Study of listvenites series along the Basal Thrust of the Semail Ophiolite : understanding of CO2-metasomatism and carbonate-forming processes of peridotites

Thierry Decrausaz

THÈSE POUR OBTENIR LE GRADE DE DOCTEUR DE L'UNIVERSITÉ DE MONTPELLIER

En Sciences de la Terre

École doctorale GAIA : Biodiversité, Agriculture, Alimentation, Environnement, Terre, Eau

Unité de recherche Géosciences Montpellier – UMR 5243

Study of listvenites series along the Basal Thrust of the Semail Ophiolite: understanding of CO_2-metasomatism and carbonate-forming processes of peridotites

Présentée par Thierry DECRAUSAZ
Le 15 décembre 2022

Sous la direction de Marguerite GODARD

Devant le jury composé de

Muriel ANDREANI, Professeure des universités, Université Claude Bernard Lyon 1	Rapporteur
Paola TARTAROTTI, Professeure des universités, Università degli Studi di Milano	Rapporteur
José Alberto PADRON-NAVARTA, Chargé de recherche, CSIC-UGR, Universidad de Granada	Examinateur
Esther SCHWARZENBACH, Professeure des universités, Université de Fribourg	Examinatrice
Manuel MUNOZ, Professeur des universités, Université de Montpellier	Président du jury
Marguerite GODARD, Directrice de recherche, CNRS, Géosciences Montpellier	Directrice de thèse

UNIVERSITÉ DE MONTPELLIER

Je dédie cette thèse à mes chers parents, Renate et Daniel

Remerciements

Bientôt quatre années se seront déroulées depuis le début de cette thèse. Pourtant je n'ai pas vu le temps passer… Et cela, je le dois en grande partie aux merveilleuses personnes que j'ai pu rencontrées.

Je tiens à exprimer toute ma gratitude envers ma directrice de thèse, Marguerite Godard, qui m'a accordé sa confiance pour mener à bien cette étude. Tu m'as toujours poussé à approfondir mes connaissances, donner mon meilleur. Merci infiniment pour tes encouragements et ta bienveillance en particulier en fin de thèse qui m'ont aidé à surmonter cette période, et pour ton humour qui m'a fait (sou)rire si souvent.

Je tiens tout particulièrement à remercier Romain Lafay et Emilien Oliot avec qui j'ai pu partager quelques journées de terrain dans les magnifiques montagnes de l'Oman. Merci à toi Romain pour avoir été un repère à mon arrivée à Montpellier et pour toutes nos parties de fléchettes. Emilien, merci d'avoir toujours su trouver un temps précieux à me consacrer pour discuter du terrain malgré un emploi du temps bien rempli.

Je souhaite également remercier Fleurice Parat et Francoise Boudier pour toutes nos discussions et l'aide que vous avez pu m'apporter durant la thèse. Un grand merci également à Manuel Menzel pour nos différentes collaborations et discussions qui m'ont toujours énormément apporté.

Je profite de ces quelques lignes pour remercier les autres membres de GM, de l'IPGP et du GET impliqués dans le projet ANR LISZT et avec qui j'ai pu intéragir lors des dernières années: Baptiste Debret, Isabelle Martinez, Giuseppe Saldi, Pascale Bénézeth, Vasileios Mavromatis, Philippe Gouze et Richard Leprovost. En particulier, je ne saurai jamais assez remercier Baptiste et Isabelle pour leur accueil chaleureux lors de mon séjour parisien et pour m'avoir formé aux différentes techniques analytiques. Le travail fut intense mais tellement apprécié à leurs côtés.

Je remercie sincèrement les membres de mon jury, Murielle Andreani, Paola Tartorotti, José Alberto Padrón-Navarta, Esther Schwarzenbach et Manuel Muñoz pour avoir accepté d'évaluer mon travail et pour leurs précieuses remarques visant à l'améliorer.

Je tiens également à remercier les membres de mon comité de suivi de thèse, à savoir Séverin Pistre, Othmar Müntener, Catherine Thoraval, Benoit Ildefonse pour leurs conseils avisés.

Je souhaite remercier le laboratoire Géosciences Montpellier et ses membres qui m'ont accueilli. Cette thèse présente une quantité de données conséquentes qui n'auraient pu être acquises sans la contribution et le savoir-faire de nombreuses personnes : Christophe Nevado, Doriane Delmas, Fabrice Barou, Olivia Mauguin, Romain Lafay, Loic Blanchard, Céline Martin, Léa Causse, Lucie Köller, Olivier Bruguier, Frédéric Fernandez, Carlos Garrido, Virginia Rojas, Moulay Sougrati, Olivier Reubi, Martin Robyr, Alexei Ulianov, et Othmar Müntener.

Cette aventure à Montpellier m'est particulièrement chère de par toutes les amitiés que j'ai pu y nouer. Un grand merci aux potos pour tous nos bons moments, rires, bières et cafés, soirées poker et fléchettes, matches de foot et sorties au stade. Du fond de mon petit cœur fondant suisse, merci à vous Romain, Clément, Jérémie, Leny, Cyprien, Enora, Carmen, Gaëtan, Juliette, Nestor, Maël, Marine, Margaux, Anda, Arthur, Fabrice, Sarah, Gaëtan K., Fadl, Manon, Aimée, Adeline, Céline, Louis, Garrance, Lionel, Alexandre, Rémi, Romain H., Timothée, Nicolas, Clara, Clément H., Coralie, Oswald, Agathe, Justine, et Lauranne.

Une pensée particulière pour Camille, Asma, François, Paul, Julie et le petit Saul, mes collocs qui m'ont apporté tant de bonheur au quotidien. Tiche, merci pour ton aide, ton soutien, ta franchise, ta patience

(il en fallait) et ta gentillesse pendant ces années. Asma, merci pour ta douceur, ton rire contagieux, ton écoute et tes plats succulents. François, merci pour tous ces wagons de rire et ta bonne humeur. Polo, une complicité instantanée avec un papa formidable. Julie, merci pour les bons moments passés et à venir.

Je tiens également à remercier Sel, Léo, Maxou et sa petite famille en Suisse pour leur soutien malgré la distance.

Pour finir je tiens à remercier mon père Daniel, ma mère Renate et mon frère Denis pour leur soutien indéfectible, leur écoute attentive depuis tant d'années, qui me sont si chers.

ABSTRACT

Mantle rocks exposed to subsurface conditions or hydrothermal fluids react in response to disequilibrium. In nature serpentinization and carbonation are the two prevalent fluid-rock reactions affecting mantle rocks. Listvenites form by the complete conversion of peridotites into Mg-carbonates-quartz rocks by interaction with reactive CO_2-bearing fluids. The geochemical and mineralogical complexity of listvenites led to the establishment of different genetic models, however the processes and conditions favouring listvenite formation are poorly documented. Our study focusses on listvenite exposures along the base of the Semail ophiolite mantle in Oman, which have been the focus of drilling Oman Drilling Project Hole BT1B.

The present PhD thesis benefited from high-resolution core sampling from Hole BT1B, further complemented by regional sampling. Aiming to better understand the processes of peridotite carbonation, our study combines a multi-scale and multi-technique approach including: fieldwork, microstructural characterization (optical and scanning electron microscopy, Raman spectroscopy, EBSD), whole rock (XRF, ICP-QMS) and mineral geochemistry (EPMA, LA-ICPMS), and isotopic studies (bulk C-Fe-Zn isotopes, C-O isotopes on carbonates).

In the Fanja region, listvenites occur as kilometre-scale tabular sheets or smaller lenses interlayering the ophiolite mantle close to or along the basal thrust of the ophiolite. On field, peridotite carbonation defined reactions fronts from serpentinized peridotites, to intensively foliated and carbonated serpentinites at the transition with listvenite. The mantle section mainly consists of (Cpx-)harzburgites to lherzolites and rare dunites. Protoliths show selective enrichments in fluid-mobile Li, Rb, Sr, Cs, Ba and Pb. This compositional signature is typical of basal peridotites in Oman. Peridotite carbonation proceeded by the infiltration of fluids rich in As, Sr, Sb, Ba and Pb, as evidenced by bulk rock and mineral trace element compositions. Spatial disparity in the occurrence of magnesite-rich and dolomite-rich listvenites suggests their formation during different metasomatic events and/or from multiple sources of fluids.

The petrological study of carbonated serpentinites and listvenites indicate that serpentinization underwent completion prior to the onset of carbonation. Carbonation progressed through distinctive stages of pervasive rock matrix replacement and veining. Incipient carbonation is texturally ascribed to pseudomorphic replacement of serpentine veins and the generation of antitaxial carbonate veins. The onset of pervasive carbonation is characterized by the formation of chemically zoned Fe-rich magnesite spheroids and aggregates in the vicinity of antitaxial Fe-rich magnesite veins. This transient stage was followed by extended matrix replacement by Mg-rich magnesite, prior to silicification of the remaining background serpentine. Variations in magnesite compositions indicate changes in fluid compositions, redox conditions and/or fluid access during carbonation.

The bulk carbon isotopes compositions of carbonated peridotites in Hole BT1B indicate a strong inorganic component in reactive fluids. This is compatible with fluids sourced from the devolatilzation of clastic sediments underlying the ophiolite triggered by burial during regional convergence. The distribution of oxygen isotope signatures of carbonates across the well suggest carbonation at low temperature (<200 °C) by infiltration of repeated fluid batches at different structural levels over time. The bulk iron and zinc isotope compositions of BT1B listvenites series are among the most variable for mantle rocks considering a single lithological suite. Fe isotopes compositions remained relatively unaffected during successive serpentinization and carbonation. In contrast, a clear correlation between $\delta^{13}C_{TC}$ and $\delta^{66}Zn$ indicate the preferential mobility and transport of Zn in reactive fluids.

RESUME

La serpentinisation et la carbonatation sont les deux réactions métasomatiques les plus fréquentes affectant les roches du manteau. Les listvénites résultent de l'interaction entre les péridotites et des fluides riches en CO_2, pour former des roches à carbonates magnésiens et quartz. Différents modèles pétrogénétiques ont été établis pour expliquer leur complexité géochimique et minéralogique. Cependant, les processus et conditions favorisant leur formation sont peu documentés. Notre étude a été menée sur des listvénites affleurant le long de la base du manteau ophiolitique de Semail en Oman, qui a fait l'objet du forage du puits BT1B dans le cadre du projet Oman Drilling Project.

Cette thèse a bénéficié d'un échantillonnage exhaustif de carottes provenant du puits, complété par un échantillonnage régional. Dans le but de mieux comprendre les processus de carbonatation des péridotites, notre étude a combiné une approche multi-échelle et multi-technique incluant : du travail de terrain, une caractérisation microstructurale des échantillons (SEM, Raman, EBSD), des analyses géochimiques en roche totale (XRF, ICP-QMS) et sur minéral (EPMA, LA-ICPMS), ainsi que des études isotopiques (isotopie du C-Fe-Zn en roche totale, isotopie du C-O sur carbonates).

Dans la région de Fanja, les listvénites forment des corps tabulaires, kilométriques, ou de lentilles plus petites intercalant le manteau ophiolitique à proximité ou le long du chevauchement basal. La carbonatation des péridotites définit des fronts réactionnels à partir de péridotites serpentinisées et fracturées, pour des serpentinites intensément foliées et carbonatées à la transition avec les listvénites. La section du manteau étudiée est principalement constituée de (Cpx-)harzburgites, de lherzolites et de rares dunites. Les protolithes montrent des enrichissements en éléments mobiles dans les fluides (Li, Rb, Sr, Cs, Ba et Pb). Ces signatures sont typiques des péridotites basales en Oman. La carbonatation des péridotites s'est effectuée par infiltration de fluides riches en As, Sr, Sb, Ba et Pb. La disparité spatiale entre des listvénites riches en magnésite et en dolomite suggère que leur formation s'est déroulée lors de différents événements métasomatiques, et/ou la présence de sources de fluides multiples.

L'étude pétrologique des péridotites carbonatées révèle une complète serpentinisation avant l'initiation de la carbonatation. Celle-ci s'est déroulée en étapes distinctes, initiée par le remplacement statique de veines de serpentine par des carbonates et par la génération de veines antitaxiales de carbonates. La carbonatation diffuse est caractérisée par la formation précoce de sphéroïdes et d'agrégats de magnésites riches en fer, à proximité de veines de magnésite antitaxiales riches en fer. Cette étape transitoire a été suivie par un remplacement plus étendu de la matrice par des magnésites riches en Mg, avant la silicification de la serpentine résiduelle. Les variations compositionnelles des magnésites témoignent d'un changement dans la composition des fluides, dans les conditions redox et/ou de l'accessibilité des fluides au cours de la carbonatation.

L'isotopie en carbone des péridotites carbonatées révèle une composante inorganique prédominante dans les fluides, cohérente la dévolatilisation de sédiments clastiques lors de leur enfouissement en contexte de convergence. La distribution le long du puits des signatures isotopiques en oxygène des carbonates suggère une carbonatation à basse température (<200 ° C) par infiltration répétée de fluides à différents niveaux structurels au fil du temps. L'isotopie du fer et du zinc des listvénites sont parmi les plus variables pour des péridotites. Alors que les compositions isotopiques du Fe sont restées inchangées au cours de la serpentinisation et de la carbonatation, une corrélation entre les compositions en $\delta^{13}C_{TC}$ et $\delta^{66}Zn$ indique la mobilité et le transport préférentiels du Zn dans les fluides réactifs.

RESUME ETENDU

Les roches du manteau exposées aux conditions de (sub-)surface et aux circulations de fluides hydrothermaux s'altèrent. Dans la nature, l'altération métasomatique des péridotites procède principalement par les réactions de serpentinisation et de carbonatation. La serpentinisation est la réaction d'hydratation déstabilisant les silicates ferromagnésiens primaires de la péridotite (olivine et pyroxènes) par interaction avec des fluides aqueux. La carbonatation est la réaction qui convertit les silicates ferromagnésiens primaires ou les produits de la serpentinisation en carbonates par interaction avec des fluides riches en CO_2, correspondant ainsi à une réaction de déshydratation si succinte à la serpentinisation.

Ces deux types de réactions opèrent dans une variété d'environnements géologiques, de l'exposition du manteau exhumé au niveau des fonds marins (e.g., Boillot et al., 1980; Cannat et al., 2010), aux ceintures orogéniques (e.g., Kelemen et Matter, 2008; Schwarzenbach et al., 2013), aux systèmes hydrothermaux profonds tels que les systèmes de failles (e.g., Klein et al., 2022) et les zones de subduction (e.g., Hyndman et Peackock, 2003; Alt et al., 2013).

L'altération des péridotites est un processus majeur impactant les cycles géochimiques globaux, participant aux transferts de matière et d'énergie entre les couches superficielles et internes de la Terre (e.g., Bekaert et al., 2021). Des études récentes ont mis en évidence le rôle de réservoirs des péridotites pour les éléments volatiles (H, C, N, S, les halogènes et gaz nobles) et les éléments mobiles dans les fluides (Li, B, As, Sr, Sb, Cs, Ba, Pb et U) (e.g., Alt et Shanks, 1998, 2003; Delacour et al., 2008; Deschamps et al., 2013; Scambelluri et al., 2016; Peters et al., 2017).

Au cours des dernières décennies, l'intérêt pour la carbonatation des roches mafiques et ultramafiques a cru en raison de la préoccupation croissante concernant le changement climatique. La carbonatation a été proposée comme une technique fiable permettant le stockage permanent du carbone et l'atténuation des émissions anthropiques de CO_2 dans l'atmosphère (Seifritz, 1990; Lackner et al., 1995; Kelemen et Matter, 2008). Les taux de carbonatation les plus élevés ont été mesurés pour les roches riches en olivine (e.g, Kelemen et al., 2011), en raison de leur proportion molaire élevée en cations métalliques divalents permettant des liaisions avec le CO_2 dissous dans les fluides (e.g., Power et al., 2013). Les massifs de péridotites sont ainsi priorisés comme cibles potentielles pour la carbonatation industrielle.

Les péridotites carbonatisées sont principalement observées: i) dans les systèmes hydrothermaux récents ou actifs au niveau des dorsales médio-océaniques (e.g., Bach et al., 2011; Schröder et al., 2015; Kendrick et al., 2020; Ternieten et al., 2021a), ou en milieu continental (e.g., Clark et Fontes, 1990; Ulrich et al., 2014; Noël et al., 2018; Ternieten et al., 2021b); ii) dans les systèmes hydrothermaux fossiles au niveau des marges passives (e.g., Schwarzenbach et al., 2013) et le long des zones de suture tectonique où ont été imbriqués des fragments de lithosphère océanique (Beinlich et al., 2012; Falk et Kelemen, 2015; Menzel et al., 2018).

Dans de nombreux complexes ophiolitiques, la carbonatation pervasive des péridotites est caractérisée par la formation de zones métasomatiques, dans la majorité des cas associées à des structures tectoniques canalisant les fluides réactifs. Sur la base d'études expérimentales et de modélisations, Johannes (1969) et Klein et Garrido (2011) ont mis en évidence le contrôle de la température et de la concentration des fluides en CO_2 dissous comme des paramètres clés contrôlant les équilibres de phase pendant la carbonatation. En particulier, l'augmentation de la concentration en CO_2 dissous dans les fluides stabilise successivement les assemblages serpentine–magnésite, talc–magnésite et enfin quartz–magnésite. Ce dernier assemblage est connu sous le nom de listvénite.

Les listvénites sont reconnues pour héberger des minéralisations concentrant des métaux précieux tels que Au, Ag, PGE (Pt, Os, Ir, Pd, Ru, Rh), As, Hg, Pb, Ni, Co, Zn, Cu (Rose, 1837; Buisson et Leblanc, 1985; Emam et Zoheir, 2013; Qiu et Zhu, 2015; Belogub et al., 2017; Gahlan et al., 2020). Plus récemment, Kelemen et Manning (2015) ont suggéré que leur formation dans le coin mantellique pouvait impacter le bilan du carbone transféré dans les zones de subduction.

Malgré un nombre croissant d'études, à ce jour, les processus naturels et les conditions conduisant à la formation de la listvénite restent peu contraints.

Objectifs et stratégie

L'objectif principal de cette thèse est d'explorer les processus pétrogénétiques impliqués dans la carbonatation des péridotites et la formation des listvénites lors de la migration de fluides riches en CO_2. Les questions scientifiques principales sont:

- **Dans quel contexte géologique/tectonique les listvénites se forment-t-elles ?**
- **Comment la carbonatation modifie-elle la minéralogie et les propriétés microstructurales des péridotites ?**
- **Comment les éléments chimiques sont-ils mobilisés et redistribués lors de la carbonatation des péridotites ?**
- **Quelle est la séquence réactionelle menant à une carbonatation complète ?**
- **Quelles peuvent être les sources des fluides réactifs ?**
- **Quelles sont les conditions (pression, température) de formation des listvénites ?**

Dans cette optique, cette thèse de doctorat s'est focalisée sur l'étude d'affleurements de listvénites situés le long de la section basale de l'ophiolite de Semail en Oman. Ces affleurements ont fait l'objet du forage du puits BT1B dans le cadre du projet Oman Drilling Project (Kelemen et al., 2020), qui a recoupé

~200 m de listvénites et de serpentinites carbonatisées, ainsi que ~100 m de métabasaltes de la semelle métamorphique sous-jacente (Fig. 1).

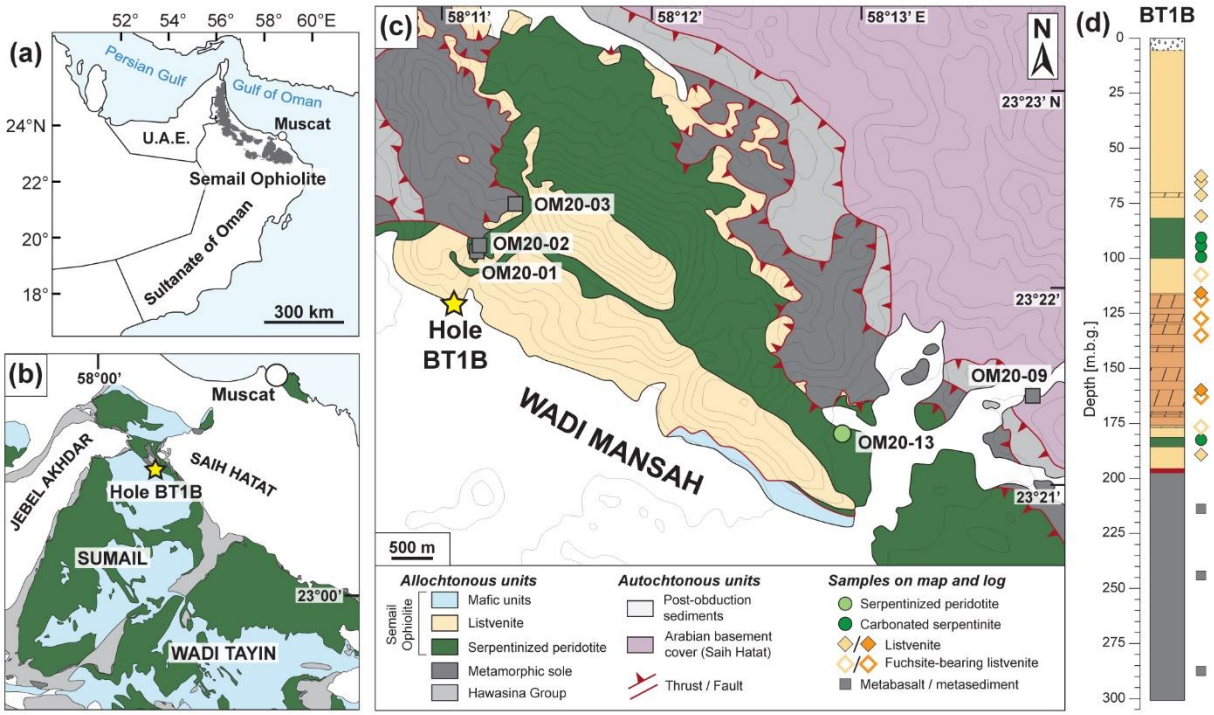

Fig. 1 (a) Position géographique de l'Ophiolite de Semail. (b) Emplacement du puits de forage BT1B dans la région de Fanja au nord du massif de Samail (modifié d'après Nicolas et al., 2000). (c) Carte géologique de la zone de Wadi Mansah (modifié d'après Villey et al., 1986; Kelemen et al., 2022), localisation du puits BT1B et des échantillons prélevés dans cette zone. (d) Colonne lithologique du puits BT1B et distribution de l'échantillonnage associé aux analyses en isotopie du fer, zinc, et carbone. Abbreviation: m.b.g.: metres below ground.

Cette thèse a bénéficié d'un échantillonnage exhaustif de carottes provenant du puits BT1B, qui a été complété par un échantillonnage régional. Dans le but de mieux comprendre les processus de carbonatation des péridotites, notre étude a combiné une approche multi-échelle et multi-technique incluant: du travail de terrain, une caractérisation minéralogique et microstructurale des échantillons (microscopie optique et électronique à balayage, spectroscopie Raman, EBSD), des analyses géochimiques en roche totale (XRF, ICP-QMS) et sur minéral (EPMA, LA-ICP-MS), ainsi que des études isotopiques (isotopie du C-Fe-Zn en roche totale, isotopie du C-O sur carbonates). Dans les paragraphes suivants sont décrits les principaux résultats produits par cette thèse.

Occurrences de listvénites dans la région de Fanja

Dans la région de Fanja, la section mantellique de l'ophiolite est amincie (<300 m), exposant des fragments démembrés et faillés de roches mantelliques juxtaposés à des gabbros, des écailles de semelle métamorphique et des sédiments para-autochtones de la marge arabique. Le manteau ophiolitique est

composé alternativement de harzburgites (à Cpx), de lherzolites et de dunites, une séquence lithologique typique des péridotites basales (« Banded Unit ») en Oman. Les listvénites se présentent sous la forme de corps tabulaires kilométriques, ou de lentilles de tailles inférieures, intercalant la section mantellique à proximité ou au contact avec le chevauchement basal de l'ophiolite avec une orientation similaire. A l'échelle de l'affleurement, la carbonatation des péridotites est caractérisée par la présence de zones réactionnelles formant une transition à partir de péridotites fracturées et modérément serpentinisées, devenant intensément foliées au contact avec les listvénites.

La séquence lithologique observée dans le puits BT1B n'est pas représentative des autres sections étudiées dans la région, où les péridotites modérément à intensément serpentinisées sont plus abondantes que les listvénites. De plus, les corps de listvénites intercalent généralement le manteau ophiolitique à proximité ou au contact des gabbros. Lorsqu'elles sont présentes au contact avec la semelle métamorphique, les listvénites forment des niveaux discontinus et peu épais. Les listvénites sont généralement bordées de serpentinites carbonatisées, foliées et pauvres en bastites évoquant des protolithes dunitiques. La localisation de la déformation lors de l'obuction de l'ophiolite ou plus tardivement dans des niveaux à faible rhéologie peut avoir favorisé la chenalisation des fluides.

Notre étude géochimique en roche totale des échantillons régionaux a mis en évidence la prédominance de la magnésite dans les listvénites affleurant dans la partie est de la zone de Fanja, tandis que les listvénites surmontant la semelle à l'ouest du site de forage sont globalement riches en dolomite. Les explications possibles sont : i) différents évènements de migrations fluides, comme suggéré par Carter et al. (2020) et Godard et al. (2021), ii) l'effet du transport des fluides, ou iii) une hétérogénéité compositionnelle à grande échelle de la source des fluides.

Deux modèles ont été proposés pour expliquer la formation des listvénites à Fanja : i) la carbonatation des péridotites au cours de l'initiation de la subduction de la marge arabique et de l'obduction de l'ophiolite au Crétacé (Kelemen et al., 2022); ii) une carbonatation du Paléocène au Miocène le long des failles d'extension post-obduction (Scharf et al., 2022). Le modèle de Scharf et al. (2022) s'appuie sur l'analyse structurale des contacts faillés entre les listvénites et la semelle métamorphique, mais aussi sur des âges U-Pb mesurés sur une listvénite (64.3 ± 6.3 Ma) et des veines de dolomites recoupant les listvénites (60.3 ± 15.4; 55.1 ± 4.7 Ma), fournissant des âges plus jeunes qu'anticipé dans le modèle de Kelemen et al. (2022). Un point critique soulevé par Kelemen et al. (2022) est que l'exhumation Paléocène–Miocène des dômes du Jebel Akhdar et du Saih Hatat peut avoir réactivé des failles plus anciennes ou en avoir créé de nouvelles.

Séquence réactionnelle

L'étude pétrologique des serpentinites carbonatisées et des listvénites révèle que la serpentinisation des roches s'est achevée avant l'initiation de la carbonatation. Cette observation est validée par : i)

l’absence de minéraux primaires dans ces deux lithologies, ainsi que par ii) la préservation locale dans les listvénites des textures « en maille » et de microstructures similaires à des bastites, typiques de la serpentinisation.

La séquence de carbonatation a été déterminée par une étude minutieuse des microstructures de remplacement de la matrice rocheuse et des différentes générations de veines, révélant ainsi des étapes de carbonatation distinctes. L’initiation de la séquence de carbonatation est caractérisée par le remplacement statique des veines de serpentine par de la magnesite et de la dolomite, notamment celles délimitant les textures en maille, et par la génération de veines antitaxiales de magnésite. La carbonatation diffuse précoce est caractérisée par la formation de sphéroïdes et d'aggrégats de magnésites chimiquement zonés et riches en fer, à proximité des veines antitaxiales de magnésite riche en fer. Cette étape transitoire a été suivie par un remplacement plus pervasif de la matrice rocheuse par des magnésites riches en Mg, avant la silicification de la serpentine résiduelle. Les variations compositionnelles des magnésites témoignent d’un changement dans la concentration des fluides en CO_2, des conditions redox, et/ou de l’accessibilité des fluides au cours de la carbonatation.

Nous documentons pour la première fois en détail les différentes réactions de carbonatation déstabilisant les oxydes de fer en magnésite riche en fer, et cohérentes avec une réaction correspondant à la conversion de la magnétite en magnésite et hématite. La modélisation thermodynamique converge vers la précipitation de magnésite riche en fer en équilibre avec la serpentine à faible XCO_2 des fluides et pour des conditions peu oxydantes. Les coeurs de sphéroïdes riches en Fe enregistrent ainsi une étape transitoire de carbonatation, suivie par la croissance majoritaire de sphéroïdes et d'agrégats riches. Même s'ils sont présents dans la majorité de nos échantillons de listvénite, la rareté des sphéroïdes au cœur riche en Fe par rapport à la magnésite riche en Mg peut être un indice d'une transition rapide d'un flux limité à un flux intensif des fluides réactifs. Cette transition peut être causée par des variations cycliques de pression fluide liée à une déformation ductile localisée et renforcée par la réaction (Menzel et al., 2022a), ou à la fracturation induite par la réaction et liée à des changements de masse volumique de la roche (par exemple Kelemen et al., 2022).

La carbonatation initie la déstabilisation des oxydes de fer, influençant ainsi la répartition du fer entre les minéraux, et induit des modifications des conditions redox. Dans les échantillons de Fanja, la carbonatation de la péridotite serpentinisée en listvénite s'accompagne d'assemblages évolutifs d'oxydes de fer et de sulfures. L'association magnétite–awaruite identifiée dans les serpentinites carbonatisées s'équilibre dans des conditions fortement réductrices lors de la serpentinisation (Klein et Bach, 2009; de Obeso et al., 2020), tandis que la conversion en sulfures riches en Fe-Cu et en hématite indique une transition vers des conditions oxydantes (Eckstrand, 1975; Frost et al., 1985).

Les sulfures sont très peu fréquents dans les échantillons de Fanja, alors qu'ils sont couramment observés dans d'autres occurrences de listvénites (e.g., Qiu et Zhu, 2018). Leur rareté ou absence peut

résulter de l'oxydation des sulfures en sulfates hautement solubles (Austrheim et al., 2021). Ces réactions peuvent participer à la mobilisation des métaux traces (en particulier Ni, Co et Cu), mais potentiellement aussi affecter la spéciation du carbone, du soufre et de l'hydrogène (e.g., Frost et al., 1985; Frost et Beard, 2007). Ces implications doivent être prises en compte pour considérer les transferts de masse à plus grande échelle, la formation de listvénites étant supposée se produire le long des sections basales des ophiolites obductées et dans les zones de subduction (Kelemen et Manning, 2015), avec un impact potentiel sur le recyclage des éléments et des métaux sensibles aux conditions redox.

Mobilité et redistribution des éléments chimiques

La mobilité et la redistribution des éléments chimiques lors de la carbonatation des péridotites a été étudiée par : i) la caractérisation des compositions en éléments majeurs et traces en roche totale et sur minéraux, ii) la caractérisation des compositions élémentaires et isotopiques du carbone, du fer et du zinc en roche totale.

Les péridotites serpentinisées de Fanja couvrent une large gamme compositionnelle reflétant l'hétérogénéité des protolithes dans la section mantellique étudiée. Elles démontrent des enrichissements en Li, Rb, Sr, Cs, Ba et Pb qui sont typiques des péridotites de la section basale de l'Ophiolite de Semail. La carbonatation des serpentinites en listvénites est accompagnée par un apport majeur de carbone inorganique et des enrichissements en As, Sr, Sb, Ba et Pb par les fluides métasomatiques. De manière générale, les éléments majeurs, les éléments de transition et les éléments lithophiles ne sont pas ou peu remobilisés. Il convient de souligner des enrichissements fréquents en Ca pour les listvénites formées au contact ou à proximité du chevauchement basal de l'ophiolite et qui pourraient indiquer une évolution compositionnelle de la source des fluides et/ou un épisode métasomatique distinct.

La variabilité compositionnelle en isotopie du fer et du zinc des échantillons de Fanja est sans précédent en comparaison aux différents types de péridotites déjà étudiées. Les concentrations et compositions isotopiques du fer des serpentinites carbonatisées et des listvénites sont comparables aux péridotites abyssales, suggérant une mobilité limitée de cet élément lors de la carbonatation. En revanche, une corrélation positive a pu être établie entre les signatures isotopiques du carbone total et les compositions isotopiques du zinc qui peut être expliquée par la complexation préférentielle du zinc « lourd » avec les ligands carbonatés dans les fluides. Des compositions isotopiques anormalement « légères » ont été mesurées sur les échantillons contenant de la fuchsite, un mica chromifère, se formant par dissolution de la chromite. Ces signatures pourraient découler de la remobilisation du fer et du zinc « lourds » dans la chromite. Toutefois, des calculs de fractionnement isotopique « ab initio » doivent être réalisés pour confirmer cette hypothése.

La quantification des compositions chimiques sur minéraux a permis de mieux appréhender la redistribution élémentaire entre les différents types de minéraux et microstructures associées. Les

compositions des carbonates en éléments lithophiles indiquent un fort contrôle des protolithes sur leur distribution. Le remplacement des serpentines de la matrice rocheuse par les magnésites est isochimique à l'exception d'enrichissements en Sb, Cs, Pb, plus modérés en Rb et Sr, et de l'appauvrissement en Li et As. Les veines précoces de magnésite présentent des compositions similaires au magnésites de la matrice, suggérant qu'elles dérivent de fluides similaires. En revanche, le remplacement de la serpentine par des dolomites s'accompagne d'un enrichissement en LREE, MREE, Sr, Sb, Ba, Pb, mais d'un appauvrissement en Li, Cs, As. La fuchsite présente les concentrations les plus élevées en Li, Rb, Sn, Sb, Cs, Ba, Th et U parmi les phases minérales.

Il convient de noter que les sphéroïdes de magnésite aux cœurs riches en fer présentent des concentrations plus élevées en Li, Sr, Sb, et Ba que les magnésites de matrice riches en Mg, mais sont appauvris en Pb et As. Les agrégats de dolomite présentent eux des teneurs plus élevées en Sr, Sb, Ba et Pb que les magnésites, mais sont appauvris en Li, Cs et As. Enfin, un enrichissement en Pb et un appauvrissement en Li, Ba et As dans les veines tardives est observé par comparaison aux carbonates de matrice. Ces résultats suggèrent une évolution dans la composition des fluides au cours de la séquence de carbonatation.

Ces interprétations doivent toutefois être considérées avec prudence. La distribution élémentaire entre les carbonates hydrothermaux et les fluides réactifs peut être contrôlée par : i) la composition des fluides (concentration en cations et ligands, espèces oxydées/réduites en solution, salinité, alcalinité, pH), ii) la composition du protolithe, ou iii) par des facteurs externes (pression et/ou température). Des études expérimentales ont démontré que l'incorporation préférentielle d'un élément entre les phases minérale et fluide est fortement dépendante des processus de sorption et de complexation (e.g., Allen et Seyfried, 2005; Migdisov et al., 2016). A ce jour, il n'existe pas d'études expérimentales ayant permis de déterminer des coefficients de partage pour la magnésite et la dolomite hydrothermale qui permettrait de modéliser les compositions initiales des fluides. La contribution de ces différents paramètres dans la redistribution élémentaire lors des réactions de carbonatation restent donc à définir.

Source des fluides réactifs et température de carbonatation

La source des fluides réactifs a été contrainte par des analyses isotopiques du carbone en roche totale et sur des microstructures de carbonates provenant de domaines homogènes sur des lamelles de roche (analyses « micro-bulk »).

Alors que les serpentinites carbonatisées ont conservé des compositions isotopiques comparables au manteau ($\delta^{13}C_{TC}$ = -6.20 à -3.96 ‰), les listvénites sont caractérisées par des compositions plus enrichies ($\delta^{13}C_{TC}$ = -3.28 á 0.8 ‰), indiquant une contribution majeure de carbone inorganique dissous par les fluides. Les compositions isotopiques "micro-bulk" des différents types de carbonates de matrice et de veines ($\delta^{13}C_{TIC}$ = -5.35 à 1.31 ‰) sont similaires aux analyses en roche totale, et cohérentes avec les signatures isotopiques en strontium des listvénites indiquant des sédiments clastiques et riches en carbonates comme source probable des fluides réactifs (de Obeso et al., 2022).

Les compositions isotopiques en oxygène des carbonates sont variables à travers le puits ($\delta^{18}O_{TIC}$ = -12.33 á -6.96 ‰), suggérant différents épisodes de migrations des fluides. Les températures de carbonatation ont été estimées en utilisant différentes compositions de fluides. Si dérivés de fluides ayant une composition semblable à l'eau de mer ($\Delta^{18}O_{min\text{-}fluid}$ = 0 ‰), les carbonates hydrothermaux se seraient formés entre 70 et 114 °C, tandis qu'entre 84 et 141 °C pour des fluides métamorphiques ($\Delta^{18}O_{min\text{-}fluid}$ = 2 ‰). En utilisant les compositions initiales des fluides les plus appauvries et enrichies ($\delta^{18}O_{fluid}$ min = -9.9 ‰ et $\delta^{18}O_{fluid}$ max = 12.2 ‰) déterminées par Beinlich et al. (2020), les températures de carbonatation minimale et maximale définissent un intervalle entre 20 °C et 313 °C.

List of contents

Chapter 1: Introduction

Mantle rocks exposed to (sub-)surface conditions and hydrothermal fluids react in response to disequilibrium. In nature peridotite metasomatism mainly proceeds by serpentinization and carbonation reactions. Serpentinization is the hydration reaction destabilizing the primary ferromagnesian silicates in peridotite (olivine and pyroxenes) by interaction with aqueous fluids. Carbonation is the reaction converting primary ferromagnesian silicates into solid carbonates by interaction with CO_2-bearing fluids, becoming a dehydration reaction if successive to serpentinization.

These two reactions proceed in a variety of geodynamic environments, from mantle exposure on the seafloor (e.g., Boillot et al., 1980; Cannat, 2010), to orogenic belts (e.g., Kelemen and Matter, 2008; Schwarzenbach et al., 2013), and deep fluid circulation zones such as fault systems (e.g., Klein et al., 2022) and subduction zones (e.g., Hyndman and Peackock, 2003; Alt et al., 2012). Altered peridotites hence play a key role in the long-term global geochemical cycling, participating to mass transfers between the atmosphere, the hydrosphere, and the Earth interior (e.g., Bekaert et al., 2021). Recent studies particularly emphasized their role as trap-and-release systems for volatile compounds (water, carbon, nitrogen, sulphur, halogens, and noble gases) and fluid mobile elements such as Li, B, As, Sr, Sb, Cs, Ba, Pb and U (Fig. 1.1, e.g., Alt and Shanks, 1998, 2003; Delacour et al., 2008; Deschamps et al., 2013; Scambelluri et al., 2016; Peters et al., 2017).

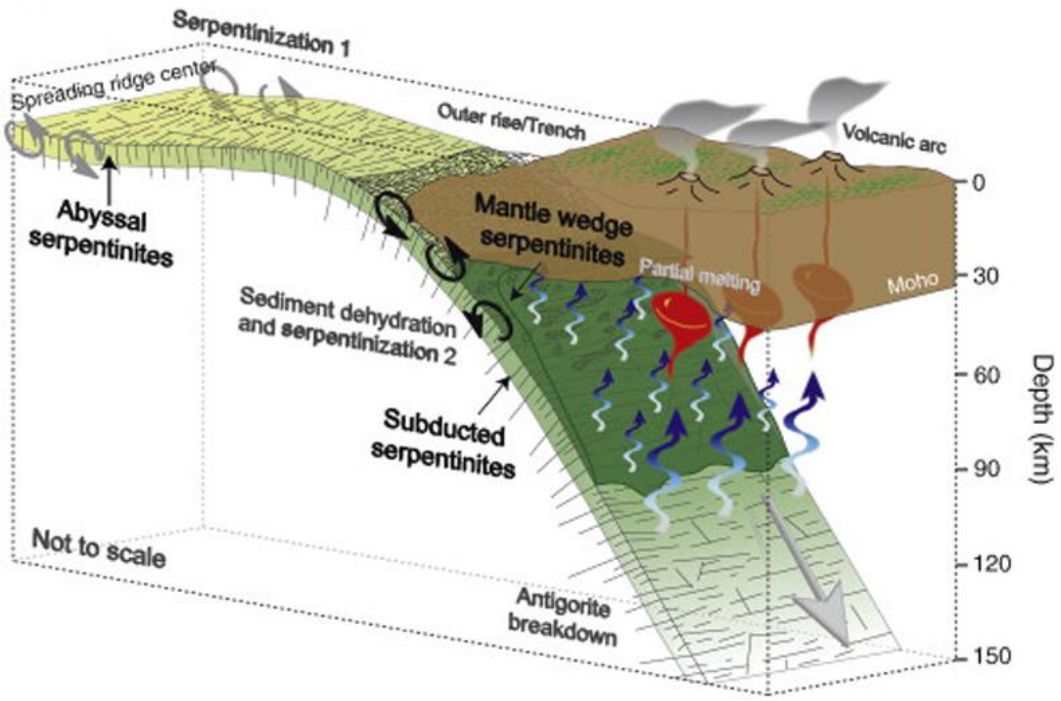

Fig. 1.1 (from Deschamps et al., 2013). Schematic sketch illustrating the geological environments from seafloor to subduction zone in which serpentinization, carbonation, and counterpart devolatilization reactions occur.

Over the past decades, interest in the carbonation of mafic and ultramafic rocks has grown in response to increasing concern on climate change. Mineral carbonation has been proposed as a reliable engineered method for permanent carbon storage and mitigation of anthropogenic CO_2 emissions in the atmosphere (Seifritz, 1990; Lackner et al., 1995; Kelemen and Matter, 2008). Most efficient mineral carbonation has been observed for olivine-rich rocks (e.g., Kelemen et al., 2011), due to their high molar proportion in divalent metallic cations to bind with dissolved CO_2 in fluids during reaction (e.g., Power et al., 2013). Peridotites are hence targeted as potential reservoirs for in-situ and ex-situ mineral carbonation.

At present day, peridotite-hosted carbonates are mostly observed: i) in recent to active hydrothermal systems at mid-ocean ridges (e.g., Bach et al., 2011; Schröder et al., 2015; Kendrick et al., 2021; Ternieten et al., 2021a), or in continental settings (e.g., Clark and Fontes, 1990; Ulrich et al., 2014; Noël et al., 2018; Ternieten et al., 2021b); ii) in fossil hydrothermal sytems at hyper-extended margins (e.g., Schwarzenbach et al., 2013), and along tectonic suture zones within dismembered oceanic lithosphere (e.g., Beinlich et al., 2012; Falk and Kelemen, 2015; Menzel et al., 2018).

In many ophiolite complexes, peridotite carbonation was pervasive and resulted in the formation of distinct metasomatic zones (e.g., Hansen, 2005; Beinlich et al., 2012; Bjerga, et al., 2015; Menzel et al., 2018). Based on experimental and modelling studies, Johannes (1969) and Klein and Garrido (2011) evidenced the control of temperature and fluid concentration in dissoved CO_2 as key parametres controlling phase equilibria during carbonation. In particular, increasing concentration of dissolved CO_2 in fluids succinctly stabilizes serpentine–magnesite, talc–magnesite and finally quartz–magnesite assemblages. This last phase assemblage is known as listvenite.

Listvenites have first attracted attention for hosting mineralizations concentrating economically-valuable metals, such as Au, Ag, PGE, As and Hg (Rose, 1837; Buisson and Leblanc, 1987; Emam and Zoheir, 2013; Qiu and Zhu, 2015; Belogub et al., 2017; Gahlan et al., 2020). More recently, several authors suggested that their formation in the mantle wedge could influence the budget of carbon in subduction zones (Kelemen and Manning, 2015; Menzel et al., 2018; Boskabadi et al., 2020). Despite an increasing number of studies, to date, natural processes and conditions leading to complete peridotite carbonation to form listvenite are still not well constrained.

Aims and strategy

The main aim addressed by this thesis is exploring the petrogenetic processes involved in peridotite carbonation and listvenite formation during reactive CO_2-fluxing. Scientific questions arising from this topic are:

- ***In which geological context do listvenite form?***
- ***How do carbonation reactions modify the mineralogy and microstructural properties of peridotite?***

- ***How are chemical elements mobilized during peridotite carbonation?***
- ***How do reaction pathways influence reaction progress?***
- ***What are the sources of reactive fluids altering mantle rocks?***
- ***What are the conditions (pressure, temperature) of listvenite formation?***

In that perspective, this PhD thesis focussed on the study of the most extended outcrops of listvenites in the world, located along the base of the Semail Ophiolite in Oman. These outcrops have been the focus of drilling Hole BT1B in the course of the Oman Drilling Project (Kelemen et al., 2020), which sampled ~ 200 m of listvenites and carbonated serpentinites, atop ~ 100 m of metabasalts from the metamorphic sole of the ophiolite.

This study benefited from high-resolution core sampling from Hole BT1B (50 samples of metasomatized peridotites), further complemented by regional sampling (48 samples). Emphasis was set to the characterization of the rock petro-structural, mineralogical, and geochemical properties. Our study combines a multi-scale and multi-technique approach including: fieldwork, microstructural characterization (optical and scanning electron microscopy, Raman spectroscopy, EBSD), whole rock (XRF, ICP-QMS) and mineral geochemistry (EPMA, LA-ICPMS), and isotopic studies (bulk C-Fe-Zn isotopes, C-O isotopes on carbonates).

Structure of the manuscript

This thesis is presented in manuscript format constituted by seven chapters. Subchapter 4.3 entitled *"Pervasive carbonation of peridotite to listvenite (Semail Ophiolite, Sultanate of Oman): clues from iron partitioning and chemical zoning"* has been accepted for publication in the European Journal of Mineralogy.

The present chapter provided a general background and motivation for this research, defining the aims of the thesis and structure of the manuscript.

Chapter 2 settles out the current knowledge on serpentinization and carbonation of peridotites. The preliminary results of a global review on listvenite occurrences are also presented. A brief summary of recent studies framing the geological background relevant to this study is provided at the end of the chapter.

Chapter 3 describes the different analytical techniques used for acquiring the dataset necessary for the production of this study. Specific protocols of sample preparation and analytical conditions are detailed.

Chapter 4 presents: i) field observations giving insights on the geological context in which listvenites formed in Oman; ii) the results of a petrographic study on core and regional samples to determine the reactional sequence and rock microstructural evolution during peridotite metasomatism. Subchapter 4.3 corresponds to a petrological study on the carbonation sequence.

Chapter 5 is composed of two subchapters presenting the results of complementary studies characterizing the bulk iron oxidation state and C-Fe-Zn isotopes compositions to constrain elemental mobility during peridotite carbonation and the compositions of reactive fluids.

Chapter 6 first presents a C-O isotopes study on carbonates that provides insights on the source of fluids and temperature of carbonation. The second subchapter presents bulk rock geochemical data of regional samples, which are compared to borehole samples to define the contribution of protoliths and reactive fluids in elemental distribution during carbonation. Elemental distribution between the different mineral phases and microstructures is also investigated in this section.

Chapter 7 depicts the main conclusions of this thesis and possible improvements by future works.

The bibliography and appendix of the different chapters are provided at the end of the manuscript.

Chapter 2: Listvenites: What, where, why?

Foreword

In nature listvenites are associated with various rock assemblages resulting from the serpentinization and carbonation of peridotites. Yet the proposed reaction pathways for listvenite formation include: i) serpentinization of peridotite followed by carbonation; or ii) carbonation after primary mantle minerals. Experiments and modelling on peridotite carbonation also stressed out the role of fluid compositions in reaction progress. The first section of this chapter settles out current knowledge on serpentinization and carbonation reactions, describing the mechanisms, thermodynamic and physico-geochemical parameters potentially favouring or limiting these reactions in natural systems.

The interest in listvenites originally stemmed from their genetic association with ore-grade mineralizations in economically-valuable metals, and was renewed recently for being considered as natural analogues to industrial carbon sequestration in ultramafic basement. Yet studies on listvenites have highlighted highly variable ore-grades, but also their structural, mineralogical, petrological complexity. Since the first review of Halls and Zhao (1995) clarifying the lithological definition of listvenite, no study attempted to provide a general overview of global listvenite distribution, geochemistry, and related genetic models. In section 2.3, we present the preliminary results of a global literature review, mostly based on studies published since 1985.

Finally, the last section of this chapter presents the geological context of the Oman Ophiolite and of the studied area. The proposed hypotheses for listvenite formation are detailed here. A brief summary of recent studies framing the geological background relevant to this study is provided at the end of the chapter.

2.1 Generalities on peridotite serpentinization and carbonation

The mantle is the most massive and voluminous reservoir on Earth (ca. 82 % and 65% of the Earth volume and mass, respectively; Helffrich and Wood, 2001), being mostly composed of refractory peridotites and subordinate pyroxenites in its uppermost section (e.g., McDonough and Rudnick, 1998). Main constituting minerals are ferromagnesian silicates, namely olivine ($(Mg,Fe)_2SiO_4$), orthopyroxene ($(Mg,Fe)_2SiO_6$) and clinopyroxene ($Ca(Mg,Fe)Si_2O_6$), along with secondary Al-rich phases (spinel, plagioclase, garnet) whose stabilities are pressure and temperature dependent.

Ferromagnesian silicates in mantle rocks react as reaching disequilibrium when exposed to (sub-)surface conditions and hydrothermal fluids (e.g., Kelemen et al., 2011). Places on Earth meeting these criteria are numerous, including mantle exposure at mid-ocean ridges and along hyper-extended passive margins (e.g., Boillot et al., 1980; Cannat, 2010), in orogenic belts (e.g., Kelemen and Matter, 2008), but also deep fluid circulation zones such as fault systems (e.g., Klein et al., 2022) or subduction zones

(e.g., Hyndman and Peackock, 2003; Alt et al., 2013). Two main fluid-rock reactions have been observed in these environments: serpentinization and carbonation.

Serpentinization

Serpentinization is the exothermic hydration reaction converting primary ferromagnesian silicates into serpentine, brucite, magnetite and releasing hydrogen, following the general reactions (e.g., Evans et al., 2011; Pens et al., 2016):

$$\text{(Mg,Fe) Olivine} + H_2O\ (aq) = \text{(Mg,Fe) Serpentine} + \text{(Mg,Fe) Brucite} + \text{Magnetite} + H_2\ (aq) \quad (R1)$$

and

$$6\ \text{Orthopyroxene} + 3\ H_2O\ (aq) = \text{Serpentine} + \text{Talc} \quad (R2)$$

Mass balance for equation R1 were investigated by Marcaillou et al. (2011). Magnetite precipitates by water reduction and hydrogen production (redox buffer), hence catalysing the conversion of dissolved CO_2 in fluids into reduced carbon species (e.g., methane, amorphous carbonaceous phases) by Fischer-Tropsch synthesis (e.g., Charlou et al., 2002; Kelley et al., 2005; McCollom et al., 2010). Magnetite formation is limited in case of high silica activity of fluids (Frost and Beard, 2007), occurring at temperature higher than 200°C. Fe-rich serpentine and Fe-rich brucite form at temperature lower than 200°C (Klein et al., 2014). Serpentinization of peridotites is typified by the formation of mesh and hourglass textures, with the hierarchical fracturing of olivine (core and rim pattern) and the static replacement of pyroxene into bastite (e.g., Wicks and Whittaker, 1977; Plümper et al., 2012; Rouméjon and Cannat, 2014).

The serpentine group is composed of three main polymorphs, namely lizardite ($Mg_3Si_2O_5(OH)_4$), chrysotile ($Mg_3Si_2O_5(OH)_4$), and antigorite ($Mg_{48}Si_{34}O_{85}(OH)_{62}$), characterized by distinctive crystallography and P-T stability field (e.g., Johannes, 1969; Evans et al., 1976; Chernovsky et al., 1988; Caruso and Chernovsky, 1979; O'Hanley and Wicks, 1995; Evans, 2004). Lizardite typically forms after olivine and pyroxenes at low temperature (<400 °C but extending to 400–600 °C if Al-rich, Andreani et al., 2007) and chrysotile (50–350°C) in veins or domains presenting a high water/rock ratio (Normand et al., 2002). Antigorite growth is generally ascribed to higher pressure and temperature range (300-650 °C; Schwartz et al., 2013).

Serpentinization modifies drastically the physical properties of the mantle protolith. Changes in rheological properties favour deformation partitioning and tectonic decoupling at the lithosphere scale (Escartin et al., 1997; Reynard, 2013). Volume increase due to reaction is estimated between 36–52 % (Klein and Le Roux, 2020) and 59–74% (Malvoisin et al., 2020). Except for water incorporation and minor mass transfers of Si, Mg and fluid mobile elements, serpentinization proceeds nearly isochemically (Mével et al., 2003; Andreani et al., 2007; Malvoisin et al., 2015, 2020).

Carbonation

Carbonation is the reaction converting ferromagnesian silicates into carbonate minerals during the fluxing of CO_2-bearing fluids (Klein and Garrido, 2011):

$$\text{Olivine} + 2\ CO_2\ (aq) = \text{Quartz} + 2\ \text{Carbonate} \quad (R3)$$
$$\text{Pyroxene} + CO_2\ (aq) = \text{Quartz} + \text{Carbonate} \quad (R4)$$

with CO_2 chemically binding with divalent cations (e.g., Mg^{2+}, Fe^{2+}, Ca^{2+}, …) in solution to grow carbonate (e.g., Lackner, 1995). When successive to serpentinization, carbonation is also a dehydration reaction:

$$\text{Serpentine} + 3\ CO_2\ (aq) = 2\ \text{Quartz} + 3\ \text{Carbonate} + H_2O\ (aq) \quad (R5)$$
$$\text{Brucite} + CO_2\ (aq) = \text{Carbonate} + H_2O\ (aq) \quad (R6)$$
$$\text{Talc} + 3\ CO_2\ (aq) = 4\ \text{Quartz} + 3\ \text{Carbonate} + H_2O\ (aq) \quad (R7)$$

Our knowledge on phase equilibria during peridotite carbonation and factors controlling the reaction progress benefited from numerous experimental studies (e.g., Johannes, 1967, 1969; Gerdemann et al., 2003; O'Connor et al., 2004; Hänchen et al., 2006; Andreani et al., 2009; Daval et al., 2013; Saldi et al., 2013; Peuble et al., 2015; Osselin et al., 2022).

Johannes et al. (1969) pointed out the role of dissolved CO_2 concentration in reactive fluids as controlling phase equilibria, with stable serpentine–brucite at low CO_2 (aq) concentration, replaced succinctly by serpentine–magnesite, talc–magnesite and finally quartz–magnesite with increasing concentration. This last phase assemblage is known in literature as listvenite. In nature, peridotite carbonation frequently resulted in the formation of distinct metasomatic zones, mimicking this reactional sequence (e.g., Hansen, 2005; Beinlich et al., 2012, Bjerga, et al., 2015; Menzel et al., 2018). In the following, we refer to the different mineral assemblages with the nomenclature provided in Table 2.1:

Lithology	Ol/En	Srp	Tlc	Qz	Carb	Fu
Serpentinized peridotite	(M)	M	(t)		(t)	
Srp-Tlc rock	(t)	M	M	(t)	m	
Carbonated serpentinite		M	(t)	(t)	M	
Soapstone		(t)	M	(m) or (t)	M	
Listvenite		(t)	(t)	M	M	
Fu-listvenite		(t)	(t)	M	M	m or t
Birbirite				M	t or m	(t)

Table 2.1 Main phase assemblages resulting from serpentinization and carbonation of peridotites in nature. Mineral abbreviations: Carb = carbonates; En = enstatite; Fu = fuchsite; Ol = olivine; Qz = quartz; Srp = serpentine; Tlc = talc. Mineral abundance: M = major; m = minor; t = trace.

Peridotite carbonation is also accompanied by changes of the rock physical properties: in open systems, the reaction induces an increase in the solid volume, despite elemental (Si, Mg and Ca) remobilization by fluids (Andreani et al., 2009).

Factors inhibiting / promoting serpentinization and carbonation

Factors controlling reaction progress in nature are: pressure, temperature, rock composition, fluid composition (nature and concentration of dissolved species), rock porosity and permeability, chemical properties of fluids (pH, alkalinity, salinity, activities of dissolved ions and molecules), and redox. These factors are key in controlling dissolution rates of minerals and fluid access to reactive surfaces.

Serpentinization experiments demonstrated a faster kinetic of dissolution for olivine compared to pyroxene at temperature below 250 °C, but slower above 250-300 °C (e.g., Martin and Fyfe, 1970; Janecky and Seyfried, 1986; Allen and Seyfried, 2003). Martin and Fyfe (1970) evidenced that serpentinization rates depend on temperature (highest rates between 250–300 °C), grain size (the lower the highest rates), and water/rock ratio (the higher the highest rates). Wegner and Ernst (1983) also measured higher serpentinization rates at high pressure. High concentration of Al-complexes in fluids has been identified as a catalyst for olivine dissolution (Andreani et al., 2013, Pens et al., 2016) but causes sluggish dissolution of orthopyroxene (Pens et al., 2016). More recently, Frost and Beard (2007) and Lemadrid et al. (2021) pointed out the correlation between high reaction rates and high water activity of fluid.

Optimal carbonation of olivine and heat-treated serpentine was experimentally constrained to the 155–185°C range (Gerdemann, 2003). In their paper, Klein and Garrido (2011) demonstrated that: i) mineral carbonation is thermodynamically promoted at low to moderate temperatures due to higher gradients in the activities of dissolved SiO_2 and CO_2 in fluids (noted $aSiO_2$ and aCO_2), ii) activity gradients are temperature-dependent, hence requiring higher aCO_2 to stabilize the quartz-magnesite assemblage at high temperature. The efficiency of carbonate precipitation is intricately related to saturation of divalent cations, HCO_3^- and CO_3^{2-} in fluids, with rates and kinetics of precipitation different for each divalent cation (Pokrovsky and Schott, 2002; Schott et al., 2009). Olivine presents the fastest dissolution rates in saline aqueous solutions with high bicarbonate concentrations (O'Connor et al., 2004; Chizmeshya et al., 2007). In turn, serpentine carbonation in similar conditions is estimated to be ~10 times slower (O'Connor et a., 2004; Gerdemann et al., 2007). If contemporaneous, carbonation is promoted over serpentinization for higher pCO_2 of fluids (Andreani et al., 2009; Peuble et al., 2015).

Both serpentinization and carbonation cause solid volume increase compared to peridotite protolith. One resulting drawback is pore clogging in case of isochemical reaction, thus limiting reaction progress. Pore clogging during serpentine carbonation is smaller than for olivine (Cipolli et al., 2004). On the other hand, solid volume change increases stresses potentially leading to rock fracturing ("reaction-

induced fracturing") hence enhancing porosity and fluid transport (e.g., Jamtveit et al., 2008; Rudge et al., 2010; Ulven et al., 2014; Lambart et al., 2018).

2.2 Listvenite: origin and related mineral assemblages

The word "listvenite", initially translated "Listwänite" from the Russian language, was first introduced by the German mineralogist Gustav Rose (1837, 1842) in his descriptions of the Uralian gold deposits from the type locality Beresovsk (Listvenya Gora). Rose (1837) used this term to designate altered rocks enclosing gold lodes, and characterized by an assemblage of quartz, carbonates (magnesite, ankerite), "greenish talc" later identified as fuchsite (or mariposite, chromian muscovite), with disseminated pyrite, and accessory chromite and Fe-oxides.

The term listvenite (or listwaenite, listwanite, listvanite in the literature) has been broadly used to describe a large variety of carbonatized mafic and ultramafic rocks discriminated by their assemblage of phyllosilicates, and not strictly respecting the original rock definition. Kashkai and Allakhverdiev (1965) distinguished listvenites depending on the nature of their protolith: ortholistvenites form by metasomatism of ultramafic and mafic rocks, paralistvenites after sedimentary rocks, and epilistvenites after metamorphic rocks. Moreover, Ploshko (1963) classified listvenites depending on their potassium content: autometamorphic listvenites are potassium-free and do not present field relationships with igneous intrusions or extrusions, while allometamorphic listvenites are produced by interaction with potassium-rich, igneous-derived fluids. More recently, Spiridonov (1991) proposed a classification for metasomatites occuring along with listvenites based on the type of phyllosilicates formed during alteration (phyllic or argillic facies) and the nature of protoliths. Accounting for an ultramafic protolith, listvenites are distinguished from zodites by the growth of Cr-micas (fuchsite, Cr-phengite) instead of Cr-clay minerals. The counterparts for mafic to felsic protoliths are beresites (quartz-carbonate-sericte assemblage) and argilizites. Among years the use of a diverse nomenclature and classifications led to misconfusion on rock assemblages, sometimes controversial genetic models, and difficulties in apprehending literature data. The first and only literature review on listvenites by Halls and Zhao (1995) highlighted this "historical" problem and listed the rock assemblages assigned as listvenites or cogenetic (Table 2.2). Their study paved consensus on two important aspects: i) listvenites result from interaction between ultramafic rocks and reactive CO_2-bearing fluids; and ii) occur in a majority of cases at terrane boundaries, near or within fault or shear zones. Halls and Zhao further recommend sticking to the original definition when willing to refer to listvenite s.s., implying alkali metasomatism (addition of potassium to the ultramafic system). Such a restriction is problematic as alkali compositions may reflect the contribution of reactive fluids or protolith inheritance.

Listvenite terminology and mineral components	Occurence and protoliths	Location	References
Ankerite, magnesite, ferroan dolomite, quartz, talc (fuchsite), pyrite	Serpentinite	Berkutskaya Gora Berezovsk ore field, Urals	Rose (1837, 1842), Murchison et al. (1845)
Carbonates, quartz, muscovite or fuchsite, pyrite	Altered serpentinite	Urals	Krotov (1915)
Quartz carbonate rocks	Skarn in contact between ultramafics and serpentinite	Urals	Lodochikov (1936)
Ferroan dolomite, quartz, muscovite, pyrite	Altered ultramafics and mafic rocks, diabase, porphyries, tuffs, greenstones and sedimentary carbonates	Berkutskaya Gora Berezovsk ore field, Urals	Borodayevskiy and Borodayevskiy (1947)
Talc-carbonate rocks, quartz-breunnerite and quartz-ferroan dolomite rocks			Korzhinskii (1953)
Carbonates, quartz, mica (muscovite, sericite and fuchsite); talc, serpentine, magnetite, hematite, sulphides (pyrite, Co-pyrite, Ni-Fe sulphides, chalcopyrite)	Serpentinite, gabbros, diabase, porphyries and other mafic rocks (with Ca)	Kazakhstan and Urals	Bok (1956)
Autometamorphic listvenites K-free and allometamorphic listvenites with K mainly quartz-carbonate rocks	At contact between ultramafics and younger granitic rocks		
Typical silica-carbonate rocks, chlorite-quartz-carbonate rocks, iron-carbonate rocks, silicified rocks, serpentine-carbonate rocks, carbonate rocks, talc-carbonate rocks	Serpentinization of ultramafic and mafic rocks	Various areas of CIS, particularly Lesser Causasus	Kashkai and Allakhverdiev (1965, 1971)
Quartz-magnesite rocks			Shcherban 1967; Shcherban and Borovikova (1969)
Talc-carbonate rocks, talc rocks, carbonate rocks, quartz-talc carbonate rocks, quartz-carbonate, rocks, potassic listvenites (muscovite/phlogopite)	Ultramafics	Northern part of the Kuznetsk Alatau	Goncharenko (1970)
Quartz-carbonate rocks (breunnerite, dolomite magnesite, calcite, serpentine, chlorite, talc, Cr-spinel, fuchsite and magnetite	Serpentinized ultramafic rocks	Armenia	Abovian (1978)
Fuchsite (muscovite)-quartz-carbonate rocks, chlorite-fuchsite-quartz-carbonate rocks, (fuchsite)-quartz-carbonate rocks	Tholeiitic basalts, peridotite komatiites, volcanogenic sedimentary stratum	Zolotye Vorota	Kuleshevich (1984)
Antigorite-talc-carbonate rocks, talc-carbonate rocks, (chlorite)-quartz-carbonate rocks, fuchsite-quartz-carbonate rocks, fuchsite-quartz rocks	Ultramafic rocks	Western Carpathians, Slovakia	Ivan (1985)
Carbonatized ultramafic rocks: Mg-Fe-Ca carbonates with accessory quartz, talc, lizardite-serpentine, chlorite, fuchsite, hematite, magnetite, pyrite and Cr-spinel	Ophiolite complexes, serpentinites	Liguria, Morocco, Mali, Saudi Arabia	Buisson and Leblanc (1985a, 1985b, 1987)
Silica-, silica and carbonate carbonate-rich rocks	Serpentinites	Araç Massif, Kastamonu, Turkey	Aydal (1989)
Carbonatized ultramafic rocks	Ophiolites	British Columbia, Canada	Nixon (!990)
Carbonatization of serpentinized ultramafic rocks (iron-magnesium carbonates and chromium mica)	Ophiolitic ultramafic rocks (serpentinite)	British Columbia, Canada	Ash and Arksey (1990a, 1990b)
Carbonate-quartz-mariposite, subordinate olivine, serpentine, magnetite, pyroxene, biotite, sericite, pyrite and chlorite	Alpine-type ultramafic precursor	British Columbia, Canada	Madu et al. (1990)
Intermediate-low temperature hydrothermal metasomatites composed of quartz, carbonates, potassic micas (Cr-muscovite, Cr-phengite), pyrite, gersdorffite, and relict Cr-spinels	Ultramafic rocks		Spiridonov (1991)
Beresite-listvenite association with aluminosilicate minerals: Quartz-carbonate rock	Serpentinite	Quebec, Canada	Auclair et al. (1993)

Table 2.2 Terminology and mineralogy of 'listvenite' from historical studies (from Halls and Zhao, 1995).

2.3 Global distribution of listvenites, genetic models and geochemical features

This section presents the preliminary results of a global review on listvenites which is mostly based on work published since the first review of Halls and Zhao (1995). This approach was motivated by: i) difficult access and, sometimes, the absence of translation for studies published prior to the eighties; ii) an increasing number of geochemical studies published since the nineties. We did not consider studies targeting listvenites for mining prospection by multispectral ASTER imaging generally lacking field and petrological data.

As a general comment, a majority of the reviewed studies describe or discuss: i) the tectonic setting in which listvenites form, ii) the reactional sequence, iii) the geochemical evolution from peridotite protolith to listvenite, iv) the likely source of reactive fluids, v) the conditions relevant of carbonation and ore formation. In contrary, the compositions of predominant rock-forming serpentine, talc and carbonate remain largely overlooked. Mechanisms allowing fluid infiltration and carbonation progress are also poorly constrained.

Listvenite distribution and geodynamic setting

Listvenite occurrences are distributed in orogenic belts resulting from the closure of oceanic domains, but were not reported from seafloor exposures (Fig. 2.1), emphasizing the need of elevated concentration of dissolved CO_2 in fluids to stabilize this rock assemblage. Listvenites have in common to form in large-scale fault and shear zones, mostly at terrane boundaries, that acted as conduits for fluid fluxes. Listvenites frequently occur as: i) decametric irregular lenses to kilometric sheets along major shear zones (e.g., Beinlich et al., 2012; Menzel et al., 2018); ii) along normal faults (e.g., Belogub et al., 2017; Qiu and Zhu, 2018;), iii) on the margins of olistoliths in tectonic mélange (e.g., Tsikouras et al., 2006; Sofiya et al., 2017).

Three types of source for reactive fluids were proposed: i) the development of hydrothermal cells after igneous activity ("magmatic" type in Table 2.2 and Fig. 2.1), such as granite emplacement in the crust; ii) fluid migration after devolatilization reactions at depth ("slab" type); iii) alteration by meteoric fluids ("meteoric" type). Most listvenite occurrences presenting ore-grade enrichments in economically-valuable metals are ascribed to the magmatic type.

Bulk geochemistry of listvenites

The geochemistry of listvenites was compiled from the studies listed in Table 2.3. The major element chemistry of listvenites were plotted in SiO_2-MgO-CaO ternary diagrams (Fig. 2.2) to illustrate the compositional variability of mineral assemblages and elemental addition/retrieval by fluids.

Metasomatized peridotites define two main trends controlled by the mineralogy, with one trend between quartz and magnesite, and the second one between quartz and dolomite. Compositions mostly cluster close to that of precursor serpentine (SiO_2:MgO = ca. 0.5). CaO contents higher than 10 wt% initiate a trend between quartz and dolomite, implying Ca addition and/or Si retrieval by fluids. In general, listvenite formation is nearly isochemical relative to peridotite protolith for most major elements (e.g., Hansen et al., 2005; Falk and Kelemen, 2015; Menzel et al., 2018; Gahlan et al., 2020). Variability mainly concern enrichment in alkali elements such as Na and K (e.g. Beinlich et al., 2012; Azer, 2013; Gahlan 2018).

Comparing the trace element compositions of serpentinized peridotites and (fuchsite-bearing) listvenites (Fig. 2.3) revealed: i) frequent enrichments in fluid mobile elements (Rb, Sr, Sb, Ba, Cs, Pb); ii) minor to absent mobility of moderately incompatible lithophile elements, except for Y and Hf. Enrichment in economically-valuable Co-Cu-Zn-Au-Ag-As-Sb have been interpreted as the result of sulphide and oxide leaching and elemental mobilization during metasomatism of serpentinized peridotites, prior to re-deposition during listvenite formation (e.g., Leblanc and Buisson, 1987; Leblanc and Fischer, 1990; Auclair et al., 1993).

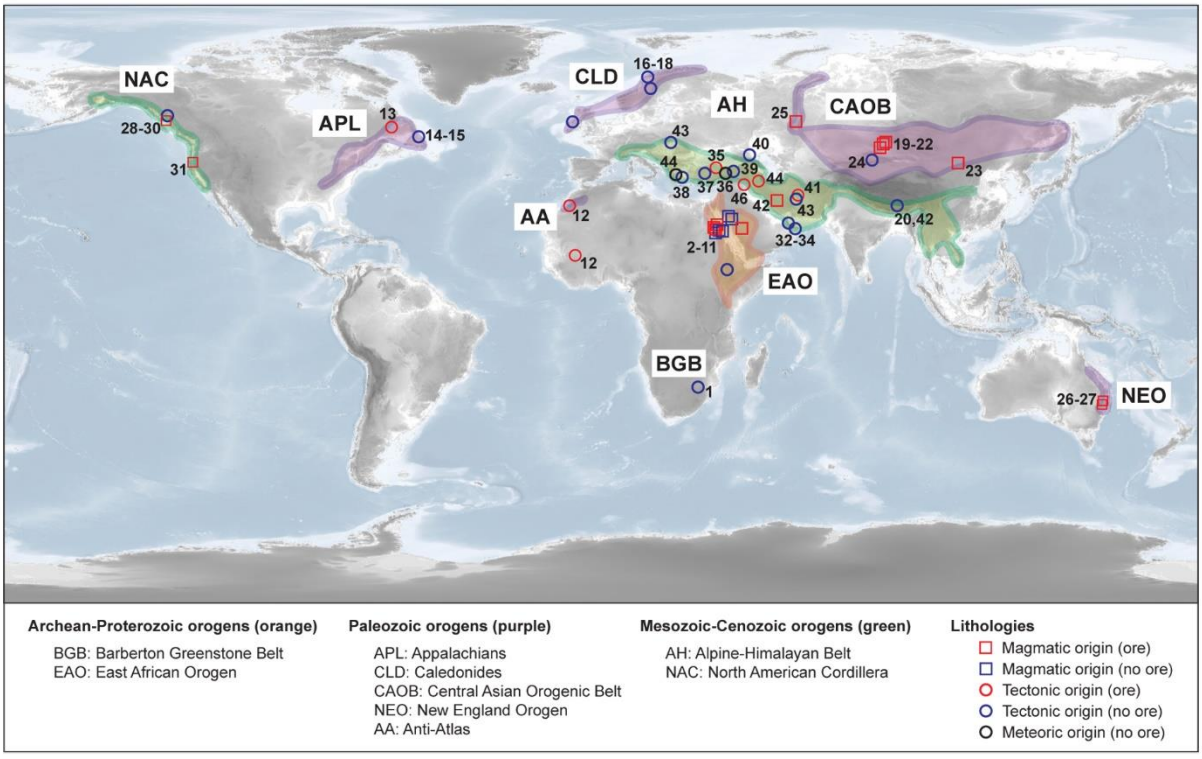

Fig. 2.1 Global map of listvenite occurences. Main orogenic belts are represented with a different color scheme depending on their period of formation. Occurences are also presented by different symbols based on the origin of metasomatic fluids and colours for the presence or absence of ore-grade enrichments in precious metals. List of references: 1 – Grosch et al. (2012); 2-11 – Azer (2013), Gahlan et al. (2018, 2020; 2022), Hamdy et al. (2022), Helmy et al. (2018), Moussa et al. (2021); Sofiya et al. (2017); 12 – Buisson and Leblanc (1987); 13-15 – Auclair et al. (1993), Escayola et al. (2009), Menzel et al. (2018); 16-18 – Austrheim et al. (2021), Beinlich et al. (2012), Halls and Zhao (1995); 19-22 – Buckman (2000), Robinson

<< et al. (2005), Qiu and Zhu (2015, 2018); 23 – Jiang and Zhu (2017); 24 – Peng et al., (2020);25 – Belogub et al. (2017); 26-27 – Ashley (1997), Buckman (2000); 28-30 – Ash and Arksey (1990), Hansen et al., (2005), Madu et al. (1990); 31 – Böhlke (1989); 32-34 – Godard et al. (2021), Falk and Kelemen (2015), Nasir et al. (2007); 35 – Aydal et al. (1990); 36 – Uçurum (2000); 37 – Akbulut et al. (2006); 38 – Tsikouras et al (2006); 39 – Çolocoĝlu (2009); 40 Aftabi and Zarrinkoub (2013); 41 – Ploshko (1963); 42 – Zhang et al. (2015); 43 – Ferenc et al. (2016); 44 –Hinsken et al. (2017); 45 – Ahankoub and Mackizadeh (2019); 46 – Pirouei et al. (2020); Üner (2020).

Orogen	Age	Country	References	Source	FO structure	LT/HT	T [°C]	Ore	Intrusion
East African Orogen	Neoproterozoic	Egypt	Azer (2013)	Tectonic	Shear zone			YES	YES
East African Orogen	Neoproterozoic	Egypt	Gahlan et al. (2018)	Tectonic	Shear zone	LT	233-300	YES	YES
East African Orogen	Cambrian	Ethiopia	Sofiya et al. (2017)	Tectonic	Shear zone				
East African Orogen	Neoproterozoic-Cambrian	Egypt	Helmy et al. (2018)	Magmatic	Shear zone			YES	YES
East African Orogen	Neoproterozoic	Saudi Arabia	Gahlan et al. (2020)	Tectonic	Shear zone	LT	200-260	YES	YES
East African Orogen	Neoproterozoic	Egypt	Moussa et al. (2021)	Magmatic?	Shear zone			YES	YES
East African Orogen	Neoproterozoic	Egypt	Hamdy et al. (2022)	Magmatic	Shear zone			YES	
East African Orogen	Neoproterozoic	Egypt	Hamdy et al. (2022)	Tectonic	Shear zone			YES	
East African Orogen	Neoproterozoic	Saudi Arabia	Gahlan et al. (2022)	Tectonic	Shear zone			YES	YES
East African Orogen	Neoproterozoic	Saudi Arabia	Gahlan et al. (2022)	Magmatic?	Shear zone			YES	YES
Appalachians	Paleozoic	Canada	Escayola et al. (2009)	Tectonic	Shear zone	LT	118-246		
Appalachians	Paleozoic	Canada	Menzel et al. (2018)	Tectonic	Shear zone	HT	ca. 300		
Caledonides	Paleozoic	Norway	Beinlich et al. (2012)	Tectonic	Shear zone	LT	250-300		
Caledonides	Paleozoic	Norway	Tominaga et al. (2017)	Tectonic	Shear zone	LT	250-300		
Caledonides	Paleozoic	Norway	Austrheim et al. (2021)			LT	<300		
Central Asian Orogenic Belt	Paleozoic	China	Buckman (2000)	Magmatic	Shear zone			YES	YES
Central Asian Orogenic Belt	Paleozoic	China	Robinson et al. (2005)	Magmatic?	Fault zone	HT	340-360	YES	YES
Central Asian Orogenic Belt	Paleozoic	China	Qiu and Zhu (2015)	Magmatic	Shear zone			YES	YES
Central Asian Orogenic Belt	Proterozoic	China	Jiang and Zhu (2017)	Magmatic	Fault zone	LT	<300	YES	YES
Central Asian Orogenic Belt	Paleozoic	China	Qiu and Zhu (2018)	Magmatic	Shear zone			YES	YES
Central Asian Orogenic Belt	Paleozoic	China	Peng et al. (2020)	Tectonic	Fault zone	HT	550-600?		
Uralides	Paleozoic	Russia	Belogub et al. (2017)	Magmatic	Shear zone	LT/HT	207-326	YES	YES
New England Orogen	Paleozoic-early Mesozoic	Australia	Ashley (1997)	Magmatic	Shear zone	LT	165-255	YES	YES
New England Orogen	Paleozoic-early Mesozoic	Australia	Buckman (2000)	Magmatic	Shear zone	LT	165-255	YES	YES
North America Cordillera	Mesozoic	Canada	Hansen et al. (2005)	Tectonic	Shear zone	LT	210-280		
Alpine-Himalayan belt	Mesozoic	Oman	Godard et al. (2021)	Tectonic	Shear zone	LT	75-250		
Alpine-Himalayan belt	Mesozoic	Oman	Falk and Kelemen (2015)	Tectonic	Shear zone	LT	80-130		
Alpine-Himalayan belt	Mesozoic	Oman	Nasir et al. (2007)	Tectonic	Shear zone				
Alpine-Himalayan belt	Mesozoic	Turkey	Aydal et al. (1990)	Tectonic	Shear zone			YES	
Alpine-Himalayan belt	Mesozoic	Turkey	Uçurum (2000)	Meteoric	Shear zone	LT	150-300		
Alpine-Himalayan belt	Cenozoic	China	Robinson et al. (2005)	Tectonic?	Fault zone				
Alpine-Himalayan belt	Mesozoic-Cenozoic	Turkey	Akbulut et al. (2006)	Tectonic	Fault zone	LT	<250		
Alpine-Himalayan belt	Cenozoic	Greece	Tsikouras et al. (2006)		Shear zone	LT	<250		
Alpine-Himalayan belt	Cenozoic	Turkey	Çolacoğlu (2009)	Tectonic	Shear zone				
Alpine-Himalayan belt	Mesozoic-Cenozoic	Iran	Aftabi and Zarrinkoub (2013)	Tectonic	Shear zone	LT	200-400	YES	
Alpine-Himalayan belt	Cenozoic	China	Zhang et al. (2015)	Tectonic?	Fault zone			YES?	
Alpine-Himalayan belt	Mesozoic	Slovakia	Ferenc et al. (2016)	Tectonic	Fault zone				
Alpine-Himalayan belt	Cenozoic	Greece	Hinsken et al. (2017)	Meteoric	Shear zone	LT/HT	250-350		
Alpine-Himalayan belt	Mesozoic-Cenozoic	Iran	Ahankoub and Mackizadeh (2019)	Magmatic	Fault zone	LT	115-300	YES	YES
Alpine-Himalayan belt	Mesozoic	Iran	Boskabadi et al. (2020)	Tectonic	Shear zone	LT	110-280		
Alpine-Himalayan belt	Cenozoic	Iran	Pirouei et al. (2020)	Tectonic	Shear zone			YES	
Alpine-Himalayan belt	Cenozoic	Turkey	Üner (2020)	Tectonic	Shear zone	LT	250-300	YES	

Table 2.3 List of studies presenting bulk geochemical data for listvenites. The source of reactive fluids and first order structures hosting listvenites are described on the fouth and fifth columns. The limit between low temperature (LT) and high temperature (HT) of carbonation was arbitrarily fixed at 300 °C.

Temperature of listvenite formation

Temperatures of listvenite formation were determined by different methods: i) clumped isotopes thermometry (Falk and Kelemen, 2015; Beinlich et al., 2020), ii) oxygen isotopes thermometry (Üner, 2020), iii) chlorite thermometry (Escayola et al., 2009; Hinsken et al., 2017 Gahlan et al., 2018; Gahlan et al., 2020), iv) fluid inclusions thermometry (Andrew et al., 1985; Spiridinov, 1991; Schandl and Wicks, 1991; Schandl and Naldrett, 1992; Schandl and Wicks, 1993; Robinson et al., 2005 and

references therein; Belogub et al., 2017; Ahankhoub and Mackizadeh, 2019), v) quartz thermometry (Ashley, 1997; Monazzami Bagherzadeh et al., 2013), vi) phase equilibria modelling (Beinlich et al., 2012; Menzel et al., 2018; Peng et al., 2020). They were also deduced from the sulphide parageneses (Jiang and Zhu, 2017). Compiled data provide ranges of carbonation temperature of 115 – 360 °C for magmatic-derived metasomatism, and 45–300 °C for tectonic-derived metasomatism.

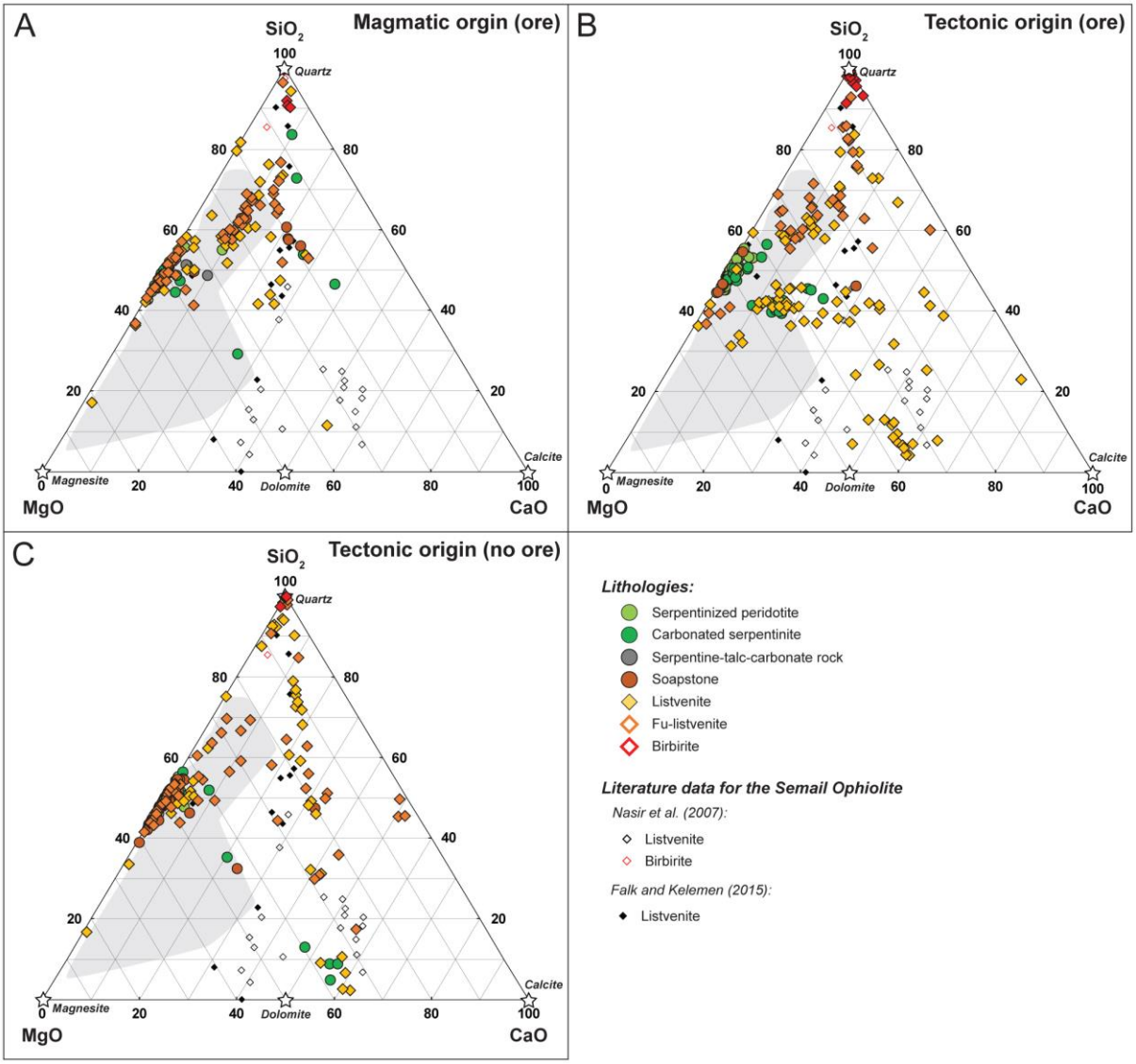

Fig. 2.2 SiO_2-MgO-CaO ternary diagrams of bulk rock compositions for metasomatized peridotites from literature data (references in Table 2.2). Separated panels are plotted for the different sources of fluids and presence of ore enrichments. SiO_2, MgO and CaO end-members are quartz, magnesite and calcite The proportions of each end-member were calculated as the fraction between oxides. The dark grey field corresponds to the bulk compositional range of BT1B core samples (Godard et al., 2021). Compositions plotted in panel (A) include 37 serpentinized peridotites, 41 listvenites and 50 fuchsite-bearing listvenites. Compositions plotted in panel (B) include 65 serpentinized peridotites, 84 listvenites and 40 fuchsite-bearing listvenites. Compositions plotted in panel (C) include 61 serpentinized peridotites, 59 listvenites and 57 fuchsite-bearing listvenites.

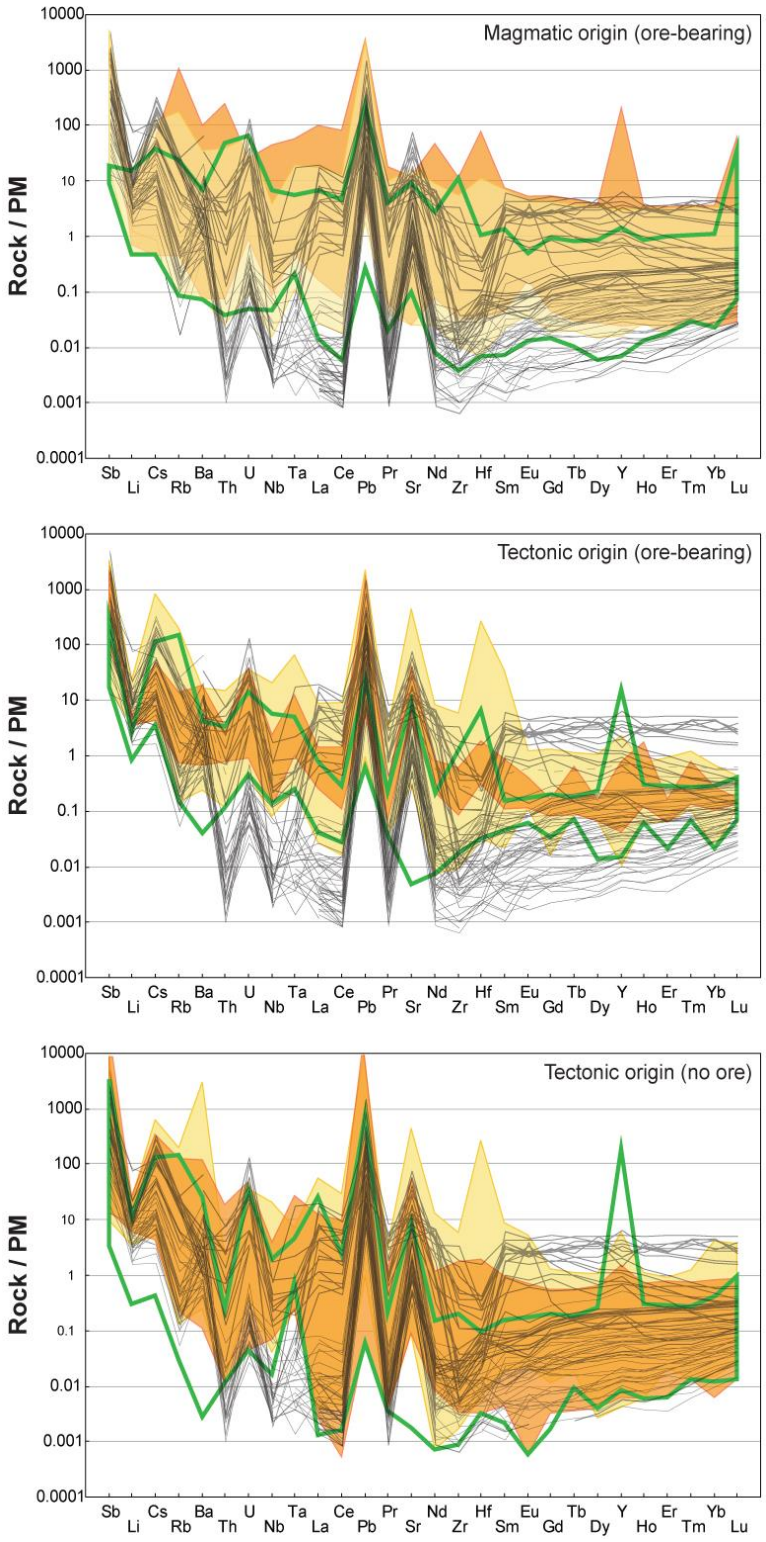

Fig. 2.3 Compiled trace element spider diagrams of metasomatized peridotites from 26 studies from references in Table 2.2. Separated panels are plotted for the different types of fluid source of and the presence of ore enrichment. The field contoured in green corresponds to compositions of peridotite protoliths, the yellow and orange fields to listvenites and fuchsite-bearing listvenites, respectively. Compositions plotted in panel (A) include 54 serpentinized peridotites, 54 listvenites and 71 fuchsite-bearing listvenites (Ahley, 1997; Buckman, 2000; Robinson et al., 2005; Jiang and Zhu, 2017; Qiu and Zhu, 2015, 2018; Helmy et al., 2018; Ahankoub and Mackizadeh, 2019; Moussa et al., 2021; Gahlan et al., 2022; Hamdy et al., 2022). Compositions plotted in panel (B) include 48 serpentinized peridotites, 73

<< listvenites and 16 fuchsite-bearing listvenites (Aydal et al., 1990; Zhang et al., 2015; Gahlan et al., 2018, 2020, 2022; Pirouei et al., 2020; Üner, 2020; Hamdy et al., 2022). Compositions plotted in panel (C) include 58 serpentinized peridotites, 126 listvenites and 53 fuchsite-bearing listvenites (Uçurum, 2000; Robinson et al., 2005; Akbulut et al., 2006; Tsikouras et al., 2006; Çolacoğlu, 2009; Hinsken et al., 2017; Sofiya et al., 2017; Boskabadi et al., 2020; Austrheim et al., 2021). Dark spectra correspond to listvenites from Oman (Nasir et al., 2007; Godard et al. 2021). Trace elements compositions were normalized to the Primitive Mantle using values from McDonough and Sun (1995).

2.4 Listvenites in the Semail Ophiolite

2.4.1 The Semail Ophiolite: structure and emplacement

The Semail Ophiolite extends over ca. 500 km along the northern coastline of the Sultanate of Oman and EAU (Fig. 2.4.1), forming the Al Hajar mountain chain and integrating the Alpine-Himalayan collisional belt. This ophiolite is a segment of oceanic lithosphere obducted on the Arabian continental margin during the closure of the Neo-Tethys realm in the Upper Cretaceous (e.g., Coleman et al., 1981). Geological records indicate a complex history from accretion at a spreading centre (e.g., Ceuleneer et al., 1988; Nicolas and Boudier, 1995), to emplacement after intra-oceanic detachment (e.g., Boudier et al., 1988) or subduction initiation in a supra-subduction zone (e.g. Searle and Cox, 1999). Ophiolite obduction and burial of autochthonous Arabian basement rocks (85–77 Ma) was followed by an extensional phase of exhumation forming the Jebel Akhdar and Saih Hatat domes (e.g., Garber et al., 2021).

Geological units in the Oman mountains can be subdivided into three main tectono-stratigraphic groups (Glennie et al., 1974; Hopson et al., 1981; Rollinson et al., 2014): i) autochthonous basement (Precambrian-Paleozoic) and cover units (Permian–Triassic, Hajar Super Group) from the Arabian margin, and discordantly overlain by para-autochthonous syn-orogenic sedimentary formations (Aruma Group, including the Muti Formation); ii) the ophiolite and allochtonous Hawasina nappes, piled up during the closure of the Hawasina proximal basin (Bechennec et al., 1990), then obducted onto the margin during the Upper Cretaceous; iii) Cenozoic post-obductional sedimentary formations.

The Semail Ophiolite is composed by 12 massifs exposing a thick mantle section (up to 9–12 km) overlain by a layered oceanic crust, comprising lower layered gabbros to upper volcanics. Asthenospheric deformation below the former oceanic spreading centre was preserved by peridotites (Boudier and Coleman, 1981), and overprinted by low temperature ductile deformation during ophiolite detachment (Boudier et al., 1988; Nicolas et al., 2000; Linckens et al., 2011). A commonly 10–100 m thick metamorphic sole outcrops discontinuously along the base of the ophiolite (e.g., Cowan et al., 2014; Soret et al., 2017).

The ophiolite mantle is composed principally of moderately to highly serpentinized refractory peridotites, mainly harzburgites and minor dunites (Lippard et al., 1986; Godard et al., 2000; Boudier et al., 2010; Hanghøj et al., 2010). Godard et al. (2000) inferred these rocks to be residues after high degree partial melting (>15%). Cpx-harzburgites (> 5% clinopyroxene) and lherzolites are locally found toward the base of the ophiolite section (Lippard et al., 1986; Takazawa et al., 2003; Khedr et al., 2014). A 50–200 m thick section of highly serpentinized, mylonitized and often amphibole-bearing Cpx-rich peridotites alternating with dunites and minor harzburgites ("Banded Unit") commonly characterizes the basal transition of the ophiolite to its metamorphic sole (e.g., Khedr et al., 2013; Prigent et al., 2018). Enrichments in B, Li and other fluid mobile elements in basal peridotites was ascribed to dehydration of the metamorphic sole during incipient subduction (Khedr et al., 2013; Prigent et al., 2018).

The metamorphic sole is made of slivers of mafic and sedimentary-derived material accreted at the base of the ophiolite mantle during intra-oceanic underthrusting (e.g., Boudier et al., 1988) or incipient subduction (e.g., Searle and Cox, 1999). It exhibits from top to bottom an inverted thermal gradient (e.g., Cowan et al., 2014; Kotowski et al., 2021), with the presence of two high-temperature units (850°C – 1 GPa, 725°C – 0.8 GPa) and low-temperature (530°C and 0.5 GPa) units gathered in a stepwise manner (Soret et al., 2017). Zircon dating indicates that the formation of the sole was in part contemporaneous to the accretion of the oceanic crust preserved by the ophiolite (96.1–95.2 Ma; Rioux et al., 2021).

2.4.2 Mantle metasomatism and listvenite occurrences in Oman

The Semail mantle has experienced multiple metasomatic events through its history, including oceanic alteration (McCulloch et al., 1981; Gregory and Taylor, 1981), serpentinization by subducting fluids during ophiolite emplacement (e.g., Prigent et al., 2018), and recent to active peridotite serpentinization and carbonation by subsurface and meteoric waters (e.g., Clark and Fontes, 1990; Clark et al., 1992; Dewandel et al., 2003, 2005; Mervine et al., 2014; Falk et al., 2016; Noël et al., 2018; Kelemen et al., 2021; Ternieten et al., 2021). In this study we focus on pervasive peridotite carbonation leading to listvenite formation.

Listvenites crop out discontinuously along the ophiolite basal thrust (Fig. 2.4). They mainly occur as decametre-thick tabular bodies replacing the ophiolite mantle near or along the basal thrust, or as blocks within tectonic mélanges in shear zones (Stanger, 1985; Wilde et al., 2022; Nasir et al., 2007; Falk and Kelemen, 2015; Scharf et al., 2022). The most extended and best exposed outcrops of listvenites in Oman are found in the Fanja region (Fig. 2.5). There, the ophiolite section is relatively thin (Fanja saddle, Boudier and Nicolas, 2018) and exposes dismembered and highly faulted fragments of mantle peridotites juxtaposed with lower gabbros atop of slices of metamorphic sole and underlying para-autochthonous sediments (Muti Formation). Listvenites are aligned along a NW–SE direction to the

northern and southern boundaries of ophiolite segments flanking the Jebel Akhdar and Saih Hatat domes.

Yet no consensus has been reached for explaining listvenite genesis in the Fanja region, with two models still debated: i) carbonation of the mantle wedge along the basal thrust by up migrating reactive fluids during ophiolite obduction (Falk and Kelemen, 2015), or ii) localized metasomatism along extensional faults during the domal exhumation of the Saih Hatat (e.g, Stanger, 1985; Wilde et al., 2002; Scharf et al., 2022). Scharf et al. (2022) recently provided U-Pb ages on listvenite (64 ± 6 Ma) and dolomite veins crosscutting listvenites (60 ± 15 Ma and 55 ± 5 Ma). However, these ages were measured on samples westwards Hole BT1B.

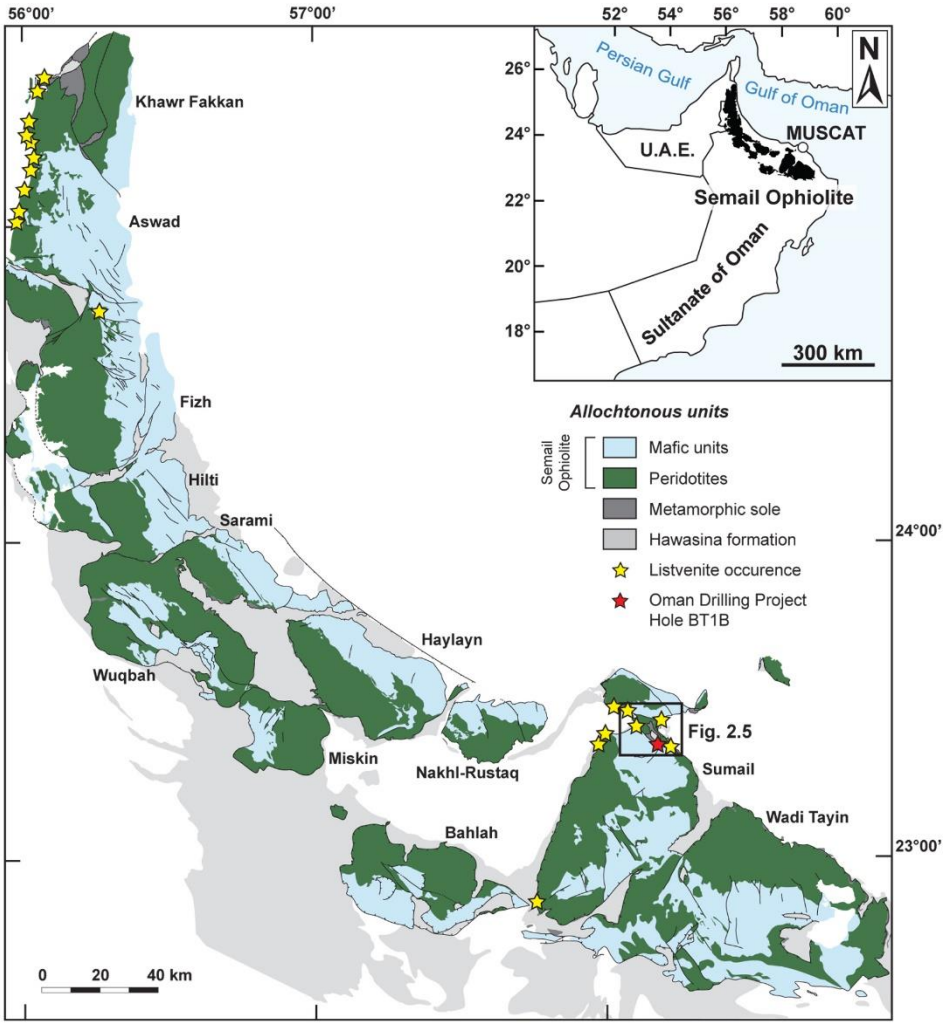

Fig. 2.4 Listvenite occurrences (yellow stars) in the Semail Ophiolite after Nasir et al. (2007) and Boudier and Nicolas (2018). The location of Hole BT1B is indicated by a red star. The insert map shows the geographical position of the ophiolite. The lithological map was adapted from Nicolas et al. (2000).

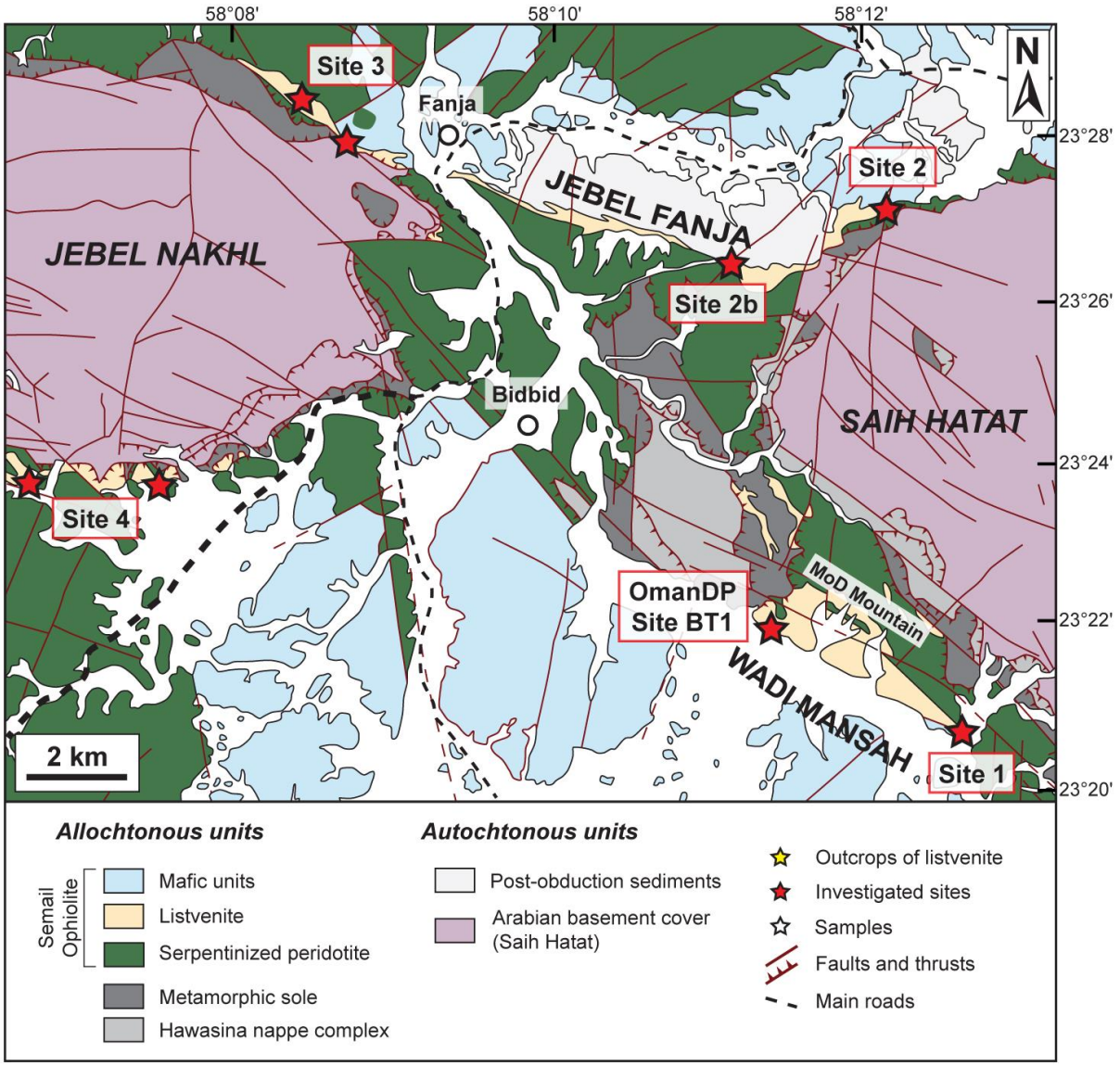

Fig. 2.5 Geological map of the Fanja area (modified after Villey et al., 1986; Kelemen at al., 2022). Investigated listvenites outcrops in this thesis are indicated as sites by red stars.

With the intent to investigate mass transfers and deformation in the leading edge of the mantle wedge in a subduction zone (Kelemen et al., 2020), listvenites from the MoD Mountain have been the focus of drilling Oman DP Hole BT1B (23°21'51.75"N; 58°10'57.69"E). Main objectives were to characterize: i) the source of reactive fluids, ii) the nature of fluids and mechanisms of transport, iii) mineralogical, chemical and rheological changes at the outcome of metasomatic reactions, and iv) deformation mechanisms in a subduction zone.

Hole BT1B was drilled using cylindrical diamond bits and wireline core retrieval in March 2017. It recovered ~200 m of listvenites interlayered by two levels of carbonated serpentinites, atop of ~100 m of metamorphic rocks (Kelemen et al., 2020; Fig. 2.6). The unmatched density and quality of borehole samples open up unique opportunities to investigate the mechanisms and reaction sequence leading to peridotite conversion into listvenite.

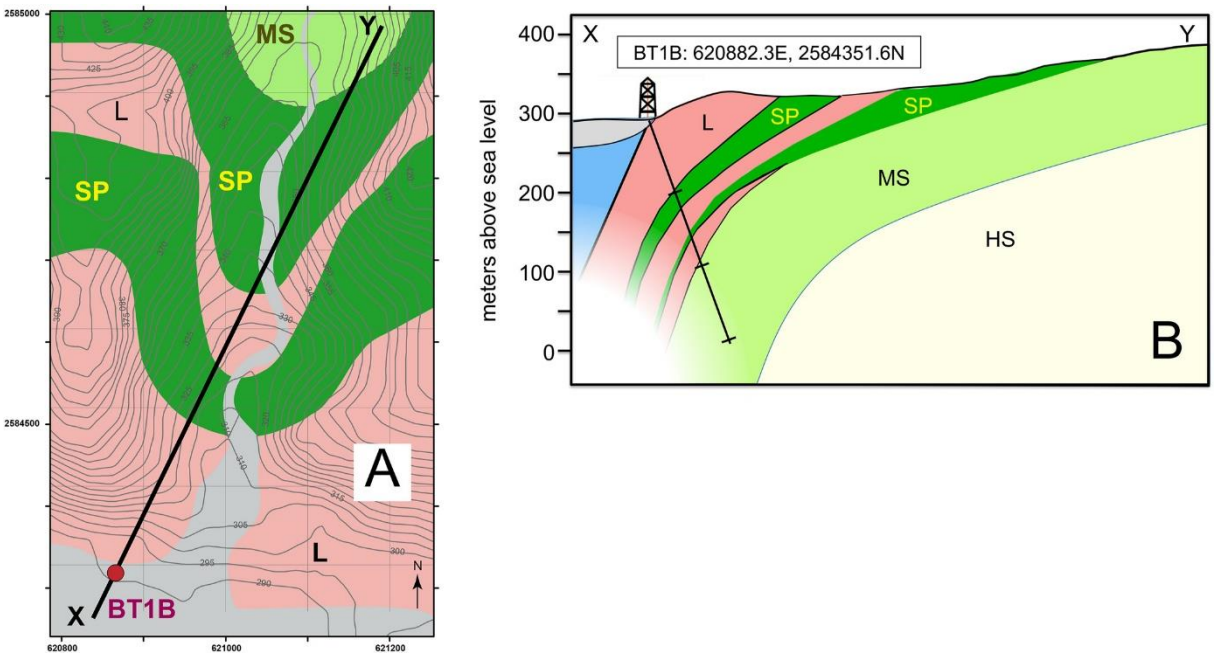

Fig. 2.6 (from Kelemen et al., 2020) Geological map (a) and idealized cross-section of drilling the ophiolite-metamorphic sole section. Abbreviations: HS= Hawasina sediments, L= listvenites, MS = metamorphic sole, SP= serpentinized peridotites

2.4.3 Summary of recent work on Oman Drilling Project Hole BT1B

Since 2020, an increasing number of studies have been published in the course of the Oman Drilling Project, providing key petrological insights on listvenite formation in Wadi Mansah. This section provides a summary of the main results establishing a petrological framework for the present thesis. Preliminary results of studies on Hole BT1B have been the object of a recent review paper by Kelemen et al. (2022).

Mineralogy and microstructures

Core description aboard D/V Chikyu shed the light on lithological and microstructural heterogeneity across the borehole (Fig. 2.7), with alternation between massive to highly veined, sheared and cataclastic domains (Kelemen et al., 2020). Listvenites are mainly composed of magnesite and quartz, with minor amount of dolomite, accessory Cr-spinel relicts and Fe-oxides. The presence of minor fuchsite in listvenites is mostly restricted to the lower part of the well. Dolomite content is variable with depth but clearly higher in the lowermost section of the borehole, and accompanied by a major decrease in magnesite and quartz abundances close to the basal thrust. A rather constant magnesite:quartz ratio of ca. 0.4 is observed at the borehole scale, indicative of carbonation being controlled by the reaction:

$$\text{Serpentine} + 3\ CO_2\ (aq) = 2\ SiO_2\ (aq) + 3\ \text{Magnesite} + H_2O$$

The absence of primary minerals points to complete serpentinization prior to carbonation. Carbonate abundance in serpentinite is low, only increasing towards the transition with listvenite. Partial carbonation in the two serpentinite intervals implies that transport of reactive fluids was limited in those structural levels.

Peridotite carbonation proceeded by a complex sequence of progressive matrix replacement and veining which is the focus of sections 4.2 and 5.1, and of a paper by Menzel et al. (2022b), to which we participated as co-authors, and added to the Appendix. To summarize, carbonation of the serpentine matrix is accompanied by the formation of isolated to clustering spherical magnesite cores, referred to as spheroids (Fig. 2.8, Beinlich et al., 2020), extended magnesite aggregates, groundmass cryptocrystalline quartz and chalcedony, and late interstitial dolomite. Magnesite spheroids are characterized by core-to-rim chemical zoning in divalent cations, with Mg-rich cores and Fe-Ca-rich rims. The discovery of less abundant but frequent spheroids with Fe-rich cores, locally related to the dissolution of Fe-oxides, motivated the writing of a paper on chemical zoning of spheroids (section 5.1). Carbonated serpentinites and listvenites host an intricate network of veins, whose sequence was unravelled by Menzel et al. (2022b). Veining during serpentinization initiated by the formation of mesh networks, cut by two types of serpentine veins: i) serpentine-magnetite veins, and ii) common, "en échelon" or branching (sub-)millimetric crack-seal veins. The onset of carbonation is marked by: i) local pseudomorphic replacement of serpentine by carbonates along mesh rims, selvages and within crack-seal veins, and ii) the generation of antitaxial, zoned magnesite veins, locally forming closely-spaced parallel vein sets. Listvenites preserved these initial microstructures however showing the complete replacement of serpentine in veins by quartz and/or carbonates. Matrix and vein microstructures are then overgrown by dendritic magnesite, followed by quartz precipitation after the remaining serpentine matrix. Late veining includes the generation of syntaxial quartz–carbonate and dolomite veins.

Menzel et al., (2022b) suggested that fluid infiltration and reaction progress is influenced by the localization of pre-existing serpentine structures and cracking during initial veining. X-ray tomography by Beinlich et al. (2020) evidenced the connectivity between early antitaxial veins and spheroids in their vicinity. However, the presence of unconnected spheroids indicate growth after diffusive fluxing. Menzel et al. (2022a) porposed that fluid infiltration was promoted by dilatant granular flow and dissolution-precipitation reactions, hence maintaining sufficient porosity for fluid transport despite solid volume increase.

Ductile and semi-brittle shear zones are abundant across the mantle-derived section in BT1B, but less frequent in the metamorphic sole (105 shear zones counted above the basal thrust; Kelemen et al., 2020). Menzel et al. (2020) estimated ca. 10 vol% of the mantle section in the borehole to be composed of cataclasite bands. Cataclasites contain lithic clasts of listvenite indicate that cataclasis postdates listvenite formation. The occurrence of reworked cataclasites, cut by thin sharp faults point to repeated

reactivation of brittle structures. Dolomite veins crosscutting cataclasites and breccias in Hole BT1B, suggesting infiltration of late Ca-rich fluids after listvenite formation. Menzel et al. (2020) proposed three possible stages relative to ophiolite evolution for cataclastic deformation: i) brittle thrusting during ophiolite obduction, ii) postobduction extensional shear zones or reactivation of previous reverse faults, and/or iii) late oblique normal or strike-slip faulting related to uplift of the Jebel Akhdar and Saih Hatat anticlinoria.

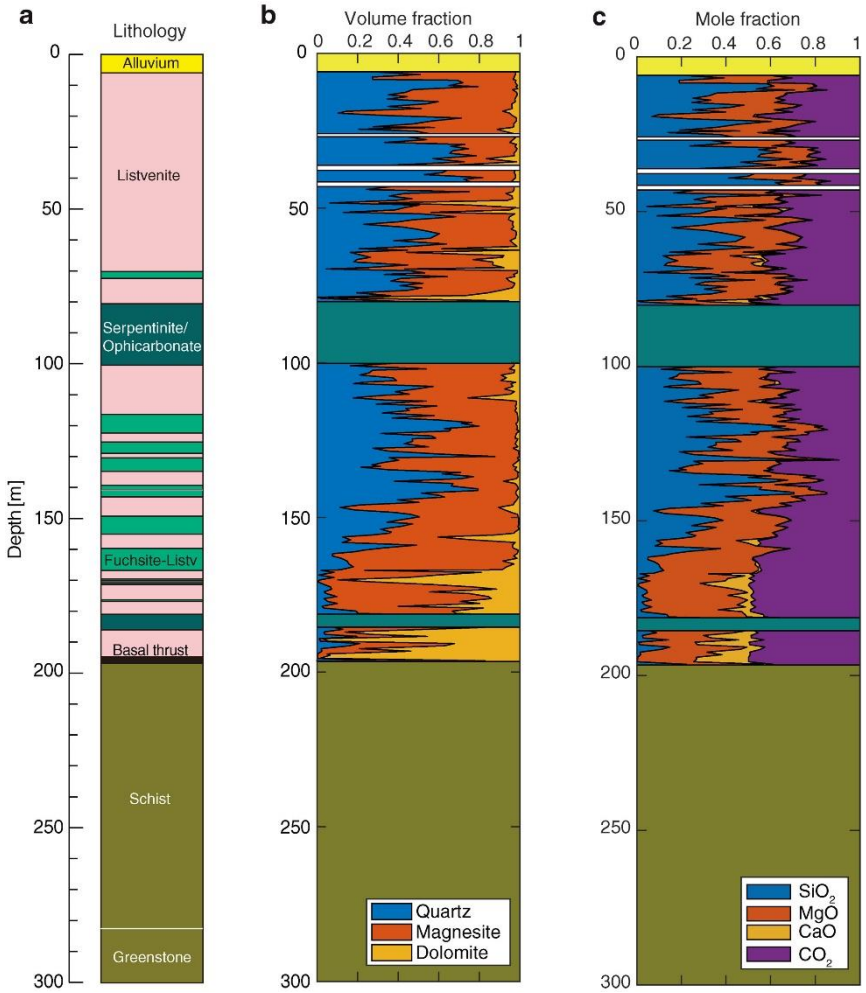

Fig. 2.7 (from Okazaki et al., 2021) Downhole (a) lithology, (b) mineral volume fraction, and (c) element molar fractions (SiO_2, MgO, CaO, and CO_2) of listvenite for Hole BT1B inferred from X-Ray CT core imaging.

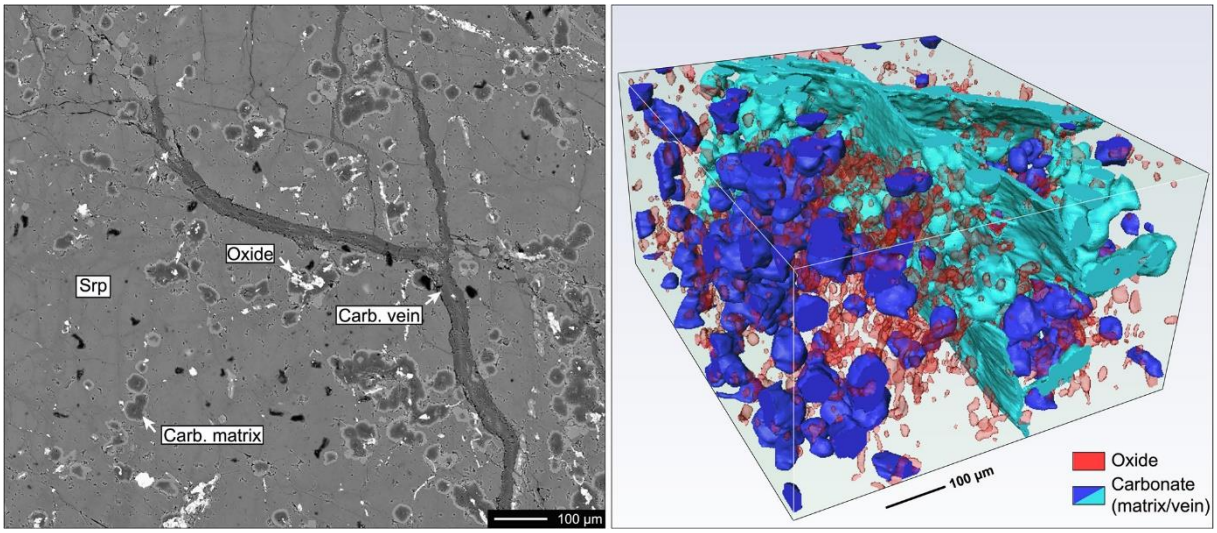

Fig. 2.8 (from Beinlich et al., 2020) 3-D reconstruction of X-ray tomography acquired on poorly carbonated serpentinite 44Z-1. The BSE image on the left shows an example of the reconstructed texture in two dimensions. The carbonate color scheme (blue/cyan) highlights connectivity between spheroids and the central vein. The pale green, translucent volume is filled by serpentine. The reconstructed volume consists of 83.0 vol.% of serpentine, 5.4 vol.% of isolated carbonate (blue), 8.2 vol.% of vein carbonate and connected spheroids (cyan), and 3.4 vol.% of oxides.

Geochemistry of listvenite series and metamorphic sole lithologies

Bulk rock geochemistry

The bulk rock volatile, major and trace element compositions of listvenites series and metamorphic rocks were determined by Godard et al. (2021), a study to which we participated as co-author and available in Appendix.

Carbonated serpentinites and listvenites show contrasted volatile abundances, the first being richer in H_2O (0.3 – 11.3 wt% vs. <0.6 wt%) but poorer in CO_2 (5.6 – 33.1 wt % vs. 21.4 – 43.2 wt%), consistent with successive hydration and dehydration reactions. Metasomatized peridotites in Hole BT1B preserved compositions close to those of basal peridotites in Oman for most major and lithophile trace elements. Three geochemical domains were identified and correspond to different protoliths: harzburgites-dunites for the upper and lowermost sections of the borehole (domains I and III) and lherzolites for the fuchsite-rich interval (domain II). Listvenite series are enriched in most fluid mobile elements compared to Semail peridotites, especially for Pb, Li, As, and Sb. Accounting for various peridotite protoliths, Godard et al. (2021) further calculated that peridotite metasomtism induced solid mass and volume increase of 13 – 31% and 14 – 35 %, respectively, for carbonate serpentinite and of 30 – 51 % and 29 – 51 %, respectively, for listvenite (Fig. 2.9). The authors also evidenced a decoupling between Sr-Ca enrichments and other FME, related to interactions with several batches of CO2-rich fluids. A similar observation was highlighted by Carter (2020), identifying two distinct fluid signatures based on compositions in halogens. One fluid signature likely relates to sedimentary pore fluids, when

the second matches with halogens compositions of the metamorphic sole. Together, these studies converge to late fluid ingress by Ca-Sr rich fluids leading to the precipitation of dolomite-rich intervals.

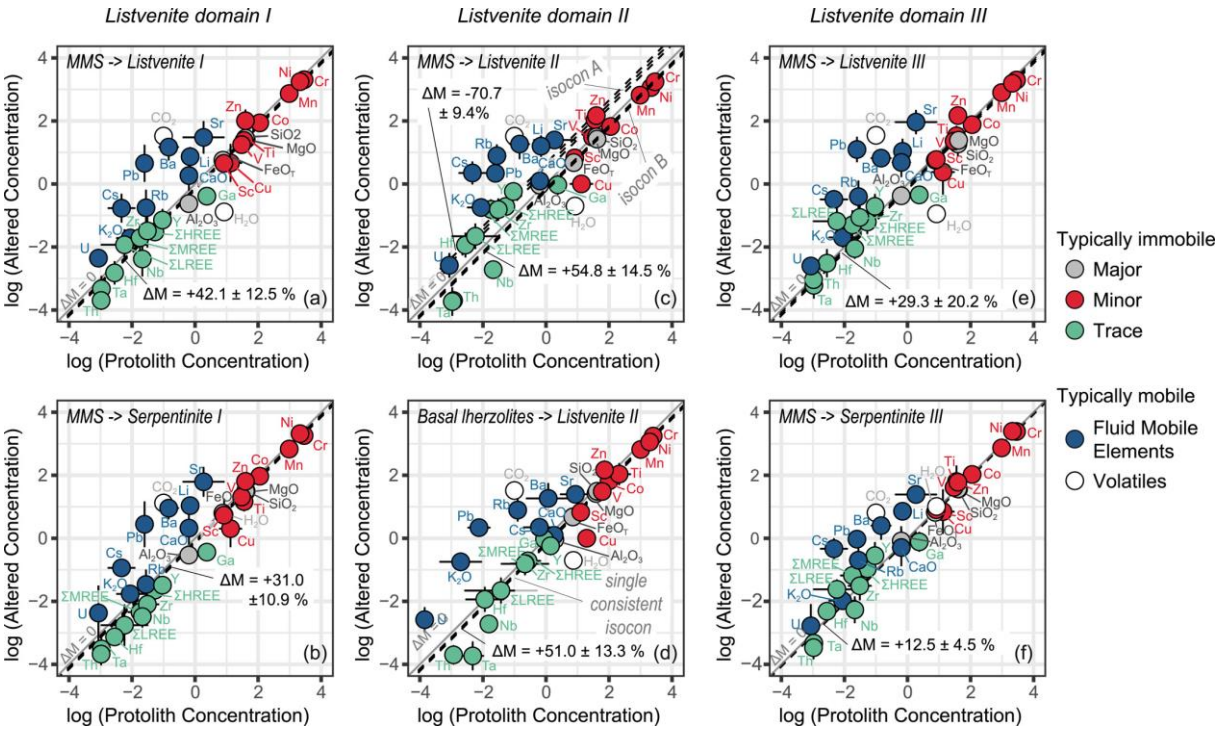

Fig. 2.9 (from Godard et al., 2021) Mass balance diagrams for listvenite series from Hole BT1B. Isocon plots comparing the average composition of listvenites and serpentinites from each listvenite domains with potential protolith compositions on log-log scales. Isocons (line of immobility) were calculated using the approach of Baumgartner and Olsen (1995). On each panel, the isocon (dotted black lines) corresponds to a protolith–altered rock pair. The gray 1:1 reference line corresponds to zero mass change during alteration. Isocons above and below this indicate mass loss and gain, respectively (noted ΔM). Using the average composition of the MMS refractory peridotites as the protolith composition for each domain, this approach gives consistent patterns of mobile and immobile elements, with the exception of Listvenites II (panel c) where two potential isocons are apparent in the data (labelled A and B). Mass balance was repeated for Listvenite II with the average composition of basal (amphibole-bearing) lherzolites, which gives a single consistent isocon and similar patterns of mobility/immobility to the other panels. Compositions are plotted as concentrations in wt.% for major and volatile elements and in µg/g for trace elements.

Insights from radiogenic and stable isotopes

Relying on the 97 ± 29 Ma Rb-Sr isochron age of fuchsite by Falk and Kelemen (2015), de Obeso et al. (2022) determined the bulk $^{87}Sr/^{86}Sr$ compositions of listvenites, carbonated serpentinites and sole lithologies on borehole samples, and Hawasina sediments sampled close to BT1B. Carbonated serpentinites and listvenites provided isotope signatures heavier ($^{87}Sr/^{86}Sr$ = 0.709–0.715) than the Semail mantle (~0.703–0.709; Gerbert-Gaillard, 2002; Lanphere et al., 1981; McCulloch et al., 1981) and the metamorphic sole (0.704–0.706), but trending to compositions of Hawasina sediments ($^{87}Sr/^{86}Sr$ = 0.708–0.724). These authors thus proposed that reactive CO_2-bearing fluids resulted from the devolatilization of clastic sediments alike Hawasina sediments at depth. In their study, de Obeso et al.

(2021) also determined the bulk carbon concentrations and isotopes signatures that provided similar results to our study in section 6.3.

Interestingly, de Obeso et al. (2021) measured the Mg isotope compositions of dolomite-rich and magnesite-rich listvenites collected by Falk and Kelemen (2015). Briefly, dolomite-rich listvenites display Mg isotope ratios (mean $\delta^{26}Mg = -1.33$ ‰) significantly lighter than for magnesite listvenites (mean $\delta^{26}Mg = -0.33$ ‰), suggesting that dolomite replaced magnesite during metasomatism at high water/rock ratio (Kelemen et al., 2022).

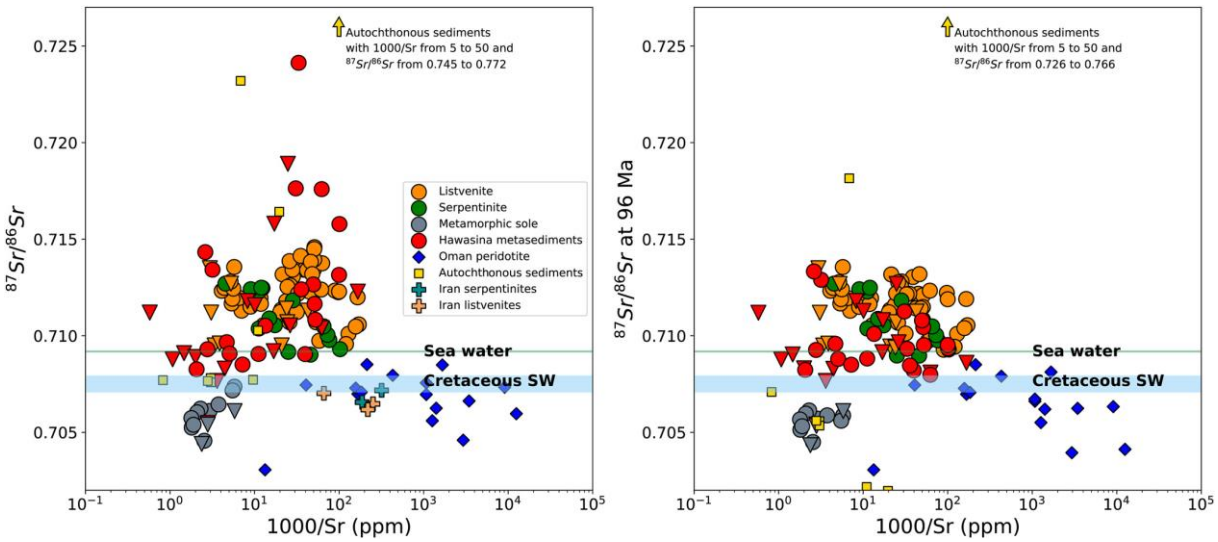

Fig. 2.10 (from de Obeso et al., 2022) Age corrected (96 Ma) $^{87}Sr/^{86}Sr$ values plotted versus inverse Sr concentration for Hole BT1B samples and other lithologies measured in Oman and Iran (Weyhenmeyer, 2000; Gerbert-Gaillard, 2002; Falk and Kelemen, 2015; Boskabadi et al., 2020). Rb concentrations Seawater and Cretaceous seawater values from McArthur et al. (2001).

Beinlich et al. (2020) determined the clumped isotope distribution (Δ47) of carbon and oxygen on matrix and vein carbonate powders, yielding a calculated temperature range of 45 ± 5 °C to 247 ± 52 °C which encompass the range of 61 ± 8 °C to 114 ± 8 °C previously obtained on Wadi Mansah listvenites by Falk and Kelemen (2015). The authors highlighted the non-systematic distribution of carbonation temperatures and calculated fluid compositions ($\delta^{18}O_{fluid}$ = -9.9 ‰ – +12.1 ‰) across the borehole (Fig. 2.11), suggesting fluid migration along different flow pathways and at different timing.

Thermodynamic modelling

Kelemen et al. (2022) modelled that decarbonation reactions involving lithologies alike the metamorphic sole and Hawasina sediments could produce fluids enough enriched in dissolved CO2 (~14'000 ppm) to convert peridotite into listvenite. Fluid cooling from 400°C to 200°C and depressurization from 1 GPa to 0.5 GPa was modelled and predicted listvenite formation with similar mineral proportions than in Hole BT1B for fluid-rock ratios of ~100.

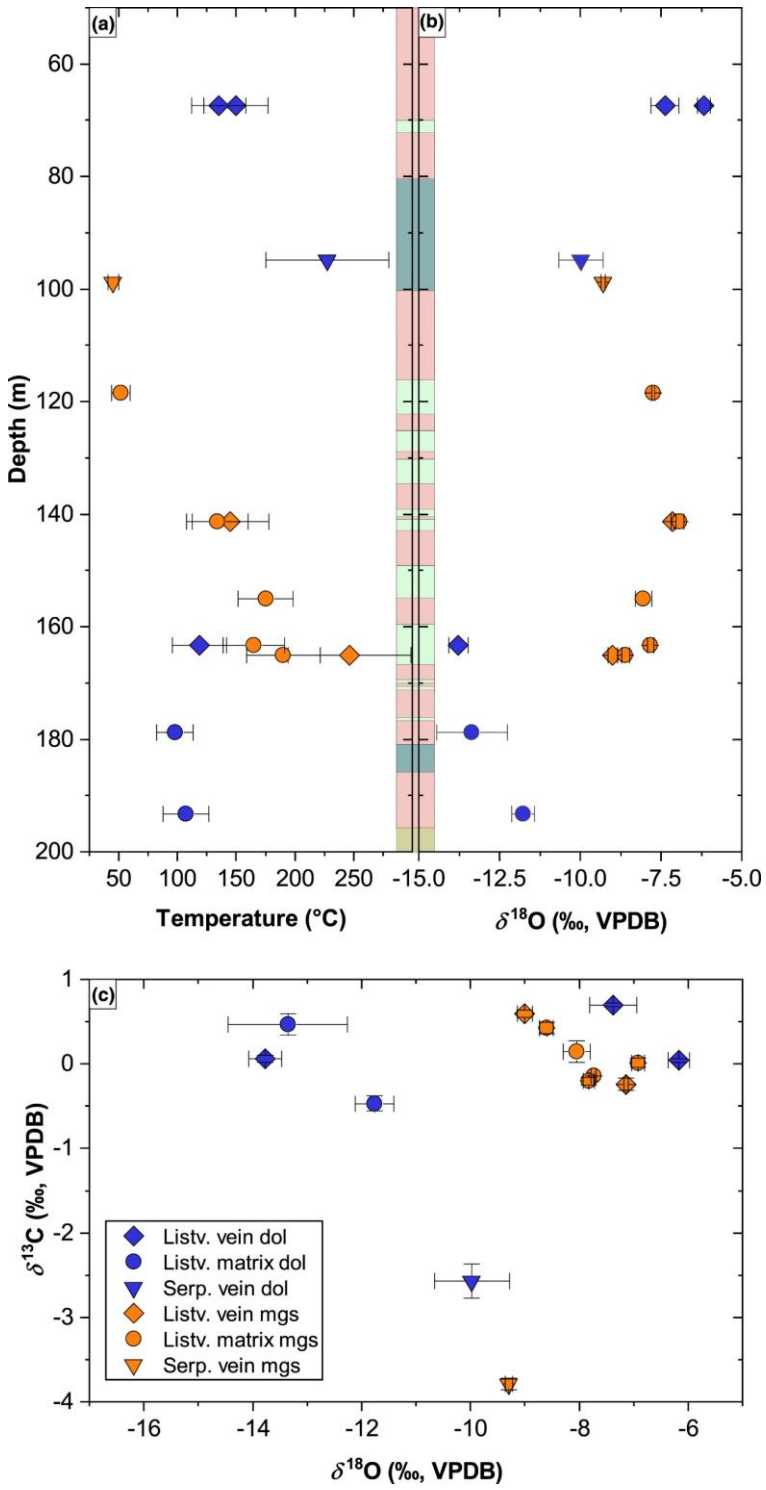

Fig. 2.11 (from Beinlich et al., 2020) Stable oxygen and carbon isotope systematics. (a) Downhole plot of clumped isotope carbonate formation temperatures for listvenite and serpentinite samples. (b) Downhole plot of magnesite and dolomite $\delta^{18}O_{VPDB}$. (c) Carbonate $\delta^{18}O_{VPDB}$ vs. $\delta^{13}C_{VPDB}$ showing clustering at high oxygen and carbon isotope ratios, lower $\delta^{18}O$ for some values of matrix and vein dolomite in listvenite and lower $\delta^{13}C$ for dolomite and magnesite veins in serpentinite 44Z-1.

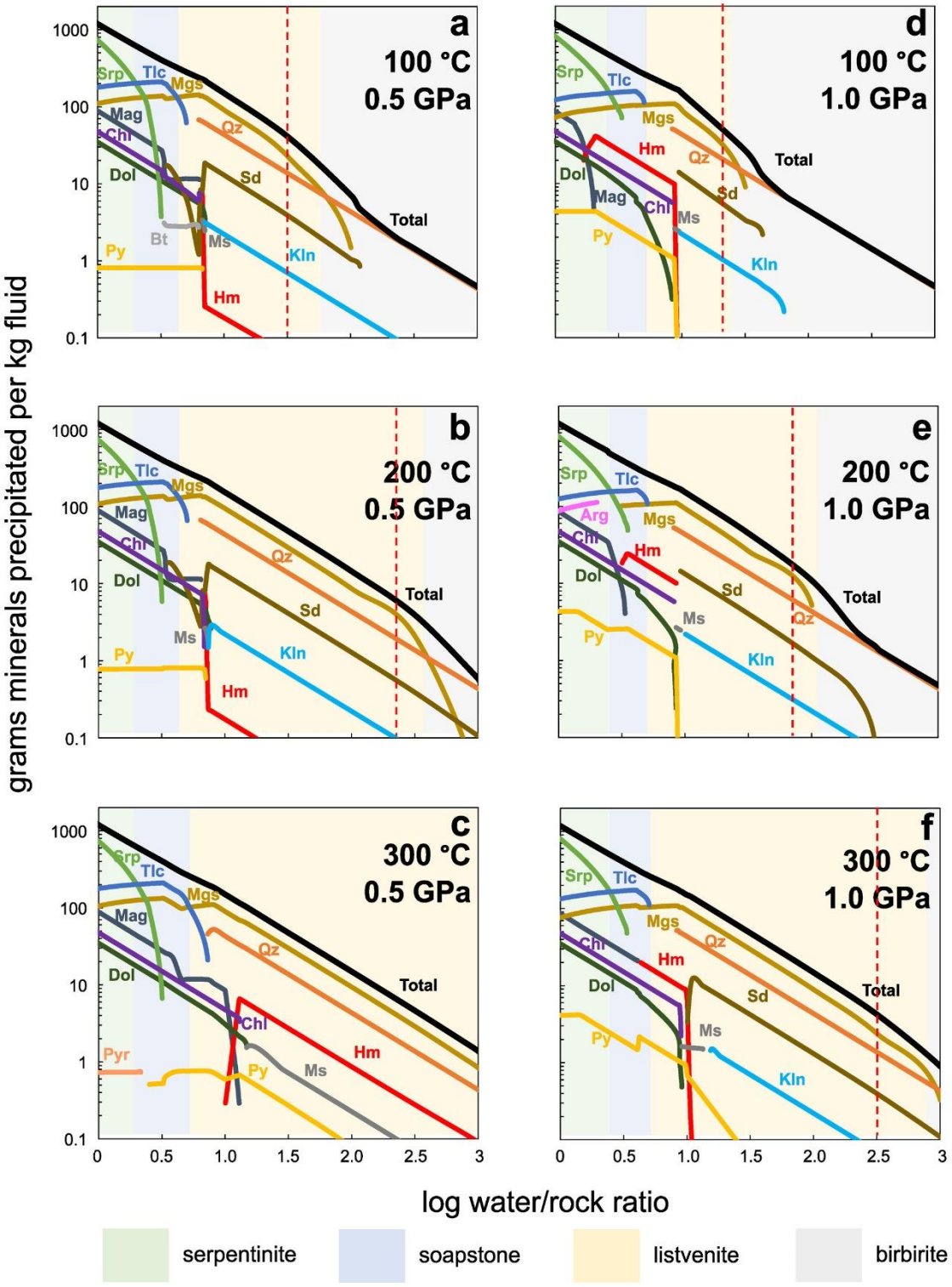

Fig. 2.12 (from Kelemen et al., 2022) Results of thermodynamic reaction path models for the reaction between fluids derived from devolatilization of Hawasina pelitic sedimentary rock OM20-17 and average Oman harzburgites. Mineral end-member abbreviations: Qz = quartz; Sd = siderite; Mgs = magnesite; Kln = kaolinite; Ms = muscovite; Dol = dolomite; Chl = chlorite; Py = pyrite; Tlc = talc; Srp = serpentine (chrysotile); Pyr = pyrrhotite. Red, vertical dashed line indicates where magnesite/quartz molar and volume proportions are ~2:1, as observed in listvenites from BT1B.

Chapter 3: Methodology

Foreword

The most extended outcrops of listvenites in the world are found along the base of the Semail Ophiolite in the Fanja region, Oman. They have been the focus of Oman Drilling Project Hole BT1B in Wadi Mansah. Drilling allowed the recovery of an exceptional continuous core section including ~200 m of listvenites and carbonated serpentinites atop of ~100 m of metabasalts from the metamorphic sole. To complement the study of core samples, listvenite outcrops were investigated and sampled in the entire region during a field campaign conducted in January 2020.

The two sample sets were examined to address the main scientific aims of the present thesis. Most analytical work was performed on core samples due to excellent preservation from weathering and to exploit the high sampling resolution. The petrography and bulk geochemistry of regional samples were characterized for comparison with BT1B samples, but also to explore geochemical features at a larger scale.

This chapter provides details on the location of sites investigated during fieldwork and sampling strategy, but also on sample selection for analysis, and a brief description of analytical methods applied for building the presented dataset.

3.1 Fieldwork

In January 2020, a field campaign was conducted in the Fanja region, where listvenite ridges are outcropping along the W-E direction on the northern and southern flanks of the Jebel Nakhl and Saih Hatat domes, Fig. 2.5). The ophiolite section is relatively thin, exposing dismembered and highly faulted fragments of mantle peridotites juxtaposed with lower gabbros atop of slices of metamorphic sole and underlying para-autochthonous sediments (Aruma Group).

A total of 8 sites exposing listvenites were investigated: i) the vicinity of Hole BT1B (MoD Mountain) and Site 1 at the eastern termination of Wadi Mansah, ii) Sites 2 and 2b along the Jebel Fanja, iii) Site 3 along the Jebel Qarn, iv) Site 4 along the Jebel Nakhl. Two samples of serpentinized pyroxenite and dunite were also collected north of the village of Fanja (Tawi), at the transition between the mantle and the lower crust. Mapping, observations and sampling were realized systematically along transects from the sole or underlying metasediments, across the ophiolite mantle, and eventually up to lower crustal gabbros. Collected samples, prefixed “OM20”, include 36 metasomatized peridotites, 6 gabbros, 3 metabasalts and 1 metasediment from the sole, and 2 limestones from the para-autochthonous units (n = 48; list of samples in Appendix).

3.2 Sample selection and preparation

This thesis benefited from the availability of two sample sets from Hole BT1B: “805GOD” core quarters (n = 50) and consortium “CHEM” rock powders (n = 76). “805GOD” core quarters were cut for the making of polished thin sections necessary to the petrological study. A subset of 15 polished thick sections were prepared for: a) investigating the occurrence of fluid inclusions; b) identifying serpentine species by Raman spectroscopy; c) quantifying the major and trace element compositions of minerals. In addition, 8 representative polished thin section billets were confectioned to conduct a “micro-bulk” carbon and oxygen isotopes study on carbonates. Bulk carbon, iron and zinc isotopes were determined on a selection of 21 “CHEM” and 5 “OM20” powders, which bulk major and trace element chemistry had previously been determined by Godard et al. (2021) or was determined by this study. Complementary Fe-titration was performed on 15 of these powders. Sample distribution across the borehole and applied analytical methods are indicated in Fig. 3.1.

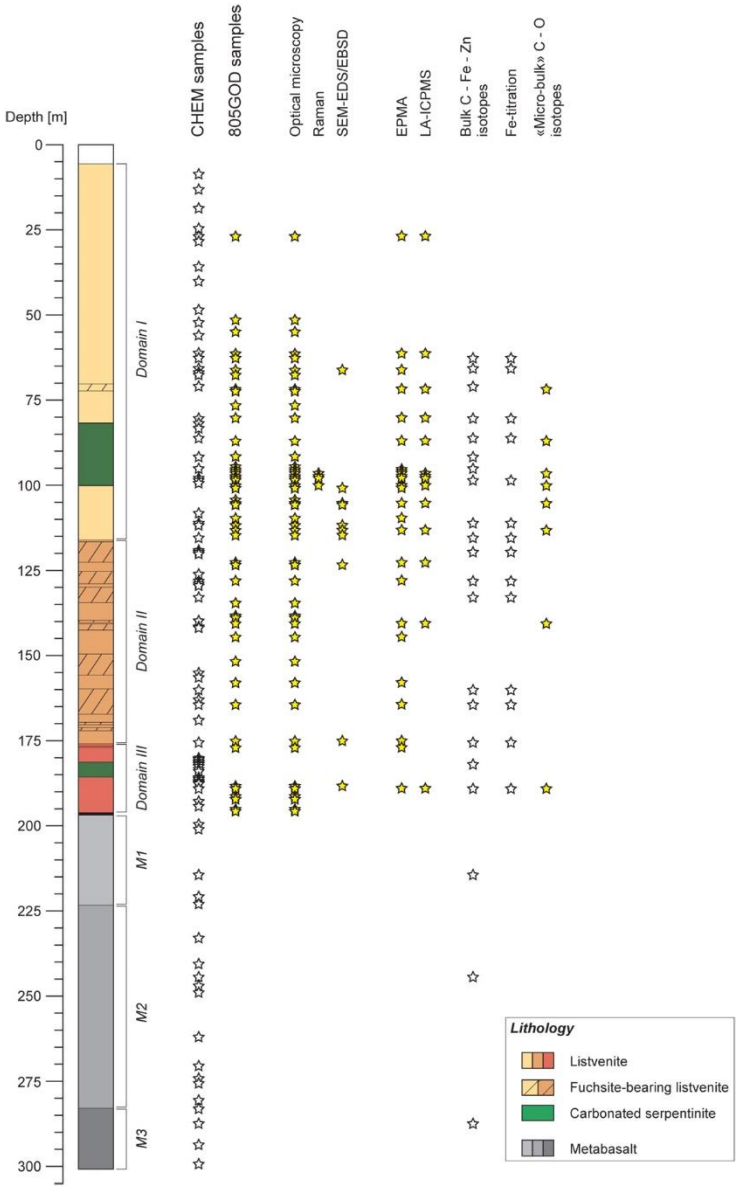

<< **Fig. 3.1** Lithological column of Hole BT1B showing sample distribution and applied analytical methods. Lithological domains in listvenites series (I-II-III) and metabasalts (M1-M2-M3) after Godard et al. (2021).

Regional samples (n=48) were cut to prepare thin sections but also to remove weathering surfaces. Rock chips were crushed with a hammer, and powdered using a Fristch PULVERISETTE 2 agate mortar grinder. All the equipment was cleaned with milliQ water and ethanol after each sample powdering. The agate mill was also cleaned by powdering quartz sand after each sample preparation to avoid contamination.

3.3 Mineral characterization

3.3.1 Raman spectroscopy

Principle:

Raman spectroscopy is a non-destructive characterization method. It is performed by irradiating a material with a monochromatic laser source. The incident radiation by high frequency photons produces inelastic light scattering (mostly Rayleigh scattering), characterized by: (i) a loss of energy to molecular vibrations, and (ii) the emission of reduced frequency photons. Key point is that vibrational energy levels of emitted photons are unique to each molecule, depending for instance on chemical bonds and molecular structure, thus providing "fingerprint" vibrational bands for each mineral (see Larkin, 2018 for further details). Raman spectroscopy is routinely used for identifying serpentine varieties (lizardite, chrysotile and antigorite) which present characteristic vibrational bands in the low frequency (0–1200 cm^{-1}) and OH-stretching (3600–3800 cm^{-1}) wavelength ranges (see Table 3.1 and Fig. 3.2; Auzende et al., 2004; Groppo et al., 2006; Petriglieri et al., 2015; Tarling et al., 2018).

Vibrational band	**Lizardite**			**Antigorite**			**Chrysotile**		
(Study)	*(1)*	*(2)*	*(3)*	*(1)*	*(2)*	*(3)*	*(1)*	*(2)*	*(3)*
O–H–O groups	230	233	241	229	230	235	232	231	235
Bending SiO_4	349	350	351	-	-	-	345	345	346
Symmetric $\nu_{5(e)}$ SiO_4	386	388	393	377	375	377	388	389	391
Deformation SiO_4–AlO_4	532	510	527	-	520	528	-	-	-
Translation OH–Mg–OH	621	630	-	631	635	-	622	620	-
ν_s Si–O_b–Si	689	690	695	687	683	685	691	692	694
ν_{as} Si–O_b–Si	-	-	-	1045	1044	-	-	-	-
ν_{as} Si–O_{nb}	-	1096	-	-	-	-	-	1105	-
ν_s outer OH	3660	n.a.	3654	-	n.a.	3641	3651	n.a.	3649
ν_s outer OH	3683	n.a.	3688	3665	n.a.	3666	3691	n.a.	3691
ν_s inner OH	3703	n.a.	3704	3695	n.a.	3693	3698	n.a.	3699

Table 3.1 Characteristic Raman peaks at low- and high-wavelength regions of main serpentine varieties (modified after Petriglieri et al., 2015). Values after: (1) Petriglieri et al. (2015); (2) Groppo et al. (2006); (3) Auzende et al. (2004). Abbreviation: n.a. = not analysed.

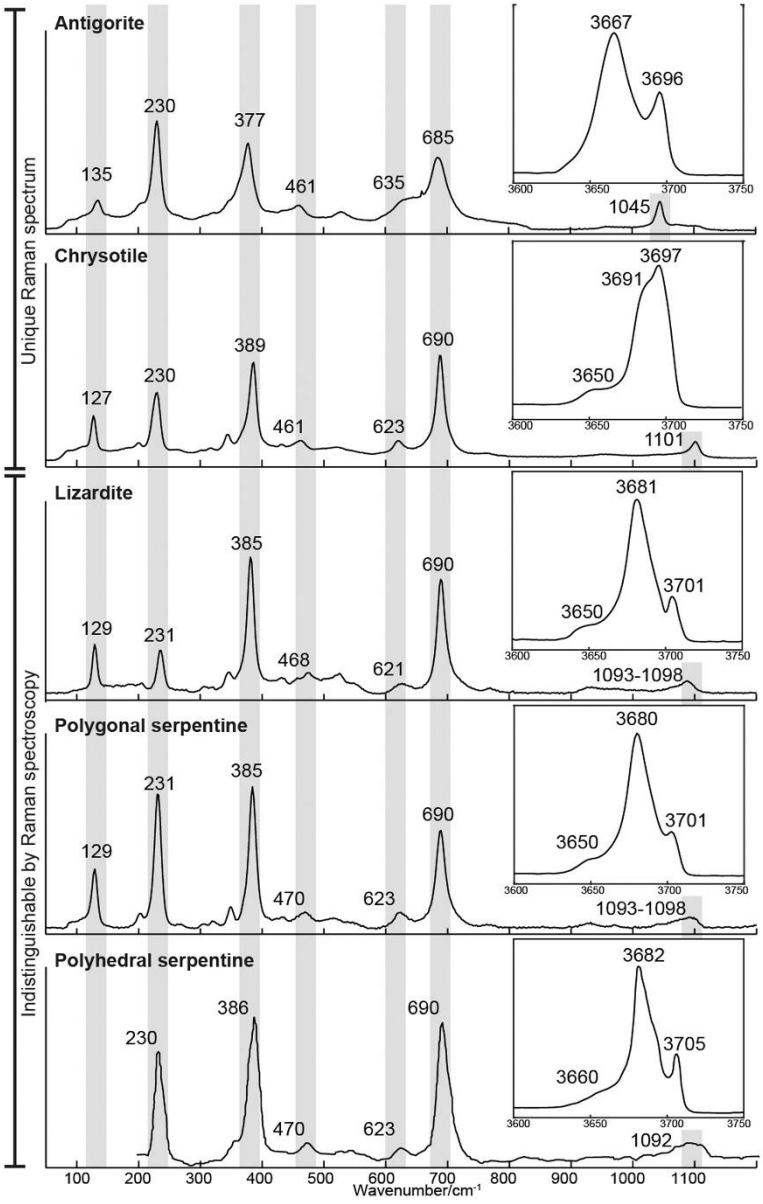

Fig. 3.2 (from Tarling et al., 2018) Type spectra of five varieties of serpentine: antigorite, chrysotile, lizardite, polygonal serpentine, and polyhedral serpentine.

Data acquisition:

Raman spectroscopy was performed at the ISTE Raman spectroscopy facility (University of Lausanne), using a HORIBA Scientific HR Raman-FTIR spectrometer, coupling an Olympus BX41 confocal microscope to an 800 mm focal-length spectrograph. Matrix and vein serpentine were measured on 4 polished thick sections of carbonated serpentinites from the borehole.

Analytical conditions:

The doubled-frequency Nd-YAG continuous-wave laser (532.12 nm wavelength) was focused on the sample surface with a laser power of ca. 1 mW. Prior to each session of measurement, the spectrometer was calibrated using a silicon standard. Excitation volume was only a few mm^3 using a

50x microscope objective, a grating of 1200 groves/mm and a split aperture of 150 µm. Raman signals were accumulated on backscattered mode for 5 acquisitions of 20 s and an exposure time of 10 s, recorded by the LabspecTm software (version 4.14).

Data treatment:

Peaks were identified using the PeakFit software (version 4).

3.3.2 Energy-dispersive X-ray spectroscopy/Electron backscatter diffraction (EDS/EBSD)

Principle:

EBSD analysis (non-destructive method) is realized by focussing high energy electrons (stationary beam) on a tilted flat solid surface (70°), hence inducing diffraction of electrons. The diffracted electrons are captured by a fluorescence (or phosphorous) screen (EBSD detector), forming electron backscattered patterns at its surface (EBSP, or backscatter Kikushi pattern – BKP), captured in real time by a video camera (Fig. 3.3a). EBSP patterns (Fig. 3.3b) are characteristic of both crystallographic structure and orientation. Coupling an EDS detector allows semi-quantitative chemical mapping of the investigated area.

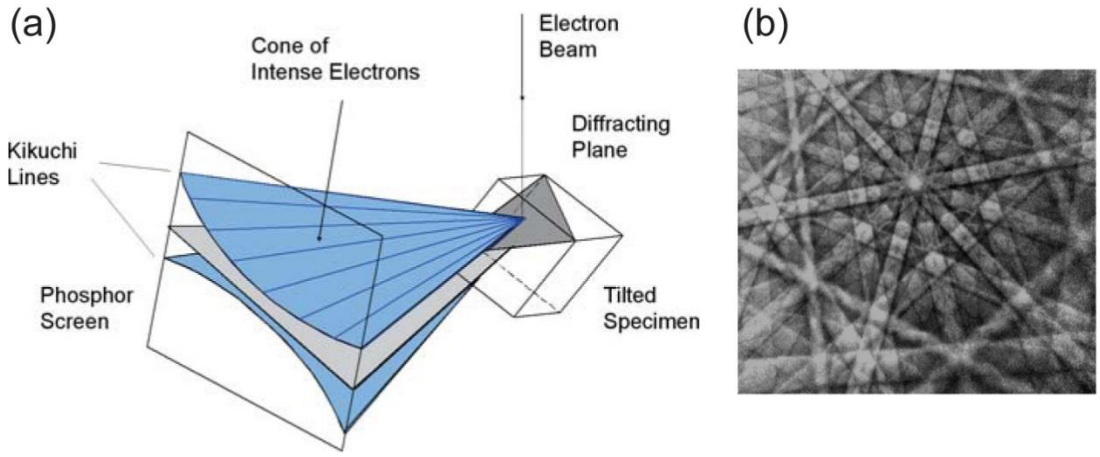

Fig. 3.3 (from Schwartz et al., 2009) (a) Simplified scheme representing an electron beam interacting with a tilted specimen, inducing electron diffraction captured by a phosphorous screen (from Schwartz et al., 2009). (b) Electron backscattered Kikushi pattern of cadmium (20 kV), acquired by video camera.

Data acquisition:

SEM-EDS and EBSD analyses were performed at the Géosciences Montpellier SEM-EBSD facility using a CamScan CrystalProbe X500FE Scanning Electron Microscope, equipped with UltimMax 100 EDS and CMOS Symmetry EBSD detectors. Chemical mapping, mineral characterization, and measurement of mineral crystallographic properties were carried out a subset of 12 polished thin sections (10 listvenites, 1 carbonated serpentinite and 1 serpentinized harzburgite).

Analytical conditions:

Mapping was acquired on tilted thin sections (70°) under low vacuum (2 Pa), at a working distance of 25 mm, an acceleration voltage of 20 kV, and a probe current of 10 nA. Step size varies from 0.5 to 1.2 μm. Data were recorded using the Oxford Instrument AZtecHKL software. Phases were indexed after the ICSD reference database.

Data treatment:

Phase indexation based on EDS data for magnesite and dolomite, removal of wild spikes, filling of non-indexed pixels (according to 8, 7 and 6 neighbouring pixel orientations), and grain boundary modelling (10° segmentation angle) was carried out with HKL Channel5 software (Tango application). Calculation of orientation distribution functions and plotting of orientation maps were achieved using Mambo application.

3.4 Major element geochemistry

3.4.1 X-ray fluorescence (XRF)

Principle:

XRF relies on measuring the spectral dispersion of XR photons generated after radiation of a glass bead or pressed pellet by XR photons. Irradiating XR photons are produced by a rhodium anode in an XR tube oriented toward the sample surface (under vacuum). Interaction between the sample and high energy photons causes the ejection of electrons from low energy levels in excited atoms, replaced by electrons from higher energy orbitals. Electronic rearrangement generates the emission of XR photons ("fluorescence"), which energy is characteristic of specific electron orbital transition in a particular element. Emitted XR photons are aligned into a primary collimator (optical instrument) prior to reach an analysing crystal diffracting X-rays into characteristic wavelengths for each chemical element present. Flow proportional and scintillation counters are the detectors used to measure the intensity of photon arrivals.

Data acquisition:

XRF was carried out at the IACT Instrumental Analysis facility (University of Granada) using a wavelength dispersive BRUKER S4 Pioneer XRF spectrometer, equipped with a rhodium anode X-ray tube (60 kV, 150 mA). Major oxides (SiO_2, TiO_2, Al_2O_3, Fe_2O_3, MnO, MgO, CaO, Na_2O, K_2O, P_2O_5) and few trace elements (V, Cr, Ni, Zn, Rb, Sr, Y, Zr, Ba, Pb) were quantified on fused glass beads and pressed pellets for all regional samples.

Sample preparation and analytical conditions:

LOI (loss on ignition) was determined after calcination of dried powders at 1000°C. The ignited powders were mixed with lithium tetraborate and fused using a FLUXANA-HD-ELEKTRONIK Vulcan

4M to produce glass beads. Pressed pellets were prepared using an automatic hydraulic press NANNETTI MIGNON S. Spectral dispersion was measured using (i) two collimators (0.23° and 0.46°), (ii) Pb, Cu, and Al beam filters, and (iii) OVO-55, LiF200 and PET analyser crystals. Photon arrivals were detected and converted into measurable electrical signals by a flow proportional counter for light elements and a scintillation counter for heavy elements.

Data treatment:

Data were acquired and processed using the SPECTRAplus software solution. The empirical calibration for major and trace elements was based on a set of 20 and 25 geostandard materials, respectively. Precision is better than 0.2-0.3 wt% for major elements (Na_2O: 0.5 wt%). Detection limits of trace elements were 2-4 ppm depending on the element (10-15 ppm for Ba and Co).

3.4.2 Iron oxidation state and partitioning

The bulk oxidation state of iron (Fe^{2+}, Fe^{3+}) and partitioning between minerals have been investigated on rock powders by chemical titration and Mössbauer spectroscopy, respectively.

Fe-titration

Principle:

Fe-titration by potentiometry allows to determine the concentration of electrolytes in solution by measuring the potential difference between indicator and reference electrodes. Abundances of electrolytes are determined by adding titrants of known concentration leading to changes in ionic concentrations till the equivalent point.

Data aquisition:

Bulk rock FeO_{TOT} analyses were carried out by potentiometry at the SARM-CRPG (Nancy, France) for a subset of rock powders including 6 listvenites, 6 fuchsite-bearing listvenites, 2 carbonated serpentinites, and 1 serpentinized harzburgite.

Sample preparation and analytical conditions:

Analyses were performed by automatic titration at the equivalent point with potassium dichromate after dissolution of the rock powder in a HF/H_2SO_4 mixture, in the presence of H_3BO_3 and H_3PO_4.

Data treatment:

Bulk Fe^{3+}/Fe_{TOT} ratios were calculated from the measured bulk $Fe_2O_{3\,TOT}$ (determined in Godard et al., 2021) and FeO_{TOT} values.

Mössbauer spectroscopy

Principle:

Mössbauer spectroscopy relies on the nuclear resonance phenomena ("Mössbauer effect"). In details, ^{57}Co decay to ^{57}Fe generates the emission of γ photons, condensed by a collimator towards an "absorber", here the sample (Fig. 3.4). Absorption of incident photons by ^{57}Fe nuclei in the sample produces "transmitted" γ photons (recoil-free transmission) measured by a detector.

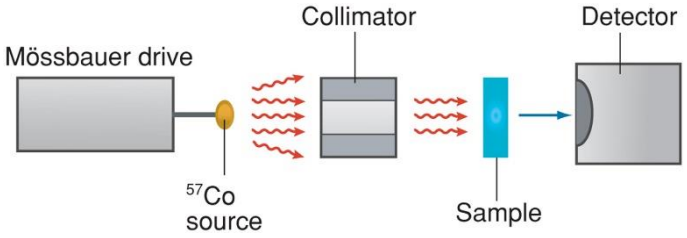

Fig. 3.4 (from Dyar et al., 2006) Simplified sketch of the instrumentation used for transmission Mössbauer spectroscopy.

To acquire a Mössbauer spectrum, the source is moving: from negative (away from sample) to positive (towards the sample) relative Doppler velocity, allowing to define levels of transmission ("%Transmission" in Fig. 3.5). Peaks in a Mössbauer sprectrum are defined by minima in transmission, attained at maximal absorption energy levels. Hence the Mössbauer spectrum of a mineral is composed of a set of characteristic peaks, generally doublets (2 peaks) or sextets (6 peaks) with specific spectral parameters: the isomer shift (IS), the quadrupole split (QS) and the magnitude of magnetic hyperfine field (B_{hf}).

Data acquisition:

Mössbauer spectroscopy was performed on a subset of 52 rock powders at the Institute Charles Gerhardt (University of Montpellier) to quantify iron oxidation state and partitioning between mineral phases. 15 samples from Hole BT1B and 37 samples from Fanja were analysed.

Analytical conditions:

Mössbauer spectra were acquired at room temperature on ~300 mg of powder using a ^{57}Co source in rhodium metal in constant acceleration mode. The spectrometer was operated using a triangular velocity waveform. Transmitted γ photons were measured by a NaI scintillation detector. In order to measure the hyperfine interaction field, spectra were acquired in the -10 to +10 mm/s velocity range. Detection limit is ~2 %.

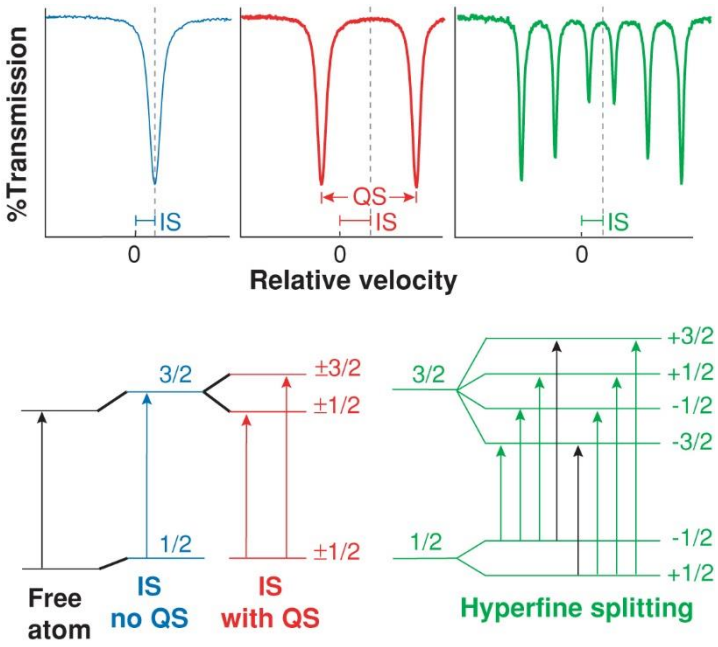

Fig 3.5 (from Dyar et al., 2006) Type transmission spectrum as a shift of the minimum away from zero velocity; this shift is generally called isomer shift (IS).

Data treatment:

Mössbauer spectra were fitted with a combination of Lorentzian lines using optimization code "Fullham". Spectral parameters (IS, QS and B_{hf}) of the best fit were compared to literature values (Table 3.2) for assessing spectral components to minerals and quality control.

>> **Table 3.2** Reference values of the isomer shift (IS), electric quadrupole splitting (QS), and magnitude of magnetic hyperfine field (B_{hf}) for minerals observed in serpentinized and carbonated peridotites. IS and QS values are in mm/s and B_{hf} in T. All IS values are referenced to the midpoint of an α-Fe spectrum.

Mineral	Fe^{2+}			Fe^{3+}			References
	IS mm/s	QS mm/s	B_{hf} T	IS mm/s	QS mm/s	B_{hf} T	
Cr-spinel	0.96 0.90	0.50 1.15		0.32 0.22	0.44 0.91	- -	Kuno et al. (2000)
Magnetite	0.67	0.00	46.0	0.26	-0.20	49.0	Preferred values from Dyar et al. (2006)
Hematite				0.37	-0.20	51.8	Preferred values from Dyar et al. (2006)
Goethite				0.37	-0.26	38.2	Murad and Johnston (1987)
Siderite	1.22	1.80					Preferred values from Dyar et al. (2006)
Ankerite	1.23	1.50					Preferred values from Dyar et al. (2006)
Lizardite	1.14	2.70					O'Hanley and Dyar (1998)
				0.40	0.70		
				0.24	0.39		
Chrysotile	1.13	2.75					O'Hanley and Dyar (1998)
				0.31	0.86		
				0.18	0.33		
Forsterite	1.14	2.93					Preferred values from Dyar et al. (2006)
Diopside	1.16	1.87					DeGrave & Eeckhout (2003)
	1.15	2.14					
Talc	1.13	2.57					Coey et al. (1991)
	1.12	2.15					
Fuchsite	0.95	3.09		0.11	0.87		Drago et al. (1977)

3.4.3 Elemental analysis (EA)

Principle:

Elemental analysis (EA) of carbon is performed by analysing gas-carried CO_2 produced by the flash dynamic combustion of a powder in a high temperature oxidation reactor (T = 1800 °C) and separated in a chromatographic column. Accurate determination of carbon concentration and isotope ratio is obtained by measuring CO_2 masses 44, 45 and 46 using an isotope ratio mass spectrometer (IRMS) connected to the column outlet.

Data aquisition:

Non-carbonate carbon (NCC), $\delta^{13}C_{NCC}$, total carbon (TC), $\delta^{13}C_{TC}$ were determined by combusting tin-capsulated powders using a FlashEA 1112 elemental analyser coupled to a ThermoFisher Scientific Delta + XP continuous-flow IRMS.

Sample preparation and analytical conditions:

For the NCC measurement, 300-500 mg of powder were previously digested by 30-50 ml of HCl 6N over 24 hours at ambient temperature, then heated at 110 °C during 3 hours for enhanced digestion. Residual powders were cleaned using distilled water to avoid acidic contamination during EA and finally

dried overnight at 60°C. Helium and oxygen were used as carrier gases. Typical amounts of encapsulated powder were ~15-30 mg for NCC analysis and ~0.5-3 mg for TC analysis of carbonated peridotites. Carbon concentrations and isotope ratios were calibrated by measuring internal reference materials, namely graphite ($\delta^{13}C_{VPDB}$ = -23.309 ‰), CAP ($\delta^{13}C_{VPDB}$ = -29.978 ‰), and LC ($\delta^{13}C_{VPDB}$ = -18.416 ‰).

Data treatment:

Data were corrected using standard linearity mass equation of graphite, and real value correction after graphite, CAP and LC. For external control of precision and accuracy, Tyrosine reference material (δ^{13}C V-PDB = -23.23 ‰) was analysed alongside samples. It provided a RSD value of 5.32% for carbon concentration and a mean analytical error of 0.19 ‰ for $\delta^{13}C_{VPDB}$ (n = 6).

3.4.4 Electron probe micro-analysis (EPMA)

Principle:

The major element chemistry of minerals was quantified using an electron probe micro-analyser, an instrument allowing to acquire: i) high-resolution quantitative analyses of minerals by wavelength-dispersive spectroscopy (WDS); ii) elemental maps by energy-dispersive spectroscopy (EDS); and iii) high-resolution images by back-scattered electron (BSE) imaging. The instrument is composed of four main devices: i) an electron source; ii) electro-magnetic optics in the instrument column to shape an electron beam; iii) a sample chamber under vacuum conditions; iv) detectors in the chamber array. EPMA analysis is performed by measuring the arrivals of X-ray photons (produced alongside Auger electrons) after bombardment of solid material by an accelerated electron beam.

Data aquisition:

The major element compositions of carbonates, silicates (serpentine, fuchsite), oxides and sulfides using a Cameca SX100 (Géosciences Montpellier) and a JEOL JXA-8530F HyperProbe (ISTE, University of Lausanne, Switzerland) electron microprobe. Operating conditions for silicates were an acceleration voltage of 15 kV, a probe current of 10 nA at Géosciences Montpellier and of 15 nA at ISTE, and a defocussed beam (10 μm) to prevent damage/devolatilization of the analysed phase. Carbonates were analysed in similar conditions except for a reduced beam size at ISTE (3-5 μm). For oxides and sulfides, the probe current was increased to 20 nA and the beam was focussed. It was eventually increased to 2 μm to measure large, homogeneous chromite or hematite grains ensuring current stability. Elemental mapping was performed at ISTE, using an acceleration voltage of 15 kV, a probe current of 20 nA, and a defocussed beam (2 μm). Step size was 1 μm and dwell times 100 ms.

Data treatment:

Quantification of elemental maps. Quantification of elemental maps was achieved by computing X-ray intensities and in-situ chemistry data through XMapTools 3.4.1 MatLab toolbox (Lanari et al., 2014,

2019), with internal standardization based on punctual EPMA analyses. Precision and detection limits of EPMA analyses are given in Appendix.

3.5 Trace element geochemistry

3.5.1 Q-ICP-MS

Principle:

Bulk rock trace element concentrations were quantified on dilute samples using a quadrupole inductively coupled plasma mass spectrometer (Q-ICP-MS). This instrument is equipped with four main devices: i) a sample introduction system including an autosampler, a nebulizer and a spray chamber, ii) a plasma torch, iii) a quadrupole mass analyser, and iv) a series of detectors. During analysis, Ar-mediated nebulized particles are conveyed to an Ar plasma hence becoming ionized. The resulting ion beam is focussed and collimated by cones and ion lenses, prior to entering a collision-reaction cell. Ions are then separated in the quadrupole mass analyser depending on their mass-to-charge ratio, and finally collected by detectors (dynodes) converting particle arrivals into measurable electrical signals.

Data aquisition:

Trace element compositions (Li, Sc, Ti, V, Mn, Co, Ni, Cu, Zn, Ga, As, Rb, Sr, Y, Zr, Mo, Cd, Sn, Sb, Nb, Cs, Ba, REE, Hf, Ta, Tl, Pb, Th, U) were quantified using an Agilent 7700X Q-ICP-MS at Géosciences Montpellier (AETE-ISO, OSU OREME, University of Montpellier). All regional samples (n = 48) were analysed.

Sample preparation and analytical conditions:

Prior to analysis, rock powders were brought into solution after $HClO_4$-HF digestion following the procedure of Ionov et al. (1992). In details, ~100 mg of powder were first dissolved by 1 ml $HClO_4$ and 2.5 ml HF in closed Savillex teflon digestion vessel and refluxed on a hot plate at 100ºC for 24 hours, followed by evaporation at 150°C. Residues were then dissolved by 0.5 ml $HClO_4$ and 1 ml HF, refluxed at 100ºC for 24 hours, followed by evaporation at 150°C. Finally, samples underwent a successive three-step digestion-evaporation cycle by adding 0.5 ml, 0.25 ml, and 0.25 ml $HClO_4$, respectively. Evaporation temperature was increased between each digestion step. Dry residues were brought into solution to a total dilution factor of 1000 for altered peridotites and 2000 for gabbros, metabasalts and metasediments. For external control of precision and accuracy, reference materials, namely DTS-2b (dunite), JP-1 (peridotite), UB-N (serpentinite), BIR-1 (basalt), BHVO-2 (basalt), OU-6 (slate) and COQ-1 (carbonatite) were prepared and analysed alongside samples (see Table 3.3)

Analyses were processed following the measurement protocol described in Godard et al. (2000). In addition to samples and reference materials, the analytic procedure involved the measurement of (i) chemical blanks for monitoring contamination during sample preparation, (ii) an instrumental blank for

instrumental calibration, (iii) internal standard solutions with determined In-Bi concentrations for monitoring instrumental contamination, analytical drift and sensibility, and (iv) external calibration solutions. Most elemental concentrations were determined using the external calibration. The helium cell gas mode of the instrument allowed avoiding most polyatomic interferences during particle transport.

Data treatment:

Concentrations of Eu, Gd, Tb, Dy, Ho, Er, Tm, Yb, Lu and Hf had to be recalculated using correction factors (Table 3.4). Concentrations of Nb and Ta were calibrated with internal standards based on Zr and Hf concentrations after the calibration method of Jochum et al. (1990). Each ICP-MS measurement is an average of three runs, with precision determined by the standard deviation. The analysis uncertainty was estimated for each sample using an error propagation approach, accounting for the precision of the measurements of (i) the instrumental blank, (ii) procedural blanks, and (iii) the sample analysis. Analyses with concentrations (i) below the instrument detection limit, (ii) for which the contribution of the procedural blank is > 70%, or (iii) having uncertainties >50 % were not considered.

Mass	Element	Blank	DTS-2b (dunite)				JP-1 (peridotite)				UB-N (serpentinite)			
		Measured (n=10)	Measured (n=4)	SD	Pref. Val.	Accuracy	Measured (n=5)	SD	Pref. Val.	Accuracy	Measured (n=8)	SD	Pref. Val.	Accuracy
		ppm	ppm	ppm	ppm	%	ppm	ppm	ppm	%	ppm	ppm	ppm	%
7	Li	0.01	1.93	0.30	1.98	2.52	1.53	0.12	1.68	8.74	25.8	2.24	26.9	4.21
9	Be	n.d.	n.d.	n.d.	-	n.d.	n.d.	n.d.	0.01	n.d.	0.06	n.d.	-	n.d.
45	Sc	0.00	2.90	0.31	3.37	13.8	7.26	0.44	7.42	2.15	12.7	1.02	13.1	3.37
47	Ti	0.09	37.8	2.98	42.9	11.7	22.4	n.d.	20.2	10.7	589	45.7	574	2.72
49	Ti	0.10	44.4	19.8	42.9	3.72	20.4	1.49	20.2	1.15	626	50.2	574	9.12
51	V	0.01	17.6	5.55	19.6	9.96	27.1	1.34	25.5	6.33	69.4	6.86	68.9	0.80
55	Mn	0.30	759	62.2	830	8.57	896	74.03	867	3.38	938	78.2	945	0.71
59	Co	0.02	123	10.8	133	7.75	118	7.25	112	4.80	105	10.0	99.3	5.70
62	Ni	0.58	3785	n.d.	3902	2.99	2371	180	2420	2.02	2010	160	1944	3.44
65	Cu	0.08	2.53	0.23	3.06	17.2	4.74	0.68	4.99	5.06	26.3	2.82	26.6	1.25
66	Zn	4.02	43.3	8.98	47.2	8.21	48.1	3.85	43.2	11.3	86.5	11.1	84.0	2.99
71	Ga	0.00	0.77	0.20	0.93	17.1	0.54	0.03	0.50	8.75	2.76	0.26	3.02	8.80
75	As	0.02	0.22	0.06	0.09	157	0.38	0.03	0.32	17.4	10.8	0.96	10.7	0.18
85	Rb	0.01	0.03	0.01	0.03	7.06	0.30	0.01	0.35	14.7	3.21	0.19	3.63	11.7
88	Sr	0.19	0.53	0.02	0.37	44.6	0.85	0.29	0.61	38.9	7.75	0.67	8.07	3.94
89	Y	0.001	0.03	0.004	0.04	9.23	0.10	0.01	0.09	7.29	2.53	0.18	2.55	0.83
90	Zr	0.01	0.14	0.02	0.20	29.2	5.71	0.28	5.41	5.55	3.57	0.19	3.72	4.25
93	Nb	0.001	0.01	0.002	0.02	36.7	0.05	0.02	0.04	20.4	0.05	0.004	0.06	12.1
95	Mo	0.00	0.03	0.003	0.07	56.2	0.14	0.02	0.13	0.67	0.36	0.03	0.39	7.24
111	Cd	0.01	0.01	n.d.	0.003	205	0.01	n.d.	0.01	18.8	0.03	0.02	0.05	45.0
118	Sn	0.05	0.59	0.05	0.65	9.40	0.03	0.01	0.04	27.1	0.31	0.07	0.33	6.47
123	Sb	0.01	0.74	n.d.	0.54	38.1	0.05	0.01	0.04	25.2	0.30	0.24	0.20	46.7
133	Cs	0.001	0.00	0.0002	0.01	80.8	0.04	0.003	0.04	7.16	11.4	0.71	11.0	3.60
138	Ba	0.17	13.5	n.d.	11.7	15.4	11.1	0.28	10.3	7.65	25.0	2.50	26.3	5.07
139	La	0.002	0.01	0.002	0.01	11.7	0.04	0.01	0.03	7.57	0.30	0.02	0.33	9.05
140	Ce	0.003	0.03	0.003	0.02	3.00	0.08	0.02	0.06	18.7	0.76	0.04	0.81	6.53
141	Pr	0.0002	0.003	0.0004	0.003	7.89	0.01	0.001	0.01	8.23	0.11	0.01	0.12	5.19
146	Nd	0.001	0.01	0.002	0.01	2.67	0.04	0.004	0.03	6.69	0.59	0.04	0.61	3.86
147	Sm	0.0002	0.003	0.0005	0.003	5.86	0.01	0.0005	0.01	1.07	0.21	0.01	0.22	2.76
151	Eu	0.00003	0.001	0.0002	0.001	1.98	0.002	0.0002	0.002	8.55	0.08	0.01	0.08	1.20
157	Gd	0.0003	0.003	0.0005	0.004	12.9	0.01	0.001	0.01	9.84	0.32	0.02	0.32	2.13
159	Tb	0.00003	0.001	0.0001	0.001	19.2	0.002	0.0003	0.002	2.19	0.06	0.004	0.06	0.31
163	Dy	0.0002	0.01	0.001	0.005	6.66	0.02	0.001	0.02	3.71	0.43	0.03	0.42	3.44
165	Ho	0.00004	0.001	0.0003	0.001	5.21	0.004	0.0003	0.004	3.79	0.10	0.01	0.09	4.47
167	Er	0.0001	0.01	0.001	0.005	10.5	0.01	0.001	0.01	2.14	0.29	0.02	0.28	3.00
169	Tm	0.00001	0.001	0.0001	0.001	4.30	0.003	0.0001	0.002	8.55	0.04	0.003	0.04	1.04
173	Yb	0.0001	0.01	0.001	0.01	19.8	0.02	0.002	0.02	7.21	0.30	0.02	0.29	4.17
175	Lu	0.00002	0.002	0.0003	0.002	17.0	0.004	0.0003	0.004	8.10	0.05	0.003	0.05	1.58
178	Hf	0.0004	0.005	0.001	0.01	10.2	0.15	0.01	0.12	18.7	0.13	0.01	0.12	9.40
181	Ta	0.00003	0.001	0.0002	0.001	45.8	0.00	0.001	0.004	23.1	0.02	0.003	0.02	14.9
203	Tl	0.0003	0.001	0.0002	0.001	27.1	0.002	0.001	0.002	1.70	0.04	0.003	-	n.d.
208	Pb	0.043	3.94	0.61	3.90	1.05	0.09	0.01	0.10	5.07	12.68	0.97	13.2	3.60
232	Th	0.0003	0.004	0.0003	0.003	23.8	0.01	0.001	0.01	6.66	0.05	0.004	0.07	28.3
238	U	0.0003	0.002	0.0002	0.002	21.5	0.01	0.002	0.01	9.51	0.05	0.01	0.06	17.0

Table 3.3 Concentrations of blanks and reference materials by ICP-MS analysis. Preferred concentrations values of reference materials are compiled from literature data (GeoRem database; Jochum et al., 2005), and used for quality control ("Accuracy" calculated as the absolute error in percent between measurements and preferred vaues)

Mass	Element	Blank	BIR-1 (basalt)				BHVO-2 (basalt)				OU-6 (slate)			COQ-1 (carbonatite)		
		Measured (n=10)	Measured (n=8)	SD	Pref. Val.	Accuracy	Measured (n=4)	SD	Pref. Val.	Accuracy	Measured (n=1)	Pref. Val.	Accuracy	Measured (n=1)	Pref. Val.	Accuracy
		ppm	ppm	ppm	ppm	%	ppm	ppm	ppm	%	ppm	ppm	%	ppm	ppm	%
7	Li	0.01	3.43	0.33	3.20	7.09	4.25	0.08	4.50	5.54	94.3	95.3	1.04	3.45	-	n.d.
9	Be	n.d.	n.d.	n.d.	-	n.d.	1.14	n.d.	1.08	6.14	n.d.	2.53	n.d.	n.d.	1.20	n.d.
45	Sc	0.00	43.3	2.95	43.21	0.28	30.8	2.52	31.8	3.21	20.0	23.1	13.6	1.07	3	64.2
47	Ti	0.09	6302	188	5746	9.67	15262	n.d.	16368	6.76	n.d.	5934	n.d.	n.d.	899	n.d.
49	Ti	0.10	5977	416	5746	4.03	17188	1549	16368	5.01	5493	5934	7.42	655	899	27.2
51	V	0.01	352.3	28.0	321	9.90	331	35.5	318	3.87	127	130	2.24	143	110	30.1
55	Mn	0.30	1309	106	1341	2.33	1284	97.6	1309	1.88	1972	2168	9.05	3408	3330	2.34
59	Co	0.02	53.9	4.33	52.2	3.20	44.9	4.06	44.9	0.01	28.2	29.2	3.41	2.62	-	n.d.
62	Ni	0.58	173	17.9	169	2.20	118	1.17	120	1.33	40.1	40.2	0.30	0.40	13	96.9
65	Cu	0.08	123	10.3	121	1.80	131	10.5	129	1.46	40.0	40.4	0.95	2.96	-	n.d.
66	Zn	4.02	74.3	7.04	70.4	5.52	105	9.98	104	1.48	116	111	3.92	96.7	87	11.1
71	Ga	0.00	16.0	1.36	15.5	3.52	23.1	2.19	21.4	7.89	25.3	24.17	4.61	37.5	6	525
75	As	0.02	0.12	0.03	0.17	30.8	1.09	0.12	0.70	55.5	14.2	13.23	7.39	7.71	-	n.d.
85	Rb	0.01	0.19	0.02	0.21	11.4	8.94	0.34	9.26	3.51	116	121.30	4.08	13.7	-	n.d.
88	Sr	0.19	108	8.02	109	0.93	411	21.4	394	4.32	130	131.70	1.48	11482	12000	4.32
89	Y	0.001	15.3	1.09	15.6	1.96	25.3	1.19	25.9	2.41	22.7	27.75	18.1	82.9	81	2.29
90	Zr	0.01	15.5	1.10	14.8	4.53	180	4.62	171	4.97	154	174.20	11.6	50.6	65	22.1
93	Nb	0.001	0.63	0.04	0.55	13.7	20.3	3.75	18.1	12.1	16.7	14.49	15.6	3207	3900	17.8
95	Mo	0.00	0.05	0.01	0.07	25.8	2.86	1.83	4.07	29.6	0.47	-	n.d.	6.90	7	6.7
111	Cd	0.01	0.05	0.02	0.10	43.7	0.08	n.d.	0.09	14.4	n.d.	-	n.d.	n.d.	-	n.d.
118	Sn	0.05	0.72	0.05	0.70	3.27	1.95	0.22	1.78	9.55	2.53	2.67	5.09	0.32	-	n.d.
123	Sb	0.01	0.53	0.07	0.46	13.8	0.16	0.09	0.10	57.2	0.56	0.56	0.35	0.20	-	n.d.
133	Cs	0.001	0.01	0.003	0.01	33.8	0.10	0.002	0.10	2.52	7.66	8.10	5.41	0.15	-	24.9
138	Ba	0.17	6.44	0.25	6.75	4.59	136	5.17	131	3.66	448	480	6.66	1106	1000	10.6
139	La	0.002	0.59	0.05	0.63	6.54	14.8	0.41	15.2	2.54	29.8	33.2	10.2	812	750	8.33
140	Ce	0.003	1.85	0.14	1.92	3.78	36.9	0.95	37.5	1.81	70.9	77.1	8.08	1684	1700	0.93
141	Pr	0.0002	0.36	0.03	0.37	2.30	5.23	0.15	5.34	2.08	7.22	7.91	8.67	144	150	3.69
146	Nd	0.001	2.34	0.19	2.40	2.52	24.1	0.62	24.3	0.64	27.3	30.2	9.69	450	480	6.34
147	Sm	0.0002	1.08	0.08	1.11	2.59	5.97	0.23	6.02	0.85	5.37	6.01	10.6	51.3	56	8.43
151	Eu	0.00003	0.53	0.04	0.52	1.00	2.06	0.08	2.04	0.68	1.20	1.36	11.7	13.9	15	7.13
157	Gd	0.0003	1.89	0.14	1.81	4.37	6.22	0.19	6.21	0.18	4.66	5.30	12.1	30.9	50	38.3
159	Tb	0.00003	0.36	0.03	0.36	0.72	0.92	0.04	0.94	2.22	0.71	0.86	16.9	3.69	4	7.83
163	Dy	0.0002	2.64	0.22	2.54	3.95	5.33	0.20	5.28	0.94	4.35	5.06	14.0	17.6	18	2.30
165	Ho	0.00004	0.59	0.05	0.57	3.64	0.99	0.04	0.99	0.01	0.88	1.04	15.5	2.95	3	1.52
167	Er	0.0001	1.72	0.14	1.68	2.20	2.48	0.09	2.51	1.05	2.60	2.93	11.2	7.60	7	8.59
169	Tm	0.00001	0.25	0.02	0.26	0.39	0.33	0.01	0.33	0.97	0.39	0.45	13.1	1.01	-	n.d.
173	Yb	0.0001	1.68	0.15	1.63	3.29	1.95	0.12	1.99	2.07	2.53	2.98	15.3	5.80	6	3.30
175	Lu	0.00002	0.26	0.02	0.25	3.18	0.27	0.01	0.28	1.20	0.39	0.45	13.4	0.79	-	n.d.
178	Hf	0.0004	0.67	0.04	0.58	14.9	4.98	0.16	4.47	11.36	4.27	4.70	9.19	0.20	-	n.d.
181	Ta	0.00003	0.04	0.01	0.04	8.39	1.15	0.29	1.15	0.54	0.97	1.02	5.33	32.9	-	n.d.
203	Tl	0.0003	0.003	0.001	-	n.d.	0.03	0.01	0.02	26.9	0.53	0.54	1.54	0.08	0.10	19.1
208	Pb	0.043	3.21	0.27	3.04	5.83	1.91	0.23	1.65	15.8	28.8	28.8	0.04	4.30	-	n.d.
232	Th	0.0003	0.03	0.003	0.03	12.2	1.15	0.05	1.22	6.43	9.21	11.3	18.5	9.72	10	2.76
238	U	0.0003	0.01	0.002	0.01	1.31	0.42	0.02	0.41	2.21	1.97	1.92	2.81	12.7	11	15.5

Table 3.3 (continued)

Element	Polyatomic interference	Correction factor
^{151}Eu	^{151}Eu= I(151) - ^{135}BaOH - ^{134}BaOH	(Eu/Ba)
^{157}Gd	I(157) - ^{141}PrO - ^{134}CeOH	(Gd-Gd/Pr*Pr)/Ce et (Gd/Pr)
^{159}Tb	I(159) - ^{143}NdO - ^{142}NdOH	(Tb/Nd)
^{163}Dy	I(163) - ^{147}SmO - ^{146}NdOH	(Dy-Dy/Sm*Sm)/Nd and (Dy/Sm)
^{165}Ho	I(165) - ^{149}SmO - ^{148}SmOH - ^{148}NdOH	(Ho-Ho/Sm*Sm)/Nd and (Ho/Sm)
^{167}Er	^{167}Er = I(167) - ^{151}EuO	Er/(Eu-Eu/Ba*Ba)
^{169}Tm	^{169}Tm = I(169) - ^{153}EuO	Tm/(Eu-Eu/Ba*Ba)
^{174}Yb	^{173}Yb = I(173) - ^{157}GdO	Yb/(Gd-Gd/Pr*Pr-Gd/Ce*Ce)
^{175}Lu	^{175}Lu = I(175) - ^{159}TbO	Lu/(Tb-Tb/Nd*Nd)
^{178}Hf	^{178}Hf = I(178) - ^{162}DyO	Hf/(Dy-Dy/Sm*Sm-Dy/Nd*Nd)

Table 3.4 Summary of polyatomic interferences and correction factors for rare elements from Eu to Lu and Hf. I(x) is the intensity measured on the mass x.

3.5.2 Laser ablation – inductively coupled plasma mass spectrometry (LA-ICP-MS)

Principle:

Minor and trace element compositions of minerals were determined by LA-ICP-MS. The analytical equipment includes 4 main devices: i) a laser ablation system; ii) an ion source (Ar plasma torch); iii) a mass spectrometer; iv) detectors. Minerals are ablated by a pulsated laser beam in a He-mediated ablation cell. Ablated particles are conveyed by He-Ar-N_2 flux to an Ar plasma torch, where they become ionized. Ionized particles are filtered in a collision cell, then separated into a quadrupole as function of mass-to-charge ratios.

Data aquisition:

Trace element compositions of minerals were determined by LA-ICP-MS over 4 sessions of measurements. A first batch of analyses was performed at ISTE (University of Lausanne), using a ThermoScientific Element XR mass spectrometer interfaced to a New Wave ArF 193 nm laser. The other batches of analysis were carried out at Géosciences Montpellier (AETE-ISO, OSU OREME), using a ThermoScientific Element 2 mass spectrometer coupled to an Excimer G2 193 nm laser.

Sample preparation and analytical conditions:

At ISTE, spot diameter for analysis was 85–100 µm, with on-sample energy density of 7 J/cm^2 and a repetition rate of 12 Hz for carbonates and spinel, while 20 Hz for serpentine and fuchsite. Data were collected in time resolved acquisition mode, with 120 s dedicated to background signal measurement followed by 45 s of sample ablation. Instrument mass bias was calibrated by 30 measurements of NIST SRM 612 reference material (synthetic glass). Calibration was controlled by 10 measurements of BCR-2G reference material (basaltic glass). At GM, spot diameter for analysis was 110 µm (pre-ablated at 130 µm), with on-sample energy density of 6 J/cm^2 and a repetition rate of 7 Hz, to avoid contamination of neighbouring crystal grains to the ablation spot. Data were collected in time resolved acquisition

mode, with 120 s dedicated to background signal measurement followed by 40 s of sample ablation. Instrument mass bias was calibrated by 26 measurements of NIST SRM 612 reference material. Calibration was controlled by 18 measurements of BIR-1G reference material (basaltic glass).

Data treatment:

Raw data were processed using the data reduction software Glitter (Griffin et al., 2008) using the linear fit to ratio method. CaO and SiO_2 content obtained by EPMA analysis was used as internal standard for quantification of carbonates and silicates compositions. Detection limits, and the values obtained for certified rock materials NIST SRM 612, BIR-1G and BCR-2G are given in Table 3.5.

		ISTE							
		NIST SRM 612 (synthetic glass)				BCR-2G (basalt glass)			
Mass	Element	Average (n=30)	SD	Pref. val.	Diff.	Average (n=10)	SD	Pref. val.	Diff.
		ppm	ppm	ppm	%	ppm	ppm	ppm	%
7	Li	41.54	0.35	40.20	3.34	9.68	0.82	9.00	7.59
9	Be	32.71	13.05	37.50	12.77	1.83	0.66	2.30	20.61
11	B	34.76	1.29	34.30	1.35	19.76	4.62	6.00	229
45	Sc	-	-	-	-	-	-	-	-
47	Ti	-	-	-	-	-	-	-	-
49	Ti	-	-	-	-	-	-	-	-
51	V	-	-	-	-	-	-	-	-
53	Cr	-	-	-	-	-	-	-	-
55	Mn	38.43	0.27	38.70	0.70	1597	26	1550	3.01
57	Fe	-	-	-	-	-	-	-	-
59	Co	38.46	0.62	38.80	0.88	14.60	0.58	13.00	12.28
62	Ni	-	-	-	-	-	-	-	-
65	Cu	36.71	0.27	37.80	2.88	17.56	0.48	21.00	16.37
66	Zn	37.92	0.29	39.10	3.01	177	5.19	125	41.52
75	As	-	-	-	-	-	-	-	-
85	Rb	31.63	0.31	31.40	0.73	47.20	0.97	47	0.43
86	Sr	-	-	-	-	-	-	-	-
88	Sr	76.15	0.85	78.40	2.87	323	10.32	342	5.42
89	Y	38.25	0.40	38.30	0.14	30.42	1.07	35.00	13.08
90	Zr	-	-	-	-	-	-	-	-
91	Zr	35.99	0.31	37.90	5.04	154	4.77	184	16.15
93	Nb	38.06	0.35	38.90	2.16	11.46	0.27	12.50	8.30
118	Sb	-	-	-	-	-	-	-	-
119	Sb	-	-	-	-	-	-	-	-
122	Sn	-	-	-	-	-	-	-	-
123	Sn	-	-	-	-	-	-	-	-
133	Cs	41.64	0.20	42.70	2.48	1.09	-	1.16	5.86
137	Ba	37.74	0.66	39.30	3.97	622	23.03	683	8.95
139	La	35.77	0.56	36.00	0.64	23.42	1.03	24.70	5.19
140	Ce	38.35	0.69	38.40	0.13	50.99	2.01	53.30	4.34
141	Pr	37.16	0.64	37.90	1.95	6.25	0.30	6.70	6.69
143	Nd	35.24	0.69	35.50	0.73	26.19	1.25	28.90	9.38
147	Sm	36.72	0.71	37.70	2.59	5.89	0.27	6.59	10.68
151	Eu	34.44	0.68	35.60	3.25	1.76	0.08	1.97	10.65
157	Gd	36.95	0.76	37.30	0.93	5.85	0.36	6.71	12.76
159	Tb	35.92	0.74	37.60	4.46	0.88	0.06	1.02	13.36
163	Dy	35.97	0.79	35.50	1.34	5.70	0.40	6.44	11.49
165	Ho	37.88	0.88	38.30	1.11	1.15	0.08	1.27	9.47
166	Er	37.44	0.85	38.00	1.49	3.20	0.20	3.70	13.57
169	Tm	37.56	0.86	36.80	2.06	0.47	0.03	0.51	7.65
172	Yb	39.96	0.96	39.20	1.93	3.09	0.22	3.39	8.81
175	Lu	37.72	0.97	37.00	1.95	0.46	0.03	0.50	9.48
178	Hf	34.78	1.07	36.70	5.22	4.11	0.33	4.84	15.17
181	Ta	-	-	-	-	-	-	-	-
208	Pb	38.97	1.10	38.57	1.04	10.81	0.60	11.00	1.76
232	Th	37.25	1.10	37.79	1.44	5.37	0.40	5.90	9.05
238	U	37.17	1.19	37.38	0.56	1.67	0.11	1.69	1.37

Table 3.5 Compiled trace element compositions of reference synthetic glass NIST SRM 612 and basaltic glasses BCR-2G and BIR-1G measured by LA-ICP-MS at the Institute of Earth Sciences (ISTE, University of Lausanne) and Géosciences Montpellier. Preferred valued were determined from a compilation of literature data downloaded in July 2022 from the GeoRem database (Jochum et al., 2005; http://georem.mpch-mainz.gwdg.de/). Diff. % is calculated as the error percentage between average measured values and preferred values.

		GM							
		NIST SRM 612 (synthetic glass)				BIR-1G (basalt glass)			
Mass	Element	Average (n=26)	SD	Pref. val.	Diff.	Average (n=18)	SD	Pref. val.	Diff.
		ppm	ppm	ppm	%	ppm	ppm	ppm	%
7	Li	42.09	1.59	40.20	4.71	3.07	0.30	3.00	2.20
9	Be	-	-	-	-	-	-	-	-
11	B	-	-	-	-	-	-	-	-
45	Sc	41.74	2.65	39.90	4.60	43.07	1.92	43.00	0.16
47	Ti	48.77	1.69	44.00	10.85	6569	265	5400	21.64
49	Ti	48.70	1.12	48.10	1.25	6972	242	5400	29.12
51	V	39.66	0.95	38.80	2.22	327	12.56	326	0.28
53	Cr	-	-	-	-	-	-	-	-
55	Mn	-	-	-	-	-	-	-	-
57	Fe	35.70	0.97	35.50	0.57	52.63	1.95	52.00	1.21
59	Co	38.90	0.95	38.80	0.26	175	7.79	178	1.94
62	Ni	37.19	1.30	37.80	1.61	115	5.81	119	3.68
65	Cu	-	-	-	-	-	-	-	-
66	Zn	38.09	1.11	39.10	2.59	88.62	5.41	78.00	13.61
75	As	37.57	1.12	35.70	5.23	0.14	0.06	-	-
85	Rb	32.06	1.34	31.40	2.09	0.21	0.02	0.20	4.20
86	Sr	76.30	1.41	78.40	2.68	103	3.58	109	5.73
88	Sr	77.39	3.97	78.40	1.29	104	4.37	109	4.20
89	Y	39.07	1.76	38.30	2.02	14.19	0.71	14.30	0.74
90	Zr	36.48	1.06	37.90	3.75	12.84	0.53	14.00	8.27
91	Zr	-	-	-	-	-	-	-	-
93	Nb	38.55	0.88	38.90	0.89	0.52	0.02	0.52	0.93
118	Sb	-	-	-	-	-	-	-	-
119	Sb	-	-	-	-	-	-	-	-
122	Sn	38.61	1.12	34.70	11.26	0.56	0.03	0.56	0.73
123	Sn	38.59	0.91	34.70	11.21	0.55	0.03	0.56	1.32
133	Cs	41.80	2.08	42.70	2.12	0.01	0.00	0.01	27.54
137	Ba	38.42	1.81	39.30	2.24	6.06	0.31	6.50	6.71
139	La	36.95	2.01	36.00	2.65	0.60	0.03	0.61	2.03
140	Ce	38.81	1.06	38.40	1.07	1.83	0.07	1.89	3.18
141	Pr	37.55	1.60	37.90	0.93	0.35	0.02	0.37	4.14
143	Nd	36.12	1.77	35.50	1.76	2.28	0.11	2.37	3.68
147	Sm	37.33	1.57	37.70	0.98	1.02	0.06	1.09	6.53
151	Eu	35.03	1.29	35.60	1.61	0.50	0.02	0.52	3.32
157	Gd	37.50	1.76	37.30	0.52	1.68	0.07	1.85	9.23
159	Tb	36.45	1.31	37.60	3.05	0.33	0.02	0.35	7.11
163	Dy	36.50	1.45	35.50	2.82	2.47	0.12	2.55	2.98
165	Ho	38.43	1.43	38.30	0.33	0.54	0.03	0.56	2.70
166	Er	37.98	1.35	38.00	0.05	1.60	0.08	1.70	5.99
169	Tm	38.09	1.30	36.80	3.49	0.24	0.01	0.24	0.02
172	Yb	40.53	1.36	39.20	3.39	1.66	0.07	1.64	1.22
175	Lu	38.23	1.19	37.00	3.32	0.24	0.01	0.25	2.60
178	Hf	35.23	0.95	36.70	4.00	0.51	0.03	0.57	9.82
181	Ta	40.29	1.03	37.60	7.14	0.04	0.00	0.04	1.74
208	Pb	39.42	1.16	38.57	2.20	3.62	0.23	3.70	2.16
232	Th	37.73	1.12	37.79	0.16	0.03	0.00	0.03	3.76
238	U	37.61	1.11	37.38	0.61	0.02	0.00	0.02	28.21

Table 3.5 (continued)

3.6 Stable isotopes geochemistry

3.6.1 Bulk iron and zinc isotopes

Principle:

Iron has four naturally occurring isotopes (Berglund and Wieser, 2011): ^{56}Fe (~91.8 %), ^{54}Fe (~5.8 %), ^{57}Fe (~2.1 %), and ^{58}Fe (~0.3 %). Zinc abundance is distributed between five isotopes (Moynier et al., 2017): ^{64}Zn (~49.2 %), ^{66}Zn (~27.8 %), ^{68}Zn (~18.4 %), ^{67}Zn (~ 4.0 %), and ^{70}Zn (~0.6 %). Over the last two decades, iron and zinc isotopes geochemistry of peridotites has developed into a powerful tool to track geological processes, being sensitive to partial melting, magmatic differentiation and metasomatism. Nowadays, Fe and Zn isotopes are mainly measured using a multiple-collector inductively coupled plasma mass spectrometer (MC-ICP-MS). This device is composed by four main components: i) a sample introduction system, ii) an inductively coupled plasma ion source; ii) an analyser; and iii) a series of collectors. Purified Fe^{3+} and Zn^{2+} in solution are sprayed and conveyed to a plasma source ionizing the nebulized particles. Ions entering the analyser are accelerated and focused to shape a beam via electrostatically charged plates and slits. The magnetic field in the analyser separates ions based on mass-to-charge ratios. Finally, mass-resolved beams are captured by collectors converting ion arrivals into voltage. Isotope ratios are determined by comparing voltages from the different collectors.

Data acquisition:

Iron and zinc isotopes were measured using a ThermoFisher Scientific Neptune Plus at the Institut de Physique du Globe (IPGP, Paris, France). 27 samples (9 listvenites, 6 fuchsite-bearing listvenites, 5 carbonated serpentinites. 1 serpentinized harzburgite, and 6 metabasalts) were analysed.

Sample preparation and analytical conditions:

Between 30 and 40 mg of powder were dissolved following a 3-step successive dissolution procedure using HF-HCl-HNO_3 developed by Debret et al. (2018a). In details, powders were first dissolved by 1.5 ml HNO_3 15.6N in 7 ml PTFE Teflon square digestion vessels with wrench top closures over a day at 120°C to dissolve carbonate phases. 1.2 ml of supernatant solution was collected prior to evaporation at 90 °C. Residues were further digested by 1:1 mixture of concentrated HF-HCl 10N (2 ml + 2 ml), refluxed for 2 days in an oven at 150 °C, then evaporated at 90 °C. Finally, samples were dissolved by "aqua regia" (0.7 ml HNO_3 15.6N + 2 ml HCl 6N), refluxed at 110 °C overnight and evaporated at 90 °C. Studies comparing this method to Parr bomb dissolution techniques (Debret et al., 2018x) have shown that it can digest all refractory phases present in serpentinites, including Cr-spinel. Prior to column chemistry, samples were brought into solution by adding 1 ml of HCl 6N and refluxed on a hotplate at 90°C over a day. Quantitative purification of Fe followed by Zn was realized by chromatographic exchange in columns filled by AG1-X8 anion exchange resin following the procedures

of Sossi et al. (2015) and Maréchal et al. (1999). All reagents used in the chemistry and mass spectrometry procedures were distilled in sub-boiling Teflon two-bottle stills. The total procedural blank contribution was <50 ng of Fe and <15 ng of Zn, which is negligible compared to the amount of Fe and Zn in samples.

Instrumental mass fractionation was corrected using the sample-standard bracketing technique for Fe and Zn following the procedures of Busigny et al. (2014) and van Kooten and Moynier (2019). Solutions consisted of 2 ppm natural Fe or 0.5 ppm natural Zn in 0.5 M HNO_3, which were introduced into the mass spectrometer using a quartz SIS (stable introduction system by ThermoFisher) and PFA 20 ml/min nebuliser, giving an intensity of 12 V for ^{54}Fe and 3 V for ^{64}Zn. Iron isotope ratios are reported as $\delta^{56}Fe$ in permil notation relative to IRMM-014 external standard. $\delta^{57}Fe$ is given to demonstrate mass dependency of the measurements (Fig. 3.6a):

$$\delta^{56}Fe = (({}^{56}Fe/{}^{54}Fe_{sample})/({}^{56}Fe/{}^{54}Fe_{IRMM\text{-}014})\text{-}1) \times 1000$$

$$\delta^{57}Fe = (({}^{57}Fe/{}^{54}Fe_{sample})/({}^{57}Fe/{}^{54}Fe_{IRMM\text{-}014})\text{-}1) \times 1000$$

In addition to all Fe masses, ^{53}Cr and ^{60}Ni were also monitored and an online Cr and Ni correction was applied to account for any isobaric interferences from ^{54}Cr and ^{58}Ni on the ^{54}Fe and ^{58}Fe masses. These corrections were either negligible or non-existent due to the effective separation of Fe from Cr and Ni during column chemistry. An in-house standard of $FeCl_2$ was analysed throughout each analytical sessions giving a mean $\delta^{56}Fe$ value of -0.72 ± 0.04 ‰ and mean $\delta^{57}Fe$ value of -1.04 ± 0.10 ‰ (n = 22), in excellent agreement with previously published measurements of this standard (e.g., Debret et al., 2016). In complement to this internal standard, reference materials, namely JP-1 (peridotite), PCC-1 (peridotite), UB-N (serpentinite), and BHVO-2 (basalt), were processed and analysed together with the samples. The obtained values are in excellent agreement with literature data and are presented in Table 3.6.

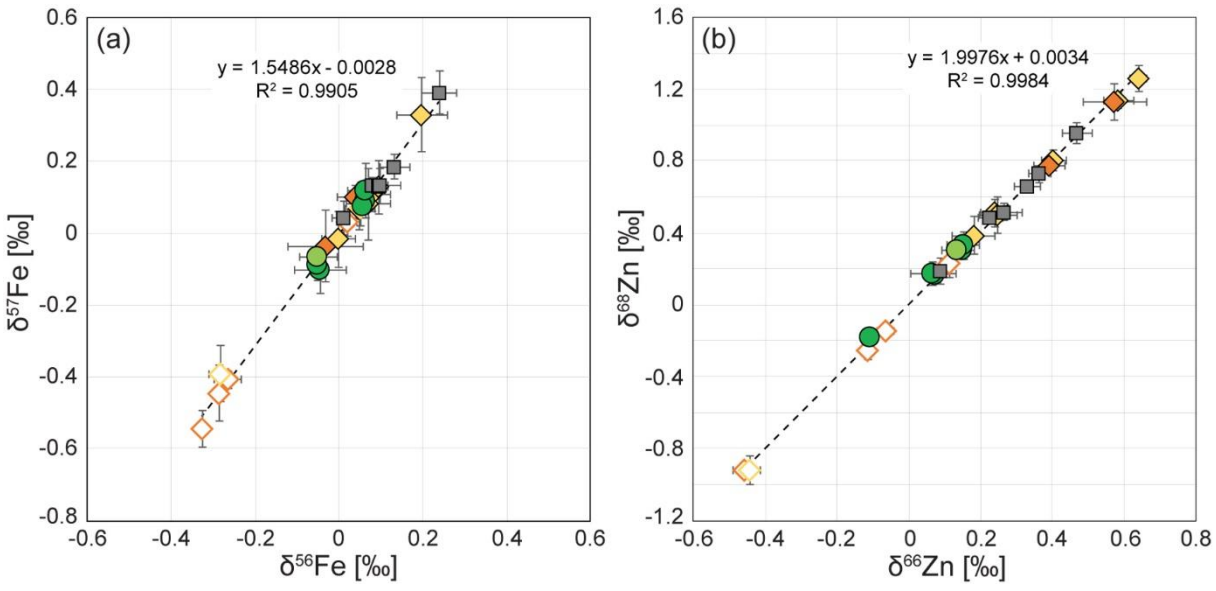

<<**Fig. 3.6** Plots of measured isotope ratios (a) $\delta^{57}Fe$ vs. $\delta^{56}Fe$, and (b) $\delta^{68}Zn$ vs. $\delta^{66}Zn$, showing mass dependency of the measurements.

The Zn isotope composition of samples is presented as $\delta^{66}Zn$ and $\delta^{68}Zn$, to demonstrate mass dependency (Fig 3.6b), in permil notation relative to the JMC-Lyon isotopic standard.

$$\delta^{66}Zn = (({}^{66}Zn/{}^{64}Zn_{sample})/({}^{66}Zn/{}^{64}Zn_{JMC\text{-}Lyon})\text{-}1) \times 1000$$

$$\delta^{68}Zn = (({}^{68}Zn/{}^{64}Zn_{sample})/({}^{68}Zn/{}^{64}Zn_{JMC\text{-}Lyon})\text{-}1) \times 1000$$

Due to a limited supply of the JMC-Lyon standard solution, samples were measured relative to the ETH standard solution. This solution was compared to JMC-Lyon throughout each analytical sessions giving a mean $\delta^{66}Zn$ value of $+0.32 \pm 0.04$ ‰ and a mean $\delta_{68}Zn$ value of 0.59 ± 0.05 ‰ (n = 18). These values are in excellent agreement with previously published measurements of the ETH standard (Archer et al., 2017). The ^{62}Ni mass was monitored to correct for the potential interference of ^{64}Ni on ^{64}Zn. The reproducibility and accuracy of the method were evaluated by analysing the external reference materials JP-1, PCC-1, UB-N, and BHVO-2. The obtained values, in excellent agreement with literature data (Wang et al., 2017; Moynier et al., 2017), are provided in Table 3.6.

Material	$\delta^{56}Fe$		$\delta^{57}Fe$		$\delta^{66}Zn$		$\delta^{68}Zn$		n
	‰	2SD	‰	2SD	‰	2SD	‰	2SD	
BHVO-2	0.098	0.005	0.202	0.062	0.286	0.052	0.588	0.084	5
PCC-1	-0.002	0.048	-0.033	0.040	0.186	0.052	0.365	0.098	5
JP-1	0.038	0.008	0.071	0.056	0.231	0.046	0.465	0.092	5
UB-N	0.038	0.017	0.067	0.033	0.366	0.035	0.735	0.067	5

Table 3.6 Iron and zinc isotopes ratios of reference materials processed and analysed together with samples.

3.6.2 "Micro-bulk" carbon and oxygen isotopes of carbonates

Principle:

Carbon and oxygen isotope compositions of carbonates are determined by measuring helium-mediated CO_2 (masses 44, 45, 46) generated by acid digestion of carbonate powders in sealed vials. CO_2-bearing gases are extracted by a dual viscous flow inlet system. Purification and molecular separation occur through successive transport into diffusion traps (water removal) and a chromatographic column. CO2 is further diluted by helium then conveyed to an isotope ratio mass spectrometer

Data aquisition:

Analyses were performed at IPGP using a Gas Bench II gas sampling system coupled to a ThermoFisher Scientific Delta + XP continuous-flow IRMS. 8 representative thin section billets (4 listvenites, 1 fuchsite-bearing listvenite, 3 carbonated serpentinites) were investigated.

Sample preparation and analytical conditions:

using a New Wave Research MicroMill at IPGP. Typical diameter and depth of single drill spot are 350 μm and 400 μm, respectively, allowing high-resolution sampling. Micro-drilling was performed on various types of matrix and vein carbonates. Drilled areas had been previously investigated by SEM (carbon coating avoided) and punctual EDS analyses to ensure sampling a single carbonate phase. Powders were weighed, then deposited in glass headspace vials with closure caps hosting a PTFE/silicone septum. Vials were flushed with helium using a Gas Bench II on-line gas preparation and introduction system. 10 droplets of 103% H_3PO_4 were injected in vials through the septum using a needle. Vials containing dolomite were heated at 80°C during 16 hours, while at 100°C for magnesite. Carbon and oxygen isotope ratios were calibrated by measuring internal reference materials, namely RII ($\delta^{13}C_{VPDB}$ = -9.77 ‰; $\delta^{18}O_{VPDB}$ = -9.15 ‰), Acros ($\delta^{13}C_{VPDB}$ = 0.26 ‰; $\delta^{18}O_{VPDB}$ = -4.14 ‰), and Merck ($\delta^{13}C_{VPDB}$ = -8.65 ‰; $\delta^{18}O_{VPDB}$ = -6.94 ‰).

Data treatment:

Data were corrected using standard linearity mass equation of RII, and real value correction after RII, Acros and Merck. In addition, $\delta^{18}O_{VPDB}$ was corrected for oxygen isotope fractionation factors of dolomite at 80 °C and magnesite at 100°C (Das Sharma et al., 2002). For external control of precision and accuracy, Reference materials, namely, dolomite Crystal ($\delta^{13}C_{VPDB}$ = 3.14 ‰; $\delta^{18}O_{VPDB}$ = -12.96 ‰), and magnesite MgS III ($\delta^{13}C_{VPDB}$ = -19.713 ‰; $\delta^{18}O_{VPDB}$ = -30.947 ‰) were analysed alongside samples. Crystal provided mean errors of 0.10 ‰ for $\delta^{13}C_{VPDB}$ and 0.32 ‰ for $\delta^{18}O_{VPDB}$ (n = 2). MgS III returned mean absolute errors of 0.05 ‰ for $\delta^{13}C_{VPDB}$ and 0.29 ‰ for $\delta^{18}O_{VPDB}$ (n = 4).

Chapter 4: Field relationships, petrography and mineralogy of listvenites and associated lithologies

4.1 Field observations

4.1.1 MoD Mountain and Site 1 (Wadi Mansah)

The MoD mountain in Wadi Mansah forms the anticlinoria of a kilometric, gently-dipping open fold exposing listvenites series on its summit, interlayered by alternating bands of serpentinized dunite, harzburgite and lherzolite on the meter to decameter scale (Fig. 4.1). The mantle section (< 250 m thick) is overlying a largely outcropping metamorphic sole due to low dip angle of lithological layering. The metamorphic sole close to the drill site is composed, from top to bottom, of quartzites or amphibolites (sample OM20-03) at the contact with the ophiolite mantle, on top of (carbonated) metabasalts (OM20-01 and -02), then siliceous cherts.

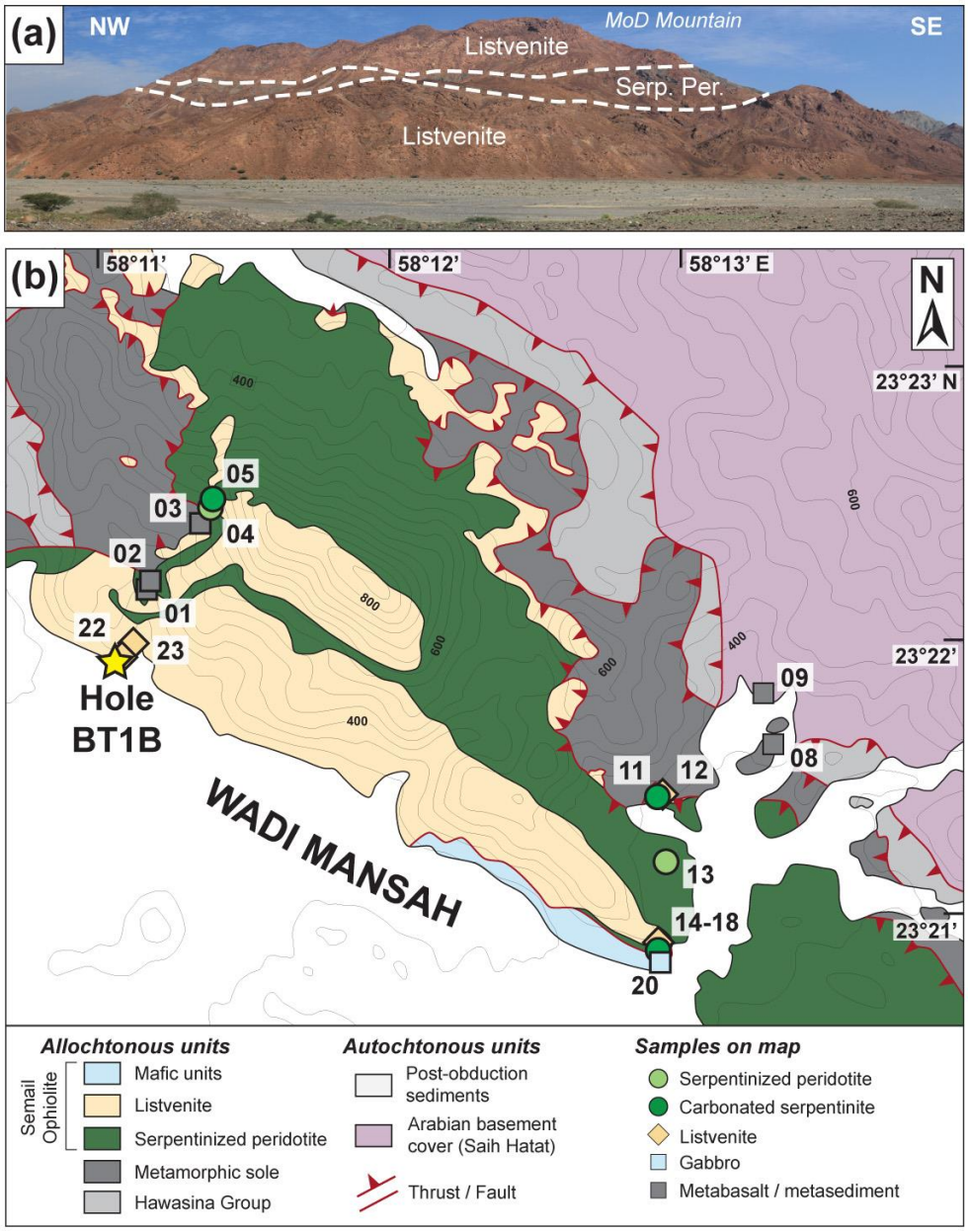

<< **Fig. 4.1** Geological map of the MoD mountain (western part) and Site 1 (eastern part) areas modified after Villey et al. (1986) and Kelemen et al. (2022), and personal observations. Sample location is indicated by a number referring to the nomenclature OM20-n (see the list of samples in Appendix). The location of Hole BT1B is indicated by a yellow star.

Listvenite occur as dm- to hm-thick tabular sheets dipping at low angle on the southern flank of the mountain (listvenite-serpentinite contact: 104/25, GPS: 23°22'5.24"N, 58°11'6.83"E). Listvenite sheets are oriented parallel to the contact with the basal thrust and to peridotite banding. Transition from massive peridotite to carbonated serpentinite and listvenite is generally marked by the development of an intense foliation (1-20 m thick; Fig. 4.2). Serpentinized peridotites are locally cut by late carbonates veins and cataclasites reworking clasts of peridotite.

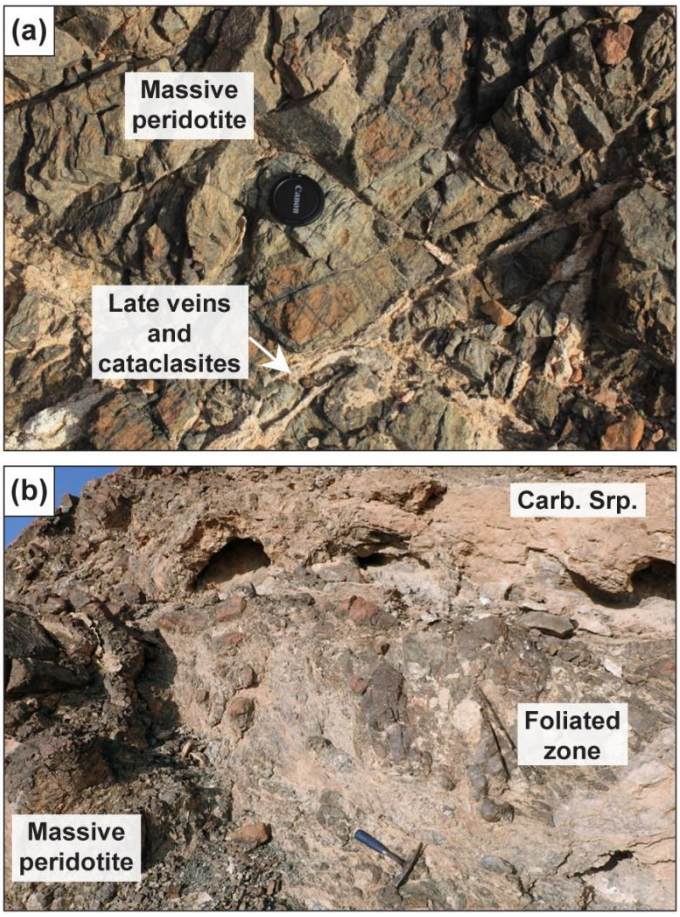

Fig. 4.2 Field photographs illustrating the lithological evolution from massive serpentinites, locally cut by late carbonates veins and cataclasites (a), to carbonated serpentinite. The lithological transition is marked by the development of an intense foliation (b).

Collected samples include one sample of serpentinized peridotite (OM20-04) and one carbonated serpentinite (OM20-05) picked close to the mountain ridge, and two listvenites (OM20-22, -23) from outcrops flooring the wadi close to Hole BT1B (Fig. 4.3).

Fig. 4.3 Samples of metasomatized peridotites collected at the MoD mountain.

Site 1 is located in the south-eastern part of Wadi Mansah. In contrast to the drilled sequence in Hole BT1B, the mantle section there is thicker (>250 m) and composed principally of massive, slightly serpentinized harzburgites and rare dunites. The underlying metamorphic sole comprises a sequence including, from top to bottom, mafic-derived rocks, shales and siliceous cherts. Listvenites are highly weathered and are found (i) atop the metamorphic sole to the North, where they form a discontinuous thin layer (~2-10 m) in contact with the main basal thrust, and below ~20 m of foliated and fractured carbonated serpentinites; and (ii) interlayered in carbonated serpentinites close to the faulted mantle–gabbros contact to the South (Fig. 4.4). All these lithological boundaries dip to the South (contact metamorphic sole–listvenites: 178/57, GPS: 23.357223°N, 58.219827°E; contact listvenites–carbonated serpentinites: 188/46; GPS: 23.345901°N, 58.221218°E). In the southern part, listvenites form a 10-50 m thick interlayer bordered by foliated and fractured carbonated serpentinites, 5-10 m away from the faulted contact with foliated gabbros. Stain orange-red listvenites host discontinuous millimetric to centimetric white quartz-carbonate veins oriented at high angle with the lithological contact. Fault contacts between listvenites, serpentinites and gabbro are highly variable, ranging from serpentinites fault gouge to foliated serpentinites, with sharp localized faults. Close to gabbros, carbonated serpentinites host scarce gabbroic dikelets (<10 cm thick) or pods. Below listvenites, ~25-50 m of foliated serpentinites show pervasive matrix replacement by carbonates.

Collected samples at Site 1 (Fig. 4.5) include one serpentinized harzburgite (OM20-13), four carbonated serpentinites (OM20-11, -16, -17, and -18), and three listvenites (OM20-12, -14, -15).

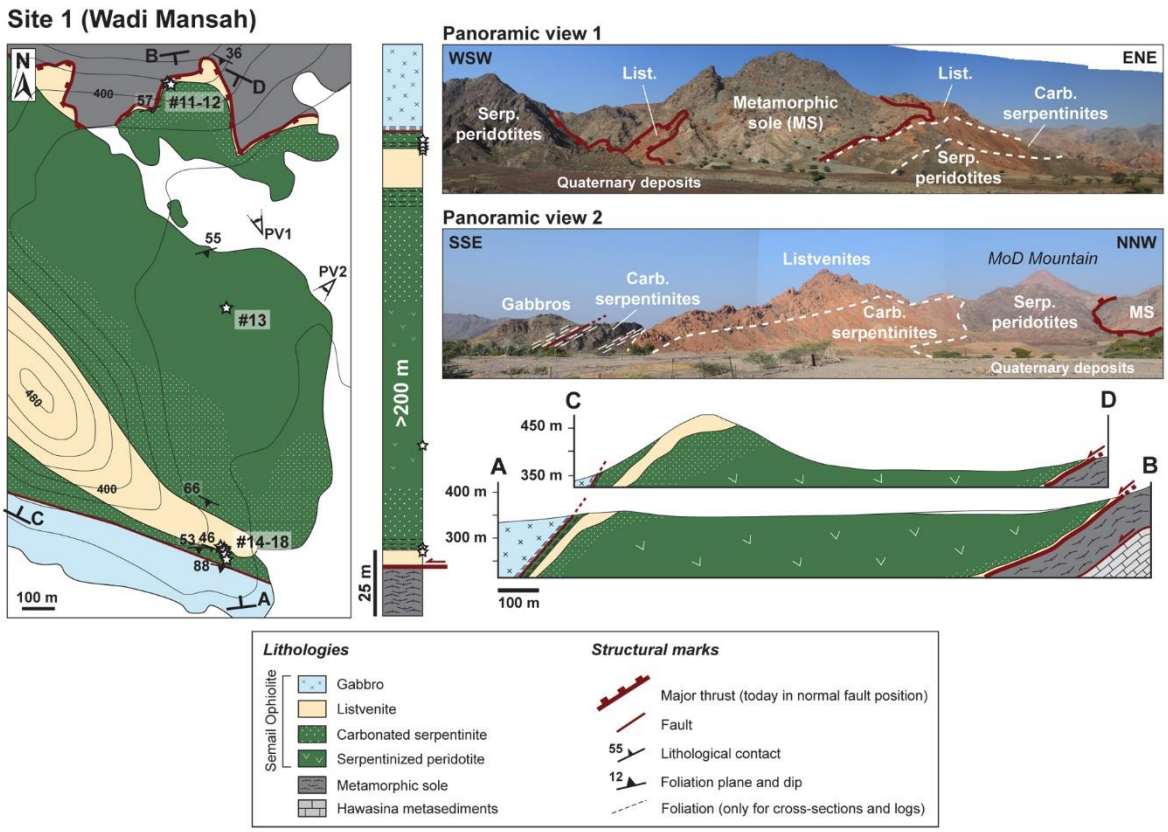

Fig. 4.4 Detailed geological map, lithological column, cross-section and field photographs for Site 1 (Wadi Mansah). The detailed map was drawn after Villey et al. (1986) and field observations The location of samples is indicated by white stars; adjacent numbers refers to sample names. The lithological column was constructed from cross-sections (A-B and C-D). The thickness of lithological layers was calculated perpendicular to the metamorphic sole. Field photographs illustrate the panoramic views (PV1 and PV2) of the investigated transect.

Fig. 4.5 Samples of metasomatized peridotites collected at Site 1.

4.1.2 Sites 2 and 2b (Jebel Fanja)

Site 2 is located in the north-eastern part of the Jebel Fanja (Fig. 2.5; GPS: 23°26'54.68"N, 58°12'6.47"E). This area is characterized by a mantle section (150-200 m thick) exposing often foliated and fractured serpentinized peridotites (~100 m thick), interlayered by bands of listvenites close to overlying lower crustal gabbros (Fig. 4.6). Serpentinized Cpx-harzburgites (~100 m thick) overly the metamorphic sole comprising a sequence composed of, from top to bottom, mafic-derived schists, locally amphibolites along the basal thrust (GPS: 23.447692°N, 58.202856°E), shales and micaschists. In this studied site, all lithological boundaries dip to the NNW (contact serpentinite–sole: 337/60; GPS: 23.446848°N, 58.203809°E; contact listvenite–carbonated serpentinite: 352/28, GPS: 23.448760°N, 58.202344°E). Two transects were investigated (cross-sections A-B and C-D).

Listvenites occur as a kilometre-scale tabular sheet draping the ridge and the southern flank of Jebel Fanja (~50-75 m), and as plurimetric lenses bordered by carbonated serpentinites. Massive stain orange-red listvenites are cut by closely spaced sub-millimetric red carbonate veins and by pluri-millimetric white quartz-carbonate veins, all being oriented perpendicular to the southern contact with underlying carbonated serpentinites (~3-20 m, Fig. 4.7). These latter are foliated close to listvenites, hosting millimetric to centimetric light orange carbonate veins, oriented sub-parallel to the contact. Vein density increases towards the serpentinites-listvenites contact. Few millimetric red carbonate veins cut through both listvenites and carbonated serpentinites. Listvenites to the North are overlain by deformed serpentinized peridotites (>20 m) crosscut by numerous gabbroic dikes and pods at proximity with gabbros.

Site 2b is located westwards compared to Site 2 (GPS: 23°26'28.66"N, 58°10'10.78"E). The investigated area shows a similar lithological sequence from sole to top of the mantle section (ca. 200 m thick), except being overlain by Cretaceous conglomerates of the Al Khod Formation westwards and by Paleogene platform carbonates of the Hadhamaut Group eastwards. The contact between with these lithologies was not investigated- Listvenites form a tabular sheet (10–<50 m thick) overlain by serpentinized peridotites hosting gabbroic intrusions (<25 m thick), and underlain by tectonized carbonated serpentinites over ca. 15 m.

Collected samples at Sites 2 and 2b (Fig. 4.8) include four serpentinized harzburgite (OM20-28, -32, -34, -35), four carbonated serpentinites (OM20-26, -30a, -30b, and -38), and four listvenites (OM20-25, -29, -31, -39).

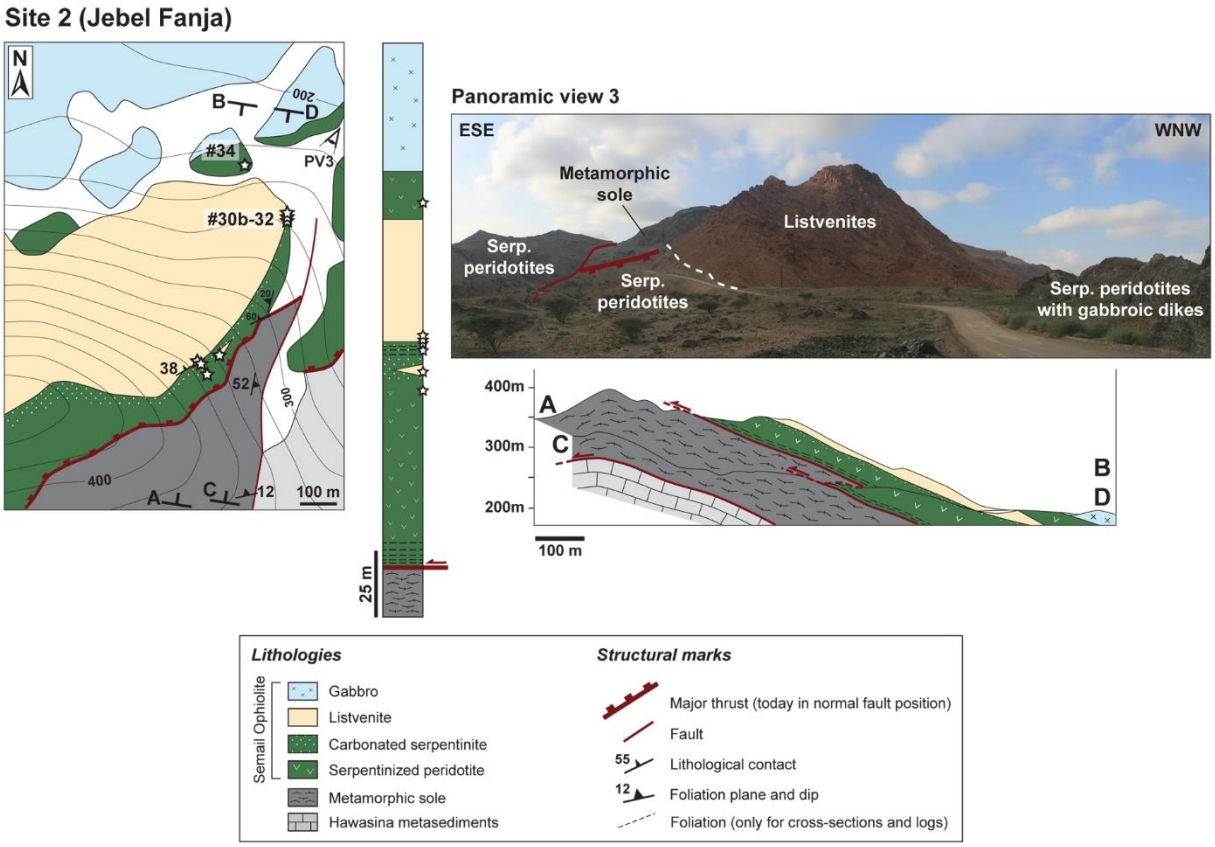

Fig. 4.6 Detailed geological map, lithological column, cross-section and field photographs for Site 2 (Jabal Fanja). The detailed map was drawn after Villey et al. (1986) and field observations The location of samples is indicated by white stars; adjacent numbers refers to sample names. The lithological column was constructed from cross-sections. The thickness of lithological layers was calculated perpendicular to the metamorphic sole. The field photograph illustrates a panoramic view (PV3) of the investigated transect.

4.1.3 Site 3 (Jabal Qarn)

Site 3 is located north-west of the village of Fanja (GPS: 23°28'22.33"N, 58°4'38.77"E). Investigations were carried on the flanks of the Jabal Qarn (Fig. 4.9). This area presents a complete sequence from lower layered gabbroic crust atop of a mantle section (> 200 m thick) interlayered by a thick tabular sheet of listvenite, and underlain by the metamorphic sole.

The ophiolite mantle overlies a metamorphic sole composed, from bottom to top, of alternating calcareous schists and shales, mafic-derived material, quartzites, and paragneisses below the basal thrust. Its thickness varies greatly laterally (10-75 m). The mantle section is composed of massive serpentinized peridotites, hosting subordinate pyroxenites, rare metric bands of fully serpentinized dunites, and gabbroic intrusions close to mantle–gabbro contact. Listvenites are found as: i) a main NW-SE-trending tabular sheet (50-100 m thick) forming the mountain ridge (Fig. 4.10a) and pinched eastwards; ii) as a metric, discontinuous, highly altered layer at the contact with the basal thrust. The listvenite sheet is dipping gently to NE.

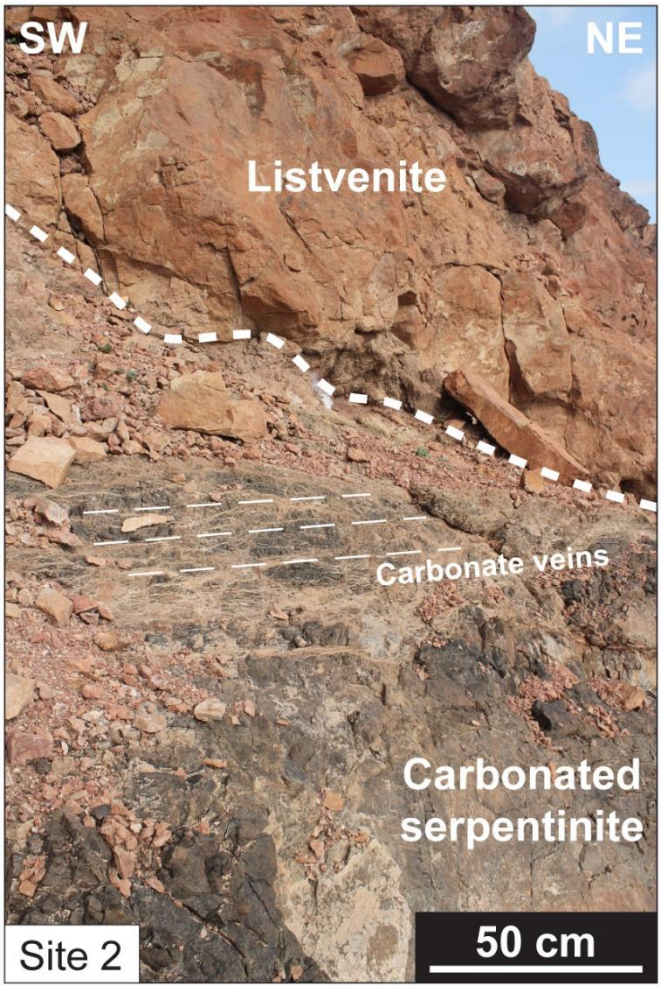

Fig. 4.7 Field photograph at Site 2 illustrating the transition from foliated carbonated serpentinites to massive listvenites. Carbonated serpentinites host magnesite veins oriented at low angle to the lithological contact, with vein density increasing towards listvenites.

The transition between listvenites and carbonated serpentinites is characterized by the development of an intense foliation within serpentinite (ca. 4 m thick, see Fig. 4.10b). The foliation is oriented similarly to the lithological boundary (045/40; GPS: 23°28'17.23"N, 58°4'42.58"E) and to that of the mantle–sole contact (320/28, GPS point: 23°28'6.46"N, 58°4'40.38"E). Carbonation of serpentinite is intense in the shear zone and progressively decrease over a distance of ca. 10 m (Fig. 4.10b-c), mainly occur along fractures (Fig. 4.10c and d). Poorly-carbonated serpentinites display an alternation between levels showing a thin banding delineated by parallel strings of magnetite and flattened mesh (Fig. 4.10d), and highly-fractured domains (4.10e). Gabbros are layered with decametric intervals alternating between mesocratic and troctolitic textures. The contact between gabbros and listvenites at the eastern termination of the Jabal Qarn likely corresponds to a high-angle normal fault.

Fig. 4.8 Samples of metasomatized peridotites collected at Sites 2 and 2b.

Collected metasomatized mantle rocks (Fig. 4.10e) include: one sample of pyroxenite (OM20-46), 2 samples of poorly carbonated serpentinite (OM20-45b, -45c), two listvenites (OM20-44c, -45a) from the tabular sheet and one from the layer at the basal thrust (OM20-45d).

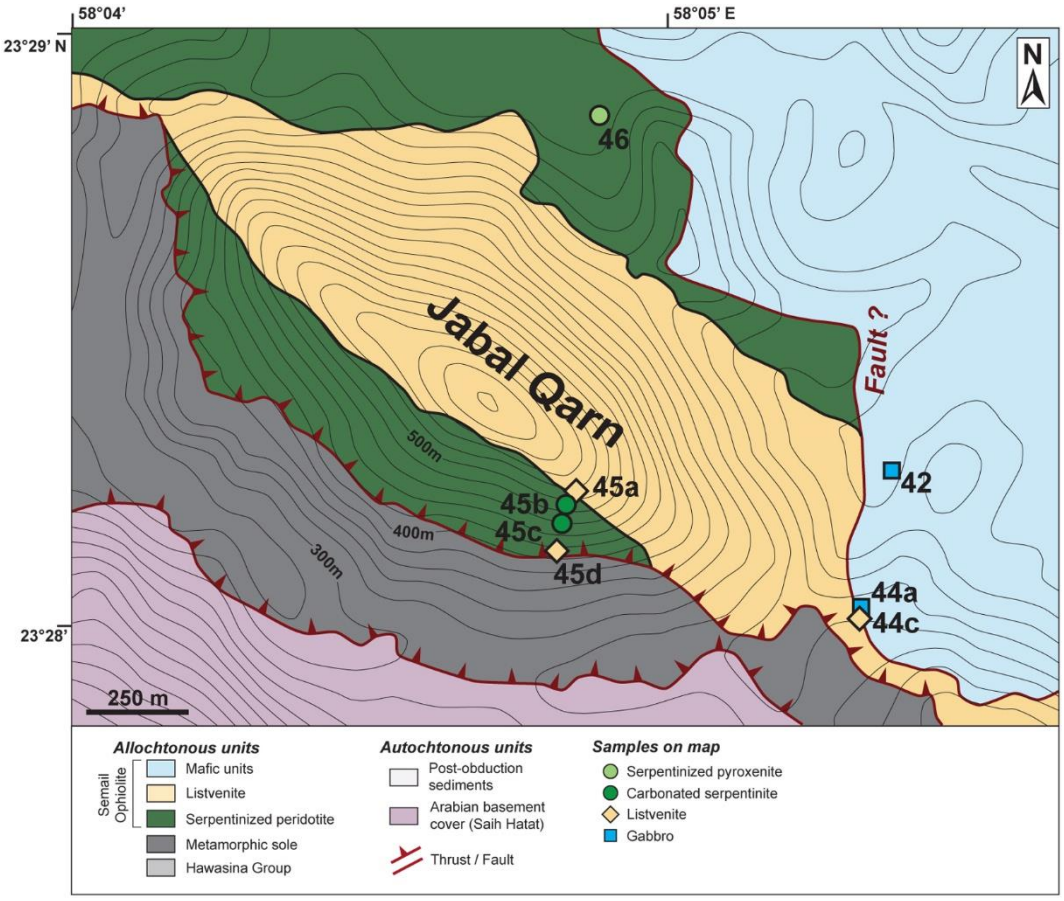

Fig. 4.9 Geological map of Site 3 alongside the Jebel Qarn, north-west of Fanja, modified after Villey et al. (1986). Sample location is indicated by a number referring to the nomenclature OM20-n (see the list of samples in Appendix).

>> **Fig. 4.10** Field and sample photographs, including: (a) a panoramic view of the Jabal Qarn ridge; (b) a photograph of the foliated contact between listvenite and carbonated serpentinites, (b-d) textural aspects of variously carbonated serpentinites; (e) collected metasomatized peridotites.

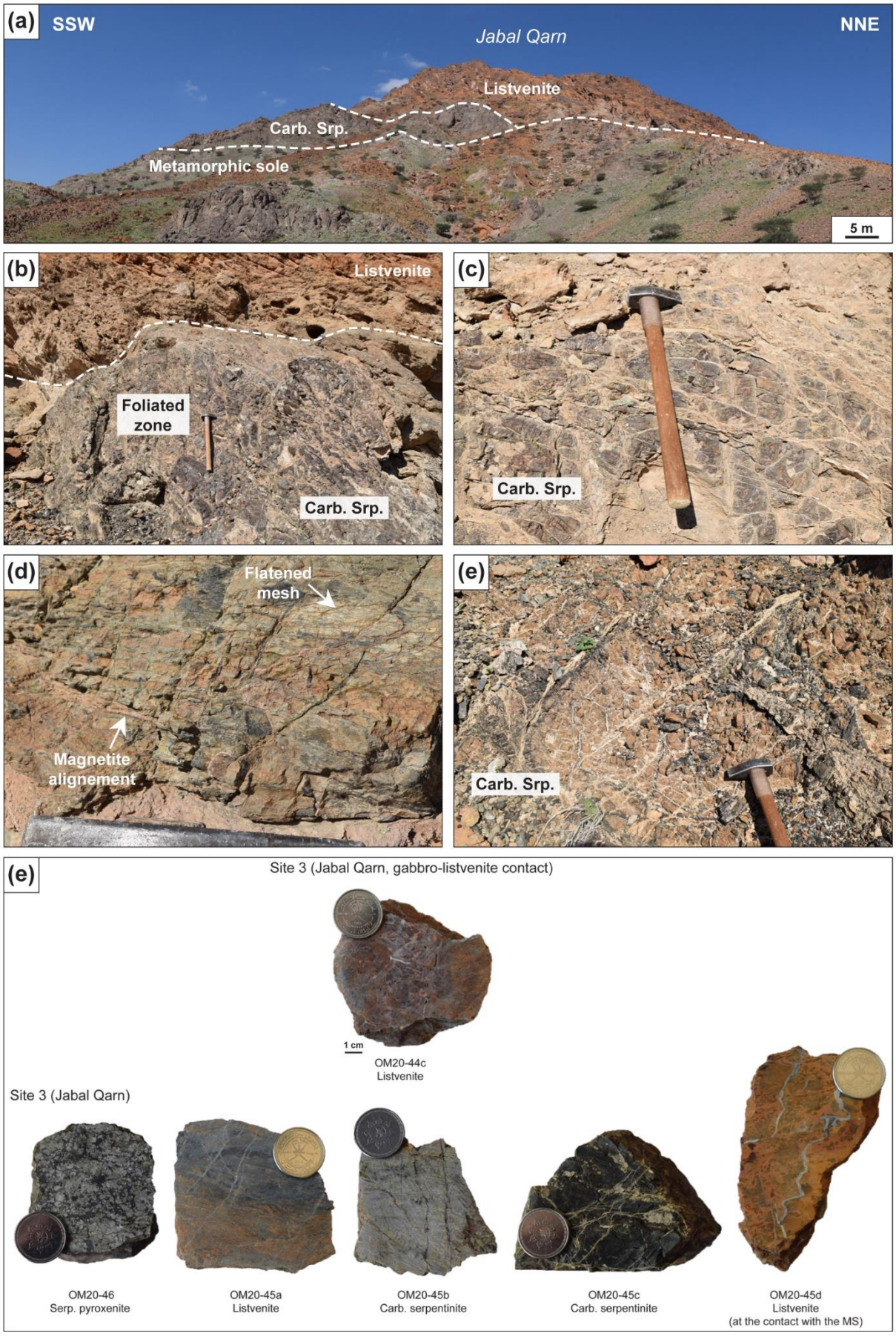
(a)
SSW
Jabal Qarn
NNE
Listvenite
Carb. Srp.
Metamorphic sole
5 m
(b)
Listvenite
Foliated zone
Carb. Srp.
(c)
Carb. Srp.
(d)
Flatened mesh
Magnetite alignement
(e)
Carb. Srp.
(e)
Site 3 (Jabal Qarn, gabbro-listvenite contact)
1 cm
OM20-44c
Listvenite
Site 3 (Jabal Qarn)
OM20-46
Serp. pyroxenite
OM20-45a
Listvenite
OM20-45b
Carb. serpentinite
OM20-45c
Carb. serpentinite
OM20-45d
Listvenite
(at the contact with the MS)

4.1.4 Site 4 (Jabal Nakhl)

Site 4 is the located on the south-eastern flank of the Jabal Nakhl (Fig. 4.11). Investigations were carried on two areas presenting a sequence from gabbroic crust atop of the mantle section (~200 m thick) underlain by the metamorphic sole to the East, and by autochthonous sediments to the West. The contact between the gabbro and the mantle section is likely faulted. All lithological layers dip to the South.

The ophiolite mantle is often foliated and tectonized, overlying a metamorphic sole composed, from top to bottom, of quartzites, sometimes in brecciated, and amphibolites. Its thickness varies greatly laterally, being pinched out to the West. The mantle section is composed of serpentinized peridotites, foliated at the contact with the sole (290/30, GPS: 23°23'55.79"N; 58°2'51.20"E) and with listvenite (162/50; GPS: 23°23'59.51"N, 58°2'52.06"E). Transition from carbonated serpentinite to listvenite is occur within over a distance less than 20 m. Listvenites are found as: i) a main W-E-trending tabular sheet (50-100 m thick) forming the mountain ridge (Fig. 4.12) at the contact with gabbros. On the western side of the area, birbirite interlayering listvenite and fuchsite-bearing listvenite were observed close to the ophiolite base.

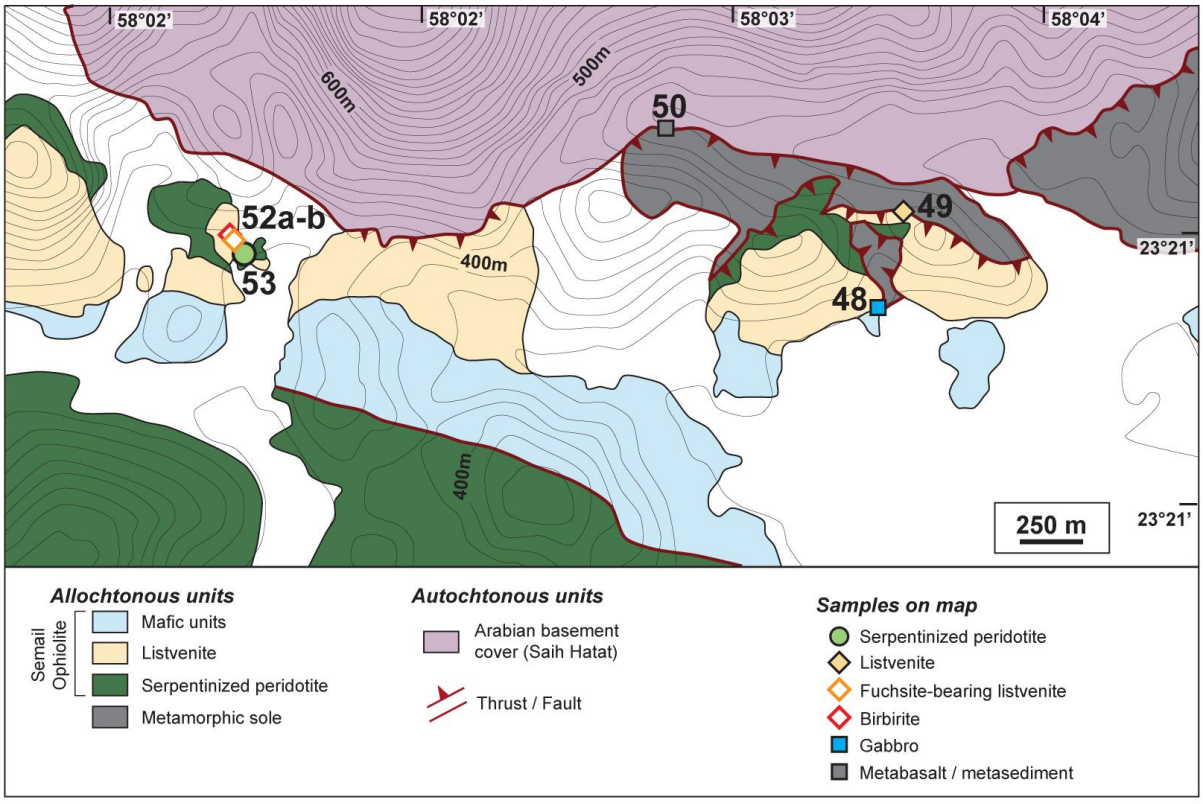

Fig. 4.11 Geological map of Site 4 on the southern flank of the Jabal Nakhl south-west of Fanja, modified after Villey et al. (1986). Sample location is indicated by a number referring to the nomenclature OM20-n (see the list of samples in Appendix).

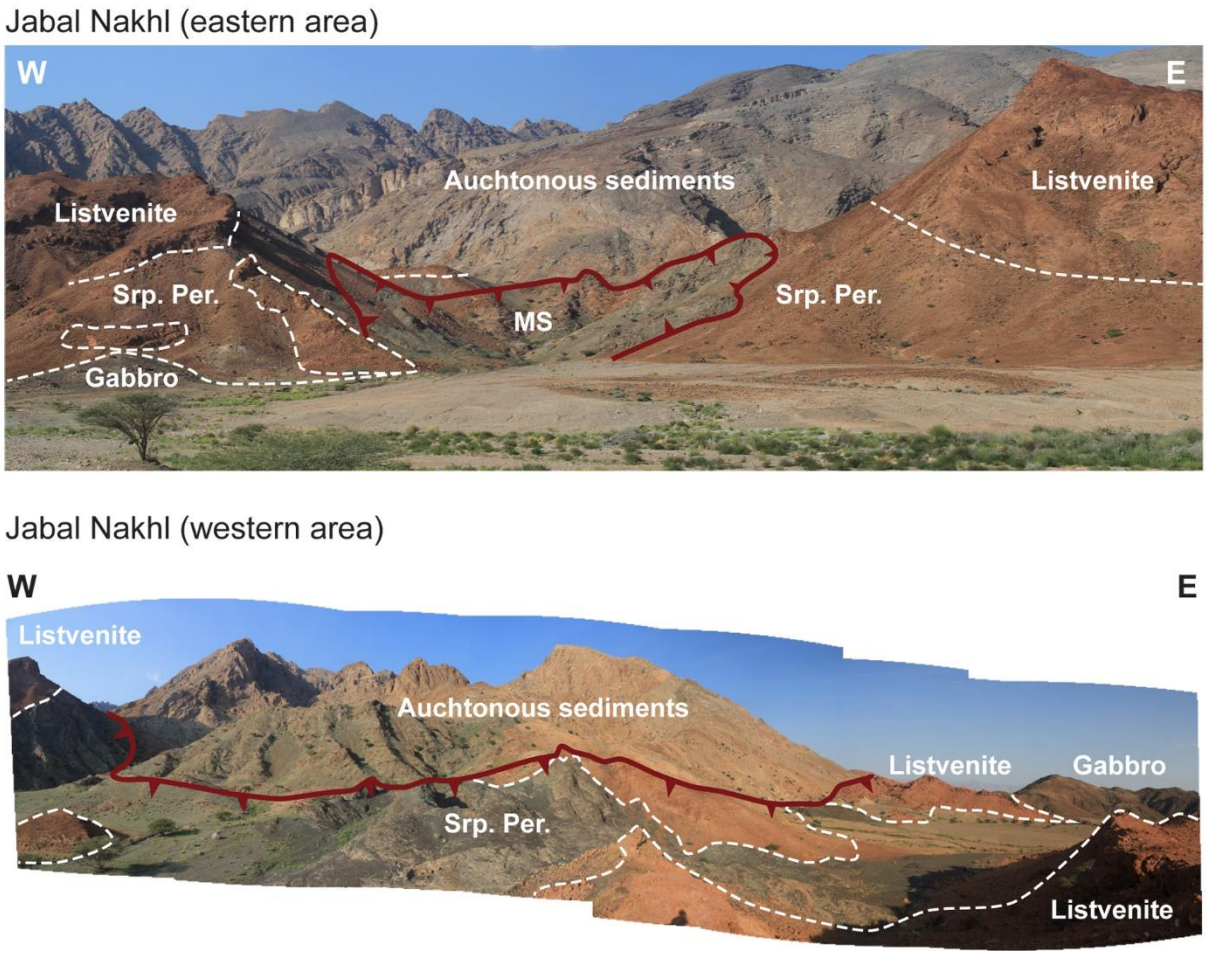

Fig. 4.12 Panoramic photographs illustrating the lithological sequence for the two investigated areas aon the southern flank of the Jabal Nakhl.

Collected metasomatized mantle rocks (Fig. 4.13) include: one serpentinized peridotite (OM20-53), one listvenite (OM20-49), one fuchsite-bearing listvenite (OM20-52b), one birbirite (OM20-52a).

Fig. 4.13 Samples of metasomatized peridotites collected at the Site 4.

4.2 Petrography of listvenites and associated rocks

4.2.1 Serpentinized peridotites

Peridotites are moderately (~70%) to completely serpentinized (Fig. 4.14). Higher degree of serpentinization is observed for samples collected closer to the transition with carbonated serpentinite and listvenite. Despite variations in grain-size, they generally display a coarse-grained, low-temperature porphyroclastic texture.

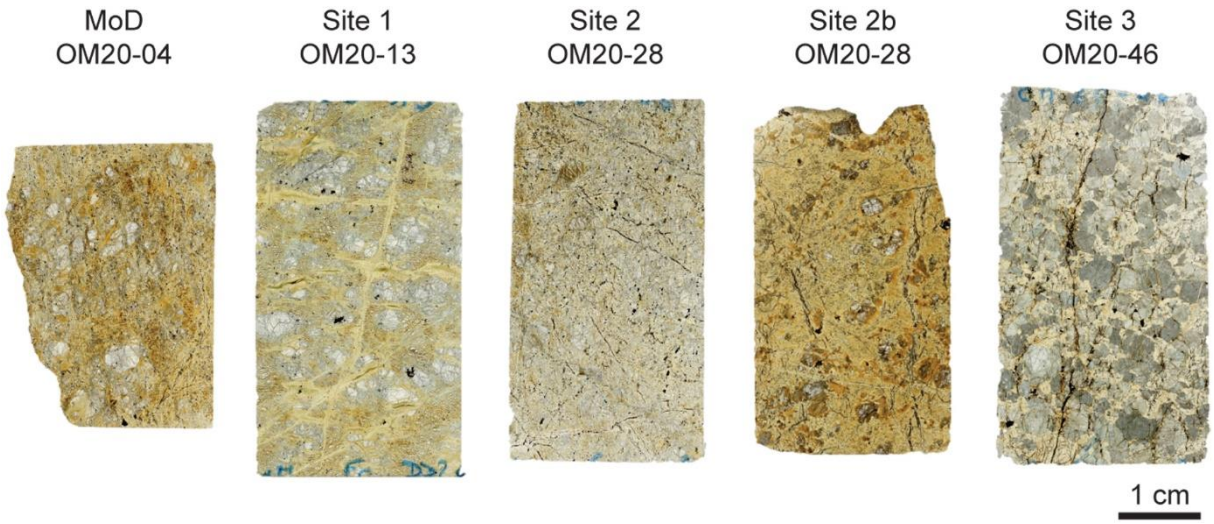

Fig. 4.14 Plane-polarized light (PPL) thin section scans of serpentinized peridotites and pyroxenite OM20-46, preserving various amounts of relict primary silicates. They show typical mesh and bastite textures. In sample OM20-46, olivine was completely altered to serpentine while pyroxenes remained mostly preserved.

Serpentinized peridotites are characterized by polygonal mesh and hourglass networks (Fig. 4.15). When preserved, olivine is found in mesh cores outlined by serpentine rims alongside abundant magnetite (Fig. 4.15a-b). Orthopyroxenes shows incipient pseudomorphic replacement to bastite, with serpentine forming along fractures and cleavages (Fig. 4.15c). Minor clinopyroxenes occur at the rim or close to orthopyroxenes (Fig. 4.15d). Accessory Cr-spinel shows subhedral to holly-leaf shapes, and are frequently rimmed by magnetite. Sulphides are rare within mesh or enclosed as tiny inclusions within Cr-spinel. In harzburgite OM20-13, they were identified as Fe-Ni-Co-bearing by SEM-EDS. Except for mesh rims, serpentine veins are rare, showing extinction patterns and repeated growth patterns typical of crack-seal veins (formed by repeated cracking and mineral growth; e.g., Andreani et al., 2004; Tarling et al., 2021).

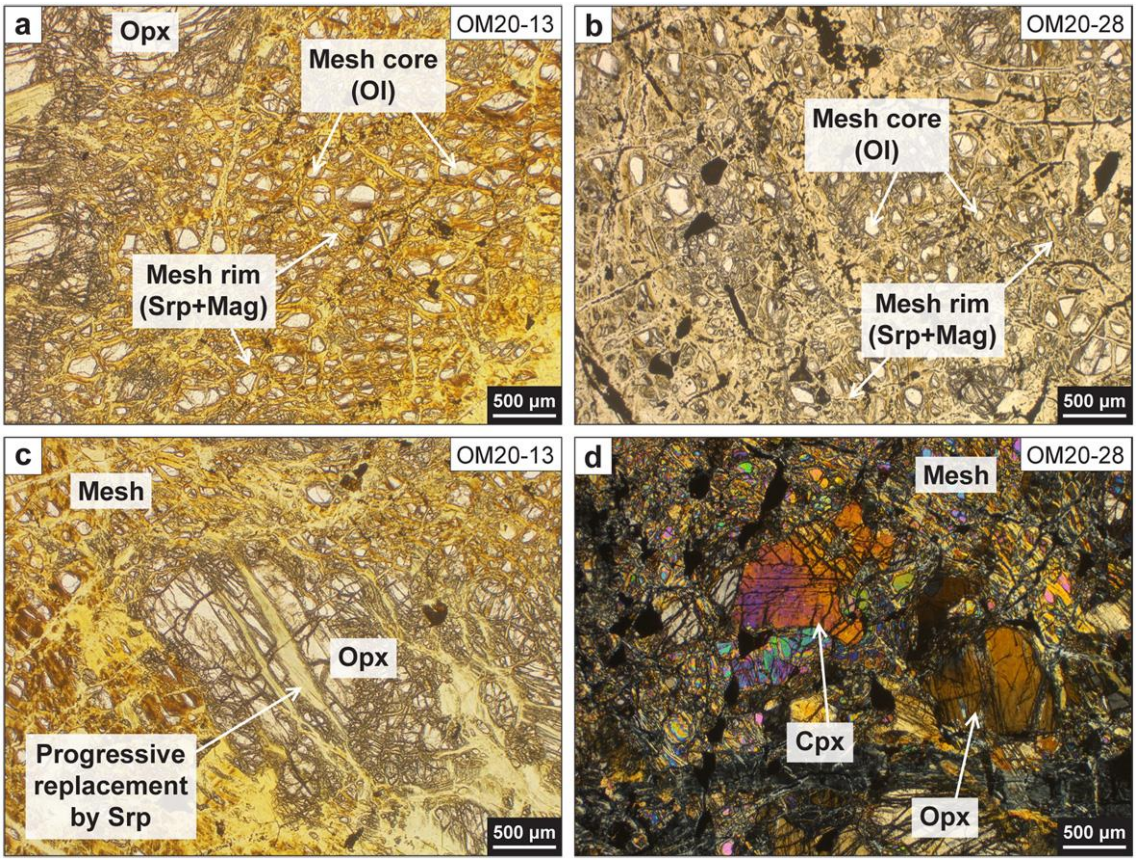

Fig. 4.15 Plane-polarized light microphotographs of serpentinized peridotites OM20-13 and OM20-28, preserving various amounts of relict primary silicates in mesh (a-b) and bastite (c) textures. Clinopyroxenes are found at the rim or close to orthopyroxene (d).

4.2.2 Carbonated serpentinites

Carbonated serpentinites are characterized by: i) the complete destabilization of primary silicates hence preserving hourglass and bastites textures in poorly deformed samples; ii) the occurrence of Mg-carbonates (magnesite-dolomite) replacing pervasively matrix serpentine, but predominantly found in veins.

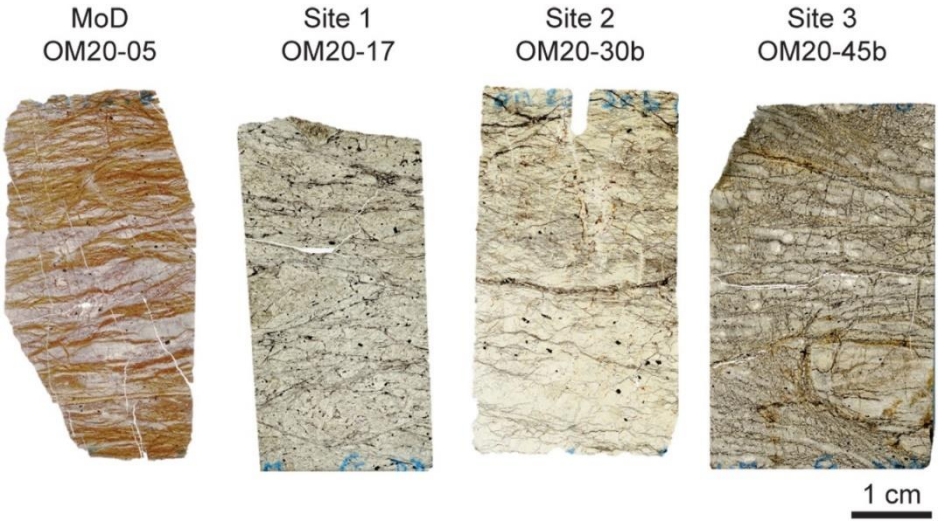

Fig. 4.16 Plane-polarized light microphotographs of carbonated serpentinites from the contact with listvenite and displaying ductile deformation. Samples are suspiciously bastite-poor, suggesting a dunitic protolith. Carbonates (reddish colour) principally occur as veins delimiting porphyroclatic domains.

We noticed that carbonated serpentinites collected at the contact with listvenites generally display ductile deformation with the formation of porphyroclatic domains. Suspiciously, these samples are also bastite-poor suggesting they might derive from a dunitic protolith (Fig. 4.16).

Poorly-deformed carbonated serpentinites in Hole BT1B preserved the serpentine hourglass and bastite textures (Fig. 4.17). Raman spectrometry indicate that mesh serpentine is mainly composed of lizardite, bastite of chrysotile (lizardite in sample 43Z-4-52-57), and veins of chrysotile (Fig. 18 and Table in Appendix). Magnetite remained localized along mesh rims but is locally destabilized to form Fe-rich magnesite. Carbonated serpentinites also contain relict Cr-spinel, often thinly rimmed by magnetite or ferri-chromite, and rare polydymite, a weathering product of pentlandite (serpentinite 44Z-4-0-5).

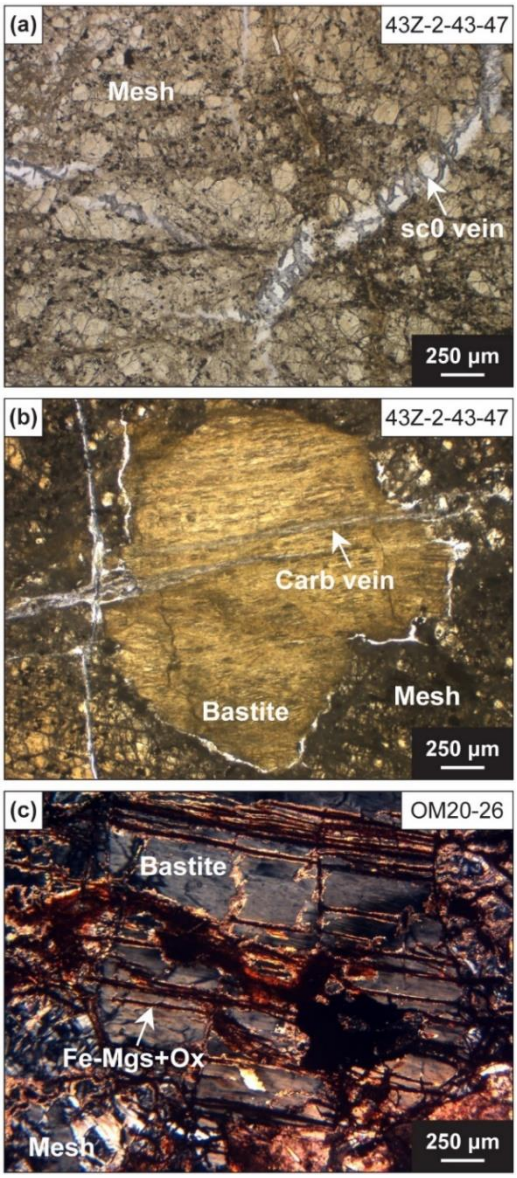

Fig. 4.17 Microphotographs of (a) mesh and (b-c) bastite textures in carbonated serpentinites. Carbonates (reddish-brownish colour) statically replaced serpentine mesh rims (a), bastite cleavages (c), or occur as thin, antitaxial veins (b).

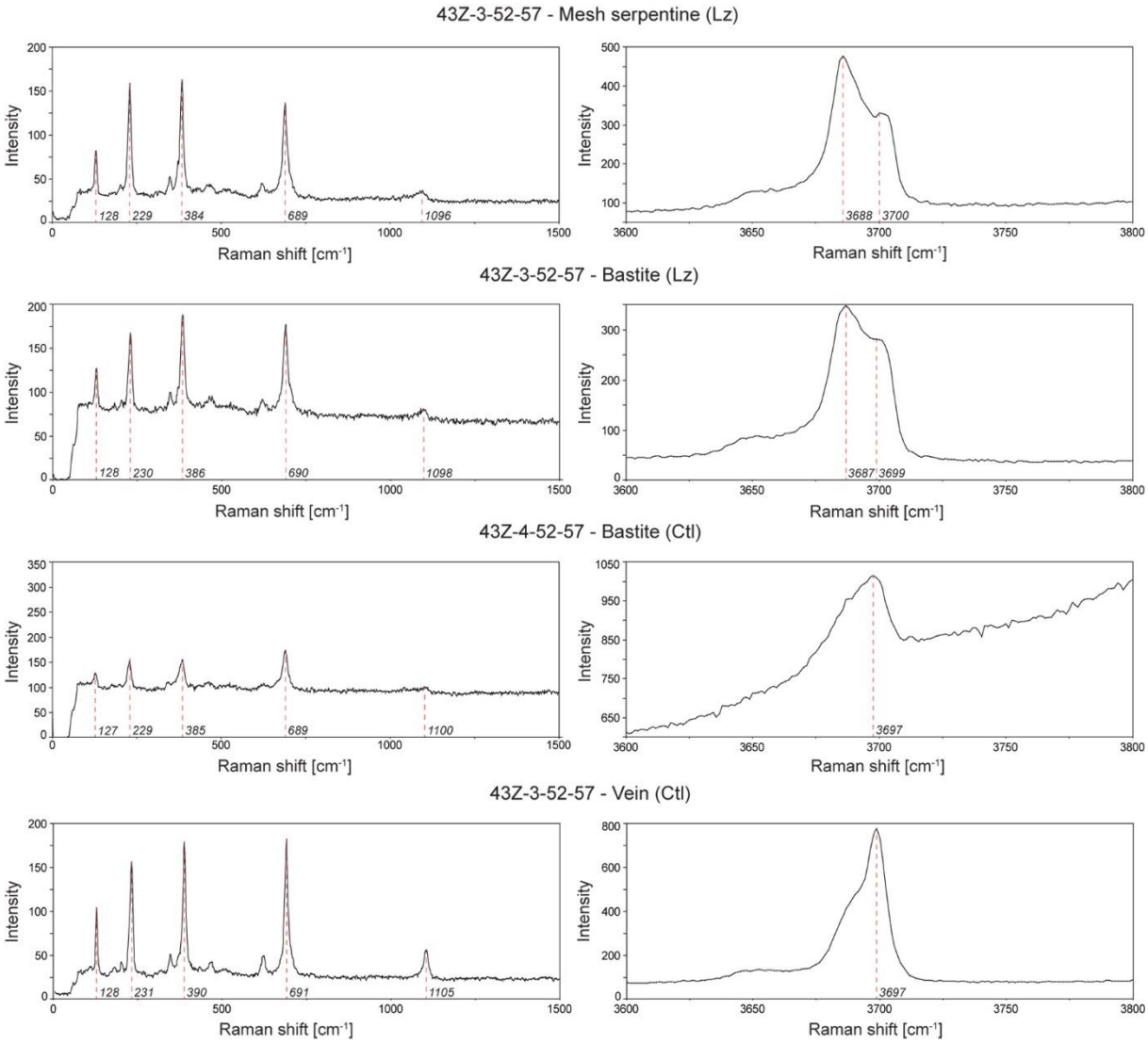

Fig. 4.18 Representative Raman spectra of the different serpentine microstructures. Serpentine species were determined using characteristic wavelength of Wang et al. (2015).

Matrix carbonates (magnesite or dolomite) occur as isolated spherical cores (spheroids), or aggregates pervasively replacing matrix serpentine (Fig. 4.19). They are found in the vicinity of carbonate veins forming aggregates developing along mesh rims Figs. 4.19a, -c), and as disperse spheroids within the mesh and cracks (Fig. 4.19b). BSE imaging and EDS mapping revealed that magnesite spheroids are chemically zoned, with Mg-rich cores and Mg-poor rims. However, magnesite spheroids with Fe-rich cores are also found in carbonated serpentinite at the transition with listvenite (44Z-2-27-29; OM20-26).

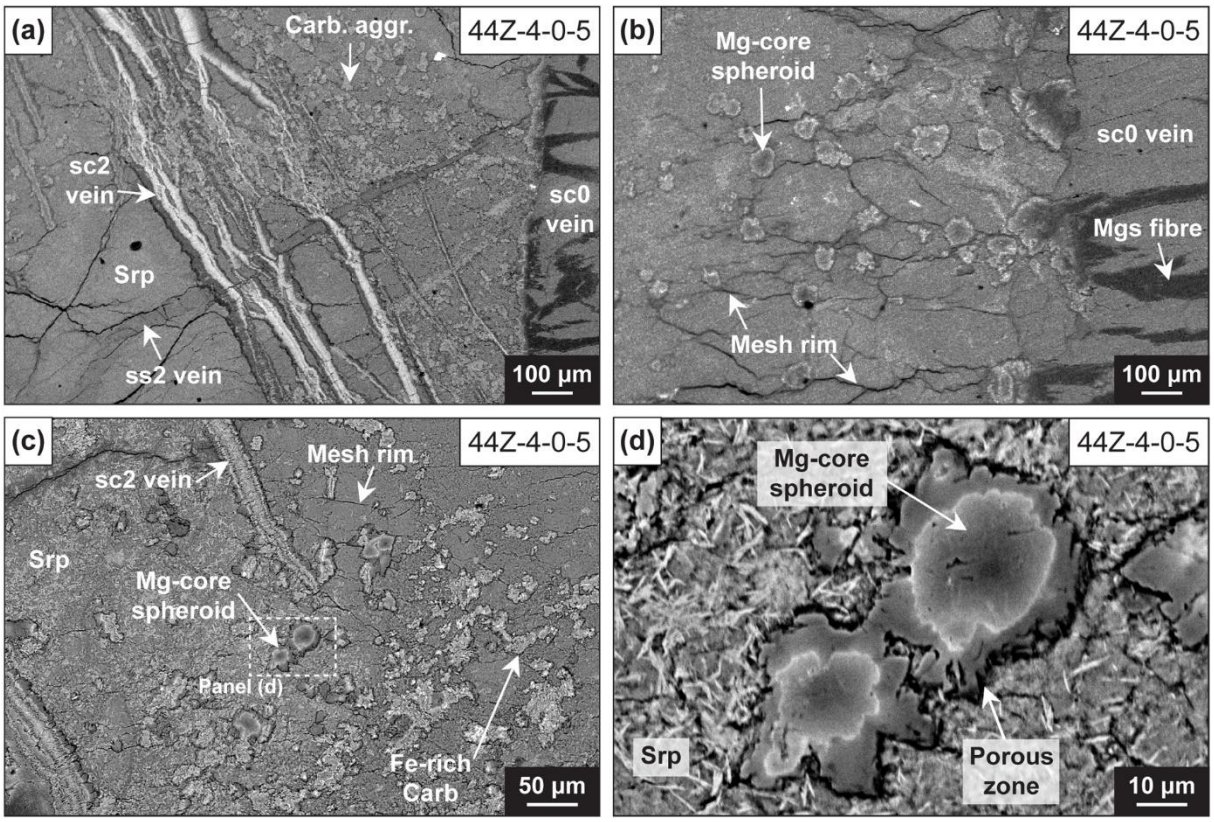

Fig. 4.19 Back-scattered electron (BSE) images illustrating the textural aspects of matrix and vein carbonates in carbonated serpentinite 44Z-4-0-5. (a) Zoned, antitaxial magnesite veins (sc2) cross-cutting perpendicularly a crack-seal serpentine vein (ss2). On the right side of the panel, a vertical crack-seal vein shows pseudomorphic replacement along the vein wall and within the structure (columnar magnesite fibres, dark grey colour). (b) Magnesite spheroids forming at crack joints in the vicinity of a slightly carbonated crack-seal vein. (c) Fe-rich magnesite aggregates developing from mesh rims, along with sparse magnesite spheroids. (d) Magnesite spheroids showing chemical zoning (dark grey: Fe-poor, light grey: Fe-rich). The rim present euhedral crystal terminations and is separated from the surrounding serpentine by a porous zone.

Distinct vein types were identified in borehole samples and are presented in order of apparition to illustrate the sequence of fluid infiltration in Hole BT1B. The used nomenclature refers to the paper of Menzel et al. (2022b).

The most common vein type corresponds to mesh rims (“ss0”; thickness: <20 µm) delineating polygonal hourglass networks where magnetite is abundant. The serpentine mesh is cut by multiple generations of serpentine–magnetite and serpentine crack-seal veins.

Discrete serpentine–magnetite veins (0.1-1.5 mm thick) are characterized by a magnetite-rich median line with flaky to fibrous serpentine on vein walls. Serpentine crack-seal veins are ubiquitous, forming parallel, en échelon, or branching networks. They show a uniform to cloudy extinction under crossed polarizers, with the fibre oriented similarly over the entire length of the vein. Crack-seal veins commonly expose vein-parallel banding with oscillatory extinction due to alternating precipitation over crack–seal

cycles (Andreani et al., 2004; Tarling et al., 2021). Pseudomorphic replacement by carbonate locally occurs along vein selvage and formation of columnar carbonate after serpentine fibres (Fig. 4.19a-b).

The most abundant early carbonate veins in serpentinite are zoned, antitaxial magnesite veins ("sc2", 50–200 μm). They often show a vein-parallel, bisymmetrical chemical zoning from vein centre to vein walls (Fig. 4.19a). Median zones are commonly made of Fe-rich magnesite, with local intervals of dolomite, while vein walls are Fe-poor. Median lines, when present, are composed of Fe-oxides. It must be noticed that chemical zoning is not always well developed. These microstructures are organized as anastomosed or parallel vein networks.

Late veining in serpentinite mainly consists in the generation of rather common quartz-bearing veins and younger carbonate veins cross-cutting all microstructures. Two types of quartz-bearing veins were identified: i) one type is made of feathery quartz intergrown with serpentine forming vein walls ("sq1", <50 μm); the second type corresponds to wider, polygranular to blocky quartz-magnesite veins ("sq2", 0.1-10 mm) commonly oriented parallel to antitaxial veins. Late syntaxial carbonate veins ("sc4", 0.1 mm to 5 cm) are partially open or brecciated, unlike all other early carbonate vein types. Menzel et al. (2022b) suggests that these veins relate to a deformation phase postdating pervasive peridotite carbonation.

In regional samples, except ubiquitous mesh, most frequently observed veins are: i) crack-seal serpentine veins, ii) early antitaxial to blocky early carbonate veins, propagating on margins of shear bands, iii) late syntaxial carbonate veins. Density of antitaxial veins increases closer to listvenite. Cross-cutting relationships are similar to BT1B.

4.2.3 Listvenites

Listvenites in Hole BT1B display a wide span of rock textures due to heterogeneous distribution between the different matrix and vein microstructures, which are locally sheared, folded, or cut by cataclasitic bands, in addition to variable abundances of matrix minerals.

A textural pattern is recurring for poorly deformed listvenites, showing a fine-grained matrix of quartz (locally chalcedony), alongside fine-grained spherical to coarser subhedral magnesite, and subordinate interstitial dolomite. Relicts of Cr-spinel are generally preserved. Fuchsite frequently grows at the expense of Cr-spinel or is intergrown with quartz in aggregates resembling bastite. Anhedral to flaky hematite (~5–20 μm) occurs within the magnesite-quartz matrix, rimming altered Cr-spinel, and replacing magnetite. Locally, hematite is in turn altered to goethite. Sulphides are rare and were only identified in few BT1B core intervals as pyrite (listvenite 46Z-4-46-51), or polydymite, chalcocite and gersdorffite (listvenite 46Z-2-19-24).

One feature of carbonated serpentinites and listvenites in Oman is the growth of magnesite spheroids after matrix serpentine. EDS mapping revealed that: i) spheroids are chemically zoned, and that ii) two main types of spheroids exist based on Mg-Fe core-to-rim zoning. Fe-core spheroids (<100 μm) are characterized by Fe-rich cores and Fe-poor rims (Fig. 4.20), and by dissolution textures involving Fe-oxides in their core. Mg-core spheroids (>100 μm) show the inverse zoning (Fig. 4.21). Both types of spheroids are overgrown by dendritic or euhedral magnesite. The distribution and abundance of matrix carbonates is local spatially correlated to the presence and density of early antitaxial carbonate veins (Fig. 4.22). Textures indicate that silicification postdated the formation of early magnesite veins and extensive matrix replacement by magnesite spheroids and aggregates (Fig. 4.23).

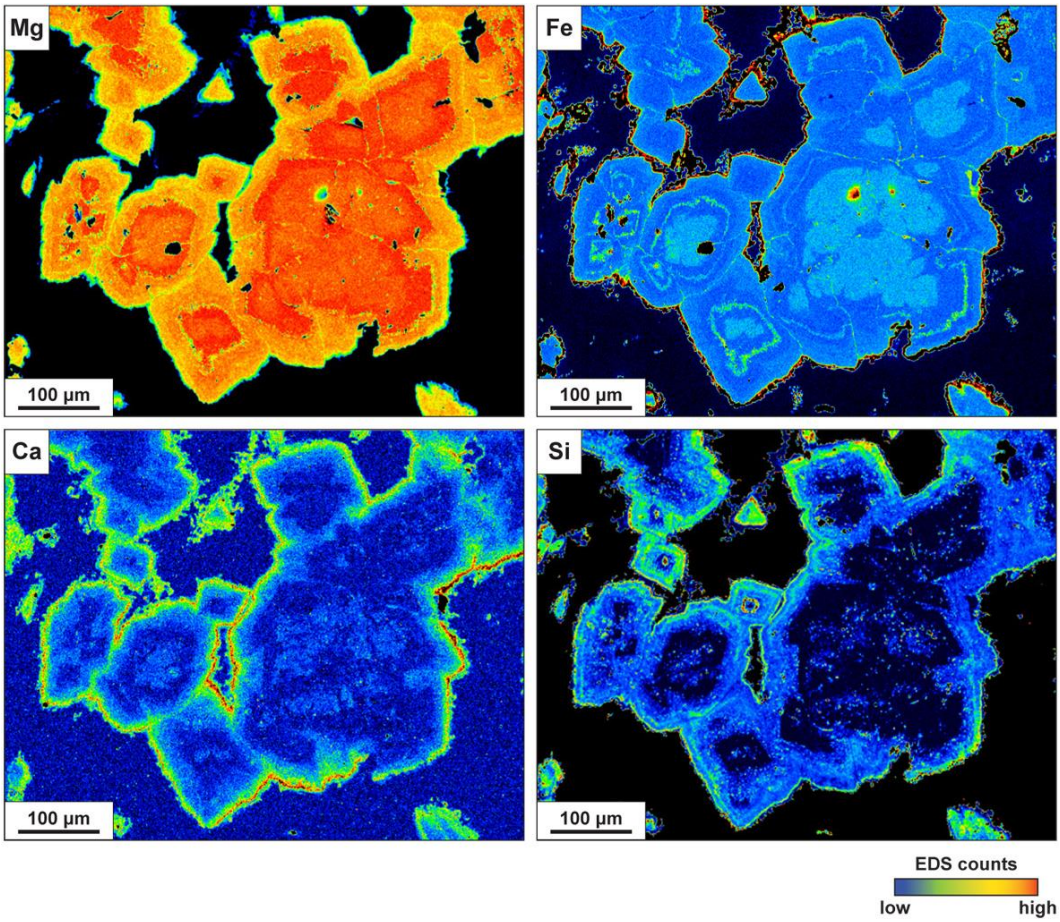

Fig. 4.20 EDS chemical mapping of Mg-core spheroids, showing Mg-rich cores and Fe-Ca-Sirich rims Their internal structure well shown for Fe suggests poly-phase growth

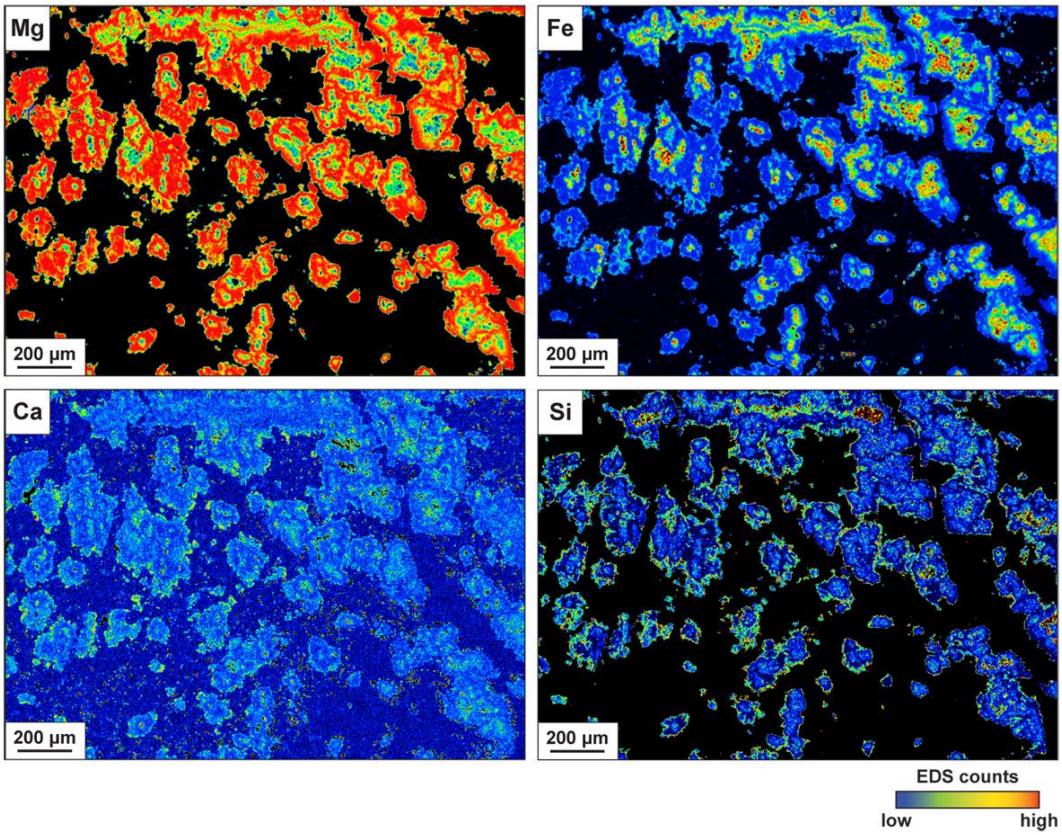

Fig. 4.21 EDS chemical mapping of Fe-core spheroids, showing Fe-rich cores and Ca-Si-rich rims. Their spatial distribution resembles that of polygonal mesh network.

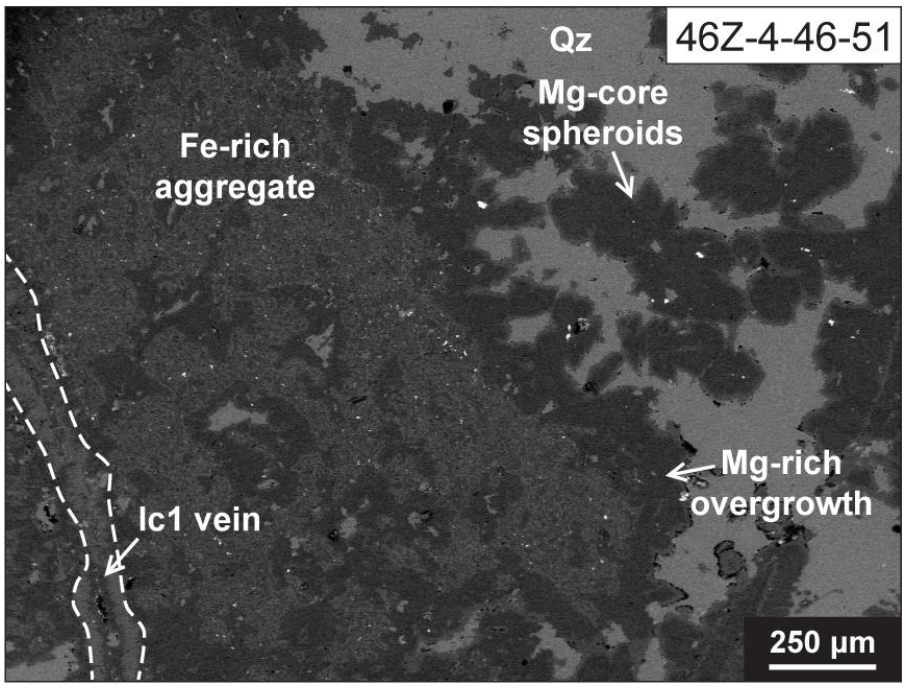

Fig. 4.22 Back-scattered electron (BSE) image of Fe-rich magnesite (light grey) clustering in the vicinity of early carbonate veins (noted lc1), and overgrown by Mg-rich magnesite (dark grey) in listvenite 46Z-4-46-51. Magnesite spheroids away from the vein are also Mg-rich. Abbreviation: Mgs: magnesite; Qz: quartz.

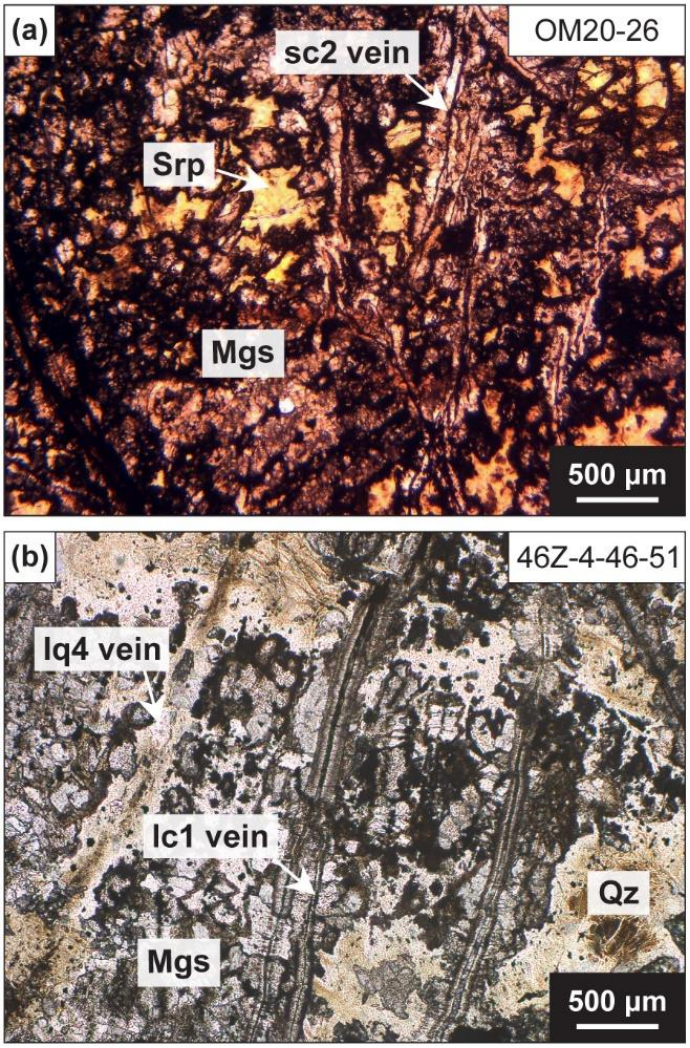

Fig. 4.23 PPL microphotographs of similar textural patterns in carbonated serpentinite OM20-16 and listvenite 46Z-4-46-51, indicating that silicification of the rock matrix postdates the pervasive magnesite replacement of serpentine and formation of early antitaxial veins. Abbreviation: Mgs: magnesite; Qz: quartz; srp = serpentine.

Listvenites in Hole BT1B host an intricate vein network resulting from the pseudomorphic replacement of pre-existing serpentine veins and superposition with newly generated veins during ongoing carbonation. In the following, we described the veining sequence in order of appearance based on cross-cutting relationships.

Pseudomorphic carbonate microstructures after serpentine veins are the oldest ones. Magnesite and/or quartz replaced serpentine in former mesh rims ("lss0", Fig. 4.24, Fig. 4.25a) and crack-seal veins ("lss2", Figs. 4.25b-c), locally preserving initial columnar magnesite fibres. These microstructures were identified as former serpentine veins due to morphological resemblance with analogous veins in carbonated serpentinites (Fig. 4.24).

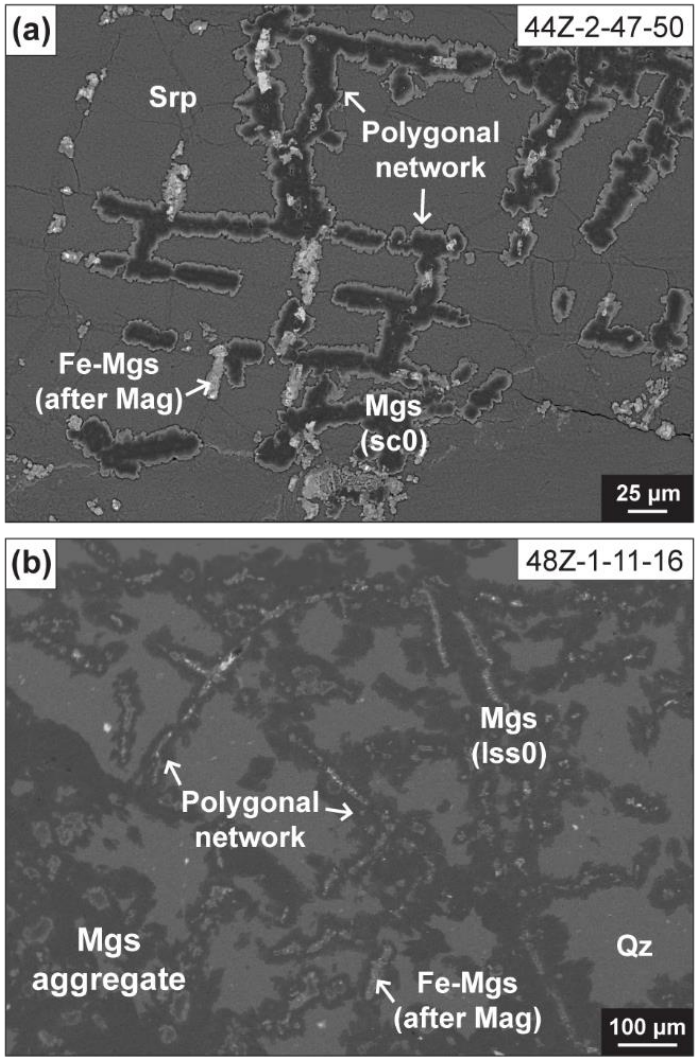

Fig. 4.24 Back-scattered electron (BSE) images of pseudomorphic replacement textures of serpentine mesh rims by carbonates (sc0 and lss0), forming characteristic polygonal networks in (a) carbonated serpentinite (44Z-2-47-49) and (b) listvenite (48Z-1-6-11). Fe-rich magnesite (light grey) formed at the expense of magnetite. Abbreviations: Mgs: magnesite, Qz: quartz, Srp: serpentine.

As for carbonated serpentinites, chemically zoned antitaxial to blocky magnesite veins (commonly 50–250 µm thick) are the most abundant. They locally form closely spaced, parallel to anastomosing networks (Fig. 4.25d). Their antitaxial habit is confirmed by euhedral crystal growth from vein walls toward rock matrix. The median zone frequently presents a line (<10 µm) rich in Fe-oxides or hydroxides. Chemical zoning is bisymmetrical, with vein centres composed of Fe-rich magnesite and Fe-poor margins (Fig. 4.26). However, vein cores can also be formed by Mg-rich magnesite or dolomite (Fig. 4.26). Abundant Fe-oxides and hydroxides may also occur on vein margins. Antitaxial veins are cut by less abundant magnesite veins ("lc2"), with cross-fibre to blocky syntaxial texture (Fig. 4.25e), and by polycrystalline magnesite-dolomite veins (lc3). Early carbonate veins are cut by cryptic and microcrystalline quartz veins (thoroughly described by Menzel et al. (2022b), that cannot be distinguished from matrix quartz by polarized-light microscopy, but are visible by

cathodoluminescence. Straight, dull quartz veins (“lq3”, 10–100 μm) are frequent and cross-cut magnesite spheroids (Fig. 4-.25h) and pseudomorphosed mesh networks. Younger quartz-magnesite (“lq4”, Fig. 4.25f) and quartz-dolomite veins (“lc4”, Fig. 4.25g) are frequent. These veins are syntaxial, with relatively straight vein walls, showing a blocky habit. Quartz-magnesite lq4 veins (<250 μm) are characterized by radial chalcedony growth on vein walls, and wide-blocky carbonate and quartz crystals along the vein center. Quartz-dolomite lc4 veins (0.1–1 mm) show a blocky habit formed by euhedral quartz and dolomite. As these veins cross-cut both matrix quartz and carbonates, their formation is younger than serpentinite carbonation and silicification. The youngest carbonates veins are wider, syntaxial to blocky, monomineralic magnesite (“lc5”, >2 mm thick) and dolomite (“lc6”, 0.1 – >5 mm thick) veins (Fig. 25h).

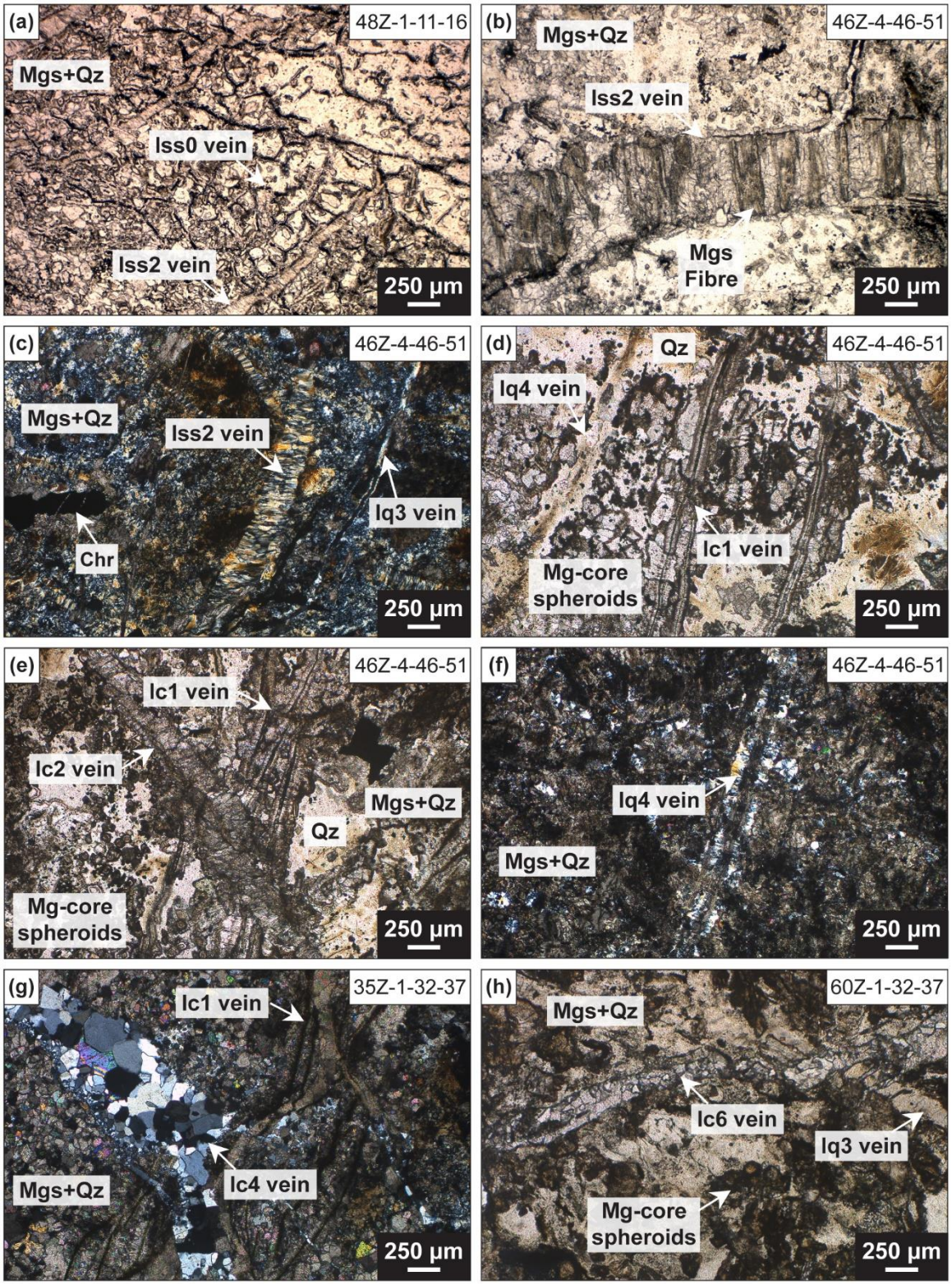

Fig. 4.25 Plane-polarized (PPL) and crossed-polarized (CPL) light microphotographs of veins hosted by listvenites. (a) Pseudomorphic lss0 and lss2 veins after mesh rims and crack-seal veins, overgrown by dendritic magnesite. (b-c) Pseudomorphosed crack-seal vein replaced by magnesite hence preserving initial columnar fibres (b), or completely replaced by quartz (c). (d) Zoned, antitaxial magnesite veins forming a parallel set. Magnesite spheroids are cut on the left side by lq4 quartz vein. (e) Large, cross-fibre lc2 vein cutting lc1 veins. (f) lq4 vein. (g) Syntaxial, polycrystalline lc4 vein cross-cutting lc1 veins. (h) Late dolomite lc6 vein cross-cutting microcrystalline lq3 quartz vein. Abbreviations: Chr = Cr-spinel; Mgs = magnesite; Qz = quartz.

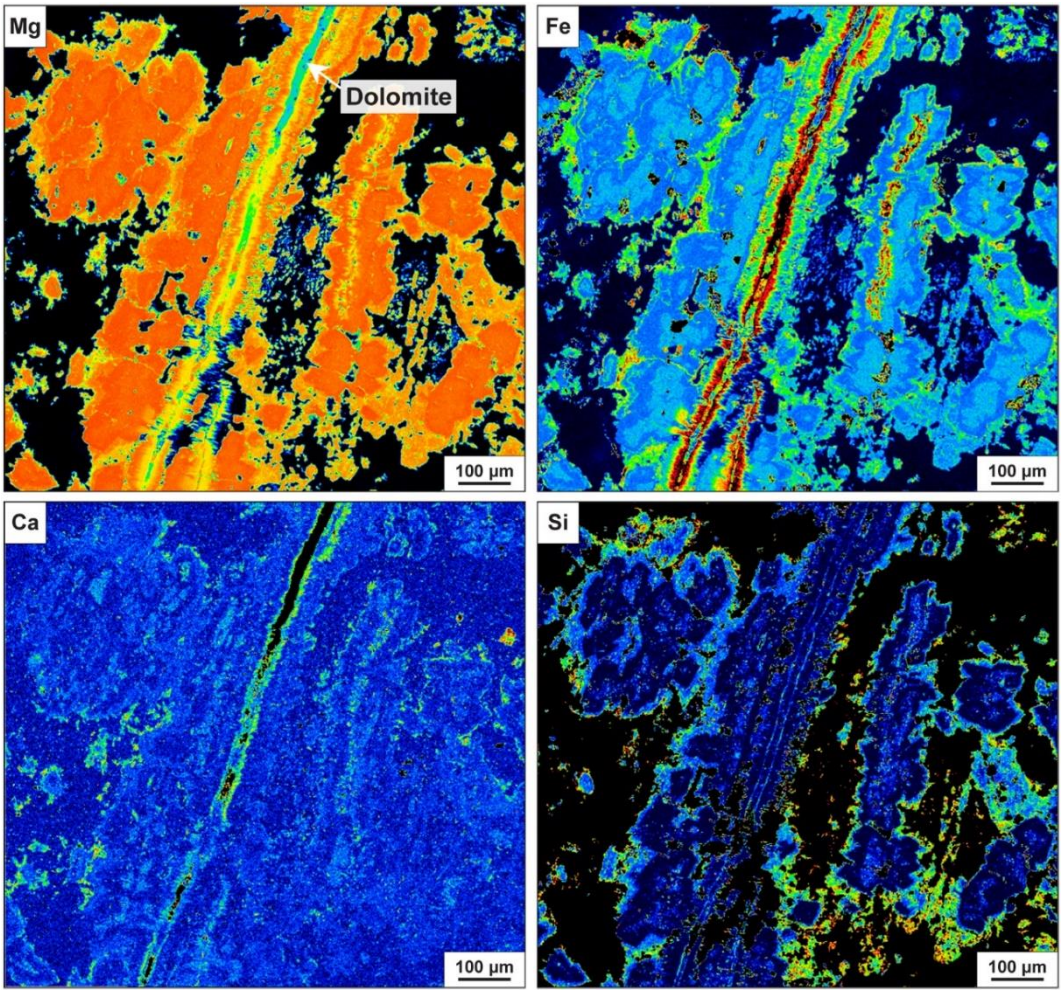

Fig. 4.26 EDS chemical mapping of antitaxial lc1 vein presented in Fig. 4.25d. The median zone is composed of Fe-rih magnesite, truncated by intervals of dolomite. The vein is overgrown by Mg-rich magesite, enriched in silica on its margin.

EBSD

EBSD analysis was performed on three samples of listvenites (Fig. 4.27): i) sample 31Z-3-26-31 presenting a strong shape preferred orientation, with a penetrative foliation aligning magnesite bands together with dolomite and quartz, ii) two samples (50Z-1-75-80 and 71Z-3-41-49) characterized by the abundant spheroids in a rock matrix showing no apparent deformation pattern. For sample 31Z, magnesite display a broad crystallographic preferred orientation (CPO) of the mineral c-axis [001] along the x-axis (here an arbitrary spatial reference as samples are not oriented). On the other hand, quartz shows a CPO perpendicular to magnesite. Magnesite and quartz in spheroid-rich samples do not present a statistically clear CPO suggesting that these minerals grew in an environment where deformation was negligible.

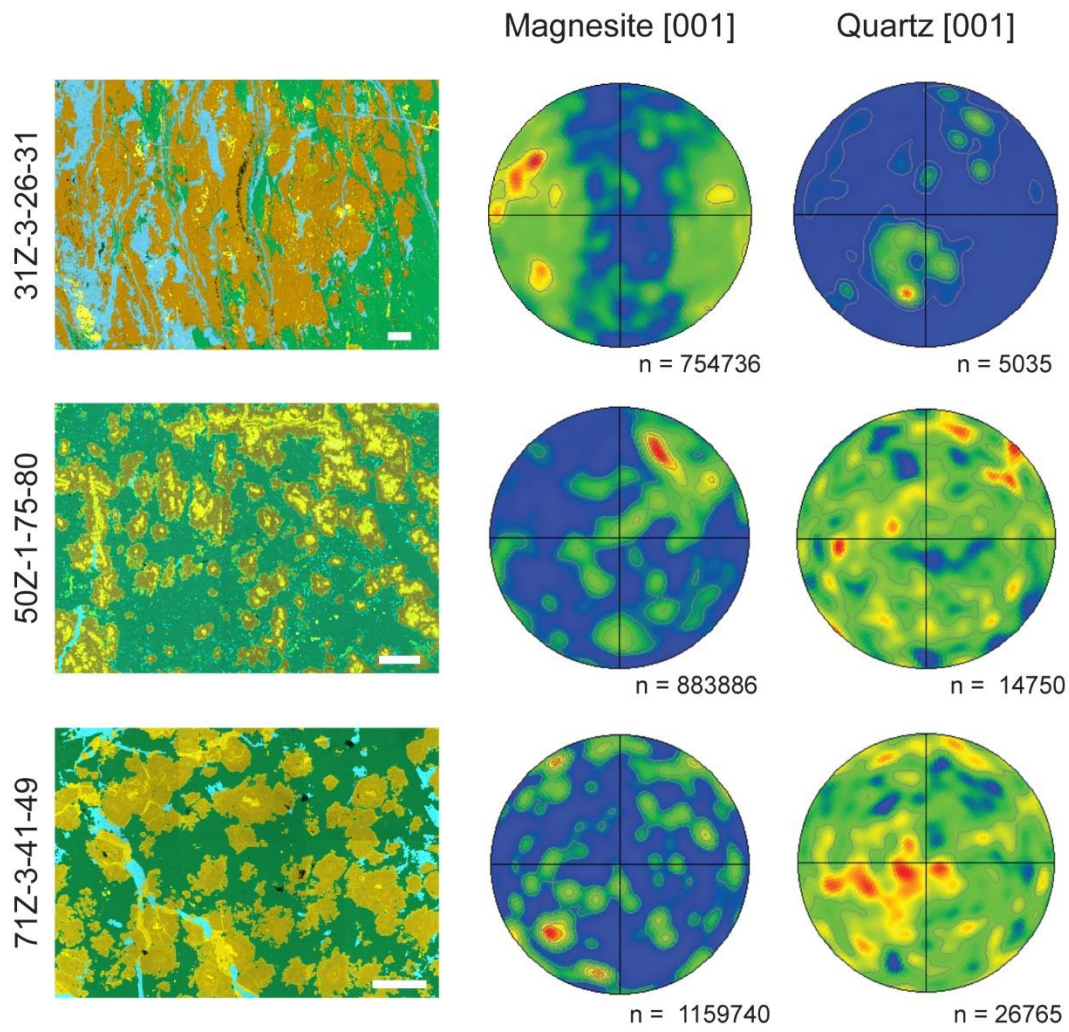

Fig. 4.27 Contoured pole figures of magnesite and quartz c-axis I an arbitrary spatial reference (all points, indicated as n; higher hemisphere). Poles figures based on 1 point per grain provided similar patterns. Colour scheme: orange = Mg-rich, yellow = Fe-rich, blue = Ca-rich; green = Si-rich.

4.3 Pervasive carbonation of peridotite to listvenite (Semail Ophiolite, Sultanate of Oman): clues from iron partitioning and chemical zoning

Thierry Decrausaz[1], Marguerite Godard[1], Manuel Menzel[2,3], Fleurice Parat[1], Emilien Oliot[1], Romain Lafay[1], Fabrice Barou[1]

[1] Géosciences Montpellier, Université de Montpellier, CNRS, Montpellier, 34095, France

[2] Tectonics and Geodynamics, RWTH Aachen University, Aachen, D–52056, Germany

[3] Instituto Andaluz de Ciencias de la Tierra (IACT), CSIC–UGR, Armilla, 18100, Spain

Accepted for publication to the European Journal of Mineralogy

Abstract

Earth's long-term cycling of carbon is regulated from mid-ocean ridges to convergent plate boundaries by mass transfers involving mantle rocks. Here we examine the conversion of peridotite to listvenite (magnesite+quartz rock) during CO_2-metasomatism along the basal thrust of the Semail Ophiolite (Fanja, Sultanate of Oman). At the outcrop scale, this transformation defines reaction zones, from serpentinized peridotites, to carbonated serpentinites and listvenites. Based on a detailed petrological and chemical study, we show that carbonation progressed through three main stages involving the development of replacive textures ascribed to early stages, whilst carbonate (± quartz) veining becomes predominant in the last stage. The pervasive replacement of serpentine by magnesite is characterized by the formation of spheroids, among which two types are identified based on the composition of their core regions: Fe-core and Mg-core spheroids. Fe-zoning is a type feature of matrix and vein magnesite formed during the onset carbonation (Stage 1). While Fe-rich magnesite is predicted to form at low fluid XCO_2 from a poorly to moderately oxidised protolith, our study evidences that the local nonredox destabilization of Fe-oxides into Fe-rich magnesite is essential to the development of Fe-core spheroids. Formation of Fe-core spheroids is followed by the pervasive (over)growth of Mg-rich spheroids and aggregates (Stage 2) at near equilibrium conditions in response to increasing fluid XCO_2. Furthermore, the compositions of carbonates indicate that most siderophile transition elements released by the dissolution of primary minerals are locally trapped in carbonate and oxides during matrix carbonation, while elements with a chalcophile affinity are the most likely to be leached out of reaction zones.

1 Introduction

(De-)serpentinization and (de-)carbonation of peridotites play a major role on the long-term cycling of volatiles, incompatible and fluid-mobile elements between the surface and the deep Earth (e.g., Alt et al., 2013; Deschamps et al., 2013; Kelemen and Manning, 2015). Carbonation of peridotites takes place in various hydrothermal systems, from seafloor exposure to convergent plate boundaries (e.g., Schwarzenbach et al., 2013; Schröder et al., 2015; Debret et al., 2018; Noël et al., 2018; Cannaò et al., 2020), or during (sub-)surface weathering (e.g., Kelemen and Matter, 2008; Ulrich et al., 2014). Listvenites represent the most extreme product of this metasomic process, with the complete conversion of the primary and secondary silicates composing the peridotites (olivine, orthopyroxene – Opx, clinopyroxene – Cpx, serpentine) into a quartz – carbonate (magnesite ± dolomite) assemblage (Halls and Zhao, 1995). Listvenites and related carbonated serpentinites are found in several orogenic and ophiolitic peridotite massifs worldwide, typically along tectonic discontinuities acting as conduits for CO_2-rich metasomatic fluids (e.g., Hansen et al., 2005; Beinlich et al., 2012; Aftabi and Zarrinkoub, 2013; Hinsken et al., 2017; Qiu and Zhu, 2018; Menzel et al., 2018; Boskabadi et al., 2020). Listvenites are well-known for hosting ore-grade mineralizations of economically-valuable metals (e.g., transition

elements such as Au, Ag, Co or Cu; e.g. Buisson and Leblanc, 1987; Auclair, 1993; Aftabi and Zarrinkoub, 2013; Emam and Zoheir, 2013; Belogub et al., 2017; Gahlan et al., 2020).

Over the years, the reaction pathways and mechanisms leading to complete peridotite carbonation have been investigated (e.g. Hansen et al., 2005; Tominaga, et al., 2017; Menzel et al., 2018). Dissolution of precursor silicates and redox evolution in response to infiltration of CO_2-rich fluids have been hypothesized as major processes driving elemental remobilization during carbonation (e.g., Buisson and Leblanc, 1987; Auclair et al., 1993). Destabilization of Fe-oxides during carbonation was also identified in a few listvenite suites (Tominaga et al., 2017; Menzel et al., 2018; Qiu and Zhu, 2018; Austrheim et al., 2021) supporting a possible impact of carbonation on local redox conditions (e.g., Frost, 1985). The redistribution of Fe and transition elements in carbonates during these processes remains however little documented.

We present a study of listvenites from the Fanja region in the Semail Ophiolite (Oman), where extensive outcrops are described (Glennie et al., 1974; Stanger, 1985; Wilde et al., 2002; Nasir et al., 2007; Falk and Kelemen, 2015; Boudier and Nicolas, 2018) and where Hole BT1B was drilled during the Oman Drilling Project (Kelemen et al., 2020). We document the relationships between the Fanja listvenites, serpentinized peridotites and adjacent lithologies in the field and downhole, with a focus on rock textures, microstructures and mineral compositions. Taking advantage of the unmatched density and quality of BT1B cores, we characterize the carbonation sequence leading to pervasive replacement of serpentinized peridotites by carbonates, with an emphasis on matrix replacement textures and Fe redistribution at the onset of the sequence. We also discuss the impact of carbonation on the remobilization of Fe and transition elements and the role of the linkages between fluid flow and changes in redox and chemical compositions in these processes.

2 Geological setting and sampling

2.1 The Semail Ophiolite and outcropping listvenites

The Semail Ophiolite is a segment of Tethyan oceanic lithosphere obducted on the Arabian continental margin during the Upper Cretaceous (e.g., Coleman, 1981; Nicolas et al., 2000) (Fig. 1a). It preserves a thick mantle section overlain by a layered oceanic crust, comprising lower layered gabbros to upper volcanics. The mantle section is composed of moderately to highly serpentinized harzburgites and minor dunites, with Cpx-harzburgites and lherzolites toward the base of the section (Lippard et al., 1986; Godard et al., 2000; Takazawa et al., 2003; Boudier et al., 2010; Hanghøj et al., 2010). A 50–200 m thick section of highly serpentinized, mylonitized and often amphibole-bearing Cpx-rich peridotites alternating with dunites and minor harzburgites characterizes the transition of the ophiolite to underlying lithologies (e.g., Khedr et al., 2013; Prigent et al., 2018). A 10–100 m thick metamorphic sole outcrops

discontinuously along the base of the ophiolite (e.g., Soret et al., 2017); it is made up of slivers of mafic and sedimentary-derived material. It records peak metamorphism in amphibolite to granulite facies ascribed to intra-oceanic underthrusting (e.g., Boudier et al., 1988) or incipient subduction (e.g., Searle and Cox, 1999). Zircon dating indicates that the formation of the sole was in part contemporaneous to the accretion of the oceanic crust preserved by the ophiolite (96.1–95.2 Ma; Rioux et al., 2021). During obduction, the ophiolite and metamorphic sole were thrusted over the allochthonous Hawasina units comprising the relicts of a wide oceanic basin (volcanics, pelagic and shelf sediments; e.g., Bechennec et al., 1990), and onto the autochthonous Arabian basement rocks. Ophiolite obduction was followed by burial then by an extensional phase of exhumation forming the Jebel Akhdar and Saih Hatat domes (Garber et al., 2021).

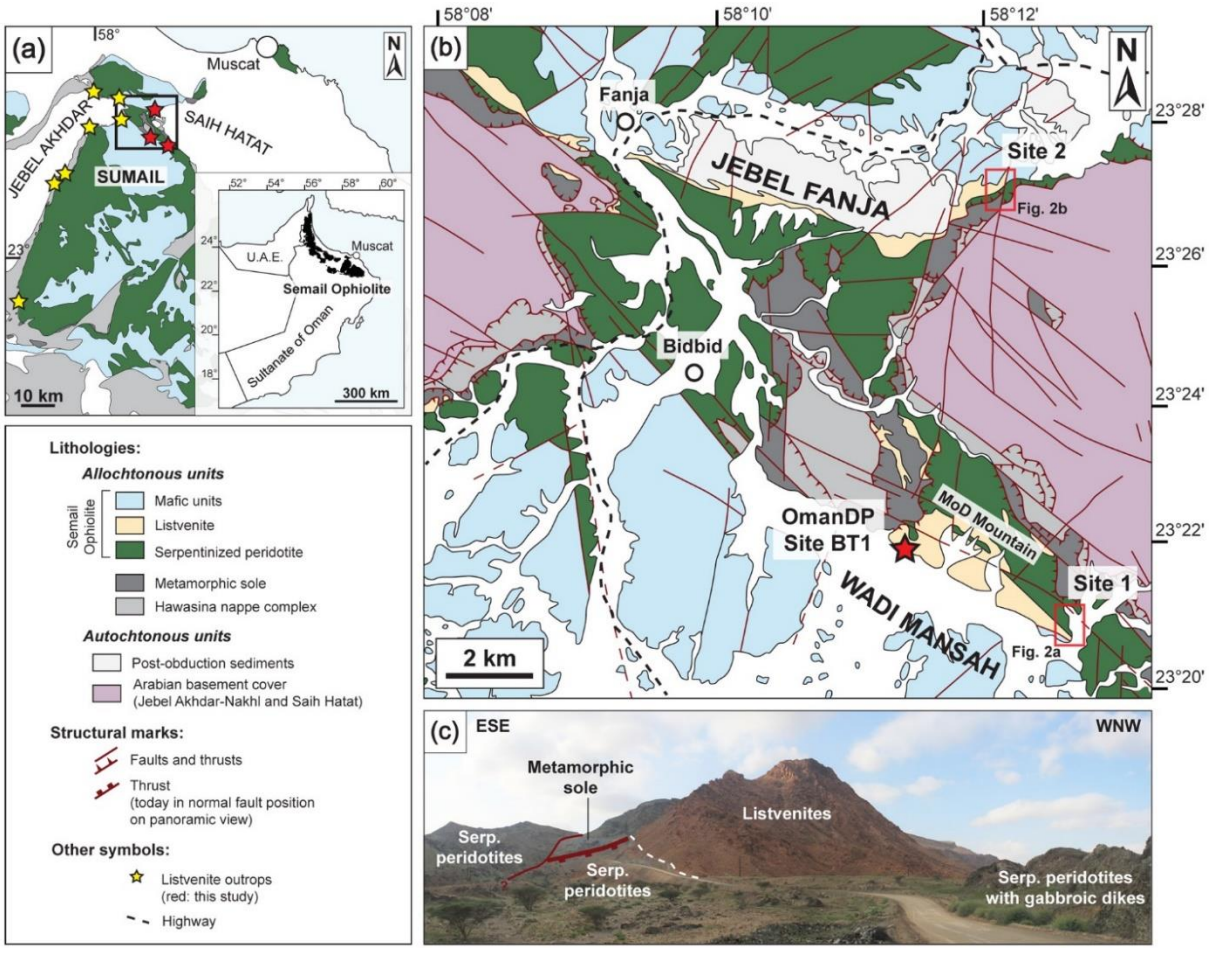

Figure 1 Listvenite outcrops in the Fanja area (Semail Ophiolite). (a) Location of the Semail Ophiolite in insert (after Nicolas et al., 2000) and Sumail massif. Listvenite occurrences (yellow stars) are reported from Nasir et al. (2007) and Boudier and Nicolas (2018). (b) Geological map of the Fanja area (modified after Villey et al. (1986), Kelemen at al. (2022)), indicated by a black rectangle in the insert map in (a). (c) Field photograph of a lithological contact between listvenites and serpentinized peridotites at Site 2 (Jebel Fanja, PV in Fig. 2b).

Listvenites crop out discontinuously along the ophiolite basal thrust (Figs. 1a-b). They occur as decametric thick layers and lenses within serpentinite oriented parallel to the basal thrust, or as blocks

within tectonic mélanges in shear zones (Nasir et al., 2007). The best exposed outcrops of listvenites are observed in the Fanja region where the ophiolite section is relatively thin (Boudier and Nicolas, 2018). It exposes dismembered and highly faulted fragments of mantle peridotites, juxtaposed with lower gabbros and slices of metamorphic sole (Fig. 1b). The Fanja listvenites are aligned along a NW–SE direction to the North and to the South of the ophiolite segments flanking the Jebel Akhdar and Saih Hatat domes. The petrologic and thermometry studies of the listvenites indicate that carbonation occurred below 250°C during cooling (Kelemen et al., 2022, Falk and Kelemen, 2015), with temperatures ranging from 247±52 to 45±5 °C for BT1B cores (Beinlich et al., 2020). The depth of formation of listvenites is however poorly constrained: it is less than 40 km assuming a subduction zone setting (Kelemen et al., 2022), and ~3.75–7.5 km for geothermal gradients expected during obduction (Beinlich et al., 2020).

Fieldwork and sampling of serpentinized peridotites, carbonated serpentinites and listvenites was realized at 3 sites (Fig. 1b), along transects from the metamorphic sole to the overlying gabbros (Figs. 2 and S1): OmanDP Hole BT1B, Site 1 in Wadi Mansah (southern alignment of listvenites) and Site 2 in the Jebel Fanja (northern alignment of listvenites).

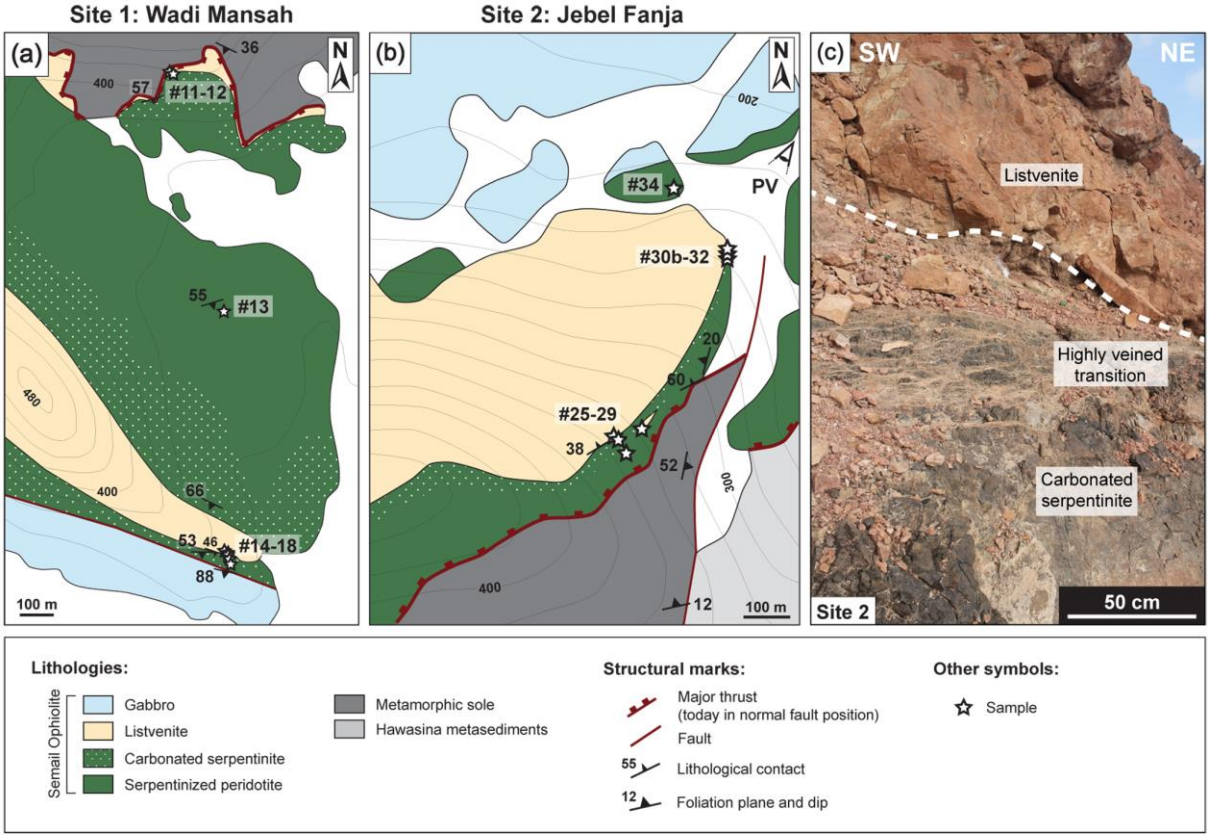

Figure 2 (a-b) Detailed geological maps of Site 1 (Wadi Mansah) and Site 2 (Jebel Fanja). Maps were drawn after Villey et al. (1986) and field observations (this study, see Text S1-1). The topography was drawn from Google Earth maps. Location of samples is indicated by white stars; adjacent numbers refers to sample names. (c) Field photograph illustrating the mesoscale transition between listvenite and carbonated serpentinite at Site 2.

2.2 Sampling

2.2.1 OmanDP Hole BT1B

Hole BT1B recovered ~200 m of listvenites interlayered by two levels of carbonated serpentinites, atop of ~100 m of metamorphic rocks (Kelemen et al., 2020; Fig. S1). Petrographic studies and bulk rock geochemical analyses of the mantle-derived section revealed three chemically distinct domains indicating that the protolith comprised serpentinized harzburgites/dunites and lherzolites as commonly observed along the ophiolite basal thrust (Godard et al., 2021). Listvenites are composed dominantly of magnesite and quartz forming the rock matrix along with minor dolomite and fuchsite (Cr-bearing muscovite), and accessory (relict) Cr-spinel, hematite and Fe-hydroxides. Fuchsite is observed only in listvenites from the lherzolitic protolith domain. Listvenites and carbonated serpentinites are cut by numerous generations of different carbonate and quartz veins (Kelemen et al., 2020; Menzel et al., 2022) and cataclasites (Menzel et al., 2020). From Hole BT1B, 15 listvenites, 5 fuchsite-bearing listvenites and 9 carbonated serpentinites were selected for this study (Fig. S1, Tables S1-2).

2.2.2 Site 1 and Site 2

Site 1 is located in the south-eastern part of Wadi Mansah, ~4.5 km east from Hole BT1B (Fig. 2 and S2). The mantle section (>250 m) is composed of massive serpentinized harzburgites and rare dunites. Listvenites are found atop the metamorphic sole to the North, and interlayering peridotites close to gabbros to the South. Lithological boundaries dip to the SSW and, except for the listvenite-peridotite interlayering, all contacts are faulted. Listvenites are orange-red due to weathering. The sole comprises, from top to bottom, mafic-derived rocks and metasediments. Listvenites in contact with the basal thrust form a 2–10 m thick layer below ~20 m of foliated and fractured carbonated serpentinites. In the southern part, listvenites form a 10–50 m thick interval bordered by foliated and fractured carbonated serpentinites, 5–10 m from the faulted contact with foliated gabbros. Listvenites are massive and host discontinuous millimetric to centimetric quartz-carbonate veins oriented at high angle with the lithological contact. Fault contacts between listvenites, serpentinites and gabbro are highly variable, ranging from serpentinite fault gouge to foliated serpentinite, with sharp localized faults. Close to gabbros, carbonated serpentinites host scarce gabbroic dikelets (<10 cm thick) or pods. Away from gabbros, ~25–50 m of deformed serpentinites show extensive matrix replacement by carbonates. Sampling includes 1 serpentinized harzburgite, 4 carbonated serpentinites and 3 listvenites (Fig S1, Tables S1-2).

Site 2 is located in the north-eastern part of the Jebel Fanja, 9.5 km north from Hole BT1B (Figs. 2 and S2). This area exposes a ~150 m thick mantle section comprising serpentinized harzburgites, interlayered by stain orange-red listvenites to the North, close to overlying gabbros. Lithological boundaries dip to the NNW. Serpentinized harzburgites (~100 m thick), often foliated and fractured,

overlie the metamorphic sole. The sole comprises mafic-derived schists, with amphibolites locally along the basal thrust, atop metasediments. Listvenites are found as a ~50–75 m thick continuous planar structural level close to gabbros, draping the ridge and southern flank of the Jebel Fanja, and as plurimetric lenses within carbonated serpentinites. Listvenites are massive and crosscut by closely spaced sub-millimetric orange-red magnesite veins and by millimetric white quartz-carbonate veins, all oriented perpendicular to the contact with the underlying carbonated serpentinites (~3–20 m). Carbonated serpentinites are often foliated at the contact with listvenites and host millimetric to centimetric light orange magnesite veins, oriented at low-angle with the contact (Fig. 1c). Vein density increases towards listvenites. Rare millimetric red magnesite veins cut through both listvenites and carbonated serpentinites. Listvenites are overlain by serpentinized peridotites (>20 m) cross-cut by numerous gabbroic dikes and pods at proximity with gabbros. Sampling includes 2 serpentinized harzburgites, 3 carbonated serpentinites and 3 listvenites collected along two transects (Fig S1, Tables S1-2).

3 Petrographic, analytical and modelling methods

The petrography, microstructure and composition of carbonated serpentinites and listvenites were determined and mapped using optical microscopy and a CamScan CrystalProbe X500FE Scanning Electron Microscope (SEM), equipped with UltimMax 100 EDS (energy-dispersive X-ray spectroscopy) detector at the Géosciences Montpellier SEM-EBSD facility. EDS data were processed with Oxford Instruments Aztec. Further back-scattered and secondary electron images were acquired using a Zeiss Gemini SUPRA 55 field-emission scanning electron microscope (FE-SEM) at the Institute of Tectonics and Geodynamics of RWTH Aachen University.

Mineral compositions of carbonates, silicates (serpentine, fuchsite), oxides and sulphides were quantified, and mapped for a subset of 25 samples, using a Cameca SX100 (Géosciences Montpellier) and a JEOL JXA-8530F HyperProbe (ISTE, University of Lausanne) Electron Probe Micro-Analyzer (EPMA). Elemental maps were quantified by coupling EDS semi-quantitative data and EPMA compositions using XMapTools 3.4.1 MatLab toolbox (Lanari et al., 2019). Transition elements were measured in carbonates and silicates for a subset of 12 samples by laser ablation inductively-coupled plasma mass spectrometry (LA-ICP-MS) on a ThermoScientific Element XR mass spectrometer (ISTE) and a ThermoScientific Element 2 mass spectrometer (Géosciences Montpellier). Data were processed using Glitter (Griffin et al., 2008). Sample preparation, operating conditions, analytical and data processing protocols are reported in Text S1. Analytical errors and measurements on reference materials are provided in Tables S3 and S9.

Thermodynamic calculations were performed using Perple_X 6.9.1 (Connolly, 2005, 2009), in a H_2O-CO_2 saturated FeO-Fe_2O_3-MgO-SiO_2 system to constrain the stability fields of metasomatic assemblages resulting from carbonation at different redox budgets. The calculations were performed

using the TC-DS622 version of the Holland and Powell (2011) thermodynamic data base with equations of state for H_2O and CO_2 after Pitzer and Sterner (1995). Solid solution models were applied for magnesite-siderite (Holland and Powell, 1998), antigorite (Padrón-Navarta et al., 2013), and ideal solution models for talc and brucite. Hematite, magnetite, and quartz were considered as pure phases.

4 Results

4.1 Textural, microstructural and geochemical study of the carbonation sequence

Based on mineral replacement textures and cross-cutting vein relationships, we identified 3 main groups of carbonates corresponding to different stages of carbonation during the conversion of serpentinized peridotite to listvenite (Table 1 in SI; this study, Kelemen et al., 2020; Beinlich et al., 2020; Menzel et al., 2022).

4.1.1 Protolith

Relics of the mantle protolith were preserved at Sites 1 and 2. They comprise moderately to fully serpentinized porphyroclastic harzburgites (Fig. S3). Serpentinized harzburgites show a typical mesh texture locally cut by millimetric crack-seal chrysotile veins. Olivine appears as mesh cores rimmed by lizardite/chrysotile and magnetite strings. Opx shows static replacement to bastite along fractures and cleavages. Minor Cpx occurs at the rim or in close proximity to Opx. Cr-spinel is often thinly rimmed by magnetite or ferri-chromite. Olivine and pyroxenes are fully serpentinized at the transition with listvenite. Bastites and serpentines display overlapping compositions in most transition elements, serpentine veins having the lowest values (see Tables S4, S10 and S11). Bastite are distinguished from serpentine by their high Sc and Ti concentrations, similarly to their respective mineral precursors, pyroxene and olivine. Sulphides are rare. They are identified as Fe-Ni-Co-bearing by SEM-EDS in serpentinized harzburgite OM20-13, and as polydymite, a weathering product of pentlandite, in carbonated serpentinite 44Z-4-0-5.

4.1.2 Stage 1: onset of carbonation

Stage 1 carbonates are identified in carbonated serpentinites and in listvenites.

The earliest occurrences of carbonates are pseudomorphic replacements of serpentine mesh and crack-seal veins by magnesite, and, in rare samples, by dolomite (Menzel et al, 2022). Pseudomorphic magnesite has XMg > 0.85 (XMg: molar Mg/(Mg+Fe)) except when growing near or at the expense of magnetite along the mesh (XMg < 0.85) (Fig. 3a). They are depleted in most transition elements compared to Semail ophiolite mantle values, except for Mn and Zn (Fig. 6).

Antitaxial magnesite veins are the most abundant veins formed in Stage 1. They crosscut serpentinites and commonly form anastomosing or closely-spaced vein networks. They are characterized by chemical zoning with a Fe-rich median zone (XMg: 0.57-0.87) and Mg-rich edges

(XMg: 0.89-0.97) (Fig. 3b). They are locally cut by cross-fibre to blocky unzoned magnesite veins (XMg: 0.93-0.97). They have transition element compositions comparable to that of pseudomorphic magnesite (Fig. 6).

Pervasive matrix carbonates occur as (a) isolated or grouped spheroidal magnesites presenting core-to-rim chemical zoning, defined as "spheroids" by Beinlich et al. (2020); and (b) aggregates formed by clustering spheroids or pervasive growth rooting from veins walls into the matrix (Figs. 3b, S3, S4). Magnesite spheroids have Fe-rich cores overgrown by Mg-rich magnesite (Figs. 5a, S5, and S6a-b); this magnesite zoning pattern is referred to in the following as Fe-core spheroids. Chemical mapping (Fig. 5a) indicates proportions of ~19% and ~81% for Fe-rich and Mg-rich magnesite respectively (Table S12). Fe-core spheroids are commonly <100 µm. They occur in the vicinity of mesh rims and zoned antitaxial veins, in domains with a low vein density. They are distinguished by the common presence of tiny inclusions of hematite (typical size: <5 µm) and characteristic destabilization textures around Fe-oxides (Figs. 4a and 4c). In carbonated serpentinite OM20-26, such a destabilization texture shows microporosity at the carbonate-oxide interface (Fig. 4a). Fe-core spheroids have high concentrations in transition elements compared to other Stage 1 carbonates, sometimes higher than Semail mantle values for Sc, Mn and Co (Figs. 6 and S6d).

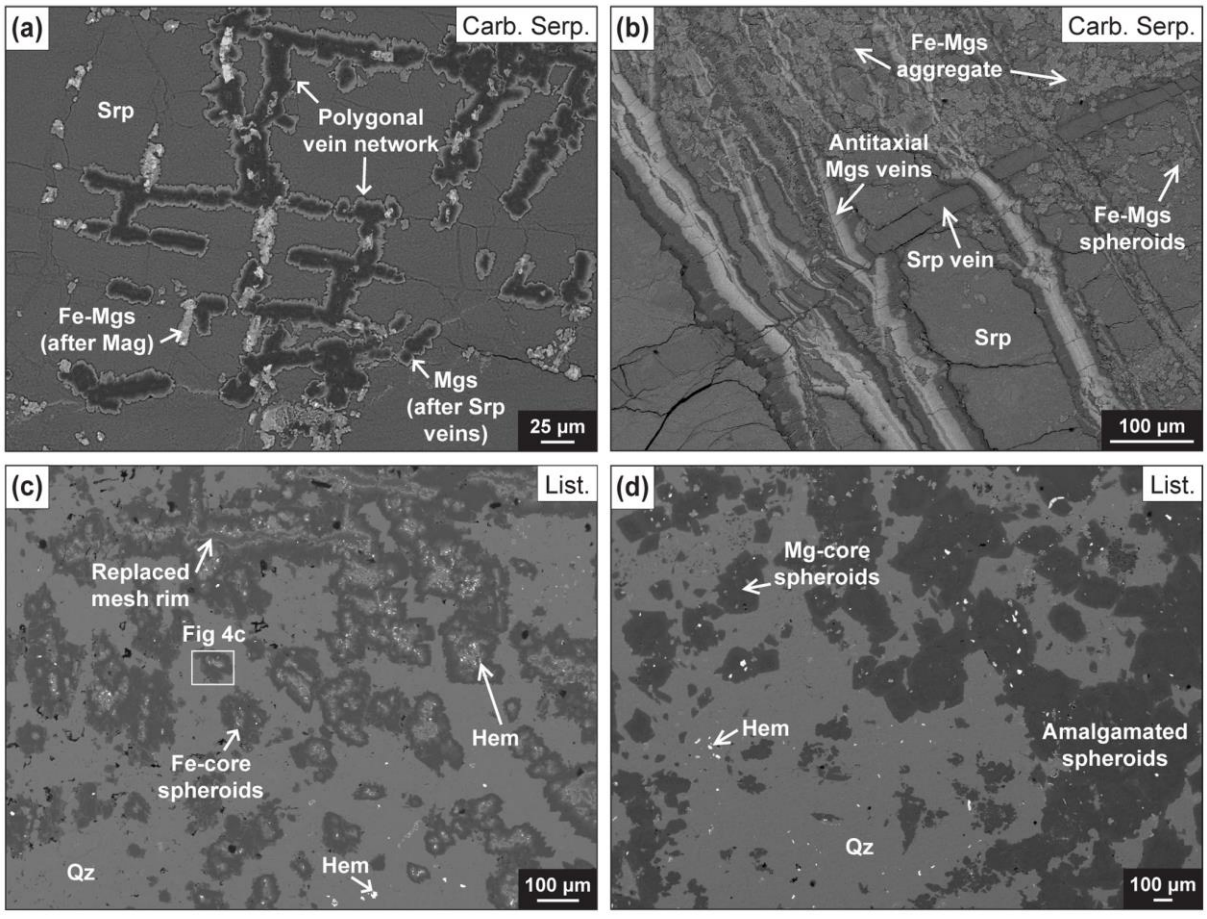

<< **Figure 3** Back-scattered electron (BSE) images of carbonate microstructures and textures representative of reaction stage 1 (a-c) and stage 2 (d). (a) Magnesite replacing serpentine mesh rims in characteristic polygonal vein networks in carbonated serpentinite 44Z-2-47-50. (b) Crack-seal serpentine vein cut by antitaxial magnesite veins showing a Fe-rich median zone (light grey) and Mg-rich vein walls (dark grey) in carbonated serpentinite 44Z-4-0-5. Fe-rich magnesite spheroids and aggregates formed in the vicinity of antitaxial veins. (c) Fe-core spheroids (light grey cores) that developed in the vicinity of a former mesh rim preserved in listvenite 50Z-1-75-80. (d) Mg-core spheroids locally amalgamated to form aggregates. Abbreviations: Hem: hematite, Mag: magnetite, Mgs: magnesite, Qz: quartz, Srp: serpentine.

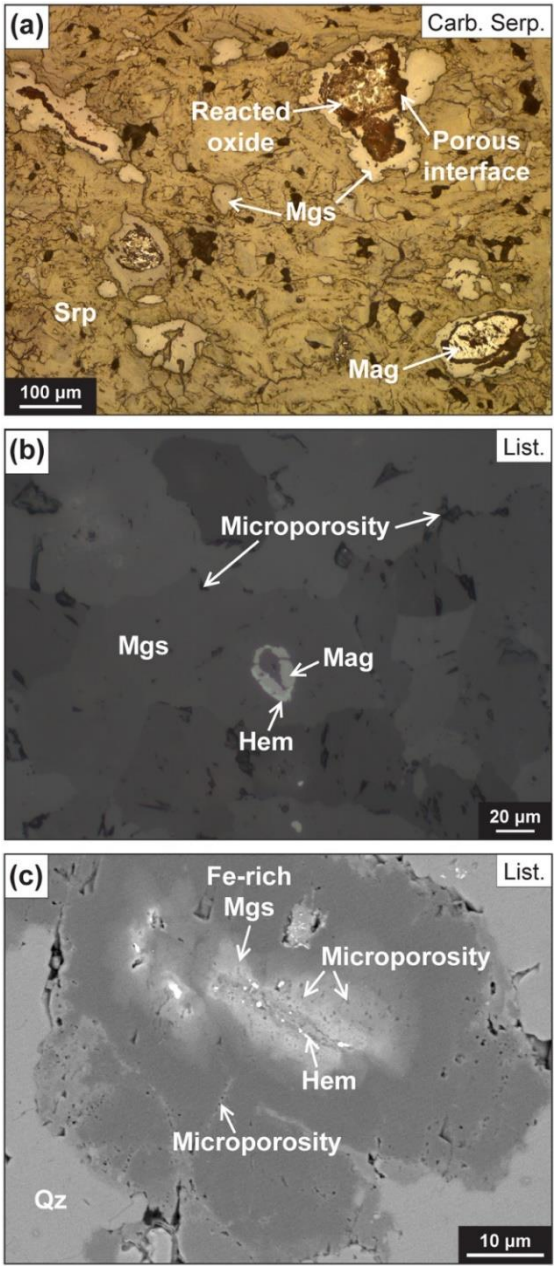

Figure 4 Textural relationships between Fe-oxides and magnesite. (a) Reflected light (RL) image of spheroids in carbonated serpentinite OM20-26. Magnesite surrounding variously reacted Fe-oxides ("reacted oxide") and magnetite. A porous interface connects oxide relicts and magnesite. (b) Magnetite destabilized into hematite and overgrown by magnesite aggregate in listvenite 71Z-2-21-26. Presence of a microporosity along (sub)grain boundaries. (c) Internal Fe-zoning of Fe- core spheroid, with hematite and a microporous zone outlining the relict of reacted Fe-oxide. Abbreviations: Hem: hematite, Mag: magnetite; Mgs: magnesite, Qz: quartz, Srp: serpentine.

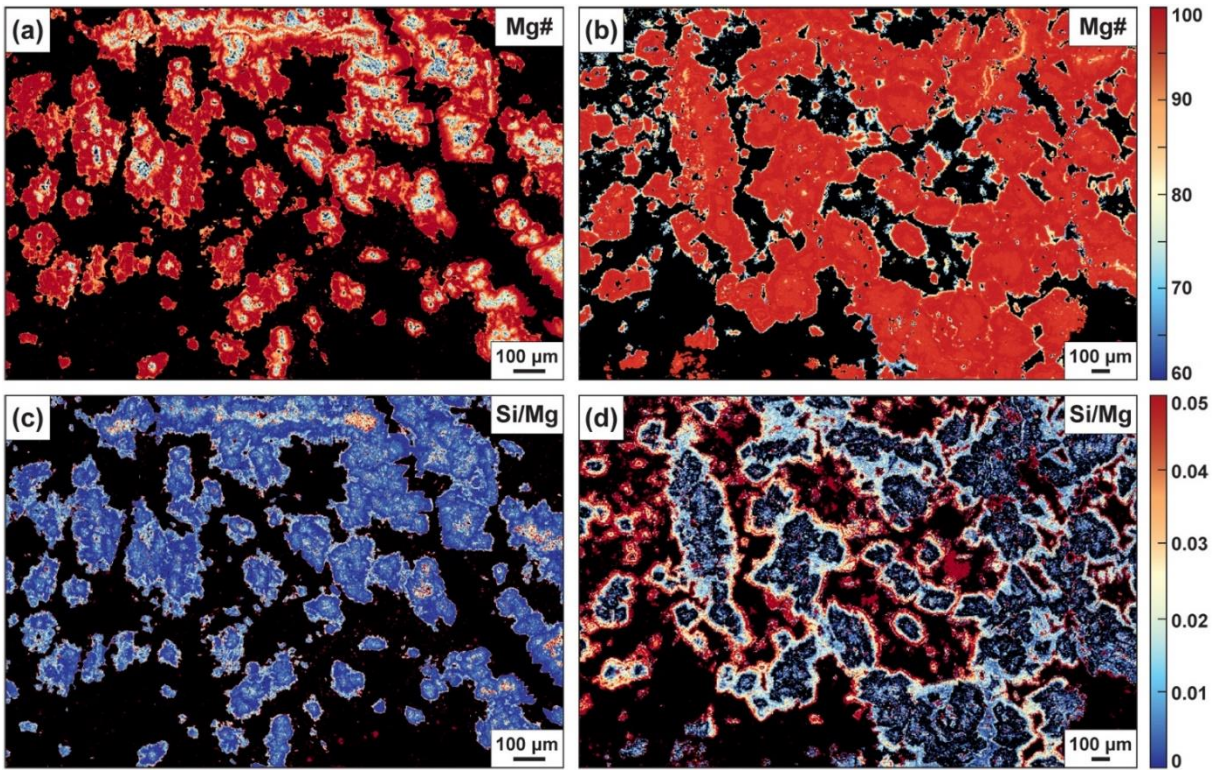

Figure 5 Quantitative Mg# and Si/Mg distribution maps of Fe-core (a and c, 50z-01-75-80) and Mg-core spheroids (b and d, 46z-4-46-51) in listvenites presented in Fig. 3c-d.

4.1.3 Stage 2: widespread replacement by Mg-rich magnesite and quartz

This stage is observed in listvenites but rarely in carbonated serpentinites; it is characterized by the complete replacement of serpentine by abundant Mg-rich magnesite and fine-grained background quartz. Chemical mapping (Figs. 5b and d) typically shows a high proportion of carbonates (~60% of volume) compared to quartz (~34 % of volume) (see Table S12).

Magnesite occur mainly as spheroids, aggregates and overgrowth on pre-existing microstructures. Magnesite spheroids have Mg-rich cores (mean XMg: ~0.96) and are referred to as Mg-core spheroids. They range in size between 50-300 µm (Fig. 3d) and show chemical zoning with Si and Fe enrichment toward the rims as illustrated on Mg# and Si/Mg maps in Figs 5b and 5d. High-resolution mapping of the largest Mg-core spheroids reveal, in the outer regions, (a) Si-Ca-rich domains incorporating nano-inclusions of quartz (Fig. S6j), and (b) the development of Mg-Fe zoning patterns and the formation of high Fe dendritic magnesites at the rims (Fig. S6g). Mg-rich magnesite aggregates (XMg = ~0.96) are composed of amalgamated Mg-core spheroids or by sub-millimetric subhedral to euhedral crystals. Mg-core spheroids and Mg-rich magnesite aggregates overlap in compositions for transition elements; they are both depleted compared to Fe-core spheroids (Figs. 6 and S6f-j). All carbonation textures are crosscut by cryptic quartz veins indicative of local silica remobilization (Menzel et al., 2022).

Anhedral to flaky hematite (~5–20 μm) occurs within the magnesite-quartz matrix, rimming altered Cr-spinel, and replacing magnetite. Fuchsite is observed in a few core samples growing at the expense of Cr-spinel (e.g., listvenite 68Z-1-60-64), or intergrown with quartz in domains resembling bastite (e.g., listvenite 53Z-2-72-77). Textures point to fuchsite growth occuring concurrently to Stage 2 carbonates. Sulphides in listvenites are extremely rare, consisting in pyrite overgrown by magnesite (e.g., listvenite 46Z-4-46-51), polydymite, chalcocite and gersdorffite (e.g., listvenite 46Z-2-19-24).

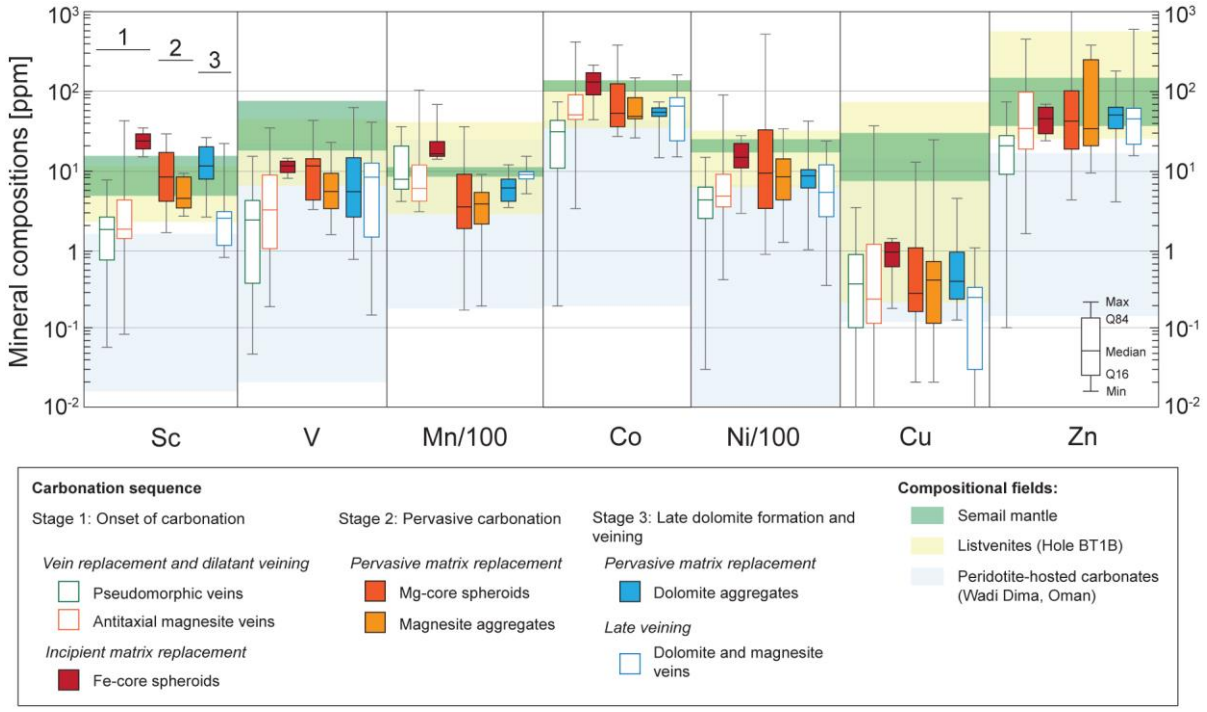

Figure 6 Caltech diagrams of the carbonates compositions in transition metals plotted on a log scale. The compositions of BT1B listvenites and the Oman mantle (data from Godard et al., 2021) and hydrothermal carbonates in the Semail Ophiolite (data from Noël et al., 2018) are represented by the couloured background fields.

4.1.4 Stage 3: late generation of quartz and carbonate veins

Stage 3 is dominated by the formation of carbonate veins (mainly dolomite) and late cataclasis. Millimetric polycrystalline syntaxial carbonate-quartz and carbonate veins cross-cut all pre-existing microstructures. Minor dolomite aggregates are also observed. Cataclasites reworking clasts of listvenite locally cut or are cut by late dolomite veins. Carbonates have transition element compositions overall similar to Stage 1 and 2 Mg-rich magnesite aggregates and veins (Fig. 6).

4.2 Thermodynamic modelling

Thermodynamic modelling is used to characterize the effects of variable CO_2 concentrations in fluids and redox conditions on mineral assemblages during carbonation at equilibrium conditions (see section 3 for further details). The protolith is modelled by a simplified harzburgite bulk composition

representative of the serpentinized Semail Ophiolite mantle section (OM94-52h, Hanghøj et al., 2010) in the FMS + fluid system. To account for its initially variable Fe^{3+}/Fe_{TOT} due to serpentinization (Mayhew et al., 2018), the Fe^{3+}/Fe_{TOT}–XCO_2 pseudosections are calculated (Fig. 7a) with: i) binary compositional mixing from reduced to fully oxidized, ii) H_2O and CO_2 considered as saturated fluid phases. Serpentine is modelled by antigorite (Atg). Reactions products include magnesite, quartz, serpentine, talc, magnetite, and hematite depending on XCO_2 ($CO_2/(CO_2+H_2O)$ molar ratio) and Fe^{3+}/Fe_{TOT} (Fig. 7). Figure 7 illustrates the results obtained at constant pressure and temperature conditions of 0.3 GPa and 200°C respectively.

Two endmember reaction pathways producing either Fe-rich or Mg-rich magnesites are identified: (A) at constant bulk Fe^{3+}/Fe_{TOT} and constant redox budget, increasing XCO_2 produces a change in phase assemblage and magnesite abundance, with magnetite reacting with CO_2 to form, first, Fe^{2+}-bearing magnesite and hematite, then, Mg-rich magnesite; (B) change in the bulk redox budget with increasing (oxidation) or decreasing (reduction) Fe^{3+}/Fe_{TOT}.

Representative of case A, the evolution of XMg in magnesite with increasing XCO_2 for a fixed bulk rock Fe^{3+}/Fe_{TOT} of 0.5 is shown in Fig. 7b. High Fe content of magnesite is predicted in the Atg–Mgs–Hem stability field (XMg = 0.7), which is primarily a consequence of disappearing magnetite as XCO_2 increases. At high XCO_2, the model predicts Mg-rich magnesite compositions despite a lack of other silicate phases that incorporate iron, because Fe is diluted within > 65% mol% of magnesite in the quartz-magnesite-hematite assemblage (Fig. 7b). Hence, the Fe redistribution during magnetite breakdown and the increasing magnesite abundance is likely to produce compositional zoning with progressive carbonation, even in a system at equilibrium. Predicted changes of XMg in magnesite between differently carbonated assemblages (corresponding to different XCO_2) vary in their intensity depending on the bulk rock Fe^{3+}/Fe_{TOT}, with only small changes of magnesite XMg in very oxidized compositions (Fig. 7a).

XMg isopleths are horizontal in most stability fields and changes in the bulk redox budget (e.g. induced by the addition of reduced or oxidized fluids) will result in variations of magnesite composition (case B in Fig. 7a). The model predicts decreasing XMg of magnesite when the bulk Fe^{3+}/Fe_{TOT} decreases. This effect is the most pronounced at low XCO_2 conditions, where serpentine is stable and magnesite abundance comparatively low. Interestingly, at these conditions, complete transformation of magnetite to hematite and Fe-bearing magnesite is predicted to occur with relatively minor magnesite precipitation, independently of the initial bulk Fe^{3+}/Fe_{TOT}.

Caveats arise when using thermodynamic modelling to interpret microstructural observations and geochemical analyses of highly reactive systems such as the Fanja listvenite series. It is important to note that fluid XCO_2 in Fig. 7 is not equivalent to the CO_2 concentration of the infiltrating fluid, but to the XCO_2 that this fluid would acquire once equilibrated with the calculated mineral assemblages. Hence

the model is applicable when the infiltrating CO_2-bearing fluids can be considered as locally buffered to the XCO_2 corresponding to the equilibrium assemblage. It is not applicable if fluid fluxes are high and CO_2 renewal fast: the buffering capacity of the local mineral assemblage can then be kinetically overstepped, and reactions will become controlled predominantly by the infiltrating fluid composition.

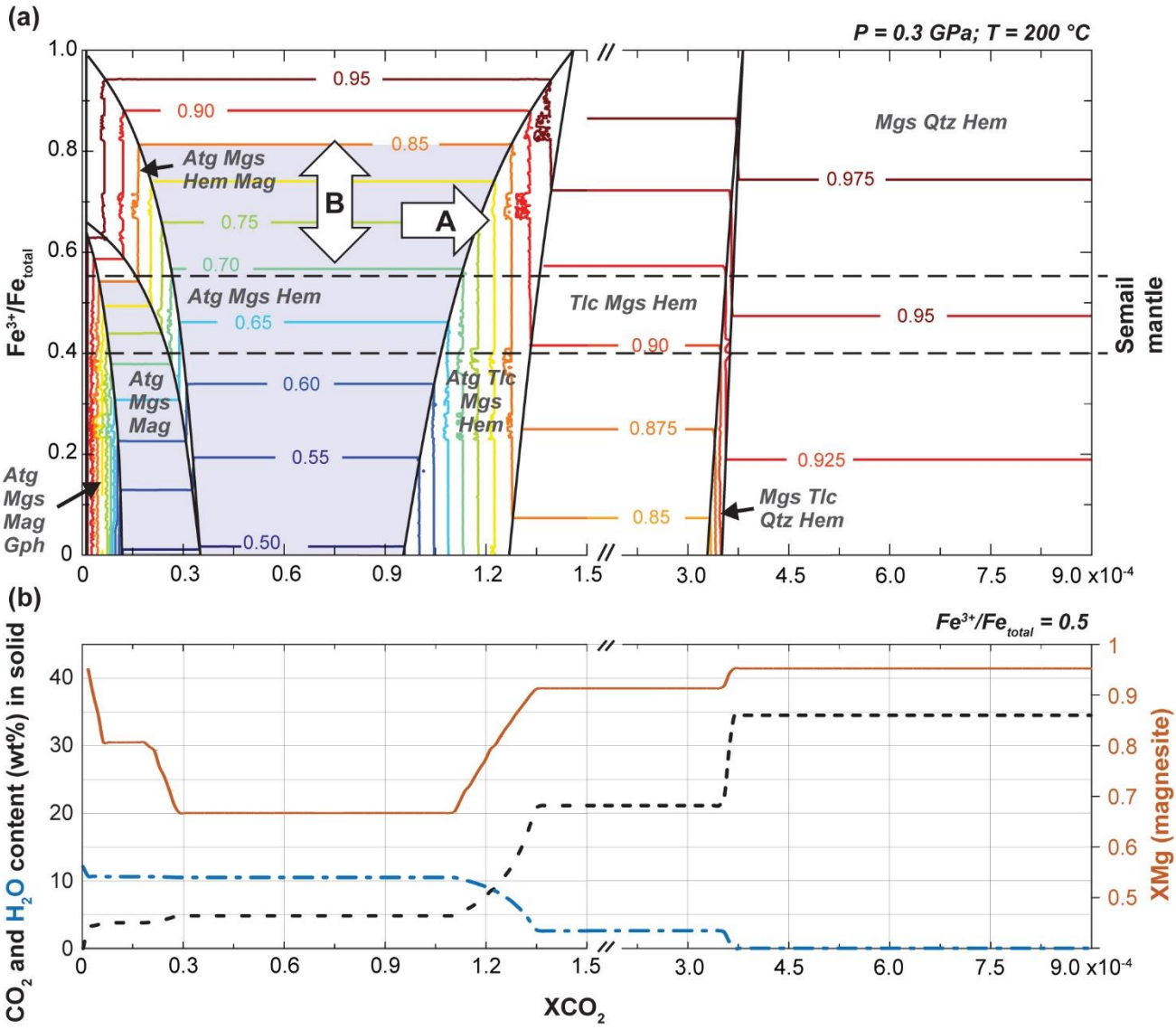

Figure 7 Model of Fe-partitioning in relation to carbonation and bulk rock redox budget. (a) Isobaric and isothermal, fluid-saturated XCO_2 pseudosection for a harzburgite bulk rock composition, with the y axis showing the redox budget expressed as Fe^{3+}/Fe_{TOT} (note that only in the small field at very low XCO_2 where graphite is predicted, the redox budget does not directly equal Fe^{3+}/Fe_{TOT} here). Predicted XMg compositions of magnesite is shown as coloured isopleths. (b) Plot of XMg of magnesite and CO_2 and H_2O content in solid assemblage at a fixed redox budget of $Fe^{3+}/Fe_{tot} = 0.5$, illustrating the expected changes of magnesite composition for the case of redox-neutral carbonation. Modelling was done using a simplified hydrated harzburgite composition with binary compositional mixing from reduced (SiO_2 – 38.77 wt%; MgO – 39.21 wt%; FeO – 6.99 wt%) to fully oxidized (SiO_2 – 38.77 wt%; MgO – 39.21 wt%; Fe_2O_3 – 7.77 wt%) with saturated H_2O and CO_2. For illustration purposes the results of two calculations at the same conditions but different ranges of XCO_2 were combined (note the change in scaling of the x-axis). Blue fields are for Fe-rich magnesite compositions (XMg < 0.85). The following mineral abbreviations are used. Atg: antigorite; Gph: graphite, Hem: hematite, Mag: magnetite, Mgs: magnesite, Qz: quartz, Tlc: talc

5 Discussion

5.1 From serpentinite to listvenite: a stepwise carbonation sequence

The conversion of serpentinites to listvenites in the Fanja region produced a wealth of vein microstructures and matrix replacement textures including zoned magnesites of highly variable compositions. The abundant veins characterizing our samples indicate efficient cracking and faulting that favoured, in turn, the recurrent redistribution of fluid pathways and the infiltration of highly reactive fluids throughout the identified sequences of carbonation (e.g., Kelemen et al, 2022; Menzel et al, 2022) despite the increase in rock volume associated to the formation of listvenites (e.g. Falk and Kelemen, 2015; Godard et al., 2021; Okazaki et al., 2021). Veins form a multi-scale discrete network with matrix replacement textures occurring as small (up to 1 mm) magnesite, or more rarely dolomite, overgrowths to aggregates around the finest veins (e.g., Figs. 3b, S3, S4). Such a discrete and recurrent (re-)organization of fluid pathways favoured the development of isolated micro-domains with matrix replacement reactions more likely to occur at rock-dominated conditions. It also allowed preserving the texture and composition of mineral assemblages formed during the earliest stages of the carbonation sequence in domains poorly or not affected by fracturation and faulting during the later stages of listvenite formation.

Our investigations indicate that the early stages of carbonation proceeded as two main steps characterized by the formation of magnesite spheroids with (i) Fe-rich core during incipient carbonation (Stage 1) and, (ii) Mg-rich cores and Fe-rich rims during extended carbonation (Stage 2). Both types are observed in carbonated serpentinites and listvenites (Figs. 5 and S5), and, we posit that they represent a type feature of the carbonation sequence. This interpretation contrasts however with models describing the formation of magnesite as resulting from single step carbonation reactions after serpentine (R1) or talc (R2) (e.g., Johannes, 1969):

$$(Mg,Fe)_3Si_2O_5(OH)_4 + 3CO_2\,(aq) = 3(Mg,Fe)CO_3 + 2SiO_2 + 2H_2O\,(aq) \quad (R1)$$

Serpentine + CO_2 (aq) = Magnesite + Quartz + H_2O (aq)

or

$$(Mg,Fe)_3Si_4O_{10}(OH)_2 + 3CO_2\,(aq) = 3(Mg,Fe)CO_3 + 4SiO_2 + 2H_2O\,(aq) \quad (R2)$$

Talc + CO_2 (aq) = Magnesite + Quartz + H_2O (aq)

The Mg-rich magnesite spheroids, aggregates and overgrowths represent the most voluminous fraction of the matrix carbonates in the Fanja listvenites (~55 vol. %; e.g., Fig 5c). Mg-rich magnesites generally have subhedral to euhedral morphologies suggesting formation at near-equilibrium conditions (Beinlich et al., 2020). This assumption is consistent with the geochemical analyses and maps of Mg-rich magnesites showing homogeneous chemical compositions at the millimetre-scale for (i) Mg-rich

overgrowths around Fe-rich core magnesites (Stage 1) and (ii) in the Mg-rich core regions of spheroids and aggregates (Stage 2) (Figs. 5b and 5d). Thermodynamic modelling predicts the formation of high XMg magnesite in the Tlc–Qz–Hem and in the Mgs–Qz–Hem stability fields (Fig. 7a) and the most favourable conditions are (i) a serpentinized protolith (Fe^{3+}/Fe_{TOT} > 0.6) and (ii) high XCO_2 fluids (>1.3 x 10^{-4}). The bulk Fe^{3+}/Fe_{TOT} of the main mantle section of the Semail ophiolite is typically of 0.4–0.55 (Mayhew et al., 2018) therefore too low to account for the Mg-rich compositions of the Fanja magnesites (XMg: ~0.96), except after equilibration with high XCO_2 fluids in the Mgs–Qz–Hem stability field. It should be noted that the stability domain of this mineral assemblage increases as temperatures decreases, and thus the formation of high XMg magnesite should be facilitated during ophiolite cooling, even when considering constant chemical and redox conditions.

Fe-rich magnesite is widespread in the studied samples although it represents only a minor fraction of the matrix carbonates (~8–19 vol. %, e.g., Fig 5). It occurs as (i) Fe-core spheroids, typical of Stage 1 features, and, (ii) thin rims around Mg-rich spheroids. Fe-rich magnesite is not uncommon in carbonated peridotites and listvenites where it occurs as Fe-rich zoning toward the rims of euhedral magnesites (e.g., Tominaga et al., 2017), or as Fe-rich overgrowth around Mg-rich magnesite (e.g., Menzel et al. 2018). Its formation is then ascribed to complete dissolution of magnetite at high XCO_2 when stabilizing the Mgs+Qz assemblage and/or to precipitation in the presence of talc (Fig. 7a, Menzel et al., 2018). The textures and compositions of the Fanja Fe-rich magnesites however differ from previously studied samples : (i) all samples have magnesite compositions too high in Fe (XMg < 0.80) to be accounted for solely by fluid-rock equilibration in the presence of talc (XMg > 0.85; Fig. 7; Menzel et al., 2018; Sieber et al., 2022), (ii) the development of Fe-rich rims of Mg-core spheroids is associated to a change in magnesite texture from euhedral and anhedral to dendritic textures suggesting changes in growth conditions (Fig. 5d), and (iii) Fe-core anhedral magnesite is often observed as coronae around Fe-oxides (Fig. 4), a texture described here for the first time in listvenites. These characteristics suggest that the Fanja Fe-rich magnesites result from different reaction pathways in contrast to previously studied carbonated serpentinites and listvenites.

5.2 Origins of two Fe-enrichment trends in the Fanja magnesites

The differences in the textures of the Fe-rich magnesites can provide insights on their growth conditions and thus on the possible origins of the two distinct types of Fe-enrichment observed in the Fanja magnesites.

Fe-rich core magnesite and associated aggregates have anhedral to subhedral textures suggesting precipitation at or near equilibrium conditions. Based on this assumption, the very low XMg (~0.55-0.70) of Fe-rich core magnesites and their volume fraction (e.g., 8 % in sample 50Z-1-75-80, Fig. 5a) can be interpreted as showing equilibration in the serpentine stability field between low XCO_2 fluids and a typical Semail serpentinized peridotite (initial bulk Fe^{3+}/Fe_{TOT} ~0.4-0.55; Mayhew et al., 2018;

Fig. 8). The Fe-rich magnesite spheroids and aggregates are typically localized in the vicinity of Stage 1 serpentine and Fe-rich magnesite veins, suggesting that precursor serpentine veins and early carbonate veins acted as fluid pathways for these low XCO_2 fluids during incipient carbonation. This hypothesis is supported by the high nanoporosity of the serpentine veins in comparison to nearby mesh lizardite (Menzel et al., 2022). In this context, the variations in Fe composition of magnesite cores and aggregates from one sample to the other is attributed to changes in (i) the degree of serpentinization of the peridotite protolith (initial bulk Fe^{3+}/Fe_{TOT}) and/or (ii) the oxygen fugacity of the low XCO_2 infiltrating fluids (oxidized to reduced fluids) (Figs. 7a and b). This interpretation however overlooks the possible impact of the partial to complete dissolution of Fe-oxides on Fe redistribution, redox changes and the role of fluid compositions (pH, ionic strength, ligands…). Fe-core spheroids preserve textures showing the growth of anhedral magnesite at the expense of magnetite in several of the carbonated serpentinite (Fig. 4a) and listvenite (Fig. 4c) samples. Some samples also preserve microporous reaction zones with tiny hematite grains, outlining relicts of dissolving magnetite (Fig. 4d). The destabilization of magnetite in presence of CO_2-rich fluids to form Fe-rich magnesite (siderite as $FeCO_3$) is written (Frost, 1985):

$$(Fe^{2+}Fe^{3+}{}_2)O_4 + 3CO_2\,(aq) = 3Fe^{2+}CO_3 + 0.5O_2\,(aq) \quad \text{(R3)}$$

Magnetite + CO_2 (aq) = Siderite + O_2 (aq)

Reaction R3 predicts an increase in oxygen fugacity, however $O_{2\,(aq)}$ solubility is negligible in hydrothermal aqueous fluids in the range of P-T conditions estimated for the formation of the Fanja listvenites. Therefore, it must be buffered by an oxidation reaction involving either infiltrating fluids and/or reacting minerals. Reaction R3 could proceed through oxidation of reduced fluid species (e.g., serpentinization derived H_2), if present, to CO_2, carbonate and/or water. Alternatively, oxidation of magnetite is suggested by the presence of hematite around destabilized magnetite and, assuming constant redox conditions, the formation of Fe-rich magnesite at the expense of magnetite can then be rewritten as:

$$(Fe^{2+}Fe^{3+}{}_2)O_4 + CO_2\,(aq) = Fe^{2+}CO_3 + Fe^{3+}{}_2O_3 \quad \text{(R4)}$$

Magnetite + CO_2 (aq) = Siderite + Hematite

However, the transformation of magnetite into hematite could also reveal interactions with low pH fluids rather than an oxidation reaction (Ohmoto, 2003; Zhao et al., 2010):

$$Fe_3O_4 + 2H^+\,(aq) = Fe_2O_3 + Fe^{2+}\,(aq) + H_2O \quad \text{(R5)}$$

Magnetite + $2H^+$ (aq) = Hematite + Fe^{2+} (aq) + H_2O (aq)

with Fe^{2+} precipitating as Fe-rich magnesite when dissolved CO_2 is present. The solubility of magnetite and the transport of Fe^{2+} would also be enhanced in saline fluids rich in ligands (CH_3COO^-, Cl^-, …; e.g., Zhao et al., 2010).

Our observations do not allow discriminating unquestionably these different reaction pathways for the formation of the Fe-core spheroids. The body of evidences suggesting that Fe-core spheroids form in low flow zones at an early stage of carbonation of the serpentinized precursor leads us however to opt for a coupled redox process (involving reduced fluids and/or solely reaction R4) as the most likely reaction pathway for their formation. Nevertheless, the migration of low pH and/or saline fluids likely represents an important vector for the remobilization of Fe, in particular for the Fe-rich rims of Mg-rich magnesite spheroids.

In contrast to Fe-core spheroids and aggregates, Fe-rich rims and associated outer cores of the Mg-rich magnesite spheroids are distinguished by their heterogeneities in textures and compositions: (i) the outer cores have euhedral to subhedral textures but contain abundant micro- to nanoscale quartz inclusions (Figs. 5d and S6j), (ii) they are also characterized by strong variations in compositions (Si, Ca, Mn; e.g., Fig. S5, Tables S10-S11), and (iii) the Fe-rich rims have dendritic textures indicating fast growth kinetics. These variations suggest a departure from equilibrium conditions from cores to rims as the formation of the Mg-rich core spheroids progressed. Another characteristic of the domains where high Mg-core spheroids dominate is the lack of Fe-bearing oxides (magnetite, Cr-spinel) except for the occurrence of small hematite grains in the outer cores and in the background quartz matrix. In contrast to what observed in Fe-core spheroids, these hematite grains have sometimes dissolution features suggesting a change in reaction conditions during the formation of the Mg-core spheroids leading to disequilibrium conditions relative to the Mgs–Qz–Hem assemblage. Decreasing temperatures would increase the stability domain for these minerals so we posit that these contrasting trends result primarily from changes in fluid composition with reacting fluids as carbonation progresses. These variations could result from (1) less efficient fluid renewal at the growing magnesite interface: carbonation reactions are typically associated to significant increases in volume (Kelemen et al., 2022) thus clogging fluid pathways (e.g., Andreani et al., 2009) and inducing, in turn, local changes in fluid compositions and reaction pathways (e.g., Peuble et al., 2015a, b) and/or (2) changes in the composition of the inlet fluids as discussed for Fe-rich spheroids.

5.3 Interplays between carbonation reactions and fluid flow: consequences on trace metal redistribution

The dissolution of serpentinized peridotites during listvenite formation releases trace elements that will be either leached out of the reaction zones by the fluids to precipitate downstream, or trapped locally by secondary minerals. The study of Hole BT1B listvenites and carbonated serpentinites shows that they have highly variable trace element bulk rock compositions compared to their serpentinized precursors,

in particular for siderophile and chalcophile transition elements, even though mass balance calculations indicate that there is no fluid addition or loss for these elements at the scale of the borehole (Godard et al., 2021). Most trace elements being highly incompatible in quartz, carbonates represent, in volume, the major trapping mineral in listvenites. They overlap in composition with the bulk rock composition of the BT1B listvenites series indicating that, except for Cu, they also account for a large part of their transition element budget (Fig. 6). These relatively rich compositions distinguish the Fanja carbonates from the hydrothermal carbonates from the Semail mantle section that are commonly depleted relative to the reacting host serpentinized peridotites (Noël et al., 2018). The Fanja carbonates have extremely variable compositions, beyond the range of Hole BT1B listvenite series, yet different trends can be distinguished between vein and matrix carbonates and, to a lesser extent, between the three carbonation stages, giving insights on the respective roles of dissolution-precipitation reactions and transport in the redistribution of transition elements during carbonation.

Matrix carbonates have on average slightly higher concentrations compared to veins, Sc showing the most systematic differences between matrix and vein compositions. These differences are related in part to the large LA-ICP-MS spot size (100 μm) compared to that of carbonate minerals, particularly those forming spheroids and aggregates: matrix carbonate measurements are likely to include the contribution of the small magnetite and hematite grains typically associated to magnesite spheroids (Fig. 4), in particular in the small Fe-core spheroids. Nevertheless, they indicate also that most transition element released by the dissolution of primary minerals will be trapped locally in carbonate and oxides when matrix carbonation occurs, in particular during the earliest stages of carbonation.

Only Mn shows significant differences in compositions from one stage of carbonation to the other for both vein and matrix carbonates: they are overall enriched in Stage 1 carbonates compared to Stage 2 and 3 carbonates. The mobility of Mn typically depends on redox conditions that are highly variable in the Fanja samples with, for example, bulk Fe^{3+}/Fe_{TOT} values of 0.13–0.61 in listvenites, and 0.3–0.74 in carbonated serpentinites at Hole BT1B (Godard et al., 2021). The overlap between the compositions of the Semail serpentinized peridotites (Mayhew et al., 2018), the carbonated serpentinites and listvenites indicate that these variable redox values are not determined solely by changes in lithologies. Our mineralogical investigations show that, in addition to the complex sequences of dissolution and precipitation of oxides discussed previously, the conversion of serpentinites to carbonated serpentinites and listvenites is associated to the progressive disappearance of sulphides initially present in the protolith. Only rare carbonated serpentinites preserve Fe-Ni(-Co) sulphides (this study) or magnetite-awaruite assemblages (BT1B core, Beinlich et al., 2020) typically indicative of highly reducing conditions typical for serpentinization (Klein and Bach, 2009; de Obeso et al., 2020). On the other hand, the rare secondary Fe-Cu rich sulphides observed in association to hematite in listvenites are indicative of oxidizing conditions, with oxygen fugacities several orders of magnitudes higher than for the magnetite-awaruite assemblages (Frost, 1985). The conversion of the magnetite and Fe-Ni sulphides to

rare Fe-Cu rich sulphides and abundant hematite in our samples points to a change to oxidizing conditions (Eckstrand, 1975; Frost, 1985). The lower Mn content of Stage 2 and 3 carbonates, predominant in listvenites, is likely related to the same process. On the same line, the scarcity or absence of sulphides in the Fanja samples may result from the oxidation of sulphide to highly soluble sulphate, as proposed for the fuchsite-bearing listvenites at the Gråberget ultramafic body (Austrheim et al., 2021). These reactions may participate to the mobilization of transition elements in fluids, especially for Cu and, to a lesser extent, Ni and Co: it could account for the depletion of carbonates in these elements compared to their serpentinized precursor. This suggests that transition elements having chalcophile affinity are the most likely to be leached out of reaction zones and act as fluid mobile elements until conditions favourable for the precipitation of sulphide are reached in fluids (supersaturation, changes in carbon, sulphur or hydrogen speciation; e.g., Frost, 1985; Frost and Beard, 2007). Such a mechanism could account for the highly localized enrichments in these elements along BT1B cores (Godard et al., 2021) and the occurrence of small Cu veins observed in some listvenite samples (Kelemen et al., 2020) or in the field in Fanja. It is interesting to note that secondary sulphides are commonly observed in ore-bearing listvenites (e.g., Qiu and Zhu, 2018).

In contrast to most transition elements, there is no straightforward relationships between the overall distribution of V and Zn in carbonates, oxides and sulphides and their bulk rock compositions. V and Zn are concentrated in Cr-spinel, a mineral well preserved until the later stages of carbonation (Kelemen et al., 2020, Beinlich et al., 2020, this study), and they are enriched mostly in fuchsite (Tables S4, S10, S11). We posit that their complex distribution trends are related to their progressive release in fluids during the dissolution of Cr-spinel combined with a preferential trapping in fuchsite-rich zones (Godard et al., 2021).

6 Summary and conclusions

The petrological and chemical study of the Fanja listvenites and associated lithologies allows identifying three stages of carbonation for the conversion of serpentinized peridotites to listvenites, with the development of replacive textures commonly observed at Stage 1 and 2, whilst carbonate (± quartz) veining becomes predominant in the later Stage 3. Carbonates are dominantly magnesite but dolomite is also commonly observed at Stage 3. This study highlights also the widespread occurrence of Fe-zoning in the matrix and vein magnesite developing during incipient carbonation. The pervasive replacement of serpentine by magnesite is characterized by the formation of spheroids, among which two types were identified based on the composition of their core regions: Mg-core and Fe-core spheroids. We also document for the first time in detail the different carbonation reactions destabilizing Fe-oxides into Fe-rich magnesite, an essential mechanism to account for the development of Fe-core magnesites. Thermodynamic modelling converges to the precipitation of Fe-rich magnesite in equilibrium with serpentine at low fluid XCO_2 composition and variable local redox conditions. Fe-core

spheroids characterize the onset of carbonation, followed by the pervasive (over)growth of Mg-rich spheroids and aggregates at increasing fluid XCO_2 and/or during cooling. The relative scarcity of Fe-core spheroids compared to Mg-rich matrix magnesite may be a hint for fast transition from limited to intensive fluxing of reactive fluid. This transition may be caused by the linkages between cyclic fluid pressure variations and brittle to cataclasic deformation under regional tectonic stress, related to reaction-enhanced deformation (Menzel et al., 2022) and reaction-induced fracturing (e.g. Kelemen et al., 2022).

Carbonation triggers the destabilization of the minerals constituting serpentinized peridotites (silicates, minor oxides and sulphides) thereby influencing the redistribution of transition elements between minerals and fluids. In Fanja, carbonation to listvenite is accompanied by evolving assemblages of Fe-oxides and sulphides. These implications have to be considered for mass transfers at a larger-scale, as listvenite formation is inferred to occur along basal sections of obducted ophiolites and in the shallow mantle wedge of subduction zones (Kelemen and Manning, 2015), with potential impact on the cycling of metals.

Data availability

All data are contained in the figures of the manuscript and supplementary information; raw images of these figures are available from the authors upon request. Data are available online on the EarthChem data repository: https://doi.org/10.26022/IEDA/112834, (Decrausaz et al., 2023).

Sample availability

Archive halves and samples of BT1B cores are available through the Oman Drilling Project (https://www.omandrilling.ac.uk/samples-data). Archive samples from Site 1 and Site 2, and all studied thin sections are stored at the Géosciences Montpellier.

Author contribution

This work is part of TD's PhD thesis at Géosciences Montpellier. MG designed the project. TD, EO and RL conducted field work. TD and EO refined geological maps. TD, MG, FP and MDM studied the petrography and the petrology. TD performed SEM imaging, EDX mapping, EPMA and LA-ICP-MS data acquisition and treatment, image processing, and drafted the figures. FB conducted EDS analyses. MDM performed thermodynamic modelling. All authors discussed and interpreted the results. TD and MG led the writing of the manuscript, to which all authors contributed.

Competing interests

The authors declare that they have no conflict of interest.

Acknowledgements

We would like to thank Carla Tiraboschi and Jörg Hermann for their constructive reviews, as well as editor Reto Gieré, whose comments helped to improve several aspects of the paper. We thank Othmar Müntener, Martin Robyr, Alexey Ulianov and Olivier Reubi for allowing access to the laboratory facilities at the University of Lausanne during the COVID-19 pandemic and for their assistance during data acquisition. We also acknowledge Olivia Mauguin and Olivier Bruguier for their assistance at the Géosciences Montpellier laboratory facilities. This work benefited from constructive and appreciated discussions with Françoise Boudier. We thank the Sultanate of Oman Public Authority for Mining for support to conduct fieldwork and export samples. We also thank Sobhi Nasir for his support during the field trip in Oman. This research used core samples provided by the Oman Drilling Project. The Oman Drilling Project (OmanDP) has been made possible through commingled funds from the International Continental Scientific Drilling Project (ICDP; Peter Kelemen, Jürg Matter, Damon Teagle lead PIs), the Sloan Foundation – Deep Carbon Observatory (grant 2014-3-01, Peter Kelemen PI), the National Science Foundation (NSF-EAR-1516300, Peter Kelemen lead PI), NASA – Astrobiology Institute (NNA15BB02A, CE3Alexis Templeton PI), the German Research Foundation (DFG: KO 1723/21-1, Jürgen Koepke PI), the Japanese Society for the Promotion of Science (JSPS no. 16H06347, Katsuyoshi Michibayashi PI; and KAKENHI 16H02742, Eiichi Takazawa PI), the European Research Council (Adv: no. 669972; Bjorn Jamtveit PI), the Swiss National Science Foundation (SNF:20FI21_163073, Gretchen Früh-Green PI), JAMSTEC, the TAMU-JR Science Operator, and contributions from the Sultanate of Oman Ministry of Regional Municipalities and Water Resources, the Oman Public Authority of Mining, Sultan Qaboos University, CNRS-Univ. Montpellier, Columbia University of New York, and the University of Southampton.

Financial support

This research has been supported by the Agence Nationale de la Recherche (grant no. ANR-18-CE01-0014-01 LISZT), the German Research Foundation (grants nos. UR64/20-1 and UR 64/17-1) and the Junta de Andalucía (Consejeria de Conocimiento y Universidades) (postdoctoral fellowship grant no. Postdoc_21_00791).

References

Alt, J.C., Schwarzenbach, E.M., Früh-Green, G.L., Shanks, W.C., Bernasconi, S.M., Garrido, C.J., Crispini, L., Gaggero, L., Padrón-Navarta, J.A., and Marchesi, C.: The role of serpentinites in cycling of carbon and sulfur: Seafloor serpentinization and subduction metamorphism, Lithos, 178, 40–54, doi:10.1016/j.lithos.2012.12.006, 2013.

Aftabi, A., and Zarrinkoub, M.H.: Petrogeochemistry of listvenite association in metaophiolites of Sahlabad region, eastern Iran: Implications for possible epigenetic Cu–Au ore exploration in metaophiolites, Lithos, 156–159, 186–203, doi:10.1016/j.lithos.2012.11.006, 2013.

Andreani, M., Luquot, L., Gouze, P., Godard, M., Hoisé, E., and Gibert, B.: Experimental Study of Carbon Sequestration Reactions Controlled by the Percolation of CO2-Rich Brine through Peridotites, Environ. Sci. Technol., 43, 4, 1226–1231, doi:10.1021/es8018429, 2009.

Auclair, M., Gauthier, M., Trottier, J., Jebrak, M., and Chartrand, F.: Mineralogy, geochemistry, and paragenesis of the Eastern Metals serpentinite-associated Ni-Cu-Zn deposit, Quebec Appalachians, Econ. Geol. 88(1), 123–138, doi:10.2113/gsecongeo.88.1.123, 1993.

Austrheim, H., Corfu, F., and Renggli, C.J.: From peridotite to fuchsite bearing quartzite via carbonation and weathering: with implications for the Pb budget of continental crust, Contrib. Mineral. Petrol., 176, 94, doi: 10.1007/s00410-021-01851-z, 2021.

Bechennec, F., Le Metour, J., Rabu, D., Bourdillon-de-Grissac, C., de Wever, P., Beurrier, M., and Villey, M.: The Hawasina Nappes: stratigraphy, palaeogeography and structural evolution of a fragment of the south-Tethyan passive continental margin, Geol. Soc. Spec. Publ., 49, 213–223, doi:10.1144/gsl.sp.1992.049.01.14, 1990.

Beinlich, A., Plümper, O., Hövelmann, J., Austrheim, H., and Jamtveit, B.: Massive serpentinite carbonation at Linnajavri, N–Norway, Terra Nova, 24(6), 446–455, doi: 10.1111/j.1365-3121.2012.01083.x, 2012.

Beinlich, A., Plümper, O., Boter, E., Müller, I.A., Kourim, F., Ziegler, M., Harigane, Y., Lafay, R., Kelemen, P.B., and the Oman Drilling Project Science Team: Ultramafic rock carbonation: Constraints from listvenite core BT1B, Oman drilling project, J. Geophys. Res. Solid Earth, 125, e2019JB019060, doi:10.1029/2019JB019060, 2020.

Belogub, E.V., Melekestseva, I.Y., Novoselov, K.A., Zabotina, M.V., Tret'yakov, G.A., Zaykov, V.V., and Yuminov, A.M.: Listvenite-related gold deposits of the South Urals (Russia): A review, Ore Geol. Rev., 85, 247–270, doi:10.1016/j.oregeorev.2016.11.008, 2017.

Boudier, F., Ceuleneer, G., and Nicolas, A.: Shear zones, thrusts and related magmatism in the Oman ophiolite: Initiation of thrusting on an oceanic ridge, Tectonophysics, 151(1–4), 275–296, doi:10.1016/0040-1951(88)90249-1, 1988.

Boudier, F., and Nicolas, A.: Synchronous Seafloor Spreading and Subduction at the Paleo-Convergent Margin of Semail and Arabia, Tectonics, 37, 2961–2982, doi:10.1029/2018TC005099, 2018.

Boudier, F., Baronnet, A., and Mainprice, D.: Serpentine mineral replacements of natural olivine and their seismic implications: Oceanic lizardite versus subduction-related antigorite. J. Petrol., 51(1–2), 495–512, doi:10.1093/petrology/egp049, 2010.

Boskabadi, A., Pitcairn, I.K., Leybourne, M.I., Teagle, D.A.H., Cooper, M.J., Hadizadeh, H., Bezenjani, R.N., and Bagherzadeh, R.M.: Carbonation of ophiolitic ultramafic rocks: Listvenite formation in the Late Cretaceous ophiolites of eastern Iran, Lithos, 352–353, 105307, doi:10.1016/j.lithos.2019.105307, 2020.

Buisson, G., and Leblanc, M.: Gold in carbonatized ultramafic rocks from ophiolite complexes, Econ. Geol., 80(7), 2028–2029, doi:10.2113/gsecongeo.80.7.2028, 1985.

Cannaò, E., Scambelluri, M., Bebout, G.E., Agostini, S., Pettke, T., Godard, M., Crispini, L., Ophicarbonate evolution from seafloor to subduction and implications for deep-Earth C cycling, Chem. Geol., 546, 119626, doi:10.1016/j.chemgeo.2020.119626, 2020.

Coleman, R.: Tectonic setting for ophiolite obduction in Oman, J. Geophys. Res. Solid Earth, 86, 2497–2508, doi:10.1029/JB086iB04p02497, 1981.

Connolly, J.A.D.: Computation of phase equilibria by linear programming: A tool for geodynamic modeling and its application to subduction zone decarbonation, Earth Planet. Sci. Lett., 236, 524–541, doi: 10.1016/j.epsl.2005.04.033, 2005.

Connolly, J.A.D.: The geodynamic equation of state: What and how, Geochemistry, Geophys. Geosystems, 10, Q10014, doi: 10.1029/2009GC002540, 2009.

de Obeso J.C., and Kelemen, P.B.: Major element mobility during serpentinization, oxidation and weathering of mantle peridotite at low temperatures, Phil. Trans. R. Soc. A, 378, 20180433, doi:10.1098/rsta.2018.0433, 2020.

Debret, B., Bouilhol, P., Pons, M.L., and Williams, H.: Carbonate Transfer during the Onset of Slab Devolatilization: New Insights from Fe and Zn Stable Isotopes, J. Petrol., 59, 1145–1166, doi:10.1093/petrology/egy057, 2018.

Decrausaz, T., Godard, M., Menzel, M.D., Parat, F., Oliot, E., Lafay, R., and Barou, F.: Major and trace element mineral compositions of carbonated serpentinites and listvenites from Oman Drilling Project Hole BT1B (Semail Ophiolite, Oman), Version 2.0, Interdisciplinary Earth Data Alliance (IEDA) [data set], https://doi.org/10.26022/IEDA/112834, 2023.

Deschamps, F., Godard, M., Guillot, S., and Hattori, K.: Geochemistry of subduction zone serpentinites: A review, Lithos, 178, 96–127, doi:10.1016/j.lithos.2013.05.019, 2013.

Eckstrand, O.R.: The Dumont serpentinite; a model for control of nickeliferous opaque mineral assemblages by alteration reactions in ultramafic rocks, Econ. Geol., 70(1), 183–201, doi:10.2113/gsecongeo.70.1.183, 1975.

Emam, A., and Zoheir, B.: Au and Cr mobilization through metasomatism: Microchemical evidence from ore-bearing listvenite, South Eastern Desert of Egypt, J. Geochem. Explor., 125, 34–45, doi:10.1016/j.gexplo.2012.11.004

Falk, E.S., and Kelemen P.B.: Geochemistry and petrology of listvenite in the Samail ophiolite, Sultanate of Oman: Complete carbonation of peridotite during ophiolite emplacement, Geochim. Cosmochim. Acta, 160, 70–90, doi:10.1016/j.gca.2015.03.014; 2015.

Frost, B.R.: On the Stability of Sulfides, Oxides, and Native Metals in Serpentinite, J. Petrol., 26(1), 31–63, doi: 10.1093/petrology/26.1.31, 1985.

Frost, B.R., and Beard, J.S.: On Silica Activity and Serpentinization, J. Petrol., 48(7), 1351–1368, doi: 10.1093/petrology/egm021, 2007.

Gahlan, H.A., Azer, M.K., Asimow, P.D., and Al-Kahtany, K.M.: Petrogenesis of gold-bearing listvenites from the carbonatized mantle section of the Neoproterozoic Ess ophiolite, Western Arabian Shield, Saudi Arabia, Lithos, 372–373, 105679, doi:10.1016/j.lithos.2020.105679, 2020.

Garber, J.M., Rioux, M., Searle, M.P., Kylander-Clark, A.R.C., Hacker, B.R., Vervoort, J.D., Warren, C.J., and Smye, A.J.: Dating continental subduction beneath the Samail Ophiolite: Garnet, zircon, and rutile petrochronology of the As Sifah eclogites, NE Oman. J. Geophys. Res. Solid Earth, 126, e2021JB022715, doi:10.1029/2021JB022715, 2021.

Glennie, K.W., Boeuf, M.G.A., Hugues Clark, M.W., Moody-Stuart, M., Pilaar, W.F.H., and Reinhardt, B.M.: Geology of the Oman Mountains, Neder. Mijn. Geol. Genoot., Delft, Netherlands, 423 pp., 1974.

Godard, M., Jousselin, D., and Bodinier, J.-L.: Relationships between geochemistry and structure beneath a paleo-spreading centre: a study of the mantle section in the Oman ophiolite, Earth Planet. Sci. Lett., 180, 133–148, doi:10.1016/S0012-821X(00)00149-7, 2000.

Godard, M., Carter, E.J., Decrausaz, T., Lafay, R., Bennett, E., Kourim, F., de Obeso, J.C., Michibayashi, K., Harris, M., Coggon, J., Teagle, D., Kelemen, P., and the Oman Drilling Project Phase 1 Science Party: Geochemical Profiles Across the Listvenite-Metamorphic Transition in the Basal Megathrust of the Semail Ophiolite: Results from Drilling at Oman DP Hole BT1B, J. Geophys. Res. Solid Earth, 126, e2021JB022733, doi:10.1029/2021JB022733, 2021.

Griffin, W., Powell, W., Pearson, N.J., and O'Reilly, S.: GLITTER: data reduction software for laser ablation ICP-MS, Short Course Series, 40, 308–311, 2008.

Halls, C., and Zhao, R.: Listvenite and related rocks: perspectives on terminology and mineralogy with reference to an occurrence at Cregganbaun, Co. Mayo, Republic of Ireland. Mineral. Deposita, 30, 303–313, doi:10.1007/BF00196366, 1995.

Hanghøj, K., Kelemen, P.B., Hassler, D., and Godard, M.: Composition and Genesis of Depleted Mantle Peridotites from the Wadi Tayin Massif, Oman Ophiolite; Major and Trace Element Geochemistry, and Os Isotope and PGE Systematics, J. Petrol., 51(1–2), 201–227, doi:10.1093/petrology/egp077, 2010.

Hansen, L.D., Dipple, G.M., Gordon, T.M., and Kellett, D.A.: Carbonated serpentinite (listwanite) at Atlin, British Columbia: a geological analogue to carbon dioxide sequestration, Can. Mineral., 43(1), 225–239, doi:10.2113/gscanmin.43.1.225, 2015.

Hinsken, T., Bröcker, M., Strauss, H., and Bulle, F.: Geochemical, isotopic and geochronological characterization of listvenite from the Upper Unit on Tinos, Cyclades, Greece, Lithos, 282–283, 281–297, doi:10.1016/j.lithos.2017.02.019, 2017.

Holland, T.J.B., and Powell, R.: An internally consistent thermodynamic data set for phases of petrological interest, J. Metamorph. Geol., 16, 309–343, doi:10.1111/j.1525-1314.1998.00140.x, 1998.

Holland, T. and Powell, R.: An improved and extended internally consistent thermodynamic dataset for phases of petrological interest, involving a new equation of state for solids, J. Metamorph. Geol., 29, 333–383, doi:10.1111/j.1525-1314.2010.00923.x, 2011.

Johannes, W.: An experimental investigation of the system MgO-SiO2–H2O-CO2, Am. J. Sci., 267(9), 1083-1104, doi:10.2475/ajs.267.9.1083, 1969.

Kelemen, P.B., and Matter, J.M.: In situ carbonation of peridotite for CO2 storage, Proc. Natl. Acad. Sci, 105(45), 17295–17300, doi:10.1073/pnas.0805794105, 2008.

Kelemen, P.B., and Manning, C.E.: Reevaluating carbon fluxes in subduction zones, what goes down, mostly comes up, Proc. Natl. Acad. Sci, 112(30), doi:10.1073/pnas.1507889112, 2015.

Kelemen, P.B., Matter, J.M., Teagle, D.A.H., Coggon, J.A., and the Oman Drilling Project Science Team: Site BT1: fluid and mass exchange on a subduction zone plate boundary, in: Proceedings of the Oman Drilling Project, College Station, Texas (International Ocean Discovery Program), doi:10.14379/OmanDP.proc.2020, 2020.

Kelemen, P.B., de Obeso, J.C., Leong, J.A., Godard, M., Okazaki, K., Kotowski, A.J., Manning, C.E., Ellison, E.T., Menzel, M.D., Urai, J.L., Hirth, G., Rioux, M., Stockli, D.F., Lafay, R., Beinlich, A.M., Coggon, J.A., Warsi, N.H., Matter, J.M., Teagle, D.A.H., Harris, M., Michibayashi, K., Takazawa, E., Al Sulaimani, Z., and the Oman Drilling Project Science Team: Listvenite formation during mass transfer into the leading edge of the mantle wedge: Initial results from Oman Drilling Project Hole BT1B, J. Geophys. Res. Solid Earth, 127, e2021JB022352, doi:10.1029/2021JB022352, 2022.

Khedr, M. Z., Arai, S. and Python, M.: Petrology and chemistry of basal lherzolites above the metamorphic sole from Wadi Sarami central Oman ophiolite, J. Mineral. Petrol. Sci., 108, 13–24, doi:10.2465/jmps.121026, 2013.

Klein, F., and Bach, W.: Fe–Ni–Co–O–S Phase Relations in Peridotite–Seawater Interactions, J. Petrol., 50(1), 37-59, doi:10.1093/petrology/egn071, 2009.

Lanari, P., Vho, A., Bovay, T., Airaghi, L., and Centrella, S.: Quantitative compositional mapping of mineral phases by electron probe micro-analyser, Geol. Soc. Spec. Publ., 478, 39–63, doi:10.1144/SP478.4, 2019.

Lippard, S.J., Shelton, A.W., and Gass, I.G.: The Ophiolite of Northern Oman, Geological Society of London Memoir 11, Blackwell Scientific Publications, Oxford, 178 pp, 1986.

Mayhew, L.E., Ellison, E.T., Miller, H.M., Kelemen, P.B., and Templeton, A.S.: Iron transformations during low temperature alteration of variably serpentinized rocks from the Samail ophiolite, Oman, Geochim. Cosmochim. Acta, 222, 704–728, doi:10.1016/j.gca.2017.11.023, 2018.

Menzel, M.D., Garrido, C.J., Sánchez-Vizcaíno V.L., Marchesi, C., Hidas, K., Escayola, M.P., and Huertas, A.D.: Carbonation of mantle peridotite by CO_2-rich fluids: the formation of listvenites in the Advocate ophiolite complex (Newfoundland, Canada), Lithos, 323, 238–261, doi: 10.1016/j.lithos.2018.06.001, 2018.

Menzel, M.D., Urai, J.L., de Obeso, J.C., Kotowski, A., Manning, C.E., Kelemen, P.B., Kettermann, M., Jesus, A.P., Harigane, Y., and the Oman Drilling Project Phase 1 Science Party: Brittle Deformation of Carbonated Peridotite-Insights From Listvenites of the Samail Ophiolite (Oman Drilling Project Hole BT1B), J. Geophys. Res. Solid Earth, 125, e2020JB020199, doi:10.1029/2020JB020199, 2020.

Menzel, M., Urai, J.L., Ukar, E., Decrausaz, T., and Godard, M.: Progressive veining during peridotite carbonation: insights from listvenites in Hole BT1B, Samail ophiolite (Oman), Solid Earth, 13, 1191–1218, doi: 0.5194/se-13-1191-2022, 2022.

Nasir, S., Al Sayigh, A.R., Al Harthy, A., Al-Khirbash, S., Al-Jaaidi, O., Musllam, A., Al-Mishwat, A., and Al-Bu'saidi, S.: Mineralogical and geochemical characterization of listwaenite from the Semail Ophiolite, Oman, Geochemistry, 67, 213–228, doi:10.1016/j.chemer.2005.01.003, 2007.

Nicolas, A., Boudier, F., Ildefonse, I., and Ball, E.: Accretion of Oman and United Arab Emirates ophiolite – Discussion of a new structural map, Mar. Geophys. Res., 21, 147-180, doi:10.1023/A:1026769727917, 2000.

Noël, J., Godard, M., Oliot, E., Martinez, I., Williams, M., Boudier, F., Rodriguez, O., Chaduteau, C., Escario, S., and Gouze, P.: Evidence of polygenetic carbon trapping in the Oman Ophiolite: Petro-structural, geochemical, and carbon and oxygen isotope study of the Wadi Dima harzburgite-hosted

carbonates (Wadi Tayin massif, Sultanate of Oman), Lithos, 323, 218–237, doi:10.1016/j.lithos.2018.08.020, 2018.

Okazaki, K., Michibayashi, K., Hatakeyama, K., Abe, N., Johnson, K.T.M., Kelemen, P.B., and the Oman Drilling Project Science Team: Major mineral fraction and physical properties of carbonated peridotite (listvenite) from ICDP Oman Drilling Project Hole BT1B inferred from X-ray CT core images, J. Geophys. Res. Solid Earth, 126, e2021JB022719, doi:10.1029/2021JB022719, 2021.

Padrón-Navarta, J.A., López Sánchez-Vizcaíno, V., Hermann, J., Connolly, J.A.D., Garrido, C.J., Gómez-Pugnaire, M.T., and Marchesi, C.: Tschermak's substitution in antigorite and consequences for phase relations and water liberation in high-grade serpentinites, Lithos, 178, 186–196, doi:10.1016/j.lithos.2013.02.001, 2013.

Peuble, S., Godard, M., Luquot, L., Andreani, M., Martinez, I., and Gouze, P.: CO2 geological storage in olivine rich basaltic aquifers: New insights from reactive-percolation experiments, Appl. Geochemistry, 52, 174–190, doi:10.1016/j.apgeochem.2014.11.024, 2015a.

Peuble, S., Andreani, M., Godard, M., Gouze, P., Barou, F., Van De Moortele, B., Mainprice, D., and Reynard, B.: Carbonate mineralization in percolated olivine aggregates: Linking effects of crystallographic orientation and fluid flow, Am. Min., 100(2-3), 474–482, doi:10.2138/am-2015-4913, 2015b.

Pitzer, K.S., and Sterner, S.M.: Equations of state valid continuously from zero to extreme pressures with H2O and CO2 as examples, Int. J. Thermophys., 16, 511–518, doi:10.1007/BF01441917, 1995.

Prigent, C., Agard, P., Guillot, S., Godard, M., and Dubacq, B.: Mantle wedge (de)formation during subduction infancy: evidence from the base of the Semail ophiolitic mantle, J. Petrol., 59, 2061–2091, doi:2010.1093/petrology/egy2090, 2018.

Qiu, T., and Zhu, Y.: Listwaenite in the Sartohay ophiolitic mélange (Xinjiang, China): A genetic model based on petrology, U-Pb chronology and trace element geochemistry, Lithos, 302–303, 427–446, doi:10.1016/j.lithos.2018.01.029, 2018.

Rioux, M., Garber, J.M., Searle, M., Kelemen, P.B., Miyashita, S., Adachi, Y., and Bowring, S.: High-Precision U-Pb Zircon Dating of Late Magmatism in the Samail Ophiolite: A Record of Subduction Initiation, J. Geophys. Res. Solid Earth, 126, e2020JB020758, doi:10.1029/2020JB020760, 2021.

Schröder, T., Bach, W., Jöns, N., Jöns, S., Monien, P., and Klügel, A.: Fluid circulation and carbonate vein precipitation in the footwall of an oceanic core complex, Ocean Drilling Program Site 175, Mid-Atlantic Ridge, Geochemistry, Geophys. Geosystems, 16, 3716–3732, doi:10.1002/2015GC006041, 2015.

Schwarzenbach, E.M., Früh-Green, G.L., Bernasconi, S.M., Alt, J.C., and Plas, A.: Serpentinization and carbon sequestration: A study of two ancient peridotite-hosted hydrothermal systems, Chem. Geol., 351, 115–133, doi:10.1016/j.chemgeo.2013.05.016, 2013.

Searle, M.J., and Cox, J.: Tectonic setting, origin, and obduction of the Oman ophiolite, Geol. Soc. Am. Bull., 111, 104–122, doi:10.1130/0016-7606(1999)111<0104:TSOAOO>2.3.CO;2, 1999.

Sieber, M.J., Yaxley, G.M., and Hermann, J.: COH-fluid induced metasomatism of peridotites in the forearc mantle. Contrib. Mineral. Petrol., 177, 44, doi:10.1007/s00410-022-01905-w, 2022.

Soret, M, Agard, P, Dubacq, B, Plunder, A, and Yamato, P.: Petrological evidence for stepwise accretion of metamorphic soles during subduction infancy (Semail ophiolite, Oman and UAE), J. Metamorph. Geol.; 35(9), 1051–1080, doi:10.1111/jmg.12267, 2017.

Stanger, G.: Silicified serpentinite in the Semail nappe of Oman, Lithos, 18, 13–22, doi:10.1016/0024-4937(85)90003-9, 1985.

Takazawa, E., Okayasu, T., and Satoh, K.: Geochemistry and origin of the basal lherzolites from the northern Oman ophiolite (northern Fizh block), Geochem. Geophys., 4(2), 1021, doi:10.1029/2001GC000232, 2013.

Tominaga, M., Beinlich, A., Lima, E.A., Tivey, M.A., Hampton, B.A., Weiss, B., and Harigane, Y.: Multi-scale magnetic mapping of serpentinite carbonation, Nat. Commun., 8, 1870, doi:10.1038/s41467-017-01610-4, 2017.

Ulrich, M., Muñoz, M., Guillot, S., Cathelineau, M., Picard, C., Quesnel, B., Boulvais, P., and Couteau, C.: Dissolution-precipitation processes governing the carbonation and silicification of the serpentinite sole of the New Caledonia ophiolite. Contrib. Mineral. Petrol., 167, 952, doi:10.1007/s00410-013-0952-8, 2014.

Villey, M., Le Metour, J., and De Gramont, X.: Geological map of Fanja, Sheet NF 40-3F. Explanatory Notes, BRGM and Oman Ministry of Petroleum & Minerals, 1986.

Wilde, A., Simpson, L., and Hanna, S., Preliminary study of Cenozoic hydrothermal alteration and platinum deposition in the Oman Ophiolite, J. Virtual Explor., 6, 7–13, 2002.

Chapter 5: Carbon, iron and zinc isotopes studies: characterization of the Fe speciation and fluid composition

Foreword

Non-traditional Fe and Zn isotope systematics have recently proven to be a powerful tool to evidence episodes of fluid transfer affecting mantle rocks in oceanic hydrothermal systems (Debret et al., 2018a), or in subduction zones (e.g., Pons et al., 2016; Inglis et al., 2017; Debret et al., 2018b, 2021). The Fe and Zn isotopes compositions of peridotites are primarily controlled by magmatic processes such as partial melting and melt impregnation (e.g., Williams et al., 2005; Weyer and Ionov, 2007; Doucet et al., 2016; Moynier et al., 2017). However, isotope fractionation may result at the outcome of metasomatism as isotopically light Fe and heavy Zn are preferentially mobilized by sulfate- and carbonate-bearing fluids (e.g., Fujii et al., 2014; Ducher et al., 2016). A recent study of Debret et al. (2020) also highlighted the correlation between the fluid redox and dramatic variability in Fe isotope compositions of serpentinized peridotites.

A complementary analytical approach was considered to constrain the nature of the reactive fluids and elemental mobility associated to the carbonation of serpentinized peridotites. Analyses were performed on an identical subset of rock powders including mainly carbonated serpentinites and listvenites from the borehole to assess: i) the oxidation state of Fe by Mössbauer spectroscopy and potentiometric titration (section 5.1), ii) the bulk carbon, iron and zinc isotopes compositions (section 5.2). The C-Fe-Zn isotopes study is presented in a draft format for a future publication to be sumitted to Geochemica Cosmochemica Acta.

5.1 Iron oxidation state and partitioning

5.1.1 Results

The bulk rock Fe^{3+}/Fe_{TOT} ratios of selected samples obtained after FeO titration are close to those provided across the borehole by Godard et al. (2021), while ratios calculated after the deconvolution of Mössbauer spectra are systematically lower (Table 5.1). For further investigations in section 5.2, we considered the Fe^{3+}/Fe_{TOT} ratios obtained by titration.

The Fe^{3+}/Fe_{TOT} ratio of the reference serpentinized harzburgite OM20-13 is 0.36, which is close to the range determined for serpentinized peridotites in Oman (0.4–0.55; Mayhew et al., 2018). Carbonated serpentinites display ratios ranging between 0.35–0.97 (BT1B: 0.21–0.85), while those of listvenites are comprised between 0.31–0.85 (BT1B: 0.21–0.92), and between 0.34–0.42 for fuchsite-bearing listvenites (BT1B: 0.13–0.58).

5.1.2 Analytical perspectives

The differences in bulk rock Fe^{3+}/Fe_{TOT} ratios obtained from FeO titration and Mössbauer spectroscopy is significative. As the duration of the Mössbauer irradiation was one week for each sample, no problem of detection is expected for Fe concentrations typical of peridotites. Discrepancy between the two methods likely result from erroneous data reduction. In particular, we identified multiple sources leading to inexact deconvolution of Mössbauer spectra by lorentzian curves for our samples: i) the consequent number of iron-bearing mineral phases which may present different Fe oxidation state depending on the distribution between the crystallographic sites, ii) overlapping peaks for Fe^{3+} in oxides, serpentine and fuchsite and for Fe^{2+} in carbonates. In addition, relatively low abundances of iron in minor and accessory phases whose contribution is close to the analytical background noise are difficult to identify and deconvolute. Determining precisely the mineral proportions in the rock powders by mass balance calculations (inversion model) or by precise XRD analyses are key in resolving issues met during data reduction.

Sample	Lithology	FeO	Fe_2O_3	Fe^{3+}/Fe_{TOT}		
				FeO titration		Mössbauer
		wt%	wt%	this study	Godard et al. (2021)	this study
30Z-2-53-58	Listvenite	1.94	11.54	0.81	-	0.68
31Z-3-31-37	Listvenite	1.47	10.95	0.85	-	0.71
35Z-1-6-11	Listvenite	2.45	6.86	-	0.46	-
38Z-3-86-91	Listvenite	1.36	7.00	0.78	-	0.78
40Z-3-3-8	Carbonated serpentinite	0.32	10.43	0.97	-	0.90
42Z-2-26-31	Carbonated serpentinite	1.51	7.76	-	0.74	-
43Z-2-3-8	Carbonated serpentinite	3.47	9.75	-	0.52	-
44Z-3-57-62	Carbonated serpentinite	4.56	8.25	0.39	0.35	0.14
47Z-3-18-23	Fu-listvenite	3.58	6.87	0.42	0.61	0.06
50Z-4-65-70	Listvenite	4.04	6.49	0.31	-	0.10
52Z-1-60-65	Fu-listvenite	3.43	6.06	0.37	0.44	0.38
55Z-1-8-13	Fu-listvenite	3.54	6.50	0.40	-	0.19
60Z-1-12-17	Fu-listvenite	2.9	5.59	0.42	-	0.15
66Z-3-66-71	Listvenite	4.93	8.28	0.34	-	-
67Z-4-39-44	Fu-listvenite	5.07	8.57	0.34	-	0.04
71Z-4-0-8	Fu-listvenite	3.63	6.21	0.35	-	0.03
74Z-1-59-62	Carbonated serpentinite	2.25	9.78	-	0.70	-
76Z-2-38-42	Listvenite	4.86	16.16	0.67	-	0.42
OM20-13	Serpentinized harzburgite	3.56	9.06	0.56	-	0.36

Table 5.1 Bulk iron oxide contents and Fe^{3+}/Fe_{TOT} ratios determined by titration and Mössbauer spectroscopy for selected samples. FeO contents were determined by titration while Fe_2O_3 contents were quantified by XRF (Godard et al., 2021).

5.2 Elemental mobility during peridotite carbonation: a combined carbon, iron and zinc isotopes study of listvenite series from Oman Drilling Project Hole BT1B (Semail Ophiolite, Oman)

Thierry Decrausaz[a], Baptiste Debret[b], Isabelle Martinez[b], Fleurice Parat[a], Virginia Rojas[b], Marguerite Godard[a]

[1] Géosciences Montpellier, Université de Montpellier, CNRS, Montpellier, France

[2] Institut de physique du globe de Paris, Université de Paris, CNRS, Paris, France

To be submitted to Geochemica Cosmochemica Acta

5.2.1 Introduction

Metasomatized peridotites constitute one of the largest reservoir of water, volatiles (e.g., C, S, N) and fluid-mobile elements (e.g., Li, K, Rb, Cs, As, Ba, Sr, U, Pb), acting as trap-and-release open systems from seafloor exposure to subduction zones (e.g. Alt et al., 2013; Deschamps et al., 2013). Non-traditional Fe and Zn stable isotopes have developed over the last decade as a powerful tool for tracing and quantifying elemental mobility during reactive fluid fluxing (e.g. Debret et al., 2016; Pons et al., 2016; Inglis et al., 2017; Debret et al., 2018b; Debret et al., 2021).

Isotopic variability of the Fe and Zn systematics in peridotites merge at the outcome of: i) high temperature petrogenetic processes, such as melt extraction or impregnation (Williams et al., 2005; Weyer and Ionov, 2007; Doucet et al., 2016), and ii) hydrothermalism (e.g. Debret et al., 2018a). Equilibrium stable isotope fractionation between minerals and fluids is controlled by contrasts in the bonding environment, coordination and oxidation state (Polyakov and Mineev, 2000; Fujii et al., 2014, Ducher et al., 2016). In particular, Fe and Zn can be mobilized by bonding to chlorine, carbonate, sulphur complexes in fluids (Hill and Schauble, 2008; Hill et al., 2010; Fujii et al., 2011, 2014; Pons et al., 2016).

In the Semail Ophiolite, the migration of reactive CO_2-bearing fluids channelized at the base of the ophiolite mantle resulted in the formation of listvenites at the expense of serpentinized peridotites (e.g. Kelemen et al., 2022). Here we present a bulk C-Fe-Zn stable isotopes study on samples from Oman Drilling Project Hole BT1B (Wadi Mansah, Oman) aiming to constrain elemental mobility during peridotite carbonation and potentially identify reaction and fluid pathways.

5.2.2 Geological background

The Semail Ophiolite is a continuous portion of oceanic lithosphere emplaced on the Arabian continental margin during Late Cretaceous closure of the Neotethys realm (e.g. Coleman et al., 1981). The ophiolite preserved a sequence including a thick mantle section (up to 12 km) and its overlying crust (4–8 km), from lower gabbros to upper volcanics (e.g. Hopson et al., 1981; Nicolas et al., 2000). Intra-oceanic underthrusting or subduction infancy (e.g. Boudier et al., 1988; Agard et al., 2016) led to the underplating of a composite metamorphic sole, recording greenschist to granulite facies peak conditions (e.g. Soret et al., 2017). Radiogenic ages of sole formation are contemporaneous with oceanic accretion (e.g. Rioux et al., 2021), and interpreted by some authors to occur in a supra-subduction zone setting (e.g. Searle and Cox, 1999). Late Creteceous convergence resulted in the obduction of the ophiolite and underlying Hawasina Formation, a nappe stack piled during the closure of the Hawasina deep-sea basin. Obduction was followed by regional extension and exhumation of subducted Arabian margin segments (e.g. Mattern and Scharf, 2018; Grobe et al., 2018; Garber et al., 2021). Formation of the Jebel Akhdar and Saih Hatat domes resulted from large-scale folding during NE–SW shortening in the Miocene-Pliocene (Grobe et al., 2018).

The Sumail Massif in the Fanja region (Fig. 5.1) exposes a dismembered and highly faulted ophiolite section juxtaposing mantle peridotites with lower gabbros, and underlying metamorphic sole, Hawasina Formation, and autochthonous sediments. Listvenites form dam- to km-scale ridges and lenses along the basal thrust or interlayering the ophiolite mantle with the same orientation to the basal thrust. Listvenites bodies are aligned on the margins of the Jebel Akhdar and Saih Hatat domes along a NW – SE direction (e.g. Scharf et al., 2022). The genesis of listvenites remains debated: they might have formed by fluxing of reactive fluids a) at the edge of the mantle wedge during obduction (Falk and Kelemen, 2015) or during post-obductional extension (Stanger, 1985; Wilde et al., 2002; Scharf et al., 2022).

Listvenites in Wadi Mansah (Fig. 5.1c) have been the target of Oman Drilling Project Hole BT1B (Kelemen et al., 2020). A borehole section including ~200 m of listvenites series and interlayered carbonated serpentinites atop of ~100 m of metabasalts from the metamorphic sole was recovered (Fig. 5.1d). A series of microstructural and geochemical studies on core samples helped to better understand the processes and conditions of peridotite carbonation. Listvenites formed by interaction between serpentinized peridotites and massive fluxes of CO_2-bearing fluids derived from the devolatilization of clastic sediments akind Hawasina sediments at depth (de Obeso et al., 2022; Kelemen et al., 2022). Pervasive carbonation was promoted by ductile deformation (Menzel et al., 2022a), or fracturation with the generation of closely-spaced vein networks (Menzel et al., 2022b), both maintaining rock permeability and favouring fluid migration. Fracturation may also result from reaction-induced volume changes, with an estimated increase of ~30-40 % from peridotite protolith to listvenites (Godard et al., 2021). Conversion into carbonated serpentinites or listvenites was accompanied by a conservative

behaviour of most major elements, transition metals and moderately incompatible lithophile elements, but also by substantial enrichment in fluid mobile elements (FME), CO_2 and water release (Godard et al., 2021). Three geochemical domains were identified across the borehole (Fig. 5.1d, Godard et al., 2021): two domains formed after a harzburgitic/dunitic protoliths (~9 mbg to ~115 mbg and ~175 mbg to ~195 mbg, mbg: metres below ground), and one fuchsite-rich domain after lherzolitic protholiths (~115 mbg to ~175 mbg). Clumped isotopes temperatures of carbonate formation range between 50 °C and 250 °C (Falk and Kelemen, 2015; Beinlich et al., 2020).

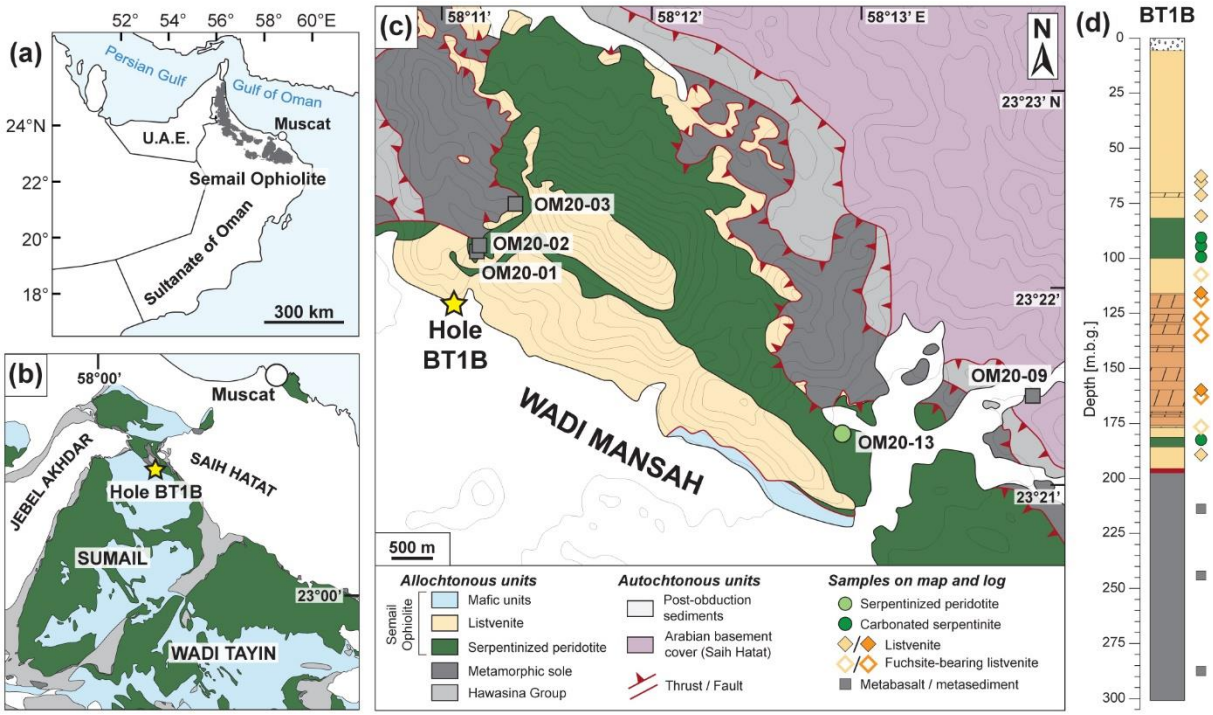

Fig. 5.1 Listvenite outcrops, Hole BT1B and sample locations in Wadi Mansah (Samail Ophiolite). (a) Location of the Semail Ophiolite. (b) Location of Hole BT1B in the Fanja region, north of the Sumail massif (modified after Nicolas et al, 2000). (c) Geological map of Wadi Mansah (modified after Villey et al., 1986; Kelemen et al., 2022), and locations of BT1B (Kelemen et al., 2020) and regional samples. (d) Simplified lithological column of Hole BT1B and sample selection across the borehole. The two main geochemical domains represented are derived from (i) harzburgite and dunite protolith (yellow), and (ii) lherzolite protolith (orange) (Godard et al., 2021). Abbreviation: m.b.g.: metres below ground.

5.2.3 Materials and methods

Hole BT1B samples include 5 carbonated serpentinites, 7 listvenites and 6 Fu-listvenites, picked regularly across the borehole (80-187 mbg). Complementary samples from Wadi Mansah consist of one reference slightly serpentinized harzburgite (OM20-13) that did not experience extensive carbonation, 3 metabasalts from the sole (OM20-01 to -03), and one metamorphosed limestone (OM20-09) from the underlying Muti Formation. Information and bulk chemistry data for core samples are provided in Godard et al. (2021).

The petrology of the carbonated serpentinites and (Fu-)listvenites from Hole BT1B was determined by the microscopic study of thin sections from neighbouring cores and by observation of high-resolution core scans.

Analytical procedures for the analyses of C-Fe-Zn concentrations and isotopes compositions is detailed in section 3.6.

5.2.4 Results

Petrology of metasomatized peridotites

The reference peridotite OM20-13 is a moderately serpentinized harzburgite displaying a porphyroclastic texture defined by mm- to cm-scale dissected orthopyroxene (Fig. 5.2a). A mesh texture developed in former olivine-rich domains, with relict olivine cores rimmed by serpentine and magnetite strings. Minor clinopyroxene is found at the rim or close to orthopyroxene. Accessory Cr-spinel is the most abundant oxide, while sulphides remain scarce. Millimetric serpentine veins cross-cut both mesh and porphyroclasts.

Carbonated serpentinites are principally composed of lizardite/chrysotile in preserved hourglass and bastite textures (Fig. 5.2b). No primary silicates are observed. Matrix replacement by carbonates proceeded with the formation of sparse spheroidal cores (<100 μm) termed “spheroids” (Beinlich et al., 2020), locally clustering into aggregates. Magnesite is dominant, but few samples are richer in dolomite (40Z-3-3-8 and 43Z-2-26-31). Accessory Cr-spinels are preserved, being frequently overgrown by a thin rim of magnetite and fractures filled by ferrit-chromite. Disseminated magnetite delineates the former mesh rims. Carbonated serpentinites host an intricate network of serpentine veins, often statically replaced by carbonates, and often cross-cut by antitaxial magnesite veins and late quartz and dolomite veins (Menzel et al., 2022b). Carbonated serpentinites at the transition with listvenites show a higher amount of carbonates, expressed by extended matrix replacement or densely-spaced veining.

Listvenites are characterized by a fine-grained matrix of magnesite and quartz after precursor serpentine. Fuchsite-bearing listvenites (later referred to as Fu-listvenites) are only distinguished by the presence of fuchsite, a chromian muscovite. Matrix carbonates mainly occur as spheroids, sometimes amalgamated, and massive aggregates. Two types of spheroids were identified based on location, size and core composition. Fe-core spheroids (<100 μm) formed during incipient carbonation and are characterized by dissolution textures involving Fe-oxides in their core. More common and abundant Mg-core spheroids (>100 μm) are related to pervasive carbonation. Quartz is cryptocrystalline and locally precipitated as chalcedony radial fibres. A microporosity is observed along quartz grain boundaries, locally forming miarolitic-like pores. Fuchsite-bearing listvenites are characterized by the

growth of fuchsite at the expense of Cr-spinel as shown in Fig. 5.2. Fuchsite grows on Cr-spinel edges and propagates in fractures and along quartz-grain boundaries (Fig. 5.2e-g), ultimately forming sheet-like flakes at the former position of Cr-spinel (Fig. 5.2h). Listvenites also host an intricate network of antitaxial magnesite veins, the earliest statically replacing serpentine mesh rims and veins, and the latest ones being mostly quartz and dolomite veins. The veining sequence is thourougly described by Menzel et al. (2022b).

Location	Lithology	Sample name	Domain	Depth	FeO_{TOT}	Zn	$\delta^{56}Fe$		$\delta^{66}Zn$		TC	$\delta^{13}C_{TC}$	NCC	$\delta^{13}C_{NCC}$
				m.b.g.	wt%	ppm	‰	2σ	‰	2σ	wt%	‰	wt%	‰
Hole BT1B	Listvenite	30Z-2-53-58	I	63.05	10.38	81	0.00	0.04	0.24	0.02	10.04	-2.60	0.26	-27.67
Hole BT1B	Listvenite	31Z-3-31-37	I	65.69	9.86	299	0.20	0.06	0.18	0.02	10.55	-2.29	0.26	-28.93
Hole BT1B	Listvenite	35Z-1-6-11	I	71.51	6.17	218	0.08	0.04	0.58	0.02	7.60	0.03	0.08	-24.66
Hole BT1B	Listvenite	35Z-1-6-11*	I	71.51	6.17	218	0.09	0.02	0.64	0.05	7.60	0.03	0.08	-24.66
Hole BT1B	Listvenite	38Z-3-86-91	I	80.87	6.30	50	0.07	0.05	0.25	0.02	5.39	-3.28	0.08	-17.50
Hole BT1B	Carbonated serpentinite	40Z-3-3-8	I	86.96	9.38	92	0.06	0.00	0.07	0.05	9.11	-5.38	0.57	-30.08
Hole BT1B	Carbonated serpentinite	42Z-2-26-31	I	91.82	6.98	50	-0.04	0.06	0.07	0.05	1.72	-5.81	0.24	-30.40
Hole BT1B	Carbonated serpentinite	43Z-2-3-8	I	94.93	8.77	49	-0.05	0.02	-0.11	0.04	1.95	-4.99	0.26	-30.18
Hole BT1B	Carbonated serpentinite	44Z-3-57-62	I	99.28	7.43	45	0.06	0.02	0.15	0.05	3.35	-3.96	0.34	-30.29
Hole BT1B	Fuchsite-bearing listvenite	47Z-3-18-23	I	107.86	6.18	161	-0.28	0.03	-0.44	0.03	9.51	0.43	0.20	-29.53
Hole BT1B	Listvenite	50Z-4-65-70	II	115.50	5.84	167	-0.03	0.09	0.57	0.03	6.70	0.22	0.18	-27.38
Hole BT1B	Fuchsite-bearing listvenite	52Z-1-60-65*	II	119.10	7.49	175	-0.28	0.01	0.11	0.04	n.a.	n.a.	n.a.	n.a.
Hole BT1B	Fuchsite-bearing listvenite	55Z-1-8-13	II	127.73	5.85	112	-0.33	0.00	-0.11	0.09	8.68	0.08	0.30	-30.30
Hole BT1B	Fuchsite-bearing listvenite	60Z-1-12-17	II	139.97	5.03	220	-0.26	0.03	-0.46	0.04	9.26	0.15	0.24	-25.79
Hole BT1B	Listvenite	66Z-3-66-71	II	160.60	7.45	420	0.04	0.04	0.39	0.02	9.06	-0.34	0.21	-24.66
Hole BT1B	Fuchsite-bearing listvenite	67Z-4-39-44	II	163.64	7.95	383	0.02	0.02	-0.06	0.03	9.15	0.80	0.21	-27.91
Hole BT1B	Fuchsite-bearing listvenite	71Z-4-0-8	II	175.59	5.59	241	0.05	0.02	n.d.	n.d.	7.90	-1.06	0.16	-29.57
Hole BT1B	Carbonated serpentinite	74Z-1-59-62	III	182.91	8.80	149	0.07	0.04	0.15	0.05	1.64	-6.20	0.36	-30.42
Hole BT1B	Listvenite	76Z-2-38-42	III	189.56	14.54	122	0.05	0.03	0.40	0.04	12.05	-1.10	0.57	-27.20
Hole BT1B	Metabasalt	88Z-2-76-82	MI	214.43	11.58	98	0.24	0.04	0.47	0.03	0.06	-20.70	0.14	-30.35
Hole BT1B	Metabasalt	100Z-2-13-21	MII	244.43	13.57	114	0.13	0.04	0.33	0.03	0.28	-3.06	0.13	-30.01
Hole BT1B	Metabasalt	118Z-2-42-50	MIII	287.41	11.64	98	0.08	0.04	0.23	0.03	0.16	-5.93	0.11	-30.25
Wadi Mansah	Carbonated metabasalt	OM20-01	-	-	12.78	354	0.09	0.02	0.09	0.06	4.79	-2.86	0.19	-30.20
Wadi Mansah	Metabasalt	OM20-02	-	-	7.53	71	0.10	0.05	0.27	0.01	0.13	-9.88	0.10	-30.09
Wadi Mansah	Amphibolite	OM20-03	-	-	7.86	92	0.01	0.03	0.36	0.06	0.02	-17.25	0.06	-30.32
Wadi Mansah	Serpentinized harzburgite	OM20-13	-	-	7.32	36	-0.05	0.04	0.14	0.02	0.12	-6.90	0.20	-31.04
Wadi Mansah	Metasediment	OM20-09	-	-	0.13	4					12.16	0.96		

Table 5.2: Bulk contents and isotope ratios of iron, zinc, Total Carbon (TC) and Total Non-Carbonate Carbon (NCC). Bulk contents and geochemical domains of samples are provided by Godard et al. (2021). The FeO_{TOT} contents are given on a volatile-free basis. Iron and zinc isotope ratios are reported as $\delta^{56}Fe$ and $\delta^{66}Zn$ in permil notation relative to IRMM-014 external standard and ETH standard solution, respectively. TC and NCC isotope ratios are reported in permil notation relative to Vienna Pee Dee Belemnite (VPDB) standard. *Bulk powders treated by $HClO_4$-HF acid digestion at Géosciences Montpellier. Abbreviations: m.b.g.: metres below ground; n.a.: not analysed: n.d.: not determined.

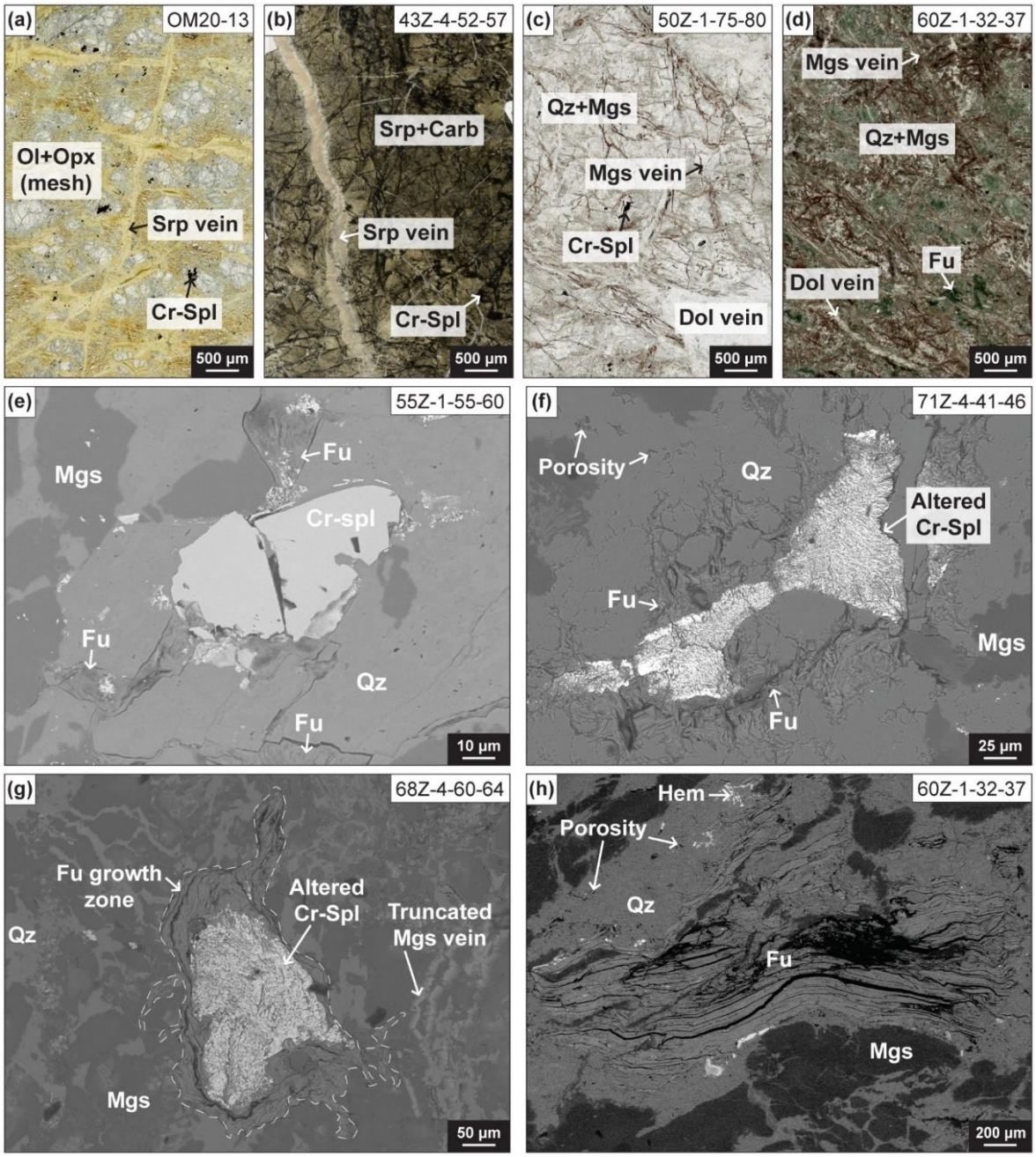

Fig. 5.2 Section scans of a type reacted peridotite rock suite (a-d) and back-scattered electron (BSE) images of Cr-spinel destabilization to fuchsite. The rock suite includes samples of (a) partially serpentinized harzburgite, (b) carbonated serpentinite, (c) listvenite, and (d) fuchsite-bearing listvenite. Carbonated peridotites are distinguished by their matrix mineral assemblage: serpentine-carbonate for carbonated serpentinite, quartz-carbonate for (fuchsite-bearing) listvenite. Fuchsite-bearing listvenite is characterized by the presence of fuchsite formed at the expense of Cr-spinel, as illustrated by BSE images (e-h). Fuchsite forming on the edge of Cr-spinel (e-g), with growth patterns showing expansion along quartz and carbonates grain boundaries in the vicinity of altered Cr-spinel (f-g), up to complete replacement (h). Matrix quartz at proximity with altered Cr-spinel frequently displays an intercrystal porosity (best observable on f or g). Abbreviations: Cr-spl: chromium spinel; Fu: fuchsite; Mgs: magnesite; Qz: quartz; Srp: serpentine.

Carbon concentration and isotopic composition

Carbon concentration and isotope composition of samples are given in Table 5.2, and plotted depth downhole for BT1B samples (Fig. 5.3). Our data are in excellent agreement with literature values of total carbon (Kelemen et al., 2020; de Obeso et al., 2022).

Total carbon

Metasomatized peridotites reveal a strong lithological control on the total carbon content reflecting the degree of carbonation completion (Fig. 5.3). Carbonated serpentinites show lower concentrations (1.64 – 3.35 wt%, n = 6) than listvenites (5.39 – 12.05 wt%, n = 7) and Fu-listvenites (7.90 – 9.51 wt%, n = 5), except for carbonated serpentinite 40Z-3-3-8 (9.38 wt%) from the transition with listvenite. The serpentinized harzburgite has a TC concentration of 0.12 wt%, comparable to the mean value of the Oman mantle in Kelemen and Manning (2015). Metabasalts display low concentrations comprised between 0.02 wt% and 0.28 wt%, except for carbonated metabasalt OM20-01 (4.79 wt%), which was sampled beneath the basal thrust. The metamorphosed limestone from the Muti Formation has a TC content of 12.16 wt%.

The serpentinized harzburgite and carbonated serpentinites preserved $\delta^{13}C_{TC}$ isotope compositions typical of the Primitive Mantle (-5.00 ± 2.50 ‰; Deines, 2002), with values of -6.90 ‰ and -6.20 ‰ to -3.96 ‰, respectively. These values are overall heavier than the compositions of serpentinized harzburgites and dunites in Wadi Dima ($\delta^{13}C_{TC}$: -11.17 ‰ to -7.87 ‰; Noël et al., 2018) and Oman Drilling Project Holes BA1B and BA3A ($\delta^{13}C_{TC}$: -15.90 ‰ to -5.78 ‰; Ternieten et al., 2021b). Listvenites and Fu-listvenites are characterized by heavier compositions (-3.28 ‰ to +0.22 ‰ and +0.08 to 0.80 ‰, respectively) indicating a strong inorganic carbon contribution from fluids. Metabasalts display highly scattered $\delta^{13}C_{TC}$ ratios between -20.7 ‰ and -2.86 ‰, with the lightest compositions assigned to samples close to the ophiolite basal thrust. $\delta^{13}C_{TC}$ of the metamorphosed limestone is 0.96 ‰.

Non-carbonate carbon

The non-carbonate carbon concentration of the serpentinized harzburgite is 0.20 wt%, comparable to carbonated serpentinites (0.24 – 0.57 wt%), listvenites (0.08 – 0.57 wt%), and Fu-listvenite (0.18 – 0.30 wt%). Metabasalts show contents comprised between 0.06 wt% and 0.19 wt%. The amount of remaining material after acid digestion of sample OM20-09 was not sufficient for analysis, indicating a predominance of inorganic carbonate.

In general, $\delta^{13}C_{NCC}$ isotope compositions of the serpentinized harzburgite and carbonated serpentinites are the lightest, with values of -31.04 ‰ and -30.42 ‰ to -30.08 ‰, respectively. Such isotope ratios are slightly lighter than the compiled range for the Oman mantle (-29.64 ‰ to -22.07 ‰;

Noël et al., 2018; Ternieten et al., 2021b), which almost encompass the complete range of compositions for listvenites (-28.93 ‰ to -17.5 ‰) and Fu-listvenites (-30.30 ‰ to -25.79 ‰). Metabasalts have light $\delta^{13}C_{NCC}$ signatures, with only minor variation (-30.35 to -30.01 ‰). Light $\delta^{13}C_{NCC}$ values may indicate the presence of organic carbon, as reported in Kelemen et al. (2022).

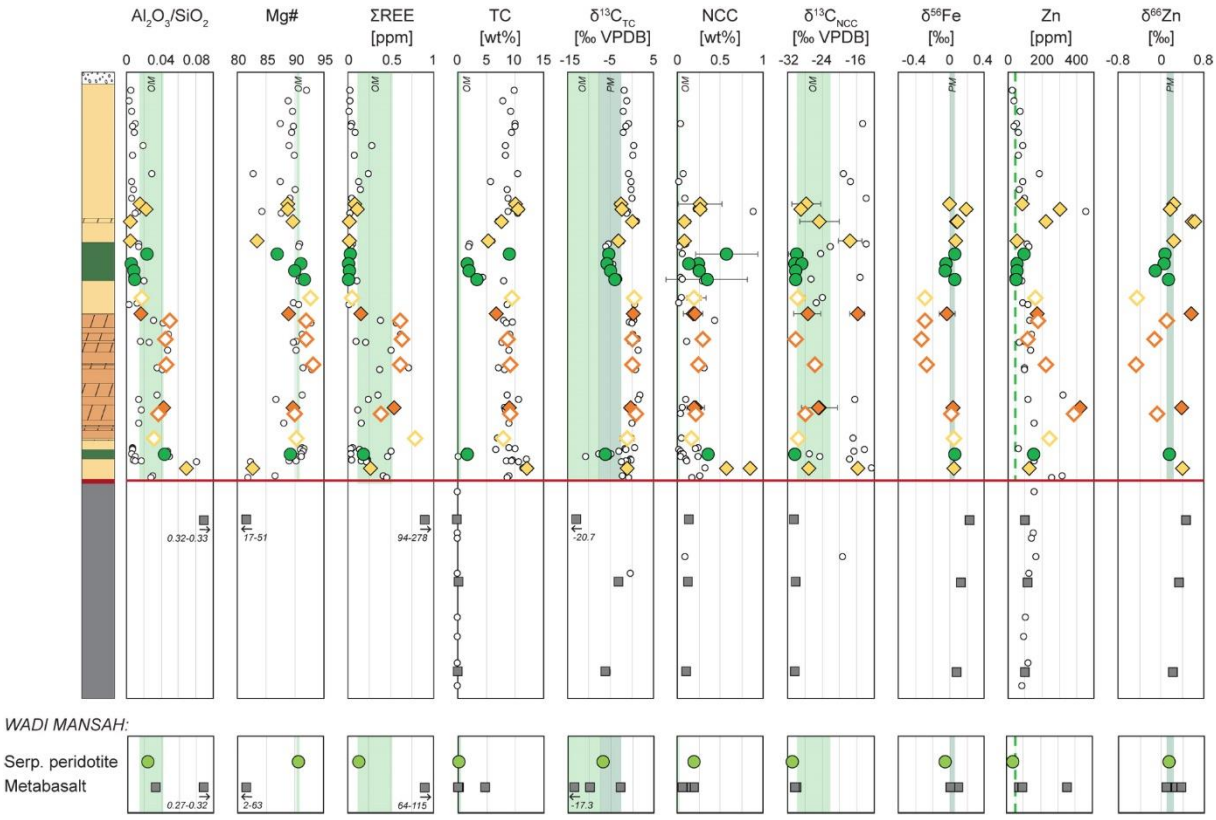

Fig. 5.3 Selected geochemical indicators, samples and reported for Wadi Mansah samples. The error bars are 2σ. The light green and dark green fields correspond to ranges of compositions for the Oman Mantle (OM) and Primitive Mantle (PM), respectively. Oman Mantle compositions after Godard et al. (2021) for Al_2O_3/SiO_2 ratios, Mg#, ΣREE and Zn; compilation of data after Kelemen and Manning (2015), Noël (2018), and Ternieten et al. (2021) for TC, $\delta^{13}C_{TC}$, NCC, and $\delta^{13}C_{NCC}$. Primitive Mantle compositions after Deines et al. (2002), Craddock et al. (2013), and Sossi et al. (2018) for $\delta^{13}C_{TC}$, $\delta^{56}Fe$ and $\delta^{66}Zn$.

Fe and Zn isotopes

Iron and zinc isotope bulk and isotope compositions of Wadi Mansah samples are given in Table 5.2, and plotted depth downhole for BT1B samples (Fig. 5.3). Binary diagrams of $\delta^{57}Fe$ vs. $\delta^{56}Fe$ and $\delta^{68}Zn$ vs. $\delta^{66}Zn$ indicate mass fractionation dependency (Fig. 3.6). $\delta^{57}Fe$ and $\delta^{68}Zn$ values of samples, and isotopic ratios for reference materials are provided in Table 3.6.

The $\delta^{56}Fe$ values of Wadi Mansah altered peridotites (n = 19) range from -0.33 ± 0.00 ‰ to +0.2 ± 0.06 ‰. $\delta^{57}Fe$ values are comprised between -0.55 ± 0.05 ‰ and +0.33 ± 0.10 ‰. The serpentinized harzburgite and carbonated serpentinites ($\delta^{56}Fe$: -0.05 ± 0.02 to +0.07 ± 0.05; n = 6), and listvenites ($\delta^{56}Fe$: -0.03 ± 0.09 to +0.2 ± 0.06; n = 7) gather isotopic ratios with median values ($\delta^{56}Fe$: +0.05 ± 0.04

‰, δ^{57}Fe: +0.08 ± 0.06 ‰) comparable within uncertainty to the Primitive Mantle (δ^{56}Fe: +0.03 ± 0.03 ‰, Craddock et al., 2013; δ^{57}Fe: ~ +0.1‰, Poitrasson et al., 2013; δ^{57}Fe: +0.05 ± 0.01 ‰; Sossi et al., 2016). Fu-listvenites show the lightest compositions with δ^{56}Fe from -0.33 ± 0.00 ‰ to +0.05 ± 0.02 ‰ (n = 6). Metabasalts of the metamorphic sole have heavy compositions (median δ^{56}Fe: +0.10 ± 0.04 ‰, median δ^{57}Fe: +0.13 ± 0.05, n = 6), in excellent agreement with proposed values for global MORBs (δ^{56}Fe: +0.11 ± 0.01 ‰, Teng et al., 2013; δ^{57}Fe: +0.10 ± 0.01 ‰, Sossi et al., 2016).

Metasomatized peridotites show an extended range of δ^{66}Zn isotope compositions ranging between -0.46 ± 0.04 ‰ and +0.64 ± 0.05 ‰. The δ^{68}Zn ratios vary from -0.92 ± 0.07 ‰ to +1.26 ± 0.06 ‰. The serpentinized harzburgite and carbonated serpentinites have δ^{66}Zn compositions comprised between -0.11 ± 0.04 ‰ and +0.15 ± 0.05 ‰, with a median value (δ^{66}Zn: +0.10 ± 0.05 ‰, n = 6) within the global range of compositions of peridotites (+0.16 ± 0.06 ‰, Sossi et al., 2018). Listvenites display heavy compositions, from +0.18 ± 0.02 ‰ to +0.58 ± 0.02 ‰ (n = 7). In contrast, fuchsite-bearing listvenites show the lightest compositions, from -0.46 ± 0.04 ‰ to +0.11 ± 0.04 ‰ (n = 5). Metabasalts have δ^{66}Zn ratios of +0.09 ± 0.02 ‰ to +0.47 ± 0.03 ‰, with a median value of +0.30 ± 0.03 ‰ (n = 6), similar to global MORBs (+0.28 ± 0.03, Wang et al., 2017).

FeO_{TOT} contents and δ^{56}Fe isotopic ratios are fairly homogeneous across Hole BT1B (Fig. 5.3), except for 4 fuchsite-bearing listvenites in the depth interval 107.86-139.97 mbg, characterized by: a) low FeO_{TOT} contents (5.03-6.18 wt%) compared to the Oman mantle (7.49-8.24 wt%, Godard et al., 2021), and b) the lightest isotope compositions (δ^{56}Fe: -0.33 ± 0.00‰ to -0.26 ± 0.03‰). The serpentinized harzburgite and carbonated serpentinites have Zn contents close the Oman mantle (40-50 ppm, Godard et al., 2021) and rather homogeneous isotopic compositions. On the other hand, Zn contents and δ^{66}Zn values of listvenites and fuchsite-bearing listvenites are highly variable with depth, with the most elemental and isotopic variability occurring within the fuchsite-bearing domain (Fig. 5.3). Both lithologies are enriched in Zn (50-420 ppm).

Fe and Zn elemental and isotopic compositions are comprised within the global range of abyssal peridotites for iron, except for the Fu-listvenites (Fig. 5.5a). For zinc, the serpentinized harzburgite and carbonated serpentinites fit in the range of abyssal perditotites, but not the carbonated lithologies (Fig. 5.5c). It must be precised here that no iron and zinc isotopes study has been carried out on abyssal peridotites having experienced conversion to listvenite. Fractionation of iron and zinc isotopes caused by their mobility in fluids during serpentinization and carbonation cannot be evidenced on δ^{56}Fe vs. FeO_{TOT} and δ^{66}Zn vs. Zn plots, as they do not show fractionation trends between serpentinized and carbonated lithologies. There is also no correlation between Fe^{3+}/Fe_{TOT}, δ^{56}Fe ratios and lithologies that could imply the addition of isotopically light or heavy Fe^{3+} by the reactive fluids (Fig. 5.5b). Overall, iron and zinc isotope compositions of Wadi Mansah peridotites encompass the entire range of mantle isotopic heterogeneities observed for the different types of peridotites on Earth (Fig. 5.4). This

variability is unprecedented at such small scale, apart from the Rainbow massif hydrothermal system at the Mid-Atlantic Ridge (Debret et al., 2018a).

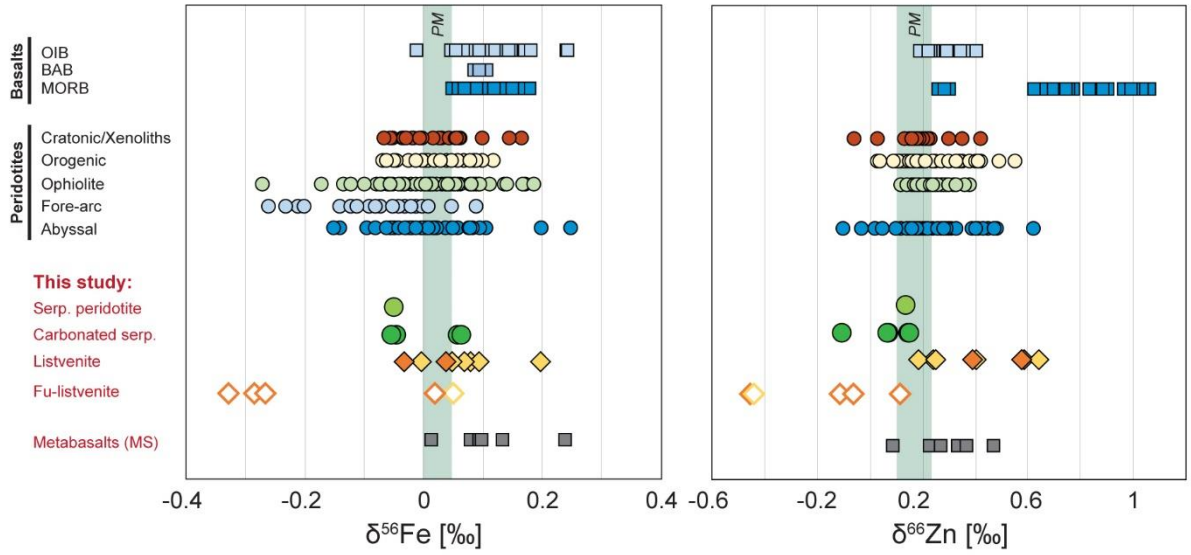

Fig. 5.4 Compiled Fe and Zn isotopic ratios of peridotites and oceanic basalts. The dark green fields show the composition of the Primitive Mantle after Craddock et al. (2013) and Sossi et al. (2018) for $\delta^{56}Fe$ and $\delta^{66}Zn$, respectively. The isotope compositions of basalts are reported from literature for mid-ocean ridges – MORB (Weyer and Ionov, 2007; Chen et al., 2013; Teng et al., 2013; Wang et al., 2017, and Zeng et al., 2021), back-arc basins – BAB (Teng et al., 2013), and oceanic islands – OIB (Weyer and Ionov, 2007; Chen et al., 2013; Teng et al., 2013; Wang et al., 2017). The isotopes compositions of peridotites are reported for mantle xenoliths and cratonic peridotites (Weyer and Ionov, 2007; Wang et al., 2017), orogenic peridotites (Weyer et al., 2005; Weyer and Ionov, 2007; Wang et al., 2017; Sossi et al., 2018; Debret et al., 2021), ophiolite peridotites (Debret et al., 2016; Pons et al., 2016; Debret et al., 2018b, Liu et al., 2019; Zhang et al., 2019); fore-arc peridotites (Debret et al., 2020) and abyssal peridotites (Craddock et al., 2013; Debret et al., 2018b; Liu et al., 2019).

>> **Fig. 5.5** Plots of (a) $\delta^{56}Fe$ vs. FeO_{TOT}, (b) $\delta^{56}Fe$ vs. Fe^{3+}/Fe_{TOT}, (c) $\delta^{66}Zn$ vs. Zn. The light blue and dark blue fields correspond to literature data for abyssal peridotites (Craddock et al., 2013; Debret et al., 2018b; Liu et al., 2019), and MORB (Weyer and Ionov, 2007; Chen et al., 2013; Teng et al., 2013; Wang et al., 2017, and Zeng et al., 2021), respectively. Yellow symbols for (Fu-)listvenites after harbzurgite/dunite protolith; Orange symbols for (Fu-)listvenites after lherzolite protolith.

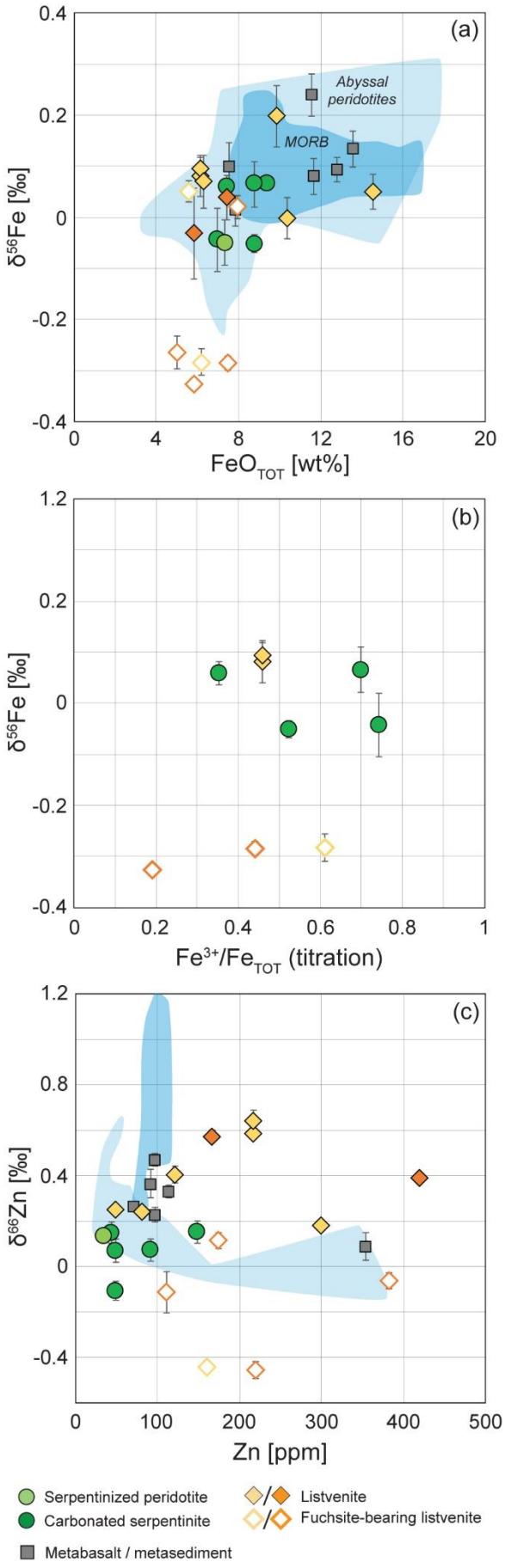
(a)
Abyssal peridotites
MORB
δ56Fe [‰]
FeOTOT [wt%]
(b)
δ56Fe [‰]
Fe3+/FeTOT (titration)
(c)
δ66Zn [‰]
Zn [ppm]
Serpentinized peridotite
Carbonated serpentinite
Metabasalt / metasediment
Listvenite
Fuchsite-bearing listvenite

5.2.5 Discussion

Isotopic fractionation from peridotite protolith to listvenite

Wadi Mansah altered peridotites are characterized by significant compositional variability revealed by stable carbon, iron and zinc isotopes. The shift from mantle-like $\delta^{13}C_{TC}$ compositions in poorly-carbonated serpentinites to heavy ones in (Fu-)listvenites indicate carbonation by reactive fluids with a strong inorganic carbon component (this study, de Obeso et al., 2021). de Obeso et al. (2021) suggest that carbon isotopic variability across Hole BT1B likely result from fractionation processes during high-temperature devolatilization of the fluid source, or during low-temperature carbonate precipitation. Moreover, isotopic variability may also arise from fluid infiltration by multiple batches along different pathways, as inferred from: a) the distribution of clumped isotopes temperatures of carbonate formation (Beinlich et al., 2021), and b) contrasted rock enrichment in Sr, Ca and FME across the borehole (Godard et al., 2021).

Fe and Zn isotope compositions are among the most scattered by comparison with other types of peridotites. Such variability could result from: a) inherited isotopic heterogeneities of protoliths, or b) the overprint by metamorphic processes. Prior to discuss the role of fluid-rock interactions on Fe and Zn mobility, isotopic inheritance from high temperature petrogenetic processes must be explored. Magmatic processes, such as partial melting or melt-rock reactions, were identified as a major cause of Fe and Zn fractionation (e.g. Williams et al., 2005; Weyer and Ionov, 2007; Doucet et al., 2016; Moynier et al., 2017), with liquids enriched in heavy Fe and Zn and depleted residues. However, no correlation is observed between $\delta^{56}Fe$ or $\delta^{66}Zn$ values and Al_2O_3/SiO_2 ratios (Fig. 5. 6), which is a good indicator of mantle fertility (Bodinier and Godard, 2007). One reason could be the local silica mobilization during pervasive carbonation or the generation of silica-bearing veins (Menzel et al., 2022b), hence shattering the precursor ratios.

The serpentinized harzburgite and carbonated serpentinites display light $\delta^{56}Fe$ values which is not surprising as their protoliths are refractory peridotites having experienced substantial melt extraction (Godard et al., 2000). Craddock et al. (2013) and Debret et al. (2016) highlighted a conservative behaviour of Fe during ocean floor serpentinization. The fact that the serpentinized harzburgite, carbonated serpentinites and listvenites have $\delta^{56}Fe$ values overlapping that of abyssal periotites and close to the Primitive Mantle indicate a low mobility of Fe in reactive fluids. Debret et al. (2020) identified a negative correlation between $\delta^{56}Fe$ and Fe^{3+}/Fe_{TOT} ratios related to the oxidation of mantle wedge peridotites by isotopically light sulphate- or carbonate-bearing slab-derived fluids in the Mariana forearc. Here, no correlation could be observed (Fig. 5.5b), possibly because of the destabilization of Fe-bearing phases and elemental redistribution during pervasive carbonation. However, few fuchsite-

bearing listvenites showing low Fe concentrations and light $\delta^{56}Fe$ ratios (Fig. 5.6a) suggest enrichment in light Fe during Fe mobilization by fluids.

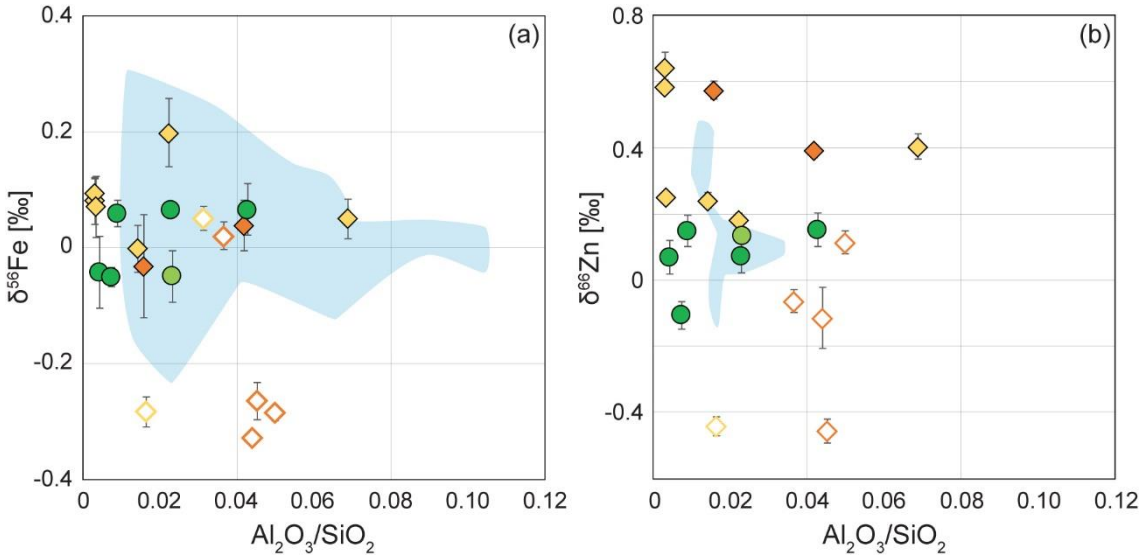

Fig. 5.6 Plots of (a) $\delta^{56}Fe$ vs. Al_2O_3/SiO_2. (b) $\delta^{66}Zn$ vs. Al_2O_3/SiO_2. Symbols as in Fig. 6.4.5. The light blue field correspond to literature data for abyssal peridotites (Craddock et al., 2013; Debret et al., 2018b; Liu et al., 2019).

Highly variable $\delta^{66}Zn$ ratios and the absence of correlation with indices of peridotite fertility (e.g. Al_2O_3/SiO_2, TiO_2 and ΣREE concentrations) imply a strong control of fluid-rock interaction on isotope fractionation. Preferential mobility of isotopically light Zn leached from peridotite by fluids can be promoted during serpentinization, and is controlled by the dissolution of spinels and sulphides (Debret et al., 2018b). The serpentinized harzburgite and carbonated serpentinites seem unaffected by this process and preserved compositions similar to abyssal peridotites and to the Primitive Mantle.

The analysed samples show a stricking positive correlation between $\delta^{66}Zn$ and $\delta^{13}C_{TC}$ ratios (Fig. 5.7a). The compositions of the serpentinized harzburgite and carbonated lithologies remained similar to the Primitive Mantle. Conversion to listvenites define a trend (1 in Fig. 5.7a) to heavier $\delta^{66}Zn$ and $\delta^{13}C_{TC}$ while Fu-listvenites define a second trend of heavy carbon but lighter Zn compositions (2 in Fig. 5.7a). The $\delta^{13}C_{TC}$ ratios express the contribution from carbonated fluids (de Obeso et al., 2022). A resembling pattern is obtained between $\delta^{66}Zn$ and TC concentration (Fig. 5.7c), clarifying the link between the mobility of carbon and zinc. Indeed, the zinc isotopes system is sensitive to the presence of carbonate ions in fluids, with heavy zinc being preferentially bonded to reduced complexes in fluids (Fujii et al., 2012; Pons et al., 2016). However, there is no clear correlation between Zn and TC (Fig. 5.7b) hinting for a complex relationship between carbon and zinc mobility.

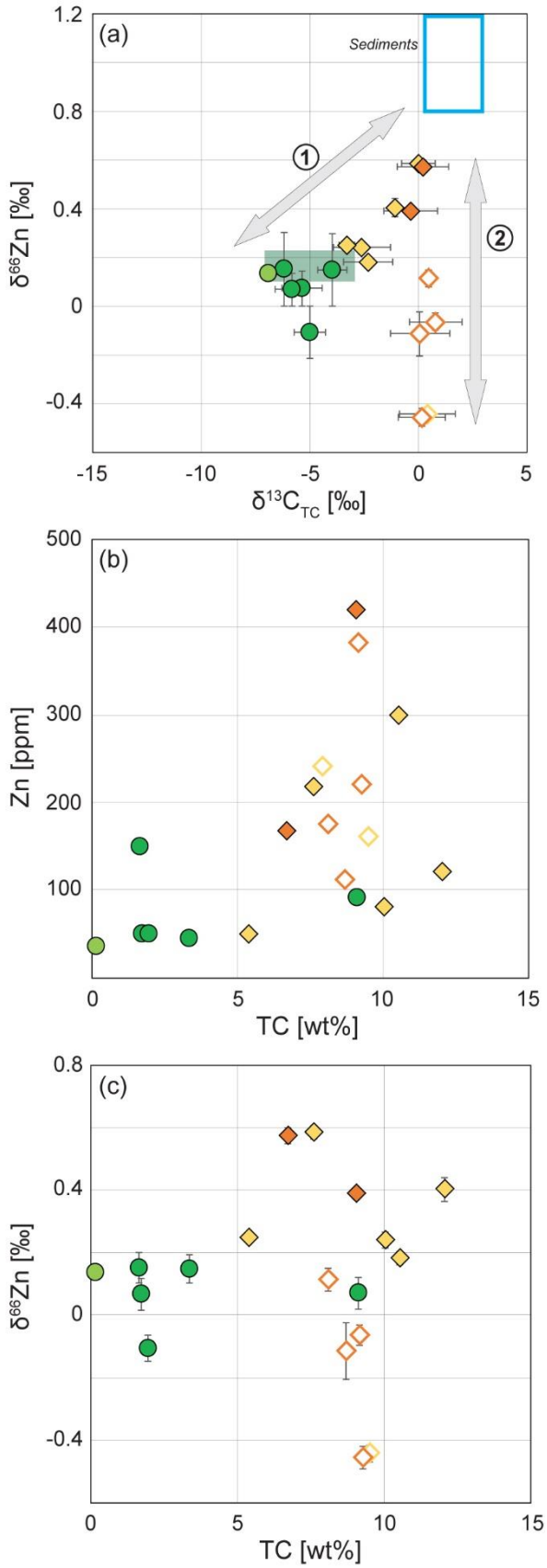

Fig. 5.7 Plots of (a) $\delta^{66}Zn$ vs. $\delta^{13}C_{TC}$, showing two distinctive trends (1) and (2) for isotopic ratios, (b) Zn concentration vs. TC concentration, and (c) $\delta^{66}Zn$ vs. TC concentration. The blue rectangle in (a) represents a sedimentary pole corresponding to $\delta^{66}Zn$ isotope compositions of deep-sea sediments after Pichat et al. (2003) and $\delta^{13}C_{TC}$ compositions of Creteceous limestones in Central Oman after Celestino et al. (2019).

Carbonation reaction and Zn mobility

Heavy $\delta^{66}Zn$ values are interpreted as an effect of the preferential mobility of heavy Zn by carbonate complexes in reactive fluids. However, the correlation between $\delta^{66}Zn$ and $\delta^{13}C_{TC}$ or TC for listvenites is not observed for carbonated serpentinites. In addition, there is no systematics between Zn and TC concentrations. These results suggest that protolith compositions, fluid transport, or reaction paths may exert a role on zinc mobility during carbonation.

Godard et al. (2021) constrained the contribution of harzburgitic/dunitic and (amphibole-bearing) lherzolitic protoliths on the geochemistry of listvenite series in Hole BT1B. A conservative behaviour during carbonation was observed for most major elements, transition metals (Sc, Ti, V, Cr, Mn, Co, Ni), and moderately incompatible lithophile trace elements (Y, Zr, Hf, MREE and HREE). On the other hand, systematic enrichment in FME (Li, Rb, Cs, Ba, Sr, Pb and U) is a feature of carbonated lithologies. Meter-scale compositional variability and local enrichment in Ca, Sr and FME in listvenite series suggest carbonation along multiple reaction paths (Godard et al., 2021). FME compositions can hence be used as a proxy to track the effect of transport and identify reaction paths on zinc mobility, similarly to FME-rich fluid release in subduction zones (e.g. Hattori and Guillot, 2007; Cannaò et al., 2016; Debret et al., 2018b).

Plots between $\delta^{66}Zn$ values and Pb (comparable for Sr, Ba, U) or Cs content (comparable for Rb) do not show any correlation between isotope compositions and elemental concentration (Fig. 5.8). Alkali-rich compositions of Oman peridotites along the basal thrust (e.g. Khedr et al., 2014; Prigent et al., 2018) are ascribed to interaction with slab-derived fluids during ophiolite cooling (Lippard et al., 1986; Prigent et al., 2018). This overprint is recorded by Wadi Mansah peridotites hence explaining high Cs content of serpentinized harzbugite OM20-13 and carbonated serpentinite 74Z-1, both sampled close to the basal thrust (Fig. 5.8b). Lherzolite-derived listvenites are also enriched in alkalis (Godard et al., 2021). Compositional heterogeneity is also illustrated by Pb (Fig. 5.8a), with listvenites after harzburgite/dunite apparently enriched compared to that derived from lherzolite, but being homogenenous at the borehole scale.

Such a small-scale compositional variability inherited from the protolith and/or fluid-rock interactions prior to carbonation hinders the establishment of linkages between the distribution of alkali elements and FME by carbonated fluids and changes in isotope compositions.

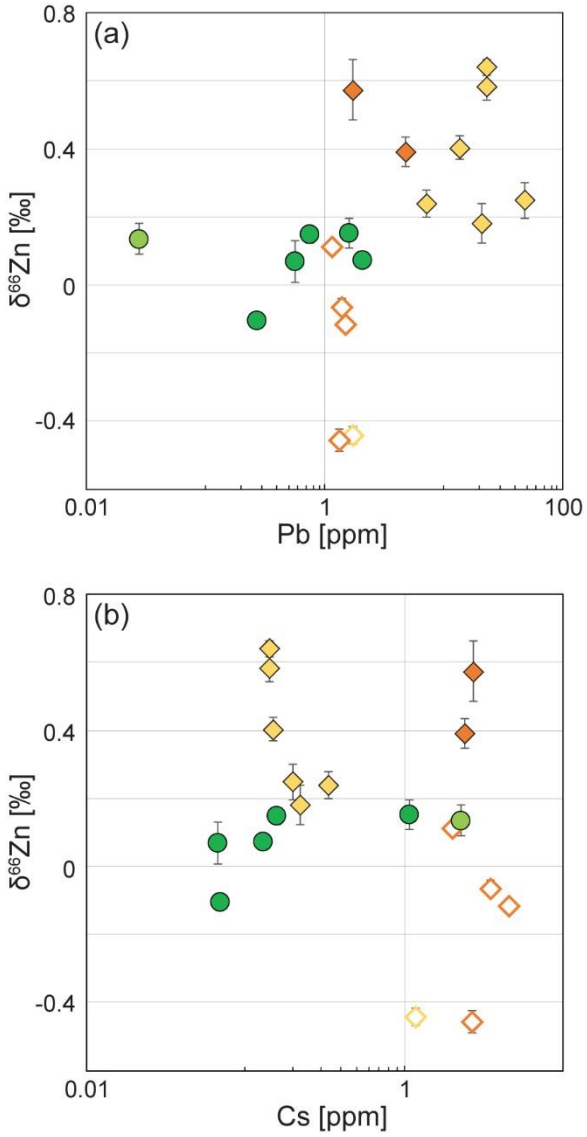

Fig. 5.8 Plots of δ^{66}Zn vs. Pb (a) and Cs (b) concentrations, illustrating the complex fluid migration record of Wadi Mansah altered peridotites.

Cr-spinel breakdown and related isotopes variations

Even if highly carbonated, Fu-listvenites display the lightest δ^{66}Zn values. We note that Zn concentrations in the fuchsite-rich domain are highly variable, suggesting that Zn remobilization was more intense than for carbonated serpentinite and listvenites. This domain is typified by fuchsite growth texturally related to Cr-spinel destabilization as shown in Fig. 5.2. Growth along quartz grain boundaries, sometimes along euhedral facets, and microfractures indicate that Cr-spinel breakdown was contemporaneous to silicification. This timing matches with the need of dissolved silica in fluids to precipitate fuchsite. Fuchsite and carbonates compositions are Zn-poor compared to parent Cr-spinel. Zn mobilization and heavy Zn leaching by fluids may thus be promoted by this reaction.

5.2.6 Perspectives

The fractionation trends observed in Fig. 5.7 suggest a strong control of: i) the fluid composition and ii) local mineral dissolution on Zn mobility. Correlations between $\delta^{66}Zn$ and $\delta^{13}C_{TC}$ or TC suggests the mobility of heavy Zn by complexation with carbonate and possibly sulphate complexes in fluids (Pons et al., 2016). At elevated pCO_2 (1.6) and temperature of 150 °C, Zn in fluids is expected to be found as $ZnHCO_3^+$ specie for pH = 4–6, while as $ZnCO_3$ at pH > 7, with the heaviest isotopic compositions obtained by complexation into $ZnCO_3$ (Fujii et al., 2011).

Mobility and isotopic fractionation of Fe and Zn driven by Cr-spinel dissolution could be modelled by *ab initio* calculations (e.g. Fujii and Albarède, 2012). In such model, the elemental and isotopic behaviour of the whole rock is approximated to that of spinel. Zn mobility can be modelled using a Rayleigh distillation law, according to:

$$10^3 \ln(\alpha_{fluid\text{-}mineral}) = 10^3 \ln(\beta_{fluid}) - 10^3 \ln(\beta_{mineral})$$

$$\delta^{56}Fe_{Final} = (1000 + \delta^{56}Fe_{Initial}) \times (F^{(\alpha-1)} - 1) + \delta^{56}Fe_{Initial}$$

and

$$10^3 \ln(\alpha_{fluid\text{-}mineral}) = 10^3 \ln(\beta_{fluid}) - 10^3 \ln(\beta_{mineral})$$

$$\delta^{66}Zn_{Final} = (1000 + \delta^{66}Zn_{Initial}) \times (F^{(\alpha-1)} - 1) + \delta^{66}Zn_{Initial}$$

where: i) α is the fractionation factor between the mineral and a fluid phase; ii) β is the reduced partition function ratio; iii) F is the fraction of Zn remaining in rock (0 if all Zn is remobilized by fluids). The recent determination β-factors for Fe and Zn species make such modelling possible at date (Dauphas et al., 2017 for Fe; Fujii et al., 2014 and Ducher et al., 2016 for Zn). The initial chemical and isotope compositions would be that of serpentinized peridotite OM20-13. Key information on the role of fluid composition may arise from testing Rayleigh distillation between spinel and carbonate complexes, but also with chlorine and sulphur complexes. Indeed, Carter (2022) evidenced the release of chlorine in fluids during the carbonation of serpentine which may have further served as carrier for Fe and Zn during carbonation.

Chapter 6: Trace element geochemistry of listvenites and associated lithologies: role of temperature and fluid composition

Foreword

This chapter is dedicated to the determination of i) fluid sources, ii) carbonation temperatures, and to iii) the study of the trace element geochemistry of Oman2020 samples and minerals of samples from the borehole.

Beinlich et al. (2020) determined the carbon and oxygen compositions of matrix and vein carbonates, and carbonation temperatures on a subset of 10 borehole samples. We complemented this work by analysing 8 additional core samples, however improving the spatial resolution of carbonate analysis by collecting powders at a microstructural scale.

The carbonation of serpentinized peridotites in Wadi Mansah is characterized by an isochemical elemental behaviour for major elements (except Ca) and lithophile elements, major addition of CO_2 and water release, and variable enrichments in FME at the borehole scale (Godard et al., 2021). However, the absence of a (partially) preserved peridotite protolith in Hole BT1B prevented from discriminating clearly elemental mobility relative to initial serpentinization and concurrent or later carbonation stages. In that regard, we carried out a bulk rock geochemical study of partially to fully serpentinized peridotites, carbonated serpentinites and listvenites collected close to the BT1B drill site and in the surroundings of Fanja to explore geochemical variability at a regional scale. The trace element compositions of minerals were also measured to better assess elemental redistribution during metasomatism.

6.1 Constraining the source of fluids and temperature of carbonation: a "micro-bulk" carbon and oxygen isotopes study on carbonates

6.1.1 Context of the study

Beinlich et al. (2020) characterized the clumped isotope distribution ($\Delta 47$) of carbon and oxygen on matrix and vein carbonate powders from 10 borehole samples. The ordering of CO_2 isotopologues in carbonate minerals is supposed to be independent on the isotope composition of the parent fluid, but is sensitive to growth temperature, thus providing a reliable paleothermometer (Ghosh et al., 2006; Eiler et al., 2007). Analyses by Beinlich et al. (2020) yielded a range of carbonation temperatures from 45 ± 5 °C to 247 ± 52 °C, encompassing those previously obtained sieved carbonate crystals from Wadi Mansah listvenites (61 ± 8 °C to 114 ± 8 °C) by Falk and Kelemen (2015). These authors assigned low-temperature carbonation respectively to obduction (Falk and Kelemen, 2015), or ophiolite uplift and cooling (Beinlich et al., 2020).

One drawback of the clumped isotope method is the amount of powder required for analysis (ca. 1–5 mg). In their study, Beinlich et al. (2020) obtained carbonate powders by micro-drilling homogeneous matrix and vein domains, however with a poor spatial resolution (drill spot size: 3.8 mm). As illustrated in chapters 4 and 5, the carbonation sequence resulted in the formation of an intricate network of matrix and vein microstructures, generally smaller than 250 μm in size and presenting distinct growth patterns. In this study, we investigated the isotope chemistry of carbonates at a higher spatial resolution (drill diameter and depth: ~300 μm and ~450 μm).

6.1.2 Sampling

The carbon and oxygen isotope compositions of carbonates were determined on a subset of 8 representative core samples (3 carbonated serpentinites, 4 listvenites and 1 fuchsite-bearing listvenite). Carbonate powder was collected by drilling identical types of microstructures in homogeneous domains. Despite high-resolution micro-sampling, the amount of powder recovered by drilling microstructures smaller than 300 μm in size was not sufficient for analysis (ca. 0.05 mg). The emplacement of drill spots is indicated in Fig. 6.1. Sample preparation, data acquisition and treatment are detailed in chapter 3.6.2.

>> **Fig. 6.1** Billet (left side) and thin section (right side) scans of the investigated samples. Drill spots are indicated by dashed contours, orange as drilling magnesite and blue for dolomite.

35Z-1-32-37 - Listvenite
(72.01 mbg)

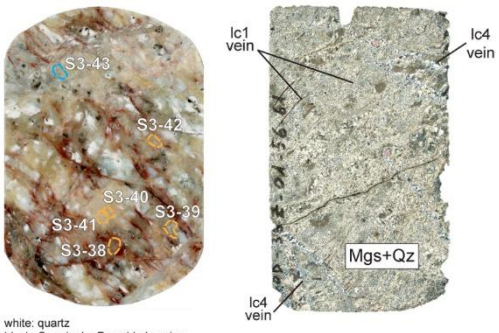

white: quartz
black: Cr-spinel + Fe-oxide in veins
red: Fe-rich magnesite
yellow-pink: Mg-rich magnesite
transparent: dolomite/quartz (veins)

40Z-3-11-16 - Carbonated serpentinite
(87.035 mbg)

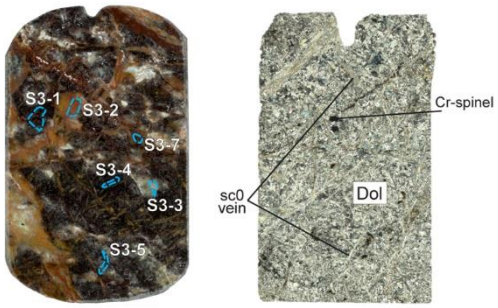

dark grey: dolomite (matrix)
black: Cr-spinel + Fe-oxide in veins
white: dolomite (matrix)

43Z-4-52-57 - Carbonated serpentinite
(96.705 mbg)

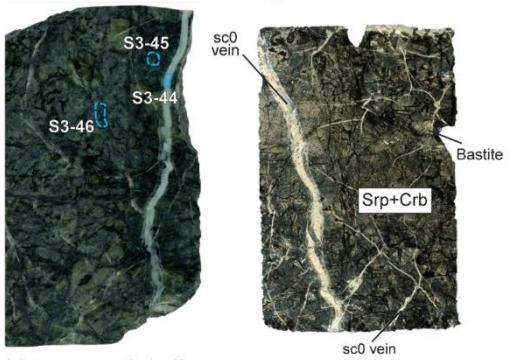

dark green-grey: serpentine (mesh)
olive-green: bastite
grey: serpentine (veins)
black: Cr-spinel + Fe-oxide in veins

44Z-4-0-5 - Carbonated serpentinite
(99.415 mbg)

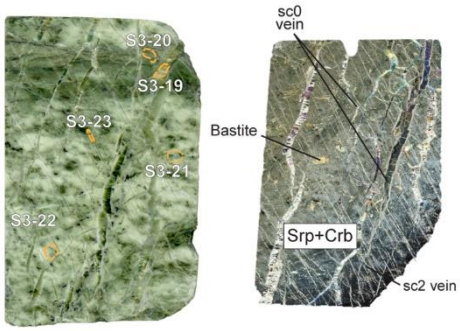

light green: serpentine (mesh)
olive green: bastite (isolated patches)
red: Fe-rich magnesite (thin veins)
black: Cr-spinel + Fe-oxide

46Z-6-46-51 - Listvenite
(106.3 mbg)

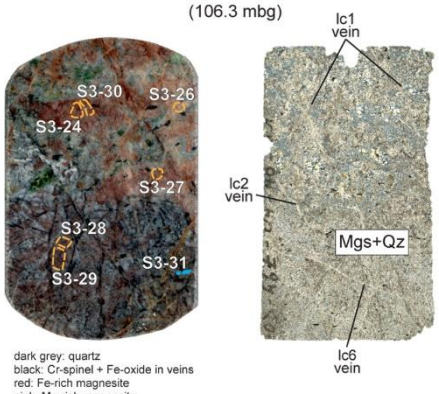

dark grey: quartz
black: Cr-spinel + Fe-oxide in veins
red: Fe-rich magnesite
pink: Mg-rich magnesite
white: Fe-oxide

50Z-1-75-80 - Listvenite
(113.2 mbg)

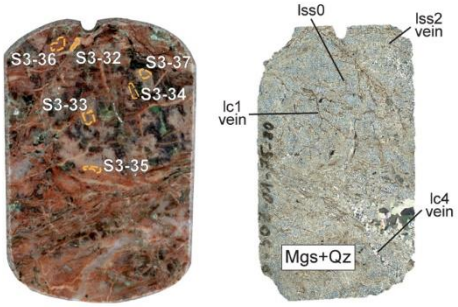

black: quartz
red: Fe-rich magnesite
pink: Mg-rich magnesite
white: Fe-oxide
transparent: dolomite and quartz (veins)

60Z-1-32-37 - Fu-listvenite
(140.17 mbg)

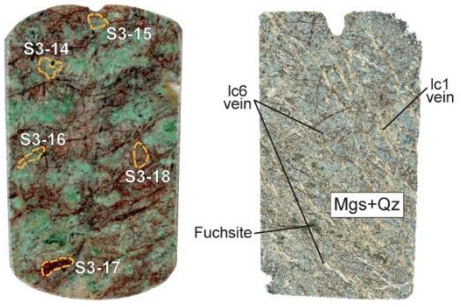

grey-light green: quartz
pink: Mg-magnesite
red: Fe-magnesite
dark green: fuchsite
white: Fe-oxide
black: Fe-oxide (veins)

76Z-1-12-20 - Listvenite
(189.3 mbg)

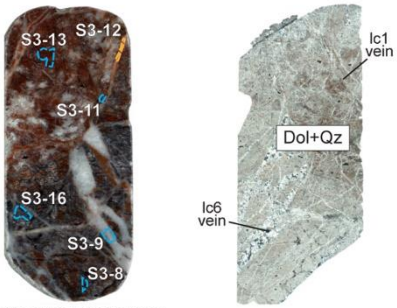

dark grey-red: dolomite +quartz
white: dolomite (veins)
orange-red: magnesite (veins)
black: Cr-spinel + Fe-oxides

6.1.3 Results

Carbon and oxygen isotope compositions of carbonates are provided in Table 6.1 and plotted depth downhole in Fig. 6.2.

Carbonates from carbonated serpentinites (n = 12) display $\delta^{13}C_{TIC}$ compositions ranging from -5.35 to -2.93 ‰. The $\delta^{18}O_{TIC}$ ratios are comprised between -12.33 ‰ and -9.47 ‰. The lightest $\delta^{18}O_{TIC}$ values correspond to carbonated serpentinite in the upper section of the serpentinite interlayer (Fig. 6.2), while the lowest ones were measure at the lower transition with listvenites. Carbonates in listvenites (n = 25) display heavier $\delta^{13}C_{TIC}$ compositions (-1.46 ‰ to +1.31 ‰), except for one outlying lc1 magnesite vein at -6.53 ‰. The $\delta^{18}O_{TIC}$ values fit in a larger compositional range than for carbonated serpentinites (-11.60 ‰ to -6.96 ‰), with higher variability within single sample. No systematic distribution in isotope compositions between matrix and vein carbonates can be inferred. In addition, there is no major difference in isotopic compositions considering single carbonate species. For example, magnesites in carbonated serpentinites ($\delta^{13}C_{TIC}$ = -3.37 ‰ to -2.91 ‰; $\delta^{18}O_{TIC}$ -10.58 ‰ to -9.47 ‰) overlap in composition with dolomites ($\delta^{13}C_{TIC}$ = -3.37 to -2.91; $\delta^{18}O_{TIC}$ = -10.58 to -9.47). Overall, the distribution of isotope compositions across the borehole is defined by changes in the host lithologies.

6.1.4 Discussion

Temperature of carbonation

The temperature of carbonate precipitation (R1b) can be estimated after the equation of oxygen exchange in a mineral-water system (R1, e.g., Aharon, 1988):

$$10^3 \ln \alpha \approx \Delta^{18}O_{min\text{-}fluid} \approx A \cdot (10^6 \cdot T^{-2}\,[K]) + B \quad (R1)$$

$$T\,[°C] = (A \cdot 10^6) / (\Delta^{18}O_{min\text{-}fluid} - B) - 273.15 \quad (R1b)$$

where $\Delta 18O_{min\text{-}fluid}$ is the difference in isotopic compositions between the mineral and its parent fluid; A and B are the oxygen isotope exchange coefficients between mineral and fluid. In our case study, the $\delta^{18}O$ composition of the fluids are unknown.

A first approach to evaluate the temperature of carbonation is to assume a fixed $\delta^{18}O$ fluid composition ($\delta^{18}O_{fluid}$). In this scenario, reactive fluids are derived from a single source and carbonation takes place under homogeneous thermal and flowing regimes at the borehole scale. For calculation, the $\delta^{18}O_{fluid}$ is fixed at +8 ‰, based on the clustering of calculated fluid compositions between +6.04 ‰ and +12.14 ‰ across BT1B (Beinlich et al., 2020). The considered A and B coefficients are from Aharon (1988) for magnesite and Horita (2014) for dolomite. Calculated temperatures range between 154–220°C for magnesite and between 138–212 °C for dolomite, broadly matching the temperature range (<200 °C) proposed by Kelemen et al. (2022). However, this scenario is unlikely accounting for: i) the

correlation between clumped temperatures and equilibrium $\delta^{18}O_{fluid}$ compositions (Falk and Kelemen, 2015; Beinlich et al., 2020), which suggest fluid migration along different flow pathways and at different timing.

The second approach corresponds to the implementation of the most fractionated fluid compositions calculated by Beinlich et al. (2020) hence providing the broadest temperature range expected for carbonation. The obtained temperatures are comprised between 35 °C and 311 °C for magnesite and between 22 °C and 313 °C for dolomites.

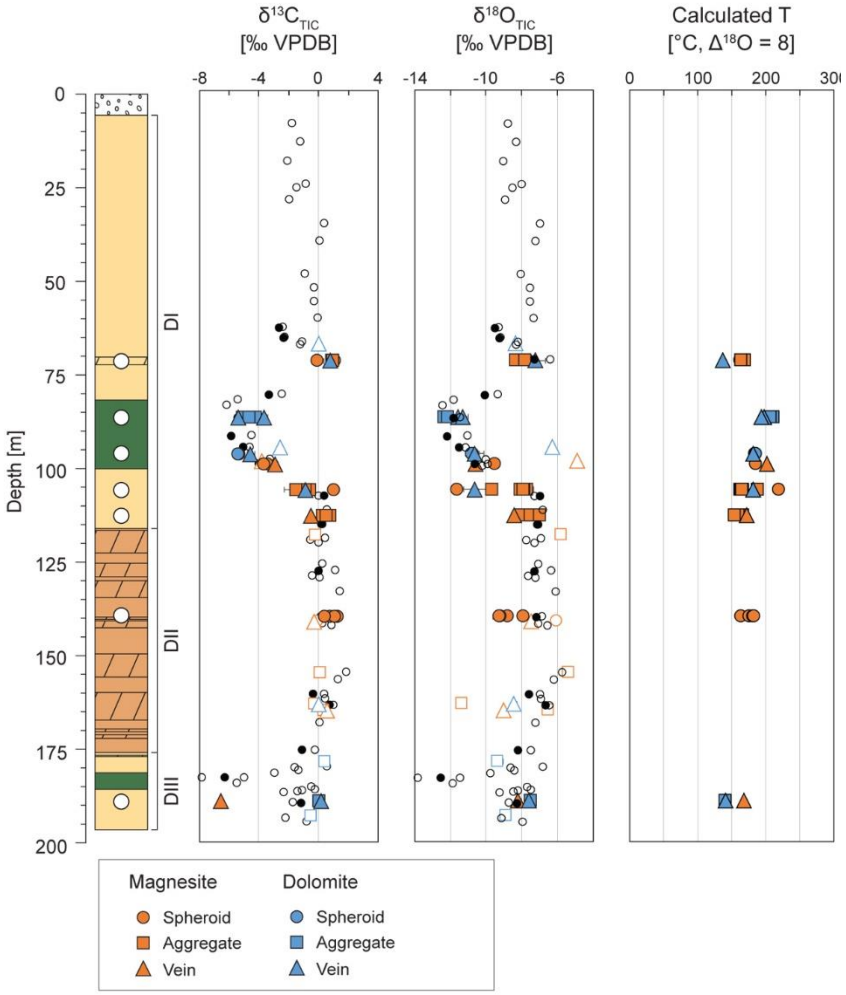

Fig. 6.2 Carbon and oxygen isotope compositions plotted depth downhole. Errors bar are 2SD. Filled symbols correspond to measured data from this study, while contoured symbols are data from Beinlich et al. (2020). Filled and contoured small circles are bulk $\delta^{13}C_{TC}$ from de Obeso et al. (2022) and this study (see chapter 5.2).

>>**Table 6.1** Carbon and oxygen isotope compositions and calculated growth temperatures of carbonate microstructures. Matrix and vein nomenclature is from Menzel et al. (2022b). $\delta^{13}C_{TIC}$ and $\delta^{18}O_{TIC}$ isotope ratios are in permil notation relative to the VPDB isotopic standard. Abbreviations: Carb. Serp. = carbonated serpentinite, List. = listvenite, Fu-List. = fuchsite-bearing listvenite.

Lithology	Sample	Depth [mbg]	Spot	Mineral	Structure	Texture	Mass [mg]	$\delta^{13}C$ ‰ VPDB	2SD ‰ VPDB	$\delta^{18}O$ ‰ VPDB	2SD ‰ VPDB	Δ18O = -9.9 ‰			Δ18O = +12.2 ‰			Δ18O = +8 ‰		
List.	35Z-1-56-61	72.01	S3-38	Mgs	Matrix	Spheroid	0.526	-0.03	0.40	-7.85	0.12	39	39	38	225	227	223	165	166	163
List.	35Z-1-56-61	72.01	S3-39	Mgs	Matrix	Spheroid	0.086	1.10	0.19	-7.65	0.30	38	39	36	222	227	217	162	166	159
List.	35Z-1-56-61	72.01	S3-40	Mgs	Matrix	Aggregate	0.238	0.92	0.17	-8.30	0.18	41	41	40	234	237	230	170	173	170
List.	35Z-1-56-61	72.01	S3-41	Mgs	Matrix	Aggregate	0.134	0.99	0.10	-7.80	0.30	38	40	37	225	230	219	164	168	164
List.	35Z-1-56-61	72.01	S3-43	Dol	Vein	lc4	0.226	0.84	0.11	-7.23	0.54	20	22	18	194	203	185	138	144	138
Carb. Serp.	40Z-3-11-16	87.035	S3-1	Dol	Matrix	Aggregate	0.166	-5.00	0.04	-12.21	0.32	43	45	42	309	320	299	210	216	210
Carb. Serp.	40Z-3-11-16	87.035	S3-3	Dol	Matrix	Aggregate	0.272	-5.05	0.07	-12.11	0.18	43	44	42	306	312	300	208	211	208
Carb. Serp.	40Z-3-11-16	87.035	S3-4	Dol	Matrix	Aggregate	0.245	-4.18	0.12	-12.33	0.23	44	45	43	313	321	305	212	216	212
Carb. Serp.	40Z-3-11-16	87.035	S3-5	Dol	Matrix	Aggregate	0.169	-4.63	0.10	-12.13	0.29	43	44	41	306	316	297	208	214	208
Carb. Serp.	40Z-3-11-16	87.035	S3-7	Dol	Vein	sc0	0.597	-5.33	0.18	-11.55	0.13	40	41	39	289	292	285	198	200	198
Carb. Serp.	40Z-3-11-16	87.035	S3-2	Dol	Vein	sc0	0.105	-3.62	0.24	-11.30	0.32	39	40	37	281	291	273	194	199	194
Carb. Serp.	43Z-4-52-57	96.705	S3-45	Dol	Matrix	Spheroid	0.695	-5.28	0.12	-10.70	0.14	36	36	35	266	269	262	184	186	184
Carb. Serp.	43Z-4-52-57	96.705	S3-46	Dol	Matrix	Spheroid	0.932	-5.35	0.20	-10.79	0.38	36	38	34	268	278	258	185	192	185
Carb. Serp.	43Z-4-52-57	96.705	S3-44	Dol	Vein	sc0	0.110	-4.53	0.24	-10.61	0.47	39	40	37	281	291	273	194	199	194
Carb. Serp.	44Z-4-0-5	99.415	S3-21	Mgs	Matrix	Spheroid	0.342	-3.37	0.08	-9.48	0.25	46	47	45	258	263	252	186	190	183
Carb. Serp.	44Z-4-0-5	99.415	S3-22	Mgs	Matrix	Spheroid	0.721	-3.60	0.14	-9.47	0.15	46	47	45	258	261	254	186	188	184
Carb. Serp.	44Z-4-0-5	99.415	S3-23	Mgs	Vein	sc2	0.422	-2.91	0.20	-10.58	0.09	51	52	51	283	286	281	203	204	203
List.	46Z-4-46-51	106.3	S3-24	Mgs	Matrix	Aggregate	0.641	-1.46	0.81	-8.02	0.10	39	40	39	228	230	227	167	168	167
List.	46Z-4-46-51	106.3	S3-25	Mgs	Matrix	Spheroid	0.098	1.08	0.22	-11.60	0.23	57	58	56	311	318	305	220	224	220
List.	46Z-4-46-51	106.3	S3-27	Mgs	Matrix	Aggregate	0.600	-1.06	0.76	-9.62	0.12	47	47	46	261	263	258	188	190	188
List.	46Z-4-46-51	106.3	S3-28	Mgs	Matrix	Aggregate	0.174	-0.56	0.15	-7.68	0.31	38	39	37	222	228	217	163	167	163
List.	46Z-4-46-51	106.3	S3-29	Mgs	Matrix	Aggregate	0.297	-0.83	0.13	-7.82	0.20	39	39	38	225	229	221	164	167	164
List.	46Z-4-46-51	106.3	S3-30	Mgs	Matrix	Aggregate	0.429	-1.46	0.22	-7.90	0.11	39	39	38	226	228	224	165	167	165
List.	46Z-4-46-51	106.3	S3-31	Dol	Vein	lc4	0.154	-0.85	0.30	-10.60	0.67	35	38	32	263	281	247	182	193	182
List.	50Z-1-75-80	113.15	S3-33	Mgs	Matrix	Aggregate	0.134	0.79	0.13	-7.44	0.29	37	38	36	218	223	213	160	163	160
List.	50Z-1-75-80	113.15	S3-35	Mgs	Matrix	Aggregate	0.089	0.50	0.17	-8.06	0.29	40	41	38	229	235	224	167	171	167
List.	50Z-1-75-80	113.15	S3-36	Mgs	Matrix	Aggregate	0.455	0.30	0.07	-7.45	0.18	37	38	36	218	221	215	160	162	160
List.	50Z-1-75-80	113.15	S3-37	Mgs	Matrix	Aggregate	0.560	0.59	0.16	-6.96	0.13	35	35	34	210	212	208	154	156	154
List.	50Z-1-75-80	113.15	S3-32	Mgs	Vein	lss2	0.351	-0.50	0.04	-8.41	0.18	41	42	40	236	239	232	172	174	172
Fu-List.	60Z-1-32-37	140.17	S3-14	Mgs	Matrix	Spheroid	0.260	1.31	0.21	-7.87	0.12	39	39	38	226	228	223	165	167	164
Fu-List.	60Z-1-32-37	140.17	S3-15	Mgs	Matrix	Spheroid	0.159	0.82	0.14	-8.74	0.17	43	43	42	242	246	239	176	178	174
Fu-List.	60Z-1-32-37	140.17	S3-16	Mgs	Matrix	Spheroid	0.251	1.11	0.23	-9.16	0.06	45	45	44	251	252	250	182	183	181
Fu-List.	60Z-1-32-37	140.17	S3-18	Mgs	Matrix	Spheroid	0.147	0.46	0.48	-9.23	0.40	45	47	43	252	261	244	183	188	177
List.	76Z-2-12-20	189.3	S3-8	Dol	Matrix	Aggregate	0.105	0.07	0.15	-7.50	0.23	21	22	20	198	202	194	141	144	141
List.	76Z-2-12-20	189.3	S3-11	Dol	Matrix	Aggregate	0.054	-0.80	0.34	-11.14	0.60	38	41	35	277	294	261	191	201	191
List.	76Z-2-12-20	189.3	S3-12	Mgs	Vein	lc1	0.042	-6.53	0.12	-8.19	0.15	40	41	40	232	234	229	169	171	169
List.	76Z-2-12-20	189.3	S3-9	Dol	Vein	lc6	0.396	0.20	0.18	-7.57	0.31	22	23	20	200	205	194	142	145	142

Isotopic variability across the borehole

Beinlich et al. (2020) highlighted the non-systematic distribution of carbonation temperatures and calculated fluid compositions ($\delta^{18}O_{fluid}$ = -9.9 ‰ – +12.1 ‰) at the borehole scale, possibly indicating fluid migration along different flow pathways and at different timing.

Carbon isotopes compositions of carbonates define two mains groups, with the lightest $\delta^{13}C$ ratios assigned to carbonated serpentinites while heavier ones were measured in (Fu-)listvenites. Homogeneous $\delta^{13}C$ ratios for listvenite-hosted carbonates indicate an identical source of fluids. It is questioning if the light $\delta^{13}C$ compositions of dolomite hosted by carbonated serpentinites derive from: i) fractionation at low temperature, resulting in mixing signatures between the host rock and fluids, or ii) a different source of fluid. Unfortunately, no clumped isotope data on matrix carbonates in this core interval are available at date. It is noteworthy that carbonated serpentinites are characterized by a high modal abundance of dolomite (Kelemen et al., 2020), enriched volatiles and Sr contents compared to surrounding listvenites (Carter et al., 2020; Godard et al., 2021), which may reflect an effect of transport on fluid composition or indicate a different source for reactive fluids. The narrow $\delta^{18}O$ compositions of matrix and veins carbonates within a single sample (except for listvenite 46Z-4) may point out carbonate precipitation under constant thermal conditions and after similar fluids.

6.2 Major and trace element chemistry of listvenites and related lithologies in the Fanja region

6.2.1 Bulk rock major and trace element geochemistry

The major element concentrations of metasomatized peridotites from Fanja are plotted on Caltech diagrams normalized to the main mantle section (MMS) of the Semail Ophiolite (Fig. 6.3), but also in SiO_2-MgO-CaO ternary diagrams (Fig. 6.4). Major element concentrations mentioned in the text were recalculated on a volatile-free basis. Trace elements compositions are presented on extended spider diagrams normalized to PM and to CI Chondrite for REE (Fig 6.5). Concentrations of selected FME and transition metals are plotted on Caltech diagrams in Fig. 6.6. Bulk rock geochemistry data are provided in Appendix.

Protolith fertility can be inferred from TiO_2 and Al_2O_3 contents, but also from the REE concentration and distribution, all these elements being considered as immobile during carbonation (Godard et al., 2021). Local mineralogical heterogeneities observed within listvenite cores and remobilization of silica through veining (see chapter 4.2) prevent using the Al_2O_3/SiO_2 ratios as a reliable proxy for peridotite fertility. Those indicators, in support to textural observations, are useful for identifying the protolith of fully serpentinized or carbonated serpentinites. Harzburgite- and dunite-derived compositions would be characterized by: i) low TiO_2 (< 0.01 wt%), Al_2O_3 (< 1 wt%), and ΣREE (< 0.1 ppm) contents, ii) depletion between MREE and HREE (Sm_N/Yb_N as proxy, N = normalized to CI Chondrite). On the other hand, lherzolite-derived compositions would be typified by: i) higher TiO_2, Al_2O_3 and ΣREE contents, ii) a REE distribution defining "spoon-shape" patterns with a strong fractionation between LREE and MREE (Ce_N/Sm_N as proxy), and limited fractionation between MREE and HREE.

Compositions of the Semail ophiolite mantle (Lippard, 1986; Godard et al., 2000; Gerbert-Gaillard, 2002; Hanghoj et al., 2010; Takazawa et al., 2003; Khedr et al., 2014) generally displays fractionation between LREE and HREE (Ce_N/Yb_N as proxy), inherited from the primary mineralogy. Such fractionation becomes less significant by precipitating Ca-carbonates such as dolomite, which incorporate high amounts of LREE (Bach et al., 2011, Schröder et al., 2015; Noël et al. 2018) compared to precursor serpentine or magnesite; also see Chapter 6.2.2).

Site 1

Serpentinized peridotites (n = 2) display SiO_2, MnO, MgO, and FeO concentrations similar to the MMS, but slightly depleted in P_2O_5 (Figs. 6.3, 6.4). Mg# range between 89.3 and 90.6. LOI values are low due to partial serpentinization (9.6 – 10.6 wt%). Compositions in transition metals are narrow to those of the MMS (Fig. 6.6; e.g. Co = 89.7 – 93.3 ppm; Zn = 35.8 – 39.7 ppm). Both serpentinized peridotites are depleted in most HFSE (U, Th, Nb, Ta, Zr, Hf, Y and REE) and LILE (Eu, Sr, Ba, Eu,

Pb). Variability in CaO, Al_2O_3 and TiO_2 contents may indicate different protoliths. Sample OM20-13 is derived from a harzburgite (CaO = 0.95 wt%; TiO_2 = 0.01 wt%; Al_2O_3 = 1.05 wt%), with trace element compositions overlapping that of the MMS (Fig. 6.5). The REE pattern ("U" shape) show high fractionation between LREE-MREE and HREE, but also between LREE and MREE (Ce_N/Yb_N = 0.03; Sm_N/Yb_N = 0.02; Ce_N/Sm_N = 1.36). The ΣREE is low (0.14 ppm). Sample OM20-04, collected close to the basal thrust, may derive from a lherzolite based on elevated CaO (1.87 wt%), TiO_2 (0.07 wt%) and Al_2O_3 (1.77 wt%) contents. The REE distribution forms a spoon-shape, typical of basal lherzolites (Ce_N/Yb_N = 0.05; Sm_N/Yb_N = 0.18; Ce_N/Sm_N = 0.3). The ΣREE is 0.61 ppm. Both samples show enrichments in few fluid mobile LILE (Li = 1.3 – 2.7 x PM; Sb = 1.6 x PM; Cs = 11.7 – 110 x PM). OM20-04 has higher abundances in Ba, As, Mo and Sr compared to OM20-13, but is poorer in alkali (Cs, Rb).

Carbonated serpentinites (n = 5) show a compositional range similar to serpentinized peridotites for most major elements, except for highly variable CaO (0.4 – 10.3 wt%) and Al_2O_3 contents (0.1 – 2.9 wt%), and an increased LOI (17.9 – 33.9 wt%). Mg# range from 88.0 to 91.4. Variations in Al_2O_3 reflect mantle compositional heterogeneity. The high Al_2O_3 content of sample OM20-18 (2.88 wt%) may be explained by abundant Cr-spinel. High CaO concentrations (6.2 – 10.3 wt%) of samples OM20-17 and OM20-18 are related to a higher content of dolomite occurring as veins, a type feature of the crust-mantle fault zone at Site 1. Carbonated serpentinites are depleted in HFSE contents and display highly variable compositions in FME (e.g. Pb = 0.66 – 39.9 x PM), with the highest concentrations in Li, Rb, Sb, Cs, Mo found in the closest samples to the sole. Dolomite-rich samples show the highest contents in Sr. Transition metals compositions are similar to serpentinized peridotites, except for abnormally low V (4.65 ppm), Cr (700 pm), and high Co (185 ppm), Cu (351 ppm), and Zn (73.0 ppm) for carbonated serpentinite OM20-11 sampled above the sole. Two types of REE patterns are observed: i) "U"-shaped patterns (n = 3; Ce_N/Yb_N = 0.58 – 0.84 Sm_N/Yb_N = 0.29 – 0.50; Ce_N/Sm_N = 1.06 – 1.98), with low ΣREE (0.08 – 0.23 ppm), and ii) spoon-shape patterns for sample OM20-17 and 18 (n = 2; Ce_N/Yb_N = 0.11 – 0.43 Sm_N/Yb_N = 0.45 – 0.73; Ce_N/Sm_N = 0.25 – 0.58), with positive Eu anomalies. Their ΣREE range between 0.23 and 0.66 ppm.

Listvenites (n = 5) are characterized by major element compositions similar to carbonated serpentinites. Few samples showing a higher CaO content (2.5 – 24.1 wt%), hence dolomite-bearing, were all collected close to the basal thrust and are highly veined or cataclasite-bearing. Na_2O and K_2O concentrations are close to that of the MMS. Mg# are comprised between 80.4 and 92.4, low ratios suggesting the mobility of Mg or Fe during carbonation and/or later alteration by fluids. Concentrations in transition metals overlap those of carbonated serpentinites, however more scattered Cu and Zn (Cu = 0.6 – 71.8 ppm; Zn = 30.1 – 387 ppm). All listvenites are enriched in As (99.4 – 1803 x PM), Sr (4.0 – 24.3 x PM), Ba (1.0 – 34.3 x PM), Cs (4.76 – 32.9 x PM), and Pb (9.64 – 142 x PM). Listvenites sampled

close to the basal thrust show the highest concentrations in Ba, U, Sr, As. "U"-shaped patterns (n = 2; Ce_N/Yb_N = 0.58 – 0.84 Sm_N/Yb_N = 0.29 – 0.50; Ce_N/Sm_N = 1.06 – 1.98), with low ΣREE (0.08 – 0.23 ppm), and ii) spoon-shape patterns for sample OM20-17 and 18 (n = 2; Ce_N/Yb_N = 0.11 – 0.43 Sm_N/Yb_N = 0.45 – 0.73; Ce_N/Sm_N = 0.25 – 0.58), with positive Eu anomalies. Their ΣREE range between 0.23 and 0.66 ppm.

Sites 2 and 2b

As for Site 1, serpentinized peridotites (n = 4) have compositions in major element and transition metals composition and SiO_2, MnO, MgO, FeO and K_2O concentrations similar to the MMS, but depleted in P_2O_5. Mg# vary from 89.5 to 90.3, with rather low LOI (9.1 – 13.8 wt%). Variable CaO, Al_2O_3 and TiO_2 contents reflect the mantle compositional heterogeneity (CaO = 0.21 – 1.7 wt%; Al_2O_3 = 0.58 – 1.85 wt%; TiO_2 = 0.04 – 0.06 wt%). Serpentinized peridotites are depleted in most HFSE and LILE relative to PM. They show variable FME contents as for As (0.54 – 89.1 x PM), Li (0.11 – 4.58 x PM), and Cs (0.71 – 9.18 x PM), less marked for Sb (0.35 – 1.04 x PM). Alkalis (Li, Rb, Sr, Cs) and U have the highest concentrations in samples collected closer to the sole than overlying gabbros. Compositions in transition metals is homogeneous between samples (e.g. Co = 102 – 122 ppm; Zn = 44.7 – 55.2 ppm). Partially serpentinized peridotites are characterized by spoon-shaped patterns (Ce_N/Yb_N = 0.02 – 0.15; Sm_N/Yb_N = 0.06 – 0.33; Ce_N/Sm_N = 0.29 – 0.46), with ΣREE varying from 0.23 to 0.54 ppm. Only the fully serpentinized peridotite at the contact with listvenite (OM20-32) display a "U-shaped" pattern (CeN/YbN = 0.10; SmN/YbN = 0.05; CeN/SmN = 1.95), in addition to a low ΣREE (0.04 ppm).

Except for CaO (0.9 – 3.6 wt%), carbonated serpentinites (n = 4) show a compositional range similar to serpentinized peridotites. LOI are higher (16.2 – 25.1 wt%). High Mg# were preserved (88.1 – 91.7). Carbonated serpentinites are characterized by depletion in most LILE and systematic enrichments in Li (1.74 – 15.7 x PM), Cs (1.16 – 5.44 x PM), Sr (1.64 – 12.9 x PM), As (51.2 –113 x PM), and Tl (5.19 – 31.4 x PM). Ba and U concentrations are scattered (Ba = 0.41 – 3.93 x PM; U = 0.01 – 21.3 x PM). Transition metals show narrow compositions overlapping those of serpentinized peridotites (e.g. Co = 94.1 – 118 ppm; Zn = 37.2 – 46.2 ppm). The REE patterns are spoon-shaped (Ce_N/Yb_N = 0.02 – 0.12; Sm_N/Yb_N = 0.01 – 0.06; Ce_N/Sm_N = 0.41 – 1.48). ΣREE are comprised between 0.06 and 0.16 ppm.

The major element chemistry of listvenites is broadly similar to serpentinized peridotites and carbonated serpentinites, except for highly altered listvenites, collected at the base of mantle interlayers. The latter are highly altered, depleted in SiO_2 (2.91 – 15.1 wt%), also showing the highest LOI (41.2 – 42.5 wt%). The high CaO content of sample OM20-38 is associated to abundant dolomite. Listvenites are poor in HSFE, but enriched in most FME (Sr, Sb, Cs, Ba, Tl, Pb, U), especially As (13.6 – 938 x PM). Site 2 samples show the highest compositions in Li and Rb, but are poorer in Mo, Sr, Sb, Ba and

U than Site 2b sample. Transitions metal contents remained overall similar to protoliths (e.g. Co = 92.3 – 115 ppm; Zn = 23.2 – 45.57 ppm). Two types of REE patterns are observed: spoon shapes for samples collected at the contact with carbonated serpentinites (Ce_N/Yb_N = 0.02 – 0.09; Sm_N/Yb_N = 0.01 – 0.13; Ce_N/Sm_N = 0.71 – 1.98), and "U" shapes for samples from Site 2 upper transect (Ce_N/Yb_N = 1.09; Sm_N/Yb_N = 0.37 – 0.52; Ce_N/Sm_N = 2.11 – 2.97). ΣREE range between 0.05 and 0.17 ppm.

Site 3

The serpentinized peridotite OM20-46 shows elevated TiO_2 (0.14 wt%) and Al_2O_3 (2.65 wt%) contents due to abundant bastites (> 50% of estimated rock volume), but also CaO (15.8 wt%). It is slightly depleted in most HFSE and LILE, but enriched in As (1.40 x PM), Sb (1.20 x PM), Ba (1.16 x PM), and Tl (13.1 x PM). The transition metal compositions are rich in V (121 ppm), Cr (3684 ppm), Cu (306 ppm) and poor in Co and Ni due to a low amount of precursor olivine. This sample display highly fractionated LREE compared to relatively flat MREE-HREE (Ce_N/Yb_N = 0.12; Sm_N/Yb_N = 0.73), and a high ΣREE (2.25 ppm).

Poorly-carbonated serpentinites (n = 2) are depleted concentrations in HSFE but enrichments in As (50.2 – 214 x PM), Sb (9.77 – 70.1 x PM), Mo, Ba (2.57 – 3.22 x PM), U (1.12 – 1.88 x PM), Pb (1.05 – 1.88 x PM), and Tl. Compositions in transition metals are comparable to serpentinized peridotites in Fanja (e.g., Co = 77.1 – 96.6 ppm, Zn = 27.9 – 45.4 ppm). Sample OM20-45b picked close to the transition with listvenite is characterized by a "U"-shaped REE pattern (Ce_N/Yb_N = 1.09; Sm_N/Yb_N = 0.28; Ce_N/Sm_N = 3.88) and a low ΣREE (0.09 ppm). Sample OM20-45c sampled closer to the basal thrust shows a relatively flat spoon-shaped pattern (Ce_N/Yb_N = 0.37; Sm_N/Yb_N = 0.35; Ce_N/Sm_N = 1.08), and a high (0.94 ppm).

Listvenites (n = 3) are depleted in HFSE, but enriched in most FME, such as Ba (2.07 – 4.70 x PM), As (20.2 – 217 x PM), Sr (7.41 – 26.3 x PM), Tl, Pb (1.45 – 54.7 x PM). Listvenites sampled at the contact with the basal thrust are enriched in most FME (e.g. U = 10.9 – 21.1 x PM), except Sr, compared to mantle interlayer (e.g. U = 0.42 x PM). Sample OM20-45d display anomalously high REE concentrations (ΣREE = 48.1 ppm) and normalized patterns resembling the ones of lithologies from the metamorphic sole (Godard et al., 2021). Such enrichment is also observed for Sc, V, Co (203 ppm) and Zn (93.8 ppm). Other listvenites display little fractionation between LREE-HREE (Ce_N/Yb_N = 0.53 – 0.64) and depletion in MREE (Ce_N/Sm_N = 1.02 – 1.96; Sm_N/Yb_N = 0.32 – 0.51), and low ΣREE (0.04 – 0.27 ppm). Their transitions metals compositions are close to that of the MMS (Co = 46.8 – 68.8 ppm;

Site 4

Serpentinized peridotite OM20-53 has high contents of TiO_2 (0.05 wt%), Al_2O_3 (2.07 wt%) and Na_2O, but low ones for CaO (0.09 wt%) and P_2O_5. Concentrations in other major elements and a high

Mg# (91.0) are alike those of the MMS and basal lherzolites. HFSE and LILE are depleted relative to PM, but enriched in alkali elements (Li = 4.37 x PM, As = 94.7 x PM; Cs = 3.18 x PM) and few FME (Mo = 6.83 x PM; Sb = 2.09 x PM, Tl: 3.37 x PM). The compositional range of transition metals is comparable to Oman peridotites (Co: 87.4 ppm; Zn: 40.8 ppm). Trace element compositions define a spoon-shape pattern (Ce_N/Yb_N = 0.01; Sm_N/Yb_N = 0.10; Ce_N/Sm_N = 0.07). The ΣREE is 0.46 ppm.

Listvenite OM20-49, sampled atop the metamorphic sole, display high concentrations of TiO_2 (0.04 wt%) and CaO (33.28 wt%), indicative of abundant Ca-carbonate (Fig. 6.4), but low for Al_2O_3 (0.13 wt%), MgO (20.1 wt%); FeO (5.13 wt %), MnO, Na_2O, and P_2O_5. The Mg # is also low 88.9. The trace element compositions are low for HFSE, but enriched in most FME (Li, Mo, Sr, Cs, Ba, Tl, U), especially for As (1770 x PM), Sb (515 x PM) and Pb (193 x PM). Depletion in transition metals is significant (Co = 24.6 ppm; Zn = 19.4 ppm). The REE distribution shows a fractionation of HREE (Ce_N/Yb_N = 2.03; Sm_N/Yb_N = 1.81) compared to rich LREE and MREE (Ce_N = 0.60 x CI; Sm_N = 0.54 x CI). The ΣREE is also elevated (1.43 ppm).

Fuchsite-bearing listvenite OM20-52b shows high concentrations in Al_2O_3 (2.12 wt%), CaO (30.5 wt %), K_2O (0.55 wt%), but low in TiO_2 (0.01 wt%), MgO (17.5 wt%), MnO, Na_2O and P_2O_5. The Mg# lies at 75.9. HFSE are depleted, but enriched in FME (), in particular for As (18937 x PM), Rb (27.5 x PM), Sb (4873 x PM), and Cs (87.7 x PM). The transition metals contents are low (e.g. Cr = 1481 ppm; Ni = 1120 ppm), except for richer in Zn (64.8 ppm). The trace element compositions for a spoon-shape pattern (Ce_N/Yb_N = 0.09; Sm_N/Yb_N = 0.34; Ce_N/Sm_N = 0.31), marked by a negative Eu anomaly. The ΣREE is 0.95 ppm.

Birbirite OM20-52a is characterized by enrichments in HFSE and LILE (except Sr, Zr and Hf), well-marked for As (5417 x PM); Rb (14.2 x PM), and Th (14.1 x PM). Transition metals contents are extremely low (Co: 2.15 ppm; Zn = 3.95 ppm). The birbirite display a relatively flat REE pattern similar to sole lithologies, as well as a high ΣREE (40.0 ppm).

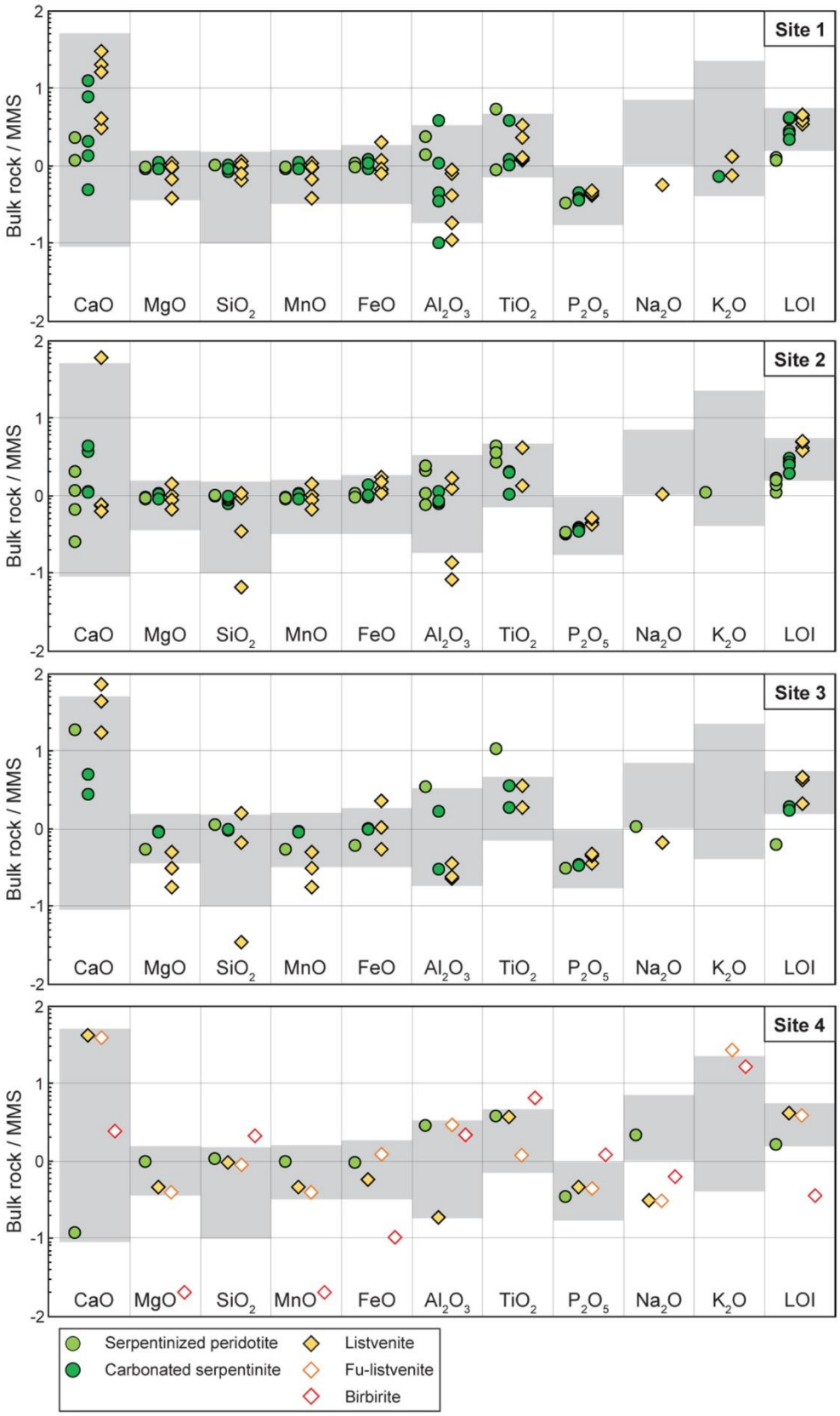

Fig. 6.3 Caltech diagrams of bulk rock compositions for metasomatized peridotites from the Fanja region. Separated panels are plotted for each investigated site. Compositions were normalized to median values of the main mantle section (Godard et al., 2000; Gerbert-Gaillard, 2002; Hanghoj et al., 2010). The dark grey field corresponds to the bulk compositional range of BT1B core samples (Godard et al., 2021).

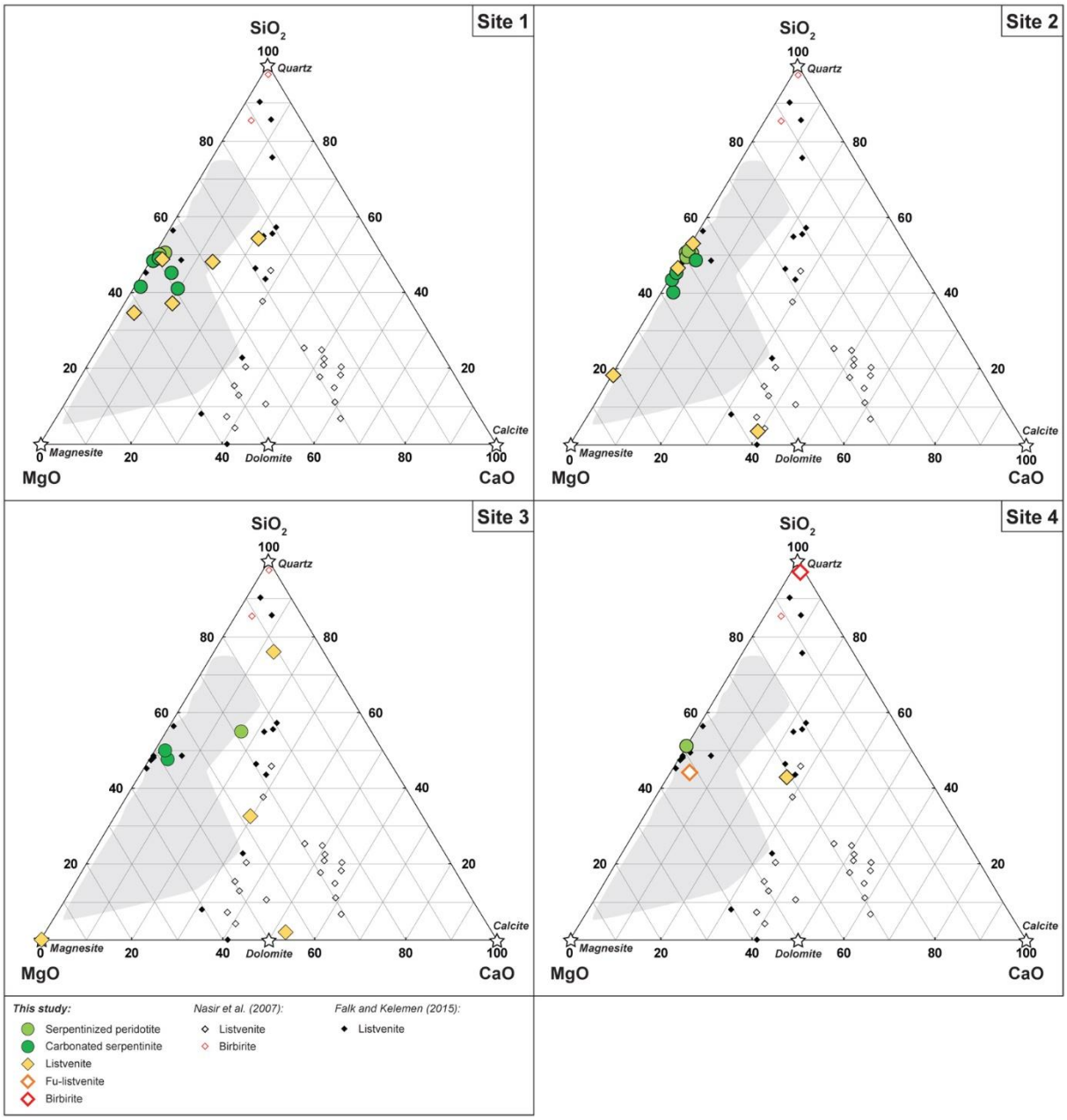

Fig. 6.4. SiO_2-MgO-CaO ternary diagrams of bulk rock compositions metasomatized peridotites from the Fanja region. SiO_2, MgO and CaO end-members are quartz, magnesite and calcite The proportions of each end-member were calculated as the fraction between oxides. The dark grey field corresponds to the bulk compositional range of BT1B core samples (Godard et al., 2021).

>> **Fig. 6.5** Trace element and rare earth elements (REE) spider diagrams for metasomatized peridotites from the Fanja region. Separated panels are plotted for the different investigated sites. Trace elements compositions were normalized to the Primitive Mantle and REE to CI-chondrite using values from McDonough and Sun (1995). The light grey field corresponds to compositions from the main mantle section of the Semail Ophiolite (Godard et al., 2000; Gerbert-Gaillard, 2002; Hanghoj et al., 2010). The dark grey field corresponds to compositions from basal lherzolite (Lippard, 1986; Takazawa et al., 2003; Khedr et al., 2014). Listvenite OM20-39 (Site 3) and birbirite OM20-52a (Site 4) are not represented on REE-normalized panels due highly enriched compositions.

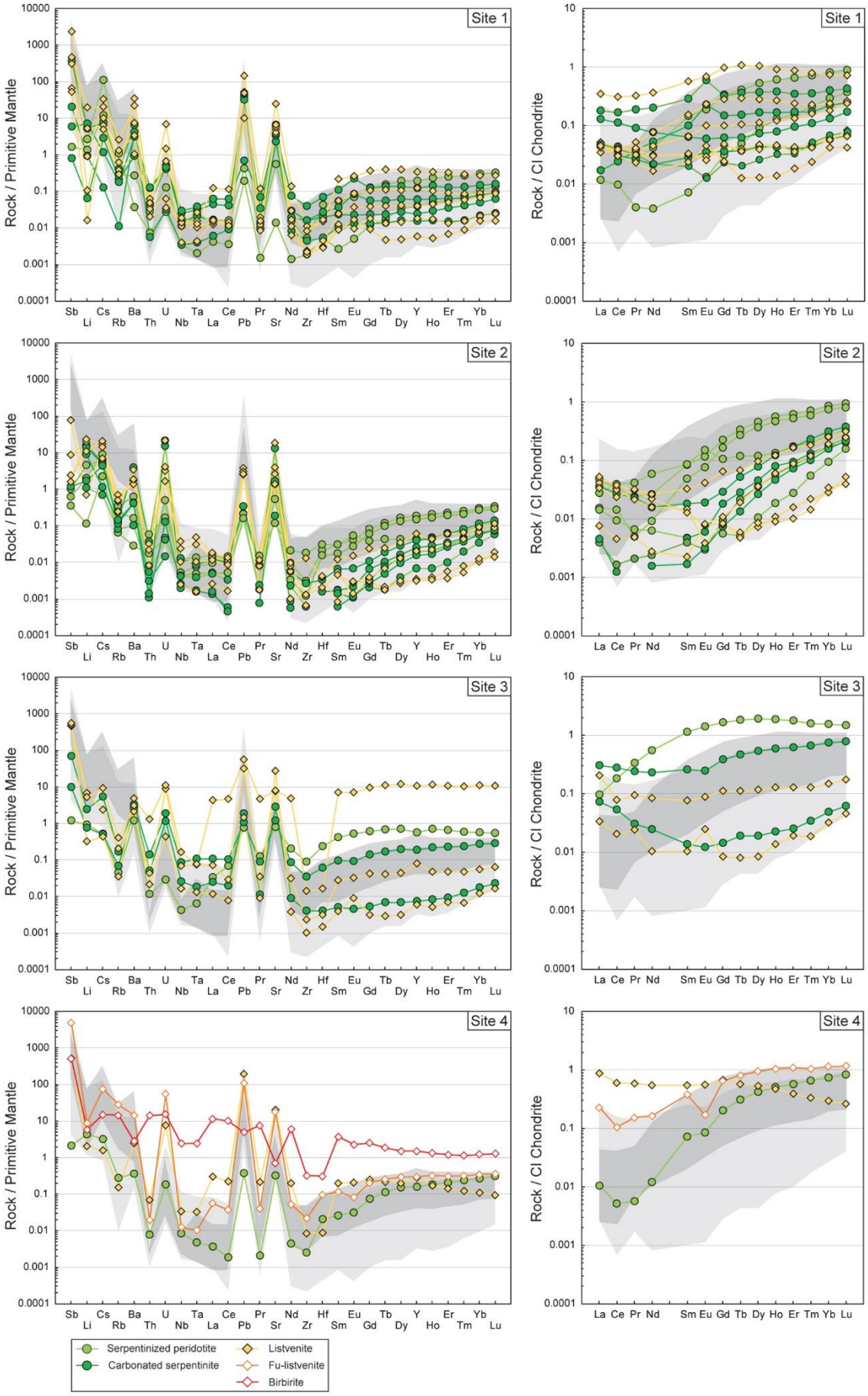
Site 1
Site 2
Site 3
Site 4
Rock / Primitive Mantle
Rock / CI Chondrite
Sb Cs Ba U Ta Ce Pr Nd Hf Eu Tb Y Er Yb
Li Rb Th Nb La Pb Sr Zr Sm Gd Dy Ho Tm Lu
La Ce Pr Nd Sm Eu Gd Tb Dy Ho Er Tm Yb Lu
Serpentinized peridotite
Carbonated serpentinite
Listvenite
Fu-listvenite
Birbirite

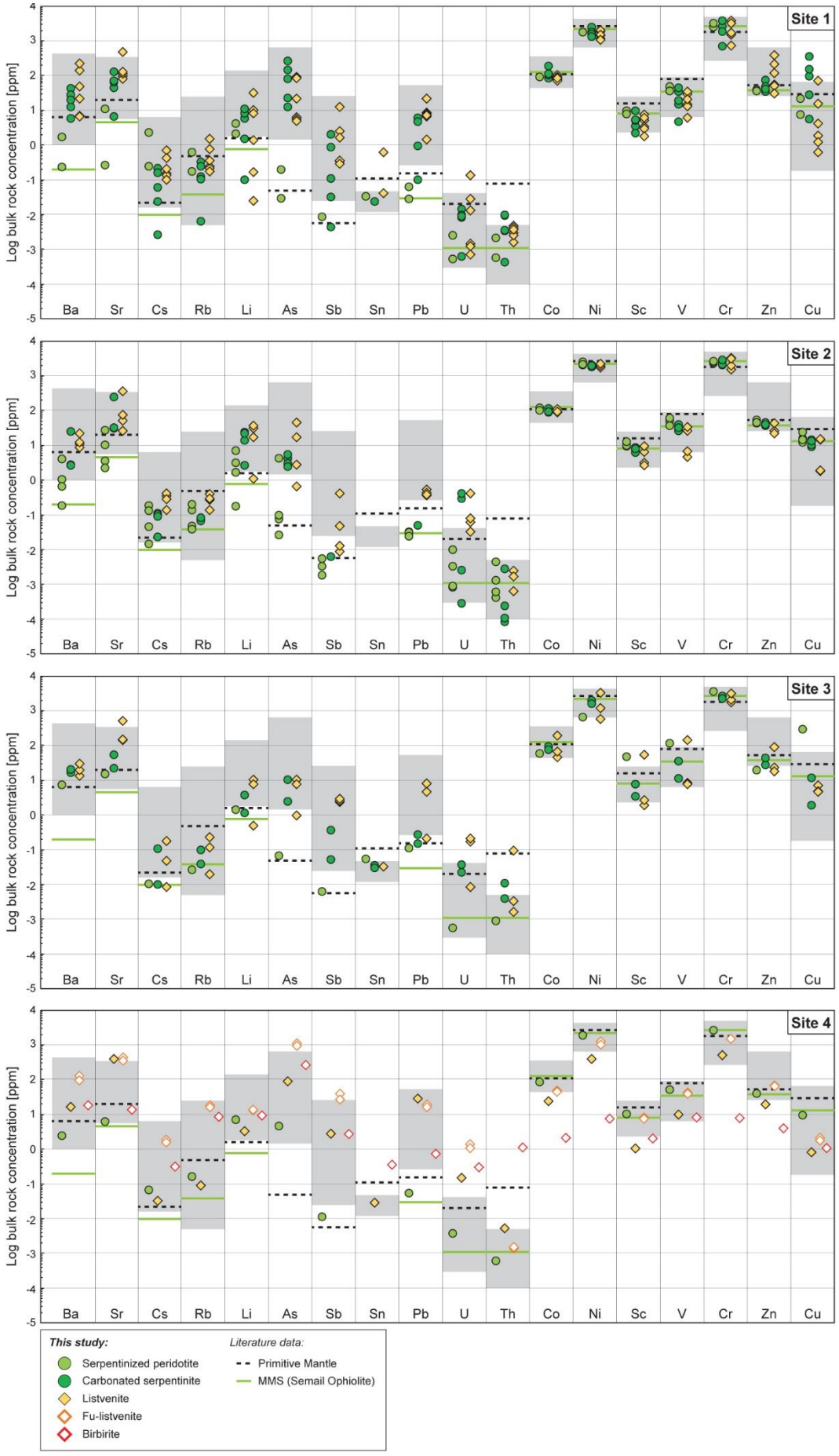
Site 1
Site 2
Site 3
Site 4
Log bulk rock concentration [ppm]
Ba Sr Cs Rb Li As Sb Sn Pb U Th Co Ni Sc V Cr Zn Cu
This study:
Serpentinized peridotite
Carbonated serpentinite
Listvenite
Fu-listvenite
Birbirite
Literature data:
Primitive Mantle
MMS (Semail Ophiolite)

<< **Fig 6.6** Caltech diagrams of the elemental abundances of selected FME and transition metals for metasomatized peridotites from the Fanja region. Separated panels are plotted for the different investigated sites. The dark grey field corresponds to the range compositions of BT1B core samples (Godard et al., 2021). Green lines represent the median values of the main mantle section of the Semail ophiolite (Godard et al., 2000; Gerbert-Gaillard, 2002; Hanghoj et al., 2010). Dashed black lines indicate the PM concentrations from McDonough and Sun (1995).

6.2.2 Trace element chemistry of silicates and carbonates

The trace element compositions of silicates (serpentine, fuchsite) and carbonates (magnesite, dolomite) are plotted on extended spider diagrams (Figs. 6.7, 6.8, 6.9) normalized to the Primitive Mantle (PM) and to CI Chondrite for REE (normalizing values from McDonough and Sun, 1995). Concentrations of fluid-mobile elements (FME) are plotted on Caltech diagrams in Fig. 6.10. Due to compositional variability between samples, concentrations mentioned in the text correspond to the Q16–Q84 range (16th and 84th percentiles). The trace element data are provided in Appendix for section 4.3.

Silicates

Mesh serpentines display extended trace element patterns comparable to the compositional range of the main mantle section from the Semail Ophiolite (Fig. 6.7a). Mesh serpentine is depleted in HFSE and LILE compared to PM, except for enriched fluid mobile Li, As, Sb, Cs and Pb (Li = 5.3 – 10.4 x PM; As = 3.2 – 12.9 x PM; Sb = 5.8 – 16.2 x PM; Cs = 3.4 – 6.4 x PM; Pb = 2.3 – 9.1 x PM). Chondrite-normalized REE patterns (Fig. 6.7b) show fractionation between LREE-MREE and HREE (Ce_N/Yb_N = 0.002 – 0.68; Sm_N/Yb_N = 0.06 – 0.28) with marked negative Ce anomalies.

Bastites are poor in HFSE and LILE (Fig. 6.7c), but variably enriched in Li, As, Sb, Cs and Pb (Li = 7.9 – 14.0 x PM; As = 9.8 – 12.2 x PM; Sb = 19.2 – 19.8 x PM; Cs = 5.2 – 17.1 x PM; Pb = 4.5 – 13.1 x PM). REE patterns seem to indicate strong fractionation between LREE-MREE and HREE (Fig. 6.7d), but data are scarce due to extremely low contents in LREE.

As for the matrix, vein serpentines are depleted in HFSE and LILE (Fig. 6.7e), and enriched in Li, As, Sb, Cs, and Pb (Li = 5.0 – 36.7 x PM; As = 2.0 – 2.9 x PM; Sb = 2.6 – 5.8 x PM; Cs = 5.0 – 13.2 x PM; Pb = 0.9 – 2.5 x PM). REE patterns display highly variable concentrations in LREE. Strong fractionation occurs between MREE and HREE (Fig. 6.7f; Sm_N/Yb_N = 0.04 – 0.36), and either depletion or enrichment between LREE and HREE (Ce_N/Yb_N = 0.03 – 2.6).

Two samples were analysed and provided very different mineral compositions. In sample 53Z-2-32-37, fuchsite is poor in most HFSE (Fig. 6.7g) but enriched in FME (As = 5.0 – 5.3 x PM; Sb = 1016 – 1418 x PM), and especially LILE (Li = 1699 – 2217 x PM; Rb = 331 – 333 x PM; Cs = 1600 – 1902 x PM; Ba = 6.9 – 7.7 x PM; Pb = 15.0 – 16.1 x PM). The REE patterns are relatively flat (Fig. 6.7h), with

slight fractionation between LREE and MREE-HREE (Ce_N/Yb_N = 0.39 – 0.70; Ce_N/Sm_N = 0.49 – 0.65; Sm_N/Yb_N = 0.65 – 1.11), thus forming "spoon" shapes. Fuchsite from sample 60Z-1-32-37 has concentrations enriched relative to PM in Hf (1.1 – 3.3 x PM) and most FME (Li, As, Rb, Sr, Sb, Cs, Ba, Pb, U) and variably in Th (0.09 – 5.3 x PM). In comparison with sample 53Z-2-32-37, compositions are close for As, Sr, Sb and Ba (As = 3.4 – 8.4 x PM; Sr = 1.0 – 1.3 x PM; Sb = 965 – 1680 x PM; Ba = 5.2 – 11.8 x PM), but richer in Rb, Cs, Pb and poorer in Li (Li = 5.5 – 11.6 x PM; Rb = 289 – 693 x PM; Cs = 1835 – 4204 x PPM; Pb = 14.4 – 26.7 x PM). REE patterns shows fractionation of flat MREE-HREE comapared to LREE (Ce_N/Yb_N = 1.37 – 3.73; Ce_N/Sm_N = 2.22 – 2.58).

Matrix carbonates

Fe-core spheroids are characterized by compositions depleted in HFSE relative to PM, but enriched in fluid mobile Li, As, Sr, Sb, Cs, Ba and Pb (Li = 7.1 – 9.5 x PM; As = 5.3 – 17.7 x PM; Sr = 4.4 – 6.9 x PM; Sb = 58.1 – 152 x PM; Cs = 6.8 – 10.2 x PM; Ba = 1.6 – 4.6 x PM; Pb = 4.3 – 9.6 x PM). Concentration in Rb is contrasted (Rb = 0.5 – 1.4 x PM). The Chondrite-normalized REE patterns have a spoon shape with strong fractionation between LREE and MREE-HREE (Ce_N/Yb_N = 0.004 – 0.1; Ce_N/Sm_N = 0.08 – 0.09), and between MREE and HREE (Sm_N/Yb_N = 0.05 – 0.09), with negative Ce anomalies (Ce/Ce* = 0.01 – 0.05).

Mg-core spheroids show a systematic enrichment in Li, As, Sb, Cs and Pb (Li = 1.8 – 9.3 x PM; As = 1.9 – 16.7 x PM; Sb = 27.8 – 227 x PM; Cs = 4.2 – 26.0 x PM; Pb = 3.5 – 17.2 x PM), but contrasted for Sr and Ba (Sr = 0.4 – 2.9 x PM; Ba = 0.2 – 1.3 x PM). Mg-core spheroids are charcterized by depletion between LREE and MREE-HREE (Ce_N/Yb_N = 0.001 – 0.05; Ce_N/Sm_N = 0.02 – 0.25), and variable fractionation of MREE to LREE (Sm_N/Yb_N = 0.02 – 0.46).

>> **Fig. 6.7** Trace elements and rare earth elements (REE) spider diagrams of silicates measured in core samples by HR-LA-ICPMS. Separated panels are plotted for the different minerals and microstructures (a-b: mesh serpentine; c-d: bastite; e-f: vein serpentine; g-h: fuchsite). Trace elements compositions were normalized to the Primitive Mantle and REE to CI Chondrite (normalizing values from McDonough and Sun, 1995). The light grey field corresponds to compositions from the main mantle section of the Semail Ophiolite (Godard et al., 2000; Gerbert-Gaillard, 2002; Hanghoj et al., 2010). The dark grey field corresponds to compositions from basal lherzolites (Lippard, 1986; Takazawa et al., 2003; Khedr et al., 2014).

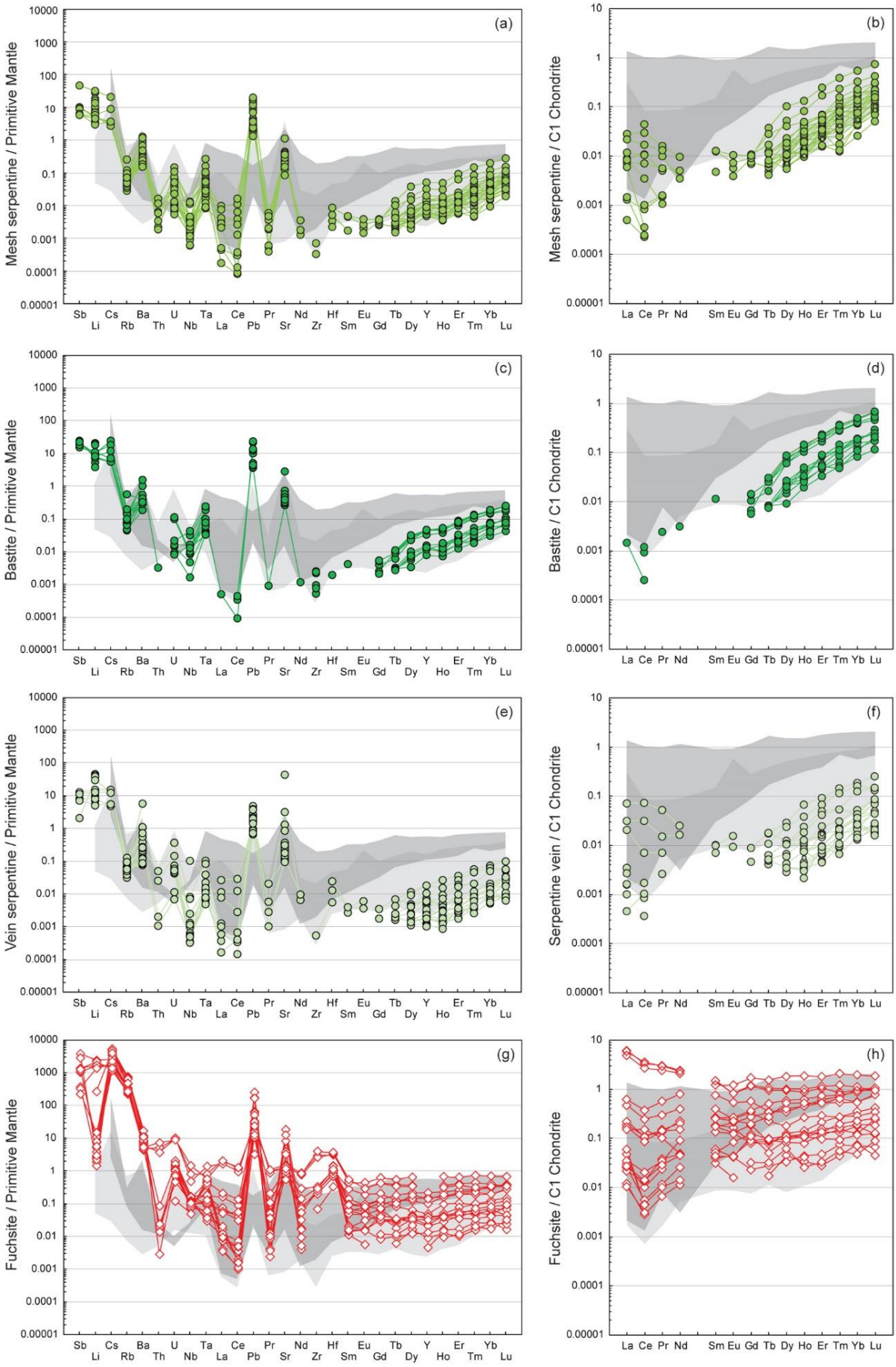
(a)
Mesh serpentine / Primitive Mantle
(b)
Mesh serpentine / C1 Chondrite
(c)
Bastite / Primitive Mantle
(d)
Bastite / C1 Chondrite
(e)
Vein serpentine / Primitive Mantle
(f)
Serpentine vein / C1 Chondrite
(g)
Fuchsite / Primitive Mantle
(h)
Fuchsite / C1 Chondrite
Sb Li Cs Rb Ba Th U Nb Ta La Ce Pb Pr Sr Nd Zr Hf Sm Eu Gd Tb Dy Y Ho Er Tm Yb Lu
La Ce Pr Nd Sm Eu Gd Tb Dy Ho Er Tm Yb Lu

Magnesite aggregates are depleted in HFSE relative to PM, but enriched for Sb, Cs, and Pb (Sb = 7.9 – 68.4 x PM; Cs: 2.0 – 3.6 x PM; Pb = 4.7 – 24.5 x PM). Li contents are variable (0.9 – 3.5 x PM). The REE patterns show depletion between LREE and MREE-HREE (Ce_N/Yb_N = 0.002 – 0.37; Ce_N/Sm_N = 0.02 – 0.58), and variable fractionation between MREE to LREE (Sm_N/Yb_N = 0.09 – 0.64).

Dolomite aggregates are depleted in HFSE and LILE (e.g., Rb = 0.04 – 0.09 x PM; Th = 0.002 – 0.03 x PM; U = 0.02 – 0.2 x PM). As, Sr, Sb, Cs, and Pb are enriched relative to PM (As = 1.9 – 2.9 x PM; Sr = 13.3 – 26.0 x PM; Sb = 369 – 618 x PM; Cs: 2.3 – 4.3 x PM; Pb = 11.3 – 153 x PM). In contrast to magnesite aggregates, the Li content is low (0.1 – 0.6 x PM) but higher for Ba (0.5 – 1.1 x PM). The concentrations in LREE and MREE are generally higher than for matrix magnesite. Interestingly, the REE patterns show fractionation between LREE and MREE-HREE (Ce_N/Sm_N = 0.08 – 0.79; Ce_N/Yb_N = 0.01 – 0.37) except for sample 76Z-2-12-20 (close to the basal thrust), which is characterized by the opposite trend (Ce_N/Sm_N = 0.95 – 1.55; Ce_N/Yb_N = 1.22 – 2.17). In addition, marked negative Eu anomalies are observed for sample 30Z-2-33-39 (Eu/Eu^* = 0.05 – 0.27).

Vein carbonates

Pseudomorphic magnesite veins after serpentine are characterized by low concentrations in HFSE (e.g., Rb = 0.005 – 0.44 x PM). Enrichments are observed for Sb and Pb (Sb = 2.5 – 20.9 x PM; Pb = 2.2 – 26.5 x PM). In turn, several mobile elements, namely As, Li, Sr, and Ba show highly variable contents (As = 0.3 – 3.3 x PM; Cs: 0.1 – 5.2 x PM; Li = 0.2 – 4.5 x PM; Sr = 0.4 – 1.7 x PM; Ba = 0.1 – 1.1 x PM). In a similar way, the REE distribution is highly variable (Ce_N/Yb_N = 0.001 – 4.9; Ce_N/Sm_N = 0.02 – 3.5; Sm_N/Yb_N = 0.04 – 1.6).

Early antitaxial magnesite veins display low concentrations in HFSE (e.g., Rb = 0.01 – 0.2 x PM). Enrichments relative to PM concern Sb and Pb (Sb = 1.8 – 23.2 x PM; Pb = 2.2 – 26.5 x PM). In turn, several mobile elements, namely As, Cs, Li, Rb, Sr, Ba show highly variable contents (As = 0.5 – 2.5 x PM; Cs: 0.2 – 6.6 x PM; Li = 0.5 – 1.4 x PM; Sr = 0.1 – 1.7 x PM; Ba = 0.1 – 1.4 x PM). As for pseudomorphic magnesite veins, the REE distribution is highly variable (Ce_N/Yb_N = 0.002 – 0.7; Ce_N/Sm_N = 0.02 – 1.6; Sm_N/Yb_N = 0.03 – 0.84).

Late dolomite veins are characterized a depletion is observed for HFSE, few LILE (e.g., Rb = 0.01 – 0.03 x PM; Ba = 0.1 – 0.5 x PM) and Li (0.1 – 0.3 x PM) compared to PM (Figs. 6.8g, 6.9). In turn, compositions are enriched in Sr, Sb, Cs, and Pb (Sr = 12.4 – 28.9 x PM; Sb = 0.6 – 101 x PM; Pb = 47.8 – 410 x PM), and contrasted for Cs (0.2 – 1.1 x PM). The normalized patterns illustrate heterogenous REE distribution, generally showing fractionation between LREE and MREE-HREE, but more scattered for sample 76Z-2-12-20 (Ce_N/Yb_N = 0.1 – 6.5; Ce_N/Sm_N = 0.04 – 4.7; Sm_N/Yb_N = 0.05 – 2.6).

6.2.3 Discussion

Contribution from protolith and reactive fluids during mass transfers

Peridotites neighbouring listvenites series in Fanja cover a large geochemical range reflecting mantle heterogeneity trending between (Cpx-)harzburgite to lherzolite protolith compositions. Frequent enrichment in Li, Rb, Sr, Cs, Ba and Pb suggests inherited geochemical signatures typical of basal peridotites, resulting from interaction with fluids enriched in those elements during oceanic detachment or ophiolite emplacement (Khedr et al., 2014). The major element geochemistry of metasomatized peridotites in Fanja reveals nearly isochemical conversion from peridotite to listvenite for SiO_2, MnO, MgO, FeO, Na_2O and P_2O_5. Rare depletion in SiO_2, MnO, MgO is restricted to samples collected close to the basal thrust and may have been caused by weathering or alteration with fluids during the reactivatuion of the basal thrust (Mattern and Scharf, 2018). Carbonation of serpentinized peridotite is accompanied by a systematic enrichment in fluid-mobile elements such as As, Sr, Sb, Ba, and Pb. It is interesting to notice that no major variation is observed accounting for trace elements compositions, but instead appears considering the major elements. In particular, substantial enrichment in Ca are observed for listvenites located westwards to BT1B and Site 2, possibly hinting: i) for regional variations of reactive CO_2-bearing fluids, or peridotite carbonation proceeding at a different tectonic stages.

>> **Fig. 6.8** Trace elements and rare earth elements (REE) spider diagrams of matrix and vein carbonates from measured in core samples by HR-LA-ICPMS. Separated panels are plotted for the different minerals and microstructures (a-b: matrix magnesite; c-d: matrix dolomite; e-f: pseudomorphic and early magnesite and dolomite veins; g-h: late magnesite and dolomite veins). Trace elements compositions were normalized to the Primitive Mantle and REE to CI Chondrite (normalizing values from McDonough and Sun, 1995). The light grey field corresponds to matrix serpentine (mesh and bastite) compositions. The dark grey field corresponds to vein serpentine compositions.

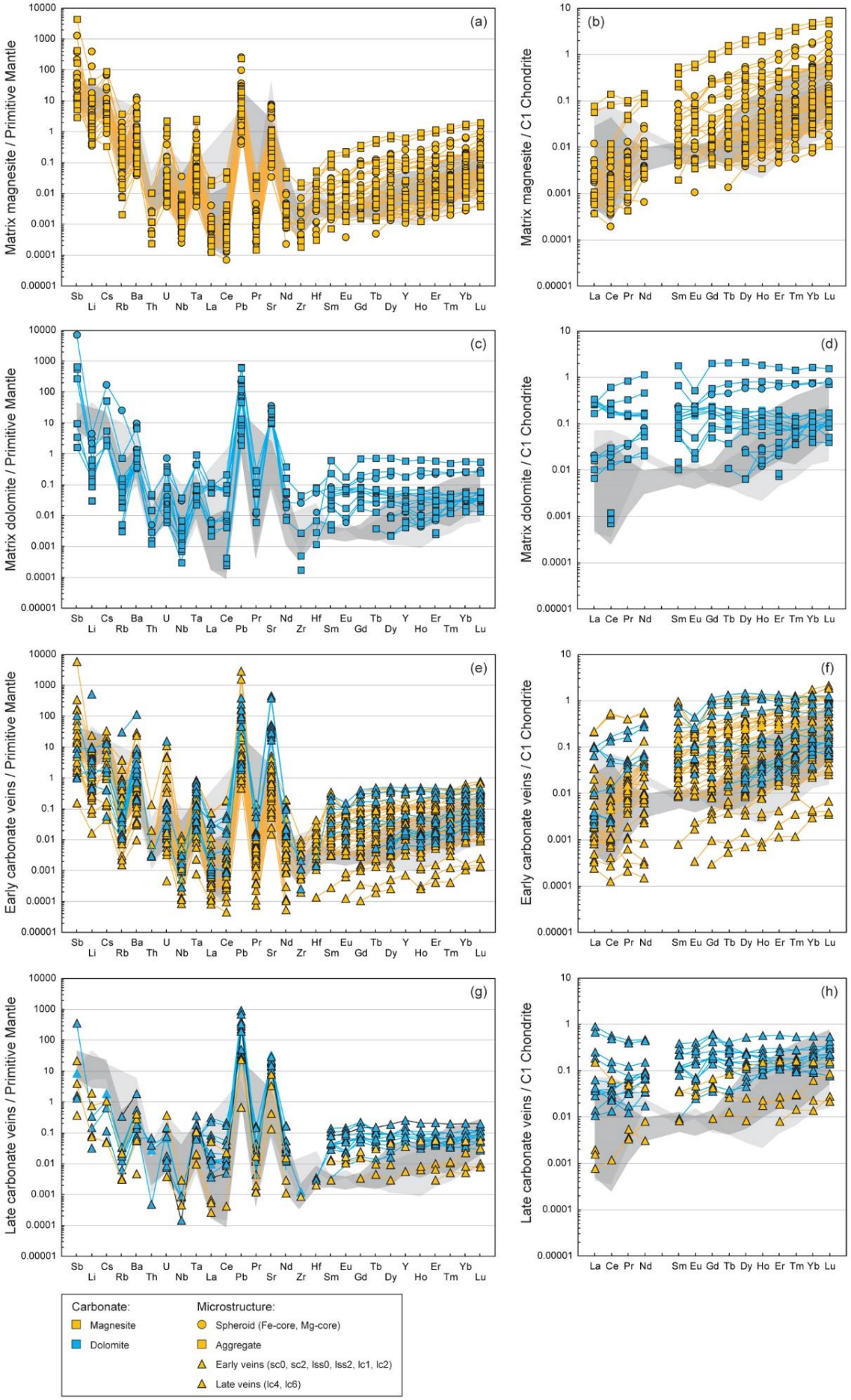
(a)
(b)
(c)
(d)
(e)
(f)
(g)
(h)
Matrix magnesite / Primitive Mantle
Matrix magnesite / C1 Chondrite
Matrix dolomite / Primitive Mantle
Matrix dolomite / C1 Chondrite
Early carbonate veins / Primitive Mantle
Early carbonate veins / C1 Chondrite
Late carbonate veins / Primitive Mantle
Late carbonate veins / C1 Chondrite
Sb Cs Ba U Ta Ce Pr Nd Hf Eu Tb Y Er Yb
Li Rb Th Nb La Pb Sr Zr Sm Gd Dy Ho Tm Lu
La Ce Pr Nd Sm Eu Gd Tb Dy Ho Er Tm Yb Lu
Carbonate:
Magnesite
Dolomite
Microstructure:
Spheroid (Fe-core, Mg-core)
Aggregate
Early veins (sc0, sc2, Iss0, Iss2, Ic1, Ic2)
Late veins (Ic4, Ic6)

Elemental redistribution between minerals

Carbonation of serpentinized peridotite in Hole BT1B proceeded in a highly reactive system where elemental distribution was primarily controlled by transport processes and reaction kinetics. Carbonate precipitation hinges on: i) the composition of reactive fluids (cationic and ligands concentrations, alkalinity, pH); ii) the composition of dissolving minerals in the host rock; iii) host rock permeability and porosity, driving fluid flow rates and access to reactive mineral surfaces; and iv) pressure and temperature determining partition coefficients between fluid and mineral. Comparing the trace element compositions of alteration minerals hence provide key insights into chemical mobility during dissolution-precipitation reaction, changes in fluid compositions and kinetics factors.

The solubility of trace elements in fluids is controlled by sorption and complexation processes (e.g., Allen and Seyfried, 2005; Migdisov et al., 2016). Preferential incorporation of an element between the mineral and fluid phases thus depend on partition coefficients. In the case of hydrothermal magnesite and dolomite, no experimental dataset is available. Hence literature data exploring fluid-carbonate elemental behaviour mainly relies of theoretical work (Wood, 1990; Rimstidt et al., 1999; Wang and Xu, 2001; Luo and Byrne, 2004) or focussing on the distribution of REE in fluorocarbonates or transport by carbonate complexes in fluids (e.g., Migdisov 2016; Louvel, 2022). To our knowledge, only one study by Wang and Xu (2001) investigated partition coefficients of few metals for magnesite, while none treated about dolomite. As abundances of fluid mobile elements in depleted mantle rocks is low (Salters and Stracke, 2004). Substantial enrichment in alteration minerals from carbonated serpentinite and listvenite are interpreted as the outcome of elemental transport by fluids. In the following, elements are distinguished by groups showing similar behaviour during the reactional sequence, or presenting contrasted chemical affinities for magnesite and dolomite.

i) High field strength elements (Zr, Hf, Nb, Ta, REE+Y, U)

Compositions of serpentines in high field strength elements (HFSE) overlap those of bulk signatures of peridotites from the main mantle section (MMS), indicating very limited elemental mobility during serpentinization. Compositions in these elements do not vary much from matrix serpentines to magnesites, also suggesting low mobility of these elements during carbonation. However, it is stricking to notice a high compositional variability for REE. Under equilibrium conditions, the REE contents of hydrothermal minerals depend upon (i) the REE compositions of the reactive fluids and host rock, (ii) pressure and temperature (Bau, 1990), (iii) the presence of REE aqueous complexes in fluids (e.g. Louvel et al., 2022).

Plotting the carbonate compositions by geochemical protolith domains (Fig. 6.9) reveals a REE distribution mimicking bulk rock compositions indicating a strong control of the protolith. Control of sorption processes on REE distribution related to changes in pressure and temperature is likely minor as

carbonation temperatures are constrained to the 100-200°C range (Kelemen et al., 2022). However, preferential tranport of LREE (T>400 °C) and HREE (T<200°C) by hydroxyl-carbonate complexes in alkaline fluids (Louvel et al., 2022) may explain local elemental variability. Carbonate compositions generally display negative Ce anomalies (Ce/Ce* ratios) potentially related to the slightly oxydising nature of fluids (Möller and Bau, 1993), also consistent with positive U anomalies compared to neighbouring Th ($(U/Th)_{CN}$ ratio). Gd positive anomalies that could indicate to the presence carboxylic ligands in fluids (Lee and Byrne, 1992) are not observed in our samples.

ii) Alkali metals (Li, Cs) and metalloids (B, As, Sb)

Serpentines are rich in metalloids and alkali metals (e.g., matrix serpentines: Li = ~19 x MMS; Cs = ~32 x MMS). Experimental work highlighted that metalloids are preferentially incorporated in serpentinization products during the hydration of olivine (Lafay et al., 2016). Alkali-rich compositions are common for Banded Unit peridotites, and have been imputed to interaction between the basal ophiolite mantle and alkali-rich fluids sourced from the dehydration of the HT metamorphic sole (e.g., Ishikawa et al., 2005; Khedr et al., 2014). Boron concentrations of serpentines in Hole BT1B overlap those reported for (partially) serpentinized basal peridotites in Oman (Prigent et al., 2018), but are slightly enriched in Li. While serpentinization of peridotites in Hole BT1B likely initiated during this early metasomatic event, reaction likely went to completion by interaction with Li-Cs rich fluids prior or concomitantly to the ingress of CO_2-rich fluids. Serpentine veins are slightly enriched in Li and Cs compared to matrix serpentines (Li = ~1.5 x mat. srp.; Cs = ~2.2 x mat. srp.), suggesting transport of these elements by serpentinizing fluids. High abundance of Li and B in fuchsite (Li = ~1.2 x mat. serp.; B = ~ 3.1 x mat. srp.) may result from: i) growth in presence of (dehydration?) fluids rich in these elements, ii) limited transport by fluids, iii) or reflect high partition coeffcients. Poorer Li, B, and As concentrations in carbonates grown after serpentines suggest: i) remobilization by fluids during rock dehydration, possibly explaining elemental variability at the borehole scale, ii) lower partition coefficients for carbonates. Li, B and As concentrations are enriched in matrix carbonates compared to veins suggesting limited transport by reactive CO_2-rich fluids. Spheroids are enriched compared to massive aggregates which could be interpreted as low transport during early carbonation or progressive depletion in fluids.

iii) Alkali Earth metals (Sr, Ba), Rb vs. Pb

Rb and alkali Earth metals (Ba, Sr) show similar compositional evolution being: i) systematically enriched in matrix magnesites compared to matrix serpentines (e.g., Rb = ~ 2.5 x mat. srp.; Sr = ~ 1.6 x mat. srp.; Ba = ~ 2.7 x mat. srp.), and ii) enriched in Fe-core spheroids compared to Mg-rich matrix magnesites, with Mg-core spheroids and magnesite aggregates displaying comparable compositions. On the other hand, Pb abundances are the highest in Mg-rich aggragtes over Mg-core spheroids and poorer

Fe-core spheroids. Dolomite aggregates show higher contents in Sr, Ba, and Pb than matrix magnesites, associated to low Li, Cs and As concentrations suggest a major change fluid compositions.

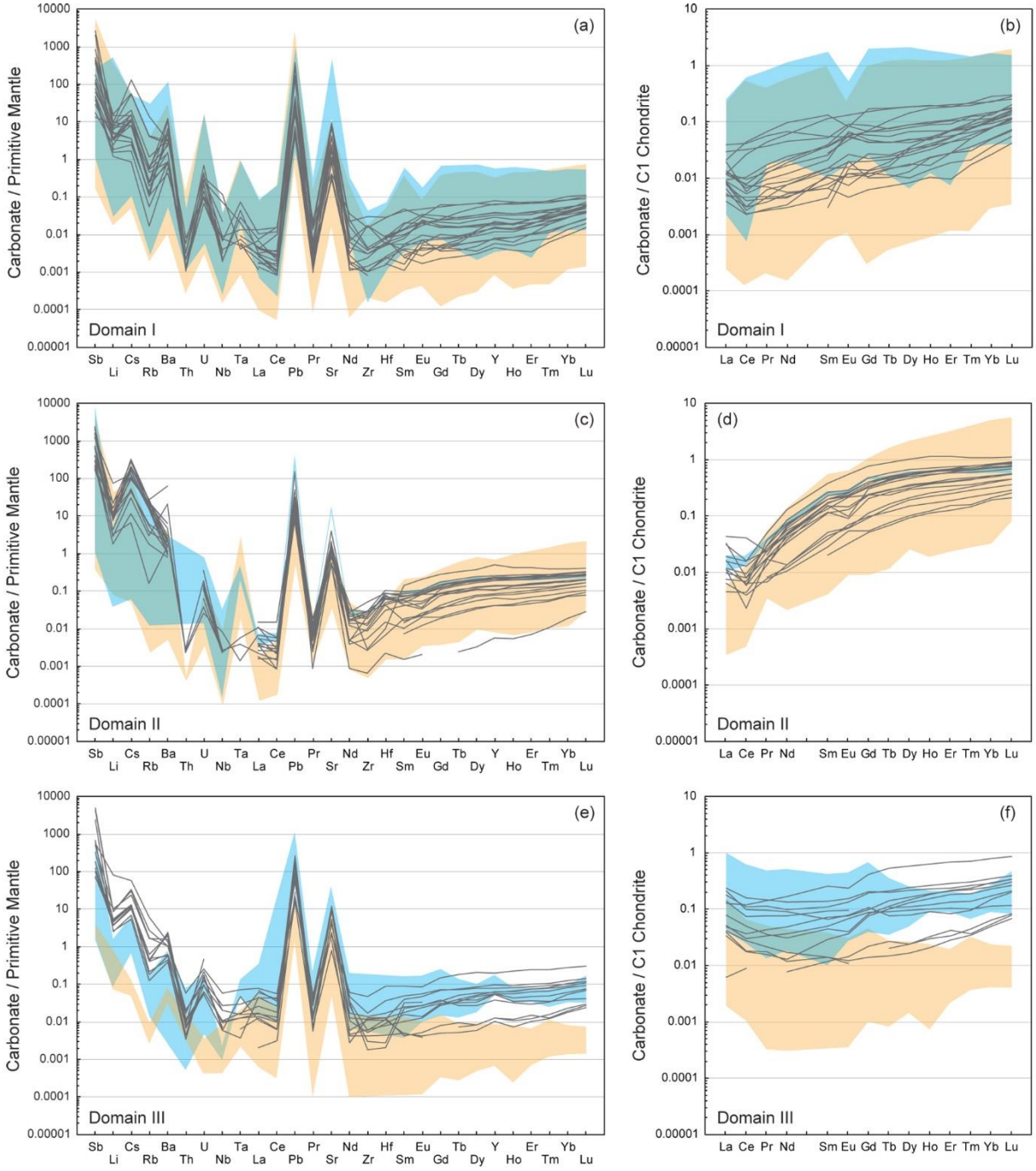

Fig. 6.9 Trace elements and rare earth elements (REE) spider diagrams of carbonates from borehole samples measured by HR-LA-ICPMS. Separated panels are plotted for the geochemical domains The blue field correspond to the compositional range of dolomites and the orange field to that of magnesites. The dark spectra correspond to bulk rock compositions from Godard et al. (2021). Trace elements compositions were normalized to the Primitive Mantle and REE to CI Chondrite (normalizing values from McDonough and Sun, 1995).

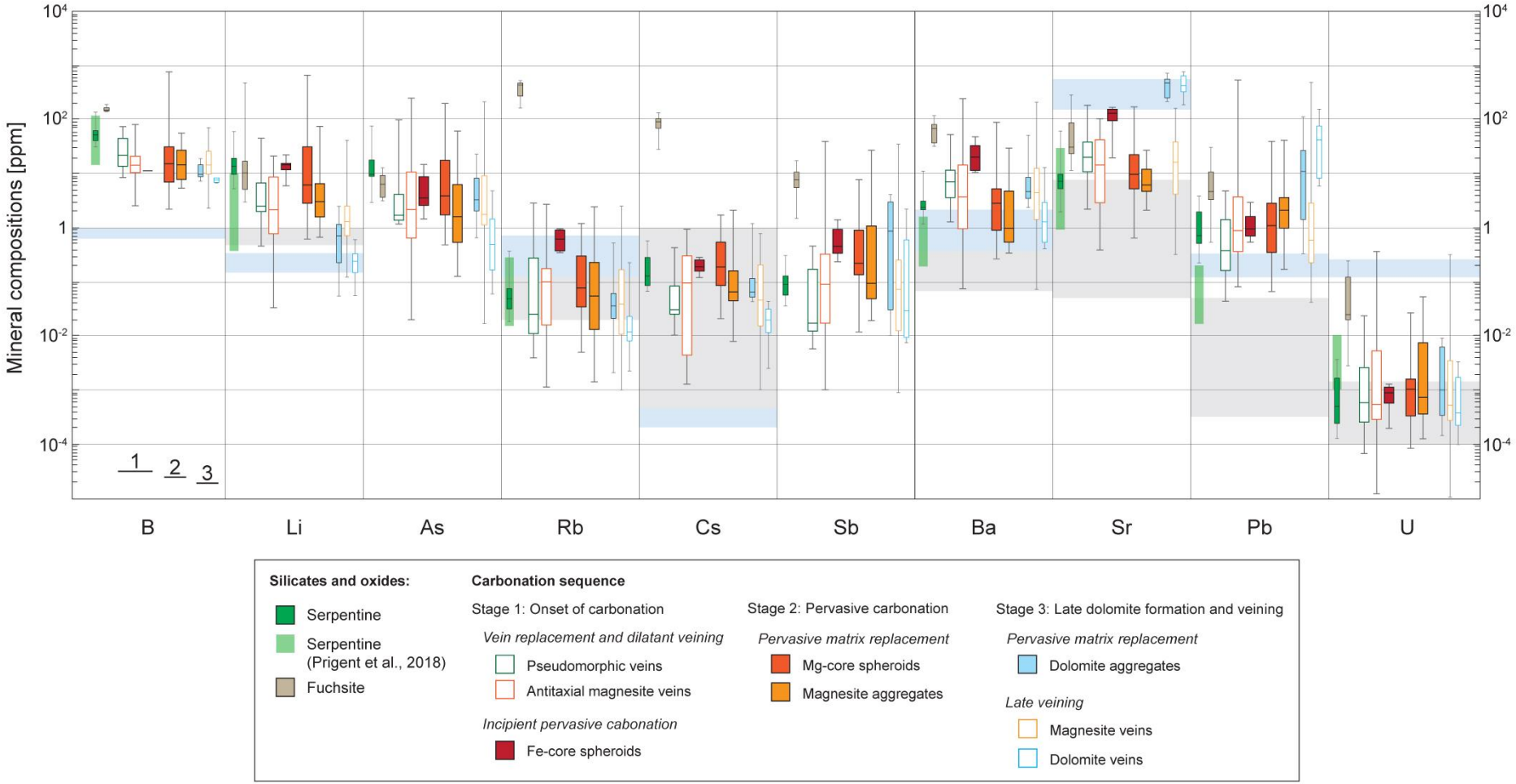

Fig. 6.10 Caltech diagrams of the compositions of silicates and carbonates , plotted on a log scale. The dark grey field correspond to the compositions of hydrothermal carbonates in the Semail Ophiolite (data from Noël et al., 2018) and the blue field to those reported from oceanic settings (Bach et al., 2011; Schröder et al., 2015, Kendrick et al., 2021).

6.2.4 Conclusions

Quantifying the trace element chemistry of the different types of carbonate microstructures highlighted the complex compositional variability within samples and between samples from different geochemical and structural levels of the borehole. Carbonate compositions in moderately incompatible lithophile elements are clearly distinguishable between the different geochemical domains, indicating a strong control of protoliths on their distribution. Enrichement in REE observed in dolomite likely result from preferential incorporation at decreasing temperature (Bau, 1991) or enhanced transport by carbonate complexes in fluids (Louvel et al., 2022).

Except for local rembobilization proceeding at the outcome of Fe-oxides destabilization (see chapter 4.3), matrix replacive magnesites preserved the distribution in transition metals of precursor serpentines, suggesting their low mobility during peridotite carbonation. High Zn abundance in pervasive magnesite aggregates suggest its mobility with carbonate lignads in fluids during advanced carbonation, possibly as an effect of changes in fluid salinity, pressure or temperature (e.g., Farsang et al., 2021).

Fluid mobile elements are excellent trackers to unravel elemental mobility and changes in fluid compositions. Alkali metals and metalloids rich serpentines related to serpentinization of peridotites prior to carbonation. Poorer Li, B, and As concentrations in carbonates grown after serpentines suggest: remobilization by fluids during rock dehydration. Systematic compositional evolution between Fe-core spheroids, Mg-core spheroids and magnesites aggregates suggest progressive depletion in Rb, Ba, Sr and enrichment in Pb in fluids as carbonation progressed. Enrichment in these elements in dolomites compared to magnesites either reflect the effect of higher partition coefficients or major changes in fluid compositions.

Chapter 7: Synthesis and concluding remarks

7.1 Synthesis

Mantle rocks exposed to subsurface conditions or hydrothermal fluids reach disequilibrium and become altered. In nature serpentinization and carbonation are the two prevalent fluid-rock reactions affecting mantle rocks. Listvenite forms by the complete conversion of peridotite to an Mg-carbonates–quartz assemblage by interaction with reactive CO_2-bearing fluids. These rocks first attracted attention for hosting ore-grade mineralizations in economically-valuable metals, or as natural analogues for industrial carbon sequestration. More recently, they have been identified as potential trap-and-release reservoirs for volatiles such as water and carbon in the shallow mantle wedge, possibly influencing global geochemical cycles. The geochemical and mineralogical complexity of listvenites led to the establishment of different genetic models, however the processes and conditions favouring listvenite formation are poorly documented.

The present PhD thesis focussed on listvenite exposures along the base of the Semail ophiolite mantle in Oman, which have been the purpose of drilling Oman Drilling Project Hole BT1B. This study benefited from high-resolution core sampling from Hole BT1B, further complemented by regional sampling. Aiming to better understand the processes of peridotite carbonation, our study combines a multi-scale and multi-technique approach consisting in fieldwork, microstructural characterization (optical and scanning electron microscopy, Raman spectroscopy, EBSD), whole rock (XRF, ICP-QMS) and mineral geochemical analyses (EPMA, LA-ICPMS), and isotopic studies (bulk C-Fe-Zn isotopes, C-O isotopes on carbonates).

Listvenite occurrences in Fanja

In the Fanja region, the ophiolite section is relatively thin (ca. <400 m), exposing dismembered and highly faulted fragments of mantle rocks juxtaposed with lower gabbros, slices of metamorphic sole, and para-autochthonous sediments of the Arabian margin. The ophiolite mantle is composed of (Cpx-)harzburgites, lherzolites and rare dunites, a rock suite proper to basal peridotites of the Banded Unit. Listvenites are found as tabular sheets extending at the kilometre-scale or smaller lenses interlayering the mantle section close to or at the contact with the basal thrust. Their orientation is similar to the basal thrust. Carbonation of peridotites defined reaction zones including (poorly-)fractured, moderately serpentinized peridotites to intensively foliated carbonated serpentinites at the contact with listvenites.

Interestingly, the drilled lithological sequence in Hole BT1B is not representative of other investigated sections in the region where moderately to highly serpentinized peridotites are more abundant than listvenites. Listvenites generally interlayer the mantle closer to or at the contact with gabbros. When present atop the metamorphic sole, listvenites only form discontinuous, thin layers. We noticed that listvenites in the borehole and other sites are bordered by bastite-poor, foliated carbonated

serpentinite reminding of dunitic protoliths. Localization of deformation in weak rheologies may have focussed fluid flows and controlled the localization of listvenites in the mantle section.

Two models have been proposed to explain the formation of listvenites in Fanja: i) Cretaceous peridotite carbonation of the mantle wedge during incipient subduction and ophiolite obduction (Kelemen et al., 2022); ii) late Paleocene–early Miocene carbonation along post-obductional extensional faults (Scharf et al., 2022). The model of Scharf et al. (2022) is based upon the structural analysis of faulted contacts between listvenites and the metamorphic sole, but also on U-Pb ages on listvenite (64.3 ± 6.3 Ma) and dolomite-veins cutting listvenites (60.3 ± 15.4; 55.1 ± 4.7 Ma) from western outcrops. Theses ages are younger than expected in the model of Kelemen et al. (2022). One critical point raised by Kelemen et al. (2022) is that Paleocene to Miocene uplift of the Jebel Akhdar and Saih Hatat domes may have reactivated older faults or created new ones. Our geochemical study of regional samples evidenced that listvenites outcropping eastwards are magnesite-rich, while listvenites atop the sole and west to the drill site are overall rich in calcite and/or dolomite. Possible explanations are: i) carbonation after different fluid batches possibly migrating at different timing of the ophiolite history; ii) large-scale compositional heterogeneity of the fluid source.

Reactional sequence

The petrological study of carbonated serpentinites and listvenites show that serpentinization underwent completion prior to the onset of carbonation. Carbonation progressed through distinctive stages of pervasive matrix replacement and veining. Incipient carbonation is texturally ascribed to pseudomorphic replacement of serpentine veins and the generation of antitaxial carbonate veins. The onset of pervasive carbonation is characterized by the formation of chemically zoned Fe-rich magnesite spheroids and aggregates in the vicinity of antitaxial Fe-rich magnesite veins. This transient stage was followed by extended matrix replacement by Mg-rich magnesite, forming Mg-core spheroids, aggregates and overgrowths on walls of pre-existing microstructures, prior to silicification of the remaining background serpentine.

Chemical zoning in matrix magnesites indicate growth under disequilibrium conditions. We document for the first time in detail the different carbonation reactions destabilizing Fe-oxides into Fe-rich magnesite and consistent with the the conversion of magnetite into Fe-rich magnesite and hematite. Thermodynamic modelling converges to the precipitation of Fe-rich magnesite as serpentine is still present in the rock assemblage, also dependent on fluid XCO_2 composition and local redox conditions. We postulate that Fe-rich cores thus record a transient step of carbonation, followed by the pervasive (over)growth of Mg-rich spheroids and aggregates under increased fluid supply. Even though present in a majority of our listvenite samples, the scarcity of Fe-core spheroids compared to Mg-rich matrix magnesite may be a hint for fast transition from limited to intensive fluxing of reactive fluids. This transition may be caused by cyclic fluid pressure variations under regional tectonic stress, related to

reaction-enhanced deformation (Menzel et al., 2021) and reaction-induced fracturing (e.g. Kelemen et al., 2022).

Elemental mobility

Elemental mobility during peridotite carbonation, and respective contribution of protoliths and fluids, were investigated by characterizing bulk rock and mineral compositions, complemented by a bulk rock C-Fe-Zn elemental and isotopes study.

Moderately to highly serpentinized peridotites in Fanja cover a large compositional range reflecting protolith heterogeneity in the investigated mantle section. They show selective enrichments in fluid-mobile Li, Rb, Sr, Cs, Ba and Pb typical of basal peridotites in Oman. Compositions of serpentines in BT1B overlap those of peridotites from the main mantle section indicating an immobile behaviour during serpentinization.

Carbonation of peridotite to listvenite is characterized by: i) the major addition by fluids of carbon; ii) enrichment in fluid-mobile As, Sr, Sb, Ba, and Pb; iii) “immobile” behaviour of most major elements, transition metals and moderately incompatible lithophile elements at the meter to decameter scale. Variations in Si, Mn, Mg and Ca abundances for samples collected atop the basal thrust likely relate to weathering and/or alteration with Ca-rich fluids precipitating abundant dolomite.

Quantifying mineral compositions allowed to better refine elemental distribution between the different minerals and microstructures. Trace element compositions of carbonates in moderately incompatible lithophile elements indicate a strong control of protoliths on their distribution. Replacement of matrix serpentine by magnesite is isochemical except for enrichment in Sb, Cs, Pb, only slightly for Rb and Sr, and depletion in Li and As. Early magnesite veins only present minor chemical variability with matrix magnesites suggesting they derive from similar fluids. On the other hand, replacement of matrix serpentine by dolomites is accompanied by an enrichment in LREE, MREE, Sr, Sb, Ba, Pb, but depletion in Li, Cs, As. It is worth noticing that Fe-core spheroids show higher concentrations in Sb and Li than for Mg-core spheroids and magnesite aggregates, but are poorer in Pb and As. In addition, Fe-core spheroids present an enrichment in Ba and Sr which is not observed for other matrix magnesites. This suggest that Fe-core spheroids formed from fluid batches different from ones responsible for late pervasive matrix replacement. Dolomite aggregates show higher contents in Sr, Sb, Ba, and Pb than matrix magnesites, and lower ones for Li, Cs and As, which may also relate to the infiltration fluids with a different composition. Finally, enrichment in Pb and depletion in Li, Ba and As in late veins point to a change in fluid chemistry during late veining.

These interpretations have to be considered with caution. Elemental distribution in carbonates is controlled by: i) the composition of the reactive fluids (concentration in cations and ligands, dissolved oxidized/reduced species, salinity, alkalinity, pH,), or ii) the composition of the host rock, or iii) external

factors (pressure and/or temperature). The distribution of trace elements is difficult to evaluate as their solubilty in fluids is controlled by sorption and complexation processes (e.g., Allen and Seyfried, 2005; Migdisov et al., 2016). Preferential incorporation of an element between the mineral and fluid phases are controlled by partition coefficients. In the case of hydrothermal magnesite and dolomite no experimental dataset is available to our knowledge for modelling the initial compositions of fluids. Hence literature data exploring fluid-carbonate elemental behaviour mainly relies of theoretical work (Wood, 1990; Rimstidt et al., 1999; Wang and Xu, 2001; Luo and Byrne, 2004) or focussing on the distribution of REE (e.g., Migdisov 2016; Louvel, 2022).

Source of fluids and temperature of carbonation

Determining the source of reactive fluids has been investigated though bulk rock and "micro-bulk" carbon isotopes study on borehole samples. While poorly carbonated serpentinites preserved mantle-like values ($\delta^{13}C_{TC}$ = -6.20 to -3.96 ‰), listvenites are characterized by heavier bulk $\delta^{13}C_{TC}$ isotope compositions ($\delta^{13}C_{TC}$ = -3.28 to +0.8 ‰) indicating a strong inorganic carbon component in fluids. "Micro-bulk" isotope compositions of the various types of matrix and vein carbonates are similar to bulk signatures, indicating a similar type of source for reactive fluids. These isotope compositions are consistent with heavy $^{87}Sr/^{86}Sr$ isotope signatures of listvenites (de Obeso et al., 2022) pointing to carbonate-bearing clastic sediments as the likely fluid source.

The oxygen isotope compositions of carbonates are variable across the borehole, suggesting multiple episodes of fluid infiltration. Temperatures of carbonation were estimated using different fluid compositions. If derived from seawater ($\Delta^{18}O_{min\text{-}fluid}$ = 0 ‰), carbonates would have formed between 70–114 °C, while between 84–141 °C for type metamorphic fluids ($\Delta^{18}O_{min\text{-}fluid}$ = +2 ‰). Calculation using the lightest ($\delta^{18}O_{fluid}$ = -9.9 ‰) and heaviest ($\delta^{18}O_{fluid}$ = +12.2 ‰) fluid compositions determined by Beinlich et al. (2020) returned minimum and maximum temperature estimates of 20 °C and 313 °C for carbonation.

7.2 Perspectives

This PhD thesis provides an inedite pretrographic and geochemical dataset for the understanding of carbonation processes and elemental mobility during CO_2-metasomatism of peridotite. Our results raised open questions that could be the scope of follow-up studies. Among all aspects presented in this study the reactional sequence and related conditions (i.e., redox, temperature), but also fluid pathways could be better constrained by a serie of complementary analyses.

Linkages between microstructure, fluid paths and compositions

The formation of matrix and vein carbonate microstructures presenting variable morphologies and compositions proceeded during distinct reactional stages. Compositional heterogeneities could result

from changes in the chemistry of fluids, likely related to infiltration of multiple fluid batches, or be locally controlled by the protolith composition, redox conditions or kinetic factors such as temperature. One key to unravel this complex Yet the spatial distribution between specific matrix and vein microstructures has only been petrographically inferred. Beinlich et al. (2020) paved the way to investigate spatial relationships between matrix and vein carbonates by X-ray tomography: these authors evidenced the occurrence of spheroids connected to early veins, suggesting fluid migration controlled by rock fracturation, and unconnected spheroids likely formed at the outcome of porous flow. One future work could be to perform XR tomography on micro-cored samples for which the presence of Fe-core spheroids, Mg-core spheroids and aggreagtes would previously be microscopically identified. The occurrence of connectivity between specific carbonate microstructures and flow structures could parameters controlling elemental mobility and reaction pathways.

Refining the temperature of carbonation and fluid signatures

In the absence of fluid inclusions in carbonates or quartz, temperature of carbonation can only be estimated by stable isotopes thermometry. The petrological study of carbonate microstructures revealed chemical zoning which arised from different growth stages and fluid arrivals. Temperatures determined by Beinlich et al. (2020) and in this study do not account for growth patterns or zoning, being based on "micro-bulk" isotopic compositions. It might therefore be of interest to measure ^{13}C and ^{18}O isotopic profiles across Fe-core and Mg-core spheroids, but also zoned magnesite veins (generally 80-300 μm wide) by secondary iron mass spectrometry (5-20 μm spot size). This will help infer if there is any isotopes systematics between chemically zoning. In such case, indicate either a different carbonation temperature or precipitation after fluids with different compositions.

Bibliography

-A-

Aftabi, A., and Zarrinkoub, M.H. (2013). Petrogeochemistry of listvenite association in metaophiolites of Sahlabad region, eastern Iran: Implications for possible epigenetic Cu–Au ore exploration in metaophiolites. Lithos, 156–159, 186–203.

Agard, P., Yamato, P., Soret, M., Prigent, C., Guillot, S., Plunder, A., Dubacq, B., Chauvet, A., Monié, P. (2016). Plate interface rheological switches during subduction infancy: Control on slab penetration and metamorphic sole formation. Earth Planet. Sci. Lett., 451, 208–220.

Ahankoub, M., Mackizadeh, M.A. (2019). Mineralogy and geochemistry of the Dehshir listvenites, central Iran. Neues Jahrb. für Mineral., 196 (1), 1–18.

Aharon, P. (1988). A stable-isotope study of magnesites from the rum jungle uranium field, Australia: Implications for the origin of strata-bound massive magnesites. Chem. Geol., 69(1), 127–145.

Akbulut, M., Pişkin. Ő., Karayiğit, A.İ. (2006). The genesis of the carbonatized and silicified ultramafics known as listvenites: a case study from the Mihalıççık region (Eskişehir), NW Turkey. Geol. J., 41, 557–580.

Allen, D.E., Seyfried, W.E. (2003). Compositional controls on vent fluids from ultramafic-hosted hydrothermal systems at mid-ocean ridges: An experimental study at 400°C, 500 bars. Geochim. Cosmochim. Acta, 67(8), 1531–1542.

Alt, J. C., Shanks, W. C. (1998). Sulfur in serpentinized oceanic peridotites: Serpentinization processes and microbial sulfate reduction. J. Geophys. Res., 103(B5), 9917–9929.

Alt, J. C., Shanks, W. C. (2003). Serpentinization of abyssal peridotites from the MARK area, Mid-Atlantic Ridge: sulfur geochemistry and reaction modeling. Geochim. Cosmochim. Acta, 67(4), 641–653.

Alt, J.C., Schwarzenbach, E.M., Früh-Green, G.L., Shanks, W.C., Bernasconi, S.M., Garrido, C.J., Crispini, L., Gaggero, L., Padrón-Navarta, J.A., Marchesi, C. (2013). The role of serpentinites in cycling of carbon and sulfur: Seafloor serpentinization and subduction metamorphism. Lithos, 178, 40–54.

Andreani, M., Mével, C., Boullier, A.M., Escartín, J. (2007). Dynamic control on serpentine crystallization in veins: Constraints on hydration processes in oceanic peridotites. Geochem. Geophys. Geosyst., 8, Q02012.

Andreani, M., Luquot, L., Gouze, P., Godard, M., Hoisé, E., Gibert, B. (2009). Experimental Study of Carbon Sequestration Reactions Controlled by the Percolation of CO2-Rich Brine through Peridotites. Environ. Sci. Technol., 43, 1226–1231.

Andreani, M., Muñoz, M., Marcaillou, C., Delacour, A. (2013). µXANES study of iron redox state in serpentine during oceanic serpentinization. Lithos, 178, 70–83.

Archer, C., Andersen, M.B., Cloquet, C., Conway, T.M., Dong, S., Ellwood, M., Moore, R., Nelson, J., Rehkämper, M., Rouxel, O., Samanta, M., Shin, K.-C., Sohrin, Y., Takanoh, S., Wasylenki, L. (2017). Inter-calibration of a proposed new primary reference standard AA-ETH Zn for zinc isotopic analysis. J. Anal. At. Spectrom., 32, 415–419.

Ash, C., Arksey, R. (1990). The listwanite - lode gold association in British Columbia. Geological fieldwork 1989.

Ashley, P.M. (1997). Silica-carbonate alteration zones and gold mineralisation in the Great Serpentinite Belt, New England Orogen, New South Wales. In: Ashley, P.M., Flood, P.G. (Eds), Tectonics and Metallogenesis of the New England Orogen, Alan H. Voisey Memorial Volume. Geological Society of Australia, 212–225.

Auclair, M., Gauthier, M., Trottier, J., Jebrak, M., Chartrand, F. (1993). Mineralogy, geochemistry, and paragenesis of the Eastern Metals serpentinite-associated Ni-Cu-Zn deposit, Quebec Appalachians. Econ. Geol., 88(1), 123–138.

Austrheim, H., Corfu, F., and Renggli, C.J. (2021). From peridotite to fuchsite bearing quartzite via carbonation and weathering: with implications for the Pb budget of continental crust. Contrib. Mineral. Petrol. 176, 94.

Auzende, A.-L., Daniel, I., Reynard, B., Lemaire, C., Guyot, F. (2004). High-pressure behaviour of serpentine minerals: a Raman spectroscopic study. Phys. Chem. Minerals, 31, 269–277.

Aydal, D. (1990). Gold-bearing listwaenites in the Araç Massif, Kastamonu, Turkey. Terra Nova, 2(1), 43–52.

Azer, M.K. (2013). Evolution and economic significance of listwaenites associated with Neoproterozoic ophiolites in South Eastern Desert, Egypt. Geol. Acta, 11(1), 113–128.

-B-

Bach, W., Garrido, C.J., Paulick, H., Harvey, J., Rosner, M. (2004). Seawater-peridotite interactions: First insights from ODP Leg 209, MAR 15°N. Geochem. Geophys. Geosyst., 5, Q09F26.

Bau, M. (1991). Rare-earth element mobility during hydrothermal and metamorphic fluid-rock interaction and the significance of the oxidation state of europium. Chem. Geol., 93, 219–230.

Bechennec, F., Le Metour, J., Rabu, D., Bourdillon-de-Grissac, C., de Wever, P., Beurrier, M., Villey, M. (1990). The Hawasina Nappes: stratigraphy, palaeogeography and structural evolution of a fragment of the south-Tethyan passive continental margin. Geol. Soc. Spec. Publ., 49, 213–223.

Beinlich, A., Plümper, O., Hövelmann, J., Austrheim, H., Jamtveit, B. (2012). Massive serpentinite carbonation at Linnajavri, N–Norway. Terra Nova, 24(6), 446–455.

Beinlich, A., Plümper, O., Boter, E., Müller, I. A., Kourim, F., Ziegler, M., Harigane, Y., Lafay, R., Kelemen, P.B., & the Oman Drilling Project Science Team (2020). Ultramafic rock carbonation: Constraints from listvenite core BT1B, Oman drilling project, J. Geophys. Res. Solid Earth, 125, e2019JB019060.

Bekaert, D.V., Turner, S.J., Broadley, M.W., Barnes, J.D., Halldórsson, S.A., Labidi, J., Wade, J., Walowski, K.J., Barry, P.H. (2021). Subduction-Driven Volatile Recycling: A Global Mass Balance. Annu. Rev. Earth Planet. Sci., 49(1), 37–70.

Belogub, E.V., Melekestseva, I.Y., Novoselov, K.A., Zabotina, M.V., Tret'yakov, G.A., Zaykov, V.V., and Yuminov, A.M. (2017). Listvenite-related gold deposits of the South Urals (Russia): A review. Ore Geol. Rev., 85, 247–270.

Berglund, M., Wieser, M.E. (2011). Isotopic compositions of the elements 2009 (IUPAC Technical Report). Pure Appl. Chem. 83(2), 397–410.

Bjerga, A., Konopásek, J., Pedersen, R.B. (2015). Talc–carbonate alteration of ultramafic rocks within the Leka Ophiolite Complex, Central Norway. Lithos, 227, 21–36.

Bodinier, J.-L., Godard, M. (2007). Orogenic, Ophiolitic, and Abyssal Peridotites. In: Holland, H.D., Turekian, K.K. (Ed.), Treatise on Geochemistry, Pergamon, 1–73.

Bohlke, J.K. (1989). Comparison of metasomatic reactions between a common CO2-rich vein fluid and diverse wall rocks; intensive variables, mass transfers, and Au mineralization at Alleghany, California. Econ. Geol., 84(2), 291–327.

Boillot, G., Grimaud, S., Mauffret, A., Mougenot, D., Mergoil-Daniel, J., Kornprobst, J., Torrent, G. (1980). Ocean-continent boundary off the Iberian margin: A serpentinite diapir west of the Galicia bank. Earth Planet. Sci. Lett., 48, 23–34.

Boskabadi, A., Pitcairn, I.K., Leybourne, M.I., Teagle, D.A.H., Cooper, M.J., Hadizadeh, H., Bezenjani, R.N., and Bagherzadeh, R.M. (2020). Carbonation of ophiolitic ultramafic rocks: Listvenite formation in the Late Cretaceous ophiolites of eastern Iran. Lithos, 352–353, 105307.

Boudier, F., Ceuleneer, G., and Nicolas, A. (1988). Shear zones, thrusts and related magmatism in the Oman ophiolite: Initiation of thrusting on an oceanic ridge. Tectonophysics, 151(1-4), 275–296.

Boudier, F., Nicolas, A. (2018) Synchronous Seafloor Spreading and Subduction at the Paleo-Convergent Margin of Semail and Arabia. Tectonics, 37, 2961–2982.

Boudier, F., Baronnet, A., Mainprice, D. (2010). Serpentine mineral replacements of natural olivine and their seismic implications: Oceanic lizardite versus subduction-related antigorite. J. Petrology, 51(1–2), 495–512.

Buckman, S. (2000). Tectonics and Mineralization of West Junggar, northwest China. Unpubl. PhD thesis, University of Hong Kong, Hong-Kong, p.304.

Busigny, V., Planavsky, N.J., Jézéquel, D., Crowe, S., Louvat, P., Moureau, J., Viollier, E., Lyons, T.W. (2014). Iron isotopes in an Archean ocean analogue. Geochim. Cosmochim. Acta, 133, 443-462.

Buisson, G., Leblanc, M. (1985). Gold in carbonatized ultramafic rocks from ophiolite complexes. Econ. Geol., 80(7), 2028–2029.

Buisson, G., Leblanc, M. (1987). Gold in Mantle Peridotites from Upper Proterozoic Ophiolites in Arabia, Mali, and Morocco. Econ. Geol., 82(8), 2091–2097.

-C-

Cannaò, E., Scambelluri, M., Agostini, S., Tonarini, S., Godard, M. (2016). Linking serpentinite geochemistry with tectonic evolution at the subduction plate-interface: the Voltri Massif case study (Ligurian Western Alps, Italy). Geochim. Cosmochim. Acta, 190, 115–133.

Cannat, M., Fontaine, F., Escartín, J. (2010). Serpentinization and Associated Hydrogen And Methane Fluxes at Slow Spreading Ridges. In: Rona, P.A., Devey, C.W., Dyment, J., Murton, B.J. (Eds.), Diversity Of Hydrothermal Systems On Slow Spreading Ocean Ridges.

Carter, E. (2020). Ophiolites as archives of hydration, carbonation and metasomatic processes in the oceanic lithosphere: insights from halogen and noble gas systematics. PhD Thesis, University of Manchester, England, p305.

Caruso, L., Chernosky, J.V. (1979). The stability of lizardite. Canad. Mineral., 17, 757–769.

Celestino, R., Wohlwend, S., Reháková, D., Weissert, H. (2017). Carbon isotope stratigraphy, biostratigraphy and sedimentology of the Upper Jurassic – Lower Cretaceous Rayda Formation, Central Oman Mountains. Newsl. Stratigr., 50, 91–109.

Charlou, J.L., Donval, J.P., Fouquet, Y., Jean-Baptiste, P., Holm, N. (2002). Geochemistry of high H2 and CH4 vent fluids issuing from ultramafic rocks at the Rainbow hydrothermal field (36°14′N, MAR). Chem. Geol., 191(4), 345–359.

Chen, H., Savage, P.S., Teng, F.-Z., Helz, R.T., Moynier, F. (2013). Zinc isotope fractionation during magmatic differentiation and the isotopic composition of the bulk Earth. Earth Planet. Sci. Lett., 369-370, 34-42.

Chernosky, J.V., Berman, R.G., Bryndzia, L.T. (1988). Stability, phase relations, and thermodynamic properties of chlorite and serpentine group minerals. Rev. Mineral. Geochem., 19, 295–346.

Clark, I.D., Fontes, J.-C. (1990). Paleoclimatic reconstruction in Northern Oman based on carbonates from hyperalkaline groundwaters. Quat. Res., 33, 320–336.

Çolacoğlu, A.R. (2009). Geology and geochemical characteristics of Gevaş listwaenites (Van-Turkey). Yerbilimleri, 30(1), 59–81.

Coleman, R. (1981). Tectonic setting for ophiolite obduction in Oman, J. Geophys. Res. Solid Earth, 86, 2497–2508.

Connolly, J.A.D. (2005). Computation of phase equilibria by linear programming: A tool for geodynamic modeling and its application to subduction zone decarbonation. Earth Planet. Sci. Lett., 236, 524–541.

Connolly, J.A.D. (2009). The geodynamic equation of state: What and how. Geochem. Geophys., 10, Q10014.

Craddock, P.R., Warren, J.M., Dauphas, N. (2013). Abyssal peridotites reveal the near-chondritic Fe isotopic composition of the Earth. Earth Planet. Sci. Lett., 365, 63–76.

-D-

de Obeso J.C., Kelemen, P.B. (2020). Major element mobility during serpentinization, oxidation and weathering of mantle peridotite at low temperatures. Phil. Trans. R. Soc. A, 378, 20180433.

Daval D., Hellmann, R., Martinez, I., Gangloff, S.F., Guyot, F. (2013). Lizardite serpentine dissolution kinetics as a function of pH and temperature, including effects of elevated pCO2. Chem. Geol., 351, 245–256.

Delacour, A., Früh-Green, G.L., Bernasconi, S.M., Schaeffer, P., and Kelley, D.S. (2008). Carbon geochemistry of serpentinites in the Lost City Hydrothermal System (30°N, MAR). Geochim. Cosmochim. Acta, 72, 3681–3702.

Deschamps, F., Godard, M., Guillot, S., and Hattori, K. (2013). Geochemistry of subduction zone serpentinites: A review. Lithos, 178, 96–127.

de Obeso, J.C., Kelemen, P.B., Leong, J.M., Menzel, M.D., Manning, C.E., Godard, M., Cai, Y., Bolge, L., Oman Drilling Project Phase 1 Science Party (2022). Deep sourced fluids for peridotite carbonation in the shallow mantle wedge of a fossil subduction zone: Sr and C isotope profiles of OmanDP Hole BT1B. J. Geophys. Res. Solid Earth, 127, e2021JB022704.

Debret, B., Millet, M.-A., Pons, M.-L., Bouilhol, P., Inglis, P., Williams, H. (2016). Isotopic evidence for iron mobility during subduction. Geology, 44, 215–218.

Debret, B., Beunon, H., Mattielli, N., Andreani, M., Ribeiro da Costa, I., Escartin, J. (2018a). Ore component mobility, transport and mineralization at mid-oceanic ridges: A stable isotopes (Zn, Cu and Fe) study of the Rainbow massif (Mid-Atlantic Ridge 36°14′N). Earth Planet. Sci. Lett., 503, 170–180.

Debret, B., Bouilhol, P., Pons, M.L., Williams, H. (2018b). Carbonate Transfer during the Onset of Slab Devolatilization: New Insights from Fe and Zn Stable Isotopes. J. Petrol., 59, 1145–1166.

Debret B., Reekie, C.D.J., Mattielli, N., Beunon, H., Ménez, B., Savov, I.P., Williams, H. (2020). Redox transfer at subduction zones: insights from Fe isotopes in the Mariana forearc. Geochem. Perspect. Lett., 12, 46–51.

Debret, B., Garrido, C.J., Pons, M.-L., Bouilhol, P., Inglis, E., López Sánchez-Vizcaíno, V., Inglis, E, Williams, H. (2021). Iron and zinc stable isotope evidence for open-system high-pressure dehydration of antigorite serpentinite in subduction zones. Geochim. Cosmochim. Acta, 296, 210–225.

Deines, P. (2002). The carbon isotope geochemistry of mantle xenoliths. Earth Sci. Rev., 58, 247–278.

Doucet, L.S., Mattielli, N., Ionov, D.A., Debouge, W., Golovin, A.V. (2016). Zn isotopic heterogeneity in the mantle: a melting control? Earth Planet. Sci. Lett., 451, 232–240.

Ducher, M., Blanchard, M., Balan, E. (2016). Equilibrium zinc isotope fractionation in Zn-bearing minerals from first-principles calculations. Chem. Geol., 443, 87–96.

-E-

Eckstrand, O.R. (1975). The Dumont serpentinite; a model for control of nickeliferous opaque mineral assemblages by alteration reactions in ultramafic rocks. Econ. Geol., 70(1), 183–201.

Eiler, J.M. (2007). “Clumped-isotope” geochemistry—The study of naturally-occurring, multiply-substituted isotopologues. Earth Planet. Sci. Lett., 262, 309–327.

Emam, A., Zoheir, B. (2013). Au and Cr mobilization through metasomatism: Microchemical evidence from ore-bearing listvenite, South Eastern Desert of Egypt. J. Geochem. Explor., 125, 34–45.

Escartín, J., Hirth, G., Evans, B. (1997). Effects of serpentinization on the lithospheric strength and the style of normal faulting at slow-spreading ridges. Earth Planet. Sci. Lett., 151, 181–189.

Escayola, M.P., Proenza, J.A., van Staal, C.R., Rogers, N., Skulski, T. (2009). The Point Rousse listvenites, Baie Vert, Newfoundland: altered ultramafic rocks with potential for gold mineralization? Current Research Newfoundland and Labrador Department of Natural Resources Geological Survey. Report 09-1, 1–12.

Evans, B.W., Johannes, W, Otterodoom, H., Tromsdorff, V. (1976). Stability of chrysotile and antigorite in the serpentine multisystem. Schweiz. Mineral. Petrogr. Mitt., 56, 79–93.

Evans, B.W. (2004). The Serpentinite Multisystem Revisited: Chrysotile Is Metastable. Int. Geol. Rev., 46, 479–506.

-F-

Falk, E.S., Kelemen, P.B. (2015). Geochemistry and petrology of listvenite in the Samail ophiolite, Sultanate of Oman: Complete carbonation of peridotite during ophiolite emplacement. Geochim. Cosmochim. Acta, 160, 70–90.

Farsang, S., Louvel, M., Rosa, A.D., Amboage, M., Anzellini, S., Widmer, R.N., Redfern, S.A.T. (2021). Effect of salinity, pressure and temperature on the solubility of smithsonite (ZnCO3) and Zn complexation in crustal and upper mantle hydrothermal fluids. Chem. Geol., 578, 120320.

Ferenc, Š, Uher, P., Spišiak, J., Šimonová, V. (2016). Chromium- and nickel-rich micas and associated minerals in listvenite from the Muránska Zdychava, Slovakia: products of hydrothermal metasomatic transformation of ultrabasic rock. J. Geosci., 61(3), 239–254.

Frost, B.R. (1985). On the Stability of Sulfides, Oxides, and Native Metals in Serpentinite. J. Petrol., 26(1), 31–63.

Frost, B.R., Beard, J.S. (2007). On Silica Activity and Serpentinization. J. Petrol., 48(7), 1351–1368.

Fujii, T., Moynier, F., Pons, M.-L., Albarède, F. (2011). The origin of Zn isotope fractionation in sulfides. Geochim. Cosmochim. Acta, 75, 7632–7643.

Fujii, T., Albarède, F. (2012). Ab initio calculation of the Zn isotope effect in phosphates, citrates, and malates and applications to plants and soil. Plos One, 7.

Fujii, T., Moynier, F., Blichert-Toft, J., Albarède, F. (2014). Density functional theory estimation of isotope fractionation of Fe, Ni, Cu, and Zn among species relevant to geochemical and biological environments. Geochim. Cosmochim. Acta, 140, 553–576.

-G-

Gahlan, H.A., Azer, M.K., Asimow, P.D. (2018). On the relative timing of listwaenite formation and chromian spinel equilibration in serpentinites. Am. Min., 103, 1087–1102.

Gahlan, H.A., Azer, M.K., Asimow, P.D., Al-Kahtany, K.M. (2020). Petrogenesis of gold-bearing listvenites from the carbonatized mantle section of the Neoproterozoic Ess ophiolite, Western Arabian Shield, Saudi Arabia. Lithos, 372–373, 105679.

Gahlan, H.A., Azer, M.K., Asimow, P.D., Al-Kahtany, K.M. (2022). Formation of gold-bearing listvenite in the mantle section of the Neoproterozoic Bir Umq ophiolite, Western Arabian Shield, Saudi Arabia. J. African Earth Sci., 190, 104517.

Garber, J.M., Rioux, M., Searle, M.P., Kylander-Clark, A.R.C., Hacker, B.R., Vervoort, J.D., Warren, C.J., Smye, A.J. (2021). Dating continental subduction beneath the Samail Ophiolite: Garnet, zircon, and rutile petrochronology of the As Sifah eclogites, NE Oman. J. Geophys. Res. Solid Earth, 126, e2021JB022715.

Gerbert-Gaillard, L. (2002). Caractérisation géochimique des peridotites de l'ophiolite d'Oman: Processus magmatiques aux limites lithosphere/asthenosphere. PhD thesis, Univ. Montpellier, France, p.266.

Gerdemann, S.J., O'Connor, W.K., Dahlin, D.C., Penner, L.R., Rush, H. (2007). Ex Situ Aqueous Mineral Carbonation. Environ. Sci. Technol., 41, 2587-2593.

Ghosh, P., Adkins, J., Affek, H., Balta, B., Guo, W., Schauble, E.A., Schrag, D., Eiler, J.M. (2006). 13C–18O bonds in carbonate minerals: a new kind of paleothermometer. Geochim. Cosmochim. Acta, 70, 1439–1456.

Glennie, K.W., Boeuf, M.G.A., Hugues Clark, M.W., Moody-Stuart, M., Pilaar, W.F.H., Reinhardt, B.M. (1974). Geology of the Oman Mountains. Neder. Mijn. Geol. Genoot., Delft, Netherlands, p.423.

Godard, M., Jousselin, D., Bodinier, J.-L. (2000). Relationships between geochemistry and structure beneath a palaeo-spreading centre: A study of the mantle section in the Oman Ophiolite. Earth Planet. Sci. Lett., 180, 133–148.

Godard, M., Carter, E., Decrausaz, T., Lafay, R., Bennett, E., Kourim, F., de Obeso, J.C., Michibayashi, K., Harris, M., Coggon, J.A., Teagle, D.A.H., Kelemen, P.B., the Oman Drilling Project Phase 1 Science Party (2021). Geochemical Profiles Across the Listvenite-Metamorphic Transition in the Basal Megathrust of the Semail Ophiolite: Results from Drilling at Oman DP Hole BT1B. J. Geophys. Res. Solid Earth, 126, e2021JB022733.

Grobe, A., Virgo, S., von Hagke, C., Urai, J.L., Littke, R. (2018). Multiphase structural evolution of a continental margin during obduction orogeny: Insights from the Jebel Akhdar Dome, Oman Mountains. Tectonics, 37, 888–913.

Groppo, C., Rinaudo, C., Cairo, S., Gastaldi, D., Compagnoni, R. (2006). Micro-Raman spectroscopy for a quick and reliable identification of serpentine minerals from ultramafics. Eur. J. Mineral., 18(3), 319–329.

Grosch, E.G., Vidal, O., Abu-Alam, T., McLoughlin, N. (2012). P–T Constraints on the Metamorphic Evolution of the Paleoarchean Kromberg Type-Section, Barberton Greenstone Belt, South Africa. J. Pet., 53(3), 513–545.

-H-

Halls, C., Zhao, R. (1995). Listvenite and related rocks: perspectives on terminology and mineralogy with reference to an occurrence at Cregganbaun, Co. Mayo, Republic of Ireland. Miner. Depos., 30, 303–313.

Hamdy, M.M., Lasheen, E.S.R., Abdelwahab, W. (2022). Gold-bearing listwaenites in ophiolitic ultramafics from the Eastern Desert of Egypt: Subduction zone-related alteration of Neoproterozoic mantle? J. African Earth Sci., 193, 104574.

Hänchen, M., Prigiobbe, V., Storti, G., Seward, T.M., Mazzotti, M. (2006). Dissolution kinetics of fosteritic olivineat 90–150 °C including effects of the presence of CO2. Geochim. Cosmochim. Acta, 70, 4403–4416.

Hanghøj, K., Kelemen, P.B., Hassler, D., Godard, M. (2010). Composition and Genesis of Depleted Mantle Peridotites from the Wadi Tayin Massif, Oman Ophiolite; Major and Trace Element Geochemistry, and Os Isotope and PGE Systematics. J. Petrol., 51(1-2), 201–227.

Hansen, L.D., Dipple, G.M., Gordon, T.M., and Kellett, D.A. (2005). Carbonated serpentinite (listwanite) at Atlin, British Columbia: a geological analogue to carbon dioxide sequestration. Can. Mineral., 43(1), 225–239.

Hattori, K. H., Guillot, S. (2007). Geochemical character of serpentinites associated with high- to ultrahigh-pressure metamorphic rocks in the Alps, Cuba, and the Himalayas: recycling of elements in subduction zones. Geochem. Geophys. Geosystems, 8, Q09010.

Helffrich, G.R., Wood, B.J. (2001). The Earth's mantle. Nature, 412, 501–507.

Helmy, H.M., Elshafei, S., Elwan, W. (2018). Mineralogy and geochemistry of metasomatized mantle peridotites from the Eastern Desert of Egypt: The role of granite-related hydrothermal fluids in gold mineralizations. J. African Earth Sci., 144, 136–150.

Hill, P.S., Schauble, E.A. (2008). Modeling the effects of bond environment on equilibriumiron isotope fractionation in ferric aquo-chloro complexes. Geochim. Cosmochim. Acta, 72, 1939–1958.

Hill, P.S., Schauble, E.A., Young, E.D. (2010). Effects of changing solution chemistry on Fe3+/Fe2+ isotope fractionation in aqueous Fe–Cl solutions. Geochim. Cosmochim. Acta, 74, 6669–6689.

Hinsken, T., Bröcker, M., Strauss, H., and Bulle, F. (2017). Geochemical, isotopic and geochronological characterization of listvenite from the Upper Unit on Tinos, Cyclades, Greece. Lithos, 282–283, 281–297.

Holland, T.J.B., Powell, R. (1998). An internally consistent thermodynamic data set for phases of petrological interest, J. Metamorph. Geol., 16, 309–343.

Holland, T. Powell, R. (2011). An improved and extended internally consistent thermodynamic dataset for phases of petrological interest, involving a new equation of state for solids. J. Metamorph. Geol., 29, 333–383.

Hopson, C.A., Coleman, R.G., Gregory, R.T., Pallister, J.S., Bailey, E.H. (1981). Geologic section through the Samail Ophiolite and associated rocks along a Muscat-Ibra Transect, southeastern Oman Mountains. J. Geophys. Res. Solid Earth, 86, 2527–2544.

Horita, J. (2014). Oxygen and carbon isotope fractionation in the system dolomite–water–CO2 to elevated temperatures. Geochim. Cosmochim. Acta, 129, 111–124.

Hyndman, R.D., Peackock, S.M. (2003). Serpentinization of the forearc mantle. Earth Planet. Sci. Lett., 212(3–4), 417–432.

-I-

Ishikawa, T., Fujisawa, S., Nagaishi, K., Masuda, T. (2005). Trace element characteristics of the fluid liberated from amphibolite-facies slab: Inference from the metamorphic sole beneath the Oman ophiolite and implication for boninite genesis. Earth Planet. Sci. Lett., 240, 355–377.

Inglis, E.C., Debret, B., Burton, K.W., Millet, M.-A., Pons, M.-L., Dale, C.W., Bouilhol, P., Cooper, M., Nowell, G.M., McCoy-West, A.J., Williams, H.M. (2017) The behavior of iron and zinc stable isotopes accompanying the subduction of mafic oceanic crust: A case study from Western Alpine ophiolites: Fe and Zn isotopes during subduction. Geochem. Geophys. Geosyst., 18, 2562–2579.

-J-

Janecky, D.R., Seyfried, W.E. (1986). Hydrothermal serpentinization of peridotite within the oceanic crust: Experimental investigations of mineralogy and major element chemistry. Geochim. Cosmochim. Acta, 50, 1357–1378.

Jiang, J., Zhu, Y. (2017). Geology and geochemistry of the Jianchaling hydrothermal nickel deposit: T–pH–fO2–fS2 conditions and nickel precipitation mechanism. Ore Geol. Rev., 91, 216–235.

Johannes, W. (1967). Zur Bildung und Stabilität von Forsterit, Talk, Serpentin, Quarz und Magnesit im System MgO-SiO2-H2O-CO2. Contr. Mineral. Petrol., 15, 233–250.

Johannes, W. (1969). An experimental investigation of the system MgO-SiO2–H2O-CO2. Am. J. Sci., 267(9), 1083–1104.

-K-

Kashkai, M.A., Allakhverdiev, S.I. (1965). Listvenites, their origin and classification. *(Listvenity, ikh genezis i klassifikatsiia: Akad. Nauk Azerbaidzhanskoi SSR)*. Institut Geologii im. akad. I.M. Gubkina. Izdat. Akad. Nauk Azerbaidzhanskoi SSR, Baku, p.142.

Kelemen, P.B., Matter, J.M. (2008). In situ carbonation of peridotite for CO2 storage. Proc. Natl. Acad. Sci., 105(45), 17295–17300.

Kelemen, P.B., Matter, J., Streit, E.E., Rudge, J.F., Curry, W.B., Blusztajn, J. (2011). Rates and Mechanisms of Mineral Carbonation in Peridotite: Natural Processes and Recipes for Enhanced, in situ CO2 Capture and Storage. Annu. Rev. Earth Planet. Sci., 39(1), 545–576.

Kelemen, P.B., Hirth, G. (2012). Reaction-driven cracking during retrograde metamorphism: Olivine hydration and carbonation. Earth Planet. Sci. Lett., 345–348, 81–89.

Kelemen, P.B., Manning, C. (2015). Reevaluating carbon fluxes in subduction zones, what goes down, mostly comes up. Proc. Natl. Acad. Sci., 112, E3997–E4006.

Kelemen, P.B., Matter, J.M., Teagle, D.A.H., Coggon, J.A., the Oman Drilling Project Science Team (2020). Site BT1: fluid and mass exchange on a subduction zone plate boundary. In: Proceedings of the Oman Drilling Project. College Station, Texas 570 (International Ocean Discovery Program).

Kelemen, P.B., de Obeso, J.C., Leong, J.A., Godard, M., Okazaki, K., Kotowski, A.J., Manning, C.E., Ellison, E.T., Menzel, M.D., Urai, J.L., Hirth, G., Rioux, M., Stockli, D.F., Lafay, R., Beinlich, A.M., Coggon, J.A., Warsi, N.H., Matter, J.M., Teagle, D.A.H., Harris, M., Michibayashi, K., Takazawa, E., Al Sulaimani, Z., the Oman Drilling Project Science Team (2022). Listvenite formation during mass transfer into the leading edge of the mantle wedge: Initial results from Oman Drilling Project 575 Hole BT1B. J. Geophys. Res. Solid Earth, 127, e2021JB022352.

Kelley, D.S., Karson, J.A., Früh-Green, G.L., Yoerger, D.R., Shank, T.M., Butterfield, D.A., Hayes, J.M., Schrenk, M.O., Olson, E.J., Proskurowski, G., Jakuba, M., Bradley, A., Larson, B., Ludwig, K., Glickson, D., Buckman, K., Bradley, A.S., Brazelton, W.J., Roe, K., Elend, M.J., Delacour, A., Bernasconi, S.M., Lilley, M.D., Baross, J.A., Summons, R.E., Sylva, S.P. (2005). A Serpentinite-Hosted Ecosystem: The Lost City Hydrothermal Field. Science, 307, 1428–1434.

Kendrick, M.A., Caulfield, J.T., Nguyen, A.D., Zhao, J.-X., Blakey, I. (2020). Halogen and trace element analysis of carbonate-veins and Fe-oxyhydroxide by LA-ICPMS: Implications for seafloor alteration, Atlantis Bank, SW Indian Ridge. Chem. Geol., 547, 119668.

Khedr, M. Z., Arai, S., Python, M., Tamura, A. (2014). Chemical variations of abyssal peridotites in the central Oman ophiolite: Evidence of oceanic mantle heterogeneity. Gondwana Res., 25, 1242–1262.

Klein, F., Bach, W. (2009). Fe–Ni–Co–O–S Phase Relations in Peridotite–Seawater Interactions. J. Petrol., 50(1), 37–59.

Klein, F., Garrido, C.J. (2011). Thermodynamic constraints on mineral carbonation of serpentinized peridotite. Lithos, 126, 147-160.

Klein, F., Bach, W., Humphris, S.E., Kahl, W.-A., Jöns, N., Moskowitz, B., Berquó, T.S. (2014). Magnetite in seafloor serpentinite—Some like it hot. Geology, 42(2), 135–138.

Klein, F., Le Roux, V. (2020). Quantifying the volume increase and chemical exchange during serpentinization. Geology, 48(6), 552–556.

Klein, F., Goldsby, D.L., Lin, J., Andreani, M. (2022). Carbonation of serpentinite in creeping faults of California. Geophys. Res. Lett., 49, e2022GL099185.

-L-

Lackner, K.S., Wendt, C.H., Butt, D.P., Joyce, E.L., Sharp, D.H. (1995). Carbon dioxide disposal in carbonate minerals. Energy, 20(11), 1153–1170.

Lafay, R., Montes-Hernandez, G., Janots, E., Munoz, M. Auzende, A.-L., Gehin, A., Chiriac, R., Proux, O. (2016). Experimental investigation of As, Sb and Cs behavior during olivine serpentinization in hydrothermal alkaline systems. Geochim. Cosmochim. Acta, 179, 177–202.

Lanari, P., Vho, A., Bovay, T., Airaghi, L., and Centrella, S. (2019). Quantitative compositional mapping of mineral phases by electron probe micro-analyser. Geol. Soc. Spec. Publ., 478, 39–63.

Lamadrid, H.M., Zajacz, Z., Klein, F., Bodnar, R.J. (2021). Synthetic fluid inclusions XXIII. Effect of temperature and fluid composition on rates of serpentinization of olivine. Geochim. Cosmochim. Acta, 292, 285–308.

Larkin, P. (2018). Infrared and Raman spectroscopy (Second Edition). Ed.: Larkin, P.J., Elsevier, Amsterdam, Netherland, p.276.

Lee, J.H., Byrne, R.H. (1992). Examination of comparative rare earth element complexation behavior using linear free-energy relationships. Geochim. Cosmochim. Acta, 56, 1127–1137.

Lippard, S.J., Shelton, A.W., Gass, I.G. (1986). The Ophiolite of Northern Oman. Geological Society of London Memoir 11, Blackwell Scientific Publications, Oxford, p.178.

Louvel, M., Etschmann, B., Guan, Q., Testemale, D., Brugger, J. (2022). Carbonate complexation enhances hydrothermal transport of rare earth elements in alkaline fluids. Nat. Commun., 13, 1456.

Liu, S.-A., Liu, P.-P., Lv, Y., Wang, Z.-Z., Dai, J.-G. (2019). Cu and Zn isotope fractionation during oceanic alteration: Implications for Oceanic Cu and Zn cycles. Geochim. Cosmochim. Acta, 257, 191–205.

Luo, Y.-R., Byrne, R.H. (2004). Carbonate complexation of yttrium and the rare earth elements in natural waters. Geochim. Cosmochim. Acta, 68(4), 691–699.

-M-

Madu, B.E., Nesbitt, B.E, Muehlenbachs, K. (1990): A mesothermal gold–stibnite–quartz vein occurrence in the Canadian Cordillera. Econ. Geol., 85, 1260–1268.

Malvoisin, B. (2015). Mass transfer in the oceanic lithosphere: Serpentinization is not isochemical. Earth Planet. Sci. Lett., 439, 75–85.

Malvoisin, B., Zhang, C., Müntener, O., Baumgartner, L.P., Kelemen, P.B., Oman Drilling Project Science Party (2020). Measurement of volume change and mass transfer during serpentinization: Insights from the Oman Drilling Project. J. Geophys. Res. Solid Earth, 125, e2019JB018877.

McCollom, T.M., Lollar, B.S., Lacrampe-Couloume, G., Seewald, J.S. (2010). The influence of carbon source on abiotic organic synthesis and carbon isotope fractionation under hydrothermal conditions. Geochim. Cosmochim. Acta, 74, 2717–2740.

Martin, B., Fyfe, W.S. (1970). Some experimental and theoretical observations on the kinetics of hydration reactions with particular reference to serpentinization. Chem. Geol., 6, 185–202.

Mayhew, L.E., Ellison, E.T., Miller, H.M., Kelemen, P.B., Templeton, A.S. (2018). Iron transformations during low temperature alteration of variably serpentinized rocks from the Samail ophiolite, Oman. Geochim. Cosmochim. Acta, 222, 704–728.

Matter, J.M., Kelemen, P.B. (2009). Permanent storage of carbon dioxide in geological reservoirs by mineral carbonation. Nature Geosci., 2, 837–841.

Mattern, F., Scharf, A. (2018). Postobductional extension along and within the Frontal Range of the Eastern Oman Mountains. J. Asian Earth Sci., 154, 369–385.

Maréchal, C.N., Télouk, P., Albarède, F. (1999). Precise analysis of copper and zinc isotopic compositions by plasma-source mass spectrometry. Chem. Geol., 156, 251–273.

McDonough, W.F., Sun, S.S. (1995). The composition of the Earth. Chem. Geol., 120, 223–253.

McDonough, W.F., Rudnick, R.L. (1998). Mineralogy and composition of the upper mantle. Rev. Mineral. Geochem., 37(1), 139–164.

Menzel, M.D., Garrido, C.J., Sánchez-Vizcaíno V.L., Marchesi, C., Hidas, K., Escayola, M.P., Huertas, A.D. (2018). Carbonation of mantle peridotite by CO2-rich fluids: the formation of listvenites in the Advocate ophiolite complex (Newfoundland, Canada). Lithos, 323, 238–261.

Menzel, M.D., Urai, J.L., de Obeso, J.C., Kotowski, A., Manning, C.E., Kelemen, P.B., Kettermann, M., Jesus, A.P., Harigane, Y., and the Oman Drilling Project Phase 1 Science Party (2020). Brittle Deformation of Carbonated Peridotite-Insights From Listvenites of the Samail Ophiolite (Oman Drilling Project Hole BT1B), J. Geophys. Res. Solid Earth, 125, e2020JB020199.

Menzel, M.D., Urai, J.L., Ukar, E., Hirth, G., Schwedt, A., Kovács, A., Kibkalo, L., Kelemen, P.B. (2022a). Ductile deformation during carbonation of serpentinized peridotite. Nat. Comm., 13, 3478.

Menzel, M.D., Urai, J.L., Ukar, E., Decrausaz, T., Godard, M. (2022b). Progressive veining during peridotite carbonation: insights from listvenites in Hole BT1B, Samail ophiolite (Oman). Solid Earth, 13, 1191–1218.

Mével, C. (2003). Serpentinization of abyssal peridotites at mid-ocean ridges. C.R.-Geosci., 335, 825–852.

Migdisov, A., Williams-Jones, A.E., Brugger, J., Caporuscio, F.A. (2016). Hydrothermal transport, deposition, and fractionation of the REE: Experimental data and thermodynamic calculations. Chem. Geol., 439, 13–42.

Möller, P., Bau, M. (1993). Rare-earth patterns with positive cerium anomaly in alkaline waters from Lake Van, Turkey. Earth Planet. Sci. Lett., 117, 671–676.

Moussa, H.E., Azer, M.K., Abou El Maaty, M.A., Maurice, A.E., Yanni, N.N., Akarish, A.I.M., Elnazer, A.A., Elsagheer, M.A. (2021). Carbonation of Neoproterozoic mantle section and formation of gold-bearing listvenite in the Northern Nubian Shield. Lithos, 406–407, 106525.

Moynier, F., Vance, D., Fujii, T., Savage, P. (2017). The isotope geochemistry of zinc and copper. Rev. Mineral. Geochem., 82, 543–600.

-N-

Nasir, S., Al Sayigh, A.R., Al Harthy, A., Al-Khirbash, S., Al-Jaaidi, O., Musllam, A., Al-Mishwat, A., Al-Bu'saidi, S. (2007). Mineralogical and geochemical characterization of listwaenite from the Semail Ophiolite, Oman. Geochemistry, 67, 213–228.

Nicolas, A., Boudier, F., Ildefonse, I., Ball, E. (2000). Accretion of Oman and United Arab Emirates ophiolite – Discussion of a new structural map, Mar. Geophys. Res., 21, 147–180.

Noël, J., Godard, M., Oliot, E., Martinez, I., Williams, M., Boudier, F., Rodriguez, O., Chaduteau, C., Escario, S., Gouze, P. (2018). Evidence of polygenetic carbon trapping in the Oman Ophiolite: Petro-structural, geochemical, and carbon and oxygen isotope study of the Wadi Dima harzburgite-hosted carbonates (Wadi Tayin massif, Sultanate of Oman). Lithos, 323, 218–237.

Normand, C., Williams-Jones, A.E., Martin, R.F. Vali, H. (2002). Hydrothermal alteration of olivine in a flow-through autoclave: Nucleation and growth of serpentine phases. Am. Min., 87(11-12), 1699–1709.

-O-

O'Connor, W.K., Dahlin, D.C., Rush, G.E., Gerdemann, S.J., Nilsen, D.N. (2004). Aqueous mineral carbonation. U.S. Dep. Energy Final Rep. DOE/ARC-TR-04-002, U.S. Dep. Energy Albany Res. Cent., Albany.

O'Hanley, D.S., Wicks, F.J. (1995). Conditions of formation of lizardite, chrysotile and antigorite, Cassiar, British Columbia. Canad. Mineral., 33(4), 753–773.

Osselin, F., Pichavant, M., Champallier, R., Ulrich, M., Raimbourg, H. (2022). Reactive transport experiments of coupled carbonation and serpentinization in a natural serpentinite. Implication for hydrogen production and carbon geological storage, Geochim. Cosmochim. Acta, 318, 165–189.

Okazaki, K., Michibayashi, K., Hatakeyama, K., Abe, N., Johnson, K.T.M., Kelemen, P.B., & the Oman Drilling Project Science Team (2021). Major mineral fraction and physical properties of carbonated peridotite (listvenite) from ICDP Oman Drilling Project Hole BT1B inferred from X-ray CT core images, J. Geophys. Res. Solid Earth, 126, e2021JB022719.

-P-

Padrón-Navarta, J.A., López Sánchez-Vizcaíno, V., Hermann, J., Connolly, J.A.D., Garrido, C.J., Gómez-Pugnaire, M.T., Marchesi, C. (2013). Tschermak's substitution in antigorite and consequences for phase relations and water liberation in high-grade serpentinites. Lithos, 178, 186–196.

Peng, W., Zhang, L., Menzel, M.D., Brovarone, A.V., Tumiati, S., Shen, T., Hu, H. (2020). Multistage CO2 sequestration in the subduction zone: Insights from exhumed carbonated serpentinites, SW Tianshan UHP belt, China. Geochim. Cosmochim. Acta, 270, 218–243.

Peuble, S., Godard, M., Luquot, L., Andreani, M., Martinez, I., Gouze, P. (2015). CO2 geological storage in olivine rich basaltic aquifers: New Insights from flow-through experiments. App. Geochem., 52, 174–190.

Pens, M., Andreani, M., Daniel, I., Perrillat, J.-Y., Cardon, H. (2016). Contrasted effect of aluminum on the serpentinization rate of olivine and orthopyroxene under hydrothermal conditions. Chem. Geol., 441, 256–264.

Peters, D., Bretscher, A., John, T., Scambelluri, M., Pettke, T. (2017). Fluid-mobile elements in serpentinites: Constraints on serpentinisation environments and element cycling in subduction zones. Chem. Geol., 466, 654–666.

Petriglieri, J.R., Salvioli-Mariani, E., Mantovani, L., Tribaudino, M., Lottici, P.P., Laporte-Magoni, C., Bersani, D. (2015). Micro-Raman mapping of the polymorphs of serpentine. J. Raman Spectrosc. 46, 953–958.

Pirouei, M., Kolo, K., Kalaitzidis, S.P. (2020). Hydrothermal listvenitization and associated mineralizations in Zagros Ophiolites: Implications for mineral exploration in Iraqi Kurdistan. J. Geochem. Explor., 208, 106404.

Pitzer, K.S., Sterner, S.M. (1995). Equations of state valid continuously from zero to extreme pressures with H2O and CO2 as examples, Int. J. Thermophys., 16, 511–518.

Pichat, S., Douchet, C., Albarède, F. (2003). Zinc isotope variations in deep-sea carbonates from the eastern equatorial Pacific over the last 175 ka. Earth Planet. Sci. Lett., 210, 167–178.

Ploshko, V.V. (1963). Listvenitization and carbonatization at terminal stages of Urushten igneous complex, North Caucasus. Int. Geol. Rev., 7, 446–463.

Plümper, O., Røyne, A., Magrasó, A., Jamtveit, B. (2012). The interface-scale mechanism of reactioninduced fracturing during serpentinization. Geology, 40, 1103–1106.

Poitrasson, F., Delpech, G., Gregoire, M. (2013). On the iron isotope heterogeneity of lithospheric mantle xenoliths: implications for mantle metasomatism, the origin of basalts and the iron isotope composition of the Earth. Contrib. Mineral. Petrol., 165, 1243–1258.

Polyakov, V.B., Mineev, S.D. (2000). The use of Mössbauer spectroscopy in stable isotope geochemistry. Geochim. Cosmochim. Acta, 64, 849–865.

Pons, M.-L., Debret, B., Bouilhol, P., Delacour, A., Williams, H. (2016). Zinc isotope evidence for sulfate-rich fluid transfer across subduction zones. Nat. Commun., 7, 13794.

Power, I.M., Wilson, S.A., Dipple, G.M. (2013). Serpentinite Carbonation for CO2 Sequestration. Elements, 9(2), 115–121.

Prigent, C., Guillot, S., Agard, P., Lemarchand, D., Soret, M., Ulrich, M. (2018). Transfer of subduction fluids into the deforming mantle wedge during nascent subduction: Evidence from trace elements and boron isotopes (Semail ophiolite, Oman). Earth Planet. Sci. Lett., 484, 213–228.

-Q-

Qiu, T., Zhu, Y. (2015). Geology and geochemistry of listwaenite-related gold mineralization in the Sayi gold deposit, Xinjiang, NW China. Ore Geol. Rev., 70, 61–79.

Qiu, T., Zhu, Y. (2018). Listwaenite in the Sartohay ophiolitic mélange (Xinjiang, China): A genetic model based on petrology, U-Pb chronology and trace element geochemistry. Lithos, 302–303, 427–446.

-R-

Reynard, B. (2013). Serpentine in active subduction zones. Lithos, 178, 171–185.

Rouméjon, S., Cannat, M. (2014). Serpentinization of mantle-derived peridotites at mid-ocean ridges: Mesh texture development in the context of tectonic exhumation. Geochem. Geophys. Geosyst., 15, 2354–2379.

Rious, M., Garber, J.M., Searle, M., Kelemen, P.B., Miyashita, S., Adachi, Y., Bowring, S. (2021). High-Precision U-Pb Zircon Dating of Late Magmatism in the Samail Ophiolite: A Record of Subduction Initiation, J. Geophys. Res. Solid Earth, 126, e2020JB020758.

Rimstidt, J.D., Balog, A., Webb, J. (1998). Distribution of trace elements between carbonate minerals and aqueous solutions. Geochim. Cosmochim. Acta, 62, 1851–1863.

Robinson, P.T., Malpas, J., Zhou, M.F., Ash, C., Yang, J.S., Bai, W.J. (2005). Geochemistry and Origin of Listwanites in the Sartohay and Luobusa Ophiolites, China. Int. Geol. Rev. 47(2), 177–202.

Rose, G. (1837). Mineralogisch-geognostiche Reise nach dem Ural, dem Altai und dem Kaspischen Meere. Volume 1: Reise nach dem nördlichen Ural und dem Altai. G.E. Reimer (Verlag der Sanderschen Buchhandlung), Berlin, 185p.

Rose, G. (1842). Mineralogisch-geognostische Reise nach dem Ural, dem Altai und dem Kaspischen Meere. Volume 2: Reise nach dem sudlichen Ural und dem Kaspischen Meere, Uebersicht der Mineralien und Gebirgsarten des Ural. G.E. Reimer (Verlag der Sanderschen Buchhandlung), Berlin, p.606.

-S-

Saldi, G.D., Schott, J., Pokrovsky, O.S., Gautier, Q., Oelkers, E.H. (2012). An experimental study of magnesite precipitation rates at neutral to alkaline conditions and 100–200°C as a function of pH, aqueous solution composition and chemical affinity. Geochim. Cosmochim. Acta, 83, 93–109.

Scambelluri, M., Bebout, G.E., Belmonte, D., Gilio, M., Campomenosi, N., Collins, N., Crispini, L. (2016). Carbonation of subduction-zone serpentinite (high-pressure ophicarbonate; Ligurian Western Alps) and implications for the deep carbon cycling. Earth Planet. Sci. Lett., 441, 155–166.

Scharf, A., Bailey, C.M., Bolhar, R., Mattern, F., Ring, U. (2022). Post-obduction listwaenite genesis in the Oman Mountains inferred from structural analysis and U-Pb carbonate dating. Earth Planet. Sci. Lett., 595, 117756.

Schröder, T., Bach, W., Jöns, N., Jöns, S., Monien, P., Klügel, A. (2015). Fluid circulation and carbonate vein precipitation in the footwall of an oceanic core complex, Ocean Drilling Program Site 175, Mid-Atlantic Ridge. Geochemistry, Geophys. Geosystems, 16(10), 3716–3732.

Schwarzenbach, E.M., Früh-Green, G.L., Bernasconi, S.M., Alt, J.C., Plas, A. (2013). Serpentinization and carbon sequestration: A study of two ancient peridotite-hosted hydrothermal systems. Chem. Geol., 351, 115–133.

Schwartz, J., Kumar, M., Adams, B.L., Field, D.P. (2009). Electron Backscatter Diffraction in Materials Science (Second Edition). Eds: Schwartz, J., Kumar, M., Adams, B.L., Field, D.P., Springer, Boston, MA, p.403.

Schwartz, S., Guillot, S., Reynard, B., Lafay, R., Debret, B., Nicollet, C., Lanari, P., Auzende, A.L. (2013). Pressure–temperature estimates of the lizardite/antigorite transition in high pressure serpentinites. Lithos, 178, 197–210.

Searle, M.P., Cox, J. (1999). Tectonic setting, origin, and obduction of the Oman ophiolite. GSA Bulletin, 111(1), 1042–1122.

Seifritz, W. (1990). CO2 disposal by means of silicates. Nature, 345, 486.

Spiridonov, E.M. (1991). Listvenites and zodites. Int. Geol. Rev., 33, 397–407.

Sofiya, A., Ishiwatari, A., Hirano, N., Tsujimori, T. (2017). Relict chromian spinels in Tulu Dimtu serpentinites and listvenite, Western Ethiopia: implications for the timing of listvenite formation, Int. Geol. Rev., 59, 1621–1631.

Soret, M., Agard, P., Dubacq, B., Plunder, A., & Yamato, P. (2017). Petrological evidence for stepwise accretion of metamorphic soles during subduction infancy (Semail ophiolite, Oman and UAE). J. Metamorph. Geol., 35, 1051–1080.

Sossi, P.A., Halverson, G.P., Nebel, O., Eggins, S.M. (2015). Combined Separation of Cu, Fe and Zn from Rock Matrices and Improved Analytical Protocols for Stable Isotope Determination. Geostand. Geoanalytical Res., 39, 129–149.

Sossi, P.A., Nebel, O., Foden, J. (2016). Iron isotope systematics in planetary reservoirs. Earth Planet. Sci. Lett., 452, 295–308.

Sossi, P.A., Nebel, O., O'Neill, H.S.C., Moynier, F. (2018). Zinc isotope composition of the Earth and its behaviour during planetary accretion. Chem. Geol., 477, 73–84.

Stanger, G. (1985). Silicified serpentinite in the Semail nappe of Oman. Lithos, 18, 13–22.

-T-

Takazawa, E., Okayasu, T., Satoh, K. (2013). Geochemistry and origin of the basal lherzolites from the northern Oman ophiolite (northern Fizh block), Geochem. Geophys., 4(2), 1021.

Tarling, M.S., Rooney, J.S., Viti, C., Smith, S.A.F., Gordon, K.C. (2018). Distinguishing the Raman spectrum of polygonal serpentine. J. Raman Spectrosc., 49, 1978–1984.

Ternieten, L., Früh-Green, G.L., Bernasconi, S.M. (2021a). Carbonate mineralogy in mantle peridotites of the Atlantis Massif (IODP Expedition 357). J. Geophys. Res. Solid Earth, 126, e2021JB021885.

Ternieten, L., Früh-Green, G.L., Bernasconi, S.M. (2021b). Carbon geochemistry of the active serpentinization site at the Wadi Tayin Massif: Insights from the ICDP Oman Drilling Project: Phase II. J. Geophys. Res. Solid Earth, 126, e2021JB022712.

Teng, F.-Z., Dauphas, N., Huang, S., Marty, B. (2013). Iron isotopic systematics of oceanic basalts. Geochim. Cosmochim. Acta, 107, 12–26.

Tominaga, M., Beinlich, A., Lima, E.A., Tivey, M.A., Hampton, B.A., Weiss, B., Harigane, Y. (2017). Multi-scale magnetic mapping of serpentinite carbonation. Nat. Commun., 8, 1870.

Tsikouras, B., Karipi, S., Grammatikopoulos, T.A., Hatzipanagiotou, K. (2006). Listwaenite evolution in the ophiolite mélange of Iti Mountain (continental Central Greece). Eur. J. Mineral., 18(2), 243–255.

-U-

Ulrich, M., Muñoz, M., Guillot, S., Cathelineau, M., Picard, C., Quesnel, B., Boulvais, P., Couteau, C. (2014). Dissolution-precipitation processes governing the carbonation and silicification of the serpentinite sole of the New Caledonia ophiolite. Contrib. Mineral. Petrol., 167, 952.

Üner, T. (2020). Listwaenitization and enrichment of precious metals in the hydrothermal mineralization zones of serpentinites in Sugeçer-Van (Eastern Anatolia, Turkey). Geochem.: Explor. Environ. Anal., 20(1), 68–79.

-V-

Villey, M., Le Metour, J., De Gramont, X. (1986) Geological map of Fanja, Sheet NF 40-3F. Explanatory Notes, BRGM and Oman Ministry of Petroleum & Minerals.

van Kooten, E., Moynier, F. (2019). Zinc isotope analyses of singularly small samples (<5 ng Zn): Investigating chondrule-matrix complementarity in Leoville. Geochim. Cosmochim. Acta, 261, 248–268.

-W-

Wang, Y., Xu, H. (2001). Prediction of trace metal partitioning between minerals and aqueous solutions: a linear free energy correlation approach. Geochim. Cosmochim. Acta, 65, 1529–1543.

Wang, Z.-Z., Liu, S.-A., Liu, J., Huang, J., Xiao, Y., Chu, Z.-Y., Zhao, X.-M., Tang, L. (2017). Zinc isotope fractionation during mantle melting and constraints on the Zn isotope composition of Earth's upper mantle. Geochim. Cosmochim. Acta, 198, 151–167.

Wegner, W.W., Ernst, W.G. (1983). Experimentally determined hydration and dehydration reaction rates in the system MgO-SiO2-H2O. Am. J. Sci., 283, 151–180.

Weyer, S., Anbar, A.D., Brey, G.P., Münker, C., Mezger, K., Woodland, A.B. (2005). Iron isotope fractionation during planetary differentiation. Earth Planet. Sci. Lett., 240, 251–264.

Weyer, S., Ionov, D.A. (2007). Partial melting and melt percolation in the mantle: The message from Fe isotopes. Earth Planet. Sci. Lett., 259, 119–133.

Wicks, F.J., Whittaker, E.J.W. (1977). Serpentine textures and serpentinization. Canad. Mineral., 15(4), 459–488.

Wilde, A., Simpson, L., Hanna, S. (2002). Preliminary study of Cenozoic hydrothermal alteration and platinum deposition in the Oman Ophiolite. In: Jessell, M.J. (Ed.), General Contributions. J. Virtual Explorer, 6, 7–13

Williams, H.M., Peslier, A.H., McCammon, C., Halliday, A.N., Levasseur, S., Teutsch, N., Burg, J.P. (2005). Systematic iron isotope variations in mantle rocks and minerals: the effects of partial melting and oxygen fugacity. Earth Planet. Sci. Lett. 235, 435–452.

Wood S.A. (1990). The aqueous geochemistry of the rare earth elements and yttrium. Review of available low temperature data for inorganic complexes and the inorganic REE speciation of natural waters. Chem. Geol., 82, 159–186.

X-Y-Z

Zeng, Z., Li, X., Chen, S., de Jong, J., Mattielli, N., Qi, H., Pearce, C., Murton, B.M. (2021). Iron, copper, and zinc isotopic fractionation in seafloor basalts and hydrothermal sulfides. Mar. Geol., 436, 106491.

Zhang, L., Yang, J., Robinson, P., Xiong, F., Chen, Y., Lai, S., Chen, M. (2015). Origin of Listwanite in the Luobusa Ophiolite, Tibet, Implications for Chromite Stability in Hydrothermal Systems. Acta Geol. Sin., 89(2), 402–417.

Zhang, L., Sun, W.-D., Zhang, Z., A, Y., Liu, F. (2019). Iron isotopic composition of supra-subduction zone ophiolitic peridotite from northern Tibet. Geochim. Cosmochim. Acta, 258, 274–289.

Appendix

Appendix to Chapter 2

JGR Solid Earth

RESEARCH ARTICLE
10.1029/2021JB022733

Special Section:
Ophiolites and Oceanic Lithosphere, with a focus on the Samail ophiolite in Oman

Geochemical Profiles Across the Listvenite-Metamorphic Transition in the Basal Megathrust of the Semail Ophiolite: Results From Drilling at OmanDP Hole BT1B

M. Godard[1], E. J. Carter[2,3], T. Decrausaz[1], R. Lafay[1], E. Bennett[4], F. Kourim[5], J.-C. de Obeso[6], K. Michibayashi[7], M. Harris[8], J. A. Coggon[9], D. A. H. Teagle[9], P. B. Kelemen[6], and the Oman Drilling Project Phase 1 Science Party[10]

[1]Géosciences Montpellier, CNRS, Université de Montpellier, Montpellier, France, [2]Department of Earth and Environmental Sciences, The University of Manchester, Manchester, UK, [3]Department of Geology, Trinity College Dublin, Dublin, Ireland, [4]School of Earth and Ocean Sciences, Cardiff University, Cardiff, UK, [5]Academia Sinica, Institute of Earth Science, Taipei, Taiwan, [6]LDEO, Columbia University, Palisades, NY, USA, [7]Department of Earth and Planetary Sciences, Graduate School of Environmental Studies, Nagoya University, Nagoya, Japan, [8]School of Geography, Earth and Environmental Sciences, Plymouth University, Plymouth, UK, [9]School of Ocean & Earth Science, University of Southampton, Southampton, UK, [10]See Appendix A

Key Points:

- BT1B listvenite series and metamorphic sole derive from partially serpentinized basal banded peridotites and alkaline basalts respectively
- Chemical redistribution suggests reactions with several batches of CO_2-rich fluids over various flow paths parallel to the basal thrust
- Listvenitization due to CO_2 metasomatism could represent a major trap-and-release mechanism for CO_2, fluid mobile elements and H_2O along convergent margins

Supporting Information:

Supporting Information may be found in the online version of this article.

Correspondence to:

M. Godard,
Marguerite.Godard@umontpellier.fr

Citation:

Godard, M., Carter, E. J., Decrausaz, T., Lafay, R., Bennett, E., Kourim, F., et al. (2021). Geochemical profiles across the listvenite-metamorphic transition in the basal megathrust of the Semail ophiolite: Results from drilling at OmanDP Hole BT1B. *Journal of Geophysical Research: Solid Earth*, *126*, e2021JB022733. https://doi.org/10.1029/2021JB022733

Received 8 JUL 2021
Accepted 25 NOV 2021

Author Contributions:

Conceptualization: M. Godard
Data curation: M. Godard, E. Bennett, F. Kourim
Formal analysis: M. Godard, E. J. Carter
Funding acquisition: M. Godard, D. A. H. Teagle, P. B. Kelemen
Investigation: M. Godard, T. Decrausaz, R. Lafay, E. Bennett, F. Kourim, J.-C. Obeso
Methodology: M. Godard, E. J. Carter

Abstract The transition from the Semail ophiolite mantle to the underlying metamorphic sole was drilled at ICDP OmanDP Hole BT1B. We analyzed the bulk major, volatile and trace element compositions of the mantle-derived listvenite series and metamorphic rocks, with the aim to constrain chemical transfers associated with peridotite carbonation along the ophiolite basal thrust. The listvenite series comprise variously carbonated serpentinites and (fuchsite-bearing) listvenites. They have high CO_2 (up to 43 wt.%) and variable H_2O (0–12 wt.%). Yet, they have compositions close to that of the basal banded peridotites for most major and lithophile trace elements, with fuchsite-bearing listvenites overlapping in composition with amphibole-bearing basal lherzolites (e.g., Al_2O_3 = 0.1–2.2 wt.%; Yb = 0.05–1 x CI-chondrite). The protolith of the listvenite series was likely similar in structure and composition to serpentinized banded peridotites which immediately overlie the metamorphic sole elsewhere in Oman. The listvenite series are enriched in fluid mobile elements (FME) compared to Semail peridotites (up to ~10^3–10^4 x Primitive Mantle), with concentrations similar to the underthrusted metabasalts and/or metasediments for Cs, Sr and Ca and sometimes even higher for Pb, Li, As, and Sb (e.g., Li up to 130 µg/g; As up to 170 µg/g). We also observe a decoupling between Sr-Ca enrichments and other FME, indicating interactions with several batches of deep CO_2-rich fluids transported along the basal thrust. These results suggest that peridotite carbonation could represent one of the major trap-and-release mechanisms for carbon, water and FME along convergent margins.

Plain Language Summary Ophiolites are sections of oceanic lithosphere emplaced on-land as tectonic plates converge. The faults developed at their base are analogues to plate interfaces in subduction zones, where mass transfers occur and play a key role in the global cycling of elements. A core was drilled at the base of the Semail Ophiolite, where variously hydrated and carbonated mantle rocks known as serpentinites and listvenites witnessed major fluid fluxes. Reactions with CO_2-bearing fluids (carbonation reaction) enhanced the mobility of elements during mass transfers along the basal thrust. We measured the elemental composition of 84 samples spaced along this core. Results indicate that CO_2-bearing fluids derive from at least two sources or pathways. As peridotites reacted, their volume increased, causing cracking, helping the ingress of reactive fluids and allowing (almost) complete carbonation of the basal ophiolite mantle. Carbon as well as many elements such as cesium, arsenic, antimony, lead, became enriched in these rocks. If forming in subduction zones, listvenites may act as temporary storage for these elements and impact global chemical cycles.

1. Introduction

Listvenites (or listwaenites) are produced by CO_2-metasomatism of mantle-derived ultramafic rocks (Falk & Kelemen, 2015; Halls & Zhao, 1995). They are composed mainly of quartz and carbonate (magnesite and/or dolomite, ±Cr- or Mg-rich micas ± chlorite) and are often associated with serpentinites, ophicarbonates and/or talc. Since their first description in the literature (Rose, 1837), they have been investigated for one of their main characteristics: the occurrence of mineralizations concentrating economically valuable metals, such as Au, Pb-Hg-Ag, Cu, Ni, Co or Sb (e.g., Belogub et al., 2017; Buisson & Leblanc, 1985; Escayola et al., 2009;

Project Administration: M. Harris, J. A. Coggon, D. A. H. Teagle, P. B. Kelemen
Resources: M. Godard
Software: E. J. Carter
Supervision: M. Godard, K. Michibayashi, D. A. H. Teagle, P. B. Kelemen
Validation: M. Godard, E. J. Carter, R. Lafay, J.-C. Obeso
Visualization: E. J. Carter, T. Decrausaz
Writing – original draft: M. Godard
Writing – review & editing: M. Godard, E. J. Carter, T. Decrausaz, R. Lafay, E. Bennett, F. Kourim, J.-C. Obeso, K. Michibayashi, M. Harris, J. A. Coggon, D. A. H. Teagle, P. B. Kelemen

Halls & Zhao, 1995; Laznicka, 2010). More recently, they have been studied also as natural analogues for industrial geological carbon storage in ultramafic basement (Falk & Kelemen, 2015; Hansen et al., 2005; Ulrich et al., 2014).

These studies have highlighted the structural, mineralogical and petrological complexity of listvenites, thus resulting in a wealth of different and sometimes contradictory genetic models (Belogub et al., 2017; Falk & Kelemen, 2015; Halls & Zhao, 1995; Nasir et al., 2007). Some authors evoke serpentinization of mantle peridotites followed by the formation, concurrent or consecutive, of carbonate (carbonation) and quartz (silicification) (Boschi et al., 2009; Nasir et al., 2007; Stanger, 1985; Ulrich et al., 2014), whilst others suggest direct reactions with primary mantle minerals (Hansen et al., 2005; Kelemen et al., 2011; Power et al., 2013). Other authors stress the role of the composition of the infiltrating CO_2-bearing fluid rather than that of the protolith in the genesis of listvenites and associated ore-grade mineralizations (Belogub et al., 2017; Escayola et al., 2009; Halls & Zhao, 1995; Menzel, Garrido, & López Sánchez-Vizcaíno, 2020; Menzel et al., 2018; Stanger, 1985), often emphasizing a possible imprint of silica and other cations scavenged from neighboring lithologies (Nasir et al., 2007; Ulrich et al., 2014). The estimated temperatures of formation and the proposed source(s) of fluids also differ: fluid-inclusions and thermodynamic analyses of carbonate-quartz assemblages suggest reaction within a temperature range from 120 to 280°C (down to 80°C and up to 400°C) and likely triggered by the infiltration of slab-derived fluids (Belogub et al., 2017; Boskabadi et al., 2020; Escayola et al., 2009; Hansen et al., 2005; Menzel et al., 2018). On the other hand, petrographic and geochemical analyses show also that some listvenite series were formed during weathering (<50°C) by silicification reactions triggered by interactions with fluids in equilibrium with atmospheric CO_2 (e.g., (Stanger, 1985; Ulrich et al., 2014) whilst others show evidence for distinct fluid infiltration and weathering episodes (e.g., Nasir et al., 2007). Finally, the mechanisms allowing the infiltration of the CO_2-rich metasomatic fluids remain speculative with suggested mechanisms including the role of large faults and deformation, reactive cracking and dissolution (Escayola et al., 2009; Falk & Kelemen, 2015; Nasir et al., 2007).

The first difficulty to unravel the genesis of listvenites stems from their environments: they crop out along ophiolitic and orogenic belts as part of highly altered rock assemblages, which often have undergone several stages of metamorphic and tectonic overprint (e.g., Azer et al., 2019; Halls & Zhao, 1995; Menzel et al., 2018; Nasir et al., 2007). For these reasons, both the protolith and potential CO_2 source(s) for listvenite-forming metasomatism are difficult to identify, and display significant structural, mineralogical and compositional variability. Only a few sites allow sampling the transition from mantle peridotites to the possible source(s) of CO_2 metasomatism: the Semail ophiolite is one of them.

The Semail ophiolite is a fragment of Tethyan oceanic lithosphere tectonically emplaced on the Arabian plate at the end of the Cretaceous (Figure 1a). Listvenite bodies occasionally crop out along its basal thrust (Falk & Kelemen, 2015; Glennie et al., 1974; Nasir et al., 2007; Figure 1a). In 2017, a 300m long section was drilled through one of the largest bodies, north of Wadi Mansah (Fanjah, Sultanate of Oman1a), as part of the ICDP Oman Drilling Project (OmanDP (Kelemen et al., 2020)). OmanDP Hole BT1B sampled the transition from a sequence of listvenites and variously carbonated serpentinites, through the basal thrust of the ophiolite, to its metamorphic sole (Figure 1b). This sampling allows us (a) to quantify the geochemical variations associated with the broad and complex range of mineralogy and rock types that are typical of listvenite suites and (b) for the first time, to correlate these variations with the distance to a major pathway for the fluids triggering their formation, here the basal thrust.

We carried out a bulk rock geochemical study (major, volatile and trace elements) of 84 samples representative of the different lithologies recovered at OmanDP Hole BT1B. Our results enable us to document the bulk composition of these different lithologies and their downhole variations from the sample scale to that of the borehole. This provides important new insights into the composition of the protolith of the Semail listvenite series and of the underlying metamorphic lithologies, and highlights the magnitude of fluid-mediated elemental transfers associated with the formation of listvenites along the basal thrust and into the overlying ophiolitic mantle.

2. Geological Setting

2.1. The Semail Ophiolite

The Semail ophiolite is composed of a dozen structural massifs outcropping over 500 km along the north-eastern margin of the Arabian Plate (~20,000 km^2); it is regarded as one of the world's largest and best documented

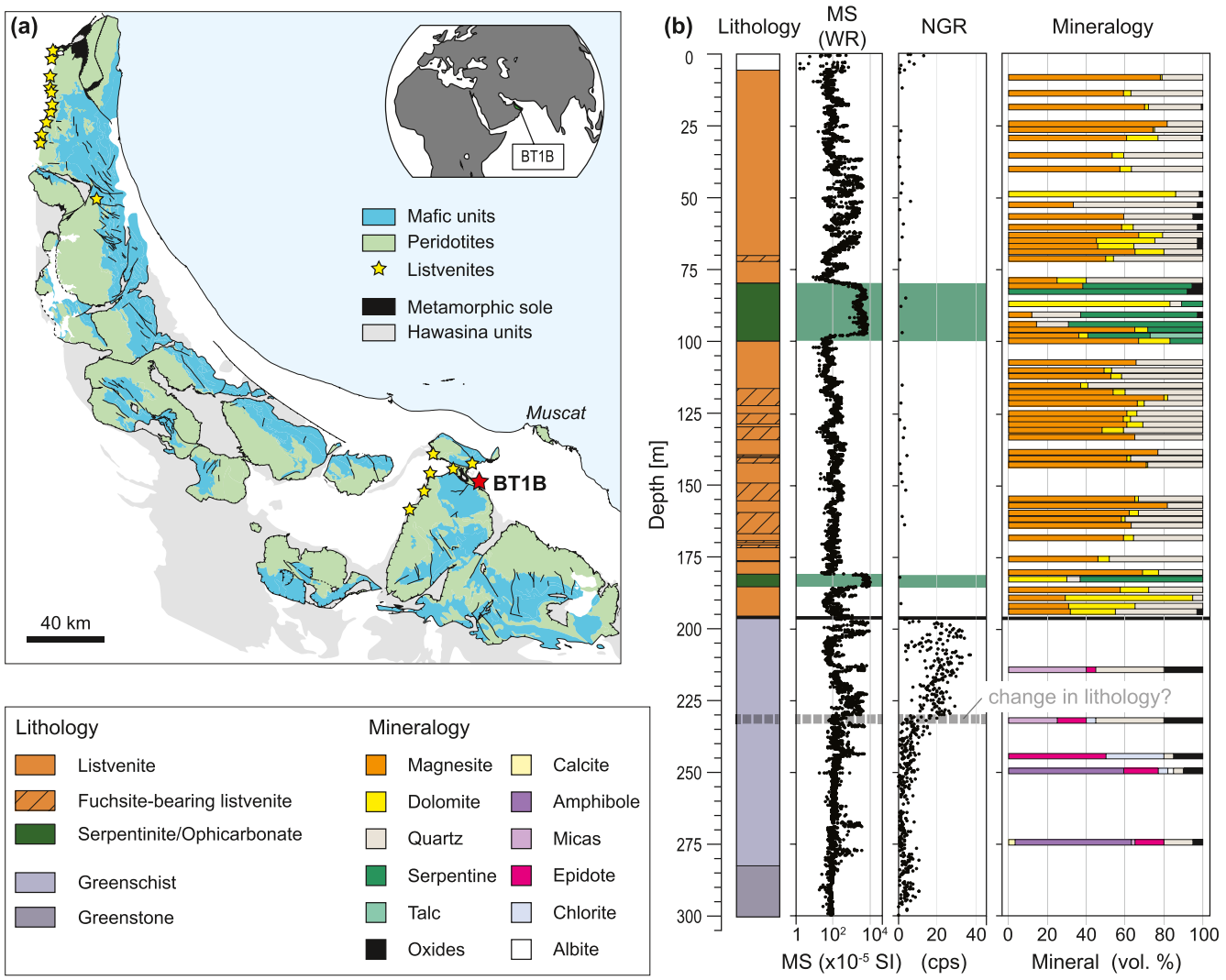

Figure 1. Location and downhole plots of lithological and physical properties of OmanDP Hole BT1B. (a) Simplified geological map of the Semail ophiolite. Yellow and red stars represent regional occurrences of listvenites and the location of OmanDP Hole BT1B, respectively (after Boudier & Nicolas, 2018); (b) Downhole plots of drilled lithologies, magnetic susceptibility (MS), natural gamma rays (NGR), and mineral proportions (data from Kelemen et al., 2020); mineral proportions are estimated based on thin section observations and X-ray diffraction analysis.

ophiolites (Figure 1a; Boudier & Nicolas, 1988; Coleman & Hopson, 1981; Goodenough et al., 2010; Lippard et al., 1986; Peters et al., 1991; Searle, 2019). The 5–7 km thick structural massifs were initially more than 12–15 km thick according to structural reconstitutions, and expose continuous fragments of the Tethyan oceanic lithosphere: the ophiolitic sequence comprises a thick mantle section overlain by a well preserved layered oceanic crust, from lower gabbros to upper volcanics (Lippard et al., 1986; Nicolas et al., 2000), formed at the end of the Cretaceous (96.1–95.2 Ma (Rioux et al., 2021)). The geochemistry of the upper volcanics indicates a transition from oceanic accretion to subduction related volcanism (e.g., Belgrano et al., 2019; Ernewein et al., 1988; Godard et al., 2003), that has been interpreted as evidence for a spontaneously initiating subduction (e.g., MacLeod et al., 2013; Pearce et al., 1981) or for a change in geodynamic settings, from mid-ocean ridge to intra-oceanic underthrusting and/or incipient subduction (e.g., Boudier et al., 1988; Godard et al., 2006; Goodenough et al., 2010).

The mantle section is predominantly made up of moderately serpentinized (40%–80%) depleted harzburgites with minor dunites (Boudier et al., 2010; Godard et al., 2000; Hanghoj et al., 2010; Hopson et al., 1981), that preserve the microstructural fabric of asthenospheric deformation below the oceanic spreading center (Boudier

& Coleman, 1981). Low temperature ductile deformation overprints this early deformation toward the base of the mantle section and has been ascribed to the onset of the ophiolite detachment (e.g., Boudier et al., 1988; Linckens et al., 2011; Nicolas et al., 2000). Local occurrences of lherzolites (>5% clinopyroxene, Cpx) and Cpx-harzburgites (>2% Cpx) are also described in this lowermost mantle section, generally in massifs where the thickest mantle sections were preserved (e.g., Fizh (Takazawa et al., 2003); Wadi Tayin (Godard et al., 2000; Hanghoj et al., 2010)) and/or close to areas where the ophiolitic metamorphic sole outcrops (Khedr et al., 2014). These Cpx-rich basal peridotites have been interpreted as the result of variable melt extraction along the palaeoridge (Khedr et al., 2014; Le Mée et al., 2004; Monnier et al., 2006) or, alternatively, as due to refertilization reactions at the base of the oceanic mantle lithosphere during off-axis cooling or early intraoceanic thrusting (Godard et al., 2000; Lippard et al., 1986; Takazawa et al., 2003).

The ophiolite lies upon a series of underthrusted sheets of pelagic and turbiditic sediments, shelf carbonates, as well as volcanics, mainly of alkaline composition (sometimes referred to as Haybi volcanics) with minor transitional to tholeiitic components (Bechennec et al., 1990; Chauvet et al., 2011; Lippard et al., 1986; Maury et al., 2003). These lithologies – commonly grouped as the Hawasina assemblages – are the relicts of a wide oceanic basin (at least 540 km across), that formed during the breakup and thinning of the Arabian continental margin during Permian to Trias (Bechennec et al., 1990).

The ophiolite *sensu stricto* and the underlying allochtonous units were thrusted atop the Arabian platform during late Cretaceous (e.g., Glennie et al., 1974; Searle & Malpas, 1980). Slivers of the ophiolite metamorphic sole are preserved at the transition from the allochtonous units to the base of the ophiolite mantle section. They are locally overlain by a <200 m thick (proto-)mylonitic "Banded Unit", deformed parallel to the basal contact, comprising basal lherzolites (or Cpx-harzburgites) alternating with harzburgites and/or dunites; all being highly serpentinized (Lippard et al., 1986; Prigent, Guillot, et al., 2018). The Banded Unit peridotites preserve evidence of secondary amphibole formed at the expense of Cpx and their constituent minerals systematically display preferential enrichments in highly incompatible and fluid mobile elements (FME) (Khedr et al., 2013; Prigent, Agard, et al., 2018). The sole is composed of slivers of metamorphosed mafic crust with subordinate metasediments and serpentinites stripped from/by the underthrusted lithosphere. It is characterized by an inverted metamorphic gradient, from low temperature (LT) greenschist facies at the base up to high temperature (HT) amphibolite/granulite facies at the upper contact with the ophiolite mantle (Ghent & Stout, 1981; Searle & Cox, 1999; Soret et al., 2017). Geochronology indicates that peak HT metamorphism is only slightly younger than the ophiolite crustal sequence (96.16–94.82 Ma (Rioux et al., 2016; Warren et al., 2005)) suggesting that the overlying mantle lithosphere was young and hot when the metamorphic sole formed.

Listvenites outcrop irregularly along the basal thrust of the the Semail Ophiolite, often as 2–50 m wide bodies within the highly altered ophiolitic and sedimentary mélange in contact with its metamorphic sole (Figure 1a; Glennie et al., 1974; Nasir et al., 2007; Stanger, 1985; Wilde et al., 2002). One of the largest listvenite bodies outcrops over $\sim 1 \times 2$ km^2 in the Wadi Mansah area (South of Muscat). It includes large lenses of serpentinites and marks the transition from mantle peridotites to underlying greenschist facies meta-basalts and silicic sediments (Falk & Kelemen, 2015; Villey et al., 1986). This site was chosen to drill OmanDP Hole BT1B with the objective of sampling the transition from the ophiolite mantle section to its metamorphic sole.

2.2. OmanDP Hole BT1B and Sampling

Drilling at OmanDP Hole BT1B (23°21.861′N, 58°20.149′E) recovered 300.05 m of continuous cores (diameter 63.5 mm (HQ) down to 167.10 mbg and 47.6 mm (NQ) below). The mineralogy, alteration and structure of the cores and their main physical and chemical properties were measured on-board drilling vessel D/V Chikyu on whole cores, core sections (Visual Core Description — VCD) and thin sections, and reported in the OmanDP proceedings (Kelemen et al., 2020). The main characteristics of the cores are summarized thereafter.

Below a few meters of alluvial material, Hole BT1B drilled first through a series of listvenites interlayered with serpentinites (hereafter grouped as the *listvenite series*), then through the basal thrust at ~197 m below ground (mbg) and into the metamorphic sole (Figure 1b).

Listvenites comprise dominantly magnesite ± dolomite and quartz; they are characterized by their pale yellow to dark reddish brown color in hand specimen. They contain relicts of chromian spinel and of magnetite alignments indicating that their protolith was a serpentinized peridotite. Between ~110 and 182 mbg, fuch-

site, a chromian mica ($(K,Na)(Al,Cr,Fe)_2(Si,Al)_3O_{10}(OH,F)_3$), is commonly observed; it occurs as light green quartz-fuchsite intergrowths forming mm- to cm-size green spots easily recognizable on hand samples. Listvenites are highly brecciated down to ~80 mbg and the presence of altered and fragmented veins and breccia, associated with occurrences of hematite and goethite, results in variable and sometimes high magnetic susceptibility (Figure 1b).

Serpentinites have dark- to olive-green colors and high magnetic susceptibility values (Figure 1b). They were recovered at 80.28–100.23 mbg and 181.26–185.47 mbg. Serpentinites are foliated to massive, they comprise mesh texture serpentine (lizardite) delineated by magnetite and subordinate bastite. They are crosscut by abundant light-green to white veins of dolomite (±magnesite) and serpentine with, locally, carbonates replacing the serpentine matrix. Variously carbonated serpentinites are distinguished from listvenites by the absence of quartz, but minor talc is found locally at ~98–100 mbg, close to the contact with listvenites.

The metamorphic sole is composed of greenish, microcrystalline and finely laminated schists (197.6–282.88 mbg) and greenstone (below 282.88 mbg) interpreted during shipboard logging as metasediments and metabasalts respectively. It comprises epidote, chlorite, albite, quartz, titanite, with carbonate and/or muscovite in schists and blue-green amphibole and minor pumpellyite in greenstones. The contact with the listvenite series occurs at 196.56–197.6 mbg. This tectonic contact is a fault gouge mixed with clasts of highly fragmented, fine-grained, chlorite- and epidote-bearing rocks. It is characterized by a strong and sharp increase in the Natural Gamma Radiation values (NGR), jumping from on average <1 cps (counts/s) in the upper parts of Hole BT1B to >30 cps at the thrust, then gradually decreasing downhole over ~30–40 m to relatively homogeneous and low values (<5 cps) (Figure 1b).

84 samples (~40 cm^3) were collected from Hole BT1B for bulk rock geochemical measurements. The VCD rocknames were used to designate geochemistry samples because of the high petrographic variability of the core, in particular for the samples from the listvenite series that typically comprised variable amounts of serpentine, carbonate and/or quartz veins. 51 listvenites, 14 serpentinites, and 19 greenshists and greenstones were analyzed. Every 20 m, a sample was taken during the drilling operations, and 15 on-site samples were thus collected. During the description of the cores on board D/V Chikyu, 59 samples were selected by the shipboard science party as representative of the different lithologies recovered from Hole BT1B. 10 additional listvenites and serpentinites were selected from Sections C5704 B-73Z-1 to −75Z-2 (180.01–186.945 mbg) for on-shore studies ("consortium samples").

3. Methods

The major element composition of BT1B samples was determined by X-ray fluorescence (XRF) on-board D/V Chikyu for the drillsite and shipboard samples and at GeoLabs (Ontario, Canada) for consortium samples. Total H_2O and CO_2 concentrations and abundances of inorganic carbon (total inorganic carbon, TIC) in the drillsite and shipboard samples were determined on-board D/V Chikyu by combustion CHNS elemental analysis (EA) and coulometry, respectively. The FeO concentration of a subset of samples (8 serpentinites and 21 Listvenites) was quantified at the University of Lausanne (ISTE) following the Fe-titration protocol of Wilson (1960). The trace element composition (Li, Sc, Ti, V, Mn, Co, Ni, Cu, Ga, As, Sn, Sb, Rb, Sr, Y, Zr, Nb, Cs, Ba, Rare Earth Elements (REE), Hf, Ta, Pb, Th, U, W) of the drillsite, shipboard and consortium samples was analyzed by Inductively Coupled-Plasma-Mass Spectrometry (ICP-MS) at Géosciences Montpellier (AETE-ISO Facility, University of Montpellier, France) using the protocol described in Godard et al. (2000). The preparation of the samples and the analytical procedures are detailed in Text S1 in Supporting Information S1. The main lithological characteristics of the analyzed samples and their major, trace and volatile element concentrations are reported in Dataset S1.

4. Results

The listvenite series and the underlying metamorphic sole are distinguished by significant downhole differences in the values of several geochemical indicators, such as loss on ignition (LOI), Mg# (100 x molar (Mg/(Mg + Fe), with all Fe as Fe^{2+}), Al_2O_3 and trace element contents as illustrated on Figures 2 and 3. These variations allow us to discriminate several lithological and geochemical domains along Hole BT1B.

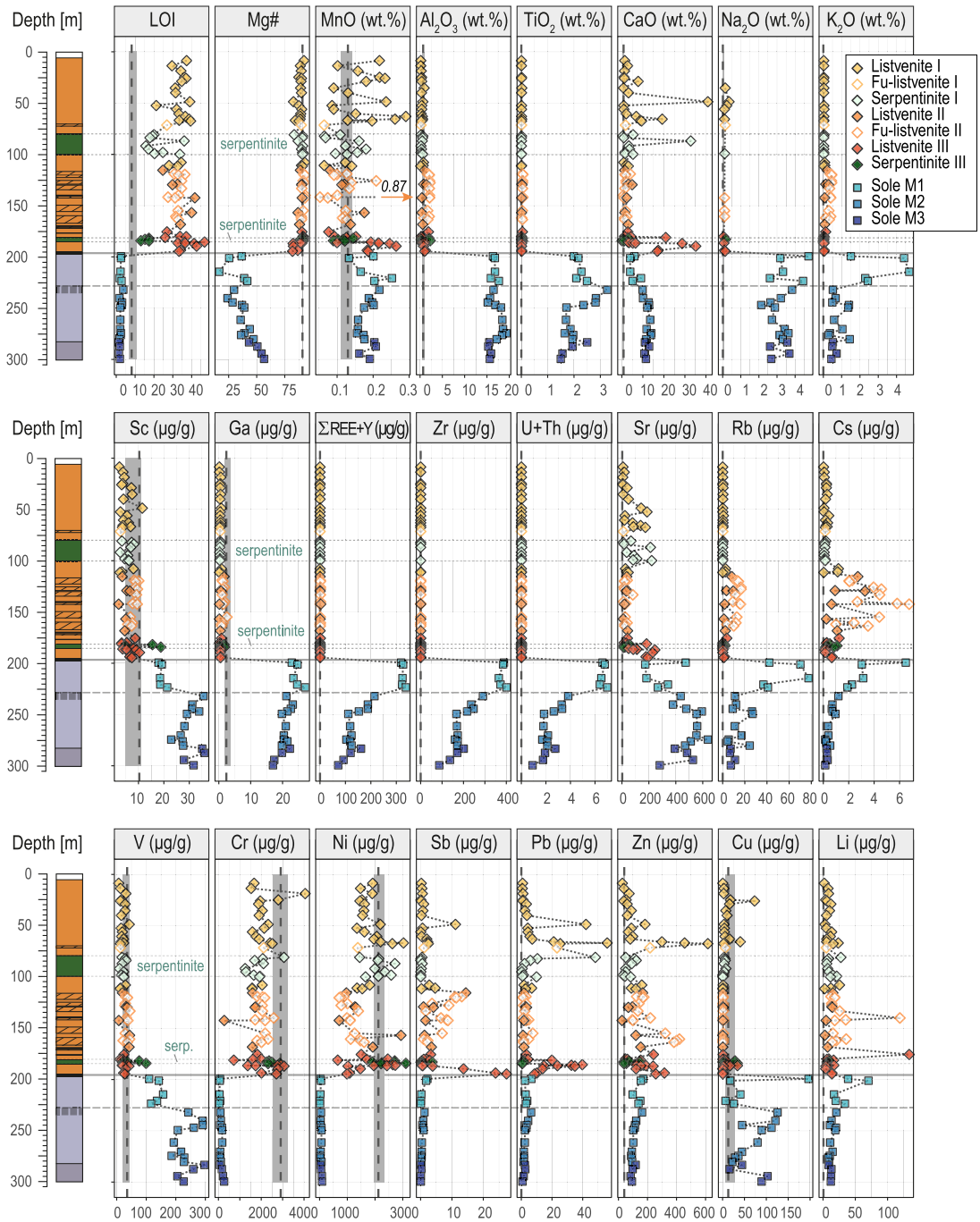

Figure 2. Concentrations of selected geochemical species plotted by depth downhole for all BT1B samples. Dashed line indicates the median concentration from literature data for peridotites from the main mantle section (MMS) of the Semail Ophiolite ($n = 92$; [Gerbert-Gaillard, 2002; Godard et al., 2000; Hanghoj et al., 2010]), and the gray field indicates ±1 standard deviation (calculated as the 16th and 84th percentile) about the median (Table S2). Major oxides are plotted on a volatile free basis. Symbols are in inset. Listvenites, fuchsite-bearing listvenites (Fu-listvenites), serpentinites and ophicarbonates (grouped as Serpentinites) from Listvenite domains I, II and III are noted I, II and III respectively. Samples from the metamorphic sole (noted sole) are grouped as M1, M2, and M3.

4.1. Geochemistry of the Listvenite Series (Depth: 6.02–196.56 mbg)

The listvenite series are characterized by high LOI (13.1–46.8 wt.%), high Mg# (~90), high concentrations in transition metals such as Ni (up to 3,110 µg/g), Co (up to 128 µg/g) and Cr (up to 4,050 µg/g), low concentrations in Al_2O_3 (<2 wt.%), Na_2O (~0.1 wt.%) and TiO_2 (<0.1 wt.%) and in incompatible lithophile trace elements, such as Th (<<0.005 µg/g), REE (ΣREE <1 µg/g) and high field strength elements (HFSE, e.g., Zr~0.1 µg/g). These

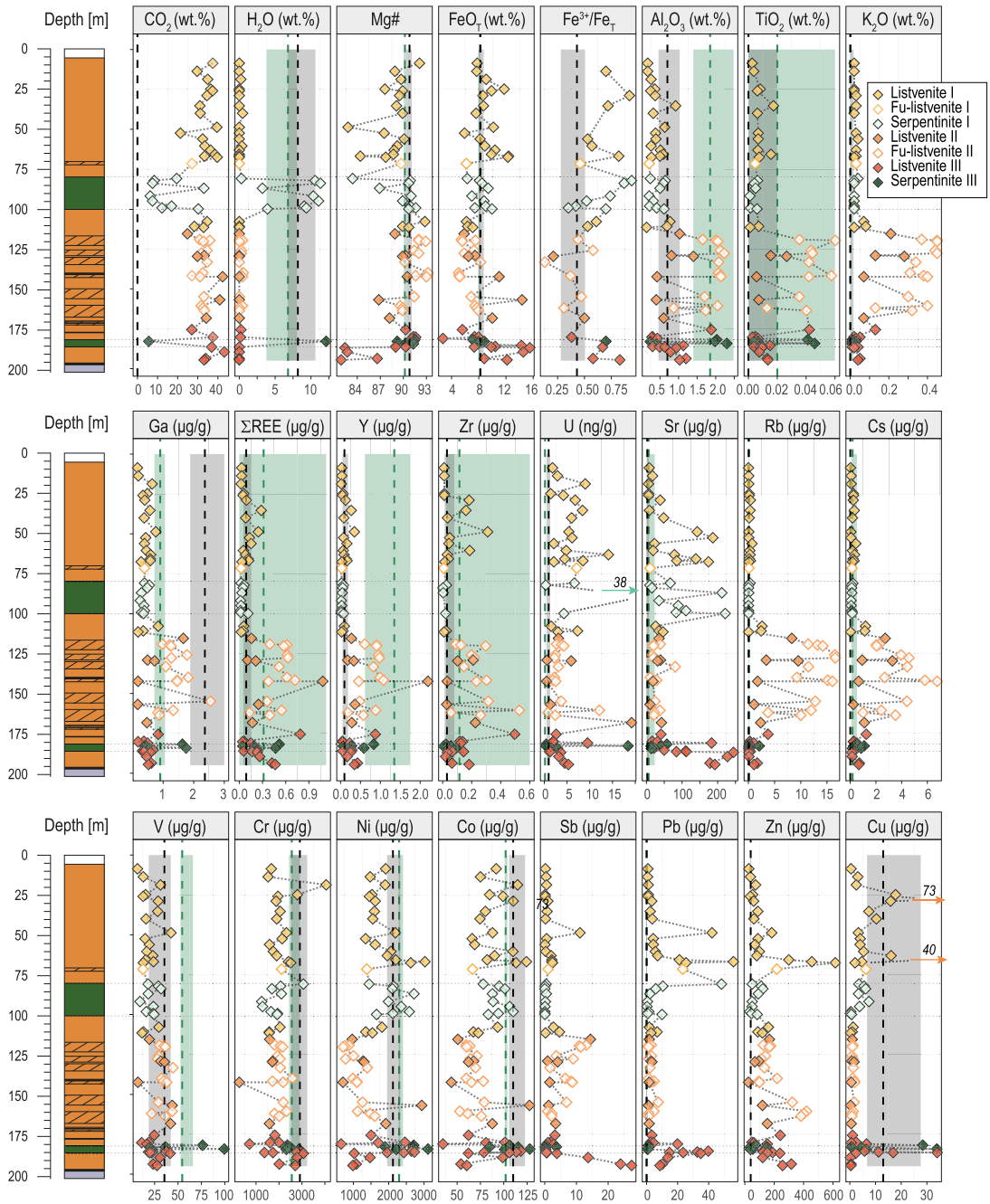

Figure 3. Concentrations of selected geochemical species plotted by depth downhole for BT1B listvenite series. Dashed gray and green lines indicate the median concentration from literature data for the MMS peridotites ($n = 92$) and basal lherzolites ([Lippard et al., 1986; Takazawa et al., 2003]; $n = 13$) of the Semail ophiolite, respectively. Fields of the corresponding color indicate ±1 standard deviation (calculated as the 16th and 84th percentile) about the median (Table S2). Symbols for are in inset, abbreviations are as in Figure 2.

compositions are highly variable downhole at the sample- to the meter scale yet they overlap, on average, that of the Semail ophiolite mantle (Figures 2–5).

Volatile elements dominate the composition of the listvenite series. Listvenites have high CO_2 indicative of the predominance of carbonates (LOI > 21.2 wt.%; CO_2 = 21.3–43.2 wt.%) but no H_2O (~0 wt.%). Serpentinites display the highest H_2O contents (up to 12.1 wt.%), primarily hosted by serpentines, which structurally comprise ~13 wt.% H_2O (Deer et al., 1996), and they have the lowest LOI (down to 13.1 wt.%) and CO_2 (down to 5.6 wt.%) values. Carbonate-rich serpentinites have intermediate compositions with LOI up to 36.1 wt.%, CO_2 up to 33.1

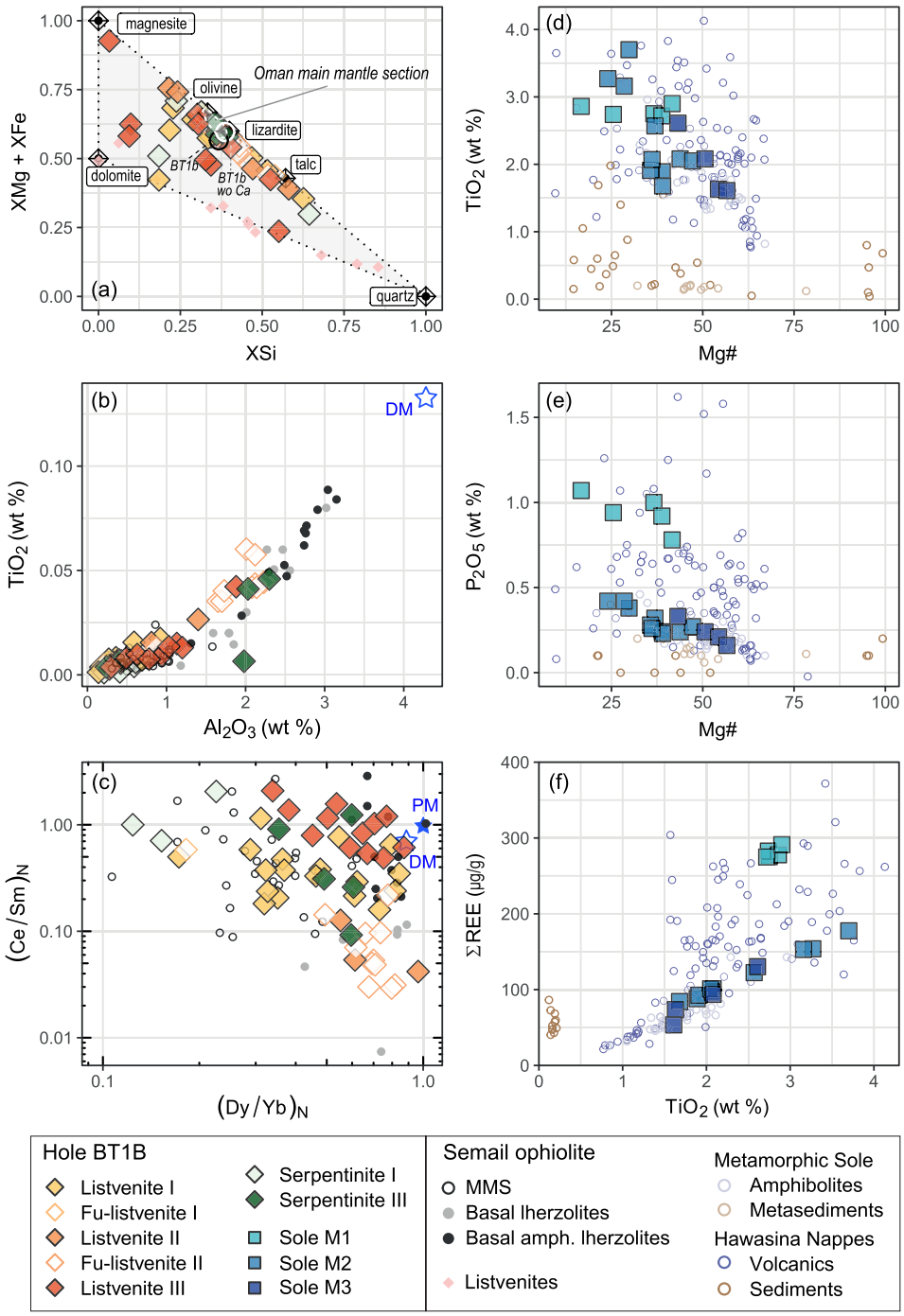

Figure 4. Scatterplots of the composition of BT1B samples. Listvenite series are plotted on (a) (XMg + XFe) versus XSi (X = cation molar proportion), (b) TiO_2 (wt.%) versus Al_2O_3 (wt.%), (c) Chondrite normalized (La/Sm) versus (Dy/Yb) diagrams. The metamorphic sole is plotted on (d) TiO_2 (wt.%) and (e) P_2O_5 (wt.%) versus Mg# and (f) Total REE (µg/g) versus TiO_2 (wt.%) diagrams. (a) The composition of listvenite series are compared to that of the refractory peridotites from the Semail Ophiolite (white field), magnesite, dolomite, quartz, talc, lizardite and olivine (Deer et al., 1996), and the mean composition of listvenite series (black circle) also, recalculated as Ca free (white circle). (b) TiO_2 and Al_2O_3 are plotted on a volatile-free basis and, when available, recalculated ICPMS data was used for plotting TiO_2. The composition of depleted mantle (DM [Salters & Stracke, 2004]), primitive mantle (PM [McDonough & Sun, 1995]) and/or literature data from the Semail mantle (MMS [Gerbert-Gaillard, 2002; Godard et al., 2000; Hanghoj et al., 2010], basal lherzolites [Lippard et al., 1986; Takazawa et al., 2003] and amphibole bearing basal lherzolites—Basal amph. lherzolites [Khedr et al., 2014]) and listvenites (Falk & Kelemen, 2015) are shown for comparison on (a), (b) and (c). The composition of Permian and Triassic volcanics ([Chauvet et al., 2011; Lapierre et al., 2004; Lippard et al., 1986; Maury et al., 2003]) and sediments (Oberhänsli et al., 1999) from the underthrusted Hawasina nappes, and of amphibolites and metasediments from the metamorphic sole (Ishikawa et al., 2005) are shown for comparison on (d), (e), and (f). Symbols are in legend, abbreviations are as in Figure 2.

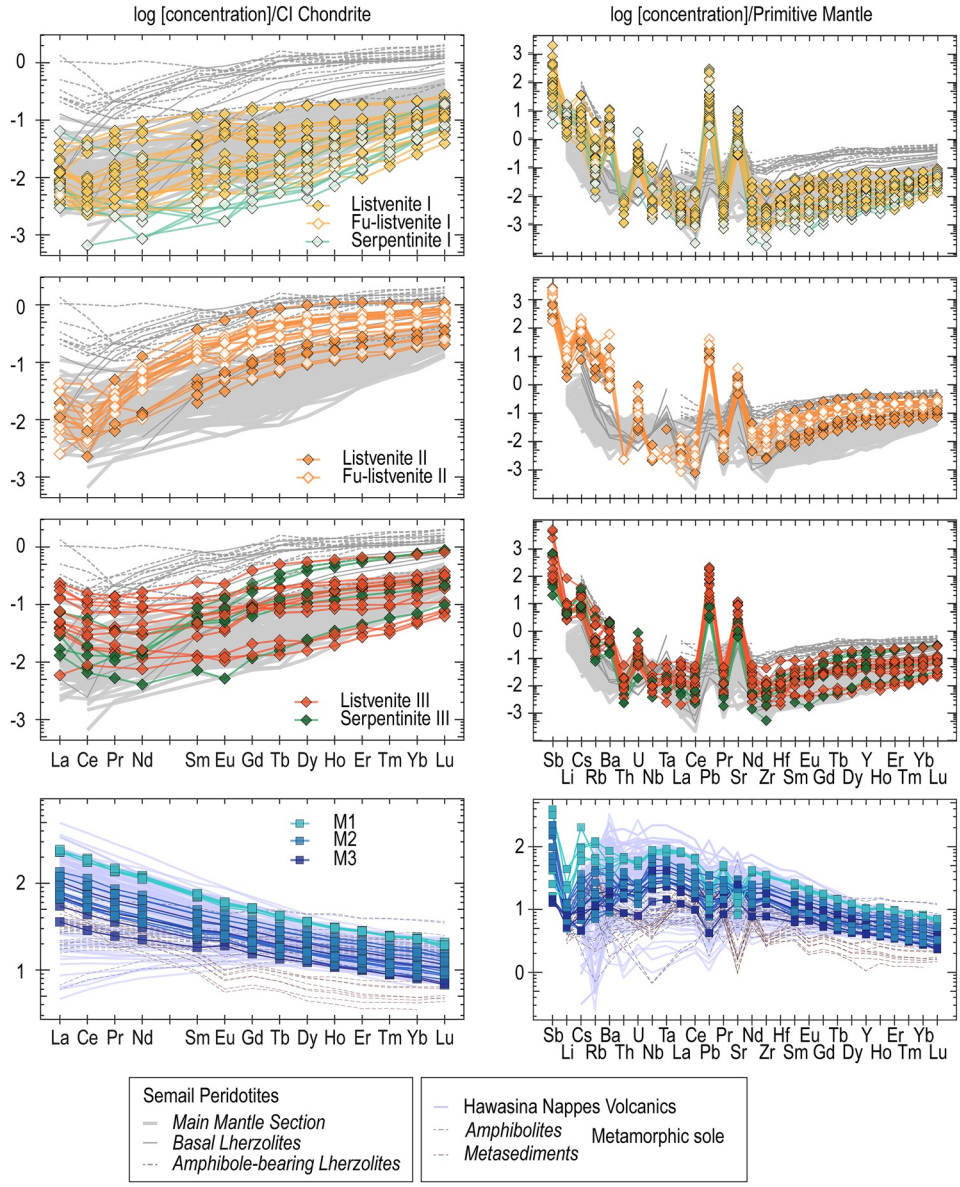

Figure 5. Rare-earth element (REE) and trace element spider diagrams for BT1B samples. Separate panels are plotted for Listvenite domains I, II and III, and for the metamorphic sole. Left: CI chondrite-normalized REE patterns. Right: Primitive mantle-normalized trace element plots; normalizing values from McDonough and Sun (1995). Literature data from Semail Ophiolite peridotites are plotted for reference in the upper three panels, and from metamorphic sole and Hawasina nappes in the lowermost panel (references in caption of Figure 4). Symbols are in inset and legend beneath the plots, abbreviations are in Figure 4.

wt.% and H_2O as low as 0.3 wt.%. As the shipboard coulometry protocol does not allow the complete dissolution of magnesite (see Text S1 in Supporting Information S1), only the samples in which dolomite is the dominant carbonate species have similar TIC and total carbon values. Most of these samples are serpentinites ($CO_{2(TIC)}$ up to 33.3 wt.%; $CO_{2(TIC)}$: TIC recalculated as CO_2).

Aside from volatile elements, the listvenite series are composed mainly of Si, Mg, Fe and Ca: these elements calculated as oxides represent ~99% of the samples volatile-free mass. Their distribution correlates primarily to the dominant mineralogy of the core (Figure 4a): variations in SiO_2 (4.4–70 wt.%) reflect changes in carbonate/quartz ratios in listvenites, and in carbonate/serpentine ratios in serpentinites, while downhole spikes in CaO (up to 32.8 wt.% in the serpentinites and up to 40.9 wt.% in listvenites) correspond to increasing TIC values ($CO_{2(TIC)}$

up to 40.1 wt.% in listvenites), indicative of the presence of dolomite (Figure 1; Kelemen et al., 2020). Correlations with these main mineralogical changes are more difficult to identify for Mg, Fe and Mg#, except for local decreases in MgO and Mg# associated with high CaO and TIC contents in dolomite-rich samples (e.g., listvenite C5704 B-23Z-1-1,37.0--42.0 cm at 48.72 mbg; Figures 2 and 3). In contrast, Al_2O_3, transition metals (e.g., Ti, Ni and Co) and lithophile trace elements (e.g., REE, Y) do not correlate with changes in volatile chemistry nor in the distribution of the dominant minerals: in particular, we do not observe major changes in their distribution between listvenites and serpentinites. These elements, generally considered as fluid-immobile, display coherent tens of meter scale downhole trends that allow us to define three geochemical domains (Figures 3–5), thereafter described as, from top to bottom, listvenite domains I, II and III.

Listvenite domain I (top to ~112 mbg) comprises listvenites (*listvenites I*), including one fuchsite-bearing listvenite, and serpentinites (*serpentinites I*). It is characterized by low concentrations in Al_2O_3 (0.14–0.92 wt.%), TiO_2 (<0.01 wt.%) and trace elements (e.g., Yb_N = 0.03–0.22; N = normalized to CI-Chondrite (McDonough & Sun, 1995)) that overlaps that of the harzburgites and dunites from the main mantle section (MMS) of the Semail ophiolite (Godard et al., 2000; Hanghoj et al., 2010; Lippard et al., 1986). It displays relatively linear REE patterns similar to that of the MMS, with normalized REE abundances decreasing from heavy (HREE) to light REE (LREE) ($(Ce/Yb)_N$ = 0.08–0.54). Several samples, in particular the serpentinites and ophicarbonates, present minor LREE enrichments relative to middle REE (MREE) (e.g., carbonate rich serpentinite C5704 B-44Z-4, 50.0–55.0 cm with $(La/Sm)_N$ = 3.7), similar to what is observed in some Ca-bearing carbonates from oceanic and ophiolitic peridotite hosted low temperature hydrothermal systems (Noel et al., 2018; Schroeder et al., 2015).

Listvenite domain II (~112 mbg to ~170 mbg) is composed of listvenites alternating with fuchsite-bearing listvenites (all grouped as *listvenites II*). It is characterized by elevated concentrations in Al_2O_3 (0.4–2.23 wt.%) and TiO_2 (0.02–0.06 wt.%) compared to Listvenite domain I. This domain has higher lithophile trace element contents (e.g., Yb_N = 0.18–1.03) and highly fractionated "spoon-shaped" REE patterns ($(Ce/Yb)_N$ = 0.007–0.061) with relatively flat convex-upward MREE-HREE segments ($(Dy/Yb)_N$ = 0.49–0.96) and slight but systematic enrichments of La relative to Ce ($(La/Ce)_N$ = 1.03–4.9), comparable to that of the (amphibole-bearing) basal lherzolites from the northern Semail ophiolite (Figures 4 and 5; Khedr et al., 2014; Takazawa et al., 2003). These REE patterns are very similar in shape to those obtained by Prigent, Agard, et al. (2018) on clinopyroxene and amphibole from the Banded Unit lherzolites close to the metamorphic sole. Listvenite domain II is also distinguished by, on average, low Ni (~1,200 µg/g) and Co (~68 µg/g) concentrations and low Fe^{3+}/Fe_{TOT} (0.1–0.6) compared to Lisvenite domain I (Ni~1,900 µg/g; Co~90 µg/g; Fe^{3+}/Fe_{TOT}~0.7).

Listvenite domain III (~170 mbg to the basal thrust) is the closest to the metamorphic sole. It comprises listvenites (*listvenites III*) and serpentinites (*serpentinites III*). It has concentrations in Al_2O_3 (0.24–2.30 wt.%), TiO_2 (<0.02 wt.%) and trace elements (e.g., Yb_N = 0.05–0.77) intermediate between that of the Lisvenite domains I and II, the most enriched samples being serpentinites and listvenites close to Listvenite domain II. It displays linear REE patterns comparable to that of Lisvenite domain I ($(Ce/Yb)_N$ = 0.08–0.67) with the exception of some samples close to Listvenite domain II that have similarly fractionated REE patterns ($(Ce/Yb)_N$ = 0.011–0.163). Listvenite domain III is characterized by systematic enrichments in LREE relative to MREE ($(La/Sm)_N$ = 0.34–3.29), a trend that overall increases toward the basal thrust. This downhole trend is accompanied by a decrease in Mg# (down to 82), an increase in Fe^{3+}/Fe_{TOT} up to Listvenite domain I values (0.38–0.83) and an increasingly scattered distribution of several elements such as Ni (650–3,100 µg/g) and Co (35–128 µg/g), or Cu (0.2–34 µg/g) and Pb (0.5–39.7 µg/g) as well as a progressive increase in the concentrations of CaO (up to 35.1 wt.%), Sr (up to 244.3 µg/g) and Sb (up to 27.4 µg/g). These variations are associated with an increase in the dolomite fraction toward the basal thrust (Figure 1b).

The listvenite series display spiked U-shaped trace element patterns that reflect the relative depletion of Zr-Hf relative to neighboring elements and significant enrichments in incompatible FME, such as alkali elements (Cs, Rb, Ba), Li, Sb, U, Pb and Sr relative to Th, Nb, Ta and LREE (Figure 5). These strong FME enrichments distinguish the listvenite series from the MMS harzburgites and dunites (Figures 2, 3 and 5). High FME concentrations appear as spikes on downhole plots (Figure 3). These spikes are however located preferentially in well-defined listvenite domains for most elements with a decoupling in the downhole distribution of alkali elements and other FME such as Sb, Pb, Sr and U. High concentrations of alkali elements including K_2O (0.07–0.45 wt.%), Ba (up to 420 µg/g), Rb (1.1–17 µg/g) and Cs (0.24–6.8 µg/g) distinguish Listvenite domain II from Listvenite domains I and III (K_2O = 0.02–0.08wt.%; Rb = 0.006–2.6 µg/g; Cs = 0.02–1.19 µg/g), with the highest concentrations

in fuchsite-bearing listvenites. In contrast, downhole spikes in concentrations for Pb, Sr and U are mainly in Listvenite domains I and III (Pb up to 56 µg/g, Sr up to 244 µg/g, U up to 0.04 µg/g). Cu (up to 73 µg/g) and to a lesser extent, Sb (up to 27.4 µg/g) and Zn (up to 610 µg/g) display similar trends with peaks in concentrations mainly in Listvenite domains I and III.

Some elements are characterized by highly scattered distributions and concentrations, and their compositions overlaps with that of the metamorphic sole (e.g., Li = 2.5–134 µg/g in listvenite series and 8–70 µg/g in metamorphic rocks; Figure 2). Some of these extreme variations can be correlated on a case-by-case basis to lithological or structural features as for MnO-rich sample C5704 B-60Z-4-1,24.0--29.0 cm(V) (MnO = 0.87 wt.%) identified as a listvenite vein crosscutting a fuchsite-bearing listvenite (C5704 B-60Z-4-1,24.0--29.0 cm(H)). This sample is also the most enriched in REE and Y (e.g., Y = 2.2 µg/g) and the most depleted in Cr (271 µg/g) indicating extensive elemental redistribution occurring at the sample scale.

4.2. Geochemistry of the Metamorphic Sole (Depth: 196.56–300.13 mbg)

BT1B metamorphic rocks have LOI of 1.3–3.8 wt.% related to the presence of H_2O (>2 wt.%) in hydrous minerals (chlorite, amphibole …) and minor CO_2 (0.04–0.97 wt.%) in carbonates, mainly calcite ($CO_{2(TIC)}$ 0.01–0.95 wt.%). They have low Mg# (16.7–56.6), low concentrations of Cr (42–265 µg/g) and Ni (15–86 µg/g) and high concentrations of Al_2O_3 (15.2–19.4 wt.%), Na_2O (2.1–4.7 wt.%), P_2O_5 (0.16–1.07 wt.%) and TiO_2 (1.6–3.7 wt.%) and they display a relatively narrow range of SiO_2 concentrations (44.5–52.6 wt.%). They are characterized by high concentrations of V (110–297 µg/g) and of incompatible trace elements, such as Th (0.75–5.9 µg/g), REE (ΣREE = 54–291 µg/g) and HFSE (e.g., Nb = 9.5–63 µg/g), and by LREE-enriched chondrite–normalized REE patterns ($(Ce/Yb)_N$ = 3.4–8.2). They overlap in composition with the amphibolites from the Semail ophiolite metamorphic sole (Ishikawa et al., 2005; Lippard et al., 1986) and the volcanic rocks from the underthrusted Hawasina assemblages (Chauvet et al., 2011; Lapierre et al., 2004; Maury et al., 2003) (Figures 4 and 5). They display trace element compositions similar to the transitional to alkali basalt series forming the Hawasina-Haybi complex indicating that the BT1B metamorphic rocks comprise only metabasalts.

We have subdivided Hole BT1B metamorphic rocks into three groups based on their lithology, physical properties, geochemistry and depth (Figure 3).

The first group (*M1*) corresponds to the high NGR cores (197.6–~230 mbg; Figure 1b). It represents the most enriched endmember of BT1B metabasalts for P_2O_5 (0.78–1.07wt.%), alkali elements (K_2O = 1.5–4.7wt.%; Ba = 192–598 µg/g; Rb = 37–78 µg/g; Cs = 1.9–6.5 µg/g) and moderately to highly incompatible lithophile elements, such as REE (Yb_N ~ 23), Th (5.1–5.9 µg/g) and U (1.0–1.3 µg/g). They have however middle range values for transition elements TiO_2 (1.9–2.4wt.%), V (110–157 µg/g) and Sc (17.9–21.3 µg/g). They are overall depleted in CaO (3.95–9.1wt.%) and in Sr (173–342 µg/g) although these elements increase with depth. *M1* metabasalts display the most fractionated REE patterns ($(Ce/Yb)_N$ = 7.7–8.2) as well as slight enrichments in Nb-Ta (e.g., Nb/Th ~ 1.27xPM), and negative anomalies in Pb and Sr relative to neighboring elements (Pb/Ce ~ 0.25xPM; Sr/Ce 0.2xPM) on extended trace element diagrams (Figure 5). Their high concentrations in K, Th and U likely explain their high NGR values (Figure 1).

The second and third groups, *M2* (~230–282.88 mbg) and *M3* (below 282.88 mbg) are composed of schists and greenstones respectively. The downhole transition from *M1* to *M2-M3* metabasalts is characterized by a sharp decrease in K_2O, and Rb, REE, HFSE, Th and U and a sharp increase in TiO_2 (up to 3.7 wt.%; Figure 2). *M2-M3* metabasalts record a continuous downhole increase in Mg# (up to 56.6), Sc (up to 36 µg/g), V (up to 297 µg/g), Co (up to 45 µg/g) and Ni (up to 87 µg/g) and a decrease in alkali elements (e.g., K_2O down to 0.3 wt.%) and in moderately to highly incompatible lithophile elements (e.g., TiO_2 down to 1.6 wt.%; Th down to 0.7 µg/g). They also show a progressive decrease in trace element concentrations and in LREE/HREE ratios with depth (Figures 2 and 4). Negative correlations between TiO_2, REE and HFSE and Co, Ni and Mg# such as those observed downhole are typical of basaltic fractional crystallization trends with the lowermost *M3* metabasalts having the least evolved compositions. Finally *M2-M3* metabasalts display positive anomalies in Nb-Ta (e.g., Nb/Th ~ 1.5xPM), minor negative anomalies in Pb (Pb/Ce = 0.43–0.88xPM) and variable Sr anomalies (Sr/Ce = 0.5–1.7xPM) relative to neighboring elements on extended trace element diagrams (Figure 5). CaO and Sr downhole trends are decoupled from other elements: they increase then stabilize with depth in *M2* (CaO up to 14.0 wt.%; Sr up to 638 µg/g) and decrease toward the bottom of the borehole (CaO down to 10.75 wt.%; Sr down to 281 µg/g).

5. Discussion

Drill cores recovered from at Hole BT1B provide the first high resolution sampling of the transition from the base of the Semail ophiolite to its metamorphic sole, thus allowing a detailed study of the geochemical processes occurring across this major tectonic structure. The mantle-derived listvenite series comprise highly fractured and veined listvenites and fuchsite-bearing listvenites and two minor intervals of variously carbonated serpentinites. In spite of the complete transformation of their mineralogy due to CO_2-metasomatism, the listvenite series preserve average compositions comparable to that of the highly serpentinized, often amphibole bearing, "Banded Unit" peridotites – a narrow zone atop the basal thrust and the metamorphic sole (Figures 2–5; Khedr et al., 2013, 2014; Prigent, Agard, et al., 2018; Yoshikawa et al., 2015). The greenschist facies BT1B metamorphic sole has basaltic compositions similar to that of the alkali metabasalts from the underthrusted Hawasina assemblages (Figures 4 and 5) from which they likely derive (e.g., Searle & Malpas, 1980). It displays progressively less evolved compositions away from the ophiolite contact (from *M1* to *M3* metabasalts), a characteristic previously documented in the amphibolitic sole (Ishikawa et al., 2005; Figure 2). There is no compositional evidence of interlayered metasediments, in contradiction to what initially hypothesized for the BT1B cores (Kelemen et al., 2020).

Hereafter, we will use our new high resolution geochemical database to evaluate the mass and volume changes associated with the formation of the listvenite series and discuss elemental mobility during these processes and its linkages to the composition of the protolith(s) and neighboring lithologies, the localization of fluid pathways along the BT1B cores and the interplay between solute transport and reaction kinetics during CO_2 metasomatism.

5.1. Mass Changes and Elemental Mobility During Listvenization

To evaluate the respective contribution of the host rock and incoming metasomatic fluids(s) to the composition of the listvenite series and to constrain elemental mobility at the scale of the borehole, we used the mass balance model of Baumgartner and Olsen (1995), a model based on Grant (1986). This approach allows us to evaluate the addition and removal of a broad range of chemical elements during the alteration of a protolith of known composition and the resulting mass changes, without a priori assumptions on elemental mobility. The main challenge for these calculations is determining consistent and representative trace element compositions for the listvenite series and for the model protoliths.

The listvenite series are characterized by strong downhole variations in mineralogy and geochemistry from the sample to the meter scale. For simplicity, mass balance calculations (Text S2 in Supporting Information S1) were carried out for listvenites (including fuchsite-bearing listvenites) and for variously carbonated serpentinites, both averaged at the scale of the listvenite domains (Table S3). The results are illustrated as isocon diagrams (Figure 6) where averaged elemental concentrations of the altered rock are plotted against those of the model protolith. Immobile elements were identified on the basis of the largest number of elements which are consistent with a single isocon (line of immobility) to within their uncertainty in the protolith and altered rock (i.e., collinear on the plot). The 1:1 reference line on isocon diagrams corresponds to zero mass change during alteration. Isocons which lie above or below the 1:1 line indicate, respectively, overall mass loss or mass gain during alteration (reflecting overall concentration or dilution of immobile elements for each of these scenarios). Elements plotting above and below the isocon are enriched and depleted, respectively, in the altered rock compared to the model protolith.

The compositions of the model protoliths were determined on the basis of the published geochemical studies of the Semail peridotites for which structural (localization, distance to the Moho and/or to the sole) and petrological (lithology, mineralogy) information were available. They were calculated including the volatile compositions of the variously serpentinized Semail peridotites. We defined two endmember protolith compositions (Table S3): (a) a refractory protolith, modeled using the compositions of MMS harzburgites and dunites (Gerbert-Gaillard, 2002; Godard et al., 2000; Hanghoj et al., 2010; Lippard et al., 1986) due to the lack of data on the composition of basal harzburgites and dunites; (b) a fertile protolith, calculated using the compositions of basal lherzolites, including amphibole-bearing samples (Khedr et al., 2014; Lippard et al., 1986; Takazawa et al., 2003). The model refractory and fertile protoliths are noted MMS and basal lherzolite respectively in Figure 6. For some trace elements, the published chemical database is limited (e.g., Ga) and/or highly variable (e.g., LREE, Cs) resulting in a large uncertainty in their distribution in the model protoliths, in particular for basal lherzolites; however, these elements represent a minor subset of the chemical database and therefore had little impact on the evaluation of the overall mass changes resulting from CO_2 metasomatism.

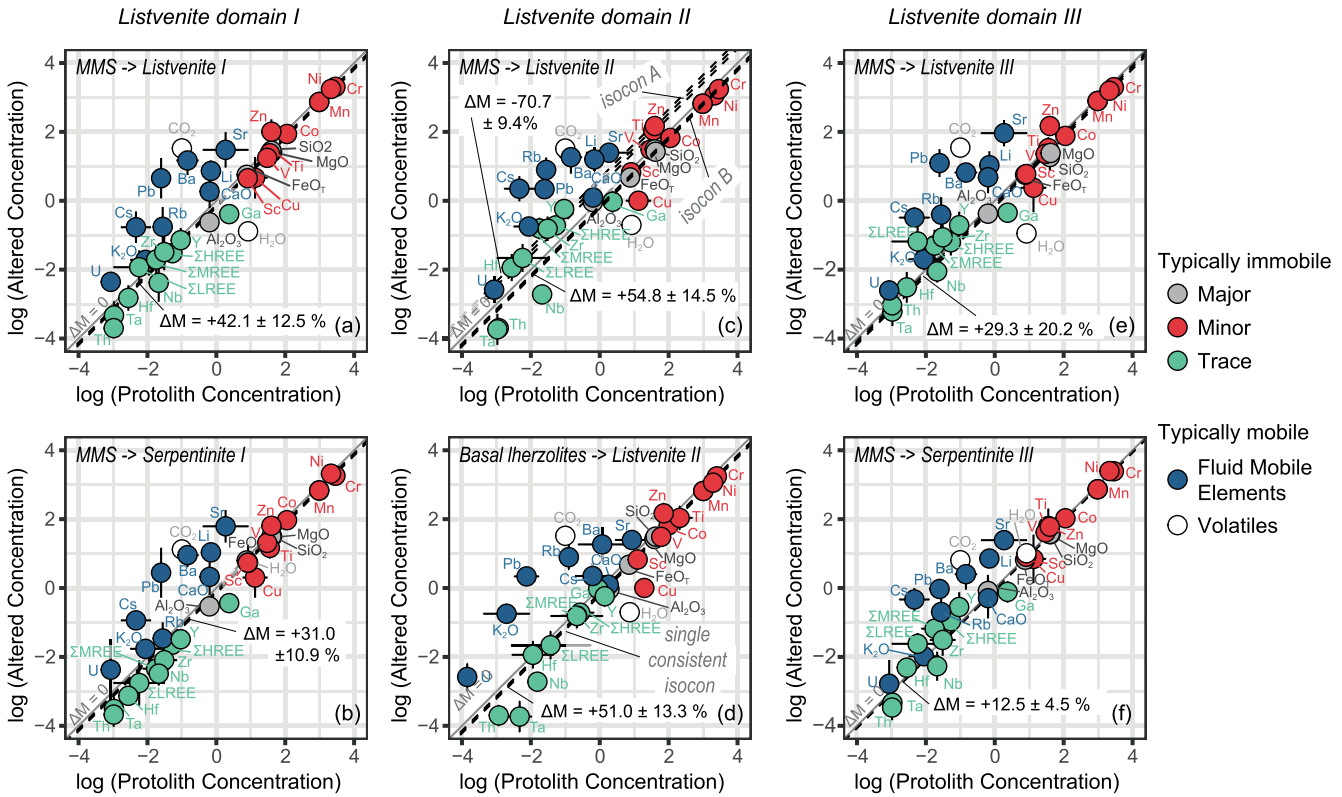

Figure 6. Mass balance diagrams for listvenite series from Hole BT1B. Isocon plots comparing the average composition of listvenites and serpentinites from each listvenite domains with potential protolith compositions on log-log scales. Isocons (line of immobility) were calculated using the approach of Baumgartner and Olsen (1995). On each panel, the isocon (dotted black lines) corresponds to a protolith–altered rock pair. The gray 1:1 reference line corresponds to zero mass change during alteration. Isocons above and below this indicate mass loss and gain, respectively (noted ΔM). Using the average composition of the MMS refractory peridotites as the protolith composition for each domain, this approach gives consistent patterns of mobile and immobile elements, with the exception of Listvenites II (panel c) where two potential isocons are apparent in the data (labeled A and B). Mass balance was repeated for Listvenite II with the average composition of basal (amphibole-bearing) lherzolites, which gives a single consistent isocon and similar patterns of mobility/immobility to the other panels. Compositions are plotted as concentrations in wt.% for major and volatile elements and in μg/g for trace elements. Compositions and calculated statistics are in Table S3. Symbols are in legend.

The mass balance calculations comparing the composition of listvenites and serpentinites to the refractory protolith show co-linearity (within uncertainty) on the isocon diagrams for most major and trace elements (Figure 6, Text S2 in Supporting Information S1). Only listvenites II display inconsistent results with two parallel collinear slopes (Figure 6c). The same calculations using the fertile model protolith for Listvenite II show collinear trends and elemental variations similar to those obtained for the adjoining domains (Figure 6d). This result supports the hypothesis that the listvenite series are replacements of a mantle section analogous to the Banded Unit, with Listvenite domains I and III being formed after a harzburgitic/dunitic protolith, and Listvenite domain II after a (amphibole bearing) lherzolitic protolith.

In each domain, most chemical elements are aligned on the same collinear trend, from SiO_2, MgO and FeO_T, the main constituents of the mantle protolith(s) of the listenite series, to Al_2O_3, Na_2O, and the transition elements generally concentrated in mantle peridotites (V, Cr, Co, Ni, Mn, Ti, and Sc) and moderately incompatible lithophile trace elements such as HREE, MREE, Y, Zr and Hf. These results indicate that these elements are immobile at the scale of the listvenite domains despite their meter-scale scattered downhole distribution. It should be noted however that the most incompatible elements, even those generally considered as fluid immobile, display minor differences from one rock type and domain to the other (e.g., depleted LREE in Serpentinite I). In particular, Nb, Ta and Th are systematically depleted relative to the model mantle protoliths. This could reveal trace element depleted protoliths compared to the models, but we posit that it most likely relates to the uncertainty due to the limited dataset on the composition of these elements in the Semail peridotites. The same consideration could explain the apparent systematic loss of Ga observed for all calculations.

A limited number of elements show significant changes in compositions relative to the model protoliths. Enrichments in CO_2 are ubiquitous in agreement with BT1B listvenitization being driven by CO_2 metasomatism as previously suggested by Falk and Kelemen (2015) for the Wadi Mansah listvenites. CO_2 enrichments are associated with the development of two reaction pathways for carbonation: on one hand, the formation of variously carbonated serpentinites (Serpentinites I and III; Figures 6b and 6f) and, on the other hand, that of listvenites (Listvenites I, II and III, Figures 6a, 6d and 6e). Listvenites are distinguished from carbonated serpentinites by their depletion in H_2O, suggesting that CO_2 addition induced the release of H_2O. This process could represent a non-negligible dehydration mechanism for serpentinized peridotites. It has been documented in several listvenite bodies from different geodynamic settings (e.g., Atlin listvenites (Hansen et al., 2005)).

Enrichments in CaO (where dolomite is present) and in most elements typically considered as fluid mobile, such as Li, K, Rb, Cs, Ba, Sr, Pb and U, relative to model peridotite protoliths are also observed (Figure 6). These enrichments vary from one domain and rock type to the other thus suggesting downhole variability in fluid-rock interactions (see Section 5.2).

Mass balance calculations indicate a significant increase of the mass of the listvenite series compared to their partially serpentinized model protoliths. The estimated mass increase was slightly less in carbonated serpentinites (12%–31%) than in listvenites (29%–51%) (Figure 6; Table S4). The density of carbonated serpentinites and listvenites (2.52 ± 0.05 and 2.86 ± 0.07 g.cm^{-3} respectively (Kelemen et al., 2020)) being relatively close to that of the variously serpentinized Semail peridotites (2.81 ± 0.50 g.cm^{-3} (Dewandel, 2002)), volume expansion is of the same order of magnitude as mass changes (Table S4). The abundant fractures and veining characterizing the listvenite series (Kelemen et al., 2020; Menzel, Urai, et al., 2020) possibly accommodated these mass and volume changes at the scale of the BT1B cored section. However these results raise the question of the mechanisms that facilitate such a large and heterogeneous increase in mass and volume at the scale of the Wadi Mansah massif.

5.2. The BT1B Listvenite Series: Sampling the Final Stage of a Protracted Sequence of Fluid Rock Interactions

BT1B listvenite series formed at low temperatures (between 245 to 45°C) and shallow depths (from 10 to 2 km) according to the study of Beinlich et al. (2020) (clumped isotope thermometry coupled to oxygen isotopes), in agreement with previous results on the Wadi Mansah listvenites (Falk & Kelemen, 2015). The fluids triggering listvenitization were particularly rich in CO_2, possibly close to saturation, according to recent thermodynamic modeling (Kelemen et al., 2021). The associated fluid-rock interactions resulted in strong mineralogical and compositional variability from the centimeter to the tens of meter-scale along the cored listvenites series (Figure 3). Geochemistry shows also a sharp geochemical transition to the presently underlying metamorphic sole (with the exception of the Ca and Sr downhole trends) (Figure 2). These jagged chemical distributions indicate localized fluid-rock interactions and limited elemental transport across the basal thrust. This implies that the CO_2-rich fluid(s) triggering the formation of the listvenites series did not originate directly from the metamorphic sole recovered at Hole BT1B. The main flow paths for these fluids were probably (sub-)parallel to the basal thrust. They followed the same direction as the fluids driving the earlier metasomatic events affecting the basal ophiolitic mantle and its metamorphic sole, and possibly reused the same pathways.

The BT1B listvenites series are systematically enriched in FME relative to the Semail ophiolite main mantle section, particularly in Cs, Rb, Ba and K (Figure 6). Alkali-rich compositions are commonly observed along the ophiolite basal thrust in the metamorphic sole (e.g., Ambrose et al., 2021; Ghent & Stout, 1981; Ishikawa et al., 2005) and in the adjacent Banded Unit peridotites, in particular in the amphibole-rich lherzolites (e.g., Khedr et al., 2013; Khedr et al., 2014; Prigent, Agard, et al., 2018; Yoshikawa et al., 2015). These enrichments are typically interpreted as resulting from interactions with alkali-rich aqueous fluids, originating from the de-volatilization of a slab (altered oceanic crust, sediments) at depth (granulite-amphibolite facies); fluid-rock interactions are however thought to occur at different pressure and temperature condition for the metamorphic sole and the Banded Unit peridotites. The extensive serpentinization characterizing the latter is also interpreted as resulting from interactions with slab-derived aqueous fluids thus suggesting that the basal thrust acted as an efficient fluid pathway also during the later stages of cooling of the ophiolite (Lippard et al., 1986; Prigent, Guillot, et al., 2018). Petrographic observations indicate that the BT1B listvenite series were formed after serpentinized peridotites (Beinlich et al., 2020; Kelemen et al., 2020) and our geochemical study shows that, when averaged at the meter to tens of meter scale, they preserved a peridotite composition for most major and trace elements in spite of their

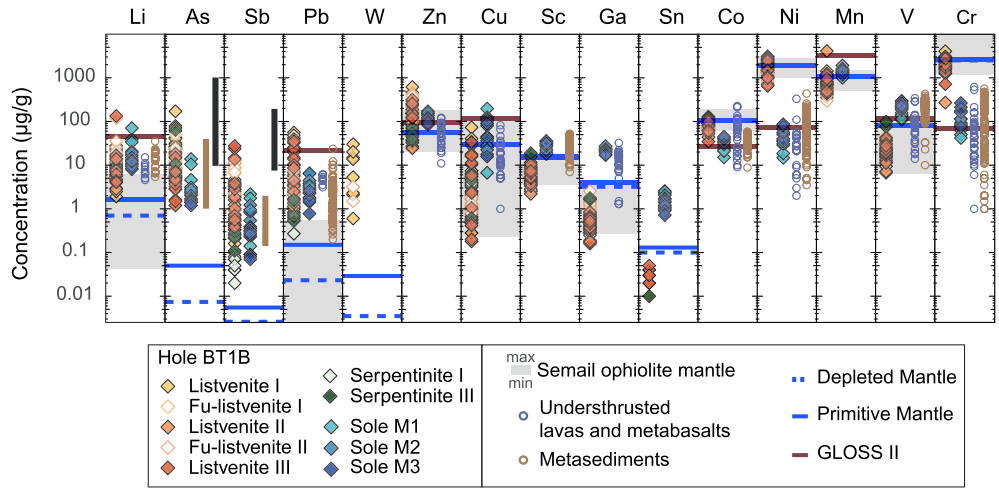

Figure 7. Caltech diagram of the composition of elemental abundance of BT1B listvenites series and metamorphic sole samples. Compositions are plotted on a log scale and compared with the compositional range of the Semail ophiolite peridotites (gray field) and lavas and sediments from the metamorphic sole and the underthrusted Hawasina assemblages (references in caption of Figure 4), and with PM (McDonough & Sun, 1995), DM (Salters & Stracke, 2004) and GLOSS II (Plank, 2014) values, Arsenic and antimony compositions are compared to the composition of abyssal plain sediments (brown line, [Plank & Ludden, 1992]) and hydrothermal sulfides (black line, [Fouquet et al., 2010]). Symbols are in legend.

strong variability (Figures 4 and 7). We propose that the BT1B listvenite series replaced a section of serpentinized Banded Unit peridotites analogous in mineralogy and composition to those exposed elsewhere along the Semail mantle section (e.g., Prigent, Agard, et al., 2018). The previous metasomatic events forming the Banded Unit peridotites may have thus contributed to the alkali-rich signature of BT1B listvenite series.

The composition and mineralogy of the three geochemical domains identified for BT1B listvenite series relate primarily to the composition of their protoliths. Compared to Listvenite domains I and III, Listvenite domain II has average compositions comparable to that of the basal amphibole-bearing lherzolites, even for alkali elements K, Ba, Cs and Rb. These enrichments are particularly prominent in the fuchsite-bearing listvenites. We posit that fuchsite is dominantly localized in Listvenite domain II because the concentrations in the chemical components allowing their formation (in particular, Al, K) were present mainly in the amphibole-rich lherzolites. Listvenite domain II is also distinguished by relatively low Fe^{3+}/Fe_T, overlapping Semail ophiolite mantle values. These variable Fe^{3+}/Fe_T could reveal variable redox conditions due to the development of different reaction paths depending on the protolith compositions (e.g., buffering of local fO_2 by Fe trapping in the fuchsite structure). They could also simply reflect changes in redox conditions during the serpentinization of the Banded Unit peridotites, previous to CO_2 metasomatism. Detailed investigations of the distribution of iron and iron speciation between minerals and along the core would allow unraveling the contributions of these different processes. Finally, although a contribution of the protoliths to the FME budget of the BT1B listvenite series is probable, it is not sufficient to explain their high concentrations in these elements as illustrated on Figure 6. This suggests that the CO_2-rich fluids triggering listvenitization contained non-negligible concentrations in FME, including in alkali elements, similar to the slab-derived fluids driving the high temperature metasomatism and serpentinization in the Banded Unit peridotites.

The Wadi Mansah listvenite series are characterized by the occurrence of variously carbonated serpentinite intervals crosscutting listvenites: BT1B core descriptions show that serpentinite-to-listenite transitions do not correspond to faults and our study shows that they have the same protoliths within a same geochemical domain (Figures 4, 6 and 7). This suggests that these changes in mineralogy reveal variable extents of reactions with CO_2-rich fluids. Beinlich et al. (2020) proposed that the variously carbonated serpentinites represented the least reacted intervals that preserved the incipient stages of carbonation of its serpentinized protolith. However, the development of dolomite-dominated Ca and Sr rich intervals in Listvenite Domains I and III reveal a possibly more complex process. The Ca-Sr rich intervals are located within, and at, the (talc-bearing) transition from serpentinites and listvenites, in the upper part of Listvenite Domains I (48–53 mbg and 63 to 67 mbg) and throughout Listvenite Domain III, with Ca-Sr enrichments increasing toward the basal thrust. This downhole trend continues

into the M1 metabasalts, drawing a shape similar to a diffusive front across the basal thrust (Figure 2). Ca-Sr rich intervals also show increasing Fe^{3+}/Fe_T values, in particular toward the basal thrust. They are systematically associated to enrichments in redox sensitive U suggesting fluid-rock interactions in an oxidized environment (e.g., Paulick et al., 2006; Peters et al., 2017). The listvenite series thus record interactions with Ca-depleted CO_2-rich fluids and with Ca-Sr-CO_2-rich oxidizing fluids. De Obeso et al. (2021) show that Sr derived from the de-volatilization at depth of Hawasina type carbonate/silicate sedimentary assemblages. Whether the interactions with Ca-depleted and -enriched CO_2-rich fluids were contemporaneous or not, is difficult to estimate in a context where flow paths are highly channelized. Because (a) dolomite-rich zones are highly localized and appear to imprint listvenites (late dolomite veins, …), and (b) they predominate in the serpentinite intervals that were initially little affected by CO_2 metasomatism, we speculate that the ingress of Ca-Sr-CO_2-rich fluids followed the onset of the formation of the listvenite series.

Selective enrichments in FME, such as Li, Pb, Sb and As or U (Figures 2, 3 and 7) are also observed, sometimes in association with slight changes in Zn and Cu compositions or in Fe^{3+}/Fe_T. The most prominent occurs at 18–35 mbg in the Listvenite domain I, and shows enrichments in Li, Mn, U, Zn and Cu, and high Fe^{3+}/Fe_T. These variations are not correlated to major changes in mineralogy or to geochemical domains, but they are observed in areas recording extensive fracturing and late re-cementation events, with locally the late precipitation of iron oxides (mostly hematite) (Menzel, Urai, et al., 2020). Efficient fracturing may have favored effective and long-lasting fluid-rock interactions and elemental redistributions, possibly until the final stages of listvenitization.

Geochemistry allows to identify the respective roles of the composition of the protoliths and of the reacting fluids on the development of distinct reactions paths along the BT1B listenite series, however determining the timing of these processes in the context of the emplacement of the Semail ophiolite remains challenging. For instance, there is an overlap in the range of temperature conditions anticipated for the serpentinization of the Banded Unit by slab derived fluids (<350°C, Prigent, Guillot, et al., 2018) and for CO_2 metasomatism along BT1B listvenite series (Beinlich et al., 2020), therefore it is possible that serpentinization and the onset of CO_2 metasomatism were contemporaneous. Also, we cannot preclude a possible contribution of the water released by the formation of listvenites to the serpentinization of neighboring peridotites, and the timing and context of the changes in the composition of reacting fluids are unclear. Further investigations coupling petro-structural and fine scale geochemical and isotopic investigations would allow to better constrain the hydrodynamic and chemical processes controlling this protracted sequence of fluid-rock interactions and their relationships to deformation and the local tectonic environment.

5.3. Contribution of Listvenites to Global Chemical Budgets

The BT1B listvenites are characterized by a dual geochemical signature: they preserve the composition(s) of their serpentinized protolith(s) for major elements (except for Ca) and most compatible (e.g., V, Sc, Ni, Cr, Co) and incompatible lithophile elements (e.g., REE, HFSE) (Figure 6) but they record significant enrichments in most of the trace elements and metals considered as fluid mobile (Li, K, Cs, Rb, K, Ba, Sr, As, Sb, and W, Figures 4, 6 and 7). They commonly have FME abundances similar, or even enriched, compared to the Semail ophiolite neighboring lithologies (sole, metabasalts and metasediments) and comparable to subduction related serpentinites (e.g., Deschamps et al., 2013; Peters et al., 2017) and ophicarbonates (Cannao et al., 2020) for alkali elements. The variously carbonated BT1B serpentinites display similar enrichments but with slightly more prominent U anomalies and, selective enrichments in Ca and Sr, and in LREE, a trend typical of carbonated oceanic serpentinites and ophicarbonates (e.g., Cannao et al., 2020; Noel et al., 2018; Peters et al., 2017). All the listvenite series show significant remobilization (Zn, Cu) and enrichments (As, Sb, Pb) of chalcophile elements and of selected siderophile elements (variable Ni, Co and Cr, and enrichments in W), a common characteristics of listvenites that typically show ore-grade compositions for these elements (e.g., Belogub et al., 2017; Buisson & Leblanc, 1985; Escayola et al., 2009; Halls & Zhao, 1995; Laznicka, 2010); such variations are also characteristic of highly serpentinized ultramafic basements hosting high temperature oceanic hydrothermal vents and sulfide deposits (e.g., Andreani et al., 2014). The redistribution of metals and FME in variously carbonated and/or serpentinized peridotites is classically interpreted in the context of their geodynamic environment, but the meter-scale chemical variability of the BT1B listvenite series suggests a key role of local and transient reactive processes associated to the ingress of CO_2-rich fluids. Laboratory experiments show that the interplay between carbonation (and/or serpentinization) kinetics, solute transport and fluid renewal at the mineral interface influences effective reaction

pathways that, in turn, modify local chemical conditions (and reaction kinetics) by changing the mineralogy of reacted samples and fluid composition (e.g., Andreani et al., 2009; Godard et al., 2013; Grozeva et al., 2017; Janecky & Seyfried, 1986; Peuble et al., 2015, 2019; Seyfried et al., 2007). Similar reactive transport mechanisms could have caused the jagged elemental redistribution along BT1B listvenite series and possibly contributed to their dual geochemical signature. Disequilibrium textures indicative of fast growth of magnesite are common (Beinlich et al., 2020): this suggests that reaction kinetics were fast compared to solute transport whatever the fluid composition. They are associated with the development of nanoporosity, that could have efficiently trap FME as fluid or solid phases (e.g., Cannaò & Malaspina, 2018). Similarly, in the absence of silica addition at the scale of the core (Figure 6), quartz-forming silicification reactions likely relate to the incomplete removal of silica during coupled silicate dissolution – carbonate precipitation reactions, as commonly observed in reactive percolation experiments when carbonation kinetics are fast (Peuble et al., 2015, 2019).

Further studies are needed to test this model of elemental redistribution for listvenites formed by CO_2 metasomatism, however it is worth to note that it accounts for some of the prominent characteristics of the BT1B listvenite series. First, fast carbonation kinetics are expected to induce reaction-driven fracturing (e.g., Jamtveit et al., 2008; Lambart et al., 2018; Ulven et al., 2014). This mechanism may have contributed to the development of the high density veining network in BT1B listvenite series, and thus helped to accommodate the large spatially heterogeneous large increase in volume associated with their formation. Second, the efficient trapping of fluid mobile trace elements combined with the preservation of the protolith mantle composition for all other trace elements produced extreme fractionation of FME relative to immobile incompatible elements (e.g., Th or, to a certain extent, Ce, Figure 8). This fractionation is particularly high for alkali elements (Li, Ba, Cs, Rb) and chalcophile elements (Pb) with Li/Th of 2,000-10^5, Ba/Th of 500-10^6, Cs/Th of 100–5,000 and Pb/Ce up to 5×10^5. Relative enrichments in U are comparatively less prominent (e.g., U/Th $\sim$ 1–100). These values are significantly higher than that of the possible sources of fluids (e.g., Li/Th $<$ 30, Ba/Th $<$ 200, Cs/Th $<$ 20, U/Th $<$ 0.5, and Pb/Ce $<$ 0.5 in metamorphic sole (this study) and sediments (GLOSS II (Plank, 2014)). These elemental fractionations follow trends similar to what is observed for forearc serpentinites when compared to oceanic serpentinites (Peters et al., 2017) but the degree of fractionation measured in the BT1B listvenite series is significantly higher. If significant amounts of listvenites were recycled, such extreme compositions could affect that of the subduction-related volcanics (e.g., by inducing a prominent alkali-rich sedimentary signature) or, over longer time scales, the mantle isotopic signature, for instance for lead isotopes due to their high Pb concentrations compared to U and Th (e.g., U/Pb $<$ 0.005). They could contribute to the development of a high Pb/Ce, low Th/Pb and U/Pb reservoir and, hence, offer a potential solution to the "first lead paradox" (Hofmann, 2008). Recent studies have shown the role of carbonation of oceanic and subduction-related peridotites in the global carbon cycle (e.g., Cannaò et al., 2020; Kelemen & Manning, 2015). Our results suggest that, similar to what proposed for (de-)serpentinization reactions (e.g., Deschamps et al., 2013; Spandler & Pirard, 2013), carbonation reactions could also impact the redistribution of fluid mobile elements and metals and play a role in their global geochemical cycles.

6. Conclusions

During ICDP Oman Drilling Project, the transition from the base of the Semail ophiolite to the underlying metamorphic sole was drilled at Hole BT1B (Wadi Mansah). We analyzed the bulk major, volatile and trace element compositions of 65 variously carbonated serpentinites and (fuchsite-bearing) listvenites, and 19 metamorphic rocks collected from recovered cores, with the aim of better constraining chemical transfers associated with peridotite carbonation along the ophiolite basal thrust.

The listvenite series record the formation of listvenites replacing a serpentinized peridotite protolith: this process is marked by CO_2 addition and H_2O removal. Their bulk geochemistry is highly variable at the meter scale yet, on average, it is close to that of the refractory peridotites of the Semail mantle section for most major and lithophile trace elements, except of the fuchsite-bearing listvenite domain that has compositions overlapping that of the more fertile, often amphibole-bearing, basal lherzolites. Thus, the type of precursor peridotite can be well recognized in spite of extensive peridotite carbonation. All samples are enriched in fluid mobile elements compared to the composition of the Semail peridotites (up to $\sim 10^3$–10^4 x PM). They have concentrations similar to the metamorphic sole and/or associated metasediments for elements such as Cs, Sr and Ca and sometimes even higher for elements such as Pb, Li, As, and Sb. Enrichments in Ca and Sr are decoupled from those in other FME, indicating interactions with several batches of CO_2-rich fluids originating in neighboring lithologies or deeper

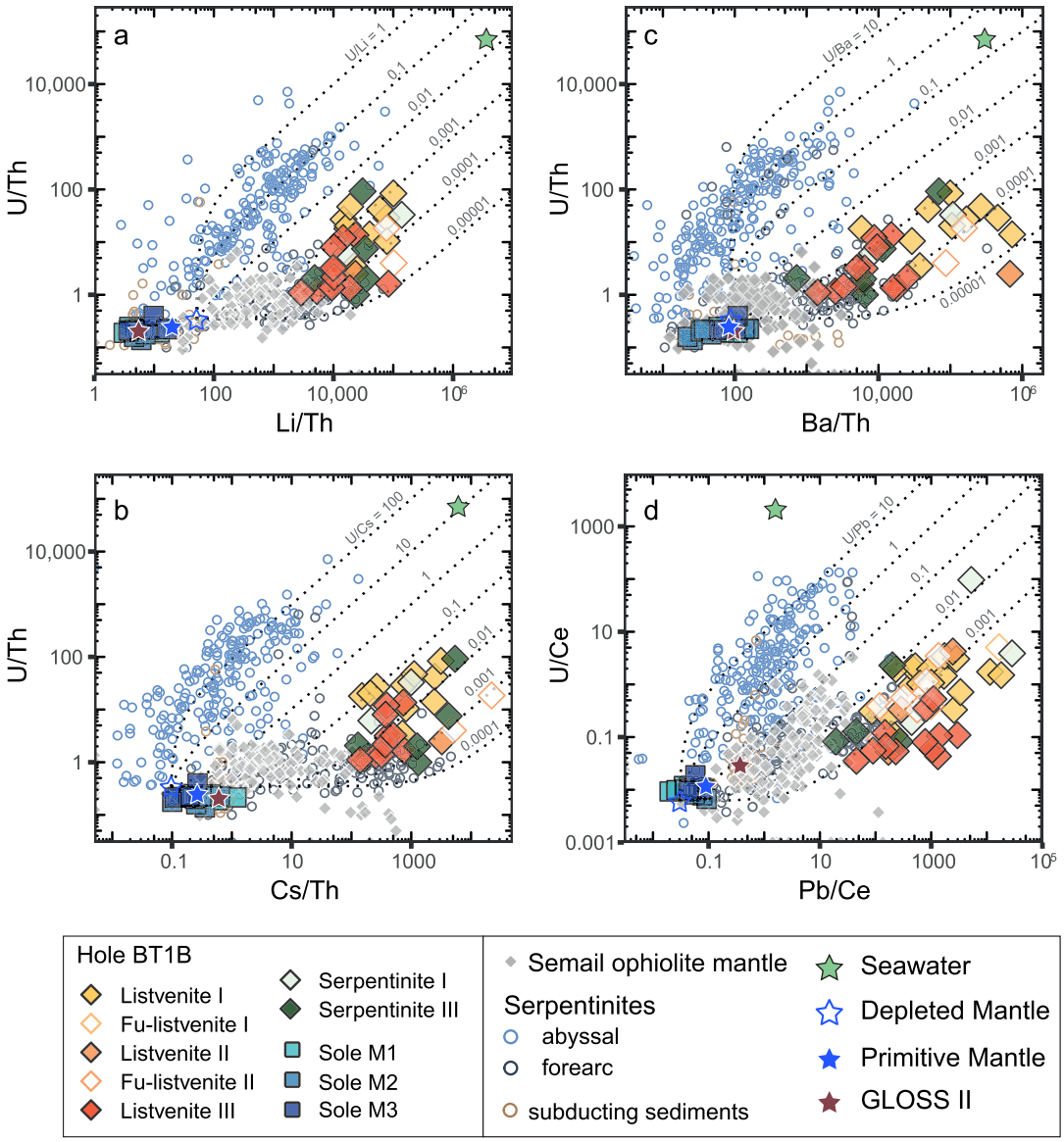

Figure 8. Scatterplots showing fluid mobile element enrichment relative to immobile trace elements in BT1B listvenites and serpentinites (a) U/Th versus Li/Th. (b) U/Th versus Cs/Th. (c) U/Th versus Ba/Th. (d) U/Ce versus Pb/Ce. Plotted for comparison are: compiled serpentinite compositions from abyssal (blue circles) and forearc (dark blue circles) settings (data from compilations in Peters et al., 2017 and Deschamps et al., 2013); compiled Semail ophiolite peridotite data; subducting sediments (Plank et al., 2007); PM (McDonough & Sun, 1995), DM (Salters & Stracke, 2004), GLOSS-II (Plank, 2014) and seawater (Li, 1991) values. Also plotted are lines of addition of fluid mobile elements in various ratios at fixed Th or Ce. Literature data sources for Semail ophiolite are as in previous plots. Symbols are in legend.

along the basal thrust. These results suggest that interactions with CO_2-rich fluids can induce extreme elemental fractionation and enrichments in carbonated peridotites. These processes could represent a major mechanism (re) mobilizing FME and volatile elements along convergent margins.

Appendix A

Phase 1

Onsite Drilling Team

Peter Kelemen, Department of Earth and Environmental Sciences, Columbia University, New York, NY, USA, peterk@ldeo.columbia.edu; Jürg M. Matte, Project Director, School of Ocean and Earth Science, University of Southampton, Southampton, UK, J.Matter@southampton.ac.uk; Damon Teagle, School of Ocean and Earth Science, University of Southampton, Southampton, UK, Damon.Teagle@southampton.ac.uk; Jude Coggon, Project Manager, School of Ocean and Earth Science, University of Southampton, Southampton, UK, jude.coggon@southampton.ac.uk; Juan Carlos de Obeso, Department of Earth and Environmental Sciences, Columbia University, New York, NY, USA, deobeso@ldeo.columbia.edu; Michelle Harris, Geography, Earth and Environmental Sciences, Plymouth University, Plymouth, UK, michelle.harris@plymouth.ac.uk; Emma Bennett, School of Earth and Ocean Sciences, Cardiff University, Cardiff, UK, bennette7@cardiff.ac.uk; Nico Bompard, School of Ocean and Earth Science, University of Southampton, Southampton, UK, N.Bompard@soton.ac.uk; Marine Boulanger, Department of Petrology, Center de Recherches Pétrographiques et Géochimiques (CRPG), Vandœuvre-lès-Nancy, France, marineb@crpg.cnrs-nancy.fr; Lyderic France, Department of Geosciences, CRPG-CNRS Université de Lorraine, France, lyde@crpg.cnrs-nancy.fr; Gretchen Früh-Green, Department of Earth Sciences, Federal Institute of Technology, Zurich, Switzerland, frueh-green@erdw.ethz.ch; Dieter Garbe-Schönberg, Institute of Geosciences, Christian-Albrecht University of Kiel, Kiel, Germany, dgs@gpi.uni-kiel.de; Benoit Ildefonse, Department of Géosciences, CNRS Université de Montpellier, Montpellier, France, benoit.ildefonse@umontpellier.fr; Ana Jesus, Department of Applied Geosciences, German University of Technology in Oman, Oman, ana.jesus@gutech.edu.om; Craig Manning, Department of Earth, Planetary and Space Sciences, University of California, Los Angeles, CA, USA, manning@epss.ucla.edu; Dominik Mock, Institute for Mineralogy, Leibniz University of Hanover, Hanover, Germany, dom.mock@web.de; Tony Morris, Geography, Earth and Environmental Sciences, Plymouth University, Plymouth, UK, amorris@plymouth.ac.uk; Samuel Müller, Institute of Geosciences, Kiel University, Kiel, Germany, mail.sam@gmx.net; Julie Noël, Department of Geosciences, Université de Montpellier, Montpellier, France, Julie.Noel@gm.univ-montp2.fr; Daniel Nothaft, Department of Geological Sciences, University of Colorado, Boulder, CL, USA, daniel.nothaft@colorado.edu; Americus Perez, Department of Earth Sciences, Kanazawa University, Kanazawa, Japan, adperez@stu.kanazawa-u.ac.jp; Philippe Pezard, Department of Geosciences, CNRS Université de Montpellier, Montpellier, France, ppezard@gulliver.fr; Nehal Warsi, Drilling Consultant, School of Ocean and Earth Science, University of Southampton, Southampton, UK, nhwarsi@gmail.com; David Zeko, Earth, Ocean and Atmospheric Sciences, University of British Columbia, Vancouver, BC, Canada, dzeko@eoas.ubc.ca; Barbara Zihlmann, School of Ocean and Earth Science, University of Southampton, Southampton, UK, barbara.zihlmann@soton.ac.uk

Onsite Wireline Logging Team

Jürg M. Matter, Project Director, School of Ocean and Earth Science, University of Southampton, Southampton, UK, J.Matter@southampton.ac.uk; Philippe A. Pezard, Geoscience Montpellier, CNRS University of Montpellier, Montpellier, France, Philippe.Pezard@GM.Uni-Montp2.Fr; Mohamed-Amine Bechkit, Houari Boumedienne University Algiers, Algeria, Mohamed-Amine.Bechkit@hotmail.fr; Laurent Brun, Geoscience Montpellier, CNRS University of Montpellier, Montpellier, France, laurent.brun@umontpellier.fr; Bernard Célérier, Geoscience Montpellier, CNRS University of Montpellier, Montpellier, France, Bernard.Celerier@gm.univ-montp2.fr; Gilles Henry, Geoscience Montpellier, CNRS University of Montpellier, Montpellier, France, Gilles.henry@gm.univ-montp2.fr; Jehanne Paris, Geoscience Montpellier, CNRS University of Montpellier, Montpellier, France, Jehanne.paris@hotmail.fr; Gérard Lods, Geoscience Montpellier, CNRS University of Montpellier, Montpellier, France, Gerard.Lods@gm.univ-montp2.fr; Pascal Robert, GeoRessources, Université de Lorraine, Nancy, France, pascal.robert@univ-lorraine.fr; Salim Al Amri, Ministry of Regional Municipalities and Water Resources, Sultanate of Oman, Salimalamri1988@gmail.com; Jürgen Koepke, Institut fuer Mineralogie, Leibniz University, Hannover, Germany, koepke@mineralogie.uni-hannover.de; Louise Koornneef, Geography, Earth and Environmental Sciences Plymouth University, Plymouth, UK louise.koornneef@plymouth.ac.uk; Romain Lafay, Institute of Earth Sciences, University of Lausanne, Lausanne, Switzerland, romain.lafay@unil.ch; Johan Lissenberg, School of Earth and Ocean Sciences, Cardiff University, Cardiff, UK, LissenbergCJ@Cardiff.ac.uk; Chris MacLeod, School of Earth and Ocean Sciences, Cardiff University, Cardiff, UK, macleod@cardiff.ac.uk; Mohsin Al Shukaili, Ministry of Regional Municipalities and Water Resource, Sultanate of Oman, alshukailimohsin@gmail.com; Ali

Al Qassabi, Ministry of Regional Municipalities and Water Resources, Sultanate of Oman, alimq7@gmail.com; Kyaw Moe, Japan Agency for Marine-Earth Science and Technology (JAMSTEC), Institute for Marine-Earth Exploration and Engineering, Yokosuka, Japan, moe@jamstec.go.jp; Yasu Yamada, Japan Agency for Marine-Earth Science and Technology (JAMSTEC), Institute for Marine-Earth Exploration and Engineering, Yokosuka, Japan, yyamada@jamstec.go.jp

ChikyuOman 2017 Description Team

Peter Kelemen, Co-Chief Scientist, Department of Earth and Environmental Sciences, Columbia University, New York, NY, USA, peterk@ldeo.columbia.edu; Damon Teagle, Co-Chief Scientist, School of Ocean and Earth Science, University of Southampton, Southampton, UK, Damon.Teagle@southampton.ac.uk; Eiichi Takazawa, Co-Chief Scientist, Department of Geology, Niigata University, Niigata, Japan takazawa@geo.sc.niigata-u.ac.jp; Katsuyoshi Michibayashi, Co-Chief Scientist, Institute of Geosciences, Shizuoka University, Shizuoka, Japan michibayashi@shizuoka.ac.jp; Michelle Harris, Alteration Lead/Staff Scientist/Co-Chief Scientist, Geography, Earth and Environmental Sciences, Plymouth University, Plymouth, UK, michelle.harris@plymouth.ac.uk; Jude Coggon, Oman Staff Scientist, School of Ocean and Earth Science, University of Southampton, Southampton, UK, jude.coggon@southampton.ac.uk; Juan Carlos de Obeso, Oman Staff Scientist/Alteration, Department of Earth and Environmental Sciences, Columbia University, New York, NY, USA, deobeso@ldeo.columbia.edu; Natsue Abe, Physical Properties, R&D Center for Ocean Drilling Science JAMSTEC, Yokosuka, Japan, abenatsu@jamstec.go.jp; Tetsu Akitou, Alteration Petrologist, Department of Earth Sciences Okayama University, Okayama, Japan, nozaka@cc.okayama-u.ac.jp; Salim Ahmed AlShahri, Omani Trainee, Geological Survey and Research, Public Authority for Mining Oman, s.alshahri1@gmail.com; Hamood Hamed Shames Al-Siyabi, Omani Trainee, Surface and Groundwater Assessment MRMWR, Oman, Aomani120@yahoo.com; Saif Masoud Alhumaimi, Omani Trainee, Geological Survey, Public Authority for Mining, Oman, saif.m@pam.gov.om; Maqbool Hussein AlRawahi, Omani Trainee, Surface and Groundwater Assessment MRMWR, Oman, maqbool.h@mrmwr.gov.om; Musaab Shaker Al Sarmi, Omani Trainee, Earth Science Department, Sultan Qaboos University, Oman, musaabs@squ.edu.om; Bader Hamed Alwaeli, Omani Trainee, Earth Science Department, Sultan Qaboos University, Oman baderw@squ.edu.om; Andreas Beinlich, Alteration Petrologist, Department of Applied Geology, Curtin University, Perth, Australia, andreas.beinlich@curtin.edu.au; Emma Bennett, Geochemistry, School of Earth and Ocean Science, Cardiff University, Cardiff, UK, bennette7@cardiff.ac.uk; Marine Boulanger, Igneous Petrologist, Department of Petrology, CRPG-CNRS Université de Lorraine, France, marineb@crpg.cnrs-nancy.fr; Elliot Carter, Geochemistry, School of Earth and Environmental Sciences University of Manchester, Manchester, UK, elliot.carter@manchester.ac.uk; Mike Cheadle, Structural Geologist, Department of Geology and Geophysics, University of Wyoming, Laramie, WY, USA, cheadle@uwyo.edu; Mark Cloos, Structural Geologist, Department of Geological Sciences, University of Texas at Austin, Austin, TX, USA, cloos@jsg.utexas.edu; Matthew Cooper, Geochemistry, School of Ocean and Earth Science, University of Southampton, Southampton, UK, mjco@noc.soton.ac.uk; Laura Crispini, Structural Geologist, Scienze della Terra dell'Ambiente e della Vita University of Genova, Genova, Italy, laura.crispini@unige.it; Joëlle D'Andres (was Ducommun), Alteration Petrologist, Research School of Earth Sciences, Australian National University, Canberra, ACT, Australia, joelle.ducommun@anu.edu.au; Luke Deamer, Structural Geologist, Department of Geology, Cardiff University, Cardiff, UK, deamerl@cardiff.ac.uk; Jeremy Deans, Structural Geologist, Department of Geography and Geology, University of Southern Mississippi, Hattiesburg, MS, USA, jeremy.deans@usm.edu; Kathi Faak, Igneous Petrologist, Institute for Geology, Mineralogy and Geophysics Ruhr-Universitaet Bochum, Bochum, Germany, Kathrin.Faak@rub.de; Marguerite Godard, Geochemistry, Department of Géosciences, CNRS Université de Montpellier, Montpellier, France, Marguerite.Godard@umontpellier.fr; Rebecca Greenberger, Infrared Spectrometry, Department of Geological and Planetary Sciences, California Institute of Technology, Pasadena, CA, USA, rgreenbe@caltech.edu; Yumiko Harigane, Structural Geologist, Research Institute of Geology and Geoinformation, National Institute of Advanced Industrial Science and Technology, Tsukuba, Japan, y-harigane@aist.go.jp; Kohei Hatakeyama, Physical Properties, Department of Earth and Planetary Systems Science, Hiroshima University, Hiroshima, Japan, kohei-hatakeyama@hiroshima-u.ac.jp; Andrew Horst, Paleomagnetist, Department of Geology, Marshall University, Huntington, WV, USA, horsta@marshall.edu; Takashi Hoshide, Igneous Petrologist, Graduate School of International Resource Sciences, Akita University, Akita, Japan, hoshide@gipc.akita-u.ac.jp; Benoit Ildefonse, Physical Properties, Department of Géosciences, CNRS Université de Montpellier, Montpellier, France, benoit.ildefonse@umontpellier.fr; Keisuke Ishii, Igneous Petrologist, Graduate school of Science and Technology, Niigata University, Nigata, Japan, f17e061a@mail.cc.niigata-u.ac.jp; Ana Jesus, Igneous

Petrologist, Department of Applied Geoscience, German University of Technology in Oman, Oman, ana.jesus@gutech.edu.om; Kevin Johnson, Igneous Petrologist, Department of Geology and Geophysics, University of Hawaii, Hawaii, USA, kjohnso2@hawaii.edu; Michael Kettermann, Structural Geologist, Structural Geology, Tectonics and Geomechanics, Aachen University, Aachen, Germany, michael.kettermann@emr.rwth-aachen.de; Hogyum Kim, Paleomagnetism, School of Earth and Environmental Sciences, Seoul National University, Seoul, Republic of Korea, kamhokam@snu.ac.kr; Jürgen Koepke, Igneous Petrologist, Institut fuer Mineralogie, Leibniz University, Hannover, Germany, koepke@mineralogie.uni-hannover.de; Kentaro Kondo, Igneous Petrologist, Graduate School of International Resource Sciences, Akita University, Akita, Japan, kentarokondo21@gmail.com; Louise Koornneef, Paleomagnetist, Geography, Earth and Environmental Sciences, Plymouth University, Plymouth, UK, louise.koornneef@plymouth.ac.uk; Alissa Kotowski, Structural Geologist, Jackson School of Geosciences, University of Texas at Austin, Austin, TX, USA, kotowski@utexas.edu; Fatna Kourim, Geochemistry, Earth Science Institute, Academia Sinica, Taipei, Taiwan, k.fatna@gmail.com; Yuki Kusano, Igneous Petrologist, Geological Survey of Japan, National Institute of Advanced Industrial Science and Technology, Tsukuba, Japan, y.kusano@aist.go.jp; Romain Lafay, Alteration Petrologist, Institute of Earth Sciences, University of Lausanne, Lausanne, Switzerland, romain.lafay@unil.ch; James Andrew Leong, Alteration Petrologist, School of Earth and Space Exploration, Arizona State University, Phoenix, AZ, USA, jmleong@asu.edu; Chris MacLeod, Structural Geologist, School of Earth and Ocean Sciences, Cardiff University, Cardiff, UK, macleod@cardiff.ac.uk; Craig Manning, Alteration Petrologist, Department of Earth, Planetary and Space Sciences, University of California, Los Angeles, CA, USA, manning@epss.ucla.edu; Catriona Menzies, Geochemist, School of Ocean and Earth Science, University of Southampton, Southampton, UK, c.menzies@soton.ac.uk; Dominik Mock, Alteration Petrologist, Institute for Mineralogy, Leibniz University of Hanover, Hanover, Germany, dom.mock@web.de; Tomoaki Morishita, Igneous Petrologist, Earth Science Course, Kanazawa University, Kanazawa, Japan, moripta@gmail.com; Tony Morris, Paleomagnetist, Geography, Earth and Environmental Sciences, Plymouth University, Plymouth, UK, amorris@plymouth.ac.uk; Du Khac Nguyen, Igneous Petrologist, School of Natural System, Kanazawa University, Kanazawa, Japan, nguyenkhacdu@humg.edu.vn; Toshio Nozaka, Alteration Petrologist, Department of Earth Sciences, Okayama University, Okayama, Japan, nozaka@cc.okayama-u.ac.jp, Keishi Okazaki, Physical Properties, Kochi Institute for Core Sample Research JAMSTEC, Yokosuka, Japan, okazakik@jamstec.go.jp; Americus Perez, Geochemist, Department of Earth Sciences, Kanazawa University, Kanazawa, Japan, adperez@stu.kanazawa-u.ac.jp; Suzanne Picazo, Igneous Petrologist, Institute of Earth Sciences, University of Lausanne, Lausanne, Switzerland, suzanne.picazo@gmail.com; Ryoko Senda, Geochemist, Faculty of Social and Cultural Studies, Kyushu University, Fukuoka, Japan, senda@scs.kyushu-u.ac.jp, Yamato Tateishi, Physical Properties, Department of Earth Sciences, Okayama University, Okayama, Japan, nozaka@cc.okayama-u.ac.jp; Jessica Till, Paleomagnetist, Geomechanics and Rheology, German Research Center for Geosciences, Potsdam, Germany, Germanyijtill@hi.is; Susumu Umino, Igneous Petrologist, School of Natural Science and Technology, Kanazawa University, Kanazawa, Japan, sesumin@staff.kanazawa-u.ac.jp, Janos Urai, Structural Geologist, Structural Geology Tectonics and Geomechanics, Aachen University, Aachen, Germany, j.urai@ged.rwth-aachen.de, Yoichi Usui, Paleomagnetist, Deep Earth Structure and Dynamics Research JAMSTEC, Yokosuka, Japan, yoichi@jamstec.go.jp; David Zeko, Alteration Petrologist, Earth, Ocean and Atmospheric Sciences, University of British Columbia, Vancouver, BC, Canada, dzeko@eoas.ubc.ca; Barbara Zihlmann, Alteration Petrologist, School of Ocean and Earth Science, University of Southampton, Southampton, UK, barbara.zihlmann@soton.ac.uk

Acknowledgments
This work benefited from fruitful discussions with Francoise Boudier, Cécile Prigent, Manuel Menzel, and Emilien Oliot. The authors thank Céline Martin and Léa Causse for their assistance for trace element analyses at the Géosciences Montpellier clean lab facility and on the AETE-ISO platform ("Analyses des Eléments en Trace dans l'Environnement et ISOtopes"; OREME observatory, University of Montpellier). The authors would like to thank also the associate editor, Phil Janney, as well as L. W. Diamond and an anonymous reviewer for their comments and suggestions on the manuscript. This research used samples and/or data provided by the Oman Drilling Project. The Oman Drilling Project (OmanDP) has been possible through co-mingled funds from the International Continental Scientific Drilling Project (ICDP; Kelemen, Matter, Teagle Lead PIs), the Sloan Foundation – Deep Carbon Observatory (Grant 2014-3-01, Kelemen PI), the National Science Foundation (NSF-EAR-1516300, Kelemen lead PI), NASA – Astrobiology Institute (NNA15BB02A, Templeton PI), the German Research Foundation (DFG: KO 1723/21-1, Koepke PI), the Japanese Society for the Promotion of Science (JSPS no:16H06347, Michibayashi PI; and KAKENHI 16H02742, Takazawa PI), the European Research Council (Adv: no.669972; Jamveit PI), the Swiss National Science Foundation (SNF:20FI21_163073, Früh-Green PI), JAMSTEC, the TAMU-JR Science Operator, and contributions from the Sultanate of Oman Ministry of Regional Municipalities and Water Resources, the Oman Public Authority of Mining, Sultan Qaboos University, CNRS-Univ. Montpellier, Columbia University of New York, and the University of Southampton. This study was funded by Project ANR-18-CE01-0014-01 LISZT.

Data Availability Statement

The dataset is available on the PANGAEA data archiving platform (https://doi.pangaea.de/10.1594/PANGAEA.937490).

References

Ambrose, T. K., Waters, D. J., Searle, M. P., Gopon, P., & Forshaw, J. B. (2021). Burial, accretion, and exhumation of the metamorphic sole of the Oman-UAE Ophiolite. *Tectonics*, *40*(4), e2020TC006392. https://doi.org/10.1029/2020TC006392

Andreani, M., Escartin, J., Delacour, A., Ildefonse, B., Godard, M., Dyment, J., et al. (2014). Tectonic structure, lithology and hydrothermal signature of the Rainbow massif (Mid-Atlantic Ridge 36°14'N). *Geochemistry, Geophysics, Geosystems*, *15*(9), 3543–3571. https://doi.org/10.1002/2014GC005269

Andreani, M., Luquot, L., Gouze, P., Godard, M., Hoise, E., & Gibert, B. (2009). Experimental study of carbon sequestration reactions controlled by the percolation of CO_2 -rich brine through peridotites. *Environmental Science & Technology*, *43*(4), 1226–1231. https://doi.org/10.1021/es8018429

Azer, M. K., Gahlan, H. A., Asimow, P. D., Mubarak, H. S., & Al-Kahtany, K. M. (2019). Multiple stages of carbonation and element redistribution during formation of ultramafic-hosted magnesite in Neoproterozoic ophiolites of the Arabian-Nubian Shield, Egypt. *The Journal of Geology*, *127*(1), 81–107. https://doi.org/10.1086/700652

Baumgartner, L. P., & Olsen, S. N. (1995). A least-squares approach to mass transport calculations using the isocon method. *Economic Geology*, *90*(5), 1261–1270. https://doi.org/10.2113/gsecongeo.90.5.1261

Bechennec, F., Le Metour, J., Rabu, D., Bourdillon-de-Grissac, C., de Wever, P., Beurrier, M., & Villey, M. (1990). The Hawasina Nappes: Stratigraphy, palaeogeography and structural evolution of a fragment of the south-Tethyan passive continental margin. *Geological Society, London, Special Publications*, *49*(1), 213–223. https://doi.org/10.1144/gsl.sp.1992.049.01.14

Beinlich, A., Plümper, O., Boter, E., Müller, I. A., Kourim, F., Ziegler, M., et al. (2020). Kelemen, and the Oman Drilling Project Science Team Ultramafic Rock Carbonation: Constraints From Listvenite Core BT1B, Oman Drilling Project. *Journal of Geophysical Research: Solid Earth*, *125*, e2019JB019060. https://doi.org/10.1029/2019JB019060

Belgrano, T. M., Diamond, L. W., Vogt, Y., Biedermann, A. R., Gilgen, S. A., & Al-Tobi, K. (2019). A revised map of volcanic units in the Oman ophiolite: Insights intothe architecture of an oceanic proto-arc volcanic sequence. *Solid Earth*, *10*, 1181–1217. https://doi.org/10.5194/se-10-1181-2019

Belogub, E. V., Melekestseva, I. Y., Novoselov, K. A., Zabotina, M. V., Tret'yakov, G. A., Zaykov, V. V., & Yuminov, A. M. (2017). Listvenite-related gold deposits of the South Urals (Russia): A review. *Ore Geology Reviews*, *85*, 247–270. https://doi.org/10.1016/j.oregeorev.2016.11.008

Boschi, C., Dini, A., Dallai, L., Ruggieri, G., & Gianelli, G. (2009). Enhanced CO_2-mineral sequestration by cyclic hydraulic fracturing and Si-rich fluid infiltration into serpentinites at Malentrata (Tuscany, Italy). *Chemical Geology*, *265*(1), 209–226. https://doi.org/10.1016/j.chemgeo.2009.03.016

Boskabadi, A., Pitcairn, I. K., Leybourne, M. I., Teagle, D. A. H., Cooper, M. J., Hadizadeh, H., et al. (2020). Carbonation of ophiolitic ultramafic rocks: Listvenite formation in the Late Cretaceous ophiolites of eastern Iran. *Lithos*, 352–353, 105307. https://doi.org/10.1016/j.lithos.2019.105307

Boudier, F., Baronnet, A., & Mainprice, D. (2010). Serpentine mineral replacements of natural olivine and their seismic implications: Oceanic lizardite versus subduction-related antigorite. *Journal of Petrology*, *51*(1–2), 495–512. https://doi.org/10.1093/petrology/egp049

Boudier, F., Ceuleneer, G., & Nicolas, A. (1988). Shear zones, thrusts and related magmatism in the Oman Ophiolite; initiation of thrusting on an oceanic ridge. *Tectonophysics*, *151*(1–4), 275–296. https://doi.org/10.1016/0040-1951(88)90249-1

Boudier, F., & Coleman, R. G. (1981). Cross section through the peridotite in the Samail ophiolite, southeastern Oman Mountains. *Journal of Geophysical Research*, *86*, 2573–2592. https://doi.org/10.1029/jb086ib04p02573

Boudier, F., & Nicolas, A. (1988). Special Issue: The ophiolites of Oman. *Tectonophysics*, *151*(1–4). https://doi.org/10.1016/0040-1951(88)90237-5

Boudier, F., & Nicolas, A. (2018). Synchronous seafloor spreading and subduction at the paleo-convergent margin of Semail and Arabia. *Tectonics*, *37*(9), 2961–2982. https://doi.org/10.1029/2018TC005099

Buisson, G., & Leblanc, M. (1985). Gold in carbonatized ultramafic rocks from ophiolite complexes. *Economic Geology*, *80*(7), 2028–2029. https://doi.org/10.2113/gsecongeo.80.7.2028

Cannaò, E., & Malaspina, N. (2018). From oceanic to continental subduction: Implications for the geochemical and redox evolution of the supra-subduction mantle. *Geosphere*, *14*(6), 2311–2336. https://doi.org/10.1130/ges01597.1

Cannao, E., Scambelluri, M., Bebout, G. E., Agostini, S., Pettke, T., Godard, M., & Crispini, L. (2020). Ophicarbonate evolution from seafloor to subduction and implications for deep-Earth C cycling. *Chemical Geology*, *546*, 119626. https://doi.org/10.1016/j.chemgeo.2020.119626

Cannaò, E., Tiepolo, M., Bebout, G. E., & Scambelluri, M. (2020). Into the deep and beyond: Carbon and nitrogen subduction recycling in secondary peridotites. *Earth and Planetary Science Letters*, *543*, 116328. https://doi.org/10.1016/j.epsl.2020.116328

Chauvet, F., Lapierre, H., Maury, R. C., Bosch, D., Basile, C., Cotten, J., et al. (2011). Triassic alkaline magmatism of the Hawasina Nappes: Post-breakup melting of the Oman lithospheric mantle modified by the Permian Neotethyan Plume. *Lithos*, *122*(1), 122–136. https://doi.org/10.1016/j.lithos.2010.12.006

Coleman, R. G., & Hopson, C. A. (1981). Oman ophiolite Special Issue. *Journal of Geophysical Research*, *B86*(4), 2497–2782. https://doi.org/10.1029/jb086ib04p02497

De Obeso, J. C., Kelemen, P., Leong, J. M., Manning, C., Menzel, M., Cai, Y., & Godard, M. (2021). Oman Drilling Project Phase 1 Science Party, Deep sourced fluids for peridotite carbonation in the shallow mantle wedge of a fossil subduction zone: Sr and C isotope profiles of OmanDP Hole BT1B. *Earth and Space Science Open Archive*. https://doi.org/10.1002/essoar.10507483.10507481

Deer, W. A., Howie, R. A., & Zussman, J. (1996). *An Introduction to the Rock-Forming Minerals* (2nd ed., p. 712). Prentice Hall.

Deschamps, F., Godard, M., Guillot, S., & Hattori, K. (2013). Geochemistry of subduction zones serpentinites: A review. In B. Reynard, M. Godard, & S. Guillot (Eds.), *Serpentinites from mid-oceanic ridges to subduction* (pp. 96–127). https://doi.org/10.1016/j.lithos.2013.05.019

Dewandel, B. (2002). *Structure et fonctionnement hydrogéologique d'un aquifère discontinu: l'ophiolite d'Oman [PhD thesis, Univ. Montpellier, France]* (p. 328).

Ernewein, M., Pflumio, C., & Whitechurch, H. (1988). The death of an accretion zone as evidenced by the magmatic history of the Sumail ophiolite (Oman). *Tectonophysics*, *151*, 247–274. Spec. Issue - The ophiolites of Oman. https://doi.org/10.1016/0040-1951(88)90248-x

Escayola, M. P., Proenza, J. A., Van Staal, C. R., Rogers, N., & Skulski, T. (2009). The Point Rousse listvenites, Baie Verte, Newfoundland: Altered ultramafic rocks with potential for gold mineralization. *Geological Survey Report. 09–1*, 1–12.

Falk, E. S., & Kelemen, P. B. (2015). Geochemistry and petrology of listvenite in the Samail ophiolite, Sultanate of Oman: Complete carbonation of peridotite during ophiolite emplacement. *Geochimica et Cosmochimica Acta*, *160*, 70–90. https://doi.org/10.1016/j.gca.2015.03.014

Fouquet, Y., Cambon, P., Etoubleau, J., Charlou, J. L., Ondréas, H., Barriga, F. J. A. S., et al. (2010). Geodiversity of hydrothermal processes along the mid-Atlantic ridge and ultramafic-hosted mineralization: A new type of oceanic Cu-Zn-Co-Au volcanogenic massive sulfide deposit. In *Diversity of hydrothermal systems on slow spreading ocean ridges* (pp. 321–367). https://doi.org/10.1029/2008GM000746

Gerbert-Gaillard, L. (2002). *Caractérisation géochimique des peridotites de l'ophiolite d'Oman: Processus magmatiques aux limites lithosphere/asthenosphere, [PhD thesis, Univ. Montpellier, France]* (p. 266).

Ghent, E. D., & Stout, M. Z. (1981). Metamorphism at the base of the Semail ophiolite, Southeastern Oman ophiolite. *Journal of Geophysical Research*, *86*, 2557–2573. https://doi.org/10.1029/jb086ib04p02557

Glennie, K. W., Boeuf, M. G. A., Hugues Clark, M. W., Moody-Stuart, M., Pilaar, W. F. H., & Reinhardt, B. M. (1974). *Geology of the Oman Mountains* (p. 423). Nederlands Geologisch Mijnbouwkundig Genootschap.

Godard, M., Bosch, D., & Einaudi, F. (2006). A MORB source for low Ti magmatism in the Semail ophiolite. *Chemical Geology*, *234*, 58–78. https://doi.org/10.1016/j.chemgeo.2006.04.005

Godard, M., Dautria, J.-M., & Perrin, M. (2003). Geochemical variability of the Oman ophiolite lavas: Relationship with spatial distribution and paleomagnetic directions. *Geochemistry, Geophysics, Geosystems*, *4*(6), 8609. https://doi.org/10.1029/2002GC000452

Godard, M., Jousselin, D., & Bodinier, J.-L. (2000). Relationships between geochemistry and structure beneath a palaeo-spreading centre: A study of the mantle section in the Oman Ophiolite. *Earth and Planetary Science Letters*, *180*, 133–148. https://doi.org/10.1016/s0012-821x(00)00149-7

Godard, M., Luquot, L., Andreani, M., & Gouze, P. (2013). Incipient hydration of mantle lithosphere at ridges: A reactive-percolation experiment. *Earth and Planetary Science Letters*, *371–372*, 92–102. https://doi.org/10.1016/j.epsl.2013.03.052

Goodenough, K. M., Styles, M. T., Schofield, D., Thomas, R. J., Crowley, Q. C., Lilly, R. M., et al. (2010). Architecture of the Oman–UAE ophiolite: Evidence for a multi-phase magmatic history. *Arabian Journal of Geosciences*, *3*(4), 439–458. https://doi.org/10.1007/s12517-010-0177-3

Grant, J. A. (1986). The isocon diagram; a simple solution to Gresens' equation for metasomatic alteration. *Economic Geology*, *81*(8), 1976–1982. https://doi.org/10.2113/gsecongeo.81.8.1976

Grozeva, N. G., Klein, F., Seewald, J. S., & Sylva, S. P. (2017). Experimental study of carbonate formation in oceanic peridotite. *Geochimica et Cosmochimica Acta*, *199*, 264–286. https://doi.org/10.1016/j.gca.2016.10.052

Halls, C., & Zhao, R. (1995). Listvenite and related rocks: Perspectives on terminology and mineralogy with reference to an occurrence at Creggan baun, Co. Mayo, Republic of Ireland. *Mineralium Deposita*, *30*(3–4), 303–313. https://doi.org/10.1007/bf00196366

Hanghoj, K., Kelemen, P., Hassler, D., & Godard, M. (2010). Composition and genesis of depleted mantle peridotites from the Wadi Tayin massif, Oman ophiolite. Major and trace element geochemistry, and Os isotope and PGE systematics. *Journal of Petrology*, *51*(1–2), 201–227. https://doi.org/10.1093/petrology/egp077

Hansen, L. D., Dipple, G. M., Gordon, T. M., & Kellett, D. A. (2005). Carbonated serpentinite (Listwanite) at Atlin, British Columbia: A geological analogue to Carbon Dioxide sequestration. *The Canadian Mineralogist*, *43*(1), 225–239. https://doi.org/10.2113/gscanmin.43.1.225

Hofmann, A. W. (2008). The enduring lead paradox. *Nature Geoscience*, *1*(12), 812–813. https://doi.org/10.1038/ngeo372

Hopson, C. A., Coleman, R. G., Gregory, R. T., Pallister, J. S., & Bailey, E. H. (1981). Geologic section through the Samail ophiolite and associated rocks along a Muscat-Ibra transect, southeastern Oman Mountains. *Journal of Geophysical Research*, *86*, 2527–2544. https://doi.org/10.1029/jb086ib04p02527

Ishikawa, T., Fujisawa, S., Nagaishi, K., & Masuda, T. (2005). Trace element characteristics of the fluid liberated from amphibolite-facies slab: Inference from the metamorphic sole beneath the Oman ophiolite and implication for boninite genesis. *Earth and Planetary Science Letters*, *240*(2), 355–377. https://doi.org/10.1016/j.epsl.2005.09.049

Jamtveit, B., Malthe-Sørenssen, A., & Kostenko, O. (2008). Reaction enhanced permeability during retrogressive metamorphism. *Earth and Planetary Science Letters*, *267*(3), 620–627. https://doi.org/10.1016/j.epsl.2007.12.016

Janecky, D. R., & Seyfried, W. E. (1986). Hydrothermal serpentinization of peridotite within the oceanic-crust- Experimental investigations of mineralogy and major element chemistry. *Geochimica et Cosmochimica Acta*, *50*(7), 1357–1378. https://doi.org/10.1016/0016-7037(86)90311-x

Kelemen, P., de Obeso, J. C., Leong, J. M., Godard, M., Kotowski, A. J., Manning, C., et al. (2021). Sulaimani, and Oman Drilling Project Science TeamMass transfer into the leading edge of the mantle wedge: Initial Results from Oman Drilling Project Hole BT1B. *Earth and Space Science Open Archive*. https://doi.org/10.1002/essoar.10507370.10507371

Kelemen, P. B., & Manning, C. E. (2015). Reevaluating carbon fluxes in subduction zones, what goes down, mostly comes up. *Proceedings of the National Academy of Sciences*, *112*(30), E3997–E4006. https://doi.org/10.1073/pnas.1507889112

Kelemen, P. B., Matter, J., Streit, E. E., Rudge, J. F., Curry, W. B., & Blusztajn, J. (2011). Rates and mechanisms of mineral carbonation in peridotite: Natural processes and recipes for enhanced, in situ CO_2 capture and storage. *Annual review of earth and planetary sciences* 39(1), 545–576). https://doi.org/10.1146/annurev-earth-092010-152509

Kelemen, P. B., Matter, J. M., Teagle, D. A. H., Coggon, J. A., & The Oman Drilling Project Science Team. (2020). *Proceedings of the Oman Drilling Project*. International Ocean Discovery Program. https://doi.org/10.14379/OmanDP.proc.2020

Khedr, M. Z., Arai, S., & Python, M. (2013). Petrology and chemistry of basal lherzolites above the metamorphic sole from Wadi Sarami central Oman ophiolite. *Journal of Mineralogical and Petrological Sciences*, *108*(1), 13–24. https://doi.org/10.2465/jmps.121026

Khedr, M. Z., Arai, S., Python, M., & Tamura, A. (2014). Chemical variations of abyssal peridotites in the central Oman ophiolite: Evidence of oceanic mantle heterogeneity. *Gondwana Research*, *25*(3), 1242–1262. https://doi.org/10.1016/j.gr.2013.05.010

Lambart, S., Savage, H. M., Robinson, B. G., & Kelemen, P. B. (2018). Experimental Investigation of the Pressure of Crystallization of Ca(OH)2: Implications for the Reactive Cracking Process. *Geochemistry, Geophysics, Geosystems*, *19*(9), 3448–3458. https://doi.org/10.1029/2018GC007609

Lapierre, H., Samper, A., Bosch, D., Maury, R. C., Béchennec, F., Cotten, J., et al. (2004). The Tethyan plume: Geochemical diversity of Middle Permian basalts from the Oman rifted margin. *Lithos*, *74*(3–4), 167–198. https://doi.org/10.1016/j.lithos.2004.02.006

Laznicka, P. (2010). *Giant Metallic Deposits: Future Sources of Industrial Metals* (p. 949). Springer.

Le Mée, L., Girardeau, J., & Monnier, C. (2004). Mantle segmentation along the Oman ophiolite fossil mid-ocean ridge. *Nature*, *432*, 167–172. https://doi.org/10.1038/nature03075

Li, Y.-H. (1991). Distribution patterns of the elements in the ocean: A synthesis. *Geochimica et Cosmochimica Acta*, *55*(11), 3223–3240. https://doi.org/10.1016/0016-7037(91)90485-n

Linckens, J., Herwegh, M., & Müntener, O. (2011). Linking temperature estimates and microstructures in deformed polymineralic mantle rocks. *Geochemistry, Geophysics, Geosystems*, *12*(8). https://doi.org/10.1029/2011GC003536

Lippard, S. J., Shelton, A. W., & Gass, I. G. (Eds.), (1986). *The ophiolite of northern Oman* (p. 178). Backwell Scientific Publications.

MacLeod, C. J., Johan Lissenberg, C., & Bibby, L. E. (2013). "Moist MORB" axial magmatism in the Oman ophiolite: The evidence against a mid-ocean ridge origin. *Geology*, *41*(4), 459–462. https://doi.org/10.1130/g33904.1

Maury, R. C., Béchennec, F., Cotten, J., Caroff, M., Cordey, F., & Marcoux, J. (2003). Middle Permian plume-related magmatism of the Hawasina Nappes and the Arabian Platform: Implications on the evolution of the Neotethyan margin in Oman. *Tectonics*, *22*(6), 1073. https://doi.org/10.1029/2002TC001483

McDonough, W. F., & Sun, S. S. (1995). The composition of the Earth. *Chemical Geology*, *120*(3–4), 223–253. https://doi.org/10.1016/0009-2541(94)00140-4

Menzel, M. D., Garrido, C. J., & López Sánchez-Vizcaíno, V. (2020). Fluid-mediated carbon release from serpentinite-hosted carbonates during dehydration of antigorite-serpentinite in subduction zones. *Earth and Planetary Science Letters*, *531*, 115964. https://doi.org/10.1016/j.epsl.2019.115964

Menzel, M. D., Garrido, C. J., López Sánchez-Vizcaíno, V., Marchesi, C., Hidas, K., Escayola, M. P., & Delgado Huertas, A. (2018). Carbonation of mantle peridotite by CO2-rich fluids: The formation of listvenites in the Advocate ophiolite complex (Newfoundland, Canada). *Lithos*, *323*, 238–261. https://doi.org/10.1016/j.lithos.2018.06.001

Menzel, M. D., Urai, J. L., de Obeso, J. C., Kotowski, A., Manning, C. E., Kelemen, P. B., et al. (2020). Brittle Deformation of Carbonated Peridotite—Insights from Listvenites of the Samail Ophiolite (Oman Drilling Project Hole BT1B). *Journal of Geophysical Research: Solid Earth*, *125*, e2020JB020199. https://doi.org/10.1029/2020JB020199

Monnier, C., Girardeau, J., Le Mée, L., & Polvé, M. (2006). Along-ridge petrological segmentation of the mantle in the Oman ophiolite. *Geochemistry, Geophysics, Geosystems*, *7*(11). https://doi.org/10.1029/2006GC001320

Nasir, S., Al Sayigh, A. R., Al Harthy, A., Al-Khirbash, S., Al-Jaaidi, O., Musllam, A., et al. (2007). Mineralogical and geochemical characterization of listwaenite from the Semail Ophiolite, Oman. *Geochemistry*, *67*(3), 213–228. https://doi.org/10.1016/j.chemer.2005.01.003

Nicolas, A., Boudier, F., Ildefonse, B., & Ball, E. (2000). Accretion of Oman ophiolite and United Emirates ophiolite. Discussion of a new structural map. *Marine Geophysical Researches*, *21*, 147–180. https://doi.org/10.1023/A:1026769727917

Noel, J., Godard, M., Oliot, E., Martinez, I., Williams, M., Boudier, F., et al. (2018). Evidence of polygenetic carbon trapping in the Oman Ophiolite: Petro-structural, geochemical, and carbon and oxygen isotope study of the Wadi Dima harzburgite-hosted carbonates (Wadi Tayin massif, Sultanate of Oman). *Lithos 323*, 218–237. https://doi.org/10.1016/j.lithos.2018.08.020

Oberhänsli, R., Wendt, A. S., Goffé, B., & Michard, A. (1999). Detrital chromites in metasediments of the East-Arabian continental margin in the Saih Hatat area: Constraints for the palaeogeographic setting of the Hawasina and Semail basins (Oman Mountains). *International Journal of Earth Sciences*, *88*(1), 13–25. https://doi.org/10.1007/s005310050242

Paulick, H., Bach, W., Godard, M., Hoog, C.-J., Suhr, G., & Harvey, J. (2006). Geochemistry of abyssal peridotites (Mid-Atlantic Ridge, 15°20'N, ODP Leg 209): Implications for fluid/rock interaction in slow spreading environments. *Chemical Geology*, *234*(3–4), 179–210. https://doi.org/10.1016/j.chemgeo.2006.04.011

Pearce, J. A., Alabaster, T., Shelton, A. W., & Searle, M. P. (1981). The Oman ophiolite as a cretaceous arc-basin complex : Evidence and implications. *Philosophical Transactions of the Royal Society of London. Series A, Mathematical and Physical Sciences*, *300*(1454), 299–317. https://doi.org/10.1098/rsta.1981.0066

Peters, D., Bretscher, A., John, T., Scambelluri, M., & Pettke, T. (2017). Fluid-mobile elements in serpentinites: Constraints on serpentinisation environments and element cycling in subduction zones. *Chemical Geology*, *466*, 654–666. https://doi.org/10.1016/j.chemgeo.2017.07.017

Peters, T. J., Nicolas, A., & Coleman, R. G. (Eds.). (1991). *Ophiolite genesis and evolution of the oceanic lithosphere* (p. 903). Kluwer Academic Press.

Peuble, S., Godard, M., Gouze, P., Leprovost, R., Martinez, I., & Shilobreeva, S. (2019). Control of CO_2 on flow and reaction paths in olivine-dominated basements: An experimental study. *Geochimica et Cosmochimica Acta*, *252*, 16–38. https://doi.org/10.1016/j.gca.2019.02.007

Peuble, S., Godard, M., Luquot, L., Gouze, P., & Martinez, I. (2015). CO_2 geological storage in olivine rich basaltic aquifers: New Insights from flow-through experiments. *Applied Geochemistry*, *52*, 174–190. https://doi.org/10.1016/j.apgeochem.2014.11.024

Plank, T. (2014). The chemical composition of subducting sediments. In H. D. Holland, & K. K. Turekian (Eds.), *Treatise on Geochemistry* (Second Edition, pp. 607–629). Elsevier. https://doi.org/10.1016/B978-0-08-095975-7.00319-3

Plank, T., Kelley, K., Murray, R., & Stern, L. Q. (2007). Chemical composition of sediments subducting at the Izu-Bonin trench. *Geochemistry, Geophysics, Geosystems*, *8*(4). https://doi.org/10.1029/2006GC001444

Plank, T., & Ludden, J. N. (1992). Geochemistry of sediments in the Argo Abyssal Plain at Site 765: A continental margin reference section for sediment recycling in subduction zone. In F. M. Gradstein, J. N. Ludden, & A. C. Adamson (Eds.), *Proceedings of Ocean Drilling Program, Scientific Results* (Vol. 123, pp. 167–189). Ocean Drilling Program. https://doi.org/10.2973/odp.proc.sr.2123.2158.1992

Power, I. M., Harrison, A. L., Dipple, G. M., Wilson, S. A., Kelemen, P. B., Hitch, M., & Southam, G. (2013). Carbon mineralization: From natural analogues to engineered systems. *Reviews in Mineralogy and Geochemistry*, *77*(1), 305–360. https://doi.org/10.2138/rmg.2013.77.9

Prigent, C., Agard, P., Guillot, S., Godard, M., & Dubacq, B. (2018). Mantle wedge (de)formation during subduction infancy: Evidence from the base of the Semail ophiolitic mantle. *Journal of Petrology*, *59*(11), 2061–2092. https://doi.org/10.1093/petrology/egy090

Prigent, C., Guillot, S., Agard, P., Lemarchand, D., Soret, M., & Ulrich, M. (2018). Transfer of subduction fluids into the deforming mantle wedge during nascent subduction: Evidence from trace elements and boron isotopes (Semail ophiolite, Oman). *Earth and Planetary Science Letters*, *484*, 213–228. https://doi.org/10.1016/j.epsl.2017.12.008

Rioux, M., Garber, J., Bauer, A., Bowring, S., Searle, M., Kelemen, P., & Hacker, B. (2016). Synchronous formation of the metamorphic sole and igneous crust of the Semail ophiolite: New constraints on the tectonic evolution during ophiolite formation from high-precision U–Pb zircon geochronology. *Earth and Planetary Science Letters*, *451*, 185–195. https://doi.org/10.1016/j.epsl.2016.06.051

Rioux, M., Garber, J. M., Searle, M. P., Kelemen, P., Miyashita, S., Adachi, Y., & Bowring, S. (2021). High-Precision U-Pb Zircon Dating of Late Magmatism in the Samail Ophiolite: A Record of Subduction Initiation. *Journal of Geophysical Research: Solid Earth*, *126*(5), e2020JB020758. https://doi.org/10.1029/2020JB020758

Rose, G. (1837). Mineralogisch-geognostiche Reise nach dem Ural, dem Altai und dem Kaspischen Meere. In G. E. Reimer (Ed.), *Reise nach dem nordlichen Ural und dem Altai - Volume 1*. Verlag der Sanderschen Buchhandlung.

Salters, V. J. M., & Stracke, A. (2004). Composition of the depleted mantle. *Geochemistry, Geophysics, Geosystems*, *5*(5). https://doi.org/10.1029/2003GC000597

Schroeder, T., Bach, W., Jöns, N., Jöns, S., Monien, P., & Klügel, A. (2015). Fluid circulation and carbonate vein precipitation in the footwall of an oceanic core complex, Ocean Drilling Program Site 175, Mid-Atlantic Ridge. *Geochemistry, Geophysics, Geosystems*, *16*(10), 3716–3732. https://doi.org/10.1002/2015GC006041

Searle, M. P., & Cox, J. (1999). Tectonic setting, origin, and obduction of the Oman ophiolite. *GSA Bulletin*, *111*(1), 1042–1122. https://doi.org/10.1130/0016-7606(1999)111<0104:tsoaoo>2.3.co;2

Searle, M. P., & Malpas, J. (1980). Structure and metamorphism of rocks beneath the Semail ophiolite of Oman and their significance in ophiolite obduction. *Transactions of the Royal Society of Edinburgh: Earth Sciences*, *71*(4), 247–262. https://doi.org/10.1017/s0263593300013614

Searle, R. C. (2019). *Geology of the Oman Mountains, Eastern Arabia* (p. 478). Springer. https://doi.org/10.1007/978-3-030-18453-7

Seyfried, W. E., Foustoukos, D. I., & Fu, Q. (2007). Redox evolution and mass transfer during serpentinization: An experimental and theoretical study at 200 degrees C, 500 bar with implications for ultramafic-hosted hydrothermal systems at Mid-Ocean Ridges. *Geochimica et Cosmochimica Acta*, *71*(15), 3872–3886. https://doi.org/10.1016/j.gca.2007.05.015

Soret, M., Agard, P., Dubacq, B., Plunder, A., & Yamato, P. (2017). Petrological evidence for stepwise accretion of metamorphic soles during subduction infancy (Semail ophiolite, Oman and UAE). *Journal of Metamorphic Geology*, *35*(9), 1051–1080. https://doi.org/10.1111/jmg.12267

Spandler, C., & Pirard, C. (2013). Element recycling from subducting slabs to arc crust: A review. *Lithos*, *170–171*, 208–223. https://doi.org/10.1016/j.lithos.2013.02.016

Stanger, G. (1985). Silicified serpentinite in the Semail nappe of Oman. *Lithos*, *18*, 13–22. https://doi.org/10.1016/0024-4937(85)90003-9

Takazawa, E., Okayasu, T., & Satoh, K. (2003). Geochemistry and origin of the basal lherzolites from the northern Oman ophiolite (northern Fizh block). *Geochemistry, Geophysics, Geosystems*, *4*(2), 1021. https://doi.org/10.1029/2001GC000232

Ulrich, M., Muñoz, M., Guillot, S., Cathelineau, M., Picard, C., Quesnel, B., et al. (2014). Dissolution–precipitation processes governing the carbonation and silicification of the serpentinite sole of the New Caledonia ophiolite. *Contributions to Mineralogy and Petrology*, *167*(1), 952. https://doi.org/10.1007/s00410-013-0952-8

Ulven, O. I., Jamtveit, B., & Malthe-Sørenssen, A. (2014). Reaction-driven fracturing of porous rock. *Journal of Geophysical Research: Solid Earth*, *119*(10), 7473–7486. https://doi.org/10.1002/2014JB011102

Villey, M., Le Metour, J., & De Gramont, X. (1986). *Geological map of Fanja, Sheet NF 40-3F*. Explanatory Notes, BRGM and Oman Ministry of Petroleum & Minerals.

Warren, C. J., Parrish, R. R., Waters, D. J., & Searle, M. P. (2005). Dating the geologic history of Oman's Semail ophiolite: Insights from U-Pb geochronology. *Contributions to Mineralogy and Petrology*, *150*, 403–422. https://doi.org/10.1007/s00410-005-0028-5

Wilde, A., Simpson, L., & Hanna, S. (2002). Preliminary study of Cenozoic hydrothermal alteration and platinum deposition in the Oman Ophiolite. *Journal of the Virtual Explorer*, *6*, 7–13. https://doi.org/10.3809/jvirtex.2002.00038

Wilson, A. D. (1960). The micro-determination of ferrous iron in silicate minerals by a volumetric and a colorimetric method. *The Analyst*, *85*(1016), 823–827. https://doi.org/10.1039/an9608500823

Yoshikawa, M., Python, M., Tamura, A., Arai, S., Takazawa, E., Shibata, T., et al. (2015). Melt extraction and metasomatism recorded in basal peridotites above the metamorphic sole of the northern Fizh massif, Oman ophiolite. *Tectonophysics*, *650*, 53–64. https://doi.org/10.1016/j.tecto.2014.12.004

Solid Earth, 13, 1191–1218, 2022
https://doi.org/10.5194/se-13-1191-2022

Solid Earth Open Access EGU

Progressive veining during peridotite carbonation: insights from listvenites in Hole BT1B, Samail ophiolite (Oman)

Manuel D. Menzel[1,a], **Janos L. Urai**[1], **Estibalitz Ukar**[2], **Thierry Decrausaz**[3], **and Marguerite Godard**[3]

[1]Tectonics and Geodynamics, RWTH Aachen University, Lochnerstrasse 4–20, 52056 Aachen, Germany
[2]Bureau of Economic Geology, The University of Texas at Austin, Austin, TX, USA
[3]Géosciences Montpellier, CNRS, Université de Montpellier, Montpellier, France
[a]now at: Instituto Andaluz de Ciencias de la Tierra (CSIC-IACT), Avenida de Palmeras 4, 18100 Armilla, Spain

Correspondence: Manuel D. Menzel (manuel.menzel@csic.es)

Received: 21 December 2021 – Discussion started: 5 January 2022
Revised: 6 May 2022 – Accepted: 11 July 2022 – Published: 1 August 2022

Abstract. The reaction of serpentinized peridotite with CO_2-bearing fluids to form listvenite (quartz–carbonate rock) requires massive fluid flux and significant permeability despite an increase in solid volume. Listvenite and serpentinite samples from Hole BT1B of the Oman Drilling Project help to understand mechanisms and feedbacks during vein formation in this process. Samples analyzed in this study contain abundant magnesite veins in closely spaced, parallel sets and younger quartz-rich veins. Cross-cutting relationships suggest that antitaxial, zoned magnesite veins with elongated grains growing from a median zone towards the wall rock are among the earliest structures to form during carbonation of serpentinite. Their bisymmetric chemical zoning of variable Ca and Fe contents, a systematic distribution of SiO_2 and Fe-oxide inclusions in these zones, and cross-cutting relations with Fe oxides and Cr spinel indicate that they record progress of reaction fronts during replacement of serpentine by carbonate in addition to dilatant vein growth. Euhedral terminations and growth textures of magnesite vein fill, together with local dolomite precipitation and voids along the vein–wall rock interface, suggest that these veins acted as preferred fluid pathways allowing infiltration of CO_2-rich fluids necessary for carbonation to progress. Fracturing and fluid flow were probably further enabled by external tectonic stress, as indicated by closely spaced sets of subparallel carbonate veins. Despite widespread subsequent quartz mineralization in the rock matrix and veins, which most likely caused a reduction in the permeability network, carbonation proceeded to completion within listvenite horizons.

1 Introduction

Listvenites (or listwanites) are the result of large-scale fluid–rock interaction that converts serpentinized peridotite into magnesite–quartz rock due to reactive flux of CO_2-bearing aqueous fluids. During this reaction, which typically occurs at low-temperature hydrothermal to sub-greenschist-facies conditions (80–350 °C) (Beinlich et al., 2020b, 2012; Falk and Kelemen, 2015; Johannes, 1969; Menzel et al., 2018), the rock gains more than 30 wt % CO_2 and an equivalent increase in rock volume. Because of the large amount of CO_2 that can be captured through this process and the fact that reaction kinetics can be fast, especially if peridotite contains brucite or remnant olivine (Kelemen et al., 2011), listvenites have attracted considerable attention as a natural analogue for carbon sequestration by mineral carbonation (Kelemen et al., 2020d; Matter and Kelemen, 2009; Power et al., 2013). The International Panel on Climate Change (IPCC) predicts that negative carbon emission techniques such as artificially enhanced mineral carbonation will become necessary even if the transition to a fossil-carbon-free economy is faster than expected (IPCC, 2021). Unfortunately, although listvenites occur in many ophiolites worldwide (e.g., Boskabadi et al., 2020; Emam and Zoheir, 2013; Hansen et al., 2005; Hinsken et al., 2017; Qiu and Zhu, 2018) and isotopic evidence suggests carbonation of serpentinized peridotite can proceed very fast in nature (Beinlich et al., 2020a), experiments have so far not been able to reproduce this reaction at a large scale and acceptable costs.

Most experimental efforts have focused on reproducing and enhancing the conditions of mineral carbonation related to hyperalkaline springs and subaerial and subaquatic weathering (Kelemen et al., 2020d; Oskierski et al., 2013; Power et al., 2013). Nonetheless, the conversion of peridotite to listvenite has higher potential for carbon sequestration in comparatively smaller rock volumes. The reasons why experimental listvenite formation at a large scale is challenging are the comparatively high temperatures ($> 80\,^{\circ}C$, but ideally about 170–200 °C; Kelemen and Matter, 2008), the low permeability of ultramafic rocks, and the volumetric expansion and permeability reduction associated with conversion to magnesite and quartz (Hövelmann et al., 2013; Peuble et al., 2018; van Noort et al., 2017). Besides the necessity for a source of CO_2-rich fluids, permeability reduction is likely one of the main limiting factors controlling the extent of listvenite formation in natural systems. Because natural fluids at sub-greenschist-facies conditions are typically not highly enriched in CO_2, listvenite formation requires high fluid–rock ratios, which implies that permeability must be maintained or repeatedly renewed over a long period to guarantee continued fluid flux.

An ingredient that is absent in most experiments but is commonplace in nature is tectonic deformation and related deviatoric stress. Listvenites occur suspiciously often along major shear zones in various ophiolites (Ash and Arksey, 1989; Belogub et al., 2017; Menzel et al., 2018; Qiu and Zhu, 2018). In listvenites of the Samail ophiolite, Oman, ductile deformation microstructures demonstrate that deformation and carbonation were synchronous (Menzel et al., 2022), suggesting that tectonic deformation plays a key role in maintaining the permeability necessary for long-lasting reactive fluid flow. Most serpentinites and listvenites formed at $T < 200\,^{\circ}C$ are expected to be brittle, although high fluid pressure can also lead to reaction-assisted ductile deformation at low temperature (Menzel et al., 2022). Deformation can enhance permeability by fracturing (e.g., Sibson, 1996) and grain-scale processes including dilatant granular flow and creep cavitation (e.g., Fusseis et al., 2009). Different sets of veins filled with carbonate and/or quartz are commonplace in listvenites and related carbonate-bearing serpentinites (Beinlich et al., 2020b, 2012; Hansen et al., 2005; Menzel et al., 2018), suggesting that dilatancy may be one of the main mechanisms by which carbonation of peridotite can progress.

Although early veins have been identified in listvenites of the Samail ophiolite (Beinlich et al., 2020b; Menzel et al., 2022), the role fractures and crystallization pressure played in allowing penetration of CO_2-rich fluids and listvenite formation is uncertain. Here we investigate the progression of microstructures within veins formed as a result of carbonation in serpentinites and listvenites of Hole BT1B, Oman Drilling Project (International Continental Drilling Project Expedition 5057-4B), using advanced high-resolution imaging and analytical methods. This natural laboratory and unmatched sample quality offer an ideal opportunity to investigate the relative timing and sequence of fracturing and mineralization, their relationship with carbonation of the unfractured matrix, the role of replacement veining, and the evolution of porosity throughout the carbonation processes in order to evaluate whether fracturing helped accommodate volumetric expansion and increased the permeability necessary for the progression of carbonation.

2 Geological setting and previous work

Due to the high quality of the drill cores recovered at site BT1 and the interdisciplinary analysis in the framework of the Oman Drilling Project, the Samail ophiolite hosts the best-studied listvenites worldwide. In the following sections, we briefly summarize the geological setting and the most important results of previous studies on listvenites in this area.

2.1 The Samail ophiolite

The Samail ophiolite (Oman) (Fig. 1) is composed of a sequence of obducted oceanic crust (4–8 km thickness) and mantle (up to 12 km thick) with characteristics similar to fast-spreading oceanic crust in the Pacific (Hopson et al., 1981; Nicolas et al., 1996; Rioux et al., 2013). Crystallization of the oceanic crust occurred during the Cenomanian (96.4–95.5 Ma) (e.g., Coleman, 1981; Rioux et al., 2013) in a mid-ocean ridge (Boudier and Coleman, 1981; Hacker et al., 1996) or, most likely, in a supra-subduction zone setting (MacLeod et al., 2013; Pearce et al., 1981; Searle and Cox, 2002). A first stage of hot oceanic subduction, broadly coeval with or shortly after oceanic crust crystallization (Garber et al., 2020), produced greenschist to granulite facies metabasalts and minor metasediments, which were underplated as a metamorphic sole below the ophiolite and are now exposed as discontinuous layers and lenses along the basal thrust fault of the ophiolite. Different parts of the metamorphic sole record temperatures of 450–550 and 700–900 °C at 0.7–1.2 GPa (Kotowski et al., 2021; Soret et al., 2017). The ophiolite and metamorphic sole were emplaced by top-to-SE thrusting onto allochthonous marine sediments (the Hawasina nappes). Further shortening subsequently culminated in NE-dipping subduction and burial of the autochthonous Arabian continental margin below the Hawasina nappes and the ophiolite (81–77 Ma) (Garber et al., 2021). The deepest burial of the underthrust margin occurred at about 79 Ma (Warren et al., 2003), reaching peak metamorphic conditions of 280–360 °C and 0.3–1.0 GPa in rocks exposed in the Jebel Akhdar and Saih Hatat domes and 450–550 °C and 2.0–2.4 GPa in eclogites at As Sifah (Agard et al., 2010; Grobe et al., 2019; Miller et al., 1999; Saddiqi et al., 2006; Searle et al., 1994). After termination of obduction, N–S extension during the Maastrichtian and early Paleocene led to top-to-NNE, mostly bedding-parallel shear zones in

the autochthonous units (Grobe et al., 2018, and references therein). This was followed by normal faulting, folding, and low-angle detachments in the Eocene and strike-slip faulting in the Oligocene related to the exhumation of the Jebel Akhdar and Saih Hatat anticlinoria as well as tectonic and erosional thinning of the ophiolite (e.g., Grobe et al., 2019; Mattern and Scharf, 2018, and references therein).

2.2 Listvenites in the Samail ophiolite

Listvenites occur along or in close proximity to the basal thrust of the Samail ophiolite at the western contact of the Aswad massif (United Arab Emirates and northwestern Oman) and in the northern Samail massif (Fanjah region, Oman) (Glennie et al., 1974; Stanger, 1985; Wilde et al., 2002) (Fig. 1a). In the area surrounding OmanDP site BT1 in the northern Samail massif, listvenites crop out as bands that are tens of meters thick along and parallel to the contact between banded peridotites and the underlying metamorphic sole, which in turn is underlain by multiply deformed, allochthonous metasediments of the Hawasina nappes (Fig. 1b). Directly north of site BT1, these units form a broad anticline (Falk and Kelemen, 2015). Early models proposed that listvenite formation was related to submeteoric fluids and normal faulting during extensional tectonics in the Paleogene, after ophiolite emplacement (Nasir et al., 2007; Stanger, 1985). However, the geometry of the listvenite outcrops and evidence for ductile deformation synchronous with carbonation (Menzel et al., 2022) indicate that listvenites formed along a shallow-dipping fault zone at the interface between ophiolite, metamorphic sole, and underlying metasediments, and not along steep normal faults (Kelemen et al., 2022). Together with an imprecise internal Rb–Sr isochron age of 97 ± 29 Ma (2σ) for Cr-muscovite-bearing listvenite close to site BT1 (Falk and Kelemen, 2015), this points to listvenite formation during subduction and/or underthrusting of the Arabian continental margin below the obducting ophiolite, consistent with a deep source of CO_2-bearing fluids as inferred from Sr and C stable isotope geochemistry (de Obeso et al., 2022). CO_2 fluid flux and carbonation concurrent with an early reactivation of the basal ophiolite thrust fault as an extensional decollement would also be consistent with the outcrop geometry, and extensional top-to-the-NE shearing in the autochthonous carbonates below the ophiolite (64 ± 4 Ma) (Hansman et al., 2018) falls just within the 2σ margin of the Rb–Sr isochron of Falk and Kelemen (2015). However, while possible, based on the currently available data this is less likely than a subduction–obduction setting (Kelemen et al., 2022). The listvenites contain abundant veins of various generations (Fig. 1c and d) and, together with adjacent units, have been overprinted by cataclasis and sharp normal to strike-slip faults that obscure the original structures, showing that multiple brittle deformation phases occurred after listvenites formed (Menzel et al., 2020).

2.3 Serpentinites and listvenites of Hole BT1B

Hole BT1B consists in its upper part of listvenite intercalated with two serpentinite layers separated by a fault at 200 m down-hole depth from underlying greenschist-facies metamafic rocks of the metamorphic sole (Fig. 1e) (Kelemen et al., 2020b). At site BT1, magnesite predominates, while dolomite and calcite are common in listvenites further north in the Fanjah area. Clumped isotope thermometry, the presence of quartz–antigorite ($\pm$ talc) intergrowths, and recrystallization microstructures of quartz after opal point to listvenite formation temperatures of 80–150 °C in this area (Falk and Kelemen, 2015). Estimates of vein and matrix carbonate precipitation in serpentinite and listvenite of core BT1B range from 45 ± 5 to 247 ± 52 °C based on clumped isotope thermometry (Beinlich et al., 2020b). The pressure and depth of listvenite formation are less well constrained. Based on data from underlying carbonate sediments (Grobe et al., 2019) and a plausible ophiolite thickness of 8–10 km, pressure was at least ~ 0.3 GPa, while the P–T conditions recorded by the metamorphic sole set an upper bound of 0.7–1.0 GPa (Kotowski et al., 2021; Soret et al., 2017). Except for some dolomite-enriched intervals, especially close to the basal fault, most BT1B listvenites are composed of magnesite, quartz, minor Cr spinel, and locally Fe (hydr)oxides or Cr-bearing muscovite (fuchsite) (Kelemen et al., 2020b). The bulk chemistry and proportions of magnesite and quartz can vary significantly on a small scale (Okazaki et al., 2021), but at the meter scale they are consistent with overall isochemical replacement of peridotite and minor addition of fluid–mobile elements (Godard et al., 2021; Kelemen et al., 2020b). Massive listvenite domains show two main types of pervasive microstructures: (i) zoned, ellipsoidal to spheroidal magnesite particles with euhedral to dendritic habit in a finer-grained quartz matrix (Beinlich et al., 2020b; Menzel et al., 2022) and (ii) variably large quartz ($\pm$ fuchsite) aggregates with microstructures resembling those of orthopyroxene or bastite surrounded by a matrix of vermicular, mesh-like magnesite–quartz intergrowths (Kelemen et al., 2020b; Menzel et al., 2022). Trace element geochemistry suggests that the protolith of the BT1B listvenites was part of the banded peridotite unit commonly found at the base of the Samail ophiolite, with compositions of fuchsite-bearing listvenite overlapping with amphibole-bearing basal lherzolite and fuchsite-free listvenite similar to the composition of refractory peridotite (Godard et al., 2021). Sr and C isotope geochemistry points to deep-sourced metamorphic fluids derived from metasediments similar to the underlying Hawasina Formation as the CO_2 source (de Obeso et al., 2022).

Visual core logging by the OmanDP science team showed that veins are abundant in serpentinite and listvenite, with densities of > 200 veins per meter of core for veins < 1 mm wide and 50–200 veins per meter for veins > 1 mm (Kelemen et al., 2020b). In serpentinites, the vein logging team distinguished between four main vein types, with a narrow

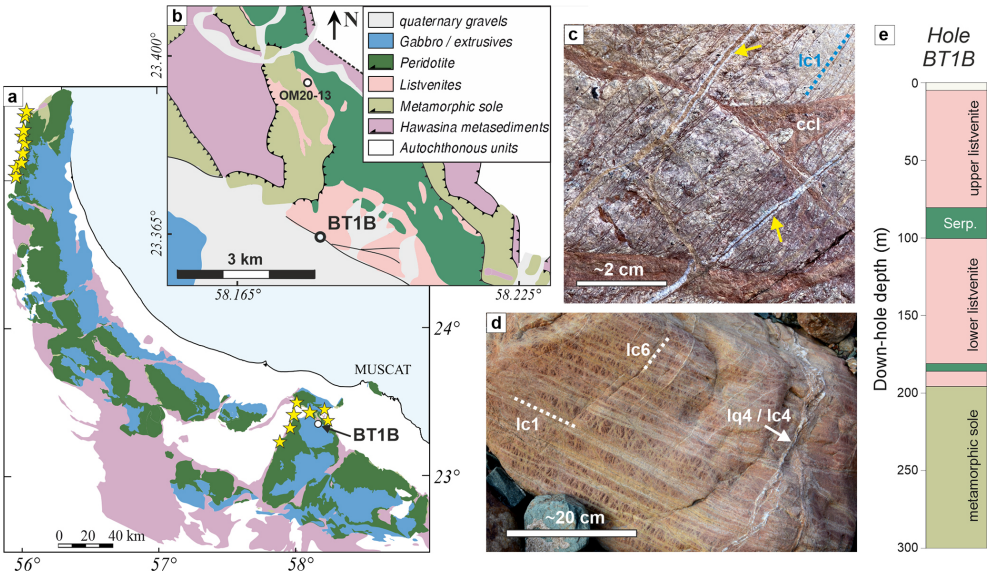

Figure 1. Geological overview map of the Samail ophiolite (common legend in **b**), with locations of known listvenite occurrences (yellow stars) (after Nicolas and Boudier, 1995). **(b)** Detailed geological overview of the area surrounding site BT1 (after de Obeso et al., 2022, and Villey et al., 1986); **(c)** Vein generations in outcrop, with closely spaced narrow carbonate veins (lc1, blue dotted line) cut by cataclasite (ccl, brown–red) and quartz–carbonate veins (yellow arrows). **(d)** Different vein generations in listvenite boulder with exceptionally wide veins, with the vein network in the matrix resembling a mesh cut by closely spaced parallel carbonate (lc1) and later quartz–carbonate (lq4 and lc4) and dolomite veins (lc6). **(e)** Lithologies in Hole BT1B (Kelemen et al., 2020b).

(< 0.1 mm) serpentine vein network that defines a mesh texture being the earliest generation. The serpentine mesh is cut by multiple generations of serpentine veins, early carbonate–oxide veins characterized by an Fe-oxide-bearing median zone and antitaxial growth habit, and younger carbonate veins with rare quartz (Kelemen et al., 2020b). In listvenites, the vein logging team identified narrow (< 0.1 mm) carbonate–oxide veins with antitaxial habit and a median line as the earliest vein generation, followed by discontinuous carbonate veins, comparatively wider carbonate–chalcedony–quartz veins (> 1 mm to > 1 cm), and late, partially open dolomite and/or magnesite veins (Kelemen et al., 2020b).

Based on deformation and overgrowth microstructures of folded and ductile transposed veins, Menzel et al. (2022) concluded that the early carbonate–oxide veins in listvenites formed during the incipient stage of the carbonation reaction while most of the rock was still composed of serpentine, confirming similar inferences from previous studies (Beinlich et al., 2020b; Kelemen et al., 2020b). In this study, we refine the preliminary vein classification of the core logging (see Tables 1 and 2) and investigate vein generations in detail that were directly involved in the carbonation reaction progress in order to understand the mechanisms controlling focused fluid flux, permeability, and reactivity during carbonation.

3 Methods and materials

3.1 Samples

The highly variable range of (micro)structures in serpentinite and listvenite of Hole BT1B was sampled during the Oman Drilling Project Phase 1 core logging onboard R/V *Chikyu* in September 2017. A few additional samples from the area north and east of Hole BT1B were obtained during a field campaign in January 2020. Thin sections produced from core samples are oriented with respect to the core reference frame (CRF), an arbitrary orientation along which contiguous core sections were split. Due to the inclination of 75° of Hole BT1B and discontinuities across which the orientation of core sections could not be reconstructed, structural measurements and sample orientations are not easily comparable between different parts of the core. Thin sections produced from field samples were either oriented in relation to structural elements, i.e., perpendicular to foliation, or, when no foliation was visible, in the geographical reference frame. For this study, vein microstructures and cross-cutting relationships were inspected in 115 thin sections, a subset of which lacking late cataclastic overprint was investigated in more detail. Our vein classification is primarily based on listvenite samples from Hole BT1B. Thin sections and samples from BT1B are named here with an abbreviated form of the ICDP convention following the scheme "Hole_Core"-"Section_top-bottom", with top and bottom denoting the distance (in cm) from the top of the section.

Table 1. Vein classification in Hole BT1B serpentinites (ordered from relatively older to younger).

No.	Vein type	Subtypes	Characteristics	Mineralogy	Width/abundance	Examples in thin section
ss0	serpentine mesh ("serp mesh")		brownish serpentine (± Brc?) forming a polygonal network, often with magnetite in median zone of veins	Serp, Mag, ± Brc?	3–20 µm *ubiquitous*	most non-foliated serpentinites
ss1	serpentine–magnetite*	various generations	transparent serpentine with magnetite aggregates in median zone	Serp (Lz), Mag	0.1–1.5 mm; *minor*	BT1B_74-1_77-80
ss2	serpentine crack–seal ("serp")	various generations	cross-fiber crack–seal veins with banded extinction patterns; pull-apart structures are common; locally parallel sets, en echelon	alternating Chr–Lz intergrowths? (Tarling et al., 2021)	50–500 µm *common*	BT1B_39-3_9-13 BT1B_44-2_47-50 BT1B_74-1_77-80
sc0	pseudomorphic carbonate*	mesh carbonate carbonate after ss2	carbonate aggregates along the serpentine mesh or parallel to fibers of serpentine crack–seal veins; locally euhedral facets at contact to serpentine	Mgs (variably Fe-bearing); ± Dol	5–30 µm *common*	BT1B_44-2_47-50 BT1B_44-3_9-11
sc1	cleavage-parallel carbonate*		patchy to feathery, in places dendritic vein aggregates parallel to serpentine cleavage, locally folded	Fe-poor Mgs ± Dol; Dol ± Qtz in some samples	0.1–1 mm *minor*	BT1B_44-2_47-50 BT1B_44-3_9-11 BT1B_42-1_19-24
sc2	zoned magnesite ("carb-oxy")	– anastomosing magnesite – composite Fe–magnesite–talc – parallel Fe–magnesite–dolomite	antitaxial–fibrous, with Fe-oxide-bearing median line and bisymmetric chemical zoning; host serpentine inclusions are common	common zoning: median line: locally Fe (hydr)oxide; zoned vein core: Ca-bearing, Fe-rich Mgs, with variable Si-inclusion content; rims: Fe-poor Mgs, Dol	typically 50–200 µm; *very common in some intervals*	BT1B_39-2_34-36 BT1B_39-3_9-13 BT1B_39-4_14-18 BT1B_44-2_47-50 BT1B_44-3_9-11
sc3	magnesite		irregular; cross-fiber to blocky	mostly Fe-poor Mgs, locally Mn-bearing	200–500 µm; *minor*	BT1B_39-4_14-18
sq1	feathery quartz*	locally two or more generations	thin splayed–feathery, highly irregular quartz vein aggregates, partly antitaxial, locally emerging from magnesite vein tips	Qtz ± Mgs, Dol in parts: impure Qtz with nm–µm Serp inclusions and intergrowths	< 50 µm *minor*	BT1B_39-2_67-72 BT1B_39-3_9-13 BT1B_42-2_19-24 BT1B_44-3_9-11
sq2	quartz and quartz–magnesite		granular–blocky quartz, locally vuggy and with euhedral magnesite	Qtz ± Fe-poor Mgs	0.1–10 mm *minor*	BT1B_44-3_9-11 BT1B_44-2_47-50
sc4	late carbonate		often brecciated, partly vuggy	Dol and/or Mgs	0.1 mm–> 5 cm	

Mineral abbreviations: Mgs – magnesite, Dol – dolomite, Qtz – quartz, Tlc – talc, Serp – serpentine, Lz – lizardite, Chr – chrysotile, Brc – brucite, Mag – magnetite, Hem – hematite, CrSp – Cr spinel, FeOx – Fe oxide and/or hydroxide.
* Cross-cutting relationships (relative timing) ambiguous; thin section samples are named with an abbreviated form of the ICDP convention following the scheme "Hole_Core-Section_top-bottom [cm]".

https://doi.org/10.5194/se-13-1191-2022

Table 2. Vein classification in Hole BT1B listvenites (ordered from relatively older to younger).

No.	Vein type	Subtypes	Characteristics	Mineralogy	Width/ abundance	Examples in thin section
l_{ss0}	magnesite or quartz network after serpentine mesh	– magnesite network – quartz network	in mesh–pseudomorphic listvenites; vein network discontinuously follows prior polygonal serpentine mesh	variably Fe-bearing Mgs (± Hem, Mag relicts); Qtz	3–20 µm *locally ubiquitous*	BT1B_21-3_35-40 BT1B_51-1_20-25 BT1B_55-3_68-72 BT1B_56-1_55-60
l_{ss2}	magnesite–quartz after serpentine crack–seal		pseudomorphic replacement of serpentine veins by vein-perpendicular magnesite columns + quartz	Mgs, Qtz	50–500 µm; *minor*	BT1B_27-2_6-8
lc1	zoned magnesite ("carb-ox veins")	– anastomosing – parallel – cross-cutting (two generations, or conjugate)	fibrous antitaxial to wide-blocky; may define a macroscopic foliation where abundant; irregular vein walls; locally folded and transposed by matrix foliation	median line: locally Fe (hydr)oxide, Dol, or Qtz; zoned vein core: Ca-bearing, Fe-rich Mgs, with variable Si-inclusion content; rims: Fe-poor Mgs, Dol	50 µm to locally up to 1 mm *very common*	BT1B_14-1_7-11 BT1B_14-3_77-80 BT1B_16-3_28-31 BT1B_20-1_64-68 BT1B_21-3_35-40 BT1B_31-4_12-14
lc2	magnesite ("carb")		irregular; cross-fiber to blocky syntaxial	Fe-poor Mgs (dull/non-luminescent)	20–500 µm; *minor*	BT1B_14-1_7-11 BT1B_14-3_77-80
lc3	magnesite–dolomite		irregular; polycrystalline	Mgs (bright pink luminescent), ± Dol	10–200 µm; *minor*	BT1B_14-3_77-80
lq1	cryptic quartz		matrix veins with irregular walls, not cutting magnesite ellipsoids; often only visible in CL	Qtz (dull luminescent)	10–100 µm	BT1B_14-3_77-80
lq2	microcrystalline quartz*	up to two generations	irregular to patchy, polygranular with domains with strong CPO; not cutting magnesite ellipsoids	Qtz (after opal?)	50 µm–1 mm; *minor*	BT1B_56-4_45-50 BT1B_67-2_36-40
lq3	quartz		straight veins cutting magnesite ellipsoids and/or cutting pseudomorphic mesh	Qtz (dull and bright luminescent), ± carbonate	10–100 µm; *minor*	BT1B_14-3_77-80
lq4	magnesite–quartz ("carb-qtz")		syntaxial; branched; host-rock inclusions common; straight vein walls; polycrystalline and radial chalcedony–quartz aggregates; often magnesite in the vein center	Qtz–chalcedony (bright luminescent), Fe-poor Mgs	typically > 1 mm *common*	BT1B_14-3_77-80 BT1B_20-1_64-68 BT1B_51-1_20-25
lc4	quartz–dolomite		syntaxial, commonly with euhedral facets; host-rock inclusions common; straight vein walls; often carbonate in the vein center	Qtz, Dol	0.1–1 mm *common*	BT1B_21-3_35-40
lc5	late magnesite		syntaxial–polygranular; irregular, with host listvenite inclusions; yellowish in drill core	Fe-bearing Mgs (not zoned)	> 2 mm *minor*	BT1B_68-3_60-65
lc6	late dolomite (various generations)	– thin en echelon – brecciated – vuggy	syntaxial to blocky, planar with straight vein walls; in parts brecciated; partly open (vuggy)	mostly Dol, with oscillatory growth zoning in CL	0.1 mm–> 5 cm *common*	BT1B_14-3_77-80 BT1B_16-3_28-31 BT1B_20-1_64-68

Mineral abbreviations: Mgs – magnesite, Dol – dolomite, Qtz – quartz, Tlc – talc, Serp – serpentine, Lz – lizardite, Chr – chrysotile, Brc – brucite, Mag – magnetite, Hem – hematite, CrSp – Cr spinel. Numbering of vein generations: subscripts indicate that veins are pseudomorphic replacements of previous serpentine vein generations. * Cross-cutting relationships (relative timing) ambiguous; thin section samples are named with an abbreviated form of the ICDP convention following the scheme "Hole_Core-Section_top-bottom [cm]".

3.2 Optical and scanning electron microscopy

A PetroScan virtual polarizing microscope (ViP; RWTH Aachen University) was used to obtain high-resolution scans of full thin sections in plane-polarized light, reflected light, and at 10 different crossed polarizer orientations with a 10× objective. A high-precision automated stage allows the interpolation of the extinction behavior of each pixel to visualize extinction at all polarization angles. A selection of these digitized thin sections is publicly available as a Supplement of the Oman Drilling Project (Kelemen et al., 2020b) at http://publications.iodp.org/other/Oman/SUPP_MAT/index.html#SUPP_MAT_Z (last access: 22 July 2022). Of these, samples of special interest regarding vein microstructures are Cores 14-3 and 77-80, Cores 31-4 and 12-14, Cores 35-1 and 30-32, Cores 44-3 and 9-11, and Cores 67-2 and 36-40.

Back-scattered electron (BSE) and energy-dispersive X-ray spectroscopy (EDX) maps were acquired for phase identification and imaging of chemical zoning using a Zeiss Gemini SUPRA 55 field-emission scanning electron microscope (FE-SEM) at the Institute of Tectonics and Geodynamics of RWTH Aachen University. Whole thin sections and specific areas of interest were mapped at an acceleration voltage of 15 kV, 8.5 mm working distance, and dwell times of 0.2–1.5 ms per point. Samples were coated with a 6–8 nm thick layer of tungsten for conductivity.

We used a Zeiss Axio Scope optical microscope equipped with a "cold" cathode luminoscope CL8200 MK5-2 to obtain optical CL panorama images of large thin section areas. Single images were taken at operating conditions of 15 kV and 320–350 µA with a 10× objective and exposure times of 5–10 s.

In selected samples and areas of specific interest, panchromatic and blue-filtered SEM-CL images were obtained using a Zeiss Sigma high-vacuum FE-SEM equipped with a Gatan MonoCL4 system at the University of Texas at Austin. Following the guidelines of Ukar and Laubach (2016), carbon-coated thin sections were imaged at 5 kV accelerating voltage, 120 µm aperture, 125 µs dwell time, and 2048 × 2048 pixel resolution at magnifications up to 2500×.

One serpentinite sample with subparallel serpentine veins was prepared with broad-ion-beam (BIB) polishing to image nano-porosity in matrix and vein serpentine. For this, a 6 × 6 × 4 mm prism was cut from a non-weathered part of the sample and mechanically pre-polished. BIB polishing was performed in a Leica TIC3X with rotary stage (RWTH Aachen) applying three Ar-ion beams for 6 h at 3 kV acceleration voltage, a beam current of 1.0 mA for each beam, and an incidence angle of 4.5°. The tungsten-coated sample surface was imaged at high resolution (10–20 nm pixel size) in secondary electron (SE) mode using the Zeiss Gemini SUPRA 55 FE-SEM (RWTH Aachen) at an acceleration voltage of 3 kV and a working distance of 5 mm.

4 Results

4.1 Veins in serpentinite

4.1.1 Serpentine mesh, magnetite–serpentine veins, and serpentine crack–seal veins

Networks of serpentine mesh veins with the typical polygonal hourglass texture of serpentinite (Wicks and Whittaker, 1977) are ubiquitous in non-foliated serpentinites (Fig. 2a; ss0 in Table 1). In these veins, serpentine is usually brownish in transmitted light, and magnetite is abundant. The serpentine mesh is cut by various generations of magnetite–serpentine veins and serpentine crack–seal veins (ss1 and ss2, Table 1; Fig. 2b and c). Similar to the serpentine mesh, magnetite–serpentine veins contain a median zone rich in magnetite with flaky to fibrous serpentine towards the vein walls. Serpentine is clear in transmitted light and the veins are discrete and continuous, occasionally forming parallel sets. Serpentine crack–seal veins are characterized by uniform to cloudy extinction under crossed polarizers with similar fiber orientations over the entire length of the vein. Commonly, these veins show vein-parallel banding with oscillatory extinction patterns that are typical of serpentine crack–seal veins (Andreani et al., 2004), likely due to alternating precipitation of chrysotile and lizardite during crack–seal cycles (Tarling et al., 2021).

Clusters of parallel, en echelon, and/or branched serpentine veins occur in foliated serpentinites of the area north of site BT1. The veins are parallel to the penetrative serpentinite foliation, which is defined by flattened mesh cells delineated by magnetite aggregates (Fig. 2d). Serpentine in these cleavage-parallel veins has the same extinction direction with the lambda plate, indicating a strong and consistent shape and crystallographic preferred orientation, which is different from the crystallographic preferred orientation of matrix serpentine (Fig. 2b).

4.1.2 Pseudomorphic carbonate

In carbonate-bearing serpentinite, small magnesite aggregates locally occur along the serpentine mesh, pseudomorphically tracing the polygonal mesh outlines (Fig. 2e, f; sc0, Table 1; Fig. S1 in the Supplement). Magnetite, partly transformed to Fe magnesite, is commonly present as inclusions within these magnesite aggregates. Pseudomorphic magnesite has core–rim zoning of variable Fe contents, and magnesite rims in the vein network commonly have euhedral crystal facets towards contacts with serpentine or a dendritic habit (Fig. 2g). In places, the pseudomorphic magnesite vein network has a preferred orientation tracing flattened serpentine mesh cells.

Pseudomorphic replacement of serpentine by carbonate also occurs within and along the walls of serpentine crack–

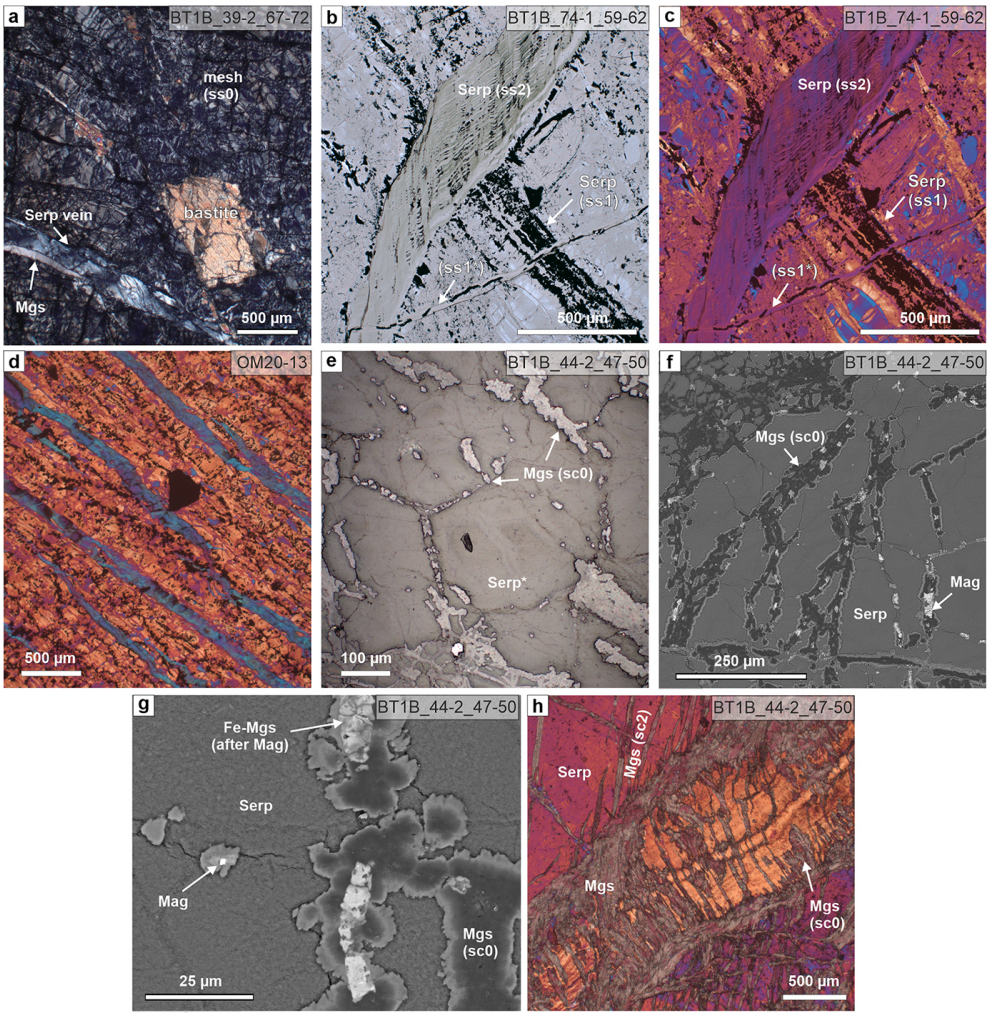

Figure 2. Serpentine veins **(a–d)** and pseudomorphic carbonate microstructures after serpentine textures **(e, f)** in serpentinite. **(a)** Mesh (ss0) and bastite textured serpentinite cut by a serpentine vein; a magnesite vein exploits the vein–host rock interface of the serpentine vein under crossed polarizers (xpol). **(b)** Plane-polarized (ppol) micrograph of a wide serpentine–magnetite vein (ss1) cut by a light green, banded serpentine crack–seal vein (ss2), which is in turn cut by a narrow serpentine–magnetite vein (ss1*). **(c)** Same area as in **(b)**, with xpol and 1λ plate. **(d)** Clustered cleavage-parallel serpentine veins in foliated serpentinite north of site BT1 with strong crystallographic preferred orientation and flattened magnetite mesh cells. The large black grain is Cr spinel (xpol with 1λ plate). **(e)** Reflected light image and **(f)** BSE image of a magnesite vein network (sc0) tracing polygonal serpentine mesh (Serp*) delineated by former magnetite in serpentinite. **(g)** Detailed BSE image of sc0 magnesite showing pseudomorphic replacement of magnetite by Fe magnesite (similar replacements are known from listvenites elsewhere; Menzel et al., 2018) and compositional zoning with Fe-bearing euhedral to dendritic magnesite rims. **(h)** Serpentine crack–seal vein (orange) in serpentinite, with partial pseudomorphic replacement by magnesite and cross-cut by zoned magnesite–dolomite veins (sc2) (xpol with 1λ plate). For abbreviations of minerals and vein generations used in all figures, see Tables 1 and 2.

seal veins (Fig. 2h). Here, vein-perpendicular magnesite columns locally replace serpentine along serpentine fibers.

4.1.3 Carbonate veins

Most carbonate in serpentinites of Hole BT1B is in veins and only occurs in minor amounts as dispersed grains within the serpentine matrix (Fig. 3). Besides pseudomorphic carbonate, two types of early carbonate veins dominate in serpentinite: patchy to feathery carbonate veins parallel to serpentine cleavage planes and zoned magnesite veins.

Cleavage-parallel carbonate veins (sc1, Table 1) have an irregular morphology with highly variable vein width and consist of Fe-poor magnesite and/or dolomite (Fig. 3c, d). These veins follow the (locally folded) serpentine cleavage and often form branched and curved, semi-isolated patches with splayed vein tips.

The most abundant carbonate vein type in serpentinite consists of zoned magnesite veins (sc2, Table 1; Fig. 3c–

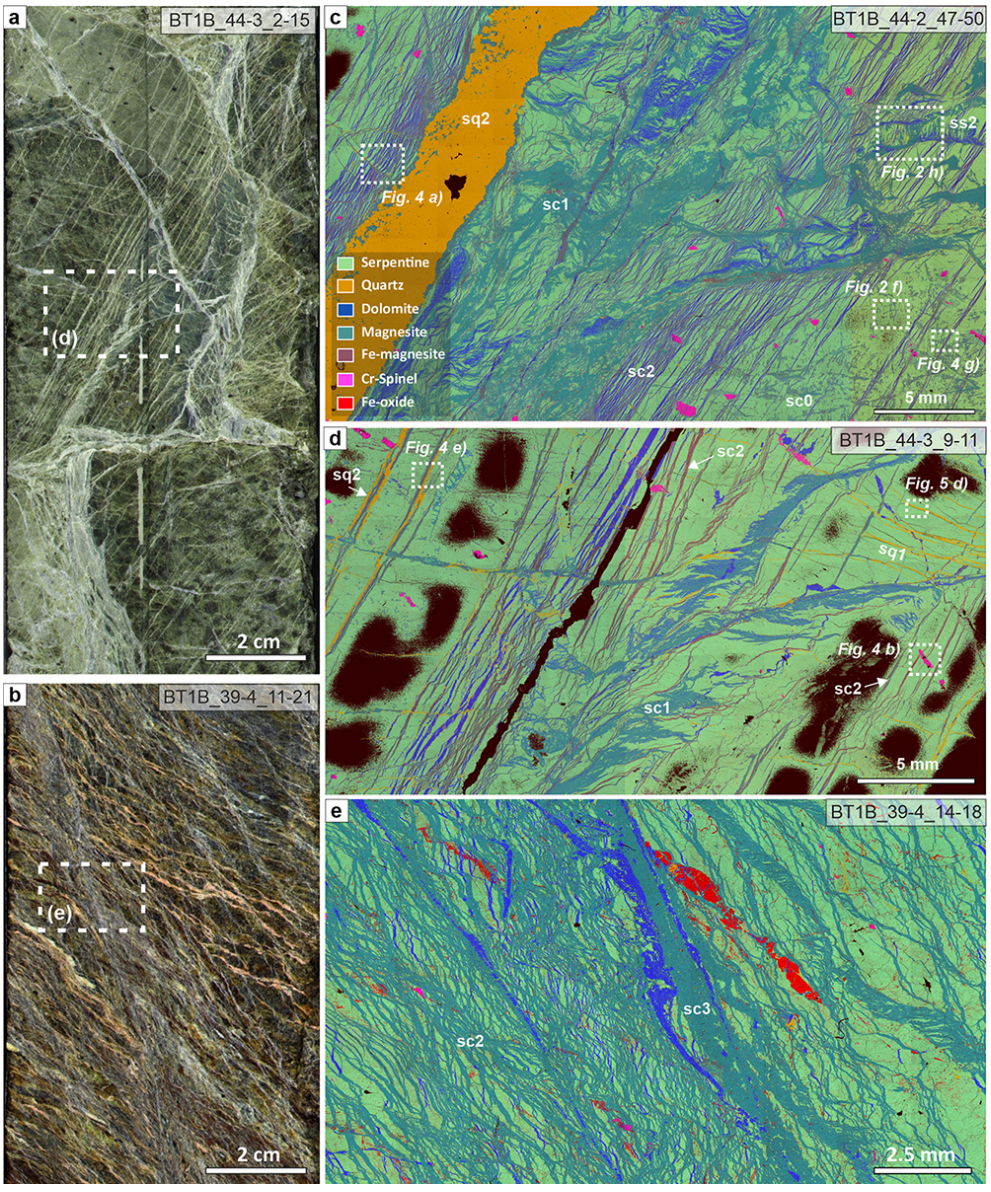

Figure 3. Veins in serpentinite of Hole BT1B. **(a)** Split-core image of serpentinite with closely spaced, parallel carbonate veins. **(b)** Split-core image of strongly veined serpentinite interval with anastomosing carbonate veins. **(c–e)** Composite-color EDX maps of carbonate-rich serpentinites showing different carbonate (sc1–sc3) and quartz (sq1, sq2) vein generations (common legend in **c**). Black patches in **(d)** are areas where soft bastite serpentine were lost during sample preparation. Core diameter in **(a)** and **(b)** is 6.3 cm.

e). During core logging, these have been named carbonate–oxide or antitaxial carb-oxy veins (Kelemen et al., 2020b). Because an Fe-oxide median line and antitaxial texture is not always present, we hereafter refer to this vein group as zoned magnesite veins (sc2). These are characterized by a planar morphology with rather constant vein width (typically 50–200 µm) and a vein-parallel, often bisymmetrical chemical zoning from a median zone towards the vein walls (Fig. 4). The veins are mostly composed of magnesite of variable composition, but dolomite can also be present along the vein walls, and minor vein segments locally consist of (or are replaced by) dolomite and rare quartz. The type of zoning and width of different zones vary between different samples and, occasionally, within the same thin section. Where present, the median line (2–10 µm wide) consists of Fe oxide and/or soft Fe hydroxides (possibly goethite) that are rarely well preserved during thin section preparation. The median zone is commonly composed of Ca- and Fe-bearing magnesite in the center, followed by Fe-rich magnesite with systematic variations in the number of SiO_2 inclusions and Fe-poor magnesite or dolomite towards the vein walls (Fig. 4d, f). Chemical zoning is not always well developed and may

consist only of slight variations in the quantity of silica impurities in magnesite. Flat or lens-shaped serpentine inclusions parallel to the vein length are common. In some zoned magnesite veins from core sections of the lower part of the upper serpentinite layer (98.7–100 m down-hole depth, see Fig. 1e) seams of talc occur along the vein walls, and locally talc is present as remnant inclusions between the Fe-rich and Fe-poor magnesite zones of the veins (Fig. 4c, f).

In some serpentinite core intervals, sc2 veins form closely spaced, parallel sets (clusters) (Figs. 3; 4a). Locally, they occur as two conjugate, anastomosing sets that resemble an s–c fabric of scaly fractured serpentinite (Fig. 3b, e). Where they intersect elongated Cr-spinel grains, zoned magnesite veins branch into numerous narrow veinlets, locally fragmenting the Cr spinel (Fig. 4b). Elongated and/or flattened Cr spinel is commonly aligned, probably showing the orientation of a remnant high-temperature plastic deformation fabric of former olivine. All carbonate veins in Hole BT1B are oblique to that early fabric. No systematic relationship between sc1–sc2 vein orientations and the serpentinite mesh texture is apparent. Cross-cutting relationships between sc2 and sc1 veins are usually ambiguous because zoned magnesite veins are locally deflected along serpentine cleavages. However, sc2 veins locally branch into narrow veinlets where they transect sc1 veins, indicating that at least some sc2 veins are relatively younger.

Cross-cutting relationships between sc2 veins and mesh–pseudomorphic magnesite aggregates in the serpentinite matrix are also often complex and ambiguous. For example, Fig. 4g shows that only the median zone of the sc2 vein cuts the matrix magnesite aggregate, while the Fe-enriched magnesite zone (II) does not. Facetted crystal terminations of carbonate towards matrix serpentine are locally present along the walls of some sc2 veins (yellow arrow in Fig. 4g). Sc2 veins commonly pinch out in narrow vein tips, but abrupt, partially corroded, wide vein terminations are also present. In places, magnesite veins show narrow talc vein terminations (Fig. 4h), Fe-oxide veinlets (Fig. 4i), or feathery quartz veins (sq1, see below) that emanate from carbonate vein tips (Fig. 5a).

4.1.4 Quartz veins

Quartz veins are common in the serpentinites of Hole BT1B, unlike typical serpentinites and peridotites of the Samail ophiolite where they are mostly absent. Quartz–serpentine intergrowths have previously been observed in samples near Hole BT1B (Falk and Kelemen, 2015), and a few quartz veins were logged during shipboard core description (Kelemen et al., 2020b). We note that their abundance in BT1B was underestimated during logging because they are usually narrow and easily overlooked (Fig. 5a). Two types are common: "feathery" quartz vein aggregates intergrown with serpentine at the microscale (sq1; Table 1) and wider, polygranular to blocky quartz and quartz–magnesite veins (sq2; Table 1). Cross-cutting relationships between the two types of quartz veins are ambiguous. Sq1 veins are strongly branched and locally emanating from the tips of carbonate veins (Fig. 5a). They commonly cut and may offset sc2 carbonate veins (Fig. 5b). Some wide sq1 veins ($> 20\,\mu m$) show an antitaxial habit, with a median zone composed of pure quartz and margins enriched in nanometer- to micrometer-sized serpentine and/or carbonate inclusions (Fig. 5c–f). Pods of dolomite or magnesite constitute parts of some veins.

Sq2 quartz and quartz–magnesite veins locally contain euhedral magnesite and are commonly oriented parallel to sc2 veins (Figs. 3d; 4e), suggesting that they formed due to preferential fracturing along the walls of zoned magnesite veins.

4.1.5 Late carbonate veins

Late, partially open or brecciated carbonate veins cut serpentinites and all previous vein generations (sc4, Table 1). These are unrelated to the formation of listvenite and possibly linked to young magnesite, dolomite, and calcite–aragonite precipitation in open joints from groundwater or hyperalkaline serpentinization fluids. Similar young carbonate veins and travertine are common in the weathering horizon of the Samail ophiolite peridotites (e.g., Chavagnac et al., 2013; Giampouras et al., 2020; Noël et al., 2018; Ternieten et al., 2021). Therefore, we do not consider them further here, but we note that they can locally obscure structures of veins synchronous with listvenite formation.

4.2 Veins in listvenite

Some listvenite intervals of Hole BT1B are highly veined such that locally $> 50\,\%$ of the listvenite volume consists of veins. This is the result of pseudomorphic replacement of previous serpentine veins and the superposition of veins formed at different time steps (Table 2).

4.2.1 Pseudomorphic veins after serpentine

Based on their strong microstructural resemblance to common serpentine veins in the serpentinites, we identify two types of pseudomorphic veins: pseudomorphic magnesite (and/or quartz) vein networks after serpentine mesh (l_{ss0}) and magnesite–quartz veins after serpentine crack–seal veins (l_{ss2}). Incipient stages of both pseudomorphic vein replacement microstructures are also present in carbonate-bearing serpentinite.

The mesh–pseudomorphic vein network (l_{ss0}) is most evident in listvenites where the volume between the magnesite mesh consists of monomineralic quartz (Fig. 6a). Magnesite usually has variable Fe contents, in parts tracing the former presence of magnetite in the serpentinite mesh, now mostly reacted to Fe magnesite. The vein network may show a preferred orientation, delineating elongated polygonal mesh cells. In contrast to serpentinite, wherein euhedral crystal facets of pseudomorphic carbonate are common, in listvenite

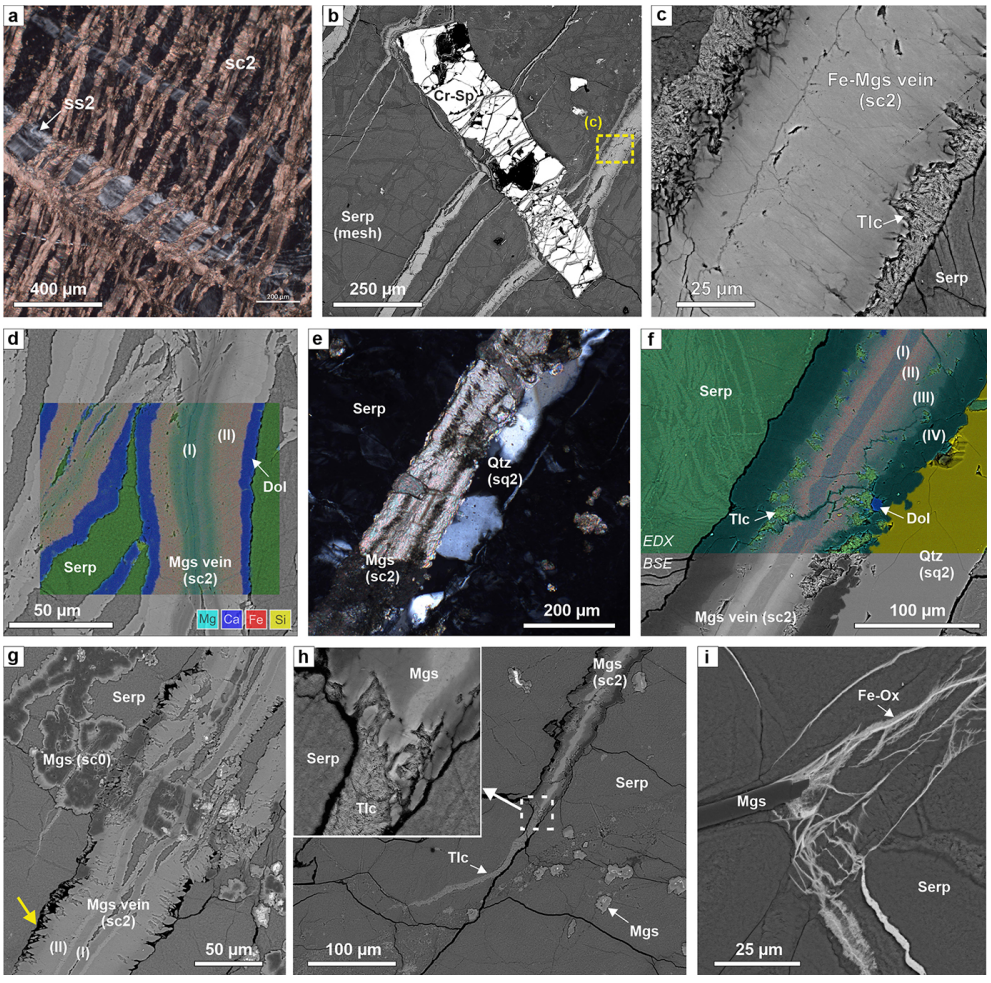

Figure 4. Microstructures of zoned magnesite veins (sc2) in serpentinite. **(a)** Close spacing of carbonate; the veins are deflected where they cut a crack–seal serpentine vein (xpol). **(b)** Elongated Cr spinel and serpentine mesh cut by zoned, Fe-magnesite–talc veins (BSE image). **(c)** Detail of **(b)**, showing talc seams along vein walls. **(d)** Composite-color EDX map superposed on a BSE image of zoned sc2 veins with dolomite rims (I: Ca-bearing magnesite; II: Fe magnesite); for phase legend see Fig. 3c. **(e)** Quartz vein exploiting the vein–host interface of a zoned magnesite vein (xpol). **(f)** Composite-color EDS map superposed on a BSE image of a part of the vein in **(e)**, with zones of (I) Ca-bearing magnesite, (II) Fe magnesite, (III) Fe-bearing magnesite with talc inclusions, and (IV) Fe-poor magnesite. Small Mg / Si variations show thin serpentine veins in the matrix. **(g)** Complex cross-cutting relations between a zoned sc2 vein and earlier mesh–pseudomorphic magnesite (sc0), showing that the core of sc2 veins formed by opening, while the vein rims are micro-reaction fronts with euhedral crystal terminations at the vein walls (yellow arrow). **(h)** Tip of a zoned sc2 carbonate vein in serpentinite. At the termination of magnesite, a talc veinlet continues over a short distance. This talc veinlet does not correspond to the open microcracks in serpentinite (black lines), showing that those are later and not related to vein formation of the zoned magnesite vein. **(i)** Fe-oxide and/or Fe-hydroxide veinlets emanating from the magnesite vein tip. (**a, d, g**: BT1B_44-2_47-50; **b, c, e, g, h**: BT1B_44-3_9-11; **i**: BT1B_39-3_9-13.)

single veinlets commonly have a corroded appearance or are overgrown by later generations of carbonate Fig. 6a).

Pseudomorphic magnesite–quartz veins after serpentine crack–seal veins (l_{ss2}) are characterized by irregular magnesite along vein walls and columnar to fibrous magnesite extending from the walls into the vein center (Fig. 6b; see Fig. 2h). Magnesite fibers are highly variable in length, ranging from small fractions of the vein aperture to fully bridging the vein. Quartz forms a polycrystalline, non-fibrous aggregate between the magnesite fibers. This vein microstructure is uncommon for classical antitaxial, syntaxial, or stretching veins (Bons et al., 2012), which supports the interpretation that they result from pseudomorphic replacement.

4.2.2 Early, zoned magnesite veins

Zoned magnesite veins (lc1, Table 2) are the most abundant in many listvenite core intervals (Fig. 6c–g) and occur in nearly all studied listvenite samples. As in serpentinites, they form closely spaced parallel or anastomosing branched to cross-cutting sets of fibrous to blocky veins. They show

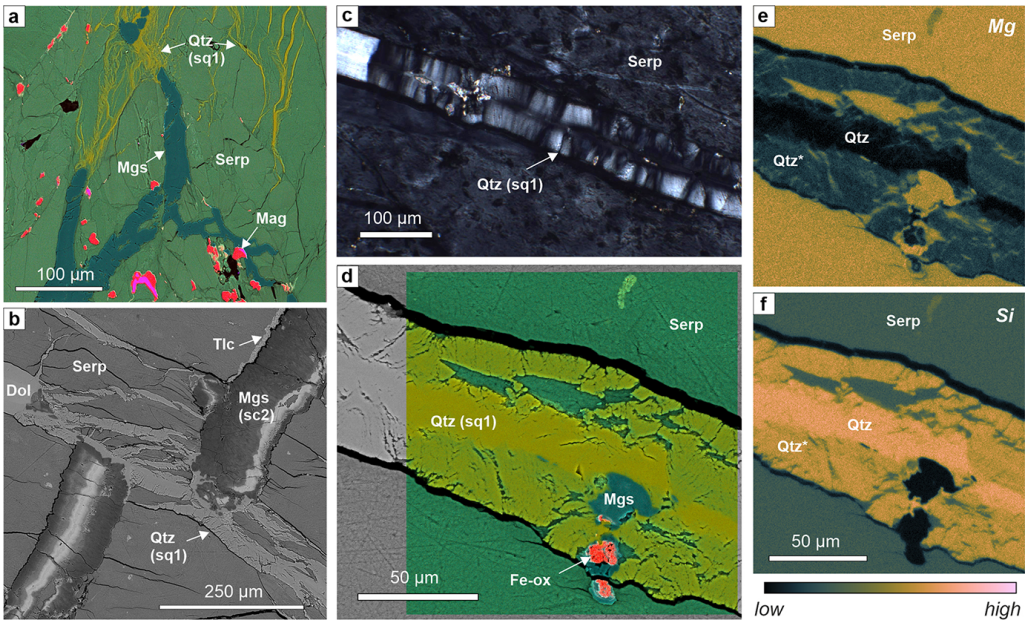

Figure 5. Quartz veins in serpentinite of Hole BT1B. **(a)** Composite-color EDX map of feathery quartz micro-veins with interstitial serpentine emanating from magnesite vein tips (sample BT1B_39-3_9-13). **(b)** BSE image of a branched quartz vein with minor dolomite cutting and offsetting a zoned magnesite vein. **(c)** Fibrous, antitaxial microstructure of a quartz vein in serpentinite (xpol). **(d–f)** Composite-color EDX map superposed on a BSE image and corresponding Mg and Si maps of a quartz vein in serpentinite (common color scale shown below **f**), showing that only the median zone consists of pure SiO_2, while the vein walls (Qtz^*) contain a high amount of serpentine and, locally, carbonate (nano-) inclusions, which result in the overall chemistry of Mg-bearing quartz at the spatial resolution of the EDX measurements. **(b–f)** Sample BT1B_44-3_9-11.

a well-defined median zone that is brown in plane-polarized light or contains Fe oxides or hydroxides and variably strong chemical zoning from the median zone towards the vein walls, indicating antitaxial growth. In most investigated thin sections, lc1 veins are the earliest generation based on cross-cutting relationships (Fig. 6e–g). In some samples, zoned magnesite veins with a wide-blocky habit form an early generation of this vein type. In some cases, wide-blocky veins are cut by fibrous carbonate veins, whereas in others fibrous segments alternate with wide-blocky sections within a single vein. Owing to these variations in texture that commonly occur together we group them into one vein type (lc1).

In listvenite samples that have a foliated matrix defined by aligned magnesite ellipsoids or dendritic magnesite–quartz intergrowths (Menzel et al., 2022), subparallel clusters of lc1 carbonate veins are oriented at various angles with respect to the matrix foliation. In samples for which the vein orientations are at a high angle to the matrix foliation, the veins are locally folded and/or transposed (Menzel et al., 2022).

Lc1 veins are mostly composed of Fe- to Ca-bearing magnesite (Fig. 7). No preserved serpentine inclusions have been observed in this type of veins, but quartz inclusions are common. In some core intervals, where these veins form anastomosing sets, vein segments composed of dolomite alternate with magnesite. The chemical zoning is similar to that of zoned magnesite veins in serpentinite (sc2) and typically bisymmetric. Lc1 veins commonly have an antitaxial habit, with elongated to fibrous crystals oriented with their long axes perpendicular to the median zone. The median zone usually shows high Fe contents ($X_{Fe} = Fe/[Fe + Mg]$ up to 0.30 in listvenites that contain little or no hematite) near the vein center and becomes progressively Fe-poor towards the vein walls (Fig. 7b). In some veins, a zone of Ca- and Fe-bearing magnesite ($X_{Fe} = 0.10$–0.15) with rare quartz inclusions occurs along the center of the Fe-rich median zone. In listvenites that contain abundant hematite, Fe contents in zoned magnesite veins are comparatively low and show less variability, although systematic chemical variations are still apparent owing to variations in minor or trace Ca contents and silica inclusions (Fig. 7f). Similar silica inclusions are common in matrix magnesite of the listvenites, wherein they have been shown to consist of SiO_2 nano-inclusions (Beinlich et al., 2020b; Menzel et al., 2022). Fe-enriched domains are commonly brown to red in the core and in plane-polarized light due to Fe oxides or hydroxides along the median zone. Cross-cutting relationships show that in some cases the presence of Fe oxides or hydroxides is due to oxidation of Fe magnesite after formation of the lc1 veins (red zones in Fig. 6d; $lc1^*$ in Fig. 6g).

SEM-CL images reveal elongated, vein-perpendicular, Fe-rich magnesite in the vein centers (dark luminescent) and Fe-poor, lighter luminescent magnesite overgrowths to-

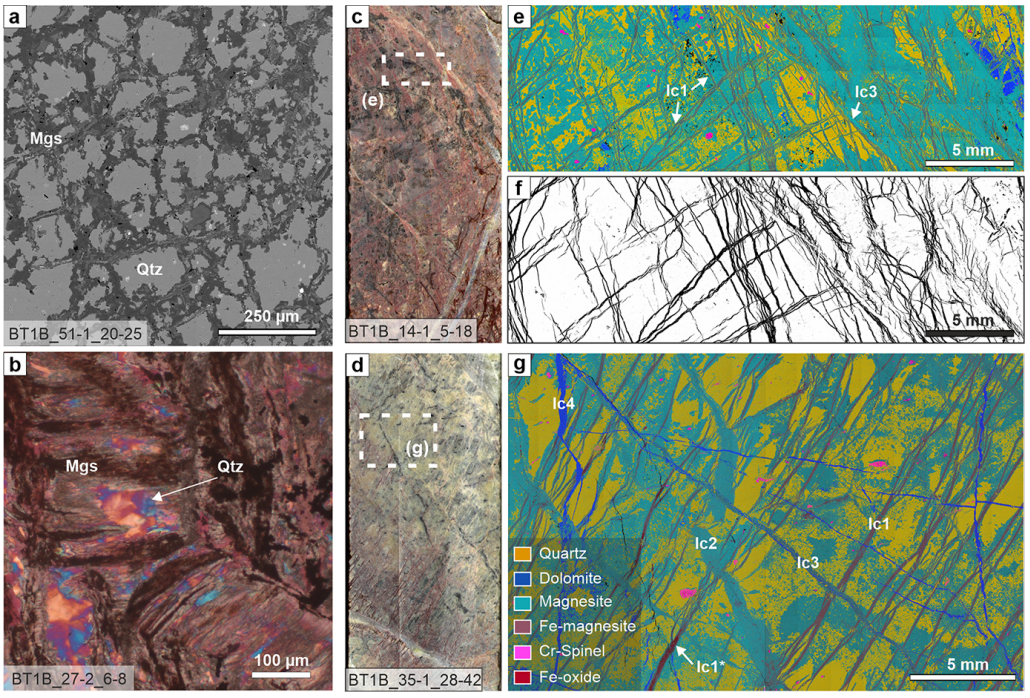

Figure 6. Veins in listvenite of Hole BT1B. **(a)** Magnesite pseudomorphic mesh vein network (l_{ss0}, BSE image). **(b)** Pseudomorphic magnesite–quartz after a serpentine crack–seal vein (l_{ss2}, xpol with 1λ plate). **(c)** Split-core image of listvenite with a conjugate cross-cutting and locally anastomosing zoned magnesite vein network. **(d)** Split-core image of listvenite with parallel carbonate veins that are locally oxidized. **(e)** Composite-color EDX map of the indicated area in **(c)**, showing different magnesite vein generations and a patchy quartz distribution in the matrix (common legend in **g**). **(f)** Same area as in **(e)**, segmented for Fe magnesite (15.8 %). **(g)** Composite-color EDX maps of the area in **(d)** showing cross-cutting relationships between different carbonate vein generations (see Table 1). Dark red veins (lc1*) contain abundant Fe oxides (red veins in **d**). Core diameter in **(a)** and **(d)** is 6.3 cm.

wards the vein walls in crystallographic continuity (Fig. 7d). Many magnesites show euhedral terminations with concentric growth zoning away from the vein center, confirming the antitaxial nature of these veins (Fig. 7d, e). Vein boundaries are irregular with dendritic embayments that extend into the listvenite matrix. A bright luminescent SiO_2 overgrowth rim separates the dendritic embayments from the quartz-rich listvenite matrix (Fig. 7d). This irregular magnesite rim with quartz overgrowth has similar microstructure, luminescence, and composition as the outermost, typically dendritic rims around matrix magnesite ellipsoids described by Menzel et al. (2022).

Cross-cutting relationships between different carbonate veins and passive markers in the form of oxide inclusions within the veins show that carbonate vein formation did not only occur by dilatancy but was accompanied by replacement of the serpentinite matrix (Fig. 8a and b). Measurement of the extent of replacement versus opening is possible in samples in which different generations of zoned magnesite veins cross-cut each other because the dilatant vein aperture is recorded by the displacement of the previous vein generation (Fig. 8b). The cumulative vein width is typically more than twice the opening aperture, showing that epitaxial carbonate growth by replacement of serpentine accounts for much of the vein volume. Moreover, Fe oxides within Fe^{3+}-rich listvenite samples and systematic variations in the content of SiO_2 may act as passive markers that document vein growth by replacement (Fig. 8c–e). While hematite may have co-precipitated during serpentine replacement, magnetite (see yellow arrow in Fig. 8d) is a remnant of the prior serpentinization stage and thus a passive marker. Fe oxides are only cut by dolomite- and quartz-bearing median lines, and oxide aggregates are preferentially aligned oblique to the lc1 carbonate veins, recording a previous fabric that appears mostly unaffected by veining. Similarly, many magnetite aggregates were passively overgrown during expansion of carbonate veins. Notably, magnesite ellipsoids in the listvenite matrix have the same, albeit concentric, patterns of silica zoning and similar cross-cutting relationships with Fe oxides (Fig. 8c), indicating that this stage of carbonate growth proceeded similarly and simultaneously in ellipsoidal matrix grains and along vein rims.

4.2.3 Magnesite and magnesite–dolomite veins

Magnesite veins (lc2) and magnesite–dolomite veins (lc3) cut zoned lc1 carbonate veins (Table 2; Fig. 6g). They are far less abundant than lc1 veins and commonly have ir-

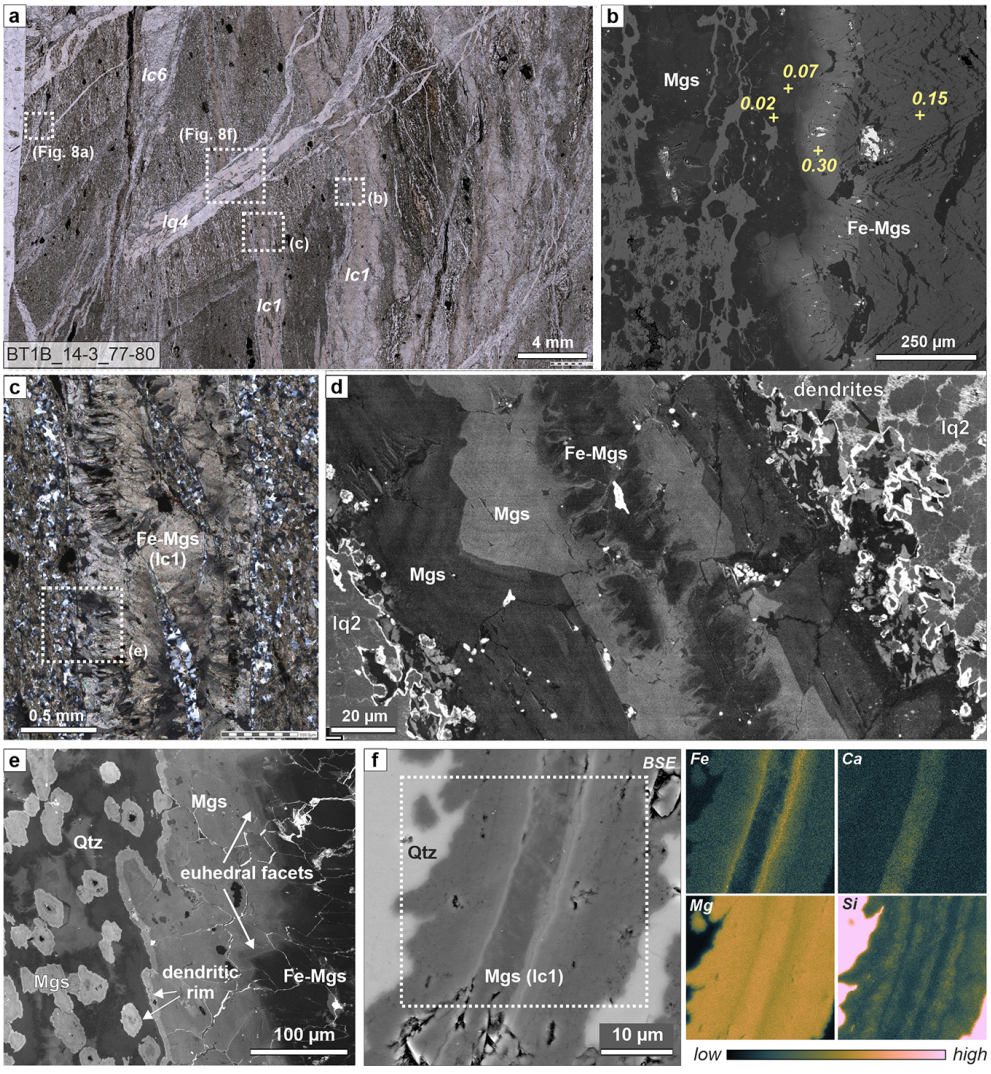

Figure 7. Zoned magnesite veins in listvenite. **(a)** Thin section overview of listvenite with comparatively wide, zoned Fe-magnesite veins (lc1), cut by a quartz–magnesite vein (lq3). **(b)** BSE image of a rim of a zoned magnesite vein, with Fe/(Fe + Mg) of magnesite shown for different zones (from EDX spot measurements). **(c)** Crossed polarized micrograph of a zoned magnesite vein with lens-shaped host listvenite inclusions. **(d)** Pan-chromatic SEM-CL image of an lc1 magnesite vein with an Fe-rich median zone, concentrically zoned growth with euhedral facets towards the vein walls, and dendritic boundaries with bright luminescent SiO_2 overgrowth. The matrix consists of microcrystalline quartz (lq2) (sample BT1B_67-2_36-40). **(e)** SEM-CL image of the area indicated in **(c)**, showing euhedral magnesite growth towards the vein walls. **(a, b, c, e)** Sample BT1B_14-3_77-80). **(f)** BSE image and EDX maps of the dotted area of a thin zoned magnesite vein in listvenite, showing systematic variations in the number of SiO_2 nano-inclusions that are apparent as variable Si-bearing magnesite at the resolution of EDX measurements (sample BT1B_27-2_6-8). Contrasts are adapted for each EDX map separately to improve visibility of zoning.

regular shapes and boundaries. Lc2 veins are composed of dull or non-luminescent magnesite with comparatively little Fe contents and without chemical zoning. They commonly have cross-fiber to blocky syntaxial textures. Lc3 carbonate veins are composed of polycrystalline magnesite with minor dolomite. Magnesite in lc3 veins may show bright pink luminescence colors under optical CL, likely due to enrichment in Mn contents, similar to sc3 veins in serpentinite (see Table 1).

4.2.4 Cryptic quartz veins

Cryptic quartz veins are one of the earliest quartz generations in listvenite (lq1, Table 2). They are usually indistinguishable from matrix quartz grains in plane- and cross-polarized light but become visible by CL due to their dull luminescence compared to brighter matrix quartz (Fig. 9a, b). Cryptic quartz veins commonly have a vermicular, highly irregular, and discontinuous geometry. Many show several stages

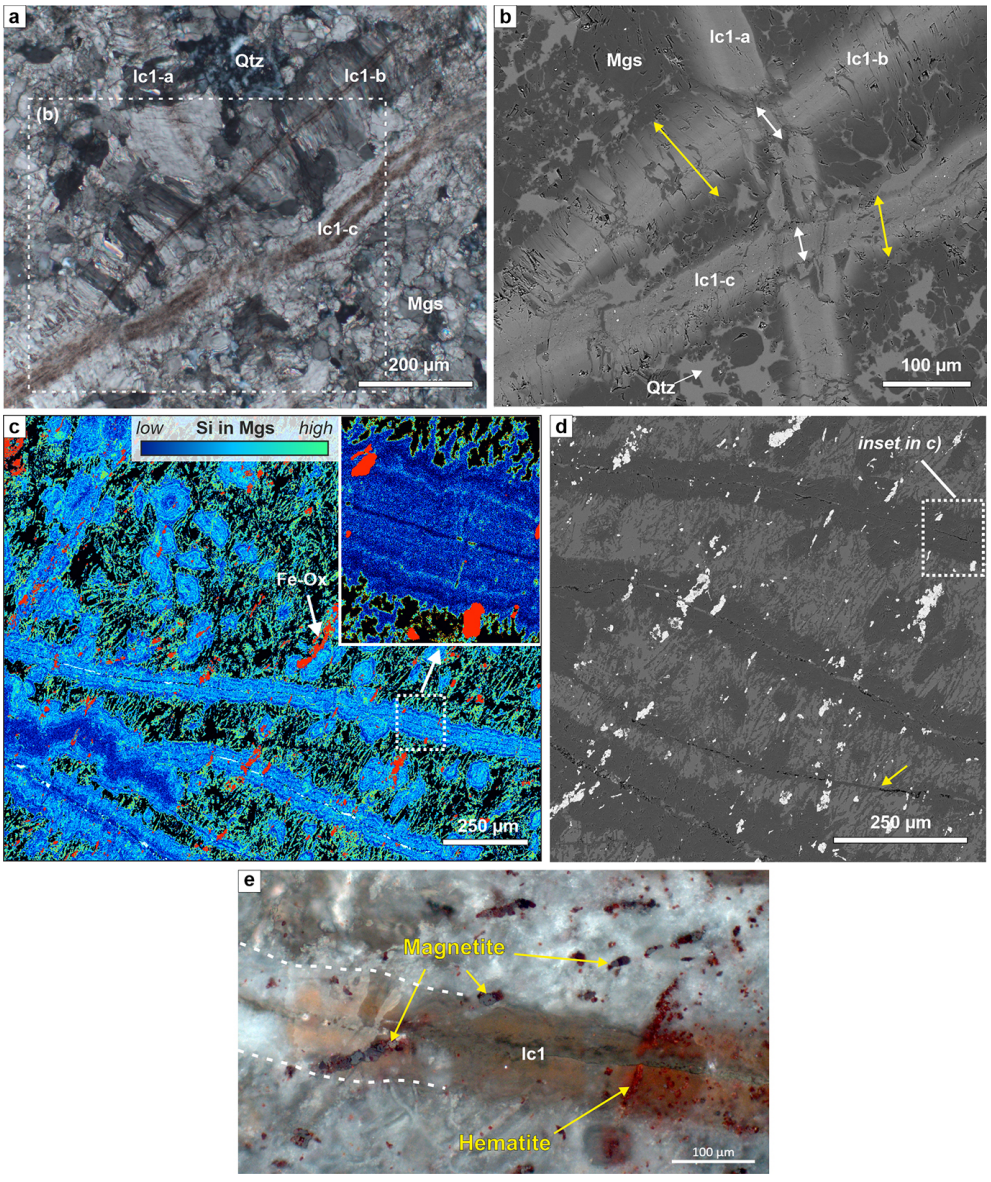

Figure 8. Microstructures showing the extent of opening versus host-rock replacement by zoned magnesite veins. **(a)** Different generations of zoned magnesite veins with a brown, Fe-enriched median zone, showing fibrous (lc1-a, lc1-b) and wide-blocky (lc1-c) habits (xpol). **(b)** BSE image of the area marked in **(a)**, showing that the true vein aperture via opening at the intersection with the earlier vein lc1-a corresponds to inclusion-bearing median zones only (white arrows), while fibrous to euhedral overgrowths indicate that a significant fraction of the total vein thickness (yellow arrows) must have formed due to replacement of the host rock (BT1B_14-1_7-11). **(c)** Si content in magnesite from EDX mapping (with Fe oxides in red; quartz – black; minor dolomite – white), showing vein-parallel zoning in carbonate veins and concentric zoning in matrix magnesite ellipsoids. Only the median zone of veins cuts the oblique Fe oxides. Local folding of an Si-poor vein core in the lower left. **(b)** BSE image of part of the area in **(c)**; the yellow arrow marks a thin vein that did not develop the common replacement rim. **(e)** Crossed polarized, reflected light image of the relationship between a wide-blocky zoned magnesite vein (lc-1), magnetite, and hematite. **(c, d, e)** BT1B_21-3_35-40.

of growth as revealed by cross-cutting or reactivated zones of different luminescence (Fig. 9b). Locally, CL reveals the presence of a thin, dark luminescent zone ($< 10\,\mu m$) with constant thickness over short length scales that could indicate a median zone or refracturing. Notably, most of these veins do not cut zoned magnesite ellipsoids of the listvenite matrix. Instead, they have highly variable thickness and deflect around magnesite ellipsoids. The cryptic quartz veins usually abut against zoned magnesite veins or exploit their wall–host rock interface. The abundance of this vein type is difficult to estimate due their cryptic nature and because matrix quartz in

places shows a similarly dull luminescence, but overall they are less abundant and younger than zoned magnesite veins.

4.2.5 Microcrystalline quartz veins

The most enigmatic vein type in listvenites of Hole BT1B is microcrystalline quartz veins (Fig. 9c–e; lq2, Table 2). They consist of microcrystalline, equigranular quartz with a strong crystallographic preferred orientation over long distances, with small variations of the preferred orientation locally producing striped or chessboard patterns under crossed polarized light. Similar microcrystalline quartz occurs as variably sized patches in the listvenite matrix, suggesting that it may be a replacement microstructure instead of a classic vein infill. SEM-CL imaging shows that the microcrystalline quartz is composed of spheroidal to equant, dull luminescent quartz grains (3–8 µm) surrounded by fibrous, bright luminescent SiO_2 matrix. Magnesite spheroids are not cut by these veins but in places occur within them. Inner parts of zoned magnesite veins appear to cut microcrystalline quartz veins and patches. However, botryoidal, euhedral, and dendritic carbonate vein rims are undisturbed by the microcrystalline quartz (Fig. 9d, e), suggesting that at least some of the microcrystalline quartz formed after zoned magnesite veins.

4.2.6 Quartz–magnesite and quartz–dolomite veins

Bimineralic quartz–magnesite as well as quartz–dolomite veins (lq4 and lc4 in Table 2) cut earlier quartz and carbonate veins (Fig. 9c, d). These veins are mostly syntaxial, with sharp, straight vein walls and abundant host-rock inclusions. Wide-blocky carbonate and quartz can be present in the vein center, while crystals at the vein walls are smaller, show growth competition textures, and commonly have euhedral terminations towards the vein center. Irregular domains of radial chalcedony growth are common, in places also nucleating on the wide-blocky carbonate and quartz crystals along the vein center (Fig. S8 in the Supplement). Cross-cutting relationships indicate that these veins cut listvenite host rock and are thus younger than carbonation of serpentinite. They are usually older than cataclasites (although in some cases also younger than cataclasis) and are cut by late, open or brecciated carbonate veins (Menzel et al., 2020).

4.2.7 Late carbonate veins

The youngest vein generations in BT1 listvenites are monomineralic magnesite (lc5) and dolomite (lc6) veins (Table 2). They have variable microstructures with mostly syntaxial to blocky habits, common euhedral crystal facets, and in places open porosity. CL imaging reveals highly oscillatory growth zoning in dolomite within some of these veins (Fig. 9g), which may be due to cyclic variations in Mn incorporation during precipitation, a common phenomenon in calcite veins elsewhere (e.g., Wang and Merino, 1992).

5 Discussion

5.1 Sequence of reactions and vein formation

Vein microstructures in carbonated peridotites are key to understanding the coupled feedbacks between deformation, fluid flow, and carbonation, and they may provide valuable insights for industrial carbon storage by mineral carbonation (van Noort et al., 2013). In the BT1B listvenites and serpentinites, vein-fill minerals may have formed due to (i) precipitation from supersaturated fluids along fluid pathways in serpentinite during an incipient stage of carbonation, (ii) precipitation of the reaction products magnesite and/or quartz *during* in situ dissolution and replacement of the host serpentine, and (iii) precipitation along fractures in listvenite after termination of the actual carbonation reaction. Microstructural evidence and cross-cutting relationships presented in this study indicate that pseudomorphic veins, zoned magnesite veins, and cryptic and microcrystalline quartz veins are coeval with different stages of the carbonation reaction sequence that consumes serpentine (Fig. 10). Some of the textures and cross-cutting relationships are ambiguous, but in general terms a first stage of carbonate veining preceded extensive crystallization of quartz in veins and the listvenite matrix. Therefore, syn-carbonation veining must have occurred in the early upper Cretaceous coinciding with the main timing of listvenite formation (Falk and Kelemen, 2015). We distinguish the following stages of microstructural evolution.

I. Early, high-temperature ($T > 700\,^{\circ}C$) deformation of the banded peridotite protolith, producing a fabric with elongated and aligned Cr spinel and orthopyroxene. The protolith was partly refertilized through high-T metasomatism (Godard et al., 2021) that is typical of the basal peridotites in the Samail ophiolite (Prigent et al., 2018).

II. Serpentinization of olivine and pyroxene to form mesh and bastite serpentine, respectively, likely at $T < 250\,^{\circ}C$ with formation of magnetite and, in dunitic protolith compositions, brucite. Deformation after and possibly also during serpentinization caused ductile shear zones with aligned lizardite and flattened magnetite mesh structures (Menzel et al., 2022). In places, serpentinization may have been accompanied by cataclasis, similar to that in partially serpentinized peridotite of the Wadi Tayin massif (Aupart et al., 2021).

III. Formation of (not mesh) serpentine–magnetite and banded serpentine crack–seal veins (ss1, ss2; Table 1). Cleavage-parallel serpentine veins formed in foliated serpentinites (Fig. 2d), although they may be obscured by carbonate in BT1B.

IV. Incipient precipitation of carbonate, in particular Fe-rich magnesite, as ellipsoidal to spheroidal grains in the

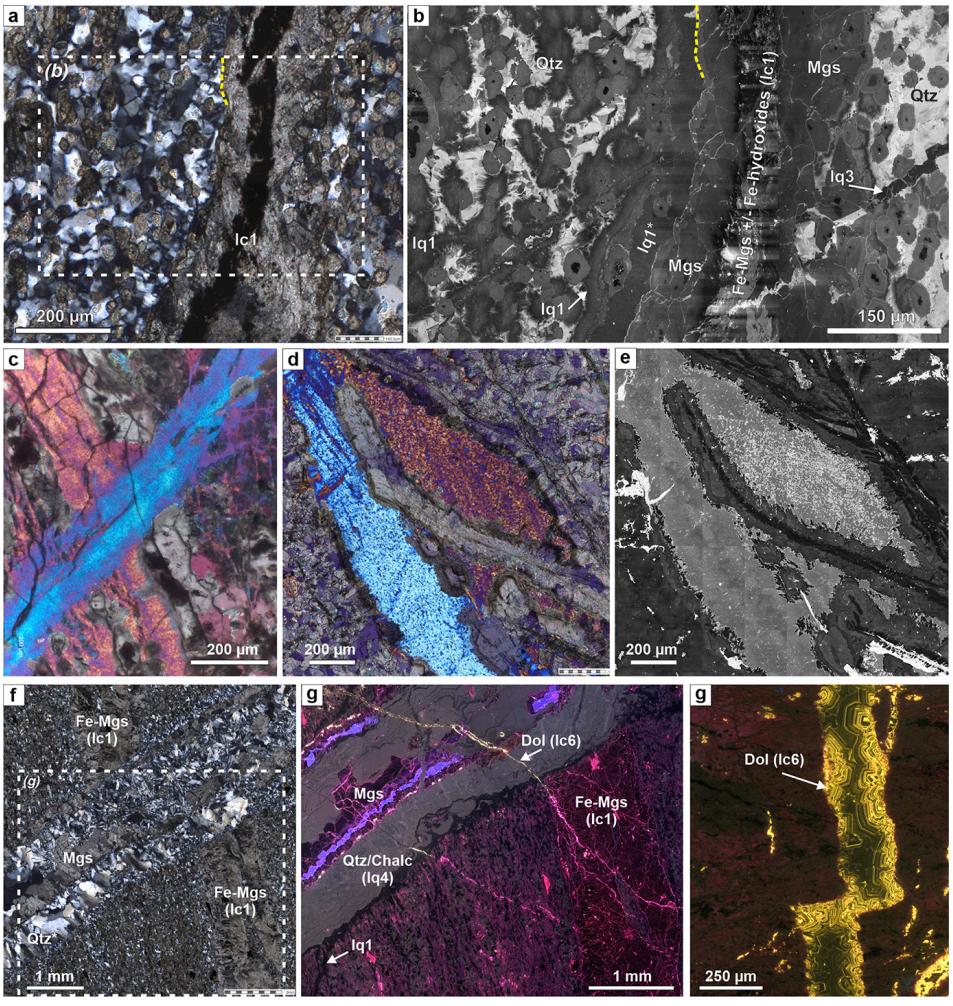

Figure 9. Quartz and late dolomite veins in listvenite. **(a)** Crossed polarized micrograph of a cryptic quartz vein adjacent to a zoned magnesite vein (lc1). **(b)** SEM-CL image of the marked area in **(a)**, showing two generations of dark luminescent cryptic quartz veins (lq1 and lq1*) in bright luminescent matrix quartz and exploiting the zoned magnesite vein interface. Cryptic quartz veins do not cut magnesite ellipsoids in the matrix. A later quartz vein (lq3) cuts both magnesite ellipsoids and the zoned magnesite vein. **(c)** Two cross-cutting generations of microcrystalline quartz veins with distinct crystal preferred orientations (xpol with 1λ plate). **(d, e)** Cross-cutting relationship between zoned magnesite veins and microcrystalline quartz (**d**: ViP xpol with 1λ plate; **e**: SEM-CL); dendritic magnesite overgrowths on the carbonate vein are undisturbed by the microcrystalline quartz. **(f, g)** Crossed polarized micrograph and optical CL mosaic image of a quartz–magnesite vein (lq4), with chalcedony cutting a zoned magnesite vein. Magnesite in the vein has luminescence distinct from that in the listvenite matrix. A late, thin dolomite vein cuts all other vein generations. **(g)** Optical CL mosaic image of a late syntaxial lc6 dolomite vein in listvenite, showing dull to bright yellow oscillatory growth zoning into an open fracture. The vein is roughly oriented vertical (parallel with respect to the core orientation) (**a, b, f, g**: sample BT1B_14-3_77-80, see marked areas in Fig. 7a, c: BT1B_56-4_45-50; **e, f**: BT1B_67-2_36-40; **g**: BT1B_32-1_17-19.)

serpentine matrix (Beinlich et al., 2020b), along the outlines of polygonal mesh cells (sc0 in Figs. 2, 10) and in early carbonate veins (sc1 and the median zone of sc2 veins; Table 1). The ellipsoidal–spheroidal grain habit is interpreted to be a result of disequilibrium precipitation at high oversaturation (Beinlich et al., 2020b) and/or under deviatoric stress (Menzel et al., 2022). Remnant olivine, pyroxene, and brucite after serpentinization may have reacted preferentially with CO_2 to form carbonate.

V. Local (about 10 %–15 % of core BT1B) ductile deformation of the reacting, serpentine-bearing assemblage, leading to folding of early carbonate veins and development of a penetrative foliation by oriented growth of ellipsoidal magnesite in the matrix (Menzel et al., 2022).

VI. Concentric growth of matrix magnesite grains and widening of zoned magnesite veins by replacement of the serpentine matrix and/or opening, in places with precipitation of some talc or quartz (Fig. 4). This is consis-

tent with the microstructures of overgrowths on folded magnesite veins in ductily deformed listvenites from Hole BT1B, which indicate that carbonate vein opening and deformation occurred before listvenite formation was completed (Menzel et al., 2022). This stage may have been accompanied by silica loss on a local scale.

VII. Incipient precipitation of quartz in the remaining serpentine matrix and formation of early, syn-carbonation quartz veins (sq1 in Table 1; lq1 and lq2 in Table 2). In places, opal may have precipitated initially and later recrystallized to quartz or chalcedony (Kelemen et al., 2022).

VIII. Dendritic growth of magnesite on ellipsoidal matrix grains and along the walls of early carbonate veins (Figs. 7; 9e) as well as precipitation of cryptic and/or microcrystalline quartz in veins and the matrix. Complete replacement of remnant matrix serpentine by quartz and minor carbonate concluded the carbonation reaction.

IX. Syntaxial to blocky quartz–carbonate veins that cut listvenite and, rarely, serpentinite (lq4, lc4; Figs. 9f, g; 10). Quartz proportions in these veins are typically higher than carbonate, pointing to silica influx or redistribution during this stage. It is possible that the formation of bimineralic quartz–carbonate veins (lq4, lc4) occurred in listvenite, while carbonation proceeded at the advancing reaction front along the serpentinite–listvenite contact. Alternatively, they may have formed due to fracturing during a first deformational overprint following carbonation.

X. Cataclasis, sharp faults, and late carbonate veins overprinting listvenite and serpentinite (Fig. 10; sc4, lc5, lc6 in Tables 1 and 2), in parts related to local Ca gain and Mg loss in listvenite (Menzel et al., 2020).

In terms of chemical reactions, we infer that the main stages of progressive transformation to listvenite proceeded by the following simplified reactions.

1. Hydration of olivine and orthopyroxene to serpentine and brucite, forming serpentine mesh veins and bastite (stage II), with brucite proportions depending on orthopyroxene abundance (for $0 \leq m \leq 1$):

$$(2-m)\,Mg_2SiO_4 + m\,MgSiO_3 + (3-m)\,H_2O = Mg_3Si_2(OH)_4 + (1-m)\,Mg(OH)_2. \quad (R1)$$

2. Incipient magnesite formation in the matrix, sc0 veins, and the center of sc1 and sc2 veins (stage IV–VI) by reaction of brucite and serpentine with CO_2, initially likely with little formation of secondary silicates but related to transfer of aqueous silica ($SiO_{2(aq)}$; for $0 \leq n \leq 2$):

$$Mg(OH)_2 + CO_{2(aq)} = MgCO_3 + H_2O, \quad (R2)$$

$$Mg_3Si_2(OH)_4 + 3\,CO_{2(aq)} = 3\,MgCO_3 + (2-n)\,SiO_2 + n\,SiO_{2\,(aq)} + 2\,H_2O. \quad (R3)$$

Isochemical replacement of serpentine by magnesite and quartz ($n = 0$ in Reaction R3) would lead to a magnesite / quartz proportion of 1.5 molar, equivalent to ~ 34 vol % quartz. Local mobility of aqueous silica is inferred from the observation that many matrix domains and magnesite veins have magnesite / quartz proportions significantly higher than 1.5 molar (Figs. 3; 4). Thus, only some of the released silica precipitated in situ, forming SiO_2 inclusions in magnesite or, rarely, talc (e.g., Fig. 4), indicating local leaching of $SiO_{2(aq)}$. In addition or alternatively to silica loss, Reaction (R3) may be complemented by influx of aqueous Mg-bearing species and local Ca mobility where early dolomite is present (see Beinlich et al., 2020b).

3. Reaction of serpentine with CO_2 to form magnesite and quartz (stages VII–VIII), locally with excess influx of aqueous silica derived from Reaction (R3), forming syn-carbonation quartz veins and (microcrystalline) quartz-rich domains:

$$Mg_3Si_2(OH)_4 + 3\,CO_{2(aq)} + n\,SiO_{2(aq)} = 3\,MgCO_3 + (2+n)\,SiO_2 + 2\,H_2O. \quad (R4)$$

4. Post-listvenite syntaxial and late veins in listvenite (stages IX–X) do not show replacement structures involving reaction of serpentine with CO_2 but are inferred to have formed primarily by precipitation from aqueous solutions with variable concentration of dissolved Si, Ca, Mg, and bicarbonate–carbonate:

$$Mg^{2+} \pm Ca^{2+} \pm HCO_3^- \pm CO_3^{2-} \pm SiO_{2(aq)} = MgCO_3 \pm SiO_2 \pm (Ca,Mg)CO_3 \pm CaCO_3. \quad (R5)$$

Some of the dolomite locally replacing early magnesite veins and filling late veins may be reflective of magnesite dissolution in combination with influx of Ca-bearing fluids, possibly related to fluid flow during brittle overprint (Menzel et al., 2020). Some of the youngest post-listvenite magnesite and dolomite vein generations (lc5, lc6) may have a similar origin as very young magnesite, dolomite, and calcite–aragonite veins related to interaction of Mg–HCO_3^-- and Ca–OH^--bearing groundwater with the Samail peridotite (Noël et al., 2018; Streit et al., 2012; Ternieten et al., 2021).

Because the transformation of serpentine into magnesite and quartz (Reactions R3 and R4) consumes CO_2 while releasing H_2O, the fluid evolves to more aqueous compositions with reaction progress. Thus, steps II–VIII and Reactions (R1)–(R4) may have occurred at the same time along different advancing reaction fronts, which correspond to the contacts between partially hydrated peridotite, serpentinite, carbonate-bearing serpentinite, and listvenite.

We note that not every stage I–X is recognizable in each core section. Moreover, field exposures around site BT1 show high variability of strongly veined domains alternating with more massive listvenite intervals. We further note that vein microstructures in dolomite and dolomite–calcite listvenites that are common further north in the Fanjah region are somewhat different from the magnesite-dominated BT1B listvenites studied here, as they are related to a massive gain of Ca through fluid influx (Reaction R5).

5.2 Influence of pre-existing serpentine structures on veining

Pseudomorphic carbonate after mesh and crack–seal serpentine veins (Figs. 2e–h; 6a, b) demonstrate that the microstructure of the precursor serpentinite determined the location and structure of vein networks to a great extent. The local presence of brucite and/or variations in Si, Al, and Fe contents of serpentine may have caused preferential carbonation at specific microstructural sites where carbonation reaction affinity is higher. Brucite, which shows very fast carbonation reaction kinetics in low-temperature experiments (Harrison et al., 2013; Hövelmann et al., 2012), is commonly observed together with magnetite along serpentine mesh veins in serpentinites (Schwarzenbach et al., 2016). The preferential replacement of previous brucite by magnesite (Reaction R1) may thus explain the polygonal, mesh–pseudomorphic carbonate vein network in some serpentinites and listvenites of Hole BT1B (Figs. 2e–f; 6a). However, brucite is typically only abundant in serpentinized dunite because its stability requires high Mg / Si of the bulk rock. As large parts of the listvenites of Hole BT1B are inferred to have had a serpentinized harzburgite and lherzolite protolith based on major and trace element geochemistry (Godard et al., 2021), we infer that brucite was only common in minor dunitic intervals. On the other hand, different parts of mesh microstructures and different veins in serpentinite can be composed of a variety of serpentine polytypes with different crystal structure. Acid-leaching experiments have shown that dissolution rates can differ greatly between these polytypes, with much higher Mg extraction rates for chrysotile, nanotubular chrysotile, and poorly ordered lizardite compared to Al-bearing lizardite, polygonal serpentine, and antigorite (Lacinska et al., 2016). It is therefore likely that different serpentine polytypes also show variable dissolution rates during reaction with moderately acidic, CO_2-bearing aqueous fluids. This may explain why specific microstructural sites are preferentially replaced by carbonate, producing pseudomorphic textures. Besides variable dissolution rates, serpentine polytypes also have different crystal habits with differing strength and surface area. Thus, we propose that the heterogeneous microstructures of different serpentine polytypes form micro-environments with different inter- and intragranular nano-porous matrix permeability as well as micron-scale permeability along fractures. These heterogeneities create complex relationships between diffusive and advective solute transfer, fluid flow rates, and kinetics that control different levels of pseudomorphic inheritance.

Banded serpentine crack–seal veins appear to have a particularly strong impact on local fracture formation and small-scale porosity morphology. Such serpentine veins typically consist of chrysotile fibers alternating with lizardite or polygonal serpentine, recording repeated crack–seal cycles (Andreani et al., 2004; Tarling et al., 2021). Due to the high tensile strength of chrysotile parallel to fiber orientations, fracturing and associated permeability are expected to occur preferentially along the vein–host rock interface, which is what we observed in pseudomorphic replacement microstructures (Figs. 2h; 6b).

5.3 Vein growth mechanisms – opening versus replacement

Opening of dilatant fractures can increase permeability and provide pathways for fluid infiltration that would allow carbonation to proceed. What type and how much permeability is created, however, depend on how soon after opening and in which direction the vein becomes filled. When crystals precipitate at the vein walls and grow inwards towards the vein center (syntaxial veins), fluid replenishment and, potentially, crack–seal events occur along the vein center (Bons et al., 2012). This potentially results in a loss of connectivity between the vein and matrix permeability network because of mineralization along the vein–matrix interface. In contrast, if crystal growth proceeds from a median zone towards the vein walls (antitaxial veins), fluid flow is focused along the vein–host rock interface, creating a connected permeability network between the fracture and rock matrix. We found examples of both types of vein growth in the BT1B serpentinites and listvenites (Tables 1 and 2). In general terms, early serpentine and carbonate veins (e.g., Figs. 2, 4) as well as some early quartz veins (Fig. 5b) tend to show antitaxial textures, whereas younger quartz–carbonate veins (lq4, lc4; Table 2) tend to be syntaxial. If the process was entirely mechanical, this would suggest a reduction in the connectivity of the permeability network over time. Owing to chemical–mineralogical replacements that occur during carbonation, however, the mechanism is more complex during listvenite formation.

Current models of vein formation treat the host rock as a non-reactive substrate with vein formation due to precipitation from aqueous solution in fluid-filled fractures (Ankit et

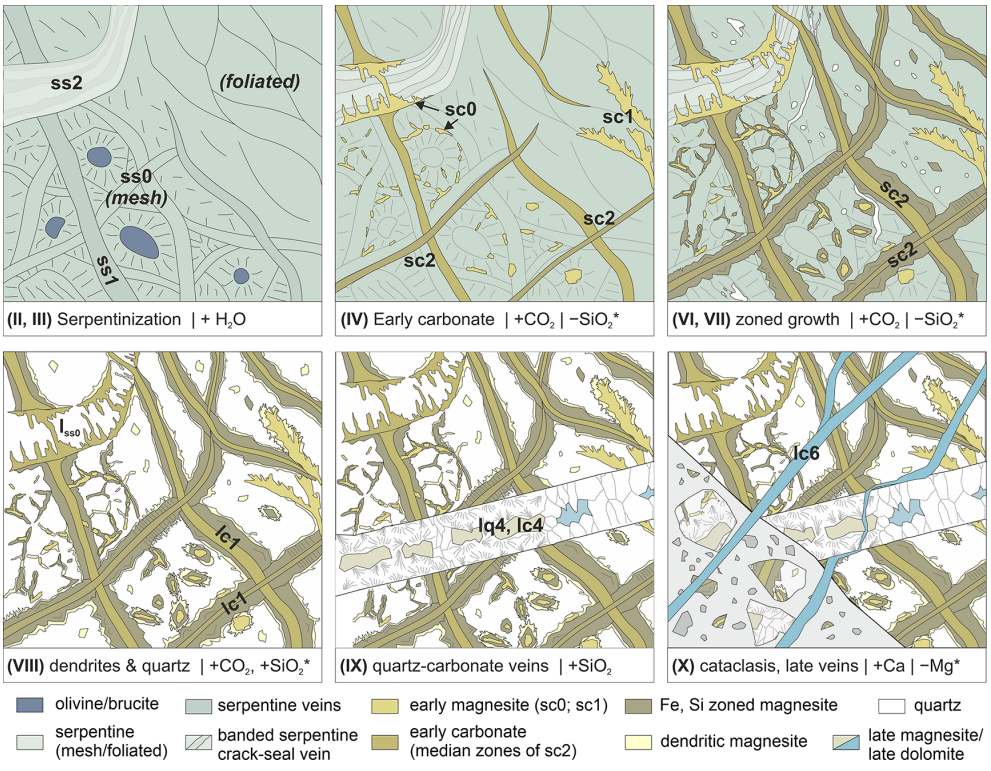

Figure 10. Sketch of the evolution of carbonation and vein formation in Hole BT1B, as inferred from serpentinite and listvenite samples (different stages, see text). Different stages were related to differing element transfer with gains (denoted by, e.g., $+H_2O$); inferred losses (e.g., $-SiO_2$*) are likely only relevant on a local scale. For clarity, not all vein generations (see Tables 1 and 2) are shown.

al., 2015; Hilgers et al., 2001; Hubert et al., 2009; Spruženiece et al., 2021a, b). This mode of vein formation is commonly observed in carbonate veins in altered oceanic crust (e.g., Quandt et al., 2020). In the case of carbonate veining during listvenite formation, however, mechanical opening was accompanied by replacement of the host serpentinite (Fig. 8) so that the morphology of the fracture wall is controlled by dissolution and replacement in addition to dilatancy. Therefore, the wall rock changes its morphology by dissolution, and vein volume is further accommodated by replacement. In addition to evidence from cross-cutting relationships and overgrown passive markers within veins and the listvenite matrix (Fig. 8), the high abundance of SiO_2 nano-inclusions within zoned magnesite veins in listvenite of Hole BT1 as confirmed by transmission electron microscope (TEM) (Beinlich et al., 2020b; Menzel et al., 2022) indicates that silica saturation and quartz nucleation rate were high during carbonate vein growth, which provides further evidence for simultaneous serpentine dissolution.

Microstructures indicative of growth zoning during carbonate vein growth from a median zone outward into the serpentine matrix (Fig. 7d) suggest that there was a reactive fluid film and significant permeability along the vein–host rock interface (Fig. 11). Compared to the fracture permeability created initially by dilatant opening of the vein, which may easily clog if mineral precipitation is fast, we postulate that this interface permeability was maintained by vein growth by replacement and coupled dissolution of serpentine. Facetted carbonate crystal terminations, partial talc infills, and secondary exploitation by quartz veins (Fig. 4) suggest that the vein–serpentinite interface was a preferential site of focused, advective fluid flow and, in places, new fracture formation. This interface permeability thus promoted continued vein growth by serpentine dissolution, in addition to supplying CO_2-bearing fluid to the nano-porous matrix of the non-veined host serpentine through diffusive solute transfer, facilitating progressive carbonation of serpentinite. Subsequent syntaxial quartz–carbonate veins most likely lacked such a reaction front, with fluid pathways concentrated along the center of the vein.

5.4 Formation of closely spaced carbonate vein sets

Because early, zoned magnesite veins are extremely abundant in serpentinite and listvenite of Hole BT1B and because of their likely role in acting as main fluid pathways early in the carbonation process, understanding their formation mechanism is integral to deciphering the factors controlling carbonation reaction progress. A key feature of these carbonate veins is that they commonly form closely spaced, subparallel sets. Similar, subparallel serpentine vein sets oc-

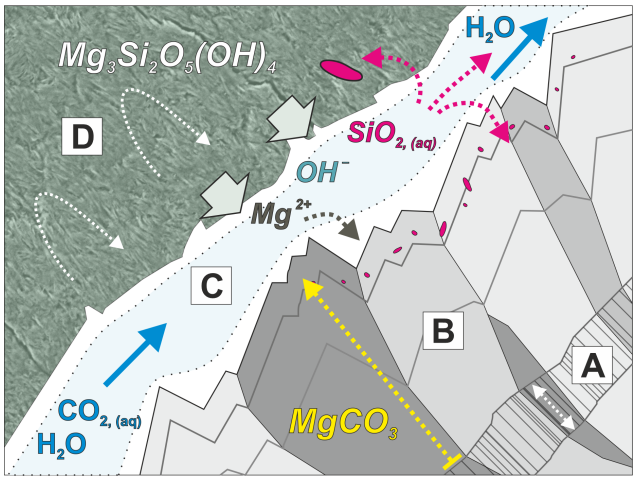

Figure 11. Conceptual sketch of magnesite vein growth by replacement of serpentine. Domain A: initial dilatant fracture with carbonate infill, forming the median lines of zoned magnesite veins. B: magnesite vein growth rim formed by replacement. C: interface permeability at vein walls causes development of a fluid film with diffusion-dominated boundary layers (white) and a central advective flow zone (light blue), which allows CO_2 influx and drives coupled serpentine dissolution and carbonate precipitation. The widths of boundary layers relative to the advective zone depend on fluid flow rate. The overall width of domain C is highly exaggerated for illustration purposes. D: nano-porous serpentine with predominantly diffusive solute transfer in matrix permeability. The observations show that only small fractions of dissolved silica precipitate in situ (red), forming nano-inclusions in magnesite; most silica is leached and precipitates in other micro-environments.

cur in serpentinites in the vicinity of listvenites in the area (Fig. 2b) and are common in other serpentinized peridotites of the Samail ophiolite (Kelemen et al., 2020a, c). Parallel, closely spaced serpentine vein sets are also known from oceanic peridotites (Andreani et al., 2007). Repeated fracturing parallel to existing veins requires the veins and the vein–host rock interface to be stronger than the host rock (Virgo et al., 2014). However, the reaction front at the vein – serpentinite interface of zoned magnesite veins (sc2 and lc1 veins; Fig. 11) speaks against a strong vein–host rock interface during this stage of reaction. Furthermore, the zoning patterns, documenting changing fluid compositions and/or redox conditions, are consistent within different veins of the same set. Hence, a sequential process of repeated parallel fracturing and sealing by zoned carbonate growth is unlikely because it would require similar cyclic variations of fluid composition and redox conditions to be repeated for each vein.

A more feasible explanation is that the zoned parts of the carbonate veins formed along a pre-existing fracture or vein set. If the vein material had a higher strength than the host serpentinite, closely spaced vein sets may form. This may have happened if the initial vein fill had a higher permeability or higher carbonation reaction affinity than serpentine of the host rock, so that the veins preferentially became replaced by carbonate. Zoned carbonate growth may then have proceeded from the narrow vein set into the serpentine matrix in a later step. A precursor vein fill of fibrous chrysotile may be a suitable candidate because chrysotile has the same or higher tensile strength compared to matrix serpentine, facilitating fracturing parallel to existing veins. Chrysotile veins may also show higher carbonation reaction rates than lizardite due to the larger surface area of fibrous aggregates, especially if they have a nano-tubular crystal morphology (Lacinska et al., 2016), in line with the observation of other pseudomorphic carbonate veins (Fig. 2c, h). High-resolution SEM imaging of a broad-ion-beam polished sample of veined serpentinite (see methods) reveals that fibrous serpentine veins can have substantially higher micro- to nano-porosity than the matrix serpentine (Fig. 12), confirming that they may be sites of preferential reactive fluid flux. Similar subparallel serpentine vein sets may thus have been the precursor of the closely spaced sc2 and lc1 carbonate veins. Such serpentine veins may form by repeated fracturing of serpentinite or during serpentinization of olivine when tectonic stress enhances widening of favorable orientations of mesh veins (see Fig. 5 of Aupart et al., 2021).

5.5 Reaction-induced fracturing?

Listvenites are inferred to form, among other settings, at the base of ophiolites or in the shallow mantle wedge of subduction zones (e.g., Kelemen and Manning, 2015). At these conditions, all principal stresses will be compressive. Thus, fracturing by tensile or shear failure typically requires a reduction of effective stress by fluid overpressure (Hilgers et al., 2006; Sibson, 2017). Experiments and numerical models of volume-expanding hydration reactions have shown that crystallization pressure may locally create gradients in differential stress, which can also facilitate fracture formation, increasing permeability and reactive surface area (Malthe-Sørenssen et al., 2006; Rudge et al., 2010; Shimizu and Okamoto, 2016). In combination with elevated fluid pressure, these local stress gradients caused by "force of crystallization" could lead to dilatant opening and propagation of existing veins, formation of new fractures, or enhanced pressure solution of the rock matrix (Fletcher and Merino, 2001). Kelemen and Hirth (2012) propose that crystallization pressure during peridotite carbonation can be large enough to exceed the stress required for frictional failure, creating a positive feedback for reaction progress via fracturing. This process has been shown to be efficient for reactions wherein volume changes are very large, such as during hydration of periclase (MgO) to brucite (Zheng et al., 2019, 2018), and important during serpentinization of olivine (Evans et al., 2020; Plümper et al., 2012; Yoshida et al., 2020). However, the extent to which crystallization pressure influences listvenite formation is less certain (van Noort et al., 2017). Full hydration and carbonation of olivine increase the solid volume

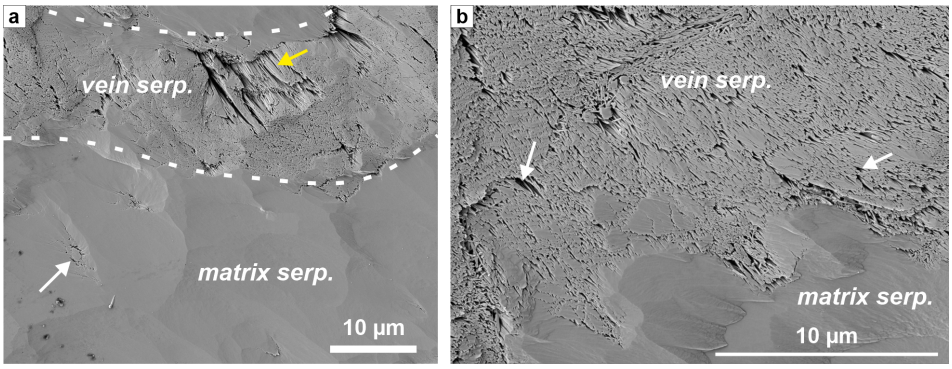

Figure 12. SE image of a broad-ion-beam polished serpentine vein in foliated serpentinite **(a)** with a close-up of the vein–wall rock interface **(b)**, showing that the vein serpentine is highly (nano-)porous in comparison to matrix serpentine. White arrows indicate examples of nano-porosity (black). In the vein, porosity is controlled by fibrous serpentine as seen in the poorly polished area (yellow arrow in **a**). The vein domain corresponds to the blue bands in Fig. 2d (sample OM20-13).

by 33 % and > 40 % (Kelemen et al., 2011), respectively, while the conversion of serpentine to magnesite and quartz is predicted to cause a solid volume expansion of 18 %–22 % (Hansen et al., 2005; Kelemen et al., 2022). Reaction-induced fracturing due to crystallization pressure and volume expansion may thus have occurred at the advancing serpentinization and carbonation reaction fronts that formed the serpentinites and listvenites at site BT1.

Zoned magnesite veins may theoretically have opened through crystallization pressure to some extent because, unlike in syntaxial veins, carbonate growth occurred from the center outwards. However, several observations argue against this mechanism dominating during early carbonation: (i) passive markers show that much of the vein width was accommodated by replacement rather than opening (Fig. 8), (ii) euhedral growth patterns point to the presence of an open fluid conduit at the vein–matrix interface (Fig. 11), and (iii) most zoned magnesite veins in serpentinites and listvenites contain a much smaller proportion of SiO_2 (mostly as inclusions in magnesite) than expected for isochemical replacement of serpentine (Figs. 4, 7, 8), indicating that silica was leached (Reaction R3). Mg isotope geochemistry and bulk chemistry mass balance calculations suggest that Mg in listvenite magnesite is derived from local dissolution of the peridotite protolith (de Obeso et al., 2021; Godard et al., 2021). Assuming that external Mg influx was negligible and that magnesite growth is rate-limited by serpentine dissolution, Reaction (R3) would cause volume expansion only if at least ∼ 22 vol % of the solid reaction products is quartz. If more $SiO_{2(aq)}$ is leached than precipitated in situ as quartz ($n > 1$ in Reaction R3), solid volume change would be negative. Since in situ quartz abundance in zoned magnesite veins is typically < 10 vol %, combined influx of CO_2 and local leaching of silica probably resulted in a solid volume decrease at the vein–serpentine interface because magnesite has a higher density than serpentine. The leached silica may have precipitated synchronously in different microstructural sites in the rock matrix, forming quartz-rich domains, or as cryptic, microcrystalline, or syntaxial quartz veins (Fig. 8; Reaction R4) further downstream along the reaction front or in listvenite. Abundant SiO_2 nano-inclusions in magnesite point to widespread quartz oversaturation and high nucleation rates. This suggests a non-trivial coupling between the surface properties, porosity, and dissolution rate of serpentine and the interface geometry, solute transport, and precipitation kinetics during vein growth. Possibly, some local silica mobilization occurred in the form of suspended silica nano-aggregates at high fluid flow rates. The occurrence of centimeter-scale bulk chemical variations in the BT1B listvenites suggests that similar local mass transfer was commonplace during listvenite formation (Godard et al., 2021).

Numerical models suggest that volume-increasing reactions with fast reaction kinetics induce polygonal and hierarchical fracture patterns (e.g., Okamoto and Shimizu, 2015; Ulven et al., 2014), in agreement with the typical mesh textures in serpentinites. In contrast, the BT1B zoned magnesite vein sets have parallel or anastomosing patterns that indicate a strong influence of tectonic stress during initial fracture formation.

Taken together, these observations suggest that although volume expansion associated with the overall transformation to listvenite (combined Reactions R3 and R4) caused some crystallization pressure, zoned magnesite veins did not primarily grow through force of crystallization. Crystallization pressure may have contributed to the external stress responsible for the initial, dilatant fractures along which the carbonate veins developed. A similar conclusion can be drawn from the microstructures of pseudomorphic carbonate (sc0) and feathery, cleavage-parallel carbonate veins (sc1) in carbonate-bearing serpentinite (Table 1): quartz is rare or absent in their vicinity, indicating that their formation did not require volume expansion if Mg was sourced locally from dissolving serpentine. Reaction-induced fracturing was, however, likely prevalent during the preceding highly volume-expanding ser-

pentinization, which created mesh and vein textures with heterogeneous permeability and carbonation affinity.

5.6 Tectonic context

CO_2 fluid flux derived from subduction and/or underthrusting of (meta)sediments below the Samail ophiolite is considered the most likely setting of listvenite formation at site BT1 (de Obeso et al., 2022; Kelemen et al., 2022), although carbonation during extensional reactivation of the thrust fault in an early phase after obduction is possible (see Sect. 2.2). While the common parallelism of zoned magnesite veins points to a strong influence of tectonic stress on vein formation, our results do not allow us to determine whether veining occurred in an overall contractional or extensional setting. This caveat is due to unoriented drill cores and the complexity arising from the observation that most of the syn-carbonation veins are replacement and not purely dilatant veins. Folding (Kelemen et al., 2022) and several phases of post-listvenite brittle faulting (Menzel et al., 2020) further complicate a reconstruction of paleo-stress directions during formation of the different vein generations. Based on ductile deformation microstructures, the morphology of preserved micro- and nano-pores, and the requirement for high fluid fluxes to form listvenite, Menzel et al. (2022) inferred that pore pressures were high during carbonation. High pore pressures can also lead to tensile and extensional fracturing in thrust settings, which may be particularly widespread at contacts and in mixtures of lithologies with disparate rheology (e.g., Sibson, 2017). Such conditions may be common at the reaction front along the contacts of comparatively strong listvenite lenses enclosed in weak, sheared serpentinite. In Oman, fluid overpressure cells formed in response to burial below the ophiolite and the Hawasina nappes, causing veining in (par)autochthonous carbonate rocks (Grobe et al., 2019). The widespread and multiphase syn-carbonation veining observed in the BT1B serpentinites and carbonates may thus be a combined effect of reaction-induced stress from serpentinization and cyclic fluctuations between sub-lithostatic and lithostatic fluid pressures in the deforming and reacting basal peridotites during subduction and/or ophiolite emplacement. With subsequent progressive cooling of the ophiolite and underlying units, CO_2 concentration in infiltrating fluids likely decreased. Thus, the fluid chemistry may have switched to more Ca and/or Mg bicarbonate ionic solutions favoring the formation of syntaxial, post-listvenite veins and precipitation of carbonate vein fill in contrast to the earlier syn-listvenite replacement veins that formed by reaction of serpentine with CO_2.

6 Conclusions

Microstructures and cross-cutting relationships in serpentinites and listvenites of Hole BT1B demonstrate that several vein generations formed during carbonation reactions. These veins constitute large volumes of the BT1B listvenites, showing that fracturing and related advective fluid flow were integral to carbonation progress. The incipient stages of carbonation are consistently related to pseudomorphic carbonate and zoned magnesite veins. Zoning of Ca, Fe, and Si contents in early carbonate veins records variations in fluid composition, changes in redox conditions, and variations of supersaturation and nucleation rates of silica during progressive serpentine replacement. Cross-cutting relations and passive markers indicate that zoned magnesite veins formed as incipient dilatant, often parallel, and closely spaced microfractures, possibly initially filled with precursor chrysotile that was preferentially replaced by carbonate. From this incipient median zone, a permeable micro-reaction front developed into the serpentine matrix upon further CO_2 influx, allowing vein growth to continue through a dilatant–reactive process. These observations indicate that vein–wall rock interfaces served as essential fluid conduits during transformation of the non-veined matrix into listvenite. Sets of parallel to anastomosing carbonate veins point to an important role of tectonic stress during early carbonation, likely complemented by deviatoric stress generated by volume expansion at the serpentinization front advancing ahead of the carbonation reaction front, whereas crystallization pressure from magnesite precipitation was most likely less significant during veining. As carbonation progressed, permeability was probably reduced during subsequent quartz veining and further silica replacement of the matrix, but a lack of remnant serpentinite in listvenite horizons indicates that penetration of CO_2-rich fluid through the vein and matrix permeability network was sufficient for carbonation to proceed to completion. Our results suggest that in this natural example, veining caused by tectonic stress and fluid overpressure is an important mechanism to create permeability despite carbonate precipitation. Without the added effect of tectonic deformation and related deviatoric stress, it is possible that permeability created through reaction-driven fracturing $\pm$ replacement veining alone is not enough to allow for the necessary fluid flux for carbonation to progress. Therefore, the extent of carbon mineralization and permanent CO_2 sequestration that can be attained via experimental in situ CO_2 injection might be limited.

Sample availability. Archive halves and samples of core BT1B are available through the Oman Drilling Project (https://www.omandrilling.ac.uk/samples-data, Oman Drilling Project, 2022). Digitized thin sections of some of the samples used in this study are available for download as a Supplement of the Oman Drilling Project (http://publications.iodp.org/other/Oman/SUPP_MAT/index.html#SUPP_MAT_Z, International Ocean Discovery Program Publications, 2022).

Data availability. All main data are contained in the figures and tables of the paper and the Supplement; raw images of figures are available from the authors upon request.

Supplement. The supplement related to this article is available online at: https://doi.org/10.5194/se-13-1191-2022-supplement.

Author contributions. MDM and JLU designed the study, conducted fieldwork, and studied the microstructures and petrography; MDM and TD refined the vein classification; MDM performed SEM imaging, EDX mapping, optical CL analysis, and image processing, as well as drafting the figures; EU conducted SEM and SEM-CL analysis. All authors discussed and interpreted the results. MDM led writing and revision of the paper, to which all authors contributed.

Competing interests. The contact author has declared that none of the authors has any competing interests.

Disclaimer. Publisher's note: Copernicus Publications remains neutral with regard to jurisdictional claims in published maps and institutional affiliations.

Acknowledgements. We would like to thank Michael Kettermann and Yumiko Harigane for sampling onboard *Chikyu* and Peter Kelemen for providing an invaluable set of additional thin sections. Werner Kraus and Jonatan Schmidt are thanked for thin section preparation and technical assistance, and Sara Elliott is thanked for assistance with SEM-CL imaging and post-processing. We are grateful to the Oman Public Authority of Mining for support to conduct fieldwork and sample export. This study has benefitted from fruitful and inspiring discussions with Peter Kelemen, Romain Lafay, Juan Carlos de Obeso, Craig Manning, and others over the past years. We further acknowledge the constructive reviews by Dennis Quandt, an anonymous referee, and the topical editor Virginia Toy, whose comments helped to improve several aspects of the paper.

This research used samples and data provided by the Oman Drilling Project. The Oman Drilling Project (OmanDP) has been possible through co-mingled funds from the International Continental Scientific Drilling Project (ICDP), the Sloan Foundation – Deep Carbon Observatory (grant 2014-3-01), the US National Science Foundation (NSF-EAR-1516300), NASA – Astrobiology Institute NNA15BB02A), the German Research Foundation (DFG: KO 1723/21-1), the Japanese Society for the Promotion of Science (JSPS no. 16H06347; and KAKENHI 16H02742), the European Research Council (Adv: no. 669972), the Swiss National Science Foundation (SNF:20FI21_163073), the Japanese Marine Science and Technology Center (JAMSTEC), the International Ocean Discovery Program (IODP), and contributions from the Sultanate of Oman Ministry of Regional Municipalities and Water Resources, the Oman Public Authority of Mining, Sultan Qaboos University, CRNS-Univ. Montpellier II, Columbia University of New York, and the University of Southampton.

Financial support. Manuel D. Menzel and Janos L. Urai were funded by the German Research Foundation (DFG grants UR 64/20-1, UR 64/17-1).

Review statement. This paper was edited by Federico Rossetti and reviewed by Dennis Quandt and one anonymous referee.

References

Agard, P., Searle, M. P., Alsop, G. I., and Dubacq, B.: Crustal stacking and expulsion tectonics during continental subduction: P-T deformation constraints from Oman, Tectonics, 29, TC5018, https://doi.org/10.1029/2010TC002669, 2010.

Andreani, M., Baronnet, A., Boullier, A.-M., and Gratier, J.-P.: A microstructural study of a "crack-seal" type serpentine vein using SEM and TEM techniques, Eur. J. Mineral., 16, 585–595, 2004.

Andreani, M., Mével, C., Boullier, A. M., and Escartín, J.: Dynamic control on serpentine crystallization in veins: Constraints on hydration processes in oceanic peridotites, Geochem. Geophy. Geosy., 8, Q02012, https://doi.org/10.1029/2006GC001373, 2007.

Ankit, K., Urai, J. L., and Nestler, B.: Microstructural evolution in bitaxial crack-seal veins: A phase-field study, J. Geophys. Res.-Sol. Ea., 120, 3096–3118, 2015.

Ash, C. H. and Arksey, R. L.: The Atlin ultramafic allochthon: ophiolitic basement within the Cache Creek terrane; tectonic and metallogenic significance, 104N/12, Geological Fieldwork 1989, 1990–1, British Columbia Ministry of Energy, Mines and Petroleum Resources Victoria, BCGS_P1990-01-41_Ash, 365–374, 1989.

Aupart, C., Morales, L., Godard, M., and Jamtveit, B.: Seismic faults triggered early stage serpentinization of peridotites from the Samail Ophiolite, Oman, Earth Planet. Sc. Lett., 574, 117137, https://doi.org/10.1016/j.epsl.2021.117137, 2021.

Beinlich, A., Plümper, O., Hövelmann, J., Austrheim, H., and Jamtveit, B.: Massive serpentinite carbonation at Linnajavri, N–Norway, Terra Nova, 24, 446–455, 2012.

Beinlich, A., John, T., Vrijmoed, J. C., Tominaga, M., Magna, T., and Podladchikov, Y. Y.: Instantaneous rock transformations in the deep crust driven by reactive fluid flow, Nat. Geosci., 13, 307–311, https://doi.org/10.1038/s41561-020-0554-9, 2020a.

Beinlich, A., Plumper, O., Boter, E., Muller, I. A., Kourim, F., Ziegler, M., Harigane, Y., Lafay, R., Kelemen, P. B., and Oman Drilling Project Science Team: Ultramafic Rock Carbonation: Constraints From Listvenite Core BT1B, Oman Drilling Project, J. Geophys. Res.-Sol. Ea., 125, e2019JB019060, https://doi.org/10.1029/2019JB019060, 2020b.

Belogub, E. V., Melekestseva, I. Y., Novoselov, K. A., Zabotina, M. V., Tret'yakov, G. A., Zaykov, V. V., and Yuminov, A. M.: Listvenite-related gold deposits of the South Urals (Russia): A review, Ore Geol. Rev., 85, 247–270, 2017.

Bons, P. D., Elburg, M. A., and Gomez-Rivas, E.: A review of the formation of tectonic veins and their microstructures, J. Struct. Geol., 43, 33–62, 2012.

Boskabadi, A., Pitcairn, I. K., Leybourne, M. I., Teagle, D. A. H., Cooper, M. J., Hadizadeh, H., Nasiri Bezenjani, R., and Monazzami Bagherzadeh, R.: Carbonation of ophiolitic

ultramafic rocks: Listvenite formation in the Late Cretaceous ophiolites of eastern Iran, Lithos, 352–353, 105307, https://doi.org/10.1016/j.lithos.2019.105307, 2020.

Boudier, F. and Coleman, R. G.: Cross section through the peridotite in the Samail Ophiolite, southeastern Oman Mountains, J. Geophys. Res.-Sol. Ea., 86, 2573–2592, 1981.

Chavagnac, V., Monnin, C., Ceuleneer, G., Boulart, C., and Hoareau, G.: Characterization of hyperalkaline fluids produced by low-temperature serpentinization of mantle peridotites in the Oman and Ligurian ophiolites, Geochem. Geophy. Geosy., 14, 2496–2522, 2013.

Coleman, R. G.: Tectonic setting for ophiolite obduction in Oman, J. Geophys. Res.-Sol. Ea., 86, 2497–2508, 1981.

de Obeso, J. C., Santiago Ramos, D. P., Higgins, J. A., and Kelemen, P. B.: A Mg Isotopic Perspective on the Mobility of Magnesium During Serpentinization and Carbonation of the Oman Ophiolite, J. Geophys. Res.-Sol. Ea., 126, e2020JB020237, https://doi.org/10.1029/2020JB020237, 2021.

de Obeso, J. C., Kelemen, P. B., Leong, J. M., Menzel, M. D., Manning, C. E., Godard, M., Cai, Y., Bolge, L., and Oman Drilling Project Phase 1 Science, P.: Deep Sourced Fluids for Peridotite Carbonation in the Shallow Mantle Wedge of a Fossil Subduction Zone: Sr and C Isotope Profiles of OmanDP Hole BT1B, J. Geophys. Res.-Sol. Ea., 127, e2021JB022704, https://doi.org/10.1029/2021JB022704, 2022.

Emam, A. and Zoheir, B.: Au and Cr mobilization through metasomatism: Microchemical evidence from ore-bearing listvenite, South Eastern Desert of Egypt, J. Geochem. Explor., 125, 34–45, 2013.

Evans, O., Spiegelman, M., and Kelemen, P. B.: Phase-Field Modeling of Reaction-Driven Cracking: Determining Conditions for Extensive Olivine Serpentinization, J. Geophys. Res.-Sol. Ea., 125, e2019JB018614, https://doi.org/10.1029/2019JB018614, 2020.

Falk, E. S. and Kelemen, P. B.: Geochemistry and petrology of listvenite in the Samail ophiolite, Sultanate of Oman: Complete carbonation of peridotite during ophiolite emplacement, Geochim. Cosmochim. Ac., 160, 70–90, 2015.

Fletcher, R. C. and Merino, E.: Mineral growth in rocks: kinetic-rheological models of replacement, vein formation, and syntectonic crystallization, Geochim. Cosmochim. Ac., 65, 3733–3748, 2001.

Fusseis, F., Regenauer-Lieb, K., Liu, J., Hough, R. M., and De Carlo, F.: Creep cavitation can establish a dynamic granular fluid pump in ductile shear zones, Nature, 459, 974–977, 2009.

Garber, J. M., Rioux, M., Kylander-Clark, A. R. C., Hacker, B. R., Vervoort, J. D., and Searle, M. P.: Petrochronology of Wadi Tayin Metamorphic Sole Metasediment, With Implications for the Thermal and Tectonic Evolution of the Samail Ophiolite (Oman/UAE), Tectonics, 39, e2020TC006135, https://doi.org/10.1029/2020TC006135, 2020.

Garber, J. M., Rioux, M., Searle, M. P., Kylander-Clark, A. R. C., Hacker, B. R., Vervoort, J. D., Warren, C. J., and Smye, A. J.: Dating continental subduction beneath the Samail Ophiolite: garnet, zircon, and rutile petrochronology of the As Sifah eclogites, NE Oman, J. Geophys. Res.-Sol. Ea., n/a, e2021JB022715, https://doi.org/10.1029/2021JB022715, 2021.

Giampouras, M., Garrido, C. J., Bach, W., Los, C., Fussmann, D., Monien, P., and García-Ruiz, J. M.: On the controls of mineral assemblages and textures in alkaline springs, Samail Ophiolite, Oman, Chem. Geol., 533, 119435, https://doi.org/10.1016/j.chemgeo.2019.119435, 2020.

Glennie, K. W., Boeuf, M. G. A., Clarke, M. W. H., Moody Stuart, M., Pilaar, W. F. H., and Reinhardt, B. M.: Geology of the Oman mountains, Verhandelingen van het Koninklink Nederlands Geologisch Mijnbouwkundig Genootschap, 31, Koninklijk Nederlands Geologisch Mijnbouwkundig Genootschap, Delft, EAN 9789001013103, 1974.

Godard, M., Carter, E. J., Decrausaz, T., Lafay, R., Bennett, E., Kourim, F., de Obeso, J. C., Michibayashi, K., Harris, M., Coggon, J. A., Teagle, D. A. H., Kelemen, P. B., and the Oman Drilling Project Phase 1 Science Party: Geochemical Profiles Across the Listvenite-Metamorphic Transition in the Basal Megathrust of the Semail Ophiolite: Results From Drilling at OmanDP Hole BT1B, J. Geophys. Res.-Sol. Ea., 126, e2021JB022733, https://doi.org/10.1029/2021JB022733, 2021.

Grobe, A., Virgo, S., von Hagke, C., Urai, J. L., and Littke, R.: Multiphase Structural Evolution of a Continental Margin During Obduction Orogeny: Insights From the Jebel Akhdar Dome, Oman Mountains, Tectonics, 37, 888–913, 2018.

Grobe, A., von Hagke, C., Littke, R., Dunkl, I., Wübbeler, F., Muchez, P., and Urai, J. L.: Tectono-thermal evolution of Oman's Mesozoic passive continental margin under the obducting Semail Ophiolite: a case study of Jebel Akhdar, Oman, Solid Earth, 10, 149–175, https://doi.org/10.5194/se-10-149-2019, 2019.

Hacker, B. R., Mosenfelder, J. L., and Gnos, E.: Rapid emplacement of the Oman ophiolite: Thermal and geochronologic constraints, Tectonics, 15, 1230–1247, 1996.

Hansen, L. D., Dipple, G. M., Gordon, T. M., and Kellett, D. A.: Carbonated serpentinite (listwanite) at Atlin, British Columbia: A geological analogue to carbon dioxide sequestration, Can. Mineral., 43, 225–239, 2005.

Hansman, R. J., Albert, R., Gerdes, A., and Ring, U.: Absolute ages of multiple generations of brittle structures by U-Pb dating of calcite, Geology, 46, 207–210, 2018.

Harrison, A. L., Power, I. M., and Dipple, G. M.: Accelerated Carbonation of Brucite in Mine Tailings for Carbon Sequestration, Environ. Sci. Technol., 47, 126–134, 2013.

Hilgers, C., Koehn, D., Bons, P. D., and Urai, J. L.: Development of crystal morphology during unitaxial growth in a progressively widening vein: II. Numerical simulations of the evolution of antitaxial fibrous veins, J. Struct. Geol., 23, 873–885, 2001.

Hilgers, C., Kirschner, D. L., Breton, J. P., and Urai, J. L.: Fracture sealing and fluid overpressures in limestones of the Jabal Akhdar dome, Oman mountains, Geofluids, 6, 168–184, 2006.

Hinsken, T., Bröcker, M., Strauss, H., and Bulle, F.: Geochemical, isotopic and geochronological characterization of listvenite from the Upper Unit on Tinos, Cyclades, Greece, Lithos, 282–283, 281–297, 2017.

Hopson, C. A., Coleman, R. G., Gregory, R. T., Pallister, J. S., and Bailey, E. H.: Geologic section through the Samail Ophiolite and associated rocks along a Muscat-Ibra Transect, southeastern Oman Mountains, J. Geophys. Res.-Sol. Ea., 86, 2527–2544, 1981.

Hövelmann, J., Putnis, C. V., Ruiz-Agudo, E., and Austrheim, H.: Direct Nanoscale Observations of CO_2 Sequestration during Brucite [$Mg(OH)_2$] Dissolution, Environ. Sci. Technol., 46, 5253–5260, 2012.

Hövelmann, J., Austrheim, H., and Jamtveit, B.: Microstructure and porosity evolution during experimental carbonation of a natural peridotite, Chem. Geol., 334, 254–265, 2013.

Hubert, J., Emmerich, H., and Urai, J. L.: Modelling the evolution of vein microstructure with phase-field techniques – a first look, J. Metamorph. Geol., 27, 523–530, 2009.

International Ocean Discovery Program Publications: Supplement of the Oman Drilling Project, International Ocean Discovery Program Publications [data set], http://publications.iodp.org/other/Oman/SUPP_MAT/index.html#SUPP_MAT_I, last access: 26 July 2022.

IPCC: Climate Change 2021: The Physical Science Basis. Contribution of Working Group I to the Sixth Assessment Report of the Intergovernmental Panel on Climate Change, edited by: Masson-Delmotte, V., Zhai, P., Pirani, A., Connors, S. L., Péan, C., Berger, S., Caud, N., Chen, Y., Goldfarb, L., Gomis, M. I., Huang, M., Leitzell, K., Lonnoy, E., Matthews, J. B. R., Maycock, T. K., Waterfield, T., Yelekçi, O., Yu, R., and Zhou, B., Cambridge University Press, in press, 2021.

Johannes, W.: An experimental investigation of the system MgO-SiO_2-H_2O-CO_2, Am. J. Sci., 267, 1083–1104, 1969.

Kelemen, P. B. and Hirth, G.: Reaction-driven cracking during retrograde metamorphism: Olivine hydration and carbonation, Earth Planet. Sc. Lett., 345–348, 81–89, 2012.

Kelemen, P. B. and Manning, C. E.: Reevaluating carbon fluxes in subduction zones, what goes down, mostly comes up, P. Natl. Acad. Sci. USA, 112, 3997–4006, https://doi.org/10.1073/pnas.1507889112, 2015.

Kelemen, P. B. and Matter, J.: In situ carbonation of peridotite for CO_2 storage, P. Natl. Acad. Sci. USA, 105, 17295–17300, 2008.

Kelemen, P. B., Matter, J., Streit, E. E., Rudge, J. F., Curry, W. B., and Blusztajn, J.: Rates and Mechanisms of Mineral Carbonation in Peridotite: Natural Processes and Recipes for Enhanced, in situ CO_2 Capture and Storage, Annu. Rev. Earth Planet. Sc., 39, 545–576, https://doi.org/10.1146/annurev-earth-092010-152509, 2011.

Kelemen, P. B., Matter, J. M., Teagle, D. A. H., Coggon, J. A., and the Oman Drilling Project Science Team: Site BA4, in: Proceedings of the Oman Drilling Project, edited by: Kelemen, P. B., Matter, J. M., Teagle, D. A. H., Coggon, J. A., and the Oman Drilling Project Science Team, International Ocean Discovery Program, College Station, TX, https://doi.org/10.14379/OmanDP.proc.2020, 2020a.

Kelemen, P. B., Matter, J. M., Teagle, D. A. H., Coggon, J. A., and the Oman Drilling Project Science Team: Site BT1: fluid and mass exchange on a subduction zone plate boundary, in: Proceedings of the Oman Drilling Project, Kelemen, P. B., Matter, J. M., Teagle, D. A. H., Coggon, J. A., and the Oman Drilling Project Science Team, International Ocean Discovery Program, College Station, TX, https://doi.org/10.14379/OmanDP.proc.2020, 2020b.

Kelemen, P. B., Matter, J. M., Teagle, D. A. H., Coggon, J. A., and the Oman Drilling Project Science Team: Site CM2: crust-mantle transition zone and into upper mantle, in: Proceedings of the Oman Drilling Project, edited by: Kelemen, P. B., Matter, J. M., Teagle, D. A. H., Coggon, J. A., and the Oman Drilling Project Science Team, International Ocean Discovery Program, College Station, TX, https://doi.org/10.14379/OmanDP.proc.2020, 2020c.

Kelemen, P. B., McQueen, N., Wilcox, J., Renforth, P., Dipple, G., and Vankeuren, A. P.: Engineered carbon mineralization in ultramafic rocks for CO_2 removal from air: Review and new insights, Chem. Geol., 550, 119628, https://doi.org/10.1016/j.chemgeo.2020.119628, 2020d.

Kelemen, P. B., Carlos de Obeso, J., Leong, J. A., Godard, M., Okazaki, K., Kotowski, A. J., Manning, C. E., Ellison, E. T., Menzel, M. D., Urai, J. L., Hirth, G., Rioux, M., Stockli, D. F., Lafay, R., Beinlich, A. M., Coggon, J. A., Warsi, N. H., Matter, J. M., Teagle, D. A. H., Harris, M., Michibayashi, K., Takazawa, E., Al Sulaimani, Z., and the Oman Drilling Project Science Team: Listvenite Formation During Mass Transfer into the Leading Edge of the Mantle Wedge: Initial Results from Oman Drilling Project Hole BT1B, J. Geophys. Res.-Sol. Ea., 127, e2021JB022352, https://doi.org/10.1029/2021JB022352, 2022.

Kotowski, A. J., Cloos, M., Stockli, D. F., and Bos Orent, E.: Structural and Thermal Evolution of an Infant Subduction Shear Zone: Insights From Sub-Ophiolite Metamorphic Rocks Recovered From Oman Drilling Project Site BT-1B, J. Geophys. Res.-Sol. Ea., 126, e2021JB021702, https://doi.org/10.1029/2021JB021702, 2021.

Lacinska, A. M., Styles, M. T., Bateman, K., Wagner, D., Hall, M. R., Gowing, C., and Brown, P. D.: Acid-dissolution of antigorite, chrysotile and lizardite for ex situ carbon capture and storage by mineralisation, Chem. Geol., 437, 153–169, 2016.

MacLeod, C. J., Johan Lissenberg, C., and Bibby, L. E.: "Moist MORB" axial magmatism in the Oman ophiolite: The evidence against a mid-ocean ridge origin, Geology, 41, 459–462, 2013.

Malthe-Sørenssen, A., Jamtveit, B., and Meakin, P.: Fracture Patterns Generated by Diffusion Controlled Volume Changing Reactions, Phys. Rev. Lett., 96, 245501, https://doi.org/10.1103/PhysRevLett.96.245501, 2006.

Matter, J. M. and Kelemen, P. B.: Permanent storage of carbon dioxide in geological reservoirs by mineral carbonation, Nat. Geosci., 2, 837–841, 2009.

Mattern, F. and Scharf, A.: Postobductional extension along and within the Frontal Range of the Eastern Oman Mountains, J. Asian Earth Sci., 154, 369–385, 2018.

Menzel, M. D., Garrido, C. J., López Sánchez-Vizcaíno, V., Marchesi, C., Hidas, K., Escayola, M. P., and Delgado Huertas, A.: Carbonation of mantle peridotite by CO_2-rich fluids: the formation of listvenites in the Advocate ophiolite complex (Newfoundland, Canada), Lithos, 323, 238–261, 2018.

Menzel, M. D., Urai, J. L., de Obeso, J. C., Kotowski, A., Manning, C. E., Kelemen, P. B., Kettermann, M., Jesus, A. P., Harigane, Y., and the Oman Drilling Project Phase 1 Science Team: Brittle Deformation of Carbonated Peridotite – Insights From Listvenites of the Samail Ophiolite (Oman Drilling Project Hole BT1B), J. Geophys. Res.-Sol. Ea., 125, e2020JB020199, https://doi.org/10.1029/2020JB020199, 2020.

Menzel, M. D., Urai, J. L., Ukar, E., Hirth, G., Schwedt, A., Kovács, A., Kibkalo, L., and Kelemen, P. B.: Ductile deformation during carbonation of serpentinized peridotite, Nat. Commun., 13, 3478, https://doi.org/10.1038/s41467-022-31049-1, 2022.

Miller, J. M., Gregory, R. T., Gray, D. R., and Foster, D. A.: Geological and geochronological constraints on the exhumation of a high-pressure metamorphic terrane, Oman, Geol. Soc. Lond. Spec. Publ., 154, 241, https://doi.org/10.1144/GSL.SP.1999.154.01.11, 1999.

Nasir, S., Al Sayigh, A. R., Al Harthy, A., Al-Khirbash, S., Al-Jaaidi, O., Musllam, A., Al-Mishwat, A., and Al-Bu'saidi, S.: Mineralogical and geochemical characterization of listwaenite from the Semail Ophiolite, Oman, Geochemistry, 67, 213–228, 2007.

Nicolas, A. and Boudier, F.: Mapping oceanic ridge segments in Oman ophiolite, J. Geophys. Res.-Sol. Ea., 100, 6179–6197, 1995.

Nicolas, A., Boudier, F., and Ildefonse, B.: Variable crustal thickness in the Oman ophiolite: Implication for oceanic crust, J. Geophys. Res.-Sol. Ea., 101, 17941–17950, 1996.

Noël, J., Godard, M., Oliot, E., Martinez, I., Williams, M., Boudier, F., Rodriguez, O., Chaduteau, C., Escario, S., and Gouze, P.: Evidence of polygenetic carbon trapping in the Oman Ophiolite: Petro-structural, geochemical, and carbon and oxygen isotope study of the Wadi Dima harzburgite-hosted carbonates (Wadi Tayin massif, Sultanate of Oman), Lithos, 323, 218–237, 2018.

Okamoto, A. and Shimizu, H.: Contrasting fracture patterns induced by volume-increasing and -decreasing reactions: Implications for the progress of metamorphic reactions, Earth Planet. Sc. Lett., 417, 9–18, 2015.

Okazaki, K., Michibayashi, K., Hatakeyama, K., Abe, N., Johnson, K. T. M., Kelemen, P. B., and the Oman Drilling Project Science Team: Major Mineral Fraction and Physical Properties of Carbonated Peridotite (Listvenite) From ICDP Oman Drilling Project Hole BT1B Inferred From X-Ray CT Core Images, J. Geophys. Res.-Sol. Ea., 126, e2021JB022719, https://doi.org/10.1029/2021JB022719, 2021.

Oman Drilling Project: Samples & Data, Oman Drilling Project [data set], https://www.omandrilling.ac.uk/samples-data#SOAC, last access: 26 July 2022.

Oskierski, H. C., Dlugogorski, B. Z., and Jacobsen, G.: Sequestration of atmospheric CO_2 in chrysotile mine tailings of the Woodsreef Asbestos Mine, Australia: Quantitative mineralogy, isotopic fingerprinting and carbonation rates, Chem. Geol., 358, 156–169, 2013.

Pearce, J. A., Alabaster, T., Shelton, A. W., Searle, M. P., Vine, F. J., and Smith, A. G.: The Oman ophiolite as a Cretaceous arc-basin complex: evidence and implications, Philos. T. Roy. Soc. A, 300, 299–317, 1981.

Peuble, S., Andreani, M., Gouze, P., Pollet-Villard, M., Reynard, B., and Van de Moortele, B.: Multi-scale characterization of the incipient carbonation of peridotite, Chem. Geol., 476, 150–160, 2018.

Plümper, O., Røyne, A., Magrasó, A., and Jamtveit, B.: The interface-scale mechanism of reaction-induced fracturing during serpentinization, Geology, 40, 1103–1106, 2012.

Power, I. M., Wilson, S. A., and Dipple, G. M.: Serpentinite Carbonation for CO_2 Sequestration, Elements, 9, 115–121, 2013.

Prigent, C., Agard, P., Guillot, S., Godard, M., and Dubacq, B.: Mantle Wedge (De)formation During Subduction Infancy: Evidence from the Base of the Semail Ophiolitic Mantle, J. Petrol., 59, 2061–2092, 2018.

Quandt, D., Micheuz, P., Kurz, W., Bernasconi, S. M., Hippler, D., Krenn, K., and Hauzenberger, C. A.: Geochemistry and Microtextures of Vein Calcites Pervading the Izu-Bonin Forearc and Rear Arc Crust: New Insights From IODP Expeditions 352 and 351, Geochem. Geophy. Geosy., 21, e2019GC008745, https://doi.org/10.1029/2019GC008745, 2020.

Qiu, T. and Zhu, Y.: Listwaenite in the Sartohay ophiolitic mélange (Xinjiang, China): A genetic model based on petrology, U-Pb chronology and trace element geochemistry, Lithos, 302–303, 427–446, 2018.

Rioux, M., Bowring, S., Kelemen, P., Gordon, S., Miller, R., and Dudás, F.: Tectonic development of the Samail ophiolite: High-precision U-Pb zircon geochronology and Sm-Nd isotopic constraints on crustal growth and emplacement, J. Geophys. Res.-Sol. Ea., 118, 2085–2101, 2013.

Rudge, J. F., Kelemen, P. B., and Spiegelman, M.: A simple model of reaction-induced cracking applied to serpentinization and carbonation of peridotite, Earth Planet. Sc. Lett., 291, 215–227, 2010.

Saddiqi, O., Michard, A., Goffe, B., Poupeau, G. R., and Oberhänsli, R.: Fission-track thermochronology of the Oman Mountains continental windows, and current problems of tectonic interpretation, B. Soc. Géol. Fr., 177, 127–134, 2006.

Schwarzenbach, E. M., Caddick, M. J., Beard, J. S., and Bodnar, R. J.: Serpentinization, element transfer, and the progressive development of zoning in veins: evidence from a partially serpentinized harzburgite, Contrib. Mineral. Petr., 171, 5, https://doi.org/10.1007/s00410-015-1219-3, 2016.

Searle, M. P. and Cox, J. O. N.: Subduction zone metamorphism during formation and emplacement of the Semail ophiolite in the Oman Mountains, Geol. Mag., 139, 241–255, 2002.

Searle, M. P., Waters, D. J., Martin, H. N., and Rex, D. C.: Structure and metamorphism of blueschist–eclogite facies rocks from the northeastern Oman Mountains, J. Geol. Soc., 151, 555, https://doi.org/10.1144/gsjgs.151.3.0555, 1994.

Shimizu, H. and Okamoto, A.: The roles of fluid transport and surface reaction in reaction-induced fracturing, with implications for the development of mesh textures in serpentinites, Contrib. Mineral. Petr., 171, 73, https://doi.org/10.1007/s00410-016-1288-y, 2016.

Sibson, R. H.: Structural permeability of fluid-driven fault-fracture meshes, J. Struct. Geol., 18, 1031–1042, 1996.

Sibson, R. H.: Tensile overpressure compartments on low-angle thrust faults, Earth Planet. Space, 69, 113, https://doi.org/10.1186/s40623-017-0699-y, 2017.

Soret, M., Agard, P., Dubacq, B., Plunder, A., and Yamato, P.: Petrological evidence for stepwise accretion of metamorphic soles during subduction infancy (Semail ophiolite, Oman and UAE), J. Metamorph. Geol., 35, 1051–1080, 2017.

Spruženiece, L., Späth, M., Urai, J. L., Ukar, E., Selzer, M., and Nestler, B.: Wide-blocky veins explained by dependency of crystal growth rate on fracture surface type: Insights from phase-field modeling, Geology, 49, 641–646, 2021a.

Spruženiece, L., Späth, M., Urai, J. L., Ukar, E., Selzer, M., Nestler, B., and Schwedt, A.: Formation of wide-blocky calcite veins by extreme growth competition, J. Geol. Soc., 178, 2020–2104, 2021b.

Stanger, G.: Silicified serpentinite in the Semail nappe of Oman, Lithos, 18, 13–22, 1985.

Streit, E., Kelemen, P., and Eiler, J.: Coexisting serpentine and quartz from carbonate-bearing serpentinized peridotite in the Samail Ophiolite, Oman, Contrib. Mineral. Petr., 164, 821–837, 2012.

Tarling, M. S., Smith, S. A. F., Rooney, J. S., Viti, C., and Gordon, K. C.: A common type of mineralogical banding in ser-

pentine crack-seal veins, Earth Planet. Sc. Lett., 564, 116930, https://doi.org/10.1016/j.epsl.2021.116930, 2021.

Ternieten, L., Früh-Green, G. L., and Bernasconi, S. M.: Carbon Geochemistry of the Active Serpentinization Site at the Wadi Tayin Massif: Insights From the ICDP Oman Drilling Project: Phase II, J. Geophys. Res.-Sol. Ea., 126, e2021JB022712, https://doi.org/10.1029/2021JB022712, 2021.

Ukar, E. and Laubach, S. E.: Syn- and postkinematic cement textures in fractured carbonate rocks: Insights from advanced cathodoluminescence imaging, Tectonophysics, 690, 190–205, 2016.

Ulven, O. I., Storheim, H., Austrheim, H., and Malthe-Sørenssen, A.: Fracture initiation during volume increasing reactions in rocks and applications for CO_2 sequestration, Earth Planet. Sc. Lett., 389, 132–142, 2014.

van Noort, R., Spiers, C. J., Drury, M. R., and Kandianis, M. T.: Peridotite dissolution and carbonation rates at fracture surfaces under conditions relevant for in situ mineralization of CO_2, Geochim. Cosmochim. Ac., 106, 1–24, 2013.

van Noort, R., Wolterbeek, T. K. T., Drury, M. R., Kandianis, M. T., and Spiers, C. J.: The force of crystallization and fracture propagation during in-situ carbonation of peridotite, Minerals, Sultanate of Oman, 7, 190, https://doi.org/10.3390/min7100190, 2017.

Villey, M., Le Metour, J., and De Gramont, X.: Geological map of Fanja, Sheet NF 40-3F, Bureau de Recherches Géologiques et Minières, Orléans, France, and Oman Ministry of Petroleum & Minerals, 1986.

Virgo, S., Abe, S., and Urai, J. L.: The evolution of crack seal vein and fracture networks in an evolving stress field: Insights from Discrete Element Models of fracture sealing, J. Geophys. Res.-Sol. Ea., 119, 8708–8727, 2014.

Wang, Y. and Merino, E.: Dynamic model of oscillatory zoning of trace elements in calcite: Double layer, inhibition, and self-organization, Geochim. Cosmochim. Ac., 56, 587–596, 1992.

Warren, C. J., Parrish, R. R., Searle, M. P., and Waters, D. J.: Dating the subduction of the Arabian continental margin beneath the Semail ophiolite, Oman, Geology, 31, 889–892, 2003.

Wicks, F. J. and Whittaker, E. J. W.: Serpentine textures and serpentinization, Can. Mineral., 15, 459–488, 1977.

Wilde, A., Simpson, L., and Hanna, S.: Preliminary study of Cenozoic hydrothermal alteration and platinum deposition in the Oman Ophiolite, Journal of the Virtual Explorer, 6, 7-13, 2002.

Yoshida, K., Okamoto, A., Shimizu, H., Oyanagi, R., Tsuchiya, N., and the Oman Drilling Project Phase 2 Science Party: Fluid Infiltration Through Oceanic Lower Crust in Response to Reaction-Induced Fracturing: Insights From Serpentinized Troctolite and Numerical Models, J. Geophys. Res.-Sol. Ea., 125, e2020JB020268, https://doi.org/10.1029/2020JB020268, 2020.

Zheng, X., Cordonnier, B., Zhu, W., Renard, F., and Jamtveit, B.: Effects of Confinement on Reaction-Induced Fracturing During Hydration of Periclase, Geochem. Geophy. Geosy., 19, 2661–2672, 2018.

Zheng, X., Cordonnier, B., McBeck, J., Boller, E., Jamtveit, B., Zhu, W., and Renard, F.: Mixed-Mode Strain Localization Generated by Hydration Reaction at Crustal Conditions, J. Geophys. Res.-Sol. Ea., 124, 4507–4522, 2019.

Appendix to Chapter 3

Oman2020 – List of rock samples

Geological unit	Location	Site	N (GPS)	E (GPS)	Sample ID	Lithology
Metamorphic Sole	Wadi Mansah	1	23°22.108'	58°11.418'	OM20-01	Metabasalt
Metamorphic Sole	Wadi Mansah	1	23°22.161'	58°11.527'	OM20-02	Metabasalt
Metamorphic Sole	Wadi Mansah	1	23°22.222'	58°11.736'	OM20-03	Amphibolite
Samail Ophiolite	Wadi Mansah	1	23°22.286'	58°11.761'	OM20-04	Serp. harzburgite
Samail Ophiolite	Wadi Mansah	1	23°22.295'	58°11.745'	OM20-05	Carb. serpentinite (trans)
Metamorphic Sole	Gharbah	1	23°21'23.22"	58°12.464'	OM20-08	Chert
Muti Formation	Gharbah	1	23°21'30.2"	58°13'51.8"	OM20-09	Limestone
Samail Ophiolite	Gharbah	1	23°21'23.02"	58°13'15.72"	OM20-11	Carb. serpentinite (trans)
Samail Ophiolite	Gharbah	1	23°21'23.02"	58°13'15.72"	OM20-12	Listvenite
Samail Ophiolite	Gharbah	1	23°21'14.5"	58°13'16.3"	OM20-13	Serp. harzburgite
Samail Ophiolite	Gharbah	1	23°20'45.0"	58°13'16.3"	OM20-14	Listvenite
Samail Ophiolite	Gharbah	1	23°20'45.0"	58°13'16.3"	OM20-15	Listvenite
Samail Ophiolite	Gharbah	1	23°20'45.0"	58°13'16.3"	OM20-16	Carb. serpentinite (trans)
Samail Ophiolite	Gharbah	1	23°20'45.0"	58°13'16.3"	OM20-17	Carb. serpentinite (trans)
Samail Ophiolite	Gharbah	1	23°20'45.0"	58°13'16.3"	OM20-18	Carb. serpentinite
Samail Ophiolite	Gharbah	1	23°20'45.0"	58°13'16.3"	OM20-20	Gabbro
Samail Ophiolite	Wadi Mansah	1	23°21'51.1"	58°10'58.3"	OM20-22	Listvenite
Samail Ophiolite	Wadi Mansah	1	23°21'51.1"	58°10'58.3"	OM20-23	Listvenite
Samail Ophiolite	Wadi Mansah	1	23°20'48.3"	58°11'32.2"	OM20-24	Gabbro
Samail Ophiolite	Mughrah	2	23°20'44.2"	58°13'16.7"	OM20-25	Listvenite
Samail Ophiolite	Mughrah	2	23°20'44.2"	58°13'16.7"	OM20-26	Carb. serpentinite (trans)
Samail Ophiolite	Mughrah	2	23°20'44.2"	58°13'16.7"	OM20-28	Serp. Harzburgite
Samail Ophiolite	Mughrah	2	23°20'44.2"	58°13'16.7"	OM20-29	Listvenite
Samail Ophiolite	Mughrah	2	23°27'7.3"	58°12'17.1"	OM20-30a	Carb. serpentinite (trans)
Samail Ophiolite	Mughrah	2	23°27'7.3"	58°12'17.1"	OM20-30b	Carb. serpentinite (trans)
Samail Ophiolite	Mughrah	2	23°27'7.3"	58°12'17.1"	OM20-31	Listvenite
Samail Ophiolite	Mughrah	2	23°27'7.3"	58°12'17.1"	OM20-32	Carb. serpentinite (trans)
Samail Ophiolite	Mughrah	2	23°27.064'	58°12.539'	OM20-33	Gabbro
Samail Ophiolite	Mughrah	2	23°27'11.7"	58°12'13.1"	OM20-34	Serp. harzburgite/dunite?
Samail Ophiolite	Jabal Fanjah	2b	23°26.288'	58°10.478'	OM20-35	Serp. peridotite
Samail Ophiolite	Jabal Fanjah	2b	23°26.319'	58°10.511'	OM20-38	Carb. serpentinite (trans)
Samail Ophiolite	Jabal Fanjah	2b	23°26.322'	58°10.514'	OM20-39	Listvenite
Samail Ophiolite	Jabal Qarn	3	23°28.009'	58°05.697'	OM20-42	Gabbro
Samail Ophiolite	Jabal Qarn	3	23°27.900'	58°05.637'	OM20-44a	Gabbro
Samail Ophiolite	Jabal Qarn	3	23°27.900'	58°05.637'	OM20-44c	Listvenite
Samail Ophiolite	Jabal Qarn	3	23°28.007'	58°05.247'	OM20-45a	Listvenite
Samail Ophiolite	Jabal Qarn	3	23°27.983'	58°05.233'	OM20-45b	Carb. serpentinite (trans)
Samail Ophiolite	Jabal Qarn	3	23°27.860'	58°05.267'	OM20-45c	Carb. serpentinite
Samail Ophiolite	Jabal Qarn	3	23°27.860'	58°05.267'	OM20-45d	Listvenite
Samail Ophiolite	Jabal Qarn	3	23°28.490'	58°05.193'	OM20-46	Serp. Px-rich peridotite
Samail Ophiolite	Jabal Akhdar	4	23°23.701'	58°03.120'	OM20-48	Gabbro
Samail Ophiolite	Jabal Akhdar	4	23°23.853'	58°03.254'	OM20-49	Listvenite
Muti Formation	Jabal Akhdar	4	23°24.036'	58°03.040'	OM20-50	Limestone
Samail Ophiolite	Jabal Akhdar	4	23°23.826'	58°01.698'	OM20-52a	Birbirite
Samail Ophiolite	Jabal Akhdar	4	23°23.826'	58°01.698'	OM20-52b	Fu-listvenite
Samail Ophiolite	Jabal Akhdar	4	23°23.826'	58°01.698'	OM20-15	Serp. peridotite
Samail Ophiolite	Tawi	-	23°29'13.9"	58°08'11.0"	OM20-54	Serp. dunite
Samail Ophiolite	Tawi	-	23°29'13.9"	58°08'11.0"	OM20-56	Serp. harzburgite

Appendix to Chapter 4.2

Table 4.2.1 Characteristic peaks of serpentine measured by Raman spectroscopy

Lithology	Sample	Analysis #	Area	Structure	Mineral	P1 [cm^{-1}]	P2 [cm^{-1}]	P3 [cm^{-1}]	P4 [cm^{-1}]	P5 [cm^{-1}]	P6 [cm^{-1}]	P7 [cm^{-1}]
Carb.serp.	43Z-3-52-57	M1	1	Mesh	Lizardite	127	229	384	689	1096 - flat	3687	3700
Carb.serp.	43Z-3-52-57	M2	1	Mesh	Lizardite	128	229	384	689	1094 - flat	3687	3700
Carb.serp.	43Z-3-52-57	M3	1	Mesh	Chrysotile	127	229	384	691	1099 - flat	3688	3698
Carb.serp.	43Z-3-52-57	M5	1	Mesh	Chrysotile	128	231	388	691	1106	3687	3698
Carb.serp.	43Z-3-52-57	V1	1	Vein	Chrysotile	128	231	389	691	1105		3697
Carb.serp.	43Z-3-52-57	V2	1	Vein	Chrysotile	128	231	390	691	1105		3697
Carb.serp.	43Z-3-52-57	B1	2	Bastite	Lizardite	128	230	386	690	1098 - flat	3687	3699
Carb.serp.	43Z-3-52-57	B2	2	Bastite	Lizardite	129	230	385	690	1097 - flat	3687	3700
Carb.serp.	43Z-3-52-57	M1	2	Mesh	Lizardite	128	228	383	690	1098 - flat	3687	3700
Carb.serp.	43Z-3-52-57	M2	2	Mesh	Lizardite	128	229	385	689	1099 - flat	3686	3698
Carb.serp.	43Z-3-52-57	M1		Mesh	Chrysotile	129	231	388	691	1104	3687	3698
Carb.serp.	43Z-3-52-57	M2	3	Mesh	Chrysotile	129	230	388	691	1104		3698
Carb.serp.	43Z-3-52-57	M3	3	Mesh	Chrysotile	129	231	388	691	1105		3699
Carb.serp.	43Z-3-52-57	M4	3	Mesh	Chrysotile	129	231	388	690	1105	3688	3698
Carb.serp.	43Z-3-52-57	V1	3	Vein	Chrysotile	128	231	389	691	1105		3697
Carb.serp.	43Z-3-52-57	M1	3	Mesh	Chrysotile	128	230	386	690	1102 - flat		3698
Carb.serp.	43Z-3-52-57	M2	4	Mesh	Chrysotile	129	230	386	690	1102	3687	3699
Carb.serp.	43Z-3-52-57	V1	4	Vein	Chrysotile	129	232	390	691	1106		3698
Carb.serp.	43Z-3-52-57	V2	4	Vein	Chrysotile	129	232	390	691	1106		3698
Carb.serp.	43Z-4-52-57	M1	4	Mesh	Chrysotile	128	230	386	690	1103	3686	3698
Carb.serp.	43Z-4-52-57	M2	1	Mesh	Lizardite	128	229	384	689	1098 - flat	3687	3700
Carb.serp.	43Z-4-52-57	M3	1	Mesh	Lizardite	128	229	385	690	1097 - flat	3686	3699
Carb.serp.	43Z-4-52-57	M4	1	Mesh	Lizardite	128	228	384	689	1100 - flat	3685	3700
Carb.serp.	43Z-4-52-57	M5	1	Mesh	Chrysotile	129	230	387	690	1104 - flat	3686	3698
Carb.serp.	43Z-4-52-57	M6	1	Mesh	Lizardite	128	230	385	691	1096 - flat	3687	3698
Carb.serp.	43Z-4-52-57	M7	1	Mesh	Chrysotile	129	232	388	691	1106 - flat	3687	3699
Carb.serp.	43Z-4-52-57	M8	1	Mesh	Chrysotile	129	232	388	691	1099 - flat		3697
Carb.serp.	43Z-4-52-57	M9	1	Mesh	Chrysotile	128	230	386	691	1107 - flat	3687	3699
Carb.serp.	43Z-4-52-57	M10	1	Mesh	Chrysotile	129	231	389	692	1106		3698
Carb.serp.	43Z-4-52-57	V1	1	Vein	Chrysotile	129	232	389	690	1105		3699
Carb.serp.	43Z-4-52-57	V2	1	Vein	Chrysotile	129	232	388	690	1105	3688	3698
Carb.serp.	43Z-4-52-57	V3	1	Vein	Chrysotile	129	232	390	690	1105		3698
Carb.serp.	43Z-4-52-57	V4	1	Vein	Chrysotile	129	232	388	690	1105		3699
Carb.serp.	43Z-4-52-57	B1	2	Bastite	Chrysotile	125	227	383	689			3696
Carb.serp.	43Z-4-52-57	B2	2	Bastite	Chrysotile	125	228	383	689			3696
Carb.serp.	43Z-4-52-57	B3	2	Bastite	Chrysotile	126	228	383	690		3689	3697
Carb.serp.	43Z-4-52-57	M1	2	Mesh	Lizardite	128	229	384	689	1097 - flat	3686	3700
Carb.serp.	43Z-4-52-57	M2	2	Mesh	Lizardite	129	230	384	688	1095 - flat	3685	3702
Carb.serp.	43Z-4-52-57	M3	2	Bastite	Chrysotile	128	229	384	689	1096 - flat	3687	3698
Carb.serp.	43Z-4-52-57	B1	3	Bastite	Chrysotile	126	229	383	690	1107 - flat	3687	3696
Carb.serp.	43Z-4-52-57	B2	3	Bastite	Chrysotile	127	229	385	690	1100 - flat		3697
Carb.serp.	43Z-4-52-57	B3	3	Bastite	Chrysotile	126	228	384	690	1097 - flat		3697
Carb.serp.	43Z-4-52-57	B4	3	Bastite	Chrysotile	126	228	383	690	1097 - flat		3696
Carb.serp.	43Z-4-52-57	B5	3	Bastite	Chrysotile	127	228	383	690	1100 - flat		3697
Carb.serp.	43Z-4-52-57	M1	3	Mesh	Lizardite	128	229	383	689	1097 - flat	3687	3699
Carb.serp.	43Z-4-52-57	M2	3	Mesh	Lizardite	128	228	383	689	1098 - flat	3687	3700
Carb.serp.	43Z-4-52-57	M3	3	Mesh	Chrysotile	128	229	385	690	1099 - flat	3687	3699
Carb.serp.	43Z-4-52-57	V1	3	Vein	Chrysotile	128	231	389	691	1106		3698
Carb.serp.	43Z-4-52-57	V2	3	Vein	Chrysotile	128	228	385	690	1101 - flat	3688	3699
Carb.serp.	44Z-1-41-46	B1	1	Bastite	Chrysotile	126	230	385	690	1096 - flat	3688	3699
Carb.serp.	44Z-1-41-46	B2	1	Bastite	Chrysotile	126	230	384	690		3686	3699
Carb.serp.	44Z-1-41-46	M1	1	Mesh	Lizardite	129	230	385	689		3685	3704
Carb.serp.	44Z-1-41-46	M2	1	Mesh	Lizardite	128	230	384	690		3682	3700
Carb.serp.	44Z-1-41-46	M3	1	Mesh	Lizardite	128	230	385	691	1095 - flat	3688	3701
Carb.serp.	44Z-1-41-46	V1	1	Vein	Chrysotile	130	232	389	693	1107		3698
Carb.serp.	44Z-1-41-46	V2	1	Vein	Chrysotile	129	232	390	693	1108		3697
Carb.serp.	44Z-1-41-46	M1	2	Mesh	Lizardite	127	230	384	689	1096 - flat	3686	3701
Carb.serp.	44Z-1-41-46	M2	2	Mesh	Lizardite	127	229	384	690		3688	3700
Carb.serp.	44Z-1-41-46	M3	2	Mesh	Lizardite	127	229	385	690		3687	3700
Carb.serp.	44Z-1-41-46	V1	2	Vein	Chrysotile	129	232	389	692	1104		3698
Carb.serp.	44Z-1-41-46	V2	2	Vein	Chrysotile	129	232	389	692	1106		3698
Carb.serp.	44Z-1-41-46	B1	3	Bastite	Chrysotile	126	229	383	689		3687	3699
Carb.serp.	44Z-1-41-46	B2	3	Bastite	Lizardite	126	229	383	690	1095 - flat	3688	3697
Carb.serp.	44Z-1-41-46	B3	3	Bastite	Chrysotile	125	228	383	689	1095 - flat	3688	3698
Carb.serp.	44Z-1-41-46	B1	4	Bastite	Lizardite	127	230	384	690		3687	3700
Carb.serp.	44Z-1-41-46	B2	4	Bastite	Lizardite	126	229	384	690	1095 - flat	3688	3697
Carb.serp.	44Z-1-41-46	B3	4	Bastite	Chrysotile	128	230	387	691	1104		3699
Carb.serp.	44Z-4-0-5	M1	1	Mesh	Chrysotile	128	231	389	691	1103		3698
Carb.serp.	44Z-4-0-5	M3	1	Mesh	Lizardite	127	228	383	688		3686	3700
Carb.serp.	44Z-4-0-5	M4	1	Mesh	Chrysotile	126	228	383	691	1095 - flat		3697
Carb.serp.	44Z-4-0-5	M5	1	Mesh	Lizardite	128	228	383	689		3687	3698
Carb.serp.	44Z-4-0-5	M6	1	Mesh	Lizardite	125	228	383	690		3687	3697
Carb.serp.	44Z-4-0-5	V1	1	Bastite	Chrysotile	128	231	389	691	1105		3699
Carb.serp.	44Z-4-0-5	V2	1	Bastite	Chrysotile	128	231	389	691	1095		3698
Carb.serp.	44Z-4-0-5	V3	1	Bastite	Chrysotile	128	231	390	691	1106		3699
Carb.serp.	44Z-4-0-5	V4	1	Bastite	Chrysotile	129	230	388	692	1097		3697

Carb.serp.	44Z-4-0-5	V5	1	Bastite	Chrysotile	128	231	389	691	1106		3698
Carb.serp.	44Z-4-0-5	V6	1	Bastite	Chrysotile	128	231	389	691	1107		3697
Carb.serp.	44Z-4-0-5	V7	1	Bastite	Chrysotile	128	231	388	691	1106		3698
Carb.serp.	44Z-4-0-5	M1	1	Mesh	Lizardite	128	229	385	689	1093 - flat	3687	3700
Carb.serp.	44Z-4-0-5	M2	2	Mesh	Chrysotile	127	229	383	690	1096 - flat	3688	3696
Carb.serp.	44Z-4-0-5	V1	2	Bastite	Chrysotile	129	231	388	692	1103		3698
Carb.serp.	44Z-4-0-5	V2	2	Bastite	Chrysotile	129	230	388	692	1106		3699

Appendix to Chapter 4.3

Table S1 : List of rock samples

Sample name	Sample name (ICDP nomenclature)	Location	GPS N	GPS E	Rock type	Depth m.b.g.	Distance to sole m.b.g.	Domain[1]
16Z-1-65-70	C5704B-16Z-1 W, 65.0--70.0 cm	OmanDP Hole BT1B	23.364374°	58.182693°	Listvenite	27.65	169.35	I
30Z-2-33-39	C5704B-30Z-2 W, 33.0--39.0 cm	OmanDP Hole BT1B	23.364374°	58.182693°	Listvenite	62.68	134.32	I
31Z-3-26-31	C5704B-31Z-3 W, 26.0--31.0 cm	OmanDP Hole BT1B	23.364374°	58.182693°	Listvenite	65.56	131.44	I
35Z-1-56-61	C5704B-35Z-1 W, 56.0--61.0 cm	OmanDP Hole BT1B	23.364374°	58.182693°	Listvenite	71.97	125.03	I
38Z-3-60-65	C5704B-38Z-3 W, 60.0--65.0 cm	OmanDP Hole BT1B	23.364374°	58.182693°	Listvenite	80.61	116.39	I
40Z-3-11-16	C5704B-40Z-3 W, 11.0--16.0 cm	OmanDP Hole BT1B	23.364374°	58.182693°	Carb. serpentinite	87.04	109.97	I
43Z-2-43-48	C5704B-43Z-2-1 W, 43.0--48.0 cm	OmanDP Hole BT1B	23.364374°	58.182693°	Carb. serpentinite	95.30	101.70	I
43Z-3-0-5	C5704B-43Z-3-1 W, 0.0--5.0 cm	OmanDP Hole BT1B	23.364374°	58.182693°	Carb. serpentinite	95.56	101.44	I
43Z-3-52-57	C5704B-43Z-3-1 W, 52.0--57.0 cm	OmanDP Hole BT1B	23.364374°	58.182693°	Carb. serpentinite	96.07	100.93	I
43Z-4-52-57	C5704B-43Z-4-1 W, 52.0--57.0 cm	OmanDP Hole BT1B	23.364374°	58.182693°	Carb. serpentinite	96.64	100.36	I
44Z-1-41-46	C5704B-44Z-1-1 W, 41.0--46.0 cm	OmanDP Hole BT1B	23.364374°	58.182693°	Carb. serpentinite	97.55	99.45	I
44Z-2-37-39	C5704B-44Z-2-1 W, 37.0--39.0 cm	OmanDP Hole BT1B	23.364374°	58.182693°	Carb. serpentinite	98.22	98.78	I
44Z-2-47-50	C5704B-44Z-2-1b W, 47.0--50.0 cm	OmanDP Hole BT1B	23.364374°	58.182693°	Carb. serpentinite	98.32	98.68	I
44Z-4-0-5	C5704B-44Z-4-1 W, 0.0--5.0 cm	OmanDP Hole BT1B	23.364374°	58.182693°	Carb. serpentinite	99.37	97.63	I
45Z-1-38-39	C5704B-45Z-1-1 W, 38.0--39.0 cm	OmanDP Hole BT1B	23.364374°	58.182693°	Listvenite	100.57	96.43	I
46Z-2-19-24	C5704B-46Z-2-1 W, 19.0--24.0 cm	OmanDP Hole BT1B	23.364374°	58.182693°	Listvenite	104.25	92.75	I
46Z-4-46-51	C5704B-46Z-4 W, 46.0--51.0 cm	OmanDP Hole BT1B	23.364374°	58.182693°	Listvenite	106.06	90.94	I
48Z-1-6-11	C5704B-48Z-1 W, 6.0--11.0 cm	OmanDP Hole BT1B	23.364374°	58.182693°	Listvenite	109.40	87.60	I
50Z-1-75-80	C5704B-50Z-1 W, 75.0--80.0 cm	OmanDP Hole BT1B	23.364374°	58.182693°	Listvenite	113.11	83.89	II
53Z-2-72-77	C5704B-53Z-2 W, 72.0--77.0 cm	OmanDP Hole BT1B	23.364374°	58.182693°	Fu-listvenite	122.87	74.13	II
53Z-4-35-40	C5704B-53Z-4 W, 35.0--40.0 cm	OmanDP Hole BT1B	23.364374°	58.182693°	Fu-listvenite	124.06	72.94	II
55Z-1-55-60	C5704B-55Z-1 W, 55.0--60.0 cm	OmanDP Hole BT1B	23.364374°	58.182693°	Fu-listvenite	128.20	68.80	II
60Z-1-32-37	C5704B-60Z-1 W, 32.0--37.0 cm	OmanDP Hole BT1B	23.364374°	58.182693°	Fu-listvenite	140.15	56.85	II
61Z-4-28-33	C5704B-61Z-4 W, 28.0--33.0 cm	OmanDP Hole BT1B	23.364374°	58.182693°	Listvenite	145.30	51.70	II
66Z-1-30-35	C5704B-66Z-1 W, 30.0--35.0 cm	OmanDP Hole BT1B	23.364374°	58.182693°	Listvenite	158.38	38.62	II
68Z-1-60-64	C5704B-68Z-1 W, 60.0--64.0 cm	OmanDP Hole BT1B	23.364374°	58.182693°	Fu-listvenite	164.67	32.33	II
71Z-3-41-49	C5704B-71Z-3 W, 41.0--49.0 cm	OmanDP Hole BT1B	23.364374°	58.182693°	Fu-listvenite	175.01	21.99	III
72Z-1-71-79	C5704B-72Z-1 W, 71.0--79.0 cm	OmanDP Hole BT1B	23.364374°	58.182693°	Listvenite	176.94	20.07	III
76Z-2-12-20	C5704B-76Z-2-1 W, 12.0--20.0 cm	OmanDP Hole BT1B	23.364374°	58.182693°	Listvenite	189.30	7.71	III
OM20-18		Site 1	23.345929°	58.221138°	Carb. serpentinite		<250	
OM20-17		Site 1	23.345820°	58.221398°	Carb. serpentinite		<250	
OM20-16		Site 1	23.345970°	58.221128°	Carb. serpentinite		<250	
OM20-15		Site 1	23.345970°	58.221128°	Listvenite		<250	
OM20-14		Site 1	23.346010°	58.221083°	Listvenite		<250	
OM20-13		Site 1	23.351069°	58.220117°	Serp. peridotite		100	
OM20-11		Site 1	23.355735°	58.221883°	Carb. serpentinite		12	
OM20-12		Site 1	23.355454°	58.221920°	Listvenite		10	
OM20-34		Site 2 - lower transect	23.453191°	58.203511°	Serp. peridotite		120	
OM20-31		Site 2 - lower transect	23.449571°	58.204111°	Listvenite		100	
OM20-30b		Site 2 - lower transect	23.449571°	58.204111°	Carb. serpentinite		100	
OM20-32		Site 2 - lower transect	23.449571°	58.204111°	Serp. peridotite		98	
OM20-25		Site 2 - upper transect	23.448299°	58.201763°	Listvenite		80	
OM20-29		Site 2 - upper transect	23.449091°	58.202924°	Listvenite		65	
OM20-26		Site 2 - upper transect	23.448299°	58.201763°	Carb. serpentinite		78	
OM20-28		Site 2 - upper transect	23.448445°	58.202033°	Serp. peridotite		65	

[1]BT1B core geochemical domains after Godard et al. (2021)

Abbreviations : m.b.g. = metres below ground

Table S2: Mineralogy and microstructures of rock samples

Sample name	Rock type	Depth	Domain[1]	Host rock proportion[2]	Vein proportion[2]	Dominant deformation structure	Matrix carbonates	Vein carbonates	Quartz	Serpentine	Fuchsite	Oxides	Sulfides	Primary silicates (Ol+Opx+Cpx)	Mg-core spheroids	Fe-core spheroids
		m.b.g.		%	%											
16Z-1-65-70	Listvenite	27.65	I	86.0	10.0	Foliated	Mgs (+), Dol (-)	Mgs (+), Dol (-)	M			t			x	x
30Z-2-33-39	Listvenite	62.68	I	89.0	5.5	Veined	Mgs (=), Dol (=)	Mgs (+), Dol (-)	M			t			x	
31Z-3-26-31	Listvenite	65.56	I	90.0	3.0	Foliated	Mgs (+), Dol (-)	Mgs (+), Dol (-)	M			t			x	
35Z-1-56-61	Listvenite	71.97	I	84.5	15.0	Veined	Mgs (+), Dol (-)	Mgs (+), Dol (-)	M			t			x	
38Z-3-60-65	Listvenite	80.61	I	79.0	2.0	Foliated	Mgs (=), Dol (=)	Mgs (+), Dol (-)	M			t				
40Z-3-11-16	Carb. serpentinite	87.04	I	87.0	6.0	Veined	Dol	Dol				t				
43Z-2-43-48	Carb. serpentinite	95.30	I	94.0	5.0	Veined	Mgs (=), Dol(=)	Mgs (+), Dol (-)		M		t	t			
43Z-3-0-5	Carb. serpentinite	95.56	I	94.0	5.0	Veined	Mgs (=), Dol(=)	Dol (+), Mgs (-)		M		t	t		x	
43Z-3-52-57	Carb. serpentinite	96.07	I	94.0	5.0	Veined	Mgs (=), Dol(=)	Dol (+), Mgs (-)		M		t	t		x	
43Z-4-52-57	Carb. serpentinite	96.64	I	94.0	5.0	Veined	Mgs (=), Dol(=)	Mgs (+), Dol (-)		M		t	t			
44Z-1-41-46	Carb. serpentinite	97.55	I	94.0	5.0	Veined	Mgs (+), Dol (-)	Mgs (+), Dol (-)		M		t	t			
44Z-2-37-39	Carb. serpentinite	98.22	I	94.0	3.0	Veined	Mgs (+), Dol (-)	Mgs (+), Dol (-)		M		t	t		x	x
44Z-2-47-50	Carb. serpentinite	98.32	I	94.0	3.0	Veined	Mgs (+), Dol (-)	Mgs (+), Dol (-)		M		t			x	
44Z-4-0-5	Carb. serpentinite	99.37	I	75.0	8.0	Veined	Mgs (+), Dol (-)	Mgs (+), Dol (-)		M		t	t		x	x
45Z-1-38-39	Listvenite	100.57	I	89.5	7.0	Veined	Mgs (+), Dol (-)	Mgs (+), Dol (-)	M			t			x	x
46Z-2-19-24	Listvenite	104.25	I	98.5	1.5	Veined	Mgs (+), Dol (-)	Mgs (+), Dol (-)	M			t	t		x	
46Z-4-46-51	Listvenite	106.06	II	88.5	10.0	Veined	Mgs (+), Dol (-)	Mgs (+), Dol (-)	M			t	t		x	
48Z-1-6-11	Listvenite	109.40	II	88.5	10.0	Veined	Mgs (+), Dol (-)	Mgs (+), Dol (-)	M			t			x	x
50Z-1-75-80	Listvenite	113.11	II	66.5	9.0	Veined	Mgs (+), Dol (-)	Mgs (+), Dol (-)	M			t			x	x
53Z-2-72-77	Fu-listvenite	122.87	II	89.5	7.0	Veined	Mgs (+), Dol (-)	Mgs (+), Dol (-)	M		m	t			x	x
53Z-4-35-40	Fu-listvenite	124.06	II	15.0	5.0	Veined	Mgs (+), Dol (-)	Mgs (+), Dol (-)	M		m	t			x	x
55Z-1-55-60	Fu-listvenite	128.20	II	79.0	11.0	Veined	Mgs (+), Dol (-)	Mgs (+), Dol (-)	M		t	t				
60Z-1-32-37	Fu-listvenite	140.15	II	90.0	7.0	Veined	Mgs (+), Dol (-)	Mgs (+), Dol (-)	M		m	t			x	x
61Z-4-28-33	Listvenite	145.30	II	79.0	13.0	Veined	Mgs (+), Dol (-)	Mgs (+), Dol (-)	M			t				
66Z-1-30-35	Listvenite	158.38	II	85.0	10.0	Veined	Mgs (+), Dol (-)	Mgs (+), Dol (-)	M			t			x	x
68Z-1-60-64	Fu-listvenite	164.67	II	40.0	7.0	Veined	Mgs (+), Dol (-)	Mgs (+), Dol (-)	M		t	t			x	
71Z-3-41-49	Fu-listvenite	175.01	III	74.0	13.0	Veined	Mgs (+), Dol (-)	Mgs (+), Dol (-)	M			t			x	x
72Z-1-71-79	Listvenite	176.94	III	87.0	10.0	Veined	Mgs (+), Dol (-)	Mgs (+), Dol (-)	M			t			x	x
76Z-2-12-20	Listvenite	189.30	III	85.0	15.0	Foliated	Dol (+), Mgs (-)	Dol (+), Mgs (-)	M			t				
OM20-18	Carb. serpentinite			90	10	Foliated		M		M		t				
OM20-17	Carb. serpentinite			60	40	Foliated	t	M		M		t				
OM20-16	Carb. serpentinite			70	30	Veined	M		m	M		t			x	x
OM20-15	Listvenite			50	50	Veined	M	M	m			t			x	x
OM20-14	Listvenite			85	15	Veined	M	M	M			t			x	x
OM20-13	Serp. peridotite			90	10	Veined				M		t		M		

OM20-11	Carb. serpentinite	95	5	Veined	M	M			t					
OM20-12	Listvenite	85	15	Veined	M	M	M		t					
OM20-34	Serp. peridotite	95	5	Veined				M	t	t	M			
OM20-31	Listvenite	0	0	Cataclasite	M	M	M		t					
OM20-30b	Carb. serpentinite	55	45	Veined	m	M		M	t				x	x
OM20-32	Serp. peridotite	95	5	Veined				M	t					
OM20-25	Listvenite	50	50	Veined	M	M	m		t				x	x
OM20-29	Listvenite	85	15	Veined	M	M	m		t				x	x
OM20-26	Carb. serpentinite	95	5	Veined	m	m		M	t				x	x
OM20-28	Serp. peridotite	95	5	Veined				M	t	t	M			

[1]BT1B core geochemical domains after Godard et al. (2021)
[2]After Kelemen et al. (2020) for OmanDP Hole BT1B samples
[3]Abbreviations of vein generations after Menzel et al. (2022)
Abbreviations : M = major, m = minor, t = trace, m.b.g. = metres below ground
Abbreviations for minerals: Cpx = clinopyroxene, Dol = Dolomite, Mgs = magnesite, Ol = olivine, Opx = orthopyroxene
Dominant deformation structure is termed “veined” in case of dense veining, “foliated” as shearing structures were recognized, or "cataclasite" as predominant cataclasites are observed
For carbonate abundance, (+) and (-) indicate the predominance of each phase
Abundance of matrix and vein carbonates and the occuence of Mg-core and Fe-core spheroids were determined based on thin-section study and SEM imaging

Table S2 (continued)

Vein generations[3]

Sample name	Serpentine-hosted										Listvenite-hosted										
	ss0	ss1	ss2	sc0	sc1	sc2	sc3	sq1	sq2	sc4	lss0	lss2	lc1	lc2	lc3	lq1	lq2	lq3	lq4	lc4	lc5	lc6
16Z-1-65-70													M	t		t		t				m
30Z-2-33-39											t		M									t
31Z-3-26-31													M									m
35Z-1-56-61													m					m		M		m
38Z-3-60-65													m								m	m
40Z-3-11-16				M		m				m												
43Z-2-43-48	m		m	m		m																
43Z-3-0-5	m		m	m		m																
43Z-3-52-57	m		m	m		m																
43Z-4-52-57	m		m	m		m	t															
44Z-1-41-46	m		m	m		m																
44Z-2-37-39	m		m	m						t												
44Z-2-47-50	m		M	M		m																
44Z-4-0-5	m		M	M		m																
45Z-1-38-39											m	m	m	m								
46Z-2-19-24											m	m	m	m								
46Z-4-46-51												t	M	m					t	t		m
48Z-1-6-11											t	m	M							m		
50Z-1-75-80											m	m	M	t						t		m
53Z-2-72-77													M	m				t	t			m
53Z-4-35-40											m	t	M					t	t	t		t
55Z-1-55-60													M	M						m		
60Z-1-32-37											m		M						m	m		m
61Z-4-28-33															m	t			t	m		M
66Z-1-30-35											m		M									m
68Z-1-60-64													M					m		m		M
71Z-3-41-49												t	t							t		M
72Z-1-71-79												t	M	m								M
76Z-2-12-20													t									M
OM20-18	M			M	M																	
OM20-17	M			M	M																	
OM20-16				m	M						m	t	M									M
OM20-15											m		M							t		t
OM20-14													M	m				m	m	m		m
OM20-13	M																					
OM20-11											M	M	m									
OM20-12											M		M						M		m	M
OM20-34																						
OM20-31													M									
OM20-30b	M		m	m	M																	
OM20-32	M		m																			
OM20-25											M	m	M									
OM20-29											M		M					m	t			m
OM20-26	M		m		M																	
OM20-28	M	m																				

Table S3 : Average standard deviation and detection limits for EPMA analyses

Géosciences Montpellier										**Institute of Earth Sciences**							
	1σ (wt%)					**Detection limit (µg/g)**					**1σ (wt%)**				**Detection limit (µg/g)**		
Major oxides	Carbonates	Silicates	Oxides	Sulfides	Element	Carbonates	Silicates	Oxides	Sulfides	Major oxides	Carbonates	Silicates	Oxides	Element	Carbonates	Silicates	Oxides
SiO2	0.08	0.25	0.02	0.02	Si	229	250	216	205	SiO2	0.01	0.05	0.01	Si	56	129	66
TiO2	-	0.05	0.03	0.06	Ti	548	1113	811	733	TiO2	-	0.01	0.00	Ti	-	87	78
Al2O3	0.04	0.06	0.15	0.02	Al	324	286	288	207	Al2O3	-	0.01	0.03	Al	-	44	64
Cr2O3	0.03	0.09	1.31	0.06	Cr	405	892	962	676	Cr2O3	-	0.03	0.06	Cr	-	141	150
FeO	0.14	0.22	0.69	0.39	Fe	638	1561	1808	736	FeO	0.05	0.03	0.07	Fe	118	97	116
MnO	0.06	0.04	0.06	0.07	Mn	712	671	878	881	MnO	0.01	0.01	0.01	Mn	128	107	158
MgO	0.32	0.51	0.13	0.05	Mg	406	625	341	410	MgO	0.04	0.05	0.02	Mg	46	102	44
CaO	0.22	0.02	0.02	0.02	Ca	228	264	265	190	CaO	0.02	0.01	-	Ca	65	53	-
Na2O	0.03	0.03	0.03	0.04	Na	296	497	570	406	Na2O	-	0.00	-	Na	-	49	-
K2O	0.03	0.14	0.01	0.01	K	236	228	190	164	K2O	-	0.02	-	K	-	47	-
NiO	0.05	0.09	0.10	0.33	Ni	684	1604	1391	751	NiO	-	0.02	0.01	Ni	-	167	130
CuO	-	-	-	0.10	Cu	914	-	1278	1059	CuO	-	-	-	Cu	-	-	-
ZnO	-	-	0.09	0.11	Zn	1166	1299	1610	1279	ZnO	-	-	-	Zn	-	-	-
SO2	-	-	-	0.86	S	361	549	464	925	SO2	-	-	-	S	-	-	-
Cl	-	0.01	0.01	-	Cl	-	182	203	-	Cl	-	0.15	-	Cl	-	31	-
BaO	-	-	-	-	Ba	597	668	-	-	BaO	0.03	-	-	Ba	284	-	-
SrO	-	-	-	-	Sr	1128	-	850	-	SrO	0.01	-	-	Sr	106	-	-

Table S4 : Major element compositions of carbonates determined by EPMA

								Major oxides																
Facility	Lithology	Sample	Mineral	Structure	Texture[2]	Zone	Transect	SiO2	TiO2	Al2O3	Cr2O3	FeO	MnO	MgO	CaO	Na2O	K2O	NiO	CuO	ZnO	SO2	Cl	BaO	SrO	Total
								wt%	wt%	wt%	wt%	wt%	wt%	wt%	wt%	wt%	wt%	wt%	wt%	wt%	wt%	wt%	wt%	wt%	
GM	Listvenite	16Z-1-65-70	Dolomite	Matrix	Aggregate			-	-	-	-	2.24	-	19.80	27.54	-	-	-	-	-	-	-	-	-	49.58
GM	Listvenite	16Z-1-65-70	Dolomite	Matrix	Aggregate			0.08	-	0.18	-	2.46	-	19.60	27.51	-	-	-	-	-	-	-	-	0.04	49.88
GM	Listvenite	16Z-1-65-70	Dolomite	Matrix	Aggregate			0.08	-	0.20	-	2.13	-	19.56	27.64	-	-	-	-	-	-	-	-	-	49.61
GM	Listvenite	16Z-1-65-70	Dolomite	Matrix	Aggregate			-	-	-	-	1.86	-	19.70	28.29	-	-	-	-	-	-	-	-	-	49.85
GM	Listvenite	16Z-1-65-70	Dolomite	Matrix	Aggregate			0.19	-	-	-	2.54	-	19.47	27.62	-	-	-	-	-	-	-	-	-	49.82
GM	Listvenite	16Z-1-65-70	Dolomite	Vein	lc6	Median zone		0.15	-	-	-	1.19	0.24	20.40	27.88	-	-	-	-	-	-	-	-	-	49.85
GM	Listvenite	16Z-1-65-70	Dolomite	Vein	lc6	Median zone		-	-	-	-	0.39	0.28	20.65	28.47	-	-	-	-	-	-	-	-	-	49.78
GM	Listvenite	16Z-1-65-70	Dolomite	Vein	lc6	Median zone		-	-	-	-	-	0.29	21.31	28.37	-	-	-	-	-	-	-	-	-	49.97
GM	Listvenite	16Z-1-65-70	Dolomite	Vein	lc6	Median zone		-	-	-	-	0.57	-	20.76	28.71	-	-	-	-	-	-	-	-	-	50.04
GM	Listvenite	16Z-1-65-70	Magnesite	Matrix	Aggregate			0.21	-	-	-	7.78	0.11	43.48	-	-	-	-	-	-	-	-	-	-	51.59
GM	Listvenite	16Z-1-65-70	Magnesite	Matrix	Aggregate			4.01	-	-	-	3.10	-	44.58	0.07	-	-	-	-	-	-	-	-	-	51.75
GM	Listvenite	16Z-1-65-70	Magnesite	Vein	lss0	Median zone		0.24	-	-	-	4.03	-	44.65	0.60	-	-	-	-	-	-	-	-	-	49.53
GM	Listvenite	16Z-1-65-70	Magnesite	Vein	lss0	Median zone		0.27	-	-	0.30	2.70	-	45.87	0.07	-	-	-	-	-	-	-	-	-	49.21
GM	Listvenite	16Z-1-65-70	Magnesite	Vein	lss0	Intermediate		1.18	-	-	-	2.71	-	45.84	0.07	-	-	-	-	-	-	-	-	-	49.80
GM	Listvenite	16Z-1-65-70	Magnesite	Vein	lss0	Rim		0.36	-	-	0.31	2.59	-	45.35	0.52	-	-	-	-	-	-	-	-	-	49.14
GM	Listvenite	16Z-1-65-70	Magnesite	Vein	lss0	Median zone		2.16	-	-	-	2.60	-	44.90	0.12	-	-	-	-	-	-	-	-	-	49.77
GM	Listvenite	16Z-1-65-70	Siderite	Vein	lc1	Median zone		3.83	-	0.90	-	35.39	0.12	14.36	0.09	-	-	0.20	-	-	-	-	-	-	54.88
GM	Listvenite	16Z-1-65-70	Siderite	Vein	lc1	Median zone		4.98	-	1.14	-	43.38	-	6.70	0.10	-	-	-	-	-	-	-	-	-	56.30
GM	Listvenite	16Z-1-65-70	Siderite	Vein	lc1	Median zone		7.27	-	1.60	-	59.39	-	0.26	0.09	-	-	-	-	-	-	-	-	-	68.61
GM	Listvenite	16Z-1-65-70	Siderite	Vein	lc1	Median zone		5.65	-	0.95	-	53.29	0.14	13.51	0.13	-	-	0.20	-	-	-	-	-	-	73.87
GM	Listvenite	16Z-1-65-70	Siderite	Vein	lc1	Intermediate		4.39	-	0.26	-	38.61	-	9.94	0.13	-	-	-	-	-	-	-	-	-	53.33
GM	Listvenite	16Z-1-65-70	Magnesite	Vein	lc1	Intermediate		0.21	-	-	-	7.78	0.11	43.48	-	-	-	-	-	-	-	-	-	-	51.59
GM	Listvenite	16Z-1-65-70	Magnesite	Vein	lc1	Rim		0.14	-	-	-	4.30	-	44.98	0.07	-	-	-	-	-	-	-	-	-	49.50
GM	Listvenite	16Z-1-65-70	Magnesite	Vein	lc1	Rim	a	0.80	-	-	0.14	2.92	-	46.17	-	-	-	-	-	-	-	-	-	-	50.03
GM	Listvenite	16Z-1-65-70	Magnesite	Vein	lc1	Rim	a	1.07	-	-	-	3.43	-	45.47	0.05	-	-	-	-	-	-	-	-	-	50.01
GM	Listvenite	16Z-1-65-70	Magnesite	Vein	lc1	Intermediate	a	2.14	-	-	-	3.64	-	43.68	0.07	-	-	-	-	-	-	-	-	-	49.53
GM	Listvenite	16Z-1-65-70	Magnesite	Vein	lc1	Intermediate	a	0.99	-	-	-	3.60	-	44.71	0.13	-	-	-	-	-	-	-	-	-	49.43
GM	Listvenite	16Z-1-65-70	Magnesite	Vein	lc1	Intermediate	a	1.30	-	-	0.13	3.50	-	45.22	-	-	-	-	-	-	-	-	-	0.03	50.17
GM	Listvenite	16Z-1-65-70	Magnesite	Vein	lc1	Intermediate	a	1.00	-	-	-	3.38	-	45.10	0.05	-	-	-	-	-	-	-	-	0.04	49.57
GM	Listvenite	16Z-1-65-70	Magnesite	Vein	lc1	Intermediate	a	3.00	-	-	-	3.81	-	43.91	0.12	-	-	-	-	-	-	-	-	-	50.85
GM	Listvenite	16Z-1-65-70	Magnesite	Vein	lc1	Intermediate	a	1.93	-	-	0.15	4.50	-	43.96	0.21	-	-	-	-	-	-	-	-	-	50.74
GM	Listvenite	16Z-1-65-70	Magnesite	Vein	lc1	Intermediate	a	0.70	-	-	-	4.11	-	44.28	0.08	-	-	-	-	-	-	-	-	0.00	49.17
GM	Listvenite	16Z-1-65-70	Magnesite	Vein	lc1	Intermediate	a	0.59	-	-	0.17	3.99	-	43.81	-	-	-	-	-	-	-	-	-	-	48.56
GM	Listvenite	16Z-1-65-70	Magnesite	Vein	lc1	Intermediate	a	1.84	-	-	-	3.28	-	44.72	0.06	-	-	-	-	-	-	-	-	-	49.90
GM	Listvenite	16Z-1-65-70	Magnesite	Vein	lc1	Intermediate	a	0.34	-	-	-	3.54	-	45.28	0.06	-	-	-	-	-	-	-	-	-	49.21
GM	Listvenite	16Z-1-65-70	Magnesite	Vein	lc1	Intermediate	a	0.31	-	-	-	4.32	-	45.25	-	-	-	-	-	-	-	-	-	0.01	49.89
GM	Listvenite	16Z-1-65-70	Magnesite	Vein	lc1	Median zone	a	0.17	-	-	-	5.64	-	44.85	0.08	-	-	-	-	-	-	-	-	-	50.74
GM	Listvenite	16Z-1-65-70	Magnesite	Vein	lc1	Median zone	a	0.09	-	-	-	7.33	-	43.40	0.47	-	-	-	-	-	-	-	-	0.01	51.30
GM	Listvenite	16Z-1-65-70	Magnesite	Vein	lc1	Intermediate	a	-	-	-	-	7.26	-	43.04	0.08	-	-	-	-	-	-	-	-	-	50.37
GM	Listvenite	16Z-1-65-70	Magnesite	Vein	lc1	Intermediate	a	-	-	-	-	6.01	-	44.22	0.07	-	-	-	-	-	-	-	-	0.01	50.30
GM	Listvenite	16Z-1-65-70	Magnesite	Vein	lc1	Rim	a	0.09	-	-	-	5.38	-	44.52	-	-	-	-	-	-	-	-	-	-	49.99
GM	Listvenite	16Z-1-65-70	Magnesite	Vein	lc1	Rim	a	0.60	-	-	-	4.82	-	44.08	0.06	-	-	-	-	-	-	-	-	-	49.56
GM	Listvenite	16Z-1-65-70	Magnesite	Vein	lc1	Rim	b	1.04	-	-	0.19	3.05	-	46.25	-	-	-	-	-	-	-	-	-	0.02	50.54
GM	Listvenite	16Z-1-65-70	Magnesite	Vein	lc1	Rim	b	0.56	-	-	0.43	8.21	-	44.69	0.07	-	-	-	-	-	-	-	-	-	53.96
GM	Listvenite	16Z-1-65-70	Magnesite	Vein	lc1	Intermediate	b	0.26	-	-	0.29	2.79	-	46.48	-	-	-	-	-	-	-	-	-	-	49.81
GM	Listvenite	16Z-1-65-70	Magnesite	Vein	lc1	Intermediate	b	0.34	-	-	0.26	2.90	-	46.68	0.05	-	-	-	-	-	-	-	-	-	50.23

GM	Listvenite	16Z-1-65-70	Magnesite	Vein	lc1	Intermediate	b	0.37	-	-	0.13	2.87	-	45.84	0.10	-	-	-	-	-	-	-	-	0.02	49.33
GM	Listvenite	16Z-1-65-70	Magnesite	Vein	lc1	Intermediate	b	1.48	-	-	-	3.11	-	44.66	0.20	-	-	-	-	-	-	-	-	0.01	49.45
GM	Listvenite	16Z-1-65-70	Magnesite	Vein	lc1	Intermediate	b	-	-	-	-	5.68	-	44.76	0.08	-	-	-	-	-	-	-	-	0.01	50.52
GM	Listvenite	16Z-1-65-70	Magnesite	Vein	lc1	Median zone	b	0.29	-	-	-	7.67	0.20	44.71	0.08	-	-	-	-	-	-	-	-	0.02	52.97
GM	Listvenite	16Z-1-65-70	Magnesite	Vein	lc1	Median zone	b	3.80	-	0.64	0.14	29.09	-	21.22	0.13	-	0.08	-	-	-	-	-	-	-	55.10
GM	Listvenite	16Z-1-65-70	Magnesite	Vein	lc1	Median zone	b	0.10	-	-	-	7.17	-	43.44	0.04	-	-	-	-	-	-	-	-	0.01	50.76
GM	Listvenite	16Z-1-65-70	Magnesite	Vein	lc1	Intermediate	b	0.12	-	-	-	5.34	-	43.90	0.07	-	-	-	-	-	-	-	-	-	49.43
GM	Listvenite	16Z-1-65-70	Magnesite	Vein	lc1	Intermediate	b	0.11	-	-	-	4.46	-	45.73	0.05	-	-	-	-	-	-	-	-	-	50.36
GM	Listvenite	16Z-1-65-70	Magnesite	Vein	lc1	Intermediate	b	0.47	-	-	0.19	3.64	-	45.16	-	-	-	-	-	-	-	-	-	0.02	49.48
GM	Listvenite	16Z-1-65-70	Magnesite	Vein	lc1	Intermediate	b	0.76	-	-	0.29	10.16	-	43.72	0.05	-	-	-	-	-	-	-	-	-	54.98
GM	Listvenite	16Z-1-65-70	Magnesite	Vein	lc1	Intermediate	b	2.45	-	-	0.19	4.06	-	41.82	0.23	-	-	-	-	-	-	-	-	-	48.76
GM	Listvenite	16Z-1-65-70	Magnesite	Vein	lc1	Rim	b	0.52	-	-	0.21	4.10	-	44.58	0.05	-	0.05	-	-	-	-	-	-	0.01	49.52
GM	Listvenite	16Z-1-65-70	Magnesite	Vein	lc1	Rim	b	0.37	-	-	0.26	9.56	-	44.67	0.07	-	-	-	-	-	-	-	-	-	54.93
ISTE	Listvenite	30Z-2-33-39	Dolomite	Matrix	Aggregate			-	-	-	-	1.02	0.06	21.21	25.15	-	-	-	-	-	-	-	-	-	47.43
ISTE	Listvenite	30Z-2-33-39	Dolomite	Matrix	Aggregate			0.02	-	-	-	3.68	0.27	18.81	25.14	-	-	-	-	-	-	-	-	-	47.92
ISTE	Listvenite	30Z-2-33-39	Dolomite	Matrix	Aggregate			-	-	-	-	1.52	0.08	20.79	27.97	-	-	-	-	-	-	-	-	-	50.36
ISTE	Listvenite	30Z-2-33-39	Dolomite	Matrix	Aggregate			0.02	-	-	-	1.20	0.07	20.95	27.74	-	-	-	-	-	-	-	-	-	49.97
ISTE	Listvenite	30Z-2-33-39	Dolomite	Matrix	Aggregate			0.02	-	-	-	1.07	0.04	21.55	28.27	-	-	-	-	-	-	-	0.12	-	51.07
ISTE	Listvenite	30Z-2-33-39	Dolomite	Matrix	Aggregate			0.03	-	-	-	4.40	0.17	17.77	28.87	-	-	-	-	-	-	-	-	-	51.24
ISTE	Listvenite	30Z-2-33-39	Dolomite	Matrix	Aggregate			0.02	-	-	-	1.33	0.08	20.86	27.95	-	-	-	-	-	-	-	-	-	50.24
ISTE	Listvenite	30Z-2-33-39	Dolomite	Vein	lc2	Median zone		-	-	-	-	1.68	0.08	20.63	24.61	-	-	-	-	-	-	-	-	0.06	47.06
ISTE	Listvenite	30Z-2-33-39	Dolomite	Vein	lc6	Median zone		-	-	-	-	1.37	0.12	20.88	27.97	-	-	-	-	-	-	-	-	-	50.34
ISTE	Listvenite	30Z-2-33-39	Magnesite	Matrix	Mg-core spheroid			0.60	-	-	-	4.46	0.09	43.32	0.41	-	-	-	-	-	-	-	-	-	48.88
ISTE	Listvenite	30Z-2-33-39	Magnesite	Matrix	Aggregate			0.97	-	-	-	4.47	0.14	43.14	0.16	-	-	-	-	-	-	-	-	-	48.88
ISTE	Listvenite	30Z-2-33-39	Magnesite	Matrix	Aggregate			1.15	-	-	-	4.18	0.05	43.11	0.22	-	-	-	-	-	-	-	-	-	48.71
ISTE	Listvenite	30Z-2-33-39	Magnesite	Matrix	Aggregate			0.62	-	-	-	3.70	0.10	44.40	0.40	-	-	-	-	-	-	-	-	-	49.22
ISTE	Listvenite	30Z-2-33-39	Magnesite	Vein	lc1	Median zone		0.45	-	-	-	4.47	0.12	41.69	1.13	-	-	-	-	-	-	-	-	-	47.86
ISTE	Listvenite	31Z-3-26-31	Dolomite	Vein	lc1	Median zone		-	-	-	-	0.30	0.05	21.82	29.13	-	-	-	-	-	-	-	-	-	51.30
ISTE	Listvenite	31Z-3-26-31	Dolomite	Vein	lc6	Median zone		0.67	-	-	-	1.08	0.43	22.83	27.92	-	-	-	-	-	-	-	-	-	52.93
ISTE	Listvenite	31Z-3-26-31	Dolomite	Vein	lc6	Median zone		-	-	-	-	0.94	0.18	22.76	28.39	-	-	-	-	-	-	-	-	-	52.27
ISTE	Listvenite	31Z-3-26-31	Dolomite	Vein	lc6	Median zone		-	-	-	-	0.73	0.34	21.80	29.57	-	-	-	-	-	-	-	-	-	52.44
ISTE	Listvenite	31Z-3-26-31	Dolomite	Vein	lc6	Median zone		-	-	-	-	0.72	0.38	21.16	29.41	-	-	-	-	-	-	-	-	-	51.67
ISTE	Listvenite	31Z-3-26-31	Magnesite	Matrix	Mg-core spheroid	Rim	c	0.15	-	-	-	5.44	0.07	41.68	0.17	-	-	-	-	-	-	-	-	-	47.51
ISTE	Listvenite	31Z-3-26-31	Dolomite	Matrix	Mg-core spheroid	Internal growth	c	0.32	-	-	-	1.86	0.23	21.08	26.74	-	-	-	-	-	-	-	-	-	50.23
ISTE	Listvenite	31Z-3-26-31	Magnesite	Matrix	Mg-core spheroid	Internal growth	c	1.37	-	-	-	3.01	0.03	45.05	0.23	-	-	-	-	-	-	-	-	-	49.69
ISTE	Listvenite	31Z-3-26-31	Magnesite	Matrix	Mg-core spheroid	Core	c	3.34	-	-	-	4.01	0.05	43.59	0.15	-	-	-	-	-	-	-	-	-	51.14
ISTE	Listvenite	31Z-3-26-31	Magnesite	Matrix	Mg-core spheroid	Core		1.47	-	-	-	3.91	0.04	44.39	0.22	-	-	-	-	-	-	-	-	-	50.03
ISTE	Listvenite	31Z-3-26-31	Magnesite	Matrix	Mg-core spheroid	Core		1.02	-	-	-	3.17	0.04	44.85	0.26	-	-	-	-	-	-	-	-	-	49.34
ISTE	Listvenite	31Z-3-26-31	Magnesite	Matrix	Mg-core spheroid	Core		1.47	-	-	-	2.81	0.05	45.12	0.29	-	-	-	-	-	-	-	-	-	49.74
ISTE	Listvenite	31Z-3-26-31	Magnesite	Matrix	Mg-core spheroid	Core		2.24	-	-	-	1.80	-	44.50	0.57	-	-	-	-	-	-	-	-	-	49.11
ISTE	Listvenite	31Z-3-26-31	Magnesite	Matrix	Mg-core spheroid	Core		1.60	-	-	-	3.32	0.04	44.72	0.25	-	-	-	-	-	-	-	-	-	49.94
ISTE	Listvenite	31Z-3-26-31	Magnesite	Matrix	Mg-core spheroid	Core		1.34	-	-	-	2.91	0.05	45.04	0.20	-	-	-	-	-	-	-	-	-	49.54
ISTE	Listvenite	31Z-3-26-31	Magnesite	Matrix	Mg-core spheroid	Core		2.07	-	-	-	3.41	0.08	44.60	0.26	-	-	-	-	-	-	-	-	-	50.42
ISTE	Listvenite	31Z-3-26-31	Magnesite	Vein	lc1	Rim		0.11	-	-	-	4.98	0.32	42.14	0.29	-	-	-	-	-	-	-	-	-	47.84
ISTE	Listvenite	31Z-3-26-31	Magnesite	Vein	lc1	Rim		0.02	-	-	-	4.57	0.17	43.78	0.25	-	-	-	-	-	-	-	-	-	48.79
ISTE	Listvenite	35Z-1-32-37	Magnesite	Matrix	Aggregate	Core		0.04	-	-	-	4.57	0.05	44.78	0.22	-	-	-	-	-	-	-	-	-	49.66
ISTE	Listvenite	35Z-1-32-37	Magnesite	Matrix	Aggregate	Core		-	-	-	-	3.11	0.04	44.90	0.76	-	-	-	-	-	-	-	-	-	48.81
ISTE	Listvenite	35Z-1-32-37	Magnesite	Matrix	Aggregate	Core		0.02	-	-	-	4.26	-	44.65	0.40	-	-	-	-	-	-	-	-	-	49.33
ISTE	Listvenite	35Z-1-32-37	Magnesite	Matrix	Aggregate			0.54	-	-	-	4.00	0.03	44.29	0.53	-	-	-	-	-	-	-	-	-	49.39
ISTE	Listvenite	35Z-1-32-37	Magnesite	Matrix	Aggregate			-	-	-	-	5.58	0.05	44.11	0.04	-	-	-	-	-	-	-	-	-	49.78
ISTE	Listvenite	35Z-1-32-37	Magnesite	Matrix	Aggregate			0.02	-	-	-	4.46	0.05	44.02	0.48	-	-	-	-	-	-	-	-	-	49.03
ISTE	Listvenite	35Z-1-32-37	Magnesite	Matrix	Aggregate			0.01	-	-	-	5.04	0.06	44.01	0.43	-	-	-	-	-	-	-	-	-	49.55
ISTE	Listvenite	35Z-1-32-37	Magnesite	Vein	lc1	Median zone		6.16				31.14	0.11	21.89	0.15	-	-	-	-	-	-	-	-	-	59.47

ISTE	Listvenite	35Z-1-32-37	Magnesite	Vein	lc1	Median zone		1.82	-	-	-	8.13	0.37	41.54	0.20	-	-	-	-	-	-	-	-	-	52.06
ISTE	Listvenite	35Z-1-32-37	Magnesite	Vein	lc1	Median zone		2.88	-	-	-	12.24	0.33	37.24	0.45	-	-	-	-	-	-	-	-	-	53.14
ISTE	Listvenite	35Z-1-32-37	Magnesite	Vein	lc1	Median zone		1.71	-	-	-	8.17	0.36	43.52	0.66	-	-	-	-	-	-	-	-	-	54.42
ISTE	Listvenite	35Z-1-32-37	Magnesite	Vein	lc1	Median zone		2.18	-	-	-	7.93	0.38	40.62	0.30	-	-	-	-	-	-	-	-	-	51.41
ISTE	Listvenite	35Z-1-32-37	Magnesite	Vein	lc1	Median zone		0.14	-	-	-	21.88	0.14	32.91	0.26	-	-	-	-	-	-	-	-	-	55.33
ISTE	Listvenite	35Z-1-32-37	Magnesite	Vein	lc1	Median zone		0.74	-	-	-	30.43	0.16	24.45	0.17	-	-	-	-	-	-	-	-	-	55.95
ISTE	Listvenite	35Z-1-32-37	Magnesite	Vein	lc1	Median zone		1.68	-	-	-	29.12	0.12	25.09	0.22	-	-	-	-	-	-	-	-	-	56.23
ISTE	Listvenite	35Z-1-32-37	Magnesite	Vein	lc1	Rim		0.86	-	-	-	24.92	0.15	28.42	0.25	-	-	-	-	-	-	-	-	-	54.59
ISTE	Listvenite	35Z-1-32-37	Magnesite	Matrix	Aggregate (clast)			0.02	-	-	-	4.62	0.06	44.52	0.28	-	-	-	-	-	-	-	-	-	49.50
ISTE	Listvenite	35Z-1-32-37	Magnesite	Matrix	Aggregate (clast)			0.02	-	-	-	4.77	0.04	43.62	0.46	-	-	-	-	-	-	-	-	-	48.91
ISTE	Listvenite	38Z-3-60-65	Dolomite	Matrix		Interstitial		0.33	-	-	-	0.72	1.06	20.91	26.55	-	-	-	-	-	-	-	-	-	49.57
ISTE	Listvenite	38Z-3-60-65	Dolomite	Matrix		Interstitial		0.03	-	-	-	1.54	0.34	20.78	26.24	-	-	-	-	-	-	-	-	-	48.93
ISTE	Listvenite	38Z-3-60-65	Dolomite	Matrix		Interstitial		-	-	-	-	0.41	1.14	21.14	25.46	-	-	-	-	-	-	-	-	-	48.14
ISTE	Listvenite	38Z-3-60-65	Dolomite	Vein	lc2			-	-	-	-	1.41	0.35	20.67	26.23	-	-	-	-	-	-	-	0.09	-	48.75
ISTE	Listvenite	38Z-3-60-65	Dolomite	Vein	lc2			-	-	-	-	0.74	0.05	21.35	26.64	-	-	-	-	-	-	-	0.09	-	48.88
ISTE	Listvenite	38Z-3-60-65	Magnesite	Vein	lc1	Median zone		-	-	-	-	4.44	0.11	44.06	0.11	-	-	-	-	-	-	-	-	-	48.72
ISTE	Listvenite	38Z-3-60-65	Magnesite	Vein	lc1	Median zone		0.19	-	-	-	3.41	0.12	44.66	0.15	-	-	-	-	-	-	-	-	-	48.54
ISTE	Listvenite	38Z-3-60-65	Magnesite	Vein	lc1	Median zone		0.47	-	-	-	3.00	0.03	44.75	0.31	-	-	-	-	-	-	-	-	-	48.55
ISTE	Listvenite	38Z-3-60-65	Magnesite	Vein	lc1	Median zone		-	-	-	-	9.23	0.65	39.48	0.11	-	-	-	-	-	-	-	-	0.03	49.50
ISTE	Listvenite	38Z-3-60-65	Magnesite	Vein	lc1	Rim		0.56	-	-	-	4.53	0.13	43.69	0.11	-	-	-	-	-	-	-	-	-	49.01
ISTE	Listvenite	38Z-3-60-65	Magnesite	Vein	lc2			0.07	-	-	-	9.49	0.61	39.59	0.05	-	-	-	-	-	-	-	-	-	49.81
ISTE	Listvenite	38Z-3-60-65	Magnesite	Vein	lc2			-	-	-	-	6.03	0.27	42.48	0.04	-	-	-	-	-	-	-	-	-	48.82
ISTE	Carb. serpentinite	40Z-3-11-16	Dolomite	Matrix	Aggregate			-	-	-	-	0.21	0.05	21.62	29.96	-	-	-	-	-	-	-	-	-	51.84
ISTE	Carb. serpentinite	40Z-3-11-16	Dolomite	Matrix	Aggregate			0.02	-	-	-	0.30	0.07	21.34	29.81	-	-	-	-	-	-	-	-	-	51.54
ISTE	Carb. serpentinite	40Z-3-11-16	Dolomite	Matrix	Aggregate			-	-	-	-	0.27	0.08	21.69	29.91	-	-	-	-	-	-	-	-	-	51.94
ISTE	Carb. serpentinite	40Z-3-11-16	Dolomite	Matrix	Aggregate			1.22	-	-	-	1.00	0.06	20.52	29.76	-	-	-	-	-	-	-	-	-	52.56
ISTE	Carb. serpentinite	40Z-3-11-16	Dolomite	Matrix	Aggregate			-	-	-	-	0.76	0.08	21.02	29.29	-	-	-	-	-	-	-	-	-	51.15
ISTE	Carb. serpentinite	40Z-3-11-16	Dolomite	Matrix	Aggregate			0.29	-	-	-	1.06	0.09	20.27	29.15	-	-	-	-	-	-	-	-	-	50.85
ISTE	Carb. serpentinite	40Z-3-11-16	Dolomite	Matrix	sc0			0.25	-	-	-	0.06	0.15	21.63	29.66	-	-	-	-	-	-	-	-	-	51.75
ISTE	Carb. serpentinite	40Z-3-11-16	Dolomite	Vein	sc0	Median zone		2.19	-	-	-	0.37	0.51	21.58	28.69	-	-	-	-	-	-	-	-	-	53.34
ISTE	Carb. serpentinite	40Z-3-11-16	Dolomite	Vein	sc0	Median zone		0.50	-	-	-	0.24	0.74	21.46	29.20	-	-	-	-	-	-	-	-	-	52.14
GM	Carb. serpentinite	43Z-2-43-48	Dolomite	Matrix	Dol-core spheroid	Internal growth		3.55	-	-	-	1.42	0.80	20.84	37.73	-	-	-	-	-	-	-	-	-	64.34
GM	Carb. serpentinite	43Z-2-43-48	Dolomite	Matrix	Mg-core spheroid	Rim		9.88	-	-	-	1.30	0.68	25.06	30.71	-	-	-	-	-	-	-	-	-	67.62
GM	Carb. serpentinite	43Z-2-43-48	Dolomite	Vein	sc0	Median zone		0.94	-	-	-	0.50	0.29	20.91	37.40	-	-	-	-	-	-	-	-	-	60.04
GM	Carb. serpentinite	43Z-2-43-48	Dolomite	Vein	sc0	Median zone		0.85	-	-	-	0.47	0.47	21.29	37.29	-	-	-	-	-	-	-	-	-	60.36
GM	Carb. serpentinite	43Z-2-43-48	Dolomite	Vein	sc0	Median zone		0.67	-	-	-	0.44	0.41	20.48	37.49	-	-	-	-	-	-	-	-	-	59.49
GM	Carb. serpentinite	43Z-2-43-49	Dolomite	Vein	sc0	Median zone		1.64	-	-	-	0.55	0.45	21.08	37.41	-	-	-	-	-	-	-	-	-	61.13
GM	Carb. serpentinite	43Z-2-43-48	Dolomite	Vein	sc2	Median zone		1.64	-	-	-	0.50	0.44	21.07	36.53	-	-	-	-	-	-	-	-	-	60.18
GM	Carb. serpentinite	43Z-2-43-48	Dolomite	Vein	sc2	Median zone		6.93	-	-	-	1.10	0.58	21.77	33.28	-	-	-	-	-	-	-	-	-	63.65
GM	Carb. serpentinite	43Z-2-43-48	Magnesite	Matrix	Dol-core spheroid	Internal growth	d	7.79	-	-	-	3.63	0.75	37.38	10.08	-	-	-	-	-	-	-	-	-	59.63
GM	Carb. serpentinite	43Z-2-43-48	Dolomite	Matrix	Dol-core spheroid	Core	d	3.61	-	-	-	0.70	0.39	22.43	37.84	-	-	-	-	-	-	-	-	-	64.97
GM	Carb. serpentinite	43Z-2-43-48	Dolomite	Matrix	Dol-core spheroid	Core	d	0.69	-	-	-	0.34	0.38	21.05	38.27	-	-	-	-	-	-	-	-	-	60.72
GM	Carb. serpentinite	43Z-2-43-48	Dolomite	Matrix	Dol-core spheroid	Core	d	1.66	-	-	-	0.46	0.43	22.20	38.58	-	-	-	-	-	-	-	-	-	63.34
GM	Carb. serpentinite	43Z-2-43-48	Magnesite	Matrix	Dol-core spheroid	Internal growth	d	0.83	-	-	-	2.05	1.22	45.75	0.96	-	-	-	-	-	-	-	-	-	50.81
GM	Carb. serpentinite	43Z-2-43-48	Dolomite	Matrix	Dol-core spheroid	Internal growth	d	3.23	-	-	-	1.41	1.02	31.23	24.05	-	-	-	-	-	-	-	-	-	60.93
GM	Carb. serpentinite	43Z-2-43-48	Dolomite	Matrix	Dol-core spheroid	Internal growth	d	6.48	-	-	-	1.24	0.54	21.55	36.22	-	-	-	-	-	-	-	-	-	66.03
GM	Carb. serpentinite	43Z-2-43-48	Magnesite	Matrix	Mg-core spheroid	Rim		5.51	-	-	-	2.70	0.96	41.73	2.10	-	-	-	-	-	-	-	-	-	53.00
GM	Carb. serpentinite	43Z-2-43-48	Magnesite	Matrix	Mg-core spheroid	Rim	e	12.07	-	-	0.11	2.46	0.94	36.88	9.06	-	-	-	-	-	-	-	-	-	61.52
GM	Carb. serpentinite	43Z-2-43-48	Magnesite	Matrix	Mg-core spheroid	Internal growth	e	11.55	-	-	0.07	2.22	1.11	37.49	8.27	-	-	-	-	-	-	-	-	-	60.71
GM	Carb. serpentinite	43Z-2-43-48	Magnesite	Matrix	Mg-core spheroid	Internal growth	e	9.96	-	-	-	2.13	1.06	36.79	9.22	-	-	-	-	-	-	-	-	-	59.16
GM	Carb. serpentinite	43Z-2-43-48	Magnesite	Matrix	Mg-core spheroid	Core	e	9.18	-	-	-	1.94	1.30	32.44	18.89	-	-	-	-	-	-	-	-	-	63.75
GM	Carb. serpentinite	43Z-2-43-48	Magnesite	Matrix	Mg-core spheroid	Core	e	8.67	-	-	-	2.36	1.19	37.71	9.01	-	-	-	-	-	-	-	-	-	58.94
GM	Carb. serpentinite	43Z-2-43-48	Magnesite	Matrix	Mg-core spheroid	Internal growth	e	10.34	-	-	-	2.26	1.05	38.20	8.16	-	-	-	-	-	-	-	-	-	60.01

GM	Carb. serpentinite	43Z-2-43-48	Magnesite	Matrix	Mg-core spheroid	Internal growth	e	7.41	-	-	-	7.82	1.02	37.59	8.34	-	-	-	-	-	-	-	-	-	62.17
GM	Carb. serpentinite	43Z-2-43-48	Dolomite	Matrix	Mg-core spheroid	Rim	e	9.95	-	-	-	1.40	0.59	25.17	31.25	-	-	-	-	-	-	-	-	-	68.35
GM	Carb. serpentinite	43Z-2-43-48	Dolomite	Matrix	Mg-core spheroid	Rim	f	9.88	-	-	-	1.30	0.68	25.06	30.71	-	-	-	-	-	-	-	-	-	67.62
GM	Carb. serpentinite	43Z-2-43-48	Magnesite	Matrix	Mg-core spheroid	Internal growth	f	5.25	-	-	-	2.69	1.31	38.85	7.35	-	-	-	-	-	-	-	-	-	55.46
GM	Carb. serpentinite	43Z-2-43-48	Magnesite	Matrix	Mg-core spheroid	Rim	f	11.24	-	-	0.08	2.22	0.99	34.25	8.16	-	-	-	-	-	-	-	-	-	56.94
GM	Carb. serpentinite	43Z-2-43-48	Magnesite	Vein	sc2	Median zone		2.94	-	-	-	4.97	0.24	43.95	0.37	-	-	-	-	-	-	-	-	-	52.47
GM	Carb. serpentinite	43Z-2-43-48	Magnesite	Vein	sc2	Median zone		3.05	-	-	-	4.64	0.26	44.05	0.41	-	-	-	-	-	-	-	-	-	52.41
GM	Carb. serpentinite	43Z-2-43-48	Magnesite	Vein	sc2	Median zone		1.05	-	-	-	2.17	1.16	37.99	11.10	-	-	-	-	-	-	-	-	-	53.47
GM	Carb. serpentinite	43Z-2-43-48	Magnesite	Vein	sc2	Median zone		1.05	-	-	-	2.06	1.39	42.09	4.84	-	-	-	-	-	-	-	-	-	51.43
GM	Carb. serpentinite	43Z-3-0-5	Dolomite	Matrix	Dol-core spheroid	Core		4.44	-	-	-	1.50	0.95	20.80	35.32	-	-	-	-	-	-	-	-	-	63.01
GM	Carb. serpentinite	43Z-3-0-5	Dolomite	Matrix	Dol-core spheroid	Core		4.87	-	-	-	1.39	0.52	21.84	35.80	-	-	-	-	-	-	-	-	-	64.42
GM	Carb. serpentinite	43Z-3-0-5	Dolomite	Matrix	Dol-core spheroid	Core		4.93	-	-	-	3.02	1.07	27.89	23.83	-	-	-	-	-	-	-	-	-	60.74
GM	Carb. serpentinite	43Z-3-0-5	Dolomite	Matrix	Dol-core spheroid	Core		3.91	-	-	-	1.66	0.92	22.10	35.43	-	-	-	-	-	-	-	-	-	64.02
GM	Carb. serpentinite	43Z-3-0-5	Dolomite	Matrix	Dol-core spheroid	Core		8.61	-	-	-	1.43	0.46	22.69	33.09	-	-	-	-	-	-	-	-	-	66.28
GM	Carb. serpentinite	43Z-3-0-5	Dolomite	Matrix	Dol-core spheroid	Core		8.48	-	-	-	1.52	0.57	22.49	34.17	-	-	-	-	-	-	-	-	-	67.23
GM	Carb. serpentinite	43Z-3-0-5	Dolomite	Matrix	Mg-core spheroid	Core		10.63	-	-	-	4.20	0.33	39.47	0.29	-	-	-	-	-	-	-	-	-	54.92
GM	Carb. serpentinite	43Z-3-0-5	Dolomite	Vein	sc2	Median zone		0.80	-	-	-	1.27	0.96	26.71	29.62	-	-	-	-	-	-	-	-	-	59.35
GM	Carb. serpentinite	43Z-3-0-5	Dolomite	Vein	sc2	Intermediate		1.03	-	-	-	0.32	0.68	21.55	38.52	-	-	-	-	-	-	-	-	-	62.11
GM	Carb. serpentinite	43Z-3-0-5	Magnesite	Vein	sc2	Rim		10.63	-	-	-	4.20	0.33	39.47	0.29	-	-	-	-	-	-	-	-	-	54.92
GM	Carb. serpentinite	43Z-3-0-5	Magnesite	Vein	sc2	Intermediate	g	0.15	-	-	-	3.95	0.31	45.20	0.24	-	-	-	-	-	-	-	-	-	49.85
GM	Carb. serpentinite	43Z-3-0-5	Magnesite	Vein	sc2	Intermediate	g	0.28	-	-	-	3.47	-	45.89	0.40	-	-	-	-	-	-	-	-	-	50.04
GM	Carb. serpentinite	43Z-3-0-5	Magnesite	Vein	sc2	Intermediate	g	3.15	-	-	-	3.65	-	44.78	0.35	-	-	-	-	-	-	-	-	-	51.92
GM	Carb. serpentinite	43Z-3-0-5	Magnesite	Vein	sc2	Median zone	g	3.99	-	-	-	4.39	0.35	43.70	0.27	-	-	-	-	-	-	-	-	-	52.69
GM	Carb. serpentinite	43Z-3-0-5	Magnesite	Vein	sc2	Median zone	g	3.08	-	-	-	6.74	2.04	41.19	0.74	-	-	-	-	-	-	-	-	-	53.79
GM	Carb. serpentinite	43Z-3-0-5	Magnesite	Vein	sc2	Median zone	g	6.74	-	-	-	5.14	1.04	41.65	0.27	-	-	-	-	-	-	-	-	-	54.82
GM	Carb. serpentinite	43Z-3-0-5	Magnesite	Vein	sc2	Intermediate	g	2.42	-	-	-	4.37	0.24	44.17	0.43	-	-	-	-	-	-	-	-	-	51.63
GM	Carb. serpentinite	43Z-3-0-5	Magnesite	Vein	sc2	Intermediate	g	7.88	-	-	-	3.81	-	42.92	0.34	-	-	-	-	-	-	-	-	-	54.95
GM	Carb. serpentinite	43Z-3-0-5	Magnesite	Vein	sc2	Intermediate	g	1.81	-	-	-	3.76	-	44.87	0.34	-	-	-	-	-	-	-	-	-	50.78
GM	Carb. serpentinite	43Z-3-0-5	Dolomite	Vein	sc2	Rim	g	1.76	-	-	-	0.42	0.99	20.55	37.72	-	-	-	-	-	-	-	-	-	61.44
GM	Carb. serpentinite	43Z-3-0-5	Dolomite	Vein	sc2	Rim	g	1.81	-	-	-	0.34	0.85	21.36	37.97	-	-	-	-	-	-	-	-	-	62.34
GM	Carb. serpentinite	43Z-4-52-57	Dolomite	Matrix	Dol-core spheroid	Core		-	-	-	-	-	-	21.11	33.40	-	-	-	-	-	-	-	-	-	54.51
GM	Carb. serpentinite	43Z-4-52-57	Dolomite	Matrix	Dol-core spheroid	Core		4.63	-	-	-	0.68	-	20.36	29.14	-	-	-	-	-	-	-	-	-	54.81
GM	Carb. serpentinite	43Z-4-52-57	Dolomite	Matrix	Dol-core spheroid	Core		0.16	-	-	-	0.28	0.23	21.08	32.52	-	-	-	-	-	-	-	-	-	54.28
GM	Carb. serpentinite	43Z-4-52-57	Dolomite	Matrix	Dol-core spheroid	Core		0.21	-	-	-	1.38	-	19.94	32.77	-	-	-	-	-	-	-	-	-	54.30
GM	Carb. serpentinite	43Z-4-52-57	Dolomite	Matrix	Dol-core spheroid	Core		4.80	-	-	-	1.20	0.65	22.01	29.89	-	-	-	-	-	-	-	-	-	58.56
GM	Carb. serpentinite	43Z-4-52-57	Dolomite	Matrix	Dol-core spheroid	Core		3.45	-	-	-	1.29	0.75	23.65	28.56	-	-	-	-	-	-	-	-	-	57.70
GM	Carb. serpentinite	43Z-4-52-57	Dolomite	Matrix	Dol-core spheroid	Core		3.25	-	-	-	1.54	0.75	24.60	27.43	-	-	-	-	-	-	-	-	-	57.57
GM	Carb. serpentinite	43Z-4-52-57	Dolomite	Matrix	Dol-core spheroid	Core		3.69	-	-	-	0.65	0.54	21.79	30.02	-	-	-	-	-	-	-	-	-	56.68
GM	Carb. serpentinite	43Z-4-52-57	Dolomite	Matrix	Dol-core spheroid	Core		8.34	-	-	-	1.03	0.59	24.36	26.80	-	-	-	-	-	-	-	-	-	61.11
GM	Carb. serpentinite	43Z-4-52-57	Dolomite	Matrix	Dol-core spheroid	Core		7.48	-	-	-	1.35	0.71	24.89	25.25	-	-	-	-	-	-	-	-	-	59.68
GM	Carb. serpentinite	43Z-4-52-57	Dolomite	Matrix	Dol-core spheroid	Core		4.37	-	-	0.45	25.27	0.50	18.87	19.31	-	-	-	-	-	-	-	-	-	68.77
GM	Carb. serpentinite	43Z-4-52-57	Dolomite	Vein	sc2	Median zone		4.27	-	-	-	0.49	0.87	22.97	29.54	-	-	-	-	-	-	-	-	-	58.14
GM	Carb. serpentinite	43Z-4-52-57	Dolomite	Vein	sc2	Median zone		5.13	-	-	-	0.68	0.74	22.40	28.97	-	-	-	-	-	-	-	-	-	57.93
GM	Carb. serpentinite	43Z-4-52-57	Dolomite	Vein	sc2	Median zone		4.71	-	-	-	0.68	0.50	23.38	30.25	-	-	-	-	-	-	-	-	-	59.53
GM	Carb. serpentinite	43Z-4-52-57	Dolomite	Vein	sc2	Median zone		3.64	-	-	-	0.62	0.52	23.03	32.10	-	-	-	-	-	-	-	-	-	59.92
GM	Carb. serpentinite	43Z-4-52-57	Magnesite	Matrix	Mg-core spheroid	Core		6.44	-	-	-	3.29	0.54	34.04	11.45	-	-	-	-	-	-	-	-	-	55.76
ISTE	Carb. serpentinite	44Z-1-41-46	Magnesite	Matrix	Mg-core spheroid	Core		5.54	-	-	-	3.85	0.33	39.15	1.01	-	-	-	-	-	-	-	-	-	49.89
ISTE	Carb. serpentinite	44Z-1-41-46	Magnesite	Matrix	Mg-core spheroid	Core		6.11	-	-	-	4.89	0.24	36.96	1.05	-	-	-	-	-	-	-	-	-	49.25
ISTE	Carb. serpentinite	44Z-1-41-46	Magnesite	Matrix	Mg-core spheroid	Core		5.94	-	-	-	4.68	0.23	37.11	2.00	-	-	-	-	-	-	-	-	-	49.96
ISTE	Carb. serpentinite	44Z-1-41-46	Dolomite	Matrix	Spheroid	Core		5.02	-	-	-	3.25	0.20	26.34	16.74	-	-	-	-	-	-	-	-	-	51.55
ISTE	Carb. serpentinite	44Z-1-41-46	Dolomite	Vein	sc0	Median zone		1.01	-	-	-	0.40	1.21	22.60	27.23	-	-	-	-	-	-	-	-	-	52.45
ISTE	Carb. serpentinite	44Z-1-41-46	Dolomite	Vein	sc2	Median zone		1.82	-	-	-	0.26	2.61	20.82	29.27	-	-	-	-	-	-	-	-	-	54.78
ISTE	Carb. serpentinite	44Z-1-41-46	Dolomite	Vein	sc2 or sc4?	Median zone		0.03	-	-	-	2.22	0.20	18.52	28.64	-	-	-	-	-	-	-	-	-	49.61

ISTE	Carb. serpentinite	44Z-1-41-46	Dolomite	Vein	sc2 or sc4?	Median zone	0.25	-	-	-	1.75	0.89	20.07	27.75	-	-	-	-	-	-	-	-	-	50.71
ISTE	Carb. serpentinite	44Z-1-41-46	Dolomite	Vein	sc2 or sc4?	Median zone	7.06	-	-	-	1.22	0.17	24.94	26.39	-	-	-	-	-	-	-	0.07	-	59.85
ISTE	Carb. serpentinite	44Z-1-41-46	Dolomite	Vein	sc2 or sc4?	Median zone	5.18	-	-	-	2.21	1.00	24.55	23.58	-	-	-	-	-	-	-	-	-	56.52
ISTE	Carb. serpentinite	44Z-1-41-46	Dolomite	Vein	sc2 or sc4?	Median zone	3.63	-	-	-	2.41	1.03	24.49	25.42	-	-	-	-	-	-	-	-	-	56.98
ISTE	Carb. serpentinite	44Z-1-41-46	Dolomite	Vein	sc2 or sc4?	Median zone	3.83	-	-	-	1.42	0.19	22.02	27.42	-	-	-	-	-	-	-	0.08	-	54.97
ISTE	Carb. serpentinite	44Z-1-41-46	Magnesite	Vein	sc2	Median zone	0.85	-	-	-	8.00	1.59	32.34	0.64	-	-	-	-	-	-	-	-	-	43.41
ISTE	Carb. serpentinite	44Z-1-41-46	Magnesite	Vein	sc0	Median zone	1.74	-	-	-	0.89	1.57	41.50	3.71	-	-	-	-	-	-	-	-	-	49.41
ISTE	Carb. serpentinite	44Z-1-41-46	Magnesite	Vein	sc0	Median zone	1.15	-	-	-	0.94	2.30	44.33	0.28	-	-	-	-	-	-	-	-	-	49.01
GM	Carb. serpentinite	44Z-4-0-5	Magnesite	Matrix	Fe-core spheroid	Core	10.01	-	-	-	17.65	-	30.18	2.55	-	-	-	-	-	-	-	-	-	60.39
GM	Carb. serpentinite	44Z-4-0-5	Magnesite	Matrix	Fe-core spheroid	Core	5.92	-	-	-	22.79	-	29.10	1.71	-	-	-	-	-	-	-	-	-	59.52
GM	Carb. serpentinite	44Z-4-0-5	Magnesite	Matrix	Fe-core spheroid	Core	3.44	-	-	0.67	28.15	-	25.00	1.89	-	-	-	-	-	-	-	-	-	59.14
ISTE	Carb. serpentinite	44Z-4-0-5	Magnesite	Matrix	Mg-core spheroid	Core	5.08	-	-	-	5.13	0.20	37.06	1.23	-	-	-	-	-	-	-	-	-	48.70
ISTE	Carb. serpentinite	44Z-4-0-5	Magnesite	Matrix	Mg-core spheroid	Core	5.31	-	-	-	6.15	0.17	34.23	0.92	-	-	-	-	-	-	-	-	-	46.78
ISTE	Carb. serpentinite	44Z-4-0-5	Magnesite	Matrix	Mg-core spheroid	Core	8.91	-	-	-	8.52	0.10	30.76	0.70	-	-	-	-	-	-	-	-	-	48.99
ISTE	Carb. serpentinite	44Z-4-0-5	Magnesite	Matrix	Mg-core spheroid	Core	8.54	-	-	-	4.45	0.23	38.02	0.57	-	-	-	-	-	-	-	-	-	51.81
ISTE	Carb. serpentinite	44Z-4-0-5	Magnesite	Matrix	Mg-core spheroid	Core	6.77	-	-	-	4.83	0.21	37.87	0.48	-	-	-	-	-	-	-	-	-	50.16
ISTE	Carb. serpentinite	44Z-4-0-5	Magnesite	Matrix	Mg-core spheroid	Internal growth	6.77	-	-	-	7.40	0.15	33.02	0.67	-	-	-	-	-	-	-	-	-	48.01
ISTE	Carb. serpentinite	44Z-4-0-5	Magnesite	Matrix	Mg-core spheroid	Rim	8.13	-	-	-	6.03	0.17	34.91	0.74	-	-	-	-	-	-	-	-	-	49.98
GM	Carb. serpentinite	44Z-4-0-5	Magnesite	Matrix	Mg-core spheroid	Rim	1.93	-	-	-	17.42	-	34.86	0.43	-	-	-	-	-	-	-	-	-	54.64
GM	Carb. serpentinite	44Z-4-0-5	Magnesite	Vein	sc0	Border	6.93	-	-	-	2.54	0.75	42.88	0.48	-	-	-	-	-	-	-	-	-	53.57
GM	Carb. serpentinite	44Z-4-0-5	Magnesite	Vein	sc0	Border	5.03	-	-	-	3.18	1.00	42.62	0.77	-	-	-	-	-	-	-	-	-	52.58
GM	Carb. serpentinite	44Z-4-0-5	Magnesite	Vein	sc0	Border	5.73	-	-	-	2.39	0.86	43.32	0.52	-	-	-	-	-	-	-	-	-	52.82
GM	Carb. serpentinite	44Z-4-0-5	Magnesite	Vein	sc0		1.51	-	-	-	2.37	0.79	44.46	0.80	-	-	-	-	-	-	-	-	-	49.94
GM	Carb. serpentinite	44Z-4-0-5	Magnesite	Vein	sc0		1.54	-	-	-	1.95	0.73	45.45	0.20	-	-	-	-	-	-	-	-	-	49.87
GM	Carb. serpentinite	44Z-4-0-5	Magnesite	Vein	sc0		-	-	-	-	28.09	-	27.33	0.81	-	-	-	-	-	-	-	-	-	56.23
GM	Carb. serpentinite	44Z-4-0-5	Magnesite	Vein	sc2	Median zone	0.73	-	-	-	11.87	-	39.80	0.52	-	-	-	-	-	-	-	-	-	52.92
GM	Carb. serpentinite	44Z-4-0-5	Magnesite	Vein	sc2	Median zone	3.98	-	-	-	12.08	-	36.91	2.65	-	-	-	-	-	-	-	-	-	55.61
GM	Carb. serpentinite	44Z-4-0-5	Magnesite	Vein	sc2	Median zone	0.48	-	-	-	11.13	-	40.86	0.22	-	-	-	-	-	-	-	-	-	52.69
GM	Carb. serpentinite	44Z-4-0-5	Magnesite	Vein	sc2	Median zone	4.07	-	-	-	15.43	-	35.25	1.31	-	-	-	-	-	-	-	-	-	56.06
GM	Carb. serpentinite	44Z-4-0-5	Magnesite	Vein	sc2	Median zone	0.19	-	-	-	18.09	-	35.86	0.43	-	-	-	-	-	-	-	-	-	54.56
GM	Carb. serpentinite	44Z-4-0-5	Magnesite	Vein	sc2	Median zone	0.43	-	-	-	10.71	-	40.66	0.06	-	-	-	-	-	-	-	-	-	51.86
GM	Carb. serpentinite	44Z-4-0-5	Magnesite	Vein	sc2	Median zone	7.17	-	-	-	14.68	-	35.68	0.79	-	-	-	-	-	-	-	-	-	58.32
GM	Carb. serpentinite	44Z-4-0-5	Magnesite	Vein	sc2	Median zone	7.46	-	-	-	10.55	-	32.65	6.05	-	-	-	-	-	-	-	-	-	56.71
GM	Carb. serpentinite	44Z-4-0-5	Magnesite	Vein	sc2	Median zone	-	-	-	-	31.07	-	26.27	0.61	-	-	-	-	-	-	-	-	-	57.94
GM	Carb. serpentinite	44Z-4-0-5	Magnesite	Vein	sc2	Median zone	-	-	-	-	28.52	-	28.73	0.32	-	-	-	-	-	-	-	-	-	57.57
GM	Carb. serpentinite	44Z-4-0-5	Magnesite	Vein	sc2	Median zone	13.88	-	-	-	7.70	-	36.35	0.22	-	-	-	-	-	-	-	-	-	58.15
ISTE	Carb. serpentinite	44Z-4-0-5	Magnesite	Vein	sc2	Border	2.03	-	-	-	2.09	0.44	43.14	0.57	-	-	-	-	-	-	-	-	-	48.27
ISTE	Listvenite	45Z-1-38-39	Dolomite	Matrix	Dol-core spheroid	Core	0.03	-	-	-	0.20	0.25	22.14	27.51	-	-	-	-	-	-	-	-	-	50.13
ISTE	Listvenite	45Z-1-38-39	Dolomite	Matrix	Aggregate		-	-	-	-	0.72	0.04	21.43	27.64	-	-	-	-	-	-	-	-	-	49.83
ISTE	Listvenite	45Z-1-38-39	Dolomite	Matrix	Aggregate		-	-	-	-	2.54	0.12	20.34	26.96	-	-	-	-	-	-	-	-	0.03	49.98
ISTE	Listvenite	45Z-1-38-39	Magnesite	Matrix	Mg-core spheroid	Core	1.28	-	-	-	3.97	0.04	44.90	0.23	-	-	-	-	-	-	-	-	0.06	50.49
ISTE	Listvenite	45Z-1-38-39	Magnesite	Matrix	Mg-core spheroid	Core	0.56	-	-	-	4.56	0.07	44.60	0.26	-	-	-	-	-	-	-	-	-	50.05
ISTE	Listvenite	45Z-1-38-39	Magnesite	Matrix	Mg-core spheroid	Core	0.21	-	-	-	4.50	0.04	44.57	0.13	-	-	-	-	-	-	-	-	-	49.45
ISTE	Listvenite	45Z-1-38-39	Magnesite	Matrix	Mg-core spheroid	Core	0.83	-	-	-	3.34	0.05	44.60	0.48	-	-	-	-	-	-	-	-	-	49.29
ISTE	Listvenite	45Z-1-38-39	Magnesite	Matrix	Mg-core spheroid	Core	0.45	-	-	-	3.67	0.03	45.43	0.33	-	-	-	-	-	-	-	-	0.03	49.95
ISTE	Listvenite	45Z-1-38-39	Magnesite	Matrix	Aggregate		0.44	-	-	-	3.09	0.10	44.19	0.26	-	-	-	-	-	-	-	-	-	48.07
ISTE	Listvenite	45Z-1-38-39	Magnesite	Matrix	Aggregate		6.98	-	-	-	3.54	-	41.62	0.22	-	-	-	-	-	-	-	-	0.15	52.50
ISTE	Listvenite	45Z-1-38-39	Magnesite	Matrix	Aggregate		-	-	-	-	5.28	0.08	43.93	0.03	-	-	-	-	-	-	-	-	-	49.32
ISTE	Listvenite	45Z-1-38-39	Magnesite	Matrix	Overgrowth		-	-	-	-	5.10	0.07	43.93	-	-	-	-	-	-	-	-	-	-	49.10
ISTE	Listvenite	45Z-1-38-39	Magnesite	Matrix	Overgrowth		0.38	-	-	-	4.31	0.07	44.72	0.23	-	-	-	-	-	-	-	-	-	49.71
GM	Listvenite	46Z-4-46-51	Dolomite	Matrix	Dol-core spheroid	Core	0.09	-	-	-	4.48	0.20	18.98	26.97	-	-	-	-	-	-	-	-	-	50.73
GM	Listvenite	46Z-4-46-51	Dolomite	Matrix	Dol-core spheroid	Core	0.13	-	-	-	4.39	-	19.75	26.85	-	-	-	-	-	-	-	-	-	51.12
GM	Listvenite	46Z-4-46-51	Dolomite	Matrix	Dol-core spheroid	Core	-	-	-	-	3.11	0.21	18.10	28.77	-	-	-	-	-	-	-	-	-	50.20

GM	Listvenite	46Z-4-46-51	Dolomite	Vein	lc1	Median zone		-	-	-	-	5.03	0.27	18.76	29.63	-	-	-	-	-	-	-	-	-	53.69
ISTE	Listvenite	46Z-4-46-51	Dolomite	Vein	lc1	Median zone		0.13	-	-	-	1.50	0.14	21.09	26.96	-	-	-	-	-	-	-	-	-	49.82
ISTE	Listvenite	46Z-4-46-51	Dolomite	Vein	lc6	Median zone		0.06	-	-	-	3.15	0.16	19.37	26.77	-	-	-	-	-	-	-	-	-	49.51
ISTE	Listvenite	46Z-4-46-51	Dolomite	Vein	lc6	Median zone		0.06	-	-	-	2.06	0.14	20.59	26.71	-	-	-	-	-	-	-	-	-	49.56
GM	Listvenite	46Z-4-46-51	Magnesite	Matrix	Mg-core spheroid	Core		0.27	-	-	-	7.30	-	41.23	0.26	-	-	-	-	-	-	-	-	-	49.07
GM	Listvenite	46Z-4-46-51	Magnesite	Matrix	Mg-core spheroid	Core		1.95	-	-	-	4.25	-	44.26	0.08	-	-	1.33	-	-	-	-	-	-	51.88
GM	Listvenite	46Z-4-46-51	Magnesite	Matrix	Mg-core spheroid	Core		3.88	-	0.13	-	3.00	-	43.14	0.67	-	-	1.22	-	-	-	-	-	-	52.04
GM	Listvenite	46Z-4-46-51	Magnesite	Matrix	Mg-core spheroid	Core		6.45	-	-	-	5.93	0.21	43.01	0.37	-	-	-	-	-	-	-	-	-	55.97
GM	Listvenite	46Z-4-46-51	Magnesite	Matrix	Mg-core spheroid	Core		0.72	-	-	-	4.48	-	44.00	0.11	-	-	-	-	-	-	-	-	-	49.31
GM	Listvenite	46Z-4-46-51	Magnesite	Matrix	Mg-core spheroid	Core		0.77	-	-	-	4.45	-	43.53	0.12	-	-	-	-	-	-	-	-	-	48.87
GM	Listvenite	46Z-4-46-51	Magnesite	Matrix	Mg-core spheroid	Core		0.09	-	-	-	12.02	-	39.26	0.49	-	-	-	-	-	-	-	-	-	51.86
GM	Listvenite	46Z-4-46-51	Magnesite	Matrix	Mg-core spheroid	Core		0.47	-	-	-	7.02	-	41.65	0.22	-	-	-	-	-	-	-	-	-	49.36
ISTE	Listvenite	46Z-4-46-51	Magnesite	Matrix	Mg-core spheroid	Core		0.43	-	-	-	3.52	0.10	45.28	0.19	-	-	-	-	-	-	-	-	-	49.52
ISTE	Listvenite	46Z-4-46-51	Magnesite	Matrix	Mg-core spheroid	Core		0.42	-	-	-	3.34	0.08	45.10	0.25	-	-	-	-	-	-	-	-	-	49.19
ISTE	Listvenite	46Z-4-46-51	Magnesite	Matrix	Mg-core spheroid	Core		0.10	-	-	-	2.51	-	45.82	0.04	-	-	-	-	-	-	-	-	-	48.47
ISTE	Listvenite	46Z-4-46-51	Magnesite	Matrix	Mg-core spheroid	Core		2.45	-	-	-	6.09	0.28	41.39	0.41	-	-	-	-	-	-	-	-	-	50.62
ISTE	Listvenite	46Z-4-46-51	Magnesite	Matrix	Mg-core spheroid	Core		0.44	-	-	-	3.56	0.07	45.34	0.24	-	-	-	-	-	-	-	-	-	49.65
ISTE	Listvenite	46Z-4-46-51	Magnesite	Matrix	Mg-core spheroid	Core		0.12	-	-	-	2.94	0.03	44.94	0.18	-	-	-	-	-	-	-	-	-	48.21
ISTE	Listvenite	46Z-4-46-51	Magnesite	Matrix	Mg-core spheroid	Internal growth		0.07	-	-	-	2.36	-	46.28	0.03	-	-	-	-	-	-	-	-	-	48.74
ISTE	Listvenite	46Z-4-46-51	Magnesite	Matrix	Mg-core spheroid	Internal growth		2.57	-	-	-	2.49	-	43.30	0.34	-	-	-	-	-	-	-	-	-	48.70
ISTE	Listvenite	46Z-4-46-51	Magnesite	Matrix	Mg-core spheroid	Internal growth		2.27	-	-	-	7.50	0.25	41.55	0.20	-	-	-	-	-	-	-	-	-	51.77
ISTE	Listvenite	46Z-4-46-51	Magnesite	Matrix	Mg-core spheroid	Rim		22.44	-	-	-	11.39	-	26.69	0.49	-	-	-	-	-	-	-	-	-	61.01
ISTE	Listvenite	46Z-4-46-51	Magnesite	Matrix	Mg-core spheroid	Rim		22.99	-	-	-	18.54	0.06	21.48	0.11	-	-	-	-	-	-	-	-	-	63.18
ISTE	Listvenite	46Z-4-46-51	Magnesite	Matrix	Mg-core spheroid	Rim		0.25	-	-	-	3.59	0.10	44.78	0.16	-	-	-	-	-	-	-	-	-	48.88
GM	Listvenite	46Z-4-46-51	Magnesite	Matrix	Mg-core spheroid	Rim	h	3.58	-	0.14	-	4.19	-	40.02	0.93	-	-	-	-	-	-	-	-	-	48.87
GM	Listvenite	46Z-4-46-51	Magnesite	Matrix	Mg-core spheroid	Rim	h	3.09	-	-	-	2.49	-	41.23	0.48	-	-	-	-	-	-	-	-	-	47.29
GM	Listvenite	46Z-4-46-51	Magnesite	Matrix	Mg-core spheroid	Internal growth	h	2.10	-	-	-	2.39	-	42.92	0.24	-	-	-	-	-	-	-	-	-	47.64
GM	Listvenite	46Z-4-46-51	Magnesite	Matrix	Mg-core spheroid	Internal growth	h	0.59	-	-	-	3.51	-	44.50	0.09	-	-	-	-	-	-	-	-	-	48.69
GM	Listvenite	46Z-4-46-51	Magnesite	Matrix	Mg-core spheroid	Internal growth	h	0.14	-	-	-	2.53	-	45.07	0.07	-	-	-	-	-	-	-	-	-	47.82
GM	Listvenite	46Z-4-46-51	Magnesite	Matrix	Mg-core spheroid	Internal growth	h	0.32	-	-	-	2.47	-	44.73	0.44	-	-	-	-	-	-	-	-	-	47.97
GM	Listvenite	46Z-4-46-51	Magnesite	Matrix	Mg-core spheroid	Internal growth	h	7.83	-	-	-	2.56	-	42.40	0.07	-	-	-	-	-	-	-	-	-	52.87
GM	Listvenite	46Z-4-46-51	Magnesite	Matrix	Mg-core spheroid	Internal growth	h	0.21	-	-	-	2.37	-	44.96	0.08	-	-	-	-	-	-	-	-	-	47.61
GM	Listvenite	46Z-4-46-51	Magnesite	Matrix	Mg-core spheroid	Internal growth	h	0.24	-	-	-	2.51	-	45.25	-	-	-	-	-	-	-	-	-	-	47.99
GM	Listvenite	46Z-4-46-51	Magnesite	Matrix	Mg-core spheroid	Internal growth	h	0.17	-	-	-	2.52	-	45.60	0.07	-	-	-	-	-	-	-	-	-	48.37
GM	Listvenite	46Z-4-46-51	Magnesite	Matrix	Mg-core spheroid	Internal growth	h	2.39	-	-	-	2.41	-	44.14	0.07	-	-	-	-	-	-	-	-	-	49.02
GM	Listvenite	46Z-4-46-51	Magnesite	Matrix	Mg-core spheroid	Internal growth	h	2.66	-	-	-	2.40	-	42.20	0.23	-	-	-	-	-	-	-	-	-	47.50
GM	Listvenite	46Z-4-46-51	Magnesite	Matrix	Mg-core spheroid	Internal growth	h	1.86	-	-	-	2.72	-	43.32	0.22	-	-	-	-	-	-	-	-	-	48.12
GM	Listvenite	46Z-4-46-51	Magnesite	Matrix	Mg-core spheroid	Internal growth	h	0.11	-	-	-	2.43	-	44.92	0.09	-	-	-	-	-	-	-	-	-	47.55
GM	Listvenite	46Z-4-46-51	Magnesite	Matrix	Mg-core spheroid	Internal growth	h	2.14	-	-	-	2.36	-	44.15	0.05	-	-	-	-	-	-	-	-	-	48.70
GM	Listvenite	46Z-4-46-51	Magnesite	Matrix	Mg-core spheroid	Internal growth	h	-	-	-	-	2.40	-	45.42	0.07	-	-	-	-	-	-	-	-	-	47.89
GM	Listvenite	46Z-4-46-51	Magnesite	Matrix	Mg-core spheroid	Internal growth	h	-	-	-	-	2.38	-	45.14	0.05	-	-	-	-	-	-	-	-	-	47.57
GM	Listvenite	46Z-4-46-51	Magnesite	Matrix	Mg-core spheroid	Core	h	0.50	-	-	-	3.88	-	44.52	0.10	-	-	-	-	-	-	-	-	-	49.00
GM	Listvenite	46Z-4-46-51	Magnesite	Matrix	Mg-core spheroid	Core	h	-	-	-	-	3.13	-	45.17	0.06	-	-	-	-	-	-	-	-	-	48.36
GM	Listvenite	46Z-4-46-51	Magnesite	Matrix	Mg-core spheroid	Core	h	-	-	-	-	3.70	-	44.97	0.82	-	-	-	-	-	-	-	-	-	49.49
GM	Listvenite	46Z-4-46-51	Magnesite	Matrix	Mg-core spheroid	Core	h	0.30	-	-	-	4.28	-	44.60	0.14	-	-	-	-	-	-	-	-	-	49.32
GM	Listvenite	46Z-4-46-51	Magnesite	Matrix	Mg-core spheroid	Core	h	0.88	-	-	-	4.76	-	43.97	0.11	-	-	-	-	-	-	-	-	-	49.73
GM	Listvenite	46Z-4-46-51	Magnesite	Matrix	Mg-core spheroid	Core	h	0.42	-	-	-	4.56	0.18	44.46	0.22	-	-	-	-	-	-	-	-	-	49.84
GM	Listvenite	46Z-4-46-51	Magnesite	Matrix	Mg-core spheroid	Core	h	0.29	-	-	-	3.91	-	40.85	0.07	-	-	-	-	-	-	-	-	-	45.11
GM	Listvenite	46Z-4-46-51	Magnesite	Matrix	Mg-core spheroid	Core	h	-	-	-	-	2.53	-	45.21	0.08	-	-	-	-	-	-	-	-	-	47.83
GM	Listvenite	46Z-4-46-51	Magnesite	Matrix	Mg-core spheroid	Internal growth	h	0.22	-	-	-	2.72	-	45.18	0.05	-	-	-	-	-	-	-	-	-	48.16
GM	Listvenite	46Z-4-46-51	Magnesite	Matrix	Mg-core spheroid	Internal growth	h	-	-	-	-	3.58	-	44.84	0.05	-	-	-	-	-	-	-	-	-	48.47
GM	Listvenite	46Z-4-46-51	Magnesite	Matrix	Mg-core spheroid	Internal growth	h	0.12	-	-	-	3.45	-	44.95	0.05	-	-	-	-	-	-	-	-	-	48.58
GM	Listvenite	46Z-4-46-51	Magnesite	Matrix	Mg-core spheroid	Internal growth	h	-	-	-	-	3.62	-	44.86	0.16	-	-	-	-	-	-	-	-	-	48.64

GM	Listvenite	46Z-4-46-51	Magnesite	Matrix	Mg-core spheroid	Internal growth	h	0.47	-	-	-	3.59	-	44.62	0.20	-	-	-	-	-	-	-	-	-	48.89
GM	Listvenite	46Z-4-46-51	Magnesite	Matrix	Mg-core spheroid	Internal growth	h	0.45	-	-	-	3.47	-	44.68	0.06	-	-	-	-	-	-	-	-	-	48.66
GM	Listvenite	46Z-4-46-51	Magnesite	Matrix	Mg-core spheroid	Internal growth	h	-	-	-	-	3.46	-	45.08	0.07	-	-	-	-	-	-	-	-	-	48.62
GM	Listvenite	46Z-4-46-51	Magnesite	Matrix	Mg-core spheroid	Internal growth	h	-	-	-	-	3.25	-	45.22	-	-	-	-	-	-	-	-	-	-	48.47
GM	Listvenite	46Z-4-46-51	Magnesite	Matrix	Mg-core spheroid	Internal growth	h	0.19	-	-	-	2.67	-	45.33	-	-	-	-	-	-	-	-	-	-	48.19
GM	Listvenite	46Z-4-46-51	Magnesite	Matrix	Mg-core spheroid	Internal growth	h	0.47	-	-	-	2.50	-	45.29	0.08	-	-	-	-	-	-	-	-	-	48.33
GM	Listvenite	46Z-4-46-51	Magnesite	Matrix	Mg-core spheroid	Internal growth	h	1.65	-	-	-	2.72	-	43.65	0.08	-	-	-	-	-	-	-	-	-	48.10
GM	Listvenite	46Z-4-46-51	Magnesite	Matrix	Mg-core spheroid	Internal growth	h	1.59	-	-	-	2.47	-	42.82	0.37	-	-	-	-	-	-	-	-	-	47.26
GM	Listvenite	46Z-4-46-51	Magnesite	Matrix	Mg-core spheroid	Internal growth	h	1.79	-	-	-	3.01	-	42.31	0.62	-	-	-	-	-	-	-	-	-	47.73
GM	Listvenite	46Z-4-46-51	Magnesite	Matrix	Mg-core spheroid	Rim	h	1.78	-	-	-	3.14	-	42.05	0.77	-	-	-	-	-	-	-	-	-	47.74
GM	Listvenite	46Z-4-46-51	Magnesite	Matrix	Mg-core spheroid	Rim	h	6.03	-	0.20	-	4.05	-	37.64	1.18	-	-	-	-	-	-	-	-	-	49.10
GM	Listvenite	46Z-4-46-51	Magnesite	Matrix	Mg-core spheroid	Rim	i	4.56	-	-	-	17.83	-	32.25	0.82	-	-	-	-	-	-	-	-	-	55.46
GM	Listvenite	46Z-4-46-51	Magnesite	Matrix	Mg-core spheroid	Rim	i	13.03	-	-	-	16.74	-	27.72	0.90	-	-	-	-	-	-	-	-	-	58.39
GM	Listvenite	46Z-4-46-51	Magnesite	Matrix	Mg-core spheroid	Internal growth	i	0.28	-	-	-	10.47	-	39.46	0.94	-	-	-	-	-	-	-	-	-	51.14
GM	Listvenite	46Z-4-46-51	Magnesite	Matrix	Mg-core spheroid	Internal growth	i	7.48	-	0.18	-	3.21	-	38.72	0.75	-	-	-	-	-	-	-	-	-	50.35
GM	Listvenite	46Z-4-46-51	Magnesite	Matrix	Mg-core spheroid	Internal growth	i	3.48	-	0.48	-	2.81	-	41.09	0.41	-	-	-	-	-	-	-	-	-	48.27
GM	Listvenite	46Z-4-46-51	Magnesite	Matrix	Mg-core spheroid	Internal growth	i	2.98	-	-	-	2.36	-	41.70	0.25	-	-	-	-	-	-	-	-	-	47.30
GM	Listvenite	46Z-4-46-51	Magnesite	Matrix	Mg-core spheroid	Internal growth	i	1.28	-	-	-	2.82	-	43.57	0.15	-	0.05	-	-	-	-	-	-	-	47.87
GM	Listvenite	46Z-4-46-51	Magnesite	Matrix	Mg-core spheroid	Internal growth	i	-	-	-	-	2.49	-	45.21	-	-	-	-	-	-	-	-	-	-	47.70
GM	Listvenite	46Z-4-46-51	Magnesite	Matrix	Mg-core spheroid	Internal growth	i	0.16	-	-	-	2.47	-	44.89	-	-	-	-	-	-	-	-	-	-	47.52
GM	Listvenite	46Z-4-46-51	Magnesite	Matrix	Mg-core spheroid	Internal growth	i	0.82	-	-	-	2.43	-	44.70	0.07	-	-	-	-	-	-	-	-	-	48.01
GM	Listvenite	46Z-4-46-51	Magnesite	Matrix	Mg-core spheroid	Internal growth	i	-	-	-	-	2.72	-	44.92	0.05	-	-	-	-	-	-	-	-	-	47.70
GM	Listvenite	46Z-4-46-51	Magnesite	Matrix	Mg-core spheroid	Core	i	-	-	-	-	3.48	-	44.77	-	-	-	-	-	-	-	-	-	-	48.26
GM	Listvenite	46Z-4-46-51	Magnesite	Matrix	Mg-core spheroid	Core	i	1.07	-	-	-	3.60	-	44.06	0.22	-	-	-	-	-	-	-	-	-	48.96
GM	Listvenite	46Z-4-46-51	Magnesite	Matrix	Mg-core spheroid	Core	i	0.69	-	-	-	3.49	-	44.32	0.21	-	-	-	-	-	-	-	-	-	48.70
GM	Listvenite	46Z-4-46-51	Magnesite	Matrix	Mg-core spheroid	Core	i	0.31	-	-	-	3.61	-	44.30	0.21	-	-	-	-	-	-	-	-	-	48.42
GM	Listvenite	46Z-4-46-51	Magnesite	Matrix	Mg-core spheroid	Core	i	0.50	-	-	-	3.61	-	44.46	0.23	-	-	-	-	-	-	-	-	-	48.79
GM	Listvenite	46Z-4-46-51	Magnesite	Matrix	Mg-core spheroid	Core	i	0.58	-	-	-	3.66	-	44.18	0.17	-	-	-	-	-	-	-	-	-	48.59
GM	Listvenite	46Z-4-46-51	Magnesite	Matrix	Mg-core spheroid	Internal growth	i	0.21	-	-	-	3.78	-	43.26	0.16	-	-	-	-	-	-	-	-	-	47.41
GM	Listvenite	46Z-4-46-51	Magnesite	Matrix	Mg-core spheroid	Internal growth	i	0.60	-	-	-	2.76	-	44.73	0.06	-	-	-	-	-	-	-	-	-	48.16
GM	Listvenite	46Z-4-46-51	Magnesite	Matrix	Mg-core spheroid	Internal growth	i	0.14	-	-	-	2.53	-	45.09	0.07	-	-	-	-	-	-	-	-	-	47.82
GM	Listvenite	46Z-4-46-51	Magnesite	Matrix	Mg-core spheroid	Internal growth	i	-	-	-	-	2.37	-	44.85	0.07	-	-	-	-	-	-	-	-	-	47.29
GM	Listvenite	46Z-4-46-51	Magnesite	Matrix	Mg-core spheroid	Internal growth	i	0.09	-	-	-	2.41	-	44.91	0.07	-	-	-	-	-	-	-	-	-	47.47
GM	Listvenite	46Z-4-46-51	Magnesite	Matrix	Mg-core spheroid	Internal growth	i	1.30	-	-	-	2.53	-	43.37	0.10	-	-	-	-	-	-	-	-	-	47.30
GM	Listvenite	46Z-4-46-51	Magnesite	Matrix	Mg-core spheroid	Internal growth	i	2.23	-	-	-	2.31	-	42.12	0.22	-	-	-	-	-	-	-	-	-	46.88
GM	Listvenite	46Z-4-46-51	Magnesite	Matrix	Mg-core spheroid	Internal growth	i	4.64	-	0.16	-	2.79	-	40.64	0.35	-	-	-	-	-	-	-	-	-	48.58
GM	Listvenite	46Z-4-46-51	Magnesite	Matrix	Mg-core spheroid	Rim	i	9.47	-	0.15	-	4.20	-	36.37	0.82	-	-	-	-	-	-	-	-	-	51.00
GM	Listvenite	46Z-4-46-51	Magnesite	Matrix	Mg-core spheroid	Rim	i	6.98	-	-	-	11.15	-	36.02	0.72	-	-	-	-	-	-	-	-	-	54.87
GM	Listvenite	46Z-4-46-51	Magnesite	Matrix	Euhedral	Core		0.12	-	-	-	3.38	-	44.91	1.24	-	-	-	-	-	-	-	-	-	49.66
GM	Listvenite	46Z-4-46-51	Magnesite	Matrix	Aggregate			3.26	-	-	-	15.12	-	38.32	0.40	-	-	-	-	-	-	-	-	-	57.10
GM	Listvenite	46Z-4-46-51	Magnesite	Vein	lc1	Median zone		-	-	-	-	3.12	-	44.67	1.49	-	-	-	-	-	-	-	-	-	49.27
GM	Listvenite	46Z-4-46-51	Magnesite	Vein	lc1	Median zone		3.76	-	-	-	7.95	-	29.63	13.61	-	-	-	-	-	-	-	-	-	54.95
ISTE	Listvenite	46Z-4-46-51	Magnesite	Vein	lc1	Intermediate		0.11	-	-	-	10.21	0.18	39.12	0.52	-	-	-	-	-	-	-	-	-	50.14
ISTE	Listvenite	46Z-4-46-51	Magnesite	Vein	lc1	Intermediate		0.14	-	-	-	4.67	0.13	44.23	0.08	-	-	-	-	-	-	-	-	-	49.25
ISTE	Listvenite	46Z-4-46-51	Magnesite	Vein	lc1	Rim		0.09	-	-	-	2.56	0.04	46.61	0.06	-	-	-	-	-	-	-	-	-	49.36
GM	Listvenite	46Z-4-46-51	Magnesite	Vein	lc1	Rim		-	-	-	-	10.93	0.13	41.35	0.46	-	-	-	-	-	-	-	-	-	52.87
GM	Listvenite	46Z-4-46-51	Magnesite	Vein	lc1	Rim		0.62	-	-	-	9.96	0.25	42.03	0.08	-	-	-	-	-	-	-	-	-	52.94
GM	Listvenite	46Z-4-46-51	Magnesite	Vein	lc1	Rim	j	3.05	-	-	-	4.23	-	40.93	0.20	-	-	-	-	-	-	-	-	-	48.41
GM	Listvenite	46Z-4-46-51	Magnesite	Vein	lc1	Rim	j	1.85	-	-	-	2.72	-	43.04	0.14	-	-	-	-	-	-	-	-	-	47.74
GM	Listvenite	46Z-4-46-51	Magnesite	Vein	lc1	Rim	j	18.58	-	0.31	-	4.23	-	36.51	0.08	-	-	-	-	-	-	-	-	-	59.70
GM	Listvenite	46Z-4-46-51	Magnesite	Vein	lc1	Intermediate	j	0.64	-	-	-	5.44	-	43.09	0.12	-	-	-	-	-	-	-	-	-	49.29
GM	Listvenite	46Z-4-46-51	Magnesite	Vein	lc1	Intermediate	j	1.24	-	-	-	2.71	-	44.72	-	-	-	-	-	-	-	-	-	-	48.67
GM	Listvenite	46Z-4-46-51	Magnesite	Vein	lc1	Intermediate	j	-	-	-	-	2.52	-	45.38	0.05	-	-	-	-	-	-	-	-	-	47.95

GM	Listvenite	46Z-4-46-51	Magnesite	Vein	lc1	Intermediate	j	0.12	-	-	-	2.68	-	45.04	0.11	-	-	-	-	-	-	-	-	-	47.96
GM	Listvenite	46Z-4-46-51	Magnesite	Vein	lc1	Intermediate	j	0.10	-	-	-	3.70	-	45.11	-	-	-	-	-	-	-	-	-	-	48.91
GM	Listvenite	46Z-4-46-51	Magnesite	Vein	lc1	Intermediate	j	3.25	-	-	-	3.41	-	43.80	0.07	-	-	-	-	-	-	-	-	-	50.52
GM	Listvenite	46Z-4-46-51	Magnesite	Vein	lc1	Intermediate	j	2.52	-	-	-	3.49	-	44.02	0.14	-	-	-	-	-	-	-	-	-	50.18
GM	Listvenite	46Z-4-46-51	Magnesite	Vein	lc1	Intermediate	j	0.22	-	-	-	3.65	-	44.93	0.18	-	-	-	-	-	-	-	-	-	48.98
GM	Listvenite	46Z-4-46-51	Magnesite	Vein	lc1	Intermediate	j	0.61	-	-	-	3.67	-	44.88	0.12	-	-	-	-	-	-	-	-	-	49.28
GM	Listvenite	46Z-4-46-51	Magnesite	Vein	lc1	Intermediate	j	0.10	-	-	-	3.74	-	45.01	-	-	-	-	-	-	-	-	-	-	48.85
GM	Listvenite	46Z-4-46-51	Magnesite	Vein	lc1	Intermediate	j	-	-	-	-	2.94	-	45.23	0.07	-	-	-	-	-	-	-	-	-	48.24
GM	Listvenite	46Z-4-46-51	Magnesite	Vein	lc1	Intermediate	j	26.07	-	0.16	-	3.38	-	30.18	0.10	-	-	-	-	-	-	-	-	-	59.90
GM	Listvenite	46Z-4-46-51	Magnesite	Vein	lc1	Intermediate	j	29.03	-	-	-	4.65	-	29.86	0.08	-	-	-	-	-	-	-	-	-	63.62
GM	Listvenite	46Z-4-46-51	Magnesite	Vein	lc1	Intermediate	j	2.13	-	-	-	6.23	-	41.89	0.20	-	-	-	-	-	-	-	-	-	50.45
GM	Listvenite	46Z-4-46-51	Magnesite	Vein	lc1	Intermediate	j	1.17	-	-	-	4.01	-	43.65	0.05	-	-	-	-	-	-	-	-	-	48.89
GM	Listvenite	46Z-4-46-51	Magnesite	Vein	lc1	Intermediate	j	0.23	-	-	-	7.09	0.19	42.31	0.17	-	-	-	-	-	-	-	-	-	49.97
GM	Listvenite	46Z-4-46-51	Magnesite	Vein	lc1	Median zone	j	-	-	-	-	11.83	-	39.24	0.76	-	-	-	-	-	-	-	-	-	51.83
GM	Listvenite	46Z-4-46-51	Magnesite	Vein	lc1	Median zone	j	2.74	-	-	-	15.47	-	35.60	0.52	-	-	-	-	-	-	-	-	-	54.33
GM	Listvenite	46Z-4-46-51	Magnesite	Vein	lc1	Median zone	j	0.20	-	-	-	23.39	0.25	27.65	0.25	-	-	-	-	-	-	-	-	-	51.73
GM	Listvenite	46Z-4-46-51	Magnesite	Vein	lc1	Median zone	j	4.92	-	-	-	20.39	0.28	22.51	0.46	-	-	-	-	-	-	-	-	-	48.56
GM	Listvenite	46Z-4-46-51	Magnesite	Vein	lc1	Intermediate	j	0.78	-	-	-	13.00	-	38.16	0.48	-	-	-	-	-	-	-	-	-	52.43
GM	Listvenite	46Z-4-46-51	Magnesite	Vein	lc1	Intermediate	j	0.11	-	-	-	11.69	-	39.08	0.99	-	-	-	-	-	-	-	-	-	51.88
GM	Listvenite	46Z-4-46-51	Magnesite	Vein	lc1	Intermediate	j	0.20	-	-	-	5.32	-	43.67	-	-	-	-	-	-	-	-	-	-	49.19
GM	Listvenite	46Z-4-46-51	Magnesite	Vein	lc1	Intermediate	j	1.45	-	-	-	3.94	-	43.61	0.11	-	-	-	-	-	-	-	-	-	49.10
GM	Listvenite	46Z-4-46-51	Magnesite	Vein	lc1	Intermediate	j	0.50	-	-	-	5.22	-	43.21	0.14	-	-	-	-	-	-	-	-	-	49.07
GM	Listvenite	46Z-4-46-51	Magnesite	Vein	lc1	Rim	j	2.65	-	-	-	5.66	-	41.19	0.12	-	-	-	-	-	-	-	-	-	49.62
GM	Listvenite	46Z-4-46-51	Magnesite	Vein	lc1	Rim	j	1.34	-	-	-	5.67	-	42.46	0.09	-	-	-	-	-	-	-	-	-	49.56
GM	Listvenite	46Z-4-46-51	Magnesite	Vein	lc1	Rim	j	1.66	-	-	-	2.61	-	43.51	0.09	-	-	-	-	-	-	-	-	-	47.88
GM	Listvenite	46Z-4-46-51	Magnesite	Vein	lc1	Rim	k	17.68	-	-	-	4.64	0.17	34.39	0.26	-	-	-	-	-	-	-	-	-	57.14
GM	Listvenite	46Z-4-46-51	Magnesite	Vein	lc1	Rim	k	0.32	-	-	-	4.95	-	42.32	0.26	-	-	-	-	-	-	-	-	-	47.85
GM	Listvenite	46Z-4-46-51	Magnesite	Vein	lc1	Intermediate	k	0.11	-	-	-	5.27	-	44.08	0.11	-	-	-	-	-	-	-	-	-	49.57
GM	Listvenite	46Z-4-46-51	Magnesite	Vein	lc1	Intermediate	k	-	-	-	-	3.71	-	44.49	0.05	-	-	-	-	-	-	-	-	-	48.25
GM	Listvenite	46Z-4-46-51	Magnesite	Vein	lc1	Intermediate	k	0.14	-	-	-	5.14	-	43.78	0.08	-	-	-	-	-	-	-	-	-	49.15
GM	Listvenite	46Z-4-46-51	Magnesite	Vein	lc1	Intermediate	k	-	-	-	-	7.16	0.27	43.14	0.11	-	-	-	-	-	-	-	-	-	50.67
GM	Listvenite	46Z-4-46-51	Magnesite	Vein	lc1	Median zone	k	0.71	-	-	-	10.97	-	37.19	2.12	-	-	-	-	-	-	-	-	-	50.98
GM	Listvenite	46Z-4-46-51	Dolomite	Vein	lc1	Median zone	k	-	-	-	-	2.33	-	20.04	28.89	-	-	-	-	-	-	-	-	-	51.26
GM	Listvenite	46Z-4-46-51	Dolomite	Vein	lc1	Median zone	k	-	-	-	-	2.34	-	18.86	29.06	-	-	-	-	-	-	-	-	-	50.26
GM	Listvenite	46Z-4-46-51	Dolomite	Vein	lc1	Median zone	k	0.56	-	-	-	4.82	-	21.96	22.73	-	-	-	-	-	-	-	-	-	50.07
GM	Listvenite	46Z-4-46-51	Magnesite	Vein	lc1	Intermediate	k	0.25	-	-	-	4.35	-	43.50	0.18	-	-	-	-	-	-	-	-	-	48.27
GM	Listvenite	46Z-4-46-51	Magnesite	Vein	lc1	Intermediate	k	0.14	-	-	-	4.28	-	43.57	0.15	-	-	-	-	-	-	-	-	-	48.14
GM	Listvenite	46Z-4-46-51	Magnesite	Vein	lc1	Intermediate	k	0.37	-	-	-	9.92	-	40.14	0.49	-	-	-	-	-	-	-	-	-	50.92
GM	Listvenite	46Z-4-46-51	Magnesite	Vein	lc1	Intermediate	k	0.13	-	-	-	7.60	0.21	39.41	0.84	-	-	-	-	-	-	-	-	-	48.19
GM	Listvenite	46Z-4-46-51	Magnesite	Vein	lc1	Intermediate	k	4.88	-	-	-	11.61	-	34.66	0.54	-	-	-	-	-	-	-	-	-	51.69
GM	Listvenite	46Z-4-46-51	Magnesite	Vein	lc1	Intermediate	k	0.44	-	-	-	8.63	-	41.04	0.26	-	-	-	-	-	-	-	-	-	50.37
GM	Listvenite	46Z-4-46-51	Magnesite	Vein	lc1	Intermediate	k	0.18	-	-	-	8.13	-	41.44	0.11	-	-	-	-	-	-	-	-	-	49.86
GM	Listvenite	46Z-4-46-51	Magnesite	Vein	lc1	Intermediate	k	0.55	-	-	-	6.78	0.19	41.89	0.13	-	-	-	-	-	-	-	-	-	49.55
GM	Listvenite	46Z-4-46-51	Magnesite	Vein	lc1	Intermediate	k	0.10	-	-	-	2.59	-	44.64	0.12	-	-	-	-	-	-	-	-	-	47.45
GM	Listvenite	46Z-4-46-51	Magnesite	Vein	lc1	Intermediate	k	0.78	-	-	-	3.71	-	43.01	0.12	-	-	-	-	-	-	-	-	-	47.62
GM	Listvenite	46Z-4-46-51	Magnesite	Vein	lc1	Intermediate	k	3.25	-	-	-	3.25	-	41.13	0.17	-	-	-	-	-	-	-	-	-	47.80
GM	Listvenite	46Z-4-46-51	Magnesite	Vein	lc1	Rim	k	2.31	-	-	-	3.61	-	40.53	0.13	-	-	-	-	-	-	-	-	-	46.59
GM	Listvenite	46Z-4-46-51	Magnesite	Vein	lc1	Rim	k	5.83	-	-	-	6.82	-	35.65	0.34	-	-	-	-	-	-	-	-	-	48.64
GM	Listvenite	46Z-4-46-51	Magnesite	Vein	lc1	Rim	l	2.07	-	-	-	2.53	-	42.63	0.13	-	-	-	-	-	-	-	-	-	47.36
GM	Listvenite	46Z-4-46-51	Magnesite	Vein	lc1	Rim	l	2.81	-	-	-	2.78	-	42.42	0.13	-	-	-	-	-	-	-	-	-	48.15
GM	Listvenite	46Z-4-46-51	Magnesite	Vein	lc1	Intermediate	l	2.77	-	-	-	2.64	-	42.06	0.19	-	-	-	-	-	-	-	-	-	47.67
GM	Listvenite	46Z-4-46-51	Magnesite	Vein	lc1	Intermediate	l	1.21	-	-	-	3.61	-	41.84	0.61	-	-	-	-	-	-	-	-	-	47.26
GM	Listvenite	46Z-4-46-51	Magnesite	Vein	lc1	Intermediate	l	0.11	-	-	-	2.66	-	44.73	0.05	-	-	-	-	-	-	-	-	-	47.55

GM	Listvenite	46Z-4-46-51	Magnesite	Vein	lc1	Intermediate	l	0.16	-	-	-	2.51	-	44.71	0.11	-	-	-	-	-	-	-	-	-	47.50
GM	Listvenite	46Z-4-46-51	Magnesite	Vein	lc1	Intermediate	l	-	-	-	-	2.80	-	45.04	-	-	-	-	-	-	-	-	-	-	47.84
GM	Listvenite	46Z-4-46-51	Magnesite	Vein	lc1	Intermediate	l	0.20	-	-	-	3.69	-	44.54	0.14	-	-	-	-	-	-	-	-	-	48.56
GM	Listvenite	46Z-4-46-51	Magnesite	Vein	lc1	Intermediate	l	-	-	-	-	3.54	-	44.18	0.22	-	-	-	-	-	-	-	-	-	47.94
GM	Listvenite	46Z-4-46-51	Magnesite	Vein	lc1	Median zone	l	2.49	-	-	-	3.51	-	43.05	0.28	-	-	-	-	-	-	-	-	-	49.33
GM	Listvenite	46Z-4-46-51	Magnesite	Vein	lc1	Median zone	l	0.96	-	-	-	3.70	-	43.77	0.31	-	-	-	-	-	-	-	-	-	48.75
GM	Listvenite	46Z-4-46-51	Magnesite	Vein	lc1	Median zone	l	0.33	-	-	-	3.57	-	44.30	0.16	-	-	-	-	-	-	-	-	-	48.36
GM	Listvenite	46Z-4-46-51	Magnesite	Vein	lc1	Median zone	l	0.14	-	-	-	3.91	-	44.36	0.17	-	-	-	-	-	-	-	-	-	48.58
GM	Listvenite	46Z-4-46-51	Magnesite	Vein	lc1	Median zone	l	6.67	-	-	-	7.38	0.25	41.25	0.30	-	-	-	-	-	-	-	-	-	55.85
GM	Listvenite	46Z-4-46-51	Magnesite	Vein	lc1	Median zone	l	0.97	-	-	-	3.13	-	43.62	0.11	-	-	-	-	-	-	-	-	-	47.83
GM	Listvenite	46Z-4-46-51	Magnesite	Vein	lc1	Median zone	l	0.44	-	-	-	3.07	-	44.37	0.08	-	-	-	-	-	-	-	-	-	47.97
GM	Listvenite	46Z-4-46-51	Magnesite	Vein	lc1	Median zone	l	1.18	-	-	-	3.27	-	44.01	0.24	-	-	-	-	-	-	-	-	-	48.70
GM	Listvenite	46Z-4-46-51	Magnesite	Vein	lc1	Intermediate	l	0.60	-	-	-	3.68	-	44.31	0.17	-	-	-	-	-	-	-	-	-	48.76
GM	Listvenite	46Z-4-46-51	Magnesite	Vein	lc1	Intermediate	l	0.76	-	-	-	3.46	-	44.25	0.15	-	-	-	-	-	-	-	-	-	48.62
GM	Listvenite	46Z-4-46-51	Magnesite	Vein	lc1	Intermediate	l	0.15	-	-	-	3.57	-	44.39	-	-	-	-	-	-	-	-	-	-	48.11
GM	Listvenite	46Z-4-46-51	Magnesite	Vein	lc1	Intermediate	l	-	-	-	-	2.69	-	44.68	0.07	-	-	-	-	-	-	-	-	-	47.44
GM	Listvenite	46Z-4-46-51	Magnesite	Vein	lc1	Intermediate	l	-	-	-	-	2.42	-	44.69	0.06	-	-	-	-	-	-	-	-	-	47.18
GM	Listvenite	46Z-4-46-51	Magnesite	Vein	lc1	Intermediate	l	0.67	-	-	-	4.60	-	42.66	0.14	-	-	-	-	-	-	-	-	-	48.08
GM	Listvenite	46Z-4-46-51	Magnesite	Vein	lc1	Intermediate	l	1.60	-	-	-	2.94	-	42.33	0.25	-	-	-	-	-	-	-	-	-	47.12
GM	Listvenite	46Z-4-46-51	Magnesite	Vein	lc1	Intermediate	l	2.88	-	-	-	2.63	-	42.13	0.22	-	-	-	-	-	-	-	-	-	47.86
GM	Listvenite	46Z-4-46-51	Magnesite	Vein	lc1	Intermediate	l	2.92	-	-	-	3.55	-	41.89	0.10	-	-	-	-	-	-	-	-	-	48.46
GM	Listvenite	46Z-4-46-51	Magnesite	Vein	lc1	Intermediate	l	5.41	-	-	-	2.97	-	40.75	0.14	-	-	-	-	-	-	-	-	-	49.26
GM	Listvenite	46Z-4-46-51	Magnesite	Vein	lc1	Rim	l	3.67	-	0.18	-	2.76	-	41.51	0.18	-	-	-	-	-	-	-	-	-	48.30
GM	Listvenite	46Z-4-46-51	Magnesite	Vein	lc1	Rim	l	3.87	-	0.70	-	4.27	-	39.74	0.14	-	-	-	-	-	-	-	-	-	48.72
GM	Listvenite	46Z-4-46-51	Magnesite	Vein	lc1	Rim	m	-	-	-	-	2.54	-	44.89	0.07	-	-	-	-	-	-	-	-	-	47.51
GM	Listvenite	46Z-4-46-51	Magnesite	Vein	lc1	Rim	m	0.10	-	-	-	3.28	-	44.85	0.11	-	-	-	-	-	-	-	-	-	48.34
GM	Listvenite	46Z-4-46-51	Magnesite	Vein	lc1	Intermediate	m	0.17	-	-	-	3.51	-	43.85	0.27	-	-	-	-	-	-	-	-	-	47.80
GM	Listvenite	46Z-4-46-51	Magnesite	Vein	lc1	Intermediate	m	-	-	-	-	3.64	-	44.44	0.17	-	-	-	-	-	-	-	-	-	48.25
GM	Listvenite	46Z-4-46-51	Magnesite	Vein	lc1	Intermediate	m	0.33	-	-	-	3.60	-	43.66	0.19	-	-	-	-	-	-	-	-	-	47.78
GM	Listvenite	46Z-4-46-51	Magnesite	Vein	lc1	Intermediate	m	0.26	-	-	0.12	3.21	-	45.16	-	-	-	-	-	-	-	-	-	-	48.75
GM	Listvenite	46Z-4-46-51	Magnesite	Vein	lc1	Intermediate	m	0.99	-	-	-	5.21	-	42.71	0.09	-	-	-	-	-	-	-	-	-	49.01
GM	Listvenite	46Z-4-46-51	Magnesite	Vein	lc1	Intermediate	m	0.56	-	-	-	3.60	-	43.76	0.21	-	-	-	-	-	-	-	-	-	48.13
GM	Listvenite	46Z-4-46-51	Magnesite	Vein	lc1	Intermediate	m	0.47	-	-	-	3.68	-	44.60	0.17	-	-	-	-	-	-	-	-	-	48.93
GM	Listvenite	46Z-4-46-51	Magnesite	Vein	lc1	Intermediate	m	0.19	-	-	-	3.65	-	44.23	0.19	-	-	-	-	-	-	-	-	-	48.26
GM	Listvenite	46Z-4-46-51	Magnesite	Vein	lc1	Intermediate	m	14.97	-	-	0.14	2.79	-	38.11	0.19	-	-	-	-	-	-	-	-	-	56.19
GM	Listvenite	46Z-4-46-51	Magnesite	Vein	lc1	Intermediate	m	2.49	-	-	-	3.66	-	43.02	0.28	-	-	-	-	-	-	-	-	-	49.45
GM	Listvenite	46Z-4-46-51	Magnesite	Vein	lc1	Intermediate	m	1.49	-	-	0.11	3.78	-	42.96	0.44	-	-	-	-	-	-	-	-	-	48.79
GM	Listvenite	46Z-4-46-51	Magnesite	Vein	lc1	Intermediate	m	2.70	-	-	-	3.65	-	42.61	0.37	-	-	-	-	-	-	-	-	-	49.33
GM	Listvenite	46Z-4-46-51	Magnesite	Vein	lc1	Intermediate	m	1.01	-	-	0.12	3.78	-	43.61	0.33	-	-	-	-	-	-	-	-	-	48.85
GM	Listvenite	46Z-4-46-51	Magnesite	Vein	lc1	Intermediate	m	0.09	-	-	-	2.95	-	44.54	0.14	-	-	-	-	-	-	-	-	-	47.73
GM	Listvenite	46Z-4-46-51	Magnesite	Vein	lc1	Intermediate	m	12.11	-	-	-	6.79	-	35.11	0.22	-	-	-	-	-	-	-	-	-	54.21
GM	Listvenite	46Z-4-46-51	Magnesite	Vein	lc1	Median zone	m	0.13	-	-	-	11.80	-	38.75	1.00	-	-	-	-	-	-	-	-	-	51.68
GM	Listvenite	46Z-4-46-51	Magnesite	Vein	lc1	Median zone	m	-	-	-	-	11.64	-	39.11	0.91	-	-	-	-	-	-	-	-	-	51.66
GM	Listvenite	46Z-4-46-51	Dolomite	Vein	lc1	Median zone	m	0.19	-	-	-	5.74	-	24.41	20.51	-	-	-	-	-	-	-	-	-	50.86
GM	Listvenite	46Z-4-46-51	Dolomite	Vein	lc1	Median zone	m	0.10	-	-	-	2.42	-	18.51	28.08	-	-	-	-	-	-	-	-	-	49.10
GM	Listvenite	46Z-4-46-51	Dolomite	Vein	lc1	Median zone	m	-	-	-	-	2.26	-	19.26	28.48	-	-	-	-	-	-	-	-	-	49.99
GM	Listvenite	46Z-4-46-51	Magnesite	Vein	lc1	Median zone	m	0.24	-	-	-	10.47	-	33.31	6.53	-	-	-	-	-	-	-	-	-	50.55
GM	Listvenite	46Z-4-46-51	Magnesite	Vein	lc1	Median zone	m	0.14	-	-	-	8.78	0.20	41.01	0.17	-	-	-	-	-	-	-	-	-	50.31
GM	Listvenite	46Z-4-46-51	Magnesite	Vein	lc1	Median zone	m	0.51	-	-	-	6.27	-	41.71	0.17	-	-	-	-	-	-	-	-	-	48.66
GM	Listvenite	46Z-4-46-51	Magnesite	Vein	lc1	Intermediate	m	9.68	-	-	-	4.92	-	37.15	0.17	-	-	-	-	-	-	-	-	-	51.92
GM	Listvenite	46Z-4-46-51	Magnesite	Vein	lc1	Intermediate	m	0.26	-	-	0.15	3.09	-	43.80	0.24	-	-	-	-	-	-	-	-	-	47.54
GM	Listvenite	46Z-4-46-51	Magnesite	Vein	lc1	Intermediate	m	0.69	-	-	0.16	3.79	-	43.43	0.28	-	-	-	-	-	-	-	-	-	48.36
GM	Listvenite	46Z-4-46-51	Magnesite	Vein	lc1	Intermediate	m	0.44	-	-	-	3.57	-	43.20	0.34	-	-	-	-	-	-	-	-	-	47.56

GM	Listvenite	46Z-4-46-51	Magnesite	Vein	lc1	Intermediate	m	1.08	-	-	-	3.65	-	42.54	0.52	-	-	-	-	-	-	-	-	-	47.79
GM	Listvenite	46Z-4-46-51	Magnesite	Vein	lc1	Intermediate	m	0.58	-	-	0.16	3.90	-	43.54	0.29	-	-	-	-	-	-	-	-	-	48.46
GM	Listvenite	46Z-4-46-51	Magnesite	Vein	lc1	Intermediate	m	0.77	-	-	0.17	3.88	-	43.52	0.32	-	-	-	-	-	-	-	-	-	48.66
GM	Listvenite	46Z-4-46-51	Magnesite	Vein	lc1	Intermediate	m	0.94	-	-	0.16	4.53	-	42.60	0.53	-	-	-	-	-	-	-	-	-	48.76
GM	Listvenite	46Z-4-46-51	Magnesite	Vein	lc1	Intermediate	m	0.33	-	-	0.13	7.35	-	41.23	0.44	-	-	-	-	-	-	-	-	-	49.48
GM	Listvenite	46Z-4-46-51	Magnesite	Vein	lc1	Intermediate	m	0.25	-	-	0.14	4.89	-	43.28	0.42	-	-	-	-	-	-	-	-	-	48.99
GM	Listvenite	46Z-4-46-51	Magnesite	Vein	lc1	Intermediate	m	0.86	-	0.35	0.18	5.09	-	41.88	0.21	-	0.09	-	-	-	-	-	-	-	48.66
GM	Listvenite	46Z-4-46-51	Magnesite	Vein	lc1	Rim	m	2.58	-	1.28	0.25	7.10	-	38.15	0.26	-	0.33	-	-	-	-	-	-	-	49.96
GM	Listvenite	46Z-4-46-51	Magnesite	Vein	lc1	Rim	m	0.13	-	-	-	4.14	-	43.67	0.13	-	-	-	-	-	-	-	-	-	48.07
GM	Listvenite	46Z-4-46-51	Magnesite	Vein	lc2	Median zone		1.09	-	0.13	-	5.98	-	43.52	0.28	-	-	1.54	-	-	-	-	-	-	52.55
ISTE	Listvenite	46Z-4-46-51	Magnesite	Vein	lq4	Rim		0.07	-	-	-	6.25	0.12	42.19	1.14	-	-	-	-	-	-	-	-	-	49.77
ISTE	Listvenite	46Z-4-46-51	Magnesite	Vein	lq4	Rim		0.21	-	-	-	6.40	0.12	41.03	1.70	-	-	-	-	-	-	-	-	-	49.46
ISTE	Listvenite	48Z-1-6-11	Magnesite	Matrix	Mg-core spheroid	Core		0.05	-	-	-	1.26	0.10	47.34	0.12	-	-	-	-	-	-	-	-	-	48.86
ISTE	Listvenite	48Z-1-6-11	Magnesite	Matrix	Mg-core spheroid	Core		0.02	-	-	-	2.06	0.10	46.13	0.44	-	-	-	-	-	-	-	-	-	48.74
ISTE	Listvenite	48Z-1-6-11	Magnesite	Matrix	Mg-core spheroid	Core		0.55	-	-	-	1.70	0.07	46.22	0.35	-	-	-	-	-	-	-	-	-	48.88
ISTE	Listvenite	48Z-1-6-11	Magnesite	Matrix	Mg-core spheroid	Core		3.28	-	-	-	7.28	0.53	42.27	0.25	-	-	-	-	-	-	-	-	-	53.60
ISTE	Listvenite	48Z-1-6-11	Magnesite	Matrix	Mg-core spheroid	Internal growth		0.20	-	-	-	20.55	0.12	31.23	0.37	-	-	-	-	-	-	-	-	-	52.47
ISTE	Listvenite	48Z-1-6-11	Magnesite	Matrix	Mg-core spheroid	Rim		0.02	-	-	-	3.09	-	44.37	0.10	-	-	-	-	-	-	-	-	-	47.57
ISTE	Listvenite	48Z-1-6-11	Magnesite	Matrix	Aggregate			0.16	-	-	-	1.73	0.04	44.52	0.24	-	-	-	-	-	-	-	-	-	46.69
ISTE	Listvenite	48Z-1-6-11	Magnesite	Vein	lss0	Median zone		8.83	-	-	-	13.24	0.10	35.30	0.29	-	-	-	-	-	-	-	-	-	57.76
ISTE	Listvenite	48Z-1-6-11	Magnesite	Vein	lss0	Median zone		0.43	-	-	-	23.60	0.13	27.14	0.46	-	-	-	-	-	-	-	-	-	51.77
ISTE	Listvenite	48Z-1-6-11	Magnesite	Vein	lss0	Rim		0.03	-	-	-	2.40	-	45.55	0.05	-	-	-	-	-	-	-	-	-	48.04
ISTE	Listvenite	48Z-1-6-11	Magnesite	Vein	lss0	Rim		0.07	-	-	-	2.19	-	46.24	0.15	-	-	-	-	-	-	-	-	-	48.65
ISTE	Listvenite	48Z-1-6-11	Magnesite	Vein	lss0	Rim		0.04	-	-	-	3.06	-	44.46	0.11	-	-	-	-	-	-	-	-	-	47.67
ISTE	Listvenite	48Z-1-6-11	Magnesite	Vein	lss2	Median zone		0.49	-	-	-	1.85	0.99	46.20	0.31	-	-	-	-	-	-	-	-	-	49.85
ISTE	Listvenite	48Z-1-6-11	Magnesite	Vein	lss2	Median zone		0.13	-	-	-	1.93	0.74	46.12	0.17	-	-	-	-	-	-	-	-	-	49.09
ISTE	Listvenite	48Z-1-6-11	Magnesite	Vein	lss2	Median zone		0.33	-	-	-	2.04	0.58	46.25	0.08	-	-	-	-	-	-	-	-	-	49.29
ISTE	Listvenite	48Z-1-6-11	Magnesite	Vein	lss2	Rim		5.24	-	-	-	10.00	0.15	37.67	0.25	-	-	-	-	-	-	-	-	-	53.32
ISTE	Listvenite	48Z-1-6-11	Magnesite	Vein	lc1	Median zone		-	-	-	-	7.39	0.07	42.04	0.03	-	-	-	-	-	-	-	-	-	49.53
ISTE	Listvenite	48Z-1-6-11	Magnesite	Vein	lc1	Median zone		-	-	-	-	3.87	0.03	44.14	0.21	-	-	-	-	-	-	-	-	-	48.26
ISTE	Listvenite	48Z-1-6-11	Magnesite	Vein	lc1	Median zone		0.02	-	-	-	7.29	0.06	42.13	0.64	-	-	-	-	-	-	-	-	-	50.14
ISTE	Listvenite	48Z-1-6-11	Magnesite	Vein	lc1	Median zone		1.65	-	-	-	31.15	0.09	23.93	0.37	-	-	-	-	-	-	-	-	-	57.20
ISTE	Listvenite	48Z-1-6-11	Magnesite	Vein	lc1	Median zone		0.34	-	-	-	17.98	0.16	33.89	0.20	-	-	-	-	-	-	-	-	-	52.57
ISTE	Listvenite	48Z-1-6-11	Magnesite	Vein	lc1	Intermediate		0.04	-	-	-	26.82	0.18	26.79	0.46	-	-	-	-	-	-	-	0.09	-	54.37
ISTE	Listvenite	48Z-1-6-11	Magnesite	Vein	lc1	Intermediate		0.10	-	-	-	24.65	0.12	28.86	0.33	-	-	-	-	-	-	-	-	-	54.05
ISTE	Listvenite	48Z-1-6-11	Magnesite	Vein	lc1	Rim		1.27	-	-	-	5.52	0.11	43.17	0.22	-	-	-	-	-	-	-	-	-	50.29
GM	Listvenite	50Z-1-75-80	Magnesite	Matrix	Mg-core spheroid	Core		-	-	-	-	3.68	-	46.11	0.13	-	-	0.20	-	-	-	-	-	-	50.13
ISTE	Listvenite	50Z-1-75-80	Magnesite	Matrix	Fe-core spheroid	Core		1.62	-	-	-	11.76	0.19	38.05	0.28	-	-	-	-	-	-	-	-	-	51.91
ISTE	Listvenite	50Z-1-75-80	Magnesite	Matrix	Fe-core spheroid	Core		2.75	-	-	-	21.62	0.20	29.34	0.63	-	-	-	-	-	-	-	-	-	54.54
ISTE	Listvenite	50Z-1-75-80	Magnesite	Matrix	Fe-core spheroid	Core		2.01	-	-	-	22.49	0.20	27.87	0.80	-	-	-	-	-	-	-	-	-	53.37
ISTE	Listvenite	50Z-1-75-80	Magnesite	Matrix	Fe-core spheroid	Internal growth		0.55	-	-	-	20.37	0.21	31.17	0.28	-	-	-	-	-	-	-	-	-	52.58
ISTE	Listvenite	50Z-1-75-80	Magnesite	Matrix	Fe-core spheroid	Internal growth		0.33	-	-	-	10.93	0.24	39.06	0.32	-	-	-	-	-	-	-	-	-	50.88
ISTE	Listvenite	50Z-1-75-80	Magnesite	Matrix	Fe-core spheroid	Internal growth		0.07	-	-	-	2.77	-	45.30	0.15	-	-	-	-	-	-	-	-	-	48.29
ISTE	Listvenite	50Z-1-75-80	Magnesite	Matrix	Fe-core spheroid	Rim		0.38	-	-	-	2.95	-	45.23	0.24	-	-	-	-	-	-	-	-	-	48.80
ISTE	Listvenite	50Z-1-75-80	Magnesite	Matrix	Fe-core spheroid	Rim		0.39	-	-	-	2.83	-	45.58	0.14	-	-	-	-	-	-	-	-	-	48.93
ISTE	Listvenite	50Z-1-75-80	Magnesite	Vein	lss2	Median zone		0.08	-	-	-	3.10	0.06	45.54	0.05	-	-	-	-	-	-	-	-	-	48.84
ISTE	Listvenite	50Z-1-75-80	Magnesite	Vein	lss2	Median zone		0.15	-	-	-	2.89	0.08	44.91	0.36	-	-	-	-	-	-	-	-	-	48.40
ISTE	Listvenite	50Z-1-75-80	Magnesite	Vein	lss2	Rim		0.18	-	-	-	2.77	-	44.17	0.17	-	-	-	-	-	-	-	-	-	47.30
ISTE	Listvenite	50Z-1-75-80	Magnesite	Vein	lss2	Median zone		0.04	-	-	-	1.69	0.09	46.66	0.18	-	-	-	-	-	-	-	-	-	48.66
ISTE	Listvenite	50Z-1-75-80	Magnesite	Vein	lss2	Rim		0.21	-	-	-	7.17	0.12	41.82	0.19	-	-	-	-	-	-	-	-	-	49.51
ISTE	Listvenite	50Z-1-75-80	Magnesite	Matrix	Aggregate			0.12	-	-	-	2.22	0.06	45.90	0.14	-	-	-	-	-	-	-	-	-	48.44
ISTE	Listvenite	50Z-1-75-80	Magnesite	Vein	lss2	Median zone		0.19	-	-	-	2.10	0.10	46.41	0.35	-	-	-	-	-	-	-	-	-	49.15
ISTE	Listvenite	50Z-1-75-80	Magnesite	Vein	lss2	Median zone		0.66	-	-	-	2.04	1.55	45.07	0.10	-	-	-	-	-	-	-	-	-	49.42

GM	Fu-listvenite	53Z-2-72-77	Magnesite	Matrix	Mg-core spheroid	Core	-	-	-	-	4.38	-	45.39	0.09	-	-	-	-	-	-	-	-	-	49.87
GM	Fu-listvenite	53Z-2-72-77	Magnesite	Matrix	Mg-core spheroid	Core	-	-	-	-	4.97	-	44.04	0.88	-	-	-	-	-	-	-	-	-	49.89
GM	Fu-listvenite	53Z-2-72-77	Magnesite	Matrix	Mg-core spheroid	Core	-	-	-	-	4.32	-	44.81	0.44	-	-	-	-	-	-	-	-	-	49.57
GM	Fu-listvenite	53Z-2-72-77	Magnesite	Matrix	Mg-core spheroid	Core	0.67	-	0.26	0.20	4.96	-	43.57	0.49	-	-	0.17	-	-	-	-	-	-	50.32
GM	Fu-listvenite	53Z-2-72-77	Magnesite	Matrix	Mg-core spheroid	Internal growth	-	-	-	-	4.35	-	44.55	1.01	-	-	-	-	-	-	-	-	-	49.91
GM	Fu-listvenite	53Z-2-72-77	Magnesite	Matrix	Mg-core spheroid	Internal growth	-	-	-	-	4.20	-	44.60	0.62	-	-	-	-	-	-	-	-	-	49.42
GM	Fu-listvenite	53Z-2-72-77	Magnesite	Matrix	Mg-core spheroid	Internal growth	-	-	-	-	4.70	-	45.01	0.78	-	-	-	-	-	-	-	-	-	50.49
GM	Fu-listvenite	53Z-2-72-77	Magnesite	Matrix	Mg-core spheroid	Internal growth	-	-	-	-	4.32	-	44.97	0.51	-	-	-	-	-	-	-	-	-	49.80
GM	Fu-listvenite	53Z-2-72-77	Magnesite	Matrix	Mg-core spheroid	Internal growth	0.16	-	-	-	4.28	-	45.24	0.36	-	-	-	-	-	-	-	-	-	50.03
GM	Fu-listvenite	53Z-2-72-77	Magnesite	Matrix	Mg-core spheroid	Internal growth	-	-	-	0.21	4.75	0.11	44.96	0.25	-	-	-	-	-	-	-	-	-	50.28
GM	Fu-listvenite	53Z-2-72-77	Magnesite	Matrix	Mg-core spheroid	Rim	-	-	-	-	4.47	-	45.09	0.27	-	-	-	-	-	-	-	-	-	49.84
GM	Fu-listvenite	53Z-2-72-77	Magnesite	Matrix	Mg-core spheroid	Rim	-	-	-	-	4.75	-	45.41	0.08	-	-	-	-	-	-	-	-	-	50.23
GM	Fu-listvenite	53Z-2-72-77	Magnesite	Matrix	Mg-core spheroid	Rim	-	-	-	-	3.92	-	44.93	0.46	-	-	-	-	-	-	-	-	-	49.30
GM	Fu-listvenite	53Z-2-72-77	Magnesite	Matrix	Mg-core spheroid	Rim	-	-	-	-	4.11	-	44.88	0.20	-	-	-	-	-	-	-	-	-	49.20
GM	Fu-listvenite	53Z-2-72-77	Magnesite	Matrix	Aggregate	Core	1.14	-	-	-	8.03	0.97	42.36	0.12	-	-	-	-	-	-	-	-	-	52.62
GM	Fu-listvenite	53Z-2-72-77	Magnesite	Matrix	Aggregate	Core	1.11	-	-	-	5.17	0.12	44.31	0.20	-	-	-	-	-	-	-	-	-	50.90
GM	Fu-listvenite	53Z-2-72-77	Magnesite	Matrix	Aggregate	Core	0.10	-	-	0.24	4.89	-	45.25	0.19	-	-	-	-	-	-	-	-	-	50.67
GM	Fu-listvenite	53Z-2-72-77	Magnesite	Matrix	Aggregate	Intermediate	6.53	-	-	-	4.37	-	42.17	0.27	-	-	-	-	-	-	-	-	-	53.35
GM	Fu-listvenite	53Z-2-72-77	Magnesite	Matrix	Aggregate	Rim	1.96	-	-	-	4.61	-	43.58	0.25	-	-	-	-	-	-	-	-	-	50.40
GM	Fu-listvenite	53Z-2-72-77	Magnesite	Vein	lc1	Median zone	0.11	-	-	-	6.21	-	44.20	0.56	-	-	-	-	-	-	-	-	-	51.09
GM	Fu-listvenite	53Z-2-72-77	Magnesite	Vein	lc1	Median zone	-	-	-	-	5.88	0.15	44.88	0.10	-	-	-	-	-	-	-	-	-	51.01
GM	Fu-listvenite	53Z-2-72-77	Magnesite	Vein	lc1	Median zone	0.46	-	-	-	8.54	0.36	42.62	0.21	-	-	-	-	-	-	-	-	-	52.18
GM	Fu-listvenite	53Z-2-72-77	Magnesite	Vein	lc1	Intermediate	0.69	-	-	-	5.12	0.37	44.67	-	-	-	-	-	-	-	-	-	-	50.84
GM	Fu-listvenite	53Z-2-72-77	Magnesite	Vein	lc1	Intermediate	-	-	-	-	4.93	-	45.28	0.17	-	-	-	-	-	-	-	-	-	50.38
GM	Fu-listvenite	53Z-2-72-77	Magnesite	Vein	lc1	Rim	-	-	-	-	4.39	-	45.26	0.47	-	-	-	-	-	-	-	-	-	50.13
GM	Fu-listvenite	53Z-2-72-77	Magnesite	Vein	lc5-6?	Median zone	-	-	-	-	3.31	-	46.02	0.15	-	-	-	-	-	-	-	-	-	49.48
GM	Fu-listvenite	53Z-2-72-77	Magnesite	Vein	lc5-6?	Median zone	-	-	-	-	3.72	-	45.62	0.35	-	-	-	-	-	-	-	-	-	49.69
ISTE	Fu-listvenite	53Z-4-35-40	Magnesite	Matrix	Aggregate		0.65	-	-	-	8.25	0.15	41.38	0.13	-	-	-	-	-	-	-	-	-	50.55
ISTE	Fu-listvenite	53Z-4-35-40	Magnesite	Matrix	Aggregate		0.18	-	-	-	10.26	0.17	39.73	0.22	-	-	-	-	-	-	-	-	-	50.56
ISTE	Fu-listvenite	53Z-4-35-40	Magnesite	Matrix	Aggregate		0.11	-	-	-	11.18	0.19	39.14	0.26	-	-	-	-	-	-	-	-	-	50.88
ISTE	Fu-listvenite	53Z-4-35-40	Magnesite	Matrix	Aggregate		0.18	-	-	-	11.84	0.22	38.48	0.14	-	-	-	-	-	-	-	-	0.03	50.90
ISTE	Fu-listvenite	53Z-4-35-40	Magnesite	Matrix	Aggregate		0.93	-	-	-	6.48	-	41.15	0.94	-	-	-	-	-	-	-	-	0.03	49.53
ISTE	Fu-listvenite	53Z-4-35-40	Magnesite	Matrix	Aggregate		0.05	-	-	-	7.22	0.14	42.58	0.14	-	-	-	-	-	-	-	-	-	50.13
ISTE	Fu-listvenite	53Z-4-35-40	Magnesite	Vein	lss0	Median zone	0.02	-	-	-	10.81	0.58	39.38	0.05	-	-	-	-	-	-	-	-	-	50.85
ISTE	Fu-listvenite	53Z-4-35-40	Magnesite	Vein	lss0	Rim	1.11	-	-	-	8.51	0.20	40.54	0.32	-	-	-	-	-	-	-	-	-	50.68
ISTE	Fu-listvenite	55Z-1-55-60	Dolomite	Vein	lc1	Median zone	-	-	-	-	4.28	0.13	26.32	21.46	-	-	-	-	-	-	-	-	-	52.19
ISTE	Fu-listvenite	55Z-1-55-60	Magnesite	Matrix	Mg-core spheroid	Core	0.18	-	-	-	6.14	0.27	41.11	0.41	-	-	-	-	-	-	-	-	-	48.10
ISTE	Fu-listvenite	55Z-1-55-60	Magnesite	Matrix	Mg-core spheroid	Core	0.94	-	-	-	2.73	0.05	44.49	0.07	-	-	-	-	-	-	-	-	-	48.27
ISTE	Fu-listvenite	55Z-1-55-60	Magnesite	Matrix	Mg-core spheroid	Core	0.13	-	-	-	2.58	0.05	43.81	0.63	-	-	-	-	-	-	-	-	-	47.21
ISTE	Fu-listvenite	55Z-1-55-60	Magnesite	Matrix	Euhedral	Core	0.02	-	-	-	3.73	0.11	43.35	0.67	-	-	-	-	-	-	-	-	-	47.88
ISTE	Fu-listvenite	55Z-1-55-60	Magnesite	Matrix	Euhedral	Core	0.02	-	-	-	3.78	0.12	42.65	0.96	-	-	-	-	-	-	-	-	-	47.53
ISTE	Fu-listvenite	55Z-1-55-60	Magnesite	Matrix	Aggregate		0.02	-	-	-	4.90	0.18	43.68	0.67	-	-	-	-	-	-	-	-	-	49.45
ISTE	Fu-listvenite	55Z-1-55-60	Magnesite	Matrix	Aggregate		0.25	-	-	-	5.04	0.17	43.79	0.36	-	-	-	-	-	-	-	-	-	49.61
ISTE	Fu-listvenite	55Z-1-55-60	Magnesite	Matrix	Aggregate		0.02	-	-	-	4.69	0.15	42.99	0.49	-	-	-	-	-	-	-	-	-	48.33
ISTE	Fu-listvenite	55Z-1-55-60	Magnesite	Matrix	Aggregate		2.09	-	-	-	4.41	0.17	42.77	0.52	-	-	-	-	-	-	-	-	-	49.96
ISTE	Fu-listvenite	55Z-1-55-60	Magnesite	Matrix	Aggregate		-	-	-	-	4.43	0.16	43.68	0.67	-	-	-	-	-	-	-	-	-	48.94
ISTE	Fu-listvenite	55Z-1-55-60	Magnesite	Matrix	Aggregate		0.13	-	-	-	4.86	0.17	43.65	0.24	-	-	-	-	-	-	-	0.10	-	49.15
ISTE	Fu-listvenite	55Z-1-55-60	Magnesite	Matrix	Aggregate		4.31	-	-	-	10.84	0.35	36.74	0.87	-	-	-	-	-	-	-	-	-	53.11
ISTE	Fu-listvenite	55Z-1-55-60	Magnesite	Vein	lss0	Median zone	0.47	-	-	-	12.02	0.31	36.68	0.23	-	-	-	-	-	-	-	-	-	49.70
ISTE	Fu-listvenite	55Z-1-55-60	Magnesite	Vein	lss0	Intermediate	-	-	-	-	9.47	0.43	38.78	0.25	-	-	-	-	-	-	-	-	-	48.94
ISTE	Fu-listvenite	55Z-1-55-60	Magnesite	Vein	lss0	Rim	0.02	-	-	-	4.82	0.17	42.23	0.88	-	-	-	-	-	-	-	-	-	48.12
ISTE	Fu-listvenite	55Z-1-55-60	Magnesite	Vein	lc1	Median zone	0.02	-	-	-	7.79	0.13	40.69	0.17	-	-	-	-	-	-	-	-	-	48.80
ISTE	Fu-listvenite	55Z-1-55-60	Magnesite	Vein	lc1	Median zone	0.70	-	-	-	4.82	0.18	42.79	0.38	-	-	-	-	-	-	-	-	-	48.87

ISTE	Fu-listvenite	55Z-1-55-60	Magnesite	Vein	lc1	Median zone	0.15	-	-	-	15.47	0.14	34.18	0.52	-	-	-	-	-	-	-	-	-	50.46
ISTE	Fu-listvenite	55Z-1-55-60	Magnesite	Vein	lc1	Intermediate	0.03	-	-	-	9.95	0.41	38.49	0.56	-	-	-	-	-	-	-	-	-	49.44
ISTE	Fu-listvenite	55Z-1-55-60	Magnesite	Vein	lc1	Intermediate	0.02	-	-	-	14.58	0.26	35.39	0.56	-	-	-	-	-	-	-	-	-	50.82
ISTE	Fu-listvenite	55Z-1-55-60	Magnesite	Vein	lc1	Intermediate	0.21	-	-	-	6.16	0.16	42.98	0.16	-	-	-	-	-	-	-	-	-	49.67
ISTE	Fu-listvenite	55Z-1-55-60	Magnesite	Vein	lc1	Intermediate	0.30	-	-	-	15.57	0.25	35.86	0.25	-	-	-	-	-	-	-	-	-	52.24
ISTE	Fu-listvenite	55Z-1-55-60	Magnesite	Vein	lc1	Intermediate	0.23	-	-	-	4.91	0.10	43.66	0.53	-	-	-	-	-	-	-	-	-	49.43
ISTE	Fu-listvenite	55Z-1-55-60	Magnesite	Vein	lc1	Intermediate	2.29	-	-	-	14.97	0.24	35.48	0.37	-	-	-	-	-	-	-	-	-	53.35
ISTE	Fu-listvenite	55Z-1-55-60	Magnesite	Vein	lc1	Rim	0.03	-	-	-	8.64	0.38	41.19	0.29	-	-	-	-	-	-	-	-	-	50.53
ISTE	Fu-listvenite	55Z-1-55-60	Magnesite	Vein	lc1	Rim	0.05	-	-	-	7.26	0.23	42.19	0.33	-	-	-	-	-	-	-	-	-	50.07
ISTE	Fu-listvenite	55Z-1-55-60	Magnesite	Vein	lc1	Rim	0.05	-	-	-	2.84	0.05	44.48	0.25	-	-	-	-	-	-	-	-	-	47.68
ISTE	Fu-listvenite	55Z-1-55-60	Magnesite	Vein	lc1	Rim	0.01	-	-	-	5.13	0.10	43.36	-	-	-	-	-	-	-	-	-	-	48.60
ISTE	Fu-listvenite	55Z-1-55-60	Magnesite	Vein	lc1	Overgrowth	0.11	-	-	-	5.65	0.17	42.17	0.52	-	-	-	-	-	-	-	-	-	48.63
ISTE	Fu-listvenite	55Z-1-55-60	Dolomite	Vein	lc6	Median zone	-	-	-	-	2.62	0.09	19.67	28.47	-	-	-	-	-	-	-	-	-	50.85
ISTE	Fu-listvenite	55Z-1-55-60	Dolomite	Vein	lc6	Median zone	-	-	-	-	4.08	0.11	18.51	28.05	-	-	-	-	-	-	-	-	-	50.75
GM	Fu-listvenite	60Z-1-32-37	Dolomite	Matrix	Spheroid	Core	0.08	-	-	-	3.57	0.18	18.70	27.59	-	-	-	-	-	-	-	-	-	50.11
GM	Fu-listvenite	60Z-1-32-37	Dolomite	Matrix	Spheroid	Core	2.59	-	1.28	0.37	2.25	-	19.08	26.89	-	0.34	-	-	-	-	-	-	-	52.80
GM	Fu-listvenite	60Z-1-32-37	Dolomite	Matrix	Spheroid	Core	2.29	-	1.44	0.46	3.70	0.14	23.14	26.01	-	0.23	-	-	-	-	-	-	-	57.40
GM	Fu-listvenite	60Z-1-32-37	Dolomite	Matrix	Spheroid	Rim	-	-	-	-	2.73	-	20.53	32.01	-	-	-	-	-	-	-	-	-	55.27
ISTE	Fu-listvenite	60Z-1-32-37	Dolomite	Vein	lc6	Median zone	-	-	-	-	2.07	0.12	20.99	27.24	-	-	-	-	-	-	-	-	-	50.42
GM	Fu-listvenite	60Z-1-32-37	Dolomite	Vein	lc6	Median zone	-	-	-	-	1.81	0.15	24.72	30.14	-	-	-	-	-	-	-	-	-	56.82
GM	Fu-listvenite	60Z-1-32-37	Magnesite	Matrix	Mg-core spheroid	Core	0.66	-	-	-	6.28	-	43.96	0.46	-	-	-	-	-	-	-	-	0.01	51.37
GM	Fu-listvenite	60Z-1-32-37	Magnesite	Matrix	Mg-core spheroid	Core	0.16	-	-	-	5.91	-	44.84	0.17	-	-	-	-	-	-	-	-	0.02	51.09
GM	Fu-listvenite	60Z-1-32-37	Magnesite	Matrix	Mg-core spheroid	Core	0.77	-	-	-	6.45	-	43.81	0.20	-	-	-	-	-	-	-	-	-	51.23
ISTE	Fu-listvenite	60Z-1-32-37	Magnesite	Matrix	Mg-core spheroid	Core	1.77	-	-	-	6.09	0.10	42.76	0.35	-	-	-	-	-	-	-	-	-	51.08
ISTE	Fu-listvenite	60Z-1-32-37	Magnesite	Matrix	Mg-core spheroid	Core	6.00	-	-	-	4.95	0.09	45.99	0.30	-	-	-	-	-	-	-	0.09	-	57.42
ISTE	Fu-listvenite	60Z-1-32-37	Magnesite	Matrix	Mg-core spheroid	Core	3.68	-	-	-	3.64	0.06	43.83	0.30	-	-	-	-	-	-	-	-	-	51.51
GM	Fu-listvenite	60Z-1-32-37	Magnesite	Matrix	Mg-core spheroid	Core	3.58	-	-	-	4.04	-	43.63	0.36	-	-	-	-	-	-	-	-	-	51.61
GM	Fu-listvenite	60Z-1-32-37	Magnesite	Matrix	Mg-core spheroid	Core	3.63	-	-	-	5.59	-	43.32	0.41	-	-	-	-	-	-	-	-	-	52.95
GM	Fu-listvenite	60Z-1-32-37	Magnesite	Matrix	Mg-core spheroid	Core	6.17	-	-	-	3.69	-	42.76	0.30	-	-	-	-	-	-	-	-	-	52.92
GM	Fu-listvenite	60Z-1-32-37	Magnesite	Matrix	Mg-core spheroid	Core	3.83	-	-	-	3.28	-	44.99	0.26	-	-	-	-	-	-	-	-	-	52.35
GM	Fu-listvenite	60Z-1-32-37	Magnesite	Matrix	Mg-core spheroid	Core	7.94	-	0.11	-	3.49	-	42.56	0.26	-	-	-	-	-	-	-	-	-	54.36
GM	Fu-listvenite	60Z-1-32-37	Magnesite	Matrix	Mg-core spheroid	Internal growth	2.34	-	0.19	-	4.76	-	43.21	0.74	-	-	0.28	-	-	-	-	-	-	51.52
GM	Fu-listvenite	60Z-1-32-37	Magnesite	Matrix	Mg-core spheroid	Internal growth	3.94	-	-	-	3.97	-	43.62	0.26	-	-	-	-	-	-	-	-	-	51.78
GM	Fu-listvenite	60Z-1-32-37	Magnesite	Matrix	Mg-core spheroid	Internal growth	7.34	-	-	-	4.62	-	42.56	0.35	-	-	-	-	-	-	-	-	-	54.86
GM	Fu-listvenite	60Z-1-32-37	Magnesite	Matrix	Mg-core spheroid	Rim	8.91	-	0.24	-	3.50	-	42.36	0.29	-	-	-	-	-	-	-	-	-	55.30
GM	Fu-listvenite	60Z-1-32-37	Magnesite	Matrix	Mg-core spheroid	Rim	1.28	-	-	-	6.99	-	33.81	7.60	-	-	0.43	-	-	-	-	-	-	50.11
GM	Fu-listvenite	60Z-1-32-37	Magnesite	Matrix	Mg-core spheroid	Rim	10.15	-	0.19	-	3.31	-	41.56	0.18	-	-	-	-	-	-	-	-	-	55.38
GM	Fu-listvenite	60Z-1-32-37	Magnesite	Matrix	Mg-core spheroid	Rim	3.20	-	1.25	-	4.08	-	43.77	1.89	-	-	0.45	-	-	-	-	-	-	54.64
GM	Fu-listvenite	60Z-1-32-37	Magnesite	Matrix	Mg-core spheroid	Rim	4.81	-	0.20	-	4.11	-	42.57	0.68	-	-	0.31	-	-	-	-	-	-	52.69
ISTE	Fu-listvenite	60Z-1-32-37	Magnesite	Vein	lc2		-	-	-	-	2.72	0.07	46.13	0.15	-	-	-	-	-	-	-	-	-	49.07
ISTE	Fu-listvenite	60Z-1-32-37	Magnesite	Matrix	Aggregate		1.77	-	-	-	6.09	0.10	42.76	0.35	-	-	-	-	-	-	-	-	-	51.08
ISTE	Fu-listvenite	60Z-1-32-37	Magnesite	Matrix	Aggregate		1.18	-	-	-	5.83	0.08	43.27	0.24	-	-	-	-	-	-	-	-	-	50.61
GM	Fu-listvenite	60Z-1-32-37	Magnesite	Matrix	Aggregate		1.28	-	-	-	4.50	-	44.73	0.26	-	-	-	-	-	-	-	-	-	50.77
ISTE	Fu-listvenite	60Z-1-32-37	Magnesite	Matrix	Aggregate		1.38	-	-	-	4.80	0.08	43.51	0.43	-	-	-	-	-	-	-	-	-	50.20
ISTE	Fu-listvenite	60Z-1-32-37	Magnesite	Matrix	Aggregate		0.81	-	-	-	4.18	0.08	44.10	0.42	-	-	-	-	-	-	-	-	-	49.59
GM	Fu-listvenite	60Z-1-32-37	Magnesite	Matrix	Aggregate		1.02	-	-	-	5.20	-	44.83	0.25	-	-	-	-	-	-	-	-	-	51.31
ISTE	Fu-listvenite	60Z-1-32-37	Magnesite	Matrix	Aggregate		1.66	-	-	-	4.42	0.05	43.77	0.36	-	-	-	-	-	-	-	-	-	50.26
ISTE	Fu-listvenite	60Z-1-32-37	Magnesite	Matrix	Aggregate		1.18	-	-	-	5.83	0.08	43.27	0.24	-	-	-	-	-	-	-	-	-	50.61
ISTE	Fu-listvenite	60Z-1-32-37	Magnesite	Vein	lss0	Median zone	5.97	-	-	-	4.33	0.04	41.77	0.56	-	-	-	-	-	-	-	-	-	52.67
GM	Fu-listvenite	60Z-1-32-37	Magnesite	Vein	lss0	Median zone	7.98	-	-	-	4.11	-	42.68	0.28	-	-	-	-	-	-	-	-	-	55.05
GM	Fu-listvenite	60Z-1-32-37	Magnesite	Vein	lss0	Median zone	6.16	-	-	-	3.79	-	44.13	0.18	-	-	-	-	-	-	-	-	-	54.26
GM	Fu-listvenite	60Z-1-32-37	Magnesite	Vein	lss0	Median zone	1.29	-	-	-	4.01	-	40.92	0.34	-	-	-	-	-	-	-	-	-	46.55
GM	Fu-listvenite	60Z-1-32-37	Magnesite	Vein	lss0	Intermediate	5.69	-	-	-	4.14	-	43.19	0.35	-	-	-	-	-	-	-	-	-	53.37

GM	Fu-listvenite	60Z-1-32-37	Magnesite	Vein	lss0	Intermediate	1.17	-	-	-	5.41	-	43.28	0.26	-	-	0.18	-	-	-	-	-	-	50.30
GM	Fu-listvenite	60Z-1-32-37	Magnesite	Vein	lss0	Rim	2.31	-	-	0.25	3.62	-	44.96	0.37	-	-	-	-	-	-	-	-	-	51.51
ISTE	Fu-listvenite	60Z-1-32-37	Magnesite	Vein	lss0	Rim	1.96	-	-	-	3.38	0.08	44.40	0.32	-	-	-	-	-	-	-	-	-	50.14
ISTE	Fu-listvenite	60Z-1-32-37	Magnesite	Vein	lss0	Rim	8.45	-	-	-	4.22	0.07	42.32	0.34	-	-	-	-	-	-	-	-	-	55.40
ISTE	Fu-listvenite	60Z-1-32-37	Magnesite	Vein	lss0	Rim	8.06	-	-	-	3.61	0.04	42.75	0.25	-	-	-	-	-	-	-	-	-	54.71
GM	Fu-listvenite	60Z-1-32-37	Magnesite	Vein	lss0	Rim	5.04	-	0.34	-	5.56	-	40.64	0.90	-	-	0.33	-	-	-	-	-	-	52.81
GM	Fu-listvenite	60Z-1-32-37	Magnesite	Vein	lc1	Median zone	4.16	-	-	-	5.30	-	43.39	0.16	-	-	-	-	-	-	-	-	-	53.02
GM	Fu-listvenite	60Z-1-32-37	Magnesite	Vein	lc1	Median zone	1.78	-	-	-	5.13	-	45.07	0.35	-	-	-	-	-	-	-	-	-	52.33
GM	Fu-listvenite	60Z-1-32-37	Magnesite	Vein	lc1	Median zone	3.34	-	-	-	5.70	-	43.62	0.22	-	-	-	-	-	-	-	-	-	52.88
ISTE	Fu-listvenite	60Z-1-32-37	Magnesite	Vein	lc1	Rim	3.05	-	-	-	4.64	0.05	43.82	0.22	-	-	-	-	-	-	-	-	-	51.79
GM	Fu-listvenite	60Z-1-32-37	Magnesite	Vein	lc2	Median zone	-	-	-	-	2.62	-	46.25	0.31	-	-	-	-	-	-	-	-	-	49.18
ISTE	Fu-listvenite	60Z-1-32-37	Magnesite	Vein	lc2	Median zone	1.31	-	-	-	5.30	0.06	43.47	0.33	-	-	-	-	-	-	-	-	-	50.46
GM	Fu-listvenite	60Z-1-32-37	Magnesite	Vein	lc2	Median zone	1.63	-	-	-	6.07	-	44.15	0.38	-	-	-	-	-	-	-	-	-	52.23
ISTE	Listvenite	61Z-4-28-33	Dolomite	Vein	lc3	Median zone	-	-	-	-	1.12	0.05	21.72	29.22	-	-	-	-	-	-	-	-	-	52.11
ISTE	Listvenite	61Z-4-28-33	Magnesite	Matrix	Aggregate		0.02	-	-	-	3.48	0.05	45.01	0.47	-	-	-	-	-	-	-	-	-	49.02
ISTE	Listvenite	61Z-4-28-33	Magnesite	Matrix	Aggregate		0.62	-	-	-	3.46	0.09	45.30	0.26	-	-	-	-	-	-	-	-	-	49.72
ISTE	Listvenite	61Z-4-28-33	Magnesite	Matrix	Aggregate		0.01	-	-	-	3.49	0.05	45.66	0.02	-	-	-	-	-	-	-	-	-	49.24
ISTE	Listvenite	61Z-4-28-33	Magnesite	Matrix	Aggregate		0.02	-	-	-	3.23	0.08	44.92	0.46	-	-	-	-	-	-	-	-	-	48.71
ISTE	Listvenite	61Z-4-28-33	Magnesite	Matrix	Aggregate		-	-	-	-	3.33	-	45.46	0.06	-	-	-	-	-	-	-	-	-	48.85
ISTE	Listvenite	61Z-4-28-33	Magnesite	Matrix	Aggregate		-	-	-	-	3.62	0.08	44.68	0.40	-	-	-	-	-	-	-	-	-	48.79
ISTE	Listvenite	61Z-4-28-33	Magnesite	Matrix	Aggregate		0.31	-	-	-	2.89	0.05	45.43	0.97	-	-	-	-	-	-	-	-	-	49.65
ISTE	Listvenite	61Z-4-28-33	Magnesite	Matrix	Aggregate		-	-	-	-	3.62	0.06	45.03	0.31	-	-	-	-	-	-	-	-	-	49.02
ISTE	Listvenite	61Z-4-28-33	Magnesite	Matrix	Aggregate		-	-	-	-	3.65	0.07	44.97	0.15	-	-	-	-	-	-	-	-	-	48.84
ISTE	Listvenite	61Z-4-28-33	Magnesite	Matrix	Aggregate		-	-	-	-	3.54	0.06	44.30	0.49	-	-	-	-	-	-	-	-	-	48.40
ISTE	Listvenite	61Z-4-28-33	Magnesite	Matrix	Aggregate		-	-	-	-	3.81	0.08	44.32	0.57	-	-	-	-	-	-	-	-	0.03	48.82
ISTE	Listvenite	61Z-4-28-33	Magnesite	Matrix	Aggregate		-	-	-	-	3.59	0.07	44.13	0.48	-	-	-	-	-	-	-	-	-	48.27
ISTE	Listvenite	61Z-4-28-33	Magnesite	Vein	lc5	Median zone	-	-	-	-	5.57	0.04	42.45	0.37	-	-	-	-	-	-	-	-	-	48.43
ISTE	Listvenite	61Z-4-28-33	Magnesite	Vein	lc5	Median zone	-	-	-	-	7.46	0.10	40.80	0.39	-	-	-	-	-	-	-	-	-	48.75
ISTE	Listvenite	61Z-4-28-33	Magnesite	Vein	lc5	Median zone	-	-	-	-	6.94	0.05	41.09	0.41	-	-	-	-	-	-	-	-	-	48.49
ISTE	Listvenite	66Z-1-30-35	Magnesite	Matrix	Mg-core spheroid	Core	-	-	-	-	3.63	-	44.61	0.08	-	-	-	-	-	-	-	-	-	48.32
ISTE	Listvenite	66Z-1-30-35	Magnesite	Matrix	Mg-core spheroid	Core	0.16	-	-	-	5.11	0.10	43.79	0.31	-	-	-	-	-	-	-	-	-	49.46
ISTE	Listvenite	66Z-1-30-35	Magnesite	Vein	lc1	Median zone	1.18	-	-	-	30.62	0.10	24.05	0.21	-	-	-	-	-	-	-	-	-	56.17
ISTE	Listvenite	66Z-1-30-35	Magnesite	Vein	lc1	Median zone	1.91	-	-	-	23.20	0.09	28.85	0.25	-	-	-	-	-	-	-	-	-	54.31
ISTE	Listvenite	66Z-1-30-35	Magnesite	Vein	lc1	Intermediate	0.44	-	-	-	28.43	0.07	25.21	0.20	-	-	-	-	-	-	-	-	-	54.34
ISTE	Listvenite	66Z-1-30-35	Magnesite	Vein	lc1	Rim	0.12	-	-	-	5.69	0.09	43.56	0.32	-	-	-	-	-	-	-	-	-	49.78
ISTE	Listvenite	66Z-1-30-35	Magnesite	Vein	lc1	Rim	1.21	-	-	-	4.49	-	43.28	0.09	-	-	-	-	-	-	-	-	-	49.07
ISTE	Listvenite	66Z-1-30-35	Dolomite	Vein	lc6	Median zone	-	-	-	-	3.64	0.14	18.85	26.68	-	-	-	-	-	-	-	-	-	49.31
ISTE	Listvenite	66Z-1-30-35	Dolomite	Vein	lc6	Median zone	0.07	-	-	-	1.88	0.09	20.64	26.03	-	-	-	-	-	-	-	-	-	48.71
ISTE	Listvenite	66Z-1-30-35	Magnesite	Vein	lc6	Median zone	0.07	-	-	-	8.44	0.10	40.86	0.11	-	-	-	-	-	-	-	-	-	49.57
ISTE	Fu-listvenite	68Z-1-60-64	Dolomite	Matrix	Aggregate		-	-	-	-	6.76	0.19	17.08	26.66	-	-	-	-	-	-	-	-	-	50.69
ISTE	Fu-listvenite	68Z-1-60-64	Magnesite	Matrix	Fe-core spheroid	Internal growth	-	-	-	-	12.27	0.17	38.08	0.73	-	-	-	-	-	-	-	-	-	51.25
ISTE	Fu-listvenite	68Z-1-60-64	Magnesite	Matrix	Fe-core spheroid	Core	1.61	-	-	-	14.13	0.29	35.69	0.91	-	-	-	-	-	-	-	-	-	52.63
ISTE	Fu-listvenite	68Z-1-60-64	Magnesite	Matrix	Fe-core spheroid	Core	0.06	-	-	-	27.90	0.17	26.31	0.46	-	-	-	-	-	-	-	-	-	54.90
ISTE	Fu-listvenite	68Z-1-60-64	Magnesite	Matrix	Fe-core spheroid	Rim	0.07	-	-	-	16.13	0.18	35.27	0.41	-	-	-	-	-	-	-	-	-	52.06
ISTE	Fu-listvenite	68Z-1-60-64	Magnesite	Matrix	Aggregate		0.03	-	-	-	4.35	0.08	44.00	0.72	-	-	-	-	-	-	-	-	-	49.17
ISTE	Fu-listvenite	68Z-1-60-64	Magnesite	Matrix	Aggregate		-	-	-	-	5.16	0.13	43.66	0.67	-	-	-	-	-	-	-	-	-	49.62
ISTE	Fu-listvenite	68Z-1-60-64	Magnesite	Matrix	Aggregate		-	-	-	-	4.61	0.11	44.64	0.46	-	-	-	-	-	-	-	-	-	49.82
ISTE	Fu-listvenite	68Z-1-60-64	Magnesite	Matrix	Aggregate		0.30	-	-	-	4.66	0.11	43.99	0.59	-	-	-	-	-	-	-	-	-	49.64
ISTE	Fu-listvenite	68Z-1-60-64	Magnesite	Matrix	Aggregate		0.02	-	-	-	5.57	0.16	43.30	0.63	-	-	-	-	-	-	-	-	-	49.67
ISTE	Fu-listvenite	68Z-1-60-64	Magnesite	Matrix	Aggregate		0.11	-	-	-	3.93	0.12	44.06	0.74	-	-	-	-	-	-	-	-	-	48.96
ISTE	Fu-listvenite	68Z-1-60-64	Magnesite	Vein	lc1	Median zone	-	-	-	-	29.80	0.17	24.93	0.12	-	-	-	-	-	-	-	-	-	55.03
ISTE	Fu-listvenite	68Z-1-60-64	Magnesite	Vein	lc1	Median zone	0.02	-	-	-	31.43	0.10	23.05	0.31	-	-	-	-	-	-	-	-	-	54.91
ISTE	Fu-listvenite	68Z-1-60-64	Magnesite	Vein	lc1	Median zone	0.03	-	-	-	9.13	0.13	40.49	0.65	-	-	-	-	-	-	-	-	-	50.43

ISTE	Fu-listvenite	68Z-1-60-64	Magnesite	Vein	lc1	Median zone	0.10	-	-	-	26.34	0.15	26.63	0.60	-	-	-	-	-	-	-	-	-	53.82
ISTE	Fu-listvenite	68Z-1-60-64	Magnesite	Vein	lc1	Median zone	0.13	-	-	-	24.04	0.11	28.81	0.64	-	-	-	-	-	-	-	-	-	53.73
ISTE	Fu-listvenite	68Z-1-60-64	Magnesite	Vein	lc1	Intermediate	0.19	-	-	-	5.52	0.09	43.38	0.42	-	-	-	-	-	-	-	-	-	49.60
ISTE	Fu-listvenite	68Z-1-60-64	Magnesite	Vein	lc1	Rim	0.19	-	-	-	18.08	0.13	33.46	0.46	-	-	-	-	-	-	-	-	-	52.31
ISTE	Fu-listvenite	71Z-3-0-8	Magnesite	Matrix	Fe-core spheroid	Core	2.21	-	-	-	15.91	0.88	33.92	0.42	-	-	-	-	-	-	-	-	-	53.34
ISTE	Fu-listvenite	71Z-3-0-8	Magnesite	Matrix	Fe-core spheroid	Internal growth	0.79	-	-	-	9.00	0.20	40.39	0.17	-	-	-	-	-	-	-	-	-	50.55
ISTE	Fu-listvenite	71Z-3-0-8	Magnesite	Matrix	Fe-core spheroid	Internal growth	0.16	-	-	-	4.84	0.04	43.87	0.12	-	-	-	-	-	-	-	-	-	49.03
ISTE	Fu-listvenite	71Z-3-0-8	Magnesite	Matrix	Fe-core spheroid	Internal growth	1.78	-	-	-	4.80	-	42.63	0.36	-	-	-	-	-	-	-	-	-	49.56
ISTE	Fu-listvenite	71Z-3-0-8	Magnesite	Matrix	Fe-core spheroid	Rim	4.65	-	-	-	7.40	0.06	37.55	0.70	-	-	-	-	-	-	-	-	-	50.37
ISTE	Fu-listvenite	71Z-3-0-8	Magnesite	Matrix	Mg-core spheroid	Core	-	-	-	-	3.63	0.08	44.65	0.74	-	-	-	-	-	-	-	-	-	49.10
ISTE	Fu-listvenite	71Z-3-0-8	Magnesite	Matrix	Mg-core spheroid	Core	0.78	-	-	-	3.86	0.08	44.72	0.40	-	-	-	-	-	-	-	-	-	49.84
ISTE	Fu-listvenite	71Z-3-0-8	Magnesite	Matrix	Mg-core spheroid	Core	0.07	-	-	-	3.47	0.12	45.00	0.35	-	-	-	-	-	-	-	-	-	49.01
ISTE	Fu-listvenite	71Z-3-0-8	Magnesite	Matrix	Mg-core spheroid	Core	1.91	-	-	-	4.32	0.11	43.44	0.20	-	-	-	-	-	-	-	-	-	49.99
ISTE	Fu-listvenite	71Z-3-0-8	Magnesite	Matrix	Mg-core spheroid	Core	0.06	-	-	-	3.86	-	44.80	0.08	-	-	-	-	-	-	-	-	-	48.80
ISTE	Fu-listvenite	71Z-3-0-8	Magnesite	Vein	lss0	Median zone	0.03	-	-	-	21.44	0.22	30.86	0.38	-	-	-	-	-	-	-	-	-	52.93
ISTE	Fu-listvenite	71Z-3-0-8	Magnesite	Vein	lss0	Rim	2.03	-	-	-	4.81	-	42.36	0.57	-	-	-	-	-	-	-	-	-	49.76
ISTE	Fu-listvenite	71Z-3-0-8	Magnesite	Vein	lc1	Median zone	0.06	-	-	-	3.86	-	44.80	0.08	-	-	-	-	-	-	-	-	-	48.80
ISTE	Fu-listvenite	71Z-3-0-8	Magnesite	Vein	lc1	Intermediate	-	-	-	-	22.09	0.26	30.31	0.66	-	-	-	-	-	-	-	-	-	53.33
ISTE	Fu-listvenite	71Z-3-0-8	Magnesite	Vein	lc1	Rim	2.16	-	-	-	5.45	-	41.48	0.45	-	-	-	-	-	-	-	-	-	49.54
ISTE	Fu-listvenite	71Z-3-0-8	Magnesite	Vein	lc1	Rim	0.67	-	-	-	3.72	0.07	44.49	0.21	-	-	-	-	-	-	-	-	-	49.16
ISTE	Listvenite	72Z-1-71-79	Dolomite	Vein	lc6	Median zone	-	-	-	-	3.34	0.13	14.70	27.97	-	-	-	-	-	-	-	-	-	46.14
ISTE	Listvenite	72Z-1-71-79	Magnesite	Matrix	Fe-core spheroid	Core	0.02	-	-	-	15.22	0.24	29.61	0.79	-	-	-	-	-	-	-	-	-	45.89
ISTE	Listvenite	72Z-1-71-79	Magnesite	Matrix	Mg-core spheroid	Core	0.12	-	-	-	6.95	0.17	41.90	0.17	-	-	-	-	-	-	-	-	-	49.31
ISTE	Listvenite	72Z-1-71-79	Magnesite	Matrix	Mg-core spheroid	Core	0.02	-	-	-	2.88	-	44.58	0.12	-	-	-	-	-	-	-	-	-	47.59
ISTE	Listvenite	72Z-1-71-79	Magnesite	Matrix	Mg-core spheroid	Core	0.22	-	-	-	5.56	0.16	42.96	0.33	-	-	-	-	-	-	-	-	-	49.23
ISTE	Listvenite	72Z-1-71-79	Magnesite	Matrix	Mg-core spheroid	Core	0.02	-	-	-	1.59	0.05	44.57	0.94	-	-	-	-	-	-	-	-	-	47.17
ISTE	Listvenite	72Z-1-71-79	Magnesite	Matrix	Mg-core spheroid	Core	2.02	-	-	-	4.52	0.70	39.00	0.43	-	-	-	-	-	-	-	-	-	46.66
ISTE	Listvenite	72Z-1-71-79	Magnesite	Matrix	Mg-core spheroid	Core	3.26	-	-	-	9.63	0.21	32.67	0.33	-	-	-	-	-	-	-	-	-	46.10
ISTE	Listvenite	72Z-1-71-79	Magnesite	Matrix	Mg-core spheroid	Core	0.15	-	-	-	1.33	0.07	42.89	0.91	-	-	-	-	-	-	-	-	-	45.34
ISTE	Listvenite	72Z-1-71-79	Magnesite	Matrix	Mg-core spheroid	Core	0.15	-	-	-	3.55	0.11	40.78	0.31	-	-	-	-	-	-	-	-	-	44.90
ISTE	Listvenite	72Z-1-71-79	Magnesite	Matrix	Mg-core spheroid	Internal growth	0.01	-	-	-	3.37	0.10	44.99	0.15	-	-	-	-	-	-	-	-	-	48.63
ISTE	Listvenite	72Z-1-71-79	Magnesite	Matrix	Mg-core spheroid	Rim	0.02	-	-	-	3.02	-	44.98	0.11	-	-	-	-	-	-	-	-	-	48.13
ISTE	Listvenite	72Z-1-71-79	Magnesite	Matrix	Aggregate		0.04	-	-	-	1.75	0.04	45.46	0.07	-	-	-	-	-	-	-	-	-	47.36
ISTE	Listvenite	72Z-1-71-79	Magnesite	Matrix	Aggregate		0.12	-	-	-	1.28	0.08	42.61	0.95	-	-	-	-	-	-	-	-	-	45.04
ISTE	Listvenite	72Z-1-71-79	Magnesite	Vein	lc1	Median zone	0.02	-	-	-	14.67	0.12	28.09	0.46	-	-	-	-	-	-	-	-	-	43.36
ISTE	Listvenite	72Z-1-71-79	Magnesite	Vein	lc1	Median zone	0.04	-	-	-	13.59	0.25	36.68	0.39	-	-	-	-	-	-	-	-	-	50.95
ISTE	Listvenite	72Z-1-71-80	Magnesite	Vein	lc6	Median zone	0.02	-	-	-	6.28	0.11	38.25	0.22	-	-	-	-	-	-	-	-	-	44.87
ISTE	Listvenite	72Z-1-71-79	Magnesite	Vein	lc1	Rim	-	-	-	-	6.89	0.16	38.21	0.26	-	-	-	-	-	-	-	-	-	45.52
ISTE	Listvenite	72Z-1-71-79	Magnesite	Vein	lc1	Rim	0.34	-	-	-	7.16	0.18	42.14	0.30	-	-	-	-	-	-	-	-	-	50.12
ISTE	Listvenite	72Z-1-71-79	Magnesite	Vein	lc1	Rim	0.09	-	-	-	6.91	0.18	42.16	0.22	-	-	-	-	-	-	-	-	-	49.56
ISTE	Listvenite	76Z-2-12-20	Dolomite	Matrix	Aggregate		0.10	-	-	-	5.23	0.07	20.79	27.35	-	-	-	-	-	-	-	-	-	53.54
ISTE	Listvenite	76Z-2-12-20	Dolomite	Matrix	Aggregate		0.05	-	-	-	5.13	0.11	19.20	25.58	-	-	-	-	-	-	-	-	-	50.07
ISTE	Listvenite	76Z-2-12-20	Dolomite	Matrix	Aggregate		0.15	-	-	-	3.86	0.14	19.08	29.32	-	-	-	-	-	-	-	-	-	52.55
ISTE	Listvenite	76Z-2-12-20	Dolomite	Vein	lc6		-	-	-	-	0.89	0.20	21.89	30.02	-	-	-	-	-	-	-	-	-	53.00
ISTE	Listvenite	76Z-2-12-20	Dolomite	Vein	lc6		0.09	-	-	-	1.42	0.24	21.85	29.39	-	-	-	-	-	-	-	-	-	52.99
ISTE	Listvenite	76Z-2-12-20	Dolomite	Vein	lc6	Median zone	-	-	-	-	1.99	0.11	20.82	29.62	-	-	-	-	-	-	-	-	-	52.54
ISTE	Listvenite	76Z-2-12-20	Dolomite	Vein	lc6	Median zone	-	-	-	-	4.85	0.12	18.03	29.64	-	-	-	-	-	-	-	-	-	52.64
ISTE	Listvenite	76Z-2-12-20	Magnesite	Matrix	lss2?		0.31	-	-	-	5.97	0.51	42.83	0.27	-	-	-	-	-	-	-	-	-	49.90
ISTE	Listvenite	76Z-2-12-20	Magnesite	Vein	lss2?		-	-	-	-	16.41	0.29	25.38	9.23	-	-	-	-	-	-	-	-	-	51.31
ISTE	Listvenite	76Z-2-12-20	Magnesite	Matrix	lss2?		0.20	-	-	-	13.88	0.31	36.86	0.20	-	-	-	-	-	-	-	-	-	51.45
ISTE	Listvenite	76Z-2-12-20	Magnesite	Vein	lc1		0.44	-	-	-	7.45	0.57	39.81	3.04	-	-	-	-	-	-	-	-	-	51.31
ISTE	Listvenite	76Z-2-12-20	Magnesite	Vein	lc1	Median zone	-	-	-	-	6.09	0.04	42.97	0.06	-	-	-	-	-	-	-	-	-	49.17
ISTE	Listvenite	76Z-2-12-20	Magnesite	Vein	lc1	Median zone	-	-	-	-	5.69	0.07	42.66	0.33	-	-	-	-	-	-	-	-	-	48.75

ISTE	Listvenite	76Z-2-12-20	Magnesite	Vein	lc1	Median zone	0.02	-	-	-	5.77	0.34	42.97	0.10	-	-	-	-	-	-	-	-	-	49.20
ISTE	Listvenite	76Z-2-12-20	Magnesite	Vein	lc1	Median zone	0.57	-	-	-	5.42	0.41	43.89	0.18	-	-	-	-	-	-	-	-	-	50.47

[1]BT1B core geochemical domains after Godard et al. (2021)

[2]Abbreviations of vein generations after Menzel et al. (2022)

Other abbreviations: m.b.g. = metres below ground, p.f.u. = per formula unit

Table S4 (continued)

								Cations p.f.u. (6O formula)																
Facility	Lithology	Sample	Mineral	Structure	Texture[2]	Zone	Transect	Si	Ti	Al	Cr	Fe	Mn	Mg	Ca	Na	K	Ni	Cu	Zn	S	Cl	Ba	Sr	Total
GM	Listvenite	16Z-1-65-70	Dolomite	Matrix	Aggregate			-	-	-	-	0.18	-	2.91	2.91	-	-	-	-	-	-	-	-	-	6.00
GM	Listvenite	16Z-1-65-70	Dolomite	Matrix	Aggregate			0.01	-	0.02	-	0.20	-	2.86	2.89	-	-	-	-	-	-	-	-	0.00	5.98
GM	Listvenite	16Z-1-65-70	Dolomite	Matrix	Aggregate			0.01	-	0.02	-	0.17	-	2.86	2.91	-	-	-	-	-	-	-	-	-	5.98
GM	Listvenite	16Z-1-65-70	Dolomite	Matrix	Aggregate			-	-	-	-	0.15	-	2.88	2.97	-	-	-	-	-	-	-	-	-	6.00
GM	Listvenite	16Z-1-65-70	Dolomite	Matrix	Aggregate			0.02	-	-	-	0.21	-	2.85	2.90	-	-	-	-	-	-	-	-	-	5.98
GM	Listvenite	16Z-1-65-70	Dolomite	Vein	lc6	Median zone		0.01	-	-	-	0.10	0.02	2.95	2.90	-	-	-	-	-	-	-	-	-	5.99
GM	Listvenite	16Z-1-65-70	Dolomite	Vein	lc6	Median zone		-	-	-	-	0.03	0.02	2.99	2.96	-	-	-	-	-	-	-	-	-	6.00
GM	Listvenite	16Z-1-65-70	Dolomite	Vein	lc6	Median zone		-	-	-	-	-	0.02	3.05	2.92	-	-	-	-	-	-	-	-	-	6.00
GM	Listvenite	16Z-1-65-70	Dolomite	Vein	lc6	Median zone		-	-	-	-	0.05	-	2.99	2.97	-	-	-	-	-	-	-	-	-	6.00
GM	Listvenite	16Z-1-65-70	Magnesite	Matrix	Aggregate			0.02	-	-	-	0.54	0.01	5.41	-	-	-	-	-	-	-	-	-	-	5.98
GM	Listvenite	16Z-1-65-70	Magnesite	Matrix	Aggregate			0.31	-	-	-	0.20	-	5.17	0.01	-	-	-	-	-	-	-	-	-	5.69
GM	Listvenite	16Z-1-65-70	Magnesite	Vein	lss0	Median zone		0.02	-	-	-	0.28	-	5.62	0.05	-	-	-	-	-	-	-	-	-	5.98
GM	Listvenite	16Z-1-65-70	Magnesite	Vein	lss0	Median zone		0.02	-	-	0.02	0.19	-	5.73	0.01	-	-	-	-	-	-	-	-	-	5.97
GM	Listvenite	16Z-1-65-70	Magnesite	Vein	lss0	Intermediate		0.10	-	-	-	0.19	-	5.61	0.01	-	-	-	-	-	-	-	-	-	5.90
GM	Listvenite	16Z-1-65-70	Magnesite	Vein	lss0	Rim		0.03	-	-	0.02	0.18	-	5.68	0.05	-	-	-	-	-	-	-	-	-	5.96
GM	Listvenite	16Z-1-65-70	Magnesite	Vein	lss0	Median zone		0.18	-	-	-	0.18	-	5.46	0.01	-	-	-	-	-	-	-	-	-	5.82
GM	Listvenite	16Z-1-65-70	Siderite	Vein	lc1	Median zone		0.38	-	0.10	-	2.93	0.01	2.12	0.01	-	-	0.02	-	-	-	-	-	-	5.57
GM	Listvenite	16Z-1-65-70	Siderite	Vein	lc1	Median zone		0.51	-	0.14	-	3.73	-	1.03	0.01	-	-	-	-	-	-	-	-	-	5.42
GM	Listvenite	16Z-1-65-70	Siderite	Vein	lc1	Median zone		0.65	-	0.17	-	4.41	-	0.03	0.01	-	-	-	-	-	-	-	-	-	5.27
GM	Listvenite	16Z-1-65-70	Siderite	Vein	lc1	Median zone		0.43	-	0.09	-	3.42	0.01	1.55	0.01	-	-	0.01	-	-	-	-	-	-	5.52
GM	Listvenite	16Z-1-65-70	Siderite	Vein	lc1	Intermediate		0.47	-	0.03	-	3.43	-	1.57	0.01	-	-	-	-	-	-	-	-	-	5.52
GM	Listvenite	16Z-1-65-70	Magnesite	Vein	lc1	Intermediate		0.02	-	-	-	0.54	0.01	5.41	-	-	-	-	-	-	-	-	-	-	5.98
GM	Listvenite	16Z-1-65-70	Magnesite	Vein	lc1	Rim		0.01	-	-	-	0.30	-	5.67	0.01	-	-	-	-	-	-	-	-	-	5.99
GM	Listvenite	16Z-1-65-70	Magnesite	Vein	lc1	Rim	a	0.07	-	-	0.01	0.20	-	5.65	-	-	-	-	-	-	-	-	-	-	5.93
GM	Listvenite	16Z-1-65-70	Magnesite	Vein	lc1	Rim	a	0.09	-	-	-	0.24	-	5.58	0.00	-	-	-	-	-	-	-	-	-	5.91
GM	Listvenite	16Z-1-65-70	Magnesite	Vein	lc1	Intermediate	a	0.18	-	-	-	0.25	-	5.39	0.01	-	-	-	-	-	-	-	-	-	5.82
GM	Listvenite	16Z-1-65-70	Magnesite	Vein	lc1	Intermediate	a	0.08	-	-	-	0.25	-	5.57	0.01	-	-	-	-	-	-	-	-	-	5.92
GM	Listvenite	16Z-1-65-70	Magnesite	Vein	lc1	Intermediate	a	0.11	-	-	0.01	0.24	-	5.53	-	-	-	-	-	-	-	-	-	0.00	5.89
GM	Listvenite	16Z-1-65-70	Magnesite	Vein	lc1	Intermediate	a	0.08	-	-	-	0.24	-	5.59	0.00	-	-	-	-	-	-	-	-	0.00	5.92
GM	Listvenite	16Z-1-65-70	Magnesite	Vein	lc1	Intermediate	a	0.24	-	-	-	0.26	-	5.25	0.01	-	-	-	-	-	-	-	-	-	5.76
GM	Listvenite	16Z-1-65-70	Magnesite	Vein	lc1	Intermediate	a	0.16	-	-	0.01	0.31	-	5.35	0.02	-	-	-	-	-	-	-	-	-	5.84
GM	Listvenite	16Z-1-65-70	Magnesite	Vein	lc1	Intermediate	a	0.06	-	-	-	0.29	-	5.58	0.01	-	-	-	-	-	-	-	-	0.00	5.94
GM	Listvenite	16Z-1-65-70	Magnesite	Vein	lc1	Intermediate	a	0.05	-	-	0.01	0.29	-	5.60	-	-	-	-	-	-	-	-	-	-	5.94
GM	Listvenite	16Z-1-65-70	Magnesite	Vein	lc1	Intermediate	a	0.15	-	-	-	0.22	-	5.47	0.01	-	-	-	-	-	-	-	-	-	5.85
GM	Listvenite	16Z-1-65-70	Magnesite	Vein	lc1	Intermediate	a	0.03	-	-	-	0.25	-	5.69	0.00	-	-	-	-	-	-	-	-	-	5.97
GM	Listvenite	16Z-1-65-70	Magnesite	Vein	lc1	Intermediate	a	0.03	-	-	-	0.30	-	5.65	-	-	-	-	-	-	-	-	-	0.00	5.97
GM	Listvenite	16Z-1-65-70	Magnesite	Vein	lc1	Median zone	a	0.01	-	-	-	0.39	-	5.57	0.01	-	-	-	-	-	-	-	-	-	5.99
GM	Listvenite	16Z-1-65-70	Magnesite	Vein	lc1	Median zone	a	0.01	-	-	-	0.51	-	5.43	0.04	-	-	-	-	-	-	-	-	0.00	5.99
GM	Listvenite	16Z-1-65-70	Magnesite	Vein	lc1	Intermediate	a	-	-	-	-	0.52	-	5.47	0.01	-	-	-	-	-	-	-	-	-	6.00
GM	Listvenite	16Z-1-65-70	Magnesite	Vein	lc1	Intermediate	a	-	-	-	-	0.42	-	5.57	0.01	-	-	-	-	-	-	-	-	0.00	6.00
GM	Listvenite	16Z-1-65-70	Magnesite	Vein	lc1	Rim	a	0.01	-	-	-	0.38	-	5.60	-	-	-	-	-	-	-	-	-	-	5.99
GM	Listvenite	16Z-1-65-70	Magnesite	Vein	lc1	Rim	a	0.05	-	-	-	0.34	-	5.55	0.01	-	-	-	-	-	-	-	-	-	5.95
GM	Listvenite	16Z-1-65-70	Magnesite	Vein	lc1	Rim	b	0.08	-	-	0.01	0.21	-	5.60	-	-	-	-	-	-	-	-	-	0.00	5.91
GM	Listvenite	16Z-1-65-70	Magnesite	Vein	lc1	Rim	b	0.04	-	-	0.03	0.55	-	5.32	0.01	-	-	-	-	-	-	-	-	-	5.94
GM	Listvenite	16Z-1-65-70	Magnesite	Vein	lc1	Intermediate	b	0.02	-	-	0.02	0.19	-	5.74	-	-	-	-	-	-	-	-	-	-	5.97
GM	Listvenite	16Z-1-65-70	Magnesite	Vein	lc1	Intermediate	b	0.03	-	-	0.02	0.20	-	5.71	0.00	-	-	-	-	-	-	-	-	-	5.96
GM	Listvenite	16Z-1-65-70	Magnesite	Vein	lc1	Intermediate	b	0.03	-	-	0.01	0.20	-	5.71	0.01	-	-	-	-	-	-	-	-	0.00	5.96

GM	Listvenite	16Z-1-65-70	Magnesite	Vein	lc1	Intermediate	b	0.12	-	-	-	0.22	-	5.52	0.02	-	-	-	-	-	-	-	-	0.00	5.88
GM	Listvenite	16Z-1-65-70	Magnesite	Vein	lc1	Intermediate	b	-	-	-	-	0.40	-	5.59	0.01	-	-	-	-	-	-	-	-	0.00	6.00
GM	Listvenite	16Z-1-65-70	Magnesite	Vein	lc1	Median zone	b	0.02	-	-	-	0.52	0.01	5.41	0.01	-	-	-	-	-	-	-	-	0.00	5.98
GM	Listvenite	16Z-1-65-70	Magnesite	Vein	lc1	Median zone	b	0.35	-	0.07	0.01	2.24	-	2.92	0.01	-	0.01	-	-	-	-	-	-	-	5.61
GM	Listvenite	16Z-1-65-70	Magnesite	Vein	lc1	Median zone	b	0.01	-	-	-	0.51	-	5.47	0.00	-	-	-	-	-	-	-	-	0.00	5.99
GM	Listvenite	16Z-1-65-70	Magnesite	Vein	lc1	Intermediate	b	0.01	-	-	-	0.38	-	5.59	0.01	-	-	-	-	-	-	-	-	-	5.99
GM	Listvenite	16Z-1-65-70	Magnesite	Vein	lc1	Intermediate	b	0.01	-	-	-	0.31	-	5.67	0.00	-	-	-	-	-	-	-	-	-	5.99
GM	Listvenite	16Z-1-65-70	Magnesite	Vein	lc1	Intermediate	b	0.04	-	-	0.01	0.26	-	5.65	-	-	-	-	-	-	-	-	-	0.00	5.95
GM	Listvenite	16Z-1-65-70	Magnesite	Vein	lc1	Intermediate	b	0.06	-	-	0.02	0.67	-	5.17	0.00	-	-	-	-	-	-	-	-	-	5.93
GM	Listvenite	16Z-1-65-70	Magnesite	Vein	lc1	Intermediate	b	0.21	-	-	0.01	0.29	-	5.26	0.02	-	-	-	-	-	-	-	-	-	5.79
GM	Listvenite	16Z-1-65-70	Magnesite	Vein	lc1	Rim	b	0.04	-	-	0.01	0.29	-	5.59	0.00	-	0.01	-	-	-	-	-	-	0.00	5.95
GM	Listvenite	16Z-1-65-70	Magnesite	Vein	lc1	Rim	b	0.03	-	-	0.02	0.63	-	5.28	0.01	-	-	-	-	-	-	-	-	-	5.96
ISTE	Listvenite	30Z-2-33-39	Dolomite	Matrix	Aggregate			-	-	-	-	0.09	0.01	3.19	2.72	-	-	-	-	-	-	-	-	-	6.00
ISTE	Listvenite	30Z-2-33-39	Dolomite	Matrix	Aggregate			0.00	-	-	-	0.32	0.02	2.88	2.77	-	-	-	-	-	-	-	-	-	6.00
ISTE	Listvenite	30Z-2-33-39	Dolomite	Matrix	Aggregate			-	-	-	-	0.12	0.01	2.98	2.89	-	-	-	-	-	-	-	-	-	6.00
ISTE	Listvenite	30Z-2-33-39	Dolomite	Matrix	Aggregate			0.00	-	-	-	0.10	0.01	3.02	2.87	-	-	-	-	-	-	-	-	-	6.00
ISTE	Listvenite	30Z-2-33-39	Dolomite	Matrix	Aggregate			0.00	-	-	-	0.08	0.00	3.04	2.87	-	-	-	-	-	-	-	0.00	-	6.00
ISTE	Listvenite	30Z-2-33-39	Dolomite	Matrix	Aggregate			0.00	-	-	-	0.36	0.01	2.59	3.03	-	-	-	-	-	-	-	-	-	6.00
ISTE	Listvenite	30Z-2-33-39	Dolomite	Matrix	Aggregate			0.00	-	-	-	0.11	0.01	3.00	2.89	-	-	-	-	-	-	-	-	-	6.00
ISTE	Listvenite	30Z-2-33-39	Dolomite	Vein	lc2	Median zone		-	-	-	-	0.14	0.01	3.15	2.70	-	-	-	-	-	-	-	-	0.00	6.00
ISTE	Listvenite	30Z-2-33-39	Dolomite	Vein	lc6	Median zone		-	-	-	-	0.11	0.01	3.00	2.88	-	-	-	-	-	-	-	-	-	6.00
ISTE	Listvenite	30Z-2-33-39	Magnesite	Matrix	Mg-core spheroid			0.05	-	-	-	0.32	0.01	5.53	0.04	-	-	-	-	-	-	-	-	-	5.95
ISTE	Listvenite	30Z-2-33-39	Magnesite	Matrix	Aggregate			0.08	-	-	-	0.32	0.01	5.49	0.01	-	-	-	-	-	-	-	-	-	5.92
ISTE	Listvenite	30Z-2-33-39	Magnesite	Matrix	Aggregate			0.10	-	-	-	0.30	0.00	5.48	0.02	-	-	-	-	-	-	-	-	-	5.90
ISTE	Listvenite	30Z-2-33-39	Magnesite	Matrix	Aggregate			0.05	-	-	-	0.26	0.01	5.59	0.04	-	-	-	-	-	-	-	-	-	5.95
ISTE	Listvenite	30Z-2-33-39	Magnesite	Vein	lc1	Median zone		0.04	-	-	-	0.33	0.01	5.48	0.11	-	-	-	-	-	-	-	-	-	5.96
ISTE	Listvenite	31Z-3-26-31	Dolomite	Vein	lc1	Median zone		-	-	-	-	0.02	0.00	3.05	2.92	-	-	-	-	-	-	-	-	-	6.00
ISTE	Listvenite	31Z-3-26-31	Dolomite	Vein	lc6	Median zone		0.06	-	-	-	0.08	0.03	3.07	2.70	-	-	-	-	-	-	-	-	-	5.94
ISTE	Listvenite	31Z-3-26-31	Dolomite	Vein	lc6	Median zone		-	-	-	-	0.07	0.01	3.12	2.80	-	-	-	-	-	-	-	-	-	6.00
ISTE	Listvenite	31Z-3-26-31	Dolomite	Vein	lc6	Median zone		-	-	-	-	0.06	0.03	3.00	2.92	-	-	-	-	-	-	-	-	-	6.00
ISTE	Listvenite	31Z-3-26-31	Dolomite	Vein	lc6	Median zone		-	-	-	-	0.06	0.03	2.96	2.96	-	-	-	-	-	-	-	-	-	6.00
ISTE	Listvenite	31Z-3-26-31	Magnesite	Matrix	Mg-core spheroid	Rim	c	0.01	-	-	-	0.41	0.01	5.55	0.02	-	-	-	-	-	-	-	-	-	5.99
ISTE	Listvenite	31Z-3-26-31	Dolomite	Matrix	Mg-core spheroid	Internal growth	c	0.03	-	-	-	0.15	0.02	3.02	2.75	-	-	-	-	-	-	-	-	-	5.97
ISTE	Listvenite	31Z-3-26-31	Magnesite	Matrix	Mg-core spheroid	Internal growth	c	0.11	-	-	-	0.21	0.00	5.54	0.02	-	-	-	-	-	-	-	-	-	5.89
ISTE	Listvenite	31Z-3-26-31	Magnesite	Matrix	Mg-core spheroid	Core	c	0.27	-	-	-	0.27	0.00	5.18	0.01	-	-	-	-	-	-	-	-	-	5.73
ISTE	Listvenite	31Z-3-26-31	Magnesite	Matrix	Mg-core spheroid	Core		0.12	-	-	-	0.27	0.00	5.46	0.02	-	-	-	-	-	-	-	-	-	5.88
ISTE	Listvenite	31Z-3-26-31	Magnesite	Matrix	Mg-core spheroid	Core		0.08	-	-	-	0.22	0.00	5.58	0.02	-	-	-	-	-	-	-	-	-	5.92
ISTE	Listvenite	31Z-3-26-31	Magnesite	Matrix	Mg-core spheroid	Core		0.12	-	-	-	0.19	0.00	5.54	0.03	-	-	-	-	-	-	-	-	-	5.88
ISTE	Listvenite	31Z-3-26-31	Magnesite	Matrix	Mg-core spheroid	Core		0.18	-	-	-	0.12	-	5.46	0.05	-	-	-	-	-	-	-	-	-	5.82
ISTE	Listvenite	31Z-3-26-31	Magnesite	Matrix	Mg-core spheroid	Core		0.13	-	-	-	0.23	0.00	5.48	0.02	-	-	-	-	-	-	-	-	-	5.87
ISTE	Listvenite	31Z-3-26-31	Magnesite	Matrix	Mg-core spheroid	Core		0.11	-	-	-	0.20	0.00	5.56	0.02	-	-	-	-	-	-	-	-	-	5.89
ISTE	Listvenite	31Z-3-26-31	Magnesite	Matrix	Mg-core spheroid	Core		0.17	-	-	-	0.23	0.01	5.40	0.02	-	-	-	-	-	-	-	-	-	5.83
ISTE	Listvenite	31Z-3-26-31	Magnesite	Vein	lc1	Rim		0.01	-	-	-	0.37	0.02	5.56	0.03	-	-	-	-	-	-	-	-	-	5.99
ISTE	Listvenite	31Z-3-26-31	Magnesite	Vein	lc1	Rim		0.00	-	-	-	0.33	0.01	5.63	0.02	-	-	-	-	-	-	-	-	-	6.00
ISTE	Listvenite	35Z-1-32-37	Magnesite	Matrix	Aggregate	Core		0.00	-	-	-	0.32	0.00	5.65	0.02	-	-	-	-	-	-	-	-	-	6.00
ISTE	Listvenite	35Z-1-32-37	Magnesite	Matrix	Aggregate	Core		-	-	-	-	0.22	0.00	5.71	0.07	-	-	-	-	-	-	-	-	-	6.00
ISTE	Listvenite	35Z-1-32-37	Magnesite	Matrix	Aggregate	Core		0.00	-	-	-	0.30	-	5.66	0.04	-	-	-	-	-	-	-	-	-	6.00
ISTE	Listvenite	35Z-1-32-37	Magnesite	Matrix	Aggregate			0.05	-	-	-	0.28	0.00	5.58	0.05	-	-	-	-	-	-	-	-	-	5.95
ISTE	Listvenite	35Z-1-32-37	Magnesite	Matrix	Aggregate			-	-	-	-	0.40	0.00	5.60	0.00	-	-	-	-	-	-	-	-	-	6.00
ISTE	Listvenite	35Z-1-32-37	Magnesite	Matrix	Aggregate			0.00	-	-	-	0.32	0.00	5.63	0.04	-	-	-	-	-	-	-	-	-	6.00
ISTE	Listvenite	35Z-1-32-37	Magnesite	Matrix	Aggregate			0.00	-	-	-	0.36	0.00	5.60	0.04	-	-	-	-	-	-	-	-	-	6.00
ISTE	Listvenite	35Z-1-32-37	Magnesite	Vein	lc1	Median zone		0.52	-	-	-	2.19	0.01	2.75	0.01	-	-	-	-	-	-	-	-	-	5.48
ISTE	Listvenite	35Z-1-32-37	Magnesite	Vein	lc1	Median zone		0.15	-	-	-	0.56	0.03	5.10	0.02	-	-	-	-	-	-	-	-	-	5.85

ISTE	Listvenite	35Z-1-32-37	Magnesite	Vein	lc1	Median zone		0.24	-	-	-	0.85	0.02	4.61	0.04	-	-	-	-	-	-	-	-	-	5.76
ISTE	Listvenite	35Z-1-32-37	Magnesite	Vein	lc1	Median zone		0.13	-	-	-	0.54	0.02	5.11	0.06	-	-	-	-	-	-	-	-	-	5.87
ISTE	Listvenite	35Z-1-32-37	Magnesite	Vein	lc1	Median zone		0.18	-	-	-	0.55	0.03	5.03	0.03	-	-	-	-	-	-	-	-	-	5.82
ISTE	Listvenite	35Z-1-32-37	Magnesite	Vein	lc1	Median zone		0.01	-	-	-	1.61	0.01	4.33	0.02	-	-	-	-	-	-	-	-	-	5.99
ISTE	Listvenite	35Z-1-32-37	Magnesite	Vein	lc1	Median zone		0.07	-	-	-	2.40	0.01	3.43	0.02	-	-	-	-	-	-	-	-	-	5.93
ISTE	Listvenite	35Z-1-32-37	Magnesite	Vein	lc1	Median zone		0.15	-	-	-	2.23	0.01	3.43	0.02	-	-	-	-	-	-	-	-	-	5.85
ISTE	Listvenite	35Z-1-32-37	Magnesite	Vein	lc1	Rim		0.08	-	-	-	1.91	0.01	3.89	0.02	-	-	-	-	-	-	-	-	-	5.92
ISTE	Listvenite	35Z-1-32-37	Magnesite	Matrix	Aggregate (clast)			0.00	-	-	-	0.33	0.00	5.64	0.03	-	-	-	-	-	-	-	-	-	6.00
ISTE	Listvenite	35Z-1-32-37	Magnesite	Matrix	Aggregate (clast)			0.00	-	-	-	0.34	0.00	5.61	0.04	-	-	-	-	-	-	-	-	-	6.00
ISTE	Listvenite	38Z-3-60-65	Dolomite	Matrix		Interstitial		0.03	-	-	-	0.06	0.09	3.03	2.76	-	-	-	-	-	-	-	-	-	5.97
ISTE	Listvenite	38Z-3-60-65	Dolomite	Matrix		Interstitial		0.00	-	-	-	0.13	0.03	3.06	2.78	-	-	-	-	-	-	-	-	-	6.00
ISTE	Listvenite	38Z-3-60-65	Dolomite	Matrix		Interstitial		-	-	-	-	0.03	0.10	3.15	2.72	-	-	-	-	-	-	-	-	-	6.00
ISTE	Listvenite	38Z-3-60-65	Dolomite	Vein	lc2			-	-	-	-	0.12	0.03	3.06	2.79	-	-	-	-	-	-	-	0.00	-	6.00
ISTE	Listvenite	38Z-3-60-65	Dolomite	Vein	lc2			-	-	-	-	0.06	0.00	3.13	2.80	-	-	-	-	-	-	-	0.00	-	6.00
ISTE	Listvenite	38Z-3-60-65	Magnesite	Vein	lc1	Median zone		-	-	-	-	0.32	0.01	5.66	0.01	-	-	-	-	-	-	-	-	-	6.00
ISTE	Listvenite	38Z-3-60-65	Magnesite	Vein	lc1	Median zone		0.02	-	-	-	0.24	0.01	5.70	0.01	-	-	-	-	-	-	-	-	-	5.98
ISTE	Listvenite	38Z-3-60-65	Magnesite	Vein	lc1	Median zone		0.04	-	-	-	0.21	0.00	5.68	0.03	-	-	-	-	-	-	-	-	-	5.96
ISTE	Listvenite	38Z-3-60-65	Magnesite	Vein	lc1	Median zone		-	-	-	-	0.69	0.05	5.25	0.01	-	-	-	-	-	-	-	-	0.00	6.00
ISTE	Listvenite	38Z-3-60-65	Magnesite	Vein	lc1	Rim		0.05	-	-	-	0.32	0.01	5.56	0.01	-	-	-	-	-	-	-	-	-	5.95
ISTE	Listvenite	38Z-3-60-65	Magnesite	Vein	lc2			0.01	-	-	-	0.70	0.05	5.23	0.00	-	-	-	-	-	-	-	-	-	5.99
ISTE	Listvenite	38Z-3-60-65	Magnesite	Vein	lc2			-	-	-	-	0.44	0.02	5.54	0.00	-	-	-	-	-	-	-	-	-	6.00
ISTE	Carb. serpentinite	40Z-3-11-16	Dolomite	Matrix	Aggregate			-	-	-	-	0.02	0.00	3.00	2.98	-	-	-	-	-	-	-	-	-	6.00
ISTE	Carb. serpentinite	40Z-3-11-16	Dolomite	Matrix	Aggregate			0.00	-	-	-	0.02	0.01	2.98	2.99	-	-	-	-	-	-	-	-	-	6.00
ISTE	Carb. serpentinite	40Z-3-11-16	Dolomite	Matrix	Aggregate			-	-	-	-	0.02	0.01	3.00	2.97	-	-	-	-	-	-	-	-	-	6.00
ISTE	Carb. serpentinite	40Z-3-11-16	Dolomite	Matrix	Aggregate			0.11	-	-	-	0.08	0.00	2.79	2.91	-	-	-	-	-	-	-	-	-	5.89
ISTE	Carb. serpentinite	40Z-3-11-16	Dolomite	Matrix	Aggregate			-	-	-	-	0.06	0.01	2.96	2.97	-	-	-	-	-	-	-	-	-	6.00
ISTE	Carb. serpentinite	40Z-3-11-16	Dolomite	Matrix	Aggregate			0.03	-	-	-	0.08	0.01	2.88	2.98	-	-	-	-	-	-	-	-	-	5.97
ISTE	Carb. serpentinite	40Z-3-11-16	Dolomite	Matrix	sc0			0.02	-	-	-	0.00	0.01	2.99	2.95	-	-	-	-	-	-	-	-	-	5.98
ISTE	Carb. serpentinite	40Z-3-11-16	Dolomite	Vein	sc0	Median zone		0.19	-	-	-	0.03	0.04	2.84	2.71	-	-	-	-	-	-	-	-	-	5.81
ISTE	Carb. serpentinite	40Z-3-11-16	Dolomite	Vein	sc0	Median zone		0.05	-	-	-	0.02	0.06	2.95	2.88	-	-	-	-	-	-	-	-	-	5.95
GM	Carb. serpentinite	43Z-2-43-48	Dolomite	Matrix	Dol-core spheroid	Internal growth		0.26	-	-	-	0.09	0.05	2.32	3.01	-	-	-	-	-	-	-	-	-	5.74
GM	Carb. serpentinite	43Z-2-43-48	Dolomite	Matrix	Mg-core spheroid	Rim		0.65	-	-	-	0.07	0.04	2.45	2.15	-	-	-	-	-	-	-	-	-	5.35
GM	Carb. serpentinite	43Z-2-43-48	Dolomite	Vein	sc0	Median zone		0.08	-	-	-	0.03	0.02	2.54	3.26	-	-	-	-	-	-	-	-	-	5.92
GM	Carb. serpentinite	43Z-2-43-48	Dolomite	Vein	sc0	Median zone		0.07	-	-	-	0.03	0.03	2.57	3.23	-	-	-	-	-	-	-	-	-	5.93
GM	Carb. serpentinite	43Z-2-43-48	Dolomite	Vein	sc0	Median zone		0.06	-	-	-	0.03	0.03	2.52	3.31	-	-	-	-	-	-	-	-	-	5.94
GM	Carb. serpentinite	43Z-2-43-49	Dolomite	Vein	sc0	Median zone		0.13	-	-	-	0.04	0.03	2.49	3.18	-	-	-	-	-	-	-	-	-	5.87
GM	Carb. serpentinite	43Z-2-43-48	Dolomite	Vein	sc2	Median zone		0.13	-	-	-	0.03	0.03	2.53	3.15	-	-	-	-	-	-	-	-	-	5.87
GM	Carb. serpentinite	43Z-2-43-48	Dolomite	Vein	sc2	Median zone		0.50	-	-	-	0.07	0.04	2.34	2.57	-	-	-	-	-	-	-	-	-	5.50
GM	Carb. serpentinite	43Z-2-43-48	Magnesite	Matrix	Dol-core spheroid	Internal growth	d	0.54	-	-	-	0.21	0.04	3.90	0.76	-	-	-	-	-	-	-	-	-	5.46
GM	Carb. serpentinite	43Z-2-43-48	Dolomite	Matrix	Dol-core spheroid	Core	d	0.26	-	-	-	0.04	0.02	2.44	2.96	-	-	-	-	-	-	-	-	-	5.74
GM	Carb. serpentinite	43Z-2-43-48	Dolomite	Matrix	Dol-core spheroid	Core	d	0.06	-	-	-	0.02	0.03	2.53	3.31	-	-	-	-	-	-	-	-	-	5.94
GM	Carb. serpentinite	43Z-2-43-48	Dolomite	Matrix	Dol-core spheroid	Core	d	0.13	-	-	-	0.03	0.03	2.53	3.16	-	-	-	-	-	-	-	-	-	5.87
GM	Carb. serpentinite	43Z-2-43-48	Magnesite	Matrix	Dol-core spheroid	Internal growth	d	0.07	-	-	-	0.14	0.08	5.56	0.08	-	-	-	-	-	-	-	-	-	5.93
GM	Carb. serpentinite	43Z-2-43-48	Dolomite	Matrix	Dol-core spheroid	Internal growth	d	0.24	-	-	-	0.09	0.06	3.46	1.91	-	-	-	-	-	-	-	-	-	5.76
GM	Carb. serpentinite	43Z-2-43-48	Dolomite	Matrix	Dol-core spheroid	Internal growth	d	0.46	-	-	-	0.07	0.03	2.26	2.73	-	-	-	-	-	-	-	-	-	5.54
GM	Carb. serpentinite	43Z-2-43-48	Magnesite	Matrix	Mg-core spheroid	Rim		0.42	-	-	-	0.17	0.06	4.75	0.17	-	-	-	-	-	-	-	-	-	5.58
GM	Carb. serpentinite	43Z-2-43-48	Magnesite	Matrix	Mg-core spheroid	Rim	e	0.79	-	-	0.01	0.13	0.05	3.59	0.63	-	-	-	-	-	-	-	-	-	5.21
GM	Carb. serpentinite	43Z-2-43-48	Magnesite	Matrix	Mg-core spheroid	Internal growth	e	0.76	-	-	0.00	0.12	0.06	3.70	0.59	-	-	-	-	-	-	-	-	-	5.23
GM	Carb. serpentinite	43Z-2-43-48	Magnesite	Matrix	Mg-core spheroid	Internal growth	e	0.68	-	-	-	0.12	0.06	3.77	0.68	-	-	-	-	-	-	-	-	-	5.32
GM	Carb. serpentinite	43Z-2-43-48	Magnesite	Matrix	Mg-core spheroid	Core	e	0.61	-	-	-	0.11	0.07	3.24	1.35	-	-	-	-	-	-	-	-	-	5.39
GM	Carb. serpentinite	43Z-2-43-48	Magnesite	Matrix	Mg-core spheroid	Core	e	0.60	-	-	-	0.14	0.07	3.91	0.67	-	-	-	-	-	-	-	-	-	5.40
GM	Carb. serpentinite	43Z-2-43-48	Magnesite	Matrix	Mg-core spheroid	Internal growth	e	0.70	-	-	-	0.13	0.06	3.83	0.59	-	-	-	-	-	-	-	-	-	5.30
GM	Carb. serpentinite	43Z-2-43-48	Magnesite	Matrix	Mg-core spheroid	Internal growth	e	0.51	-	-	-	0.45	0.06	3.86	0.61	-	-	-	-	-	-	-	-	-	5.49

GM	Carb. serpentinite	43Z-2-43-48	Dolomite	Matrix	Mg-core spheroid	Rim	e	0.65	-	-	-	0.08	0.03	2.43	2.17	-	-	-	-	-	-	-	-	-	5.35
GM	Carb. serpentinite	43Z-2-43-48	Dolomite	Matrix	Mg-core spheroid	Rim	f	0.65	-	-	-	0.07	0.04	2.45	2.15	-	-	-	-	-	-	-	-	-	5.35
GM	Carb. serpentinite	43Z-2-43-48	Magnesite	Matrix	Mg-core spheroid	Internal growth	f	0.40	-	-	-	0.17	0.08	4.36	0.59	-	-	-	-	-	-	-	-	-	5.60
GM	Carb. serpentinite	43Z-2-43-48	Magnesite	Matrix	Mg-core spheroid	Rim	f	0.79	-	-	0.00	0.13	0.06	3.60	0.62	-	-	-	-	-	-	-	-	-	5.20
GM	Carb. serpentinite	43Z-2-43-48	Magnesite	Vein	sc2	Median zone		0.23	-	-	-	0.33	0.02	5.16	0.03	-	-	-	-	-	-	-	-	-	5.77
GM	Carb. serpentinite	43Z-2-43-48	Magnesite	Vein	sc2	Median zone		0.24	-	-	-	0.31	0.02	5.16	0.03	-	-	-	-	-	-	-	-	-	5.76
GM	Carb. serpentinite	43Z-2-43-48	Magnesite	Vein	sc2	Median zone		0.09	-	-	-	0.15	0.08	4.63	0.97	-	-	-	-	-	-	-	-	-	5.91
GM	Carb. serpentinite	43Z-2-43-48	Magnesite	Vein	sc2	Median zone		0.09	-	-	-	0.14	0.10	5.16	0.43	-	-	-	-	-	-	-	-	-	5.91
GM	Carb. serpentinite	43Z-3-0-5	Dolomite	Matrix	Dol-core spheroid	Core		0.33	-	-	-	0.09	0.06	2.33	2.85	-	-	-	-	-	-	-	-	-	5.67
GM	Carb. serpentinite	43Z-3-0-5	Dolomite	Matrix	Dol-core spheroid	Core		0.36	-	-	-	0.08	0.03	2.38	2.80	-	-	-	-	-	-	-	-	-	5.64
GM	Carb. serpentinite	43Z-3-0-5	Dolomite	Matrix	Dol-core spheroid	Core		0.37	-	-	-	0.19	0.07	3.10	1.91	-	-	-	-	-	-	-	-	-	5.63
GM	Carb. serpentinite	43Z-3-0-5	Dolomite	Matrix	Dol-core spheroid	Core		0.29	-	-	-	0.10	0.06	2.44	2.82	-	-	-	-	-	-	-	-	-	5.71
GM	Carb. serpentinite	43Z-3-0-5	Dolomite	Matrix	Dol-core spheroid	Core		0.59	-	-	-	0.08	0.03	2.30	2.42	-	-	-	-	-	-	-	-	-	5.41
GM	Carb. serpentinite	43Z-3-0-5	Dolomite	Matrix	Dol-core spheroid	Core		0.57	-	-	-	0.09	0.03	2.26	2.47	-	-	-	-	-	-	-	-	-	5.43
GM	Carb. serpentinite	43Z-3-0-5	Dolomite	Matrix	Mg-core spheroid	Core		0.76	-	-	-	0.25	0.02	4.19	0.02	-	-	-	-	-	-	-	-	-	5.24
GM	Carb. serpentinite	43Z-3-0-5	Dolomite	Vein	sc2	Median zone		0.06	-	-	-	0.08	0.06	3.18	2.54	-	-	-	-	-	-	-	-	-	5.94
GM	Carb. serpentinite	43Z-3-0-5	Dolomite	Vein	sc2	Intermediate		0.08	-	-	-	0.02	0.05	2.53	3.24	-	-	-	-	-	-	-	-	-	5.92
GM	Carb. serpentinite	43Z-3-0-5	Magnesite	Vein	sc2	Rim		0.76	-	-	-	0.25	0.02	4.19	0.02	-	-	-	-	-	-	-	-	-	5.24
GM	Carb. serpentinite	43Z-3-0-5	Magnesite	Vein	sc2	Intermediate	g	0.01	-	-	-	0.28	0.02	5.65	0.02	-	-	-	-	-	-	-	-	-	5.99
GM	Carb. serpentinite	43Z-3-0-5	Magnesite	Vein	sc2	Intermediate	g	0.02	-	-	-	0.24	-	5.68	0.04	-	-	-	-	-	-	-	-	-	5.98
GM	Carb. serpentinite	43Z-3-0-5	Magnesite	Vein	sc2	Intermediate	g	0.25	-	-	-	0.24	-	5.24	0.03	-	-	-	-	-	-	-	-	-	5.75
GM	Carb. serpentinite	43Z-3-0-5	Magnesite	Vein	sc2	Median zone	g	0.31	-	-	-	0.28	0.02	5.05	0.02	-	-	-	-	-	-	-	-	-	5.69
GM	Carb. serpentinite	43Z-3-0-5	Magnesite	Vein	sc2	Median zone	g	0.24	-	-	-	0.45	0.14	4.87	0.06	-	-	-	-	-	-	-	-	-	5.76
GM	Carb. serpentinite	43Z-3-0-5	Magnesite	Vein	sc2	Median zone	g	0.50	-	-	-	0.32	0.07	4.60	0.02	-	-	-	-	-	-	-	-	-	5.50
GM	Carb. serpentinite	43Z-3-0-5	Magnesite	Vein	sc2	Intermediate	g	0.19	-	-	-	0.29	0.02	5.27	0.04	-	-	-	-	-	-	-	-	-	5.81
GM	Carb. serpentinite	43Z-3-0-5	Magnesite	Vein	sc2	Intermediate	g	0.57	-	-	-	0.23	-	4.61	0.03	-	-	-	-	-	-	-	-	-	5.43
GM	Carb. serpentinite	43Z-3-0-5	Magnesite	Vein	sc2	Intermediate	g	0.15	-	-	-	0.26	-	5.42	0.03	-	-	-	-	-	-	-	-	-	5.85
GM	Carb. serpentinite	43Z-3-0-5	Dolomite	Vein	sc2	Rim	g	0.14	-	-	-	0.03	0.07	2.43	3.20	-	-	-	-	-	-	-	-	-	5.86
GM	Carb. serpentinite	43Z-3-0-5	Dolomite	Vein	sc2	Rim	g	0.14	-	-	-	0.02	0.06	2.48	3.16	-	-	-	-	-	-	-	-	-	5.86
GM	Carb. serpentinite	43Z-4-52-57	Dolomite	Matrix	Dol-core spheroid	Core		-	-	-	-	-	-	2.81	3.19	-	-	-	-	-	-	-	-	-	6.00
GM	Carb. serpentinite	43Z-4-52-57	Dolomite	Matrix	Dol-core spheroid	Core		0.39	-	-	-	0.05	-	2.55	2.62	-	-	-	-	-	-	-	-	-	5.61
GM	Carb. serpentinite	43Z-4-52-57	Dolomite	Matrix	Dol-core spheroid	Core		0.01	-	-	-	0.02	0.02	2.81	3.12	-	-	-	-	-	-	-	-	-	5.99
GM	Carb. serpentinite	43Z-4-52-57	Dolomite	Matrix	Dol-core spheroid	Core		0.02	-	-	-	0.10	-	2.69	3.17	-	-	-	-	-	-	-	-	-	5.98
GM	Carb. serpentinite	43Z-4-52-57	Dolomite	Matrix	Dol-core spheroid	Core		0.38	-	-	-	0.08	0.04	2.59	2.53	-	-	-	-	-	-	-	-	-	5.62
GM	Carb. serpentinite	43Z-4-52-57	Dolomite	Matrix	Dol-core spheroid	Core		0.28	-	-	-	0.09	0.05	2.84	2.47	-	-	-	-	-	-	-	-	-	5.72
GM	Carb. serpentinite	43Z-4-52-57	Dolomite	Matrix	Dol-core spheroid	Core		0.26	-	-	-	0.10	0.05	2.95	2.37	-	-	-	-	-	-	-	-	-	5.74
GM	Carb. serpentinite	43Z-4-52-57	Dolomite	Matrix	Dol-core spheroid	Core		0.30	-	-	-	0.04	0.04	2.67	2.64	-	-	-	-	-	-	-	-	-	5.70
GM	Carb. serpentinite	43Z-4-52-57	Dolomite	Matrix	Dol-core spheroid	Core		0.60	-	-	-	0.06	0.04	2.62	2.07	-	-	-	-	-	-	-	-	-	5.40
GM	Carb. serpentinite	43Z-4-52-57	Dolomite	Matrix	Dol-core spheroid	Core		0.56	-	-	-	0.08	0.04	2.75	2.01	-	-	-	-	-	-	-	-	-	5.44
GM	Carb. serpentinite	43Z-4-52-57	Dolomite	Matrix	Dol-core spheroid	Core		0.33	-	-	0.03	1.59	0.03	2.12	1.56	-	-	-	-	-	-	-	-	-	5.66
GM	Carb. serpentinite	43Z-4-52-57	Dolomite	Vein	sc2	Median zone		0.34	-	-	-	0.03	0.06	2.72	2.51	-	-	-	-	-	-	-	-	-	5.66
GM	Carb. serpentinite	43Z-4-52-57	Dolomite	Vein	sc2	Median zone		0.41	-	-	-	0.04	0.05	2.64	2.45	-	-	-	-	-	-	-	-	-	5.59
GM	Carb. serpentinite	43Z-4-52-57	Dolomite	Vein	sc2	Median zone		0.36	-	-	-	0.04	0.03	2.69	2.50	-	-	-	-	-	-	-	-	-	5.64
GM	Carb. serpentinite	43Z-4-52-57	Dolomite	Vein	sc2	Median zone		0.28	-	-	-	0.04	0.03	2.68	2.68	-	-	-	-	-	-	-	-	-	5.72
GM	Carb. serpentinite	43Z-4-52-57	Magnesite	Matrix	Mg-core spheroid	Core		0.49	-	-	-	0.21	0.03	3.85	0.93	-	-	-	-	-	-	-	-	-	5.51
ISTE	Carb. serpentinite	44Z-1-41-46	Magnesite	Matrix	Mg-core spheroid	Core		0.45	-	-	-	0.26	0.02	4.73	0.09	-	-	-	-	-	-	-	-	-	5.55
ISTE	Carb. serpentinite	44Z-1-41-46	Magnesite	Matrix	Mg-core spheroid	Core		0.50	-	-	-	0.34	0.02	4.54	0.09	-	-	-	-	-	-	-	-	-	5.50
ISTE	Carb. serpentinite	44Z-1-41-46	Magnesite	Matrix	Mg-core spheroid	Core		0.49	-	-	-	0.32	0.02	4.52	0.18	-	-	-	-	-	-	-	-	-	5.51
ISTE	Carb. serpentinite	44Z-1-41-46	Dolomite	Matrix	Spheroid	Core		0.43	-	-	-	0.23	0.01	3.36	1.53	-	-	-	-	-	-	-	-	-	5.57
ISTE	Carb. serpentinite	44Z-1-41-46	Dolomite	Vein	sc0	Median zone		0.09	-	-	-	0.03	0.09	3.05	2.64	-	-	-	-	-	-	-	-	-	5.91
ISTE	Carb. serpentinite	44Z-1-41-46	Dolomite	Vein	sc2	Median zone		0.16	-	-	-	0.02	0.19	2.72	2.75	-	-	-	-	-	-	-	-	-	5.84
ISTE	Carb. serpentinite	44Z-1-41-46	Dolomite	Vein	sc2 or sc4?	Median zone		0.00	-	-	-	0.18	0.02	2.74	3.05	-	-	-	-	-	-	-	-	-	6.00
ISTE	Carb. serpentinite	44Z-1-41-46	Dolomite	Vein	sc2 or sc4?	Median zone		0.02	-	-	-	0.14	0.07	2.88	2.86	-	-	-	-	-	-	-	-	-	5.98

ISTE	Carb. serpentinite	44Z-1-41-46	Dolomite	Vein	sc2 or sc4?	Median zone	0.52	-	-	-	0.08	0.01	2.76	2.10	-	-	-	-	-	-	-	0.00	-	5.48
ISTE	Carb. serpentinite	44Z-1-41-46	Dolomite	Vein	sc2 or sc4?	Median zone	0.41	-	-	-	0.15	0.07	2.93	2.02	-	-	-	-	-	-	-	-	-	5.59
ISTE	Carb. serpentinite	44Z-1-41-46	Dolomite	Vein	sc2 or sc4?	Median zone	0.29	-	-	-	0.16	0.07	2.96	2.21	-	-	-	-	-	-	-	-	-	5.71
ISTE	Carb. serpentinite	44Z-1-41-46	Dolomite	Vein	sc2 or sc4?	Median zone	0.32	-	-	-	0.10	0.01	2.76	2.47	-	-	-	-	-	-	-	0.00	-	5.68
ISTE	Carb. serpentinite	44Z-1-41-46	Magnesite	Vein	sc2	Median zone	0.09	-	-	-	0.68	0.14	4.93	0.07	-	-	-	-	-	-	-	-	-	5.91
ISTE	Carb. serpentinite	44Z-1-41-46	Magnesite	Vein	sc0	Median zone	0.15	-	-	-	0.06	0.11	5.20	0.33	-	-	-	-	-	-	-	-	-	5.85
ISTE	Carb. serpentinite	44Z-1-41-46	Magnesite	Vein	sc0	Median zone	0.10	-	-	-	0.07	0.16	5.55	0.03	-	-	-	-	-	-	-	-	-	5.90
GM	Carb. serpentinite	44Z-4-0-5	Magnesite	Matrix	Fe-core spheroid	Core	0.73	-	-	-	1.07	-	3.27	0.20	-	-	-	-	-	-	-	-	-	5.27
GM	Carb. serpentinite	44Z-4-0-5	Magnesite	Matrix	Fe-core spheroid	Core	0.47	-	-	-	1.50	-	3.42	0.14	-	-	-	-	-	-	-	-	-	5.53
GM	Carb. serpentinite	44Z-4-0-5	Magnesite	Matrix	Fe-core spheroid	Core	0.29	-	-	0.04	2.00	-	3.17	0.17	-	-	-	-	-	-	-	-	-	5.68
ISTE	Carb. serpentinite	44Z-4-0-5	Magnesite	Matrix	Mg-core spheroid	Core	0.43	-	-	-	0.36	0.01	4.66	0.11	-	-	-	-	-	-	-	-	-	5.57
ISTE	Carb. serpentinite	44Z-4-0-5	Magnesite	Matrix	Mg-core spheroid	Core	0.47	-	-	-	0.45	0.01	4.51	0.09	-	-	-	-	-	-	-	-	-	5.53
ISTE	Carb. serpentinite	44Z-4-0-5	Magnesite	Matrix	Mg-core spheroid	Core	0.75	-	-	-	0.60	0.01	3.84	0.06	-	-	-	-	-	-	-	-	-	5.25
ISTE	Carb. serpentinite	44Z-4-0-5	Magnesite	Matrix	Mg-core spheroid	Core	0.65	-	-	-	0.29	0.01	4.34	0.05	-	-	-	-	-	-	-	-	-	5.35
ISTE	Carb. serpentinite	44Z-4-0-5	Magnesite	Matrix	Mg-core spheroid	Core	0.54	-	-	-	0.32	0.01	4.53	0.04	-	-	-	-	-	-	-	-	-	5.46
ISTE	Carb. serpentinite	44Z-4-0-5	Magnesite	Matrix	Mg-core spheroid	Internal growth	0.58	-	-	-	0.53	0.01	4.23	0.06	-	-	-	-	-	-	-	-	-	5.42
ISTE	Carb. serpentinite	44Z-4-0-5	Magnesite	Matrix	Mg-core spheroid	Rim	0.66	-	-	-	0.41	0.01	4.20	0.06	-	-	-	-	-	-	-	-	-	5.34
GM	Carb. serpentinite	44Z-4-0-5	Magnesite	Matrix	Mg-core spheroid	Rim	0.16	-	-	-	1.23	-	4.40	0.04	-	-	-	-	-	-	-	-	-	5.84
GM	Carb. serpentinite	44Z-4-0-5	Magnesite	Vein	sc0	Border	0.51	-	-	-	0.16	0.05	4.73	0.04	-	-	-	-	-	-	-	-	-	5.49
GM	Carb. serpentinite	44Z-4-0-5	Magnesite	Vein	sc0	Border	0.39	-	-	-	0.20	0.06	4.89	0.06	-	-	-	-	-	-	-	-	-	5.61
GM	Carb. serpentinite	44Z-4-0-5	Magnesite	Vein	sc0	Border	0.43	-	-	-	0.15	0.06	4.88	0.04	-	-	-	-	-	-	-	-	-	5.57
GM	Carb. serpentinite	44Z-4-0-5	Magnesite	Vein	sc0		0.12	-	-	-	0.16	0.06	5.46	0.07	-	-	-	-	-	-	-	-	-	5.88
GM	Carb. serpentinite	44Z-4-0-5	Magnesite	Vein	sc0		0.13	-	-	-	0.13	0.05	5.55	0.02	-	-	-	-	-	-	-	-	-	5.87
GM	Carb. serpentinite	44Z-4-0-5	Magnesite	Vein	sc0		-	-	-	-	2.17	-	3.75	0.08	-	-	-	-	-	-	-	-	-	6.00
GM	Carb. serpentinite	44Z-4-0-5	Magnesite	Vein	sc2	Median zone	0.06	-	-	-	0.84	-	4.99	0.05	-	-	-	-	-	-	-	-	-	5.94
GM	Carb. serpentinite	44Z-4-0-5	Magnesite	Vein	sc2	Median zone	0.31	-	-	-	0.80	-	4.35	0.22	-	-	-	-	-	-	-	-	-	5.69
GM	Carb. serpentinite	44Z-4-0-5	Magnesite	Vein	sc2	Median zone	0.04	-	-	-	0.78	-	5.12	0.02	-	-	-	-	-	-	-	-	-	5.96
GM	Carb. serpentinite	44Z-4-0-5	Magnesite	Vein	sc2	Median zone	0.33	-	-	-	1.03	-	4.20	0.11	-	-	-	-	-	-	-	-	-	5.67
GM	Carb. serpentinite	44Z-4-0-5	Magnesite	Vein	sc2	Median zone	0.02	-	-	-	1.31	-	4.62	0.04	-	-	-	-	-	-	-	-	-	5.98
GM	Carb. serpentinite	44Z-4-0-5	Magnesite	Vein	sc2	Median zone	0.04	-	-	-	0.76	-	5.16	0.01	-	-	-	-	-	-	-	-	-	5.96
GM	Carb. serpentinite	44Z-4-0-5	Magnesite	Vein	sc2	Median zone	0.53	-	-	-	0.91	-	3.96	0.06	-	-	-	-	-	-	-	-	-	5.47
GM	Carb. serpentinite	44Z-4-0-5	Magnesite	Vein	sc2	Median zone	0.57	-	-	-	0.67	-	3.70	0.49	-	-	-	-	-	-	-	-	-	5.43
GM	Carb. serpentinite	44Z-4-0-5	Magnesite	Vein	sc2	Median zone	-	-	-	-	2.37	-	3.57	0.06	-	-	-	-	-	-	-	-	-	6.00
GM	Carb. serpentinite	44Z-4-0-5	Magnesite	Vein	sc2	Median zone	-	-	-	-	2.14	-	3.83	0.03	-	-	-	-	-	-	-	-	-	6.00
GM	Carb. serpentinite	44Z-4-0-5	Magnesite	Vein	sc2	Median zone	0.94	-	-	-	0.44	-	3.67	0.02	-	-	-	-	-	-	-	-	-	5.06
ISTE	Carb. serpentinite	44Z-4-0-5	Magnesite	Vein	sc2	Border	0.17	-	-	-	0.15	0.03	5.43	0.05	-	-	-	-	-	-	-	-	-	5.83
ISTE	Listvenite	45Z-1-38-39	Dolomite	Matrix	Dol-core spheroid	Core	0.00	-	-	-	0.02	0.02	3.15	2.81	-	-	-	-	-	-	-	-	-	6.00
ISTE	Listvenite	45Z-1-38-39	Dolomite	Matrix	Aggregate		-	-	-	-	0.06	0.00	3.08	2.86	-	-	-	-	-	-	-	-	-	6.00
ISTE	Listvenite	45Z-1-38-39	Dolomite	Matrix	Aggregate		-	-	-	-	0.21	0.01	2.96	2.82	-	-	-	-	-	-	-	-	0.00	6.00
ISTE	Listvenite	45Z-1-38-39	Magnesite	Matrix	Mg-core spheroid	Core	0.11	-	-	-	0.27	0.00	5.49	0.02	-	-	-	-	-	-	-	-	0.00	5.89
ISTE	Listvenite	45Z-1-38-39	Magnesite	Matrix	Mg-core spheroid	Core	0.05	-	-	-	0.32	0.01	5.56	0.02	-	-	-	-	-	-	-	-	-	5.95
ISTE	Listvenite	45Z-1-38-39	Magnesite	Matrix	Mg-core spheroid	Core	0.02	-	-	-	0.32	0.00	5.63	0.01	-	-	-	-	-	-	-	-	-	5.98
ISTE	Listvenite	45Z-1-38-39	Magnesite	Matrix	Mg-core spheroid	Core	0.07	-	-	-	0.23	0.00	5.58	0.04	-	-	-	-	-	-	-	-	-	5.93
ISTE	Listvenite	45Z-1-38-39	Magnesite	Matrix	Mg-core spheroid	Core	0.04	-	-	-	0.26	0.00	5.64	0.03	-	-	-	-	-	-	-	-	0.00	5.96
ISTE	Listvenite	45Z-1-38-39	Magnesite	Matrix	Aggregate		0.04	-	-	-	0.22	0.01	5.67	0.02	-	-	-	-	-	-	-	-	-	5.96
ISTE	Listvenite	45Z-1-38-39	Magnesite	Matrix	Aggregate		0.53	-	-	-	0.22	-	4.70	0.02	-	-	-	-	-	-	-	-	0.01	5.47
ISTE	Listvenite	45Z-1-38-39	Magnesite	Matrix	Aggregate		-	-	-	-	0.38	0.01	5.61	0.00	-	-	-	-	-	-	-	-	-	6.00
ISTE	Listvenite	45Z-1-38-39	Magnesite	Matrix	Overgrowth		-	-	-	-	0.37	0.00	5.63	-	-	-	-	-	-	-	-	-	-	6.00
ISTE	Listvenite	45Z-1-38-39	Magnesite	Matrix	Overgrowth		0.03	-	-	-	0.30	0.00	5.61	0.02	-	-	-	-	-	-	-	-	-	5.97
GM	Listvenite	46Z-4-46-51	Dolomite	Matrix	Dol-core spheroid	Core	0.01	-	-	-	0.37	0.02	2.77	2.83	-	-	-	-	-	-	-	-	-	5.99
GM	Listvenite	46Z-4-46-51	Dolomite	Matrix	Dol-core spheroid	Core	0.01	-	-	-	0.35	-	2.84	2.78	-	-	-	-	-	-	-	-	-	5.99
GM	Listvenite	46Z-4-46-51	Dolomite	Matrix	Dol-core spheroid	Core	-	-	-	-	0.26	0.02	2.67	3.05	-	-	-	-	-	-	-	-	-	6.00
GM	Listvenite	46Z-4-46-51	Dolomite	Vein	lc1	Median zone	-	-	-	-	0.39	0.02	2.62	2.97	-	-	-	-	-	-	-	-	-	6.00

ISTE	Listvenite	46Z-4-46-51	Dolomite	Vein	lc1	Median zone		0.01	-	-	-	0.12	0.01	3.04	2.80	-	-	-	-	-	-	-	-	-	5.99
ISTE	Listvenite	46Z-4-46-51	Dolomite	Vein	lc6	Median zone		0.01	-	-	-	0.26	0.01	2.87	2.85	-	-	-	-	-	-	-	-	-	5.99
ISTE	Listvenite	46Z-4-46-51	Dolomite	Vein	lc6	Median zone		0.01	-	-	-	0.17	0.01	3.01	2.80	-	-	-	-	-	-	-	-	-	5.99
GM	Listvenite	46Z-4-46-51	Magnesite	Matrix	Mg-core spheroid	Core		0.02	-	-	-	0.54	-	5.39	0.02	-	-	-	-	-	-	-	-	-	5.98
GM	Listvenite	46Z-4-46-51	Magnesite	Matrix	Mg-core spheroid	Core		0.16	-	-	-	0.29	-	5.31	0.01	-	-	0.09	-	-	-	-	-	-	5.84
GM	Listvenite	46Z-4-46-51	Magnesite	Matrix	Mg-core spheroid	Core		0.30	-	0.01	-	0.20	-	5.04	0.06	-	-	0.08	-	-	-	-	-	-	5.69
GM	Listvenite	46Z-4-46-51	Magnesite	Matrix	Mg-core spheroid	Core		0.47	-	-	-	0.36	0.01	4.66	0.03	-	-	-	-	-	-	-	-	-	5.53
GM	Listvenite	46Z-4-46-51	Magnesite	Matrix	Mg-core spheroid	Core		0.06	-	-	-	0.32	-	5.55	0.01	-	-	-	-	-	-	-	-	-	5.94
GM	Listvenite	46Z-4-46-51	Magnesite	Matrix	Mg-core spheroid	Core		0.07	-	-	-	0.32	-	5.54	0.01	-	-	-	-	-	-	-	-	-	5.93
GM	Listvenite	46Z-4-46-51	Magnesite	Matrix	Mg-core spheroid	Core		0.01	-	-	-	0.87	-	5.07	0.05	-	-	-	-	-	-	-	-	-	5.99
GM	Listvenite	46Z-4-46-51	Magnesite	Matrix	Mg-core spheroid	Core		0.04	-	-	-	0.51	-	5.39	0.02	-	-	-	-	-	-	-	-	-	5.96
ISTE	Listvenite	46Z-4-46-51	Magnesite	Matrix	Mg-core spheroid	Core		0.04	-	-	-	0.25	0.01	5.66	0.02	-	-	-	-	-	-	-	-	-	5.96
ISTE	Listvenite	46Z-4-46-51	Magnesite	Matrix	Mg-core spheroid	Core		0.04	-	-	-	0.24	0.01	5.67	0.02	-	-	-	-	-	-	-	-	-	5.96
ISTE	Listvenite	46Z-4-46-51	Magnesite	Matrix	Mg-core spheroid	Core		0.01	-	-	-	0.18	-	5.80	0.00	-	-	-	-	-	-	-	-	-	5.99
ISTE	Listvenite	46Z-4-46-51	Magnesite	Matrix	Mg-core spheroid	Core		0.20	-	-	-	0.42	0.02	5.12	0.04	-	-	-	-	-	-	-	-	-	5.80
ISTE	Listvenite	46Z-4-46-51	Magnesite	Matrix	Mg-core spheroid	Core		0.04	-	-	-	0.25	0.00	5.65	0.02	-	-	-	-	-	-	-	-	-	5.96
ISTE	Listvenite	46Z-4-46-51	Magnesite	Matrix	Mg-core spheroid	Core		0.01	-	-	-	0.21	0.00	5.75	0.02	-	-	-	-	-	-	-	-	-	5.99
ISTE	Listvenite	46Z-4-46-51	Magnesite	Matrix	Mg-core spheroid	Internal growth		0.01	-	-	-	0.17	-	5.82	0.00	-	-	-	-	-	-	-	-	-	5.99
ISTE	Listvenite	46Z-4-46-51	Magnesite	Matrix	Mg-core spheroid	Internal growth		0.21	-	-	-	0.17	-	5.37	0.03	-	-	-	-	-	-	-	-	-	5.79
ISTE	Listvenite	46Z-4-46-51	Magnesite	Matrix	Mg-core spheroid	Internal growth		0.19	-	-	-	0.51	0.02	5.08	0.02	-	-	-	-	-	-	-	-	-	5.81
ISTE	Listvenite	46Z-4-46-51	Magnesite	Matrix	Mg-core spheroid	Rim		1.42	-	-	-	0.60	-	2.52	0.03	-	-	-	-	-	-	-	-	-	4.58
ISTE	Listvenite	46Z-4-46-51	Magnesite	Matrix	Mg-core spheroid	Rim		1.47	-	-	-	0.99	0.00	2.05	0.01	-	-	-	-	-	-	-	-	-	4.53
ISTE	Listvenite	46Z-4-46-51	Magnesite	Matrix	Mg-core spheroid	Rim		0.02	-	-	-	0.26	0.01	5.68	0.01	-	-	-	-	-	-	-	-	-	5.98
GM	Listvenite	46Z-4-46-51	Magnesite	Matrix	Mg-core spheroid	Rim	h	0.30	-	0.01	-	0.29	-	5.00	0.08	-	-	-	-	-	-	-	-	-	5.69
GM	Listvenite	46Z-4-46-51	Magnesite	Matrix	Mg-core spheroid	Rim	h	0.26	-	-	-	0.18	-	5.25	0.04	-	-	-	-	-	-	-	-	-	5.74
GM	Listvenite	46Z-4-46-51	Magnesite	Matrix	Mg-core spheroid	Internal growth	h	0.18	-	-	-	0.17	-	5.45	0.02	-	-	-	-	-	-	-	-	-	5.82
GM	Listvenite	46Z-4-46-51	Magnesite	Matrix	Mg-core spheroid	Internal growth	h	0.05	-	-	-	0.25	-	5.64	0.01	-	-	-	-	-	-	-	-	-	5.95
GM	Listvenite	46Z-4-46-51	Magnesite	Matrix	Mg-core spheroid	Internal growth	h	0.01	-	-	-	0.18	-	5.79	0.01	-	-	-	-	-	-	-	-	-	5.99
GM	Listvenite	46Z-4-46-51	Magnesite	Matrix	Mg-core spheroid	Internal growth	h	0.03	-	-	-	0.18	-	5.73	0.04	-	-	-	-	-	-	-	-	-	5.97
GM	Listvenite	46Z-4-46-51	Magnesite	Matrix	Mg-core spheroid	Internal growth	h	0.58	-	-	-	0.16	-	4.68	0.01	-	-	-	-	-	-	-	-	-	5.42
GM	Listvenite	46Z-4-46-51	Magnesite	Matrix	Mg-core spheroid	Internal growth	h	0.02	-	-	-	0.17	-	5.79	0.01	-	-	-	-	-	-	-	-	-	5.98
GM	Listvenite	46Z-4-46-51	Magnesite	Matrix	Mg-core spheroid	Internal growth	h	0.02	-	-	-	0.18	-	5.78	-	-	-	-	-	-	-	-	-	-	5.98
GM	Listvenite	46Z-4-46-51	Magnesite	Matrix	Mg-core spheroid	Internal growth	h	0.01	-	-	-	0.18	-	5.78	0.01	-	-	-	-	-	-	-	-	-	5.99
GM	Listvenite	46Z-4-46-51	Magnesite	Matrix	Mg-core spheroid	Internal growth	h	0.20	-	-	-	0.17	-	5.43	0.01	-	-	-	-	-	-	-	-	-	5.80
GM	Listvenite	46Z-4-46-51	Magnesite	Matrix	Mg-core spheroid	Internal growth	h	0.23	-	-	-	0.17	-	5.35	0.02	-	-	-	-	-	-	-	-	-	5.77
GM	Listvenite	46Z-4-46-51	Magnesite	Matrix	Mg-core spheroid	Internal growth	h	0.16	-	-	-	0.19	-	5.47	0.02	-	-	-	-	-	-	-	-	-	5.84
GM	Listvenite	46Z-4-46-51	Magnesite	Matrix	Mg-core spheroid	Internal growth	h	0.01	-	-	-	0.18	-	5.80	0.01	-	-	-	-	-	-	-	-	-	5.99
GM	Listvenite	46Z-4-46-51	Magnesite	Matrix	Mg-core spheroid	Internal growth	h	0.18	-	-	-	0.16	-	5.48	0.00	-	-	-	-	-	-	-	-	-	5.82
GM	Listvenite	46Z-4-46-51	Magnesite	Matrix	Mg-core spheroid	Internal growth	h	-	-	-	-	0.17	-	5.82	0.01	-	-	-	-	-	-	-	-	-	6.00
GM	Listvenite	46Z-4-46-51	Magnesite	Matrix	Mg-core spheroid	Internal growth	h	-	-	-	-	0.17	-	5.82	0.00	-	-	-	-	-	-	-	-	-	6.00
GM	Listvenite	46Z-4-46-51	Magnesite	Matrix	Mg-core spheroid	Core	h	0.04	-	-	-	0.28	-	5.63	0.01	-	-	-	-	-	-	-	-	-	5.96
GM	Listvenite	46Z-4-46-51	Magnesite	Matrix	Mg-core spheroid	Core	h	-	-	-	-	0.22	-	5.77	0.01	-	-	-	-	-	-	-	-	-	6.00
GM	Listvenite	46Z-4-46-51	Magnesite	Matrix	Mg-core spheroid	Core	h	-	-	-	-	0.26	-	5.66	0.07	-	-	-	-	-	-	-	-	-	6.00
GM	Listvenite	46Z-4-46-51	Magnesite	Matrix	Mg-core spheroid	Core	h	0.03	-	-	-	0.30	-	5.63	0.01	-	-	-	-	-	-	-	-	-	5.97
GM	Listvenite	46Z-4-46-51	Magnesite	Matrix	Mg-core spheroid	Core	h	0.07	-	-	-	0.33	-	5.51	0.01	-	-	-	-	-	-	-	-	-	5.93
GM	Listvenite	46Z-4-46-51	Magnesite	Matrix	Mg-core spheroid	Core	h	0.04	-	-	-	0.32	0.01	5.58	0.02	-	-	-	-	-	-	-	-	-	5.96
GM	Listvenite	46Z-4-46-51	Magnesite	Matrix	Mg-core spheroid	Core	h	0.03	-	-	-	0.30	-	5.64	0.01	-	-	-	-	-	-	-	-	-	5.97
GM	Listvenite	46Z-4-46-51	Magnesite	Matrix	Mg-core spheroid	Core	h	-	-	-	-	0.18	-	5.81	0.01	-	-	-	-	-	-	-	-	-	6.00
GM	Listvenite	46Z-4-46-51	Magnesite	Matrix	Mg-core spheroid	Internal growth	h	0.02	-	-	-	0.19	-	5.76	0.00	-	-	-	-	-	-	-	-	-	5.98
GM	Listvenite	46Z-4-46-51	Magnesite	Matrix	Mg-core spheroid	Internal growth	h	-	-	-	-	0.26	-	5.74	0.01	-	-	-	-	-	-	-	-	-	6.00
GM	Listvenite	46Z-4-46-51	Magnesite	Matrix	Mg-core spheroid	Internal growth	h	0.01	-	-	-	0.25	-	5.73	0.00	-	-	-	-	-	-	-	-	-	5.99
GM	Listvenite	46Z-4-46-51	Magnesite	Matrix	Mg-core spheroid	Internal growth	h	-	-	-	-	0.26	-	5.73	0.01	-	-	-	-	-	-	-	-	-	6.00
GM	Listvenite	46Z-4-46-51	Magnesite	Matrix	Mg-core spheroid	Internal growth	h	0.04	-	-	-	0.25	-	5.65	0.02	-	-	-	-	-	-	-	-	-	5.96

GM	Listvenite	46Z-4-46-51	Magnesite	Matrix	Mg-core spheroid	Internal growth	h	0.04	-	-	-	0.25	-	5.67	0.01	-	-	-	-	-	-	-	-	-	5.96
GM	Listvenite	46Z-4-46-51	Magnesite	Matrix	Mg-core spheroid	Internal growth	h	-	-	-	-	0.25	-	5.75	0.01	-	-	-	-	-	-	-	-	-	6.00
GM	Listvenite	46Z-4-46-51	Magnesite	Matrix	Mg-core spheroid	Internal growth	h	-	-	-	-	0.23	-	5.77	-	-	-	-	-	-	-	-	-	-	6.00
GM	Listvenite	46Z-4-46-51	Magnesite	Matrix	Mg-core spheroid	Internal growth	h	0.02	-	-	-	0.19	-	5.78	-	-	-	-	-	-	-	-	-	-	5.98
GM	Listvenite	46Z-4-46-51	Magnesite	Matrix	Mg-core spheroid	Internal growth	h	0.04	-	-	-	0.18	-	5.74	0.01	-	-	-	-	-	-	-	-	-	5.96
GM	Listvenite	46Z-4-46-51	Magnesite	Matrix	Mg-core spheroid	Internal growth	h	0.14	-	-	-	0.19	-	5.52	0.01	-	-	-	-	-	-	-	-	-	5.86
GM	Listvenite	46Z-4-46-51	Magnesite	Matrix	Mg-core spheroid	Internal growth	h	0.14	-	-	-	0.18	-	5.51	0.03	-	-	-	-	-	-	-	-	-	5.86
GM	Listvenite	46Z-4-46-51	Magnesite	Matrix	Mg-core spheroid	Internal growth	h	0.15	-	-	-	0.22	-	5.42	0.06	-	-	-	-	-	-	-	-	-	5.85
GM	Listvenite	46Z-4-46-51	Magnesite	Matrix	Mg-core spheroid	Rim	h	0.15	-	-	-	0.23	-	5.40	0.07	-	-	-	-	-	-	-	-	-	5.85
GM	Listvenite	46Z-4-46-51	Magnesite	Matrix	Mg-core spheroid	Rim	h	0.49	-	0.02	-	0.28	-	4.60	0.10	-	-	-	-	-	-	-	-	-	5.50
GM	Listvenite	46Z-4-46-51	Magnesite	Matrix	Mg-core spheroid	Rim	i	0.37	-	-	-	1.23	-	3.95	0.07	-	-	-	-	-	-	-	-	-	5.63
GM	Listvenite	46Z-4-46-51	Magnesite	Matrix	Mg-core spheroid	Rim	i	0.95	-	-	-	1.02	-	3.01	0.07	-	-	-	-	-	-	-	-	-	5.05
GM	Listvenite	46Z-4-46-51	Magnesite	Matrix	Mg-core spheroid	Internal growth	i	0.02	-	-	-	0.76	-	5.11	0.09	-	-	-	-	-	-	-	-	-	5.98
GM	Listvenite	46Z-4-46-51	Magnesite	Matrix	Mg-core spheroid	Internal growth	i	0.59	-	0.02	-	0.21	-	4.53	0.06	-	-	-	-	-	-	-	-	-	5.40
GM	Listvenite	46Z-4-46-51	Magnesite	Matrix	Mg-core spheroid	Internal growth	i	0.29	-	0.05	-	0.20	-	5.12	0.04	-	-	-	-	-	-	-	-	-	5.69
GM	Listvenite	46Z-4-46-51	Magnesite	Matrix	Mg-core spheroid	Internal growth	i	0.25	-	-	-	0.17	-	5.30	0.02	-	-	-	-	-	-	-	-	-	5.75
GM	Listvenite	46Z-4-46-51	Magnesite	Matrix	Mg-core spheroid	Internal growth	i	0.11	-	-	-	0.20	-	5.56	0.01	-	0.01	-	-	-	-	-	-	-	5.89
GM	Listvenite	46Z-4-46-51	Magnesite	Matrix	Mg-core spheroid	Internal growth	i	-	-	-	-	0.18	-	5.82	-	-	-	-	-	-	-	-	-	-	6.00
GM	Listvenite	46Z-4-46-51	Magnesite	Matrix	Mg-core spheroid	Internal growth	i	0.01	-	-	-	0.18	-	5.79	-	-	-	-	-	-	-	-	-	-	5.99
GM	Listvenite	46Z-4-46-51	Magnesite	Matrix	Mg-core spheroid	Internal growth	i	0.07	-	-	-	0.17	-	5.68	0.01	-	-	-	-	-	-	-	-	-	5.93
GM	Listvenite	46Z-4-46-51	Magnesite	Matrix	Mg-core spheroid	Internal growth	i	-	-	-	-	0.20	-	5.80	0.00	-	-	-	-	-	-	-	-	-	6.00
GM	Listvenite	46Z-4-46-51	Magnesite	Matrix	Mg-core spheroid	Core	i	-	-	-	-	0.25	-	5.75	-	-	-	-	-	-	-	-	-	-	6.00
GM	Listvenite	46Z-4-46-51	Magnesite	Matrix	Mg-core spheroid	Core	i	0.09	-	-	-	0.25	-	5.54	0.02	-	-	-	-	-	-	-	-	-	5.91
GM	Listvenite	46Z-4-46-51	Magnesite	Matrix	Mg-core spheroid	Core	i	0.06	-	-	-	0.25	-	5.62	0.02	-	-	-	-	-	-	-	-	-	5.94
GM	Listvenite	46Z-4-46-51	Magnesite	Matrix	Mg-core spheroid	Core	i	0.03	-	-	-	0.26	-	5.67	0.02	-	-	-	-	-	-	-	-	-	5.97
GM	Listvenite	46Z-4-46-51	Magnesite	Matrix	Mg-core spheroid	Core	i	0.04	-	-	-	0.26	-	5.64	0.02	-	-	-	-	-	-	-	-	-	5.96
GM	Listvenite	46Z-4-46-51	Magnesite	Matrix	Mg-core spheroid	Core	i	0.05	-	-	-	0.26	-	5.62	0.02	-	-	-	-	-	-	-	-	-	5.95
GM	Listvenite	46Z-4-46-51	Magnesite	Matrix	Mg-core spheroid	Internal growth	i	0.02	-	-	-	0.28	-	5.67	0.02	-	-	-	-	-	-	-	-	-	5.98
GM	Listvenite	46Z-4-46-51	Magnesite	Matrix	Mg-core spheroid	Internal growth	i	0.05	-	-	-	0.20	-	5.69	0.01	-	-	-	-	-	-	-	-	-	5.95
GM	Listvenite	46Z-4-46-51	Magnesite	Matrix	Mg-core spheroid	Internal growth	i	0.01	-	-	-	0.18	-	5.79	0.01	-	-	-	-	-	-	-	-	-	5.99
GM	Listvenite	46Z-4-46-51	Magnesite	Matrix	Mg-core spheroid	Internal growth	i	-	-	-	-	0.17	-	5.82	0.01	-	-	-	-	-	-	-	-	-	6.00
GM	Listvenite	46Z-4-46-51	Magnesite	Matrix	Mg-core spheroid	Internal growth	i	0.01	-	-	-	0.17	-	5.80	0.01	-	-	-	-	-	-	-	-	-	5.99
GM	Listvenite	46Z-4-46-51	Magnesite	Matrix	Mg-core spheroid	Internal growth	i	0.11	-	-	-	0.18	-	5.58	0.01	-	-	-	-	-	-	-	-	-	5.89
GM	Listvenite	46Z-4-46-51	Magnesite	Matrix	Mg-core spheroid	Internal growth	i	0.19	-	-	-	0.17	-	5.43	0.02	-	-	-	-	-	-	-	-	-	5.81
GM	Listvenite	46Z-4-46-51	Magnesite	Matrix	Mg-core spheroid	Internal growth	i	0.38	-	0.02	-	0.19	-	4.99	0.03	-	-	-	-	-	-	-	-	-	5.61
GM	Listvenite	46Z-4-46-51	Magnesite	Matrix	Mg-core spheroid	Rim	i	0.73	-	0.01	-	0.27	-	4.18	0.07	-	-	-	-	-	-	-	-	-	5.26
GM	Listvenite	46Z-4-46-51	Magnesite	Matrix	Mg-core spheroid	Rim	i	0.54	-	-	-	0.72	-	4.14	0.06	-	-	-	-	-	-	-	-	-	5.46
GM	Listvenite	46Z-4-46-51	Magnesite	Matrix	Euhedral	Core		0.01	-	-	-	0.24	-	5.63	0.11	-	-	-	-	-	-	-	-	-	5.99
GM	Listvenite	46Z-4-46-51	Magnesite	Matrix	Aggregate			0.26	-	-	-	0.99	-	4.47	0.03	-	-	-	-	-	-	-	-	-	5.74
GM	Listvenite	46Z-4-46-51	Magnesite	Vein	lc1	Median zone		-	-	-	-	0.22	-	5.64	0.14	-	-	-	-	-	-	-	-	-	6.00
GM	Listvenite	46Z-4-46-51	Magnesite	Vein	lc1	Median zone		0.31	-	-	-	0.55	-	3.63	1.20	-	-	-	-	-	-	-	-	-	5.69
ISTE	Listvenite	46Z-4-46-51	Magnesite	Vein	lc1	Intermediate		0.01	-	-	-	0.76	0.01	5.16	0.05	-	-	-	-	-	-	-	-	-	5.99
ISTE	Listvenite	46Z-4-46-51	Magnesite	Vein	lc1	Intermediate		0.01	-	-	-	0.33	0.01	5.63	0.01	-	-	-	-	-	-	-	-	-	5.99
ISTE	Listvenite	46Z-4-46-51	Magnesite	Vein	lc1	Rim		0.01	-	-	-	0.18	0.00	5.80	0.01	-	-	-	-	-	-	-	-	-	5.99
GM	Listvenite	46Z-4-46-51	Magnesite	Vein	lc1	Rim		-	-	-	-	0.77	0.01	5.18	0.04	-	-	-	-	-	-	-	-	-	6.00
GM	Listvenite	46Z-4-46-51	Magnesite	Vein	lc1	Rim		0.05	-	-	-	0.69	0.02	5.18	0.01	-	-	-	-	-	-	-	-	-	5.95
GM	Listvenite	46Z-4-46-51	Magnesite	Vein	lc1	Rim	j	0.26	-	-	-	0.30	-	5.17	0.02	-	-	-	-	-	-	-	-	-	5.74
GM	Listvenite	46Z-4-46-51	Magnesite	Vein	lc1	Rim	j	0.16	-	-	-	0.19	-	5.48	0.01	-	-	-	-	-	-	-	-	-	5.84
GM	Listvenite	46Z-4-46-51	Magnesite	Vein	lc1	Rim	j	1.16	-	0.02	-	0.22	-	3.41	0.01	-	-	-	-	-	-	-	-	-	4.82
GM	Listvenite	46Z-4-46-51	Magnesite	Vein	lc1	Intermediate	j	0.05	-	-	-	0.39	-	5.49	0.01	-	-	-	-	-	-	-	-	-	5.95
GM	Listvenite	46Z-4-46-51	Magnesite	Vein	lc1	Intermediate	j	0.10	-	-	-	0.19	-	5.60	-	-	-	-	-	-	-	-	-	-	5.90
GM	Listvenite	46Z-4-46-51	Magnesite	Vein	lc1	Intermediate	j	-	-	-	-	0.18	-	5.81	0.00	-	-	-	-	-	-	-	-	-	6.00
GM	Listvenite	46Z-4-46-51	Magnesite	Vein	lc1	Intermediate	j	0.01	-	-	-	0.19	-	5.78	0.01	-	-	-	-	-	-	-	-	-	5.99

GM	Listvenite	46Z-4-46-51	Magnesite	Vein	lc1	Intermediate	j	0.01	-	-	-	0.26	-	5.72	-	-	-	-	-	-	-	-	-	-	-	5.99
GM	Listvenite	46Z-4-46-51	Magnesite	Vein	lc1	Intermediate	j	0.26	-	-	-	0.23	-	5.24	0.01	-	-	-	-	-	-	-	-	-	-	5.74
GM	Listvenite	46Z-4-46-51	Magnesite	Vein	lc1	Intermediate	j	0.21	-	-	-	0.24	-	5.34	0.01	-	-	-	-	-	-	-	-	-	-	5.79
GM	Listvenite	46Z-4-46-51	Magnesite	Vein	lc1	Intermediate	j	0.02	-	-	-	0.26	-	5.69	0.02	-	-	-	-	-	-	-	-	-	-	5.98
GM	Listvenite	46Z-4-46-51	Magnesite	Vein	lc1	Intermediate	j	0.05	-	-	-	0.26	-	5.63	0.01	-	-	-	-	-	-	-	-	-	-	5.95
GM	Listvenite	46Z-4-46-51	Magnesite	Vein	lc1	Intermediate	j	0.01	-	-	-	0.27	-	5.72	-	-	-	-	-	-	-	-	-	-	-	5.99
GM	Listvenite	46Z-4-46-51	Magnesite	Vein	lc1	Intermediate	j	-	-	-	-	0.21	-	5.78	0.01	-	-	-	-	-	-	-	-	-	-	6.00
GM	Listvenite	46Z-4-46-51	Magnesite	Vein	lc1	Intermediate	j	1.56	-	0.01	-	0.17	-	2.69	0.01	-	-	-	-	-	-	-	-	-	-	4.44
GM	Listvenite	46Z-4-46-51	Magnesite	Vein	lc1	Intermediate	j	1.63	-	-	-	0.22	-	2.51	0.00	-	-	-	-	-	-	-	-	-	-	4.37
GM	Listvenite	46Z-4-46-51	Magnesite	Vein	lc1	Intermediate	j	0.18	-	-	-	0.43	-	5.19	0.02	-	-	-	-	-	-	-	-	-	-	5.82
GM	Listvenite	46Z-4-46-51	Magnesite	Vein	lc1	Intermediate	j	0.10	-	-	-	0.28	-	5.51	0.00	-	-	-	-	-	-	-	-	-	-	5.90
GM	Listvenite	46Z-4-46-51	Magnesite	Vein	lc1	Intermediate	j	0.02	-	-	-	0.51	0.01	5.42	0.02	-	-	-	-	-	-	-	-	-	-	5.98
GM	Listvenite	46Z-4-46-51	Magnesite	Vein	lc1	Median zone	j	-	-	-	-	0.86	-	5.07	0.07	-	-	-	-	-	-	-	-	-	-	6.00
GM	Listvenite	46Z-4-46-51	Magnesite	Vein	lc1	Median zone	j	0.23	-	-	-	1.08	-	4.42	0.05	-	-	-	-	-	-	-	-	-	-	5.77
GM	Listvenite	46Z-4-46-51	Magnesite	Vein	lc1	Median zone	j	0.02	-	-	-	1.90	0.02	4.01	0.03	-	-	-	-	-	-	-	-	-	-	5.98
GM	Listvenite	46Z-4-46-51	Magnesite	Vein	lc1	Median zone	j	0.48	-	-	-	1.67	0.02	3.29	0.05	-	-	-	-	-	-	-	-	-	-	5.52
GM	Listvenite	46Z-4-46-51	Magnesite	Vein	lc1	Intermediate	j	0.07	-	-	-	0.93	-	4.89	0.04	-	-	-	-	-	-	-	-	-	-	5.93
GM	Listvenite	46Z-4-46-51	Magnesite	Vein	lc1	Intermediate	j	0.01	-	-	-	0.85	-	5.04	0.09	-	-	-	-	-	-	-	-	-	-	5.99
GM	Listvenite	46Z-4-46-51	Magnesite	Vein	lc1	Intermediate	j	0.02	-	-	-	0.38	-	5.58	-	-	-	-	-	-	-	-	-	-	-	5.98
GM	Listvenite	46Z-4-46-51	Magnesite	Vein	lc1	Intermediate	j	0.12	-	-	-	0.28	-	5.47	0.01	-	-	-	-	-	-	-	-	-	-	5.88
GM	Listvenite	46Z-4-46-51	Magnesite	Vein	lc1	Intermediate	j	0.04	-	-	-	0.37	-	5.53	0.01	-	-	-	-	-	-	-	-	-	-	5.96
GM	Listvenite	46Z-4-46-51	Magnesite	Vein	lc1	Rim	j	0.22	-	-	-	0.40	-	5.15	0.01	-	-	-	-	-	-	-	-	-	-	5.78
GM	Listvenite	46Z-4-46-51	Magnesite	Vein	lc1	Rim	j	0.11	-	-	-	0.40	-	5.36	0.01	-	-	-	-	-	-	-	-	-	-	5.89
GM	Listvenite	46Z-4-46-51	Magnesite	Vein	lc1	Rim	j	0.14	-	-	-	0.19	-	5.52	0.01	-	-	-	-	-	-	-	-	-	-	5.86
GM	Listvenite	46Z-4-46-51	Magnesite	Vein	lc1	Rim	k	1.17	-	-	-	0.26	0.01	3.38	0.02	-	-	-	-	-	-	-	-	-	-	4.83
GM	Listvenite	46Z-4-46-51	Magnesite	Vein	lc1	Rim	k	0.03	-	-	-	0.36	-	5.55	0.02	-	-	-	-	-	-	-	-	-	-	5.97
GM	Listvenite	46Z-4-46-51	Magnesite	Vein	lc1	Intermediate	k	0.01	-	-	-	0.38	-	5.60	0.01	-	-	-	-	-	-	-	-	-	-	5.99
GM	Listvenite	46Z-4-46-51	Magnesite	Vein	lc1	Intermediate	k	-	-	-	-	0.27	-	5.73	0.00	-	-	-	-	-	-	-	-	-	-	6.00
GM	Listvenite	46Z-4-46-51	Magnesite	Vein	lc1	Intermediate	k	0.01	-	-	-	0.37	-	5.60	0.01	-	-	-	-	-	-	-	-	-	-	5.99
GM	Listvenite	46Z-4-46-51	Magnesite	Vein	lc1	Intermediate	k	-	-	-	-	0.51	0.02	5.46	0.01	-	-	-	-	-	-	-	-	-	-	6.00
GM	Listvenite	46Z-4-46-51	Magnesite	Vein	lc1	Median zone	k	0.06	-	-	-	0.81	-	4.87	0.20	-	-	-	-	-	-	-	-	-	-	5.94
GM	Listvenite	46Z-4-46-51	Dolomite	Vein	lc1	Median zone	k	-	-	-	-	0.19	-	2.86	2.96	-	-	-	-	-	-	-	-	-	-	6.00
GM	Listvenite	46Z-4-46-51	Dolomite	Vein	lc1	Median zone	k	-	-	-	-	0.19	-	2.76	3.05	-	-	-	-	-	-	-	-	-	-	6.00
GM	Listvenite	46Z-4-46-51	Dolomite	Vein	lc1	Median zone	k	0.05	-	-	-	0.39	-	3.16	2.35	-	-	-	-	-	-	-	-	-	-	5.95
GM	Listvenite	46Z-4-46-51	Magnesite	Vein	lc1	Intermediate	k	0.02	-	-	-	0.32	-	5.63	0.02	-	-	-	-	-	-	-	-	-	-	5.98
GM	Listvenite	46Z-4-46-51	Magnesite	Vein	lc1	Intermediate	k	0.01	-	-	-	0.31	-	5.65	0.01	-	-	-	-	-	-	-	-	-	-	5.99
GM	Listvenite	46Z-4-46-51	Magnesite	Vein	lc1	Intermediate	k	0.03	-	-	-	0.72	-	5.17	0.05	-	-	-	-	-	-	-	-	-	-	5.97
GM	Listvenite	46Z-4-46-51	Magnesite	Vein	lc1	Intermediate	k	0.01	-	-	-	0.57	0.02	5.30	0.08	-	-	-	-	-	-	-	-	-	-	5.99
GM	Listvenite	46Z-4-46-51	Magnesite	Vein	lc1	Intermediate	k	0.41	-	-	-	0.81	-	4.32	0.05	-	-	-	-	-	-	-	-	-	-	5.59
GM	Listvenite	46Z-4-46-51	Magnesite	Vein	lc1	Intermediate	k	0.04	-	-	-	0.62	-	5.28	0.02	-	-	-	-	-	-	-	-	-	-	5.96
GM	Listvenite	46Z-4-46-51	Magnesite	Vein	lc1	Intermediate	k	0.02	-	-	-	0.59	-	5.37	0.01	-	-	-	-	-	-	-	-	-	-	5.98
GM	Listvenite	46Z-4-46-51	Magnesite	Vein	lc1	Intermediate	k	0.05	-	-	-	0.49	0.01	5.39	0.01	-	-	-	-	-	-	-	-	-	-	5.95
GM	Listvenite	46Z-4-46-51	Magnesite	Vein	lc1	Intermediate	k	0.01	-	-	-	0.19	-	5.78	0.01	-	-	-	-	-	-	-	-	-	-	5.99
GM	Listvenite	46Z-4-46-51	Magnesite	Vein	lc1	Intermediate	k	0.07	-	-	-	0.27	-	5.58	0.01	-	-	-	-	-	-	-	-	-	-	5.93
GM	Listvenite	46Z-4-46-51	Magnesite	Vein	lc1	Intermediate	k	0.28	-	-	-	0.23	-	5.20	0.02	-	-	-	-	-	-	-	-	-	-	5.72
GM	Listvenite	46Z-4-46-51	Magnesite	Vein	lc1	Rim	k	0.20	-	-	-	0.27	-	5.31	0.01	-	-	-	-	-	-	-	-	-	-	5.80
GM	Listvenite	46Z-4-46-51	Magnesite	Vein	lc1	Rim	k	0.49	-	-	-	0.48	-	4.50	0.03	-	-	-	-	-	-	-	-	-	-	5.51
GM	Listvenite	46Z-4-46-51	Magnesite	Vein	lc1	Rim	l	0.18	-	-	-	0.18	-	5.45	0.01	-	-	-	-	-	-	-	-	-	-	5.82
GM	Listvenite	46Z-4-46-51	Magnesite	Vein	lc1	Rim	l	0.24	-	-	-	0.20	-	5.32	0.01	-	-	-	-	-	-	-	-	-	-	5.76
GM	Listvenite	46Z-4-46-51	Magnesite	Vein	lc1	Intermediate	l	0.24	-	-	-	0.19	-	5.32	0.02	-	-	-	-	-	-	-	-	-	-	5.76
GM	Listvenite	46Z-4-46-51	Magnesite	Vein	lc1	Intermediate	l	0.11	-	-	-	0.26	-	5.47	0.06	-	-	-	-	-	-	-	-	-	-	5.89
GM	Listvenite	46Z-4-46-51	Magnesite	Vein	lc1	Intermediate	l	0.01	-	-	-	0.19	-	5.78	0.00	-	-	-	-	-	-	-	-	-	-	5.99
GM	Listvenite	46Z-4-46-51	Magnesite	Vein	lc1	Intermediate	l	0.01	-	-	-	0.18	-	5.78	0.01	-	-	-	-	-	-	-	-	-	-	5.99

GM	Listvenite	46Z-4-46-51	Magnesite	Vein	lc1	Intermediate	l	-	-	-	-	0.20	-	5.80	-	-	-	-	-	-	-	-	-	-	-	-	6.00
GM	Listvenite	46Z-4-46-51	Magnesite	Vein	lc1	Intermediate	l	0.02	-	-	-	0.26	-	5.69	0.01	-	-	-	-	-	-	-	-	-	-	-	5.98
GM	Listvenite	46Z-4-46-51	Magnesite	Vein	lc1	Intermediate	l	-	-	-	-	0.26	-	5.72	0.02	-	-	-	-	-	-	-	-	-	-	-	6.00
GM	Listvenite	46Z-4-46-51	Magnesite	Vein	lc1	Median zone	l	0.21	-	-	-	0.24	-	5.32	0.02	-	-	-	-	-	-	-	-	-	-	-	5.79
GM	Listvenite	46Z-4-46-51	Magnesite	Vein	lc1	Median zone	l	0.08	-	-	-	0.26	-	5.55	0.03	-	-	-	-	-	-	-	-	-	-	-	5.92
GM	Listvenite	46Z-4-46-51	Magnesite	Vein	lc1	Median zone	l	0.03	-	-	-	0.26	-	5.67	0.02	-	-	-	-	-	-	-	-	-	-	-	5.97
GM	Listvenite	46Z-4-46-51	Magnesite	Vein	lc1	Median zone	l	0.01	-	-	-	0.28	-	5.68	0.02	-	-	-	-	-	-	-	-	-	-	-	5.99
GM	Listvenite	46Z-4-46-51	Magnesite	Vein	lc1	Median zone	l	0.49	-	-	-	0.45	0.02	4.53	0.02	-	-	-	-	-	-	-	-	-	-	-	5.51
GM	Listvenite	46Z-4-46-51	Magnesite	Vein	lc1	Median zone	l	0.08	-	-	-	0.23	-	5.60	0.01	-	-	-	-	-	-	-	-	-	-	-	5.92
GM	Listvenite	46Z-4-46-51	Magnesite	Vein	lc1	Median zone	l	0.04	-	-	-	0.22	-	5.69	0.01	-	-	-	-	-	-	-	-	-	-	-	5.96
GM	Listvenite	46Z-4-46-51	Magnesite	Vein	lc1	Median zone	l	0.10	-	-	-	0.23	-	5.55	0.02	-	-	-	-	-	-	-	-	-	-	-	5.90
GM	Listvenite	46Z-4-46-51	Magnesite	Vein	lc1	Intermediate	l	0.05	-	-	-	0.26	-	5.62	0.02	-	-	-	-	-	-	-	-	-	-	-	5.95
GM	Listvenite	46Z-4-46-51	Magnesite	Vein	lc1	Intermediate	l	0.06	-	-	-	0.25	-	5.61	0.01	-	-	-	-	-	-	-	-	-	-	-	5.94
GM	Listvenite	46Z-4-46-51	Magnesite	Vein	lc1	Intermediate	l	0.01	-	-	-	0.26	-	5.72	-	-	-	-	-	-	-	-	-	-	-	-	5.99
GM	Listvenite	46Z-4-46-51	Magnesite	Vein	lc1	Intermediate	l	-	-	-	-	0.20	-	5.80	0.01	-	-	-	-	-	-	-	-	-	-	-	6.00
GM	Listvenite	46Z-4-46-51	Magnesite	Vein	lc1	Intermediate	l	-	-	-	-	0.18	-	5.82	0.01	-	-	-	-	-	-	-	-	-	-	-	6.00
GM	Listvenite	46Z-4-46-51	Magnesite	Vein	lc1	Intermediate	l	0.06	-	-	-	0.34	-	5.53	0.01	-	-	-	-	-	-	-	-	-	-	-	5.94
GM	Listvenite	46Z-4-46-51	Magnesite	Vein	lc1	Intermediate	l	0.14	-	-	-	0.21	-	5.49	0.02	-	-	-	-	-	-	-	-	-	-	-	5.86
GM	Listvenite	46Z-4-46-51	Magnesite	Vein	lc1	Intermediate	l	0.24	-	-	-	0.19	-	5.31	0.02	-	-	-	-	-	-	-	-	-	-	-	5.76
GM	Listvenite	46Z-4-46-51	Magnesite	Vein	lc1	Intermediate	l	0.25	-	-	-	0.25	-	5.25	0.01	-	-	-	-	-	-	-	-	-	-	-	5.75
GM	Listvenite	46Z-4-46-51	Magnesite	Vein	lc1	Intermediate	l	0.44	-	-	-	0.20	-	4.91	0.01	-	-	-	-	-	-	-	-	-	-	-	5.56
GM	Listvenite	46Z-4-46-51	Magnesite	Vein	lc1	Rim	l	0.31	-	0.02	-	0.19	-	5.15	0.02	-	-	-	-	-	-	-	-	-	-	-	5.69
GM	Listvenite	46Z-4-46-51	Magnesite	Vein	lc1	Rim	l	0.32	-	0.07	-	0.30	-	4.94	0.01	-	-	-	-	-	-	-	-	-	-	-	5.64
GM	Listvenite	46Z-4-46-51	Magnesite	Vein	lc1	Rim	m	-	-	-	-	0.18	-	5.81	0.01	-	-	-	-	-	-	-	-	-	-	-	6.00
GM	Listvenite	46Z-4-46-51	Magnesite	Vein	lc1	Rim	m	0.01	-	-	-	0.24	-	5.74	0.01	-	-	-	-	-	-	-	-	-	-	-	5.99
GM	Listvenite	46Z-4-46-51	Magnesite	Vein	lc1	Intermediate	m	0.01	-	-	-	0.26	-	5.69	0.03	-	-	-	-	-	-	-	-	-	-	-	5.99
GM	Listvenite	46Z-4-46-51	Magnesite	Vein	lc1	Intermediate	m	-	-	-	-	0.26	-	5.72	0.02	-	-	-	-	-	-	-	-	-	-	-	6.00
GM	Listvenite	46Z-4-46-51	Magnesite	Vein	lc1	Intermediate	m	0.03	-	-	-	0.26	-	5.66	0.02	-	-	-	-	-	-	-	-	-	-	-	5.97
GM	Listvenite	46Z-4-46-51	Magnesite	Vein	lc1	Intermediate	m	0.02	-	-	0.01	0.23	-	5.72	-	-	-	-	-	-	-	-	-	-	-	5.97
GM	Listvenite	46Z-4-46-51	Magnesite	Vein	lc1	Intermediate	m	0.08	-	-	-	0.37	-	5.45	0.01	-	-	-	-	-	-	-	-	-	-	-	5.92
GM	Listvenite	46Z-4-46-51	Magnesite	Vein	lc1	Intermediate	m	0.05	-	-	-	0.26	-	5.62	0.02	-	-	-	-	-	-	-	-	-	-	-	5.95
GM	Listvenite	46Z-4-46-51	Magnesite	Vein	lc1	Intermediate	m	0.04	-	-	-	0.26	-	5.64	0.02	-	-	-	-	-	-	-	-	-	-	-	5.96
GM	Listvenite	46Z-4-46-51	Magnesite	Vein	lc1	Intermediate	m	0.02	-	-	-	0.26	-	5.69	0.02	-	-	-	-	-	-	-	-	-	-	-	5.98
GM	Listvenite	46Z-4-46-51	Magnesite	Vein	lc1	Intermediate	m	1.00	-	-	0.01	0.16	-	3.81	0.01	-	-	-	-	-	-	-	-	-	-	-	4.99
GM	Listvenite	46Z-4-46-51	Magnesite	Vein	lc1	Intermediate	m	0.21	-	-	-	0.25	-	5.31	0.02	-	-	-	-	-	-	-	-	-	-	-	5.79
GM	Listvenite	46Z-4-46-51	Magnesite	Vein	lc1	Intermediate	m	0.13	-	-	0.01	0.27	-	5.43	0.04	-	-	-	-	-	-	-	-	-	-	-	5.87
GM	Listvenite	46Z-4-46-51	Magnesite	Vein	lc1	Intermediate	m	0.22	-	-	-	0.25	-	5.27	0.03	-	-	-	-	-	-	-	-	-	-	-	5.78
GM	Listvenite	46Z-4-46-51	Magnesite	Vein	lc1	Intermediate	m	0.09	-	-	0.01	0.27	-	5.52	0.03	-	-	-	-	-	-	-	-	-	-	-	5.91
GM	Listvenite	46Z-4-46-51	Magnesite	Vein	lc1	Intermediate	m	0.01	-	-	-	0.21	-	5.76	0.01	-	-	-	-	-	-	-	-	-	-	-	5.99
GM	Listvenite	46Z-4-46-51	Magnesite	Vein	lc1	Intermediate	m	0.88	-	-	-	0.41	-	3.81	0.02	-	-	-	-	-	-	-	-	-	-	-	5.12
GM	Listvenite	46Z-4-46-51	Magnesite	Vein	lc1	Median zone	m	0.01	-	-	-	0.86	-	5.02	0.09	-	-	-	-	-	-	-	-	-	-	-	5.99
GM	Listvenite	46Z-4-46-51	Magnesite	Vein	lc1	Median zone	m	-	-	-	-	0.85	-	5.07	0.08	-	-	-	-	-	-	-	-	-	-	-	6.00
GM	Listvenite	46Z-4-46-51	Dolomite	Vein	lc1	Median zone	m	0.02	-	-	-	0.45	-	3.44	2.07	-	-	-	-	-	-	-	-	-	-	-	5.98
GM	Listvenite	46Z-4-46-51	Dolomite	Vein	lc1	Median zone	m	0.01	-	-	-	0.20	-	2.76	3.01	-	-	-	-	-	-	-	-	-	-	-	5.99
GM	Listvenite	46Z-4-46-51	Dolomite	Vein	lc1	Median zone	m	-	-	-	-	0.19	-	2.82	3.00	-	-	-	-	-	-	-	-	-	-	-	6.00
GM	Listvenite	46Z-4-46-51	Magnesite	Vein	lc1	Median zone	m	0.02	-	-	-	0.80	-	4.52	0.64	-	-	-	-	-	-	-	-	-	-	-	5.98
GM	Listvenite	46Z-4-46-51	Magnesite	Vein	lc1	Median zone	m	0.01	-	-	-	0.64	0.01	5.31	0.02	-	-	-	-	-	-	-	-	-	-	-	5.99
GM	Listvenite	46Z-4-46-51	Magnesite	Vein	lc1	Median zone	m	0.04	-	-	-	0.46	-	5.44	0.02	-	-	-	-	-	-	-	-	-	-	-	5.96
GM	Listvenite	46Z-4-46-51	Magnesite	Vein	lc1	Intermediate	m	0.73	-	-	-	0.31	-	4.20	0.01	-	-	-	-	-	-	-	-	-	-	-	5.27
GM	Listvenite	46Z-4-46-51	Magnesite	Vein	lc1	Intermediate	m	0.02	-	-	0.01	0.23	-	5.69	0.02	-	-	-	-	-	-	-	-	-	-	-	5.97
GM	Listvenite	46Z-4-46-51	Magnesite	Vein	lc1	Intermediate	m	0.06	-	-	0.01	0.27	-	5.57	0.03	-	-	-	-	-	-	-	-	-	-	-	5.94
GM	Listvenite	46Z-4-46-51	Magnesite	Vein	lc1	Intermediate	m	0.04	-	-	-	0.26	-	5.63	0.03	-	-	-	-	-	-	-	-	-	-	-	5.96
GM	Listvenite	46Z-4-46-51	Magnesite	Vein	lc1	Intermediate	m	0.09	-	-	-	0.26	-	5.50	0.05	-	-	-	-	-	-	-	-	-	-	-	5.91

GM	Listvenite	46Z-4-46-51	Magnesite	Vein	lc1	Intermediate	m	0.05	-	-	0.01	0.28	-	5.58	0.03	-	-	-	-	-	-	-	-	-	5.95
GM	Listvenite	46Z-4-46-51	Magnesite	Vein	lc1	Intermediate	m	0.07	-	-	0.01	0.28	-	5.55	0.03	-	-	-	-	-	-	-	-	-	5.93
GM	Listvenite	46Z-4-46-51	Magnesite	Vein	lc1	Intermediate	m	0.08	-	-	0.01	0.32	-	5.45	0.05	-	-	-	-	-	-	-	-	-	5.91
GM	Listvenite	46Z-4-46-51	Magnesite	Vein	lc1	Intermediate	m	0.03	-	-	0.01	0.54	-	5.35	0.04	-	-	-	-	-	-	-	-	-	5.97
GM	Listvenite	46Z-4-46-51	Magnesite	Vein	lc1	Intermediate	m	0.02	-	-	0.01	0.35	-	5.55	0.04	-	-	-	-	-	-	-	-	-	5.97
GM	Listvenite	46Z-4-46-51	Magnesite	Vein	lc1	Intermediate	m	0.07	-	0.04	0.01	0.37	-	5.39	0.02	-	0.01	-	-	-	-	-	-	-	5.91
GM	Listvenite	46Z-4-46-51	Magnesite	Vein	lc1	Rim	m	0.22	-	0.13	0.02	0.50	-	4.80	0.02	-	0.04	-	-	-	-	-	-	-	5.73
GM	Listvenite	46Z-4-46-51	Magnesite	Vein	lc1	Rim	m	0.01	-	-	-	0.30	-	5.66	0.01	-	-	-	-	-	-	-	-	-	5.99
GM	Listvenite	46Z-4-46-51	Magnesite	Vein	lc2	Median zone		0.09	-	0.01	-	0.41	-	5.27	0.02	-	-	0.10	-	-	-	-	-	-	5.91
ISTE	Listvenite	46Z-4-46-51	Magnesite	Vein	lq4	Rim		0.01	-	-	-	0.45	0.01	5.42	0.10	-	-	-	-	-	-	-	-	-	5.99
ISTE	Listvenite	46Z-4-46-51	Magnesite	Vein	lq4	Rim		0.02	-	-	-	0.47	0.01	5.33	0.16	-	-	-	-	-	-	-	-	-	5.98
ISTE	Listvenite	48Z-1-6-11	Magnesite	Matrix	Mg-core spheroid	Core		0.00	-	-	-	0.09	0.01	5.89	0.01	-	-	-	-	-	-	-	-	-	6.00
ISTE	Listvenite	48Z-1-6-11	Magnesite	Matrix	Mg-core spheroid	Core		0.00	-	-	-	0.15	0.01	5.81	0.04	-	-	-	-	-	-	-	-	-	6.00
ISTE	Listvenite	48Z-1-6-11	Magnesite	Matrix	Mg-core spheroid	Core		0.05	-	-	-	0.12	0.00	5.75	0.03	-	-	-	-	-	-	-	-	-	5.95
ISTE	Listvenite	48Z-1-6-11	Magnesite	Matrix	Mg-core spheroid	Core		0.26	-	-	-	0.48	0.04	4.95	0.02	-	-	-	-	-	-	-	-	-	5.74
ISTE	Listvenite	48Z-1-6-11	Magnesite	Matrix	Mg-core spheroid	Internal growth		0.02	-	-	-	1.60	0.01	4.32	0.04	-	-	-	-	-	-	-	-	-	5.98
ISTE	Listvenite	48Z-1-6-11	Magnesite	Matrix	Mg-core spheroid	Rim		0.00	-	-	-	0.23	-	5.76	0.01	-	-	-	-	-	-	-	-	-	6.00
ISTE	Listvenite	48Z-1-6-11	Magnesite	Matrix	Aggregate			0.01	-	-	-	0.13	0.00	5.82	0.02	-	-	-	-	-	-	-	-	-	5.99
ISTE	Listvenite	48Z-1-6-11	Magnesite	Vein	lss0	Median zone		0.65	-	-	-	0.81	0.01	3.86	0.02	-	-	-	-	-	-	-	-	-	5.35
ISTE	Listvenite	48Z-1-6-11	Magnesite	Vein	lss0	Median zone		0.04	-	-	-	1.92	0.01	3.94	0.05	-	-	-	-	-	-	-	-	-	5.96
ISTE	Listvenite	48Z-1-6-11	Magnesite	Vein	lss0	Rim		0.00	-	-	-	0.17	-	5.82	0.00	-	-	-	-	-	-	-	-	-	6.00
ISTE	Listvenite	48Z-1-6-11	Magnesite	Vein	lss0	Rim		0.01	-	-	-	0.15	-	5.82	0.01	-	-	-	-	-	-	-	-	-	5.99
ISTE	Listvenite	48Z-1-6-11	Magnesite	Vein	lss0	Rim		0.00	-	-	-	0.22	-	5.76	0.01	-	-	-	-	-	-	-	-	-	6.00
ISTE	Listvenite	48Z-1-6-11	Magnesite	Vein	lss2	Median zone		0.04	-	-	-	0.13	0.07	5.69	0.03	-	-	-	-	-	-	-	-	-	5.96
ISTE	Listvenite	48Z-1-6-11	Magnesite	Vein	lss2	Median zone		0.01	-	-	-	0.14	0.05	5.77	0.02	-	-	-	-	-	-	-	-	-	5.99
ISTE	Listvenite	48Z-1-6-11	Magnesite	Vein	lss2	Median zone		0.03	-	-	-	0.14	0.04	5.75	0.01	-	-	-	-	-	-	-	-	-	5.97
ISTE	Listvenite	48Z-1-6-11	Magnesite	Vein	lss2	Rim		0.42	-	-	-	0.67	0.01	4.47	0.02	-	-	-	-	-	-	-	-	-	5.58
ISTE	Listvenite	48Z-1-6-11	Magnesite	Vein	lc1	Median zone		-	-	-	-	0.54	0.00	5.45	0.00	-	-	-	-	-	-	-	-	-	6.00
ISTE	Listvenite	48Z-1-6-11	Magnesite	Vein	lc1	Median zone		-	-	-	-	0.28	0.00	5.70	0.02	-	-	-	-	-	-	-	-	-	6.00
ISTE	Listvenite	48Z-1-6-11	Magnesite	Vein	lc1	Median zone		0.00	-	-	-	0.52	0.00	5.41	0.06	-	-	-	-	-	-	-	-	-	6.00
ISTE	Listvenite	48Z-1-6-11	Magnesite	Vein	lc1	Median zone		0.15	-	-	-	2.39	0.01	3.27	0.04	-	-	-	-	-	-	-	-	-	5.85
ISTE	Listvenite	48Z-1-6-11	Magnesite	Vein	lc1	Median zone		0.03	-	-	-	1.36	0.01	4.55	0.02	-	-	-	-	-	-	-	-	-	5.97
ISTE	Listvenite	48Z-1-6-11	Magnesite	Vein	lc1	Intermediate		0.00	-	-	-	2.13	0.01	3.80	0.05	-	-	-	-	-	-	-	0.00	-	6.00
ISTE	Listvenite	48Z-1-6-11	Magnesite	Vein	lc1	Intermediate		0.01	-	-	-	1.92	0.01	4.02	0.03	-	-	-	-	-	-	-	-	-	5.99
ISTE	Listvenite	48Z-1-6-11	Magnesite	Vein	lc1	Rim		0.11	-	-	-	0.39	0.01	5.38	0.02	-	-	-	-	-	-	-	-	-	5.89
GM	Listvenite	50Z-1-75-80	Magnesite	Matrix	Mg-core spheroid	Core		-	-	-	-	0.26	-	5.72	0.01	-	-	0.01	-	-	-	-	-	-	6.00
ISTE	Listvenite	50Z-1-75-80	Magnesite	Matrix	Fe-core spheroid	Core		0.14	-	-	-	0.84	0.01	4.84	0.03	-	-	-	-	-	-	-	-	-	5.86
ISTE	Listvenite	50Z-1-75-80	Magnesite	Matrix	Fe-core spheroid	Core		0.24	-	-	-	1.59	0.01	3.85	0.06	-	-	-	-	-	-	-	-	-	5.76
ISTE	Listvenite	50Z-1-75-80	Magnesite	Matrix	Fe-core spheroid	Core		0.18	-	-	-	1.73	0.02	3.81	0.08	-	-	-	-	-	-	-	-	-	5.82
ISTE	Listvenite	50Z-1-75-80	Magnesite	Matrix	Fe-core spheroid	Internal growth		0.05	-	-	-	1.57	0.02	4.28	0.03	-	-	-	-	-	-	-	-	-	5.95
ISTE	Listvenite	50Z-1-75-80	Magnesite	Matrix	Fe-core spheroid	Internal growth		0.03	-	-	-	0.80	0.02	5.09	0.03	-	-	-	-	-	-	-	-	-	5.97
ISTE	Listvenite	50Z-1-75-80	Magnesite	Matrix	Fe-core spheroid	Internal growth		0.01	-	-	-	0.20	-	5.78	0.01	-	-	-	-	-	-	-	-	-	5.99
ISTE	Listvenite	50Z-1-75-80	Magnesite	Matrix	Fe-core spheroid	Rim		0.03	-	-	-	0.21	-	5.71	0.02	-	-	-	-	-	-	-	-	-	5.97
ISTE	Listvenite	50Z-1-75-80	Magnesite	Matrix	Fe-core spheroid	Rim		0.03	-	-	-	0.20	-	5.72	0.01	-	-	-	-	-	-	-	-	-	5.97
ISTE	Listvenite	50Z-1-75-80	Magnesite	Vein	lss2	Median zone		0.01	-	-	-	0.22	0.00	5.76	0.00	-	-	-	-	-	-	-	-	-	5.99
ISTE	Listvenite	50Z-1-75-80	Magnesite	Vein	lss2	Median zone		0.01	-	-	-	0.21	0.01	5.73	0.03	-	-	-	-	-	-	-	-	-	5.99
ISTE	Listvenite	50Z-1-75-80	Magnesite	Vein	lss2	Rim		0.02	-	-	-	0.20	-	5.75	0.02	-	-	-	-	-	-	-	-	-	5.98
ISTE	Listvenite	50Z-1-75-80	Magnesite	Vein	lss2	Median zone		0.00	-	-	-	0.12	0.01	5.85	0.02	-	-	-	-	-	-	-	-	-	6.00
ISTE	Listvenite	50Z-1-75-80	Magnesite	Vein	lss2	Rim		0.02	-	-	-	0.52	0.01	5.42	0.02	-	-	-	-	-	-	-	-	-	5.98
ISTE	Listvenite	50Z-1-75-80	Magnesite	Matrix	Aggregate			0.01	-	-	-	0.16	0.00	5.81	0.01	-	-	-	-	-	-	-	-	-	5.99
ISTE	Listvenite	50Z-1-75-80	Magnesite	Vein	lss2	Median zone		0.02	-	-	-	0.15	0.01	5.78	0.03	-	-	-	-	-	-	-	-	-	5.98
ISTE	Listvenite	50Z-1-75-80	Magnesite	Vein	lss2	Median zone		0.06	-	-	-	0.14	0.11	5.63	0.01	-	-	-	-	-	-	-	-	-	5.94
GM	Fuchsite-bearing listvenite	53Z-2-72-77	Magnesite	Matrix	Mg-core spheroid	Core		-	-	-	-	0.31	-	5.68	0.01	-	-	-	-	-	-	-	-	-	6.00

GM	Fu-listvenite	53Z-2-72-77	Magnesite	Matrix	Mg-core spheroid	Core	-	-	-	-	0.35	-	5.57	0.08	-	-	-	-	-	-	-	-	-	6.00
GM	Fu-listvenite	53Z-2-72-77	Magnesite	Matrix	Mg-core spheroid	Core	-	-	-	-	0.31	-	5.65	0.04	-	-	-	-	-	-	-	-	-	6.00
GM	Fu-listvenite	53Z-2-72-77	Magnesite	Matrix	Mg-core spheroid	Core	0.06	-	0.03	0.01	0.35	-	5.43	0.04	-	-	0.01	-	-	-	-	-	-	5.92
GM	Fu-listvenite	53Z-2-72-77	Magnesite	Matrix	Mg-core spheroid	Internal growth	-	-	-	-	0.31	-	5.60	0.09	-	-	-	-	-	-	-	-	-	6.00
GM	Fu-listvenite	53Z-2-72-77	Magnesite	Matrix	Mg-core spheroid	Internal growth	-	-	-	-	0.30	-	5.65	0.06	-	-	-	-	-	-	-	-	-	6.00
GM	Fu-listvenite	53Z-2-72-77	Magnesite	Matrix	Mg-core spheroid	Internal growth	-	-	-	-	0.33	-	5.60	0.07	-	-	-	-	-	-	-	-	-	6.00
GM	Fu-listvenite	53Z-2-72-77	Magnesite	Matrix	Mg-core spheroid	Internal growth	-	-	-	-	0.30	-	5.65	0.05	-	-	-	-	-	-	-	-	-	6.00
GM	Fu-listvenite	53Z-2-72-77	Magnesite	Matrix	Mg-core spheroid	Internal growth	0.01	-	-	-	0.30	-	5.64	0.03	-	-	-	-	-	-	-	-	-	5.99
GM	Fu-listvenite	53Z-2-72-77	Magnesite	Matrix	Mg-core spheroid	Internal growth	-	-	-	0.01	0.33	0.01	5.62	0.02	-	-	-	-	-	-	-	-	-	5.99
GM	Fu-listvenite	53Z-2-72-77	Magnesite	Matrix	Mg-core spheroid	Rim	-	-	-	-	0.31	-	5.66	0.02	-	-	-	-	-	-	-	-	-	6.00
GM	Fu-listvenite	53Z-2-72-77	Magnesite	Matrix	Mg-core spheroid	Rim	-	-	-	-	0.33	-	5.66	0.01	-	-	-	-	-	-	-	-	-	6.00
GM	Fu-listvenite	53Z-2-72-77	Magnesite	Matrix	Mg-core spheroid	Rim	-	-	-	-	0.28	-	5.68	0.04	-	-	-	-	-	-	-	-	-	6.00
GM	Fu-listvenite	53Z-2-72-77	Magnesite	Matrix	Mg-core spheroid	Rim	-	-	-	-	0.29	-	5.69	0.02	-	-	-	-	-	-	-	-	-	6.00
GM	Fu-listvenite	53Z-2-72-77	Magnesite	Matrix	Aggregate	Core	0.09	-	-	-	0.55	0.07	5.18	0.01	-	-	-	-	-	-	-	-	-	5.91
GM	Fu-listvenite	53Z-2-72-77	Magnesite	Matrix	Aggregate	Core	0.09	-	-	-	0.36	0.01	5.44	0.02	-	-	-	-	-	-	-	-	-	5.91
GM	Fu-listvenite	53Z-2-72-77	Magnesite	Matrix	Aggregate	Core	0.01	-	-	0.02	0.34	-	5.60	0.02	-	-	-	-	-	-	-	-	-	5.98
GM	Fu-listvenite	53Z-2-72-77	Magnesite	Matrix	Aggregate	Intermediate	0.49	-	-	-	0.27	-	4.72	0.02	-	-	-	-	-	-	-	-	-	5.51
GM	Fu-listvenite	53Z-2-72-77	Magnesite	Matrix	Aggregate	Rim	0.16	-	-	-	0.32	-	5.34	0.02	-	-	-	-	-	-	-	-	-	5.84
GM	Fu-listvenite	53Z-2-72-77	Magnesite	Vein	lc1	Median zone	0.01	-	-	-	0.43	-	5.50	0.05	-	-	-	-	-	-	-	-	-	5.99
GM	Fu-listvenite	53Z-2-72-77	Magnesite	Vein	lc1	Median zone	-	-	-	-	0.41	0.01	5.57	0.01	-	-	-	-	-	-	-	-	-	6.00
GM	Fu-listvenite	53Z-2-72-77	Magnesite	Vein	lc1	Median zone	0.04	-	-	-	0.59	0.03	5.29	0.02	-	-	-	-	-	-	-	-	-	5.96
GM	Fu-listvenite	53Z-2-72-77	Magnesite	Vein	lc1	Intermediate	0.06	-	-	-	0.35	0.03	5.51	-	-	-	-	-	-	-	-	-	-	5.94
GM	Fu-listvenite	53Z-2-72-77	Magnesite	Vein	lc1	Intermediate	-	-	-	-	0.34	-	5.64	0.02	-	-	-	-	-	-	-	-	-	6.00
GM	Fu-listvenite	53Z-2-72-77	Magnesite	Vein	lc1	Rim	-	-	-	-	0.31	-	5.65	0.04	-	-	-	-	-	-	-	-	-	6.00
GM	Fu-listvenite	53Z-2-72-77	Magnesite	Vein	lc5-6?	Median zone	-	-	-	-	0.23	-	5.75	0.01	-	-	-	-	-	-	-	-	-	6.00
GM	Fu-listvenite	53Z-2-72-77	Magnesite	Vein	lc5-6?	Median zone	-	-	-	-	0.26	-	5.71	0.03	-	-	-	-	-	-	-	-	-	6.00
ISTE	Fu-listvenite	53Z-4-35-40	Magnesite	Matrix	Aggregate		0.06	-	-	-	0.59	0.01	5.28	0.01	-	-	-	-	-	-	-	-	-	5.94
ISTE	Fu-listvenite	53Z-4-35-40	Magnesite	Matrix	Aggregate		0.02	-	-	-	0.75	0.01	5.18	0.02	-	-	-	-	-	-	-	-	-	5.98
ISTE	Fu-listvenite	53Z-4-35-40	Magnesite	Matrix	Aggregate		0.01	-	-	-	0.82	0.01	5.12	0.02	-	-	-	-	-	-	-	-	-	5.99
ISTE	Fu-listvenite	53Z-4-35-40	Magnesite	Matrix	Aggregate		0.02	-	-	-	0.87	0.02	5.06	0.01	-	-	-	-	-	-	-	-	0.00	5.98
ISTE	Fu-listvenite	53Z-4-35-40	Magnesite	Matrix	Aggregate		0.08	-	-	-	0.47	-	5.28	0.09	-	-	-	-	-	-	-	-	0.00	5.92
ISTE	Fu-listvenite	53Z-4-35-40	Magnesite	Matrix	Aggregate		0.00	-	-	-	0.52	0.01	5.45	0.01	-	-	-	-	-	-	-	-	-	6.00
ISTE	Fu-listvenite	53Z-4-35-40	Magnesite	Vein	lss0	Median zone	0.00	-	-	-	0.79	0.04	5.15	0.00	-	-	-	-	-	-	-	-	-	6.00
ISTE	Fu-listvenite	53Z-4-35-40	Magnesite	Vein	lss0	Rim	0.09	-	-	-	0.61	0.01	5.16	0.03	-	-	-	-	-	-	-	-	-	5.91
ISTE	Fu-listvenite	55Z-1-55-60	Dolomite	Vein	lc1	Median zone	-	-	-	-	0.33	0.01	3.57	2.09	-	-	-	-	-	-	-	-	-	6.00
ISTE	Fu-listvenite	55Z-1-55-60	Magnesite	Matrix	Mg-core spheroid	Core	0.02	-	-	-	0.46	0.02	5.45	0.04	-	-	-	-	-	-	-	-	-	5.98
ISTE	Fu-listvenite	55Z-1-55-60	Magnesite	Matrix	Mg-core spheroid	Core	0.08	-	-	-	0.19	0.00	5.64	0.01	-	-	-	-	-	-	-	-	-	5.92
ISTE	Fu-listvenite	55Z-1-55-60	Magnesite	Matrix	Mg-core spheroid	Core	0.01	-	-	-	0.19	0.00	5.72	0.06	-	-	-	-	-	-	-	-	-	5.99
ISTE	Fu-listvenite	55Z-1-55-60	Magnesite	Matrix	Euhedral	Core	0.00	-	-	-	0.27	0.01	5.65	0.06	-	-	-	-	-	-	-	-	-	6.00
ISTE	Fu-listvenite	55Z-1-55-60	Magnesite	Matrix	Euhedral	Core	0.00	-	-	-	0.28	0.01	5.62	0.09	-	-	-	-	-	-	-	-	-	6.00
ISTE	Fu-listvenite	55Z-1-55-60	Magnesite	Matrix	Aggregate		0.00	-	-	-	0.35	0.01	5.57	0.06	-	-	-	-	-	-	-	-	-	6.00
ISTE	Fu-listvenite	55Z-1-55-60	Magnesite	Matrix	Aggregate		0.02	-	-	-	0.36	0.01	5.55	0.03	-	-	-	-	-	-	-	-	-	5.98
ISTE	Fu-listvenite	55Z-1-55-60	Magnesite	Matrix	Aggregate		0.00	-	-	-	0.34	0.01	5.60	0.05	-	-	-	-	-	-	-	-	-	6.00
ISTE	Fu-listvenite	55Z-1-55-60	Magnesite	Matrix	Aggregate		0.17	-	-	-	0.31	0.01	5.29	0.05	-	-	-	-	-	-	-	-	-	5.83
ISTE	Fu-listvenite	55Z-1-55-60	Magnesite	Matrix	Aggregate		-	-	-	-	0.32	0.01	5.61	0.06	-	-	-	-	-	-	-	-	-	6.00
ISTE	Fu-listvenite	55Z-1-55-60	Magnesite	Matrix	Aggregate		0.01	-	-	-	0.35	0.01	5.59	0.02	-	-	-	-	-	-	-	0.00	-	5.99
ISTE	Fu-listvenite	55Z-1-55-60	Magnesite	Matrix	Aggregate		0.35	-	-	-	0.74	0.02	4.46	0.08	-	-	-	-	-	-	-	-	-	5.65
ISTE	Fu-listvenite	55Z-1-55-60	Magnesite	Vein	lss0	Median zone	0.04	-	-	-	0.91	0.02	4.96	0.02	-	-	-	-	-	-	-	-	-	5.96
ISTE	Fu-listvenite	55Z-1-55-60	Magnesite	Vein	lss0	Intermediate	-	-	-	-	0.72	0.03	5.23	0.02	-	-	-	-	-	-	-	-	-	6.00
ISTE	Fu-listvenite	55Z-1-55-60	Magnesite	Vein	lss0	Rim	0.00	-	-	-	0.36	0.01	5.55	0.08	-	-	-	-	-	-	-	-	-	6.00
ISTE	Fu-listvenite	55Z-1-55-60	Magnesite	Vein	lc1	Median zone	0.00	-	-	-	0.58	0.01	5.39	0.02	-	-	-	-	-	-	-	-	-	6.00
ISTE	Fu-listvenite	55Z-1-55-60	Magnesite	Vein	lc1	Median zone	0.06	-	-	-	0.35	0.01	5.48	0.03	-	-	-	-	-	-	-	-	-	5.94
ISTE	Fu-listvenite	55Z-1-55-60	Magnesite	Vein	lc1	Median zone	0.01	-	-	-	1.20	0.01	4.71	0.05	-	-	-	-	-	-	-	-	-	5.99

ISTE	Fu-listvenite	55Z-1-55-60	Magnesite	Vein	lc1	Intermediate	0.00	-	-	-	0.75	0.03	5.16	0.05	-	-	-	-	-	-	-	-	-	6.00
ISTE	Fu-listvenite	55Z-1-55-60	Magnesite	Vein	lc1	Intermediate	0.00	-	-	-	1.11	0.02	4.81	0.06	-	-	-	-	-	-	-	-	-	6.00
ISTE	Fu-listvenite	55Z-1-55-60	Magnesite	Vein	lc1	Intermediate	0.02	-	-	-	0.44	0.01	5.50	0.01	-	-	-	-	-	-	-	-	-	5.98
ISTE	Fu-listvenite	55Z-1-55-60	Magnesite	Vein	lc1	Intermediate	0.03	-	-	-	1.16	0.02	4.75	0.02	-	-	-	-	-	-	-	-	-	5.97
ISTE	Fu-listvenite	55Z-1-55-60	Magnesite	Vein	lc1	Intermediate	0.02	-	-	-	0.35	0.01	5.55	0.05	-	-	-	-	-	-	-	-	-	5.98
ISTE	Fu-listvenite	55Z-1-55-60	Magnesite	Vein	lc1	Intermediate	0.19	-	-	-	1.06	0.02	4.50	0.03	-	-	-	-	-	-	-	-	-	5.81
ISTE	Fu-listvenite	55Z-1-55-60	Magnesite	Vein	lc1	Rim	0.00	-	-	-	0.63	0.03	5.31	0.03	-	-	-	-	-	-	-	-	-	6.00
ISTE	Fu-listvenite	55Z-1-55-60	Magnesite	Vein	lc1	Rim	0.00	-	-	-	0.52	0.02	5.42	0.03	-	-	-	-	-	-	-	-	-	6.00
ISTE	Fu-listvenite	55Z-1-55-60	Magnesite	Vein	lc1	Rim	0.00	-	-	-	0.21	0.00	5.76	0.02	-	-	-	-	-	-	-	-	-	6.00
ISTE	Fu-listvenite	55Z-1-55-60	Magnesite	Vein	lc1	Rim	0.00	-	-	-	0.37	0.01	5.62	-	-	-	-	-	-	-	-	-	-	6.00
ISTE	Fu-listvenite	55Z-1-55-60	Magnesite	Vein	lc1	Overgrowth	0.01	-	-	-	0.41	0.01	5.50	0.05	-	-	-	-	-	-	-	-	-	5.99
ISTE	Fu-listvenite	55Z-1-55-60	Dolomite	Vein	lc6	Median zone	-	-	-	-	0.21	0.01	2.83	2.95	-	-	-	-	-	-	-	-	-	6.00
ISTE	Fu-listvenite	55Z-1-55-60	Dolomite	Vein	lc6	Median zone	-	-	-	-	0.33	0.01	2.71	2.95	-	-	-	-	-	-	-	-	-	6.00
GM	Fu-listvenite	60Z-1-32-37	Dolomite	Matrix	Spheroid	Core	0.01	-	-	-	0.29	0.02	2.75	2.92	-	-	-	-	-	-	-	-	-	5.99
GM	Fu-listvenite	60Z-1-32-37	Dolomite	Matrix	Spheroid	Core	0.23	-	0.13	0.03	0.17	-	2.54	2.57	-	0.04	-	-	-	-	-	-	-	5.71
GM	Fu-listvenite	60Z-1-32-37	Dolomite	Matrix	Spheroid	Core	0.19	-	0.14	0.03	0.25	0.01	2.82	2.28	-	0.02	-	-	-	-	-	-	-	5.74
GM	Fu-listvenite	60Z-1-32-37	Dolomite	Matrix	Spheroid	Rim	-	-	-	-	0.20	-	2.73	3.06	-	-	-	-	-	-	-	-	-	6.00
ISTE	Fu-listvenite	60Z-1-32-37	Dolomite	Vein	lc6	Median zone	-	-	-	-	0.17	0.01	3.01	2.81	-	-	-	-	-	-	-	-	-	6.00
GM	Fu-listvenite	60Z-1-32-37	Dolomite	Vein	lc6	Median zone	-	-	-	-	0.13	0.01	3.12	2.74	-	-	-	-	-	-	-	-	-	6.00
GM	Fu-listvenite	60Z-1-32-37	Magnesite	Matrix	Mg-core spheroid	Core	0.05	-	-	-	0.43	-	5.42	0.04	-	-	-	-	-	-	-	-	0.00	5.95
GM	Fu-listvenite	60Z-1-32-37	Magnesite	Matrix	Mg-core spheroid	Core	0.01	-	-	-	0.41	-	5.55	0.01	-	-	-	-	-	-	-	-	0.00	5.99
GM	Fu-listvenite	60Z-1-32-37	Magnesite	Matrix	Mg-core spheroid	Core	0.06	-	-	-	0.45	-	5.41	0.02	-	-	-	-	-	-	-	-	-	5.94
ISTE	Fu-listvenite	60Z-1-32-37	Magnesite	Matrix	Mg-core spheroid	Core	0.15	-	-	-	0.42	0.01	5.25	0.03	-	-	-	-	-	-	-	-	-	5.85
ISTE	Fu-listvenite	60Z-1-32-37	Magnesite	Matrix	Mg-core spheroid	Core	0.42	-	-	-	0.29	0.01	4.83	0.02	-	-	-	-	-	-	-	0.00	-	5.58
ISTE	Fu-listvenite	60Z-1-32-37	Magnesite	Matrix	Mg-core spheroid	Core	0.29	-	-	-	0.24	0.00	5.15	0.03	-	-	-	-	-	-	-	-	-	5.71
GM	Fu-listvenite	60Z-1-32-37	Magnesite	Matrix	Mg-core spheroid	Core	0.28	-	-	-	0.27	-	5.14	0.03	-	-	-	-	-	-	-	-	-	5.72
GM	Fu-listvenite	60Z-1-32-37	Magnesite	Matrix	Mg-core spheroid	Core	0.28	-	-	-	0.36	-	5.04	0.03	-	-	-	-	-	-	-	-	-	5.72
GM	Fu-listvenite	60Z-1-32-37	Magnesite	Matrix	Mg-core spheroid	Core	0.47	-	-	-	0.23	-	4.81	0.02	-	-	-	-	-	-	-	-	-	5.53
GM	Fu-listvenite	60Z-1-32-37	Magnesite	Matrix	Mg-core spheroid	Core	0.30	-	-	-	0.21	-	5.18	0.02	-	-	-	-	-	-	-	-	-	5.70
GM	Fu-listvenite	60Z-1-32-37	Magnesite	Matrix	Mg-core spheroid	Core	0.58	-	0.01	-	0.21	-	4.60	0.02	-	-	-	-	-	-	-	-	-	5.42
GM	Fu-listvenite	60Z-1-32-37	Magnesite	Matrix	Mg-core spheroid	Internal growth	0.19	-	0.02	-	0.32	-	5.19	0.06	-	-	0.02	-	-	-	-	-	-	5.80
GM	Fu-listvenite	60Z-1-32-37	Magnesite	Matrix	Mg-core spheroid	Internal growth	0.31	-	-	-	0.26	-	5.10	0.02	-	-	-	-	-	-	-	-	-	5.69
GM	Fu-listvenite	60Z-1-32-37	Magnesite	Matrix	Mg-core spheroid	Internal growth	0.53	-	-	-	0.28	-	4.62	0.03	-	-	-	-	-	-	-	-	-	5.47
GM	Fu-listvenite	60Z-1-32-37	Magnesite	Matrix	Mg-core spheroid	Rim	0.63	-	0.02	-	0.21	-	4.48	0.02	-	-	-	-	-	-	-	-	-	5.36
GM	Fu-listvenite	60Z-1-32-37	Magnesite	Matrix	Mg-core spheroid	Rim	0.11	-	-	-	0.52	-	4.49	0.73	-	-	0.03	-	-	-	-	-	-	5.89
GM	Fu-listvenite	60Z-1-32-37	Magnesite	Matrix	Mg-core spheroid	Rim	0.71	-	0.02	-	0.19	-	4.35	0.01	-	-	-	-	-	-	-	-	-	5.28
GM	Fu-listvenite	60Z-1-32-37	Magnesite	Matrix	Mg-core spheroid	Rim	0.24	-	0.11	-	0.26	-	4.92	0.15	-	-	0.03	-	-	-	-	-	-	5.70
GM	Fu-listvenite	60Z-1-32-37	Magnesite	Matrix	Mg-core spheroid	Rim	0.37	-	0.02	-	0.26	-	4.89	0.06	-	-	0.02	-	-	-	-	-	-	5.62
ISTE	Fu-listvenite	60Z-1-32-37	Magnesite	Vein	lc2		-	-	-	-	0.19	0.00	5.79	0.01	-	-	-	-	-	-	-	-	-	6.00
ISTE	Fu-listvenite	60Z-1-32-37	Magnesite	Matrix	Aggregate		0.15	-	-	-	0.42	0.01	5.25	0.03	-	-	-	-	-	-	-	-	-	5.85
ISTE	Fu-listvenite	60Z-1-32-37	Magnesite	Matrix	Aggregate		0.10	-	-	-	0.41	0.01	5.37	0.02	-	-	-	-	-	-	-	-	-	5.90
GM	Fu-listvenite	60Z-1-32-37	Magnesite	Matrix	Aggregate		0.10	-	-	-	0.31	-	5.46	0.02	-	-	-	-	-	-	-	-	-	5.90
ISTE	Fu-listvenite	60Z-1-32-37	Magnesite	Matrix	Aggregate		0.11	-	-	-	0.33	0.01	5.39	0.04	-	-	-	-	-	-	-	-	-	5.89
ISTE	Fu-listvenite	60Z-1-32-37	Magnesite	Matrix	Aggregate		0.07	-	-	-	0.29	0.01	5.53	0.04	-	-	-	-	-	-	-	-	-	5.93
GM	Fu-listvenite	60Z-1-32-37	Magnesite	Matrix	Aggregate		0.08	-	-	-	0.36	-	5.46	0.02	-	-	-	-	-	-	-	-	-	5.92
ISTE	Fu-listvenite	60Z-1-32-37	Magnesite	Matrix	Aggregate		0.14	-	-	-	0.31	0.00	5.39	0.03	-	-	-	-	-	-	-	-	-	5.86
ISTE	Fu-listvenite	60Z-1-32-37	Magnesite	Matrix	Aggregate		0.10	-	-	-	0.41	0.01	5.37	0.02	-	-	-	-	-	-	-	-	-	5.90
ISTE	Fu-listvenite	60Z-1-32-37	Magnesite	Vein	lss0	Median zone	0.46	-	-	-	0.28	0.00	4.76	0.05	-	-	-	-	-	-	-	-	-	5.54
GM	Fu-listvenite	60Z-1-32-37	Magnesite	Vein	lss0	Median zone	0.57	-	-	-	0.25	-	4.58	0.02	-	-	-	-	-	-	-	-	-	5.43
GM	Fu-listvenite	60Z-1-32-37	Magnesite	Vein	lss0	Median zone	0.45	-	-	-	0.23	-	4.84	0.01	-	-	-	-	-	-	-	-	-	5.55
GM	Fu-listvenite	60Z-1-32-37	Magnesite	Vein	lss0	Median zone	0.11	-	-	-	0.30	-	5.44	0.03	-	-	-	-	-	-	-	-	-	5.89
GM	Fu-listvenite	60Z-1-32-37	Magnesite	Vein	lss0	Intermediate	0.43	-	-	-	0.26	-	4.85	0.03	-	-	-	-	-	-	-	-	-	5.57
GM	Fu-listvenite	60Z-1-32-37	Magnesite	Vein	lss0	Intermediate	0.10	-	-	-	0.38	-	5.39	0.02	-	-	0.01	-	-	-	-	-	-	5.90

GM	Fu-listvenite	60Z-1-32-37	Magnesite	Vein	lss0	Rim	0.18	-	-	0.02	0.24	-	5.34	0.03	-	-	-	-	-	-	-	-	-	5.81
ISTE	Fu-listvenite	60Z-1-32-37	Magnesite	Vein	lss0	Rim	0.16	-	-	-	0.23	0.01	5.41	0.03	-	-	-	-	-	-	-	-	-	5.84
ISTE	Fu-listvenite	60Z-1-32-37	Magnesite	Vein	lss0	Rim	0.60	-	-	-	0.25	0.00	4.51	0.03	-	-	-	-	-	-	-	-	-	5.40
ISTE	Fu-listvenite	60Z-1-32-37	Magnesite	Vein	lss0	Rim	0.58	-	-	-	0.22	0.00	4.60	0.02	-	-	-	-	-	-	-	-	-	5.42
GM	Fu-listvenite	60Z-1-32-37	Magnesite	Vein	lss0	Rim	0.39	-	0.03	-	0.36	-	4.71	0.07	-	-	0.02	-	-	-	-	-	-	5.59
GM	Fu-listvenite	60Z-1-32-37	Magnesite	Vein	lc1	Median zone	0.32	-	-	-	0.34	-	5.00	0.01	-	-	-	-	-	-	-	-	-	5.68
GM	Fu-listvenite	60Z-1-32-37	Magnesite	Vein	lc1	Median zone	0.14	-	-	-	0.34	-	5.35	0.03	-	-	-	-	-	-	-	-	-	5.86
GM	Fu-listvenite	60Z-1-32-37	Magnesite	Vein	lc1	Median zone	0.26	-	-	-	0.37	-	5.09	0.02	-	-	-	-	-	-	-	-	-	5.74
ISTE	Fu-listvenite	60Z-1-32-37	Magnesite	Vein	lc1	Rim	0.24	-	-	-	0.31	0.00	5.19	0.02	-	-	-	-	-	-	-	-	-	5.76
GM	Fu-listvenite	60Z-1-32-37	Magnesite	Vein	lc2	Median zone	-	-	-	-	0.18	-	5.79	0.03	-	-	-	-	-	-	-	-	-	6.00
ISTE	Fu-listvenite	60Z-1-32-37	Magnesite	Vein	lc2	Median zone	0.11	-	-	-	0.37	0.00	5.38	0.03	-	-	-	-	-	-	-	-	-	5.89
GM	Fu-listvenite	60Z-1-32-37	Magnesite	Vein	lc2	Median zone	0.13	-	-	-	0.41	-	5.30	0.03	-	-	-	-	-	-	-	-	-	5.87
ISTE	Listvenite	61Z-4-28-33	Dolomite	Vein	lc3	Median zone	-	-	-	-	0.09	0.00	3.00	2.91	-	-	-	-	-	-	-	-	-	6.00
ISTE	Listvenite	61Z-4-28-33	Magnesite	Matrix	Aggregate		0.00	-	-	-	0.25	0.00	5.70	0.04	-	-	-	-	-	-	-	-	-	6.00
ISTE	Listvenite	61Z-4-28-33	Magnesite	Matrix	Aggregate		0.05	-	-	-	0.24	0.01	5.63	0.02	-	-	-	-	-	-	-	-	-	5.95
ISTE	Listvenite	61Z-4-28-33	Magnesite	Matrix	Aggregate		0.00	-	-	-	0.25	0.00	5.75	0.00	-	-	-	-	-	-	-	-	-	6.00
ISTE	Listvenite	61Z-4-28-33	Magnesite	Matrix	Aggregate		0.00	-	-	-	0.23	0.01	5.72	0.04	-	-	-	-	-	-	-	-	-	6.00
ISTE	Listvenite	61Z-4-28-33	Magnesite	Matrix	Aggregate		-	-	-	-	0.24	-	5.76	0.01	-	-	-	-	-	-	-	-	-	6.00
ISTE	Listvenite	61Z-4-28-33	Magnesite	Matrix	Aggregate		-	-	-	-	0.26	0.01	5.70	0.04	-	-	-	-	-	-	-	-	-	6.00
ISTE	Listvenite	61Z-4-28-33	Magnesite	Matrix	Aggregate		0.03	-	-	-	0.20	0.00	5.66	0.09	-	-	-	-	-	-	-	-	-	5.97
ISTE	Listvenite	61Z-4-28-33	Magnesite	Matrix	Aggregate		-	-	-	-	0.26	0.00	5.71	0.03	-	-	-	-	-	-	-	-	-	6.00
ISTE	Listvenite	61Z-4-28-33	Magnesite	Matrix	Aggregate		-	-	-	-	0.26	0.00	5.72	0.01	-	-	-	-	-	-	-	-	-	6.00
ISTE	Listvenite	61Z-4-28-33	Magnesite	Matrix	Aggregate		-	-	-	-	0.26	0.00	5.69	0.05	-	-	-	-	-	-	-	-	-	6.00
ISTE	Listvenite	61Z-4-28-33	Magnesite	Matrix	Aggregate		-	-	-	-	0.27	0.01	5.67	0.05	-	-	-	-	-	-	-	-	0.00	6.00
ISTE	Listvenite	61Z-4-28-33	Magnesite	Matrix	Aggregate		-	-	-	-	0.26	0.01	5.69	0.04	-	-	-	-	-	-	-	-	-	6.00
ISTE	Listvenite	61Z-4-28-33	Magnesite	Vein	lc5	Median zone	-	-	-	-	0.41	0.00	5.55	0.03	-	-	-	-	-	-	-	-	-	6.00
ISTE	Listvenite	61Z-4-28-33	Magnesite	Vein	lc5	Median zone	-	-	-	-	0.55	0.01	5.40	0.04	-	-	-	-	-	-	-	-	-	6.00
ISTE	Listvenite	61Z-4-28-33	Magnesite	Vein	lc5	Median zone	-	-	-	-	0.52	0.00	5.44	0.04	-	-	-	-	-	-	-	-	-	6.00
ISTE	Listvenite	66Z-1-30-35	Magnesite	Matrix	Mg-core spheroid	Core	-	-	-	-	0.26	-	5.73	0.01	-	-	-	-	-	-	-	-	-	6.00
ISTE	Listvenite	66Z-1-30-35	Magnesite	Matrix	Mg-core spheroid	Core	0.01	-	-	-	0.36	0.01	5.57	0.03	-	-	-	-	-	-	-	-	-	5.99
ISTE	Listvenite	66Z-1-30-35	Magnesite	Vein	lc1	Median zone	0.11	-	-	-	2.40	0.01	3.35	0.02	-	-	-	-	-	-	-	-	-	5.89
ISTE	Listvenite	66Z-1-30-35	Magnesite	Vein	lc1	Median zone	0.17	-	-	-	1.75	0.01	3.88	0.02	-	-	-	-	-	-	-	-	-	5.83
ISTE	Listvenite	66Z-1-30-35	Magnesite	Vein	lc1	Intermediate	0.04	-	-	-	2.28	0.01	3.61	0.02	-	-	-	-	-	-	-	-	-	5.96
ISTE	Listvenite	66Z-1-30-35	Magnesite	Vein	lc1	Rim	0.01	-	-	-	0.41	0.01	5.54	0.03	-	-	-	-	-	-	-	-	-	5.99
ISTE	Listvenite	66Z-1-30-35	Magnesite	Vein	lc1	Rim	0.10	-	-	-	0.32	-	5.47	0.01	-	-	-	-	-	-	-	-	-	5.90
ISTE	Listvenite	66Z-1-30-35	Dolomite	Vein	lc6	Median zone	-	-	-	-	0.31	0.01	2.82	2.87	-	-	-	-	-	-	-	-	-	6.00
ISTE	Listvenite	66Z-1-30-35	Dolomite	Vein	lc6	Median zone	0.01	-	-	-	0.16	0.01	3.05	2.77	-	-	-	-	-	-	-	-	-	5.99
ISTE	Listvenite	66Z-1-30-35	Magnesite	Vein	lc6	Median zone	0.01	-	-	-	0.62	0.01	5.35	0.01	-	-	-	-	-	-	-	-	-	5.99
ISTE	Fu-listvenite	68Z-1-60-64	Dolomite	Matrix	Aggregate		-	-	-	-	0.57	0.02	2.55	2.86	-	-	-	-	-	-	-	-	-	6.00
ISTE	Fu-listvenite	68Z-1-60-64	Magnesite	Matrix	Fe-core spheroid	Internal growth	-	-	-	-	0.91	0.01	5.01	0.07	-	-	-	-	-	-	-	-	-	6.00
ISTE	Fu-listvenite	68Z-1-60-64	Magnesite	Matrix	Fe-core spheroid	Core	0.14	-	-	-	1.02	0.02	4.60	0.08	-	-	-	-	-	-	-	-	-	5.86
ISTE	Fu-listvenite	68Z-1-60-64	Magnesite	Matrix	Fe-core spheroid	Core	0.01	-	-	-	2.21	0.01	3.72	0.05	-	-	-	-	-	-	-	-	-	5.99
ISTE	Fu-listvenite	68Z-1-60-64	Magnesite	Matrix	Fe-core spheroid	Rim	0.01	-	-	-	1.21	0.01	4.72	0.04	-	-	-	-	-	-	-	-	-	5.99
ISTE	Fu-listvenite	68Z-1-60-64	Magnesite	Matrix	Aggregate		0.00	-	-	-	0.31	0.01	5.61	0.07	-	-	-	-	-	-	-	-	-	6.00
ISTE	Fu-listvenite	68Z-1-60-64	Magnesite	Matrix	Aggregate		-	-	-	-	0.37	0.01	5.56	0.06	-	-	-	-	-	-	-	-	-	6.00
ISTE	Fu-listvenite	68Z-1-60-64	Magnesite	Matrix	Aggregate		-	-	-	-	0.33	0.01	5.62	0.04	-	-	-	-	-	-	-	-	-	6.00
ISTE	Fu-listvenite	68Z-1-60-64	Magnesite	Matrix	Aggregate		0.03	-	-	-	0.33	0.01	5.56	0.05	-	-	-	-	-	-	-	-	-	5.97
ISTE	Fu-listvenite	68Z-1-60-64	Magnesite	Matrix	Aggregate		0.00	-	-	-	0.40	0.01	5.53	0.06	-	-	-	-	-	-	-	-	-	6.00
ISTE	Fu-listvenite	68Z-1-60-64	Magnesite	Matrix	Aggregate		0.01	-	-	-	0.28	0.01	5.62	0.07	-	-	-	-	-	-	-	-	-	5.99
ISTE	Fu-listvenite	68Z-1-60-64	Magnesite	Vein	lc1	Median zone	-	-	-	-	2.40	0.01	3.58	0.01	-	-	-	-	-	-	-	-	-	6.00
ISTE	Fu-listvenite	68Z-1-60-64	Magnesite	Vein	lc1	Median zone	0.00	-	-	-	2.58	0.01	3.37	0.03	-	-	-	-	-	-	-	-	-	6.00
ISTE	Fu-listvenite	68Z-1-60-64	Magnesite	Vein	lc1	Median zone	0.00	-	-	-	0.67	0.01	5.26	0.06	-	-	-	-	-	-	-	-	-	6.00
ISTE	Fu-listvenite	68Z-1-60-64	Magnesite	Vein	lc1	Median zone	0.01	-	-	-	2.11	0.01	3.80	0.06	-	-	-	-	-	-	-	-	-	5.99

ISTE	Fu-listvenite	68Z-1-60-64	Magnesite	Vein	lc1	Median zone	0.01	-	-	-	1.88	0.01	4.02	0.06	-	-	-	-	-	-	-	-	5.99
ISTE	Fu-listvenite	68Z-1-60-64	Magnesite	Vein	lc1	Intermediate	0.02	-	-	-	0.39	0.01	5.53	0.04	-	-	-	-	-	-	-	-	5.98
ISTE	Fu-listvenite	68Z-1-60-64	Magnesite	Vein	lc1	Rim	0.02	-	-	-	1.38	0.01	4.54	0.04	-	-	-	-	-	-	-	-	5.98
ISTE	Fu-listvenite	71Z-3-0-8	Magnesite	Matrix	Fe-core spheroid	Core	0.19	-	-	-	1.15	0.06	4.37	0.04	-	-	-	-	-	-	-	-	5.81
ISTE	Fu-listvenite	71Z-3-0-8	Magnesite	Matrix	Fe-core spheroid	Internal growth	0.07	-	-	-	0.65	0.01	5.19	0.02	-	-	-	-	-	-	-	-	5.93
ISTE	Fu-listvenite	71Z-3-0-8	Magnesite	Matrix	Fe-core spheroid	Internal growth	0.01	-	-	-	0.35	0.00	5.61	0.01	-	-	-	-	-	-	-	-	5.99
ISTE	Fu-listvenite	71Z-3-0-8	Magnesite	Matrix	Fe-core spheroid	Internal growth	0.15	-	-	-	0.34	-	5.33	0.03	-	-	-	-	-	-	-	-	5.85
ISTE	Fu-listvenite	71Z-3-0-8	Magnesite	Matrix	Fe-core spheroid	Rim	0.39	-	-	-	0.51	0.00	4.65	0.06	-	-	-	-	-	-	-	-	5.61
ISTE	Fu-listvenite	71Z-3-0-8	Magnesite	Matrix	Mg-core spheroid	Core	-	-	-	-	0.26	0.01	5.67	0.07	-	-	-	-	-	-	-	-	6.00
ISTE	Fu-listvenite	71Z-3-0-8	Magnesite	Matrix	Mg-core spheroid	Core	0.06	-	-	-	0.27	0.01	5.56	0.04	-	-	-	-	-	-	-	-	5.94
ISTE	Fu-listvenite	71Z-3-0-8	Magnesite	Matrix	Mg-core spheroid	Core	0.01	-	-	-	0.25	0.01	5.70	0.03	-	-	-	-	-	-	-	-	5.99
ISTE	Fu-listvenite	71Z-3-0-8	Magnesite	Matrix	Mg-core spheroid	Core	0.16	-	-	-	0.30	0.01	5.36	0.02	-	-	-	-	-	-	-	-	5.84
ISTE	Fu-listvenite	71Z-3-0-8	Magnesite	Matrix	Mg-core spheroid	Core	0.01	-	-	-	0.28	-	5.71	0.01	-	-	-	-	-	-	-	-	5.99
ISTE	Fu-listvenite	71Z-3-0-8	Magnesite	Vein	lss0	Median zone	0.00	-	-	-	1.67	0.02	4.27	0.04	-	-	-	-	-	-	-	-	6.00
ISTE	Fu-listvenite	71Z-3-0-8	Magnesite	Vein	lss0	Rim	0.17	-	-	-	0.34	-	5.27	0.05	-	-	-	-	-	-	-	-	5.83
ISTE	Fu-listvenite	71Z-3-0-8	Magnesite	Vein	lc1	Median zone	0.01	-	-	-	0.28	-	5.71	0.01	-	-	-	-	-	-	-	-	5.99
ISTE	Fu-listvenite	71Z-3-0-8	Magnesite	Vein	lc1	Intermediate	-	-	-	-	1.72	0.02	4.20	0.07	-	-	-	-	-	-	-	-	6.00
ISTE	Fu-listvenite	71Z-3-0-8	Magnesite	Vein	lc1	Rim	0.18	-	-	-	0.38	-	5.21	0.04	-	-	-	-	-	-	-	-	5.82
ISTE	Fu-listvenite	71Z-3-0-8	Magnesite	Vein	lc1	Rim	0.06	-	-	-	0.26	0.00	5.60	0.02	-	-	-	-	-	-	-	-	5.94
ISTE	Listvenite	72Z-1-71-79	Dolomite	Vein	lc6	Median zone	-	-	-	-	0.31	0.01	2.40	3.28	-	-	-	-	-	-	-	-	6.00
ISTE	Listvenite	72Z-1-71-79	Magnesite	Matrix	Fe-core spheroid	Core	0.00	-	-	-	1.32	0.02	4.57	0.09	-	-	-	-	-	-	-	-	6.00
ISTE	Listvenite	72Z-1-71-79	Magnesite	Matrix	Mg-core spheroid	Core	0.01	-	-	-	0.51	0.01	5.44	0.02	-	-	-	-	-	-	-	-	5.99
ISTE	Listvenite	72Z-1-71-79	Magnesite	Matrix	Mg-core spheroid	Core	0.00	-	-	-	0.21	-	5.78	0.01	-	-	-	-	-	-	-	-	6.00
ISTE	Listvenite	72Z-1-71-79	Magnesite	Matrix	Mg-core spheroid	Core	0.02	-	-	-	0.40	0.01	5.52	0.03	-	-	-	-	-	-	-	-	5.98
ISTE	Listvenite	72Z-1-71-79	Magnesite	Matrix	Mg-core spheroid	Core	0.00	-	-	-	0.12	0.00	5.79	0.09	-	-	-	-	-	-	-	-	6.00
ISTE	Listvenite	72Z-1-71-79	Magnesite	Matrix	Mg-core spheroid	Core	0.18	-	-	-	0.34	0.05	5.21	0.04	-	-	-	-	-	-	-	-	5.82
ISTE	Listvenite	72Z-1-71-79	Magnesite	Matrix	Mg-core spheroid	Core	0.31	-	-	-	0.76	0.02	4.58	0.03	-	-	-	-	-	-	-	-	5.69
ISTE	Listvenite	72Z-1-71-79	Magnesite	Matrix	Mg-core spheroid	Core	0.01	-	-	-	0.10	0.00	5.78	0.09	-	-	-	-	-	-	-	-	5.99
ISTE	Listvenite	72Z-1-71-79	Magnesite	Matrix	Mg-core spheroid	Core	0.01	-	-	-	0.28	0.01	5.66	0.03	-	-	-	-	-	-	-	-	5.99
ISTE	Listvenite	72Z-1-71-79	Magnesite	Matrix	Mg-core spheroid	Internal growth	0.00	-	-	-	0.24	0.01	5.74	0.01	-	-	-	-	-	-	-	-	6.00
ISTE	Listvenite	72Z-1-71-79	Magnesite	Matrix	Mg-core spheroid	Rim	0.00	-	-	-	0.22	-	5.77	0.01	-	-	-	-	-	-	-	-	6.00
ISTE	Listvenite	72Z-1-71-79	Magnesite	Matrix	Aggregate		0.00	-	-	-	0.13	0.00	5.86	0.01	-	-	-	-	-	-	-	-	6.00
ISTE	Listvenite	72Z-1-71-79	Magnesite	Matrix	Aggregate		0.01	-	-	-	0.10	0.01	5.78	0.09	-	-	-	-	-	-	-	-	5.99
ISTE	Listvenite	72Z-1-71-79	Magnesite	Vein	lc1	Median zone	0.00	-	-	-	1.34	0.01	4.59	0.05	-	-	-	-	-	-	-	-	6.00
ISTE	Listvenite	72Z-1-71-79	Magnesite	Vein	lc1	Median zone	0.00	-	-	-	1.02	0.02	4.91	0.04	-	-	-	-	-	-	-	-	6.00
ISTE	Listvenite	72Z-1-71-80	Magnesite	Vein	lc6	Median zone	0.00	-	-	-	0.50	0.01	5.46	0.02	-	-	-	-	-	-	-	-	6.00
ISTE	Listvenite	72Z-1-71-79	Magnesite	Vein	lc1	Rim	-	-	-	-	0.55	0.01	5.41	0.03	-	-	-	-	-	-	-	-	6.00
ISTE	Listvenite	72Z-1-71-79	Magnesite	Vein	lc1	Rim	0.03	-	-	-	0.51	0.01	5.39	0.03	-	-	-	-	-	-	-	-	5.97
ISTE	Listvenite	72Z-1-71-79	Magnesite	Vein	lc1	Rim	0.01	-	-	-	0.50	0.01	5.45	0.02	-	-	-	-	-	-	-	-	5.99
ISTE	Listvenite	76Z-2-12-20	Dolomite	Matrix	Aggregate		0.01	-	-	-	0.40	0.01	2.86	2.71	-	-	-	-	-	-	-	-	5.99
ISTE	Listvenite	76Z-2-12-20	Dolomite	Matrix	Aggregate		0.00	-	-	-	0.43	0.01	2.84	2.72	-	-	-	-	-	-	-	-	6.00
ISTE	Listvenite	76Z-2-12-20	Dolomite	Matrix	Aggregate		0.01	-	-	-	0.31	0.01	2.69	2.97	-	-	-	-	-	-	-	-	5.99
ISTE	Listvenite	76Z-2-12-20	Dolomite	Vein	lc6		-	-	-	-	0.07	0.02	2.98	2.94	-	-	-	-	-	-	-	-	6.00
ISTE	Listvenite	76Z-2-12-20	Dolomite	Vein	lc6		0.01	-	-	-	0.11	0.02	2.98	2.88	-	-	-	-	-	-	-	-	5.99
ISTE	Listvenite	76Z-2-12-20	Dolomite	Vein	lc6	Median zone	-	-	-	-	0.15	0.01	2.89	2.95	-	-	-	-	-	-	-	-	6.00
ISTE	Listvenite	76Z-2-12-20	Dolomite	Vein	lc6	Median zone	-	-	-	-	0.39	0.01	2.57	3.03	-	-	-	-	-	-	-	-	6.00
ISTE	Listvenite	76Z-2-12-20	Magnesite	Matrix	lss2?		0.03	-	-	-	0.43	0.04	5.46	0.03	-	-	-	-	-	-	-	-	5.97
ISTE	Listvenite	76Z-2-12-20	Magnesite	Vein	lss2?		-	-	-	-	1.33	0.02	3.68	0.96	-	-	-	-	-	-	-	-	6.00
ISTE	Listvenite	76Z-2-12-20	Magnesite	Matrix	lss2?		0.02	-	-	-	1.03	0.02	4.89	0.02	-	-	-	-	-	-	-	-	5.98
ISTE	Listvenite	76Z-2-12-20	Magnesite	Vein	lc1		0.04	-	-	-	0.53	0.04	5.07	0.28	-	-	-	-	-	-	-	-	5.96
ISTE	Listvenite	76Z-2-12-20	Magnesite	Vein	lc1	Median zone	-	-	-	-	0.44	0.00	5.55	0.01	-	-	-	-	-	-	-	-	6.00
ISTE	Listvenite	76Z-2-12-20	Magnesite	Vein	lc1	Median zone	-	-	-	-	0.42	0.00	5.55	0.03	-	-	-	-	-	-	-	-	6.00
ISTE	Listvenite	76Z-2-12-20	Magnesite	Vein	lc1	Median zone	0.00	-	-	-	0.42	0.02	5.54	0.01	-	-	-	-	-	-	-	-	6.00

ISTE	Listvenite	76Z-2-12-20	Magnesite	Vein	lc1	Median zone	0.05	-	-	-	0.38	0.03	5.48	0.02	-	-	-	-	-	-	-	-	-	-	5.95

Table S4 (continued)

											Site ratios			Site ratios (including Si)		
Facility	Lithology	Sample	Mineral	Structure	Texture[2]	Zone	Transect	Mg#	Fe/Mn	Mg/Si	XMg	XCa	XFe	XMg+Ca	XSi	XFe
GM	Listvenite	16Z-1-65-70	Dolomite	Matrix	Aggregate			0.94	-	n.d.	0.48	0.48	0.03	0.97	0.00	0.03
GM	Listvenite	16Z-1-65-70	Dolomite	Matrix	Aggregate			0.93	-	347	0.48	0.49	0.03	0.97	0.00	0.03
GM	Listvenite	16Z-1-65-70	Dolomite	Matrix	Aggregate			0.94	-	349	0.48	0.49	0.03	0.97	0.00	0.03
GM	Listvenite	16Z-1-65-70	Dolomite	Matrix	Aggregate			0.95	-	n.d.	0.48	0.49	0.03	0.97	0.00	0.03
GM	Listvenite	16Z-1-65-70	Dolomite	Matrix	Aggregate			0.93	-	150	0.48	0.49	0.03	0.97	0.00	0.03
GM	Listvenite	16Z-1-65-70	Dolomite	Vein	lc6	Median zone		0.97	5	197	0.50	0.49	0.02	0.98	0.00	0.02
GM	Listvenite	16Z-1-65-70	Dolomite	Vein	lc6	Median zone		0.99	1	n.d.	0.50	0.50	0.01	0.99	0.00	0.01
GM	Listvenite	16Z-1-65-70	Dolomite	Vein	lc6	Median zone		1.00	-	n.d.	0.51	0.49	0.00	1.00	0.00	0.00
GM	Listvenite	16Z-1-65-70	Dolomite	Vein	lc6	Median zone		0.98	-	n.d.	0.50	0.49	0.01	0.99	0.00	0.01
GM	Listvenite	16Z-1-65-70	Magnesite	Matrix	Aggregate			0.91	67	305	0.91	0.00	0.09	0.91	0.00	0.09
GM	Listvenite	16Z-1-65-70	Magnesite	Matrix	Aggregate			0.96	-	17	0.96	0.00	0.04	0.96	0.06	0.04
GM	Listvenite	16Z-1-65-70	Magnesite	Vein	lss0	Median zone		0.95	-	273	0.94	0.01	0.05	0.95	0.00	0.05
GM	Listvenite	16Z-1-65-70	Magnesite	Vein	lss0	Median zone		0.97	-	258	0.97	0.00	0.03	0.97	0.00	0.03
GM	Listvenite	16Z-1-65-70	Magnesite	Vein	lss0	Intermediate		0.97	-	58	0.97	0.00	0.03	0.97	0.02	0.03
GM	Listvenite	16Z-1-65-70	Magnesite	Vein	lss0	Rim		0.97	-	187	0.96	0.01	0.03	0.97	0.01	0.03
GM	Listvenite	16Z-1-65-70	Magnesite	Vein	lss0	Median zone		0.97	-	31	0.97	0.00	0.03	0.97	0.03	0.03
GM	Listvenite	16Z-1-65-70	Siderite	Vein	lc1	Median zone		0.42	296	6	0.42	0.00	0.58	0.42	0.07	0.58
GM	Listvenite	16Z-1-65-70	Siderite	Vein	lc1	Median zone		0.22	-	2	0.22	0.00	0.78	0.22	0.11	0.78
GM	Listvenite	16Z-1-65-70	Siderite	Vein	lc1	Median zone		0.01	-	0	0.01	0.00	0.99	0.01	0.14	0.99
GM	Listvenite	16Z-1-65-70	Siderite	Vein	lc1	Median zone		0.31	387	4	0.31	0.00	0.69	0.31	0.09	0.69
GM	Listvenite	16Z-1-65-70	Siderite	Vein	lc1	Intermediate		0.31	-	3	0.31	0.00	0.68	0.32	0.09	0.68
GM	Listvenite	16Z-1-65-70	Magnesite	Vein	lc1	Intermediate		0.91	67	305	0.91	0.00	0.09	0.91	0.00	0.09
GM	Listvenite	16Z-1-65-70	Magnesite	Vein	lc1	Rim		0.95	-	475	0.95	0.00	0.05	0.95	0.00	0.05
GM	Listvenite	16Z-1-65-70	Magnesite	Vein	lc1	Rim	a	0.97	-	86	0.97	0.00	0.03	0.97	0.01	0.03
GM	Listvenite	16Z-1-65-70	Magnesite	Vein	lc1	Rim	a	0.96	-	63	0.96	0.00	0.04	0.96	0.02	0.04
GM	Listvenite	16Z-1-65-70	Magnesite	Vein	lc1	Intermediate	a	0.96	-	30	0.95	0.00	0.04	0.96	0.03	0.04
GM	Listvenite	16Z-1-65-70	Magnesite	Vein	lc1	Intermediate	a	0.96	-	67	0.95	0.00	0.04	0.96	0.01	0.04
GM	Listvenite	16Z-1-65-70	Magnesite	Vein	lc1	Intermediate	a	0.96	-	52	0.96	0.00	0.04	0.96	0.02	0.04
GM	Listvenite	16Z-1-65-70	Magnesite	Vein	lc1	Intermediate	a	0.96	-	68	0.96	0.00	0.04	0.96	0.01	0.04
GM	Listvenite	16Z-1-65-70	Magnesite	Vein	lc1	Intermediate	a	0.95	-	22	0.95	0.00	0.05	0.95	0.04	0.05
GM	Listvenite	16Z-1-65-70	Magnesite	Vein	lc1	Intermediate	a	0.95	-	34	0.94	0.00	0.05	0.95	0.03	0.05
GM	Listvenite	16Z-1-65-70	Magnesite	Vein	lc1	Intermediate	a	0.95	-	94	0.95	0.00	0.05	0.95	0.01	0.05
GM	Listvenite	16Z-1-65-70	Magnesite	Vein	lc1	Intermediate	a	0.95	-	110	0.95	0.00	0.05	0.95	0.01	0.05
GM	Listvenite	16Z-1-65-70	Magnesite	Vein	lc1	Intermediate	a	0.96	-	36	0.96	0.00	0.04	0.96	0.03	0.04
GM	Listvenite	16Z-1-65-70	Magnesite	Vein	lc1	Intermediate	a	0.96	-	199	0.96	0.00	0.04	0.96	0.00	0.04
GM	Listvenite	16Z-1-65-70	Magnesite	Vein	lc1	Intermediate	a	0.95	-	218	0.95	0.00	0.05	0.95	0.00	0.05
GM	Listvenite	16Z-1-65-70	Magnesite	Vein	lc1	Median zone	a	0.93	-	405	0.93	0.00	0.07	0.93	0.00	0.07
GM	Listvenite	16Z-1-65-70	Magnesite	Vein	lc1	Median zone	a	0.91	-	712	0.91	0.01	0.09	0.91	0.00	0.09
GM	Listvenite	16Z-1-65-70	Magnesite	Vein	lc1	Intermediate	a	0.91	-	n.d.	0.91	0.00	0.09	0.91	0.00	0.09
GM	Listvenite	16Z-1-65-70	Magnesite	Vein	lc1	Intermediate	a	0.93	-	n.d.	0.93	0.00	0.07	0.93	0.00	0.07
GM	Listvenite	16Z-1-65-70	Magnesite	Vein	lc1	Rim	a	0.94	-	732	0.94	0.00	0.06	0.94	0.00	0.06
GM	Listvenite	16Z-1-65-70	Magnesite	Vein	lc1	Rim	a	0.94	-	110	0.94	0.00	0.06	0.94	0.01	0.06
GM	Listvenite	16Z-1-65-70	Magnesite	Vein	lc1	Rim	b	0.96	-	67	0.96	0.00	0.04	0.96	0.01	0.04
GM	Listvenite	16Z-1-65-70	Magnesite	Vein	lc1	Rim	b	0.91	-	119	0.91	0.00	0.09	0.91	0.01	0.09
GM	Listvenite	16Z-1-65-70	Magnesite	Vein	lc1	Intermediate	b	0.97	-	263	0.97	0.00	0.03	0.97	0.00	0.03
GM	Listvenite	16Z-1-65-70	Magnesite	Vein	lc1	Intermediate	b	0.97	-	202	0.97	0.00	0.03	0.97	0.00	0.03
GM	Listvenite	16Z-1-65-70	Magnesite	Vein	lc1	Intermediate	b	0.97	-	184	0.96	0.00	0.03	0.97	0.01	0.03

GM	Listvenite	16Z-1-65-70	Magnesite	Vein	lc1	Intermediate	b	0.96	-	45	0.96	0.00	0.04	0.96	0.02	0.04
GM	Listvenite	16Z-1-65-70	Magnesite	Vein	lc1	Intermediate	b	0.93	-	n.d.	0.93	0.00	0.07	0.93	0.00	0.07
GM	Listvenite	16Z-1-65-70	Magnesite	Vein	lc1	Median zone	b	0.91	37	231	0.91	0.00	0.09	0.91	0.00	0.09
GM	Listvenite	16Z-1-65-70	Magnesite	Vein	lc1	Median zone	b	0.57	-	8	0.56	0.00	0.43	0.57	0.07	0.43
GM	Listvenite	16Z-1-65-70	Magnesite	Vein	lc1	Median zone	b	0.92	-	620	0.91	0.00	0.08	0.92	0.00	0.08
GM	Listvenite	16Z-1-65-70	Magnesite	Vein	lc1	Intermediate	b	0.94	-	538	0.94	0.00	0.06	0.94	0.00	0.06
GM	Listvenite	16Z-1-65-70	Magnesite	Vein	lc1	Intermediate	b	0.95	-	593	0.95	0.00	0.05	0.95	0.00	0.05
GM	Listvenite	16Z-1-65-70	Magnesite	Vein	lc1	Intermediate	b	0.96	-	144	0.96	0.00	0.04	0.96	0.01	0.04
GM	Listvenite	16Z-1-65-70	Magnesite	Vein	lc1	Intermediate	b	0.88	-	86	0.88	0.00	0.12	0.88	0.01	0.12
GM	Listvenite	16Z-1-65-70	Magnesite	Vein	lc1	Intermediate	b	0.95	-	25	0.94	0.00	0.05	0.95	0.04	0.05
GM	Listvenite	16Z-1-65-70	Magnesite	Vein	lc1	Rim	b	0.95	-	127	0.95	0.00	0.05	0.95	0.01	0.05
GM	Listvenite	16Z-1-65-70	Magnesite	Vein	lc1	Rim	b	0.89	-	181	0.89	0.00	0.11	0.89	0.00	0.11
ISTE	Listvenite	30Z-2-33-39	Dolomite	Matrix	Aggregate			0.97	17	n.d.	0.53	0.45	0.01	0.99	0.00	0.01
ISTE	Listvenite	30Z-2-33-39	Dolomite	Matrix	Aggregate			0.90	13	1375	0.48	0.46	0.05	0.95	0.00	0.05
ISTE	Listvenite	30Z-2-33-39	Dolomite	Matrix	Aggregate			0.96	18	n.d.	0.50	0.48	0.02	0.98	0.00	0.02
ISTE	Listvenite	30Z-2-33-39	Dolomite	Matrix	Aggregate			0.97	17	1602	0.50	0.48	0.02	0.98	0.00	0.02
ISTE	Listvenite	30Z-2-33-39	Dolomite	Matrix	Aggregate			0.97	26	1746	0.51	0.48	0.01	0.99	0.00	0.01
ISTE	Listvenite	30Z-2-33-39	Dolomite	Matrix	Aggregate			0.88	25	974	0.43	0.51	0.06	0.94	0.00	0.06
ISTE	Listvenite	30Z-2-33-39	Dolomite	Matrix	Aggregate			0.97	17	1358	0.50	0.48	0.02	0.98	0.00	0.02
ISTE	Listvenite	30Z-2-33-39	Dolomite	Vein	lc2	Median zone		0.96	20	n.d.	0.53	0.45	0.02	0.98	0.00	0.02
ISTE	Listvenite	30Z-2-33-39	Dolomite	Vein	lc6	Median zone		0.96	11	n.d.	0.50	0.48	0.02	0.98	0.00	0.02
ISTE	Listvenite	30Z-2-33-39	Magnesite	Matrix	Mg-core spheroid			0.95	47	108	0.94	0.01	0.05	0.95	0.01	0.05
ISTE	Listvenite	30Z-2-33-39	Magnesite	Matrix	Aggregate			0.95	32	66	0.94	0.00	0.05	0.95	0.01	0.05
ISTE	Listvenite	30Z-2-33-39	Magnesite	Matrix	Aggregate			0.95	80	56	0.95	0.00	0.05	0.95	0.02	0.05
ISTE	Listvenite	30Z-2-33-39	Magnesite	Matrix	Aggregate			0.96	38	106	0.95	0.01	0.04	0.96	0.01	0.04
ISTE	Listvenite	30Z-2-33-39	Magnesite	Vein	lc1	Median zone		0.94	38	138	0.93	0.02	0.06	0.94	0.01	0.06
ISTE	Listvenite	31Z-3-26-31	Dolomite	Vein	lc1	Median zone		0.99	6	n.d.	0.51	0.49	0.00	1.00	0.00	0.00
ISTE	Listvenite	31Z-3-26-31	Dolomite	Vein	lc6	Median zone		0.97	2	51	0.52	0.46	0.01	0.99	0.01	0.01
ISTE	Listvenite	31Z-3-26-31	Dolomite	Vein	lc6	Median zone		0.98	5	n.d.	0.52	0.47	0.01	0.99	0.00	0.01
ISTE	Listvenite	31Z-3-26-31	Dolomite	Vein	lc6	Median zone		0.98	2	n.d.	0.50	0.49	0.01	0.99	0.00	0.01
ISTE	Listvenite	31Z-3-26-31	Dolomite	Vein	lc6	Median zone		0.98	2	n.d.	0.50	0.50	0.01	0.99	0.00	0.01
ISTE	Listvenite	31Z-3-26-31	Magnesite	Matrix	Mg-core spheroid	Rim	c	0.93	79	416	0.93	0.00	0.07	0.93	0.00	0.07
ISTE	Listvenite	31Z-3-26-31	Dolomite	Matrix	Mg-core spheroid	Internal growth	c	0.95	8	98	0.51	0.46	0.03	0.97	0.01	0.03
ISTE	Listvenite	31Z-3-26-31	Magnesite	Matrix	Mg-core spheroid	Internal growth	c	0.96	98	49	0.96	0.00	0.04	0.96	0.02	0.04
ISTE	Listvenite	31Z-3-26-31	Magnesite	Matrix	Mg-core spheroid	Core	c	0.95	83	19	0.95	0.00	0.05	0.95	0.05	0.05
ISTE	Listvenite	31Z-3-26-31	Magnesite	Matrix	Mg-core spheroid	Core		0.95	87	45	0.95	0.00	0.05	0.95	0.02	0.05
ISTE	Listvenite	31Z-3-26-31	Magnesite	Matrix	Mg-core spheroid	Core		0.96	75	66	0.96	0.00	0.04	0.96	0.01	0.04
ISTE	Listvenite	31Z-3-26-31	Magnesite	Matrix	Mg-core spheroid	Core		0.97	60	46	0.96	0.00	0.03	0.97	0.02	0.03
ISTE	Listvenite	31Z-3-26-31	Magnesite	Matrix	Mg-core spheroid	Core		0.98	-	30	0.97	0.01	0.02	0.98	0.03	0.02
ISTE	Listvenite	31Z-3-26-31	Magnesite	Matrix	Mg-core spheroid	Core		0.96	74	42	0.96	0.00	0.04	0.96	0.02	0.04
ISTE	Listvenite	31Z-3-26-31	Magnesite	Matrix	Mg-core spheroid	Core		0.97	61	50	0.96	0.00	0.03	0.97	0.02	0.03
ISTE	Listvenite	31Z-3-26-31	Magnesite	Matrix	Mg-core spheroid	Core		0.96	42	32	0.95	0.00	0.04	0.96	0.03	0.04
ISTE	Listvenite	31Z-3-26-31	Magnesite	Vein	lc1	Rim		0.94	15	558	0.93	0.00	0.06	0.94	0.00	0.06
ISTE	Listvenite	31Z-3-26-31	Magnesite	Vein	lc1	Rim		0.94	27	3606	0.94	0.00	0.06	0.94	0.00	0.06
ISTE	Listvenite	35Z-1-32-37	Magnesite	Matrix	Aggregate	Core		0.95	99	1703	0.94	0.00	0.05	0.95	0.00	0.05
ISTE	Listvenite	35Z-1-32-37	Magnesite	Matrix	Aggregate	Core		0.96	86	n.d.	0.95	0.01	0.04	0.96	0.00	0.04
ISTE	Listvenite	35Z-1-32-37	Magnesite	Matrix	Aggregate	Core		0.95	-	3362	0.94	0.01	0.05	0.95	0.00	0.05
ISTE	Listvenite	35Z-1-32-37	Magnesite	Matrix	Aggregate			0.95	119	122	0.94	0.01	0.05	0.95	0.01	0.05
ISTE	Listvenite	35Z-1-32-37	Magnesite	Matrix	Aggregate			0.93	109	n.d.	0.93	0.00	0.07	0.93	0.00	0.07
ISTE	Listvenite	35Z-1-32-37	Magnesite	Matrix	Aggregate			0.95	91	3201	0.94	0.01	0.05	0.95	0.00	0.05
ISTE	Listvenite	35Z-1-32-37	Magnesite	Matrix	Aggregate			0.94	79	5291	0.93	0.01	0.06	0.94	0.00	0.06
ISTE	Listvenite	35Z-1-32-37	Magnesite	Vein	lc1	Median zone		0.56	284	5	0.55	0.00	0.44	0.56	0.10	0.44
ISTE	Listvenite	35Z-1-32-37	Magnesite	Vein	lc1	Median zone		0.90	22	34	0.90	0.00	0.10	0.90	0.03	0.10

ISTE	Listvenite	35Z-1-32-37	Magnesite	Vein	lc1	Median zone		0.84	37	19	0.84	0.01	0.15	0.85	0.04	0.15
ISTE	Listvenite	35Z-1-32-37	Magnesite	Vein	lc1	Median zone		0.90	23	38	0.90	0.01	0.09	0.91	0.02	0.09
ISTE	Listvenite	35Z-1-32-37	Magnesite	Vein	lc1	Median zone		0.90	21	28	0.90	0.00	0.10	0.90	0.03	0.10
ISTE	Listvenite	35Z-1-32-37	Magnesite	Vein	lc1	Median zone		0.73	157	353	0.73	0.00	0.27	0.73	0.00	0.27
ISTE	Listvenite	35Z-1-32-37	Magnesite	Vein	lc1	Median zone		0.59	188	50	0.59	0.00	0.41	0.59	0.01	0.41
ISTE	Listvenite	35Z-1-32-37	Magnesite	Vein	lc1	Median zone		0.61	234	22	0.60	0.00	0.39	0.61	0.03	0.39
ISTE	Listvenite	35Z-1-32-37	Magnesite	Vein	lc1	Rim		0.67	169	49	0.67	0.00	0.33	0.67	0.01	0.33
ISTE	Listvenite	35Z-1-32-37	Magnesite	Matrix	Aggregate (clast)			0.94	71	3750	0.94	0.00	0.05	0.95	0.00	0.05
ISTE	Listvenite	35Z-1-32-37	Magnesite	Matrix	Aggregate (clast)			0.94	117	3318	0.94	0.01	0.06	0.94	0.00	0.06
ISTE	Listvenite	38Z-3-60-65	Dolomite	Matrix		Interstitial		0.98	1	95	0.52	0.47	0.01	0.99	0.01	0.01
ISTE	Listvenite	38Z-3-60-65	Dolomite	Matrix		Interstitial		0.96	5	956	0.51	0.47	0.02	0.98	0.00	0.02
ISTE	Listvenite	38Z-3-60-65	Dolomite	Matrix		Interstitial		0.99	0.4	n.d.	0.53	0.46	0.01	0.99	0.00	0.01
ISTE	Listvenite	38Z-3-60-65	Dolomite	Vein	lc2			0.96	4	n.d.	0.51	0.47	0.02	0.98	0.00	0.02
ISTE	Listvenite	38Z-3-60-65	Dolomite	Vein	lc2			0.98	14	n.d.	0.52	0.47	0.01	0.99	0.00	0.01
ISTE	Listvenite	38Z-3-60-65	Magnesite	Vein	lc1	Median zone		0.95	42	n.d.	0.94	0.00	0.05	0.95	0.00	0.05
ISTE	Listvenite	38Z-3-60-65	Magnesite	Vein	lc1	Median zone		0.96	28	349	0.96	0.00	0.04	0.96	0.00	0.04
ISTE	Listvenite	38Z-3-60-65	Magnesite	Vein	lc1	Median zone		0.96	98	143	0.96	0.00	0.04	0.96	0.01	0.04
ISTE	Listvenite	38Z-3-60-65	Magnesite	Vein	lc1	Median zone		0.88	14	n.d.	0.88	0.00	0.12	0.88	0.00	0.12
ISTE	Listvenite	38Z-3-60-65	Magnesite	Vein	lc1	Rim		0.95	35	116	0.94	0.00	0.05	0.95	0.01	0.05
ISTE	Listvenite	38Z-3-60-65	Magnesite	Vein	lc2			0.88	15	844	0.88	0.00	0.12	0.88	0.00	0.12
ISTE	Listvenite	38Z-3-60-65	Magnesite	Vein	lc2			0.93	22	n.d.	0.93	0.00	0.07	0.93	0.00	0.07
ISTE	Carbonated serpentinite	40Z-3-11-16	Dolomite	Matrix	Aggregate			0.99	4	n.d.	0.50	0.50	0.00	1.00	0.00	0.00
ISTE	Carbonated serpentinite	40Z-3-11-16	Dolomite	Matrix	Aggregate			0.99	4	1701	0.50	0.50	0.00	1.00	0.00	0.00
ISTE	Carbonated serpentinite	40Z-3-11-16	Dolomite	Matrix	Aggregate			0.99	3	n.d.	0.50	0.50	0.00	1.00	0.00	0.00
ISTE	Carbonated serpentinite	40Z-3-11-16	Dolomite	Matrix	Aggregate			0.97	16	25	0.48	0.50	0.01	0.99	0.02	0.01
ISTE	Carbonated serpentinite	40Z-3-11-16	Dolomite	Matrix	Aggregate			0.98	9	n.d.	0.49	0.50	0.01	0.99	0.00	0.01
ISTE	Carbonated serpentinite	40Z-3-11-16	Dolomite	Matrix	Aggregate			0.97	12	106	0.48	0.50	0.01	0.99	0.00	0.01
ISTE	Carbonated serpentinite	40Z-3-11-16	Dolomite	Matrix	sc0			1.00	0	127	0.50	0.50	0.00	1.00	0.00	0.00
ISTE	Carbonated serpentinite	40Z-3-11-16	Dolomite	Vein	sc0	Median zone		0.99	1	15	0.51	0.49	0.00	1.00	0.03	0.00
ISTE	Carbonated serpentinite	40Z-3-11-16	Dolomite	Vein	sc0	Median zone		0.99	0.3	65	0.50	0.49	0.00	1.00	0.01	0.00
GM	Carbonated serpentinite	43Z-2-43-48	Dolomite	Matrix	Dol-core spheroid	Internal growth		0.96	2	9	0.43	0.56	0.02	0.98	0.05	0.02
GM	Carbonated serpentinite	43Z-2-43-48	Dolomite	Matrix	Mg-core spheroid	Rim		0.97	2	4	0.52	0.46	0.02	0.98	0.14	0.02
GM	Carbonated serpentinite	43Z-2-43-48	Dolomite	Vein	sc0	Median zone		0.99	2	33	0.43	0.56	0.01	0.99	0.01	0.01
GM	Carbonated serpentinite	43Z-2-43-48	Dolomite	Vein	sc0	Median zone		0.99	1	37	0.44	0.55	0.01	0.99	0.01	0.01
GM	Carbonated serpentinite	43Z-2-43-48	Dolomite	Vein	sc0	Median zone		0.99	1	45	0.43	0.57	0.01	0.99	0.01	0.01
GM	Carbonated serpentinite	43Z-2-43-49	Dolomite	Vein	sc0	Median zone		0.99	1	19	0.44	0.56	0.01	0.99	0.02	0.01
GM	Carbonated serpentinite	43Z-2-43-48	Dolomite	Vein	sc2	Median zone		0.99	1	19	0.44	0.55	0.01	0.99	0.02	0.01
GM	Carbonated serpentinite	43Z-2-43-48	Dolomite	Vein	sc2	Median zone		0.97	2	5	0.47	0.52	0.01	0.99	0.10	0.01
GM	Carbonated serpentinite	43Z-2-43-48	Magnesite	Matrix	Dol-core spheroid	Internal growth	d	0.95	5	7	0.80	0.16	0.04	0.96	0.11	0.04
GM	Carbonated serpentinite	43Z-2-43-48	Dolomite	Matrix	Dol-core spheroid	Core	d	0.98	2	9	0.45	0.54	0.01	0.99	0.05	0.01
GM	Carbonated serpentinite	43Z-2-43-48	Dolomite	Matrix	Dol-core spheroid	Core	d	0.99	1	46	0.43	0.56	0.00	1.00	0.01	0.00
GM	Carbonated serpentinite	43Z-2-43-48	Dolomite	Matrix	Dol-core spheroid	Core	d	0.99	1	20	0.44	0.55	0.01	0.99	0.02	0.01
GM	Carbonated serpentinite	43Z-2-43-48	Magnesite	Matrix	Dol-core spheroid	Internal growth	d	0.98	2	82	0.96	0.01	0.02	0.98	0.01	0.02
GM	Carbonated serpentinite	43Z-2-43-48	Dolomite	Matrix	Dol-core spheroid	Internal growth	d	0.98	1	14	0.63	0.35	0.02	0.98	0.04	0.02
GM	Carbonated serpentinite	43Z-2-43-48	Dolomite	Matrix	Dol-core spheroid	Internal growth	d	0.97	2	5	0.45	0.54	0.01	0.99	0.09	0.01
GM	Carbonated serpentinite	43Z-2-43-48	Magnesite	Matrix	Mg-core spheroid	Rim		0.96	3	11	0.93	0.03	0.03	0.97	0.08	0.03
GM	Carbonated serpentinite	43Z-2-43-48	Magnesite	Matrix	Mg-core spheroid	Rim	e	0.96	3	5	0.82	0.15	0.03	0.97	0.18	0.03
GM	Carbonated serpentinite	43Z-2-43-48	Magnesite	Matrix	Mg-core spheroid	Internal growth	e	0.97	2	5	0.84	0.13	0.03	0.97	0.17	0.03
GM	Carbonated serpentinite	43Z-2-43-48	Magnesite	Matrix	Mg-core spheroid	Internal growth	e	0.97	2	6	0.82	0.15	0.03	0.97	0.15	0.03
GM	Carbonated serpentinite	43Z-2-43-48	Magnesite	Matrix	Mg-core spheroid	Core	e	0.97	1	5	0.69	0.29	0.02	0.98	0.13	0.02
GM	Carbonated serpentinite	43Z-2-43-48	Magnesite	Matrix	Mg-core spheroid	Core	e	0.97	2	6	0.83	0.14	0.03	0.97	0.13	0.03
GM	Carbonated serpentinite	43Z-2-43-48	Magnesite	Matrix	Mg-core spheroid	Internal growth	e	0.97	2	6	0.84	0.13	0.03	0.97	0.15	0.03
GM	Carbonated serpentinite	43Z-2-43-48	Magnesite	Matrix	Mg-core spheroid	Internal growth	e	0.90	8	8	0.78	0.12	0.09	0.91	0.10	0.09

GM	Carbonated serpentinite	43Z-2-43-48	Dolomite	Matrix	Mg-core spheroid	Rim	e	0.97	2	4	0.52	0.46	0.02	0.98	0.14	0.02
GM	Carbonated serpentinite	43Z-2-43-48	Dolomite	Matrix	Mg-core spheroid	Rim	f	0.97	2	4	0.52	0.46	0.02	0.98	0.14	0.02
GM	Carbonated serpentinite	43Z-2-43-48	Magnesite	Matrix	Mg-core spheroid	Internal growth	f	0.96	2	11	0.85	0.12	0.03	0.97	0.08	0.03
GM	Carbonated serpentinite	43Z-2-43-48	Magnesite	Matrix	Mg-core spheroid	Rim	f	0.96	2	5	0.83	0.14	0.03	0.97	0.18	0.03
GM	Carbonated serpentinite	43Z-2-43-48	Magnesite	Vein	sc2	Median zone		0.94	21	22	0.94	0.01	0.06	0.94	0.04	0.06
GM	Carbonated serpentinite	43Z-2-43-48	Magnesite	Vein	sc2	Median zone		0.94	18	22	0.94	0.01	0.06	0.94	0.04	0.06
GM	Carbonated serpentinite	43Z-2-43-48	Magnesite	Vein	sc2	Median zone		0.97	2	54	0.81	0.17	0.03	0.97	0.01	0.03
GM	Carbonated serpentinite	43Z-2-43-48	Magnesite	Vein	sc2	Median zone		0.97	1	60	0.90	0.07	0.02	0.98	0.02	0.02
GM	Carbonated serpentinite	43Z-3-0-5	Dolomite	Matrix	Dol-core spheroid	Core		0.96	2	7	0.44	0.54	0.02	0.98	0.06	0.02
GM	Carbonated serpentinite	43Z-3-0-5	Dolomite	Matrix	Dol-core spheroid	Core		0.97	3	7	0.45	0.53	0.02	0.98	0.07	0.02
GM	Carbonated serpentinite	43Z-3-0-5	Dolomite	Matrix	Dol-core spheroid	Core		0.94	3	8	0.60	0.37	0.04	0.96	0.07	0.04
GM	Carbonated serpentinite	43Z-3-0-5	Dolomite	Matrix	Dol-core spheroid	Core		0.96	2	8	0.46	0.53	0.02	0.98	0.05	0.02
GM	Carbonated serpentinite	43Z-3-0-5	Dolomite	Matrix	Dol-core spheroid	Core		0.97	3	4	0.48	0.50	0.02	0.98	0.12	0.02
GM	Carbonated serpentinite	43Z-3-0-5	Dolomite	Matrix	Dol-core spheroid	Core		0.96	3	4	0.47	0.51	0.02	0.98	0.12	0.02
GM	Carbonated serpentinite	43Z-3-0-5	Dolomite	Matrix	Mg-core spheroid	Core		0.94	13	6	0.94	0.01	0.06	0.94	0.17	0.06
GM	Carbonated serpentinite	43Z-3-0-5	Dolomite	Vein	sc2	Median zone		0.97	1	50	0.55	0.44	0.01	0.99	0.01	0.01
GM	Carbonated serpentinite	43Z-3-0-5	Dolomite	Vein	sc2	Intermediate		0.99	0	31	0.44	0.56	0.00	1.00	0.01	0.00
GM	Carbonated serpentinite	43Z-3-0-5	Magnesite	Vein	sc2	Rim		0.94	13	6	0.94	0.01	0.06	0.94	0.17	0.06
GM	Carbonated serpentinite	43Z-3-0-5	Magnesite	Vein	sc2	Intermediate	g	0.95	13	449	0.95	0.00	0.05	0.95	0.00	0.05
GM	Carbonated serpentinite	43Z-3-0-5	Magnesite	Vein	sc2	Intermediate	g	0.96	-	245	0.95	0.01	0.04	0.96	0.00	0.04
GM	Carbonated serpentinite	43Z-3-0-5	Magnesite	Vein	sc2	Intermediate	g	0.96	-	21	0.95	0.01	0.04	0.96	0.04	0.04
GM	Carbonated serpentinite	43Z-3-0-5	Magnesite	Vein	sc2	Median zone	g	0.95	12	16	0.94	0.00	0.05	0.95	0.06	0.05
GM	Carbonated serpentinite	43Z-3-0-5	Magnesite	Vein	sc2	Median zone	g	0.92	3	20	0.91	0.01	0.08	0.92	0.05	0.08
GM	Carbonated serpentinite	43Z-3-0-5	Magnesite	Vein	sc2	Median zone	g	0.94	5	9	0.93	0.00	0.06	0.94	0.10	0.06
GM	Carbonated serpentinite	43Z-3-0-5	Magnesite	Vein	sc2	Intermediate	g	0.95	18	27	0.94	0.01	0.05	0.95	0.03	0.05
GM	Carbonated serpentinite	43Z-3-0-5	Magnesite	Vein	sc2	Intermediate	g	0.95	-	8	0.95	0.01	0.05	0.95	0.12	0.05
GM	Carbonated serpentinite	43Z-3-0-5	Magnesite	Vein	sc2	Intermediate	g	0.96	-	37	0.95	0.01	0.04	0.96	0.03	0.04
GM	Carbonated serpentinite	43Z-3-0-5	Dolomite	Vein	sc2	Rim	g	0.99	0.4	17	0.43	0.57	0.00	1.00	0.02	0.00
GM	Carbonated serpentinite	43Z-3-0-5	Dolomite	Vein	sc2	Rim	g	0.99	0.4	18	0.44	0.56	0.00	1.00	0.02	0.00
GM	Carbonated serpentinite	43Z-4-52-57	Dolomite	Matrix	Dol-core spheroid	Core		1.00	-	n.d.	0.47	0.53	0.00	1.00	0.00	0.00
GM	Carbonated serpentinite	43Z-4-52-57	Dolomite	Matrix	Dol-core spheroid	Core		0.98	-	7	0.49	0.50	0.01	0.99	0.07	0.01
GM	Carbonated serpentinite	43Z-4-52-57	Dolomite	Matrix	Dol-core spheroid	Core		0.99	1	197	0.47	0.52	0.00	1.00	0.00	0.00
GM	Carbonated serpentinite	43Z-4-52-57	Dolomite	Matrix	Dol-core spheroid	Core		0.96	-	140	0.45	0.53	0.02	0.98	0.00	0.02
GM	Carbonated serpentinite	43Z-4-52-57	Dolomite	Matrix	Dol-core spheroid	Core		0.97	2	7	0.50	0.49	0.02	0.98	0.07	0.02
GM	Carbonated serpentinite	43Z-4-52-57	Dolomite	Matrix	Dol-core spheroid	Core		0.97	2	10	0.53	0.46	0.02	0.98	0.05	0.02
GM	Carbonated serpentinite	43Z-4-52-57	Dolomite	Matrix	Dol-core spheroid	Core		0.97	2	11	0.54	0.44	0.02	0.98	0.05	0.02
GM	Carbonated serpentinite	43Z-4-52-57	Dolomite	Matrix	Dol-core spheroid	Core		0.98	1	9	0.50	0.49	0.01	0.99	0.06	0.01
GM	Carbonated serpentinite	43Z-4-52-57	Dolomite	Matrix	Dol-core spheroid	Core		0.98	2	4	0.55	0.44	0.01	0.99	0.13	0.01
GM	Carbonated serpentinite	43Z-4-52-57	Dolomite	Matrix	Dol-core spheroid	Core		0.97	2	5	0.57	0.41	0.02	0.98	0.11	0.02
GM	Carbonated serpentinite	43Z-4-52-57	Dolomite	Matrix	Dol-core spheroid	Core		0.57	50	6	0.40	0.30	0.30	0.70	0.06	0.30
GM	Carbonated serpentinite	43Z-4-52-57	Dolomite	Vein	sc2	Median zone		0.99	1	8	0.52	0.48	0.01	0.99	0.06	0.01
GM	Carbonated serpentinite	43Z-4-52-57	Dolomite	Vein	sc2	Median zone		0.98	1	7	0.51	0.48	0.01	0.99	0.08	0.01
GM	Carbonated serpentinite	43Z-4-52-57	Dolomite	Vein	sc2	Median zone		0.98	1	7	0.51	0.48	0.01	0.99	0.07	0.01
GM	Carbonated serpentinite	43Z-4-52-57	Dolomite	Vein	sc2	Median zone		0.99	1	9	0.50	0.50	0.01	0.99	0.05	0.01
GM	Carbonated serpentinite	43Z-4-52-57	Magnesite	Matrix	Mg-core spheroid	Core		0.95	6	8	0.77	0.19	0.04	0.96	0.10	0.04
ISTE	Carbonated serpentinite	44Z-1-41-46	Magnesite	Matrix	Mg-core spheroid	Core		0.95	12	11	0.93	0.02	0.05	0.95	0.09	0.05
ISTE	Carbonated serpentinite	44Z-1-41-46	Magnesite	Matrix	Mg-core spheroid	Core		0.93	20	9	0.91	0.02	0.07	0.93	0.10	0.07
ISTE	Carbonated serpentinite	44Z-1-41-46	Magnesite	Matrix	Mg-core spheroid	Core		0.93	20	9	0.90	0.03	0.06	0.94	0.10	0.06
ISTE	Carbonated serpentinite	44Z-1-41-46	Dolomite	Matrix	Spheroid	Core		0.94	16	8	0.66	0.30	0.05	0.95	0.08	0.05
ISTE	Carbonated serpentinite	44Z-1-41-46	Dolomite	Vein	sc0	Median zone		0.99	0	33	0.53	0.46	0.01	0.99	0.02	0.01
ISTE	Carbonated serpentinite	44Z-1-41-46	Dolomite	Vein	sc2	Median zone		0.99	0	17	0.50	0.50	0.00	1.00	0.03	0.00
ISTE	Carbonated serpentinite	44Z-1-41-46	Dolomite	Vein	sc2 or sc4?	Median zone		0.94	11	917	0.46	0.51	0.03	0.97	0.00	0.03
ISTE	Carbonated serpentinite	44Z-1-41-46	Dolomite	Vein	sc2 or sc4?	Median zone		0.95	2	121	0.49	0.49	0.02	0.98	0.00	0.02

ISTE	Carbonated serpentinite	44Z-1-41-46	Dolomite	Vein	sc2 or sc4?	Median zone	0.97	7	5	0.56	0.43	0.02	0.98	0.11	0.02
ISTE	Carbonated serpentinite	44Z-1-41-46	Dolomite	Vein	sc2 or sc4?	Median zone	0.95	2	7	0.57	0.40	0.03	0.97	0.08	0.03
ISTE	Carbonated serpentinite	44Z-1-41-46	Dolomite	Vein	sc2 or sc4?	Median zone	0.95	2	10	0.56	0.41	0.03	0.97	0.06	0.03
ISTE	Carbonated serpentinite	44Z-1-41-46	Dolomite	Vein	sc2 or sc4?	Median zone	0.97	7	9	0.52	0.46	0.02	0.98	0.06	0.02
ISTE	Carbonated serpentinite	44Z-1-41-46	Magnesite	Vein	sc2	Median zone	0.88	5	57	0.87	0.01	0.12	0.88	0.02	0.12
ISTE	Carbonated serpentinite	44Z-1-41-46	Magnesite	Vein	sc0	Median zone	0.99	1	36	0.93	0.06	0.01	0.99	0.03	0.01
ISTE	Carbonated serpentinite	44Z-1-41-46	Magnesite	Vein	sc0	Median zone	0.99	0.4	57	0.98	0.00	0.01	0.99	0.02	0.01
GM	Carbonated serpentinite	44Z-4-0-5	Magnesite	Matrix	Fe-core spheroid	Core	0.75	-	4	0.72	0.04	0.24	0.76	0.16	0.24
GM	Carbonated serpentinite	44Z-4-0-5	Magnesite	Matrix	Fe-core spheroid	Core	0.69	-	7	0.67	0.03	0.30	0.70	0.09	0.30
GM	Carbonated serpentinite	44Z-4-0-5	Magnesite	Matrix	Fe-core spheroid	Core	0.61	-	11	0.59	0.03	0.37	0.63	0.05	0.37
ISTE	Carbonated serpentinite	44Z-4-0-5	Magnesite	Matrix	Mg-core spheroid	Core	0.93	25	11	0.91	0.02	0.07	0.93	0.08	0.07
ISTE	Carbonated serpentinite	44Z-4-0-5	Magnesite	Matrix	Mg-core spheroid	Core	0.91	35	10	0.89	0.02	0.09	0.91	0.09	0.09
ISTE	Carbonated serpentinite	44Z-4-0-5	Magnesite	Matrix	Mg-core spheroid	Core	0.87	81	5	0.85	0.01	0.13	0.87	0.17	0.13
ISTE	Carbonated serpentinite	44Z-4-0-5	Magnesite	Matrix	Mg-core spheroid	Core	0.94	19	7	0.93	0.01	0.06	0.94	0.14	0.06
ISTE	Carbonated serpentinite	44Z-4-0-5	Magnesite	Matrix	Mg-core spheroid	Core	0.93	22	8	0.93	0.01	0.07	0.93	0.11	0.07
ISTE	Carbonated serpentinite	44Z-4-0-5	Magnesite	Matrix	Mg-core spheroid	Internal growth	0.89	49	7	0.88	0.01	0.11	0.89	0.12	0.11
ISTE	Carbonated serpentinite	44Z-4-0-5	Magnesite	Matrix	Mg-core spheroid	Rim	0.91	34	6	0.90	0.01	0.09	0.91	0.14	0.09
GM	Carbonated serpentinite	44Z-4-0-5	Magnesite	Matrix	Mg-core spheroid	Rim	0.78	-	27	0.78	0.01	0.22	0.78	0.03	0.22
GM	Carbonated serpentinite	44Z-4-0-5	Magnesite	Vein	sc0	Border	0.97	3	9	0.96	0.01	0.03	0.97	0.10	0.03
GM	Carbonated serpentinite	44Z-4-0-5	Magnesite	Vein	sc0	Border	0.96	3	13	0.95	0.01	0.04	0.96	0.07	0.04
GM	Carbonated serpentinite	44Z-4-0-5	Magnesite	Vein	sc0	Border	0.97	3	11	0.96	0.01	0.03	0.97	0.09	0.03
GM	Carbonated serpentinite	44Z-4-0-5	Magnesite	Vein	sc0		0.97	3	44	0.96	0.01	0.03	0.97	0.02	0.03
GM	Carbonated serpentinite	44Z-4-0-5	Magnesite	Vein	sc0		0.98	3	44	0.97	0.00	0.02	0.98	0.02	0.02
GM	Carbonated serpentinite	44Z-4-0-5	Magnesite	Vein	sc0		0.63	-	n.d.	0.63	0.01	0.36	0.64	0.00	0.36
GM	Carbonated serpentinite	44Z-4-0-5	Magnesite	Vein	sc2	Median zone	0.86	-	81	0.85	0.01	0.14	0.86	0.01	0.14
GM	Carbonated serpentinite	44Z-4-0-5	Magnesite	Vein	sc2	Median zone	0.84	-	14	0.81	0.04	0.15	0.85	0.06	0.15
GM	Carbonated serpentinite	44Z-4-0-5	Magnesite	Vein	sc2	Median zone	0.87	-	126	0.86	0.00	0.13	0.87	0.01	0.13
GM	Carbonated serpentinite	44Z-4-0-5	Magnesite	Vein	sc2	Median zone	0.80	-	13	0.79	0.02	0.19	0.81	0.06	0.19
GM	Carbonated serpentinite	44Z-4-0-5	Magnesite	Vein	sc2	Median zone	0.78	-	287	0.77	0.01	0.22	0.78	0.00	0.22
GM	Carbonated serpentinite	44Z-4-0-5	Magnesite	Vein	sc2	Median zone	0.87	-	141	0.87	0.00	0.13	0.87	0.01	0.13
GM	Carbonated serpentinite	44Z-4-0-5	Magnesite	Vein	sc2	Median zone	0.81	-	7	0.80	0.01	0.19	0.81	0.11	0.19
GM	Carbonated serpentinite	44Z-4-0-5	Magnesite	Vein	sc2	Median zone	0.85	-	7	0.76	0.10	0.14	0.86	0.12	0.14
GM	Carbonated serpentinite	44Z-4-0-5	Magnesite	Vein	sc2	Median zone	0.60	-	n.d.	0.60	0.01	0.39	0.61	0.00	0.39
GM	Carbonated serpentinite	44Z-4-0-5	Magnesite	Vein	sc2	Median zone	0.64	-	n.d.	0.64	0.01	0.36	0.64	0.00	0.36
GM	Carbonated serpentinite	44Z-4-0-5	Magnesite	Vein	sc2	Median zone	0.89	-	4	0.89	0.00	0.11	0.89	0.23	0.11
ISTE	Carbonated serpentinite	44Z-4-0-5	Magnesite	Vein	sc2	Border	0.97	5	32	0.96	0.01	0.03	0.97	0.03	0.03
ISTE	Listvenite	45Z-1-38-39	Dolomite	Matrix	Dol-core spheroid	Core	1.00	1	1166	0.53	0.47	0.00	1.00	0.00	0.00
ISTE	Listvenite	45Z-1-38-39	Dolomite	Matrix	Aggregate		0.98	19	n.d.	0.51	0.48	0.01	0.99	0.00	0.01
ISTE	Listvenite	45Z-1-38-39	Dolomite	Matrix	Aggregate		0.93	22	n.d.	0.49	0.47	0.03	0.97	0.00	0.03
ISTE	Listvenite	45Z-1-38-39	Magnesite	Matrix	Mg-core spheroid	Core	0.95	91	52	0.95	0.00	0.05	0.95	0.02	0.05
ISTE	Listvenite	45Z-1-38-39	Magnesite	Matrix	Mg-core spheroid	Core	0.95	61	119	0.94	0.00	0.05	0.95	0.01	0.05
ISTE	Listvenite	45Z-1-38-39	Magnesite	Matrix	Mg-core spheroid	Core	0.95	99	322	0.94	0.00	0.05	0.95	0.00	0.05
ISTE	Listvenite	45Z-1-38-39	Magnesite	Matrix	Mg-core spheroid	Core	0.96	72	80	0.95	0.01	0.04	0.96	0.01	0.04
ISTE	Listvenite	45Z-1-38-39	Magnesite	Matrix	Mg-core spheroid	Core	0.96	109	150	0.95	0.01	0.04	0.96	0.01	0.04
ISTE	Listvenite	45Z-1-38-39	Magnesite	Matrix	Aggregate		0.96	32	151	0.96	0.00	0.04	0.96	0.01	0.04
ISTE	Listvenite	45Z-1-38-39	Magnesite	Matrix	Aggregate		0.95	-	9	0.95	0.00	0.05	0.95	0.11	0.05
ISTE	Listvenite	45Z-1-38-39	Magnesite	Matrix	Aggregate		0.94	67	n.d.	0.94	0.00	0.06	0.94	0.00	0.06
ISTE	Listvenite	45Z-1-38-39	Magnesite	Matrix	Overgrowth		0.94	75	n.d.	0.94	0.00	0.06	0.94	0.00	0.06
ISTE	Listvenite	45Z-1-38-39	Magnesite	Matrix	Overgrowth		0.95	62	177	0.95	0.00	0.05	0.95	0.01	0.05
GM	Listvenite	46Z-4-46-51	Dolomite	Matrix	Dol-core spheroid	Core	0.88	22	324	0.46	0.47	0.06	0.94	0.00	0.06
GM	Listvenite	46Z-4-46-51	Dolomite	Matrix	Dol-core spheroid	Core	0.89	-	231	0.48	0.46	0.06	0.94	0.00	0.06
GM	Listvenite	46Z-4-46-51	Dolomite	Matrix	Dol-core spheroid	Core	0.91	14	n.d.	0.45	0.51	0.04	0.96	0.00	0.04
GM	Listvenite	46Z-4-46-51	Dolomite	Vein	lc1	Median zone	0.87	18	n.d.	0.44	0.50	0.07	0.93	0.00	0.07

ISTE	Listvenite	46Z-4-46-51	Dolomite	Vein	lc1	Median zone		0.96	11	234	0.51	0.47	0.02	0.98	0.00	0.02
ISTE	Listvenite	46Z-4-46-51	Dolomite	Vein	lc6	Median zone		0.92	20	453	0.48	0.48	0.04	0.96	0.00	0.04
ISTE	Listvenite	46Z-4-46-51	Dolomite	Vein	lc6	Median zone		0.95	14	502	0.50	0.47	0.03	0.97	0.00	0.03
GM	Listvenite	46Z-4-46-51	Magnesite	Matrix	Mg-core spheroid	Core		0.91	-	229	0.91	0.00	0.09	0.91	0.00	0.09
GM	Listvenite	46Z-4-46-51	Magnesite	Matrix	Mg-core spheroid	Core		0.95	-	34	0.95	0.00	0.05	0.95	0.03	0.05
GM	Listvenite	46Z-4-46-51	Magnesite	Matrix	Mg-core spheroid	Core		0.96	-	17	0.95	0.01	0.04	0.96	0.06	0.04
GM	Listvenite	46Z-4-46-51	Magnesite	Matrix	Mg-core spheroid	Core		0.93	28	10	0.92	0.01	0.07	0.93	0.09	0.07
GM	Listvenite	46Z-4-46-51	Magnesite	Matrix	Mg-core spheroid	Core		0.95	-	91	0.94	0.00	0.05	0.95	0.01	0.05
GM	Listvenite	46Z-4-46-51	Magnesite	Matrix	Mg-core spheroid	Core		0.95	-	84	0.94	0.00	0.05	0.95	0.01	0.05
GM	Listvenite	46Z-4-46-51	Magnesite	Matrix	Mg-core spheroid	Core		0.85	-	639	0.85	0.01	0.15	0.85	0.00	0.15
GM	Listvenite	46Z-4-46-51	Magnesite	Matrix	Mg-core spheroid	Core		0.91	-	133	0.91	0.00	0.09	0.91	0.01	0.09
ISTE	Listvenite	46Z-4-46-51	Magnesite	Matrix	Mg-core spheroid	Core		0.96	36	158	0.96	0.00	0.04	0.96	0.01	0.04
ISTE	Listvenite	46Z-4-46-51	Magnesite	Matrix	Mg-core spheroid	Core		0.96	41	159	0.96	0.00	0.04	0.96	0.01	0.04
ISTE	Listvenite	46Z-4-46-51	Magnesite	Matrix	Mg-core spheroid	Core		0.97	-	712	0.97	0.00	0.03	0.97	0.00	0.03
ISTE	Listvenite	46Z-4-46-51	Magnesite	Matrix	Mg-core spheroid	Core		0.92	21	25	0.92	0.01	0.08	0.92	0.04	0.08
ISTE	Listvenite	46Z-4-46-51	Magnesite	Matrix	Mg-core spheroid	Core		0.96	51	153	0.95	0.00	0.04	0.96	0.01	0.04
ISTE	Listvenite	46Z-4-46-51	Magnesite	Matrix	Mg-core spheroid	Core		0.96	86	560	0.96	0.00	0.04	0.96	0.00	0.04
ISTE	Listvenite	46Z-4-46-51	Magnesite	Matrix	Mg-core spheroid	Internal growth		0.97	-	1047	0.97	0.00	0.03	0.97	0.00	0.03
ISTE	Listvenite	46Z-4-46-51	Magnesite	Matrix	Mg-core spheroid	Internal growth		0.97	-	25	0.96	0.01	0.03	0.97	0.04	0.03
ISTE	Listvenite	46Z-4-46-51	Magnesite	Matrix	Mg-core spheroid	Internal growth		0.91	30	27	0.91	0.00	0.09	0.91	0.03	0.09
ISTE	Listvenite	46Z-4-46-51	Magnesite	Matrix	Mg-core spheroid	Rim		0.81	-	2	0.80	0.01	0.19	0.81	0.45	0.19
ISTE	Listvenite	46Z-4-46-51	Magnesite	Matrix	Mg-core spheroid	Rim		0.67	295	1	0.67	0.00	0.33	0.67	0.48	0.33
ISTE	Listvenite	46Z-4-46-51	Magnesite	Matrix	Mg-core spheroid	Rim		0.96	36	262	0.95	0.00	0.04	0.96	0.00	0.04
GM	Listvenite	46Z-4-46-51	Magnesite	Matrix	Mg-core spheroid	Rim	h	0.94	-	17	0.93	0.02	0.05	0.95	0.06	0.05
GM	Listvenite	46Z-4-46-51	Magnesite	Matrix	Mg-core spheroid	Rim	h	0.97	-	20	0.96	0.01	0.03	0.97	0.05	0.03
GM	Listvenite	46Z-4-46-51	Magnesite	Matrix	Mg-core spheroid	Internal growth	h	0.97	-	31	0.97	0.00	0.03	0.97	0.03	0.03
GM	Listvenite	46Z-4-46-51	Magnesite	Matrix	Mg-core spheroid	Internal growth	h	0.96	-	112	0.96	0.00	0.04	0.96	0.01	0.04
GM	Listvenite	46Z-4-46-51	Magnesite	Matrix	Mg-core spheroid	Internal growth	h	0.97	-	468	0.97	0.00	0.03	0.97	0.00	0.03
GM	Listvenite	46Z-4-46-51	Magnesite	Matrix	Mg-core spheroid	Internal growth	h	0.97	-	208	0.96	0.01	0.03	0.97	0.00	0.03
GM	Listvenite	46Z-4-46-51	Magnesite	Matrix	Mg-core spheroid	Internal growth	h	0.97	-	8	0.97	0.00	0.03	0.97	0.12	0.03
GM	Listvenite	46Z-4-46-51	Magnesite	Matrix	Mg-core spheroid	Internal growth	h	0.97	-	326	0.97	0.00	0.03	0.97	0.00	0.03
GM	Listvenite	46Z-4-46-51	Magnesite	Matrix	Mg-core spheroid	Internal growth	h	0.97	-	285	0.97	0.00	0.03	0.97	0.00	0.03
GM	Listvenite	46Z-4-46-51	Magnesite	Matrix	Mg-core spheroid	Internal growth	h	0.97	-	390	0.97	0.00	0.03	0.97	0.00	0.03
GM	Listvenite	46Z-4-46-51	Magnesite	Matrix	Mg-core spheroid	Internal growth	h	0.97	-	28	0.97	0.00	0.03	0.97	0.04	0.03
GM	Listvenite	46Z-4-46-51	Magnesite	Matrix	Mg-core spheroid	Internal growth	h	0.97	-	24	0.97	0.00	0.03	0.97	0.04	0.03
GM	Listvenite	46Z-4-46-51	Magnesite	Matrix	Mg-core spheroid	Internal growth	h	0.97	-	35	0.96	0.00	0.03	0.97	0.03	0.03
GM	Listvenite	46Z-4-46-51	Magnesite	Matrix	Mg-core spheroid	Internal growth	h	0.97	-	584	0.97	0.00	0.03	0.97	0.00	0.03
GM	Listvenite	46Z-4-46-51	Magnesite	Matrix	Mg-core spheroid	Internal growth	h	0.97	-	31	0.97	0.00	0.03	0.97	0.03	0.03
GM	Listvenite	46Z-4-46-51	Magnesite	Matrix	Mg-core spheroid	Internal growth	h	0.97	-	n.d.	0.97	0.00	0.03	0.97	0.00	0.03
GM	Listvenite	46Z-4-46-51	Magnesite	Matrix	Mg-core spheroid	Internal growth	h	0.97	-	n.d.	0.97	0.00	0.03	0.97	0.00	0.03
GM	Listvenite	46Z-4-46-51	Magnesite	Matrix	Mg-core spheroid	Core	h	0.95	-	133	0.95	0.00	0.05	0.95	0.01	0.05
GM	Listvenite	46Z-4-46-51	Magnesite	Matrix	Mg-core spheroid	Core	h	0.96	-	n.d.	0.96	0.00	0.04	0.96	0.00	0.04
GM	Listvenite	46Z-4-46-51	Magnesite	Matrix	Mg-core spheroid	Core	h	0.96	-	n.d.	0.94	0.01	0.04	0.96	0.00	0.04
GM	Listvenite	46Z-4-46-51	Magnesite	Matrix	Mg-core spheroid	Core	h	0.95	-	224	0.95	0.00	0.05	0.95	0.00	0.05
GM	Listvenite	46Z-4-46-51	Magnesite	Matrix	Mg-core spheroid	Core	h	0.94	-	75	0.94	0.00	0.06	0.94	0.01	0.06
GM	Listvenite	46Z-4-46-51	Magnesite	Matrix	Mg-core spheroid	Core	h	0.95	25	158	0.94	0.00	0.05	0.95	0.01	0.05
GM	Listvenite	46Z-4-46-51	Magnesite	Matrix	Mg-core spheroid	Core	h	0.95	-	208	0.95	0.00	0.05	0.95	0.00	0.05
GM	Listvenite	46Z-4-46-51	Magnesite	Matrix	Mg-core spheroid	Core	h	0.97	-	n.d.	0.97	0.00	0.03	0.97	0.00	0.03
GM	Listvenite	46Z-4-46-51	Magnesite	Matrix	Mg-core spheroid	Internal growth	h	0.97	-	309	0.97	0.00	0.03	0.97	0.00	0.03
GM	Listvenite	46Z-4-46-51	Magnesite	Matrix	Mg-core spheroid	Internal growth	h	0.96	-	n.d.	0.96	0.00	0.04	0.96	0.00	0.04
GM	Listvenite	46Z-4-46-51	Magnesite	Matrix	Mg-core spheroid	Internal growth	h	0.96	-	558	0.96	0.00	0.04	0.96	0.00	0.04
GM	Listvenite	46Z-4-46-51	Magnesite	Matrix	Mg-core spheroid	Internal growth	h	0.96	-	n.d.	0.95	0.00	0.04	0.96	0.00	0.04
GM	Listvenite	46Z-4-46-51	Magnesite	Matrix	Mg-core spheroid	Internal growth	h	0.96	-	142	0.95	0.00	0.04	0.96	0.01	0.04

GM	Listvenite	46Z-4-46-51	Magnesite	Matrix	Mg-core spheroid	Internal growth	h	0.96	-	149	0.96	0.00	0.04	0.96	0.01	0.04
GM	Listvenite	46Z-4-46-51	Magnesite	Matrix	Mg-core spheroid	Internal growth	h	0.96	-	n.d.	0.96	0.00	0.04	0.96	0.00	0.04
GM	Listvenite	46Z-4-46-51	Magnesite	Matrix	Mg-core spheroid	Internal growth	h	0.96	-	n.d.	0.96	0.00	0.04	0.96	0.00	0.04
GM	Listvenite	46Z-4-46-51	Magnesite	Matrix	Mg-core spheroid	Internal growth	h	0.97	-	350	0.97	0.00	0.03	0.97	0.00	0.03
GM	Listvenite	46Z-4-46-51	Magnesite	Matrix	Mg-core spheroid	Internal growth	h	0.97	-	145	0.97	0.00	0.03	0.97	0.01	0.03
GM	Listvenite	46Z-4-46-51	Magnesite	Matrix	Mg-core spheroid	Internal growth	h	0.97	-	39	0.97	0.00	0.03	0.97	0.02	0.03
GM	Listvenite	46Z-4-46-51	Magnesite	Matrix	Mg-core spheroid	Internal growth	h	0.97	-	40	0.96	0.01	0.03	0.97	0.02	0.03
GM	Listvenite	46Z-4-46-51	Magnesite	Matrix	Mg-core spheroid	Internal growth	h	0.96	-	35	0.95	0.01	0.04	0.96	0.03	0.04
GM	Listvenite	46Z-4-46-51	Magnesite	Matrix	Mg-core spheroid	Rim	h	0.96	-	35	0.95	0.01	0.04	0.96	0.03	0.04
GM	Listvenite	46Z-4-46-51	Magnesite	Matrix	Mg-core spheroid	Rim	h	0.94	-	9	0.92	0.02	0.06	0.94	0.10	0.06
GM	Listvenite	46Z-4-46-51	Magnesite	Matrix	Mg-core spheroid	Rim	i	0.76	-	11	0.75	0.01	0.23	0.77	0.07	0.23
GM	Listvenite	46Z-4-46-51	Magnesite	Matrix	Mg-core spheroid	Rim	i	0.75	-	3	0.73	0.02	0.25	0.75	0.23	0.25
GM	Listvenite	46Z-4-46-51	Magnesite	Matrix	Mg-core spheroid	Internal growth	i	0.87	-	214	0.86	0.01	0.13	0.87	0.00	0.13
GM	Listvenite	46Z-4-46-51	Magnesite	Matrix	Mg-core spheroid	Internal growth	i	0.96	-	8	0.94	0.01	0.04	0.96	0.12	0.04
GM	Listvenite	46Z-4-46-51	Magnesite	Matrix	Mg-core spheroid	Internal growth	i	0.96	-	18	0.96	0.01	0.04	0.96	0.05	0.04
GM	Listvenite	46Z-4-46-51	Magnesite	Matrix	Mg-core spheroid	Internal growth	i	0.97	-	21	0.97	0.00	0.03	0.97	0.05	0.03
GM	Listvenite	46Z-4-46-51	Magnesite	Matrix	Mg-core spheroid	Internal growth	i	0.96	-	51	0.96	0.00	0.03	0.97	0.02	0.03
GM	Listvenite	46Z-4-46-51	Magnesite	Matrix	Mg-core spheroid	Internal growth	i	0.97	-	n.d.	0.97	0.00	0.03	0.97	0.00	0.03
GM	Listvenite	46Z-4-46-51	Magnesite	Matrix	Mg-core spheroid	Internal growth	i	0.97	-	416	0.97	0.00	0.03	0.97	0.00	0.03
GM	Listvenite	46Z-4-46-51	Magnesite	Matrix	Mg-core spheroid	Internal growth	i	0.97	-	81	0.97	0.00	0.03	0.97	0.01	0.03
GM	Listvenite	46Z-4-46-51	Magnesite	Matrix	Mg-core spheroid	Internal growth	i	0.97	-	n.d.	0.97	0.00	0.03	0.97	0.00	0.03
GM	Listvenite	46Z-4-46-51	Magnesite	Matrix	Mg-core spheroid	Core	i	0.96	-	n.d.	0.96	0.00	0.04	0.96	0.00	0.04
GM	Listvenite	46Z-4-46-51	Magnesite	Matrix	Mg-core spheroid	Core	i	0.96	-	61	0.95	0.00	0.04	0.96	0.02	0.04
GM	Listvenite	46Z-4-46-51	Magnesite	Matrix	Mg-core spheroid	Core	i	0.96	-	96	0.95	0.00	0.04	0.96	0.01	0.04
GM	Listvenite	46Z-4-46-51	Magnesite	Matrix	Mg-core spheroid	Core	i	0.96	-	214	0.95	0.00	0.04	0.96	0.00	0.04
GM	Listvenite	46Z-4-46-51	Magnesite	Matrix	Mg-core spheroid	Core	i	0.96	-	133	0.95	0.00	0.04	0.96	0.01	0.04
GM	Listvenite	46Z-4-46-51	Magnesite	Matrix	Mg-core spheroid	Core	i	0.96	-	114	0.95	0.00	0.04	0.96	0.01	0.04
GM	Listvenite	46Z-4-46-51	Magnesite	Matrix	Mg-core spheroid	Internal growth	i	0.95	-	309	0.95	0.00	0.05	0.95	0.00	0.05
GM	Listvenite	46Z-4-46-51	Magnesite	Matrix	Mg-core spheroid	Internal growth	i	0.97	-	111	0.97	0.00	0.03	0.97	0.01	0.03
GM	Listvenite	46Z-4-46-51	Magnesite	Matrix	Mg-core spheroid	Internal growth	i	0.97	-	482	0.97	0.00	0.03	0.97	0.00	0.03
GM	Listvenite	46Z-4-46-51	Magnesite	Matrix	Mg-core spheroid	Internal growth	i	0.97	-	n.d.	0.97	0.00	0.03	0.97	0.00	0.03
GM	Listvenite	46Z-4-46-51	Magnesite	Matrix	Mg-core spheroid	Internal growth	i	0.97	-	756	0.97	0.00	0.03	0.97	0.00	0.03
GM	Listvenite	46Z-4-46-51	Magnesite	Matrix	Mg-core spheroid	Internal growth	i	0.97	-	50	0.97	0.00	0.03	0.97	0.02	0.03
GM	Listvenite	46Z-4-46-51	Magnesite	Matrix	Mg-core spheroid	Internal growth	i	0.97	-	28	0.97	0.00	0.03	0.97	0.03	0.03
GM	Listvenite	46Z-4-46-51	Magnesite	Matrix	Mg-core spheroid	Internal growth	i	0.96	-	13	0.96	0.01	0.04	0.96	0.07	0.04
GM	Listvenite	46Z-4-46-51	Magnesite	Matrix	Mg-core spheroid	Rim	i	0.94	-	6	0.93	0.01	0.06	0.94	0.16	0.06
GM	Listvenite	46Z-4-46-51	Magnesite	Matrix	Mg-core spheroid	Rim	i	0.85	-	8	0.84	0.01	0.15	0.85	0.11	0.15
GM	Listvenite	46Z-4-46-51	Magnesite	Matrix	Euhedral	Core		0.96	-	537	0.94	0.02	0.04	0.96	0.00	0.04
GM	Listvenite	46Z-4-46-51	Magnesite	Matrix	Aggregate			0.82	-	18	0.81	0.01	0.18	0.82	0.05	0.18
GM	Listvenite	46Z-4-46-51	Magnesite	Vein	lc1	Median zone		0.96	-	n.d.	0.94	0.02	0.04	0.96	0.00	0.04
GM	Listvenite	46Z-4-46-51	Magnesite	Vein	lc1	Median zone		0.87	-	12	0.68	0.22	0.10	0.90	0.06	0.10
ISTE	Listvenite	46Z-4-46-51	Magnesite	Vein	lc1	Intermediate		0.87	55	533	0.87	0.01	0.13	0.87	0.00	0.13
ISTE	Listvenite	46Z-4-46-51	Magnesite	Vein	lc1	Intermediate		0.94	35	484	0.94	0.00	0.06	0.94	0.00	0.06
ISTE	Listvenite	46Z-4-46-51	Magnesite	Vein	lc1	Rim		0.97	69	748	0.97	0.00	0.03	0.97	0.00	0.03
GM	Listvenite	46Z-4-46-51	Magnesite	Vein	lc1	Rim		0.87	82	n.d.	0.86	0.01	0.13	0.87	0.00	0.13
GM	Listvenite	46Z-4-46-51	Magnesite	Vein	lc1	Rim		0.88	39	101	0.88	0.00	0.12	0.88	0.01	0.12
GM	Listvenite	46Z-4-46-51	Magnesite	Vein	lc1	Rim	j	0.95	-	20	0.94	0.00	0.05	0.95	0.05	0.05
GM	Listvenite	46Z-4-46-51	Magnesite	Vein	lc1	Rim	j	0.97	-	35	0.96	0.00	0.03	0.97	0.03	0.03
GM	Listvenite	46Z-4-46-51	Magnesite	Vein	lc1	Rim	j	0.94	-	3	0.94	0.00	0.06	0.94	0.32	0.06
GM	Listvenite	46Z-4-46-51	Magnesite	Vein	lc1	Intermediate	j	0.93	-	101	0.93	0.00	0.07	0.93	0.01	0.07
GM	Listvenite	46Z-4-46-51	Magnesite	Vein	lc1	Intermediate	j	0.97	-	54	0.97	0.00	0.03	0.97	0.02	0.03
GM	Listvenite	46Z-4-46-51	Magnesite	Vein	lc1	Intermediate	j	0.97	-	n.d.	0.97	0.00	0.03	0.97	0.00	0.03
GM	Listvenite	46Z-4-46-51	Magnesite	Vein	lc1	Intermediate	j	0.97	-	543	0.97	0.00	0.03	0.97	0.00	0.03

GM	Listvenite	46Z-4-46-51	Magnesite	Vein	lc1	Intermediate	j	0.96	-	647	0.96	0.00	0.04	0.96	0.00	0.04
GM	Listvenite	46Z-4-46-51	Magnesite	Vein	lc1	Intermediate	j	0.96	-	20	0.96	0.00	0.04	0.96	0.05	0.04
GM	Listvenite	46Z-4-46-51	Magnesite	Vein	lc1	Intermediate	j	0.96	-	26	0.96	0.00	0.04	0.96	0.04	0.04
GM	Listvenite	46Z-4-46-51	Magnesite	Vein	lc1	Intermediate	j	0.96	-	309	0.95	0.00	0.04	0.96	0.00	0.04
GM	Listvenite	46Z-4-46-51	Magnesite	Vein	lc1	Intermediate	j	0.96	-	110	0.95	0.00	0.04	0.96	0.01	0.04
GM	Listvenite	46Z-4-46-51	Magnesite	Vein	lc1	Intermediate	j	0.96	-	703	0.96	0.00	0.04	0.96	0.00	0.04
GM	Listvenite	46Z-4-46-51	Magnesite	Vein	lc1	Intermediate	j	0.96	-	n.d.	0.96	0.00	0.04	0.96	0.00	0.04
GM	Listvenite	46Z-4-46-51	Magnesite	Vein	lc1	Intermediate	j	0.94	-	2	0.94	0.00	0.06	0.94	0.54	0.06
GM	Listvenite	46Z-4-46-51	Magnesite	Vein	lc1	Intermediate	j	0.92	-	2	0.92	0.00	0.08	0.92	0.60	0.08
GM	Listvenite	46Z-4-46-51	Magnesite	Vein	lc1	Intermediate	j	0.92	-	29	0.92	0.00	0.08	0.92	0.03	0.08
GM	Listvenite	46Z-4-46-51	Magnesite	Vein	lc1	Intermediate	j	0.95	-	55	0.95	0.00	0.05	0.95	0.02	0.05
GM	Listvenite	46Z-4-46-51	Magnesite	Vein	lc1	Intermediate	j	0.91	38	277	0.91	0.00	0.09	0.91	0.00	0.09
GM	Listvenite	46Z-4-46-51	Magnesite	Vein	lc1	Median zone	j	0.86	-	n.d.	0.85	0.01	0.14	0.86	0.00	0.14
GM	Listvenite	46Z-4-46-51	Magnesite	Vein	lc1	Median zone	j	0.80	-	19	0.80	0.01	0.19	0.81	0.04	0.19
GM	Listvenite	46Z-4-46-51	Magnesite	Vein	lc1	Median zone	j	0.68	93	204	0.68	0.00	0.32	0.68	0.00	0.32
GM	Listvenite	46Z-4-46-51	Magnesite	Vein	lc1	Median zone	j	0.66	72	7	0.66	0.01	0.33	0.67	0.10	0.33
GM	Listvenite	46Z-4-46-51	Magnesite	Vein	lc1	Intermediate	j	0.84	-	73	0.83	0.01	0.16	0.84	0.01	0.16
GM	Listvenite	46Z-4-46-51	Magnesite	Vein	lc1	Intermediate	j	0.86	-	508	0.84	0.02	0.14	0.86	0.00	0.14
GM	Listvenite	46Z-4-46-51	Magnesite	Vein	lc1	Intermediate	j	0.94	-	326	0.94	0.00	0.06	0.94	0.00	0.06
GM	Listvenite	46Z-4-46-51	Magnesite	Vein	lc1	Intermediate	j	0.95	-	45	0.95	0.00	0.05	0.95	0.02	0.05
GM	Listvenite	46Z-4-46-51	Magnesite	Vein	lc1	Intermediate	j	0.94	-	130	0.93	0.00	0.06	0.94	0.01	0.06
GM	Listvenite	46Z-4-46-51	Magnesite	Vein	lc1	Rim	j	0.93	-	23	0.93	0.00	0.07	0.93	0.04	0.07
GM	Listvenite	46Z-4-46-51	Magnesite	Vein	lc1	Rim	j	0.93	-	47	0.93	0.00	0.07	0.93	0.02	0.07
GM	Listvenite	46Z-4-46-51	Magnesite	Vein	lc1	Rim	j	0.97	-	39	0.97	0.00	0.03	0.97	0.02	0.03
GM	Listvenite	46Z-4-46-51	Magnesite	Vein	lc1	Rim	k	0.93	26	3	0.93	0.00	0.07	0.93	0.32	0.07
GM	Listvenite	46Z-4-46-51	Magnesite	Vein	lc1	Rim	k	0.94	-	199	0.93	0.00	0.06	0.94	0.00	0.06
GM	Listvenite	46Z-4-46-51	Magnesite	Vein	lc1	Intermediate	k	0.94	-	586	0.94	0.00	0.06	0.94	0.00	0.06
GM	Listvenite	46Z-4-46-51	Magnesite	Vein	lc1	Intermediate	k	0.96	-	n.d.	0.95	0.00	0.04	0.96	0.00	0.04
GM	Listvenite	46Z-4-46-51	Magnesite	Vein	lc1	Intermediate	k	0.94	-	469	0.94	0.00	0.06	0.94	0.00	0.06
GM	Listvenite	46Z-4-46-51	Magnesite	Vein	lc1	Intermediate	k	0.91	26	n.d.	0.91	0.00	0.09	0.91	0.00	0.09
GM	Listvenite	46Z-4-46-51	Magnesite	Vein	lc1	Median zone	k	0.86	-	78	0.83	0.03	0.14	0.86	0.01	0.14
GM	Listvenite	46Z-4-46-51	Dolomite	Vein	lc1	Median zone	k	0.94	-	n.d.	0.48	0.49	0.03	0.97	0.00	0.03
GM	Listvenite	46Z-4-46-51	Dolomite	Vein	lc1	Median zone	k	0.93	-	n.d.	0.46	0.51	0.03	0.97	0.00	0.03
GM	Listvenite	46Z-4-46-51	Dolomite	Vein	lc1	Median zone	k	0.89	-	59	0.54	0.40	0.07	0.93	0.01	0.07
GM	Listvenite	46Z-4-46-51	Magnesite	Vein	lc1	Intermediate	k	0.95	-	264	0.94	0.00	0.05	0.95	0.00	0.05
GM	Listvenite	46Z-4-46-51	Magnesite	Vein	lc1	Intermediate	k	0.95	-	460	0.95	0.00	0.05	0.95	0.00	0.05
GM	Listvenite	46Z-4-46-51	Magnesite	Vein	lc1	Intermediate	k	0.88	-	161	0.87	0.01	0.12	0.88	0.01	0.12
GM	Listvenite	46Z-4-46-51	Magnesite	Vein	lc1	Intermediate	k	0.90	36	448	0.89	0.01	0.10	0.90	0.00	0.10
GM	Listvenite	46Z-4-46-51	Magnesite	Vein	lc1	Intermediate	k	0.84	-	11	0.83	0.01	0.16	0.84	0.08	0.16
GM	Listvenite	46Z-4-46-51	Magnesite	Vein	lc1	Intermediate	k	0.89	-	138	0.89	0.00	0.11	0.89	0.01	0.11
GM	Listvenite	46Z-4-46-51	Magnesite	Vein	lc1	Intermediate	k	0.90	-	346	0.90	0.00	0.10	0.90	0.00	0.10
GM	Listvenite	46Z-4-46-51	Magnesite	Vein	lc1	Intermediate	k	0.92	35	113	0.91	0.00	0.08	0.92	0.01	0.08
GM	Listvenite	46Z-4-46-51	Magnesite	Vein	lc1	Intermediate	k	0.97	-	701	0.97	0.00	0.03	0.97	0.00	0.03
GM	Listvenite	46Z-4-46-51	Magnesite	Vein	lc1	Intermediate	k	0.95	-	82	0.95	0.00	0.05	0.95	0.01	0.05
GM	Listvenite	46Z-4-46-51	Magnesite	Vein	lc1	Intermediate	k	0.96	-	19	0.95	0.00	0.04	0.96	0.05	0.04
GM	Listvenite	46Z-4-46-51	Magnesite	Vein	lc1	Rim	k	0.95	-	26	0.95	0.00	0.05	0.95	0.04	0.05
GM	Listvenite	46Z-4-46-51	Magnesite	Vein	lc1	Rim	k	0.90	-	9	0.90	0.01	0.10	0.90	0.10	0.10
GM	Listvenite	46Z-4-46-51	Magnesite	Vein	lc1	Rim	l	0.97	-	31	0.97	0.00	0.03	0.97	0.03	0.03
GM	Listvenite	46Z-4-46-51	Magnesite	Vein	lc1	Rim	l	0.96	-	23	0.96	0.00	0.04	0.96	0.04	0.04
GM	Listvenite	46Z-4-46-51	Magnesite	Vein	lc1	Intermediate	l	0.97	-	23	0.96	0.00	0.03	0.97	0.04	0.03
GM	Listvenite	46Z-4-46-51	Magnesite	Vein	lc1	Intermediate	l	0.95	-	52	0.94	0.01	0.05	0.95	0.02	0.05
GM	Listvenite	46Z-4-46-51	Magnesite	Vein	lc1	Intermediate	l	0.97	-	632	0.97	0.00	0.03	0.97	0.00	0.03
GM	Listvenite	46Z-4-46-51	Magnesite	Vein	lc1	Intermediate	l	0.97	-	422	0.97	0.00	0.03	0.97	0.00	0.03

GM	Listvenite	46Z-4-46-51	Magnesite	Vein	lc1	Intermediate	l	0.97	-	n.d.	0.97	0.00	0.03	0.97	0.00	0.03
GM	Listvenite	46Z-4-46-51	Magnesite	Vein	lc1	Intermediate	l	0.96	-	338	0.95	0.00	0.04	0.96	0.00	0.04
GM	Listvenite	46Z-4-46-51	Magnesite	Vein	lc1	Intermediate	l	0.96	-	n.d.	0.95	0.00	0.04	0.96	0.00	0.04
GM	Listvenite	46Z-4-46-51	Magnesite	Vein	lc1	Median zone	l	0.96	-	26	0.95	0.00	0.04	0.96	0.04	0.04
GM	Listvenite	46Z-4-46-51	Magnesite	Vein	lc1	Median zone	l	0.95	-	68	0.95	0.00	0.05	0.95	0.01	0.05
GM	Listvenite	46Z-4-46-51	Magnesite	Vein	lc1	Median zone	l	0.96	-	199	0.95	0.00	0.04	0.96	0.00	0.04
GM	Listvenite	46Z-4-46-51	Magnesite	Vein	lc1	Median zone	l	0.95	-	460	0.95	0.00	0.05	0.95	0.00	0.05
GM	Listvenite	46Z-4-46-51	Magnesite	Vein	lc1	Median zone	l	0.91	30	9	0.90	0.00	0.09	0.91	0.10	0.09
GM	Listvenite	46Z-4-46-51	Magnesite	Vein	lc1	Median zone	l	0.96	-	67	0.96	0.00	0.04	0.96	0.01	0.04
GM	Listvenite	46Z-4-46-51	Magnesite	Vein	lc1	Median zone	l	0.96	-	149	0.96	0.00	0.04	0.96	0.01	0.04
GM	Listvenite	46Z-4-46-51	Magnesite	Vein	lc1	Median zone	l	0.96	-	56	0.96	0.00	0.04	0.96	0.02	0.04
GM	Listvenite	46Z-4-46-51	Magnesite	Vein	lc1	Intermediate	l	0.96	-	110	0.95	0.00	0.04	0.96	0.01	0.04
GM	Listvenite	46Z-4-46-51	Magnesite	Vein	lc1	Intermediate	l	0.96	-	86	0.96	0.00	0.04	0.96	0.01	0.04
GM	Listvenite	46Z-4-46-51	Magnesite	Vein	lc1	Intermediate	l	0.96	-	447	0.96	0.00	0.04	0.96	0.00	0.04
GM	Listvenite	46Z-4-46-51	Magnesite	Vein	lc1	Intermediate	l	0.97	-	n.d.	0.97	0.00	0.03	0.97	0.00	0.03
GM	Listvenite	46Z-4-46-51	Magnesite	Vein	lc1	Intermediate	l	0.97	-	n.d.	0.97	0.00	0.03	0.97	0.00	0.03
GM	Listvenite	46Z-4-46-51	Magnesite	Vein	lc1	Intermediate	l	0.94	-	94	0.94	0.00	0.06	0.94	0.01	0.06
GM	Listvenite	46Z-4-46-51	Magnesite	Vein	lc1	Intermediate	l	0.96	-	40	0.96	0.00	0.04	0.96	0.02	0.04
GM	Listvenite	46Z-4-46-51	Magnesite	Vein	lc1	Intermediate	l	0.97	-	22	0.96	0.00	0.03	0.97	0.04	0.03
GM	Listvenite	46Z-4-46-51	Magnesite	Vein	lc1	Intermediate	l	0.95	-	21	0.95	0.00	0.05	0.95	0.04	0.05
GM	Listvenite	46Z-4-46-51	Magnesite	Vein	lc1	Intermediate	l	0.96	-	11	0.96	0.00	0.04	0.96	0.09	0.04
GM	Listvenite	46Z-4-46-51	Magnesite	Vein	lc1	Rim	l	0.96	-	17	0.96	0.00	0.04	0.96	0.06	0.04
GM	Listvenite	46Z-4-46-51	Magnesite	Vein	lc1	Rim	l	0.94	-	15	0.94	0.00	0.06	0.94	0.06	0.06
GM	Listvenite	46Z-4-46-51	Magnesite	Vein	lc1	Rim	m	0.97	-	n.d.	0.97	0.00	0.03	0.97	0.00	0.03
GM	Listvenite	46Z-4-46-51	Magnesite	Vein	lc1	Rim	m	0.96	-	668	0.96	0.00	0.04	0.96	0.00	0.04
GM	Listvenite	46Z-4-46-51	Magnesite	Vein	lc1	Intermediate	m	0.96	-	386	0.95	0.00	0.04	0.96	0.00	0.04
GM	Listvenite	46Z-4-46-51	Magnesite	Vein	lc1	Intermediate	m	0.96	-	n.d.	0.95	0.00	0.04	0.96	0.00	0.04
GM	Listvenite	46Z-4-46-51	Magnesite	Vein	lc1	Intermediate	m	0.96	-	199	0.95	0.00	0.04	0.96	0.00	0.04
GM	Listvenite	46Z-4-46-51	Magnesite	Vein	lc1	Intermediate	m	0.96	-	256	0.96	0.00	0.04	0.96	0.00	0.04
GM	Listvenite	46Z-4-46-51	Magnesite	Vein	lc1	Intermediate	m	0.94	-	64	0.93	0.00	0.06	0.94	0.01	0.06
GM	Listvenite	46Z-4-46-51	Magnesite	Vein	lc1	Intermediate	m	0.96	-	117	0.95	0.00	0.04	0.96	0.01	0.04
GM	Listvenite	46Z-4-46-51	Magnesite	Vein	lc1	Intermediate	m	0.96	-	140	0.95	0.00	0.04	0.96	0.01	0.04
GM	Listvenite	46Z-4-46-51	Magnesite	Vein	lc1	Intermediate	m	0.96	-	351	0.95	0.00	0.04	0.96	0.00	0.04
GM	Listvenite	46Z-4-46-51	Magnesite	Vein	lc1	Intermediate	m	0.96	-	4	0.96	0.00	0.04	0.96	0.25	0.04
GM	Listvenite	46Z-4-46-51	Magnesite	Vein	lc1	Intermediate	m	0.95	-	26	0.95	0.00	0.05	0.95	0.04	0.05
GM	Listvenite	46Z-4-46-51	Magnesite	Vein	lc1	Intermediate	m	0.95	-	43	0.95	0.01	0.05	0.95	0.02	0.05
GM	Listvenite	46Z-4-46-51	Magnesite	Vein	lc1	Intermediate	m	0.95	-	24	0.95	0.01	0.05	0.95	0.04	0.05
GM	Listvenite	46Z-4-46-51	Magnesite	Vein	lc1	Intermediate	m	0.95	-	64	0.95	0.01	0.05	0.95	0.01	0.05
GM	Listvenite	46Z-4-46-51	Magnesite	Vein	lc1	Intermediate	m	0.96	-	735	0.96	0.00	0.04	0.96	0.00	0.04
GM	Listvenite	46Z-4-46-51	Magnesite	Vein	lc1	Intermediate	m	0.90	-	4	0.90	0.00	0.10	0.90	0.21	0.10
GM	Listvenite	46Z-4-46-51	Magnesite	Vein	lc1	Median zone	m	0.85	-	439	0.84	0.02	0.14	0.86	0.00	0.14
GM	Listvenite	46Z-4-46-51	Magnesite	Vein	lc1	Median zone	m	0.86	-	n.d.	0.84	0.01	0.14	0.86	0.00	0.14
GM	Listvenite	46Z-4-46-51	Dolomite	Vein	lc1	Median zone	m	0.88	-	189	0.58	0.35	0.08	0.92	0.00	0.08
GM	Listvenite	46Z-4-46-51	Dolomite	Vein	lc1	Median zone	m	0.93	-	277	0.46	0.50	0.03	0.97	0.00	0.03
GM	Listvenite	46Z-4-46-51	Dolomite	Vein	lc1	Median zone	m	0.94	-	n.d.	0.47	0.50	0.03	0.97	0.00	0.03
GM	Listvenite	46Z-4-46-51	Magnesite	Vein	lc1	Median zone	m	0.85	-	211	0.76	0.11	0.13	0.87	0.00	0.13
GM	Listvenite	46Z-4-46-51	Magnesite	Vein	lc1	Median zone	m	0.89	43	422	0.89	0.00	0.11	0.89	0.00	0.11
GM	Listvenite	46Z-4-46-51	Magnesite	Vein	lc1	Median zone	m	0.92	-	121	0.92	0.00	0.08	0.92	0.01	0.08
GM	Listvenite	46Z-4-46-51	Magnesite	Vein	lc1	Intermediate	m	0.93	-	6	0.93	0.00	0.07	0.93	0.16	0.07
GM	Listvenite	46Z-4-46-51	Magnesite	Vein	lc1	Intermediate	m	0.96	-	255	0.96	0.00	0.04	0.96	0.00	0.04
GM	Listvenite	46Z-4-46-51	Magnesite	Vein	lc1	Intermediate	m	0.95	-	94	0.95	0.00	0.05	0.95	0.01	0.05
GM	Listvenite	46Z-4-46-51	Magnesite	Vein	lc1	Intermediate	m	0.96	-	146	0.95	0.01	0.04	0.96	0.01	0.04
GM	Listvenite	46Z-4-46-51	Magnesite	Vein	lc1	Intermediate	m	0.95	-	59	0.95	0.01	0.05	0.95	0.02	0.05

GM	Listvenite	46Z-4-46-51	Magnesite	Vein	lc1	Intermediate	m	0.95	-	113	0.95	0.00	0.05	0.95	0.01	0.05
GM	Listvenite	46Z-4-46-51	Magnesite	Vein	lc1	Intermediate	m	0.95	-	85	0.95	0.01	0.05	0.95	0.01	0.05
GM	Listvenite	46Z-4-46-51	Magnesite	Vein	lc1	Intermediate	m	0.94	-	68	0.94	0.01	0.06	0.94	0.01	0.06
GM	Listvenite	46Z-4-46-51	Magnesite	Vein	lc1	Intermediate	m	0.91	-	189	0.90	0.01	0.09	0.91	0.00	0.09
GM	Listvenite	46Z-4-46-51	Magnesite	Vein	lc1	Intermediate	m	0.94	-	256	0.93	0.01	0.06	0.94	0.00	0.06
GM	Listvenite	46Z-4-46-51	Magnesite	Vein	lc1	Intermediate	m	0.94	-	72	0.93	0.00	0.06	0.94	0.01	0.06
GM	Listvenite	46Z-4-46-51	Magnesite	Vein	lc1	Rim	m	0.91	-	22	0.90	0.00	0.09	0.91	0.04	0.09
GM	Listvenite	46Z-4-46-51	Magnesite	Vein	lc1	Rim	m	0.95	-	498	0.95	0.00	0.05	0.95	0.00	0.05
GM	Listvenite	46Z-4-46-51	Magnesite	Vein	lc2	Median zone		0.93	-	59	0.92	0.00	0.07	0.93	0.02	0.07
ISTE	Listvenite	46Z-4-46-51	Magnesite	Vein	lq4	Rim		0.92	50	887	0.91	0.02	0.08	0.92	0.00	0.08
ISTE	Listvenite	46Z-4-46-51	Magnesite	Vein	lq4	Rim		0.92	53	295	0.90	0.03	0.08	0.92	0.00	0.08
ISTE	Listvenite	48Z-1-6-11	Magnesite	Matrix	Mg-core spheroid	Core		0.99	13	1440	0.98	0.00	0.01	0.99	0.00	0.01
ISTE	Listvenite	48Z-1-6-11	Magnesite	Matrix	Mg-core spheroid	Core		0.98	21	4271	0.97	0.01	0.02	0.98	0.00	0.02
ISTE	Listvenite	48Z-1-6-11	Magnesite	Matrix	Mg-core spheroid	Core		0.98	25	125	0.97	0.01	0.02	0.98	0.01	0.02
ISTE	Listvenite	48Z-1-6-11	Magnesite	Matrix	Mg-core spheroid	Core		0.91	14	19	0.91	0.00	0.09	0.91	0.05	0.09
ISTE	Listvenite	48Z-1-6-11	Magnesite	Matrix	Mg-core spheroid	Internal growth		0.73	175	234	0.73	0.01	0.27	0.73	0.00	0.27
ISTE	Listvenite	48Z-1-6-11	Magnesite	Matrix	Mg-core spheroid	Rim		0.96	-	3937	0.96	0.00	0.04	0.96	0.00	0.04
ISTE	Listvenite	48Z-1-6-11	Magnesite	Matrix	Aggregate			0.98	45	417	0.97	0.00	0.02	0.98	0.00	0.02
ISTE	Listvenite	48Z-1-6-11	Magnesite	Vein	lss0	Median zone		0.83	126	6	0.82	0.00	0.17	0.83	0.14	0.17
ISTE	Listvenite	48Z-1-6-11	Magnesite	Vein	lss0	Median zone		0.67	177	93	0.67	0.01	0.33	0.67	0.01	0.33
ISTE	Listvenite	48Z-1-6-11	Magnesite	Vein	lss0	Rim		0.97	-	1997	0.97	0.00	0.03	0.97	0.00	0.03
ISTE	Listvenite	48Z-1-6-11	Magnesite	Vein	lss0	Rim		0.97	-	1030	0.97	0.00	0.03	0.97	0.00	0.03
ISTE	Listvenite	48Z-1-6-11	Magnesite	Vein	lss0	Rim		0.96	-	1894	0.96	0.00	0.04	0.96	0.00	0.04
ISTE	Listvenite	48Z-1-6-11	Magnesite	Vein	lss2	Median zone		0.98	2	140	0.97	0.00	0.02	0.98	0.01	0.02
ISTE	Listvenite	48Z-1-6-11	Magnesite	Vein	lss2	Median zone		0.98	3	533	0.97	0.00	0.02	0.98	0.00	0.02
ISTE	Listvenite	48Z-1-6-11	Magnesite	Vein	lss2	Median zone		0.98	3	209	0.97	0.00	0.02	0.98	0.00	0.02
ISTE	Listvenite	48Z-1-6-11	Magnesite	Vein	lss2	Rim		0.87	64	11	0.87	0.00	0.13	0.87	0.08	0.13
ISTE	Listvenite	48Z-1-6-11	Magnesite	Vein	lc1	Median zone		0.91	109	n.d.	0.91	0.00	0.09	0.91	0.00	0.09
ISTE	Listvenite	48Z-1-6-11	Magnesite	Vein	lc1	Median zone		0.95	122	n.d.	0.95	0.00	0.05	0.95	0.00	0.05
ISTE	Listvenite	48Z-1-6-11	Magnesite	Vein	lc1	Median zone		0.91	121	2881	0.90	0.01	0.09	0.91	0.00	0.09
ISTE	Listvenite	48Z-1-6-11	Magnesite	Vein	lc1	Median zone		0.58	331	22	0.57	0.01	0.42	0.58	0.03	0.42
ISTE	Listvenite	48Z-1-6-11	Magnesite	Vein	lc1	Median zone		0.77	111	150	0.77	0.00	0.23	0.77	0.01	0.23
ISTE	Listvenite	48Z-1-6-11	Magnesite	Vein	lc1	Intermediate		0.64	146	1131	0.64	0.01	0.36	0.64	0.00	0.36
ISTE	Listvenite	48Z-1-6-11	Magnesite	Vein	lc1	Intermediate		0.68	202	452	0.67	0.01	0.32	0.68	0.00	0.32
ISTE	Listvenite	48Z-1-6-11	Magnesite	Vein	lc1	Rim		0.93	48	51	0.93	0.00	0.07	0.93	0.02	0.07
GM	Listvenite	50Z-1-75-80	Magnesite	Matrix	Mg-core spheroid	Core		0.96	-	n.d.	0.96	0.00	0.04	0.96	0.00	0.04
ISTE	Listvenite	50Z-1-75-80	Magnesite	Matrix	Fe-core spheroid	Core		0.85	60	35	0.85	0.00	0.15	0.85	0.02	0.15
ISTE	Listvenite	50Z-1-75-80	Magnesite	Matrix	Fe-core spheroid	Core		0.71	107	16	0.70	0.01	0.29	0.71	0.04	0.29
ISTE	Listvenite	50Z-1-75-80	Magnesite	Matrix	Fe-core spheroid	Core		0.69	113	21	0.68	0.01	0.31	0.69	0.03	0.31
ISTE	Listvenite	50Z-1-75-80	Magnesite	Matrix	Fe-core spheroid	Internal growth		0.73	96	84	0.73	0.00	0.27	0.73	0.01	0.27
ISTE	Listvenite	50Z-1-75-80	Magnesite	Matrix	Fe-core spheroid	Internal growth		0.86	45	176	0.86	0.01	0.13	0.87	0.00	0.13
ISTE	Listvenite	50Z-1-75-80	Magnesite	Matrix	Fe-core spheroid	Internal growth		0.97	-	958	0.96	0.00	0.03	0.97	0.00	0.03
ISTE	Listvenite	50Z-1-75-80	Magnesite	Matrix	Fe-core spheroid	Rim		0.96	-	178	0.96	0.00	0.04	0.96	0.01	0.04
ISTE	Listvenite	50Z-1-75-80	Magnesite	Matrix	Fe-core spheroid	Rim		0.97	-	176	0.96	0.00	0.03	0.97	0.01	0.03
ISTE	Listvenite	50Z-1-75-80	Magnesite	Vein	lss2	Median zone		0.96	48	804	0.96	0.00	0.04	0.96	0.00	0.04
ISTE	Listvenite	50Z-1-75-80	Magnesite	Vein	lss2	Median zone		0.97	35	434	0.96	0.01	0.03	0.97	0.00	0.03
ISTE	Listvenite	50Z-1-75-80	Magnesite	Vein	lss2	Rim		0.97	-	361	0.96	0.00	0.03	0.97	0.00	0.03
ISTE	Listvenite	50Z-1-75-80	Magnesite	Vein	lss2	Median zone		0.98	19	1688	0.98	0.00	0.02	0.98	0.00	0.02
ISTE	Listvenite	50Z-1-75-80	Magnesite	Vein	lss2	Rim		0.91	59	298	0.91	0.00	0.09	0.91	0.00	0.09
ISTE	Listvenite	50Z-1-75-80	Magnesite	Matrix	Aggregate			0.97	36	593	0.97	0.00	0.03	0.97	0.00	0.03
ISTE	Listvenite	50Z-1-75-80	Magnesite	Vein	lss2	Median zone		0.98	20	367	0.97	0.01	0.02	0.98	0.00	0.02
ISTE	Listvenite	50Z-1-75-80	Magnesite	Vein	lss2	Median zone		0.98	1	102	0.97	0.00	0.02	0.98	0.01	0.02
GM	Fuchsite-bearing listvenite	53Z-2-72-77	Magnesite	Matrix	Mg-core spheroid	Core		0.95	-	n.d.	0.95	0.00	0.05	0.95	0.00	0.05

GM	Fuchsite-bearing listvenite	53Z-2-72-77	Magnesite	Matrix	Mg-core spheroid	Core	0.94	-	n.d.	0.93	0.01	0.06	0.94	0.00	0.06
GM	Fuchsite-bearing listvenite	53Z-2-72-77	Magnesite	Matrix	Mg-core spheroid	Core	0.95	-	n.d.	0.94	0.01	0.05	0.95	0.00	0.05
GM	Fuchsite-bearing listvenite	53Z-2-72-77	Magnesite	Matrix	Mg-core spheroid	Core	0.94	-	97	0.93	0.01	0.06	0.94	0.01	0.06
GM	Fuchsite-bearing listvenite	53Z-2-72-77	Magnesite	Matrix	Mg-core spheroid	Internal growth	0.95	-	n.d.	0.93	0.02	0.05	0.95	0.00	0.05
GM	Fuchsite-bearing listvenite	53Z-2-72-77	Magnesite	Matrix	Mg-core spheroid	Internal growth	0.95	-	n.d.	0.94	0.01	0.05	0.95	0.00	0.05
GM	Fuchsite-bearing listvenite	53Z-2-72-77	Magnesite	Matrix	Mg-core spheroid	Internal growth	0.94	-	n.d.	0.93	0.01	0.05	0.95	0.00	0.05
GM	Fuchsite-bearing listvenite	53Z-2-72-77	Magnesite	Matrix	Mg-core spheroid	Internal growth	0.95	-	n.d.	0.94	0.01	0.05	0.95	0.00	0.05
GM	Fuchsite-bearing listvenite	53Z-2-72-77	Magnesite	Matrix	Mg-core spheroid	Internal growth	0.95	-	434	0.94	0.01	0.05	0.95	0.00	0.05
GM	Fuchsite-bearing listvenite	53Z-2-72-77	Magnesite	Matrix	Mg-core spheroid	Internal growth	0.94	42	n.d.	0.94	0.00	0.06	0.94	0.00	0.06
GM	Fuchsite-bearing listvenite	53Z-2-72-77	Magnesite	Matrix	Mg-core spheroid	Rim	0.95	-	n.d.	0.94	0.00	0.05	0.95	0.00	0.05
GM	Fuchsite-bearing listvenite	53Z-2-72-77	Magnesite	Matrix	Mg-core spheroid	Rim	0.94	-	n.d.	0.94	0.00	0.06	0.94	0.00	0.06
GM	Fuchsite-bearing listvenite	53Z-2-72-77	Magnesite	Matrix	Mg-core spheroid	Rim	0.95	-	n.d.	0.95	0.01	0.05	0.95	0.00	0.05
GM	Fuchsite-bearing listvenite	53Z-2-72-77	Magnesite	Matrix	Mg-core spheroid	Rim	0.95	-	n.d.	0.95	0.00	0.05	0.95	0.00	0.05
GM	Fuchsite-bearing listvenite	53Z-2-72-77	Magnesite	Matrix	Aggregate	Core	0.90	8	55	0.90	0.00	0.10	0.90	0.02	0.10
GM	Fuchsite-bearing listvenite	53Z-2-72-77	Magnesite	Matrix	Aggregate	Core	0.94	44	60	0.94	0.00	0.06	0.94	0.02	0.06
GM	Fuchsite-bearing listvenite	53Z-2-72-77	Magnesite	Matrix	Aggregate	Core	0.94	-	684	0.94	0.00	0.06	0.94	0.00	0.06
GM	Fuchsite-bearing listvenite	53Z-2-72-77	Magnesite	Matrix	Aggregate	Intermediate	0.95	-	10	0.94	0.00	0.05	0.95	0.10	0.05
GM	Fuchsite-bearing listvenite	53Z-2-72-77	Magnesite	Matrix	Aggregate	Rim	0.94	-	33	0.94	0.00	0.06	0.94	0.03	0.06
GM	Fuchsite-bearing listvenite	53Z-2-72-77	Magnesite	Vein	lc1	Median zone	0.93	-	576	0.92	0.01	0.07	0.93	0.00	0.07
GM	Fuchsite-bearing listvenite	53Z-2-72-77	Magnesite	Vein	lc1	Median zone	0.93	39	n.d.	0.93	0.00	0.07	0.93	0.00	0.07
GM	Fuchsite-bearing listvenite	53Z-2-72-77	Magnesite	Vein	lc1	Median zone	0.90	24	138	0.90	0.00	0.10	0.90	0.01	0.10
GM	Fuchsite-bearing listvenite	53Z-2-72-77	Magnesite	Vein	lc1	Intermediate	0.94	14	97	0.94	0.00	0.06	0.94	0.01	0.06
GM	Fuchsite-bearing listvenite	53Z-2-72-77	Magnesite	Vein	lc1	Intermediate	0.94	-	n.d.	0.94	0.00	0.06	0.94	0.00	0.06
GM	Fuchsite-bearing listvenite	53Z-2-72-77	Magnesite	Vein	lc1	Rim	0.95	-	n.d.	0.94	0.01	0.05	0.95	0.00	0.05
GM	Fuchsite-bearing listvenite	53Z-2-72-77	Magnesite	Vein	lc5-6?	Median zone	0.96	-	n.d.	0.96	0.00	0.04	0.96	0.00	0.04
GM	Fuchsite-bearing listvenite	53Z-2-72-77	Magnesite	Vein	lc5-6?	Median zone	0.96	-	n.d.	0.95	0.01	0.04	0.96	0.00	0.04
ISTE	Fuchsite-bearing listvenite	53Z-4-35-40	Magnesite	Matrix	Aggregate		0.90	54	95	0.90	0.00	0.10	0.90	0.01	0.10
ISTE	Fuchsite-bearing listvenite	53Z-4-35-40	Magnesite	Matrix	Aggregate		0.87	59	338	0.87	0.00	0.13	0.87	0.00	0.13
ISTE	Fuchsite-bearing listvenite	53Z-4-35-40	Magnesite	Matrix	Aggregate		0.86	57	511	0.86	0.00	0.14	0.86	0.00	0.14
ISTE	Fuchsite-bearing listvenite	53Z-4-35-40	Magnesite	Matrix	Aggregate		0.85	54	313	0.85	0.00	0.15	0.85	0.00	0.15
ISTE	Fuchsite-bearing listvenite	53Z-4-35-40	Magnesite	Matrix	Aggregate		0.92	-	66	0.91	0.01	0.08	0.92	0.01	0.08
ISTE	Fuchsite-bearing listvenite	53Z-4-35-40	Magnesite	Matrix	Aggregate		0.91	52	1195	0.91	0.00	0.09	0.91	0.00	0.09
ISTE	Fuchsite-bearing listvenite	53Z-4-35-40	Magnesite	Vein	lss0	Median zone	0.87	18	2935	0.87	0.00	0.13	0.87	0.00	0.13
ISTE	Fuchsite-bearing listvenite	53Z-4-35-40	Magnesite	Vein	lss0	Rim	0.89	42	55	0.89	0.01	0.10	0.90	0.02	0.10
ISTE	Fuchsite-bearing listvenite	55Z-1-55-60	Dolomite	Vein	lc1	Median zone	0.92	34	n.d.	0.60	0.35	0.05	0.95	0.00	0.05
ISTE	Fuchsite-bearing listvenite	55Z-1-55-60	Magnesite	Matrix	Mg-core spheroid	Core	0.92	23	349	0.92	0.01	0.08	0.92	0.00	0.08
ISTE	Fuchsite-bearing listvenite	55Z-1-55-60	Magnesite	Matrix	Mg-core spheroid	Core	0.97	56	71	0.97	0.00	0.03	0.97	0.01	0.03
ISTE	Fuchsite-bearing listvenite	55Z-1-55-60	Magnesite	Matrix	Mg-core spheroid	Core	0.97	51	486	0.96	0.01	0.03	0.97	0.00	0.03
ISTE	Fuchsite-bearing listvenite	55Z-1-55-60	Magnesite	Matrix	Euhedral	Core	0.95	34	2681	0.94	0.01	0.05	0.95	0.00	0.05
ISTE	Fuchsite-bearing listvenite	55Z-1-55-60	Magnesite	Matrix	Euhedral	Core	0.95	31	3654	0.94	0.02	0.05	0.95	0.00	0.05
ISTE	Fuchsite-bearing listvenite	55Z-1-55-60	Magnesite	Matrix	Aggregate		0.94	27	3658	0.93	0.01	0.06	0.94	0.00	0.06
ISTE	Fuchsite-bearing listvenite	55Z-1-55-60	Magnesite	Matrix	Aggregate		0.94	30	262	0.93	0.01	0.06	0.94	0.00	0.06
ISTE	Fuchsite-bearing listvenite	55Z-1-55-60	Magnesite	Matrix	Aggregate		0.94	31	3815	0.94	0.01	0.06	0.94	0.00	0.06
ISTE	Fuchsite-bearing listvenite	55Z-1-55-60	Magnesite	Matrix	Aggregate		0.95	26	30	0.94	0.01	0.05	0.95	0.03	0.05
ISTE	Fuchsite-bearing listvenite	55Z-1-55-60	Magnesite	Matrix	Aggregate		0.95	27	n.d.	0.94	0.01	0.05	0.95	0.00	0.05
ISTE	Fuchsite-bearing listvenite	55Z-1-55-60	Magnesite	Matrix	Aggregate		0.94	29	499	0.94	0.00	0.06	0.94	0.00	0.06
ISTE	Fuchsite-bearing listvenite	55Z-1-55-60	Magnesite	Matrix	Aggregate		0.86	31	13	0.85	0.01	0.14	0.86	0.07	0.14
ISTE	Fuchsite-bearing listvenite	55Z-1-55-60	Magnesite	Vein	lss0	Median zone	0.84	39	117	0.84	0.00	0.15	0.85	0.01	0.15
ISTE	Fuchsite-bearing listvenite	55Z-1-55-60	Magnesite	Vein	lss0	Intermediate	0.88	22	n.d.	0.88	0.00	0.12	0.88	0.00	0.12
ISTE	Fuchsite-bearing listvenite	55Z-1-55-60	Magnesite	Vein	lss0	Rim	0.94	29	3148	0.93	0.01	0.06	0.94	0.00	0.06
ISTE	Fuchsite-bearing listvenite	55Z-1-55-60	Magnesite	Vein	lc1	Median zone	0.90	60	3176	0.90	0.00	0.10	0.90	0.00	0.10
ISTE	Fuchsite-bearing listvenite	55Z-1-55-60	Magnesite	Vein	lc1	Median zone	0.94	27	91	0.93	0.01	0.06	0.94	0.01	0.06
ISTE	Fuchsite-bearing listvenite	55Z-1-55-60	Magnesite	Vein	lc1	Median zone	0.80	110	347	0.79	0.01	0.20	0.80	0.00	0.20

ISTE	Fuchsite-bearing listvenite	55Z-1-55-60	Magnesite	Vein	lc1	Intermediate	0.87	24	1810	0.87	0.01	0.13	0.87	0.00	0.13
ISTE	Fuchsite-bearing listvenite	55Z-1-55-60	Magnesite	Vein	lc1	Intermediate	0.81	55	2304	0.80	0.01	0.19	0.81	0.00	0.19
ISTE	Fuchsite-bearing listvenite	55Z-1-55-60	Magnesite	Vein	lc1	Intermediate	0.93	38	307	0.92	0.00	0.07	0.93	0.00	0.07
ISTE	Fuchsite-bearing listvenite	55Z-1-55-60	Magnesite	Vein	lc1	Intermediate	0.80	61	176	0.80	0.00	0.20	0.80	0.00	0.20
ISTE	Fuchsite-bearing listvenite	55Z-1-55-60	Magnesite	Vein	lc1	Intermediate	0.94	51	280	0.93	0.01	0.06	0.94	0.00	0.06
ISTE	Fuchsite-bearing listvenite	55Z-1-55-60	Magnesite	Vein	lc1	Intermediate	0.81	62	23	0.80	0.01	0.19	0.81	0.03	0.19
ISTE	Fuchsite-bearing listvenite	55Z-1-55-60	Magnesite	Vein	lc1	Rim	0.89	22	1968	0.89	0.00	0.10	0.90	0.00	0.10
ISTE	Fuchsite-bearing listvenite	55Z-1-55-60	Magnesite	Vein	lc1	Rim	0.91	31	1169	0.91	0.01	0.09	0.91	0.00	0.09
ISTE	Fuchsite-bearing listvenite	55Z-1-55-60	Magnesite	Vein	lc1	Rim	0.97	53	1275	0.96	0.00	0.03	0.97	0.00	0.03
ISTE	Fuchsite-bearing listvenite	55Z-1-55-60	Magnesite	Vein	lc1	Rim	0.94	50	5090	0.94	0.00	0.06	0.94	0.00	0.06
ISTE	Fuchsite-bearing listvenite	55Z-1-55-60	Magnesite	Vein	lc1	Overgrowth	0.93	32	568	0.92	0.01	0.07	0.93	0.00	0.07
ISTE	Fuchsite-bearing listvenite	55Z-1-55-60	Dolomite	Vein	lc6	Median zone	0.93	30	n.d.	0.47	0.49	0.04	0.96	0.00	0.04
ISTE	Fuchsite-bearing listvenite	55Z-1-55-60	Dolomite	Vein	lc6	Median zone	0.89	38	n.d.	0.45	0.49	0.06	0.94	0.00	0.06
GM	Fuchsite-bearing listvenite	60Z-1-32-37	Dolomite	Matrix	Spheroid	Core	0.90	19	335	0.46	0.49	0.05	0.95	0.00	0.05
GM	Fuchsite-bearing listvenite	60Z-1-32-37	Dolomite	Matrix	Spheroid	Core	0.94	-	11	0.48	0.49	0.03	0.97	0.04	0.03
GM	Fuchsite-bearing listvenite	60Z-1-32-37	Dolomite	Matrix	Spheroid	Core	0.92	25	15	0.53	0.43	0.05	0.95	0.03	0.05
GM	Fuchsite-bearing listvenite	60Z-1-32-37	Dolomite	Matrix	Spheroid	Rim	0.93	-	n.d.	0.46	0.51	0.03	0.97	0.00	0.03
ISTE	Fuchsite-bearing listvenite	60Z-1-32-37	Dolomite	Vein	lc6	Median zone	0.95	18	n.d.	0.50	0.47	0.03	0.97	0.00	0.03
GM	Fuchsite-bearing listvenite	60Z-1-32-37	Dolomite	Vein	lc6	Median zone	0.96	12	n.d.	0.52	0.46	0.02	0.98	0.00	0.02
GM	Fuchsite-bearing listvenite	60Z-1-32-37	Magnesite	Matrix	Mg-core spheroid	Core	0.93	-	99	0.92	0.01	0.07	0.93	0.01	0.07
GM	Fuchsite-bearing listvenite	60Z-1-32-37	Magnesite	Matrix	Mg-core spheroid	Core	0.93	-	415	0.93	0.00	0.07	0.93	0.00	0.07
GM	Fuchsite-bearing listvenite	60Z-1-32-37	Magnesite	Matrix	Mg-core spheroid	Core	0.92	-	85	0.92	0.00	0.08	0.92	0.01	0.08
ISTE	Fuchsite-bearing listvenite	60Z-1-32-37	Magnesite	Matrix	Mg-core spheroid	Core	0.93	59	36	0.92	0.01	0.07	0.93	0.03	0.07
ISTE	Fuchsite-bearing listvenite	60Z-1-32-37	Magnesite	Matrix	Mg-core spheroid	Core	0.94	57	11	0.94	0.00	0.06	0.94	0.08	0.06
ISTE	Fuchsite-bearing listvenite	60Z-1-32-37	Magnesite	Matrix	Mg-core spheroid	Core	0.96	60	18	0.95	0.00	0.04	0.96	0.05	0.04
GM	Fuchsite-bearing listvenite	60Z-1-32-37	Magnesite	Matrix	Mg-core spheroid	Core	0.95	-	18	0.95	0.01	0.05	0.95	0.05	0.05
GM	Fuchsite-bearing listvenite	60Z-1-32-37	Magnesite	Matrix	Mg-core spheroid	Core	0.93	-	18	0.93	0.01	0.07	0.93	0.05	0.07
GM	Fuchsite-bearing listvenite	60Z-1-32-37	Magnesite	Matrix	Mg-core spheroid	Core	0.95	-	10	0.95	0.00	0.05	0.95	0.09	0.05
GM	Fuchsite-bearing listvenite	60Z-1-32-37	Magnesite	Matrix	Mg-core spheroid	Core	0.96	-	18	0.96	0.00	0.04	0.96	0.05	0.04
GM	Fuchsite-bearing listvenite	60Z-1-32-37	Magnesite	Matrix	Mg-core spheroid	Core	0.96	-	8	0.95	0.00	0.04	0.96	0.12	0.04
GM	Fuchsite-bearing listvenite	60Z-1-32-37	Magnesite	Matrix	Mg-core spheroid	Internal growth	0.94	-	28	0.93	0.01	0.06	0.94	0.03	0.06
GM	Fuchsite-bearing listvenite	60Z-1-32-37	Magnesite	Matrix	Mg-core spheroid	Internal growth	0.95	-	16	0.95	0.00	0.05	0.95	0.06	0.05
GM	Fuchsite-bearing listvenite	60Z-1-32-37	Magnesite	Matrix	Mg-core spheroid	Internal growth	0.94	-	9	0.94	0.01	0.06	0.94	0.11	0.06
GM	Fuchsite-bearing listvenite	60Z-1-32-37	Magnesite	Matrix	Mg-core spheroid	Rim	0.96	-	7	0.95	0.00	0.04	0.96	0.13	0.04
GM	Fuchsite-bearing listvenite	60Z-1-32-37	Magnesite	Matrix	Mg-core spheroid	Rim	0.90	-	39	0.78	0.13	0.09	0.91	0.02	0.09
GM	Fuchsite-bearing listvenite	60Z-1-32-37	Magnesite	Matrix	Mg-core spheroid	Rim	0.96	-	6	0.95	0.00	0.04	0.96	0.16	0.04
GM	Fuchsite-bearing listvenite	60Z-1-32-37	Magnesite	Matrix	Mg-core spheroid	Rim	0.95	-	20	0.92	0.03	0.05	0.95	0.05	0.05
GM	Fuchsite-bearing listvenite	60Z-1-32-37	Magnesite	Matrix	Mg-core spheroid	Rim	0.95	-	13	0.94	0.01	0.05	0.95	0.07	0.05
ISTE	Fuchsite-bearing listvenite	60Z-1-32-37	Magnesite	Vein	lc2		0.97	41	n.d.	0.97	0.00	0.03	0.97	0.00	0.03
ISTE	Fuchsite-bearing listvenite	60Z-1-32-37	Magnesite	Matrix	Aggregate		0.93	59	36	0.92	0.01	0.07	0.93	0.03	0.07
ISTE	Fuchsite-bearing listvenite	60Z-1-32-37	Magnesite	Matrix	Aggregate		0.93	71	55	0.93	0.00	0.07	0.93	0.02	0.07
GM	Fuchsite-bearing listvenite	60Z-1-32-37	Magnesite	Matrix	Aggregate		0.95	-	52	0.94	0.00	0.05	0.95	0.02	0.05
ISTE	Fuchsite-bearing listvenite	60Z-1-32-37	Magnesite	Matrix	Aggregate		0.94	61	47	0.94	0.01	0.06	0.94	0.02	0.06
ISTE	Fuchsite-bearing listvenite	60Z-1-32-37	Magnesite	Matrix	Aggregate		0.95	55	82	0.94	0.01	0.05	0.95	0.01	0.05
GM	Fuchsite-bearing listvenite	60Z-1-32-37	Magnesite	Matrix	Aggregate		0.94	-	65	0.94	0.00	0.06	0.94	0.01	0.06
ISTE	Fuchsite-bearing listvenite	60Z-1-32-37	Magnesite	Matrix	Aggregate		0.95	83	39	0.94	0.01	0.05	0.95	0.02	0.05
ISTE	Fuchsite-bearing listvenite	60Z-1-32-37	Magnesite	Matrix	Aggregate		0.93	71	55	0.93	0.00	0.07	0.93	0.02	0.07
ISTE	Fuchsite-bearing listvenite	60Z-1-32-37	Magnesite	Vein	lss0	Median zone	0.95	111	10	0.94	0.01	0.05	0.95	0.09	0.05
GM	Fuchsite-bearing listvenite	60Z-1-32-37	Magnesite	Vein	lss0	Median zone	0.95	-	8	0.94	0.00	0.05	0.95	0.12	0.05
GM	Fuchsite-bearing listvenite	60Z-1-32-37	Magnesite	Vein	lss0	Median zone	0.95	-	11	0.95	0.00	0.05	0.95	0.09	0.05
GM	Fuchsite-bearing listvenite	60Z-1-32-37	Magnesite	Vein	lss0	Median zone	0.95	-	47	0.94	0.01	0.05	0.95	0.02	0.05
GM	Fuchsite-bearing listvenite	60Z-1-32-37	Magnesite	Vein	lss0	Intermediate	0.95	-	11	0.94	0.01	0.05	0.95	0.08	0.05
GM	Fuchsite-bearing listvenite	60Z-1-32-37	Magnesite	Vein	lss0	Intermediate	0.93	-	55	0.93	0.00	0.07	0.93	0.02	0.07

GM	Fuchsite-bearing listvenite	60Z-1-32-37	Magnesite	Vein	lss0	Rim	0.96	-	29	0.95	0.01	0.04	0.96	0.03	0.04
ISTE	Fuchsite-bearing listvenite	60Z-1-32-37	Magnesite	Vein	lss0	Rim	0.96	42	34	0.95	0.00	0.04	0.96	0.03	0.04
ISTE	Fuchsite-bearing listvenite	60Z-1-32-37	Magnesite	Vein	lss0	Rim	0.95	59	7	0.94	0.01	0.05	0.95	0.13	0.05
ISTE	Fuchsite-bearing listvenite	60Z-1-32-37	Magnesite	Vein	lss0	Rim	0.95	97	8	0.95	0.00	0.05	0.95	0.12	0.05
GM	Fuchsite-bearing listvenite	60Z-1-32-37	Magnesite	Vein	lss0	Rim	0.93	-	12	0.92	0.01	0.07	0.93	0.08	0.07
GM	Fuchsite-bearing listvenite	60Z-1-32-37	Magnesite	Vein	lc1	Median zone	0.94	-	16	0.93	0.00	0.06	0.94	0.06	0.06
GM	Fuchsite-bearing listvenite	60Z-1-32-37	Magnesite	Vein	lc1	Median zone	0.94	-	38	0.94	0.01	0.06	0.94	0.02	0.06
GM	Fuchsite-bearing listvenite	60Z-1-32-37	Magnesite	Vein	lc1	Median zone	0.93	-	19	0.93	0.00	0.07	0.93	0.05	0.07
ISTE	Fuchsite-bearing listvenite	60Z-1-32-37	Magnesite	Vein	lc1	Rim	0.94	84	21	0.94	0.00	0.06	0.94	0.04	0.06
GM	Fuchsite-bearing listvenite	60Z-1-32-37	Magnesite	Vein	lc2	Median zone	0.97	-	n.d.	0.96	0.00	0.03	0.97	0.00	0.03
ISTE	Fuchsite-bearing listvenite	60Z-1-32-37	Magnesite	Vein	lc2	Median zone	0.94	93	49	0.93	0.01	0.06	0.94	0.02	0.06
GM	Fuchsite-bearing listvenite	60Z-1-32-37	Magnesite	Vein	lc2	Median zone	0.93	-	40	0.92	0.01	0.07	0.93	0.02	0.07
ISTE	Listvenite	61Z-4-28-33	Dolomite	Vein	lc3	Median zone	0.97	23	n.d.	0.50	0.48	0.01	0.99	0.00	0.01
ISTE	Listvenite	61Z-4-28-33	Magnesite	Matrix	Aggregate		0.96	72	3273	0.95	0.01	0.04	0.96	0.00	0.04
ISTE	Listvenite	61Z-4-28-33	Magnesite	Matrix	Aggregate		0.96	39	109	0.96	0.00	0.04	0.96	0.01	0.04
ISTE	Listvenite	61Z-4-28-33	Magnesite	Matrix	Aggregate		0.96	65	5489	0.96	0.00	0.04	0.96	0.00	0.04
ISTE	Listvenite	61Z-4-28-33	Magnesite	Matrix	Aggregate		0.96	39	3086	0.95	0.01	0.04	0.96	0.00	0.04
ISTE	Listvenite	61Z-4-28-33	Magnesite	Matrix	Aggregate		0.96	-	n.d.	0.96	0.00	0.04	0.96	0.00	0.04
ISTE	Listvenite	61Z-4-28-33	Magnesite	Matrix	Aggregate		0.96	43	n.d.	0.95	0.01	0.04	0.96	0.00	0.04
ISTE	Listvenite	61Z-4-28-33	Magnesite	Matrix	Aggregate		0.97	57	220	0.95	0.01	0.03	0.97	0.00	0.03
ISTE	Listvenite	61Z-4-28-33	Magnesite	Matrix	Aggregate		0.96	64	n.d.	0.95	0.00	0.04	0.96	0.00	0.04
ISTE	Listvenite	61Z-4-28-33	Magnesite	Matrix	Aggregate		0.96	52	n.d.	0.95	0.00	0.04	0.96	0.00	0.04
ISTE	Listvenite	61Z-4-28-33	Magnesite	Matrix	Aggregate		0.96	55	n.d.	0.95	0.01	0.04	0.96	0.00	0.04
ISTE	Listvenite	61Z-4-28-33	Magnesite	Matrix	Aggregate		0.95	45	n.d.	0.95	0.01	0.05	0.95	0.00	0.05
ISTE	Listvenite	61Z-4-28-33	Magnesite	Matrix	Aggregate		0.96	49	n.d.	0.95	0.01	0.04	0.96	0.00	0.04
ISTE	Listvenite	61Z-4-28-33	Magnesite	Vein	lc5	Median zone	0.93	140	n.d.	0.93	0.01	0.07	0.93	0.00	0.07
ISTE	Listvenite	61Z-4-28-33	Magnesite	Vein	lc5	Median zone	0.91	73	n.d.	0.90	0.01	0.09	0.91	0.00	0.09
ISTE	Listvenite	61Z-4-28-33	Magnesite	Vein	lc5	Median zone	0.91	136	n.d.	0.91	0.01	0.09	0.91	0.00	0.09
ISTE	Listvenite	66Z-1-30-35	Magnesite	Matrix	Mg-core spheroid	Core	0.96	-	n.d.	0.96	0.00	0.04	0.96	0.00	0.04
ISTE	Listvenite	66Z-1-30-35	Magnesite	Matrix	Mg-core spheroid	Core	0.94	52	412	0.93	0.00	0.06	0.94	0.00	0.06
ISTE	Listvenite	66Z-1-30-35	Magnesite	Vein	lc1	Median zone	0.58	309	30	0.58	0.00	0.42	0.58	0.02	0.42
ISTE	Listvenite	66Z-1-30-35	Magnesite	Vein	lc1	Median zone	0.69	241	22	0.69	0.00	0.31	0.69	0.03	0.31
ISTE	Listvenite	66Z-1-30-35	Magnesite	Vein	lc1	Intermediate	0.61	413	85	0.61	0.00	0.39	0.61	0.01	0.39
ISTE	Listvenite	66Z-1-30-35	Magnesite	Vein	lc1	Rim	0.93	61	557	0.93	0.00	0.07	0.93	0.00	0.07
ISTE	Listvenite	66Z-1-30-35	Magnesite	Vein	lc1	Rim	0.95	-	53	0.94	0.00	0.05	0.95	0.02	0.05
ISTE	Listvenite	66Z-1-30-35	Dolomite	Vein	lc6	Median zone	0.90	27	n.d.	0.47	0.48	0.05	0.95	0.00	0.05
ISTE	Listvenite	66Z-1-30-35	Dolomite	Vein	lc6	Median zone	0.95	21	445	0.51	0.46	0.03	0.97	0.00	0.03
ISTE	Listvenite	66Z-1-30-35	Magnesite	Vein	lc6	Median zone	0.90	85	919	0.89	0.00	0.10	0.90	0.00	0.10
ISTE	Fuchsite-bearing listvenite	68Z-1-60-64	Dolomite	Matrix	Aggregate		0.82	35	n.d.	0.43	0.48	0.09	0.91	0.00	0.09
ISTE	Fuchsite-bearing listvenite	68Z-1-60-64	Magnesite	Matrix	Fe-core spheroid	Internal growth	0.85	70	n.d.	0.84	0.01	0.15	0.85	0.00	0.15
ISTE	Fuchsite-bearing listvenite	68Z-1-60-64	Magnesite	Matrix	Fe-core spheroid	Core	0.82	48	33	0.81	0.01	0.18	0.82	0.02	0.18
ISTE	Fuchsite-bearing listvenite	68Z-1-60-64	Magnesite	Matrix	Fe-core spheroid	Core	0.63	162	634	0.62	0.01	0.37	0.63	0.00	0.37
ISTE	Fuchsite-bearing listvenite	68Z-1-60-64	Magnesite	Matrix	Fe-core spheroid	Rim	0.80	86	798	0.79	0.01	0.20	0.80	0.00	0.20
ISTE	Fuchsite-bearing listvenite	68Z-1-60-64	Magnesite	Matrix	Aggregate		0.95	55	2572	0.94	0.01	0.05	0.95	0.00	0.05
ISTE	Fuchsite-bearing listvenite	68Z-1-60-64	Magnesite	Matrix	Aggregate		0.94	38	n.d.	0.93	0.01	0.06	0.94	0.00	0.06
ISTE	Fuchsite-bearing listvenite	68Z-1-60-64	Magnesite	Matrix	Aggregate		0.95	42	n.d.	0.94	0.01	0.05	0.95	0.00	0.05
ISTE	Fuchsite-bearing listvenite	68Z-1-60-64	Magnesite	Matrix	Aggregate		0.94	42	222	0.94	0.01	0.06	0.94	0.00	0.06
ISTE	Fuchsite-bearing listvenite	68Z-1-60-64	Magnesite	Matrix	Aggregate		0.93	35	3415	0.92	0.01	0.07	0.93	0.00	0.07
ISTE	Fuchsite-bearing listvenite	68Z-1-60-64	Magnesite	Matrix	Aggregate		0.95	32	599	0.94	0.01	0.05	0.95	0.00	0.05
ISTE	Fuchsite-bearing listvenite	68Z-1-60-64	Magnesite	Vein	lc1	Median zone	0.60	170	n.d.	0.60	0.00	0.40	0.60	0.00	0.40
ISTE	Fuchsite-bearing listvenite	68Z-1-60-64	Magnesite	Vein	lc1	Median zone	0.57	325	1548	0.56	0.01	0.43	0.57	0.00	0.43
ISTE	Fuchsite-bearing listvenite	68Z-1-60-64	Magnesite	Vein	lc1	Median zone	0.89	68	2148	0.88	0.01	0.11	0.89	0.00	0.11
ISTE	Fuchsite-bearing listvenite	68Z-1-60-64	Magnesite	Vein	lc1	Median zone	0.64	171	401	0.64	0.01	0.35	0.65	0.00	0.35

ISTE	Fuchsite-bearing listvenite	68Z-1-60-64	Magnesite	Vein	lc1	Median zone	0.68	218	326	0.67	0.01	0.32	0.68	0.00	0.32
ISTE	Fuchsite-bearing listvenite	68Z-1-60-64	Magnesite	Vein	lc1	Intermediate	0.93	62	338	0.93	0.01	0.07	0.93	0.00	0.07
ISTE	Fuchsite-bearing listvenite	68Z-1-60-64	Magnesite	Vein	lc1	Rim	0.77	139	267	0.76	0.01	0.23	0.77	0.00	0.23
ISTE	Fuchsite-bearing listvenite	71Z-3-0-8	Magnesite	Matrix	Fe-core spheroid	Core	0.79	18	23	0.79	0.01	0.21	0.79	0.03	0.21
ISTE	Fuchsite-bearing listvenite	71Z-3-0-8	Magnesite	Matrix	Fe-core spheroid	Internal growth	0.89	44	76	0.89	0.00	0.11	0.89	0.01	0.11
ISTE	Fuchsite-bearing listvenite	71Z-3-0-8	Magnesite	Matrix	Fe-core spheroid	Internal growth	0.94	116	410	0.94	0.00	0.06	0.94	0.00	0.06
ISTE	Fuchsite-bearing listvenite	71Z-3-0-8	Magnesite	Matrix	Fe-core spheroid	Internal growth	0.94	-	36	0.94	0.01	0.06	0.94	0.03	0.06
ISTE	Fuchsite-bearing listvenite	71Z-3-0-8	Magnesite	Matrix	Fe-core spheroid	Rim	0.90	118	12	0.89	0.01	0.10	0.90	0.07	0.10
ISTE	Fuchsite-bearing listvenite	71Z-3-0-8	Magnesite	Matrix	Mg-core spheroid	Core	0.96	45	n.d.	0.95	0.01	0.04	0.96	0.00	0.04
ISTE	Fuchsite-bearing listvenite	71Z-3-0-8	Magnesite	Matrix	Mg-core spheroid	Core	0.95	46	86	0.95	0.01	0.05	0.95	0.01	0.05
ISTE	Fuchsite-bearing listvenite	71Z-3-0-8	Magnesite	Matrix	Mg-core spheroid	Core	0.96	29	938	0.95	0.01	0.04	0.96	0.00	0.04
ISTE	Fuchsite-bearing listvenite	71Z-3-0-8	Magnesite	Matrix	Mg-core spheroid	Core	0.95	39	34	0.94	0.00	0.05	0.95	0.03	0.05
ISTE	Fuchsite-bearing listvenite	71Z-3-0-8	Magnesite	Matrix	Mg-core spheroid	Core	0.95	-	1121	0.95	0.00	0.05	0.95	0.00	0.05
ISTE	Fuchsite-bearing listvenite	71Z-3-0-8	Magnesite	Vein	lss0	Median zone	0.72	94	1710	0.72	0.01	0.28	0.72	0.00	0.28
ISTE	Fuchsite-bearing listvenite	71Z-3-0-8	Magnesite	Vein	lss0	Rim	0.94	-	31	0.93	0.01	0.06	0.94	0.03	0.06
ISTE	Fuchsite-bearing listvenite	71Z-3-0-8	Magnesite	Vein	lc1	Median zone	0.95	-	1121	0.95	0.00	0.05	0.95	0.00	0.05
ISTE	Fuchsite-bearing listvenite	71Z-3-0-8	Magnesite	Vein	lc1	Intermediate	0.71	83	n.d.	0.70	0.01	0.29	0.71	0.00	0.29
ISTE	Fuchsite-bearing listvenite	71Z-3-0-8	Magnesite	Vein	lc1	Rim	0.93	-	29	0.92	0.01	0.07	0.93	0.03	0.07
ISTE	Fuchsite-bearing listvenite	71Z-3-0-8	Magnesite	Vein	lc1	Rim	0.96	56	99	0.95	0.00	0.04	0.96	0.01	0.04
ISTE	Listvenite	72Z-1-71-79	Dolomite	Vein	lc6	Median zone	0.89	26	n.d.	0.40	0.55	0.05	0.95	0.00	0.05
ISTE	Listvenite	72Z-1-71-79	Magnesite	Matrix	Fe-core spheroid	Core	0.78	62	2025	0.76	0.01	0.22	0.78	0.00	0.22
ISTE	Listvenite	72Z-1-71-79	Magnesite	Matrix	Mg-core spheroid	Core	0.91	40	535	0.91	0.00	0.08	0.92	0.00	0.08
ISTE	Listvenite	72Z-1-71-79	Magnesite	Matrix	Mg-core spheroid	Core	0.97	-	3979	0.96	0.00	0.03	0.97	0.00	0.03
ISTE	Listvenite	72Z-1-71-79	Magnesite	Matrix	Mg-core spheroid	Core	0.93	35	295	0.93	0.01	0.07	0.93	0.00	0.07
ISTE	Listvenite	72Z-1-71-79	Magnesite	Matrix	Mg-core spheroid	Core	0.98	29	3841	0.97	0.01	0.02	0.98	0.00	0.02
ISTE	Listvenite	72Z-1-71-79	Magnesite	Matrix	Mg-core spheroid	Core	0.94	6	29	0.93	0.01	0.06	0.94	0.03	0.06
ISTE	Listvenite	72Z-1-71-79	Magnesite	Matrix	Mg-core spheroid	Core	0.86	46	15	0.85	0.01	0.14	0.86	0.06	0.14
ISTE	Listvenite	72Z-1-71-79	Magnesite	Matrix	Mg-core spheroid	Core	0.98	20	430	0.97	0.01	0.02	0.98	0.00	0.02
ISTE	Listvenite	72Z-1-71-79	Magnesite	Matrix	Mg-core spheroid	Core	0.95	32	415	0.95	0.01	0.05	0.95	0.00	0.05
ISTE	Listvenite	72Z-1-71-79	Magnesite	Matrix	Mg-core spheroid	Internal growth	0.96	34	4723	0.96	0.00	0.04	0.96	0.00	0.04
ISTE	Listvenite	72Z-1-71-79	Magnesite	Matrix	Mg-core spheroid	Rim	0.96	-	3421	0.96	0.00	0.04	0.96	0.00	0.04
ISTE	Listvenite	72Z-1-71-79	Magnesite	Matrix	Aggregate		0.98	42	1606	0.98	0.00	0.02	0.98	0.00	0.02
ISTE	Listvenite	72Z-1-71-79	Magnesite	Matrix	Aggregate		0.98	16	518	0.97	0.02	0.02	0.98	0.00	0.02
ISTE	Listvenite	72Z-1-71-79	Magnesite	Vein	lc1	Median zone	0.77	119	2366	0.77	0.01	0.22	0.78	0.00	0.22
ISTE	Listvenite	72Z-1-71-79	Magnesite	Vein	lc1	Median zone	0.83	53	1384	0.82	0.01	0.17	0.83	0.00	0.17
ISTE	Listvenite	72Z-1-71-80	Magnesite	Vein	lc6	Median zone	0.92	58	2880	0.91	0.00	0.08	0.92	0.00	0.08
ISTE	Listvenite	72Z-1-71-79	Magnesite	Vein	lc1	Rim	0.91	43	n.d.	0.90	0.00	0.09	0.91	0.00	0.09
ISTE	Listvenite	72Z-1-71-79	Magnesite	Vein	lc1	Rim	0.91	40	188	0.91	0.00	0.09	0.91	0.00	0.09
ISTE	Listvenite	72Z-1-71-79	Magnesite	Vein	lc1	Rim	0.92	38	711	0.91	0.00	0.08	0.92	0.00	0.08
ISTE	Listvenite	76Z-2-12-20	Dolomite	Matrix	Aggregate		0.88	78	304	0.48	0.45	0.07	0.93	0.00	0.07
ISTE	Listvenite	76Z-2-12-20	Dolomite	Matrix	Aggregate		0.87	47	568	0.47	0.45	0.07	0.93	0.00	0.07
ISTE	Listvenite	76Z-2-12-20	Dolomite	Matrix	Aggregate		0.90	27	195	0.45	0.50	0.05	0.95	0.00	0.05
ISTE	Listvenite	76Z-2-12-20	Dolomite	Vein	lc6		0.98	4	n.d.	0.50	0.49	0.01	0.99	0.00	0.01
ISTE	Listvenite	76Z-2-12-20	Dolomite	Vein	lc6		0.96	6	346	0.50	0.48	0.02	0.98	0.00	0.02
ISTE	Listvenite	76Z-2-12-20	Dolomite	Vein	lc6	Median zone	0.95	18	n.d.	0.48	0.49	0.03	0.97	0.00	0.03
ISTE	Listvenite	76Z-2-12-20	Dolomite	Vein	lc6	Median zone	0.87	41	n.d.	0.43	0.51	0.06	0.94	0.00	0.06
ISTE	Listvenite	76Z-2-12-20	Magnesite	Matrix	lss2?		0.93	12	205	0.92	0.00	0.07	0.93	0.00	0.07
ISTE	Listvenite	76Z-2-12-20	Magnesite	Vein	lss2?		0.73	55	n.d.	0.62	0.16	0.22	0.78	0.00	0.22
ISTE	Listvenite	76Z-2-12-20	Magnesite	Matrix	lss2?		0.83	45	269	0.82	0.00	0.17	0.83	0.00	0.17
ISTE	Listvenite	76Z-2-12-20	Magnesite	Vein	lc1		0.90	13	135	0.86	0.05	0.09	0.91	0.01	0.09
ISTE	Listvenite	76Z-2-12-20	Magnesite	Vein	lc1	Median zone	0.93	138	n.d.	0.93	0.00	0.07	0.93	0.00	0.07
ISTE	Listvenite	76Z-2-12-20	Magnesite	Vein	lc1	Median zone	0.93	86	n.d.	0.93	0.01	0.07	0.93	0.00	0.07
ISTE	Listvenite	76Z-2-12-20	Magnesite	Vein	lc1	Median zone	0.93	17	2822	0.93	0.00	0.07	0.93	0.00	0.07

ISTE	Listvenite	76Z-2-12-20	Magnesite	Vein	lc1	Median zone	0.94	13	114	0.93	0.00	0.06	0.94	0.01	0.06

Table S5 : Major element compositions of silicates determined by EPMA

								Major oxides													
Facility	Lithology	Sample	Mineral	Structure	Texture[2]	Zone	Transect	SiO2	TiO2	Al2O3	Cr2O3	FeO	MnO	MgO	CaO	Na2O	K2O	NiO	CuO	ZnO	SO2	Cl	BaO	SrO	Total
								wt%	wt%	wt%	wt%	wt%	wt%	wt%	wt%	wt%	wt%	wt%	wt%	wt%	wt%	wt%	wt%	wt%	wt%
GM	Carb. serpentinite	43Z-2-43-48	Serpentine	Matrix	Mesh			42.94	-	0.38	-	2.58	-	40.06	-	-	-	-	-	-	-	0.05	-	-	86.01
GM	Carb. serpentinite	43Z-2-43-48	Serpentine	Matrix	Mesh			42.82	-	0.36	-	2.30	-	39.93	-	-	-	-	-	-	-	-	-	-	85.41
GM	Carb. serpentinite	43Z-2-43-48	Serpentine	Matrix	Mesh			42.91	-	0.44	-	2.45	-	39.49	-	-	-	-	-	-	-	-	-	-	85.30
GM	Carb. serpentinite	43Z-2-43-48	Serpentine	Matrix	Mesh			43.79	-	0.33	-	1.95	-	40.08	-	-	-	-	-	-	-	-	-	-	86.15
GM	Carb. serpentinite	43Z-2-43-48	Serpentine	Matrix	Mesh			42.96	-	0.27	-	2.06	-	40.08	-	-	-	-	-	-	-	0.05	-	-	85.42
GM	Carb. serpentinite	43Z-2-43-48	Serpentine	Matrix	Mesh			43.09	-	0.30	-	2.45	-	40.11	-	-	-	-	-	-	-	0.04	-	-	86.00
GM	Carb. serpentinite	43Z-2-43-48	Serpentine	Matrix	Mesh			42.90	-	0.31	-	2.50	-	40.21	-	-	-	-	-	-	-	0.06	-	-	85.99
GM	Carb. serpentinite	43Z-2-43-48	Serpentine	Matrix	Mesh			42.79	-	0.24	-	2.72	-	40.71	-	-	-	-	-	-	-	0.06	-	-	86.53
GM	Carb. serpentinite	43Z-2-43-48	Serpentine	Matrix	Mesh			43.47	-	0.23	-	2.63	-	40.38	-	-	-	-	-	-	-	0.04	-	-	86.74
GM	Carb. serpentinite	43Z-2-43-48	Serpentine	Matrix	Mesh			43.03	-	0.11	-	1.95	-	40.88	-	-	-	-	-	-	-	-	-	-	85.98
GM	Carb. serpentinite	43Z-2-43-48	Serpentine	Matrix	Mesh			43.00	-	0.16	-	1.98	-	41.07	-	-	-	-	-	-	-	0.04	-	-	86.25
GM	Carb. serpentinite	43Z-2-43-48	Serpentine	Matrix	Mesh			43.92	-	0.31	-	3.23	-	39.44	-	-	-	-	-	-	-	-	-	-	86.90
GM	Carb. serpentinite	43Z-2-43-48	Serpentine	Matrix	Mesh			42.61	-	0.28	-	4.27	-	39.02	-	-	-	-	-	-	-	0.05	-	-	86.22
GM	Carb. serpentinite	43Z-2-43-48	Serpentine	Matrix	Mesh			43.53	-	0.86	0.51	5.00	-	36.60	0.08	-	-	-	-	-	-	0.09	-	-	86.66
GM	Carb. serpentinite	43Z-2-43-48	Serpentine	Matrix	Mesh			43.13	-	0.28	-	4.25	-	40.00	0.10	-	-	-	-	-	-	-	-	-	87.76
GM	Carb. serpentinite	43Z-2-43-48	Serpentine	Matrix	Mesh			42.61	-	0.32	-	3.99	-	38.95	-	-	-	-	-	-	-	0.04	-	-	85.92
GM	Carb. serpentinite	43Z-2-43-48	Serpentine	Matrix	Mesh			44.17	-	0.31	-	3.64	-	40.11	-	-	-	-	-	-	-	-	-	-	88.23
GM	Carb. serpentinite	43Z-2-43-48	Serpentine	Matrix	Mesh			44.46	-	0.63	0.60	4.50	-	36.64	0.09	-	-	-	-	-	-	-	-	-	86.91
GM	Carb. serpentinite	43Z-2-43-48	Serpentine	Matrix	Mesh			42.80	-	0.24	-	2.35	-	40.29	-	-	-	-	-	-	-	0.07	-	-	85.74
GM	Carb. serpentinite	43Z-2-43-48	Serpentine	Matrix	Mesh			43.10	-	0.19	-	2.27	-	41.72	-	-	-	0.53	-	-	-	0.06	-	-	87.86
GM	Carb. serpentinite	43Z-2-43-48	Serpentine	Matrix	Mesh			43.54	-	0.18	-	2.04	-	39.71	-	-	-	-	-	-	-	-	-	-	85.47
GM	Carb. serpentinite	43Z-2-43-48	Serpentine	Matrix	Mesh			43.36	-	0.13	-	2.18	-	41.12	-	-	-	-	-	-	-	-	-	-	86.79
GM	Carb. serpentinite	43Z-2-43-48	Serpentine	Matrix	Mesh			42.41	-	0.24	-	2.37	-	40.05	-	-	-	-	-	-	-	0.07	-	-	85.14
GM	Carb. serpentinite	43Z-2-43-48	Serpentine	Matrix	Mesh			43.08	-	0.17	-	1.93	-	40.06	-	-	-	-	-	-	-	-	-	-	85.24
GM	Carb. serpentinite	43Z-2-43-48	Serpentine	Matrix	Bastite			42.74	-	0.92	0.74	3.35	-	37.85	-	-	-	-	-	-	-	0.07	-	-	85.66
GM	Carb. serpentinite	43Z-2-43-48	Serpentine	Matrix	Bastite			42.83	-	1.05	0.75	4.19	-	37.80	0.08	-	-	-	-	-	-	0.07	-	-	86.78
GM	Carb. serpentinite	43Z-2-43-48	Serpentine	Matrix	Bastite			42.12	-	1.00	0.67	3.68	-	37.39	0.09	-	-	-	-	-	-	0.08	-	-	85.04
GM	Carb. serpentinite	43Z-2-43-48	Serpentine	Matrix	Bastite			42.17	-	0.78	0.71	7.44	-	36.16	-	-	-	-	-	-	-	-	-	-	87.26
GM	Carb. serpentinite	43Z-2-43-48	Serpentine	Matrix	Bastite			42.90	-	0.73	0.78	7.39	-	36.64	-	-	-	-	-	-	-	-	-	-	88.45
GM	Carb. serpentinite	43Z-2-43-48	Serpentine	Matrix	Bastite			42.77	-	0.67	0.93	8.54	-	35.66	-	-	-	-	-	-	-	-	-	-	88.56
GM	Carb. serpentinite	43Z-2-43-48	Serpentine	Matrix	Bastite			41.82	-	0.58	1.00	8.50	-	36.00	-	-	-	-	-	-	-	-	-	-	87.90
GM	Carb. serpentinite	43Z-2-43-48	Serpentine	Matrix	Bastite			42.19	-	0.95	1.02	7.81	-	35.60	-	-	-	-	-	-	-	0.04	-	-	87.61
GM	Carb. serpentinite	43Z-2-43-48	Serpentine	Matrix	Bastite			42.10	-	0.86	0.83	6.89	-	36.63	-	-	-	-	-	-	-	-	-	-	87.32
GM	Carb. serpentinite	43Z-2-43-48	Serpentine	Matrix	Bastite			42.00	-	0.65	0.79	6.74	-	35.56	-	-	-	-	-	-	-	-	-	-	85.74
GM	Carb. serpentinite	43Z-2-43-48	Serpentine	Matrix	Bastite			42.10	-	0.78	0.92	6.14	-	36.49	0.07	-	-	-	-	-	-	0.06	-	-	86.57
GM	Carb. serpentinite	43Z-2-43-48	Serpentine	Matrix	Bastite			42.72	-	0.56	0.55	4.50	-	37.24	0.14	-	-	-	-	-	-	0.06	-	-	85.77
GM	Carb. serpentinite	43Z-2-43-48	Serpentine	Matrix	Bastite			42.25	-	0.46	0.54	5.43	-	37.51	0.12	-	-	0.46	-	-	-	0.07	-	-	86.83
GM	Carb. serpentinite	43Z-2-43-48	Serpentine	Matrix	Bastite			42.93	-	0.44	0.55	5.18	-	37.39	0.13	-	-	-	-	-	-	0.05	-	-	86.68
GM	Carb. serpentinite	43Z-2-43-48	Serpentine	Matrix	Bastite			43.52	-	0.54	0.33	4.79	-	36.64	0.11	-	-	-	-	-	-	0.05	-	-	85.97
GM	Carb. serpentinite	43Z-2-43-48	Serpentine	Matrix	Bastite			44.10	-	0.63	0.33	5.29	-	36.12	0.15	-	-	-	-	-	-	-	-	-	86.62
GM	Carb. serpentinite	43Z-2-43-48	Serpentine	Matrix	Bastite			44.18	-	0.54	0.32	4.59	-	36.20	0.13	-	-	-	-	-	-	0.04	-	-	85.99
GM	Carb. serpentinite	43Z-2-43-48	Serpentine	Matrix	Bastite			43.14	-	0.56	0.48	4.72	-	36.43	0.12	-	-	-	-	-	-	0.05	-	-	85.51
GM	Carb. serpentinite	43Z-2-43-48	Serpentine	Matrix	Bastite			43.90	-	0.57	0.49	5.11	-	37.22	0.13	-	-	-	-	-	-	0.06	-	-	87.49
GM	Carb. serpentinite	43Z-2-43-48	Serpentine	Matrix	Bastite			42.58	-	0.58	0.50	6.04	-	36.41	0.13	-	-	-	-	-	-	0.05	-	-	86.29
GM	Carb. serpentinite	43Z-2-43-48	Serpentine	Vein	sc0	Median zone		44.57	-	0.43	-	2.52	-	41.24	0.12	-	-	-	-	-	-	0.05	-	-	88.93
GM	Carb. serpentinite	43Z-2-43-48	Serpentine	Vein	sc0	Median zone		43.78	-	0.40	-	2.36	-	41.14	0.16	-	0.05	-	-	-	-	0.09	-	-	87.97
GM	Carb. serpentinite	43Z-2-43-48	Serpentine	Vein	sc0	Median zone		43.87	-	0.42	-	2.18	-	40.82	0.15	-	-	-	-	-	-	0.08	-	-	87.51

GM	Carb. serpentinite	43Z-2-43-48	Serpentine	Vein	sc0	Rim		44.57	-	0.39	-	2.32	-	41.32	0.12	-	-	-	-	-	-	0.05	-	-	88.77
GM	Carb. serpentinite	43Z-2-43-48	Serpentine	Vein	sc0	Rim		44.11	-	0.36	-	2.15	-	40.41	0.17	-	-	-	-	-	-	0.07	-	-	87.27
GM	Carb. serpentinite	43Z-2-43-48	Serpentine	Vein	sc0	Rim		44.76	-	0.44	-	2.45	-	40.88	0.14	-	-	-	-	-	-	0.08	-	-	88.74
GM	Carb. serpentinite	43Z-2-43-48	Serpentine	Vein	sc0	Rim		44.51	-	0.38	-	1.99	-	40.79	0.10	-	-	-	-	-	-	0.04	-	-	87.81
GM	Carb. serpentinite	43Z-3-0-5	Serpentine	Matrix	Mesh			44.12	-	0.27	-	4.33	-	37.10	0.17	-	-	-	-	-	-	-	-	-	85.99
GM	Carb. serpentinite	43Z-3-0-5	Serpentine	Matrix	Mesh			44.41	-	0.23	-	4.31	-	38.73	0.12	-	-	-	-	-	-	-	-	-	87.79
GM	Carb. serpentinite	43Z-3-0-5	Serpentine	Matrix	Mesh			43.76	-	0.26	-	3.93	-	36.89	0.14	-	-	-	-	-	-	-	-	-	84.99
GM	Carb. serpentinite	43Z-3-0-5	Serpentine	Matrix	Mesh			43.44	-	0.56	0.33	5.02	-	35.79	0.20	-	-	-	-	-	-	0.06	-	-	85.41
GM	Carb. serpentinite	43Z-3-0-5	Serpentine	Matrix	Mesh			44.04	-	0.20	-	3.53	-	39.28	0.07	-	-	-	-	-	-	-	-	-	87.11
GM	Carb. serpentinite	43Z-3-0-5	Serpentine	Matrix	Mesh			42.99	-	0.18	-	4.56	-	38.56	0.08	-	-	-	-	-	-	-	-	-	86.37
GM	Carb. serpentinite	43Z-3-0-5	Serpentine	Matrix	Mesh			43.44	-	0.21	-	5.81	-	39.11	0.07	-	-	-	-	-	-	-	-	-	88.65
GM	Carb. serpentinite	43Z-3-0-5	Serpentine	Matrix	Bastite			42.72	-	0.56	0.55	4.50	-	37.24	0.14	-	-	-	-	-	-	0.06	-	-	85.77
GM	Carb. serpentinite	43Z-3-0-5	Serpentine	Matrix	Bastite			42.25	-	0.46	0.54	5.43	-	37.51	0.12	-	-	0.46	-	-	-	0.07	-	-	86.83
GM	Carb. serpentinite	43Z-3-0-5	Serpentine	Matrix	Bastite			42.93	-	0.44	0.55	5.18	-	37.39	0.13	-	-	-	-	-	-	0.05	-	-	86.68
GM	Carb. serpentinite	43Z-3-0-5	Serpentine	Matrix	Bastite			43.52	-	0.54	0.33	4.79	-	36.64	0.11	-	-	-	-	-	-	0.05	-	-	85.97
GM	Carb. serpentinite	43Z-3-0-5	Serpentine	Matrix	Bastite			44.10	-	0.63	0.33	5.29	-	36.12	0.15	-	-	-	-	-	-	-	-	-	86.62
GM	Carb. serpentinite	43Z-3-0-5	Serpentine	Matrix	Bastite			44.18	-	0.54	0.32	4.59	-	36.20	0.13	-	-	-	-	-	-	0.04	-	-	85.99
GM	Carb. serpentinite	43Z-3-0-5	Serpentine	Matrix	Bastite			43.14	-	0.56	0.48	4.72	-	36.43	0.12	-	-	-	-	-	-	0.05	-	-	85.51
GM	Carb. serpentinite	43Z-3-0-5	Serpentine	Matrix	Bastite			43.90	-	0.57	0.49	5.11	-	37.22	0.13	-	-	-	-	-	-	0.06	-	-	87.49
GM	Carb. serpentinite	43Z-3-0-5	Serpentine	Matrix	Bastite			42.58	-	0.58	0.50	6.04	-	36.41	0.13	-	-	-	-	-	-	0.05	-	-	86.29
GM	Carb. serpentinite	43Z-3-0-5	Serpentine	Vein	ss1	Median zone		44.06	-	0.20	-	1.15	-	41.12	-	-	-	-	-	-	-	-	-	-	86.53
GM	Carb. serpentinite	43Z-3-0-5	Serpentine	Vein	ss1	Median zone		44.44	-	0.17	-	1.13	-	41.58	-	-	-	-	-	-	-	-	-	-	87.32
GM	Carb. serpentinite	43Z-3-0-5	Serpentine	Vein	ss1	Median zone		43.84	-	0.21	0.29	1.50	-	40.45	-	-	-	-	-	-	-	-	-	-	86.30
GM	Carb. serpentinite	43Z-3-0-5	Serpentine	Vein	ss1	Rim		43.77	-	0.19	-	1.35	-	40.71	-	-	-	-	-	-	-	0.04	-	-	86.06
GM	Carb. serpentinite	43Z-3-0-5	Serpentine	Vein	ss1	Rim		44.80	-	0.19	-	1.17	-	41.78	0.07	-	-	-	-	-	-	-	-	-	88.00
GM	Carb. serpentinite	43Z-3-52-57	Serpentine	Matrix	Mesh			42.98	-	0.22	-	2.40	-	39.73	0.09	-	-	-	-	-	-	-	-	-	85.42
GM	Carb. serpentinite	43Z-3-52-57	Serpentine	Matrix	Mesh			43.06	-	0.25	-	1.99	-	39.52	0.11	-	-	-	-	-	-	-	-	-	84.94
GM	Carb. serpentinite	43Z-3-52-57	Serpentine	Matrix	Mesh			43.75	-	0.29	-	2.27	-	40.04	-	-	-	-	-	-	-	-	-	-	86.35
GM	Carb. serpentinite	43Z-3-52-57	Serpentine	Matrix	Mesh			44.10	-	0.26	-	2.11	-	40.17	0.08	-	-	-	-	-	-	-	-	-	86.72
GM	Carb. serpentinite	43Z-3-52-57	Serpentine	Matrix	Mesh			43.05	-	0.28	-	2.60	-	38.51	0.09	-	-	-	-	-	-	-	-	-	84.54
GM	Carb. serpentinite	43Z-3-52-57	Serpentine	Matrix	Mesh			41.82	-	0.31	-	2.52	-	39.03	-	-	-	-	-	-	-	0.04	-	-	83.72
GM	Carb. serpentinite	43Z-3-52-57	Serpentine	Matrix	Mesh			42.61	-	0.26	-	2.07	-	38.76	0.09	-	-	-	-	-	-	0.04	-	-	83.82
GM	Carb. serpentinite	43Z-3-52-57	Serpentine	Matrix	Mesh			42.63	-	0.69	0.51	4.01	-	37.03	0.45	-	-	-	-	-	-	0.08	-	-	85.40
GM	Carb. serpentinite	43Z-3-52-57	Serpentine	Matrix	Mesh			41.86	-	0.30	-	2.74	-	38.19	0.07	-	-	-	-	-	-	-	-	-	83.17
GM	Carb. serpentinite	43Z-3-52-57	Serpentine	Matrix	Mesh			42.22	-	0.33	0.43	2.92	-	39.18	0.07	-	-	-	-	-	-	0.05	-	-	85.21
GM	Carb. serpentinite	43Z-3-52-57	Serpentine	Matrix	Mesh			42.64	-	0.32	-	1.54	-	39.08	-	-	-	-	-	-	-	-	-	-	83.58
GM	Carb. serpentinite	43Z-3-52-57	Serpentine	Matrix	Mesh			43.20	-	0.29	-	2.15	-	39.57	0.07	-	-	-	-	-	-	0.04	-	-	85.33
GM	Carb. serpentinite	43Z-3-52-57	Serpentine	Matrix	Mesh			42.86	-	0.30	-	2.46	-	39.35	0.08	-	-	-	-	-	-	0.05	-	-	85.09
GM	Carb. serpentinite	43Z-3-52-57	Serpentine	Matrix	Mesh			43.03	-	0.31	-	2.32	-	39.67	0.09	-	-	-	-	-	-	-	-	-	85.41
GM	Carb. serpentinite	43Z-3-52-57	Serpentine	Matrix	Mesh			43.24	-	0.17	-	2.92	-	39.69	-	-	-	-	-	-	-	-	-	-	86.02
GM	Carb. serpentinite	43Z-3-52-57	Serpentine	Matrix	Mesh			43.08	-	0.21	-	2.90	-	39.76	-	-	-	-	-	-	-	0.04	-	-	85.99
GM	Carb. serpentinite	43Z-3-52-57	Serpentine	Matrix	Mesh			43.43	-	0.24	-	3.09	-	40.16	-	-	-	-	-	-	-	-	-	-	86.92
GM	Carb. serpentinite	43Z-3-52-57	Serpentine	Matrix	Mesh			43.37	-	0.23	-	2.51	-	39.47	-	-	-	-	-	-	-	-	-	-	85.58
GM	Carb. serpentinite	43Z-3-52-57	Serpentine	Matrix	Bastite			42.33	-	0.66	0.52	4.51	-	36.43	0.17	-	-	-	-	-	-	0.05	-	-	84.67
GM	Carb. serpentinite	43Z-3-52-57	Serpentine	Matrix	Bastite			42.43	-	0.67	0.40	4.36	-	36.05	0.17	-	-	-	-	-	-	0.05	-	-	84.13
GM	Carb. serpentinite	43Z-3-52-57	Serpentine	Matrix	Bastite			42.93	-	0.68	0.50	3.86	-	35.52	0.21	-	-	-	-	-	-	0.04	-	-	83.74
GM	Carb. serpentinite	43Z-3-52-57	Serpentine	Vein	sc0	Rim		44.83	-	0.28	-	2.46	-	40.13	0.08	-	-	-	-	-	-	-	-	-	87.78
GM	Carb. serpentinite	43Z-3-52-57	Serpentine	Vein	sc0	Rim		44.00	-	0.25	-	1.91	-	40.38	-	-	-	-	-	-	-	-	-	-	86.54
GM	Carb. serpentinite	43Z-3-52-57	Serpentine	Vein	sc0	Median zone	a	43.75	-	0.22	-	2.15	-	39.94	-	-	-	-	-	-	-	0.04	-	-	86.11
GM	Carb. serpentinite	43Z-3-52-57	Serpentine	Vein	sc0	Median zone	a	44.19	-	0.30	-	2.38	-	40.95	0.09	-	-	-	-	-	-	-	-	-	87.91
GM	Carb. serpentinite	43Z-3-52-57	Serpentine	Vein	sc0	Median zone	a	43.96	-	0.23	-	1.97	-	40.50	-	-	-	-	-	-	-	-	-	-	86.66
GM	Carb. serpentinite	43Z-3-52-57	Serpentine	Vein	sc0	Median zone	a	43.88	-	0.28	-	2.01	-	39.70	-	-	-	-	-	-	-	-	-	-	85.87
GM	Carb. serpentinite	43Z-3-52-57	Serpentine	Vein	sc0	Median zone	a	42.99	-	0.27	-	2.04	-	38.82	-	-	-	-	-	-	-	-	-	-	84.12

GM	Carb. serpentinite	43Z-3-52-57	Serpentine	Vein	sc0	Median zone	a	43.60	-	0.24	-	1.83	-	40.35	-	-	-	-	-	-	-	-	-	-	-	86.02
GM	Carb. serpentinite	43Z-3-52-57	Serpentine	Vein	sc0	Rim		44.83	-	0.28	-	2.46	-	40.13	0.08	-	-	-	-	-	-	-	-	-	-	87.78
GM	Carb. serpentinite	43Z-3-52-57	Serpentine	Vein	sc0	Rim		44.00	-	0.25	-	1.91	-	40.38	-	-	-	-	-	-	-	-	-	-	-	86.54
GM	Carb. serpentinite	43Z-3-52-57	Serpentine	Vein	sc0	Rim		44.51	-	0.23	-	2.12	-	40.77	0.09	-	-	-	-	-	-	-	-	-	-	87.71
GM	Carb. serpentinite	43Z-3-52-57	Serpentine	Vein	sc0	Rim		44.49	-	0.26	-	1.99	-	40.60	0.09	-	-	-	-	-	-	-	-	-	-	87.43
GM	Carb. serpentinite	43Z-3-52-57	Serpentine	Vein	sc0	Median zone		42.72	-	0.51	0.35	4.69	-	35.71	0.16	-	-	-	-	-	-	-	-	-	-	84.13
GM	Carb. serpentinite	43Z-3-52-57	Serpentine	Vein	sc0	Median zone		42.79	-	0.75	0.37	3.21	-	37.39	0.13	-	-	-	-	-	-	0.09	-	-	-	84.73
GM	Carb. serpentinite	43Z-3-52-57	Serpentine	Vein	sc0	Median zone		43.13	-	0.79	0.39	2.95	-	36.54	0.15	-	-	-	-	-	-	0.06	-	-	-	84.00
GM	Carb. serpentinite	43Z-3-52-57	Serpentine	Vein	sc0	Median zone	b	42.43	-	0.29	-	2.70	-	39.18	-	-	-	-	-	-	-	-	-	-	-	84.61
GM	Carb. serpentinite	43Z-3-52-57	Serpentine	Vein	sc0	Median zone	b	42.83	-	0.25	-	2.40	-	39.28	-	-	-	-	-	-	-	-	-	-	-	84.76
GM	Carb. serpentinite	43Z-3-52-57	Serpentine	Vein	sc0	Median zone	b	42.93	-	0.28	-	2.08	-	39.51	0.09	-	-	-	-	-	-	0.04	-	-	-	84.93
GM	Carb. serpentinite	43Z-3-52-57	Serpentine	Vein	sc0	Median zone	b	43.63	-	0.26	-	1.94	-	39.73	-	-	-	-	-	-	-	-	-	-	-	85.57
GM	Carb. serpentinite	43Z-3-52-57	Serpentine	Vein	sc0	Median zone	b	43.56	-	0.33	-	1.94	-	39.90	-	-	-	-	-	-	-	-	-	-	-	85.73
GM	Carb. serpentinite	43Z-3-52-57	Serpentine	Vein	sc0	Median zone	b	43.71	-	0.26	-	1.82	-	39.13	-	-	-	-	-	-	-	-	-	-	-	84.91
GM	Carb. serpentinite	43Z-3-52-57	Serpentine	Vein	sc0	Median zone	b	42.86	-	0.32	-	2.22	-	39.52	-	-	-	-	-	-	-	-	-	-	-	84.92
GM	Carb. serpentinite	43Z-3-52-57	Serpentine	Vein	sc0	Median zone	b	43.40	-	0.32	-	1.96	-	39.29	-	-	-	-	-	-	-	-	-	-	-	84.97
GM	Carb. serpentinite	43Z-4-52-57	Serpentine	Matrix	Mesh			44.33	-	0.11	-	2.20	-	40.35	-	-	-	-	-	-	-	-	-	-	-	87.00
GM	Carb. serpentinite	43Z-4-52-57	Serpentine	Matrix	Mesh			43.72	-	-	-	3.13	-	40.69	0.09	-	-	-	-	-	-	-	-	-	-	87.64
GM	Carb. serpentinite	43Z-4-52-57	Serpentine	Matrix	Mesh			43.78	-	-	-	2.83	-	40.41	-	-	-	-	-	-	-	-	-	-	-	87.03
GM	Carb. serpentinite	43Z-4-52-57	Serpentine	Matrix	Mesh			43.58	-	-	-	2.54	-	40.45	-	-	-	-	-	-	-	-	-	-	-	86.57
GM	Carb. serpentinite	43Z-4-52-57	Serpentine	Matrix	Mesh			43.59	-	-	-	2.54	-	40.69	-	-	-	-	-	-	-	-	-	-	-	86.83
GM	Carb. serpentinite	43Z-4-52-57	Serpentine	Matrix	Mesh			43.67	-	-	-	3.27	-	39.68	-	-	-	-	-	-	-	-	-	-	-	86.62
GM	Carb. serpentinite	43Z-4-52-57	Serpentine	Matrix	Bastite			43.70	-	0.66	0.73	4.53	-	37.29	-	-	-	-	-	-	-	-	-	-	-	86.92
GM	Carb. serpentinite	43Z-4-52-57	Serpentine	Matrix	Bastite			43.09	-	0.32	0.76	4.90	-	37.27	-	-	-	-	-	-	-	-	-	-	-	86.34
GM	Carb. serpentinite	43Z-4-52-57	Serpentine	Matrix	Bastite			42.59	-	0.78	0.72	4.90	-	36.54	0.10	-	-	0.49	-	-	-	-	-	-	-	86.11
GM	Carb. serpentinite	43Z-4-52-57	Serpentine	Vein	sc0	Median zone		44.49	-	0.17	-	1.12	-	40.52	-	-	-	-	-	-	-	-	-	-	-	86.30
GM	Carb. serpentinite	43Z-4-52-57	Serpentine	Vein	sc0	Median zone		42.76	-	0.15	-	2.51	-	38.38	-	-	-	-	-	-	-	-	-	-	-	83.80
GM	Carb. serpentinite	43Z-4-52-57	Serpentine	Vein	sc0	Median zone		43.03	-	0.11	-	2.48	-	38.65	-	-	-	-	-	-	-	-	-	-	-	84.28
GM	Carb. serpentinite	43Z-4-52-57	Serpentine	Vein	sc0	Rim	c	45.08	-	0.15	-	1.29	-	42.12	-	-	-	-	-	-	-	-	-	-	-	88.64
GM	Carb. serpentinite	43Z-4-52-57	Serpentine	Vein	sc0	Rim	c	45.24	-	0.15	-	1.25	-	41.99	-	-	-	-	-	-	-	-	-	-	-	88.63
GM	Carb. serpentinite	43Z-4-52-57	Serpentine	Vein	sc0	Rim	c	44.40	-	0.12	-	1.41	-	41.35	-	-	-	-	-	-	-	-	-	-	-	87.27
GM	Carb. serpentinite	43Z-4-52-57	Serpentine	Vein	sc0	Rim	c	44.38	-	0.11	-	1.72	-	41.28	-	-	-	-	-	-	-	-	-	-	-	87.48
GM	Carb. serpentinite	43Z-4-52-57	Serpentine	Vein	sc0	Median zone	c	43.46	-	-	-	1.80	-	41.18	0.07	-	-	-	-	-	-	-	-	-	-	86.52
GM	Carb. serpentinite	43Z-4-52-57	Serpentine	Vein	sc0	Median zone	c	43.44	-	-	-	1.65	-	41.21	-	-	-	-	-	-	-	-	-	-	-	86.31
GM	Carb. serpentinite	43Z-4-52-57	Serpentine	Vein	sc0	Median zone	c	44.05	-	0.10	-	1.52	-	41.28	0.10	-	-	-	-	-	-	-	-	-	-	87.07
GM	Carb. serpentinite	43Z-4-52-57	Serpentine	Vein	sc0	Median zone	c	44.68	-	-	-	1.71	-	41.89	-	-	-	-	-	-	-	-	-	-	-	88.28
GM	Carb. serpentinite	43Z-4-52-57	Serpentine	Vein	sc0	Median zone	c	45.30	-	0.10	-	1.68	-	42.33	-	-	-	-	-	-	-	-	-	-	-	89.41
GM	Carb. serpentinite	43Z-4-52-57	Serpentine	Vein	sc0	Median zone	c	44.30	-	-	-	2.41	-	41.74	-	-	-	-	-	-	-	-	-	-	-	88.46
GM	Carb. serpentinite	43Z-4-52-57	Serpentine	Vein	sc0	Median zone	c	44.02	-	-	-	1.52	-	43.15	-	-	-	-	-	-	-	-	-	-	-	88.68
GM	Carb. serpentinite	43Z-4-52-57	Serpentine	Vein	sc0	Median zone	c	44.35	-	0.11	-	1.89	-	41.69	-	-	-	-	-	-	-	-	-	-	-	88.04
GM	Carb. serpentinite	43Z-4-52-57	Serpentine	Vein	sc0	Median zone	c	43.84	-	-	-	1.97	-	41.29	-	-	-	-	-	-	-	-	-	-	-	87.10
GM	Carb. serpentinite	43Z-4-52-57	Serpentine	Vein	sc0	Median zone	c	43.62	-	0.12	-	2.14	-	40.59	-	-	-	-	-	-	-	-	-	-	-	86.46
GM	Carb. serpentinite	43Z-4-52-57	Serpentine	Vein	sc0	Median zone	c	43.88	-	-	-	2.25	-	41.41	-	-	-	-	-	-	-	-	-	-	-	87.54
GM	Carb. serpentinite	43Z-4-52-57	Serpentine	Vein	sc0	Median zone	c	43.95	-	-	-	1.96	-	41.38	-	-	-	-	-	-	-	-	-	-	-	87.30
GM	Carb. serpentinite	43Z-4-52-57	Serpentine	Vein	sc0	Median zone	c	43.91	-	0.14	-	1.83	-	41.26	-	-	-	-	-	-	-	-	-	-	-	87.13
GM	Carb. serpentinite	43Z-4-52-57	Serpentine	Vein	sc0	Median zone	c	44.17	-	0.10	-	1.84	-	41.42	-	-	-	-	-	-	-	-	-	-	-	87.54
GM	Carb. serpentinite	43Z-4-52-57	Serpentine	Vein	sc0	Median zone	c	44.02	-	0.11	-	2.02	-	41.39	-	-	-	-	-	-	-	-	-	-	-	87.54
GM	Carb. serpentinite	43Z-4-52-57	Serpentine	Vein	sc0	Median zone	c	43.11	-	-	-	2.21	-	40.84	0.34	-	-	-	-	-	-	-	-	-	-	86.50
GM	Carb. serpentinite	43Z-4-52-57	Serpentine	Vein	sc0	Median zone	c	44.14	-	0.12	-	2.28	-	41.14	-	-	-	-	-	-	-	-	-	-	-	87.68
GM	Carb. serpentinite	43Z-4-52-57	Serpentine	Vein	sc0	Median zone	c	44.11	-	-	-	2.66	-	40.92	-	-	-	-	-	-	-	-	-	-	-	87.68
GM	Carb. serpentinite	43Z-4-52-57	Serpentine	Vein	sc0	Median zone	c	43.78	-	-	-	1.66	-	41.07	-	-	-	-	-	-	-	-	-	-	-	86.51
GM	Carb. serpentinite	43Z-4-52-57	Serpentine	Vein	sc0	Median zone	c	44.13	-	-	-	2.24	-	40.99	-	-	-	-	-	-	-	-	-	-	-	87.37
GM	Carb. serpentinite	43Z-4-52-57	Serpentine	Vein	sc0	Rim	c	44.48	-	0.14	-	1.69	-	41.12	-	-	-	-	-	-	-	-	-	-	-	87.43

GM	Carb. serpentinite	43Z-4-52-57	Serpentine	Vein	sc0	Rim	c	44.49	-	0.13	-	1.25	-	41.21	-	-	-	-	-	-	-	-	-	-	87.08
GM	Carb. serpentinite	43Z-4-52-57	Serpentine	Vein	sc0	Rim	c	44.79	-	0.13	-	1.25	-	41.93	-	-	-	-	-	-	-	-	-	-	88.10
GM	Carb. serpentinite	43Z-4-52-57	Serpentine	Vein	sc0	Median zone		42.76	-	0.15	-	2.51	-	38.38	-	-	-	-	-	-	-	-	-	-	83.80
GM	Carb. serpentinite	43Z-4-52-57	Serpentine	Vein	sc0	Median zone		43.03	-	0.11	-	2.48	-	38.65	-	-	-	-	-	-	-	-	-	-	84.28
ISTE	Carb. serpentinite	44Z-1-41-46	Serpentine	Matrix	Mesh			40.14	0.01	0.42	0.03	2.66	0.03	36.83	0.04	0.01	-	0.34	-	-	-	0.05	-	-	80.56
ISTE	Carb. serpentinite	44Z-1-41-46	Serpentine	Matrix	Mesh			41.90	-	0.31	0.01	1.02	0.02	37.57	0.03	0.01	0.01	0.23	-	-	-	0.04	-	-	81.14
ISTE	Carb. serpentinite	44Z-1-41-46	Serpentine	Matrix	Mesh			40.98	-	0.37	0.01	1.32	0.02	37.47	0.02	-	-	0.18	-	-	-	0.04	-	-	80.41
ISTE	Carb. serpentinite	44Z-1-41-46	Serpentine	Matrix	Mesh			40.22	-	0.42	0.00	1.92	0.04	36.75	0.04	0.01	-	0.28	-	-	-	0.06	-	-	79.72
ISTE	Carb. serpentinite	44Z-1-41-46	Serpentine	Matrix	Bastite			40.56	0.01	1.36	0.56	2.68	0.07	33.65	0.05	0.01	-	0.69	-	-	-	0.10	-	-	79.75
ISTE	Carb. serpentinite	44Z-1-41-46	Serpentine	Matrix	Bastite			39.55	0.02	1.90	0.87	2.59	0.07	34.14	0.02	0.01	-	0.25	-	-	-	0.15	-	-	79.56
ISTE	Carb. serpentinite	44Z-1-41-46	Serpentine	Matrix	Bastite			42.05	-	2.03	0.58	3.11	0.09	33.14	0.05	0.01	0.01	0.31	-	-	-	0.05	-	-	81.45
ISTE	Carb. serpentinite	44Z-1-41-46	Serpentine	Vein	sc0			41.25	-	0.61	0.03	4.51	0.16	35.58	0.07	-	0.01	0.18	-	-	-	0.04	-	-	82.44
ISTE	Carb. serpentinite	44Z-1-41-46	Serpentine	Vein	sc0			42.38	-	0.55	0.00	1.63	0.10	37.24	0.04	0.01	-	0.22	-	-	-	0.07	-	-	82.23
GM	Carb. serpentinite	44Z-4-0-5	Serpentine	Matrix	Mesh			43.74	-	0.16	-	2.21	-	40.50	-	-	-	-	-	-	-	0.04	-	-	86.64
GM	Carb. serpentinite	44Z-4-0-5	Serpentine	Matrix	Mesh			44.77	-	0.30	-	3.10	-	39.60	0.10	-	-	-	-	-	-	0.05	-	-	87.92
GM	Carb. serpentinite	44Z-4-0-5	Serpentine	Matrix	Mesh			43.20	-	0.23	-	2.64	-	39.75	-	-	-	-	-	-	-	0.07	-	-	85.88
GM	Carb. serpentinite	44Z-4-0-5	Serpentine	Matrix	Mesh			44.47	-	0.33	-	2.76	-	39.28	0.10	-	-	-	-	-	-	0.05	-	-	86.99
GM	Carb. serpentinite	44Z-4-0-5	Serpentine	Matrix	Mesh			43.95	-	0.22	-	2.23	-	40.58	-	-	-	-	-	-	-	0.04	-	-	87.02
GM	Carb. serpentinite	44Z-4-0-5	Serpentine	Matrix	Mesh			44.45	-	0.25	-	3.79	-	39.58	0.09	-	-	-	-	-	-	0.05	-	-	88.20
GM	Carb. serpentinite	44Z-4-0-5	Serpentine	Matrix	Mesh			43.99	-	0.28	-	2.71	-	39.17	0.10	-	-	-	-	-	-	0.04	-	-	86.30
GM	Carb. serpentinite	44Z-4-0-5	Serpentine	Matrix	Mesh			46.39	-	0.31	-	3.58	-	36.88	-	-	-	-	-	-	-	0.04	-	-	87.19
GM	Carb. serpentinite	44Z-4-0-5	Serpentine	Matrix	Mesh			45.30	-	0.34	-	3.74	-	38.52	0.09	-	-	-	-	-	-	-	-	-	87.98
GM	Carb. serpentinite	44Z-4-0-5	Serpentine	Matrix	Mesh			42.49	-	0.28	-	5.30	-	38.00	-	-	-	-	-	-	-	0.04	-	-	86.11
GM	Carb. serpentinite	44Z-4-0-5	Serpentine	Matrix	Mesh			42.00	-	0.31	-	4.45	-	37.51	-	-	-	-	-	-	-	-	-	-	84.26
GM	Carb. serpentinite	44Z-4-0-5	Serpentine	Matrix	Mesh			42.72	-	0.32	-	4.79	-	38.02	-	-	-	-	-	-	-	0.04	-	-	85.89
GM	Carb. serpentinite	44Z-4-0-5	Serpentine	Matrix	Mesh			45.24	-	0.22	-	2.75	-	38.65	0.11	-	0.05	-	-	-	-	0.05	-	-	87.06
GM	Carb. serpentinite	44Z-4-0-5	Serpentine	Matrix	Mesh			45.80	-	0.25	-	2.83	-	38.26	0.08	-	-	-	-	-	-	0.04	-	-	87.26
GM	Carb. serpentinite	44Z-4-0-5	Serpentine	Matrix	Mesh			44.68	-	0.26	-	3.22	-	39.67	-	-	-	-	-	-	-	-	-	-	87.83
GM	Carb. serpentinite	44Z-4-0-5	Serpentine	Matrix	Mesh			43.65	-	0.27	-	3.73	-	38.69	0.07	-	0.04	-	-	-	-	0.05	-	-	86.50
ISTE	Carb. serpentinite	44Z-4-0-5	Serpentine	Matrix	Mesh			43.43	-	0.33	0.17	3.61	-	37.85	0.05	0.05	-	0.36	-	-	-	0.03	-	-	85.88
ISTE	Carb. serpentinite	44Z-4-0-5	Serpentine	Matrix	Mesh			43.35	-	0.34	0.08	1.83	-	35.94	0.05	0.06	-	0.43	-	-	-	0.03	-	-	82.11
ISTE	Carb. serpentinite	44Z-4-0-5	Serpentine	Matrix	Mesh			43.95	-	0.34	0.09	1.36	0.04	36.44	0.05	0.03	-	0.38	-	-	-	0.04	-	-	82.71
ISTE	Carb. serpentinite	44Z-4-0-5	Serpentine	Matrix	Mesh			43.88	0.03	0.32	0.05	2.96	0.03	36.37	0.05	0.03	-	0.23	-	-	-	0.05	-	-	84.00
GM	Carb. serpentinite	44Z-4-0-5	Serpentine	Matrix	Bastite			42.34	-	0.67	0.54	3.33	-	38.69	-	-	-	-	-	-	-	0.10	-	-	85.66
GM	Carb. serpentinite	44Z-4-0-5	Serpentine	Matrix	Bastite			41.95	-	0.68	0.51	3.78	-	38.46	-	-	-	-	-	-	-	0.13	-	-	85.50
GM	Carb. serpentinite	44Z-4-0-5	Serpentine	Matrix	Bastite			42.63	-	0.70	0.56	3.59	-	38.43	0.08	-	-	-	-	-	-	0.09	-	-	86.08
GM	Carb. serpentinite	44Z-4-0-5	Serpentine	Matrix	Bastite			42.19	-	0.63	0.64	3.30	-	38.72	-	-	-	-	-	-	-	0.10	-	-	85.57
GM	Carb. serpentinite	44Z-4-0-5	Serpentine	Matrix	Bastite			44.36	-	0.82	0.55	5.44	-	36.36	0.14	-	-	-	-	-	-	0.08	-	-	87.75
GM	Carb. serpentinite	44Z-4-0-5	Serpentine	Matrix	Bastite			49.96	-	0.57	0.48	4.17	-	31.50	-	-	-	-	-	-	-	0.05	-	-	86.72
GM	Carb. serpentinite	44Z-4-0-5	Serpentine	Matrix	Bastite			42.38	-	0.78	0.52	4.72	-	34.60	0.16	-	-	-	-	-	-	0.10	-	-	83.26
GM	Carb. serpentinite	44Z-4-0-5	Serpentine	Matrix	Bastite			44.31	-	0.82	0.58	5.21	-	34.30	0.12	-	-	-	-	-	-	0.08	-	-	85.41
ISTE	Carb. serpentinite	44Z-4-0-5	Serpentine	Matrix	Bastite			43.22	-	0.72	0.46	7.74	0.08	33.47	0.06	0.04	-	0.41	-	-	-	0.06	-	-	86.26
ISTE	Carb. serpentinite	44Z-4-0-5	Serpentine	Matrix	Bastite			42.05	0.03	0.68	0.49	4.72	0.12	33.59	0.08	0.07	-	0.41	-	-	-	0.05	-	-	82.29
GM	Carb. serpentinite	44Z-4-0-5	Serpentine	Vein	sc0	Median zone		43.30	-	0.36	-	1.99	-	39.04	-	-	-	-	-	-	-	0.08	-	-	84.77
GM	Carb. serpentinite	44Z-4-0-5	Serpentine	Vein	sc0	Median zone		44.16	-	0.32	-	2.01	-	39.17	-	-	-	-	-	-	-	0.07	-	-	85.73
GM	Carb. serpentinite	44Z-4-0-5	Serpentine	Vein	sc0	Median zone		43.87	-	0.33	-	2.25	-	38.85	-	-	-	-	-	-	-	-	-	-	85.31
GM	Carb. serpentinite	44Z-4-0-5	Serpentine	Vein	sc0	Median zone		43.80	-	0.23	-	2.38	-	38.20	-	-	-	-	-	-	-	-	-	-	84.62
GM	Carb. serpentinite	44Z-4-0-5	Serpentine	Vein	sc0	Median zone		43.13	-	0.22	-	2.95	-	39.09	-	-	-	-	-	-	-	-	-	-	85.39
GM	Carb. serpentinite	44Z-4-0-5	Serpentine	Vein	sc0	Median zone		43.16	-	0.25	-	2.95	-	38.89	-	-	-	-	-	-	-	-	-	-	85.24
GM	Carb. serpentinite	44Z-4-0-5	Serpentine	Vein	sc0	Median zone		44.10	-	0.23	-	2.50	-	39.31	-	-	-	-	-	-	-	-	-	-	86.14
GM	Carb. serpentinite	44Z-4-0-5	Serpentine	Vein	sc0	Median zone		43.26	-	0.20	-	2.65	-	39.58	-	-	-	-	-	-	-	-	-	-	85.69
GM	Carb. serpentinite	44Z-4-0-5	Serpentine	Vein	sc0	Median zone		43.87	-	0.32	-	2.60	-	38.63	0.08	-	-	-	-	-	-	-	-	-	85.51
GM	Carb. serpentinite	44Z-4-0-5	Serpentine	Vein	sc0	Median zone		43.17	-	0.28	-	2.37	-	38.16	0.08	-	-	-	-	-	-	-	-	-	84.07

GM	Carb. serpentinite	44Z-4-0-5	Serpentine	Vein	sc0	Median zone		43.77	-	0.27	-	2.47	-	38.93	-	-	-	-	-	-	-	-	-	-	-	85.44
ISTE	Carb. serpentinite	44Z-4-0-5	Serpentine	Vein	sc0	Median zone		44.33	-	0.33	-	2.31	0.07	39.33	0.04	0.04	-	0.26	-	-	-	0.04	-	-	86.76
ISTE	Carb. serpentinite	44Z-4-0-5	Serpentine	Vein	sc0	Median zone		43.98	-	0.59	0.23	4.03	-	36.07	0.06	0.07	-	0.50	-	-	-	0.03	-	-	85.56
ISTE	Carb. serpentinite	44Z-4-0-5	Serpentine	Vein	sc0	Median zone		42.83	-	0.27	-	2.19	0.05	37.95	0.02	-	-	0.27	-	-	-	0.05	-	-	83.62
ISTE	Carb. serpentinite	44Z-4-0-5	Serpentine	Vein	sc0	Median zone		43.84	-	0.34	-	2.38	0.09	38.86	0.04	0.03	-	0.36	-	-	-	0.05	-	-	86.00
ISTE	Carb. serpentinite	44Z-4-0-5	Serpentine	Vein	sc0	Median zone		43.93	-	0.32	-	2.09	0.07	38.22	0.04	0.02	-	0.27	-	-	-	0.05	-	-	85.00
ISTE	Carb. serpentinite	44Z-4-0-5	Serpentine	Vein	sc0	Median zone		44.97	-	0.34	-	2.13	0.06	39.19	0.01	-	-	0.16	-	-	-	0.04	-	-	86.91
ISTE	Carb. serpentinite	44Z-4-0-5	Serpentine	Vein	sc0	Median zone		43.69	-	0.25	-	2.60	0.07	37.39	0.05	0.03	-	0.15	-	-	-	0.02	-	-	84.24
ISTE	Carb. serpentinite	44Z-4-0-5	Serpentine	Vein	sc0	Median zone		44.30	-	0.23	-	1.61	0.10	38.41	-	0.03	-	0.15	-	-	-	0.01	-	-	84.85
GM	Carb. serpentinite	44Z-4-0-5	Serpentine	Vein	sc0	Rim	d	44.82	-	0.28	-	1.74	-	39.58	-	-	-	-	-	-	-	0.04	-	-	86.46
GM	Carb. serpentinite	44Z-4-0-5	Serpentine	Vein	sc0	Rim	d	44.32	-	0.29	-	1.85	-	40.25	-	-	-	-	-	-	-	0.06	-	-	86.77
GM	Carb. serpentinite	44Z-4-0-5	Serpentine	Vein	sc0	Rim	d	44.33	-	0.31	-	2.15	-	39.52	-	-	-	-	-	-	-	0.04	-	-	86.35
GM	Carb. serpentinite	44Z-4-0-5	Serpentine	Vein	sc0	Median zone	d	43.80	-	0.37	-	2.42	-	39.10	-	-	-	-	-	-	-	0.06	-	-	85.76
GM	Carb. serpentinite	44Z-4-0-5	Serpentine	Vein	sc0	Median zone	d	44.03	-	0.30	-	2.11	-	39.22	-	-	-	-	-	-	-	0.05	-	-	85.71
GM	Carb. serpentinite	44Z-4-0-5	Serpentine	Vein	sc0	Median zone	d	43.24	-	0.30	-	2.01	-	38.86	-	-	-	-	-	-	-	0.07	-	-	84.48
GM	Carb. serpentinite	44Z-4-0-5	Serpentine	Vein	sc0	Median zone	d	43.72	-	0.31	-	1.89	-	38.82	-	-	-	-	-	-	-	0.06	-	-	84.79
GM	Carb. serpentinite	44Z-4-0-5	Serpentine	Vein	sc0	Median zone	d	43.82	-	0.29	-	1.78	-	39.56	-	-	-	-	-	-	-	0.06	-	-	85.51
GM	Carb. serpentinite	44Z-4-0-5	Serpentine	Vein	sc0	Median zone	d	43.84	-	0.28	-	1.83	-	39.53	-	-	-	-	-	-	-	0.07	-	-	85.55
GM	Carb. serpentinite	44Z-4-0-5	Serpentine	Vein	sc0	Median zone	d	43.89	-	0.27	-	1.44	-	39.45	-	-	-	-	-	-	-	0.07	-	-	85.12
GM	Carb. serpentinite	44Z-4-0-5	Serpentine	Vein	sc0	Rim	d	45.11	-	0.30	-	3.58	-	38.32	0.09	-	-	-	-	-	-	0.05	-	-	87.45
GM	Carb. serpentinite	44Z-4-0-5	Serpentine	Vein	sc0	Rim	d	46.34	-	0.25	-	2.44	-	38.49	-	-	-	-	-	-	-	-	-	-	87.52
GM	Fu-listvenite	53Z-2-72-77	Fuchsite	Matrix				44.66	-	32.16	5.19	1.28	-	3.08	0.29	0.26	4.73	1.82	-	-	-	-	-	-	93.48
GM	Fu-listvenite	53Z-2-72-77	Fuchsite	Matrix				43.57	-	34.41	4.87	1.65	-	2.89	0.34	0.13	3.50	2.05	-	-	-	-	-	-	93.42
GM	Fu-listvenite	53Z-2-72-77	Fuchsite	Matrix				44.91	0.21	34.59	4.86	1.38	-	2.65	0.38	0.31	4.44	1.85	-	-	-	-	-	-	95.57
GM	Fu-listvenite	53Z-2-72-77	Fuchsite	Matrix				43.30	-	35.51	4.28	1.10	0.11	2.67	0.29	0.24	3.89	1.97	-	-	-	-	-	-	93.34
GM	Fu-listvenite	53Z-2-72-77	Fuchsite	Matrix				43.53	0.39	34.20	5.29	1.41	-	3.09	0.29	0.25	3.64	2.16	-	-	-	-	-	-	94.25
GM	Fu-listvenite	60Z-1-32-37	Fuchsite	Matrix				50.38	-	28.62	4.73	2.09	-	1.60	0.44	0.35	7.07	0.41	-	-	-	-	-	-	95.68
GM	Fu-listvenite	60Z-1-32-37	Fuchsite	Matrix				54.39	-	22.88	5.77	3.17	-	1.31	1.52	0.88	6.26	-	-	-	-	-	-	-	96.19
GM	Fu-listvenite	60Z-1-32-37	Fuchsite	Matrix				51.21	-	23.40	6.04	2.19	-	0.96	0.48	0.18	6.94	-	-	-	-	-	-	-	91.38
GM	Fu-listvenite	60Z-1-32-37	Fuchsite	Matrix				50.27	-	26.09	6.49	-	-	-	0.70	-	7.89	-	-	-	-	-	-	-	91.43
GM	Fu-listvenite	60Z-1-32-37	Fuchsite	Matrix				51.00	-	27.49	6.78	2.77	-	1.18	0.67	0.22	7.42	0.15		-	-	-	-	-	97.86
GM	Fu-listvenite	60Z-1-32-37	Fuchsite	Matrix				47.24	-	26.16	6.12	2.98	-	1.19	0.72	-	7.78	-	-	-	-	-	-	-	92.18
GM	Fu-listvenite	60Z-1-32-37	Fuchsite	Matrix				48.76	-	25.01	6.35	2.59	-	1.05	0.61	-	7.88	-	-	-	-	-	-	-	92.24
GM	Fu-listvenite	60Z-1-32-37	Fuchsite	Matrix				50.02	-	24.90	6.37	2.39	-	1.14	0.76	-	7.73	-	-	-	-	-	-	-	93.30
GM	Fu-listvenite	60Z-1-32-37	Fuchsite	Matrix				48.48	-	23.37	6.65	2.62	-	1.17	0.70	-	7.61	-	-	-	-	-	-	-	90.59
GM	Fu-listvenite	60Z-1-32-37	Fuchsite	Matrix				50.01	-	25.57	5.91	3.17	-	1.18	0.65	-	8.04	-	-	-	-	-	-	-	94.54
GM	Fu-listvenite	60Z-1-32-37	Fuchsite	Matrix				45.59	0.04	30.79	6.54	2.84	-	1.13	0.41	0.37	7.26	0.40	-	-	-	-	-	-	95.38
GM	Fu-listvenite	60Z-1-32-37	Fuchsite	Matrix				42.59	-	31.42	5.69	1.92	-	0.99	0.39	0.16	7.15	0.30	-	-	-	0.02	-	-	90.62

Table S5 (continued)

								Cations p.f.u. (7O formula for serpentine, 22O formula for fuchsite)																	
Facility	Lithology	Sample	Mineral	Structure	Texture[2]	Zone	Transect	Si	Ti	Al	Cr	Fe	Mn	Mg	Ca	Na	K	Ni	Cu	Zn	S	Cl	Ba	Sr	Total	Mg#	Cr#	Mg/Si
GM	Carb. serpentinite	43Z-2-43-48	Serpentine	Matrix	Mesh			2.03	-	0.02	-	0.10	-	2.82	-	-	-	-	-	-	-	0.00	-	-	4.97	97	-	1.39
GM	Carb. serpentinite	43Z-2-43-48	Serpentine	Matrix	Mesh			2.03	-	0.02	-	0.09	-	2.82	-	-	-	-	-	-	-	-	-	-	4.96	97	-	1.39
GM	Carb. serpentinite	43Z-2-43-48	Serpentine	Matrix	Mesh			2.04	-	0.02	-	0.10	-	2.79	-	-	-	-	-	-	-	-	-	-	4.95	97	-	1.37
GM	Carb. serpentinite	43Z-2-43-48	Serpentine	Matrix	Mesh			2.05	-	0.02	-	0.08	-	2.80	-	-	-	-	-	-	-	-	-	-	4.94	97	-	1.36
GM	Carb. serpentinite	43Z-2-43-48	Serpentine	Matrix	Mesh			2.03	-	0.02	-	0.08	-	2.83	-	-	-	-	-	-	-	0.00	-	-	4.96	97	-	1.39
GM	Carb. serpentinite	43Z-2-43-48	Serpentine	Matrix	Mesh			2.03	-	0.02	-	0.10	-	2.82	-	-	-	-	-	-	-	0.00	-	-	4.96	97	-	1.39
GM	Carb. serpentinite	43Z-2-43-48	Serpentine	Matrix	Mesh			2.02	-	0.02	-	0.10	-	2.83	-	-	-	-	-	-	-	0.00	-	-	4.97	97	-	1.40
GM	Carb. serpentinite	43Z-2-43-48	Serpentine	Matrix	Mesh			2.01	-	0.01	-	0.11	-	2.85	-	-	-	-	-	-	-	0.01	-	-	4.99	96	-	1.42
GM	Carb. serpentinite	43Z-2-43-48	Serpentine	Matrix	Mesh			2.03	-	0.01	-	0.10	-	2.81	-	-	-	-	-	-	-	0.00	-	-	4.96	96	-	1.38
GM	Carb. serpentinite	43Z-2-43-48	Serpentine	Matrix	Mesh			2.02	-	0.01	-	0.08	-	2.87	-	-	-	-	-	-	-	-	-	-	4.97	97	-	1.42
GM	Carb. serpentinite	43Z-2-43-48	Serpentine	Matrix	Mesh			2.02	-	0.01	-	0.08	-	2.87	-	-	-	-	-	-	-	0.00	-	-	4.98	97	-	1.42
GM	Carb. serpentinite	43Z-2-43-48	Serpentine	Matrix	Mesh			2.05	-	0.02	-	0.13	-	2.75	-	-	-	-	-	-	-	-	-	-	4.94	96	-	1.34
GM	Carb. serpentinite	43Z-2-43-48	Serpentine	Matrix	Mesh			2.02	-	0.02	-	0.17	-	2.76	-	-	-	-	-	-	-	0.00	-	-	4.97	94	-	1.37
GM	Carb. serpentinite	43Z-2-43-48	Serpentine	Matrix	Mesh			2.06	-	0.05	0.02	0.20	-	2.58	0.00	-	-	-	-	-	-	0.01	-	-	4.91	93	29	1.25
GM	Carb. serpentinite	43Z-2-43-48	Serpentine	Matrix	Mesh			2.01	-	0.02	-	0.17	-	2.78	0.01	-	-	-	-	-	-	-	-	-	4.98	94	-	1.38
GM	Carb. serpentinite	43Z-2-43-48	Serpentine	Matrix	Mesh			2.03	-	0.02	-	0.16	-	2.76	-	-	-	-	-	-	-	0.00	-	-	4.97	95	-	1.36
GM	Carb. serpentinite	43Z-2-43-48	Serpentine	Matrix	Mesh			2.04	-	0.02	-	0.14	-	2.76	-	-	-	-	-	-	-	-	-	-	4.95	95	-	1.35
GM	Carb. serpentinite	43Z-2-43-48	Serpentine	Matrix	Mesh			2.09	-	0.03	0.02	0.18	-	2.56	0.00	-	-	-	-	-	-	-	-	-	4.89	94	39	1.23
GM	Carb. serpentinite	43Z-2-43-48	Serpentine	Matrix	Mesh			2.02	-	0.01	-	0.09	-	2.84	-	-	-	-	-	-	-	0.01	-	-	4.98	97	-	1.40
GM	Carb. serpentinite	43Z-2-43-48	Serpentine	Matrix	Mesh			2.00	-	0.01	-	0.09	-	2.88	-	-	-	0.02	-	-	-	0.00	-	-	5.00	97	-	1.44
GM	Carb. serpentinite	43Z-2-43-48	Serpentine	Matrix	Mesh			2.06	-	0.01	-	0.08	-	2.79	-	-	-	-	-	-	-	-	-	-	4.94	97	-	1.36
GM	Carb. serpentinite	43Z-2-43-48	Serpentine	Matrix	Mesh			2.02	-	0.01	-	0.08	-	2.86	-	-	-	-	-	-	-	-	-	-	4.97	97	-	1.41
GM	Carb. serpentinite	43Z-2-43-48	Serpentine	Matrix	Mesh			2.02	-	0.01	-	0.09	-	2.84	-	-	-	-	-	-	-	0.01	-	-	4.98	97	-	1.41
GM	Carb. serpentinite	43Z-2-43-48	Serpentine	Matrix	Mesh			2.04	-	0.01	-	0.08	-	2.83	-	-	-	-	-	-	-	-	-	-	4.95	97	-	1.39
GM	Carb. serpentinite	43Z-2-43-48	Serpentine	Matrix	Bastite			2.03	-	0.05	0.03	0.13	-	2.68	-	-	-	-	-	-	-	0.01	-	-	4.93	95	35	1.32
GM	Carb. serpentinite	43Z-2-43-48	Serpentine	Matrix	Bastite			2.02	-	0.06	0.03	0.17	-	2.66	0.00	-	-	-	-	-	-	0.01	-	-	4.94	94	32	1.32
GM	Carb. serpentinite	43Z-2-43-48	Serpentine	Matrix	Bastite			2.02	-	0.06	0.03	0.15	-	2.68	0.00	-	-	-	-	-	-	0.01	-	-	4.94	95	31	1.32
GM	Carb. serpentinite	43Z-2-43-48	Serpentine	Matrix	Bastite			2.01	-	0.04	0.03	0.30	-	2.57	-	-	-	-	-	-	-	-	-	-	4.95	90	38	1.28
GM	Carb. serpentinite	43Z-2-43-48	Serpentine	Matrix	Bastite			2.02	-	0.04	0.03	0.29	-	2.57	-	-	-	-	-	-	-	-	-	-	4.95	90	42	1.27
GM	Carb. serpentinite	43Z-2-43-48	Serpentine	Matrix	Bastite			2.02	-	0.04	0.03	0.34	-	2.51	-	-	-	-	-	-	-	-	-	-	4.94	88	48	1.24
GM	Carb. serpentinite	43Z-2-43-48	Serpentine	Matrix	Bastite			2.00	-	0.03	0.04	0.34	-	2.56	-	-	-	-	-	-	-	-	-	-	4.97	88	54	1.28
GM	Carb. serpentinite	43Z-2-43-48	Serpentine	Matrix	Bastite			2.01	-	0.05	0.04	0.31	-	2.53	-	-	-	-	-	-	-	0.00	-	-	4.95	89	42	1.26
GM	Carb. serpentinite	43Z-2-43-48	Serpentine	Matrix	Bastite			2.00	-	0.05	0.03	0.27	-	2.60	-	-	-	-	-	-	-	-	-	-	4.96	90	39	1.30
GM	Carb. serpentinite	43Z-2-43-48	Serpentine	Matrix	Bastite			2.03	-	0.04	0.03	0.27	-	2.56	-	-	-	-	-	-	-	-	-	-	4.94	90	45	1.26
GM	Carb. serpentinite	43Z-2-43-48	Serpentine	Matrix	Bastite			2.01	-	0.04	0.03	0.25	-	2.60	0.00	-	-	-	-	-	-	0.00	-	-	4.95	91	44	1.29
GM	Carb. serpentinite	43Z-2-43-48	Serpentine	Matrix	Bastite			2.04	-	0.03	0.02	0.18	-	2.65	0.01	-	-	-	-	-	-	0.00	-	-	4.94	94	40	1.30
GM	Carb. serpentinite	43Z-2-43-48	Serpentine	Matrix	Bastite			2.01	-	0.03	0.02	0.22	-	2.66	0.01	-	-	0.02	-	-	-	0.01	-	-	4.97	92	44	1.32
GM	Carb. serpentinite	43Z-2-43-48	Serpentine	Matrix	Bastite			2.04	-	0.02	0.02	0.21	-	2.65	0.01	-	-	-	-	-	-	0.00	-	-	4.94	93	45	1.30
GM	Carb. serpentinite	43Z-2-43-48	Serpentine	Matrix	Bastite			2.07	-	0.03	0.01	0.19	-	2.60	0.01	-	-	-	-	-	-	0.00	-	-	4.91	93	29	1.26
GM	Carb. serpentinite	43Z-2-43-48	Serpentine	Matrix	Bastite			2.08	-	0.04	0.01	0.21	-	2.54	0.01	-	-	-	-	-	-	-	-	-	4.89	92	26	1.22
GM	Carb. serpentinite	43Z-2-43-48	Serpentine	Matrix	Bastite			2.09	-	0.03	0.01	0.18	-	2.56	0.01	-	-	-	-	-	-	0.00	-	-	4.89	93	29	1.22
GM	Carb. serpentinite	43Z-2-43-48	Serpentine	Matrix	Bastite			2.06	-	0.03	0.02	0.19	-	2.60	0.01	-	-	-	-	-	-	0.00	-	-	4.91	93	37	1.26
GM	Carb. serpentinite	43Z-2-43-48	Serpentine	Matrix	Bastite			2.06	-	0.03	0.02	0.20	-	2.60	0.01	-	-	-	-	-	-	0.00	-	-	4.92	93	37	1.26
GM	Carb. serpentinite	43Z-2-43-48	Serpentine	Matrix	Bastite			2.04	-	0.03	0.02	0.24	-	2.60	0.01	-	-	-	-	-	-	0.00	-	-	4.94	91	37	1.27
GM	Carb. serpentinite	43Z-2-43-48	Serpentine	Vein	sc0	Median zone		2.03	-	0.02	-	0.10	-	2.80	0.01	-	-	-	-	-	-	0.00	-	-	4.96	97	-	1.38
GM	Carb. serpentinite	43Z-2-43-48	Serpentine	Vein	sc0	Median zone		2.02	-	0.02	-	0.09	-	2.83	0.01	-	0.00	-	-	-	-	0.01	-	-	4.98	97	-	1.40

GM	Carb. serpentinite	43Z-2-43-48	Serpentine	Vein	sc0	Median zone		2.03	-	0.02	-	0.08	-	2.82	0.01	-	-	-	-	-	-	0.01	-	-	4.97	97	-	1.39
GM	Carb. serpentinite	43Z-2-43-48	Serpentine	Vein	sc0	Rim		2.03	-	0.02	-	0.09	-	2.81	0.01	-	-	-	-	-	-	0.00	-	-	4.96	97	-	1.38
GM	Carb. serpentinite	43Z-2-43-48	Serpentine	Vein	sc0	Rim		2.04	-	0.02	-	0.08	-	2.79	0.01	-	-	-	-	-	-	0.01	-	-	4.95	97	-	1.37
GM	Carb. serpentinite	43Z-2-43-48	Serpentine	Vein	sc0	Rim		2.04	-	0.02	-	0.09	-	2.78	0.01	-	-	-	-	-	-	0.01	-	-	4.95	97	-	1.36
GM	Carb. serpentinite	43Z-2-43-48	Serpentine	Vein	sc0	Rim		2.05	-	0.02	-	0.08	-	2.80	0.01	-	-	-	-	-	-	0.00	-	-	4.95	97	-	1.37
GM	Carb. serpentinite	43Z-3-0-5	Serpentine	Matrix	Mesh			2.09	-	0.02	-	0.17	-	2.62	0.01	-	-	-	-	-	-	-	-	-	4.90	94	-	1.25
GM	Carb. serpentinite	43Z-3-0-5	Serpentine	Matrix	Mesh			2.06	-	0.01	-	0.17	-	2.68	0.01	-	-	-	-	-	-	-	-	-	4.93	94	-	1.30
GM	Carb. serpentinite	43Z-3-0-5	Serpentine	Matrix	Mesh			2.09	-	0.01	-	0.16	-	2.63	0.01	-	-	-	-	-	-	-	-	-	4.90	94	-	1.26
GM	Carb. serpentinite	43Z-3-0-5	Serpentine	Matrix	Mesh			2.08	-	0.03	0.01	0.20	-	2.56	0.01	-	-	-	-	-	-	0.00	-	-	4.90	93	28	1.23
GM	Carb. serpentinite	43Z-3-0-5	Serpentine	Matrix	Mesh			2.06	-	0.01	-	0.14	-	2.73	0.00	-	-	-	-	-	-	-	-	-	4.94	95	-	1.33
GM	Carb. serpentinite	43Z-3-0-5	Serpentine	Matrix	Mesh			2.04	-	0.01	-	0.18	-	2.72	0.00	-	-	-	-	-	-	-	-	-	4.96	94	-	1.34
GM	Carb. serpentinite	43Z-3-0-5	Serpentine	Matrix	Mesh			2.02	-	0.01	-	0.23	-	2.71	0.00	-	-	-	-	-	-	-	-	-	4.97	92	-	1.34
GM	Carb. serpentinite	43Z-3-0-5	Serpentine	Matrix	Bastite			2.04	-	0.03	0.02	0.18	-	2.65	0.01	-	-	-	-	-	-	0.00	-	-	4.94	94	40	1.30
GM	Carb. serpentinite	43Z-3-0-5	Serpentine	Matrix	Bastite			2.01	-	0.03	0.02	0.22	-	2.66	0.01	-	-	0.02	-	-	-	0.01	-	-	4.97	92	44	1.32
GM	Carb. serpentinite	43Z-3-0-5	Serpentine	Matrix	Bastite			2.04	-	0.02	0.02	0.21	-	2.65	0.01	-	-	-	-	-	-	0.00	-	-	4.94	93	45	1.30
GM	Carb. serpentinite	43Z-3-0-5	Serpentine	Matrix	Bastite			2.07	-	0.03	0.01	0.19	-	2.60	0.01	-	-	-	-	-	-	0.00	-	-	4.91	93	29	1.26
GM	Carb. serpentinite	43Z-3-0-5	Serpentine	Matrix	Bastite			2.08	-	0.04	0.01	0.21	-	2.54	0.01	-	-	-	-	-	-	-	-	-	4.89	92	26	1.22
GM	Carb. serpentinite	43Z-3-0-5	Serpentine	Matrix	Bastite			2.09	-	0.03	0.01	0.18	-	2.56	0.01	-	-	-	-	-	-	0.00	-	-	4.89	93	29	1.22
GM	Carb. serpentinite	43Z-3-0-5	Serpentine	Matrix	Bastite			2.06	-	0.03	0.02	0.19	-	2.60	0.01	-	-	-	-	-	-	0.00	-	-	4.91	93	37	1.26
GM	Carb. serpentinite	43Z-3-0-5	Serpentine	Matrix	Bastite			2.06	-	0.03	0.02	0.20	-	2.60	0.01	-	-	-	-	-	-	0.00	-	-	4.92	93	37	1.26
GM	Carb. serpentinite	43Z-3-0-5	Serpentine	Matrix	Bastite			2.04	-	0.03	0.02	0.24	-	2.60	0.01	-	-	-	-	-	-	0.00	-	-	4.94	91	37	1.27
GM	Carb. serpentinite	43Z-3-0-5	Serpentine	Vein	ss1	Median zone		2.05	-	0.01	-	0.04	-	2.85	-	-	-	-	-	-	-	-	-	-	4.95	98	-	1.39
GM	Carb. serpentinite	43Z-3-0-5	Serpentine	Vein	ss1	Median zone		2.05	-	0.01	-	0.04	-	2.85	-	-	-	-	-	-	-	-	-	-	4.95	99	-	1.39
GM	Carb. serpentinite	43Z-3-0-5	Serpentine	Vein	ss1	Median zone		2.05	-	0.01	0.01	0.06	-	2.81	-	-	-	-	-	-	-	-	-	-	4.94	98	48	1.38
GM	Carb. serpentinite	43Z-3-0-5	Serpentine	Vein	ss1	Rim		2.05	-	0.01	-	0.05	-	2.84	-	-	-	-	-	-	-	0.00	-	-	4.95	98	-	1.39
GM	Carb. serpentinite	43Z-3-0-5	Serpentine	Vein	ss1	Rim		2.05	-	0.01	-	0.04	-	2.84	0.00	-	-	-	-	-	-	-	-	-	4.95	98	-	1.39
GM	Carb. serpentinite	43Z-3-52-57	Serpentine	Matrix	Mesh			2.04	-	0.01	-	0.10	-	2.81	0.00	-	-	-	-	-	-	-	-	-	4.96	97	-	1.38
GM	Carb. serpentinite	43Z-3-52-57	Serpentine	Matrix	Mesh			2.05	-	0.01	-	0.08	-	2.80	0.01	-	-	-	-	-	-	-	-	-	4.95	97	-	1.37
GM	Carb. serpentinite	43Z-3-52-57	Serpentine	Matrix	Mesh			2.05	-	0.02	-	0.09	-	2.79	-	-	-	-	-	-	-	-	-	-	4.95	97	-	1.36
GM	Carb. serpentinite	43Z-3-52-57	Serpentine	Matrix	Mesh			2.05	-	0.01	-	0.08	-	2.79	0.00	-	-	-	-	-	-	-	-	-	4.94	97	-	1.36
GM	Carb. serpentinite	43Z-3-52-57	Serpentine	Matrix	Mesh			2.06	-	0.02	-	0.10	-	2.75	0.00	-	-	-	-	-	-	-	-	-	4.93	96	-	1.33
GM	Carb. serpentinite	43Z-3-52-57	Serpentine	Matrix	Mesh			2.03	-	0.02	-	0.10	-	2.82	-	-	-	-	-	-	-	0.00	-	-	4.97	97	-	1.39
GM	Carb. serpentinite	43Z-3-52-57	Serpentine	Matrix	Mesh			2.05	-	0.01	-	0.08	-	2.78	0.00	-	-	-	-	-	-	0.00	-	-	4.94	97	-	1.36
GM	Carb. serpentinite	43Z-3-52-57	Serpentine	Matrix	Mesh			2.04	-	0.04	0.02	0.16	-	2.64	0.02	-	-	-	-	-	-	0.01	-	-	4.94	94	33	1.30
GM	Carb. serpentinite	43Z-3-52-57	Serpentine	Matrix	Mesh			2.04	-	0.02	-	0.11	-	2.78	0.00	-	-	-	-	-	-	-	-	-	4.95	96	-	1.36
GM	Carb. serpentinite	43Z-3-52-57	Serpentine	Matrix	Mesh			2.02	-	0.02	0.02	0.12	-	2.79	0.00	-	-	-	-	-	-	0.00	-	-	4.97	96	47	1.38
GM	Carb. serpentinite	43Z-3-52-57	Serpentine	Matrix	Mesh			2.05	-	0.02	-	0.06	-	2.80	-	-	-	-	-	-	-	-	-	-	4.94	98	-	1.37
GM	Carb. serpentinite	43Z-3-52-57	Serpentine	Matrix	Mesh			2.05	-	0.02	-	0.09	-	2.79	0.00	-	-	-	-	-	-	0.00	-	-	4.95	97	-	1.37
GM	Carb. serpentinite	43Z-3-52-57	Serpentine	Matrix	Mesh			2.04	-	0.02	-	0.10	-	2.79	0.00	-	-	-	-	-	-	0.00	-	-	4.96	97	-	1.37
GM	Carb. serpentinite	43Z-3-52-57	Serpentine	Matrix	Mesh			2.04	-	0.02	-	0.09	-	2.80	0.00	-	-	-	-	-	-	-	-	-	4.95	97	-	1.37
GM	Carb. serpentinite	43Z-3-52-57	Serpentine	Matrix	Mesh			2.04	-	0.01	-	0.12	-	2.79	-	-	-	-	-	-	-	-	-	-	4.96	96	-	1.37
GM	Carb. serpentinite	43Z-3-52-57	Serpentine	Matrix	Mesh			2.03	-	0.01	-	0.11	-	2.80	-	-	-	-	-	-	-	0.00	-	-	4.96	96	-	1.38
GM	Carb. serpentinite	43Z-3-52-57	Serpentine	Matrix	Mesh			2.03	-	0.01	-	0.12	-	2.80	-	-	-	-	-	-	-	-	-	-	4.96	96	-	1.38
GM	Carb. serpentinite	43Z-3-52-57	Serpentine	Matrix	Mesh			2.05	-	0.01	-	0.10	-	2.78	-	-	-	-	-	-	-	-	-	-	4.94	97	-	1.36
GM	Carb. serpentinite	43Z-3-52-57	Serpentine	Matrix	Bastite			2.05	-	0.04	0.02	0.18	-	2.63	0.01	-	-	-	-	-	-	0.00	-	-	4.93	94	34	1.28
GM	Carb. serpentinite	43Z-3-52-57	Serpentine	Matrix	Bastite			2.06	-	0.04	0.02	0.18	-	2.61	0.01	-	-	-	-	-	-	0.00	-	-	4.92	94	28	1.27
GM	Carb. serpentinite	43Z-3-52-57	Serpentine	Matrix	Bastite			2.09	-	0.04	0.02	0.16	-	2.57	0.01	-	-	-	-	-	-	0.00	-	-	4.89	94	33	1.23
GM	Carb. serpentinite	43Z-3-52-57	Serpentine	Vein	sc0	Rim		2.06	-	0.02	-	0.09	-	2.75	0.00	-	-	-	-	-	-	-	-	-	4.93	97	-	1.33
GM	Carb. serpentinite	43Z-3-52-57	Serpentine	Vein	sc0	Rim		2.05	-	0.01	-	0.07	-	2.80	-	-	-	-	-	-	-	-	-	-	4.94	97	-	1.37
GM	Carb. serpentinite	43Z-3-52-57	Serpentine	Vein	sc0	Median zone	a	2.05	-	0.01	-	0.08	-	2.79	-	-	-	-	-	-	-	0.00	-	-	4.94	97	-	1.36
GM	Carb. serpentinite	43Z-3-52-57	Serpentine	Vein	sc0	Median zone	a	2.03	-	0.02	-	0.09	-	2.81	0.00	-	-	-	-	-	-	-	-	-	4.96	97	-	1.38
GM	Carb. serpentinite	43Z-3-52-57	Serpentine	Vein	sc0	Median zone	a	2.05	-	0.01	-	0.08	-	2.81	-	-	-	-	-	-	-	-	-	-	4.95	97	-	1.37

GM	Carb. serpentinite	43Z-3-52-57	Serpentine	Vein	sc0	Median zone	a	2.06	-	0.02	-	0.08	-	2.78	-	-	-	-	-	-	-	-	-	4.93	97	-	1.35
GM	Carb. serpentinite	43Z-3-52-57	Serpentine	Vein	sc0	Median zone	a	2.06	-	0.02	-	0.08	-	2.77	-	-	-	-	-	-	-	-	-	4.93	97	-	1.35
GM	Carb. serpentinite	43Z-3-52-57	Serpentine	Vein	sc0	Median zone	a	2.04	-	0.01	-	0.07	-	2.82	-	-	-	-	-	-	-	-	-	4.95	98	-	1.38
GM	Carb. serpentinite	43Z-3-52-57	Serpentine	Vein	sc0	Rim		2.06	-	0.02	-	0.09	-	2.75	0.00	-	-	-	-	-	-	-	-	4.93	97	-	1.33
GM	Carb. serpentinite	43Z-3-52-57	Serpentine	Vein	sc0	Rim		2.05	-	0.01	-	0.07	-	2.80	-	-	-	-	-	-	-	-	-	4.94	97	-	1.37
GM	Carb. serpentinite	43Z-3-52-57	Serpentine	Vein	sc0	Rim		2.05	-	0.01	-	0.08	-	2.80	0.00	-	-	-	-	-	-	-	-	4.94	97	-	1.37
GM	Carb. serpentinite	43Z-3-52-57	Serpentine	Vein	sc0	Rim		2.05	-	0.01	-	0.08	-	2.79	0.00	-	-	-	-	-	-	-	-	4.94	97	-	1.36
GM	Carb. serpentinite	43Z-3-52-57	Serpentine	Vein	sc0	Median zone		2.08	-	0.03	0.01	0.19	-	2.59	0.01	-	-	-	-	-	-	-	-	4.90	93	31	1.25
GM	Carb. serpentinite	43Z-3-52-57	Serpentine	Vein	sc0	Median zone		2.05	-	0.04	0.01	0.13	-	2.67	0.01	-	-	-	-	-	-	0.01	-	4.93	95	25	1.30
GM	Carb. serpentinite	43Z-3-52-57	Serpentine	Vein	sc0	Median zone		2.08	-	0.04	0.01	0.12	-	2.63	0.01	-	-	-	-	-	-	0.00	-	4.90	96	25	1.26
GM	Carb. serpentinite	43Z-3-52-57	Serpentine	Vein	sc0	Median zone	b	2.03	-	0.02	-	0.11	-	2.80	-	-	-	-	-	-	-	-	-	4.96	96	-	1.38
GM	Carb. serpentinite	43Z-3-52-57	Serpentine	Vein	sc0	Median zone	b	2.04	-	0.01	-	0.10	-	2.79	-	-	-	-	-	-	-	-	-	4.95	97	-	1.37
GM	Carb. serpentinite	43Z-3-52-57	Serpentine	Vein	sc0	Median zone	b	2.04	-	0.02	-	0.08	-	2.80	0.00	-	-	-	-	-	-	0.00	-	4.95	97	-	1.37
GM	Carb. serpentinite	43Z-3-52-57	Serpentine	Vein	sc0	Median zone	b	2.06	-	0.01	-	0.08	-	2.79	-	-	-	-	-	-	-	-	-	4.94	97	-	1.36
GM	Carb. serpentinite	43Z-3-52-57	Serpentine	Vein	sc0	Median zone	b	2.05	-	0.02	-	0.08	-	2.80	-	-	-	-	-	-	-	-	-	4.94	97	-	1.37
GM	Carb. serpentinite	43Z-3-52-57	Serpentine	Vein	sc0	Median zone	b	2.07	-	0.01	-	0.07	-	2.76	-	-	-	-	-	-	-	-	-	4.92	97	-	1.33
GM	Carb. serpentinite	43Z-3-52-57	Serpentine	Vein	sc0	Median zone	b	2.04	-	0.02	-	0.09	-	2.80	-	-	-	-	-	-	-	-	-	4.95	97	-	1.37
GM	Carb. serpentinite	43Z-3-52-57	Serpentine	Vein	sc0	Median zone	b	2.06	-	0.02	-	0.08	-	2.78	-	-	-	-	-	-	-	-	-	4.93	97	-	1.35
GM	Carb. serpentinite	43Z-4-52-57	Serpentine	Matrix	Mesh			2.06	-	0.01	-	0.09	-	2.79	-	-	-	-	-	-	-	-	-	4.94	97	-	1.36
GM	Carb. serpentinite	43Z-4-52-57	Serpentine	Matrix	Mesh			2.03	-	-	-	0.12	-	2.82	0.00	-	-	-	-	-	-	-	-	4.97	96	n.d.	1.39
GM	Carb. serpentinite	43Z-4-52-57	Serpentine	Matrix	Mesh			2.04	-	-	-	0.11	-	2.81	-	-	-	-	-	-	-	-	-	4.96	96	n.d.	1.38
GM	Carb. serpentinite	43Z-4-52-57	Serpentine	Matrix	Mesh			2.04	-	-	-	0.10	-	2.82	-	-	-	-	-	-	-	-	-	4.96	97	n.d.	1.38
GM	Carb. serpentinite	43Z-4-52-57	Serpentine	Matrix	Mesh			2.03	-	-	-	0.10	-	2.83	-	-	-	-	-	-	-	-	-	4.97	97	n.d.	1.39
GM	Carb. serpentinite	43Z-4-52-57	Serpentine	Matrix	Mesh			2.05	-	-	-	0.13	-	2.77	-	-	-	-	-	-	-	-	-	4.95	96	n.d.	1.35
GM	Carb. serpentinite	43Z-4-52-57	Serpentine	Matrix	Bastite			2.06	-	0.04	0.03	0.18	-	2.61	-	-	-	-	-	-	-	-	-	4.91	94	43	1.27
GM	Carb. serpentinite	43Z-4-52-57	Serpentine	Matrix	Bastite			2.05	-	0.02	0.03	0.19	-	2.64	-	-	-	-	-	-	-	-	-	4.93	93	62	1.29
GM	Carb. serpentinite	43Z-4-52-57	Serpentine	Matrix	Bastite			2.04	-	0.04	0.03	0.20	-	2.60	0.01	-	-	0.02	-	-	-	-	-	4.93	93	38	1.28
GM	Carb. serpentinite	43Z-4-52-57	Serpentine	Vein	sc0	Median zone		2.07	-	0.01	-	0.04	-	2.81	-	-	-	-	-	-	-	-	-	4.93	98	-	1.36
GM	Carb. serpentinite	43Z-4-52-57	Serpentine	Vein	sc0	Median zone		2.06	-	0.01	-	0.10	-	2.76	-	-	-	-	-	-	-	-	-	4.93	96	-	1.34
GM	Carb. serpentinite	43Z-4-52-57	Serpentine	Vein	sc0	Median zone		2.06	-	0.01	-	0.10	-	2.76	-	-	-	-	-	-	-	-	-	4.93	97	-	1.34
GM	Carb. serpentinite	43Z-4-52-57	Serpentine	Vein	sc0	Rim	c	2.05	-	0.01	-	0.05	-	2.85	-	-	-	-	-	-	-	-	-	4.95	98	-	1.39
GM	Carb. serpentinite	43Z-4-52-57	Serpentine	Vein	sc0	Rim	c	2.05	-	0.01	-	0.05	-	2.84	-	-	-	-	-	-	-	-	-	4.94	98	-	1.38
GM	Carb. serpentinite	43Z-4-52-57	Serpentine	Vein	sc0	Rim	c	2.05	-	0.01	-	0.05	-	2.84	-	-	-	-	-	-	-	-	-	4.95	98	-	1.39
GM	Carb. serpentinite	43Z-4-52-57	Serpentine	Vein	sc0	Rim	c	2.04	-	0.01	-	0.07	-	2.84	-	-	-	-	-	-	-	-	-	4.95	98	-	1.39
GM	Carb. serpentinite	43Z-4-52-57	Serpentine	Vein	sc0	Median zone	c	2.03	-	-	-	0.07	-	2.87	0.00	-	-	-	-	-	-	-	-	4.97	98	n.d.	1.41
GM	Carb. serpentinite	43Z-4-52-57	Serpentine	Vein	sc0	Median zone	c	2.03	-	-	-	0.06	-	2.87	-	-	-	-	-	-	-	-	-	4.97	98	n.d.	1.41
GM	Carb. serpentinite	43Z-4-52-57	Serpentine	Vein	sc0	Median zone	c	2.04	-	0.01	-	0.06	-	2.85	0.01	-	-	-	-	-	-	-	-	4.96	98	-	1.40
GM	Carb. serpentinite	43Z-4-52-57	Serpentine	Vein	sc0	Median zone	c	2.04	-	-	-	0.07	-	2.85	-	-	-	-	-	-	-	-	-	4.96	98	n.d.	1.40
GM	Carb. serpentinite	43Z-4-52-57	Serpentine	Vein	sc0	Median zone	c	2.04	-	0.01	-	0.06	-	2.84	-	-	-	-	-	-	-	-	-	4.96	98	-	1.39
GM	Carb. serpentinite	43Z-4-52-57	Serpentine	Vein	sc0	Median zone	c	2.03	-	-	-	0.09	-	2.85	-	-	-	-	-	-	-	-	-	4.97	97	n.d.	1.40
GM	Carb. serpentinite	43Z-4-52-57	Serpentine	Vein	sc0	Median zone	c	2.01	-	-	-	0.06	-	2.93	-	-	-	-	-	-	-	-	-	4.99	98	n.d.	1.46
GM	Carb. serpentinite	43Z-4-52-57	Serpentine	Vein	sc0	Median zone	c	2.03	-	0.01	-	0.07	-	2.85	-	-	-	-	-	-	-	-	-	4.96	98	-	1.40
GM	Carb. serpentinite	43Z-4-52-57	Serpentine	Vein	sc0	Median zone	c	2.03	-	-	-	0.08	-	2.86	-	-	-	-	-	-	-	-	-	4.97	97	n.d.	1.40
GM	Carb. serpentinite	43Z-4-52-57	Serpentine	Vein	sc0	Median zone	c	2.04	-	0.01	-	0.08	-	2.83	-	-	-	-	-	-	-	-	-	4.96	97	-	1.39
GM	Carb. serpentinite	43Z-4-52-57	Serpentine	Vein	sc0	Median zone	c	2.03	-	-	-	0.09	-	2.85	-	-	-	-	-	-	-	-	-	4.97	97	n.d.	1.41
GM	Carb. serpentinite	43Z-4-52-57	Serpentine	Vein	sc0	Median zone	c	2.03	-	-	-	0.08	-	2.86	-	-	-	-	-	-	-	-	-	4.97	97	n.d.	1.40
GM	Carb. serpentinite	43Z-4-52-57	Serpentine	Vein	sc0	Median zone	c	2.03	-	0.01	-	0.07	-	2.85	-	-	-	-	-	-	-	-	-	4.96	98	-	1.40
GM	Carb. serpentinite	43Z-4-52-57	Serpentine	Vein	sc0	Median zone	c	2.04	-	0.01	-	0.07	-	2.85	-	-	-	-	-	-	-	-	-	4.96	98	-	1.40
GM	Carb. serpentinite	43Z-4-52-57	Serpentine	Vein	sc0	Median zone	c	2.03	-	0.01	-	0.08	-	2.85	-	-	-	-	-	-	-	-	-	4.96	97	-	1.40
GM	Carb. serpentinite	43Z-4-52-57	Serpentine	Vein	sc0	Median zone	c	2.02	-	-	-	0.09	-	2.85	0.02	-	-	-	-	-	-	-	-	4.98	97	n.d.	1.41
GM	Carb. serpentinite	43Z-4-52-57	Serpentine	Vein	sc0	Median zone	c	2.04	-	0.01	-	0.09	-	2.83	-	-	-	-	-	-	-	-	-	4.96	97	-	1.39
GM	Carb. serpentinite	43Z-4-52-57	Serpentine	Vein	sc0	Median zone	c	2.04	-	-	-	0.10	-	2.82	-	-	-	-	-	-	-	-	-	4.96	96	n.d.	1.38

GM	Carb. serpentinite	43Z-4-52-57	Serpentine	Vein	sc0	Median zone	c	2.04	-	-	-	0.06	-	2.85	-	-	-	-	-	-	-	-	-	-	4.96	98	n.d.	1.40
GM	Carb. serpentinite	43Z-4-52-57	Serpentine	Vein	sc0	Median zone	c	2.04	-	-	-	0.09	-	2.83	-	-	-	-	-	-	-	-	-	-	4.96	97	n.d.	1.38
GM	Carb. serpentinite	43Z-4-52-57	Serpentine	Vein	sc0	Rim	c	2.05	-	0.01	-	0.07	-	2.82	-	-	-	-	-	-	-	-	-	-	4.95	98	-	1.38
GM	Carb. serpentinite	43Z-4-52-57	Serpentine	Vein	sc0	Rim	c	2.05	-	0.01	-	0.05	-	2.83	-	-	-	-	-	-	-	-	-	-	4.94	98	-	1.38
GM	Carb. serpentinite	43Z-4-52-57	Serpentine	Vein	sc0	Rim	c	2.04	-	0.01	-	0.05	-	2.85	-	-	-	-	-	-	-	-	-	-	4.95	98	-	1.40
GM	Carb. serpentinite	43Z-4-52-57	Serpentine	Vein	sc0	Median zone		2.06	-	0.01	-	0.10	-	2.76	-	-	-	-	-	-	-	-	-	-	4.93	96	-	1.34
GM	Carb. serpentinite	43Z-4-52-57	Serpentine	Vein	sc0	Median zone		2.06	-	0.01	-	0.10	-	2.76	-	-	-	-	-	-	-	-	-	-	4.93	97	-	1.34
ISTE	Carb. serpentinite	44Z-1-41-46	Serpentine	Matrix	Mesh			2.03	0.00	0.02	0.00	0.11	0.00	2.77	0.00	0.00	-	0.01	-	-	-	0.00	-	-	4.96	1	0	1.37
ISTE	Carb. serpentinite	44Z-1-41-46	Serpentine	Matrix	Mesh			2.07	-	0.02	0.00	0.04	0.00	2.77	0.00	0.00	0.00	0.01	-	-	-	0.00	-	-	4.92	1	0	1.34
ISTE	Carb. serpentinite	44Z-1-41-46	Serpentine	Matrix	Mesh			2.05	-	0.02	0.00	0.06	0.00	2.80	0.00	-	-	0.01	-	-	-	0.00	-	-	4.94	1	0	1.36
ISTE	Carb. serpentinite	44Z-1-41-46	Serpentine	Matrix	Mesh			2.04	-	0.02	0.00	0.08	0.00	2.78	0.00	0.00	-	0.01	-	-	-	0.01	-	-	4.95	1	0	1.36
ISTE	Carb. serpentinite	44Z-1-41-46	Serpentine	Matrix	Bastite			2.07	0.00	0.08	0.02	0.11	0.00	2.56	0.00	0.00	-	0.03	-	-	-	0.01	-	-	4.89	1	0	1.24
ISTE	Carb. serpentinite	44Z-1-41-46	Serpentine	Matrix	Bastite			2.02	0.00	0.11	0.03	0.11	0.00	2.60	0.00	0.00	-	0.01	-	-	-	0.01	-	-	4.91	1	0	1.29
ISTE	Carb. serpentinite	44Z-1-41-46	Serpentine	Matrix	Bastite			2.09	-	0.12	0.02	0.13	0.00	2.46	0.00	0.00	0.00	0.01	-	-	-	0.00	-	-	4.84	1	0	1.17
ISTE	Carb. serpentinite	44Z-1-41-46	Serpentine	Vein	sc0			2.05	-	0.04	0.00	0.19	0.01	2.64	0.00	-	0.00	0.01	-	-	-	0.00	-	-	4.93	1	0	1.29
ISTE	Carb. serpentinite	44Z-1-41-46	Serpentine	Vein	sc0			2.08	-	0.03	0.00	0.07	0.00	2.72	0.00	0.00	-	0.01	-	-	-	0.01	-	-	4.91	1	0	1.31
GM	Carb. serpentinite	44Z-4-0-5	Serpentine	Matrix	Mesh			2.04	-	0.01	-	0.09	-	2.82	-	-	-	-	-	-	-	0.00	-	-	4.96	97	-	1.38
GM	Carb. serpentinite	44Z-4-0-5	Serpentine	Matrix	Mesh			2.06	-	0.02	-	0.12	-	2.72	0.01	-	-	-	-	-	-	0.00	-	-	4.93	96	-	1.32
GM	Carb. serpentinite	44Z-4-0-5	Serpentine	Matrix	Mesh			2.04	-	0.01	-	0.10	-	2.80	-	-	-	-	-	-	-	0.01	-	-	4.96	96	-	1.37
GM	Carb. serpentinite	44Z-4-0-5	Serpentine	Matrix	Mesh			2.07	-	0.02	-	0.11	-	2.72	0.00	-	-	-	-	-	-	0.00	-	-	4.93	96	-	1.32
GM	Carb. serpentinite	44Z-4-0-5	Serpentine	Matrix	Mesh			2.04	-	0.01	-	0.09	-	2.81	-	-	-	-	-	-	-	0.00	-	-	4.96	97	-	1.38
GM	Carb. serpentinite	44Z-4-0-5	Serpentine	Matrix	Mesh			2.05	-	0.01	-	0.15	-	2.72	0.00	-	-	-	-	-	-	0.00	-	-	4.95	95	-	1.33
GM	Carb. serpentinite	44Z-4-0-5	Serpentine	Matrix	Mesh			2.06	-	0.02	-	0.11	-	2.74	0.01	-	-	-	-	-	-	0.00	-	-	4.93	96	-	1.33
GM	Carb. serpentinite	44Z-4-0-5	Serpentine	Matrix	Mesh			2.15	-	0.02	-	0.14	-	2.54	-	-	-	-	-	-	-	0.00	-	-	4.85	95	-	1.19
GM	Carb. serpentinite	44Z-4-0-5	Serpentine	Matrix	Mesh			2.09	-	0.02	-	0.14	-	2.65	0.00	-	-	-	-	-	-	-	-	-	4.90	95	-	1.27
GM	Carb. serpentinite	44Z-4-0-5	Serpentine	Matrix	Mesh			2.03	-	0.02	-	0.21	-	2.71	-	-	-	-	-	-	-	0.00	-	-	4.97	93	-	1.33
GM	Carb. serpentinite	44Z-4-0-5	Serpentine	Matrix	Mesh			2.04	-	0.02	-	0.18	-	2.71	-	-	-	-	-	-	-	-	-	-	4.95	94	-	1.33
GM	Carb. serpentinite	44Z-4-0-5	Serpentine	Matrix	Mesh			2.04	-	0.02	-	0.19	-	2.70	-	-	-	-	-	-	-	0.00	-	-	4.96	93	-	1.33
GM	Carb. serpentinite	44Z-4-0-5	Serpentine	Matrix	Mesh			2.10	-	0.01	-	0.11	-	2.67	0.01	-	0.00	-	-	-	-	0.00	-	-	4.90	96	-	1.27
GM	Carb. serpentinite	44Z-4-0-5	Serpentine	Matrix	Mesh			2.12	-	0.01	-	0.11	-	2.63	0.00	-	-	-	-	-	-	0.00	-	-	4.88	96	-	1.25
GM	Carb. serpentinite	44Z-4-0-5	Serpentine	Matrix	Mesh			2.06	-	0.01	-	0.12	-	2.73	-	-	-	-	-	-	-	-	-	-	4.93	96	-	1.32
GM	Carb. serpentinite	44Z-4-0-5	Serpentine	Matrix	Mesh			2.06	-	0.01	-	0.15	-	2.72	0.00	-	0.00	-	-	-	-	0.00	-	-	4.94	95	-	1.32
ISTE	Carb. serpentinite	44Z-4-0-5	Serpentine	Matrix	Mesh			2.06	-	0.02	0.01	0.14	-	2.68	0.00	0.00	-	0.01	-	-	-	0.00	-	-	4.93	95	26	1.30
ISTE	Carb. serpentinite	44Z-4-0-5	Serpentine	Matrix	Mesh			2.12	-	0.02	0.00	0.07	-	2.62	0.00	0.01	-	0.02	-	-	-	0.00	-	-	4.87	97	14	1.24
ISTE	Carb. serpentinite	44Z-4-0-5	Serpentine	Matrix	Mesh			2.13	-	0.02	0.00	0.06	0.00	2.63	0.00	0.00	-	0.01	-	-	-	0.00	-	-	4.86	98	15	1.24
ISTE	Carb. serpentinite	44Z-4-0-5	Serpentine	Matrix	Mesh			2.11	0.00	0.02	0.00	0.12	0.00	2.61	0.00	0.00	-	0.01	-	-	-	0.00	-	-	4.88	96	10	1.24
GM	Carb. serpentinite	44Z-4-0-5	Serpentine	Matrix	Bastite			2.02	-	0.04	0.02	0.13	-	2.75	-	-	-	-	-	-	-	0.01	-	-	4.96	95	35	1.36
GM	Carb. serpentinite	44Z-4-0-5	Serpentine	Matrix	Bastite			2.01	-	0.04	0.02	0.15	-	2.75	-	-	-	-	-	-	-	0.01	-	-	4.97	95	34	1.37
GM	Carb. serpentinite	44Z-4-0-5	Serpentine	Matrix	Bastite			2.02	-	0.04	0.02	0.14	-	2.72	0.00	-	-	-	-	-	-	0.01	-	-	4.95	95	35	1.34
GM	Carb. serpentinite	44Z-4-0-5	Serpentine	Matrix	Bastite			2.01	-	0.04	0.02	0.13	-	2.75	-	-	-	-	-	-	-	0.01	-	-	4.97	95	41	1.37
GM	Carb. serpentinite	44Z-4-0-5	Serpentine	Matrix	Bastite			2.07	-	0.05	0.02	0.21	-	2.53	0.01	-	-	-	-	-	-	0.01	-	-	4.90	92	31	1.22
GM	Carb. serpentinite	44Z-4-0-5	Serpentine	Matrix	Bastite			2.30	-	0.03	0.02	0.16	-	2.16	-	-	-	-	-	-	-	0.00	-	-	4.68	93	36	0.94
GM	Carb. serpentinite	44Z-4-0-5	Serpentine	Matrix	Bastite			2.08	-	0.05	0.02	0.19	-	2.53	0.01	-	-	-	-	-	-	0.01	-	-	4.89	93	31	1.22
GM	Carb. serpentinite	44Z-4-0-5	Serpentine	Matrix	Bastite			2.12	-	0.05	0.02	0.21	-	2.45	0.01	-	-	-	-	-	-	0.01	-	-	4.85	92	32	1.15
ISTE	Carb. serpentinite	44Z-4-0-5	Serpentine	Matrix	Bastite			2.08	-	0.04	0.02	0.31	0.00	2.41	0.00	0.00	-	0.02	-	-	-	0.01	-	-	4.89	89	30	1.15
ISTE	Carb. serpentinite	44Z-4-0-5	Serpentine	Matrix	Bastite			2.09	0.00	0.04	0.02	0.20	0.00	2.49	0.00	0.01	-	0.02	-	-	-	0.00	-	-	4.88	93	33	1.19
GM	Carb. serpentinite	44Z-4-0-5	Serpentine	Vein	sc0	Median zone		2.06	-	0.02	-	0.08	-	2.77	-	-	-	-	-	-	-	0.01	-	-	4.94	97	-	1.34
GM	Carb. serpentinite	44Z-4-0-5	Serpentine	Vein	sc0	Median zone		2.08	-	0.02	-	0.08	-	2.74	-	-	-	-	-	-	-	0.01	-	-	4.92	97	-	1.32
GM	Carb. serpentinite	44Z-4-0-5	Serpentine	Vein	sc0	Median zone		2.07	-	0.02	-	0.09	-	2.74	-	-	-	-	-	-	-	-	-	-	4.92	97	-	1.32
GM	Carb. serpentinite	44Z-4-0-5	Serpentine	Vein	sc0	Median zone		2.09	-	0.01	-	0.09	-	2.71	-	-	-	-	-	-	-	-	-	-	4.91	97	-	1.30
GM	Carb. serpentinite	44Z-4-0-5	Serpentine	Vein	sc0	Median zone		2.05	-	0.01	-	0.12	-	2.77	-	-	-	-	-	-	-	-	-	-	4.95	96	-	1.35
GM	Carb. serpentinite	44Z-4-0-5	Serpentine	Vein	sc0	Median zone		2.05	-	0.01	-	0.12	-	2.76	-	-	-	-	-	-	-	-	-	-	4.94	96	-	1.34

GM	Carb. serpentinite	44Z-4-0-5	Serpentine	Vein	sc0	Median zone		2.07	-	0.01	-	0.10	-	2.75	-	-	-	-	-	-	-	-	-	-	4.93	97	-	1.33
GM	Carb. serpentinite	44Z-4-0-5	Serpentine	Vein	sc0	Median zone		2.04	-	0.01	-	0.10	-	2.79	-	-	-	-	-	-	-	-	-	-	4.95	96	-	1.36
GM	Carb. serpentinite	44Z-4-0-5	Serpentine	Vein	sc0	Median zone		2.07	-	0.02	-	0.10	-	2.72	0.00	-	-	-	-	-	-	-	-	-	4.92	96	-	1.31
GM	Carb. serpentinite	44Z-4-0-5	Serpentine	Vein	sc0	Median zone		2.07	-	0.02	-	0.10	-	2.73	0.00	-	-	-	-	-	-	-	-	-	4.92	97	-	1.32
GM	Carb. serpentinite	44Z-4-0-5	Serpentine	Vein	sc0	Median zone		2.07	-	0.01	-	0.10	-	2.74	-	-	-	-	-	-	-	-	-	-	4.92	97	-	1.33
ISTE	Carb. serpentinite	44Z-4-0-5	Serpentine	Vein	sc0	Median zone		2.07	-	0.02	-	0.09	0.00	2.73	0.00	0.00	-	0.01	-	-	-	0.00	-	-	4.93	97	-	1.32
ISTE	Carb. serpentinite	44Z-4-0-5	Serpentine	Vein	sc0	Median zone		2.09	-	0.03	0.01	0.16	-	2.56	0.00	0.01	-	0.02	-	-	-	0.00	-	-	4.89	94	21	1.22
ISTE	Carb. serpentinite	44Z-4-0-5	Serpentine	Vein	sc0	Median zone		2.07	-	0.02	-	0.09	0.00	2.73	0.00	-	-	0.01	-	-	-	0.00	-	-	4.93	97	-	1.32
ISTE	Carb. serpentinite	44Z-4-0-5	Serpentine	Vein	sc0	Median zone		2.06	-	0.02	-	0.09	0.00	2.73	0.00	0.00	-	0.01	-	-	-	0.00	-	-	4.93	97	-	1.32
ISTE	Carb. serpentinite	44Z-4-0-5	Serpentine	Vein	sc0	Median zone		2.08	-	0.02	-	0.08	0.00	2.70	0.00	0.00	-	0.01	-	-	-	0.00	-	-	4.91	97	-	1.30
ISTE	Carb. serpentinite	44Z-4-0-5	Serpentine	Vein	sc0	Median zone		2.09	-	0.02	-	0.08	0.00	2.71	0.00	-	-	0.01	-	-	-	0.00	-	-	4.91	97	-	1.30
ISTE	Carb. serpentinite	44Z-4-0-5	Serpentine	Vein	sc0	Median zone		2.09	-	0.01	-	0.10	0.00	2.67	0.00	0.00	-	0.01	-	-	-	0.00	-	-	4.90	96	-	1.28
ISTE	Carb. serpentinite	44Z-4-0-5	Serpentine	Vein	sc0	Median zone		2.10	-	0.01	-	0.06	0.00	2.71	-	0.00	-	0.01	-	-	-	0.00	-	-	4.90	98	-	1.29
GM	Carb. serpentinite	44Z-4-0-5	Serpentine	Vein	sc0	Rim	d	2.08	-	0.02	-	0.07	-	2.74	-	-	-	-	-	-	-	0.00	-	-	4.91	98	-	1.32
GM	Carb. serpentinite	44Z-4-0-5	Serpentine	Vein	sc0	Rim	d	2.06	-	0.02	-	0.07	-	2.79	-	-	-	-	-	-	-	0.00	-	-	4.94	97	-	1.35
GM	Carb. serpentinite	44Z-4-0-5	Serpentine	Vein	sc0	Rim	d	2.07	-	0.02	-	0.08	-	2.75	-	-	-	-	-	-	-	0.00	-	-	4.92	97	-	1.33
GM	Carb. serpentinite	44Z-4-0-5	Serpentine	Vein	sc0	Median zone	d	2.06	-	0.02	-	0.10	-	2.75	-	-	-	-	-	-	-	0.01	-	-	4.93	97	-	1.33
GM	Carb. serpentinite	44Z-4-0-5	Serpentine	Vein	sc0	Median zone	d	2.07	-	0.02	-	0.08	-	2.75	-	-	-	-	-	-	-	0.00	-	-	4.92	97	-	1.33
GM	Carb. serpentinite	44Z-4-0-5	Serpentine	Vein	sc0	Median zone	d	2.06	-	0.02	-	0.08	-	2.77	-	-	-	-	-	-	-	0.01	-	-	4.93	97	-	1.34
GM	Carb. serpentinite	44Z-4-0-5	Serpentine	Vein	sc0	Median zone	d	2.08	-	0.02	-	0.08	-	2.75	-	-	-	-	-	-	-	0.00	-	-	4.92	97	-	1.32
GM	Carb. serpentinite	44Z-4-0-5	Serpentine	Vein	sc0	Median zone	d	2.06	-	0.02	-	0.07	-	2.78	-	-	-	-	-	-	-	0.00	-	-	4.93	98	-	1.35
GM	Carb. serpentinite	44Z-4-0-5	Serpentine	Vein	sc0	Median zone	d	2.06	-	0.02	-	0.07	-	2.78	-	-	-	-	-	-	-	0.01	-	-	4.93	97	-	1.34
GM	Carb. serpentinite	44Z-4-0-5	Serpentine	Vein	sc0	Median zone	d	2.07	-	0.02	-	0.06	-	2.78	-	-	-	-	-	-	-	0.01	-	-	4.93	98	-	1.34
GM	Carb. serpentinite	44Z-4-0-5	Serpentine	Vein	sc0	Rim	d	2.09	-	0.02	-	0.14	-	2.65	0.00	-	-	-	-	-	-	0.00	-	-	4.90	95	-	1.27
GM	Carb. serpentinite	44Z-4-0-5	Serpentine	Vein	sc0	Rim	d	2.13	-	0.01	-	0.09	-	2.63	-	-	-	-	-	-	-	-	-	-	4.87	97	-	1.24
GM	Fu-listvenite	53Z-2-72-77	Fuchsite	Matrix				6.02	-	5.11	0.55	0.14	-	0.62	0.04	0.07	0.81	0.20	-	-	-	-	-	-	13.56	81	10	0.10
GM	Fu-listvenite	53Z-2-72-77	Fuchsite	Matrix				5.85	-	5.44	0.52	0.19	-	0.58	0.05	0.03	0.60	0.22	-	-	-	-	-	-	13.47	76	9	0.10
GM	Fu-listvenite	53Z-2-72-77	Fuchsite	Matrix				5.90	0.02	5.36	0.50	0.15	-	0.52	0.05	0.08	0.74	0.20	-	-	-	-	-	-	13.52	77	9	0.09
GM	Fu-listvenite	53Z-2-72-77	Fuchsite	Matrix				5.80	-	5.60	0.45	0.12	0.01	0.53	0.04	0.06	0.66	0.21	-	-	-	-	-	-	13.50	81	7	0.09
GM	Fu-listvenite	53Z-2-72-77	Fuchsite	Matrix				5.80	0.04	5.37	0.56	0.16	-	0.61	0.04	0.07	0.62	0.23	-	-	-	-	-	-	13.50	80	9	0.11
GM	Fu-listvenite	60Z-1-32-37	Fuchsite	Matrix				6.63	-	4.44	0.49	0.23	-	0.31	0.06	0.09	1.19	0.04	-	-	-	-	-	-	13.49	58	10	0.05
GM	Fu-listvenite	60Z-1-32-37	Fuchsite	Matrix				7.12	-	3.53	0.60	0.35	-	0.26	0.21	0.22	1.05	-	-	-	-	-	-	-	13.34	42	14	0.04
GM	Fu-listvenite	60Z-1-32-37	Fuchsite	Matrix				7.06	-	3.80	0.66	0.25	-	0.20	0.07	0.05	1.22	-	-	-	-	-	-	-	13.31	44	15	0.03
GM	Fu-listvenite	60Z-1-32-37	Fuchsite	Matrix				6.91	-	4.22	0.70	-	-	-	0.10	-	1.38	-	-	-	-	-	-	-	13.32	n.d.	14	0.00
GM	Fu-listvenite	60Z-1-32-37	Fuchsite	Matrix				6.65	-	4.22	0.70	0.30	-	0.23	0.09	0.05	1.23	0.02	-	-	-	-	-	-	13.50	43	14	0.03
GM	Fu-listvenite	60Z-1-32-37	Fuchsite	Matrix				6.58	-	4.29	0.67	0.35	-	0.25	0.11	-	1.38	-	-	-	-	-	-	-	13.63	42	14	0.04
GM	Fu-listvenite	60Z-1-32-37	Fuchsite	Matrix				6.76	-	4.09	0.70	0.30	-	0.22	0.09	-	1.39	-	-	-	-	-	-	-	13.54	42	15	0.03
GM	Fu-listvenite	60Z-1-32-37	Fuchsite	Matrix				6.83	-	4.01	0.69	0.27	-	0.23	0.11	-	1.35	-	-	-	-	-	-	-	13.49	46	15	0.03
GM	Fu-listvenite	60Z-1-32-37	Fuchsite	Matrix				6.85	-	3.89	0.74	0.31	-	0.25	0.11	-	1.37	-	-	-	-	-	-	-	13.52	44	16	0.04
GM	Fu-listvenite	60Z-1-32-37	Fuchsite	Matrix				6.77	-	4.08	0.63	0.36	-	0.24	0.09	-	1.39	-	-	-	-	-	-	-	13.57	40	13	0.04
GM	Fu-listvenite	60Z-1-32-37	Fuchsite	Matrix				6.13	0.00	4.88	0.70	0.32	-	0.23	0.06	0.10	1.25	0.04	-	-	-	-	-	-	13.70	42	12	0.04
GM	Fu-listvenite	60Z-1-32-37	Fuchsite	Matrix				6.00	-	5.22	0.63	0.23	-	0.21	0.06	0.04	1.29	0.03	-	-	-	0.00	-	-	13.72	48	11	0.03

Table S6: Major element compositions of Cr-spinel determined by EPMA

									Major oxides																
Facility	Lithology	Sample	Depth m.b.g	Domain[1]	Mineral	Structure	Texture	Zone	SiO2 wt%	TiO2 wt%	Al2O3 wt%	Cr2O3 wt%	FeO wt%	MnO wt%	MgO wt%	CaO wt%	Na2O wt%	K2O wt%	NiO wt%	CuO wt%	ZnO wt%	SO2 wt%	Cl wt%	BaO wt%	SrO wt%	Total wt%
GM	Listvenite	16Z-1-65-70	27.65	I	Cr-spinel	Matrix		Core	-	-	19.92	46.28	21.87	0.62	10.65	-	-	-	-	-	-	-	-	-	0.22	99.55
GM	Listvenite	16Z-1-65-70	27.65	I	Cr-spinel	Matrix		Border	-	-	19.29	46.66	21.80	0.56	10.59	-	-	-	-	-	-	-	-	-	0.20	99.12
GM	Listvenite	30Z-2-33-39	113.113	I	Cr-spinel	Matrix		Core	-	0.16	31.08	37.41	20.88	0.49	10.23	-	-	-	-	-	-	-	-	-	-	100.25
GM	Listvenite	30Z-2-33-39	113.113	I	Cr-spinel	Matrix		Core	-	0.26	32.79	33.57	23.98	0.59	9.32	-	-	-	-	-	0.37	-	-	-	-	100.87
GM	Listvenite	30Z-2-33-39	113.113	I	Cr-spinel	Matrix		Core	-	0.32	33.06	34.06	23.88	0.46	9.70	-	-	-	-	-	-	-	-	-	-	101.50
GM	Listvenite	30Z-2-33-39	113.113	I	Cr-spinel	Matrix		Core	-	0.26	33.06	33.95	23.74	0.52	9.18	-	-	-	-	-	0.39	-	-	-	-	101.10
GM	Listvenite	30Z-2-33-39	113.113	I	Cr-spinel	Matrix		Core	-	0.18	30.98	36.88	21.12	0.54	9.66	-	-	-	-	-	0.45	-	-	-	-	99.80
GM	Listvenite	30Z-2-33-39	113.113	I	Cr-spinel	Matrix		Core	-	0.30	32.97	34.68	22.32	0.48	9.99	-	-	-	-	-	0.42	-	-	-	-	101.14
ISTE	Listvenite	31Z-3-26-31	65.635	I	Cr-spinel	Matrix		Core	-	0.27	15.26	50.60	23.30	0.20	9.88	-	-	-	0.07	-	-	-	-	-	-	99.59
ISTE	Listvenite	31Z-3-26-31	65.635	I	Cr-spinel	Matrix		Core	-	0.25	15.32	50.20	23.54	0.20	9.98	-	-	-	0.09	-	-	-	-	-	-	99.58
ISTE	Listvenite	31Z-3-26-31	65.635	I	Cr-spinel	Matrix		Core	-	0.40	12.11	51.44	25.91	0.24	9.17	-	-	-	0.07	-	-	-	-	-	-	99.34
ISTE	Listvenite	31Z-3-26-31	65.635	I	Cr-spinel	Matrix		Core	-	0.34	21.56	40.68	24.67	0.23	10.90	-	-	-	0.12	-	-	-	-	-	-	98.49
ISTE	Listvenite	31Z-3-26-31	65.635	I	Cr-spinel	Matrix		Core	0.14	0.19	13.36	42.29	33.50	0.22	7.84	-	-	-	1.34	-	-	-	-	-	-	98.88
GM	Carb. serpentinite	43Z-2-43-48	95.33	I	Cr-spinel	Matrix		Core	0.47	-	24.28	31.52	32.25	-	10.46	-	-	-	-	-	-	-	-	-	-	98.99
GM	Carb. serpentinite	43Z-2-43-48	95.33	I	Cr-spinel	Matrix		Core	0.44	-	28.00	36.17	23.83	-	12.04	0.10	-	-	-	-	-	-	-	-	-	100.58
GM	Carb. serpentinite	43Z-2-43-48	95.33	I	Cr-spinel	Matrix		Core	-	-	24.72	43.12	20.04	-	12.58	-	-	-	-	-	-	-	-	-	-	100.45
GM	Carb. serpentinite	43Z-2-43-48	95.33	I	Cr-spinel	Matrix		Core	-	-	24.24	44.16	19.71	-	12.57	-	-	-	-	-	-	-	-	-	-	100.67
GM	Carb. serpentinite	43Z-2-43-48	95.33	I	Cr-spinel	Matrix		Core	-	-	24.35	42.56	19.93	-	12.60	-	-	-	-	-	-	-	-	-	-	99.44
GM	Carb. serpentinite	43Z-2-43-48	95.33	I	Cr-spinel	Matrix		Core	0.13	-	24.14	42.49	19.81	-	12.79	-	-	-	-	-	-	-	-	-	-	99.36
GM	Carb. serpentinite	43Z-2-43-48	95.33	I	Cr-spinel	Matrix		Core	0.53	-	24.75	42.17	20.15	-	12.62	-	-	-	-	-	-	-	0.06	-	-	100.28
GM	Carb. serpentinite	43Z-2-43-48	95.33	I	Cr-spinel	Matrix		Core	-	-	26.55	42.80	19.04	-	12.94	-	-	-	-	-	-	-	-	-	-	101.34
GM	Carb. serpentinite	43Z-2-43-48	95.33	I	Cr-spinel	Matrix		Core	0.62	-	24.04	41.97	21.60	-	12.56	-	-	0.06	-	-	-	-	0.09	-	-	100.93
GM	Carb. serpentinite	43Z-2-43-48	95.33	I	Cr-spinel	Matrix		Core	0.14	-	11.83	54.60	26.07	-	8.78	-	-	-	-	-	-	-	-	-	-	101.43
GM	Carb. serpentinite	43Z-2-43-48	95.33	I	Cr-spinel	Matrix		Core	-	-	12.28	56.12	22.29	-	9.37	-	-	-	-	-	-	-	-	-	-	100.05
GM	Carb. serpentinite	43Z-2-43-48	95.33	I	Cr-spinel	Matrix		Core	0.47	-	10.13	44.91	36.05	-	8.10	-	-	-	-	-	-	-	-	-	-	99.66
GM	Carb. serpentinite	43Z-2-43-48	95.33	I	Cr-spinel	Matrix		Core	-	-	12.51	54.89	21.88	-	9.54	-	-	-	-	-	-	-	-	-	-	98.82
GM	Carb. serpentinite	43Z-2-43-48	95.33	I	Cr-spinel	Matrix		Core	-	-	12.58	55.90	21.45	-	9.67	-	-	-	-	-	-	-	-	-	-	99.59
GM	Carb. serpentinite	43Z-2-43-48	95.33	I	Cr-spinel	Matrix		Core	-	-	12.36	55.05	22.36	-	9.50	-	-	-	-	-	-	-	-	-	-	99.27
GM	Carb. serpentinite	43Z-2-43-48	95.33	I	Ferrit-chromite	Matrix		Core	0.61	-	7.25	33.69	51.58	-	5.98	-	-	-	-	-	-	-	-	-	-	99.10
GM	Carb. serpentinite	43Z-2-43-48	95.33	I	Cr-spinel	Matrix		Core	0.12	-	11.76	57.41	23.70	-	9.44	-	-	-	-	-	-	-	-	-	-	102.43
GM	Carb. serpentinite	43Z-2-43-48	95.33	I	Cr-spinel	Matrix		Core	-	-	12.24	56.70	22.00	-	9.80	-	-	-	-	-	-	-	-	-	-	100.75
GM	Carb. serpentinite	43Z-2-43-48	95.33	I	Cr-spinel	Matrix		Core	-	-	12.81	54.66	22.22	-	9.85	-	-	-	-	-	-	-	-	-	-	99.53
GM	Carb. serpentinite	43Z-2-43-48	95.33	I	Cr-spinel	Matrix		Core	0.11	-	12.93	50.09	25.60	-	9.36	-	-	-	-	-	-	-	-	-	-	98.10
GM	Carb. serpentinite	43Z-2-43-48	95.33	I	Cr-spinel	Matrix		Core	-	-	13.37	51.97	22.61	-	9.52	-	-	-	-	-	-	-	-	-	-	97.48
GM	Carb. serpentinite	43Z-2-43-48	95.33	I	Cr-spinel	Matrix		Core	-	-	13.49	52.53	21.86	-	9.60	-	-	-	-	-	-	-	-	-	-	97.49
GM	Carb. serpentinite	43Z-3-0-5	95.595	I	Cr-spinel	Matrix		Core	-	-	14.93	50.76	23.84	-	9.22	0.08	-	-	-	-	-	-	-	-	-	98.83
GM	Carb. serpentinite	43Z-4-52-57	96.705	I	Cr-spinel	Matrix		Core	0.11	-	15.91	48.89	22.96	-	10.84	-	-	-	-	-	-	-	-	-	-	98.70
GM	Carb. serpentinite	43Z-4-52-57	96.705	I	Cr-spinel	Matrix		Core	-	-	16.08	50.00	21.55	-	10.37	-	-	-	-	-	-	-	-	-	-	98.00
GM	Carb. serpentinite	43Z-4-52-57	96.705	I	Cr-spinel	Matrix		Core	-	-	16.04	49.68	22.04	-	10.18	-	-	-	-	-	-	-	-	-	-	97.93
GM	Carb. serpentinite	44Z-4-0-5	99.415	I	Cr-spinel	Matrix		Core	0.26	-	17.90	52.62	20.15	0.67	10.32	-	-	-	-	-	-	-	-	-	0.00	101.92
GM	Carb. serpentinite	44Z-4-0-5	99.415	I	Cr-spinel	Matrix		Core	-	-	15.57	55.04	20.90	0.76	9.74	-	-	-	-	-	-	-	-	-	-	102.00
GM	Carb. serpentinite	44Z-4-0-5	99.415	I	Cr-spinel	Matrix		Core	-	-	17.23	52.96	21.28	0.69	9.58	-	-	-	-	-	0.37	-	-	-	-	102.11
GM	Carb. serpentinite	44Z-4-0-5	99.415	I	Cr-spinel	Matrix		Core	-	-	15.42	55.82	19.49	0.64	10.44	-	-	-	-	-	-	-	-	-	-	101.81
GM	Carb. serpentinite	44Z-4-0-5	99.415	I	Cr-spinel	Matrix		Core	-	-	16.03	54.65	20.04	0.62	10.22	-	-	-	-	-	-	-	-	-	-	101.56
GM	Carb. serpentinite	44Z-4-0-5	99.415	I	Cr-spinel	Matrix		Core	-	-	15.44	55.18	21.25	0.67	9.83	-	-	-	-	-	-	-	-	-	-	102.36
GM	Carb. serpentinite	44Z-4-0-5	99.415	I	Cr-spinel	Matrix		Core	-	-	17.07	54.18	19.99	0.66	10.50	-	-	-	-	-	-	-	-	-	-	102.40
GM	Carb. serpentinite	44Z-4-0-5	99.415	I	Cr-spinel	Matrix		Core	-	-	19.85	51.29	20.02	0.60	10.13	-	-	-	-	-	-	-	-	-	-	101.89

GM	Carb. serpentinite	44Z-4-0-5	99.415	I	Cr-spinel	Matrix	Core	-	-	16.51	53.67	19.04	0.60	10.88	-	-	-	-	-	-	-	-	-	-	100.70
GM	Carb. serpentinite	44Z-4-0-5	99.415	I	Cr-spinel	Matrix	Core	-	-	20.58	49.93	20.02	0.58	11.22	-	-	-	-	-	-	-	-	-	-	102.33
GM	Carb. serpentinite	44Z-4-0-5	99.415	I	Cr-spinel	Matrix	Core	-	-	24.97	44.63	18.97	0.57	12.12	-	-	-	-	-	-	-	-	-	-	101.26
ISTE	Listvenite	46Z-4-46-51	106.3	I	Cr-spinel	Matrix	Core	-	0.06	26.12	46.68	15.60	0.12	14.34	-	-	-	0.07	-	-	-	-	-	-	102.98
ISTE	Listvenite	46Z-4-46-51	106.3	I	Cr-spinel	Matrix	Core	-	0.11	23.00	49.70	16.14	0.15	13.67	-	-	-	0.10	-	-	-	-	-	-	102.87
ISTE	Listvenite	46Z-4-46-51	106.3	I	Cr-spinel	Matrix	Core	-	0.09	24.74	46.49	16.19	0.11	13.66	-	-	-	0.06	-	-	-	-	-	-	101.34
GM	Listvenite	46Z-4-46-51	106.3	I	Cr-spinel	Matrix	Border	-	-	26.73	45.29	15.20	0.49	14.30	-	-	-	-	-	-	-	-	-	-	102.02
GM	Listvenite	46Z-4-46-51	106.3	I	Cr-spinel	Matrix	Core	-	-	26.32	45.52	14.82	0.46	14.32	-	-	-	-	-	-	-	-	-	-	101.45
GM	Listvenite	46Z-4-46-51	106.3	I	Cr-spinel	Matrix	Core	-	-	28.94	41.95	15.72	0.50	13.99	-	-	-	-	-	-	-	-	-	-	101.09
GM	Listvenite	46Z-4-46-51	106.3	I	Cr-spinel	Matrix	Core	-	-	23.39	48.70	15.79	0.60	13.79	-	-	-	-	-	-	-	-	-	-	102.27
GM	Listvenite	46Z-4-46-51	106.3	I	Cr-spinel	Matrix	Border	-	-	24.09	47.56	15.96	0.63	13.68	-	-	-	-	-	-	-	-	-	-	101.92
GM	Listvenite	46Z-4-46-51	106.3	I	Cr-spinel	Matrix	Core	-	-	23.29	48.81	16.46	0.48	13.29	-	-	-	-	-	-	-	-	-	-	102.33
ISTE	Listvenite	48Z-1-6-11	109.41	I	Cr-spinel	Matrix	Core	-	0.07	16.46	53.56	19.30	0.16	10.97	-	-	-	0.06	-	-	-	-	-	-	100.58
ISTE	Listvenite	48Z-1-6-11	109.41	I	Cr-spinel	Matrix	Core	-	0.08	17.02	52.99	20.00	0.19	10.85	-	-	-	0.07	-	-	-	-	-	-	101.20
ISTE	Listvenite	48Z-1-6-11	109.41	I	Cr-spinel	Matrix	Core	-	0.06	16.57	53.16	21.25	0.25	9.99	-	-	-	-	-	-	-	-	-	-	101.27
ISTE	Listvenite	50Z-1-75-80	113.113	II	Cr-spinel	Matrix	Core	0.02	0.11	17.16	54.62	19.36	0.20	10.79	-	-	-	-	-	-	-	-	-	-	102.25
ISTE	Listvenite	50Z-1-75-80	113.113	II	Cr-spinel	Matrix	Core	-	0.11	17.22	54.23	20.40	0.22	10.40	-	-	-	0.05	-	-	-	-	-	-	102.63
ISTE	Listvenite	50Z-1-75-80	113.113	II	Cr-spinel	Matrix	Core	-	0.10	17.34	54.52	19.86	0.22	10.49	-	-	-	0.04	-	-	-	-	-	-	102.58
ISTE	Listvenite	50Z-1-75-80	113.113	II	Cr-spinel	Matrix	Core	0.02	0.13	16.82	54.80	20.10	0.18	10.51	-	-	-	0.07	-	-	-	-	-	-	102.63
ISTE	Listvenite	50Z-1-75-80	113.113	II	Cr-spinel	Matrix	Core	-	0.10	22.04	49.73	17.87	0.17	12.40	-	-	-	0.09	-	-	-	-	-	-	102.40
ISTE	Listvenite	50Z-1-75-80	113.113	II	Cr-spinel	Matrix	Core	0.02	0.09	21.79	50.04	17.54	0.16	12.48	-	-	-	0.08	-	-	-	-	-	-	102.20
ISTE	Listvenite	50Z-1-75-80	113.113	II	Cr-spinel	Matrix	Core	0.02	0.09	24.06	47.63	18.18	0.16	12.30	-	-	-	0.07	-	-	-	-	-	-	102.51
ISTE	Listvenite	50Z-1-75-80	113.113	II	Cr-spinel	Matrix	Core	-	0.08	23.57	48.10	18.29	0.18	12.29	-	-	-	0.06	-	-	-	-	-	-	102.57
GM	Listvenite	50Z-1-75-80	113.113	II	Cr-spinel	Matrix	Core	-	-	33.67	37.14	16.39	0.39	14.80	-	-	-	-	-	-	-	-	-	-	102.39
GM	Listvenite	50Z-1-75-80	113.113	II	Cr-spinel	Matrix	Core	-	-	23.44	47.48	18.61	0.52	11.89	-	-	-	-	-	-	-	-	-	-	101.95
GM	Listvenite	50Z-1-75-80	113.113	II	Cr-spinel	Matrix	Core	-	-	33.46	37.20	16.20	0.43	14.57	-	-	-	-	-	-	-	-	-	-	101.86
GM	Listvenite	50Z-1-75-80	113.113	II	Cr-spinel	Matrix	Core	-	-	25.36	44.74	18.50	0.58	12.46	-	-	-	-	-	-	-	-	-	-	101.63
GM	Listvenite	50Z-1-75-80	113.113	II	Cr-spinel	Matrix	Core	-	-	25.42	45.43	18.25	0.53	12.68	-	-	-	-	-	-	-	-	-	-	102.31
GM	Listvenite	50Z-1-75-80	113.113	II	Cr-spinel	Matrix	Core	-	-	25.35	45.60	17.83	0.46	12.56	-	-	-	-	-	-	-	-	-	-	101.80
ISTE	Fu-listvenite	55Z-1-55-60	128.2	II	Cr-spinel	Matrix	Core	-	0.11	30.70	34.40	18.64	0.19	14.21	-	-	-	0.16	-	-	-	-	-	-	98.41
ISTE	Listvenite	61Z-4-28-33	145.45	II	Cr-spinel	Matrix	Core	-	0.12	11.88	55.80	22.22	0.22	8.95	-	-	-	0.04	-	-	-	-	-	-	99.23
ISTE	Listvenite	61Z-4-28-33	145.45	II	Cr-spinel	Matrix	Core	-	0.14	12.25	55.82	21.85	0.20	8.96	-	-	-	-	-	-	-	-	-	-	99.22
ISTE	Listvenite	61Z-4-28-33	145.45	II	Cr-spinel	Matrix	Core	-	0.12	12.78	56.18	22.07	0.19	8.50	-	-	-	0.08	-	-	-	-	-	-	99.92
ISTE	Listvenite	66Z-1-30-35	158.4	II	Cr-spinel	Matrix	Core	-	0.15	17.10	51.33	24.94	0.31	8.78	-	-	-	0.05	-	-	-	-	-	-	102.66
ISTE	Listvenite	66Z-1-30-35	158.4	II	Cr-spinel	Matrix	Core	-	0.15	17.40	50.43	25.17	0.29	8.70	-	-	-	0.08	-	-	-	-	-	-	102.22
ISTE	Listvenite	66Z-1-30-35	158.4	II	Cr-spinel	Matrix	Core	-	0.17	16.91	49.60	26.84	0.36	7.83	-	-	-	0.09	-	-	-	-	-	-	101.80
ISTE	Listvenite	66Z-1-30-35	158.4	II	Cr-spinel	Matrix	Core	-	0.17	17.15	50.21	24.98	0.30	8.67	-	-	-	0.07	-	-	-	-	-	-	101.55
ISTE	Listvenite	72Z-1-71-79	176.96	III	Cr-spinel	Matrix	Core	-	0.10	11.85	57.76	21.60	0.20	9.26	-	-	-	0.04	-	-	-	-	-	-	100.81
ISTE	Listvenite	72Z-1-71-79	176.96	III	Cr-spinel	Matrix	Core	-	0.09	11.96	56.46	23.16	0.26	8.53	-	-	-	0.04	-	-	-	-	-	-	100.50
ISTE	Listvenite	72Z-1-71-79	176.96	III	Cr-spinel	Matrix	Core	-	0.09	11.90	56.81	22.73	0.22	8.85	-	-	-	0.07	-	-	-	-	-	-	100.68
ISTE	Listvenite	72Z-1-71-79	176.96	III	Cr-spinel	Matrix	Core	-	0.08	11.81	56.25	22.71	0.20	8.62	-	-	-	0.07	-	-	-	-	-	-	99.74
ISTE	Listvenite	72Z-1-71-79	176.96	III	Cr-spinel	Matrix	Core	-	0.08	12.64	56.81	22.44	0.21	9.03	-	-	-	0.03	-	-	-	-	-	-	101.25
ISTE	Listvenite	72Z-1-71-79	176.96	III	Cr-spinel	Matrix	Core	-	0.07	13.15	55.26	22.67	0.22	8.77	-	-	-	0.03	-	-	-	-	-	-	100.17
GM	Listvenite	76Z-2-12-20	189.295	III	Cr-spinel	Matrix	Core	-	-	12.12	51.81	28.73	0.87	7.64	0.06	-	-	-	-	-	-	-	-	-	101.24
GM	Listvenite	76Z-2-12-20	190.295	III	Cr-spinel	Matrix	Core	-	-	12.11	51.72	29.85	0.71	6.62	-	-	-	-	-	0.39	-	-	-	-	101.39

Table S6 (continued)

									Cations p.f.u. (4O formula)																					
Facility	Lithology	Sample	Depth m.b.g	Domain[1]	Mineral	Structure	Texture	Zone	Si	Ti	Al	Cr	Fe	Mn	Mg	Ca	Na	K	Ni	Cu	Zn	S	Cl	Ba	Sr	Total	Mg#	Cr#
GM	Listvenite	16Z-1-65-70	27.65	I	Cr-spinel	Matrix		Core	-	-	0.75	1.17	0.59	0.02	0.51	-	-	-	-	-	-	-	-	-	0.00	3.04	46	61
GM	Listvenite	16Z-1-65-70	27.65	I	Cr-spinel	Matrix		Border	-	-	0.73	1.19	0.59	0.02	0.51	-	-	-	-	-	-	-	-	-	0.00	3.04	46	62
GM	Listvenite	30Z-2-33-39	113.113	I	Cr-spinel	Matrix		Core	-	0.00	1.10	0.89	0.53	0.01	0.46	-	-	-	-	-	-	-	-	-	-	3.00	47	45
GM	Listvenite	30Z-2-33-39	113.113	I	Cr-spinel	Matrix		Core	-	0.01	1.16	0.80	0.60	0.01	0.42	-	-	-	-	-	0.01	-	-	-	-	3.01	41	41
GM	Listvenite	30Z-2-33-39	113.113	I	Cr-spinel	Matrix		Core	-	0.01	1.16	0.80	0.60	0.01	0.43	-	-	-	-	-	-	-	-	-	-	3.01	42	41
GM	Listvenite	30Z-2-33-39	113.113	I	Cr-spinel	Matrix		Core	-	0.01	1.17	0.80	0.59	0.01	0.41	-	-	-	-	-	0.01	-	-	-	-	3.00	41	41
GM	Listvenite	30Z-2-33-39	113.113	I	Cr-spinel	Matrix		Core	-	0.00	1.11	0.88	0.54	0.01	0.44	-	-	-	-	-	0.01	-	-	-	-	2.99	45	44
GM	Listvenite	30Z-2-33-39	113.113	I	Cr-spinel	Matrix		Core	-	0.01	1.16	0.82	0.56	0.01	0.44	-	-	-	-	-	0.01	-	-	-	-	3.00	44	41
ISTE	Listvenite	31Z-3-26-31	65.635	I	Cr-spinel	Matrix		Core	-	0.01	0.59	1.31	0.64	0.01	0.48	-	-	-	0.00	-	-	-	-	-	-	3.04	43	69
ISTE	Listvenite	31Z-3-26-31	65.635	I	Cr-spinel	Matrix		Core	-	0.01	0.59	1.30	0.65	0.01	0.49	-	-	-	0.00	-	-	-	-	-	-	3.05	43	69
ISTE	Listvenite	31Z-3-26-31	65.635	I	Cr-spinel	Matrix		Core	-	0.01	0.48	1.37	0.73	0.01	0.46	-	-	-	0.00	-	-	-	-	-	-	3.06	39	74
ISTE	Listvenite	31Z-3-26-31	65.635	I	Cr-spinel	Matrix		Core	-	0.01	0.82	1.04	0.67	0.01	0.52	-	-	-	0.00	-	-	-	-	-	-	3.06	44	56
ISTE	Listvenite	31Z-3-26-31	65.635	I	Cr-spinel	Matrix		Core	0.00	0.01	0.55	1.16	0.97	0.01	0.41	-	-	-	0.04	-	-	-	-	-	-	3.14	29	68
GM	Carb. serpentinite	43Z-2-43-48	95.33	I	Cr-spinel	Matrix		Core	0.02	-	0.92	0.81	0.87	-	0.50	-	-	-	-	-	-	-	-	-	-	3.12	37	47
GM	Carb. serpentinite	43Z-2-43-48	95.33	I	Cr-spinel	Matrix		Core	0.01	-	1.01	0.87	0.61	-	0.55	0.00	-	-	-	-	-	-	-	-	-	3.05	47	46
GM	Carb. serpentinite	43Z-2-43-48	95.33	I	Cr-spinel	Matrix		Core	-	-	0.89	1.05	0.51	-	0.58	-	-	-	-	-	-	-	-	-	-	3.03	53	54
GM	Carb. serpentinite	43Z-2-43-48	95.33	I	Cr-spinel	Matrix		Core	-	-	0.88	1.07	0.51	-	0.57	-	-	-	-	-	-	-	-	-	-	3.03	53	55
GM	Carb. serpentinite	43Z-2-43-48	95.33	I	Cr-spinel	Matrix		Core	-	-	0.89	1.04	0.52	-	0.58	-	-	-	-	-	-	-	-	-	-	3.03	53	54
GM	Carb. serpentinite	43Z-2-43-48	95.33	I	Cr-spinel	Matrix		Core	0.00	-	0.88	1.04	0.51	-	0.59	-	-	-	-	-	-	-	-	-	-	3.03	54	54
GM	Carb. serpentinite	43Z-2-43-48	95.33	I	Cr-spinel	Matrix		Core	0.02	-	0.89	1.02	0.52	-	0.58	-	-	-	-	-	-	-	0.00	-	-	3.03	53	53
GM	Carb. serpentinite	43Z-2-43-48	95.33	I	Cr-spinel	Matrix		Core	-	-	0.94	1.02	0.48	-	0.58	-	-	-	-	-	-	-	-	-	-	3.02	55	52
GM	Carb. serpentinite	43Z-2-43-48	95.33	I	Cr-spinel	Matrix		Core	0.02	-	0.87	1.02	0.55	-	0.57	-	-	0.00	-	-	-	-	0.00	-	-	3.04	51	54
GM	Carb. serpentinite	43Z-2-43-48	95.33	I	Cr-spinel	Matrix		Core	0.00	-	0.46	1.43	0.72	-	0.43	-	-	-	-	-	-	-	-	-	-	3.05	38	76
GM	Carb. serpentinite	43Z-2-43-48	95.33	I	Cr-spinel	Matrix		Core	-	-	0.48	1.47	0.62	-	0.46	-	-	-	-	-	-	-	-	-	-	3.03	43	75
GM	Carb. serpentinite	43Z-2-43-48	95.33	I	Cr-spinel	Matrix		Core	0.02	-	0.42	1.24	1.05	-	0.42	-	-	-	-	-	-	-	-	-	-	3.15	29	75
GM	Carb. serpentinite	43Z-2-43-48	95.33	I	Cr-spinel	Matrix		Core	-	-	0.49	1.45	0.61	-	0.48	-	-	-	-	-	-	-	-	-	-	3.03	44	75
GM	Carb. serpentinite	43Z-2-43-48	95.33	I	Cr-spinel	Matrix		Core	-	-	0.49	1.46	0.59	-	0.48	-	-	-	-	-	-	-	-	-	-	3.02	45	75
GM	Carb. serpentinite	43Z-2-43-48	95.33	I	Cr-spinel	Matrix		Core	-	-	0.49	1.45	0.62	-	0.47	-	-	-	-	-	-	-	-	-	-	3.03	43	75
GM	Carb. serpentinite	43Z-2-43-48	95.33	I	Ferrit-chromite	Matrix		Core	0.02	-	0.32	1.00	1.63	-	0.34	-	-	-	-	-	-	-	-	-	-	3.31	17	76
GM	Carb. serpentinite	43Z-2-43-48	95.33	I	Cr-spinel	Matrix		Core	0.00	-	0.45	1.48	0.64	-	0.46	-	-	-	-	-	-	-	-	-	-	3.03	42	77
GM	Carb. serpentinite	43Z-2-43-48	95.33	I	Cr-spinel	Matrix		Core	-	-	0.47	1.47	0.60	-	0.48	-	-	-	-	-	-	-	-	-	-	3.03	44	76
GM	Carb. serpentinite	43Z-2-43-48	95.33	I	Cr-spinel	Matrix		Core	-	-	0.50	1.43	0.62	-	0.49	-	-	-	-	-	-	-	-	-	-	3.03	44	74
GM	Carb. serpentinite	43Z-2-43-48	95.33	I	Cr-spinel	Matrix		Core	0.00	-	0.52	1.34	0.73	-	0.47	-	-	-	-	-	-	-	-	-	-	3.07	39	72
GM	Carb. serpentinite	43Z-2-43-48	95.33	I	Cr-spinel	Matrix		Core	-	-	0.53	1.39	0.64	-	0.48	-	-	-	-	-	-	-	-	-	-	3.04	43	72
GM	Carb. serpentinite	43Z-2-43-48	95.33	I	Cr-spinel	Matrix		Core	-	-	0.54	1.40	0.62	-	0.48	-	-	-	-	-	-	-	-	-	-	3.03	44	72
GM	Carb. serpentinite	43Z-3-0-5	95.595	I	Cr-spinel	Matrix		Core	-	-	0.58	1.33	0.66	-	0.46	0.00	-	-	-	-	-	-	-	-	-	3.04	41	70
GM	Carb. serpentinite	43Z-4-52-57	96.705	I	Cr-spinel	Matrix		Core	0.00	-	0.62	1.27	0.63	-	0.53	-	-	-	-	-	-	-	-	-	-	3.05	46	67
GM	Carb. serpentinite	43Z-4-52-57	96.705	I	Cr-spinel	Matrix		Core	-	-	0.63	1.30	0.59	-	0.51	-	-	-	-	-	-	-	-	-	-	3.03	46	68
GM	Carb. serpentinite	43Z-4-52-57	96.705	I	Cr-spinel	Matrix		Core	-	-	0.63	1.30	0.61	-	0.50	-	-	-	-	-	-	-	-	-	-	3.04	45	68
GM	Carb. serpentinite	44Z-4-0-5	99.415	I	Cr-spinel	Matrix		Core	0.01	-	0.66	1.31	0.53	0.02	0.48	-	-	-	-	-	-	-	-	-	-	3.01	48	66
GM	Carb. serpentinite	44Z-4-0-5	99.415	I	Cr-spinel	Matrix		Core	-	-	0.59	1.39	0.56	0.02	0.46	-	-	-	-	-	-	-	-	-	-	3.01	45	70
GM	Carb. serpentinite	44Z-4-0-5	99.415	I	Cr-spinel	Matrix		Core	-	-	0.64	1.32	0.56	0.02	0.45	-	-	-	-	-	0.01	-	-	-	-	3.01	45	67
GM	Carb. serpentinite	44Z-4-0-5	99.415	I	Cr-spinel	Matrix		Core	-	-	0.58	1.40	0.52	0.02	0.49	-	-	-	-	-	-	-	-	-	-	3.01	49	71
GM	Carb. serpentinite	44Z-4-0-5	99.415	I	Cr-spinel	Matrix		Core	-	-	0.60	1.38	0.53	0.02	0.49	-	-	-	-	-	-	-	-	-	-	3.01	48	70
GM	Carb. serpentinite	44Z-4-0-5	99.415	I	Cr-spinel	Matrix		Core	-	-	0.58	1.39	0.57	0.02	0.47	-	-	-	-	-	-	-	-	-	-	3.02	45	71
GM	Carb. serpentinite	44Z-4-0-5	99.415	I	Cr-spinel	Matrix		Core	-	-	0.63	1.35	0.53	0.02	0.49	-	-	-	-	-	-	-	-	-	-	3.01	48	68
GM	Carb. serpentinite	44Z-4-0-5	99.415	I	Cr-spinel	Matrix		Core	-	-	0.73	1.26	0.52	0.02	0.47	-	-	-	-	-	-	-	-	-	-	3.00	47	63

GM	Carb. serpentinite	44Z-4-0-5	99.415	I	Cr-spinel	Matrix	Core	-	-	0.62	1.35	0.51	0.02	0.52	-	-	-	-	-	-	-	-	-	-	3.01	50	69
GM	Carb. serpentinite	44Z-4-0-5	99.415	I	Cr-spinel	Matrix	Core	-	-	0.75	1.22	0.52	0.02	0.52	-	-	-	-	-	-	-	-	-	-	3.02	50	62
GM	Carb. serpentinite	44Z-4-0-5	99.415	I	Cr-spinel	Matrix	Core	-	-	0.90	1.07	0.48	0.01	0.55	-	-	-	-	-	-	-	-	-	-	3.02	53	55
ISTE	Listvenite	46Z-4-46-51	106.3	I	Cr-spinel	Matrix	Core	-	0.00	0.90	1.08	0.38	0.00	0.63	-	-	-	0.00	-	-	-	-	-	-	3.00	62	55
ISTE	Listvenite	46Z-4-46-51	106.3	I	Cr-spinel	Matrix	Core	-	0.00	0.81	1.17	0.40	0.00	0.61	-	-	-	0.00	-	-	-	-	-	-	3.01	60	59
ISTE	Listvenite	46Z-4-46-51	106.3	I	Cr-spinel	Matrix	Core	-	0.00	0.88	1.11	0.41	0.00	0.61	-	-	-	0.00	-	-	-	-	-	-	3.01	60	56
GM	Listvenite	46Z-4-46-51	106.3	I	Cr-spinel	Matrix	Border	-	-	0.93	1.06	0.38	0.01	0.63	-	-	-	-	-	-	-	-	-	-	3.01	63	53
GM	Listvenite	46Z-4-46-51	106.3	I	Cr-spinel	Matrix	Core	-	-	0.92	1.07	0.37	0.01	0.63	-	-	-	-	-	-	-	-	-	-	3.00	63	54
GM	Listvenite	46Z-4-46-51	106.3	I	Cr-spinel	Matrix	Core	-	-	1.01	0.98	0.39	0.01	0.62	-	-	-	-	-	-	-	-	-	-	3.01	61	49
GM	Listvenite	46Z-4-46-51	106.3	I	Cr-spinel	Matrix	Core	-	-	0.83	1.15	0.40	0.02	0.62	-	-	-	-	-	-	-	-	-	-	3.01	61	58
GM	Listvenite	46Z-4-46-51	106.3	I	Cr-spinel	Matrix	Border	-	-	0.85	1.13	0.40	0.02	0.61	-	-	-	-	-	-	-	-	-	-	3.01	60	57
GM	Listvenite	46Z-4-46-51	106.3	I	Cr-spinel	Matrix	Core	-	-	0.83	1.16	0.41	0.01	0.60	-	-	-	-	-	-	-	-	-	-	3.01	59	58
ISTE	Listvenite	48Z-1-6-11	109.41	I	Cr-spinel	Matrix	Core	-	0.00	0.62	1.35	0.51	0.00	0.52	-	-	-	0.00	-	-	-	-	-	-	3.01	50	69
ISTE	Listvenite	48Z-1-6-11	109.41	I	Cr-spinel	Matrix	Core	-	0.00	0.64	1.33	0.53	0.01	0.51	-	-	-	0.00	-	-	-	-	-	-	3.02	49	68
ISTE	Listvenite	48Z-1-6-11	109.41	I	Cr-spinel	Matrix	Core	-	0.00	0.62	1.34	0.57	0.01	0.48	-	-	-	-	-	-	-	-	-	-	3.02	46	68
ISTE	Listvenite	50Z-1-75-80	113.113	II	Cr-spinel	Matrix	Core	0.00	0.00	0.63	1.35	0.51	0.01	0.50	-	-	-	-	-	-	-	-	-	-	3.00	50	68
ISTE	Listvenite	50Z-1-75-80	113.113	II	Cr-spinel	Matrix	Core	-	0.00	0.64	1.34	0.53	0.01	0.49	-	-	-	0.00	-	-	-	-	-	-	3.01	48	68
ISTE	Listvenite	50Z-1-75-80	113.113	II	Cr-spinel	Matrix	Core	-	0.00	0.64	1.35	0.52	0.01	0.49	-	-	-	0.00	-	-	-	-	-	-	3.00	48	68
ISTE	Listvenite	50Z-1-75-80	113.113	II	Cr-spinel	Matrix	Core	0.00	0.00	0.62	1.36	0.53	0.00	0.49	-	-	-	0.00	-	-	-	-	-	-	3.01	48	69
ISTE	Listvenite	50Z-1-75-80	113.113	II	Cr-spinel	Matrix	Core	-	0.00	0.79	1.19	0.45	0.00	0.56	-	-	-	0.00	-	-	-	-	-	-	3.01	55	60
ISTE	Listvenite	50Z-1-75-80	113.113	II	Cr-spinel	Matrix	Core	0.00	0.00	0.78	1.20	0.45	0.00	0.57	-	-	-	0.00	-	-	-	-	-	-	3.01	56	61
ISTE	Listvenite	50Z-1-75-80	113.113	II	Cr-spinel	Matrix	Core	0.00	0.00	0.85	1.13	0.46	0.00	0.55	-	-	-	0.00	-	-	-	-	-	-	3.00	55	57
ISTE	Listvenite	50Z-1-75-80	113.113	II	Cr-spinel	Matrix	Core	-	0.00	0.84	1.15	0.46	0.00	0.55	-	-	-	0.00	-	-	-	-	-	-	3.01	54	58
GM	Listvenite	50Z-1-75-80	113.113	II	Cr-spinel	Matrix	Core	-	-	1.14	0.84	0.39	0.01	0.63	-	-	-	-	-	-	-	-	-	-	3.01	62	43
GM	Listvenite	50Z-1-75-80	113.113	II	Cr-spinel	Matrix	Core	-	-	0.84	1.14	0.47	0.01	0.54	-	-	-	-	-	-	-	-	-	-	3.01	53	58
GM	Listvenite	50Z-1-75-80	113.113	II	Cr-spinel	Matrix	Core	-	-	1.14	0.85	0.39	0.01	0.63	-	-	-	-	-	-	-	-	-	-	3.01	62	43
GM	Listvenite	50Z-1-75-80	113.113	II	Cr-spinel	Matrix	Core	-	-	0.90	1.07	0.47	0.01	0.56	-	-	-	-	-	-	-	-	-	-	3.01	55	54
GM	Listvenite	50Z-1-75-80	113.113	II	Cr-spinel	Matrix	Core	-	-	0.90	1.08	0.46	0.01	0.57	-	-	-	-	-	-	-	-	-	-	3.01	55	55
GM	Listvenite	50Z-1-75-80	113.113	II	Cr-spinel	Matrix	Core	-	-	0.90	1.08	0.45	0.01	0.56	-	-	-	-	-	-	-	-	-	-	3.01	56	55
ISTE	Fu-listvenite	55Z-1-55-60	128.2	II	Cr-spinel	Matrix	Core	-	0.00	1.09	0.82	0.47	0.00	0.64	-	-	-	0.00	-	-	-	-	-	-	3.04	58	43
ISTE	Listvenite	61Z-4-28-33	145.45	II	Cr-spinel	Matrix	Core	-	0.00	0.47	1.48	0.62	0.01	0.45	-	-	-	0.00	-	-	-	-	-	-	3.02	42	76
ISTE	Listvenite	61Z-4-28-33	145.45	II	Cr-spinel	Matrix	Core	-	0.00	0.48	1.47	0.61	0.01	0.45	-	-	-	-	-	-	-	-	-	-	3.02	42	75
ISTE	Listvenite	61Z-4-28-33	145.45	II	Cr-spinel	Matrix	Core	-	0.00	0.50	1.47	0.61	0.01	0.42	-	-	-	0.00	-	-	-	-	-	-	3.01	41	75
ISTE	Listvenite	66Z-1-30-35	158.4	II	Cr-spinel	Matrix	Core	-	0.00	0.64	1.29	0.66	0.01	0.42	-	-	-	0.00	-	-	-	-	-	-	3.03	39	67
ISTE	Listvenite	66Z-1-30-35	158.4	II	Cr-spinel	Matrix	Core	-	0.00	0.66	1.27	0.67	0.01	0.41	-	-	-	0.00	-	-	-	-	-	-	3.03	38	66
ISTE	Listvenite	66Z-1-30-35	158.4	II	Cr-spinel	Matrix	Core	-	0.00	0.65	1.27	0.73	0.01	0.38	-	-	-	0.00	-	-	-	-	-	-	3.04	34	66
ISTE	Listvenite	66Z-1-30-35	158.4	II	Cr-spinel	Matrix	Core	-	0.00	0.65	1.28	0.67	0.01	0.42	-	-	-	0.00	-	-	-	-	-	-	3.03	38	66
ISTE	Listvenite	72Z-1-71-79	176.96	III	Cr-spinel	Matrix	Core	-	0.00	0.46	1.50	0.59	0.01	0.45	-	-	-	0.00	-	-	-	-	-	-	3.02	43	77
ISTE	Listvenite	72Z-1-71-79	176.96	III	Cr-spinel	Matrix	Core	-	0.00	0.47	1.48	0.64	0.01	0.42	-	-	-	0.00	-	-	-	-	-	-	3.02	40	76
ISTE	Listvenite	72Z-1-71-79	176.96	III	Cr-spinel	Matrix	Core	-	0.00	0.46	1.48	0.63	0.01	0.44	-	-	-	0.00	-	-	-	-	-	-	3.02	41	76
ISTE	Listvenite	72Z-1-71-79	176.96	III	Cr-spinel	Matrix	Core	-	0.00	0.46	1.49	0.63	0.01	0.43	-	-	-	0.00	-	-	-	-	-	-	3.02	40	76
ISTE	Listvenite	72Z-1-71-79	176.96	III	Cr-spinel	Matrix	Core	-	0.00	0.49	1.47	0.61	0.01	0.44	-	-	-	0.00	-	-	-	-	-	-	3.02	42	75
ISTE	Listvenite	72Z-1-71-79	176.96	III	Cr-spinel	Matrix	Core	-	0.00	0.51	1.44	0.63	0.01	0.43	-	-	-	0.00	-	-	-	-	-	-	3.02	41	74
GM	Listvenite	76Z-2-12-20	189.295	III	Cr-spinel	Matrix	Core	-	-	0.48	1.38	0.81	0.02	0.38	0.00	-	-	-	-	-	-	-	-	-	3.07	32	74
GM	Listvenite	76Z-2-12-20	190.295	III	Cr-spinel	Matrix	Core	-	-	0.48	1.38	0.84	0.02	0.33	-	-	-	-	-	0.01	-	-	-	-	3.06	28	74

Table S7: Major element compositions of Fe oxides determined by EPMA

									Major oxides																
Facility	Lithology	Sample	Depth	Domain[1]	Mineral	Structure	Texture	Zone	SiO2	TiO2	Al2O3	Cr2O3	FeO	MnO	MgO	CaO	Na2O	K2O	NiO	CuO	ZnO	SO2	Cl	BaO	SrO	Total
			m.b.g						wt%	wt%	wt%	wt%	wt%	wt%	wt%	wt%	wt%	wt%	wt%	wt%	wt%	wt%	wt%	wt%	wt%	
GM	Listvenite	46Z-4-46-51	106.3	I	Fe oxide	Matrix	Flaky	Inclusion in Mgs aggregate (close to core)	0.42	-	-	0.42	89.30	-	-	-	-	-	-	-	-	-	-	-	-	90.14
GM	Listvenite	46Z-4-46-51	106.3	I	Fe oxide	Matrix	Flaky	Inclusion in Mgs aggregate (close to core)	0.66	0.18	-	0.92	87.60	-	-	-	-	-	-	-	-	-	-	-	-	89.37
GM	Listvenite	46Z-4-46-51	106.3	I	Fe oxide	Matrix	Elongated	Inclusion in Mg-core spheroid (close to core)	0.54	-	-	-	86.49	-	5.87	0.09	-	-	-	-	-	-	-	-	-	92.98
GM	Listvenite	50Z-1-75-80	113.113	II	Fe oxide	Matrix	Anhedral	Inclusion in Mgs aggregate (close to core)	0.37	-	-	-	88.04	-	1.56	0.13	-	-	0.32	-	-	-	-	-	-	90.43
GM	Listvenite	50Z-1-75-80	113.113	II	Fe oxide	Matrix	Anhedral	Inclusion in Mgs aggregate (close to core)	0.38	-	-	-	88.97	-	0.20	-	-	-	0.33	-	-	-	-	-	-	89.88
GM	Listvenite	50Z-1-75-80	113.113	II	Fe oxide	Matrix	Anhedral	Inclusion in lss0	0.31	-	-	-	89.46	-	0.23	-	-	-	-	-	-	-	-	-	-	90.00
GM	Listvenite	50Z-1-75-80	113.113	II	Fe oxide	Matrix	Anhedral	Inclusion in lss0	0.35	-	-	-	89.34	-	0.27	-	-	-	-	-	-	-	-	-	-	89.96
GM	Listvenite	50Z-1-75-80	113.113	II	Fe oxide	Matrix	Anhedral	Inclusion in lss0	0.49	-	-	-	88.23	-	1.67	-	-	-	-	-	-	-	-	-	-	90.39
GM	Listvenite	50Z-1-75-80	113.113	II	Fe oxide	Matrix	Anhedral	Inclusion in lss0	0.29	-	-	-	82.96	-	7.08	0.08	-	-	0.33	-	-	-	-	-	-	90.74
GM	Listvenite	50Z-1-75-80	113.113	II	Fe oxide	Matrix	Subhedral	Inclusion in lss0	0.40	-	-	0.18	83.87	-	2.24	0.10	-	-	0.26	-	-	-	-	-	-	87.04
GM	Listvenite	50Z-1-75-80	113.113	II	Fe oxide	Matrix	Subhedral	Inclusion in lss0	0.14	-	-	0.52	89.01	-	0.11	-	-	-	0.39	-	-	-	-	-	-	90.16
GM	Listvenite	50Z-1-75-80	113.113	II	Fe oxide	Matrix	Anhedral	Within Qz matrix	0.24	-	-	-	87.29	-	2.36	-	-	-	-	-	-	-	-	-	-	89.89
GM	Fu-listvenite	60Z-1-32-37	140.17	II	Fe oxide	Matrix	Elongated	Inclusion in Mg-core spheroid (border)	0.86	-	0.13	-	89.71	-	0.14	-	-	-	-	-	-	-	-	-	-	90.83
GM	Fu-listvenite	60Z-1-32-37	140.17	II	Fe oxide	Matrix	Subhedral	Inclusion in Mg-core spheroid (border)	0.74	-	-	-	89.09	-	0.21	-	-	-	0.59	-	-	-	-	-	-	90.63
GM	Fu-listvenite	60Z-1-32-37	140.17	II	Fe oxide	Matrix	Subhedral	Inclusion in Mg-core spheroid (border)	0.64	-	-	-	88.83	-	0.32	-	-	-	0.67	-	-	-	-	-	-	90.46
GM	Listvenite	76Z-2-12-18	189.295	III	Fe oxide	Matrix	Elongated	Within Dol-Qz matrix	0.48	-	-	0.56	90.81	-	-	0.25	-	-	-	-	-	-	-	-	-	92.10
GM	Listvenite	76Z-2-12-18	189.295	III	Fe oxide	Matrix	Elongated	Within Dol-Qz matrix	0.46	-	-	0.21	90.85	-	-	0.47	-	-	-	-	-	-	-	-	-	91.99
GM	Listvenite	76Z-2-12-18	189.295	III	Fe oxide	Matrix	Elongated	Within Dol-Qz matrix	0.26	-	-	1.18	90.70	-	0.11	0.14	-	-	-	-	-	-	-	-	-	92.38
GM	Listvenite	76Z-2-12-18	189.295	III	Fe oxide	Matrix	Elongated	Within Dol-Qz matrix	0.24	-	-	-	90.84	-	-	0.63	0.12	-	-	-	-	-	-	-	-	91.83
GM	Listvenite	76Z-2-12-18	189.295	III	Fe oxide	Matrix	Elongated	Within Dol-Qz matrix	-	-	-	-	89.81	-	-	0.58	-	-	-	-	-	-	-	-	-	90.39
GM	Listvenite	76Z-2-12-18	189.295	III	Fe oxide	Matrix	Elongated	Within Dol-Qz matrix	0.76	-	-	-	90.45	-	-	0.21	-	-	-	-	-	-	-	-	-	91.42
GM	Listvenite	76Z-2-12-18	189.295	III	Fe oxide	Matrix	Elongated	Within Dol-Qz matrix	0.10	-	-	-	91.49	-	0.11	0.34	-	-	-	-	-	-	-	-	-	92.03
GM	Listvenite	76Z-2-12-18	189.295	III	Fe oxide	Matrix	Elongated	Within Dol-Qz matrix	0.43	-	-	-	90.78	-	-	0.26	-	-	-	-	-	-	-	-	-	91.47

Table S7 (continued)

									Cations p.f.u. (3O formula)																	
Facility	Lithology	Sample	Depth m.b.g	Domain[1]	Mineral	Structure	Texture	Zone	Si	Ti	Al	Cr	Fe	Mn	Mg	Ca	Na	K	Ni	Cu	Zn	S	Cl	Ba	Sr	Total
GM	Listvenite	46Z-4-46-51	106.3	I	Fe oxide	Matrix	Flaky	Inclusion in Mgs aggregate (close to core)	0.01	-	-	0.01	1.97	-	-	-	-	-	-	-	-	-	-	-	-	2.00
GM	Listvenite	46Z-4-46-51	106.3	I	Fe oxide	Matrix	Flaky	Inclusion in Mgs aggregate (close to core)	0.02	0.00	-	0.02	1.95	-	-	-	-	-	-	-	-	-	-	-	-	1.99
GM	Listvenite	46Z-4-46-51	106.3	I	Fe oxide	Matrix	Elongated	Inclusion in Mg-core spheroid (close to core)	0.01	-	-	-	1.82	-	0.24	0.00	-	-	-	-	-	-	-	-	-	2.08
GM	Listvenite	50Z-1-75-80	113.113	II	Fe oxide	Matrix	Anhedral	Inclusion in Mgs aggregate (close to core)	0.01	-	-	-	1.93	-	0.07	0.00	-	-	0.01	-	-	-	-	-	-	2.02
GM	Listvenite	50Z-1-75-80	113.113	II	Fe oxide	Matrix	Anhedral	Inclusion in Mgs aggregate (close to core)	0.01	-	-	-	1.97	-	0.01	-	-	-	0.01	-	-	-	-	-	-	2.00
GM	Listvenite	50Z-1-75-80	113.113	II	Fe oxide	Matrix	Anhedral	Inclusion in lss0	0.01	-	-	-	1.98	-	0.01	-	-	-	-	-	-	-	-	-	-	2.00
GM	Listvenite	50Z-1-75-80	113.113	II	Fe oxide	Matrix	Anhedral	Inclusion in lss0	0.01	-	-	-	1.98	-	0.01	-	-	-	-	-	-	-	-	-	-	2.00
GM	Listvenite	50Z-1-75-80	113.113	II	Fe oxide	Matrix	Anhedral	Inclusion in lss0	0.01	-	-	-	1.93	-	0.07	-	-	-	-	-	-	-	-	-	-	2.02
GM	Listvenite	50Z-1-75-80	113.113	II	Fe oxide	Matrix	Anhedral	Inclusion in lss0	0.01	-	-	-	1.78	-	0.30	0.00	-	-	0.01	-	-	-	-	-	-	2.10
GM	Listvenite	50Z-1-75-80	113.113	II	Fe oxide	Matrix	Subhedral	Inclusion in lss0	0.01	-	-	0.00	1.91	-	0.10	0.00	-	-	0.01	-	-	-	-	-	-	2.03
GM	Listvenite	50Z-1-75-80	113.113	II	Fe oxide	Matrix	Subhedral	Inclusion in lss0	0.00	-	-	0.01	1.97	-	0.00	-	-	-	0.01	-	-	-	-	-	-	2.00
GM	Listvenite	50Z-1-75-80	113.113	II	Fe oxide	Matrix	Anhedral	Within Qz matrix	0.01	-	-	-	1.92	-	0.10	-	-	-	-	-	-	-	-	-	-	2.03
GM	Fuchsite-bearing listvenite	60Z-1-32-37	140.17	II	Fe oxide	Matrix	Elongated	Inclusion in Mg-core spheroid (border)	0.02	-	0.00	-	1.96	-	0.01	-	-	-	-	-	-	-	-	-	-	1.99
GM	Fuchsite-bearing listvenite	60Z-1-32-37	140.17	II	Fe oxide	Matrix	Subhedral	Inclusion in Mg-core spheroid (border)	0.02	-	-	-	1.96	-	0.01	-	-	-	0.01	-	-	-	-	-	-	2.00
GM	Fuchsite-bearing listvenite	60Z-1-32-37	140.17	II	Fe oxide	Matrix	Subhedral	Inclusion in Mg-core spheroid (border)	0.02	-	-	-	1.96	-	0.01	-	-	-	0.02	-	-	-	-	-	-	2.00
GM	Listvenite	76Z-2-12-18	189.295	III	Fe oxide	Matrix	Elongated	Within Dol-Qz matrix	0.01	-	-	0.01	1.96	-	-	0.01	-	-	-	-	-	-	-	-	-	2.00
GM	Listvenite	76Z-2-12-18	189.295	III	Fe oxide	Matrix	Elongated	Within Dol-Qz matrix	0.01	-	-	0.00	1.97	-	-	0.01	-	-	-	-	-	-	-	-	-	2.00
GM	Listvenite	76Z-2-12-18	189.295	III	Fe oxide	Matrix	Elongated	Within Dol-Qz matrix	0.01	-	-	0.03	1.96	-	0.00	0.00	-	-	-	-	-	-	-	-	-	2.00
GM	Listvenite	76Z-2-12-18	189.295	III	Fe oxide	Matrix	Elongated	Within Dol-Qz matrix	0.01	-	-	-	1.97	-	-	0.02	0.01	-	-	-	-	-	-	-	-	2.01
GM	Listvenite	76Z-2-12-18	189.295	III	Fe oxide	Matrix	Elongated	Within Dol-Qz matrix	-	-	-	-	1.99	-	-	0.02	-	-	-	-	-	-	-	-	-	2.01
GM	Listvenite	76Z-2-12-18	189.295	III	Fe oxide	Matrix	Elongated	Within Dol-Qz matrix	0.02	-	-	-	1.97	-	-	0.01	-	-	-	-	-	-	-	-	-	1.99
GM	Listvenite	76Z-2-12-18	189.295	III	Fe oxide	Matrix	Elongated	Within Dol-Qz matrix	0.00	-	-	-	1.99	-	0.00	0.01	-	-	-	-	-	-	-	-	-	2.00
GM	Listvenite	76Z-2-12-18	189.295	III	Fe oxide	Matrix	Elongated	Within Dol-Qz matrix	0.01	-	-	-	1.98	-	-	0.01	-	-	-	-	-	-	-	-	-	2.00

Table S8: Major element compositions of sulfides determined by EPMA

Weight

Facility	Lithology	Sample	Depth m.b.g	Domain[1]	Mineral	Structure	Texture	Zone	Si %	Ti %	Al %	Cr %	Fe %	Mn %	Mg %	Ca %	Na %	K %	Ni %	Cu %	Zn %	S %	Cl %	Ba %	Sr %	O %	Total %
GM	Carb. serpentinite	44Z-4-0-5	99.415	I	Polydymite	Matrix		Core	0.04	-	-	0.06	0.76	0.02	0.03	-	-	-	53.37	0.33	0.04	41.61	-	-	-	-	96.26
GM	Carb. serpentinite	44Z-4-0-5	99.415	I	Polydymite	Matrix		Core	0.06	0.00	-	-	0.58	-	0.01	-	0.02	-	54.25	0.06	0.00	41.54	-	-	-	-	96.54
GM	Listvenite	46Z-4-46-51	106.3	I	Pyrite	Matrix		Core	0.02	0.03	0.01	-	45.83	0.04	-	-	0.10	0.01	0.19	0.33	0.10	53.30	-	-	-	-	99.95
GM	Listvenite	46Z-4-46-51	106.3	I	Pyrite	Matrix		Core	0.06	-	0.01	0.02	46.04	0.04	-	-	0.02	-	0.07	0.15	0.04	53.28	-	-	-	-	99.71
GM	Listvenite	46Z-4-46-51	106.3	I	Pyrite	Matrix		Core	0.22	0.00	0.01	0.01	44.96	0.02	0.02	0.04	0.01	-	0.53	0.47	-	52.81	-	-	-	-	99.08
GM	Listvenite	46Z-4-46-51	106.3	I	Pyrite	Matrix		Core	0.01	-	-	0.01	46.24	-	-	0.01	0.00	-	0.11	0.06	0.08	53.40	-	-	-	-	99.92
GM	Listvenite	46Z-4-46-51	106.3	I	Pyrite	Matrix		Core	0.01	0.02	-	0.01	43.09	0.02	0.02	-	0.03	-	3.63	0.00	-	52.55	-	-	-	-	99.36

Cations p.f.u. (7 for polydymite and 2 for pyrite)

Facility	Lithology	Sample	Depth m.b.g	Domain[1]	Mineral	Structure	Texture	Zone	Si	Ti	Al	Cr	Fe	Mn	Mg	Ca	Na	K	Ni	Cu	Zn	S	Cl	Ba	Sr	Total
GM	Carb. serpentinite	44Z-4-0-5	99.415	I	Polydymite	Matrix		Core	0.00	-	-	0.00	0.05	0.00	0.00	-	-	-	3.62	0.02	0.00	3.29	-	-	-	7.00
GM	Carb. serpentinite	44Z-4-0-5	99.415	I	Polydymite	Matrix		Core	0.01	0.00	-	-	0.04	-	0.00	-	0.00	-	3.67	0.00	0.00	3.28	-	-	-	7.00
GM	Listvenite	46Z-4-46-51	106.3	I	Pyrite	Matrix		Core	0.00	0.00	0.00	-	0.86	0.00	-	-	0.00	0.00	0.00	0.01	0.00	1.12	-	-	-	2.00
GM	Listvenite	46Z-4-46-51	106.3	I	Pyrite	Matrix		Core	0.00	-	0.00	0.00	0.87	0.00	-	-	0.00	-	0.00	0.00	0.00	1.13	-	-	-	2.00
GM	Listvenite	46Z-4-46-51	106.3	I	Pyrite	Matrix		Core	0.00	0.00	0.00	0.00	0.85	0.00	0.00	0.00	0.00	-	0.01	0.01	-	1.12	-	-	-	2.00
GM	Listvenite	46Z-4-46-51	106.3	I	Pyrite	Matrix		Core	0.00	-	-	0.00	0.87	-	-	0.00	0.00	-	0.00	0.00	0.00	1.13	-	-	-	2.00
GM	Listvenite	46Z-4-46-51	106.3	I	Pyrite	Matrix		Core	0.00	0.00	-	0.00	0.82	0.00	0.00	-	0.00	-	0.07	0.00	-	1.12	-	-	-	2.00

Table S9: Trace element concentrations and preferred values of certified rock standards NIST-612, BIR-1G, BCR-2G determined by LA-ICP-MS

		ISTE										GM									
		NIST SRM 612					BCR-2G					NIST SRM 612					BIR-1G				
Mass	Element	n	Average µg/g	SD µg/g	Pref. val. µg/g	Accuracy %	n	Average µg/g	SD µg/g	Pref. Val. µg/g	Accuracy %		Average µg/g	SD µg/g	Pref. val. µg/g	Accuracy %		Average µg/g	SD µg/g	Pref. Val. µg/g	Accuracy %
7	Li	30	41.54	0.35	40.20	3.34	10	9.68	0.82	9.00	7.59	26	42.09	1.59	40.20	4.71	18	3.07	0.30	3.00	2.20
9	Be	30	32.71	13.05	37.50	12.77	10	1.83	0.66	2.30	20.61	0	-	-	-	-	0	-	-	-	-
11	B	30	34.76	1.29	34.30	1.35	10	19.76	4.62	6.00	229	0	-	-	-	-	0	-	-	-	-
45	Sc	0	-	-	-	-	0	-	-	-	-	26	41.74	2.65	39.90	4.60	18	43.07	1.92	43.00	0.16
47	Ti	0	-	-	-	-	0	-	-	-	-	26	48.77	1.69	44.00	10.85	18	6569	265	5400	21.64
49	Ti	0	-	-	-	-	0	-	-	-	-	26	48.70	1.12	48.10	1.25	18	6972	242	5400	29.12
51	V	0	-	-	-	-	0	-	-	-	-	26	39.66	0.95	38.80	2.22	18	327	12.56	326	0.28
53	Cr	0	-	-	-	-	0	-	-	-	-	0	-	-	-	-	0	-	-	-	-
55	Mn	26	38.43	0.27	38.70	0.70	9	1597	26	1550	3.01	0	-	-	-	-	0	-	-	-	-
59	Co	0	-	-	-	-	0	-	-	-	-	26	35.70	0.97	35.50	0.57	18	52.63	1.95	52.00	1.21
62	Ni	30	38.46	0.62	38.80	0.88	10	14.60	0.58	13.00	12.28	26	38.90	0.95	38.80	0.26	18	175	7.79	178	1.94
63	Cu	0	-	-	-	-	0	-	-	-	-	26	37.19	1.30	37.80	1.61	18	115	5.81	119	3.68
65	Cu	30	36.71	0.27	37.80	2.88	10	17.56	0.48	21.00	16.37	0	-	-	-	-	0	-	-	-	-
66	Zn	26	37.92	0.29	39.10	3.01	9	177	5.19	125	41.52	20	38.09	1.11	39.10	2.59	13	88.62	5.41	78.00	13.61
75	As	0	-	-	-	-	0	-	-	-	-	20	37.57	1.12	35.70	5.23	12	0.14	0.06	-	-
85	Rb	30	31.63	0.31	31.40	0.73	10	47.20	0.97	47	0.43	26	32.06	1.34	31.40	2.09	18	0.21	0.02	0.20	4.20
86	Sr	0	-	-	-	-	0	-	-	-	-	24	76.30	1.41	78.40	2.68	17	103	3.58	109	5.73
88	Sr	30	76.15	0.85	78.40	2.87	10	323	10.32	342	5.42	26	77.39	3.97	78.40	1.29	18	104	4.37	109	4.20
89	Y	30	38.25	0.40	38.30	0.14	10	30.42	1.07	35.00	13.08	15	39.07	1.76	38.30	2.02	11	14.19	0.71	14.30	0.74
90	Zr	0	-	-	-	-	0	-	-	-	-	26	36.48	1.06	37.90	3.75	18	12.84	0.53	14.00	8.27
91	Zr	30	35.99	0.31	37.90	5.04	10	154	4.77	184	16.15	0	-	-	-	-	0	-	-	-	-
93	Nb	30	38.06	0.35	38.90	2.16	10	11.46	0.27	12.50	8.30	26	38.55	0.88	38.90	0.89	18	0.52	0.02	0.52	0.93
118	Sn	0	-	-	-	-	0	-	-	-	-	0	-	-	-	-	0	-	-	-	-
119	Sn	0	-	-	-	-	0	-	-	-	-	0	-	-	-	-	0	-	-	-	-
121	Sb	0	-	-	-	-	0	-	-	-	-	20	38.61	1.12	34.70	11.26	13	0.56	0.03	0.56	0.73
123	Sb	0	-	-	-	-	0	-	-	-	-	20	38.59	0.91	34.70	11.21	13	0.55	0.03	0.56	1.32
133	Cs	4	41.64	0.20	42.70	2.48	1	1.09	-	1.16	5.86	26	41.80	2.08	42.70	2.12	18	0.01	0.00	0.01	27.54
137	Ba	30	37.74	0.66	39.30	3.97	10	622	23.03	683	8.95	26	38.42	1.81	39.30	2.24	18	6.06	0.31	6.50	6.71
139	La	30	35.77	0.56	36.00	0.64	10	23.42	1.03	24.70	5.19	26	36.95	2.01	36.00	2.65	18	0.60	0.03	0.61	2.03
140	Ce	30	38.35	0.69	38.40	0.13	10	50.99	2.01	53.30	4.34	26	38.81	1.06	38.40	1.07	18	1.83	0.07	1.89	3.18
141	Pr	30	37.16	0.64	37.90	1.95	10	6.25	0.30	6.70	6.69	26	37.55	1.60	37.90	0.93	18	0.35	0.02	0.37	4.14
143	Nd	30	35.24	0.69	35.50	0.73	10	26.19	1.25	28.90	9.38	26	36.12	1.77	35.50	1.76	18	2.28	0.11	2.37	3.68
147	Sm	30	36.72	0.71	37.70	2.59	10	5.89	0.27	6.59	10.68	26	37.33	1.57	37.70	0.98	18	1.02	0.06	1.09	6.53
151	Eu	30	34.44	0.68	35.60	3.25	10	1.76	0.08	1.97	10.65	26	35.03	1.29	35.60	1.61	18	0.50	0.02	0.52	3.32
157	Gd	30	36.95	0.76	37.30	0.93	10	5.85	0.36	6.71	12.76	26	37.50	1.76	37.30	0.52	18	1.68	0.07	1.85	9.23
159	Tb	30	35.92	0.74	37.60	4.46	10	0.88	0.06	1.02	13.36	26	36.45	1.31	37.60	3.05	18	0.33	0.02	0.35	7.11
163	Dy	30	35.97	0.79	35.50	1.34	10	5.70	0.40	6.44	11.49	26	36.50	1.45	35.50	2.82	18	2.47	0.12	2.55	2.98
165	Ho	30	37.88	0.88	38.30	1.11	10	1.15	0.08	1.27	9.47	26	38.43	1.43	38.30	0.33	18	0.54	0.03	0.56	2.70
166	Er	30	37.44	0.85	38.00	1.49	10	3.20	0.20	3.70	13.57	26	37.98	1.35	38.00	0.05	18	1.60	0.08	1.70	5.99
169	Tm	30	37.56	0.86	36.80	2.06	10	0.47	0.03	0.51	7.65	26	38.09	1.30	36.80	3.49	18	0.24	0.01	0.24	0.02
172	Yb	30	39.96	0.96	39.20	1.93	10	3.09	0.22	3.39	8.81	26	40.53	1.36	39.20	3.39	18	1.66	0.07	1.64	1.22
175	Lu	30	37.72	0.97	37.00	1.95	10	0.46	0.03	0.50	9.48	26	38.23	1.19	37.00	3.32	18	0.24	0.01	0.25	2.60
178	Hf	30	34.78	1.07	36.70	5.22	10	4.11	0.33	4.84	15.17	26	35.23	0.95	36.70	4.00	18	0.51	0.03	0.57	9.82
181	Ta	0	-	-	-	-	0	-	-	-	-	26	40.29	1.03	37.60	7.14	18	0.04	0.00	0.04	1.74
208	Pb	30	38.97	1.10	38.57	1.04	10	10.81	0.60	11.00	1.76	26	39.42	1.16	38.57	2.20	18	3.62	0.23	3.70	2.16
232	Th	30	37.25	1.10	37.79	1.44	10	5.37	0.40	5.90	9.05	26	37.73	1.12	37.79	0.16	18	0.03	0.00	0.03	3.76
238	U	30	37.17	1.19	37.38	0.56	10	1.67	0.11	1.69	1.37	26	37.61	1.11	37.38	0.61	18	0.02	0.00	0.02	28.21

Table S10: Trace element compositions of silicates and carbonates determined by LA-ICP-MS

Facility	Lithology	Sample	Depth m	Domain[1]	Mineral	Structure	Texture	Location	Analysis #	Element	Normalization value (EPMA wt%)	Repetition rate Hz	Energy density J/cm2	Spot size µm
ISTE	Carb. serpentinite	43Z-3-52-57	96.115	I	Serpentine	Matrix	Mesh		au24e03	Si	43.06	12	7	100
ISTE	Carb. serpentinite	43Z-3-52-57	96.115	I	Serpentine	Matrix	Mesh		au24e04	Si	43.03	12	7	100
ISTE	Carb. serpentinite	43Z-3-52-57	96.115	I	Serpentine	Matrix	Mesh		au24e05	Si	43.20	12	7	100
ISTE	Carb. serpentinite	43Z-3-52-57	96.115	I	Serpentine	Matrix	Mesh		au24e09	Si	43.05	12	7	100
ISTE	Carb. serpentinite	43Z-3-52-57	96.115	I	Serpentine	Matrix	Mesh		au24e11	Si	42.22	12	7	100
GM	Carb. serpentinite	43Z-3-52-57	96.115	I	Serpentine	Matrix	Mesh		mb_1	Si	43.20	7	6	110
GM	Carb. serpentinite	43Z-3-52-57	96.115	I	Serpentine	Matrix	Mesh		mb_6	Si	43.05	7	6	110
GM	Carb. serpentinite	43Z-3-52-57	96.115	I	Serpentine	Matrix	Mesh		mb_7	Si	42.22	7	6	110
ISTE	Carb. serpentinite	43Z-4-52-57	96.705	I	Serpentine	Matrix	Mesh		au24e14	Si	43.78	12	7	100
ISTE	Carb. serpentinite	43Z-4-52-57	96.705	I	Serpentine	Matrix	Mesh		au24e17	Si	43.67	12	7	100
ISTE	Carb. serpentinite	43Z-4-52-57	96.705	I	Serpentine	Matrix	Mesh		au24f03	Si	43.67	12	7	100
ISTE	Carb. serpentinite	43Z-4-52-57	96.705	I	Serpentine	Matrix	Mesh		au24f05	Si	43.78	12	7	100
ISTE	Carb. serpentinite	44Z-1-41-46	97.56	I	Serpentine	Matrix	Mesh		au24f08	Si	40.14	12	7	100
ISTE	Carb. serpentinite	44Z-1-41-46	97.56	I	Serpentine	Matrix	Mesh		au24f10	Si	40.22	12	7	100
ISTE	Carb. serpentinite	44Z-1-41-46	97.56	I	Serpentine	Matrix	Mesh		au24f11	Si	41.90	12	7	100
ISTE	Carb. serpentinite	44Z-1-41-46	97.56	I	Serpentine	Matrix	Mesh		au24f14	Si	40.98	12	7	100
GM	Carb. serpentinite	44Z-1-41-46	97.56	I	Serpentine	Matrix	Mesh		kb_3	Si	40.98	7	6	110
GM	Carb. serpentinite	44Z-1-41-46	97.56	I	Serpentine	Matrix	Mesh		kb_8	Si	40.14	7	6	110
GM	Carb. serpentinite	44Z-1-41-46	97.56	I	Serpentine	Matrix	Mesh		kb_10	Si	40.22	7	6	110
ISTE	Carb. serpentinite	44Z-4-0-5	99.415	I	Serpentine	Matrix	Mesh		au24f17	Si	43.99	12	7	100
ISTE	Carb. serpentinite	44Z-4-0-5	99.415	I	Serpentine	Matrix	Mesh		au24g04	Si	43.35	12	7	100
ISTE	Carb. serpentinite	44Z-4-0-5	99.415	I	Serpentine	Matrix	Mesh		au24g08	Si	43.43	12	7	100
ISTE	Carb. serpentinite	44Z-4-0-5	99.415	I	Serpentine	Matrix	Mesh		au24g15	Si	43.95	12	7	100
ISTE	Carb. serpentinite	44Z-4-0-5	99.415	I	Serpentine	Matrix	Mesh		au24g16	Si	43.88	12	7	100
GM	Carb. serpentinite	44Z-4-0-5	99.415	I	Serpentine	Matrix	Mesh		ha29	Ca	0.10	7	6	110
ISTE	Carb. serpentinite	43Z-3-52-57	96.115	I	Serpentine	Matrix	Bastite		au24e06	Si	42.93	12	7	100
GM	Carb. serpentinite	43Z-3-52-57	96.115	I	Serpentine	Matrix	Bastite		mb_3	Si	42.33	7	6	110
GM	Carb. serpentinite	43Z-3-52-57	96.115	I	Serpentine	Matrix	Bastite		mb_4	Si	42.33	7	6	110
ISTE	Carb. serpentinite	44Z-1-41-46	97.56	I	Serpentine	Matrix	Bastite		au24f07	Si	40.56	12	7	100
ISTE	Carb. serpentinite	44Z-1-41-46	97.56	I	Serpentine	Matrix	Bastite		au24f12	Si	39.55	12	7	100
ISTE	Carb. serpentinite	44Z-1-41-46	97.56	I	Serpentine	Matrix	Bastite		au24f13	Si	42.05	12	7	100
GM	Carb. serpentinite	44Z-1-41-46	97.56	I	Serpentine	Matrix	Bastite		kb_1	Si	39.55	7	6	110
GM	Carb. serpentinite	44Z-1-41-46	97.56	I	Serpentine	Matrix	Bastite		kb_2	Si	42.05	7	6	110
GM	Carb. serpentinite	44Z-1-41-46	97.56	I	Serpentine	Matrix	Bastite		kb_5	Si	40.56	7	6	110
ISTE	Carb. serpentinite	44Z-4-0-5	99.415	I	Serpentine	Matrix	Bastite		au24g05	Si	42.05	12	7	100
ISTE	Carb. serpentinite	44Z-4-0-5	99.415	I	Serpentine	Matrix	Bastite		au24g07	Si	43.22	12	7	100
ISTE	Carb. serpentinite	43Z-3-52-57	96.115	I	Serpentine	Vein	sc0		au24e07	Si	43.88	12	7	100
ISTE	Carb. serpentinite	43Z-3-52-57	96.115	I	Serpentine	Vein	sc0		au24e10	Si	43.88	12	7	100
GM	Carb. serpentinite	43Z-3-52-57	96.115	I	Serpentine	Vein	sc0	Median zone	mb_2	Si	43.88	7	6	110
GM	Carb. serpentinite	43Z-3-52-57	96.115	I	Serpentine	Vein	sc0	Median zone	mb_8	Si	43.88	7	6	110
ISTE	Carb. serpentinite	43Z-4-52-57	96.705	I	Serpentine	Vein	sc0	Median zone	au24e12	Si	44.02	12	7	100
ISTE	Carb. serpentinite	43Z-4-52-57	96.705	I	Serpentine	Vein	sc0	Median zone	au24e15	Si	44.68	12	7	100
ISTE	Carb. serpentinite	43Z-4-52-57	96.705	I	Serpentine	Vein	sc0	Rim	au24e16	Si	44.40	12	7	100
ISTE	Carb. serpentinite	43Z-4-52-57	96.705	I	Serpentine	Vein	sc0		au24f04	Si	43.03	12	7	100
GM	Carb. serpentinite	44Z-1-41-46	97.56	I	Serpentine	Vein	sc0		kb_4	Si	41.25	7	6	110
GM	Carb. serpentinite	44Z-1-41-46	97.56	I	Serpentine	Vein	sc0		kb_9	Si	42.38	7	6	110

ISTE	Carb. serpentinite	44Z-4-0-5	99.415	I	Serpentine	Vein	sc0		au24f16	Si	43.98	12	7	100
ISTE	Carb. serpentinite	44Z-4-0-5	99.415	I	Serpentine	Vein	sc0		au24g03	Si	43.93	12	7	100
ISTE	Carb. serpentinite	44Z-4-0-5	99.415	I	Serpentine	Vein	sc0		au24g06	Si	44.97	12	7	100
ISTE	Carb. serpentinite	44Z-4-0-5	99.415	I	Serpentine	Vein	sc0		au24g14	Si	43.69	12	7	100
ISTE	Carb. serpentinite	44Z-4-0-5	99.415	I	Serpentine	Vein	sc0		au24g17	Si	44.30	12	7	100
GM	Carb. serpentinite	44Z-4-0-5	99.415	I	Serpentine	Vein	sc0	Median zone	ha28	Si	44.33	7	6	110
GM	Fu-listvenite	53Z-2-32-37	122.87	II	Fuchsite	Matrix			ha1	Si	44.66	7	6	110
GM	Fu-listvenite	53Z-2-32-37	122.87	II	Fuchsite	Matrix			ha2	Si	43.57	7	6	110
GM	Fu-listvenite	53Z-2-32-37	122.87	II	Fuchsite	Matrix			ha3	Si	43.30	7	6	110
GM	Fu-listvenite	53Z-2-32-37	122.87	II	Fuchsite	Matrix			ha4	Si	44.91	7	6	110
GM	Fu-listvenite	53Z-2-32-37	122.87	II	Fuchsite	Matrix			ha5	Si	43.53	7	6	110
ISTE	Fu-listvenite	60Z-1-32-37	140.17	II	Fuchsite	Matrix			au25c03	Al	27.49	20	7	100
ISTE	Fu-listvenite	60Z-1-32-37	140.17	II	Fuchsite	Matrix			au25c04	Al	27.49	20	7	100
ISTE	Fu-listvenite	60Z-1-32-37	140.17	II	Fuchsite	Matrix			au25c11	Al	28.62	20	7	100
GM	Fu-listvenite	60Z-1-32-37	140.17	II	Fuchsite	Matrix			mb_43	Si	54.39	7	6	110
GM	Fu-listvenite	60Z-1-32-37	140.17	II	Fuchsite	Matrix			mb_44	Si	50.38	7	6	110
GM	Fu-listvenite	60Z-1-32-37	140.17	II	Fuchsite	Matrix			mb_45	Si	50.27	7	6	110
GM	Fu-listvenite	60Z-1-32-37	140.17	II	Fuchsite	Matrix			mb_46	Si	51.00	7	6	110
ISTE	Carb. serpentinite	43Z-4-52-57	96.705	I	Dolomite	Matrix	Spheroid		au24c09	Ca	29.89	12	7	100
ISTE	Carb. serpentinite	43Z-4-52-57	96.705	I	Dolomite	Matrix	Spheroid		au24c12	Ca	19.31	12	7	100
GM	Carb. serpentinite	44Z-1-41-46	97.56	I	Dolomite	Matrix	Spheroid		kb_15	Ca	16.74	7	6	110
GM	Fu-listvenite	60Z-1-32-37	140.2	II	Dolomite	Matrix	Spheroid		mb_56	Ca	26.01	7	6	110
ISTE	Carb. serpentinite	40Z-3-11-16	87.035	I	Dolomite	Matrix	Aggregate		au24d08	Ca	29.96	12	7	100
ISTE	Carb. serpentinite	40Z-3-11-16	87.035	I	Dolomite	Matrix	Aggregate		au24d09	Ca	29.91	12	7	100
ISTE	Carb. serpentinite	40Z-3-11-16	87.035	I	Dolomite	Matrix	Aggregate		au24d11	Ca	29.76	12	7	100
ISTE	Carb. serpentinite	40Z-3-11-16	87.035	I	Dolomite	Matrix	Aggregate		au24d12	Ca	29.29	12	7	100
GM	Carb. serpentinite	40Z-3-11-16	87.035	I	Dolomite	Matrix	Aggregate		kb_28	Ca	29.76	7	6	110
GM	Carb. serpentinite	40Z-3-11-16	87.035	I	Dolomite	Matrix	Aggregate		kb_30	Ca	29.91	7	6	110
ISTE	Listvenite	30Z-2-33-39	63.7	I	Dolomite	Matrix	Aggregate		au25d03	Ca	27.97	12	7	100
ISTE	Listvenite	30Z-2-33-39	63.7	I	Dolomite	Matrix	Aggregate		au25d07	Ca	25.15	12	7	100
ISTE	Listvenite	30Z-2-33-39	63.7	I	Dolomite	Matrix	Aggregate		au25d08	Ca	25.14	12	7	100
ISTE	Listvenite	30Z-2-33-39	63.7	I	Dolomite	Matrix	Aggregate		au25d10	Ca	28.27	12	7	100
GM	Listvenite	30Z-2-33-39	63.7	I	Dolomite	Matrix	Aggregate		kb_22	Ca	27.97	7	6	110
GM	Listvenite	30Z-2-33-39	63.7	I	Dolomite	Matrix	Aggregate		kb_25	Ca	28.27	7	6	110
ISTE	Listvenite	76Z-2-12-20	189.3	III	Dolomite	Matrix	Aggregate		au25f13	Ca	27.35	12	7	100
ISTE	Listvenite	76Z-2-12-20	189.3	III	Dolomite	Matrix	Aggregate		au25f15	Ca	25.58	12	7	100
ISTE	Listvenite	76Z-2-12-20	189.3	III	Dolomite	Matrix	Aggregate		au25g05	Ca	29.32	12	7	100
GM	Listvenite	76Z-2-12-20	189.3	III	Dolomite	Matrix	Aggregate		mb_53	Ca	29.32	7	6	110
ISTE	Listvenite	76Z-2-12-20	189.3	III	Dolomite	Matrix	Aggregate		au25g06	Ca	29.32	12	7	100
GM	Listvenite	76Z-2-12-20	189.3	III	Dolomite	Matrix	Aggregate		mb_49	Ca	25.58	7	6	110
GM	Listvenite	76Z-2-12-20	189.3	III	Dolomite	Matrix	Aggregate		mb_55	Ca	29.32	7	6	110
ISTE	Carb. serpentinite	43Z-4-52-57	96.705	I	Dolomite	Vein	sc0		au24c08	Ca	29.54	12	7	100
ISTE	Carb. serpentinite	43Z-4-52-57	96.705	I	Dolomite	Vein	sc0		au24c11	Ca	29.54	12	7	100
GM	Carb. serpentinite	44Z-1-41-46	97.56	I	Dolomite	Vein	sc0		kb_12	Ca	27.23	7	6	110
GM	Carb. serpentinite	44Z-1-41-46	97.56	I	Dolomite	Vein	sc0		kb_14	Ca	27.23	7	6	110
ISTE	Carb. serpentinite	44Z-1-41-46	97.56	I	Dolomite	Vein	sc2		au24c17	Ca	29.27	12	7	100
ISTE	Listvenite	46Z-4-46-51	106.3	I	Dolomite	Vein	lc1		au25e14	Ca	29.06	12	7	100
GM	Listvenite	46Z-4-46-51	106.3	I	Dolomite	Vein	lc1	Median zone	mb_16	Ca	29.63	7	6	110
ISTE	Listvenite	30Z-2-33-39	63.7	I	Dolomite	Vein	lc2		au25d05	Ca	24.61	12	7	100
GM	Listvenite	30Z-2-33-39	63.7	I	Dolomite	Vein	lc2		kb_24	Ca	24.61	7	6	110
ISTE	Listvenite	38Z-3-60-65	80.61	I	Dolomite	Vein	lc2		au24d13	Ca	26.64	12	7	100
ISTE	Listvenite	38Z-3-60-65	80.61	I	Dolomite	Vein	lc2		au24d14	Ca	26.23	12	7	100

ISTE	Listvenite	38Z-3-60-65	80.61	I	Dolomite	Vein	lc2		au24d17	Ca	26.23	12	7	100
GM	Listvenite	16Z-1-65-70	27.65	I	Dolomite	Vein	lc6	Median zone	ha22	Ca	28.47	7	6	110
ISTE	Listvenite	30Z-2-33-39	63.7	I	Dolomite	Vein	lc6		au25d12	Ca	27.97	12	7	100
GM	Listvenite	30Z-2-33-39	63.7	I	Dolomite	Vein	lc6		kb_27	Ca	27.97	7	6	110
ISTE	Listvenite	46Z-4-46-51	106.3	I	Dolomite	Vein	lc6		au25e17	Ca	26.71	12	7	100
ISTE	Listvenite	76Z-2-12-20	189.3	III	Dolomite	Vein	lc6		au25f14	Ca	30.02	12	7	100
ISTE	Listvenite	76Z-2-12-20	189.3	III	Dolomite	Vein	lc6		au25f16	Ca	29.62	12	7	100
ISTE	Listvenite	76Z-2-12-20	189.3	III	Dolomite	Vein	lc6		au25f17	Ca	29.64	12	7	100
GM	Listvenite	76Z-2-12-20	189.3	III	Dolomite	Vein	lc6		mb_48	Ca	30.02	7	6	110
GM	Listvenite	76Z-2-12-20	189.3	III	Dolomite	Vein	lc6		mb_50	Ca	29.64	7	6	110
GM	Listvenite	76Z-2-12-20	189.3	III	Dolomite	Vein	lc6		mb_52	Ca	29.62	7	6	110
ISTE	Fu-listvenite	60Z-1-32-37	140.17	II	Dolomite	Vein	lc6		au25g12	Ca	27.24	12	7	100
GM	Fu-listvenite	60Z-1-32-37	140.17	II	Dolomite	Vein	lc6	Median zone	mb_35	Ca	30.14	7	6	110
ISTE	Listvenite	50Z-1-75-80	113.15	II	Magnesite	Matrix	Fe-core spheroid		au25d17	Ca	0.28	12	7	100
GM	Listvenite	50Z-1-75-80	113.15	II	Magnesite	Matrix	Fe-core spheroid	Core	mb_26	Ca	0.80	7	6	110
GM	Listvenite	50Z-1-75-80	113.15	II	Magnesite	Matrix	Fe-core spheroid	Core	ha26	Ca	0.80	7	6	110
GM	Listvenite	50Z-1-75-80	113.15	II	Magnesite	Matrix	Fe-core spheroid	Core	ha27	Ca	0.80	7	6	110
ISTE	Carb. serpentinite	44Z-1-41-46	97.56	I	Magnesite	Matrix	Mg-core spheroid		au24c13	Ca	1.02	12	7	100
ISTE	Carb. serpentinite	44Z-1-41-46	97.56	I	Magnesite	Matrix	Mg-core spheroid		au24c15	Ca	1.05	12	7	100
ISTE	Carb. serpentinite	44Z-4-0-5	99.415	I	Magnesite	Matrix	Mg-core spheroid		au24d03	Ca	0.70	12	7	100
ISTE	Carb. serpentinite	44Z-4-0-5	99.415	I	Magnesite	Matrix	Mg-core spheroid		au24d05	Ca	1.23	12	7	100
ISTE	Carb. serpentinite	44Z-4-0-5	99.415	I	Magnesite	Matrix	Mg-core spheroid		au24d06	Ca	0.92	12	7	100
ISTE	Listvenite	50Z-1-75-80	113.15	II	Magnesite	Matrix	Mg-core spheroid		au25d14	Ca	0.13	12	7	100
ISTE	Listvenite	46Z-4-46-51	106.3	I	Magnesite	Matrix	Mg-core spheroid		au25e08	Ca	0.21	12	7	100
ISTE	Listvenite	46Z-4-46-51	106.3	I	Magnesite	Matrix	Mg-core spheroid	Internal growth	au25e09	Ca	0.22	12	7	100
ISTE	Listvenite	46Z-4-46-51	106.3	I	Magnesite	Matrix	Mg-core spheroid		au25e10	Ca	0.04	12	7	100
ISTE	Listvenite	46Z-4-46-51	106.3	I	Magnesite	Matrix	Mg-core spheroid		au25e11	Ca	0.21	12	7	100
ISTE	Listvenite	46Z-4-46-51	106.3	I	Magnesite	Matrix	Mg-core spheroid		au25e12	Ca	0.25	12	7	100
ISTE	Listvenite	46Z-4-46-51	106.3	I	Magnesite	Matrix	Mg-core spheroid		au25e13	Ca	0.04	12	7	100
GM	Carb. serpentinite	44Z-4-0-5	99.415	I	Magnesite	Matrix	Mg-core spheroid	Core	ha31	Ca	0.70	7	6	85
GM	Listvenite	50Z-1-75-80	113.15	II	Magnesite	Matrix	Mg-core spheroid	Core	mb_29	Ca	0.13	7	6	110
GM	Listvenite	50Z-1-75-80	113.15	II	Magnesite	Matrix	Mg-core spheroid	Core	mb_30	Ca	0.13	7	6	110
GM	Fu-listvenite	53Z-2-32-37	122.87	II	Magnesite	Matrix	Mg-core spheroid	Core	ha13	Ca	0.09	7	6	110
GM	Fu-listvenite	60Z-1-32-37	140.17	II	Magnesite	Matrix	Mg-core spheroid	Core	mb_38	Ca	0.41	7	6	110
GM	Fu-listvenite	60Z-1-32-37	140.17	II	Magnesite	Matrix	Mg-core spheroid	Core	mb_39	Ca	0.36	7	6	110
GM	Fu-listvenite	53Z-2-32-37	122.87	II	Magnesite	Matrix	Mg-core spheroid	Core	ha7	Ca	0.49	7	6	110
GM	Listvenite	46Z-4-46-51	106.3	I	Magnesite	Matrix	Mg-core spheroid	Core	mb_14	Ca	0.67	7	6	110
GM	Listvenite	46Z-4-46-51	106.3	I	Magnesite	Matrix	Mg-core spheroid	Core	mb_15	Ca	0.08	7	6	110
GM	Listvenite	46Z-4-46-51	106.3	I	Magnesite	Matrix	Mg-core spheroid	Core	mb_17	Ca	0.37	7	6	110
ISTE	Fu-listvenite	60Z-1-32-37	140.17	II	Magnesite	Matrix	Mg-core spheroid		au25g13	Ca	0.30	12	7	100
GM	Listvenite	46Z-4-46-51	106.3	I	Magnesite	Matrix	Euhedral	Core	mb_18	Ca	1.25	7	6	110
ISTE	Listvenite	50Z-1-75-80	113.15	II	Magnesite	Matrix	Aggregate		au25e06	Ca	0.14	12	7	100
ISTE	Listvenite	30Z-2-33-39	63.7	I	Magnesite	Matrix	Aggregate		au25d11	Ca	0.40	12	7	100
ISTE	Listvenite	35Z-1-56-61	72.01	I	Magnesite	Matrix	Aggregate		au25f03	Ca	0.22	12	7	100
ISTE	Listvenite	35Z-1-56-61	72.01	I	Magnesite	Matrix	Aggregate		au25f04	Ca	0.53	12	7	100
ISTE	Listvenite	35Z-1-56-61	72.01	I	Magnesite	Matrix	Aggregate		au25f08	Ca	0.04	12	7	100
ISTE	Listvenite	35Z-1-56-61	72.01	I	Magnesite	Matrix	Aggregate		au25f09	Ca	0.40	12	7	100
ISTE	Listvenite	35Z-1-56-61	72.01	I	Magnesite	Matrix	Aggregate (clast)		au25f10	Ca	0.28	12	7	100
ISTE	Listvenite	35Z-1-56-61	72.01	I	Magnesite	Matrix	Aggregate		au25f12	Ca	0.43	12	7	100
ISTE	Fu-listvenite	60Z-1-32-37	140.17	II	Magnesite	Matrix	Aggregate		au25g08	Ca	0.26	12	7	100
ISTE	Fu-listvenite	60Z-1-32-37	140.17	II	Magnesite	Matrix	Aggregate		au25g09	Ca	0.36	12	7	100
GM	Listvenite	46Z-4-46-51	106.3	I	Magnesite	Matrix	Aggregate		mb_24	Ca	0.40	7	6	110
GM	Fu-listvenite	53Z-2-32-37	122.87	II	Magnesite	Matrix	Aggregate		ha9	Ca	0.19	7	6	110

GM	Fu-listvenite	53Z-2-32-37	122.87	II	Magnesite	Matrix	Aggregate		ha15	Ca	0.12	7	6	110
GM	Listvenite	16Z-1-65-70	27.65	I	Magnesite	Matrix	Aggregate		ha18	Ca	0.07	7	6	110
GM	Listvenite	35Z-1-56-61	72.01	I	Magnesite	Matrix	Aggregate		kb_16	Ca	0.53	7	6	110
GM	Listvenite	35Z-1-56-61	72.01	I	Magnesite	Matrix	Aggregate		kb_18	Ca	0.22	7	6	110
GM	Listvenite	35Z-1-56-61	72.01	I	Magnesite	Matrix	Aggregate		kb_19	Ca	0.22	7	6	110
GM	Listvenite	35Z-1-56-61	72.01	I	Magnesite	Matrix	Aggregate		kb_20	Ca	0.22	7	6	110
GM	Listvenite	30Z-2-33-39	63.7	I	Magnesite	Matrix	Aggregate		kb_26	Ca	0.40	7	6	110
ISTE	Carb. serpentinite	44Z-1-41-46	97.56	I	Magnesite	Vein	sc0		au24c16	Ca	0.28	12	7	100
GM	Listvenite	16Z-1-65-70	27.65	I	Magnesite	Vein	lss0	Median zone	ha19	Ca	0.07	7	6	110
GM	Listvenite	16Z-1-65-70	27.65	I	Magnesite	Vein	lss0	Intermediate	ha20	Ca	0.07	7	6	110
GM	Listvenite	16Z-1-65-70	27.65	I	Magnesite	Vein	lss0	Median zone	ha21	Ca	0.12	7	6	110
ISTE	Fu-listvenite	60Z-1-32-37	140.17	II	Magnesite	Vein	lss0		au25g15	Ca	0.56	12	7	100
ISTE	Fu-listvenite	60Z-1-32-37	140.17	II	Magnesite	Vein	lss0		au25g16	Ca	0.34	12	7	100
ISTE	Fu-listvenite	60Z-1-32-37	140.17	II	Magnesite	Vein	lss0		au25g17	Ca	0.28	12	7	100
GM	Fu-listvenite	60Z-1-32-37	140.2	II	Magnesite	Vein	lss0		mb_57	Ca	0.18	7	6	110
GM	Fu-listvenite	60Z-1-32-37	140.17	II	Magnesite	Vein	lss0	Median zone	mb_41	Ca	0.34	7	6	110
ISTE	Listvenite	50Z-1-75-80	113.15	II	Magnesite	Vein	lss2		au25e03	Ca	0.35	12	7	100
ISTE	Listvenite	50Z-1-75-80	113.15	II	Magnesite	Vein	lss2	Rim	au25e05	Ca	0.19	12	7	100
ISTE	Listvenite	76Z-2-12-20	189.3	III	Magnesite	Vein	lss2		au25g03	Ca	9.23	12	7	100
GM	Listvenite	76Z-2-12-20	189.3	III	Magnesite	Vein	lss2		mb_51	Ca	9.23	7	6	110
GM	Listvenite	50Z-1-75-80	113.15	II	Magnesite	Vein	lss2	Median zone	mb_25	Ca	0.05	7	6	110
GM	Listvenite	50Z-1-75-80	113.15	II	Magnesite	Vein	lss2	Median zone	mb_33	Ca	0.18	7	6	110
ISTE	Carb. serpentinite	44Z-1-41-46	97.56	I	Magnesite	Vein	sc2		au24c14	Ca	0.64	12	7	100
GM	Carb. serpentinite	44Z-1-41-46	97.56	I	Magnesite	Vein	sc2		kb_11	Ca	0.64	7	6	110
ISTE	Carb. serpentinite	44Z-4-0-5	99.415	I	Magnesite	Vein	sc2		au24d04	Ca	0.52	12	7	100
ISTE	Carb. serpentinite	44Z-4-0-5	99.415	I	Magnesite	Vein	sc2		au24d07	Ca	0.43	12	7	100
GM	Carb. serpentinite	44Z-4-0-5	99.415	I	Magnesite	Vein	sc2	Median zone	ha30	Ca	0.22	7	6	85
GM	Listvenite	16Z-1-65-70	27.65	I	Siderite	Vein	lc1	Median zone	ha16	Ca	0.13	7	6	110
GM	Listvenite	16Z-1-65-70	27.65	I	Magnesite	Vein	lc1	Intermediate	ha17	Ca	0.04	7	6	110
GM	Listvenite	16Z-1-65-70	27.65	I	Magnesite	Vein	lc1	MZ-intermediate	ha23	Ca	0.06	7	6	110
GM	Listvenite	16Z-1-65-70	27.65	I	Magnesite	Vein	lc1	Rim	ha24	Ca	0.03	7	6	110
GM	Listvenite	16Z-1-65-70	27.65	I	Magnesite	Vein	lc1	Median zone	ha25	Ca	0.08	7	6	110
ISTE	Listvenite	30Z-2-33-39	63.7	I	Magnesite	Vein	lc1		au25d04	Ca	1.13	12	7	100
GM	Listvenite	30Z-2-33-39	63.7	I	Magnesite	Vein	lc1		kb_23	Ca	1.13	7	6	110
ISTE	Listvenite	35Z-1-56-61	72.01	I	Magnesite	Vein	lc1		au25f05	Ca	0.15	12	7	100
ISTE	Listvenite	35Z-1-56-61	72.01	I	Magnesite	Vein	lc1		au25f11	Ca	0.26	12	7	100
GM	Listvenite	35Z-1-56-61	72.01	I	Magnesite	Vein	lc1		kb_17	Ca	0.15	7	6	110
ISTE	Listvenite	38Z-3-60-65	80.61	I	Magnesite	Vein	lc1		au24d16	Ca	0.11	12	7	100
ISTE	Listvenite	46Z-4-46-51	106.3	I	Magnesite	Vein	lc1		au25e16	Ca	0.52	12	7	100
GM	Listvenite	46Z-4-46-51	106.3	I	Magnesite	Vein	lc1	Median zone	mb_13	Ca	1.49	7	6	110
GM	Listvenite	46Z-4-46-51	106.3	I	Magnesite	Vein	lc1		mb_20	Ca	0.08	7	6	110
GM	Fu-listvenite	53Z-2-32-37	122.87	II	Magnesite	Vein	lc1	Median zone	ha6	Ca	0.21	7	6	110
GM	Fu-listvenite	53Z-2-32-37	122.87	II	Magnesite	Vein	lc1	Median zone	ha10	Ca	0.10	7	6	110
GM	Fu-listvenite	53Z-2-32-37	122.87	II	Magnesite	Vein	lc1	Intermediate	ha11	Ca	0.17	7	6	110
ISTE	Fu-listvenite	60Z-1-32-37	140.17	II	Magnesite	Vein	lc1	Rim	au25g14	Ca	0.22	12	7	100
GM	Fu-listvenite	60Z-1-32-37	140.17	II	Magnesite	Vein	lc1	Median zone	mb_36	Ca	0.22	7	6	110
GM	Fu-listvenite	60Z-1-32-37	140.17	II	Magnesite	Vein	lc1	Median zone	mb_40	Ca	0.35	7	6	110
ISTE	Listvenite	76Z-2-12-20	189.3	III	Magnesite	Vein	lc1		au25g04	Ca	3.04	12	7	100
ISTE	Listvenite	76Z-2-12-20	189.3	III	Magnesite	Vein	lc1		au25g07	Ca	0.06	12	7	100
GM	Listvenite	76Z-2-12-20	189.3	III	Magnesite	Vein	lc1		mb_54	Ca	0.06	7	6	110
ISTE	Listvenite	46Z-4-46-51	106.3	I	Magnesite	Vein	lc2		au25e15	Ca	0.28	12	7	100
GM	Listvenite	46Z-4-46-51	106.3	I	Magnesite	Vein	lc2	Median zone	mb_19	Ca	0.28	7	6	110
ISTE	Fu-listvenite	60Z-1-32-37	140.17	II	Magnesite	Vein	lc2		au25g11	Ca	0.15	12	7	100

GM	Fu-listvenite	60Z-1-32-37	140.17	II	Magnesite	Vein	lc2	Median zone	mb_37	Ca	0.31	7	6	110
GM	Listvenite	46Z-4-46-51	106.3	I	Magnesite	Vein	lq4	Rim	mb_22	Ca	1.14	7	6	110
GM	Fu-listvenite	53Z-2-32-37	122.87	II	Magnesite	Vein	lc5 or lc6	Median zone	ha12	Ca	0.35	7	6	110

Table S10 (continued)

Analysis #	Li7 µg/g	Be9 µg/g	B11 µg/g	Sc45 µg/g	Ti47 µg/g	Ti49 µg/g	V51 µg/g	Cr53 µg/g	Mn55 µg/g	Co59 µg/g	Ni62 µg/g	Cu63 µg/g	Cu65 µg/g	Zn66 µg/g	As75 µg/g	Rb85 µg/g	Sr86 µg/g	Sr88 µg/g	Y89 µg/g	Zr90 µg/g	Zr91 µg/g	Nb93 µg/g	Sn118 µg/g	Sn119 µg/g
au24e03	6.97	-	-	-	-	-	-	-	230	-	2152	-	0.76	27.83	-	0.02	-	3.49	0.03	-	-	0.001	-	-
au24e04	8.71	-	-	-	-	-	-	-	266	-	2648	-	1.54	30.30	-	0.03	-	2.56	0.02	-	-	0.001	-	-
au24e05	12.64	-	-	-	-	-	-	-	381	-	3014	-	0.54	43.72	-	0.04	-	5.85	0.05	-	-	0.003	-	-
au24e09	11.55	-	-	-	-	-	-	-	304	-	2390	-	0.59	41.64	-	0.03	-	5.56	0.04	-	-	0.002	-	-
au24e11	15.37	-	-	-	-	-	-	-	344	-	2093	-	0.45	39.64	-	0.03	-	5.74	0.05	-	-	0.002	-	-
mb_1	8.77	-	-	7.05	11.03	10.16	7.65	-	-	77.55	2625	0.60	0.60	22.74	2.73	0.03	1.77	1.72	-	-	-	-	-	-
mb_6	8.78	-	-	7.99	8.32	7.95	9.33	-	-	55.52	2669	1.34	1.34	24.68	3.75	0.04	3.78	3.80	-	-	-	0.001	-	-
mb_7	7.91	-	-	7.61	6.95	6.91	10.52	-	-	61.52	3697	0.62	0.62	24.64	3.41	0.04	3.66	3.92	-	-	-	0.001	-	-
au24e14	8.54	-	-	-	-	-	-	-	270	-	2530	-	6.55	46.39	-	0.02	-	4.49	0.02	-	0.028	0.001	-	-
au24e17	10.65	-	-	-	-	-	-	-	282	-	2664	-	0.63	45.18	-	0.03	-	3.74	0.02	-	0.119	0.002	-	-
au24f03	11.08	-	-	-	-	-	-	-	257	-	2432	-	0.94	45.87	-	0.02	-	4.92	0.02	-	-	0.000	-	-
au24f05	13.72	-	-	-	-	-	-	-	363	-	2271	-	0.66	59.68	-	0.02	-	6.40	0.03	-	0.048	0.003	-	-
au24f08	5.46	-	-	-	-	-	-	-	199	-	3350	-	0.43	14.87	-	0.02	-	6.98	0.06	-	0.004	-	-	-
au24f10	6.46	-	-	-	-	-	-	-	201	-	3032	-	0.58	15.15	-	0.03	-	8.88	0.06	-	0.031	0.001	-	-
au24f11	16.62	-	-	-	-	-	-	-	461	-	3328	-	0.40	34.30	-	0.07	-	8.21	0.22	-	0.005	0.009	-	-
au24f14	11.11	-	-	-	-	-	-	-	499	-	2858	-	0.69	25.37	-	0.07	-	8.66	0.14	-	0.007	0.002	-	-
kb_3	9.49	-	-	12.31	36.46	37.29	25.19	-	-	94.12	2898	0.24	0.24	-	-	0.06	5.70	5.79	0.09	0.004	-	0.002	-	-
kb_8	4.74	-	-	7.74	20.92	21.03	12.04	-	-	63.08	2772	0.13	0.13	-	-	0.03	6.96	7.20	0.05	-	-	-	-	-
kb_10	7.18	-	-	5.12	13.76	14.08	8.38	-	-	78.83	3275	0.56	0.56	-	-	0.04	2.95	3.03	0.04	-	-	0.000	-	-
au24f17	25.82	-	-	-	-	-	-	-	217	-	2258	-	1.20	45.67	-	0.05	-	22.33	0.03	-	0.016	0.001	-	-
au24g04	44.35	-	-	-	-	-	-	-	96	-	3598	-	0.44	52.37	-	0.05	-	4.51	0.02	-	0.002	0.001	-	-
au24g08	28.84	-	-	-	-	-	-	-	283	-	2483	-	1.40	57.50	-	0.07	-	6.42	0.04	-	0.007	0.003	-	-
au24g15	25.58	-	-	-	-	-	-	-	229	-	2321	-	0.49	50.17	-	0.05	-	8.47	0.03	-	0.002	0.002	-	-
au24g16	21.66	-	-	-	-	-	-	-	478	-	2639	-	3.32	63.30	-	0.06	-	8.58	0.05	-	0.007	0.007	-	-
ha29	31.91	-	-	12.57	36.69	37.29	27.54	-	-	96.78	2612	2.92	2.92	53.55	40.18	0.10	4.98	4.94	0.04	0.005	-	0.005	-	-
au24e06	13.12	-	-	-	-	-	-	-	419	-	3063	-	0.55	46.19	-	0.04	-	5.55	0.05	-	0.004	0.003	-	-
mb_3	12.74	-	-	20.79	55.73	60.06	51.10	-	-	68.64	2823	0.42	0.42	43.54	8.59	0.05	6.72	7.14	-	0.006	-	0.008	-	-
mb_4	10.79	-	-	21.58	58.47	60.89	53.08	-	-	67.78	2944	0.19	0.19	46.18	13.44	0.04	5.41	5.67	-	0.012	-	0.010	-	-
au24f07	15.36	-	-	-	-	-	-	-	455	-	2786	-	0.45	31.85	-	0.08	-	9.26	0.19	-	0.007	0.008	-	-
au24f12	5.87	-	-	-	-	-	-	-	191	-	3412	-	0.40	14.44	-	0.03	-	4.92	0.06	-	-	-	-	-
au24f13	31.85	-	-	-	-	-	-	-	561	-	2930	-	0.47	37.48	-	0.32	-	10.19	0.14	-	0.005	0.005	-	-
kb_1	15.29	-	-	27.46	134.64	141.85	110.11	-	-	134.35	3196	0.03	0.03	-	-	0.08	-	6.24	0.18	0.025	-	0.027	-	-
kb_2	16.51	-	-	23.54	97.16	101.01	88.90	-	-	134.43	3255	0.60	0.60	-	-	0.11	-	8.64	0.19	0.022	-	0.020	-	-
kb_5	12.48	-	-	22.80	111.83	117.96	88.96	-	-	122.18	2877	0.06	0.06	-	-	0.06	-	7.39	0.19	0.024	-	0.027	-	-
au24g05	29.87	-	-	-	-	-	-	-	500	-	2629	-	0.43	66.01	-	0.09	-	13.78	0.05	-	0.005	0.006	-	-
au24g07	28.23	-	-	-	-	-	-	-	362	-	3057	-	1.37	68.14	-	0.09	-	10.96	0.06	-	0.007	0.006	-	-
au24e07	14.26	-	-	-	-	-	-	-	676	-	3172	-	0.47	57.36	-	0.03	-	7.01	0.08	-	0.005	0.005	-	-
au24e10	7.86	-	-	-	-	-	-	-	520	-	1598	-	0.68	27.98	-	0.02	-	2.39	0.01	-	-	-	-	-
mb_2	11.89	-	-	4.94	4.19	3.22	10.49	-	-	45.53	1793	1.22	1.22	25.85	3.50	0.04	1.93	2.05	-	-	-	0.001	-	-
mb_8	8.07	-	-	6.04	4.97	3.90	8.96	-	-	46.29	1620	0.48	0.48	21.51	1.81	0.03	2.25	2.21	-	-	-	0.001	-	-
au24e12	8.01	-	-	-	-	-	-	-	430	-	1819	-	0.69	34.31	-	0.02	-	3.39	0.01	-	-	-	-	-
au24e15	7.93	-	-	-	-	-	-	-	398	-	1849	-	0.68	34.97	-	0.02	-	2.09	0.01	-	0.007	0.000	-	-
au24e16	7.68	-	-	-	-	-	-	-	399	-	1911	-	0.58	37.73	-	0.03	-	2.15	0.02	-	0.276	0.004	-	-
au24f04	12.19	-	-	-	-	-	-	-	325	-	2728	-	0.53	45.55	-	0.03	-	4.00	0.01	-	-	-	-	-
kb_4	23.26	-	-	6.74	7.44	6.09	9.86	-	-	130.32	1922	0.03	0.03	-	-	0.03	-	2.01	0.04	-	-	-	-	-
kb_9	19.37	-	-	4.40	5.51	4.51	7.72	-	-	109.36	1884	0.52	0.52	-	-	0.07	4.23	2.72	0.02	4.020	-	0.065	-	-
au24f16	58.63	-	-	-	-	-	-	-	619	-	1545	-	0.54	34.80	-	0.04	-	3.53	0.01	-	-	0.000	-	-
au24g03	65.01	-	-	-	-	-	-	-	505	-	1822	-	0.47	46.90	-	0.03	-	4.91	0.01	-	0.002	0.002	-	-

au24g06	69.78	-	-	-	-	-	-	-	551	-	1742	-	0.51	40.06	-	0.03	-	4.87	0.01	-	0.003	0.000	-	-
au24g14	63.09	-	-	-	-	-	-	-	510	-	1784	-	0.51	35.22	-	0.04	-	5.90	0.01	-	-	0.000	-	-
au24g17	59.21	-	-	-	-	-	-	-	656	-	1456	-	0.66	33.23	-	0.03	-	3.32	0.00	-	-	0.000	-	-
ha28	52.63	-	-	4.34	6.71	5.23	8.72	-	-	83.46	1250	1.31	1.31	28.76	2.25	0.06	2.01	2.01	0.00	0.006	-	0.001	-	-
ha1	2718.74	-	-	9.22	1376.33	1522.34	332.45	-	-	36.51	14052	13.05	13.05	61.29	5.06	198.36	21.36	21.71	0.21	3.290	-	0.114	-	-
ha2	3987.30	-	-	13.60	2490.29	2811.81	297.98	-	-	250.59	14230	4.66	4.66	253.51	10.06	211.32	21.54	22.14	0.43	3.590	-	0.103	-	-
ha3	3547.82	-	-	8.03	990.97	1078.01	299.03	-	-	32.40	12894	16.68	16.68	54.65	5.01	138.44	15.84	16.26	0.15	2.150	-	0.082	-	-
ha4	2739.84	-	-	7.55	953.13	1053.28	319.64	-	-	30.53	11150	15.84	15.84	51.83	5.33	199.96	16.49	17.26	0.10	2.660	-	0.093	-	-
ha5	2216.74	-	-	8.06	555.40	613.91	344.86	-	-	31.74	12328	7.74	7.74	58.79	5.31	199.78	14.66	15.43	0.09	2.640	-	0.110	-	-
au25c03	12.17	0.00	-	-	-	-	-	-	-	-	1229	-	5.74	-	-	463.40	-	18.95	0.04	-	3.840	0.084	-	-
au25c04	8.53	0.00	-	-	-	-	-	-	-	-	1032	-	6.12	-	-	431.92	-	24.07	0.06	-	3.470	0.076	-	-
au25c11	436.21	0.00	-	-	-	-	-	-	-	-	2396	-	5.01	-	-	399.61	-	19.22	0.02	-	2.790	0.059	-	-
mb_43	12.75	-	-	7.76	471.42	515.96	89.74	-	-	7.65	519	6.57	6.57	52.51	3.59	186.81	30.86	31.04	-	32.300	-	0.531	-	-
mb_44	4.91	-	-	13.31	432.21	445.84	75.98	-	-	38.40	772	7.27	7.27	13.46	7.30	288.80	26.60	27.65	-	27.820	-	0.329	-	-
mb_45	9.09	-	-	6.49	93.57	94.60	64.23	-	-	2.38	332	4.79	4.79	6.75	11.80	147.20	10.73	10.97	-	0.730	-	0.033	-	-
mb_46	24.22	-	-	7.26	366.86	395.97	77.64	-	-	2.87	369	8.58	8.58	22.98	3.01	160.00	23.78	24.24	-	42.410	-	0.963	-	-
au24c09	5.17	-	-	-	-	-	-	-	7096	-	1865	-	1.28	110.62	-	-	-	727.02	0.08	-	-	-	-	-
au24c12	3.64	-	-	-	-	-	-	-	4414	-	741	-	1.00	53.25	-	-	-	500.98	0.06	-	-	-	-	-
kb_15	74.03	-	-	14.27	42.76	43.68	36.52	-	-	227.25	1039	-	-	-	-	0.13	1322.38	1353.77	0.28	-	-	0.007	-	-
mb_56	7.62	-	-	17.37	1184.57	1253.11	69.62	-	-	70.59	1024	0.95	0.95	68.96	9.76	16.25	247.88	258.81	-	0.278	-	0.021	-	-
au24d08	-	-	-	-	-	-	-	-	804	-	811	-	0.74	39.03	-	0.05	-	315.82	0.03	-	-	0.005	-	-
au24d09	-	0.07	-	-	-	-	-	-	384	-	817	-	1.07	80.03	-	0.02	-	218.03	0.06	-	0.005	0.000	-	-
au24d11	-	0.05	-	-	-	-	-	-	767	-	792	-	2.49	186.06	-	-	-	212.88	0.03	-	-	-	-	-
au24d12	-	0.06	-	-	-	-	-	-	372	-	843	-	0.42	134.72	-	0.01	-	199.00	0.03	-	-	-	-	-
kb_28	0.26	-	-	10.25	2.68	2.98	2.05	-	-	55.31	892	0.21	0.21	-	-	0.04	192.92	199.66	0.02	0.002	-	0.001	-	-
kb_30	0.40	-	-	10.78	2.91	3.69	5.87	-	-	77.38	841	1.55	1.55	-	-	0.02	215.48	219.35	0.03	0.006	-	0.002	-	-
au25d03	0.05	0.02	-	-	-	-	-	-	440	-	273	-	0.45	8.35	-	0.00	-	611.69	0.13	-	0.010	0.000	-	-
au25d07	0.18	0.04	-	-	-	-	-	-	376	-	406	-	0.92	13.62	-	0.03	-	515.15	0.09	-	0.070	0.001	-	-
au25d08	0.15	0.03	-	-	-	-	-	-	1165	-	103	-	0.43	4.24	-	0.00	-	311.55	2.60	-	0.017	0.001	-	-
au25d10	0.87	0.21	-	-	-	-	-	-	650	-	4190	-	3.07	37.27	-	0.08	-	517.80	0.24	-	0.195	0.003	-	-
kb_22	1.06	-	-	26.10	776.20	813.44	62.37	-	-	68.37	925	5.45	5.45	-	-	0.52	445.01	452.23	0.92	0.557	-	0.030	-	-
kb_25	0.19	-	-	23.49	1.97	2.20	16.02	-	-	15.39	321	0.20	0.20	-	-	0.03	558.18	590.28	0.08	0.033	-	0.001	-	-
au25f13	1.05	0.22	-	-	-	-	-	-	785	-	1184	-	0.34	51.56	-	0.03	-	444.21	0.22	-	-	-	-	-
au25f15	0.65	0.27	-	-	-	-	-	-	628	-	891	-	0.27	36.24	-	0.04	-	476.92	0.24	-	0.002	-	-	-
au25g05	1.21	0.29	-	-	-	-	-	-	724	-	1178	-	0.39	48.12	-	0.06	-	663.89	0.28	-	-	-	-	-
mb_53	1.22	-	-	4.53	0.84	1.08	1.47	-	-	58.75	1122	0.13	0.13	48.10	1.08	0.04	537.66	541.55	-	-	-	-	-	-
au25g06	0.70	0.10	-	-	-	-	-	-	858	-	579	-	0.33	47.08	-	0.05	-	509.81	0.30	-	-	0.001	-	-
mb_49	1.07	-	-	2.72	0.44	0.94	0.75	-	-	57.92	1143	0.11	0.11	47.28	3.11	0.04	453.90	430.28	-	-	-	-	-	-
mb_55	2.31	-	-	14.21	3.49	3.31	13.87	-	-	47.57	742	0.17	0.17	56.64	2.65	0.10	502.34	500.50	-	-	-	-	-	-
au24c08	7.32	-	-	-	-	-	-	-	5329	-	1543	-	1.16	48.63	-	0.02	-	673.83	0.06	-	-	-	-	-
au24c11	2.95	-	-	-	-	-	-	-	6430	-	885	-	0.72	41.98	-	0.01	-	635.86	0.05	-	-	-	-	-
kb_12	3.22	-	-	1.56	7.03	7.77	2.78	-	-	44.96	327	0.03	0.03	-	-	0.01	972.99	993.42	0.08	0.003	-	-	-	-
kb_14	15.75	-	-	3.71	8.30	7.77	6.12	-	-	104.79	1750	-	-	-	-	0.04	1067.82	1105.82	0.06	-	-	-	-	-
au24c17	-	-	-	-	-	-	-	-	12578	-	314	-	0.54	9.56	-	-	-	945.11	0.11	-	-	-	-	-
au25e14	6.21	0.22	-	-	-	-	-	-	2420	-	4047	-	1.30	879.01	-	0.42	-	435.88	0.29	-	0.019	0.002	-	-
mb_16	2.23	-	-	6.45	1.98	2.45	9.98	-	-	210.36	1898	0.18	0.18	316.27	64.96	0.03	492.76	532.83	-	0.023	-	-	-	-
au25d05	0.79	0.01	-	-	-	-	-	-	402	-	29	-	0.80	13.75	-	0.01	-	9577.79	2.09	-	0.013	-	-	-
kb_24	0.93	-	-	2.40	7.35	8.06	1.50	-	-	6.75	26	0.37	0.37	-	-	0.01	7869.74	8159.21	1.58	0.013	-	0.000	-	-
au24d13	0.78	-	-	-	-	-	-	-	5071	-	315	-	0.38	13.09	-	0.01	-	446.72	0.03	-	-	0.001	-	-
au24d14	-	-	-	-	-	-	-	-	2917	-	42	-	0.53	39.49	-	-	-	739.62	0.07	-	-	-	-	-
au24d17	-	-	-	-	-	-	-	-	1210	-	21	-	0.31	5.87	-	-	-	603.73	0.09	-	-	-	-	-
ha22	-	-	-	22.88	0.18	0.11	1.82	-	-	72.29	1138	0.54	0.54	66.93	0.45	-	217.58	224.40	0.53	-	-	0.001	-	-
au25d12	-	0.03	-	-	-	-	-	-	722	-	444	-	0.74	14.38	-	0.01	-	610.79	0.33	-	0.026	0.001	-	-

kb_27	0.04	-	-	4.68	2.02	2.43	41.32	-	-	21.95	559	1.04	1.04	-	-	0.02	673.30	682.42	0.40	0.013	-	0.001	-	-
au25e17	-	0.03	-	-	-	-	-	-	983	-	687	-	0.26	51.50	-	0.00	-	373.65	0.25	-	0.002	-	-	-
au25f14	0.31	0.04	-	-	-	-	-	-	1509	-	147	-	0.29	18.85	-	0.02	-	687.11	0.20	-	-	0.001	-	-
au25f16	-	0.05	-	-	-	-	-	-	535	-	627	-	0.38	34.80	-	-	-	472.73	0.32	-	0.005	-	-	-
au25f17	0.14	0.16	-	-	-	-	-	-	944	-	1042	-	0.38	47.09	-	0.01	-	403.39	0.70	-	-	-	-	-
mb_48	0.56	-	-	2.47	0.43	0.43	0.15	-	-	23.65	219	0.02	0.02	20.08	1.59	0.02	622.25	610.25	-	-	-	-	-	-
mb_50	0.24	-	-	1.18	0.50	0.19	4.80	-	-	67.31	1162	0.04	0.04	48.74	0.06	0.01	443.04	439.40	-	-	-	-	-	-
mb_52	-	-	-	1.59	-	-	14.68	-	-	117.09	2244	0.10	0.10	237.45	0.06	-	181.77	181.37	-	-	-	-	-	-
au25g12	0.05	0.04	-	-	-	-	-	-	972	-	100	-	0.35	16.61	-	0.22	-	317.09	1.14	-	0.002	0.000	-	-
mb_35	-	-	-	1.66	0.45	0.54	11.75	-	-	12.62	36	0.03	0.03	21.50	0.06	0.01	324.18	345.95	-	-	-	-	-	-
au25d17	5.74	0.08	-	-	-	-	-	-	276	-	2840	-	0.78	31.86	-	0.85	-	18.97	0.09	-	0.007	0.003	-	-
mb_26	13.81	-	-	12.53	1.69	1.79	7.89	-	-	42.89	323	0.19	0.19	21.97	1.36	0.30	125.21	133.12	-	-	-	0.002	-	-
ha26	19.55	-	-	23.01	30.14	33.01	12.97	-	-	198.99	1880	1.25	1.25	67.07	12.51	0.33	141.72	146.04	1.15	-	-	0.003	-	-
ha27	13.14	-	-	34.21	15.86	17.52	10.81	-	-	135.49	1273	1.14	1.14	70.47	3.30	0.80	110.26	110.47	0.25	-	-	0.005	-	-
au24c13	2.51	-	-	-	-	-	-	-	391	-	123	-	0.13	8.51	-	0.00	-	66.85	0.02	-	-	-	-	-
au24c15	8.89	-	-	-	-	-	-	-	867	-	87	-	0.22	18.33	-	0.01	-	96.15	0.01	-	-	-	-	-
au24d03	655.16	-	-	-	-	-	-	-	3679	-	56266	-	12.32	1175.07	-	1.20	-	103.62	0.65	-	-	-	-	-
au24d05	210.94	-	-	-	-	-	-	-	3102	-	19845	-	7.96	472.24	-	0.58	-	160.16	0.29	-	-	0.024	-	-
au24d06	29.34	-	-	-	-	-	-	-	1879	-	2637	-	1.19	99.16	-	0.11	-	137.34	0.05	-	-	-	-	-
au25d14	4.29	0.01	-	-	-	-	-	-	305	-	497	-	0.35	9.14	-	0.07	-	16.61	0.07	-	0.003	0.000	-	-
au25e08	5.83	0.05	-	-	-	-	-	-	272	-	4036	-	1.10	294.08	-	0.13	-	6.80	0.05	-	0.009	0.002	-	-
au25e09	3.11	0.05	-	-	-	-	-	-	345	-	3434	-	1.03	26.56	-	0.05	-	8.07	0.09	-	0.006	0.001	-	-
au25e10	1.30	0.01	-	-	-	-	-	-	16	-	574	-	0.13	4.66	-	0.06	-	1.34	0.00	-	0.002	0.000	-	-
au25e11	4.37	0.07	-	-	-	-	-	-	54	-	3107	-	0.55	21.49	-	0.16	-	6.32	0.01	-	0.005	0.000	-	-
au25e12	6.89	0.17	-	-	-	-	-	-	191	-	6965	-	1.15	47.34	-	0.38	-	9.19	0.04	-	0.033	0.001	-	-
au25e13	2.34	0.04	-	-	-	-	-	-	64	-	1185	-	0.29	239.04	-	0.15	-	1.89	0.01	-	0.007	0.001	-	-
ha31	20.26	-	-	8.83	24.06	24.60	13.12	-	-	144.18	1593	0.30	0.30	52.62	15.78	0.07	86.92	87.36	0.04	-	-	0.002	-	-
mb_29	3.04	-	-	8.19	6.07	5.95	3.11	-	-	30.57	294	0.18	0.18	22.22	3.70	0.29	15.56	16.10	-	0.004	-	-	-	-
mb_30	3.88	-	-	5.80	19.63	20.02	13.52	-	-	47.00	603	0.30	0.30	303.28	2.13	0.10	11.71	11.69	-	0.009	-	0.006	-	-
ha13	0.71	-	-	2.38	5.52	5.96	4.55	-	-	29.56	226	0.05	0.05	15.88	0.52	0.07	0.65	0.68	0.11	0.005	-	0.001	-	-
mb_38	29.13	-	-	12.41	54.58	55.88	10.68	-	-	85.80	802	0.43	0.43	8.98	17.81	0.35	22.12	22.53	-	0.076	-	-	-	-
mb_39	5.61	-	-	1.70	8.66	9.12	4.15	-	-	24.99	370	0.18	0.18	8.25	5.00	0.17	10.23	10.24	-	0.013	-	-	-	-
ha7	1.79	-	-	28.77	21.71	23.57	13.90	-	-	58.81	236	0.02	0.02	61.83	1.68	0.11	8.56	8.58	0.38	0.024	-	0.001	-	-
mb_14	13.58	-	-	4.86	12.06	13.12	44.19	-	-	385.71	18137	0.17	0.17	87.33	12.17	0.30	19.02	19.59	-	0.036	-	0.003	-	-
mb_15	1.35	-	-	3.50	9.54	10.37	5.33	-	-	42.79	996	0.16	0.16	21.82	29.97	0.06	3.47	3.49	-	0.003	-	0.001	-	-
mb_17	4.14	-	-	26.57	60.31	63.06	19.62	-	-	207.13	2664	0.66	0.66	51.58	185.72	0.07	19.79	20.56	-	0.035	-	-	-	-
au25g13	18.75	0.02	-	-	-	-	-	-	460	-	806	-	1.19	45.36	-	0.31	-	13.84	0.26	-	0.060	0.000	-	-
mb_18	5.18	-	-	23.62	2.84	3.09	3.25	-	-	64.11	268	0.04	0.04	102.87	0.45	0.82	55.96	55.81	-	-	-	0.002	-	-
au25e06	6.18	0.11	-	-	-	-	-	-	699	-	851	-	0.79	19.06	-	0.15	-	40.87	0.07	-	0.036	0.001	-	-
au25d11	1.55	0.15	-	-	-	-	-	-	882	-	2297	-	25.27	48.78	-	0.05	-	21.35	0.50	-	0.356	0.006	-	-
au25f03	0.65	-	-	-	-	-	-	-	186	-	630	-	0.34	150.85	-	0.00	-	4.21	0.02	-	-	0.000	-	-
au25f04	3.87	-	-	-	-	-	-	-	390	-	2797	-	0.65	335.78	-	0.01	-	7.50	0.01	-	0.001	0.001	-	-
au25f08	0.14	0.02	-	-	-	-	-	-	19	-	118	-	0.07	36.85	-	0.00	-	0.75	0.00	-	0.001	0.001	-	-
au25f09	2.81	0.04	-	-	-	-	-	-	415	-	1267	-	0.54	295.94	-	0.01	-	7.66	0.02	-	-	0.002	-	-
au25f10	0.84	-	-	-	-	-	-	-	166	-	190	-	0.32	299.88	-	-	-	6.44	0.01	-	0.002	0.000	-	-
au25f12	8.89	0.01	-	-	-	-	-	-	246	-	2348	-	0.69	419.93	-	0.03	-	4.70	0.00	-	0.004	0.002	-	-
au25g08	14.09	0.04	-	-	-	-	-	-	402	-	337	-	0.46	9.03	-	0.13	-	16.08	2.10	-	0.062	0.001	-	-
au25g09	19.92	0.02	-	-	-	-	-	-	605	-	485	-	0.72	9.93	-	0.40	-	21.98	2.79	-	0.134	0.001	-	-
mb_24	2.35	-	-	4.13	2.25	2.44	3.59	-	-	90.32	783	0.04	0.04	37.82	1.13	0.02	12.30	12.48	-	-	-	-	-	-
ha9	5.07	-	-	8.31	8.57	9.57	7.12	-	-	45.80	365	0.02	0.02	29.86	0.19	0.25	2.96	3.05	0.11	0.010	-	0.001	-	-
ha15	5.58	-	-	7.57	95.69	100.69	9.26	-	-	26.04	174	0.08	0.08	15.44	0.49	0.59	1.85	1.87	0.28	0.042	-	0.001	-	-
ha18	3.01	-	-	5.10	11.02	11.71	5.78	-	-	41.58	522	0.30	0.30	22.75	5.64	0.05	3.56	3.58	0.02	0.011	-	0.002	-	-
kb_16	5.72	-	-	9.54	1.99	2.43	15.04	-	-	139.76	3394	0.11	0.11	-	-	0.01	5.62	5.57	0.01	0.003	-	0.005	-	-

kb_18	1.06	-	-	3.91	3.47	4.05	4.66	-	-	46.59	844	0.97	0.97	-	-	0.00	3.76	3.92	0.02	0.003	-	0.002	-	-
kb_19	1.48	-	-	3.24	14.57	15.68	3.44	-	-	58.56	917	2.49	2.49	-	-	0.08	5.29	5.44	0.04	0.003	-	0.001	-	-
kb_20	1.29	-	-	2.64	1.30	1.61	1.40	-	-	49.75	834	0.11	0.11	-	-	0.05	4.21	4.17	0.04	0.002	-	0.000	-	-
kb_26	2.28	-	-	2.87	45.89	49.77	20.66	-	-	80.20	1653	14.74	14.74	-	-	0.18	23.10	23.98	0.40	0.179	-	0.003	-	-
au24c16	1.34	-	-	-	-	-	-	-	959	-	171	-	0.14	3.17	-	0.00	-	15.41	0.00	-	-	-	-	-
ha19	2.02	-	-	7.56	11.33	11.60	3.79	-	-	47.63	560	0.43	0.43	20.76	3.11	0.02	2.52	2.58	0.02	0.007	-	0.002	-	-
ha20	0.00	-	-	0.06	0.05	0.05	0.05	-	-	0.21	3	0.00	0.00	0.10	0.04	0.00	1.15	1.18	0.00	0.000	-	0.000	-	-
ha21	0.04	-	-	0.32	0.88	0.96	0.45	-	-	1.36	20	0.01	0.01	0.77	0.37	0.00	1.59	1.61	0.00	0.001	-	0.000	-	-
au25g15	40.78	0.04	-	-	-	-	-	-	736	-	1442	-	2.58	15.73	-	1.19	-	28.00	0.46	-	0.052	0.001	-	-
au25g16	9.06	0.10	-	-	-	-	-	-	413	-	433	-	0.74	36.36	-	0.27	-	19.70	0.13	-	0.022	-	-	-
au25g17	15.70	0.03	-	-	-	-	-	-	486	-	1106	-	3.65	35.67	-	0.38	-	11.62	0.42	-	0.082	0.001	-	-
mb_57	5.29	-	-	1.82	14.08	14.69	5.90	-	-	32.88	447	0.18	0.18	14.88	3.90	0.13	7.40	7.38	-	0.032	-	-	-	-
mb_41	14.97	-	-	5.51	74.44	76.12	15.41	-	-	71.23	820	0.65	0.65	20.89	10.25	0.26	15.40	15.69	-	0.086	-	0.001	-	-
au25e03	4.73	0.26	-	-	-	-	-	-	3779	-	482	-	1.13	32.01	-	0.60	-	74.73	0.10	-	0.008	0.001	-	-
au25e05	3.16	0.18	-	-	-	-	-	-	3009	-	449	-	1.33	23.21	-	0.04	-	40.03	0.02	-	0.003	-	-	-
au25g03	0.14	0.13	-	-	-	-	-	-	769	-	1355	-	0.13	72.55	-	0.00	-	192.60	0.05	-	-	0.000	-	-
mb_51	0.12	-	-	0.47	-	0.07	0.23	-	-	30.63	534	0.04	0.04	26.39	0.04	0.00	163.04	159.47	-	-	-	0.000	-	-
mb_25	0.40	-	-	0.78	2.31	2.50	0.99	-	-	13.50	77	0.08	0.08	3.33	1.01	0.02	8.82	9.01	-	-	-	-	-	-
mb_33	1.21	-	-	0.65	0.51	0.75	1.46	-	-	40.13	318	0.40	0.40	13.00	1.51	0.02	24.73	24.58	-	-	-	-	-	-
au24c14	2.25	-	-	-	-	-	-	-	10387	-	1156	-	1.91	133.81	-	-	-	10.44	0.03	-	-	-	-	-
kb_11	0.82	-	-	1.05	3.26	3.71	3.07	-	-	135.62	710	0.03	0.03	-	-	0.01	11.27	11.33	0.03	-	-	-	-	-
au24d04	2.04	-	-	-	-	-	-	-	619	-	333	-	0.45	46.15	-	0.01	-	155.17	0.01	-	0.007	-	-	-
au24d07	2.40	-	-	-	-	-	-	-	296	-	337	-	0.25	34.55	-	0.01	-	96.37	0.00	-	-	-	-	-
ha30	2.22	-	-	0.60	1.36	1.48	1.07	-	-	32.46	174	0.03	0.03	15.31	1.13	0.01	47.78	48.79	0.01	-	-	0.000	-	-
ha16	-	-	-	4.38	4.53	5.17	32.47	-	-	51.42	789	5.65	5.65	20.48	77.64	0.09	15.80	15.63	0.24	0.043	-	0.003	-	-
ha17	-	-	-	3.94	2.55	2.93	1.03	-	-	45.01	497	0.25	0.25	19.27	1.25	-	0.49	0.52	0.57	-	-	0.001	-	-
ha23	1.23	-	-	1.57	1.49	1.88	1.25	-	-	52.54	249	0.27	0.27	19.59	1.82	0.03	1.92	1.94	0.05	-	-	0.001	-	-
ha24	-	-	-	1.65	1.28	1.33	0.99	-	-	37.93	382	0.13	0.13	18.64	0.46	0.01	0.34	0.32	0.21	0.013	-	0.001	-	-
ha25	0.87	-	-	1.78	1.89	2.05	1.48	-	-	48.65	235	0.23	0.23	28.74	2.71	0.01	1.41	1.44	0.06	0.002	-	0.001	-	-
au25d04	0.67	0.30	-	-	-	-	-	-	2205	-	4179	-	28.86	80.60	-	0.09	-	83.09	1.42	-	0.089	0.001	-	-
kb_23	0.29	-	-	9.39	35.11	38.74	27.03	-	-	147.71	2834	32.03	32.03	-	-	0.08	75.66	76.79	1.38	0.112	-	0.004	-	-
au25f05	2.24	0.54	-	-	-	-	-	-	526	-	1246	-	9.47	493.98	-	0.04	-	12.89	0.03	-	0.021	0.002	-	-
au25f11	1.70	0.01	-	-	-	-	-	-	315	-	546	-	0.82	177.38	-	0.00	-	4.35	0.02	-	-	0.001	-	-
kb_17	1.86	-	-	2.08	40.87	45.03	11.61	-	-	147.78	1948	36.31	36.31	-	-	0.03	9.66	9.79	0.03	0.014	-	0.002	-	-
au24d16	1.22	-	-	-	-	-	-	-	455	-	423	-	0.47	113.38	-	-	-	2.59	0.03	-	-	-	-	-
au25e16	0.94	0.04	-	-	-	-	-	-	1289	-	1082	-	0.57	117.78	-	0.02	-	27.98	0.05	-	-	-	-	-
mb_13	16.98	-	-	43.08	9.00	8.89	14.68	-	-	407.89	5057	1.85	1.85	184.77	200.73	0.52	88.23	86.73	-	-	-	-	-	-
mb_20	0.03	-	-	0.08	0.04	0.04	0.19	-	-	3.47	43	0.00	0.00	1.61	0.11	0.00	1.38	1.41	-	-	-	-	-	-
ha6	1.97	-	-	4.29	8.62	9.41	6.11	-	-	89.21	553	0.25	0.25	37.73	1.73	2.34	8.28	8.25	1.66	0.038	-	0.001	-	-
ha10	0.12	-	-	0.66	0.69	0.82	0.99	-	-	38.89	170	0.03	0.03	9.96	0.35	0.00	3.74	3.76	0.56	-	-	0.000	-	-
ha11	0.16	-	-	1.33	0.52	0.80	3.34	-	-	50.32	161	0.04	0.04	9.38	0.63	0.00	7.54	7.72	0.69	-	-	-	-	-
au25g14	12.69	0.03	-	-	-	-	-	-	352	-	591	-	0.87	20.27	-	0.34	-	12.66	0.15	-	0.068	0.000	-	-
mb_36	4.30	-	-	2.96	11.35	11.83	6.32	-	-	60.87	646	0.15	0.15	29.03	1.73	0.16	5.12	5.29	-	0.008	-	0.001	-	-
mb_40	16.13	-	-	10.63	68.36	71.24	8.33	-	-	61.63	456	0.10	0.10	15.21	8.39	0.15	15.08	15.51	-	0.084	-	0.002	-	-
au25g04	0.74	0.04	-	-	-	-	-	-	600	-	500	-	0.18	58.73	-	0.01	-	56.23	0.04	-	-	-	-	-
au25g07	1.40	0.02	-	-	-	-	-	-	825	-	508	-	0.14	64.13	-	0.01	-	2.50	0.00	-	-	-	-	-
mb_54	0.40	-	-	0.26	-	0.04	0.58	-	-	54.13	518	0.02	0.02	94.39	0.02	0.00	1.18	1.13	-	-	-	-	-	-
au25e15	2.98	0.06	-	-	-	-	-	-	2329	-	629	-	0.76	34.23	-	0.02	-	22.42	0.05	-	0.003	-	-	-
mb_19	1.84	-	-	9.64	3.18	3.93	4.52	-	-	101.61	1766	0.13	0.13	37.49	8.02	0.08	12.75	13.50	-	-	-	0.001	-	-
au25g11	0.45	-	-	-	-	-	-	-	539	-	212	-	0.50	16.11	-	0.00	-	1.66	0.51	-	-	0.000	-	-
mb_37	0.57	-	-	0.08	-	0.53	1.87	-	-	43.47	148	0.04	0.04	14.73	0.81	0.02	7.01	7.12	-	-	-	-	-	-
mb_22	1.26	-	-	0.79	-	0.23	0.16	-	-	151.38	1691	0.02	0.02	626.73	0.63	0.01	69.53	70.00	-	-	-	-	-	-
ha12	-	-	-	0.85	1.15	1.36	12.17	-	-	78.40	557	0.01	0.01	57.55	0.06	-	2.75	2.79	0.16	0.009	-	-	-	-

Table S10 (continued)

Analysis #	Sb121 µg/g	Sb123 µg/g	Cs133 µg/g	Ba137 µg/g	La139 µg/g	Ce140 µg/g	Pr141 µg/g	Nd146 µg/g	Sm147 µg/g	Eu151 µg/g	Gd157 µg/g	Tb159 µg/g	Dy163 µg/g	Ho165 µg/g	Er167 µg/g	Tm169 µg/g	Yb173 µg/g	Lu175 µg/g	Hf177 µg/g	Ta181 µg/g	Pb208 µg/g	Th232 µg/g	U238 µg/g
au24e03	-	-	-	1.72	-	-	-	-	-	-	0.0014	-	0.0021	0.0008	0.0038	0.0006	0.0081	0.0024	-	-	0.32	-	0.00025
au24e04	-	-	-	1.35	-	-	-	-	-	-	-	-	0.0016	0.0005	0.0025	0.0004	0.0067	0.0018	-	-	0.26	-	0.00014
au24e05	-	-	-	2.22	-	-	-	-	-	0.0003	-	-	0.0035	0.0012	0.0059	0.0024	0.0156	0.0047	-	-	0.48	-	0.00022
au24e09	-	-	-	2.04	-	-	-	-	-	0.0004	-	0.0004	0.0025	0.0013	0.0058	0.0009	0.0144	0.0040	-	-	0.41	-	-
au24e11	-	-	-	1.92	-	-	-	-	-	-	-	0.0002	0.0030	0.0016	0.0087	0.0014	0.0158	0.0041	-	-	0.44	-	0.00011
mb_1	0.033	0.031	0.065	1.39	-	-	-	-	-	-	-	0.0003	0.0009	0.0005	0.0053	0.0003	0.0040	0.0013	-	-	0.19	0.0005	-
mb_6	0.056	0.063	0.057	1.94	-	-	-	-	-	-	-	-	0.0018	0.0008	0.0037	0.0011	0.0133	0.0026	-	-	0.33	-	0.00027
mb_7	0.049	0.033	0.080	1.93	-	-	-	-	-	-	-	-	0.0035	0.0006	0.0036	0.0018	0.0090	0.0022	-	-	0.37	-	0.00017
au24e14	-	-	-	2.14	0.0021	0.0066	0.0005	-	-	-	-	-	0.0015	0.0006	0.0027	0.0003	0.0077	0.0021	0.0010	-	0.43	0.0005	0.00083
au24e17	-	-	-	2.09	0.0067	0.0185	0.0015	0.0044	0.0018	0.0004	0.0019	-	0.0030	0.0006	0.0040	0.0010	0.0072	0.0017	0.0024	-	0.28	0.0013	0.00304
au24f03	-	-	-	2.35	-	-	-	-	-	-	-	-	-	0.0011	0.0040	0.0008	0.0090	0.0034	-	-	0.26	-	-
au24f05	-	-	-	2.07	0.0029	0.0066	0.0010	0.0017	0.0007	-	0.0015	0.0002	0.0028	0.0007	0.0048	0.0009	0.0113	0.0028	0.0015	-	0.35	0.0009	0.00078
au24f08	-	-	-	1.45	0.0003	0.0005	0.0001	-	-	-	-	0.0005	0.0049	0.0025	0.0100	0.0032	0.0297	0.0056	-	-	0.68	-	-
au24f10	-	-	-	1.77	0.0017	0.0043	0.0005	0.0023	-	-	-	0.0003	0.0031	0.0023	0.0111	0.0024	0.0262	0.0052	-	-	0.65	0.0002	0.00062
au24f11	-	-	-	2.09	-	-	-	-	-	0.0002	0.0018	0.0014	0.0259	0.0074	0.0403	0.0098	0.0875	0.0185	-	-	1.93	-	-
au24f14	-	-	-	2.21	-	0.0006	0.0002	-	-	-	0.0021	0.0006	0.0130	0.0046	0.0275	0.0059	0.0534	0.0105	-	-	1.40	-	0.00018
kb_3	-	-	0.190	1.59	-	0.0272	-	-	0.0019	0.0006	0.0020	0.0010	0.0100	0.0027	0.0110	0.0039	0.0369	0.0077	-	-	1.06	-	-
kb_8	-	-	0.077	1.22	-	-	-	-	-	-	-	-	0.0039	0.0017	0.0087	0.0022	0.0220	0.0045	-	-	0.56	-	-
kb_10	-	-	0.079	1.00	-	-	-	-	-	-	-	-	0.0045	0.0011	0.0055	0.0020	0.0123	0.0039	-	-	0.56	-	-
au24f17	-	-	-	5.76	0.0020	0.0021	0.0001	-	-	-	-	0.0003	0.0022	0.0010	0.0064	0.0020	0.0137	0.0035	0.0006	-	1.36	0.0002	0.00135
au24g04	-	-	-	2.46	0.0001	0.0001	-	-	-	-	-	0.0003	0.0026	0.0007	0.0056	0.0012	0.0148	0.0025	-	-	1.07	-	0.00046
au24g08	-	-	-	4.39	0.0004	0.0002	-	-	-	-	-	0.0003	0.0050	0.0012	0.0075	0.0025	0.0190	0.0057	-	-	2.42	-	0.00153
au24g15	-	-	-	3.13	-	-	-	-	-	-	-	0.0002	0.0027	0.0014	0.0054	0.0017	0.0191	0.0045	-	-	1.82	-	0.00102
au24g16	-	-	-	8.42	0.0014	0.0002	-	-	-	-	-	0.0004	0.0048	0.0015	0.0075	0.0024	0.0272	0.0074	-	-	2.64	-	0.00226
ha29	0.163	0.166	0.279	4.86	0.0033	0.0067	0.0008	-	-	-	-	0.0003	0.0036	0.0014	0.0051	0.0016	0.0198	0.0034	-	0.0033	1.91	0.0002	0.00137
au24e06	-	-	-	2.32	-	-	-	0.0014	-	-	-	0.0003	0.0035	0.0015	0.0073	0.0015	0.0189	0.0042	-	-	0.52	-	0.00027
mb_3	0.114	0.104	0.109	3.39	-	-	-	-	-	-	-	0.0003	0.0053	0.0013	0.0074	0.0021	0.0243	0.0040	-	-	0.56	-	0.00016
mb_4	0.129	0.111	0.109	2.35	-	-	-	-	-	-	0.0027	-	0.0064	0.0018	0.0141	0.0027	0.0293	0.0059	-	-	0.61	-	0.00031
au24f07	-	-	-	2.12	-	0.0006	-	-	-	-	0.0013	0.0010	0.0190	0.0063	0.0319	0.0080	0.0732	0.0160	0.0005	-	1.69	-	-
au24f12	-	-	-	1.18	-	-	-	-	-	-	-	0.0003	0.0061	0.0025	0.0118	0.0027	0.0327	0.0056	-	-	0.74	-	-
au24f13	-	-	-	2.56	-	-	-	-	-	-	0.0021	0.0006	0.0144	0.0054	0.0261	0.0067	0.0607	0.0111	-	-	1.43	-	-
kb_1	-	-	0.493	1.83	-	-	-	-	0.0016	-	0.0028	0.0009	0.0171	0.0069	0.0361	0.0087	0.0773	0.0156	-	-	1.81	-	-
kb_2	-	-	0.359	2.64	-	0.0007	-	-	-	-	-	0.0009	0.0143	0.0066	0.0308	0.0067	0.0641	0.0128	-	-	1.98	-	-
kb_5	-	-	0.238	2.08	-	-	-	-	-	-	-	0.0011	0.0206	0.0077	0.0344	0.0085	0.0780	0.0162	-	-	1.96	-	0.00042
au24g05	-	-	-	2.43	-	0.0002	-	-	-	-	-	0.0003	0.0042	0.0023	0.0090	0.0027	0.0260	0.0070	-	-	3.14	-	0.00191
au24g07	-	-	-	6.41	0.0003	0.0002	-	-	-	-	0.0011	-	0.0056	0.0015	0.0130	0.0035	0.0300	0.0060	-	-	3.42	-	0.00216
au24e07	-	-	-	2.35	-	-	-	-	0.0011	-	0.0018	0.0006	0.0073	0.0037	0.0151	0.0036	0.0309	0.0063	-	-	0.69	0.0002	0.00022
au24e10	-	-	-	0.78	-	-	0.0003	-	-	-	-	0.0002	-	0.0004	0.0008	0.0004	0.0035	0.0012	-	-	0.12	-	-
mb_2	0.042	0.045	0.097	1.64	0.0008	-	-	-	-	-	-	-	-	-	0.0016	0.0006	0.0065	0.0018	-	0.0010	0.14	-	-
mb_8	0.040	0.019	0.106	1.07	-	-	-	-	-	-	-	-	-	0.0003	0.0028	-	0.0069	0.0012	-	-	0.12	-	-
au24e12	-	-	-	1.44	0.0002	-	-	-	-	-	-	-	0.0007	-	0.0011	0.0002	0.0035	0.0006	-	-	0.10	-	-
au24e15	-	-	-	1.32	0.0004	0.0011	-	-	-	-	-	0.0002	0.0009	0.0002	0.0007	0.0002	0.0039	0.0005	-	-	0.10	-	0.00013
au24e16	-	-	-	1.58	0.0169	0.0462	0.0050	0.0115	0.0015	0.0009	-	0.0006	0.0031	0.0007	0.0024	-	0.0046	0.0005	0.0067	-	0.20	0.0037	0.00702
au24f04	-	-	-	1.71	-	-	-	-	-	-	-	-	-	-	0.0027	-	-	0.0033	-	-	0.20	-	-
kb_4	-	-	0.299	0.47	-	-	-	-	-	-	-	-	0.0027	0.0013	0.0080	0.0014	0.0207	0.0037	-	-	0.32	-	-
kb_9	-	-	0.251	0.81	-	-	-	-	-	-	-	-	0.0026	0.0010	0.0068	0.0014	0.0070	0.0022	-	-	0.24	-	-
au24f16	-	-	-	1.56	-	-	-	-	-	-	-	-	-	0.0003	0.0013	0.0002	0.0036	0.0005	-	-	0.32	-	0.00140
au24g03	-	-	-	0.52	-	-	-	-	-	-	-	-	-	0.0005	0.0016	-	0.0027	0.0007	-	-	0.53	-	0.00114

au24g06	-	-	-	0.72	0.0001	0.0006	-	-	-	-	0.0009	-	0.0011	0.0004	0.0015	0.0005	0.0060	0.0011	-	-	0.56	-	0.00116
au24g14	-	-	-	0.55	-	-	-	-	-	-	-	-	0.0009	0.0002	0.0013	0.0004	0.0043	0.0011	-	-	0.55	-	0.00082
au24g17	-	-	-	1.61	-	-	-	-	-	-	-	-	-	0.0001	0.0015	0.0002	0.0024	0.0005	-	-	0.28	-	0.00089
ha28	0.013	0.010	0.278	5.18	0.0057	0.0050	0.0008	-	-	-	-	-	0.0017	-	-	0.0003	-	0.0005	0.0017	0.0019	0.23	-	0.00113
ha1	5.860	5.590	33.590	46.68	0.1124	0.1512	0.0281	0.1840	0.0583	0.0140	0.0685	0.0081	0.0441	0.0147	0.0466	0.0066	0.0571	0.0103	0.3210	0.0215	2.29	-	0.04040
ha2	21.060	20.730	54.020	29.71	0.1469	0.2320	0.0532	0.3630	0.1140	0.0302	0.1140	0.0128	0.0850	0.0252	0.0995	0.0177	0.1560	0.0266	0.2990	0.0044	5.04	-	0.04280
ha3	7.620	7.650	27.850	45.67	0.0447	0.0689	0.0126	0.1045	0.0278	0.0094	0.0167	0.0028	0.0309	0.0078	0.0346	0.0069	0.0466	0.0084	0.1950	0.0257	2.41	-	0.02980
ha4	7.770	7.800	34.280	54.64	0.0522	0.0673	0.0141	0.0925	0.0259	0.0073	0.0371	0.0031	0.0246	0.0067	0.0217	0.0033	0.0287	0.0030	0.2550	0.0337	2.25	0.0014	0.02750
ha5	2.080	2.005	39.940	50.67	0.0405	0.0536	0.0133	0.0694	0.0200	0.0071	0.0160	0.0033	0.0202	0.0044	0.0193	0.0037	0.0203	0.0060	0.2360	0.0149	1.65	-	0.03240
au25c03	-	-	92.290	77.32	0.0073	0.0062	0.0022	-	0.0046	0.0009	-	0.0006	0.0110	0.0019	0.0045	0.0011	0.0122	0.0011	0.4080	-	3.51	0.0016	0.02430
au25c04	-	-	75.370	67.61	0.0360	0.0939	0.0094	0.0227	0.0088	0.0024	0.0046	0.0010	0.0082	0.0024	0.0076	0.0018	0.0113	0.0017	0.3450	-	2.41	0.0068	0.03420
au25c11	-	-	99.880	74.78	0.0025	0.0019	-	-	-	-	-	-	-	0.0023	-	-	-	-	0.2810	-	1.91	-	0.01490
mb_43	6.400	6.630	47.910	32.50	1.4570	2.0450	0.2820	1.1060	0.2210	0.0460	0.2400	0.0383	0.2500	0.0556	0.1850	0.0303	0.1800	0.0234	0.8840	1.0320	4.30	0.4180	0.20100
mb_44	15.930	15.880	84.290	39.62	1.1630	1.6520	0.2270	0.9660	0.1800	0.0683	0.3430	0.0559	0.4490	0.1025	0.2890	0.0515	0.3160	0.0458	0.9720	0.1337	4.97	0.3020	0.20900
mb_45	7.120	7.030	25.280	32.25	0.0065	-	-	-	-	-	-	-	-	-	-	-	-	-	0.0950	0.0136	0.50	-	0.00248
mb_46	1.280	1.349	29.180	35.92	1.4140	2.1900	0.2740	1.0660	0.2230	0.0464	0.2310	0.0345	0.2330	0.0481	0.1660	0.0216	0.1540	0.0233	1.0450	4.1500	3.70	0.5920	0.18500
au24c09	-	-	-	65.29	-	-	-	-	-	-	-	-	-	0.0016	-	-	-	-	-	-	0.70	-	-
au24c12	-	-	-	48.47	-	-	-	-	-	-	-	-	0.0067	0.0007	0.0032	0.0021	-	-	-	-	0.40	-	-
kb_15	-	-	0.309	303.98	0.0117	0.0027	-	-	-	-	-	0.0020	0.0186	0.0083	0.0233	0.0151	0.0750	0.0169	-	-	1.39	-	-
mb_56	40.950	39.270	3.690	9.42	0.0048	0.0119	0.0030	0.0360	0.0348	0.0131	0.0848	0.0163	0.1399	0.0309	0.1008	0.0167	0.1169	0.0198	0.0159	0.0006	33.97	-	0.01544
au24d08	-	-	-	3.07	-	0.0004	-	-	-	-	-	-	-	-	0.0012	-	-	-	-	-	2.14	-	0.00169
au24d09	-	-	-	9.57	-	-	-	-	-	-	-	-	0.0059	0.0014	0.0040	0.0009	0.0240	0.0042	-	-	1.27	-	0.00564
au24d11	-	-	-	6.27	-	-	-	-	-	-	-	-	-	0.0008	0.0045	0.0015	0.0084	0.0033	-	-	1.04	-	0.00800
au24d12	-	-	-	5.88	-	-	-	-	-	-	-	-	-	-	0.0013	-	0.0063	0.0010	-	-	0.30	-	0.00041
kb_28	-	-	0.057	7.63	-	0.0005	-	-	0.0015	-	-	0.0004	0.0016	0.0009	0.0037	0.0009	0.0099	0.0024	-	-	0.46	0.0003	0.00189
kb_30	-	-	0.043	9.68	-	0.0007	-	-	-	-	-	-	0.0016	0.0016	0.0064	0.0013	0.0166	0.0037	-	-	0.86	-	0.00669
au25d03	-	-	-	3.14	0.0016	0.0085	0.0016	0.0117	0.0072	0.0013	0.0176	0.0028	0.0185	0.0051	0.0153	0.0021	0.0135	0.0026	0.0004	-	40.65	0.0001	0.00020
au25d07	-	-	-	2.92	0.0038	0.0154	0.0035	0.0241	0.0093	0.0010	0.0154	0.0026	0.0228	0.0047	0.0116	0.0019	0.0139	0.0023	0.0039	-	16.43	0.0004	0.00089
au25d08	-	-	-	7.43	0.0626	0.3700	0.0762	0.5120	0.2604	0.0293	0.3970	0.0746	0.5200	0.0995	0.2637	0.0354	0.2628	0.0384	0.0008	-	100.53	0.0035	0.00013
au25d10	-	-	-	3.36	0.0042	0.0180	0.0034	0.0311	0.0132	0.0028	0.0298	0.0055	0.0345	0.0084	0.0217	0.0032	0.0277	0.0032	0.0241	-	24.65	0.0001	0.00550
kb_22	-	-	1.267	51.47	0.0452	0.1894	0.0349	0.2390	0.1100	0.0155	0.1316	0.0295	0.2185	0.0492	0.1351	0.0201	0.1390	0.0188	0.0201	0.0041	106.14	0.0048	0.00619
kb_25	-	-	0.063	4.25	0.0018	0.0058	0.0013	0.0086	0.0022	-	0.0098	0.0013	0.0166	0.0030	0.0108	0.0019	0.0134	0.0012	0.0020	-	20.52	0.0012	0.00032
au25f13	-	-	-	2.95	0.0750	0.1114	0.0134	0.0668	0.0173	0.0084	0.0364	0.0038	0.0271	0.0068	0.0154	0.0019	0.0177	0.0022	-	-	9.89	-	0.00063
au25f15	-	-	-	2.16	0.0686	0.1133	0.0135	0.0759	0.0201	0.0094	0.0379	0.0053	0.0301	0.0063	0.0189	0.0024	0.0137	0.0021	-	-	8.77	-	0.00054
au25g05	-	-	-	3.20	0.0828	0.1279	0.0169	0.0785	0.0265	0.0124	0.0448	0.0068	0.0417	0.0076	0.0185	0.0022	0.0119	0.0017	-	-	13.04	-	0.00091
mb_53	0.904	0.859	0.052	3.66	0.0892	0.1744	0.0207	0.1299	0.0407	0.0161	0.0774	0.0099	0.0538	0.0133	0.0304	0.0033	0.0142	0.0028	0.0017	-	9.79	-	0.00050
au25g06	-	-	-	3.99	0.0599	0.1120	0.0154	0.0772	0.0234	0.0115	0.0484	0.0064	0.0393	0.0107	0.0226	0.0036	0.0241	0.0038	-	-	23.07	-	0.00016
mb_49	3.200	3.200	0.040	2.50	0.0647	0.0958	0.0136	0.0691	0.0201	0.0098	0.0446	0.0070	0.0391	0.0061	0.0136	0.0016	0.0178	0.0025	-	-	7.10	-	0.00021
mb_55	3.860	3.600	0.120	4.88	0.0799	0.1224	0.0143	0.0746	0.0312	0.0112	0.0434	0.0073	0.0449	0.0099	0.0315	0.0027	0.0241	0.0042	-	0.0009	19.10	-	0.00160
au24c08	-	-	-	47.30	-	-	-	-	-	-	-	-	-	-	0.0056	-	0.0064	-	-	-	0.29	-	-
au24c11	-	-	-	50.89	0.0008	-	-	-	-	-	-	-	-	-	0.0031	-	0.0043	0.0011	-	-	0.29	-	-
kb_12	-	-	0.033	49.31	0.0005	-	-	-	-	-	-	0.0006	0.0051	0.0017	0.0085	0.0024	0.0179	0.0033	-	-	0.46	-	-
kb_14	-	-	0.283	56.85	-	-	-	-	-	-	-	-	0.0049	0.0027	0.0048	-	0.0154	0.0024	-	-	0.48	-	-
au24c17	-	-	-	39.93	-	-	-	-	-	-	-	-	0.0074	0.0024	0.0092	0.0024	0.0212	0.0030	-	-	0.35	-	-
au25e14	-	-	-	8.33	0.0240	0.0363	0.0045	0.0331	0.0148	0.0060	0.0263	0.0046	0.0252	0.0089	0.0223	0.0054	0.0418	0.0069	-	-	37.83	-	0.00286
mb_16	0.601	0.611	0.046	10.17	0.0257	0.0290	0.0040	0.0179	0.0068	0.0032	0.0166	0.0028	0.0257	0.0066	0.0169	0.0048	0.0259	0.0047	-	0.0010	27.09	-	0.00201
au25d05	-	-	-	61.97	0.0236	0.1040	0.0216	0.1467	0.1145	0.0251	0.2326	0.0490	0.3600	0.0754	0.2184	0.0289	0.2084	0.0317	0.0004	-	17.86	0.0003	0.00119
kb_24	-	-	0.009	40.08	0.0151	0.0843	0.0144	0.1309	0.0819	0.0148	0.1702	0.0334	0.2740	0.0605	0.1534	0.0206	0.1330	0.0219	-	-	12.87	-	0.00062
au24d13	-	-	-	13.52	0.0007	-	-	-	-	0.0015	-	-	0.0032	0.0009	0.0037	0.0010	0.0112	0.0022	-	-	37.80	-	-
au24d14	-	-	-	5.03	0.0008	0.0018	-	-	-	-	0.0048	-	0.0056	0.0012	0.0075	0.0008	0.0135	0.0017	-	-	14.74	-	-
au24d17	-	-	-	1.37	0.0010	0.0015	-	-	-	-	-	-	0.0033	0.0021	0.0077	0.0016	0.0165	0.0033	-	-	24.50	-	-
ha22	-	0.004	-	0.38	0.0094	0.0257	0.0062	0.0461	0.0357	0.0134	0.0555	0.0101	0.0632	0.0170	0.0507	0.0070	0.0568	0.0083	-	-	30.71	-	0.00018
au25d12	-	-	-	1.93	0.0034	0.0170	0.0038	0.0310	0.0195	0.0036	0.0374	0.0064	0.0571	0.0112	0.0314	0.0048	0.0373	0.0060	0.0009	-	105.94	0.0033	0.00165

kb_27	-	-	0.040	2.51	0.0070	0.0236	0.0064	0.0376	0.0196	0.0041	0.0539	0.0089	0.0640	0.0139	0.0425	0.0071	0.0466	0.0076	-	-	145.49	0.0023	0.00142
au25e17	-	-	-	0.94	0.0157	0.0350	0.0052	0.0396	0.0172	0.0081	0.0392	0.0044	0.0280	0.0067	0.0205	0.0034	0.0317	0.0052	-	-	61.98	-	0.00033
au25f14	-	-	-	4.10	0.0090	0.0153	0.0016	0.0081	0.0014	0.0015	0.0075	0.0012	0.0149	0.0046	0.0204	0.0041	0.0396	0.0092	-	-	7.10	-	0.00009
au25f16	-	-	-	0.45	0.0612	0.0984	0.0118	0.0712	0.0192	0.0096	0.0386	0.0058	0.0394	0.0090	0.0218	0.0029	0.0235	0.0036	-	-	140.07	0.0057	-
au25f17	-	-	-	1.19	0.2211	0.3690	0.0433	0.2270	0.0612	0.0236	0.1260	0.0121	0.0591	0.0097	0.0241	0.0025	0.0149	0.0019	-	-	7.37	-	0.00291
mb_48	2.001	1.933	0.023	3.76	0.0105	0.0146	0.0012	0.0167	-	0.0021	0.0098	0.0014	0.0115	0.0062	0.0178	0.0027	0.0342	0.0110	-	-	5.52	-	0.00035
mb_50	-	-	0.014	1.28	0.1656	0.3060	0.0385	0.2117	0.0448	0.0187	0.1257	0.0107	0.0569	0.0113	0.0255	0.0024	0.0170	0.0036	-	-	8.00	-	0.00325
mb_52	0.007	-	-	0.50	0.0456	0.0706	0.0074	0.0425	0.0187	0.0082	0.0426	0.0058	0.0358	0.0075	0.0289	0.0045	0.0243	0.0057	-	-	35.61	-	0.00037
au25g12	-	-	-	12.75	0.0026	0.0085	0.0031	0.0326	0.0335	0.0155	0.0855	0.0155	0.1332	0.0321	0.0970	0.0137	0.0934	0.0139	-	-	52.41	-	0.00027
mb_35	0.006	-	0.001	19.39	0.0025	0.0078	0.0033	0.0288	0.0392	0.0158	0.0964	0.0178	0.1489	0.0344	0.1081	0.0140	0.0919	0.0148	-	-	60.15	-	-
au25d17	-	-	-	10.56	0.0005	0.0005	0.0003	-	0.0015	-	0.0041	0.0008	0.0101	0.0032	0.0117	0.0028	0.0174	0.0046	0.0008	-	0.49	-	0.00018
mb_26	0.216	0.221	0.111	9.28	-	-	-	-	-	-	-	-	0.0023	0.0004	0.0044	0.0009	0.0078	0.0009	-	-	0.69	-	-
ha26	1.250	1.280	0.253	43.70	0.0029	0.0042	0.0008	0.0132	0.0131	0.0074	0.0470	0.0129	0.1349	0.0392	0.1680	0.0353	0.2770	0.0507	-	-	2.66	-	0.00084
ha27	0.424	0.393	0.175	26.13	0.0013	0.0023	0.0006	-	-	0.0014	0.0062	0.0026	0.0309	0.0123	0.0417	0.0091	0.0868	0.0268	-	-	1.03	-	0.00120
au24c13	-	-	-	10.14	-	-	-	-	-	-	-	-	0.0018	0.0004	0.0022	0.0006	0.0032	0.0008	-	-	0.08	-	-
au24c15	-	-	-	29.51	-	-	-	-	-	-	-	-	0.0033	-	0.0009	0.0005	0.0040	-	-	-	0.06	-	-
au24d03	-	-	-	86.46	-	-	-	-	-	-	-	-	-	-	0.0660	0.0230	0.1350	0.0380	-	-	39.31	-	0.02600
au24d05	-	-	-	71.61	-	-	-	-	-	-	0.0610	-	0.0670	0.0103	-	-	0.0960	0.0270	-	-	14.97	-	0.01420
au24d06	-	-	-	44.60	-	-	-	-	-	-	-	-	-	0.0030	0.0090	-	-	0.0025	-	-	1.90	-	-
au25d14	-	-	-	5.56	0.0003	0.0009	0.0001	0.0004	0.0008	0.0003	0.0031	0.0009	0.0076	0.0023	0.0108	0.0022	0.0200	0.0043	0.0002	-	0.46	0.0001	0.00033
au25e08	-	-	-	1.46	0.0004	0.0006	-	-	-	0.0003	-	0.0003	0.0047	0.0016	0.0075	0.0019	0.0196	0.0040	-	-	1.03	-	0.00087
au25e09	-	-	-	2.85	0.0002	0.0004	-	0.0014	-	-	0.0013	0.0010	0.0098	0.0032	0.0172	0.0039	0.0380	0.0085	-	-	1.75	-	0.00248
au25e10	-	-	-	0.48	0.0001	0.0001	0.0000	0.0004	0.0002	0.0001	0.0004	0.0001	0.0003	0.0002	0.0005	0.0001	0.0010	0.0002	0.0001	-	0.30	-	0.00021
au25e11	-	-	-	2.17	0.0002	0.0002	-	-	-	-	-	0.0001	0.0011	0.0004	0.0025	0.0006	0.0036	0.0005	0.0002	-	1.45	-	0.00101
au25e12	-	-	-	2.82	0.0004	0.0005	-	0.0018	-	-	0.0022	0.0005	0.0027	0.0021	0.0074	0.0012	0.0121	0.0023	0.0013	-	2.57	-	0.00332
au25e13	-	-	-	0.65	0.0002	0.0002	0.0001	-	-	-	-	0.0002	0.0020	0.0003	0.0022	0.0003	0.0053	0.0008	0.0004	-	0.59	-	0.00035
ha31	0.058	0.056	0.236	28.12	-	0.0012	-	-	-	-	-	0.0010	0.0028	0.0013	0.0054	0.0015	0.0141	0.0045	-	-	1.49	-	0.00053
mb_29	7.250	7.630	0.163	5.42	-	-	-	-	-	0.0006	0.0025	0.0012	0.0068	0.0027	0.0107	0.0023	0.0295	0.0054	-	-	0.29	-	0.00024
mb_30	2.120	2.120	0.093	4.91	-	0.0010	0.0002	0.0016	0.0010	0.0012	0.0049	0.0023	0.0259	0.0084	0.0319	0.0054	0.0511	0.0104	-	-	0.64	-	0.00116
ha13	0.191	0.194	0.020	0.26	-	0.0003	-	0.0010	0.0006	0.0007	0.0045	0.0015	0.0161	0.0045	0.0164	0.0026	0.0193	0.0029	0.0009	-	0.08	-	0.00008
mb_38	0.177	0.168	1.533	4.63	-	0.0008	0.0006	0.0117	0.0093	0.0046	0.0464	0.0111	0.1214	0.0325	0.1224	0.0305	0.2970	0.0705	0.0065	-	4.54	-	-
mb_39	0.314	0.302	0.488	2.70	-	0.0006	-	0.0013	0.0021	0.0005	0.0019	0.0004	0.0062	0.0010	0.0043	0.0009	0.0071	0.0021	0.0016	-	2.60	-	-
ha7	0.217	0.227	0.064	0.73	-	0.0014	0.0007	0.0062	0.0125	0.0034	0.0234	0.0065	0.0748	0.0173	0.0698	0.0114	0.0800	0.0140	0.0035	0.0006	0.58	-	0.00028
mb_14	0.137	0.139	1.428	2.74	-	0.0015	-	-	0.0038	-	-	0.0015	0.0059	0.0028	0.0122	0.0028	0.0088	0.0039	-	-	5.78	-	-
mb_15	0.367	0.377	0.084	1.18	0.0002	0.0005	0.0002	-	-	-	-	-	0.0025	0.0013	0.0066	0.0012	0.0140	0.0032	-	-	0.54	-	0.00044
mb_17	2.240	2.130	0.177	8.43	0.0011	0.0034	0.0012	-	-	-	0.0060	0.0022	0.0195	0.0059	0.0428	0.0088	0.0886	0.0189	-	-	3.73	-	0.00317
au25g13	-	-	-	2.96	0.0002	0.0009	0.0006	0.0046	0.0051	0.0034	0.0231	0.0047	0.0428	0.0121	0.0436	0.0095	0.0835	0.0196	0.0050	-	2.35	-	0.00033
mb_18	-	0.008	0.602	0.91	0.0006	0.0007	-	-	-	-	-	0.0008	0.0058	0.0019	0.0084	0.0022	0.0246	0.0042	-	-	2.12	-	-
au25e06	-	-	-	12.33	0.0032	0.0119	0.0010	0.0035	0.0014	0.0007	0.0036	0.0005	0.0064	0.0019	0.0080	0.0012	0.0103	0.0020	0.0014	-	0.45	0.0006	0.00219
au25d11	-	-	-	7.81	0.0135	0.0506	0.0085	0.0531	0.0304	0.0047	0.0529	0.0119	0.0908	0.0226	0.0693	0.0125	0.0792	0.0111	0.0140	-	4.35	0.0009	0.01897
au25f03	-	-	-	0.31	-	0.0005	0.0001	0.0016	-	0.0002	0.0009	0.0004	0.0022	0.0005	0.0029	0.0006	0.0062	0.0017	-	-	0.78	-	0.00020
au25f04	-	-	-	0.81	-	0.0005	-	-	-	-	-	-	0.0016	0.0005	0.0016	0.0006	0.0045	0.0010	-	-	2.44	-	-
au25f08	-	-	-	0.08	0.0000	0.0001	0.0000	0.0001	0.0001	0.0000	0.0002	0.0000	0.0002	0.0000	0.0001	0.0000	0.0002	0.0000	-	-	0.36	0.0000	0.00601
au25f09	-	-	-	1.72	0.0002	0.0007	0.0003	-	0.0011	-	0.0017	0.0004	0.0019	0.0009	0.0040	0.0007	0.0091	0.0020	-	-	3.77	-	0.00690
au25f10	-	-	-	0.35	0.0003	0.0006	0.0001	0.0011	0.0004	0.0001	0.0006	0.0002	0.0021	0.0004	0.0016	0.0004	0.0039	0.0010	-	-	1.01	0.0001	0.00004
au25f12	-	-	-	0.90	0.0001	0.0004	-	-	-	-	-	-	-	0.0003	0.0008	0.0001	0.0013	0.0003	-	-	4.67	-	0.00800
au25g08	-	-	-	3.93	0.0001	0.0058	0.0038	0.0410	0.0585	0.0301	0.1625	0.0435	0.4190	0.1059	0.4120	0.0802	0.6700	0.1159	0.0061	-	3.57	0.0000	0.00011
au25g09	-	-	-	4.56	0.0002	0.0074	0.0047	0.0598	0.0818	0.0357	0.2070	0.0576	0.5270	0.1405	0.5060	0.0977	0.8000	0.1376	0.0157	-	3.01	-	-
mb_24	0.036	0.039	0.055	1.92	-	0.0014	0.0003	0.0019	-	0.0008	0.0032	0.0011	0.0178	0.0066	0.0299	0.0079	0.0658	0.0157	-	-	0.83	-	0.00040
ha9	0.043	0.045	0.139	0.32	-	0.0006	0.0003	0.0032	0.0029	0.0012	0.0086	0.0020	0.0200	0.0055	0.0190	0.0025	0.0158	0.0026	0.0013	-	0.15	-	0.00012
ha15	0.967	0.936	0.051	0.40	0.0006	0.0010	0.0005	0.0055	0.0069	0.0028	0.0211	0.0054	0.0521	0.0135	0.0496	0.0092	0.0786	0.0132	0.0026	0.0001	0.56	-	0.00077
ha18	0.203	0.190	0.076	1.58	-	0.0004	-	0.0016	-	0.0003	0.0030	0.0004	0.0052	0.0006	0.0026	0.0005	0.0032	0.0007	-	-	0.50	-	0.00039
kb_16	-	-	0.029	0.53	0.0011	0.0005	0.0005	-	-	-	-	-	0.0018	0.0007	0.0035	0.0005	0.0073	0.0011	-	0.0005	2.01	-	-

kb_18	-	-	0.007	0.32	0.0006	0.0007	0.0002	-	0.0012	-	0.0012	0.0002	0.0025	0.0010	0.0018	0.0009	0.0082	0.0022	-	0.0006	0.86	-	0.00052
kb_19	-	-	0.058	1.49	0.0005	0.0032	0.0005	0.0034	-	-	0.0022	0.0007	0.0051	0.0012	0.0050	0.0014	0.0215	0.0037	-	-	37.06	-	0.00034
kb_20	-	-	0.042	0.59	0.0007	0.0014	-	0.0030	0.0017	0.0016	0.0032	0.0005	0.0038	0.0016	0.0046	0.0016	0.0121	0.0037	-	-	1.52	-	-
kb_26	-	-	0.143	19.22	0.0189	0.0861	0.0097	0.0660	0.0361	0.0051	0.0473	0.0100	0.0828	0.0188	0.0513	0.0079	0.0614	0.0103	0.0075	-	3.92	0.0002	0.02760
au24c16	-	-	-	2.93	0.0002	-	-	-	-	-	-	-	-	-	-	-	0.0007	-	-	-	0.04	-	-
ha19	0.085	0.085	0.024	1.20	0.0002	0.0007	-	0.0038	0.0015	0.0005	0.0023	0.0008	0.0029	0.0011	0.0034	0.0006	0.0059	0.0012	-	0.0004	0.43	-	0.00051
ha20	0.001	0.001	0.000	0.00	-	0.0000	0.0000	0.0000	0.0000	0.0000	0.0000	0.0000	0.0001	0.0000	0.0001	0.0000	0.0001	0.0000	0.0000	-	0.04	-	-
ha21	0.012	0.012	0.001	0.03	0.0000	0.0000	0.0000	0.0000	0.0001	0.0000	0.0001	0.0000	0.0002	0.0001	0.0002	0.0000	0.0002	0.0000	-	0.0000	0.33	-	0.00003
au25g15	-	-	-	10.05	-	0.0007	0.0005	0.0029	0.0082	0.0061	0.0262	0.0081	0.0815	0.0223	0.0942	0.0172	0.2260	0.0487	0.0050	-	4.23	-	-
au25g16	-	-	-	9.52	0.0007	0.0015	0.0006	0.0071	0.0052	0.0023	0.0097	0.0028	0.0187	0.0056	0.0197	0.0043	0.0359	0.0076	0.0018	-	4.16	-	0.00053
au25g17	-	-	-	5.22	0.0013	0.0035	0.0013	0.0142	0.0113	0.0057	0.0246	0.0088	0.0727	0.0221	0.0973	0.0218	0.2277	0.0475	0.0086	-	2.98	-	0.00113
mb_57	0.214	0.204	0.366	2.45	-	-	-	0.0019	0.0026	0.0005	0.0018	0.0010	0.0068	0.0019	0.0064	0.0014	0.0091	0.0020	0.0026	-	2.72	-	0.00025
mb_41	0.925	0.936	0.744	5.55	-	0.0011	-	0.0045	0.0051	0.0020	0.0145	0.0039	0.0356	0.0103	0.0435	0.0101	0.1139	0.0233	0.0043	-	3.36	-	0.00031
au25e03	-	-	-	23.28	0.0006	0.0012	0.0004	0.0011	0.0009	0.0007	0.0053	0.0015	0.0149	0.0030	0.0170	0.0035	0.0260	0.0053	-	-	1.18	-	0.00171
au25e05	-	-	-	12.65	0.0009	0.0015	-	0.0019	-	0.0006	0.0017	0.0002	0.0012	0.0007	0.0032	0.0004	0.0044	0.0009	-	-	0.79	-	0.00344
au25g03	-	-	-	0.37	0.0582	0.0463	0.0039	0.0203	0.0032	0.0013	0.0092	0.0007	0.0033	0.0009	0.0020	0.0001	0.0025	0.0005	-	-	7.02	-	0.00009
mb_51	0.023	0.020	0.001	0.39	0.0376	0.0399	0.0047	0.0200	0.0057	0.0017	0.0089	0.0010	0.0066	0.0013	0.0031	0.0008	0.0038	0.0006	-	-	3.70	-	0.00008
mb_25	0.013	0.015	0.010	3.03	0.0001	-	-	-	-	-	0.0009	0.0002	0.0026	0.0007	0.0041	0.0004	0.0037	0.0007	-	-	0.15	-	0.00012
mb_33	0.009	0.014	0.021	5.29	0.0004	0.0006	-	-	-	-	-	0.0002	-	0.0002	-	-	-	-	-	-	0.43	-	0.00023
au24c14	-	-	-	8.02	-	-	-	-	-	-	-	-	-	-	-	-	-	-	-	-	0.27	-	-
kb_11	-	-	0.102	6.01	-	-	-	-	-	-	-	-	-	0.0010	0.0053	-	0.0147	-	-	-	0.27	-	-
au24d04	-	-	-	12.40	-	-	-	-	-	-	-	-	-	-	-	-	-	-	-	-	0.04	-	-
au24d07	-	-	-	7.76	0.0003	-	-	-	-	-	-	-	-	-	-	-	-	-	-	-	0.07	-	-
ha30	0.005	0.004	0.026	3.85	0.0002	0.0005	0.0002	-	-	-	-	0.0001	-	0.0002	0.0007	0.0003	0.0037	0.0006	-	-	0.16	-	0.00006
ha16	0.964	0.958	0.184	28.89	0.0050	0.0096	0.0022	0.0233	0.0096	0.0057	0.0203	0.0054	0.0394	0.0084	0.0243	0.0052	0.0440	0.0072	0.0013	-	7.41	0.0003	0.03910
ha17	0.011	-	0.003	0.27	-	0.0044	0.0019	0.0207	0.0232	0.0102	0.0504	0.0094	0.0827	0.0191	0.0722	0.0109	0.0799	0.0135	0.0005	0.0002	0.11	-	0.00027
ha23	0.015	0.024	0.041	1.04	0.0007	0.0034	0.0008	0.0050	0.0043	0.0017	0.0045	0.0009	0.0079	0.0020	0.0079	0.0008	0.0056	0.0015	-	-	0.31	-	0.00016
ha24	0.007	0.009	0.004	0.20	0.0023	0.0053	0.0008	0.0112	0.0060	0.0031	0.0154	0.0024	0.0228	0.0068	0.0217	0.0041	0.0414	0.0059	-	0.0039	0.16	0.0017	0.00023
ha25	0.090	0.086	0.026	1.01	0.0009	0.0046	0.0007	0.0071	0.0036	0.0019	0.0069	0.0016	0.0102	0.0022	0.0066	0.0014	0.0061	0.0016	-	-	0.35	-	0.00029
au25d04	-	-	-	29.49	0.0518	0.3110	0.0387	0.2550	0.1362	0.0096	0.2120	0.0400	0.3030	0.0634	0.1849	0.0285	0.2030	0.0282	0.0023	-	5.80	0.0002	0.10770
kb_23	-	-	0.099	30.13	0.0539	0.3370	0.0376	0.2660	0.1382	0.0125	0.2030	0.0438	0.3180	0.0676	0.2031	0.0325	0.2010	0.0291	0.0027	-	8.07	-	0.09740
au25f05	-	-	-	46.19	0.0019	0.0022	0.0004	0.0016	0.0008	0.0007	0.0015	0.0003	0.0031	0.0007	0.0039	0.0006	0.0062	0.0011	0.0007	-	101.27	0.0025	0.05290
au25f11	-	-	-	0.85	0.0001	0.0005	0.0001	0.0011	0.0003	0.0006	0.0008	0.0001	0.0016	0.0007	0.0036	0.0006	0.0053	0.0014	-	-	1.55	0.0000	0.00193
kb_17	-	-	0.049	37.09	0.0019	0.0018	0.0003	-	-	0.0012	0.0019	0.0005	0.0030	0.0008	0.0025	0.0004	0.0060	0.0011	-	-	56.82	-	0.07360
au24d16	-	-	-	0.50	-	-	0.0001	-	-	-	-	-	0.0011	0.0005	0.0042	0.0009	0.0126	0.0019	-	-	5.63	-	-
au25e16	-	-	-	2.55	0.0003	0.0005	-	0.0013	-	-	0.0018	0.0004	0.0045	0.0019	0.0074	0.0014	0.0121	0.0026	-	-	0.53	-	-
mb_13	1.970	1.990	0.461	19.37	-	-	-	-	0.0086	0.0047	-	0.0036	0.0459	0.0239	0.1140	0.0264	0.2900	0.0540	-	-	4.59	-	0.00740
mb_20	0.001	0.001	0.001	0.07	0.0001	0.0001	0.0000	0.0001	-	-	0.0001	0.0000	0.0002	0.0001	0.0002	0.0000	0.0005	0.0001	-	-	0.07	-	-
ha6	0.139	0.128	0.309	3.33	0.0009	0.0082	0.0051	0.0632	0.0559	0.0144	0.1266	0.0306	0.2500	0.0635	0.1908	0.0269	0.2170	0.0258	0.0077	-	1.07	-	0.00051
ha10	0.019	0.015	0.004	0.80	0.0006	0.0035	0.0017	0.0247	0.0236	0.0117	0.0407	0.0109	0.0999	0.0250	0.0963	0.0178	0.1469	0.0285	-	-	0.22	-	0.00017
ha11	0.029	0.039	-	1.27	-	0.0046	0.0027	0.0335	0.0305	0.0133	0.0639	0.0158	0.1444	0.0352	0.1149	0.0209	0.1662	0.0311	-	-	0.54	-	0.00041
au25g14	-	-	-	3.99	0.0001	0.0007	0.0004	0.0048	0.0043	0.0033	0.0121	0.0025	0.0259	0.0069	0.0239	0.0042	0.0293	0.0042	0.0055	-	1.49	-	0.00007
mb_36	0.283	0.267	0.124	1.71	-	0.0016	0.0015	0.0203	0.0182	0.0112	0.0674	0.0120	0.1355	0.0323	0.1067	0.0181	0.1653	0.0259	-	-	0.91	-	0.00030
mb_40	0.055	0.053	0.344	3.44	-	0.0019	0.0011	0.0106	0.0130	0.0053	0.0424	0.0099	0.0931	0.0239	0.0602	0.0144	0.0868	0.0159	0.0129	-	2.71	-	-
au25g04	-	-	-	0.63	0.0082	0.0135	0.0016	0.0065	0.0020	0.0011	0.0041	0.0005	0.0032	0.0009	0.0035	0.0004	0.0050	0.0010	-	-	1.49	0.0000	0.00017
au25g07	-	-	-	0.55	0.0005	0.0006	0.0000	0.0001	-	0.0000	0.0002	0.0000	0.0004	0.0000	0.0003	0.0001	0.0007	0.0001	-	-	0.48	-	0.00001
mb_54	0.011	0.010	0.003	0.22	0.0007	0.0007	0.0001	0.0004	-	0.0001	0.0006	0.0001	0.0009	0.0002	0.0007	0.0002	0.0007	0.0002	-	-	0.23	-	-
au25e15	-	-	-	4.48	-	0.0003	-	-	-	-	-	0.0003	0.0055	0.0017	0.0082	0.0017	0.0202	0.0046	-	-	0.98	-	0.00009
mb_19	0.080	0.089	0.064	1.48	-	-	-	-	-	-	-	-	0.0023	0.0018	0.0097	0.0035	0.0206	0.0054	-	-	0.77	-	0.00036
au25g11	-	-	-	0.25	-	0.0029	0.0014	0.0176	0.0199	0.0148	0.0429	0.0092	0.0670	0.0167	0.0464	0.0075	0.0466	0.0059	-	-	0.14	-	-
mb_37	0.079	0.084	0.042	0.56	-	0.0013	0.0007	0.0058	0.0070	0.0043	0.0107	0.0027	0.0235	0.0045	0.0089	0.0014	0.0101	0.0019	-	-	0.25	-	-
mb_22	0.121	0.099	0.023	2.77	0.0005	-	0.0005	0.0015	-	-	0.0019	-	-	-	0.0013	0.0004	0.0023	0.0007	-	-	4.00	-	-
ha12	0.002	0.004	0.001	0.03	0.0004	-	0.0003	0.0038	0.0054	0.0027	0.0137	0.0032	0.0322	0.0085	0.0265	0.0041	0.0257	0.0040	0.0006	-	0.11	-	-

Table S10 (continued) 1σ error

Analysis #	Li7 µg/g	Be9 µg/g	B11 µg/g	Sc45 µg/g	Ti47 µg/g	Ti49 µg/g	V51 µg/g	Cr53 µg/g	Mn55 µg/g	Co59 µg/g	Ni62 µg/g	Cu63 µg/g	Cu65 µg/g	Zn66 µg/g	As75 µg/g	Rb85 µg/g	Sr86 µg/g	Sr88 µg/g	Y89 µg/g	Zr90 µg/g	Zr91 µg/g	Nb93 µg/g	Sn118 µg/g	Sn119 µg/g
au24e03	0.23	0.01	1.29	-	-	-	-	-	8.5	-	71.6	-	0.03	0.93	-	0.00	-	0.14	0.0015	-	0.0007	0.0002	-	-
au24e04	0.29	0.01	1.13	-	-	-	-	-	9.9	-	88.2	-	0.05	1.01	-	0.00	-	0.10	0.0012	-	0.0009	0.0002	-	-
au24e05	0.42	0.01	1.67	-	-	-	-	-	14.2	-	100.7	-	0.02	1.46	-	0.00	-	0.24	0.0021	-	0.0011	0.0003	-	-
au24e09	0.39	0.01	1.48	-	-	-	-	-	11.7	-	81.4	-	0.02	1.39	-	0.00	-	0.23	0.0018	-	0.0009	0.0002	-	-
au24e11	0.53	0.01	1.43	-	-	-	-	-	13.6	-	72.4	-	0.02	1.33	-	0.00	-	0.25	0.0022	-	0.0009	0.0002	-	-
mb_1	0.35	-	-	0.23	0.41	0.35	0.26	-	-	2.53	90.4	0.02	-	0.82	0.13	0.00	0.08	0.06	-	0.0022	-	0.0003	0.0180	0.0210
mb_6	0.41	-	-	0.29	0.35	0.29	0.36	-	-	1.96	103.0	0.05	-	0.90	0.17	0.00	0.16	0.13	-	0.0022	-	0.0004	0.0210	0.0260
mb_7	0.38	-	-	0.28	0.30	0.25	0.42	-	-	2.21	145.9	0.02	-	0.91	0.16	0.00	0.16	0.14	-	0.0021	-	0.0003	0.0170	0.0230
au24e14	0.30	0.01	1.51	-	-	-	-	-	11.2	-	89.8	-	0.23	1.57	-	0.00	-	0.21	0.0013	-	0.0036	0.0002	-	-
au24e17	0.39	0.01	1.69	-	-	-	-	-	12.2	-	97.5	-	0.03	1.54	-	0.00	-	0.18	0.0013	-	0.0077	0.0002	-	-
au24f03	0.35	0.01	1.66	-	-	-	-	-	7.8	-	77.0	-	0.04	1.49	-	0.00	-	0.17	0.0014	-	0.0017	0.0002	-	-
au24f05	0.43	0.01	1.46	-	-	-	-	-	11.0	-	72.1	-	0.02	1.91	-	0.00	-	0.22	0.0013	-	0.0040	0.0002	-	-
au24f08	0.17	0.01	1.73	-	-	-	-	-	6.0	-	107.1	-	0.02	0.48	-	0.00	-	0.24	0.0026	-	0.0011	0.0001	-	-
au24f10	0.20	0.01	1.58	-	-	-	-	-	6.1	-	97.7	-	0.02	0.50	-	0.00	-	0.31	0.0025	-	0.0035	0.0001	-	-
au24f11	0.52	0.01	4.98	-	-	-	-	-	14.0	-	107.7	-	0.02	1.10	-	0.00	-	0.29	0.0079	-	0.0012	0.0005	-	-
au24f14	0.35	0.01	2.20	-	-	-	-	-	15.1	-	93.9	-	0.03	0.82	-	0.00	-	0.31	0.0052	-	0.0015	0.0002	-	-
kb_3	0.72	1.30	-	1.62	2.92	2.14	1.10	-	-	6.23	142.1	0.02	-	4.09	2.19	0.01	0.64	0.67	0.0075	0.0010	-	0.0004	0.0140	0.0160
kb_8	0.36	1.27	-	1.02	1.68	1.22	0.53	-	-	4.18	135.9	0.01	-	2.86	1.75	0.00	0.78	0.83	0.0041	0.0009	-	0.0001	0.0100	0.0120
kb_10	0.55	1.27	-	0.67	1.11	0.82	0.37	-	-	5.22	160.6	0.04	-	3.84	1.79	0.00	0.33	0.35	0.0035	0.0010	-	0.0002	0.0140	0.0170
au24f17	0.83	0.01	2.43	-	-	-	-	-	6.6	-	75.6	-	0.04	1.47	-	0.00	-	0.84	0.0015	-	0.0024	0.0002	-	-
au24g04	1.36	0.00	0.88	-	-	-	-	-	2.9	-	113.2	-	0.02	1.74	-	0.00	-	0.15	0.0012	-	0.0008	0.0002	-	-
au24g08	0.89	0.00	1.46	-	-	-	-	-	8.5	-	78.7	-	0.05	1.91	-	0.00	-	0.21	0.0016	-	0.0013	0.0002	-	-
au24g15	0.80	0.00	1.83	-	-	-	-	-	6.9	-	75.6	-	0.02	1.70	-	0.00	-	0.30	0.0015	-	0.0010	0.0002	-	-
au24g16	0.68	0.00	2.16	-	-	-	-	-	14.4	-	86.3	-	0.11	2.16	-	0.00	-	0.31	0.0022	-	0.0018	0.0005	-	-
ha29	3.10	-	-	2.13	4.15	2.99	1.61	-	-	6.53	147.9	0.26	-	4.50	3.19	0.01	0.65	0.64	0.0049	0.0018	-	0.0006	0.1300	0.1100
au24e06	0.44	0.01	1.72	-	-	-	-	-	15.7	-	102.7	-	0.02	1.54	-	0.00	-	0.23	0.0023	-	0.0013	0.0003	-	-
mb_3	0.52	-	-	0.70	1.91	1.91	1.80	-	-	2.28	99.4	0.02	-	1.55	0.38	0.00	0.25	0.24	-	0.0022	-	0.0008	0.0200	0.0220
mb_4	0.45	-	-	0.73	2.03	1.94	1.90	-	-	2.27	105.2	0.01	-	1.65	0.59	0.00	0.21	0.19	-	0.0026	-	0.0009	0.0180	0.0220
au24f07	0.48	0.01	2.45	-	-	-	-	-	13.8	-	88.9	-	0.02	1.03	-	0.00	-	0.32	0.0068	-	0.0015	0.0005	-	-
au24f12	0.19	0.01	2.70	-	-	-	-	-	5.8	-	110.9	-	0.02	0.47	-	0.00	-	0.17	0.0027	-	0.0008	0.0001	-	-
au24f13	1.00	0.01	2.57	-	-	-	-	-	17.0	-	95.8	-	0.02	1.21	-	0.01	-	0.37	0.0053	-	0.0013	0.0004	-	-
kb_1	1.16	1.25	-	3.61	10.74	8.10	4.79	-	-	8.90	156.7	0.00	-	6.53	3.42	0.01	0.68	0.72	0.0150	0.0025	-	0.0019	0.0120	0.0170
kb_2	1.26	1.33	-	3.09	7.75	5.78	3.87	-	-	8.90	159.6	0.04	-	6.38	3.41	0.01	0.92	1.00	0.0160	0.0024	-	0.0015	0.0130	0.0160
kb_5	0.95	1.28	-	2.99	8.92	6.74	3.87	-	-	8.09	141.1	0.01	-	6.95	3.68	0.01	0.82	0.85	0.0160	0.0024	-	0.0019	0.0110	0.0130
au24g05	0.92	0.00	1.68	-	-	-	-	-	15.1	-	82.8	-	0.02	2.19	-	0.00	-	0.46	0.0020	-	0.0011	0.0004	-	-
au24g07	0.87	0.00	1.98	-	-	-	-	-	10.9	-	96.7	-	0.05	2.26	-	0.00	-	0.36	0.0022	-	0.0013	0.0004	-	-
au24e07	0.48	0.01	1.78	-	-	-	-	-	25.5	-	106.9	-	0.02	1.91	-	0.00	-	0.29	0.0034	-	0.0016	0.0004	-	-
au24e10	0.27	0.01	1.13	-	-	-	-	-	20.3	-	54.8	-	0.03	0.94	-	0.00	-	0.10	0.0007	-	0.0007	0.0001	-	-
mb_2	0.48	-	-	0.17	0.20	0.13	0.37	-	-	1.50	62.4	0.04	-	0.93	0.16	0.00	0.09	0.07	-	0.0021	-	0.0003	0.0180	0.0200
mb_8	0.40	-	-	0.23	0.26	0.17	0.37	-	-	1.69	65.5	0.02	-	0.80	0.09	0.00	0.11	0.08	-	0.0027	-	0.0004	0.0150	0.0210
au24e12	0.28	0.01	1.25	-	-	-	-	-	17.2	-	63.4	-	0.03	1.16	-	0.00	-	0.15	0.0005	-	0.0007	0.0001	-	-
au24e15	0.28	0.01	1.42	-	-	-	-	-	16.7	-	66.3	-	0.03	1.19	-	0.00	-	0.10	0.0006	-	0.0014	0.0001	-	-
au24e16	0.28	0.01	1.47	-	-	-	-	-	17.1	-	69.3	-	0.03	1.29	-	0.00	-	0.10	0.0015	-	0.0160	0.0004	-	-
au24f04	0.39	0.03	2.45	-	-	-	-	-	9.8	-	86.6	-	0.03	1.51	-	0.00	-	0.14	0.0017	-	0.0034	0.0004	-	-
kb_4	1.77	1.30	-	0.89	0.61	0.36	0.43	-	-	8.63	94.2	0.00	-	4.76	1.73	0.00	0.20	0.23	0.0038	0.0009	-	0.0001	0.0100	0.0120
kb_9	1.47	1.34	-	0.58	0.46	0.28	0.34	-	-	7.24	92.4	0.03	-	4.78	1.90	0.01	0.47	0.31	0.0023	0.2700	-	0.0039	0.0140	0.0180
au24f16	1.87	0.01	1.36	-	-	-	-	-	18.8	-	51.4	-	0.02	1.13	-	0.00	-	0.13	0.0008	-	0.0009	0.0001	-	-
au24g03	1.99	0.01	0.86	-	-	-	-	-	15.2	-	57.3	-	0.02	1.56	-	0.00	-	0.16	0.0006	-	0.0009	0.0002	-	-

au24g06	2.14	0.00	0.82	-	-	-	-	-	16.6	-	55.0	-	0.02	1.33	-	0.00	-	0.16	0.0006	-	0.0008	0.0001	-	-
au24g14	1.96	0.00	1.04	-	-	-	-	-	15.4	-	57.8	-	0.02	1.20	-	0.00	-	0.21	0.0006	-	0.0005	0.0001	-	-
au24g17	1.85	0.00	0.96	-	-	-	-	-	19.8	-	47.9	-	0.02	1.14	-	0.00	-	0.12	0.0004	-	0.0004	0.0001	-	-
ha28	5.03	-	-	0.72	0.76	0.43	0.50	-	-	5.55	69.9	0.11	-	2.40	0.18	0.01	0.26	0.26	0.0008	0.0022	-	0.0003	0.0460	0.0420
ha1	173.20	-	-	0.80	88.74	77.29	13.72	-	-	1.64	575.9	0.73	-	4.54	0.38	13.79	1.53	1.53	0.0150	0.1900	-	0.0067	0.6700	0.5900
ha2	255.25	-	-	1.19	161.58	143.37	12.33	-	-	11.27	584.7	0.26	-	18.60	0.75	14.79	1.56	1.57	0.0300	0.2100	-	0.0067	0.4200	0.3700
ha3	228.32	-	-	0.71	64.76	55.25	12.42	-	-	1.46	531.3	0.94	-	4.00	0.37	9.76	1.15	1.16	0.0110	0.1300	-	0.0050	0.6900	0.6100
ha4	177.37	-	-	0.67	62.78	54.30	13.32	-	-	1.39	461.0	0.89	-	3.77	0.39	14.22	1.21	1.24	0.0072	0.1600	-	0.0056	1.4400	1.2700
ha5	144.42	-	-	0.73	36.92	31.86	14.44	-	-	1.45	511.7	0.44	-	4.26	0.39	14.34	1.09	1.12	0.0067	0.1600	-	0.0066	0.8100	0.7100
au25c03	0.41	0.19	4.74	-	-	-	-	-	-	-	38.2	-	0.20	-	-	14.42	-	0.57	0.0020	-	0.1200	0.0035	-	-
au25c04	0.29	0.17	4.43	-	-	-	-	-	-	-	32.2	-	0.21	-	-	13.47	-	0.73	0.0026	-	0.1100	0.0032	-	-
au25c11	15.96	0.18	5.71	-	-	-	-	-	-	-	75.8	-	0.20	-	-	12.91	-	0.59	0.0018	-	0.1000	0.0035	-	-
mb_43	1.04	-	-	0.45	18.93	19.11	3.37	-	-	0.34	25.6	0.27	-	3.45	0.38	8.46	1.78	1.47	-	1.8700	-	0.0260	0.3200	0.3200
mb_44	0.41	-	-	0.78	17.43	16.56	2.86	-	-	1.73	38.3	0.30	-	0.90	0.77	13.18	1.55	1.32	-	1.6300	-	0.0160	0.3200	0.3000
mb_45	0.76	-	-	0.39	3.85	3.58	2.43	-	-	0.11	16.6	0.20	-	0.47	1.24	6.78	0.64	0.53	-	0.0460	-	0.0027	0.0150	0.0220
mb_46	2.05	-	-	0.44	14.97	14.84	2.96	-	-	0.13	18.7	0.35	-	1.55	0.32	7.43	1.41	1.18	-	2.5300	-	0.0430	0.3200	0.3000
au24c09	0.20	0.03	7.33	-	-	-	-	-	229.2	-	98.5	-	0.07	6.54	-	0.01	-	26.87	0.0058	-	0.0097	0.0008	-	-
au24c12	0.13	0.02	4.74	-	-	-	-	-	143.1	-	41.7	-	0.05	3.15	-	0.00	-	19.17	0.0037	-	0.0046	0.0005	-	-
kb_15	6.31	########	-	0.87	1.81	2.30	2.40	-	-	8.89	57.0	0.02	-	41.95	1.95	0.01	58.55	65.36	0.0140	0.0047	-	0.0017	0.0340	0.0380
mb_56	0.31	-	-	0.57	41.34	41.85	2.25	-	-	2.22	32.7	0.03	-	3.01	0.65	0.50	7.64	7.94	-	0.0110	-	0.0015	0.0080	0.0130
au24d08	0.05	0.01	1.80	-	-	-	-	-	26.0	-	40.8	-	0.04	2.27	-	0.00	-	13.39	0.0019	-	0.0011	0.0005	-	-
au24d09	0.02	0.02	1.82	-	-	-	-	-	12.4	-	41.9	-	0.05	4.63	-	0.00	-	9.41	0.0035	-	0.0018	0.0002	-	-
au24d11	0.04	0.02	1.93	-	-	-	-	-	24.9	-	42.3	-	0.10	10.78	-	0.00	-	9.57	0.0022	-	0.0027	0.0003	-	-
au24d12	0.02	0.02	2.45	-	-	-	-	-	12.1	-	46.1	-	0.02	7.82	-	0.00	-	9.15	0.0021	-	0.0021	0.0003	-	-
kb_28	0.03	451.59	-	0.62	0.14	0.16	0.14	-	-	2.16	48.9	0.01	-	39.69	0.54	0.00	8.54	9.63	0.0011	0.0008	-	0.0002	0.0150	0.0150
kb_30	0.04	379.98	-	0.65	0.15	0.20	0.39	-	-	3.02	46.1	0.10	-	43.54	6.36	0.00	9.53	10.58	0.0015	0.0011	-	0.0003	0.0100	0.0100
au25d03	0.01	0.01	0.44	-	-	-	-	-	14.8	-	10.2	-	0.02	0.43	-	0.00	-	18.81	0.0045	-	0.0018	0.0001	-	-
au25d07	0.01	0.01	0.41	-	-	-	-	-	12.8	-	15.5	-	0.04	0.69	-	0.00	-	15.85	0.0033	-	0.0043	0.0001	-	-
au25d08	0.01	0.01	0.34	-	-	-	-	-	39.7	-	4.0	-	0.02	0.22	-	0.00	-	9.59	0.0810	-	0.0021	0.0001	-	-
au25d10	0.03	0.06	0.43	-	-	-	-	-	22.4	-	164.6	-	0.12	1.88	-	0.00	-	15.94	0.0079	-	0.0092	0.0002	-	-
kb_22	0.09	2077.79	-	1.58	29.23	40.53	4.09	-	-	2.67	50.7	0.36	-	20.32	3.26	0.02	19.68	21.82	0.0320	0.0240	-	0.0019	0.0074	0.0078
kb_25	0.02	282.79	-	1.42	0.12	0.13	1.05	-	-	0.60	17.6	0.01	-	3.19	0.18	0.00	24.69	28.48	0.0034	0.0023	-	0.0002	0.0067	0.0074
au25f13	0.04	0.06	0.51	-	-	-	-	-	24.9	-	50.7	-	0.02	2.75	-	0.00	-	14.39	0.0075	-	0.0006	0.0001	-	-
au25f15	0.03	0.07	0.42	-	-	-	-	-	19.9	-	39.3	-	0.01	1.95	-	0.00	-	15.58	0.0080	-	0.0006	0.0000	-	-
au25g05	0.04	0.08	0.42	-	-	-	-	-	23.1	-	47.2	-	0.02	2.51	-	0.00	-	20.82	0.0091	-	0.0004	0.0000	-	-
mb_53	0.05	-	-	0.15	0.11	0.07	0.05	-	-	1.85	35.9	0.01	-	2.19	0.08	0.00	16.58	16.60	-	0.0021	-	0.0003	0.0046	0.0066
au25g06	0.03	0.03	0.37	-	-	-	-	-	27.5	-	23.4	-	0.01	2.47	-	0.00	-	16.01	0.0098	-	0.0004	0.0002	-	-
mb_49	0.05	-	-	0.09	0.09	0.06	0.03	-	-	1.83	36.6	0.01	-	2.30	0.25	0.00	14.03	13.19	-	0.0018	-	0.0002	0.0042	0.0060
mb_55	0.10	-	-	0.46	0.19	0.15	0.45	-	-	1.50	23.7	0.01	-	2.51	0.18	0.00	15.47	15.35	-	0.0025	-	0.0002	0.0062	0.0099
au24c08	0.26	0.03	5.01	-	-	-	-	-	171.9	-	80.0	-	0.06	2.90	-	0.01	-	24.66	0.0044	-	0.0061	0.0007	-	-
au24c11	0.11	0.02	5.01	-	-	-	-	-	208.2	-	48.7	-	0.04	2.48	-	0.00	-	24.02	0.0031	-	0.0036	0.0003	-	-
kb_12	0.28	3118.54	-	0.10	0.31	0.41	0.18	-	-	1.76	17.9	0.00	-	4.62	0.53	0.00	43.04	47.93	0.0034	0.0011	-	0.0001	0.0130	0.0140
kb_14	1.35	########	-	0.23	0.46	0.45	0.40	-	-	4.10	95.9	0.01	-	8.86	2.58	0.00	47.25	53.37	0.0042	0.0026	-	0.0003	0.0250	0.0270
au24c17	0.05	0.02	7.78	-	-	-	-	-	411.9	-	20.0	-	0.03	0.60	-	0.00	-	38.90	0.0060	-	0.0058	0.0004	-	-
au25e14	0.25	0.06	1.43	-	-	-	-	-	77.8	-	194.9	-	0.05	47.49	-	0.02	-	13.43	0.0100	-	0.0035	0.0003	-	-
mb_16	0.11	-	-	0.23	0.27	0.16	0.46	-	-	8.61	92.2	0.01	-	21.92	7.02	0.00	16.46	18.95	-	0.0052	-	0.0007	0.0140	0.0210
au25d05	0.03	0.01	0.35	-	-	-	-	-	13.6	-	1.1	-	0.03	0.70	-	0.00	-	294.52	0.0650	-	0.0021	0.0001	-	-
kb_24	0.08	159.20	-	0.15	0.30	0.41	0.10	-	-	0.26	1.5	0.02	-	6.90	0.27	0.00	348.04	393.68	0.0540	0.0012	-	0.0001	0.0032	0.0036
au24d13	0.03	0.01	2.61	-	-	-	-	-	165.3	-	17.6	-	0.02	0.78	-	0.00	-	21.02	0.0022	-	0.0024	0.0003	-	-
au24d14	0.02	0.01	2.51	-	-	-	-	-	95.3	-	2.5	-	0.03	2.31	-	0.00	-	35.67	0.0042	-	0.0020	0.0002	-	-
au24d17	0.02	0.01	1.95	-	-	-	-	-	39.9	-	1.4	-	0.02	0.36	-	0.00	-	31.49	0.0052	-	0.0011	0.0001	-	-
ha22	0.08	-	-	1.39	0.07	0.03	0.12	-	-	4.08	83.8	0.04	-	6.37	0.05	0.00	11.26	10.19	0.0240	0.0016	-	0.0002	0.0180	0.0190
au25d12	0.00	0.01	0.38	-	-	-	-	-	25.1	-	17.9	-	0.03	0.73	-	0.00	-	18.81	0.0110	-	0.0025	0.0001	-	-

kb_27	0.01	130.18	-	0.28	0.12	0.14	2.71	-	-	0.86	30.6	0.07	-	7.85	1.40	0.00	29.78	32.93	0.0140	0.0014	-	0.0002	0.0054	0.0065
au25e17	0.01	0.01	0.43	-	-	-	-	-	31.8	-	35.1	-	0.01	2.84	-	0.00	-	11.53	0.0081	-	0.0006	0.0000	-	-
au25f14	0.01	0.01	0.45	-	-	-	-	-	47.9	-	6.4	-	0.01	1.01	-	0.00	-	22.35	0.0068	-	0.0007	0.0001	-	-
au25f16	0.00	0.01	0.45	-	-	-	-	-	17.0	-	28.1	-	0.02	1.89	-	0.00	-	15.52	0.0110	-	0.0012	0.0000	-	-
au25f17	0.01	0.04	0.40	-	-	-	-	-	30.0	-	47.5	-	0.02	2.56	-	0.00	-	13.31	0.0230	-	0.0005	0.0000	-	-
mb_48	0.03	-	-	0.08	0.13	0.06	0.01	-	-	0.75	7.0	0.00	-	1.01	0.13	0.00	19.25	18.71	-	0.0025	-	0.0003	0.0063	0.0100
mb_50	0.01	-	-	0.04	0.10	0.04	0.16	-	-	2.12	37.2	0.00	-	2.33	0.01	0.00	13.69	13.47	-	0.0019	-	0.0002	0.0044	0.0069
mb_52	0.01	-	-	0.05	0.13	0.04	0.48	-	-	3.69	71.7	0.01	-	10.95	0.01	0.00	5.61	5.56	-	0.0028	-	0.0003	0.0054	0.0080
au25g12	0.00	0.01	0.35	-	-	-	-	-	31.3	-	4.4	-	0.02	0.90	-	0.01	-	10.07	0.0360	-	0.0006	0.0000	-	-
mb_35	0.01	-	-	0.06	0.11	0.06	0.66	-	-	0.61	2.2	0.00	-	1.69	0.01	0.00	11.65	13.84	-	0.0021	-	0.0002	0.0056	0.0069
au25d17	0.23	0.03	0.53	-	-	-	-	-	10.1	-	123.0	-	0.04	1.63	-	0.03	-	0.59	0.0038	-	0.0021	0.0004	-	-
mb_26	0.67	-	-	0.45	0.14	0.11	0.40	-	-	1.90	17.3	0.01	-	1.61	0.16	0.02	4.33	4.99	-	0.0021	-	0.0004	0.0071	0.0088
ha26	3.21	-	-	1.53	1.43	1.52	0.88	-	-	12.03	148.9	0.11	-	6.50	1.40	0.03	7.91	7.09	0.0550	0.0027	-	0.0006	0.0190	0.0180
ha27	2.18	-	-	2.31	0.79	0.84	0.74	-	-	8.29	102.1	0.10	-	6.85	0.37	0.07	6.24	5.43	0.0130	0.0035	-	0.0008	0.0170	0.0180
au24c13	0.08	0.00	0.89	-	-	-	-	-	12.7	-	7.1	-	0.01	0.50	-	0.00	-	2.59	0.0009	-	0.0005	0.0001	-	-
au24c15	0.29	0.01	2.08	-	-	-	-	-	28.3	-	5.3	-	0.01	1.09	-	0.00	-	3.84	0.0011	-	0.0020	0.0002	-	-
au24d03	38.00	0.42	86.90	-	-	-	-	-	209.0	-	3749.8	-	0.99	87.89	-	0.18	-	6.42	0.0680	-	0.0660	0.0120	-	-
au24d05	7.61	0.21	43.30	-	-	-	-	-	105.4	-	980.2	-	0.44	28.01	-	0.06	-	6.76	0.0260	-	0.0340	0.0060	-	-
au24d06	1.03	0.08	8.97	-	-	-	-	-	61.3	-	129.4	-	0.08	5.83	-	0.02	-	5.70	0.0058	-	0.0099	0.0009	-	-
au25d14	0.16	0.00	0.26	-	-	-	-	-	10.8	-	20.6	-	0.01	0.46	-	0.00	-	0.51	0.0023	-	0.0006	0.0001	-	-
au25e08	0.22	0.02	0.54	-	-	-	-	-	8.7	-	176.5	-	0.04	15.50	-	0.00	-	0.21	0.0018	-	0.0017	0.0002	-	-
au25e09	0.12	0.02	0.60	-	-	-	-	-	11.1	-	152.2	-	0.04	1.41	-	0.00	-	0.25	0.0034	-	0.0012	0.0001	-	-
au25e10	0.05	0.00	0.08	-	-	-	-	-	0.5	-	25.8	-	0.01	0.25	-	0.00	-	0.04	0.0002	-	0.0004	0.0000	-	-
au25e11	0.17	0.02	0.35	-	-	-	-	-	1.7	-	141.9	-	0.02	1.15	-	0.01	-	0.20	0.0007	-	0.0010	0.0001	-	-
au25e12	0.27	0.05	0.83	-	-	-	-	-	6.2	-	324.1	-	0.05	2.55	-	0.01	-	0.29	0.0022	-	0.0045	0.0002	-	-
au25e13	0.09	0.01	0.19	-	-	-	-	-	2.1	-	56.3	-	0.01	12.88	-	0.01	-	0.06	0.0006	-	0.0010	0.0001	-	-
ha31	3.50	-	-	0.65	1.21	1.20	0.97	-	-	9.44	137.0	0.03	-	5.21	1.74	0.01	5.30	4.58	0.0029	0.0028	-	0.0005	0.0300	0.0260
mb_29	0.15	-	-	0.30	0.30	0.29	0.16	-	-	1.40	16.4	0.01	-	1.66	0.43	0.02	0.56	0.62	-	0.0016	-	0.0002	0.0052	0.0060
mb_30	0.19	-	-	0.21	0.93	0.93	0.71	-	-	2.16	33.8	0.02	-	22.74	0.25	0.01	0.42	0.45	-	0.0013	-	0.0005	0.0044	0.0047
ha13	0.11	-	-	0.13	0.24	0.25	0.26	-	-	1.49	14.7	0.00	-	1.50	0.06	0.00	0.03	0.03	0.0045	0.0006	-	0.0001	0.0170	0.0140
mb_38	1.52	-	-	0.47	2.78	2.81	0.62	-	-	4.29	50.0	0.03	-	0.73	2.26	0.02	0.82	0.93	-	0.0051	-	0.0003	0.0130	0.0150
mb_39	0.29	-	-	0.06	0.44	0.46	0.24	-	-	1.26	23.3	0.01	-	0.67	0.64	0.01	0.38	0.42	-	0.0011	-	0.0001	0.0035	0.0035
ha7	0.26	-	-	1.40	0.89	0.96	0.73	-	-	2.79	14.4	0.00	-	6.05	0.22	0.01	0.37	0.34	0.0150	0.0022	-	0.0003	0.0380	0.0350
mb_14	0.63	-	-	0.17	0.61	0.60	2.01	-	-	15.62	864.1	0.01	-	6.03	1.31	0.02	0.66	0.70	-	0.0056	-	0.0007	0.0180	0.0220
mb_15	0.06	-	-	0.12	0.42	0.45	0.25	-	-	1.76	48.0	0.01	-	1.51	3.22	0.00	0.12	0.13	-	0.0011	-	0.0002	0.0037	0.0042
mb_17	0.20	-	-	0.94	2.67	2.73	0.93	-	-	8.66	131.9	0.04	-	3.62	20.19	0.00	0.70	0.75	-	0.0053	-	0.0005	0.0180	0.0190
au25g13	0.67	0.01	1.42	-	-	-	-	-	14.9	-	36.0	-	0.05	2.48	-	0.01	-	0.44	0.0088	-	0.0051	0.0001	-	-
mb_18	0.24	-	-	0.82	0.17	0.16	0.15	-	-	2.66	13.3	0.00	-	7.18	0.05	0.04	1.89	2.00	-	0.0021	-	0.0004	0.0067	0.0091
au25e06	0.23	0.03	0.88	-	-	-	-	-	22.4	-	36.5	-	0.03	1.01	-	0.01	-	1.26	0.0026	-	0.0035	0.0001	-	-
au25d11	0.06	0.04	0.58	-	-	-	-	-	30.6	-	91.3	-	0.94	2.46	-	0.00	-	0.66	0.0160	-	0.0140	0.0004	-	-
au25f03	0.03	0.00	0.27	-	-	-	-	-	5.9	-	24.6	-	0.02	7.89	-	0.00	-	0.13	0.0009	-	0.0001	0.0001	-	-
au25f04	0.14	0.00	0.83	-	-	-	-	-	12.4	-	109.5	-	0.03	17.56	-	0.00	-	0.24	0.0006	-	0.0007	0.0002	-	-
au25f08	0.01	0.01	0.04	-	-	-	-	-	0.6	-	4.7	-	0.00	1.94	-	0.00	-	0.02	0.0001	-	0.0001	0.0000	-	-
au25f09	0.11	0.01	0.72	-	-	-	-	-	13.2	-	51.5	-	0.02	15.58	-	0.00	-	0.25	0.0010	-	0.0007	0.0002	-	-
au25f10	0.03	0.00	0.30	-	-	-	-	-	5.3	-	7.8	-	0.01	15.83	-	0.00	-	0.21	0.0006	-	0.0006	0.0001	-	-
au25f12	0.35	0.01	1.04	-	-	-	-	-	7.8	-	99.1	-	0.03	22.32	-	0.00	-	0.15	0.0005	-	0.0012	0.0002	-	-
au25g08	0.49	0.01	1.49	-	-	-	-	-	12.9	-	13.9	-	0.02	0.48	-	0.00	-	0.51	0.0660	-	0.0035	0.0001	-	-
au25g09	0.70	0.01	2.32	-	-	-	-	-	19.5	-	20.3	-	0.03	0.53	-	0.01	-	0.70	0.0880	-	0.0076	0.0001	-	-
mb_24	0.11	-	-	0.15	0.16	0.13	0.18	-	-	3.94	41.3	0.00	-	2.74	0.13	0.00	0.43	0.47	-	0.0020	-	0.0002	0.0082	0.0091
ha9	0.74	-	-	0.41	0.35	0.39	0.38	-	-	2.20	22.6	0.00	-	2.88	0.03	0.02	0.13	0.12	0.0047	0.0009	-	0.0001	0.0330	0.0280
ha15	0.84	-	-	0.41	4.05	4.18	0.53	-	-	1.34	11.6	0.01	-	1.46	0.06	0.04	0.09	0.08	0.0120	0.0020	-	0.0001	0.0630	0.0520
ha18	0.46	-	-	0.29	0.49	0.51	0.35	-	-	2.23	36.2	0.02	-	2.16	0.66	0.00	0.18	0.16	0.0011	0.0013	-	0.0002	0.0180	0.0140
kb_16	0.49	297.10	-	0.58	0.13	0.14	0.99	-	-	5.49	186.3	0.01	-	162.17	0.04	0.00	0.26	0.27	0.0008	0.0010	-	0.0006	0.0062	0.0073

kb_18	0.09	279.04	-	0.24	0.15	0.21	0.31	-	-	1.83	46.4	0.06	-	58.34	0.43	0.00	0.17	0.19	0.0009	0.0006	-	0.0002	0.0037	0.0041
kb_19	0.13	2860.65	-	0.20	0.58	0.80	0.23	-	-	2.32	50.6	0.16	-	104.27	0.90	0.00	0.24	0.26	0.0021	0.0009	-	0.0002	0.0067	0.0079
kb_20	0.11	1103.40	-	0.16	0.08	0.09	0.09	-	-	1.96	45.9	0.01	-	83.52	0.19	0.00	0.19	0.20	0.0019	0.0007	-	0.0001	0.0041	0.0056
kb_26	0.20	7348.02	-	0.17	1.75	2.50	1.36	-	-	3.14	90.7	0.96	-	14.68	16.28	0.01	1.03	1.16	0.0140	0.0081	-	0.0004	0.0054	0.0056
au24c16	0.05	0.00	1.27	-	-	-	-	-	31.4	-	10.6	-	0.01	0.19	-	0.00	-	0.63	0.0003	-	0.0007	0.0001	-	-
ha19	0.31	-	-	0.45	0.51	0.51	0.23	-	-	2.63	40.0	0.03	-	1.97	0.36	0.00	0.13	0.12	0.0012	0.0010	-	0.0002	0.1100	0.0940
ha20	0.00	-	-	0.00	0.00	0.00	0.00	-	-	0.01	0.2	0.00	-	0.01	0.01	0.00	0.06	0.05	0.0000	0.0000	-	0.0000	0.0001	0.0001
ha21	0.01	-	-	0.02	0.04	0.04	0.03	-	-	0.08	1.5	0.00	-	0.07	0.04	0.00	0.08	0.07	0.0001	0.0001	-	0.0000	0.0026	0.0022
au25g15	1.48	0.02	2.70	-	-	-	-	-	23.9	-	67.0	-	0.11	0.89	-	0.04	-	0.90	0.0160	-	0.0072	0.0002	-	-
au25g16	0.33	0.03	0.94	-	-	-	-	-	13.5	-	20.5	-	0.03	2.04	-	0.01	-	0.64	0.0048	-	0.0034	0.0001	-	-
au25g17	0.58	0.01	1.28	-	-	-	-	-	15.8	-	53.4	-	0.14	2.02	-	0.01	-	0.38	0.0140	-	0.0053	0.0001	-	-
mb_57	0.22	-	-	0.06	0.51	0.51	0.19	-	-	1.05	14.4	0.01	-	0.65	0.25	0.00	0.23	0.23	-	0.0018	-	0.0001	0.0029	0.0040
mb_41	0.80	-	-	0.21	3.93	3.98	0.95	-	-	3.73	54.0	0.04	-	1.74	1.35	0.02	0.59	0.67	-	0.0054	-	0.0003	0.0120	0.0120
au25e03	0.17	0.07	0.84	-	-	-	-	-	120.5	-	20.3	-	0.04	1.68	-	0.02	-	2.30	0.0037	-	0.0017	0.0001	-	-
au25e05	0.12	0.05	0.75	-	-	-	-	-	96.2	-	19.1	-	0.05	1.22	-	0.00	-	1.24	0.0013	-	0.0011	0.0001	-	-
au25g03	0.01	0.03	0.19	-	-	-	-	-	24.6	-	53.6	-	0.01	3.76	-	0.00	-	6.03	0.0016	-	0.0001	0.0000	-	-
mb_51	0.01	-	-	0.02	0.03	0.01	0.01	-	-	0.97	17.1	0.00	-	1.24	0.00	0.00	5.03	4.89	-	0.0007	-	0.0001	0.0017	0.0025
mb_25	0.02	-	-	0.03	0.11	0.12	0.05	-	-	0.60	4.1	0.00	-	0.24	0.12	0.00	0.31	0.34	-	0.0004	-	0.0001	0.0016	0.0019
mb_33	0.06	-	-	0.03	0.08	0.05	0.08	-	-	1.92	18.8	0.03	-	1.01	0.19	0.00	0.90	0.98	-	0.0014	-	0.0002	0.0050	0.0064
au24c14	0.17	0.04	8.37	-	-	-	-	-	346.5	-	68.9	-	0.12	8.02	-	0.01	-	0.43	0.0050	-	0.0140	0.0016	-	-
kb_11	0.09	2405.92	-	0.07	0.27	0.23	0.20	-	-	5.36	39.2	0.01	-	30.35	0.46	0.00	0.52	0.55	0.0022	0.0027	-	0.0003	0.0150	0.0210
au24d04	0.08	0.02	1.47	-	-	-	-	-	20.0	-	16.0	-	0.03	2.69	-	0.00	-	6.26	0.0011	-	0.0033	0.0003	-	-
au24d07	0.09	0.01	0.98	-	-	-	-	-	9.6	-	16.7	-	0.01	2.00	-	0.00	-	4.02	0.0005	-	0.0004	0.0001	-	-
ha30	0.38	-	-	0.04	0.08	0.08	0.08	-	-	2.05	14.4	0.00	-	1.50	0.13	0.00	2.80	2.47	0.0005	0.0007	-	0.0001	0.0060	0.0055
ha16	0.03	-	-	0.24	0.22	0.24	1.90	-	-	2.70	53.4	0.40	-	1.94	9.21	0.01	0.76	0.67	0.0110	0.0029	-	0.0004	0.1200	0.1000
ha17	0.08	-	-	0.25	0.19	0.17	0.07	-	-	2.75	37.2	0.02	-	1.92	0.15	0.00	0.06	0.03	0.0300	0.0026	-	0.0001	0.0190	0.0200
ha23	0.20	-	-	0.10	0.09	0.09	0.08	-	-	3.03	18.7	0.02	-	1.88	0.21	0.00	0.10	0.09	0.0025	0.0009	-	0.0002	0.0270	0.0220
ha24	0.02	-	-	0.11	0.08	0.08	0.07	-	-	2.31	29.8	0.01	-	1.82	0.05	0.00	0.03	0.02	0.0110	0.0014	-	0.0002	0.0360	0.0300
ha25	0.14	-	-	0.12	0.10	0.10	0.10	-	-	2.92	18.4	0.02	-	2.78	0.30	0.00	0.08	0.07	0.0030	0.0007	-	0.0001	0.0210	0.0180
au25d04	0.03	0.08	0.85	-	-	-	-	-	74.2	-	157.2	-	1.05	4.06	-	0.01	-	2.56	0.0460	-	0.0098	0.0003	-	-
kb_23	0.03	2284.35	-	0.57	1.35	1.95	1.77	-	-	5.78	155.4	2.09	-	23.98	52.36	0.00	3.36	3.71	0.0480	0.0058	-	0.0005	0.0073	0.0098
au25f05	0.08	0.14	0.81	-	-	-	-	-	16.7	-	49.1	-	0.33	25.85	-	0.00	-	0.41	0.0010	-	0.0018	0.0002	-	-
au25f11	0.07	0.00	0.42	-	-	-	-	-	10.0	-	22.8	-	0.03	9.39	-	0.00	-	0.14	0.0008	-	0.0003	0.0001	-	-
kb_17	0.16	422.84	-	0.13	1.56	2.26	0.76	-	-	5.82	107.2	2.37	-	200.93	852.50	0.00	0.43	0.48	0.0015	0.0011	-	0.0002	0.0059	0.0061
au24d16	0.05	0.01	2.00	-	-	-	-	-	15.0	-	25.6	-	0.02	6.64	-	0.00	-	0.13	0.0018	-	0.0003	0.0001	-	-
au25e16	0.04	0.01	0.58	-	-	-	-	-	41.6	-	54.3	-	0.02	6.44	-	0.00	-	0.86	0.0020	-	0.0004	0.0000	-	-
mb_13	0.79	-	-	1.50	0.73	0.50	0.67	-	-	16.46	239.7	0.10	-	12.74	21.48	0.03	2.99	3.08	-	0.0100	-	0.0014	0.0470	0.0510
mb_20	0.00	-	-	0.00	0.00	0.00	0.01	-	-	0.15	2.2	0.00	-	0.11	0.01	0.00	0.05	0.05	-	0.0001	-	0.0000	0.0002	0.0003
ha6	0.29	-	-	0.21	0.38	0.40	0.32	-	-	4.21	33.4	0.02	-	3.80	0.24	0.13	0.36	0.32	0.0660	0.0034	-	0.0003	0.2800	0.2400
ha10	0.03	-	-	0.03	0.05	0.04	0.05	-	-	1.90	10.6	0.00	-	0.96	0.05	0.00	0.17	0.15	0.0230	0.0009	-	0.0001	0.0200	0.0190
ha11	0.04	-	-	0.07	0.06	0.05	0.18	-	-	2.46	10.1	0.00	-	0.90	0.08	0.00	0.34	0.31	0.0280	0.0012	-	0.0001	0.0140	0.0140
au25g14	0.46	0.01	1.26	-	-	-	-	-	11.4	-	26.9	-	0.03	1.12	-	0.01	-	0.41	0.0052	-	0.0041	0.0001	-	-
mb_36	0.22	-	-	0.11	0.59	0.60	0.36	-	-	3.00	39.5	0.01	-	2.30	0.22	0.01	0.20	0.22	-	0.0022	-	0.0003	0.0093	0.0098
mb_40	0.85	-	-	0.40	3.53	3.64	0.50	-	-	3.14	29.1	0.01	-	1.24	1.08	0.01	0.57	0.65	-	0.0054	-	0.0004	0.0110	0.0120
au25g04	0.03	0.01	0.15	-	-	-	-	-	19.2	-	19.9	-	0.01	3.06	-	0.00	-	1.76	0.0013	-	0.0001	0.0000	-	-
au25g07	0.05	0.01	0.40	-	-	-	-	-	26.5	-	20.7	-	0.01	3.37	-	0.00	-	0.08	0.0002	-	0.0001	0.0000	-	-
mb_54	0.02	-	-	0.01	0.02	0.01	0.02	-	-	1.73	16.8	0.00	-	4.25	0.00	0.00	0.04	0.04	-	0.0005	-	0.0001	0.0015	0.0019
au25e15	0.12	0.02	1.17	-	-	-	-	-	75.2	-	31.0	-	0.03	1.87	-	0.00	-	0.69	0.0020	-	0.0011	0.0000	-	-
mb_19	0.09	-	-	0.34	0.20	0.20	0.22	-	-	4.28	88.5	0.01	-	2.64	0.88	0.00	0.45	0.49	-	0.0025	-	0.0004	0.0089	0.0110
au25g11	0.02	0.00	0.28	-	-	-	-	-	17.4	-	9.2	-	0.02	0.87	-	0.00	-	0.05	0.0170	-	0.0004	0.0000	-	-
mb_37	0.03	-	-	0.01	0.15	0.07	0.11	-	-	2.16	9.2	0.01	-	1.18	0.10	0.00	0.27	0.29	-	0.0029	-	0.0003	0.0130	0.0150
mb_22	0.06	-	-	0.03	0.11	0.04	0.01	-	-	6.49	87.2	0.00	-	44.72	0.07	0.00	2.38	2.57	-	0.0021	-	0.0003	0.0075	0.0096
ha12	0.03	-	-	0.04	0.07	0.07	0.67	-	-	3.85	35.3	0.00	-	5.48	0.01	0.00	0.13	0.11	0.0068	0.0014	-	0.0001	0.0200	0.0210

Table S10 (continued) 1σ error

Analysis #	Sb121 µg/g	Sb123 µg/g	Cs133 µg/g	Ba137 µg/g	La139 µg/g	Ce140 µg/g	Pr141 µg/g	Nd146 µg/g	Sm147 µg/g	Eu151 µg/g	Gd157 µg/g	Tb159 µg/g	Dy163 µg/g	Ho165 µg/g	Er167 µg/g	Tm169 µg/g	Yb173 µg/g	Lu175 µg/g	Hf177 µg/g	Ta181 µg/g	Pb208 µg/g	Th232 µg/g	U238 µg/g
au24e03	-	-	-	0.0810	0.0001	0.0001	0.0001	0.0003	0.0002	0.0001	0.0005	0.0000	0.0005	0.0002	0.0006	0.0002	0.0013	0.0003	0.0000	-	0.0180	0.0001	0.0001
au24e04	-	-	-	0.0650	0.0001	0.0001	0.0001	0.0004	0.0001	0.0001	0.0007	0.0001	0.0006	0.0002	0.0006	0.0002	0.0012	0.0003	0.0001	-	0.0150	0.0001	0.0001
au24e05	-	-	-	0.1000	0.0001	0.0001	0.0001	0.0002	0.0004	0.0002	0.0008	0.0001	0.0007	0.0002	0.0008	0.0003	0.0018	0.0005	0.0003	-	0.0260	0.0000	0.0001
au24e09	-	-	-	0.1000	0.0001	0.0001	0.0001	0.0003	0.0003	0.0002	0.0004	0.0001	0.0006	0.0002	0.0008	0.0002	0.0018	0.0005	0.0003	-	0.0240	0.0000	0.0000
au24e11	-	-	-	0.0980	0.0001	0.0001	0.0001	0.0003	0.0002	0.0002	0.0004	0.0001	0.0006	0.0002	0.0010	0.0002	0.0018	0.0005	0.0003	-	0.0260	0.0000	0.0001
mb_1	0.0037	0.0042	0.0030	0.0490	0.0001	0.0002	0.0001	0.0004	0.0004	0.0001	0.0008	0.0001	0.0005	0.0002	0.0010	0.0001	0.0012	0.0003	0.0003	0.0002	0.0073	0.0002	0.0000
mb_6	0.0042	0.0051	0.0031	0.0670	0.0002	0.0001	0.0000	0.0005	0.0002	0.0002	0.0009	0.0001	0.0006	0.0002	0.0009	0.0002	0.0021	0.0004	0.0004	0.0002	0.0120	0.0001	0.0001
mb_7	0.0038	0.0037	0.0042	0.0670	0.0002	0.0002	0.0001	0.0004	0.0003	0.0000	0.0008	0.0001	0.0008	0.0002	0.0008	0.0003	0.0016	0.0003	0.0005	0.0002	0.0140	0.0001	0.0001
au24e14	-	-	-	0.1200	0.0003	0.0006	0.0001	0.0006	0.0004	0.0001	0.0005	0.0001	0.0006	0.0002	0.0006	0.0001	0.0014	0.0004	0.0004	-	0.0270	0.0001	0.0002
au24e17	-	-	-	0.1200	0.0005	0.0013	0.0002	0.0010	0.0006	0.0002	0.0007	0.0000	0.0007	0.0001	0.0007	0.0002	0.0012	0.0003	0.0005	-	0.0190	0.0002	0.0003
au24f03	-	-	-	0.0860	0.0001	0.0001	0.0000	0.0002	0.0004	0.0002	0.0008	0.0001	0.0007	0.0003	0.0009	0.0003	0.0018	0.0005	0.0001	-	0.0120	0.0000	0.0001
au24f05	-	-	-	0.0730	0.0003	0.0005	0.0002	0.0006	0.0004	0.0001	0.0007	0.0001	0.0006	0.0002	0.0007	0.0002	0.0013	0.0003	0.0004	-	0.0150	0.0002	0.0001
au24f08	-	-	-	0.0530	0.0001	0.0001	0.0001	0.0003	0.0002	0.0001	0.0006	0.0001	0.0008	0.0003	0.0010	0.0003	0.0024	0.0005	0.0002	-	0.0280	0.0000	0.0000
au24f10	-	-	-	0.0660	0.0003	0.0004	0.0001	0.0008	0.0004	0.0001	0.0005	0.0001	0.0007	0.0003	0.0012	0.0003	0.0025	0.0005	0.0002	-	0.0280	0.0001	0.0001
au24f11	-	-	-	0.0770	0.0001	0.0001	0.0001	0.0003	0.0001	0.0001	0.0006	0.0002	0.0020	0.0006	0.0025	0.0007	0.0052	0.0012	0.0002	-	0.0840	0.0000	0.0000
au24f14	-	-	-	0.0840	0.0001	0.0002	0.0001	0.0001	0.0003	0.0001	0.0007	0.0001	0.0014	0.0004	0.0020	0.0005	0.0037	0.0008	0.0002	-	0.0650	0.0000	0.0001
kb_3	0.0092	0.0086	0.0160	0.1800	0.0000	0.0021	0.0001	0.0001	0.0008	0.0002	0.0009	0.0002	0.0015	0.0004	0.0017	0.0005	0.0043	0.0008	0.0001	0.0001	0.0470	0.0001	0.0001
kb_8	0.0068	0.0075	0.0069	0.1400	0.0001	0.0002	0.0000	0.0005	0.0002	0.0001	0.0005	0.0001	0.0010	0.0003	0.0015	0.0004	0.0032	0.0006	0.0002	0.0001	0.0260	0.0000	0.0001
kb_10	0.0062	0.0081	0.0070	0.1100	0.0001	0.0001	0.0000	0.0005	0.0005	0.0001	0.0010	0.0001	0.0010	0.0003	0.0011	0.0004	0.0022	0.0005	0.0003	0.0001	0.0250	0.0001	0.0001
au24f17	-	-	-	0.2200	0.0003	0.0003	0.0001	0.0004	0.0004	0.0001	0.0004	0.0001	0.0006	0.0002	0.0009	0.0003	0.0017	0.0004	0.0003	-	0.0670	0.0001	0.0002
au24g04	-	-	-	0.0890	0.0001	0.0001	0.0000	0.0001	0.0002	0.0001	0.0003	0.0001	0.0005	0.0001	0.0007	0.0002	0.0015	0.0003	0.0001	-	0.0460	0.0001	0.0001
au24g08	-	-	-	0.1600	0.0001	0.0001	0.0000	0.0002	0.0003	0.0001	0.0002	0.0001	0.0007	0.0002	0.0008	0.0003	0.0017	0.0005	0.0001	-	0.1100	0.0000	0.0002
au24g15	-	-	-	0.1200	0.0001	0.0001	0.0000	0.0003	0.0002	0.0001	0.0005	0.0001	0.0006	0.0002	0.0008	0.0003	0.0020	0.0005	0.0002	-	0.0870	0.0001	0.0002
au24g16	-	-	-	0.3300	0.0002	0.0001	0.0001	0.0003	0.0003	0.0001	0.0004	0.0001	0.0009	0.0003	0.0010	0.0003	0.0026	0.0007	0.0002	-	0.1300	0.0001	0.0003
ha29	0.0130	0.0110	0.0370	0.6500	0.0005	0.0008	0.0002	0.0005	0.0003	0.0001	0.0008	0.0001	0.0008	0.0003	0.0010	0.0003	0.0028	0.0005	0.0003	0.0004	0.2100	0.0001	0.0002
au24e06	-	-	-	0.1100	0.0001	0.0001	0.0001	0.0006	0.0002	0.0002	0.0005	0.0001	0.0007	0.0002	0.0009	0.0003	0.0021	0.0005	0.0002	-	0.0290	0.0000	0.0001
mb_3	0.0061	0.0065	0.0048	0.1100	0.0002	0.0002	0.0001	0.0004	0.0001	0.0001	0.0009	0.0001	0.0009	0.0002	0.0011	0.0003	0.0027	0.0005	0.0003	0.0001	0.0190	0.0001	0.0001
mb_4	0.0069	0.0071	0.0050	0.0790	0.0002	0.0003	0.0001	0.0008	0.0005	0.0003	0.0011	0.0001	0.0012	0.0003	0.0018	0.0004	0.0032	0.0006	0.0005	0.0001	0.0210	0.0000	0.0001
au24f07	-	-	-	0.0760	0.0001	0.0002	0.0001	0.0005	0.0001	0.0001	0.0006	0.0002	0.0017	0.0005	0.0022	0.0006	0.0045	0.0010	0.0002	-	0.0690	0.0000	0.0000
au24f12	-	-	-	0.0460	0.0001	0.0001	0.0001	0.0001	0.0002	0.0001	0.0005	0.0001	0.0010	0.0003	0.0012	0.0003	0.0028	0.0006	0.0002	-	0.0330	0.0001	0.0001
au24f13	-	-	-	0.0960	0.0000	0.0001	0.0000	0.0003	0.0003	0.0001	0.0008	0.0001	0.0015	0.0005	0.0020	0.0006	0.0041	0.0008	0.0002	-	0.0650	0.0000	0.0000
kb_1	0.0200	0.0230	0.0420	0.2000	0.0002	0.0001	0.0001	0.0002	0.0008	0.0002	0.0011	0.0002	0.0023	0.0008	0.0040	0.0009	0.0078	0.0014	0.0005	0.0001	0.0800	0.0001	0.0001
kb_2	0.0170	0.0170	0.0310	0.2900	0.0002	0.0002	0.0000	0.0004	0.0001	0.0002	0.0007	0.0002	0.0021	0.0008	0.0036	0.0008	0.0068	0.0012	0.0001	0.0001	0.0880	0.0001	0.0001
kb_5	0.0200	0.0220	0.0210	0.2300	0.0001	0.0002	0.0001	0.0005	0.0001	0.0001	0.0009	0.0002	0.0026	0.0009	0.0037	0.0009	0.0077	0.0014	0.0005	0.0001	0.0870	0.0001	0.0001
au24g05	-	-	-	0.0880	0.0001	0.0001	0.0000	0.0001	0.0001	0.0001	0.0004	0.0001	0.0006	0.0003	0.0009	0.0003	0.0020	0.0005	0.0001	-	0.1300	0.0000	0.0002
au24g07	-	-	-	0.2300	0.0001	0.0001	0.0000	0.0002	0.0002	0.0001	0.0005	0.0001	0.0008	0.0002	0.0011	0.0003	0.0022	0.0005	0.0001	-	0.1500	0.0000	0.0002
au24e07	-	-	-	0.1100	0.0001	0.0001	0.0000	0.0005	0.0005	0.0002	0.0008	0.0002	0.0011	0.0004	0.0015	0.0004	0.0030	0.0007	0.0002	-	0.0380	0.0001	0.0001
au24e10	-	-	-	0.0400	0.0001	0.0001	0.0001	0.0004	0.0003	0.0001	0.0004	0.0001	0.0003	0.0001	0.0003	0.0001	0.0008	0.0002	0.0002	-	0.0073	0.0000	0.0000
mb_2	0.0038	0.0044	0.0043	0.0560	0.0003	0.0001	0.0001	0.0008	0.0003	0.0001	0.0005	0.0001	0.0004	0.0001	0.0005	0.0002	0.0013	0.0003	0.0003	0.0003	0.0056	0.0000	0.0001
mb_8	0.0039	0.0036	0.0058	0.0410	0.0001	0.0003	0.0000	0.0002	0.0006	0.0001	0.0009	0.0001	0.0004	0.0001	0.0008	0.0001	0.0016	0.0003	0.0004	0.0001	0.0054	0.0001	0.0001
au24e12	-	-	-	0.0760	0.0001	0.0001	0.0000	0.0003	0.0003	0.0001	0.0003	0.0000	0.0003	0.0001	0.0004	0.0001	0.0008	0.0002	0.0002	-	0.0063	0.0000	0.0000
au24e15	-	-	-	0.0730	0.0001	0.0002	0.0001	0.0007	0.0002	0.0001	0.0006	0.0001	0.0004	0.0001	0.0003	0.0001	0.0009	0.0001	0.0002	-	0.0070	0.0001	0.0001
au24e16	-	-	-	0.0900	0.0012	0.0029	0.0005	0.0020	0.0007	0.0003	0.0011	0.0002	0.0008	0.0002	0.0006	0.0001	0.0012	0.0002	0.0011	-	0.0140	0.0005	0.0007
au24f04	-	-	-	0.0730	0.0002	0.0002	0.0003	0.0017	0.0004	0.0007	0.0014	0.0003	0.0014	0.0002	0.0012	0.0003	0.0016	0.0008	0.0008	-	0.0120	0.0000	0.0001
kb_4	0.0120	0.0120	0.0260	0.0540	0.0001	0.0001	0.0001	0.0006	0.0006	0.0002	0.0005	0.0001	0.0007	0.0003	0.0014	0.0003	0.0030	0.0005	0.0001	0.0001	0.0150	0.0001	0.0001
kb_9	0.0110	0.0120	0.0220	0.0910	0.0002	0.0002	0.0001	0.0001	0.0005	0.0001	0.0005	0.0001	0.0008	0.0002	0.0013	0.0003	0.0017	0.0004	0.0001	0.0001	0.0120	0.0000	0.0001
au24f16	-	-	-	0.0630	0.0001	0.0001	0.0000	0.0004	0.0003	0.0000	0.0002	0.0001	0.0003	0.0001	0.0005	0.0001	0.0010	0.0002	0.0003	-	0.0160	0.0001	0.0002
au24g03	-	-	-	0.0210	0.0001	0.0000	0.0001	0.0003	0.0002	0.0001	0.0005	0.0001	0.0001	0.0001	0.0004	0.0001	0.0007	0.0002	0.0001	-	0.0230	0.0001	0.0002

au24g06	-	-	-	0.0270	0.0001	0.0001	0.0000	0.0002	0.0002	0.0000	0.0004	0.0000	0.0003	0.0001	0.0003	0.0001	0.0008	0.0002	0.0001	-	0.0240	0.0000	0.0001
au24g14	-	-	-	0.0240	0.0000	0.0001	0.0000	0.0005	0.0003	0.0001	0.0003	0.0000	0.0004	0.0001	0.0004	0.0001	0.0009	0.0002	0.0002	-	0.0260	0.0001	0.0001
au24g17	-	-	-	0.0660	0.0000	0.0000	0.0000	0.0001	0.0001	0.0000	0.0002	0.0000	0.0001	0.0001	0.0003	0.0001	0.0005	0.0001	0.0001	-	0.0140	0.0000	0.0001
ha28	0.0024	0.0023	0.0360	0.6800	0.0008	0.0007	0.0002	0.0007	0.0005	0.0002	0.0009	0.0001	0.0006	0.0001	0.0004	0.0001	0.0007	0.0002	0.0007	0.0004	0.0240	0.0001	0.0003
ha1	0.3500	0.2600	2.5000	3.3700	0.0067	0.0090	0.0024	0.0150	0.0069	0.0017	0.0075	0.0009	0.0045	0.0014	0.0046	0.0008	0.0060	0.0011	0.0190	0.0018	0.1500	0.0001	0.0029
ha2	1.2300	0.9700	4.0500	2.1700	0.0091	0.0140	0.0045	0.0290	0.0130	0.0034	0.0130	0.0014	0.0084	0.0023	0.0091	0.0018	0.0140	0.0025	0.0200	0.0010	0.3400	0.0001	0.0033
ha3	0.4500	0.3600	2.1000	3.3500	0.0031	0.0045	0.0013	0.0095	0.0042	0.0013	0.0033	0.0005	0.0035	0.0009	0.0037	0.0008	0.0052	0.0010	0.0130	0.0020	0.1600	0.0000	0.0022
ha4	0.4500	0.3700	2.6100	4.0500	0.0035	0.0044	0.0014	0.0086	0.0039	0.0011	0.0048	0.0005	0.0029	0.0008	0.0027	0.0005	0.0038	0.0005	0.0160	0.0023	0.1500	0.0003	0.0021
ha5	0.1200	0.0980	3.0700	3.7900	0.0029	0.0037	0.0014	0.0072	0.0036	0.0012	0.0031	0.0005	0.0027	0.0006	0.0026	0.0005	0.0033	0.0008	0.0150	0.0014	0.1100	0.0001	0.0024
au25c03	-	-	2.8300	2.3600	0.0009	0.0008	0.0004	0.0012	0.0017	0.0004	0.0013	0.0003	0.0021	0.0004	0.0012	0.0004	0.0025	0.0003	0.0140	-	0.1100	0.0003	0.0015
au25c04	-	-	2.3200	2.0700	0.0021	0.0042	0.0009	0.0040	0.0023	0.0007	0.0019	0.0003	0.0018	0.0005	0.0015	0.0004	0.0024	0.0004	0.0120	-	0.0780	0.0007	0.0019
au25c11	-	-	3.1400	2.3300	0.0008	0.0007	0.0003	0.0015	0.0001	0.0001	0.0024	0.0002	0.0013	0.0007	0.0011	0.0002	0.0016	0.0002	0.0120	-	0.0680	0.0001	0.0016
mb_43	0.5100	0.3600	3.2300	1.6900	0.0760	0.0950	0.0190	0.0780	0.0220	0.0055	0.0220	0.0037	0.0220	0.0053	0.0190	0.0033	0.0200	0.0029	0.0670	0.0670	0.3100	0.0330	0.0180
mb_44	1.2800	0.8400	5.7600	2.0700	0.0610	0.0770	0.0150	0.0660	0.0160	0.0060	0.0260	0.0046	0.0330	0.0084	0.0260	0.0045	0.0280	0.0042	0.0710	0.0097	0.3600	0.0240	0.0190
mb_45	0.5800	0.3800	1.7500	1.7000	0.0011	0.0007	0.0003	0.0019	0.0012	0.0005	0.0021	0.0003	0.0008	0.0002	0.0011	0.0002	0.0002	0.0002	0.0100	0.0017	0.0370	0.0001	0.0005
mb_46	0.1100	0.0760	2.0400	1.9100	0.0740	0.1000	0.0180	0.0720	0.0170	0.0042	0.0180	0.0029	0.0180	0.0042	0.0160	0.0021	0.0150	0.0023	0.0760	0.2700	0.2700	0.0460	0.0170
au24c09	-	-	-	3.5000	0.0008	0.0007	0.0005	0.0018	0.0021	0.0012	0.0041	0.0006	0.0026	0.0007	0.0007	0.0005	0.0035	0.0010	0.0016	-	0.0570	0.0005	0.0001
au24c12	-	-	-	2.7900	0.0004	0.0005	0.0004	0.0024	0.0019	0.0006	0.0031	0.0004	0.0023	0.0003	0.0012	0.0007	0.0019	0.0005	0.0009	-	0.0350	0.0001	0.0001
kb_15	0.0240	0.0430	0.0140	14.3200	0.0023	0.0013	0.0006	0.0033	0.0028	0.0003	0.0041	0.0008	0.0046	0.0015	0.0054	0.0022	0.0130	0.0025	0.0001	0.0001	0.0870	0.0001	0.0001
mb_56	1.3400	1.2800	0.1100	0.3000	0.0007	0.0010	0.0005	0.0040	0.0043	0.0014	0.0060	0.0010	0.0070	0.0016	0.0059	0.0011	0.0076	0.0013	0.0024	0.0003	1.0400	0.0001	0.0010
au24d08	-	-	-	0.1800	0.0000	0.0002	0.0001	0.0005	0.0001	0.0001	0.0009	0.0000	0.0006	0.0002	0.0005	0.0001	0.0006	0.0002	0.0001	-	0.1900	0.0001	0.0004
au24d09	-	-	-	0.5500	0.0002	0.0002	0.0001	0.0003	0.0001	0.0002	0.0007	0.0001	0.0013	0.0003	0.0009	0.0003	0.0033	0.0007	0.0001	-	0.1200	0.0001	0.0008
au24d11	-	-	-	0.3900	0.0003	0.0003	0.0002	0.0012	0.0004	0.0003	0.0016	0.0002	0.0010	0.0003	0.0012	0.0004	0.0022	0.0007	0.0008	-	0.1000	0.0000	0.0012
au24d12	-	-	-	0.3700	0.0002	0.0002	0.0001	0.0010	0.0009	0.0004	0.0017	0.0002	0.0012	0.0002	0.0006	0.0003	0.0018	0.0004	0.0005	-	0.0310	0.0001	0.0002
kb_28	0.0030	0.0043	0.0023	0.3600	0.0002	0.0002	0.0001	0.0003	0.0007	0.0001	0.0005	0.0001	0.0005	0.0002	0.0008	0.0002	0.0016	0.0003	0.0001	0.0000	0.0280	0.0001	0.0003
kb_30	0.0056	0.0042	0.0019	0.4600	0.0002	0.0002	0.0001	0.0006	0.0002	0.0005	0.0022	0.0001	0.0005	0.0002	0.0010	0.0002	0.0021	0.0004	0.0002	0.0001	0.0520	0.0001	0.0006
au25d03	-	-	-	0.0990	0.0002	0.0005	0.0002	0.0015	0.0011	0.0003	0.0018	0.0003	0.0015	0.0004	0.0012	0.0003	0.0014	0.0003	0.0002	-	1.2500	0.0001	0.0001
au25d07	-	-	-	0.0910	0.0003	0.0007	0.0003	0.0019	0.0010	0.0002	0.0014	0.0002	0.0014	0.0003	0.0009	0.0002	0.0012	0.0002	0.0004	-	0.5100	0.0001	0.0001
au25d08	-	-	-	0.2300	0.0022	0.0120	0.0026	0.0180	0.0098	0.0014	0.0140	0.0026	0.0170	0.0034	0.0092	0.0014	0.0097	0.0015	0.0002	-	3.1100	0.0003	0.0000
au25d10	-	-	-	0.1100	0.0003	0.0008	0.0003	0.0024	0.0013	0.0003	0.0022	0.0004	0.0020	0.0005	0.0014	0.0003	0.0019	0.0003	0.0014	-	0.7600	0.0000	0.0003
kb_22	0.4400	0.4400	0.0420	2.4200	0.0026	0.0087	0.0017	0.0120	0.0070	0.0013	0.0075	0.0014	0.0095	0.0022	0.0068	0.0011	0.0078	0.0012	0.0025	0.0006	6.3300	0.0006	0.0006
kb_25	0.0140	0.0130	0.0026	0.2000	0.0003	0.0006	0.0002	0.0015	0.0010	0.0001	0.0016	0.0002	0.0017	0.0004	0.0014	0.0003	0.0019	0.0003	0.0007	0.0001	1.2200	0.0003	0.0001
au25f13	-	-	-	0.1000	0.0029	0.0043	0.0007	0.0041	0.0017	0.0007	0.0027	0.0003	0.0019	0.0005	0.0012	0.0002	0.0016	0.0003	0.0001	-	0.5100	0.0001	0.0001
au25f15	-	-	-	0.0770	0.0027	0.0044	0.0007	0.0041	0.0016	0.0006	0.0025	0.0004	0.0018	0.0004	0.0013	0.0002	0.0012	0.0002	0.0001	-	0.4800	0.0001	0.0001
au25g05	-	-	-	0.1000	0.0028	0.0044	0.0007	0.0041	0.0019	0.0008	0.0028	0.0004	0.0023	0.0005	0.0012	0.0002	0.0011	0.0002	0.0001	-	0.4400	0.0001	0.0001
mb_53	0.0320	0.0310	0.0021	0.1200	0.0034	0.0060	0.0011	0.0069	0.0037	0.0013	0.0047	0.0006	0.0032	0.0008	0.0024	0.0004	0.0019	0.0004	0.0006	0.0002	0.3000	0.0000	0.0001
au25g06	-	-	-	0.1300	0.0022	0.0040	0.0007	0.0042	0.0019	0.0008	0.0031	0.0004	0.0023	0.0006	0.0015	0.0003	0.0018	0.0004	0.0001	-	0.7900	0.0001	0.0001
mb_49	0.1100	0.1100	0.0017	0.0820	0.0026	0.0035	0.0008	0.0045	0.0025	0.0010	0.0033	0.0005	0.0025	0.0005	0.0015	0.0002	0.0021	0.0003	0.0001	0.0001	0.2200	0.0000	0.0001
mb_55	0.1300	0.1200	0.0044	0.1600	0.0034	0.0046	0.0010	0.0055	0.0037	0.0012	0.0039	0.0006	0.0032	0.0008	0.0028	0.0004	0.0029	0.0005	0.0001	0.0003	0.5800	0.0001	0.0003
au24c08	-	-	-	2.4900	0.0006	0.0005	0.0005	0.0038	0.0007	0.0008	0.0036	0.0006	0.0027	0.0002	0.0020	0.0006	0.0031	0.0008	0.0016	-	0.0240	0.0001	0.0001
au24c11	-	-	-	2.8500	0.0003	0.0003	0.0002	0.0010	0.0010	0.0005	0.0020	0.0003	0.0010	0.0002	0.0010	0.0002	0.0016	0.0005	0.0006	-	0.0240	0.0001	0.0001
kb_12	0.0030	0.0043	0.0017	2.3200	0.0002	0.0002	0.0001	0.0002	0.0007	0.0003	0.0008	0.0002	0.0010	0.0003	0.0014	0.0004	0.0026	0.0005	0.0002	0.0002	0.0280	0.0001	0.0001
kb_14	0.0140	0.0240	0.0110	2.6900	0.0006	0.0004	0.0002	0.0021	0.0003	0.0006	0.0021	0.0002	0.0018	0.0006	0.0019	0.0003	0.0040	0.0007	0.0001	0.0004	0.0310	0.0000	0.0000
au24c17	-	-	-	2.6300	0.0005	0.0003	0.0003	0.0028	0.0010	0.0006	0.0036	0.0004	0.0024	0.0007	0.0023	0.0007	0.0046	0.0009	0.0010	-	0.0350	0.0001	0.0001
au25e14	-	-	-	0.2900	0.0014	0.0018	0.0005	0.0037	0.0023	0.0008	0.0032	0.0005	0.0025	0.0008	0.0021	0.0006	0.0037	0.0007	0.0003	-	1.7800	0.0001	0.0004
mb_16	0.0470	0.0400	0.0027	0.3600	0.0020	0.0021	0.0007	0.0036	0.0024	0.0009	0.0032	0.0005	0.0032	0.0008	0.0027	0.0007	0.0041	0.0007	0.0011	0.0004	1.1900	0.0001	0.0004
au25d05	-	-	-	1.8900	0.0011	0.0036	0.0010	0.0072	0.0057	0.0014	0.0098	0.0019	0.0130	0.0028	0.0081	0.0013	0.0086	0.0014	0.0002	-	0.5500	0.0001	0.0002
kb_24	0.0092	0.0089	0.0006	1.8900	0.0010	0.0040	0.0008	0.0070	0.0053	0.0011	0.0087	0.0015	0.0110	0.0025	0.0072	0.0011	0.0070	0.0012	0.0002	0.0000	0.7700	0.0001	0.0001
au24d13	-	-	-	0.8800	0.0003	0.0002	0.0001	0.0007	0.0005	0.0006	0.0021	0.0002	0.0014	0.0003	0.0011	0.0004	0.0027	0.0006	0.0006	-	3.9700	0.0001	0.0001
au24d14	-	-	-	0.3400	0.0003	0.0004	0.0002	0.0012	0.0006	0.0004	0.0021	0.0002	0.0016	0.0003	0.0014	0.0003	0.0026	0.0004	0.0005	-	1.6100	0.0000	0.0000
au24d17	-	-	-	0.1100	0.0003	0.0004	0.0001	0.0001	0.0002	0.0003	0.0005	0.0001	0.0010	0.0004	0.0014	0.0004	0.0029	0.0006	0.0003	-	3.0300	0.0001	0.0001
ha22	0.0011	0.0015	0.0003	0.0190	0.0007	0.0017	0.0005	0.0035	0.0032	0.0011	0.0040	0.0007	0.0038	0.0010	0.0033	0.0005	0.0040	0.0006	0.0003	0.0001	2.9700	0.0000	0.0001
au25d12	-	-	-	0.0610	0.0003	0.0008	0.0003	0.0022	0.0016	0.0004	0.0024	0.0004	0.0027	0.0006	0.0016	0.0003	0.0022	0.0004	0.0002	-	3.2900	0.0002	0.0002

kb_27	0.0130	0.0150	0.0018	0.1200	0.0007	0.0014	0.0005	0.0032	0.0024	0.0006	0.0039	0.0006	0.0036	0.0008	0.0029	0.0006	0.0037	0.0006	0.0004	0.0001	8.6700	0.0004	0.0002
au25e17	-	-	-	0.0350	0.0008	0.0014	0.0003	0.0027	0.0015	0.0006	0.0026	0.0003	0.0018	0.0004	0.0013	0.0003	0.0021	0.0004	0.0001	-	3.1300	0.0001	0.0001
au25f14	-	-	-	0.1400	0.0005	0.0008	0.0002	0.0012	0.0005	0.0003	0.0011	0.0002	0.0013	0.0004	0.0015	0.0004	0.0027	0.0007	0.0001	-	0.3800	0.0001	0.0000
au25f16	-	-	-	0.0180	0.0025	0.0040	0.0007	0.0044	0.0018	0.0007	0.0029	0.0004	0.0025	0.0006	0.0016	0.0003	0.0020	0.0004	0.0001	-	7.8700	0.0005	0.0000
au25f17	-	-	-	0.0440	0.0084	0.0140	0.0019	0.0100	0.0035	0.0012	0.0066	0.0007	0.0032	0.0006	0.0016	0.0002	0.0013	0.0002	0.0001	-	0.4300	0.0001	0.0003
mb_48	0.0710	0.0690	0.0014	0.1200	0.0009	0.0011	0.0003	0.0025	0.0006	0.0005	0.0019	0.0003	0.0016	0.0006	0.0021	0.0004	0.0036	0.0009	0.0001	0.0001	0.1700	0.0001	0.0002
mb_50	0.0020	0.0022	0.0009	0.0450	0.0059	0.0100	0.0017	0.0098	0.0040	0.0014	0.0065	0.0007	0.0033	0.0007	0.0022	0.0003	0.0021	0.0004	0.0001	0.0001	0.2400	0.0001	0.0003
mb_52	0.0024	0.0027	0.0004	0.0220	0.0022	0.0030	0.0007	0.0040	0.0028	0.0010	0.0038	0.0005	0.0028	0.0007	0.0026	0.0005	0.0029	0.0006	0.0005	0.0001	1.0800	0.0001	0.0001
au25g12	-	-	-	0.4000	0.0002	0.0005	0.0002	0.0022	0.0022	0.0009	0.0043	0.0007	0.0054	0.0013	0.0040	0.0007	0.0043	0.0007	0.0001	-	1.8700	0.0001	0.0001
mb_35	0.0018	0.0018	0.0004	0.7200	0.0004	0.0007	0.0004	0.0030	0.0038	0.0014	0.0060	0.0011	0.0078	0.0019	0.0062	0.0009	0.0062	0.0010	0.0001	0.0000	3.2300	0.0001	0.0000
au25d17	-	-	-	0.3300	0.0002	0.0002	0.0001	0.0001	0.0007	0.0002	0.0012	0.0002	0.0015	0.0004	0.0014	0.0004	0.0022	0.0006	0.0003	-	0.0170	0.0001	0.0001
mb_26	0.0190	0.0160	0.0043	0.3300	0.0002	0.0002	0.0001	0.0005	0.0004	0.0002	0.0005	0.0001	0.0006	0.0001	0.0009	0.0002	0.0015	0.0002	0.0004	0.0001	0.0340	0.0000	0.0001
ha26	0.1100	0.1000	0.0220	2.0400	0.0006	0.0006	0.0002	0.0024	0.0026	0.0011	0.0047	0.0010	0.0083	0.0023	0.0100	0.0021	0.0160	0.0028	0.0006	0.0002	0.2800	0.0001	0.0002
ha27	0.0390	0.0340	0.0160	1.2400	0.0005	0.0006	0.0003	0.0009	0.0013	0.0006	0.0023	0.0005	0.0034	0.0011	0.0042	0.0009	0.0079	0.0019	0.0006	0.0003	0.1100	0.0000	0.0003
au24c13	-	-	-	0.6000	0.0001	0.0001	0.0000	0.0002	0.0001	0.0001	0.0003	0.0001	0.0004	0.0001	0.0004	0.0001	0.0006	0.0002	0.0002	-	0.0070	0.0000	0.0000
au24c15	-	-	-	1.8400	0.0002	0.0002	0.0001	0.0010	0.0005	0.0003	0.0012	0.0002	0.0011	0.0002	0.0005	0.0002	0.0012	0.0002	0.0005	-	0.0063	0.0001	0.0001
au24d03	-	-	-	6.1800	0.0080	0.0070	0.0039	0.0001	0.0001	0.0055	0.0450	0.0020	0.0270	0.0064	0.0300	0.0100	0.0560	0.0150	0.0160	-	3.6000	0.0001	0.0100
au24d05	-	-	-	3.9100	0.0029	0.0022	0.0007	0.0001	0.0001	0.0017	0.0300	0.0022	0.0220	0.0043	0.0075	0.0032	0.0300	0.0077	0.0001	-	1.2300	0.0001	0.0047
au24d06	-	-	-	2.4100	0.0009	0.0005	0.0001	0.0008	0.0001	0.0004	0.0078	0.0001	0.0005	0.0013	0.0037	0.0012	0.0036	0.0012	0.0005	-	0.1600	0.0001	0.0001
au25d14	-	-	-	0.1700	0.0001	0.0001	0.0000	0.0002	0.0002	0.0001	0.0004	0.0001	0.0006	0.0002	0.0006	0.0002	0.0011	0.0003	0.0001	-	0.0150	0.0000	0.0000
au25e08	-	-	-	0.0510	0.0001	0.0001	0.0000	0.0003	0.0003	0.0001	0.0003	0.0001	0.0007	0.0002	0.0008	0.0002	0.0017	0.0004	0.0001	-	0.0440	0.0001	0.0001
au25e09	-	-	-	0.0970	0.0001	0.0001	0.0000	0.0005	0.0002	0.0001	0.0005	0.0002	0.0010	0.0003	0.0012	0.0003	0.0024	0.0006	0.0000	-	0.0750	0.0001	0.0002
au25e10	-	-	-	0.0170	0.0000	0.0000	0.0000	0.0001	0.0001	0.0000	0.0001	0.0000	0.0001	0.0000	0.0001	0.0000	0.0002	0.0000	0.0000	-	0.0130	0.0001	0.0000
au25e11	-	-	-	0.0750	0.0001	0.0001	0.0000	0.0002	0.0002	0.0001	0.0002	0.0001	0.0003	0.0001	0.0004	0.0001	0.0006	0.0001	0.0001	-	0.0650	0.0001	0.0001
au25e12	-	-	-	0.1000	0.0002	0.0002	0.0001	0.0008	0.0004	0.0001	0.0008	0.0002	0.0008	0.0003	0.0011	0.0003	0.0018	0.0004	0.0004	-	0.1200	0.0000	0.0004
au25e13	-	-	-	0.0240	0.0001	0.0001	0.0000	0.0002	0.0001	0.0000	0.0001	0.0000	0.0003	0.0001	0.0003	0.0001	0.0006	0.0001	0.0001	-	0.0270	0.0000	0.0001
ha31	0.0073	0.0075	0.0230	1.4100	0.0004	0.0003	0.0002	0.0014	0.0001	0.0003	0.0013	0.0003	0.0009	0.0003	0.0012	0.0003	0.0025	0.0006	0.0003	0.0002	0.1700	0.0000	0.0002
mb_29	0.6200	0.5100	0.0061	0.2000	0.0001	0.0002	0.0001	0.0005	0.0004	0.0002	0.0008	0.0002	0.0009	0.0003	0.0012	0.0003	0.0026	0.0005	0.0001	0.0001	0.0150	0.0000	0.0001
mb_30	0.1800	0.1400	0.0035	0.1800	0.0001	0.0002	0.0001	0.0005	0.0004	0.0002	0.0008	0.0002	0.0017	0.0005	0.0020	0.0004	0.0032	0.0006	0.0000	0.0001	0.0330	0.0001	0.0002
ha13	0.0150	0.0140	0.0014	0.0120	0.0001	0.0001	0.0000	0.0003	0.0002	0.0001	0.0006	0.0001	0.0010	0.0003	0.0010	0.0002	0.0014	0.0002	0.0002	0.0000	0.0065	0.0000	0.0000
mb_38	0.0180	0.0140	0.0550	0.1800	0.0003	0.0004	0.0002	0.0020	0.0020	0.0008	0.0042	0.0009	0.0071	0.0020	0.0073	0.0017	0.0160	0.0035	0.0014	0.0001	0.2500	0.0001	0.0001
mb_39	0.0300	0.0230	0.0170	0.1000	0.0001	0.0001	0.0000	0.0004	0.0005	0.0001	0.0004	0.0001	0.0006	0.0001	0.0005	0.0001	0.0008	0.0002	0.0003	0.0000	0.1500	0.0000	0.0001
ha7	0.0180	0.0170	0.0042	0.0310	0.0002	0.0003	0.0002	0.0011	0.0018	0.0005	0.0023	0.0005	0.0041	0.0010	0.0040	0.0007	0.0050	0.0009	0.0008	0.0002	0.0450	0.0001	0.0001
mb_14	0.0130	0.0120	0.0490	0.1100	0.0003	0.0006	0.0003	0.0002	0.0018	0.0004	0.0014	0.0004	0.0016	0.0005	0.0022	0.0005	0.0023	0.0007	0.0002	0.0002	0.2500	0.0000	0.0001
mb_15	0.0270	0.0230	0.0031	0.0430	0.0001	0.0002	0.0001	0.0003	0.0003	0.0001	0.0004	0.0001	0.0005	0.0002	0.0008	0.0002	0.0014	0.0003	0.0002	0.0000	0.0240	0.0000	0.0001
mb_17	0.1700	0.1300	0.0072	0.3100	0.0005	0.0007	0.0004	0.0014	0.0003	0.0004	0.0020	0.0004	0.0027	0.0007	0.0042	0.0009	0.0078	0.0015	0.0006	0.0002	0.1700	0.0001	0.0005
au25g13	-	-	-	0.0970	0.0001	0.0002	0.0001	0.0010	0.0010	0.0005	0.0023	0.0004	0.0028	0.0008	0.0026	0.0007	0.0047	0.0011	0.0007	-	0.0860	0.0000	0.0001
mb_18	0.0018	0.0023	0.0210	0.0370	0.0002	0.0003	0.0001	0.0006	0.0004	0.0002	0.0009	0.0002	0.0010	0.0003	0.0013	0.0003	0.0028	0.0005	0.0001	0.0001	0.0950	0.0001	0.0001
au25e06	-	-	-	0.4100	0.0003	0.0007	0.0002	0.0008	0.0005	0.0002	0.0008	0.0001	0.0008	0.0002	0.0008	0.0002	0.0012	0.0003	0.0003	-	0.0190	0.0001	0.0002
au25d11	-	-	-	0.2400	0.0007	0.0019	0.0005	0.0032	0.0021	0.0005	0.0031	0.0006	0.0040	0.0010	0.0030	0.0007	0.0038	0.0006	0.0010	-	0.1400	0.0001	0.0008
au25f03	-	-	-	0.0130	0.0000	0.0001	0.0000	0.0005	0.0001	0.0001	0.0004	0.0001	0.0005	0.0001	0.0005	0.0001	0.0009	0.0002	0.0000	-	0.0340	0.0000	0.0001
au25f04	-	-	-	0.0300	0.0001	0.0001	0.0000	0.0004	0.0003	0.0001	0.0001	0.0001	0.0004	0.0001	0.0004	0.0001	0.0008	0.0002	0.0001	-	0.1100	0.0000	0.0000
au25f08	-	-	-	0.0029	0.0000	0.0000	0.0000	0.0000	0.0000	0.0000	0.0000	0.0000	0.0000	0.0000	0.0000	0.0000	0.0000	0.0000	0.0000	-	0.0170	0.0000	0.0003
au25f09	-	-	-	0.0590	0.0001	0.0001	0.0001	0.0003	0.0004	0.0001	0.0005	0.0001	0.0004	0.0001	0.0005	0.0001	0.0010	0.0002	0.0001	-	0.1800	0.0000	0.0005
au25f10	-	-	-	0.0130	0.0001	0.0001	0.0000	0.0003	0.0002	0.0001	0.0003	0.0000	0.0004	0.0001	0.0003	0.0001	0.0005	0.0001	0.0000	-	0.0490	0.0000	0.0000
au25f12	-	-	-	0.0340	0.0001	0.0001	0.0000	0.0002	0.0002	0.0001	0.0001	0.0001	0.0001	0.0001	0.0003	0.0001	0.0004	0.0001	0.0001	-	0.2400	0.0000	0.0006
au25g08	-	-	-	0.1200	0.0000	0.0003	0.0002	0.0023	0.0028	0.0012	0.0066	0.0016	0.0150	0.0036	0.0140	0.0029	0.0230	0.0041	0.0005	-	0.1200	0.0000	0.0000
au25g09	-	-	-	0.1400	0.0001	0.0005	0.0004	0.0038	0.0044	0.0017	0.0092	0.0022	0.0190	0.0050	0.0180	0.0037	0.0290	0.0051	0.0012	-	0.1100	0.0001	0.0001
mb_24	0.0040	0.0040	0.0024	0.0730	0.0002	0.0003	0.0001	0.0008	0.0001	0.0003	0.0010	0.0002	0.0018	0.0006	0.0025	0.0006	0.0048	0.0010	0.0001	0.0001	0.0400	0.0001	0.0001
ha9	0.0037	0.0037	0.0090	0.0140	0.0001	0.0001	0.0001	0.0005	0.0005	0.0002	0.0008	0.0002	0.0012	0.0003	0.0012	0.0002	0.0012	0.0002	0.0003	0.0000	0.0120	0.0000	0.0000
ha15	0.0760	0.0680	0.0037	0.0170	0.0001	0.0001	0.0001	0.0006	0.0008	0.0003	0.0015	0.0003	0.0026	0.0007	0.0025	0.0005	0.0039	0.0006	0.0004	0.0001	0.0490	0.0001	0.0001
ha18	0.0170	0.0150	0.0057	0.0690	0.0001	0.0001	0.0001	0.0005	0.0003	0.0001	0.0007	0.0001	0.0006	0.0001	0.0005	0.0001	0.0006	0.0001	0.0002	0.0000	0.0450	0.0001	0.0001
kb_16	0.0048	0.0034	0.0015	0.0290	0.0003	0.0002	0.0002	0.0007	0.0006	0.0000	0.0007	0.0001	0.0006	0.0002	0.0008	0.0002	0.0014	0.0002	0.0001	0.0002	0.1200	0.0001	0.0001

kb_18	0.0210	0.0220	0.0005	0.0170	0.0001	0.0002	0.0001	0.0004	0.0005	0.0001	0.0005	0.0001	0.0005	0.0001	0.0004	0.0001	0.0011	0.0003	0.0000	0.0002	0.0520	0.0000	0.0001
kb_19	0.0190	0.0170	0.0025	0.0750	0.0002	0.0004	0.0002	0.0010	0.0004	0.0001	0.0009	0.0002	0.0009	0.0002	0.0010	0.0003	0.0026	0.0005	0.0001	0.0000	2.2200	0.0001	0.0001
kb_20	0.0076	0.0079	0.0018	0.0310	0.0002	0.0002	0.0000	0.0008	0.0007	0.0004	0.0008	0.0001	0.0007	0.0002	0.0008	0.0002	0.0016	0.0004	0.0001	0.0001	0.0920	0.0001	0.0001
kb_26	0.5900	0.6100	0.0051	0.9100	0.0012	0.0041	0.0006	0.0042	0.0030	0.0006	0.0033	0.0006	0.0041	0.0010	0.0031	0.0005	0.0040	0.0007	0.0012	0.0001	0.2300	0.0001	0.0016
au24c16	-	-	-	0.1900	0.0001	0.0001	0.0001	0.0002	0.0003	0.0001	0.0004	0.0001	0.0002	0.0001	0.0001	0.0001	0.0003	0.0000	0.0002	-	0.0040	0.0001	0.0000
ha19	0.0074	0.0071	0.0019	0.0540	0.0001	0.0001	0.0001	0.0007	0.0004	0.0002	0.0006	0.0001	0.0005	0.0001	0.0005	0.0001	0.0008	0.0002	0.0002	0.0001	0.0400	0.0000	0.0001
ha20	0.0001	0.0001	0.0000	0.0002	0.0000	0.0000	0.0000	0.0000	0.0000	0.0000	0.0000	0.0000	0.0000	0.0000	0.0000	0.0000	0.0000	0.0000	0.0000	0.0000	0.0035	0.0001	0.0000
ha21	0.0010	0.0010	0.0001	0.0014	0.0000	0.0000	0.0000	0.0000	0.0000	0.0000	0.0000	0.0000	0.0000	0.0000	0.0000	0.0000	0.0000	0.0000	0.0000	0.0000	0.0310	0.0000	0.0000
au25g15	-	-	-	0.3300	0.0001	0.0003	0.0002	0.0013	0.0020	0.0010	0.0038	0.0008	0.0059	0.0016	0.0059	0.0014	0.0120	0.0028	0.0010	-	0.1600	0.0001	0.0001
au25g16	-	-	-	0.3100	0.0002	0.0003	0.0002	0.0015	0.0012	0.0004	0.0017	0.0004	0.0019	0.0005	0.0018	0.0005	0.0031	0.0007	0.0005	-	0.1600	0.0000	0.0001
au25g17	-	-	-	0.1700	0.0002	0.0003	0.0002	0.0016	0.0013	0.0005	0.0021	0.0005	0.0036	0.0010	0.0044	0.0011	0.0095	0.0021	0.0008	-	0.1100	0.0000	0.0001
mb_57	0.0080	0.0079	0.0120	0.0790	0.0001	0.0001	0.0000	0.0005	0.0006	0.0002	0.0005	0.0001	0.0007	0.0002	0.0007	0.0002	0.0011	0.0002	0.0005	0.0001	0.0840	0.0001	0.0001
mb_41	0.0940	0.0740	0.0280	0.2200	0.0002	0.0004	0.0002	0.0013	0.0016	0.0005	0.0022	0.0005	0.0030	0.0009	0.0035	0.0008	0.0078	0.0015	0.0011	0.0001	0.2000	0.0001	0.0001
au25e03	-	-	-	0.7600	0.0001	0.0002	0.0001	0.0005	0.0004	0.0002	0.0010	0.0002	0.0014	0.0003	0.0013	0.0004	0.0021	0.0005	0.0002	-	0.0480	0.0001	0.0002
au25e05	-	-	-	0.4200	0.0002	0.0002	0.0001	0.0007	0.0003	0.0002	0.0006	0.0001	0.0004	0.0001	0.0006	0.0001	0.0008	0.0002	0.0001	-	0.0320	0.0000	0.0003
au25g03	-	-	-	0.0120	0.0019	0.0016	0.0002	0.0012	0.0004	0.0001	0.0007	0.0001	0.0003	0.0001	0.0002	0.0000	0.0003	0.0001	0.0001	-	0.2400	0.0001	0.0000
mb_51	0.0015	0.0016	0.0002	0.0140	0.0014	0.0015	0.0003	0.0015	0.0008	0.0003	0.0009	0.0001	0.0006	0.0001	0.0004	0.0001	0.0006	0.0001	0.0001	0.0000	0.1100	0.0001	0.0000
mb_25	0.0013	0.0013	0.0004	0.1100	0.0001	0.0001	0.0000	0.0001	0.0001	0.0001	0.0003	0.0001	0.0003	0.0001	0.0004	0.0001	0.0005	0.0001	0.0001	0.0000	0.0076	0.0000	0.0000
mb_33	0.0016	0.0021	0.0011	0.2000	0.0002	0.0002	0.0001	0.0003	0.0003	0.0001	0.0004	0.0001	0.0003	0.0001	0.0002	0.0001	0.0004	0.0001	0.0000	0.0001	0.0230	0.0001	0.0001
au24c14	-	-	-	0.5200	0.0008	0.0017	0.0012	0.0049	0.0039	0.0014	0.0087	0.0011	0.0044	0.0004	0.0034	0.0010	0.0060	0.0011	0.0022	-	0.0300	0.0001	0.0001
kb_11	0.0068	0.0130	0.0047	0.3000	0.0005	0.0003	0.0001	0.0017	0.0014	0.0003	0.0013	0.0001	0.0011	0.0003	0.0017	0.0003	0.0033	0.0003	0.0003	0.0002	0.0180	0.0002	0.0001
au24d04	-	-	-	0.6400	0.0002	0.0002	0.0002	0.0001	0.0001	0.0002	0.0011	0.0001	0.0005	0.0001	0.0001	0.0001	0.0007	0.0001	0.0001	-	0.0049	0.0001	0.0001
au24d07	-	-	-	0.4200	0.0001	0.0001	0.0001	0.0001	0.0001	0.0001	0.0006	0.0000	0.0004	0.0001	0.0001	0.0001	0.0001	0.0001	0.0002	-	0.0061	0.0001	0.0001
ha30	0.0009	0.0009	0.0024	0.1900	0.0001	0.0001	0.0001	0.0001	0.0001	0.0001	0.0003	0.0001	0.0002	0.0001	0.0002	0.0001	0.0006	0.0001	0.0001	0.0000	0.0170	0.0001	0.0000
ha16	0.0770	0.0710	0.0130	1.2100	0.0005	0.0008	0.0003	0.0023	0.0015	0.0007	0.0021	0.0004	0.0027	0.0006	0.0020	0.0004	0.0035	0.0006	0.0005	0.0001	0.6500	0.0001	0.0026
ha17	0.0017	0.0023	0.0007	0.0160	0.0003	0.0006	0.0002	0.0019	0.0022	0.0008	0.0036	0.0007	0.0049	0.0011	0.0044	0.0007	0.0052	0.0009	0.0002	0.0001	0.0100	0.0001	0.0001
ha23	0.0018	0.0026	0.0035	0.0490	0.0002	0.0003	0.0001	0.0008	0.0008	0.0003	0.0008	0.0001	0.0008	0.0002	0.0008	0.0001	0.0008	0.0002	0.0001	0.0001	0.0300	0.0000	0.0001
ha24	0.0012	0.0015	0.0004	0.0120	0.0003	0.0005	0.0001	0.0013	0.0010	0.0004	0.0016	0.0002	0.0017	0.0005	0.0017	0.0003	0.0031	0.0005	0.0002	0.0004	0.0160	0.0002	0.0001
ha25	0.0081	0.0072	0.0023	0.0480	0.0001	0.0004	0.0001	0.0008	0.0006	0.0003	0.0008	0.0002	0.0008	0.0002	0.0007	0.0002	0.0008	0.0002	0.0001	0.0000	0.0360	0.0000	0.0001
au25d04	-	-	-	0.9100	0.0026	0.0110	0.0020	0.0150	0.0092	0.0013	0.0120	0.0022	0.0140	0.0030	0.0090	0.0018	0.0110	0.0019	0.0007	-	0.1800	0.0001	0.0041
kb_23	0.0250	0.0320	0.0039	1.4200	0.0031	0.0150	0.0018	0.0130	0.0085	0.0012	0.0110	0.0020	0.0130	0.0029	0.0097	0.0017	0.0110	0.0017	0.0009	0.0001	0.4800	0.0001	0.0054
au25f05	-	-	-	1.5100	0.0002	0.0002	0.0001	0.0004	0.0002	0.0001	0.0004	0.0001	0.0004	0.0001	0.0004	0.0001	0.0006	0.0001	0.0002	-	4.4900	0.0002	0.0027
au25f11	-	-	-	0.0300	0.0000	0.0001	0.0000	0.0003	0.0001	0.0001	0.0003	0.0000	0.0003	0.0001	0.0004	0.0001	0.0006	0.0002	0.0000	-	0.0770	0.0000	0.0002
kb_17	1.8700	1.9400	0.0019	1.7600	0.0002	0.0002	0.0001	0.0003	0.0002	0.0002	0.0006	0.0001	0.0005	0.0001	0.0005	0.0001	0.0009	0.0002	0.0003	0.0001	3.4000	0.0001	0.0040
au24d16	-	-	-	0.0380	0.0001	0.0001	0.0001	0.0004	0.0001	0.0001	0.0005	0.0000	0.0004	0.0001	0.0008	0.0002	0.0020	0.0004	0.0002	-	0.6700	0.0001	0.0001
au25e16	-	-	-	0.0910	0.0001	0.0001	0.0000	0.0005	0.0002	0.0001	0.0006	0.0001	0.0007	0.0002	0.0008	0.0002	0.0013	0.0003	0.0001	-	0.0260	0.0001	0.0000
mb_13	0.1500	0.1200	0.0180	0.6900	0.0008	0.0013	0.0004	0.0030	0.0038	0.0017	0.0028	0.0009	0.0062	0.0023	0.0110	0.0025	0.0220	0.0040	0.0003	0.0006	0.2000	0.0001	0.0012
mb_20	0.0001	0.0001	0.0001	0.0025	0.0000	0.0000	0.0000	0.0000	0.0000	0.0000	0.0000	0.0000	0.0000	0.0000	0.0000	0.0000	0.0001	0.0000	0.0000	0.0000	0.0033	0.0001	0.0000
ha6	0.0120	0.0110	0.0190	0.1300	0.0003	0.0008	0.0005	0.0047	0.0048	0.0013	0.0076	0.0016	0.0120	0.0029	0.0094	0.0015	0.0110	0.0015	0.0015	0.0002	0.0820	0.0001	0.0001
ha10	0.0021	0.0019	0.0004	0.0330	0.0001	0.0003	0.0002	0.0019	0.0020	0.0008	0.0026	0.0006	0.0047	0.0012	0.0046	0.0009	0.0071	0.0013	0.0002	0.0001	0.0170	0.0001	0.0001
ha11	0.0031	0.0038	0.0003	0.0530	0.0002	0.0004	0.0003	0.0025	0.0026	0.0010	0.0039	0.0008	0.0067	0.0016	0.0056	0.0010	0.0082	0.0015	0.0000	0.0001	0.0430	0.0001	0.0001
au25g14	-	-	-	0.1300	0.0000	0.0001	0.0001	0.0007	0.0006	0.0003	0.0012	0.0002	0.0016	0.0004	0.0014	0.0003	0.0018	0.0003	0.0005	-	0.0550	0.0001	0.0000
mb_36	0.0270	0.0210	0.0049	0.0690	0.0001	0.0004	0.0003	0.0025	0.0025	0.0011	0.0048	0.0008	0.0073	0.0019	0.0062	0.0011	0.0095	0.0015	0.0003	0.0001	0.0500	0.0001	0.0001
mb_40	0.0065	0.0057	0.0130	0.1400	0.0002	0.0004	0.0003	0.0021	0.0024	0.0009	0.0041	0.0008	0.0060	0.0016	0.0045	0.0011	0.0067	0.0012	0.0020	0.0001	0.1600	0.0001	0.0001
au25g04	-	-	-	0.0210	0.0004	0.0006	0.0001	0.0007	0.0004	0.0002	0.0005	0.0001	0.0004	0.0001	0.0004	0.0001	0.0005	0.0001	0.0001	-	0.0510	0.0000	0.0000
au25g07	-	-	-	0.0180	0.0000	0.0001	0.0000	0.0001	0.0000	0.0000	0.0001	0.0000	0.0001	0.0000	0.0001	0.0000	0.0001	0.0000	0.0001	-	0.0160	0.0001	0.0000
mb_54	0.0008	0.0009	0.0002	0.0083	0.0001	0.0001	0.0000	0.0002	0.0001	0.0001	0.0002	0.0000	0.0002	0.0000	0.0002	0.0001	0.0002	0.0001	0.0000	0.0000	0.0073	0.0000	0.0000
au25e15	-	-	-	0.1600	0.0001	0.0001	0.0001	0.0004	0.0001	0.0001	0.0005	0.0001	0.0009	0.0003	0.0009	0.0003	0.0020	0.0005	0.0002	-	0.0480	0.0000	0.0000
mb_19	0.0074	0.0075	0.0028	0.0580	0.0002	0.0003	0.0001	0.0006	0.0002	0.0002	0.0007	0.0000	0.0007	0.0003	0.0015	0.0004	0.0027	0.0006	0.0002	0.0001	0.0360	0.0001	0.0001
au25g11	-	-	-	0.0100	0.0000	0.0003	0.0002	0.0018	0.0018	0.0009	0.0030	0.0006	0.0034	0.0009	0.0025	0.0005	0.0029	0.0005	0.0001	-	0.0055	0.0000	0.0001
mb_37	0.0086	0.0080	0.0022	0.0270	0.0003	0.0004	0.0003	0.0016	0.0019	0.0008	0.0021	0.0004	0.0024	0.0005	0.0015	0.0003	0.0020	0.0004	0.0005	0.0001	0.0150	0.0000	0.0001
mb_22	0.0110	0.0080	0.0013	0.1000	0.0002	0.0003	0.0002	0.0007	0.0001	0.0001	0.0009	0.0001	0.0001	0.0001	0.0006	0.0001	0.0009	0.0002	0.0001	0.0001	0.1900	0.0000	0.0002
ha12	0.0009	0.0012	0.0003	0.0028	0.0001	0.0001	0.0001	0.0008	0.0009	0.0004	0.0014	0.0003	0.0020	0.0005	0.0018	0.0003	0.0021	0.0003	0.0003	0.0001	0.0088	0.0000	0.0000

Table S11: Compiled compositions of silicates and carbonates in transition metals determined by LA-ICP-MS

Mineral	Structure		Sc µg/g	Ti µg/g	V µg/g	Mn µg/g	Co µg/g	Ni µg/g	Cu µg/g	Zn µg/g
Fuchsite		*n*	*9*	*9*	*9*	-	*9*	*12*	*12*	*9*
		Q16	7.55	446	77.6	-	7.65	708	5.56	23.0
		Median	**8.03**	**614**	**298**	**-**	**31.7**	**1813**	**6.92**	**52.5**
		Q84	9.22	1078	320	-	36.5	12470	9.70	58.8
		Min	6.49	94.6	64.2	-	2.38	332	4.66	6.75
		Max	13.6	2812	345	-	251	14230	16.7	254
Serpentine	All	*n*	*17*	*17*	*17*	*35*	*17*	*52*	*52*	*44*
		Q16	6.04	6.09	8.96	268	63.1	1919	0.45	28.6
		Median	**7.74**	**14.1**	**10.5**	**381**	**78.8**	**2634**	**0.56**	**38.7**
		Q84	20.8	60.1	51.1	499	109	2962	0.69	46.2
		Min	4.34	3.22	7.65	96.4	45.5	1250	0.03	14.4
		Max	27.5	142	110	675.8	134	3697	7	68
Serpentine	Mesh	*n*	*7*	*7*	*7*	*18*	*7*	*25*	*25*	*22*
		Q16	7.33	9.055	8.86	229	62.3	2432	0.49	26.0
		Median	**7.74**	**14.1**	**10.5**	**276**	**77.55**	**2648**	**0.62**	**42.7**
		Q84	10.2	29.2	18.6	359	86.5	3014	1.20	49.2
		Min	5.12	6.91	7.65	96.4	55.5	2093	0.13	14.9
		Max	12.6	37.3	27.5	499	97	3697	6.55	63.3
Serpentine	Bastite	*n*	*5*	*5*	*5*	*6*	*5*	*11*	*11*	*8*
		Q16	21.6	60.9	53.1	377	68.6	2850	0.29	36.1
		Median	**22.8**	**101**	**88.9**	**437**	**122**	**2944**	**0.43**	**44.9**
		Q84	23.5	118	89.0	489	134	3129	0.51	51.1
		Min	20.8	60.1	51.1	191	67.8	2629	0.03	14.4
		Max	27.5	142	110	561	134	3412	1.37	68.1
Serpentine	Veins	*n*	*5*	*5*	*5*	*11*	*5*	*16*	*16*	*14*
		Q16	4.4	3.9	8.72	414	46.3	1614	0.50	29.9
		Median	**4.94**	**4.51**	**8.96**	**510**	**83.5**	**1806**	**0.53**	**34.9**
		Q84	6.04	5.23	9.86	585	109	1891	0.68	39.5
		Min	4.34	3.22	7.72	325	45.5	1250	0.03	21.5
		Max	6.74	6.09	10.5	676	130	3172	1.31	57.4
Magnesite	Fe-core spheroids	*n*	*3*	*3*	*3*	*1*	*3*	*4*	*4*	*4*
		Q16	17.8	9.66	9.35	276	89.2	1035	0.63	29.4
		Median	**23.0**	**17.5**	**10.8**	**276**	**135**	**1576**	**0.96**	**49.5**
		Q84	28.6	25.3	11.9	276	167	2120	1.17	67.9
		Min	12.5	1.79	7.89	276	42.9	323	0.19	22.0
		Max	34.2	33.0	13.0	276	199	2840	1.25	70.5
Magnesite	Mg-core spheroids	*n*	*11*	*11*	*11*	*13*	*11*	*24*	*24*	*24*
		Q16	4.18	7.54	4.35	191	36.7	351	0.16	17.7
		Median	**8.19**	**13.1**	**10.68**	**345**	**58.8**	**901**	**0.30**	**46.4**
		Q84	18.0	24.1	13.7	867	115	3188	1.05	100
		Min	1.70	3.09	3.11	15.6	25.0	87.1	0.02	4.66
		Max	28.8	63.1	44.2	3679	386	56266	12.3	1175
Magnesite	Aggregates	*n*	*9*	*9*	*9*	*10*	*9*	*19*	*19*	*14*
		Q16	3.24	2.44	3.59	201	45.8	425	0.11	20.0
		Median	**4.13**	**9.6**	**5.78**	**396**	**49.8**	**834**	**0.46**	**37.3**
		Q84	7.57	15.7	9.26	558	80.2	1460	0.75	260
		Min	2.64	1.61	1.398	19.3	26.0	118	0.02	9.03
		Max	9.5	100.7	20.7	882	140	3394	25.3	420
Magnesite	Pseudomorphic veins	*n*	*8*	*8*	*8*	*7*	*8*	*15*	*15*	*15*
		Q16	0.43	0.58	0.39	611	10.5	245	0.10	8.2
		Median	**0.71**	**1.73**	**1.22**	**769**	**31.8**	**449**	**0.40**	**20.8**
		Q84	2.74	12.37	4.32	1984	42.0	690	0.94	29.2
		Min	0.06	0.05	0.05	413	0.21	3.4	0.001	0.10
		Max	7.56	76.1	15.41	3779	71	1442	3.65	73
Magnesite	Antitaxial veins	*n*	*17*	*17*	*17*	*11*	*17*	*28*	*28*	*25*
		Q16	1.05	1.33	1.03	403	45.0	336	0.12	19.3
		Median	**1.78**	**2.93**	**3.07**	**600**	**52.5**	**513**	**0.25**	**34.6**
		Q84	4.29	9.4	8.3	1057	89.2	863	1.12	94.4
		Min	0.08	0.04	0.19	296	3.5	42.9	0.003	1.61
		Max	43.1	71.2	32.5	10387	407.9	5057	36.3	494

Table S11 (continued)

Dolomite	Aggregates	*n*	*7*	*7*	*7*	*12*	*7*	*19*	*19*	*15*
		Q16	7.4	1.64	1.76	426	51.4	661	0.24	36.8
		Median	**10.8**	**2.98**	**5.87**	**687**	**57.9**	**841**	**0.42**	**47.3**
		Q84	18.9	3.50	14.9	790	63.6	1024	0.99	54.1
		Min	2.72	0.94	0.75	372	15.4	103	0.11	4.24
		Max	26.1	813	62.4	1165	77.4	4190	5.45	186
Dolomite and magnesite	Late veins	*n*	*8*	*8*	*8*	*6*	*8*	*14*	*14*	*13*
		Q16	1.10	0.21	1.40	777	23.2	275	0.03	20.1
		Median	**1.63**	**0.43**	**8.28**	**958**	**69.8**	**593**	**0.27**	**47.1**
		Q84	3.02	0.95	12.8	980	88.1	1114	0.38	57.6
		Min	0.79	0.11	0.15	535	12.6	35.8	0.01	14.4
		Max	22.9	2.43	41.3	1509	151	2244	1.04	627

Table S12: Phase proportions from quantitative element distribution maps of Fe-core and Mg-core spheroids

Fe-core spheroids (50Z-1-75-80)

Phase	Phase proportion (%)	Magnesite proportion (%)
Mg-rich magnesite	35.6	80.5
Fe-rich magnesite (core)	8.6	19.5
Quartz	53.0	-
Fe oxide	2.8	-
Magnesite	**44.2**	
Non-magnesite	**55.9**	

Mg-core spheroids (46Z-4-46-51)

Phase	Phase proportion (%)	Magnesite proportion (%)
Mg-rich magnesite (core)	54.6	91.9
Fe-Ca-Si-rich magnesite (rim)	4.8	8.1
Dolomite	0.2	-
Quartz	34.3	-
Fe oxide	6.2	-
Magnesite	**59.4**	
Non-magnesite	**40.6**	

Appendix to Chapter 6

Sample	Lithology	SiO_2	TiO_2	Al_2O_3	Fe_2O_3	MnO	MgO	CaO	Na_2O	K_2O	P_2O_5	LOI	Sum	Mg#
		wt%	wt%	wt%	wt%	wt%	wt%	wt%	wt%	wt%	wt%	wt%	wt%	
OM20-01	Carb. metabasalt	34.50	1.12	14.20	7.77	0.11	7.26	11.58	0.02	0.31	0.17	22.89	99.93	64.93
OM20-02	Metabasalt	49.39	1.24	16.03	8.37	0.12	7.09	8.68	4.09	0.56	0.17	3.95	99.69	62.66
OM20-03	Amphibolite	53.88	1.30	14.38	8.74	0.21	4.74	9.86	4.95	0.11	0.10	1.19	99.46	51.80
OM20-04	Serp. peridotite	39.68	0.06	1.58	8.83	0.12	37.12	1.67	n.d.	n.d.	0.01	10.56	99.63	89.28
OM20-05	Carb. serpentinite	28.43	n.d.	0.22	6.98	0.09	29.96	0.26	n.d.	0.01	0.01	33.78	99.74	89.48
OM20-08	Radiolarite	97.40	n.d.	0.86	0.37	0.01	0.15	0.30	0.02	0.20	0.01	0.63	99.95	44.55
OM20-09	Limestone	2.44	0.01	0.12	0.15	n.d.	0.37	54.24	0.02	0.01	0.02	42.47	99.85	83.01
OM20-11	Carb. serpentinite	29.51	0.01	0.05	5.53	0.08	29.53	1.09	n.d.	n.d.	0.01	33.9	99.71	91.36
OM20-12	Listvenite	35.55	0.03	0.42	5.99	0.13	12.41	17.35	0.02	0.02	0.01	27.94	99.87	80.41
OM20-13	Serp. peridotite	40.38	0.01	0.94	8.14	0.11	39.42	0.85	n.d.	n.d.	0.01	9.63	99.49	90.56
OM20-14	Listvenite	28.85	0.01	0.09	7.30	0.08	28.60	1.63	n.d.	n.d.	0.01	33.2	99.77	88.59
OM20-15	Listvenite	17.64	0.01	0.42	11.67	0.11	31.03	2.10	n.d.	0.01	0.01	36.49	99.49	84.05
OM20-16	Carb. serpentinite	28.62	0.01	0.20	7.63	0.13	39.33	0.85	n.d.	n.d.	0.01	22.91	99.69	91.08
OM20-17	Carb. serpentinite	28.13	n.d.	0.63	8.75	0.08	32.38	8.01	n.d.	n.d.	0.01	21.41	99.4	88.00
OM20-18	Carb. serpentinite	32.18	0.04	2.35	8.07	0.11	33.81	5.10	n.d.	n.d.	0.01	17.92	99.59	89.25
OM20-20	Gabbro	41.54	0.07	21.52	4.33	0.06	11.73	15.27	0.60	n.d.	0.01	4.37	99.5	84.30
OM20-22	Listvenite	30.01	0.02	0.21	5.83	0.11	20.90	11.20	n.d.	n.d.	0.01	31.37	99.66	87.66
OM20-23	Listvenite	21.27	0.01	0.05	4.52	0.24	27.69	8.17	n.d.	n.d.	0.01	37.87	99.83	92.39
OM20-24	Gabbro	46.57	0.74	18.96	8.58	0.15	7.30	16.08	1.17	n.d.	0.01	0.35	99.91	62.77
OM20-25	Listvenite	26.74	n.d.	0.04	7.31	0.07	30.24	0.39	n.d.	n.d.	0.01	34.93	99.73	89.13
OM20-26	Carb. serpentinite	25.70	0.01	0.64	9.67	0.12	36.01	2.27	n.d.	n.d.	0.01	25.09	99.52	88.06
OM20-28	Serp. peridotite	40.22	0.05	1.44	8.84	0.12	38.05	1.50	n.d.	n.d.	0.01	9.13	99.36	89.51
OM20-29	Listvenite	32.53	n.d.	0.07	6.92	0.07	28.32	0.43	n.d.	n.d.	0.01	31.31	99.66	89.02
OM20-30a	Carb. serpentinite	30.11	0.02	0.45	6.87	0.07	38.52	0.71	n.d.	n.d.	0.01	22.83	99.59	91.74
OM20-30b	Carb. serpentinite	32.14	0.02	0.49	7.09	0.08	38.05	0.72	n.d.	n.d.	0.01	21.03	99.63	91.40
OM20-31	Listvenite	8.84	0.01	0.54	9.49	0.14	39.10	0.30	n.d.	n.d.	0.01	41.17	99.6	89.09
OM20-32	Serpentinite	38.72	0.03	0.50	8.40	0.09	37.75	0.18	n.d.	0.02	0.01	13.84	99.54	89.90
OM20-33	Gabbro	34.05	0.48	11.91	6.31	0.13	20.15	15.72	0.06	n.d.	0.02	10.79	99.62	86.35
OM20-34	Serp. peridotite	38.58	0.05	0.71	8.89	0.12	38.75	0.85	n.d.	n.d.	0.01	11.58	99.54	89.62
OM20-35	Serp. peridotite	39.19	0.04	1.60	7.87	0.12	37.07	0.47	n.d.	n.d.	0.01	13.33	99.7	90.32
OM20-38	Serpentinite	36.31	n.d.	0.54	7.95	0.06	35.37	3.00	n.d.	n.d.	0.01	16.18	99.42	89.81
OM20-39	Listvenite	1.66	0.03	0.73	8.16	0.12	17.75	28.55	0.03	n.d.	0.01	42.52	99.56	81.17
OM20-42	Gabbro	45.61	0.10	22.70	6.33	0.10	9.28	7.12	3.23	0.13	0.01	5.24	99.85	74.39
OM20-44a	Gabbro	46.34	0.22	26.95	2.81	0.04	5.53	12.66	2.00	0.29	0.02	2.98	99.84	79.59
OM20-44c	Listvenite	58.98	0.02	0.22	4.22	0.07	6.67	11.93	0.00	n.d.	0.01	17.72	99.84	75.80
OM20-45a	Listvenite	18.83	0.03	0.11	6.35	0.07	15.12	23.67	n.d.	n.d.	0.01	35.41	99.6	82.51
OM20-45b	Carb. serpentinite	35.80	0.02	0.19	7.89	0.10	35.88	3.45	n.d.	n.d.	0.01	16.33	99.67	90.01
OM20-45c	Carb. serpentinite	37.80	0.04	1.10	7.99	0.12	36.03	1.98	n.d.	n.d.	0.01	14.61	99.68	89.93
OM20-45d	Listvenite	0.93	n.d.	0.11	13.07	0.41	8.87	36.98	0.02	n.d.	0.01	39.11	99.51	57.35
OM20-46	Serpentinite	47.14	0.13	2.49	5.47	0.09	23.85	14.82	0.05	n.d.	0.01	5.21	99.26	89.63
OM20-48	Gabbro	44.13	0.08	29.37	1.46	0.02	5.50	13.20	1.90	0.47	0.01	3.46	99.6	88.19
OM20-49	Listvenite	27.04	0.03	0.09	3.42	0.10	13.82	22.21	0.01	n.d.	0.01	33	99.73	88.90
OM20-50	Limestone	4.92	0.03	0.31	0.18	0.01	0.37	52.36	0.02	0.08	0.03	41.2	99.51	80.29
OM20-52a	Birbirite	90.95	0.08	1.57	0.94	0.03	0.89	1.92	0.03	0.34	0.04	2.92	99.71	65.23
OM20-52b	Listvenite	26.35	0.01	1.47	7.63	0.16	12.12	21.13	0.01	0.38	0.01	30.51	99.78	75.89
OM20-53a	Serpentinite	39.40	0.04	1.79	7.37	0.10	37.56	0.08	0.09	0.00	0.01	13.06	99.5	90.99
OM20-54	Serpentinite	35.93	0.00	1.04	14.50	0.17	34.97	0.51	n.d.	n.d.	0.01	12.28	99.41	82.69
OM20-56	Serpentinite	41.51	0.15	2.31	10.14	0.16	28.35	8.72	0.04	n.d.	0.01	8.26	99.65	84.71

SI Table 6.1 Bulk major element compositions (in wt%) of Fanja metasomatized peridotites, gabbros and metamorphic sole lithologies. Powdered samples were measured by XRF. Mg# calculated as Mg/(Mg+Fe), all Fe being Fe^{2+}. Abbreviation: n.d.: beyond detection limit

Sample	Lithology	V	Cr	Ni	Zn	Rb	Sr	Y	Zr	Ba	Pb
		ppm	ppm	ppm	ppm	ppm	ppm	ppm	ppm	ppm	ppm
OM20-01	Carb. metabasalt	94	534	342	364	10	99	27	84.9	n.d.	87
OM20-02	Metabasalt	111	327	108	52	15	129	24	85.4	33	13
OM20-03	Amphibolite	45	56	33	64	6	202	32	110	n.d.	22
OM20-04	Serp. peridotite	10	2498	2173	39	5	13	9	3.7	n.d.	11
OM20-05	Carb. serpentinite	n.d.	2590	2061	64	8	12	10	4.6	n.d.	13
OM20-08	Radiolarite	n.d.	8	40	n.d.	16	17	10	9	n.d.	10
OM20-09	Limestone	n.d.	17	n.d.	n.d.	2	600	15	20.6	n.d.	11
OM20-11	Carb. serpentinite	n.d.	700	2629	71	7	46	10	3.7	n.d.	17
OM20-12	Listvenite	n.d.	1503	1041	396	4	510	10	16.1	48	27
OM20-13	Serp. peridotite	5	3161	2254	36	6	1	9	2.3	n.d.	14
OM20-14	Listvenite	n.d.	1674	1878	57	6	117	10	6.2	n.d.	14
OM20-15	Listvenite	7	3774	2105	261	7	86	10	6	n.d.	15
OM20-16	Carb. serpentinite	n.d.	1812	1869	36	6	67	11	4.6	n.d.	10
OM20-17	Carb. serpentinite	n.d.	3765	1566	40	6	137	10	5.2	n.d.	10
OM20-18	Carb. serpentinite	n.d.	3752	1263	32	6	67	12	5	n.d.	10
OM20-20	Gabbro	n.d.	409	333	8	4	336	11	12	n.d.	13
OM20-22	Listvenite	n.d.	3175	1527	121	6	119	10	6.2	n.d.	16
OM20-23	Listvenite	n.d.	737	1079	19	5	136	10	7	191	8
OM20-24	Gabbro	191	185	52	49	2	172	18	11.4	n.d.	8
OM20-25	Listvenite	n.d.	1595	2141	25	6	60	9	4.5	n.d.	8
OM20-26	Carb. serpentinite	10	2610	2205	44	8	272	9	8.4	n.d.	14
OM20-28	Serp. peridotite	8	2415	2237	34	4	13	11	3.8	n.d.	8
OM20-29	Listvenite	n.d.	2005	1878	21	8	77	9	4.9	n.d.	13
OM20-30a	Carb. serpentinite	n.d.	2076	1883	32	6	35	9	4.5	n.d.	8
OM20-30b	Carb. serpentinite	n.d.	2242	1948	39	6	35	9	2.8	n.d.	7
OM20-31	Listvenite	n.d.	3330	2237	44	7	31	8	4	n.d.	11
OM20-32	Serpentinite	n.d.	2670	2377	80	7	9	10	4.5	n.d.	13
OM20-33	Gabbro	116	913	729	24	4	61	19	7.3	n.d.	4
OM20-34	Serp. peridotite	n.d.	2540	2083	42	4	3	12	4.4	n.d.	8
OM20-35	Serp. peridotite	23	2726	2304	45	4	30	12	4.1	n.d.	7
OM20-38	Serpentinite	n.d.	3011	2179	29	8	36	10	3.8	n.d.	9
OM20-39	Listvenite	n.d.	3183	2384	47	6	396	9	13.9	n.d.	13
OM20-42	Gabbro	n.d.	18	324	19	7	455	9	17.3	n.d.	9
OM20-44a	Gabbro	n.d.	493	180	5	10	259	12	17	n.d.	8
OM20-44c	Listvenite	n.d.	1786	797	20	3	178	11	6.9	n.d.	15
OM20-45a	Listvenite	n.d.	2116	1390	22	5	638	7	18.3	n.d.	7
OM20-45b	Carb. serpentinite	n.d.	2738	2513	28	4	65	9	4	n.d.	7
OM20-45c	Carb. serpentinite	n.d.	2319	2065	44	8	29	10	5	n.d.	8
OM20-45d	Listvenite	78	3244	3408	104	7	149	51	6.6	n.d.	22
OM20-46	Serpentinite	61	3684	753	5	5	16	12	4	n.d.	10
OM20-48	Gabbro	n.d.	116	205	n.d.	18	410	7	13.6	70	12
OM20-49	Listvenite	n.d.	519	446	15	2	472	10	15.9	n.d.	41
OM20-50	Limestone	n.d.	n.d.	5	n.d.	6	204	15	11.2	n.d.	10
OM20-52a	Birbirite	n.d.	8	17	n.d.	13	17	18	21.2	n.d.	5
OM20-52b	Listvenite	n.d.	1481	1156	62	24	397	9	13.9	22	23
OM20-53a	Serpentinite	20	2679	2339	48	5	10	11	3.6	n.d.	6
OM20-54	Serpentinite	20	4319	1746	75	7	21	10	4.5	n.d.	10
OM20-56	Serpentinite	63	2653	736	24	5	15	12	4.9	n.d.	5

SI Table 6.2 Bulk minor and trace element compositions (in ppm) of Fanja metasomatized peridotites, gabbros and metamorphic sole lithologies. Powdered samples were measured by XRF. Abbreviation: n.d.: beyond detection limit.

Sample	Lithology	Li	Sc	Ti	V	Mn	Co	Ni	Cu	Zn	Ga	As	Rb	Sr	Y	Zr	Nb	Mo	Cd	Sn	Sb	Cs	Ba
		ppm	ppm	ppm	ppm	ppm	ppm	ppm	ppm	ppm	ppm	ppm	ppm	ppm	ppm	ppm	ppm	ppm	ppm	ppm	ppm	ppm	ppm
OM20-01	Carb. metabasalt	13.4	25.3	6504	145	840	31.2	340	13.9	354	15.3	45.5	6.10	95.3	13.4	93.0	12.8	0.58	n.d.	0.83	9.49	0.50	81.7
OM20-02	Metabasalt	14.4	31.4	7632	191	1002	44.8	124	88.4	70.9	16.2	1.00	10.6	142	14.4	104	14.0	0.33	n.d.	1.01	0.11	0.76	136
OM20-03	Amphibolite	26.1	25.8	8113	204	1690	35.0	72	1.96	91.7	16.3	0.91	0.86	243	26.1	24.5	14.1	0.20	n.d.	1.89	0.20	0.05	34.1
OM20-04	Serp. peridotite	2.09	9.51	143	48.1	740	93.3	1806	21.4	39.7	1.21	0.20	0.17	10.8	0.80	0.05	0.01	0.05	0.01	0.03	0.01	0.25	1.74
OM20-05	Carb. serpentinite	5.84	3.48	14.2	15.1	571	83.7	1730	5.56	33.9	0.19	22.6	0.32	6.53	0.05	0.04	0.01	0.13	0.01	n.d.	0.89	0.22	12.6
OM20-08	Radiolarite	0.88	0.94	143	7.16	73.1	1.26	5.58	2.29	7.81	1.25	0.66	9.01	14.3	0.88	5.39	0.53	0.04	n.d.	0.13	0.07	0.32	21.9
OM20-09	Limestone	6.49	0.55	76.4	3.34	46.9	0.24	0.96	0.73	3.82	0.38	0.17	1.23	657	6.49	2.73	0.30	0.10	n.d.	0.04	n.d.	0.04	14.5
OM20-11	Carb. serpentinite	8.28	2.17	10.0	4.65	566	185	2456	351	73.0	0.19	262	0.24	45.1	0.06	0.05	0.01	0.15	0.16	n.d.	2.00	0.16	43.0
OM20-12	Listvenite	1.41	5.21	29.8	28.7	1099	75.9	1156	71.8	387	2.70	90.1	1.53	483	1.41	0.11	0.01	0.25	n.d.	n.d.	12.6	0.69	139
OM20-13	Serp. peridotite	4.24	7.72	49.5	35.4	692	89.7	1803	7.41	35.8	0.70	0.03	0.63	0.27	0.17	0.02	0.002	0.01	n.d.	n.d.	n.d.	2.31	0.24
OM20-14	Listvenite	10.0	3.42	20.0	14.9	576	83.5	1830	1.88	55.8	0.28	6.38	0.24	114	0.08	0.09	0.01	0.02	0.02	n.d.	0.34	0.15	6.99
OM20-14	Listvenite	8.28	2.91	16.8	12.9	447	70.5	1459	4.10	51.4	0.26	5.68	0.22	95.2	0.07	0.02	0.01	0.01	0.05	0.62	0.35	0.13	6.69
OM20-15	Listvenite	31.1	7.58	77.2	35.0	715	105	1975	0.62	217	0.69	4.97	0.76	78.9	0.52	0.08	0.01	0.01	0.06	n.d.	2.48	0.42	22.0
OM20-16	Carb. serpentinite	0.10	5.20	32.5	18.9	821	85.3	1801	97.3	42.1	0.35	12.3	0.13	64.3	0.10	0.16	0.02	0.08	n.d.	n.d.	0.00	0.06	5.92
OM20-17	Carb. serpentinite	1.48	5.45	108	34.8	597	104	1532	27.8	47.6	1.26	148	0.01	129	0.25	0.16	0.002	0.03	0.005	n.d.	0.11	0.003	27.4
OM20-18	Carb. serpentinite	11.2	9.60	191	44.2	900	113	1339	153	41.7	1.97	81.7	0.10	72.1	0.51	0.40	0.02	0.02	0.34	0.02	0.03	0.02	19.6
OM20-20	Gabbro	0.50	7.71	186	21.4	470	51.8	383	85.3	21.7	10.7	1.54	0.19	327	0.50	0.50	0.01	0.01	n.d.	n.d.	0.01	0.56	7.21
OM20-22	Listvenite	0.17	6.21	31.0	20.6	788	90.3	1512	15.4	115	0.43	83.3	0.36	111	0.17	0.02	0.01	0.07	n.d.	n.d.	1.64	0.20	48.2
OM20-23	Listvenite	0.02	1.78	12.5	6.15	1824	82.8	1075	1.22	30.1	0.08	22.1	0.17	127	0.02	0.02	0.003	0.08	n.d.	0.04	0.28	0.10	226
OM20-24	Gabbro	7.63	60.0	4519	310	1241	35.5	27.7	39.9	46.7	16.2	0.64	0.04	184	7.63	3.90	0.03	0.01	n.d.	0.09	n.d.	0.02	3.15
OM20-25	Listvenite	31.7	3.27	3.74	4.82	462	95.1	1887	1.91	26.8	0.08	2.90	0.28	52.6	0.02	0.01	0.02	0.03	0.05	n.d.	0.05	0.14	11.2
OM20-26	Carb. serpentinite	14.6	8.99	42.7	41.4	907	118	2161	14.9	46.2	0.71	4.43	0.08	257	0.17	0.03	0.01	0.16	n.d.	n.d.	n.d.	0.02	26.0
OM20-28	Serp. peridotite	3.22	12.8	130	59.8	914	106	2170	12.5	44.7	1.40	0.08	0.14	10.7	0.79	0.03	0.01	0.05	0.02	n.d.	0.003	0.19	1.08
OM20-29	Listvenite	37.6	2.80	4.66	6.91	535	92.3	1798	1.98	23.2	0.16	0.68	0.41	78.6	0.01	0.01	0.02	0.03	0.02	n.d.	0.01	0.36	9.01
OM20-30a	Carb. serpentinite	25.2	7.14	63.7	28.9	568	94.1	1889	9.43	37.9	0.58	3.15	0.07	32.2	0.11	n.d.	0.002	0.05	0.02	n.d.	n.d.	0.11	2.83
OM20-30b	Carb. serpentinite	22.7	6.44	57.1	26.5	627	94.7	1857	10.8	37.2	0.55	2.56	0.07	32.6	0.08	n.d.	n.d.	0.04	0.03	n.d.	n.d.	0.10	2.74
OM20-31	Listvenite	17.4	6.73	56.5	26.7	903	115	2009	15.1	45.6	0.54	17.7	0.30	26.9	0.09	0.01	0.002	0.08	0.03	n.d.	0.01	0.43	12.4
OM20-32	Serpentinite	1.73	9.85	30.4	50.4	762	122	2582	16.6	55.2	0.64	0.10	0.05	3.74	0.03	0.01	0.003	0.30	0.01	n.d.	n.d.	0.01	0.68
OM20-33	Gabbro	7.35	52.4	2790	211	1065	65.6	846	155	38.1	5.93	0.13	0.06	57.5	7.35	2.39	0.01	0.05	n.d.	0.14	n.d.	0.01	1.99
OM20-34	Serp. peridotite	0.18	10.2	60.7	38.0	887	103	2084	24.7	45.5	0.84	0.03	0.04	2.36	0.18	0.19	0.004	0.02	n.d.	n.d.	0.002	0.05	0.19
OM20-35	Serp. peridotite	7.33	12.9	138	62.0	846	103	2192	15.2	47.6	1.35	4.45	0.21	28.3	0.64	0.01	0.003	0.47	0.03	n.d.	0.01	0.13	4.15
OM20-38	Serpentinite	2.78	8.35	31.6	34.0	432	96.7	2006	14.0	40.8	0.55	5.69	0.09	32.7	0.07	n.d.	0.001	0.06	0.01	n.d.	0.01	0.09	2.69
OM20-39	Listvenite	1.12	9.84	42.7	34.9	870	97.8	2279	15.9	45.5	0.47	46.9	0.14	373	0.26	0.13	0.01	0.46	0.03	n.d.	0.42	0.29	22.8
OM20-42	Gabbro	1.20	4.49	532	16.9	835	54.8	384	72.4	38.7	12.0	1.12	2.03	481	1.20	3.23	0.12	0.03	n.d.	0.04	0.01	1.35	33.7
OM20-44a	Gabbro	3.61	15.8	1429	76.0	453	21.0	246	127	26.2	19.3	1.11	6.80	298	3.61	9.98	0.54	0.07	n.d.	0.12	0.01	3.28	38.8
OM20-44c	Listvenite	10.9	2.02	11.6	8.85	487	46.8	608	7.26	24.3	0.50	10.9	0.12	147	0.34	0.02	0.04	0.17	0.08	n.d.	2.48	0.05	13.7
OM20-45a	Listvenite	8.14	2.83	10.5	7.87	475	68.8	1251	5.12	18.3	0.22	1.01	0.24	532	0.03	0.01	0.01	0.04	0.01	n.d.	2.69	0.19	20.1
OM20-45b	Carb. serpentinite	1.19	3.54	18.0	11.5	653	95.6	2072	1.98	27.9	0.28	2.51	0.04	56.2	0.03	0.04	0.02	0.15	n.d.	0.04	0.05	0.01	16.9
OM20-45c	Carb. serpentinite	3.91	8.02	117	37.1	778	77.1	1682	12.2	45.4	0.69	10.7	0.10	23.3	0.80	0.36	0.06	0.30	0.02	0.03	0.39	0.11	21.3
OM20-45d	Listvenite	0.51	56.9	13.9	151	3015	203	3356	4.81	93.9	0.55	7.97	0.02	156	45.6	0.15	0.10	1.32	0.45	0.03	3.01	0.01	31.0
OM20-46	Serpentinite	1.45	48.9	522	121	598	61.1	691	306	20.1	1.99	0.07	0.03	15.6	2.43	0.93	0.003	0.02	0.03	0.06	0.01	0.01	7.7
OM20-48	Gabbro	0.30	1.26	154	5.20	182	18.2	236	27.6	9.22	13.9	1.02	12.8	403	0.30	0.26	0.005	0.02	n.d.	n.d.	0.02	26.3	158
OM20-49	Listvenite	3.28	1.07	5.37	10.0	668	24.6	391	0.81	19.4	0.16	88.5	0.09	396	1.19	0.09	0.02	0.07	0.10	0.03	2.83	0.03	16.5
OM20-50	Limestone	5.63	0.80	144	7.82	152	0.54	2.48	3.34	6.48	0.67	0.87	3.25	262	5.63	5.20	0.83	0.13	n.d.	0.11	0.13	0.05	14.6
OM20-52a	Birbirite	9.19	2.02	341	8.19	204	2.15	7.50	1.07	3.95	1.75	271	8.54	13.7	6.45	3.33	1.58	0.26	n.d.	0.36	2.74	0.31	18.3
OM20-52b	Listvenite	13.0	8.09	242	42.9	1295	49.4	1259	2.17	68.5	1.37	1130	18.4	440	1.44	0.32	0.01	2.30	0.01	n.d.	39.0	1.84	128
OM20-52b	Listvenite	14.0	7.50	224	39.4	1120	45.1	1015	1.78	64.8	1.23	947	16.5	353	1.29	0.23	0.01	1.69	0.04	n.d.	26.8	1.56	94.4
OM20-53a	Serpentinite	6.99	10.5	147	52.8	611	87.4	1871	9.41	40.8	1.24	4.73	0.17	6.38	0.67	0.03	0.01	0.34	n.d.	n.d.	0.01	0.07	2.43
OM20-54	Serpentinite	0.67	5.46	134	46.3	1064	130	1553	95.3	73.6	1.90	0.19	0.01	17.4	0.16	0.07	0.005	0.19	0.01	0.02	0.01	0.001	1.99
OM20-56	Serpentinite	1.12	35.0	678	109	1044	87.2	645	115	28.9	2.00	0.14	0.08	12.8	2.83	0.98	0.01	0.05	0.05	0.06	0.01	0.01	4.81

SI Table 6.3 Bulk trace elements compositions of Fanja metasomatized peridotites, gabbros and metamorphic sole lithologies. Samples in solution were measured by ICP-QMS. Abbreviation: n.d.: not determined.

Sample	Lithology	La ppm	Ce ppm	Pr ppm	Nd ppm	Sm ppm	Eu ppm	Gd ppm	Tb ppm	Dy ppm	Ho ppm	Er ppm	Tm ppm	Yb ppm	Lu ppm	Hf ppm	Ta ppm	Tl ppm	Pb ppm	Th ppm	U ppm
OM20-01	Carb. metabasalt	11.4	23.9	3.05	12.7	2.77	0.99	2.89	0.44	2.67	0.52	1.42	0.20	1.17	0.17	2.60	0.77	0.07	74.7	1.17	0.38
OM20-02	Metabasalt	9.95	22.8	2.91	12.5	2.89	1.05	3.01	0.47	2.82	0.55	1.51	0.21	1.26	0.18	2.74	0.83	0.07	0.89	1.03	0.43
OM20-03	Amphibolite	20.6	43.0	5.35	21.9	4.91	1.34	4.99	0.80	4.87	0.96	2.68	0.38	2.34	0.35	0.88	0.81	0.01	10.00	5.62	1.07
OM20-04	Serp. peridotite	0.01	0.03	0.002	0.02	0.02	0.01	0.07	0.01	0.13	0.03	0.10	0.02	0.13	0.02	0.01	0.001	0.004	0.06	0.002	0.003
OM20-05	Carb. serpentinite	0.01	0.02	0.003	0.01	0.003	0.001	0.004	0.001	0.01	0.002	0.01	0.001	0.01	0.002	0.001	0.001	0.01	0.94	0.003	0.01
OM20-08	Radiolarite	0.82	2.32	0.21	0.89	0.19	0.04	0.15	0.03	0.15	0.03	0.10	0.01	0.10	0.01	0.13	0.02	0.09	0.80	0.47	0.10
OM20-09	Limestone	4.02	2.72	0.53	2.18	0.39	0.10	0.51	0.07	0.48	0.11	0.33	0.04	0.25	0.04	0.06	0.02	0.01	0.28	0.15	0.37
OM20-11	Carb. serpentinite	0.01	0.02	0.002	0.01	0.004	0.002	0.01	0.001	0.01	0.002	0.01	0.001	0.01	0.002	0.001	0.001	0.04	5.98	0.004	0.01
OM20-12	Listvenite	0.08	0.19	0.03	0.17	0.08	0.04	0.19	0.04	0.25	0.05	0.14	0.02	0.12	0.02	0.004	0.001	0.05	21.4	0.005	0.14
OM20-13	Serp. peridotite	0.003	0.01	0.0004	0.002	0.001	0.001	0.01	0.002	0.02	0.01	0.02	0.01	0.05	0.01	0.001	0.0001	n.d.	0.03	0.001	0.001
OM20-14	Listvenite	0.01	0.03	0.003	0.01	0.005	0.002	0.01	0.001	0.01	0.002	0.01	0.001	0.01	0.002	0.002	0.001	n.d.	8.47	0.004	0.001
OM20-14	Listvenite	0.01	0.02	0.003	0.01	0.005	0.001	0.01	0.001	0.01	0.002	0.01	0.001	0.01	0.002	0.001	0.0004	0.003	7.78	0.003	0.001
OM20-15	Listvenite	0.01	0.02	0.005	0.04	0.02	0.01	0.06	0.01	0.07	0.01	0.04	0.01	0.04	0.01	0.005	0.0005	0.01	6.53	0.002	0.001
OM20-16	Carb. serpentinite	0.03	0.07	0.01	0.04	0.01	0.003	0.01	0.002	0.02	0.004	0.02	0.003	0.02	0.004	0.01	0.001	0.005	4.75	0.01	0.01
OM20-17	Carb. serpentinite	0.004	0.01	0.003	0.02	0.01	0.01	0.03	0.01	0.04	0.01	0.03	0.004	0.04	0.01	0.01	0.0001	0.07	n.d.	0.0004	0.001
OM20-18	Carb. serpentinite	0.04	0.10	0.02	0.09	0.04	0.03	0.06	0.01	0.09	0.02	0.06	0.01	0.06	0.01	0.02	0.001	0.12	0.10	0.01	0.01
OM20-20	Gabbro	0.07	0.18	0.03	0.16	0.06	0.09	0.08	0.01	0.10	0.02	0.05	0.01	0.05	0.01	0.02	0.001	0.02	0.08	0.002	0.003
OM20-22	Listvenite	0.01	0.02	0.004	0.02	0.01	0.01	0.02	0.004	0.03	0.01	0.02	0.004	0.03	0.01	0.001	0.001	0.01	7.16	0.003	0.03
OM20-23	Listvenite	0.01	0.02	0.002	0.01	0.003	0.003	0.005	0.0004	0.003	0.001	0.00	0.001	0.01	0.001	0.001	0.0002	0.005	1.45	0.004	0.01
OM20-24	Gabbro	0.22	0.81	0.18	1.26	0.66	0.44	1.13	0.21	1.48	0.32	0.90	0.13	0.75	0.11	0.21	0.003	0.004	0.07	0.003	0.002
OM20-25	Listvenite	0.01	0.02	0.002	0.01	0.002	0.0002	0.002	0.0002	0.002	0.001	0.002	0.001	0.00	0.001	n.d.	0.001	0.02	0.56	0.003	0.03
OM20-26	Carb. serpentinite	0.01	0.02	0.002	0.01	0.003	0.001	0.01	0.002	0.02	0.01	0.03	0.01	0.05	0.01	0.001	0.0003	0.11	0.05	0.003	0.31
OM20-28	Serp. peridotite	0.01	0.02	0.002	0.01	0.01	0.01	0.04	0.01	0.11	0.03	0.10	0.02	0.14	0.02	0.01	0.0005	0.003	0.03	0.005	0.003
OM20-29	Listvenite	0.01	0.02	0.003	0.01	0.002	0.0004	0.002	0.0002	0.002	0.0005	0.002	0.0003	0.01	0.001	0.001	0.002	0.03	0.38	0.003	0.06
OM20-30a	Carb. serpentinite	n.d.	n.d.	n.d.	n.d.	0.001	0.0003	0.004	0.001	0.01	0.004	0.01	0.003	0.03	0.01	0.0004	0.0001	0.04	n.d.	0.0001	0.003
OM20-30b	Carb. serpentinite	0.001	0.001	0.0002	0.001	0.001	0.0002	0.002	0.001	0.01	0.003	0.01	0.003	0.03	0.01	n.d.	0.0001	0.05	n.d.	0.0002	0.0003
OM20-31	Listvenite	0.002	0.003	0.0004	0.001	0.0003	0.0005	0.002	0.001	0.01	0.003	0.01	0.003	0.03	0.01	0.001	0.0001	0.08	0.45	0.001	0.08
OM20-32	Serpentinite	0.003	0.01	0.001	0.003	0.001	n.d.	0.001	0.0002	0.003	0.001	0.004	0.001	0.02	0.004	n.d.	0.0001	0.08	n.d.	0.0004	0.001
OM20-33	Gabbro	0.05	0.39	0.14	1.25	0.75	0.41	1.24	0.23	1.56	0.32	0.88	0.12	0.69	0.10	0.26	0.001	0.002	0.07	0.001	0.005
OM20-34	Serp. peridotite	0.01	0.02	0.004	0.03	0.01	0.01	0.02	0.004	0.03	0.01	0.03	0.005	0.04	0.01	0.01	0.0003	n.d.	0.03	0.001	0.001
OM20-35	Serp. peridotite	0.004	0.01	0.0005	0.004	0.007	0.004	0.03	0.01	0.09	0.03	0.08	0.01	0.12	0.02	0.004	0.0002	0.01	0.02	0.001	0.01
OM20-38	Serpentinite	0.001	0.001	n.d.	0.001	0.0002	0.0002	0.001	0.0005	0.01	0.003	0.01	0.002	0.03	0.01	n.d.	n.d.	0.02	n.d.	0.0001	0.43
OM20-39	Listvenite	0.01	0.01	0.003	0.01	0.005	0.002	0.01	0.002	0.02	0.01	0.03	0.004	0.04	0.01	0.001	0.0004	0.09	0.39	0.002	0.43
OM20-42	Gabbro	0.26	0.67	0.10	0.53	0.15	0.25	0.20	0.03	0.21	0.04	0.13	0.02	0.12	0.02	0.09	0.01	0.02	0.12	0.01	0.01
OM20-44a	Gabbro	0.66	1.58	0.24	1.22	0.40	0.35	0.57	0.10	0.64	0.14	0.38	0.06	0.35	0.05	0.28	0.03	0.05	0.20	0.02	0.01
OM20-44c	Listvenite	0.05	0.05	0.01	0.04	0.01	0.01	0.02	0.004	0.03	0.01	0.02	0.003	0.02	0.004	0.001	0.003	0.01	4.73	0.003	0.18
OM20-45a	Listvenite	0.01	0.01	0.002	0.005	0.002	0.001	0.002	0.0003	0.002	0.001	0.003	0.0005	0.01	0.001	0.0004	0.0005	0.02	0.22	0.002	0.01
OM20-45b	Carb. serpentinite	0.02	0.03	0.003	0.01	0.002	0.001	0.003	0.001	0.005	0.001	0.004	0.001	0.01	0.002	0.001	0.001	0.33	0.28	0.004	0.02
OM20-45c	Carb. serpentinite	0.07	0.17	0.02	0.11	0.04	0.01	0.08	0.02	0.13	0.03	0.10	0.02	0.12	0.02	0.02	0.004	0.06	0.16	0.01	0.04
OM20-45d	Listvenite	2.96	7.62	1.17	6.00	2.77	1.09	5.13	1.09	7.78	1.70	4.68	0.69	4.77	0.70	0.005	0.003	0.02	8.20	0.10	0.22
OM20-46	Serpentinite	0.02	0.11	0.03	0.25	0.17	0.08	0.33	0.07	0.48	0.10	0.28	0.04	0.25	0.04	0.07	0.0002	0.05	0.11	0.001	0.001
OM20-48	Gabbro	0.11	0.29	0.05	0.23	0.06	0.16	0.07	0.01	0.06	0.01	0.03	0.004	0.02	0.004	0.01	0.001	0.16	0.08	0.002	0.004
OM20-49	Listvenite	0.21	0.37	0.05	0.25	0.08	0.03	0.13	0.02	0.13	0.03	0.06	0.01	0.05	0.01	0.002	0.001	0.01	28.9	0.01	0.15
OM20-50	Limestone	4.84	3.30	0.89	3.64	0.67	0.16	0.70	0.10	0.60	0.13	0.35	0.05	0.29	0.04	0.13	0.05	0.02	0.83	0.26	0.52
OM20-52a	Birbirite	7.87	16.9	1.93	7.49	1.49	0.35	1.37	0.18	1.02	0.20	0.53	0.08	0.54	0.09	0.09	0.09	0.04	0.73	1.12	0.31
OM20-52b	Listvenite	0.05	0.06	0.01	0.07	0.06	0.01	0.13	0.03	0.23	0.06	0.17	0.03	0.18	0.03	0.03	0.0004	0.92	19.4	0.001	1.37
OM20-52b	Listvenite	0.04	0.06	0.01	0.07	0.05	0.01	0.11	0.03	0.20	0.05	0.13	0.02	0.15	0.02	0.03	0.0004	0.74	16.1	0.002	1.10
OM20-53a	Serpentinite	0.002	0.003	0.001	0.01	0.01	0.00	0.04	0.01	0.10	0.03	0.09	0.02	0.12	0.02	0.01	0.0002	0.01	0.06	0.001	0.004
OM20-54	Serpentinite	0.05	0.18	0.04	0.32	0.19	0.10	0.38	0.07	0.55	0.12	0.33	0.05	0.31	0.05	0.07	0.001	0.00	0.16	0.01	0.02
OM20-56	Serpentinite	11.4	23.9	3.05	12.7	2.77	0.99	2.89	0.44	2.67	0.52	1.42	0.20	1.17	0.17	2.60	0.77	0.07	74.7	1.17	0.38

SI Table 6.3 (continued)